PB96-168646

Proceedings of the Twentieth Annual Climate Diagnostics Workshop

Seattle, Washington **October 23-27, 1995**

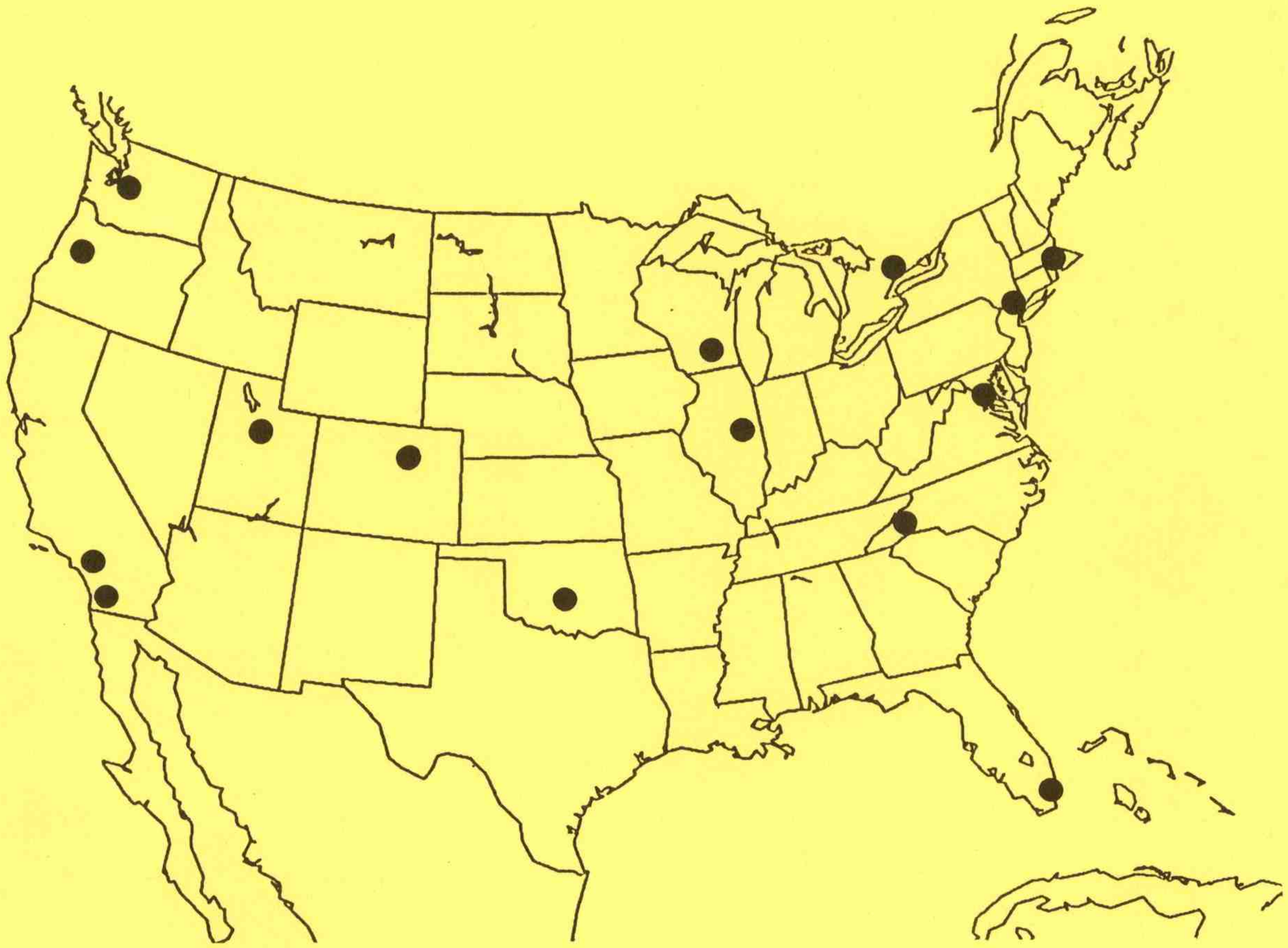

U.S. DEPARTMENT OF COMMERCE
National Oceanic and Atmospheric Administration
National Weather Service
Climate Prediction Center / NCEP

NOAA MIAMI BRANCH LIBRARY
3 9282 1000 0922 3

Publications listed below are available in both hard copy and microfiche form from the National Technical Information Service, U.S. Department of Commerce, Sills Building, 5285 Port Royal Road, Springfield, VA 22161. (Prices on request; order by accession number.)

If an author wishes to reference an article from any of the Proceedings, please include the appropriate accession number at the end of the reference. This will allow journals to accept these references more readily.

PROCEEDINGS	ACCESSION NO
First Climate Diagnostics Workshop	PB264993
Second Climate Diagnostics Workshop	PB282151
Third Climate Diagnostics Workshop	PB298355
Fourth Climate Diagnostics Workshop	PB80-201130
Fifth Climate Diagnostics Workshop	PB81-222200
Sixth Climate Diagnostics Workshop	PB82-219486
Seventh Climate Diagnostics Workshop	PB83-208033
Eighth Climate Diagnostics Workshop	PB84-192418
Ninth Climate Diagnostics Workshop	PB85-183911
Tenth Climate Diagnostics Workshop	*
Eleventh Climate Diagnostics Workshop	PB87-175741
Twelfth Climate Diagnostics Workshop	PB88-191747
Thirteenth Climate Diagnostics Workshop	PB89-178115
Fourteenth Climate Diagnostics Workshop	PB90-198573
Fifteenth Climate Diagnostics Workshop	PB91-171082
Sixteenth Climate Diagnostics Workshop	PB92-167378
Seventeenth Climate Diagnostics Workshop	PB93-183895
Eighteenth Climate Diagnostics Workshop	PB94-177078
Nineteenth Climate Diagnostics Workshop	PB95-225546

Cover Figure: Map depicting the locations of all twenty Climate Diagnostics Workshops.

1976 Washington, D.C.
1977 La Jolla, CA
1978 Miami, FL
1979 Madison, WI
1980 Seattle. WA
1981 Palisades, NY
1982 Boulder, CO
1983 Downsview,Ontario
1984 Corvallis, OR
1985 College Park, MD
1986 Champaign, IL
1987 Salt Lake City, UT
1988 Cambridge, MA
1989 La Jolla, CA
1990 Asheville, NC
1991 Los Angeles, CA
1992 Norman, OK
1993 Boulder, CO
1994 College Park, MD
1995 Seattle, WA

* Reference is WMO/Long-Range Forecasting Research Report Series No. 6, Volume I and II, WMO/TD-No. 87, January 1986.

QC
980
C 3
1995

Proceedings of the Twentieth Annual Climate Diagnostics Workshop

Property of
NOAA Miami Library / AOML
4301 Rickenbacker Causeway
Miami, Florida 33149

Held at the NOAA Pacific Marine Enviornmental Laboratory in Seattle, Washington

Co- sponsored by:

NOAA / Climate Prediction Center and the Joint Institute for the Study of Atmosphere and Ocean / University of Washington

016678

U.S. DEPARTMENT OF COMMERCE
Ronald H. Brown, Secretary

National Oceanic and Atmospheric Administration
Dr. D. James Baker, Under Secretary

National Weather Service
Elbert W. Friday, Jr., Assistant Administrator

PREFACE

The Twentieth Annual Climate Diagnostics Workshop was held in Seattle, Washington at the University of Washington and the NOAA Pacific Marine Environmental Laboratory (PMEL). The meeting was hosted by the Joint Institute for the Study of the Atmosphere and Oceans (JISAO; Department of Meteorology, University of Washington) and was jointly planned and organized by Professor J. M. Wallace and his staff, and John Janowiak of the Climate Prediction Center of NCEP. In particular, I would like to thank Ingrid Quertermous for administrative support. The conference facilities at PMEL and the use of the campus faculty club for poster sessions and dinner made our intense week very comfortable and enjoyable.

Much of the success of the Workshop is attributable to the speakers and to the ninety-four poster presenters. We also appreciate the help of the Session Chairpersons: Mike Wallace, Ed Sarachik, Chet Ropelewski, Todd Mitchell, Gene Rasmusson, Gerry Bell, Tom Smith, Harry van Loon, Art Douglas, Clara Deser, Phil Arkin, Kingtse Mo, Muthu Chelliah, M. Kanamitsu, Bob Livezey, and Huug van den Dool.

Now, I would like to add a personal note. I have had the pleasure of co-hosting the Workshops during the past ten years and participating in the growth and excitement of a new understanding of global climate anomalies. Starting in the late 1980s with a focus on the El Niño/Southern Oscillation, the Workshops have documented the progress from observations and diagnostics, to prediction and applications. The "CAC" has changed its name along with a new method for presenting climate outlooks in the U.S. Results from the great observational programs of TOGA and TOGA-COARE, GEWEX, and PACS as well as from smaller observational studies have been presented at the Workshop. Now extending from the upper ocean to the land surface, the lower atmosphere and up into the stratosphere, climate diagnostics have been the foundation studies for new understanding leading to improved monitoring, new research directions, and ultimately to some form of predictive capacity. In the years ahead we can expect to see more practical applications of this knowledge of the climate system put into service for social and economic benefit in many different regions of the globe. Altogether, the data analysis and derived benefits of these Workshops define an emerging field of climate services which join the interests of both the university research community and several NOAA centers and offices.

It has been a pleasure.

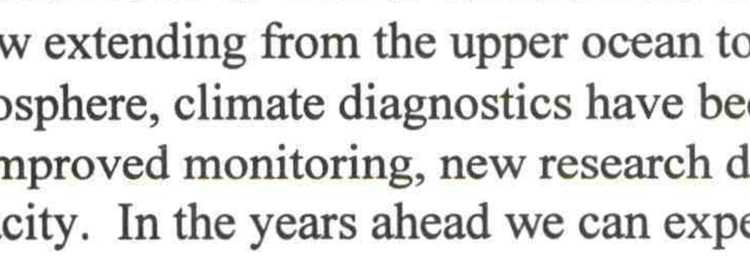

David Rodenhuis
Director (1985-1995)
Climate Prediction Center
National Centers for Environmental Prediction (NCEP)

TABLE OF CONTENTS

TWENTIETH ANNUAL CLIMATE DIAGNOSTICS WORKSHOP

Page

iii **PREFACE**

xiv **ATTENDEES**

xx **AUTHOR INDEX**

SESSION 1: RECENT CLIMATE ANOMALIES
Chairperson: D.R. Rodenhuis

1 THE EVOLUTION OF RECENT OCEANIC AND ATMOSPHERIC ANOMALIES IN THE GLOBAL TROPICS. *V.E. Kousky and C.F. Ropelewski*

5 RECENT WARMTH IN 1994/95 AND THE ROLE OF THE CIRCULATION IN THE DIVERGENCE BETWEEN SURFACE AND MSU2R TEMPERATURES SINCE THE MID 1980s. *P.D. Jones and P.M. Kelly*

* OBSERVED GLOBAL TRENDS IN MAXIMUM AND MINIMUM TEMPERATURE WITH URBAN WARMING REMOVED. *T.C. Peterson, D.R. Easterling, and T.R. Karl*

* DYNAMICAL CONTRIBUTION TO HEMISPHERIC TEMPERATURE TRENDS. *J.M. Wallace, Y. Zhang and J.A. Renwick*

SESSION 2: TROPICAL-EXTRATROPICAL INTERACTIONS
Chairperson: M. Wallace

9 DIAGNOSING THE MIDLATITUDE ATMOSPHERIC RESPONSE TO ENSO. *G.D. Bell and V.E. Kousky*

13 PHYSICAL MECHANISMS FOR THE 1995 CALIFORNIA FLOODS. *M. Masutani and K.C. Mo*

* SHORT-TERM CLIMATE EXTREMES IN PRECIPITATION OVER THE CONTINENTAL U.S. AND ENSO. *R.M. Dole, K.I. Paine and K. Wolter*

17 ENSO CYCLE MODULATION OF TRANSIENT BEHAVIOR OVER THE PACIFIC-NORTH AMERICAN SECTOR. *Z. Dai and E.M. Rasmusson*

* RELATIONSHIPS BETWEEN TROPICAL SEA SURFACE TEMPERATURE ANOMALIES AND NORTHERN HEMISPHERIC CIRCULATION PATTERNS. *M.B. Richman*

*Manuscript not available

Page

21 PERSISTENT NORTH PACIFIC CIRCULATION ANOMALIES AND INTERHEMISPHERIC TELECONNECTIONS. *R.W. Higgins, S.D. Schubert and K.C. Mo*

* EL NIÑO, LA NIÑA AND THE NONLINEARITY OF TELECONNECTIONS. *M.P. Hoerling and A. Kumar*

SESSION 2: TROPICAL-EXTRATROPICAL INTERACTIONS (Continued)
Chairperson: E. Sarachik

25 TROPICAL-EXTRATROPICAL INTERACTION AS REVEALED BY ANALYSIS OF COMBINED OCEAN-ATMOSPHERE VARIABILITY DURING 1985-1994. *Y. Dai and S. Nigam*

29 HADLEY CIRCULATION AS A MODULATOR OF THE WINTER EXTRATROPICAL CLIMATE. *A.Y. Hou*

32 THE SIGNATURE OF ENSO IN THE MIDLATITUDE HIGH-FREQUENCY VARIABILITY. *W. May and L. Bengtsson*

36 EXTRATROPICAL EDDY-MEAN FLOW INTERACTIONS INDUCED BY ZONALLY SYMMETRICAL HEAT AND MOMENTUM SOURCES IN THE TROPICS. *E.K.M. Chang*

40 RAPID DEVELOPMENT OF UPPER-LEVEL ANTICYCLONES DURING THE 1988 U.S. DROUGHT. *P. Chen and M. Newman*

* WINTERTIME ATMOSPHERIC VARIABILITY INDUCED BY ZONAL FLOW AND TROPICAL SST ANOMALIES. *M. Ting, M. Hoerling ,T. Xu, AND A. Kumar*

POSTER SESSION: 1
Coordinator: S. Chen

42 ON THE ANNUAL CYCLE OF TROPOSPHERIC WINDS OBSERVED ABOVE CHRISTMAS ISLAND IN THE CENTRAL EQUATORIAL PACIFIC. *K.S. Gage, J.R. McAfee and C.R. Williams*

46 GAUGE-BASED ANALYSES OF PRECIPITATION DURING 1971-1994. *P. Xie and P.A. Arkin*

50 THE DIURNAL CYCLE OF PRECIPITATION OVER THE U.S. AS DETERMINED FROM A COMPREHENSIVE HOURLY RAINGAUGE DATASET. *J. Janowiak and W. Higgins*

53 SEASONAL CHARACTERISTICS OF PRECIPITATION OVER THE UNITED STATES IN AMIP SIMULATIONS. *J.S. Boyle*

*Manuscript not available

Page

57 SST REGULATION IN THE INDIAN OCEAN: A COUNTERPOINT TO THE PACIFIC WARM POOL. *J.P. Loschnigg and P.J. Webster*

61 MONSOON RAINFALL IN THE GEOS-1 ASSIMILATION: SENSITIVITY TO INPUT DATA. *C-K. Park, S.D. Schubert, D.J. Lamich and Y. Kondratyeva*

65 SYSTEMATIC ERRORS IN PHASE SPEED OF TRANSIENTS AND THEIR INTERACTION WITH THE MEAN STATE. *J. Qin and H.M. van den Dool*

69 A NEW GLOBAL SEA-ICE AND SEA SURFACE TEMPERATURE DATA SET. *N.A. Rayner and D.E. Parker*

73 VERTICAL AND HORIZONTAL RESOLUTION COMPARISONS OF CPTEC/COLA GCM. *I.F.A. Cavalcanti, P. Nobre, M.L. Abreu, M. Quadro and L.P. Pezzi*

77 RELATIONSHIP BETWEEN SST ANOMALY PATTERNS AND ATMOSPHERIC FLOW PATTERNS IN THE NORTHERN HEMISPHERE. *H. Feddersen and E. Kaas*

81 WINTERTIME CIRCULATION REGIMES IN THE WESTERN HALF OF THE NORTHERN HEMISPHERE EXTRATROPICS, DEFINED BY H500 DATA IN "KEY REGIONS", AND CLIMATOLOGICAL APPLICATIONS. *M.Yu. Bardin*

85 ASYMMETRIC IMPACT OF TROPICAL SST ANOMALIES ON THE ATMOSPHERIC INTERNAL VARIABILITY OVER THE NORTH PACIFIC. *W.Y. Chen and H.M. van den Dool*

89 PREDICTION OF TROPICAL PACIFIC SST WITH THE NCEP CCA MODEL. *A.G. Barnston and Y. He*

93 THE RELATIONSHIP BETWEEN TROPICAL WESTERN PACIFIC WESTERLY ANOMALIES AND EAST ASIAN PRESSURE SURGES. *G.P. Compo, B.E. Mapes, G.N. Kiladis and P.J. Webster*

97 ON THE RELATIONSHIP BETWEEN SEA SURFACE TEMPERATURE, PRESSURE AND ZONAL WINDS IN THE EQUATORIAL PACIFIC. *M.J. McPhaden, W. Wang and C. Zhang*

101 CLIMATOLOGICAL VARIATIONS OF ATLANTIC SEA LEVEL PRESSURES. *J. Knaff*

105 EFFECTS OF VARIOUS PROCESSING METHODS APPLIED TO SHIP-BASED SURFACE WINDS DURING TOGA COARE. *L.M. Hartten*

109 ON THE GEOGRAPHICAL DISTRIBUTION OF FORECAST SKILL IN 500 HPA HEIGHT IN THE 6-10 DAY RANGE FOR NH WINTER. *J. Pan and H.M. van den Dool*

*Manuscript not available

Page

113 TROPICAL CYCLONE ACTIVITY AS A DIAGNOSTIC CLIMATE INDICATOR. *J.D. Sheaffer*

117 TEMPORAL AND SPATIAL VARIABILITY OF THE CANADIAN POLAR TROUGH. *J. Knox, A. Shabbar, W. Skinner, and K. Higuchi*

121 REVISED ATLANTIC BASIN SEASONAL TROPICAL CYCLONE PREDICTION METHODS FOR 1 JUNE AND 1 AUGUST FORECAST DATES. *C.W. Landsea, W.M. Gray, P.W. Mielke Jr. and K.J. Berry*

125 A WEST-PACIFIC UPPER TROPOSPHERIC WESTERLY WIND SURGE DURING TOGA-COARE. *H. Iskenderian and L.F. Bosart*

129 APPLICATION OF EOF ANALYSIS TO TROPICAL WIND PROFILER DATA. *C.R. Williams*

132 IMPACT OF SLOWLY-VARYING BOUNDARY FORCINGS ON THE BROAD-SCALE ASIAN MONSOON. *S. Yang and K.-M. Lau*

136 COHERENT 3-D-PROPAGATION-PATTERNS IN THE ENERGETIC EXCHANGE BETWEEN TROPO- AND STRATOSPHERE. *G. Schmitz and N. Grieger*

140 LAND SURFACE TEMPERATURES. *A. Basist and T. Peterson*

144 EARLY COMPARISONS OF THE GPCP COMBINED DATA SET SUITE WITH INDIVIDUAL ESTIMATES AND CLIMATOLOGY. *G.J. Huffman and R.F. Adler*

SESSION 3: REANALYSES
Chairperson: C.F. Ropelewski

148 NASA REANALYSIS: AN OVERVIEW OF RESULTS AND FUTURE PLANS. *S. Schubert, H.M. Helfand and C.-Y. Wu*

152 EVALUATION OF THE ECMWF RE-ANALYSIS WITH EMPHASIS ON THE PRECIPITATION. *K. Arpe and M. Stendel*

156 AN EVALUATION OF THE SURFACE FLUXES IN THE NMC/NCAR REANALYSIS. *S. Saha, G. White and R. Reynolds*

160 A COMPARISON OF MONTHLY PRECIPITATION AMONG THE NCEP/NCAR AND NASA/DAO REANALYSES AND A SATELLITE-RAINGAUGE MERGED ANALYSIS. *J. Janowiak, P. Xie and P. Arkin*

*Manuscript not available

Page

SESSION 3: REANALYSES (Continued)
Chairperson: T. Mitchell

164 ON THE ANNUAL CYCLE OF THE MEAN MERIDIONAL AND EAST-WEST CIRCULATIONS FROM THE NMC/NCAR REANALYZED FIELDS DURING 1985-94. *M. Chelliah*

168 THE ANNUAL CYCLE OF LOW-FREQUENCY STORM TRACK AS REVEALED IN NCEP/NCAR REANALYSIS. *X.L. Wang*

172 COMPONENTS OF THE EARTH RADIATION BUDGET IN NCEP/NCAR REANALYSIS. *S-K. Yang, A.J. Miller, Y-T. Hou and C.F. Ropelewski*

* LOW FREQUENCY INTRASEASONAL VARIABILITY OVER THE ATLANTIC: COMPARISON OF REANALYSES. *D.M. Straus*

176 THE MAINTENANCE OF INTRASEASONAL TRANSIENT EDDY ACTIVITY IN THE GEOS-1 ASSIMILATED DATA SET. *R.X. Black*

SESSION 4. INTERNATIONAL PROGRAM STUDIES
Chairperson: E.M. Rasmusson

180 THE MEAN ANNUAL CYCLE OF WATER VAPOR OVER THE MISSISSIPPI RIVER BASIN (1973-1992). *E.S. Yarosh and C.F. Ropelewski*

* THE MOISTURE BUDGET IN A HIGH RESOLUTION SUMMER SIMULATION OVER UNITED STATES. *H. Juang, S. Saha and M. Kanamitsu*

184 GCIP ENERGY AND MOISTURE BUDGETS. *J. Roads, S. Chen, S. Yang, M. Kanamitsu and H. Juang*

188 RECENT PROGRESS IN THE STUDY OF WATER VAPOR BUDGETS USING EDAS ANALYSES. *E.H. Berbery and E.M. Rasmusson*

191 NEW RESULTS ON THE HYDROLOGY OF THE NORTH AFRICAN DESERT, BASED ON THE NMC REANALYSES. *F. Vitart, A.H. Oort and K.C. Mo*

SESSION 5: ENSO AND ENSO VARIABILITY
Chairperson: G.D. Bell

195 ENSO-LIKE DECADE-TO-CENTURY SCALE VARIABILITY: 1900-93. *Y. Zhang, J.M. Wallace and D.S. Battisti*

* OBSERVATIONS OF ENSO VARIABILITY IN 1950-78 AND 1979-92. *T.P. Mitchell and J.M. Wallace*

*Manuscript not available

Page

* INTERDECADAL CHANGES OF THE EL NIÑO/SOUTHERN OSCILLATION. *B. Wang*

199 DECADAL AND INTERANNUAL VARIABILITY IN THE TROPICAL WESTERN PACIFIC. *D.S. Gutzler*

203 ON THE PHASE-LOCKING BETWEEN EL NIÑO AND THE ANNUAL CYCLE. *C. Penland*

* A NEW LOOK AT THE ATMOSPHERIC RESPONSE TO EL NIÑO. *A. Kumar and M.P. Hoerling*

POSTER SESSION: 2
Coordinator: C. Zhang

207 AN ANALYSIS OF THE STARTING DATE FOR THE SUMMER MONSOON IN WESTERN MEXICO AND SOUTHEAST ARIZONA. *A.V. Douglas and P.J. Englehart*

212 THE EXTRATROPICAL RESPONSE OF THE ATMOSPHERE TO TROPICAL INTRASEASONAL HEATING IN A SIMPLE GCM: IMPLICATIONS FOR DETECTION AND FORECASTING. *I. Bladé and D.L. Hartmann*

216 ZONAL MEAN FLOW/EDDY RELATIONSHIP IN A PERPETUAL JANUARY GCM EXPERIMENT. *P. Peng and N-C. Lau*

220 ON THE FORCING OF THE MARCH-TO-MAY CIRCULATION-CHANGE OVER THE EASTERN EQUATORIAL PACIFIC. *S. Nigam*

222 SURFACE FLUX VARIABILITY IN OVER THE NORTH PACIFIC IN A GCM. *M.A. Alexander and J.D. Scott*

226 SPATIAL PATTERN OF TENDENCIES IN SURFACE AIR TEMPERATURE CHANGE OVER THE LAST DECADES. *V.N. Razuvaev, E.G. Apasova, O.N. Bulygina, N.N. Korshunova and R.A. Martuganov*

229 DECADAL VARIATIONS OF THE ANNUAL CYCLE. *H.L. Rui and X.L. Wang*

232 CONSISTENCY OF THE DIABATIC HEATING THE NMC/NCAR REANALYSIS. *W. Ebisuzaki*

235 THE INFLUENCE OF ENSO ON THE TEMPERATURE FIELD OVER CANADA. *A. Shabbar and M. Khandekar*

239 THE PREDICTION OF SEASONAL WILDFIRE SEVERITY IN THE WESTERN USA. *J.W. Benoit, F.M. Fujioka and M.H. McCutchan*

*Manuscript not available

Page

243 THE 1992-95 RAINY SEASONS IN NORTHEAST BRAZIL: REAL-TIME FORECASTS AND VERIFICATION. *L. Greischar and S. Hastenrath*

246 A REVIEW OF SSM/I DERIVED CLIMATE PRODUCTS. *R. Ferraro, F. Weng, N. Grody, A. Gruber, A. Basist, J. Janowiak and C. Kondragunta*

250 AN INFLUENCE OF 11-YEAR SUNSPOT CYCLE IN THE LOWER STRATOSPHERIC-UPPER TROPOSPHERE ON THE NORTHERN HEMISPHERE. *H. van Loon and K. Labitzke*

254 A SPECTRAL ANALYSIS OF THE GEOS-1 ASSIMILATION AND SIMULATION. *W. Min, S.D. Schubert, and C-K. Park*

256 DAILY CYCLES OF SST AND SURFACE WINDS OVER THE TROPICAL PACIFIC FROM THE TAO MOORED BUOY ARRAY. *C. Deser and C. Smith*

260 ASSIMILATION VARIABILITY IN THE GEOS-1 DATA ASSIMILATION SYSTEM. *M. Sienkiewicz*

263 POTENTIAL PREDICTABILITY OF TROPICAL STORMS IN AN ENSEMBLE OF FORECASTS. *F. Vitart, J.L. Anderson and W.F. Stern*

267 STATISTICAL ANALYSIS OF CHILEAN PRECIPITATION ANOMALIES ASSOCIATED WITH ENSO. *R.H. Nuñez, T.S. Richard and J.J. O'Brien*

271 FIRST YEAR OF OBSERVATIONS FROM THE GALÁPAGOS UTILIZING A 915 MHz WIND PROFILER. *K.S. Gage and C.R. Williams*

275 STATISTICAL PREDICTION OF GLOBAL CONTINENTAL TEMPERATURE AND PRECIPITATION TO 1 YEAR IN ADVANCE USING GLOBAL SST. *A.G. Barnston and T.M. Smith*

279 MAJOR CLIMATE EVENTS AND ANOMALIES AROUND THE WORLD DURING 1995. *R. Tinker*

283 DECADAL VARIABILITY OF SNOW IN THE WESTERN UNITED STATES. *D.R. Cayan and L. Riddle*

284 THREE-DIMENSIONAL DIABATIC HEATING FIELDS FROM THE NMC/NCAR REANALYSIS. *G. White and S. Saha*

288 DYNAMICAL IMPACT OF LOCALIZED GWD FORCING IN GCM. *J. ZHOU, Y.C. Sud and K.-M. Lau*

*Manuscript not available

Page

SESSION 6: OCEANIC AND COUPLED MODEL STUDIES
Chairperson: T.M. Smith

292 DECADAL CHANGES IN THE CIRCULATION OF THE NORTHERN HEMISPHERE: RELATION TO SURFACE TEMPERATURE. *J.W. Hurrell and H. van Loon*

296 EL NIÑO PREDICTIONS BY THE NCEP COUPLED OCEAN-ATMOSPHERE MODEL: A VIEW FROM THE OCEAN SUBSURFACE THERMAL VARIABILITY. *Deng-Hua Wu, M. Ji and A. Leetmaa*

300 EXTRATROPICAL AIR-SEA INTERACTION ON WEEKLY TIME SCALES. *C. Deser and M. Timlin*

SESSION 6: OCEANIC AND COUPLED MODEL STUDIES (Continued)
Chairperson: H. van Loon

304 COUPLED PREDICTIONS AT COLA. *B.P. Kirtman*

308 INTERDECADAL RELATIONS AMONG ANOMALOUS 400M OCEAN CURRENTS, TEMPERATURE AND ATMOSPHERIC FORCING IN THE NORTH PACIFIC. *Arthur J. Miller, D.R. Cayan and W.B. White*

312 MODELING THE INTRASEASONAL THERMOCLINE VARIATIONS IN THE EASTERN PACIFIC. *B. Liebmann, H. Hendon and J. Glick*

SESSION 7: REGIONAL STUDIES
Chairperson: A.V. Douglas

314 A SIMPLE MODEL FOR THE CLIMATOLOGY AND ENSO OF EQUATORIAL PACIFIC OCEAN-ATMOSPHERE SYSTEM. *M. Cai*

318 TROPICAL CONVECTION LOW FREQUENCY VARIATIONS OVER THE AMERICAS AND ASSOCIATED BOUNDARY LAYER CURRENTS. *J. Nogués-Paegle and K.C. Mo*

322 A COMPARISON OF EQUATORIAL PACIFIC WINDS OBSERVED BY WIND PROFILERS AND MODELED BY NUMERICAL WEATHER PREDICTION ANALYSES. *C.R. Williams and K.S. Gage*

325 A VORTICITY BUDGET OF TROPICAL-EXTRATROPICAL INTERACTIONS. *G.N. Kiladis*

329 THE ROLE OF LARGE SCALE ATMOSPHERIC CIRCULATION IN THE RELATIONSHIP BETWEEN TOPICAL CONVECTION AND SEA SURFACE TEMPERATURE. *W.K.-M. Lau and H-T. Wu*

*Manuscript not available

Page

SESSION 8: LOW FREQUENCY VARIABILITY
Chairperson: C. Deser

333 SCATTEROMETER WINDS COMPOSITED ACCORDING TO THE PHASE OF THE TROPICAL INTRASEASONAL OSCILLATIONS. *R.A. Madden, T.J. Hoar and R.F. Milliff*

* STATISTICAL CHARACTERIZATION OF BLOCKING SYSTEMS OVER THE NORTHERN HEMISPHERE: 1946-1994. *I. Halevy, K. Higuchi and J.L. Knox*

337 ANGULAR MOMENTUM AND ENERGETICS IN REANALYSIS PRODUCTS. *D.A. Salstein and R.D. Rosen*

* A COMPOSITE INTRASEASONAL ATMOSPHERIC ANGULAR MOMENTUM BUDGET DURING NORTHERN WINTER. *K. Weickmann, G.N. Kiladis, P.D. Sardeshmukh*

341 DETECTING GREENHOUSE CLIMATE CHANGE DURING THE 20TH CENTURY. *D.M.H. Sexton, D.J. Karoly, C.K. Folland, J.F.B. Mitchell and D.P. Rowell*

345 NOAA'S MSU TIME SERIES FOR DETECTING CLIMATE CHANGE. *M.D. Goldberg, D.S. Crosby and W. Chung*

SESSION 9: PRECIPITATION
Chairperson: P.A. Arkin

349 VARIATIONS IN CENTRAL AND EASTERN NORTH AMERICAN PRECIPITATION TELECONNECTIONS DURING WARM AND COLD TROPICAL PACIFIC SSTA EVENTS. *D.L. Montroy and M.B. Richman*

* GLOBAL PRECIPITATION CLIMATOLOGY PROJECT (GPCP) COMBINED DATA SETS. *A. Gruber, R.F. Adler, G.J. Huffman, P. Arkin and P. Xie*

353 ANNUAL AND INTERANNUAL VARIABILITY IN LARGE-SCALE PRECIPITATION DURING 1987-1994. *P. Xie and P.A. Arkin*

357 THE ROLE OF INERTIAL INSTABILITY IN DETERMINING THE STRENGTH AND LOCATION OF NEAR-EQUATORIAL CONVECTION. *R.A. Tomas and P.J. Webster*

SESSION 10: GENERAL CIRCULATION STUDIES
Chairperson: K.C. Mo

362 TROPOSPHERIC EQUATORIAL ROSSBY WAVES: OBSERVATIONS AND MODELING. *M. Wheeler and G.N. Kiladis*

* DYNAMICALLY CONSISTENT 200 MB WIND DIVERGENCES 1980-93. *P.D. Sardeshmukh, M. Newman and B. Liebmann*

*Manuscript not available

Page

366 ON THE CLIMATOLOGICAL ANNUAL CYCLE IN GLOBAL MEAN ATMOSPHERIC SURFACE PRESSURE AND HYDROLOGY AS REVEALED BY NCEP/NCAR REANALYSIS. *H.M. van den Dool, J. Schemm and S. Saha*

370 POTENTIAL VORTICITY FLUX DIAGNOSTICS OF THE WINTER MEAN CIRCULATION USING TWO REANALYSIS DATA SETS. *J.S. Whitaker and A.F. Loughe*

SESSION 11: MODELING STUDIES
Chairperson: M. Chelliah

374 INTERACTION OF TROPICAL HEATING-INDUCED ATMOSPHERIC FLOW WITH MIDLATITUDE OROGRAPHY. *E. DeWeaver and S. Nigam*

378 INTRASEASONAL TIME SCALES OF CONVECTION IN GCMs. *K.R. Sperber and J.M. Slingo*

382 SYSTEMATIC TENDENCY ERROR IN BUDGET CALCULATIONS. *M. Kanamitsu and S. Saha*

386 APPLICATION OF ESTIMATED SOIL MOISTURE TO MODEL CLIMATE SIMULATION. *J. Huang, H.M. van den Dool and J.E. Schemm*

SESSION 12: ASPECTS OF PREDICTABILITY
Chairperson: M. Kanamitsu

390 INHERENT LIMITS TO INTERANNUAL PREDICTABILITY? *C. Torrence and P.J. Webster*

394 THE ATMOSPHERIC RESPONSE TO TROPICAL CONVECTION AND IMPLICATIONS FOR LONG RANGE FORECASTING. *K.C. Mo and P. Peng*

398 CLIMATE PREDICTION METHODOLOGY. *W.M. Gray*

402 A MULTI-YEAR DERF EXPERIMENT AT NCEP. *J.E. Schemm and H.M. van den Dool*

406 INFERENCE OF THE POTENTIAL PREDICTABILITY OF SEASONAL LAND-SURFACE CLIMATE FROM AMIP ENSEMBLE INTEGRATIONS. *T.J. Phillips and B.D. Santer*

410 SPECIFICATION OF CONTINENTAL TEMPERATURE AND PRECIPITATION USING GLOBAL SST. *T.M. Smith and A.G. Barnston*

*Manuscript not available

Page

SESSION 13- FORECASTING AND VERIFICATION
Chairperson: R.E. Livezey

413 TELECONNECTIONS AND SEASONAL RAINFALL PREDICTION IN AFRICA. *W. Thiao, A.G. Barnston and V. Kumar*

417 CLIMATE ENSEMBLE FORECASTING AT CPTEC. *P. Nobre, M.L. Abreu, I.F.A. Cavalcanti, M. Quadro, and L. Pezzi*

421 SEASONAL PREDICTION OF CANADIAN SURFACE CLIMATE BY CANONICAL CORRELATION ANALYSIS. *A. Shabbar*

* SHORT-TERM CLIMATE PREDICTIVE SKILL IN NORTHERN EUROPE. *A. Johansson, A. Barnston, S. Saha, and H.M. van den Dool*

SESSION 13: FORECASTING AND VERIFICATION (Continued)
Chairperson: H.M. van den Dool

425 LONG LEAD CLIMATE PREDICTION USING SCREENING MULTIPLE LINEAR REGRESSION. *D.A. Unger*

429 POTENTIAL FOR LONG-LEAD PREDICTION OF SEASONAL PRECIPITATION OVER THE PACIFIC ISLANDS USING THE NCEP CCA MODEL. *Y. He and A.G. Barnston*

433 VERIFICATION OF SEASONAL 'FORECASTS' FROM ENSEMBLE GCM INTEGRATIONS. *J.L. Anderson*

437 PNA-REGION TELECONNECTIONS TO TROPICAL-PACIFIC SST ANOMALIES IN OBSERVATIONS AND THE NCEP CLIMATE MODEL. *R.E. Livezey, M. Masutani, M. Ji and A. Leetmaa*

*Manuscript not available

List of Attendees to the
Twentieth Climate Diagnostics Workshop
Seattle, WA
October 23-27, 1995

Jimmy Adegoke	University of Washington, Visiting Scientist
Michael A. Alexander	NOAA/CIRES - University of Colorado
Jeffrey Anderson	NOAA/ERL/Geophysical Fluid Dynamics Laboratory
Phillip A. Arkin	NOAA/NWS/NCEP
Klaus Arpe	Max-Planck-Institute for Meteorology
Ferdinand Baer	University of Maryland
Mark Baldwin	Northwest Research Associates, Inc.
Christian Bantzer	University of Washington
Anthony G. Barnston	NOAA/NWS/NCEP/Climate Prediction Center
Joe Barsugli	NOAA/CIRES - University of Colorado
Alan Basist	NOAA/NWS/NCEP/Climate Prediction Center
Gerald D. Bell	NOAA/NWS/NCEP/Climate Prediction Center
John W. Benoit	USDA Forest Service
Ernesto H. Berberry	CICS-University of Maryland
Kenneth H. Bergman	NASA
Robert X. Black	Georgia Institute of Technology
Ileana Bladé	University of Washington
Lance F. Bosart	State University of New York - Albany, NY
James S. Boyle	Lawrence Livermore National Laboratory
Iracema F. A. Cavalcanti	INPE, Brazil
Ming Cai	CICS - University of Maryland
Bridget Callahan	University of Washington
Daniel R. Cayan	Scripps Institution of Oceanography
Edmund K. M. Chang	Massachusetts Institute of Technology
Hui Ho Chang	
Yehui Chang	NASA/Goddard Space Flight Center
Muthuvel Chelliah	NOAA/NWS/NCEP/Climate Prediction Center
Ping Chen	NOAA/CIRES - University of Colorado
Shuyi Chen	University of Washington
Wilbur Y. Chen	NOAA/NWS/NCEP/Climate Prediction Center
Yin-Quei Chen	University of Washington
Gilbert P. Compo	University of Colorado
Ying Dai	University of Maryland
Clara Deser	NOAA/CIRES - University of Colorado
Eric DeWeaver	University of Maryland
Jean O. Dickens	JPL - California Inst. of Technology
James Dodge	NASA
Randall Dole	NOAA/ERL/Climate Research Division
Arthur V. Douglas	Creighton University
John Dracup	UCLA

Greg Duane	PAOS - University of Colorado
Imke Durre	University of Washington
Wesley Ebisuzaki	NOAA/NWS/NCEP/Climate Prediction Center
Henrik Feddersen	Danish Meteorological Institute
Ralph Ferraro	NOAA/NESDIS - Satellite Research Laboratory
Kenneth S. Gage	NOAA/ERL - Boulder, CO
Mitchell D. Goldberg	NOAA/NESDIS
William M. Gray	Colorado State University
Norbert Grieger	German Atmospheric Institute
Arnold Gruber	NOAA/NESDIS
Georgiy V. Gruza	Institute for Global Climate - Russia
David S. Gutzler	University of New Mexico
Leslie M. Hartten	NOAA/CIRES - University of Colorado
Stefan Hastenrath	University of Wisconsin
Luke He	NOAA/NWS/NCEP/Climate Prediction Center
Yuxiang He	NOAA/NWS/NCEP/Climate Prediction Center
R. Wayne Higgins	NOAA/NWS/NCEP/Climate Prediction Center
Martin P. Hoerling	NOAA/CIRES - University of Colorado
Jon Hoopingarner	NOAA/NWS/NCEP/Climate Prediction Center
Arthur Y. Hou	NASA/Goddard Space Flight Center
Jin Huang	NOAA/NWS/NCEP/Climate Prediction Center
George J. Huffman	NASA/Goddard Space Flight Center
James W. Hurrell	National Center for Atmospheric Research
Haig Iskenderian	State University of New York - Albany, NY
John Janowiak	NOAA/NWS/NCEP/Climate Prediction Center
Roy Jenne	National Center for Atmospheric Research
Ake Johansson	SMHI, Sweden
Scott Johnson	University of Washington
P. D. Jones	University of East Anglia/UK
Hann Ming Henry Juang	
Masao Kanamitsu	NOAA/NWS/NCEP/Climate Prediction Center
George N. Kiladis	NOAA/CIRES - University of Colorado
Ben P. Kirtman	COLA - Calverton, MD
John Knaff	Colorado State University
John L. Knox	Environment Canada
Jennifer Kolar	PAOS - University of Colorado
Gunter Konnen	KNMI, Netherlands
Arun Kumar	NOAA/NWS/NCEP/Climate Prediction Center
Won Tae Kwon	Meteorological Research Institute - Seoul, Korea
Christopher W. Landsea	Colorado State University
William K.-M. Lau	NASA/Goddard Space Flight Center
David Lawrence	PAOS - University of Colorado
David Ledvina	NASA/Goddard Space Flight Center
Sukyong Lee	Pennsylvania State University
Brant Liebmann	NOAA/CIRES - University of Colorado
Robert E. Livezey	NOAA/NCEP/NMC/Climate Prediction Center
G. Robert Lofgren	University of Arizona
Johannes P. Loschnigg	University of Colorado

Roland A. Madden	National Center for Atmospheric Research
Nat Mantua	University of Washington
Brian E. Mapes	University of Colorado
Michiko Masutani	NOAA/NCEP/NMC/Climate Prediction Center
Wilhelm May	Danish Meteorological Institute
Ed Miles	University of Washington
Alvin J. Miller	NOAA/NWS/NCEP/Climate Prediction Center
Arthur J. Miller	Scripps Institution of Oceanography
Neal Millet	NOAA/NWS/NCEP/Climate Prediction Center
Wei Min	NASA/Goddard Space Flight Center
Todd Mitchell	University of Washington
Kingtse C. Mo	NOAA/NWS/NCEP/Climate Prediction Center
David L. Montroy	University of Oklahoma
S. Nakamoto	Japan Marine Science & Technology Center
Matthew Newman	NOAA/CIRES - University of Colorado
Sumant Nigam	University of Maryland
Gregor Nitche	University of Washington
Abraham H. Oort	NOAA/ERL/Geophysical Fluid Dynamics Laboratory
Carlos Pabon Ortiz	NASA/Goddard Space Flight Center
Julia Nogués-Paegle	University of Utah
Jianfu Pan	NOAA/NWS/NCEP/Climate Prediction Center
Chung-Kyu Park	NASA/Goddard Space Flight Center
Jeong-Gyoo Park	Meteorological Research Institute - Seoul, Korea
Peitao Peng	Princeton University
Cécile Penland	NOAA/CIRES - University of Colorado
Thomas C. Peterson	NOAA/NESDIS/National Climatic Data Center
Thomas J. Phillips	Lawrence Livermore National Laboratory
Andre Plante	Environment Canada
Gerald L. Potter	Lawrence Livermore National Laboratory
Jianchun Qin	NOAA/NWS/NCEP/Climate Prediction Center
M. Sanker Rao	National Science Foundation
V. B. Rao	INPE, Brazil
Eugene M. Rasmusson	CICS/University of Maryland
N. A. Rayner	Hadley Center - UK Meteorological Office
Kelly Redmond	Desert Research Institute
Todd S. Richards	Florida State University
John O. Roads	Scripps Institution of Oceanography
David R. Rodenhuis	NOAA/NWS/NCEP/Climate Prediction Center
Chester F. Ropelewski	NOAA/NWS/NCEP/Climate Prediction Center
Richard D. Rosen	Atmosphere and Environment Research, Inc.
Suranjana Saha	NOAA/NWS/NMC
David A. Salstein	Atmosphere and Environment Research, Inc.
Ed S. Sarachik	University of Washington
Prashant Sardeshmukh	NOAA/CIRES - University of Colorado
Jae E. Schemm	NOAA/NWS/NCEP/Climate Prediction Center
Siegfried D. Schubert	NASA/Goddard Space Flight Center
D. M. H. Sexton	Hadley Center - UK Meteorological Office
Amir Shabbar	Canadian Climate Centre

John D. Sheaffer	Colorado State University
Meta Sienkiewicz	NASA/Goddard Space Flight Center
Catherine Smith	NOAA/CIRES - University of Colorado
Thomas Smith	NOAA/NCEP/NMC/Climate Prediction Center
Kenneth R. Sperber	Lawrence Livermore National Laboratory
David M. Straus	COLA - Calverton, MD
Youichi Tannimoto	University of Washington
Karl Taylor	Lawrence Livermore National Laboratory
Wassila Thiao	NOAA/NWS/NCEP/Climate Prediction Center
Robert A. Tomas	NOAA/NCAR
Mingfang Ting	University of Illinois
Richard Tinker	NOAA/NWS/NCEP/Climate Prediction Center
Chrisopher Torrence	University of Colorado
David A. Unger	NOAA/NWS/NCEP/Climate Prediction Center
Huug M. van den Dool	NOAA/NWS/NCEP/Climate Prediction Center
Harry van Loon	NOAA/NCAR
John Michael Wallace	University of Washington
Bing Wang	University of Hawaii
Xueliang Wang	NOAA/NWS/NCEP/Climate Prediction Center
Klaus W. Weickmann	NOAA/ERL/Climate Research Division
Matthew Wheeler	NOAA/CIRES - University of Colorado
Jeffrey S. Whitaker	NOAA/CIRES - University of Colorado
Christopher R. Williams	NOAA/CIRES - University of Colorado
Klaus Wolter	NOAA/CIRES - University of Colorado
Deng-Hua Wu	NOAA/NWS/NCEP/Climate Prediction Center
Man Li C. Wu	NASA/Goddard Space Flight Center
Zhongxiang Wu	Massachusetts Institute of Technology
Pingping Xie	NOAA/NWS/NCEP/Climate Prediction Center
Shi-Keng Yang	NOAA/NWS/NCEP/Climate Prediction Center
Evgeney Yarosh	NOAA/NWS/NCEP/Climate Prediction Center
Fenglin Yin	University of Washington
Zhi-Ping Yu	University of Hawaii
Chidong Zhang	University of Washington
Yuan Zhang	University of Washington
Jiayu Zhou	NASA/Goddard Space Flight Center
F. Zwiers	Environment Canada

AUTHOR INDEX
TWENTIETH ANNUAL CLIMATE DIAGNOSTICS WORKSHOP

Author . . . . . Page

A
Abreu, M.L. 73
Abreu, M.L. 417
Adler, R.F. 144
Alexander, M.A. 222
Anderson, J.L. 263
Anderson, J.L. 433
Apasova, E.G. 226
Arkin, P.A. 46
Arkin, P.A. 160
Arkin, P.A. 353
Arpe, K. 152

B
Bardin, M.Yu. 81
Barnston, A.G. 89
Barnston, A.G. 275
Barnston, A.G. 410
Barnston, A.G. 413
Barnston, A.G. 429
Basist, A. 140
Basist, A. 246
Battisti, D.S. 195
Bell, G.D. 9
Bengtsson, L. 32
Benoit, J.W. 239
Berbery, E.H. 188
Berry, K.J. 121
Black, R.X. 176
Bladé, I. 212
Bosart, L.F. 125
Boyle, J.S. 53
Bulygina, O.N. 226

C
Cai, M. 314
Cavalcanti, I.F.A. 73
Cavalcanti, I.F.A. 417
Cayan, D.R. 283
Cayan, D.R. 308
Chang, E.K.M. 36

Author . . . . . Page

Chelliah, M. 164
Chen, P. 40
Chen, S. 184
Chen, W.Y. 85
Chung, W. 345
Compo, G.P. 93
Crosby, D.S. 345

D
Dai, Y. 25
Dai, Z. 17
Deser, C. 256
Deser, C. 300
DeWeaver, E. 374
Douglas, A.V. 207

E
Ebisuzaki, W. 232
Englehart, P.J. 207

F
Feddersen, H. 77
Ferraro, R. 246
Folland, C.K. 341
Fujioka, F.M. 239

G
Gage, K.S. 42
Gage, K.S. 271
Gage, K.S. 322
Glick, J. 312
Goldberg, M.D. 345
Gray, W.M. 121
Gray, W.M. 398
Greischar, L. 243
Grieger, N. 136
Grody, N. 246
Gruber, A. 246
Gutzler, D.S. 199

H
Hartmann, D.L. 212
Hartten, L.M. 105
Hastenrath, S. 243
He, Y. 429
He, Y. 89
Helfand, H.M. 148
Hendon, H. 312
Higgins, R.W. 21
Higgins, R.W. 50
Higuchi, K. 117
Hoar, T.J. 333
Hou, A.Y. 29
Hou, Y-T. 172
Huang, J. 386
Huffman, G.J. 144
Hurrell, J.W. 292

I
Iskenderian, H. 125

J
Janowiak, J. 50
Janowiak, J. 160
Janowiak, J. 246
Ji, M. 296
Ji, M. 437
Jones, P.D. 5
Juang, H. 184

K
Kaas, E. 77
Kanamitsu, M. 184
Kanamitsu, M. 382
Karoly, D.J. 341
Kelly, P.M. 5
Khandekar, M. 235
Kiladis, G.N. 93
Kiladis, G.N. 325
Kiladis, G.N. 362
Kirtman, B.P. 304
Knaff, J. 101
Knox, J. 117
Kondragunta, C. 246
Kondratyeva, Y. 61
Korshunova, N.N. 226
Kousky, V.E. 1
Kousky, V.E. 9
Kumar, V. 413

L
Labitzke, K. 250
Lamich, D.J. 61
Landsea, C.W. 121
Lau, K.-M. 132
Lau, K.-M. 288
Lau, W.K.-M. 329
Lau, N-C. 216
Leetmaa, A. 296
Leetmaa, A. 437
Liebmann, B. 312
Livezey, R.E. 437
Loschnigg, J.P. 57
Loughe, A.F. 370

M
Madden, R.A. 333
Mapes, B.E. 93
Martuganov, R.A. 226
Masutani, M. 13
Masutani, M. 437
May, W. 32
McAfee, J.R. 42
McCutchan, M.H. 239
McPhaden, M.J. 97
Mielke, P.W., Jr. 121
Miller, Alvin J. 172
Miller, Arthur J. 308
Milliff, R.F. 333
Min, W. 254
Mitchell, J.F.B. 341
Mo, K.C. 13
Mo, K.C. 21
Mo, K.C. 191
Mo, K.C. 318
Mo, K.C. 394
Montroy, D.L. 349

N
Newman, M. 40
Nigam, S. 25
Nigam, S. 220
Nigam, S. 374
Nobre, P. 73

Nobre, P. 417
Nogués-Paegle, J. 318
Nuñez, R.H. 267

O

O'Brien, J.J. 267
Oort, A.H. 191

P

Pan, J. 109
Park, C-K. 61
Park, C-K. 254
Parker, D.E. 69
Peng, P. 216
Peng, P. 394
Penland, C. 203
Peterson, T. 140
Pezzi, L.P. 73
Pezzi, L.P. 417
Phillips, T.J. 406

Q

Qin, J. 65
Quadro, M. 73
Quadro, M. 417

R

Rasmusson, E.M. 17
Rasmusson, E.M. 188
Rayner, N.A. 69
Razuvaev, V.N. 226
Reynolds, R. 156
Richard, T.S. 267
Richman, M.B. 349
Riddle, L. 283
Roads, J. 184
Ropelewski, C.F. 1
Ropelewski, C.F. 172
Ropelewski, C.F. 180
Rosen, R.D. 337
Rowell, D.P. 341
Rui, H.L. 229

S

Saha, S. 156
Saha, S. 284
Saha, S. 366
Saha, S. 382
Salstein, D.A. 337
Santer, B.D. 406
Schemm, J.E. 366
Schemm, J.E. 386
Schemm, J.E. 402
Schmitz, G. 136
Schubert, S.D. 21
Schubert, S.D. 61
Schubert, S. 148
Schubert, S.D. 254
Scott, J.D. 222
Sexton, D.M.H. 341
Shabbar, A. 117
Shabbar, A. 235
Shabbar, A. 421
Sheaffer, J.D. 113
Sienkiewicz, M. 260
Skinner, W. 117
Slingo, J.M. 378
Smith, C. 256
Smith, T.M. 275
Smith, T.M. 410
Sperber, K.R. 378
Stendel, M. 152
Stern, W.F. 263
Sud, Y.C. 288

T

Thiao, W. 413
Timlin, M. 300
Tinker, R. 279
Tomas, R.A. 357
Torrence, C. 390

U

Unger, D.A. 425

V

van den Dool, H.M. 65
van den Dool, H.M. 85
van den Dool, H.M. 109
van den Dool, H.M. 366
van den Dool, H.M. 386
van den Dool, H.M. 402
van Loon, H. 250
van Loon, H. 292

Vitart, F. 263
Vitart, F. 191

W
Wallace, J.M. 195
Wang, X.L. 168
Wang, X.L. 229
Wang, W. 97
Webster, P.J. 57
Webster, P.J. 93
Webster, P.J. 357
Webster, P.J. 390
Weng, F. 246
Wheeler, M. 362
Whitaker, J.S. 370
White, W.B. 308
White, G. 156
White, G. 284
Williams, C.R. 42
Williams, C.R. 129
Williams, C.R. 271
Williams, C.R. 322
Wu, C.-Y. 148
Wu, D-H. 296
Wu, H-T. 329

X
Xie, P. 46
Xie, P. 160
Xie, P. 353

Y
Yang, S. 184
Yang, S-K. 172
Yang, Song 132
Yarosh, E.S. 180

Z
Zhang, C. 97
Zhang, Y. 195
Zhou, J. 288

The Evolution of Recent Oceanic and Atmospheric Anomalies in the Global Tropics

Vernon E. Kousky and Chester F. Ropelewski

NOAA/NWS/NCEP, Climate Prediction Center, Washington, DC 20233

1. Introduction

The period 1990-1994 featured persistent positive sea surface temperature (SST) anomalies in the central equatorial Pacific and was the warmest 5-year period on record for the tropical Pacific as a whole. Mature warm episode conditions occurred during late 1991 through mid-1992, during the first half of 1993, and from mid-1994 through early 1995. In retrospect, the warming during early 1993 should probably be considered as a continuation of the 1991-1992 warm episode, and the 1994-1995 warming should be considered a separate warm episode. In this paper we describe the evolution of oceanic and atmospheric anomalies in the tropical Pacific as the 1994-1995 warm episode peaked and then decayed to be replaced by weak cold episode conditions by the end of 1995.

2. Warm Episode Conditions Decay and Cold Episode Conditions Develop During 1995

The gradual evolution toward mature warm episode conditions in the tropical Pacific culminated during December 1994-January 1995. At that time SST anomalies reached +2C in portions of the central equatorial Pacific (Fig. 1, top) and convection was enhanced in the vicinity of the anomalously warm water (Fig. 1, bottom). Anomalous anticyclonic circulation centers developed in the upper troposphere to the north and to the south of the enhanced convection, and the mid-latitudes westerlies were enhanced over the North and South Pacific. The anomalously enhanced and eastward extended North Pacific jet stream was associated with a series of intense extratropical storms that developed over the central North Pacific and then proceeded to strike the west coast of the United States resulting in severe flooding in many sections of California.

The low-level equatorial easterlies returned to near normal intensity during January and remained near normal through May. Thereafter, the easterlies became stronger than normal over the western equatorial Pacific and gradually increased to stronger than normal over the central equatorial Pacific. By November 1995, the equatorial easterlies were stronger than normal throughout the Pacific basin, marking the first time that this had happened since the 1988-89 cold episode.

With the return to near-normal or stronger-than-normal easterlies, SST anomalies steadily decreased after January 1995, and during the last half of the year anomalies were generally negative throughout the central and eastern equatorial Pacific (Fig. 2). For the first time since the 1988-89 cold episode all three Niño regions registered negative anomalies. Negative SST anomalies also spread both north and south from the equator so that by November a rather broad band of negative anomalies covered the tropical Pacific east of the date line (Fig. 3, top). Associated with this reversal in the pattern of SST anomalies, the pattern of anomalous tropical convection also reversed with suppressed convective activity near the date line and enhanced convective activity over Indonesia (Fig. 3, bottom).

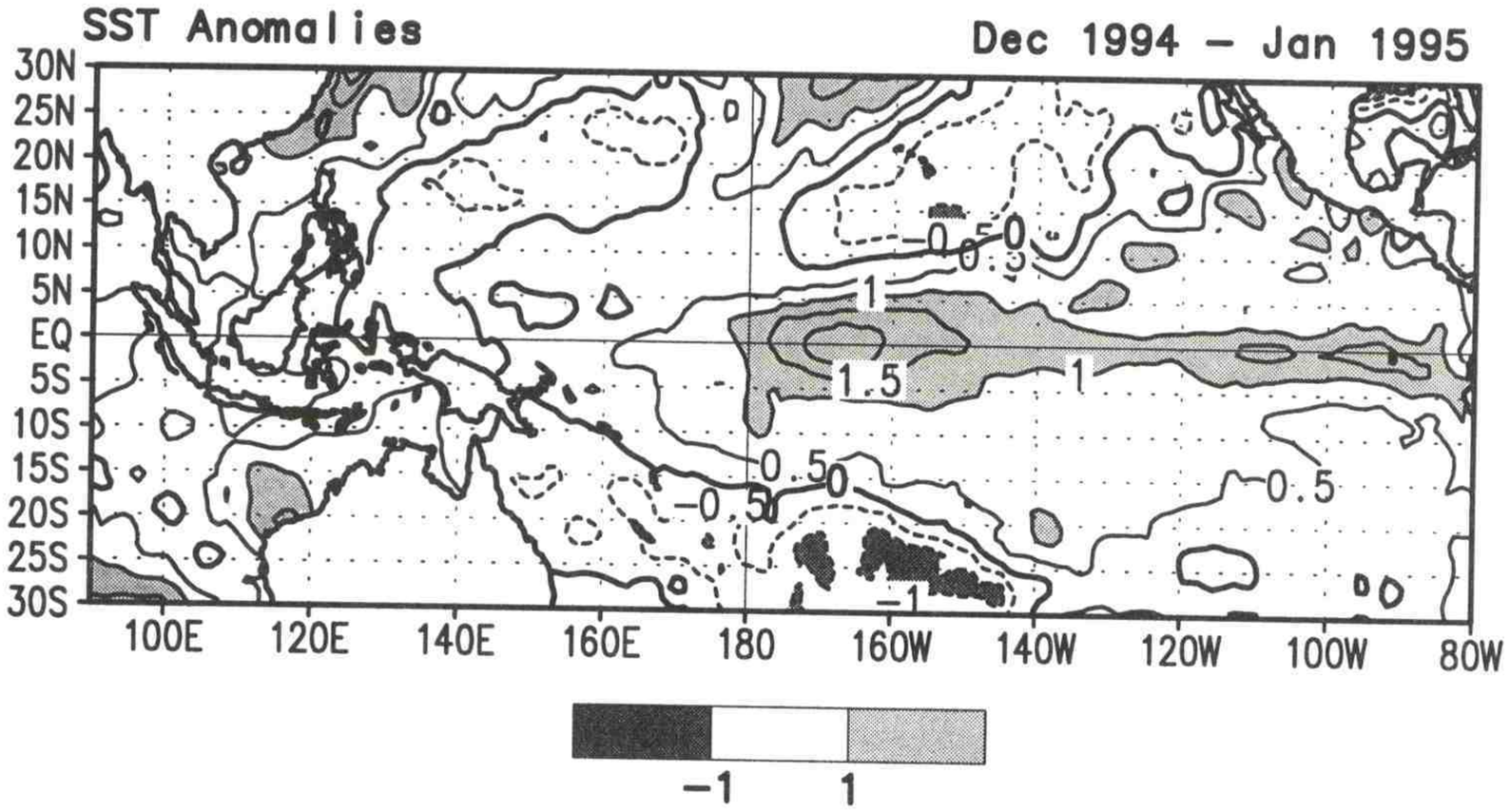

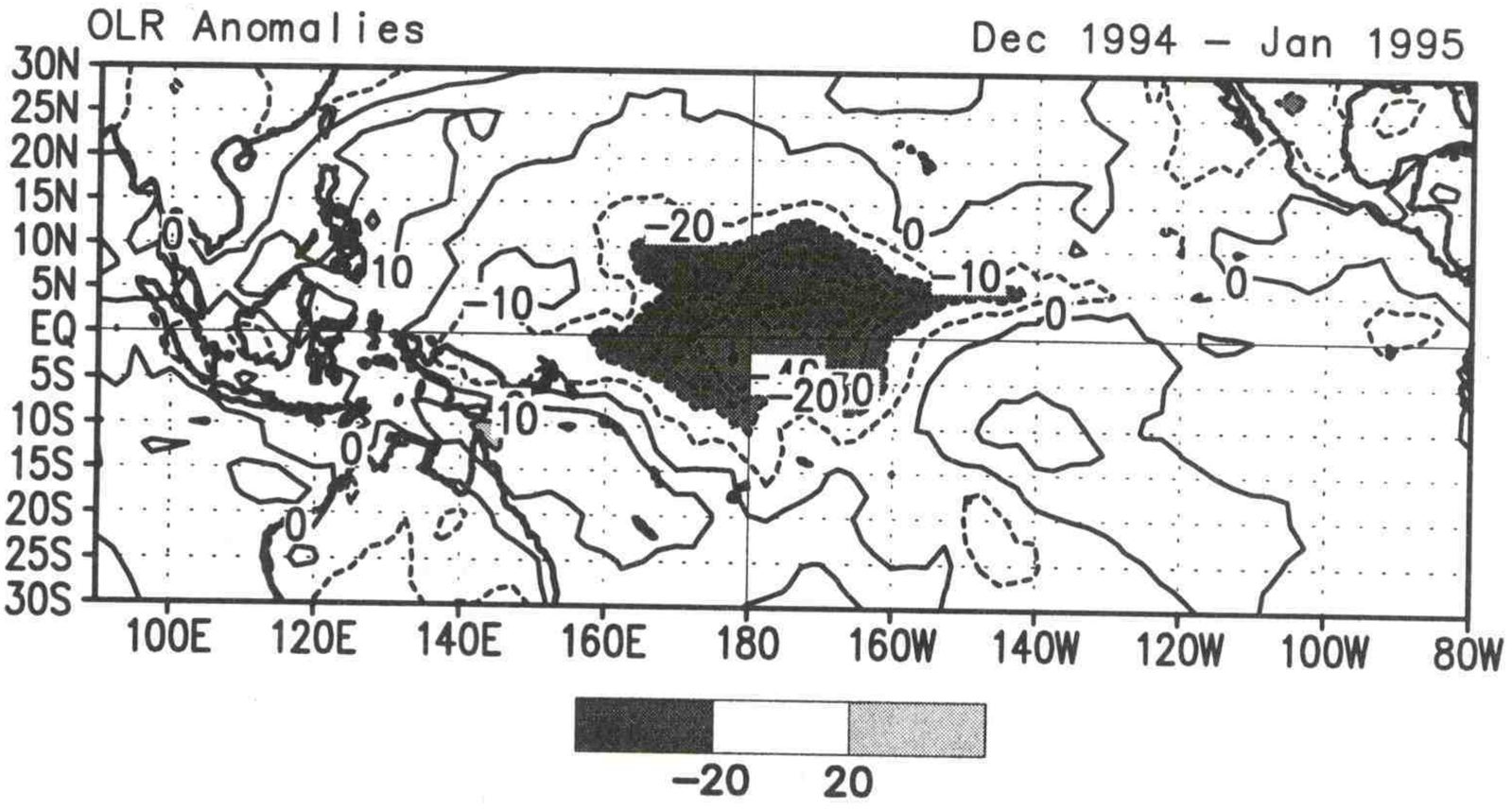

FIGURE 1. Sea surface temperature (SST) anomalies (top) and outgoing longwave radiation (OLR) anomalies (bottom) for December 1994-January 1995. Contour interval is 0.5°C (10 Wm^{-2}) for SST (OLR) anomalies. Negative OLR anomalies are indicative of enhanced tropical convection.

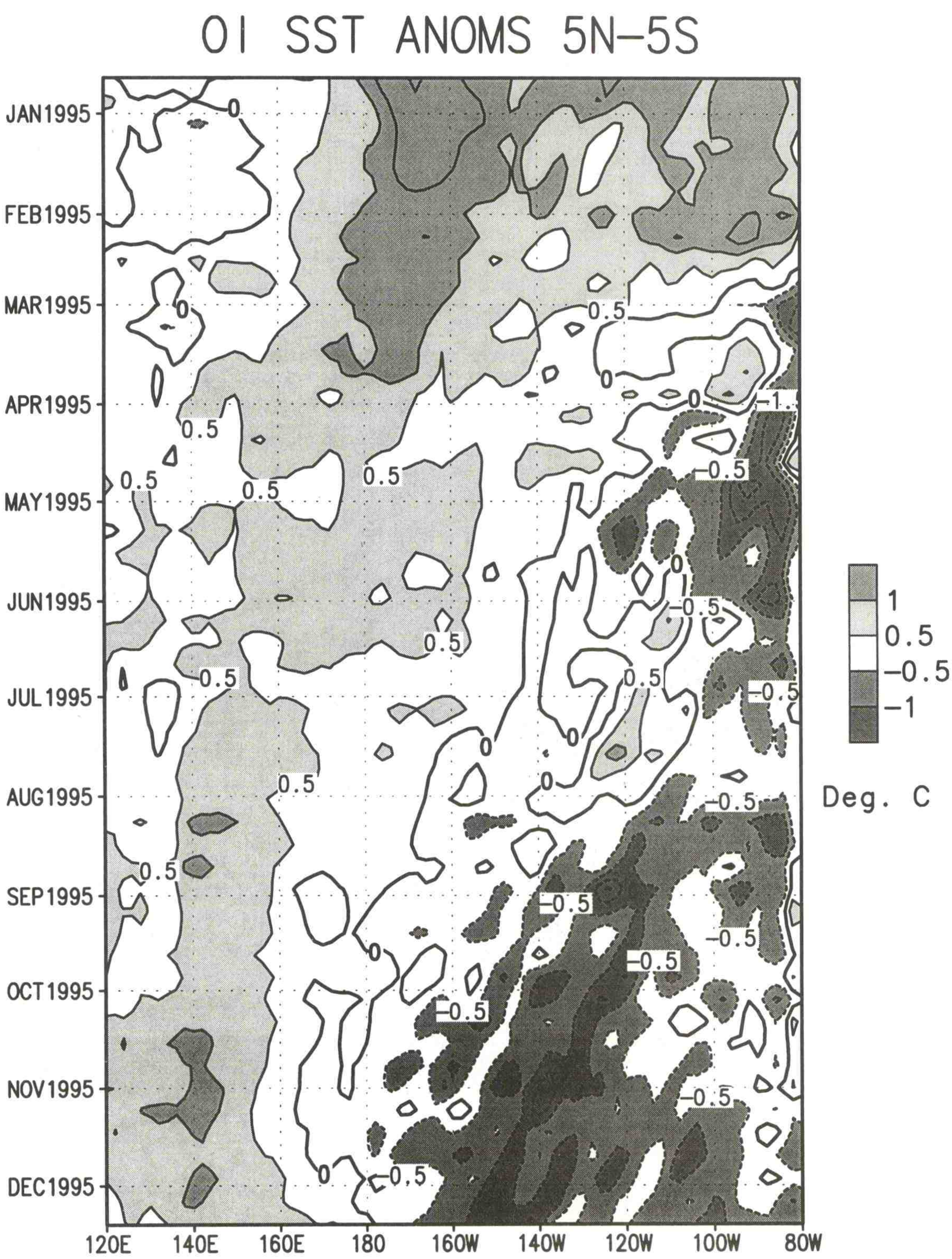

FIGURE 2. Time-longitude section of sea surface temperature anomalies for 5°N-5°S. Contour interval is 0.5°C.

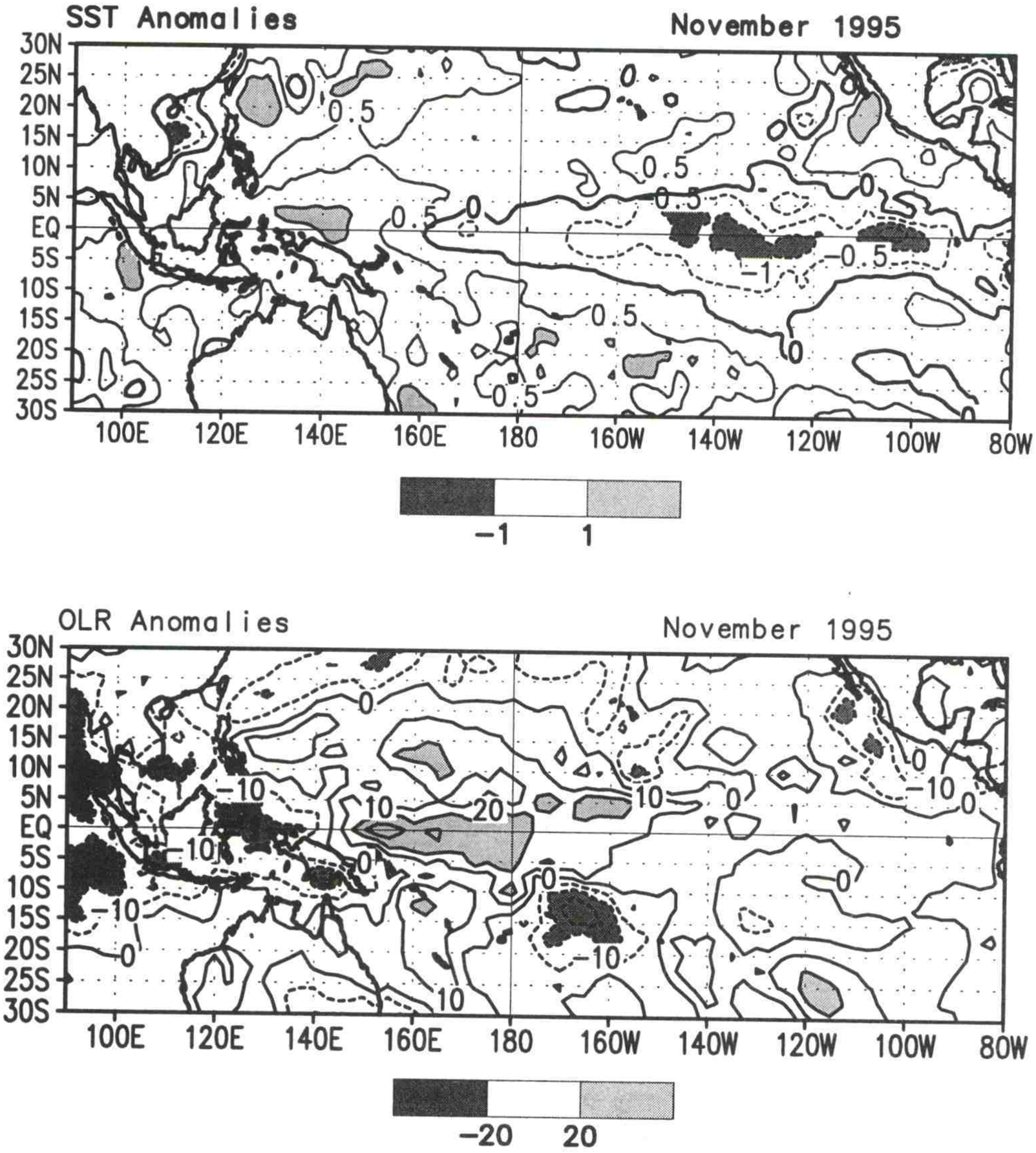

FIGURE 3. Sea surface temperature (SST) anomalies (top) and outgoing longwave radiation (OLR) anomalies (bottom) for November 1995. Contour interval is 0.5°C (10 Wm^{-2}) for SST (OLR) anomalies. Negative OLR anomalies are indicative of enhanced tropical convection.

RECENT WARMTH IN 1994/95 AND THE ROLE OF THE CIRCULATION IN THE DIVERGENCE BETWEEN SURFACE AND MSU2R TEMPERATURES SINCE THE MID 1980s

P. D. Jones and P. M. Kelly
Climatic Research Unit
University of East Anglia
Norwich NR4 7TJ
United Kingdom

1. INTRODUCTION

The warmest two years in the instrumental record of global surface air temperature, which extends back to 1854, were 1990 and 1991 (Jones and Briffa, 1992). The eruption of Mount Pinatubo in June 1991 cooled both hemispheres, particularly during 1992 and 1993 (Kelly *et al.*, in press). The effects of the dust and the subsequent secondary aerosols from this event have now diminished and the globe has begun to warm again (Nicholls *et al.*, in press).

March 1994 to February 1995 has been the warmest 12-month period of the entire Northern Hemisphere record. This warmth has continued into the spring and, on the basis of data through to September 1995, it is likely that 1995 will be the warmest year yet recorded. In contrast, temperature levels in the Southern Hemisphere, while still warmer than the 1961-90 reference level, have not been exceptional. Here, 1987 and 1988 were clearly warmer.

In this paper, we consider the pattern of temperature departures during 1994 and 1995 and discuss characteristics of the recent surface warming and a concomitant change in the circulation which may explain differences between the surface observational record and lower tropospheric temperature changes derived from satellite data.

2. TEMPERATURES DURING LATE 1994 AND 1995

Figure 1 shows the spatial pattern of temperature departures during the seasons of northern winter (DJF 1994/5), spring (MAM 1995) and summer (JJA 1995) in both hemispheres. In both northern winter and spring, the warmth in the Northern Hemisphere was centred over Siberia (+4 to +5°C with respect to 1961-90) and western North America (+2 to +3°C). The North Atlantic and North Pacific Oceans were slightly cooler than normal. In the northern summer, temperatures in most regions were slightly above normal, especially over eastern North America, Europe and eastern Siberia.

In the Southern Hemisphere, temperatures during the southern summer and autumn were near or slightly above normal except over much of Antarctica and the Australian sector of the Southern Ocean. The southern winter season saw marked contrasts between the mid-latitudes (40-60°N) and most of Antarctica. New Zealand and southern South America were exceptionally cold with many regions experiencing their coldest winters since the early 1930s. In contrast, all of Antarctica, except for the Peninsula which was colder than normal, experienced temperatures much higher than normal. Most of the warmth occurred during July which was 10°C above the 1961-90 level at many stations.

The temperature pattern in the Northern Hemisphere during the northern cold season (November-April), whilst somewhat exceptional in magnitude, has been a recurrent characteristic of the past 10-15 years. The mild winters in northern Eurasia and northern North America have occurred at the same time as enhanced zonal circulation over the North Atlantic and North Pacific oceans. In the North Atlantic, the North Atlantic Oscillation (NAO) has been in its most consistently positive phase over this time since the record began (Hurrell, 1995).

3. INCREASED ZONALITY

Similar cold-season temperature patterns to that observed in the surface record have been evident in the MSU2R satellite data for the troposphere (Spencer and Christy, 1992) though the magnitude of the anomalies over northern Eurasia has been somewhat less. There is a difference in the trend evident in the surface and lower troposphere data since 1979; the warming trend at the surface has been greater. Christy and McNider (1994) and Jones (1994) have both sought to explain this difference in terms of the differing responses of the two series to El Niño/Southern Oscillation (ENSO) and volcanic events. The increased zonality of the flow, especially in the North Atlantic, may also help to explain the divergence.

Table 1 lists dates when the Northern Hemisphere surface has been at least 0.5°C warmer than the lower

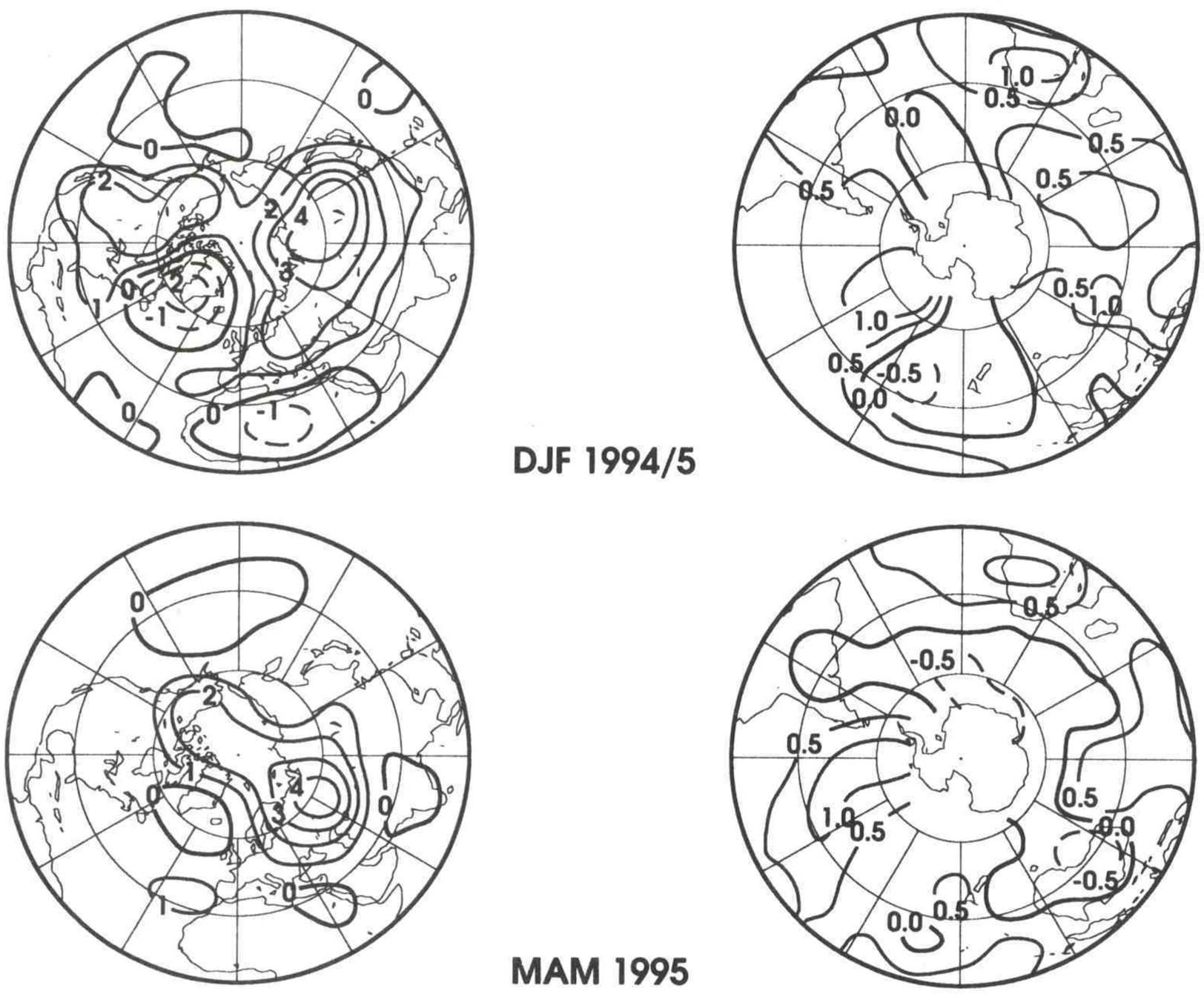

Figure 1: Surface air temperature departures from the 1961-90 reference period mean (°C) for northern winter 1994/95, spring (MAM) 1995 and, based on land data alone, summer (JJA)1995.

troposphere according to the MSU2R estimates during the period December to March. Figure 2 shows surface temperature and mean-sea-level pressure anomalies (with respect to 1961-90) as composite maps for the months given in Table 1. Each monthly composite (based on 10 years for January, 9 for February, 8 for March and 6 for December) shows similar features. Lower than normal pressure is evident north of about 60°N with higher pressure to the south. Increases in zonal flow are particularly marked over the North Atlantic/European sector and to a lesser extent over the North Pacific, increasing the maritime influence over the adjacent, downstream landmasses. The temperature composites show warm anomalies over northern Eurasia and western North America with cool anomalies over eastern Canada/Greenland and, in some months, North Africa. The similarity between the monthly composites is striking and, in the North Atlantic sector, clearly related to more positive values of the NAO.

This analysis goes some way towards explaining why there is a difference in the long-term trends observed in the surface and MSU2R data over the common period of record. If the months listed in Table 1 are omitted in

	1979	1980	1981	1982	1983	1984	1985	1986	1987	1988	1989	1990	1991	1992	1993	1994
January			X		X	X		X			X	X	X	X	X	X
February			X		X			X	X		X	X	X	X	X	
March			X			X		X			X	X		X	X	X
December	X			X						X			X	X		X

Table 1: Months with a difference of more than +0.5°C between the Northern Hemisphere surface and MSU2R data.

surface/MSU2R comparisons, the difference between the trends disappears. The "additional" warming observed in the surface record is confined to shallow levels in the atmosphere and has not penetrated to all levels of the troposphere. A similar strengthening of the North Pacific Oscillation (corresponding to a deeper and slightly southward position of the Aleutian Low) has been noted since the late 1970s by Trenberth (1990). In this region, modelling studies suggested a link to the greater number of warm episodes of ENSO in the central Pacific. Links over to the ENSO region in the North Atlantic are less clear.

4. CONCLUSIONS

Further work is necessary to assess the role of circulation changes in inducing differential trends at the surface and at height in the troposphere by, for example, considering temperatures at the 500 mb level. Comparisons with the radiosonde network record at the 850-300 mb level back to 1958 (Angell, 1988) indicate that the circulation anomaly was much less prevalent prior to the mid-to-late 1970s. This is to be expected given the more negative period of the NAO in the 1950s (Hurrell, 1995). While upper air data are not available for the earlier period of marked surface warming early in the present century, relationships between circulation anomalies and surface temperature trends during this period are broadly consistent with those during the recent period. The NAO was predominantly positive during the 1910s and 1920s, giving mild winters in northern Eurasia (Hurrell, 1995). At this time, though, fluctuations in ENSO phenomenon were at their quietest since the 1870s so conditions in the Pacific may have been dissimilar.

ACKNOWLEDGEMENTS

The authors thank John Christy for supplying the MSU2R data and Jim Angell for supplying the 850-300 mb data. This work was supported by the U.S. Department of Energy, Atmospheric and Climate Research Division under Grant No. DE-FG02-8EER60397.

REFERENCES

Angell, J. K., 1988: Variations and trends in tropospheric and stratospheric global temperature, 1958-87. *Journal of Climate* 1, 1296-1313.

Christy, J. R. and McNider, R. T., 1994: Satellite greenhouse signal. *Nature* 367, 325.

Hurrell, J. W., 1995: Decadal trends in the North Atlantic Oscillation and relationships to regional temperature and precipitation. *Science* 269, 676-679.

Jones, P. D., 1994: Recent warming in global temperature series. *Geophysical Research Letters* 21, 1149-1152.

Jones, P. D. and Briffa, K. R., 1992: Global surface air temperature variations over the twentieth century: Part 1 Spatial, Temporal and seasonal details. *The Holocene* 2, 174-188.

Kelly, P. M., Jia, P., and Jones, P. D., in press. The spatial response of the climate system to explosive volcanic eruptions. *International Journal of Climatology*.

Nicholls, N., Gruza, G. V., Jouzel, J., Karl, T. R., Ogallo, L. A. and Parker, D. E., in press: Observed climate variability and change. In: *Climate Change: The Second IPCC Assessment.* Cambridge University Press, Cambridge.

Spencer, R. W. and Christy, J. R., 1992: Precision and radiosonde validation of satellite grid point temperature anomalies, Part II: A tropospheric retrieval and trends during 1979-90. *Journal of Climate* 5, 858-868.

Trenberth, K. E., 1990: Recent observed interdecadal climate changes in the Northern Hemisphere. *Bulletin of the American Meteorological Society* 71, 988-993.

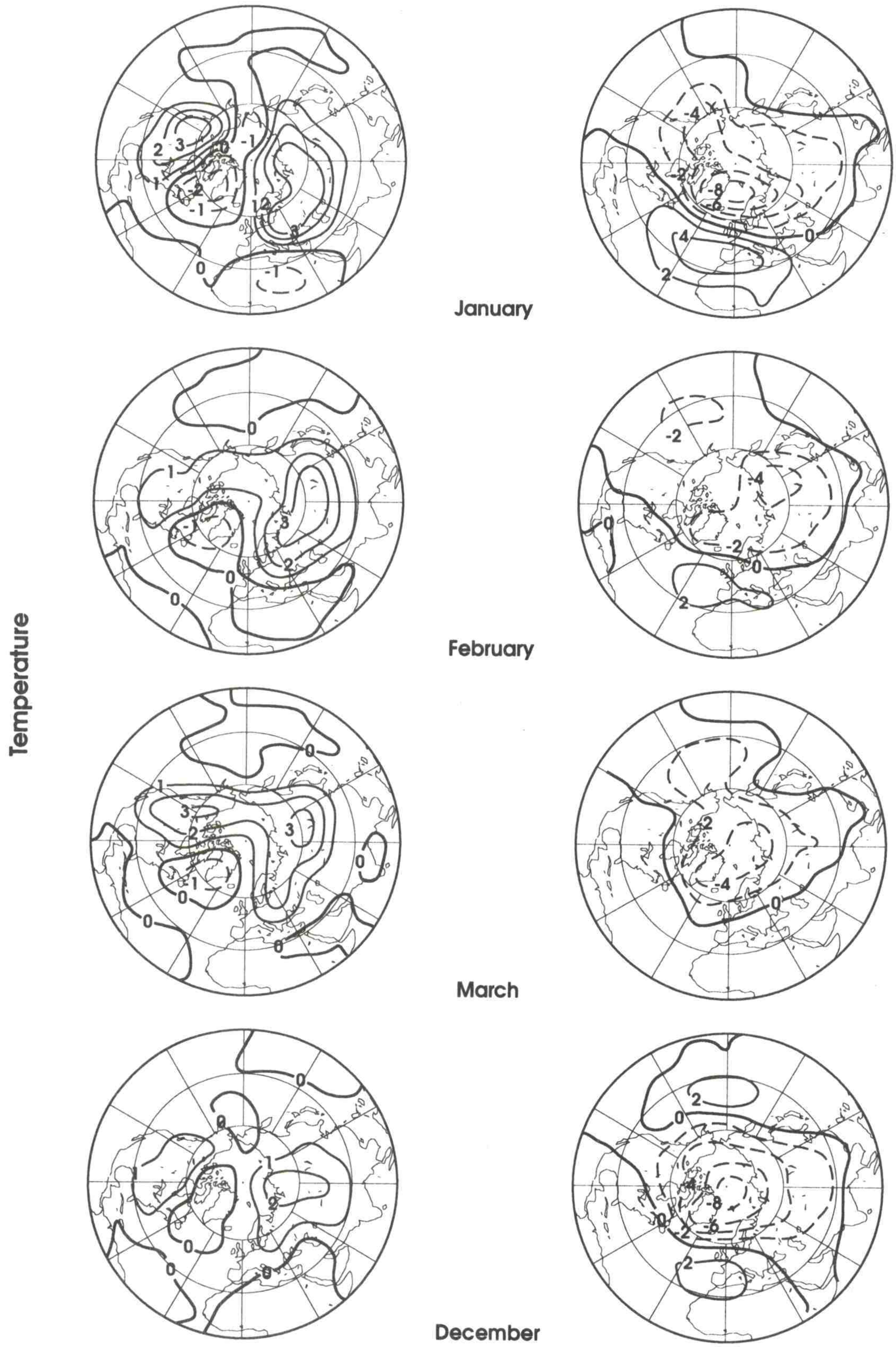

Figure 2: Surface air temperature (°C) and mean-sea-level pressure (mb) departures from the 1961-90 mean for the months with a difference of more than +0.5°C between the Northern Hemisphere surface and MSU2R data (Table 1).

DIAGNOSING THE MIDLATITUDE ATMOSPHERIC RESPONSE TO ENSO

Gerald D. Bell* and Vernon E. Kousky

NOAA/NWS/NCEP/ Climate Prediction Center
Camp Springs, MD

1. INTRODUCTION

A detailed observational diagnosis of the kinematic and dynamic response of the extratropical atmospheric circulation to ENSO during January 1995 is presented. The analysis is based on midlatitude circulation diagnostics, which have long been applied to the study of phenomena such as baroclinic midlatitude jets and waves. However, they have not been previously used to diagnose large-scale changes in the Pacific jet stream and North American circulation anomalies that are known to accompany ENSO.

2. PACIFIC JET STREAM STRUCTURE

The Pacific jet stream (Fig. 1a) is a primary dynamical interface between the tropics and the Northem Hemisphere extratropics. One of the most fundamental consequences of the tropical/extratropical interactions that occur during ENSO is a dramatic large-scale alteration of this interface, as manifested by an eastward extension of the jet to well east of the date line (Fig. 1b). This evolution occurs in conjunction with a large-scale eastward shift of the normal jet exit region to the extreme eastem North Pacific (from the date line to 135°W). This jet exit region is characterized by (1) strong diffluence in the height field (Figs. 1c, d), indicating significant along-stream decreases in the geostrophic wind speed and an accompanying weakening of the meridional temperature and height gradients, (2) strong along-stream decreases in wind speed (Figs. 1a, b), (3) strong along-stream variations in relative vorticity (Figs. 1e, f), and (4) strong parcel decelerations [denoted by the maxima of strong equatorward flow directed toward higher geopotential height, see also Fig. 2].

This large-scale alteration of the extratropical wind and mass fields in the form of an extended Pacific jet appears to serve as the catalyst for the generation of low frequency height anomalies which subsequently extend downstream over the eastem North Pacific and North America (Fig. 1d, seel also Fig. 4). During January 1995, this anomaly pattem was characterized by below-normal heights over the eastem North Pacific and the Gulf of Akaska and by above-normal heights over north-central and northeastem North America.

*Corresponding Author Address: Gerald D. Bell, NOAA/NWS/NCEP Climate Prediction Center, NOAA Science Center Rm. 605, Camp Springs, MD 20746; e-mail:wd52gb@hp32.wwb.noaa.gov

3. BAROCLINIC FEATURES OF THE PACIFIC JET

In general, the jet stream structure, as well as the meridional and vertical wind fields accompanying the jet entrance and exit regions, are traditionally viewed as a necessary and required baroclinic response to the interaction between a large-scale geostrophic flow and a baroclinic zone. For example, this geostrophic flow is manifested in the entrance region of the Pacific jet by a confluent configuration in the height field, and in the exit region by a diffluent configuration in the height field (Figs. 1c, d). It is well-known that these conditions produce large increases in the magnitude of the cross-jet component of the thermal and geostrophic vorticity gradients along parcel trajectories throughout the jet entrance region (not shown), and large decreases in the magnitude of the these gradients along parcel trajectories throughout the jet exit region (Fig. 2).

These changes in the thermal and vorticity gradients along parcel trajectories trigger large geostrophic imbalances throughout the jet, resulting in (1) a thermally- direct circulation and strong speed acceleration (cross-contour flow to lower geopotential height) in the entrance region and (2) a thermally- indirect circulation and strong speed deceleration (cross-contour flow to higher geopotential height) in the exit region (Fig. 2). All of these features characterize the climatological jet exit region which is located in the vicinity of the date line (Figs. 2a, c), the observed jet exit region which is shifted to the eastem North Pacific during January 1995 (Figs. 2b, d).

4. BAROCLINIC RESPONSE OF THE PACIFIC JET TO ENSO

The extension of the Pacific jet and shift of the jet exit region to the eastem North Pacific during January 1995 is linked to ENSO as follows. An eastward extension of convection to the central equatorial Pacific resulted in abnormal warmth and above-normal heights throughout the subtropical eastem North Pacific (Fig. 1d). These conditions increased the meridional temperature and height gradients in the subtropics and lower extratropics, resulting in (1) an eastward extension of strong geostrophic westerlies to well east of the date line, and (2) an eastward shift in the area of geostrophic flow diffluence to the extreme eastem North Pacific.

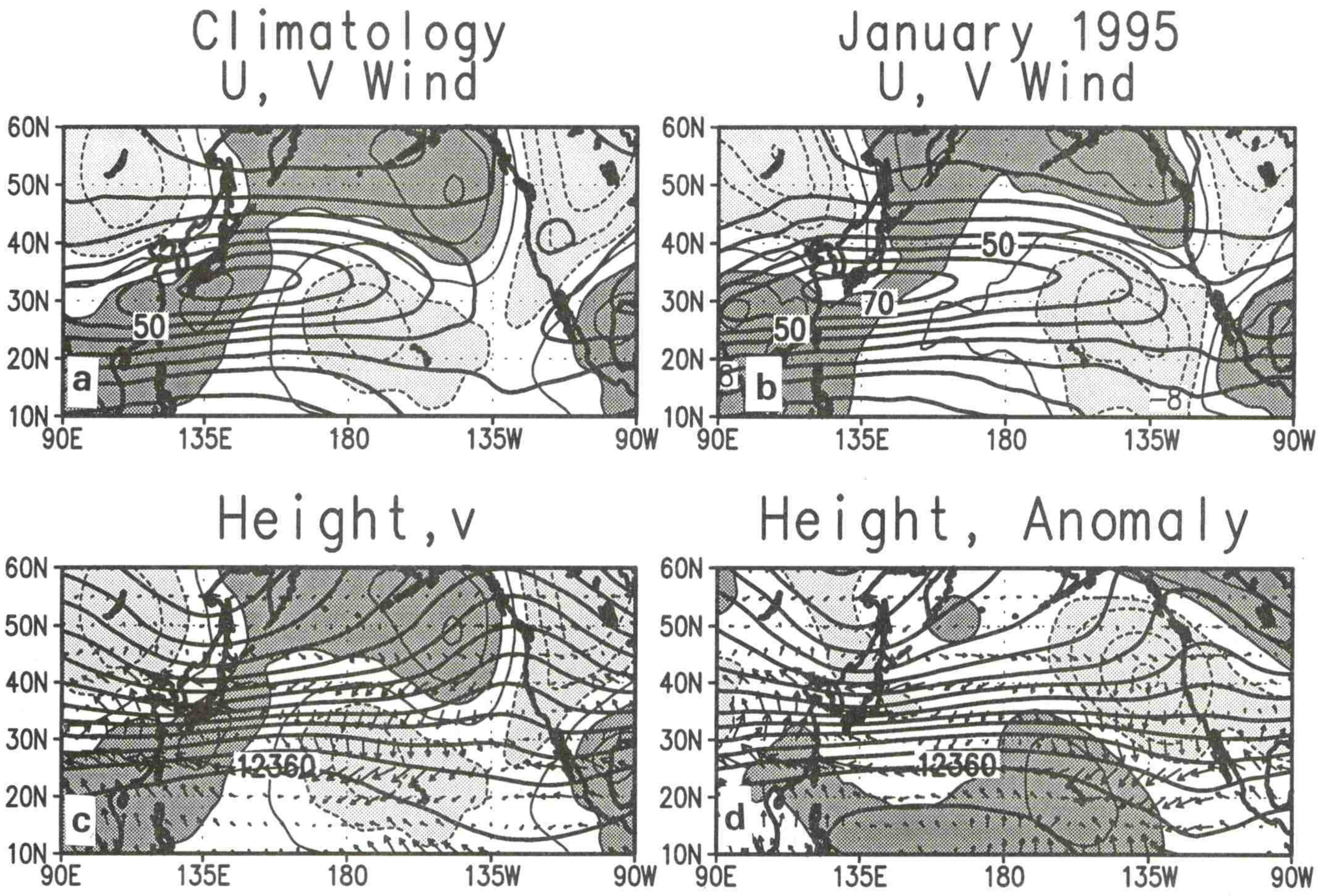

Fig. 1. (Left) January climatological mean, and (Right) January 1995 mean fields. Top panels (a, b) show meridional wind (shading and light contours, interval is 4 ms^{-1}) and zonal wind contours (thick, interval is 10 ms^{-1}). Middle panels (c, d) show geopotential height contours with ageostrophic wind vectors. Shading and light contours in panel (c) duplicate the meridional wind field shown in (a). Shading and light contours in panel (d) show height anomalies (interval is 60 m, with ±30 m contour also plotted) during January 1995. Bottom panels (e, f) show relative vorticity fields (shading and light contours, interval is $1x10^{-5}$ s^{-1}), overlayed with zonal wind contours. In all panels, positive values are shaded dark and contoured solid. Negative values are shaded light and contoured dashed. Climatological January mean is based on the 1985-1995 base period. Height anomalies are calculated as departures from the 1985-1995 mean.

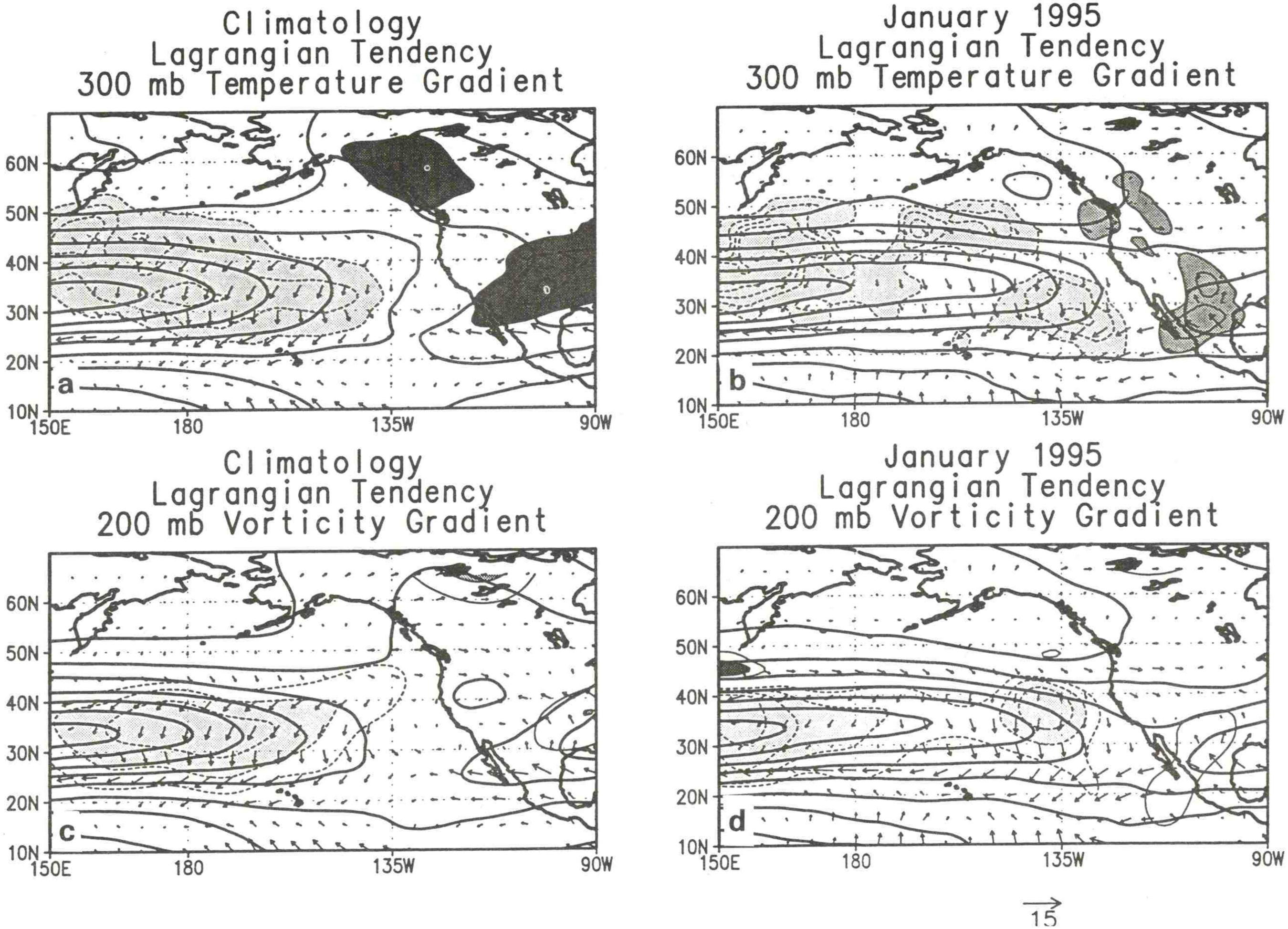

Fig. 2. (Left) January climatological mean, and (Right) January 1995 mean fields. Top panels (a, b) show the Lagrangian tendency of the 300-hPa potential temperature gradient (shaded, interval is 2 x 10^{-11} K $(ms)^{-1}$, beginning with ±4 x 10^{-11} K $(ms)^{-1}$) overlayed with zonal wind contours (thick, interval is 10 ms^{-1}). Bottom panels (c, d) show the Lagrangian tendency of the 200-hPa absolute vorticity gradient (shaded, interval is 1 x 10^{-16} $m^{-1}s^{-2}$, beginning with ±2 x 10^{-16} $m^{-1}s^{-2}$) overlayed with zonal wind contours. In all panels, positive tendencies are shaded dark and contoured solid. Negative tendencies are shaded light and contoured dashed. All panels show the corresponding ageostrophic wind vector at 200 hPa. Climatology values are calculated from the mean of the individual monthly January values between 1985-1995.

The result was a shift to the eastem North Pacific of the area of diffluent geostrophic flow and baroclinic forcing (Figs. 1d, 2b, d) which drives the jet exit region, and a nearly complete elimination of these conditions near the date line in the vicinity of the climatological jet exit region. Thus, air parcels migrating across the central North Pacific experienced virtually no deceleration and meridional displacement, resulting in a more zonal orientation to the jet and a concurrent downstream extension of the jet and accompanying vorticity (and divergence) distribution to the eastem North Pacific.

5. CONCLUSIONS

1. A primary extratropical atmospheric response to ENSO is an eastward extension of the Pacific jet to well east of the date line, along with an eastward shift in the normal jet exit region to the eastem North Pacific.

2. This response is baroclinic, and appears to be ultimately linked to an eastward extension of enhanced convection and associated heating anomaly to the central equatorial Pacific. In particular, these conditions strengthen the north-south thermal gradient at low latitudes and reduce the zonal asymmetries normally observed in the temperature field over the central and east-central subtropical North Pacific.

3. This altered thermal pattem favors a more zonally symmetric height field and geostrophic wind field across the lower extratropics of the central North Pacific, and a more diffluent geostrophic flow over the eastem North Pacific.

4. The subsequent interaction between the midlatitude baroclinic zone and this anomalous geostrophic flow field in the subtropics acts to shift the Pacific jet exit region and its attendant meridional/ vertical circulations to the eastem North Pacific.

5. This evolution represents a massive baroclinic change in the extratropical wind and mass fields over the North Pacific, and results in an extension of the Pacific jet and accompanying vorticity (and divergence) distribution to well east of the date line.

6. This large-scale alteration of the jet and its attendant circulations appears to serve as the catalyst for the generation of low frequency height anomalies which subsequently extend downstream over North America.

7. This extratropical height anomaly pattem during January 1995 (Fig. 3) is remarkably similar to the composite Northem Hemisphere wintertime midlatitude circulation during ENSO (not shown), and actually reflects a de-amplification of the primary climatological mean wave features throughout the region (Fig. 3).

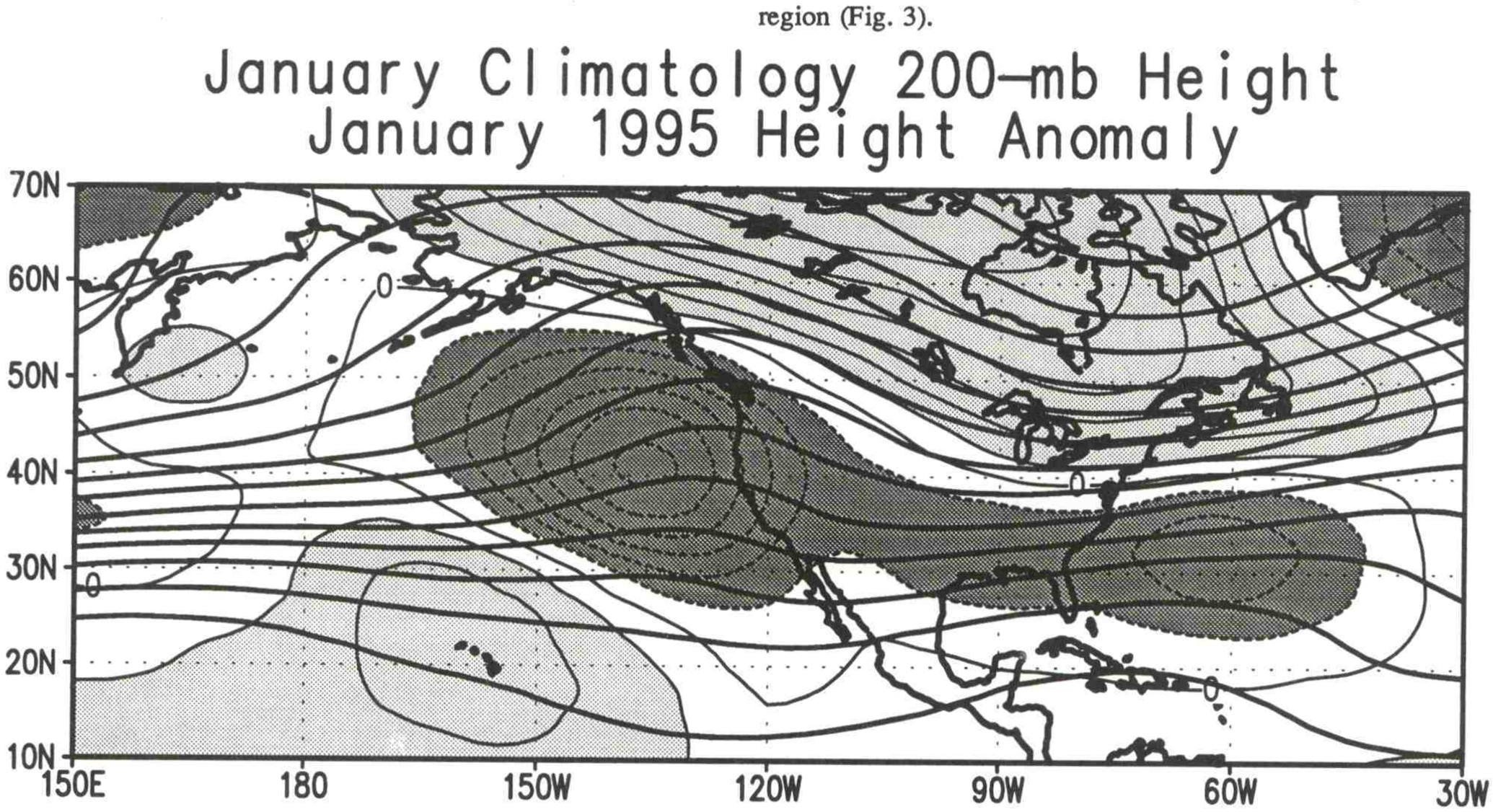

Fig. 3. January 1995 height anomalies at 200-hPa (shading and light contours), overlayed with *climatological* mean 200-hPa height contours (thick). Contour interval of height anomalies is 60 m, with ±30 m contour also plotted. Contour interval of heights is 120 m. Positive anomalies are shaded dark and contoured solid. Negative anomalies are shaded light and contoured dashed. Height anomalies are calculated as departures from the 1985-1995 January mean.

Physical Mechanisms for the 1995 California Floods

Michiko Masutani
Research and Data System Corporation, Greenbelt, Maryland 20770

And

Kingtse C. Mo
NCEP/NWS/NOAA, Washington D.C., 20233

1. Introduction

The west coast of the United States receives most of the rainfall from October to April which is an important water resource throughout the year. During the 1994/ 1995 winter, record rainfall reported in January and March caused wide spread floods and mud slides.

Several studies (Schonher and Nicholson 1989, Cayan and Webb 1992, and Cayan and Redmond 1994) have investigated the large scale circulation patterns and forcing related to the California floods. They found that heavy rainfall is likely to occur during the type one warm ENSO events, but floods do occur during non ENSO years. The 1994/95 winter was classified as a warm ENSO event. The warm sea surface temperature anomalies (SSTAs) greater than 1 °C in the equatorial Pacific appeared during November, but floods did not start until late December. During March, heavy rainfall was reported when the warm SSTAs had already subsided.

In this paper, the 1994/95 California floods and related circulation patterns are examined. Physical mechanisms responsible for the floods are proposed and are tested by diagnosing the GCM experiments.

2. Circulation anomalies during the 1994/95 winter

The total daily rainfall (Fig.1) summed over seven California stations (San Diego,Los Angeles, San Francisco, Blue Canyon, Sacramento, Riverside and Red Bluff) shows near normal rainfall during November and December. There were two intense rainfall periods in January. Rainfall was about normal during February, but heavy rain returned during March.

To describe the oceanic conditions during the 1994/95 winter, the area-mean SSTAs are shown in (Fig.2). The tropical SSTAs in the central Pacific were above 1.5 °C from November to the end of January and then gradually decayed. During March, the SSTAs were near normal. Meanwhile, in the Indian ocean, SSTAs nearly stayed between 0.9 and 1.1°C throughout the period. In the North Pacific, warm SSTAs persisted during December but returned to normal during January.

The evolution of upper level circulation is represented by the 200 hPa zonal wind anomalies (Fig.3). During the flooding periods, the subtropical jet in the North Pacific was strong and extended all the way to the west coast of the United States. The synoptic eddies located at the exit region of the jet brought rain to California.

3. Proposed Mechanisms

Based on the observational results, we propose the following causes for the California floods:

1. Tropical convection in the central Pacific over the warm SSTAs causes the intensification of the local Hadley circulation, which in turn provides a forcing to move the subtropical jet eastward. After the jet moves to the new location near the west coast of the United States, the synoptic eddies at the exit region of the jet caused rain.
2. During December, the warm SSTAs in midlatitudes prevented the jet from moving eastward, so California was dry. The flooding started only after the SSTAs in the North Pacific diminished.

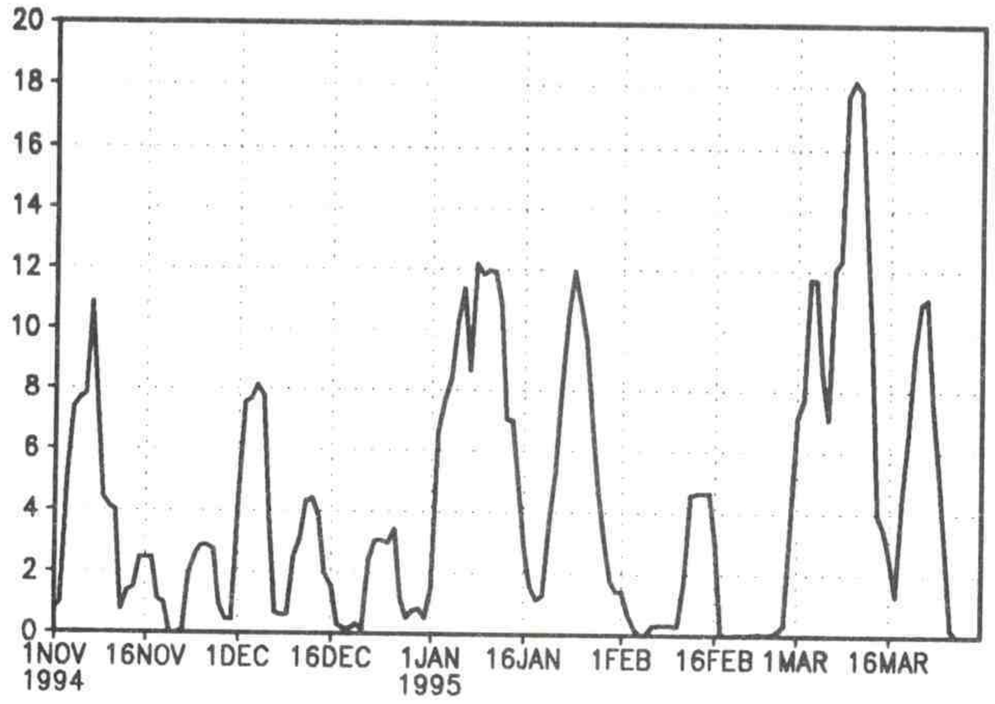

Fig.1 Total rainfall summed over seven stations on the California Coast. (mm/day.)

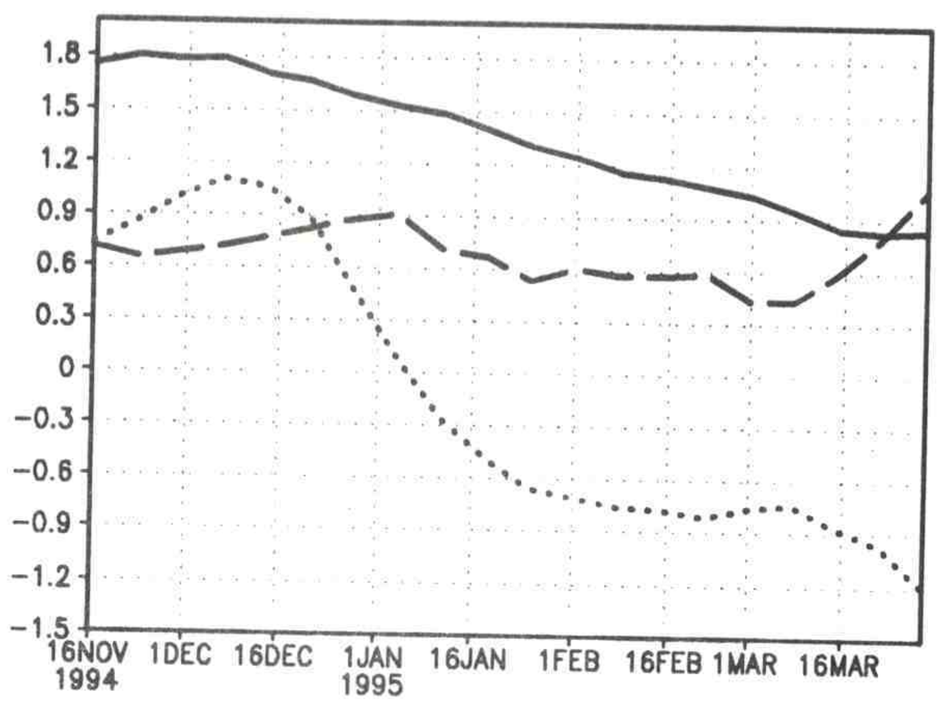

Fig.2 Three week running mean weekly SST anomaly from climatology in central Pacific(5S-5N, 180W-150W) (Solid), Pacific midlatitude (30N-40N,170W-135W) (Dashed), and Indian Ocean (5S-5N, 60E-90E).

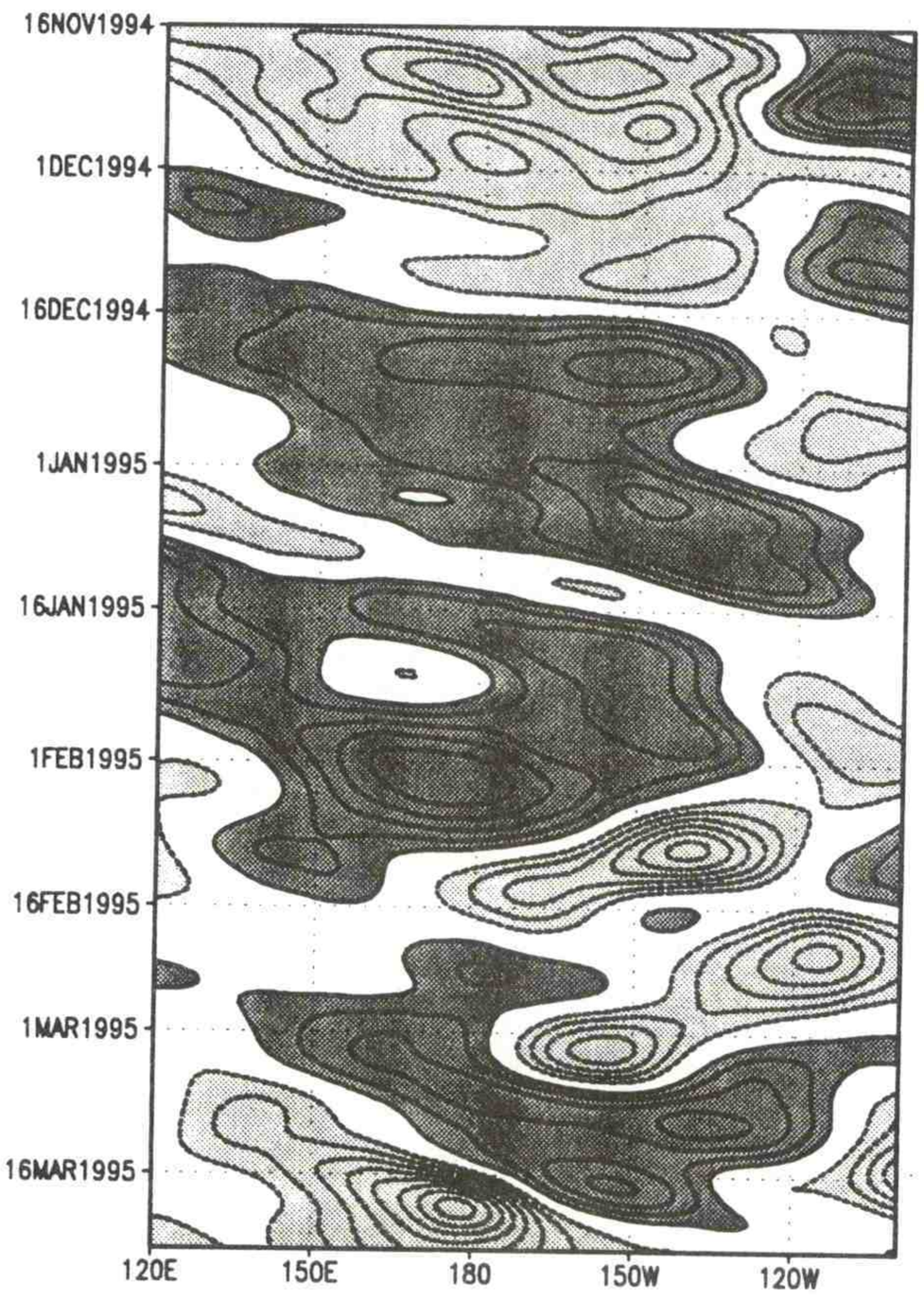

Fig.3. Time-longitude section (30N-40N) of 10 day low-pass filtered 200hPa zonal wind anomaly. Contour interval: 5m/s. Zero contours are omitted.

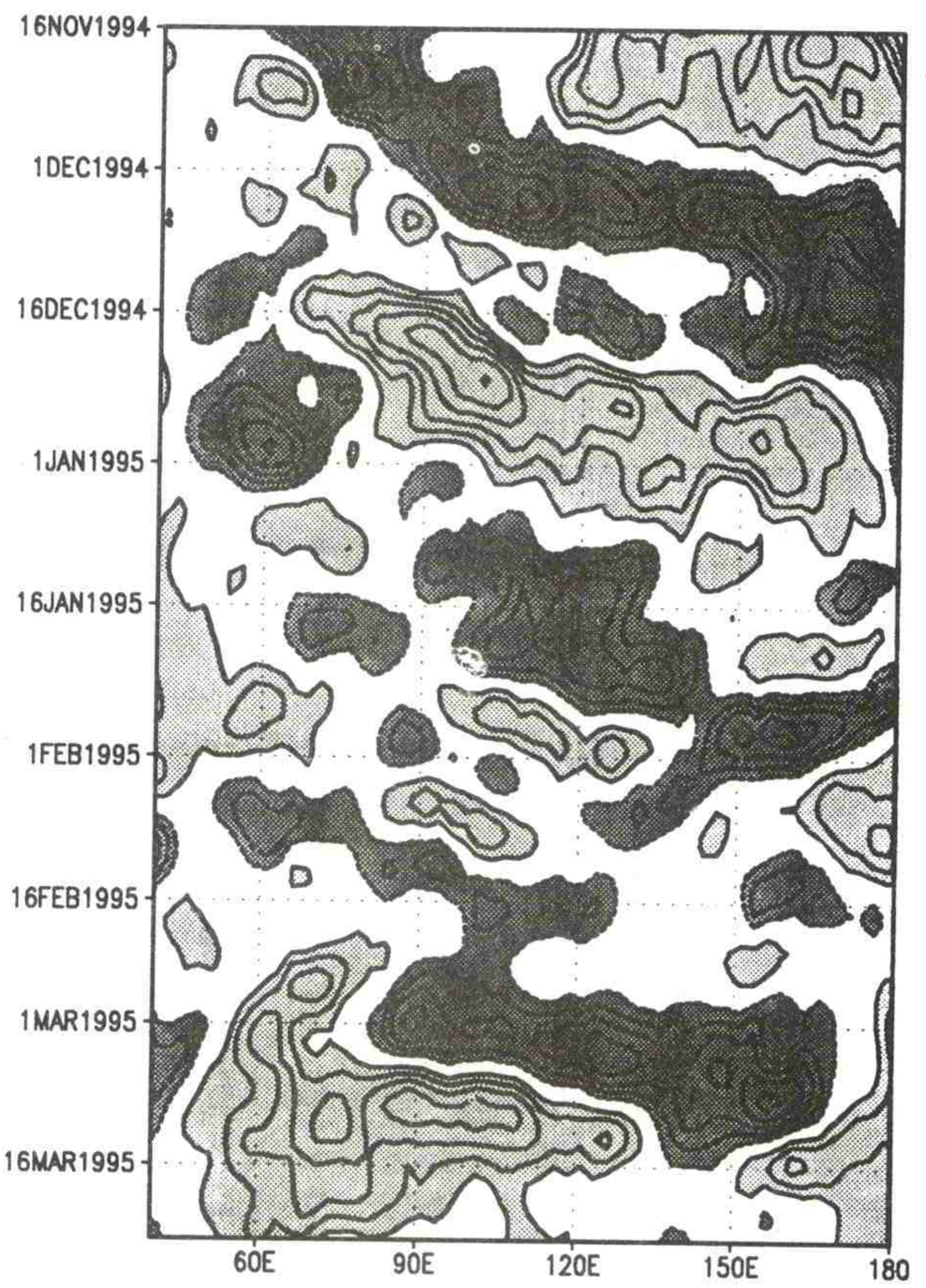

Fig.7 Time-longitude section (10S-10N) 10 day low-pass filtered OLR anomaly. Contour interval $10Wm^{-2}$. Values less than $10Wm^{-2}$ are dashed and shaded darker. Values larger than $10Wm^{-2}$ are shaded lighter. Zero contours are omitted

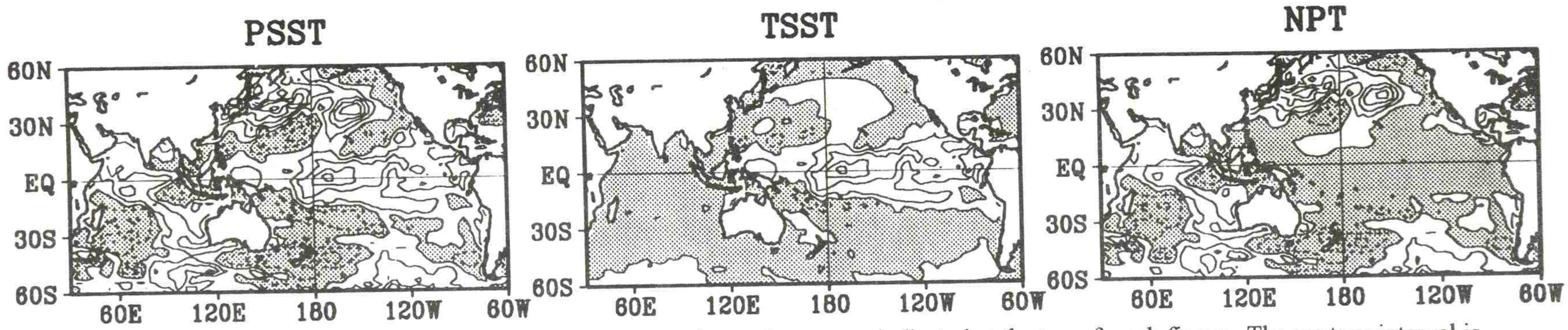

Fig.4 SST anomaly used for the GCM experiments. The names of experiments are indicated at the top of each figure. The contour interval is 0.5°C. Negative values are shaded.

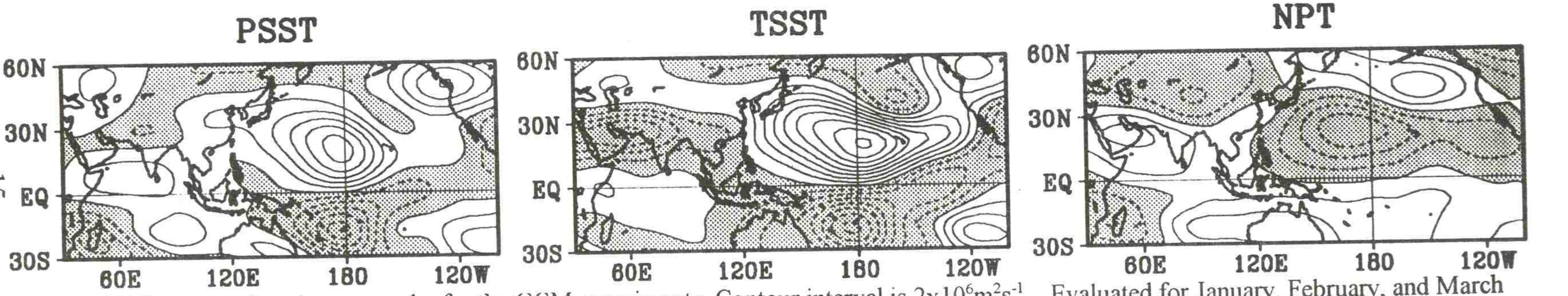

Fig.5 200hPa stream function anomaly for the GCM experiments. Contour interval is $2 \times 10^6 m^2 s^{-1}$. Evaluated for January, February, and March mean. Negative values are shaded.

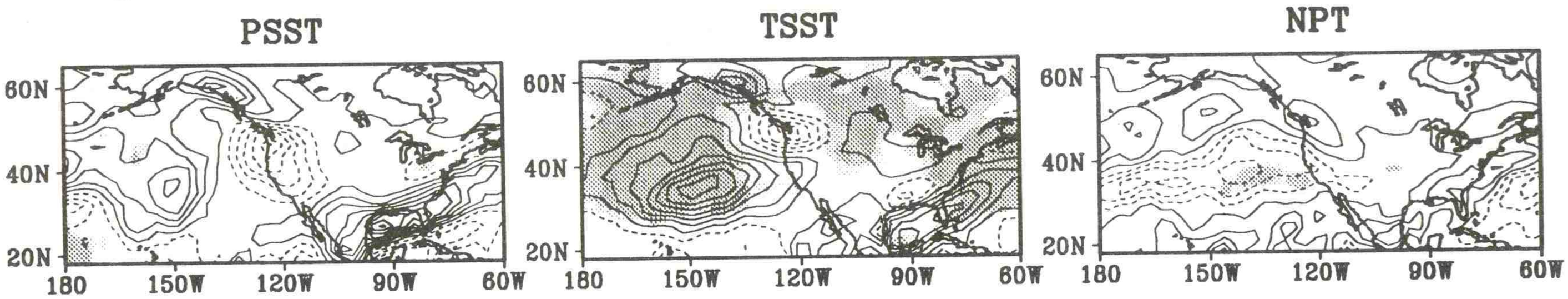

Fig.6 Rainfall anomaly over the United States and its statistical significance of the GCM results. Contour interval is 10mm/month. Evaluated for January, February, and March mean. More than10% significance is shaded lightly, more than 5% significance is shaded darker.

3. During March, the intensified tropical convection in the central Pacific and suppressed convection in the Indian ocean were responsible for the shift of the subtropical jet. The heating pattern was associated with the tropical intra-seasonal oscillation.

The above hypotheses are tested by diagnosing GCM experiments.

4. GCM experiments

We diagnose the GCM experiments performed for the NCEP seasonal prediction. (Ji , Kumer and Leetmaa, 1994) The model was integrated from 15 Nov, 1994 to the end of March 1995. The SSTAs were fixed during the integration so there is no feedback between the atmosphere and oceans. The seasonal cycle for climatological SSTs was added to form daily SSTs. The initial conditions are obtained from a balanced state from previous GCM integration. For each set, there were nine integrations with slightly different initial conditions to form an ensemble. Results reported here are from the seasonal ensemble means for the winter season. Anomalies were obtained by subtracting the model's climatology from a 12-year integration. There are three sets of experiments to examine the responses to different SSTAs. Including all SSTA, PSST experiment (Fig.4a), no eastward extension of the jet (Fig.5a) and no floods in California (Fig. 6a) are produced. The TSST experiments with SSTAs in the central Pacific (Fig.4b) only shows the eastward extension of the jet (Fig. 5b) and significant positive rainfall anomalies along the California coast (Fig.6b). The NST experiments with the tropical SSTAs removed (Fig.4c) but with warm SSTAs in both midlatitudes and in the Indian ocean show dry California (Fig.6c). Jin and Hoskins (1995) suggested that heating anomaly in Indian Ocean and tropical Pacific cause oposite circulation over thw PNA region. Reverse sign in stream function in Fig.5a and Fig.5c support this relation and suppress the rainfall in California. Midlatitude warm SSTA is also block the jet which caused by central Pacific SST and cause dry California in PSST experiment.

5. The March episode

In March, the SSTAs in the central Pacific were near normal so the floods were not caused by the SSTAs. During that winter, the OLR anomalies showed strong intraseasonal oscillations in the tropics. Fig.7 shows intensified tropical convection in the central Pacific and suppressed convection in the Indian ocean, which may provide forcing needed to shift the subtropical jet eastward. Rain followed afterwards.

Acknowledgments:

We would like to thank Dr. Ming Ji to make the GCM data avaliable to us, Dr. George Kiladis to give us the OLR data and Dr. Ants Leetmaa for stiulationg discussion. This work is partially supported by by the Office of Global Programs, NOAA.

Reference

Cayen, D. R., and K. T. Redmond 1994: ENSO influences on atmospheric circulation and precipitation in the western United States. *Proceedings of the tenth Annual Pacific Climate (PACLIM) Workshop*, April 4-7, 1993. California.p5-26.

Ji, M,, A, Kumer, and A. Leetmaa, 1994: A multiseason climate Forecaset system at the National Meteorological Center. *Bul. Amer. Met. Soc.*, 75, 569-577.

Jin, F.-F., and B.J. Hoskins, 1995: The response to tropical heating in baroclinic atmosphere. *J.Atmos. Sci.* 52, 307-319.

Kahya, E., and J. A. Dracup 1994: The influences of type I El Nino and La Nina events on steamflows in the Pacific southwest of the United States. *J. Climate* 7,965-976.

Sardeshmukh, P. D., and B. J. Hoskins 1988: The generation of global rotational flow by steady idealized tropical divergence. *J. Atmos. Sci.*, 45, 1228-1251.

Schonher, T., and S. E. Nicholson 1989: The relationship between California rainfall and the ENSO events. *J. Climate* 2, 1258-1269.

ENSO CYCLE MODULATION OF TRANSIENT BEHAVIOR OVER THE PACIFIC-NORTH AMERICAN SECTOR

Zhiyuan Dai and Eugene M. Rasmusson
University of Maryland
College Park, MD 20742

1. INTRODUCTION

Using 13 years (79-92) of twice daily NMC 200 mb wind analyses, we have re-examined the nature of transient behavior over the North Pacific-North American sector in terms of its relationship to and modulation by the ENSO cycle throughout the year. Band-pass filtering and envelope functions are used to characterize the baroclinic storm tracks (2-6 day band) and determine their relationship to and possible coupling with 6-14 day and lower frequency variability. Year-to-year variations in these features are in turn examined to identify relationships with ENSO cycle variations in the seasonally averaged circulation.

2. RESULTS

Composites were formed for the three years when OLR in the central Pacific equatorial index area routinely published in the Climate Diagnostics Bulletin (5° N-5° S; 160° E-160°) were a maximum (diminished convection) and a minimum (enhanced convection). Overall, there was little persuasive evidence during this 13 year period of a significant ENSO cycle modulation of the time averaged circulation or transient activity in this sector during the warm season. In contrast, the cold season relationships were quite pronounced. Therefore, the remainder of the discussion will be limited to the winter season (DJF) composites.

The strong modulation of the westerly flow by the ENSO cycle is well illustrated by Figure 1. The zonal wind field is more zonally uniform during the warm phase as the Pacific jet extends eastward across Baja California to form a continuous westerly maximum between the Pacific to the North Atlantic jets, and equatorial easterlies extend eastward into the eastern Pacific. During the cold phase, the axis of maximum westerlies splits into two branches of more or less equal magnitude in the jet exit region of the central North Pacific, in a manner reminiscent of synoptic blocking situations. The low-latitude branch of the westerlies is associated with the equatorial westerly duct in the central and eastern Pacific, which develops during the Northern Hemisphere cold season. A similar but weaker equatorial duct appears in the Atlantic.

Previous observational studies e.g. Kiladis and Weickmann (1992) support the conclusions based on modeling and theoretical studies that the Pacific jet acts as a waveguide for transient activity, and the equatorial duct is the preferred latitude belt for tropical-extratropical transient interaction (Kiladis and Weickmann (1992), Tomas and Webster (1994). The modulation of these features by the ENSO cycle therefore makes this sector a particularly interesting area for examining the relationships between ENSO cycle on transient activity and the time-averaged circulation.

Figures 2 and 3 illustrate the cold season modulation of transient activity by the ENSO cycle, and its' relationship to changes in the time-averaged zonal flow. The primary ENSO cycle modulation of the 2-6 day band can be summarized as an intensification and eastern extension of the North Pacific storm track during the ENSO warm phase. This is associated with increased winter and springtime precipitation and storminess across Northern Mexico and the southern U.S. The correspondence between the changes in the storm track and the changes in the jet configuration is consistent with the role of the Pacific jet as a waveguide.

The ENSO cycle modulation of the 6-14 day transient activity involves significant changes in both branches of the westerlies in the jet exit region (Figure 3). Warm phase activity diminishes in the extreme northeast Pacific, and in the south central North Pacific. The diminished warm phase activity over the low-latitude Pacific seems clearly related to the narrowing and weakening of the equatorial duct which is in contrast to the small changes in the 2-6 day band, where there is little southeastward extension of transient activity into the deep tropics of the central and eastern North Pacific during either phase of the ENSO cycle. The 6-14 day band composites are consistent with previous studies e.g. Kiladis and Weickmann (1992), which showed equatorward propagation of 6-14 day transients into the westerly duct from the jet exit region.

4. CONCLUSIONS AND COMMENTS

(1) Interannual modulation of the time-averaged circulation and transient activity in the North Pacific-North American sector associated with the ENSO cycle is strongly seasonal in nature. No significant effect of the ENSO cycle could be identified during the Northern Hemisphere warm season in the extratropical latitudes of this sector. In contrast, cold season differences in the time averaged state and transient activity between cold and warm phases of the ENSO cycle were large and consistent.

(2) The cold season modulation of 2-6 day and 6-14 day transient activity in this sector that can be associated with the ENSO cycle is substantial and consistent with what would be expected from previous studies of "normal" behavior. The 6-14 day transients strongly reflect changes in the strength and position of the Pacific jet, and in the character of the western Pacific equatorial duct. The changes in the 2-6 day "storm tracks" primarily reflect changes in the strength and position of the Pacific jet, and show only a weak sensitivity to the ENSO-related changes in the western Pacific equatorial duct. The implication is that of much more vigorous extratropical-tropical propagation in the 6-14 day band.

REFERENCES

Berbery, E. H., and C. S. Vera, 1995: Characteristics of the Southern Hemisphere winter storm track with filtered and unfiltered data. *J. Atmos. Sci.*, (Accepted).

Chang, E. K. M., 1993: Downstream development of baroclinic waves as inferred from regression analysis. *J. Atmos. Sci.*, **50**, 2038-2053.

Kiladis, G. N., and K. M. Weickmann, 1992: Extratropical forcing of tropical Pacific convection during northern winter. *Mon.Wea.Rev.*, **120,** 1924-1938.

Tomas, R. A., and P. J. Webster, 1994: Horizontal and vertical structure of cross-equatorial wave propagation. *J. Atmos. Sci.*, **51,** 2209-2220.
Wallace, J. M., G. H. Lim, and M. L. Blackmon, 1988: Relationship between cyclone tracks, anticyclone tracks, and baroclinic waveguides. *J. Atmos. Sci.*, **45**, 439-462.
Webster, P. J., and J. R. Holton., 1982: Cross-equatorial Response to Middle-latitude forcing in a zonally varying basic state. *J. Atmos. Sci.*, **39,** 722-733.

Figure Captions

Fig. 1. ENSO warm and cold phase composite for December-February (DJF) for the 200 mb zonal wind component derived from the NMC global analyses. (a) ENSO warm phases: 82-83, 86-87, 91-92; (b) ENSO cold phases: 81-82, 84-85, 88-89;
(c) difference between (a) and (b). Zonal wind speeds greater than 20m/s are shaded. Contour interval is 10m/s for (a) (b), 5m/s for (c).
Fig. 2. The ENSO warm and cold phases composite of DJF seasonal mean variance of 2-6 days bandfiltered streamfunction at 200 mb based upon NMC global analyses. (a) ENSO warm phases: 82-83, 86-87, 91-92; (b) ENSO cold phases: 81-82,84-85,88-89; (c) difference between (a) and (b). The shading areas are zonal wind with speed greater than 20 m/s for (a) (b), 5m/s for (c). Contours are for the 2-6 days bandfiltered varinace. Contour interval is 1.E+13 m**4/s**2.
Fig. 3. Same as Fig. 2 except for 6-14 days bandfiltered streamfunction.

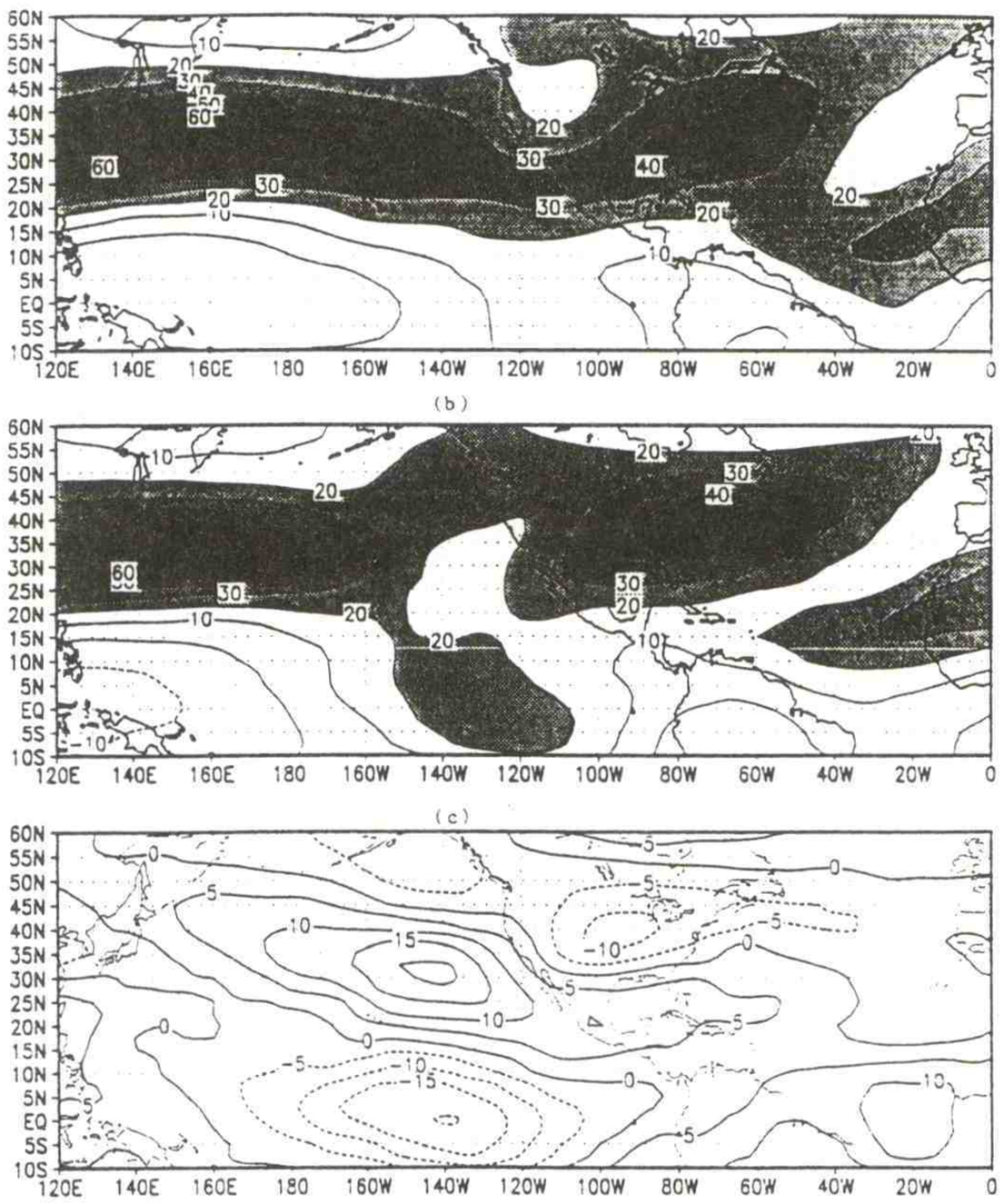

Figure 1

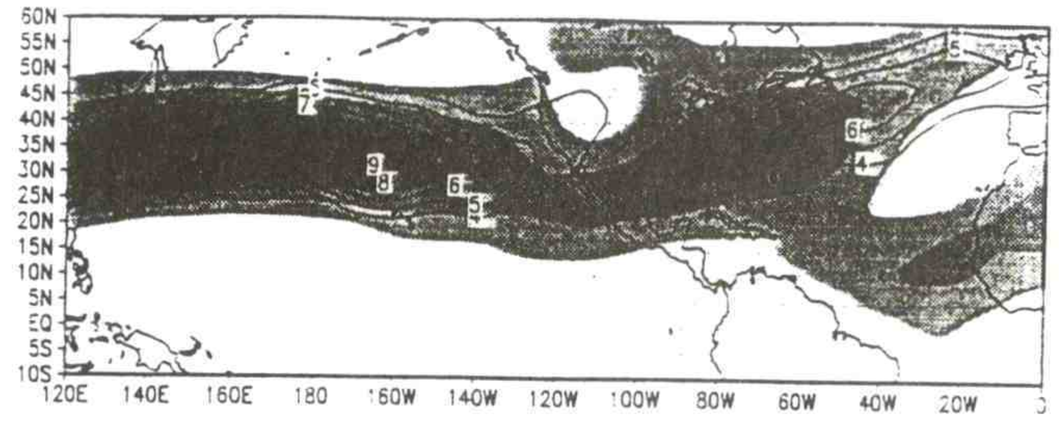

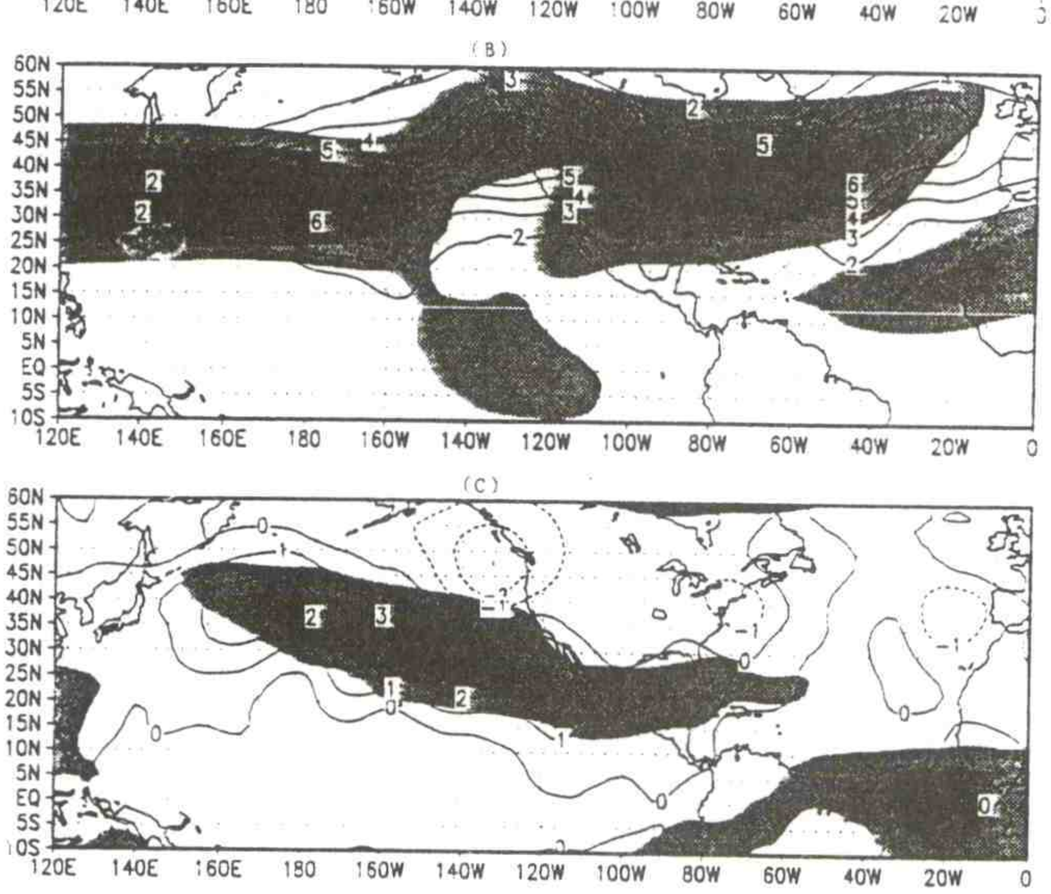

Figure 2

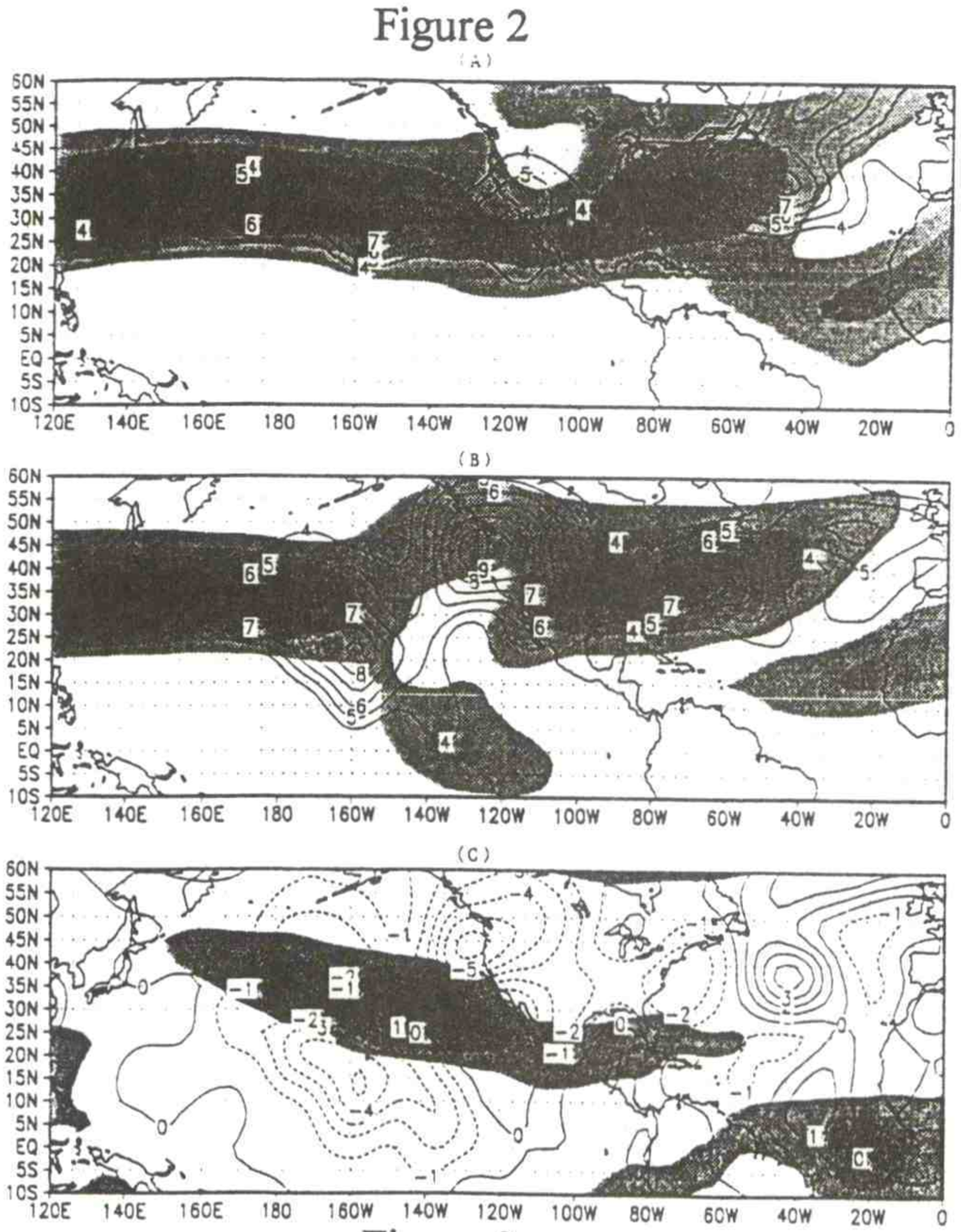

Figure 3

PERSISTENT NORTH PACIFIC CIRCULATION ANOMALIES AND INTERHEMISPHERIC TELECONNECTIONS

R. W. Higgins[1], S. D. Schubert[2] and K. C. Mo[1]

1. Climate Prediction Center, NOAA/NWS/NCEP
2. NASA/Goddard Laboratory for Atmospheres

1. INTRODUCTION

Several recent observational studies have examined the possible role of tropical heating in the development of persistent North Pacific (PNP) atmospheric circulation anomalies but little evidence has been found for a strong tropical connection. A number of observational studies have focused on the potential coupling between the extratropical circulation and the tropical Intraseasonal Oscillation (IO). Many results suggest a mutual forcing over the Indian Ocean and western Pacific in which extratropical wave trains both force and respond to tropical convection. The above studies are also not inconsistent with the idea that, on the intraseasonal time scale, the tropics act primarily to excite extratropical modes which then grow through energy exchanges with the mean jet.

The current study uses two recent 9-year (1985-1993) global reanalysis datasets produced by the Data Assimilation Office of NASA/Goddard (hereafter DAO) and the NCEP/NCAR (hereafter NCEP) to re-examine the role of the tropics in the initiation of PNP anomalies and to examine potential interhemispheric coupling of the events. Evidence is presented that PNP anomalies often appear in response to a pattern of tropical heating anomalies linked to the IO.

2. DATA ANALYSIS

The dataset from each reanalysis consists of daily averages of 500 mb heights, 200 mb winds, precipitation, and column integrated moisture flux for the eight 90-day NH winter seasons (starting 1 December) from 1985/86-1992/93. Daily averages of the NOAA Satellite OLR (gridded to 2.5^0 x 2.5^0) are used to validate the precipitation anomalies. Persistent flow anomaly cases are selected using the threshold crossing procedure discussed in Dole and Gordon (1983). The 500 mb height anomaly magnitude and duration criteria are (+100 m, 10 days) and (-100 m, 10 days) for positive and negative persistent anomaly cases, respectively. To obtain the index used to select persistent anomaly cases, we first remove the time mean and the first two harmonics of the seasonal cycle (computed from the average of all 8 years in each assimilation separately) from daily values of the 500 mb height field. Next we apply a lowpass filter which removes periods less than approximately ten days. Case onset and termination dates are determined from the resulting time series at a "key" point (50° N, 162.5° W) where large numbers of persistent anomaly cases occur. For the eight winter period 14 PNP events were identified (6 Pacific positive (PP) and 8 Pacific negative (PN)) and all 14 were common to both reanalyses. The average duration of the PP events is 20.3 (20.5) days and of the PN events is 19.6 (17.2) days in the DAO (NMC) reanalysis. Overall, 99.2% (87.9%) of the days satisfying the PP (PN) anomaly criteria are in common in the composites. Composite evolution fields for cases of a given sign are obtained by averaging over all of the cases relative to the time when the height anomaly at the key point first crosses the threshold value; this time is designated as the onset day or day 0. Anomalies are calculated with respect to the seasonal cycle (defined above) for each reanalysis separately. Prior to compositing, a lowpass filter which retains periods greater than approximately 10 days has been applied to all fields.

3. CIRCULATION FEATURES DURING PNP EVENTS

Composite mean (days 0-9) 200 mb streamfunction anomalies represented as the composite difference in the DAO (Fig. 1a) and the NMC (Fig. 1b) reanalyses show that the main PNP anomaly center is accompanied by significant downstream development across North America and subtropical anomalies of opposite sign. Overall, the streamfunction composites in both reanalyses may be interpreted as a single basic pattern with one polarity associated with blocking and the other with a regionally intensified zonal flow. Note that the subtropical anomalies tend to be zonally elongated in both reanalyses. Comparison of streamfunction and precipitation

composites (Fig. 1c) shows that the PNP anomalies are accompanied by precipitation anomalies consistent with the shift of the storm track. There are also positive precipitation anomalies to the south of the main anomaly center in the subtropics and a dipole like feature along the equator (poles over Indonesia and near the dateline). These tropical precipitation anomalies and the associated streamfunction anomalies are indicative of a strong connection between the PNP anomalies and the tropics.

Validation of the reanalysis precipitation anomalies is given in Fig. 2 which shows a comparison of the composite mean precipitation anomalies from both reanalyses to the composite mean NOAA / OLR anomalies (Fig. 2c; these data were not assimilated) for the same dates used to produce the NMC composite. The patterns of OLR and precipitation anomalies correspond quite well with the dipole like feature along (and just south of) the equator apparent in each panel. Weickmann (1983) and Lau and Chan (1985) showed that the intraseasonal variability of tropical convection is dominated by a similar dipole heating anomaly which suggests that the IO may be linked to (many of) these events.

During PNP events the tropical heating anomalies are linked to variations in the strength and location of the jet as demonstrated in Fig. 3 which shows the composite mean 200 mb vector wind and precipitation anomalies expressed as the composite difference in the NMC reanalysis (Fig. 3a) and the time mean 200 mb vector wind and its divergence from the NMC reanalysis (Fig. 3b); the patterns are similar in the DAO reanalysis. Relative to the seasonal mean, there is weaker convergence (divergence) in the jet entrance (exit) region which tends to weaken (strengthen) the thermal gradients consistent with the jet retraction during the mature phase.

Another view of the tropical / extratropical teleconnection during PNP events is presented in Fig. 4 which shows that the mature phase is associated with a coherent pattern of anomalous moisture transport spanning the tropics and extratropics in the NMC reanalysis (Fig. 4a); as the PNP anomalies mature they gradually push equatorward into the subtropics leading to modified tropical moisture transports that help to reinforce the associated tropical precipitation anomalies. The divergence of the anomalous moisture flux (Fig. 4b) during the mature phase shows that there is convergence (divergence) of moisture into the regions of heating (cooling) in both reanalyses. Calculations of the separate terms in the moisture flux convergence show that the pattern is primarily determined by the anomalous circulation.

4. LINKAGE TO THE TROPICAL IO

We have already shown that a significant fraction of PNP events are associated with tropical heating anomalies during the mature phase. Figure 5 shows that these tropical heating anomalies along (and just south of) the equator are actually present *more than a week prior to the development of the PNP anomalies*. Throughout the evolution they show a tendency to move slowly eastward with the dynamical signal associated with the tropical IO. After onset, the heating anomalies in the NH subtropics become particularly well organized apparently in response to modifications to the moisture transport as the mature PNP anomalies extend into the tropics (Higgins and Schubert 1995).

In the immediate vicinity of the tropical heating, the upper tropospheric response is characterized by a cyclonic (anticyclonic) pair of circulation anomalies that is almost symmetric about the equator and located near the node of the tropical forcing (Fig. 6). This configuration of heating and circulation anomalies has been noted in other studies. After onset a couplet of the opposite phase tends to appear, though the SH member is quite weak. Both reanalyses show extratropical wave trains extending from the tropical western Pacific towards North America prior to onset. Examination of the evolution of individual cases suggests that this wavetrain is relatively insensitive to the exact longitudinal position of the heating, and is surprisingly similar even when the heating shifts to near the dateline over the central Pacific as during the mature phase of an ENSO episode. Prior to onset there is also evidence of a similar, though weaker and less well defined, wave train in the SH.

The largest differences between the reanalyses are in the details of the pre-onset evolution; while both reanalyses show large amplitude streamfunction anomalies directly north of the tropical forcing plus a series of downstream anomalies extending towards North America, the amplitudes and phases are considerably different. In view of the slightly different position and intensity of the heating anomalies in each case, the difference in the evolution of the initial NH response is not too surprising. The best agreement between the reanalyses occurs during and after the onset phase. During this time local energy sources associated with the mean flow, synoptic-scale eddies and / or effective Rossby wave sources which develop outside the tropics and also depend on the mean flow appear to be important. However, the remarkably similar evolution in the extratropics after onset suggests that the tropical forcing acts primarily as a catalyst for the development of the PNP anomalies, and that the most useful predictors of PNP events may lie not in the extratropics but in the tropical western and central Pacific.

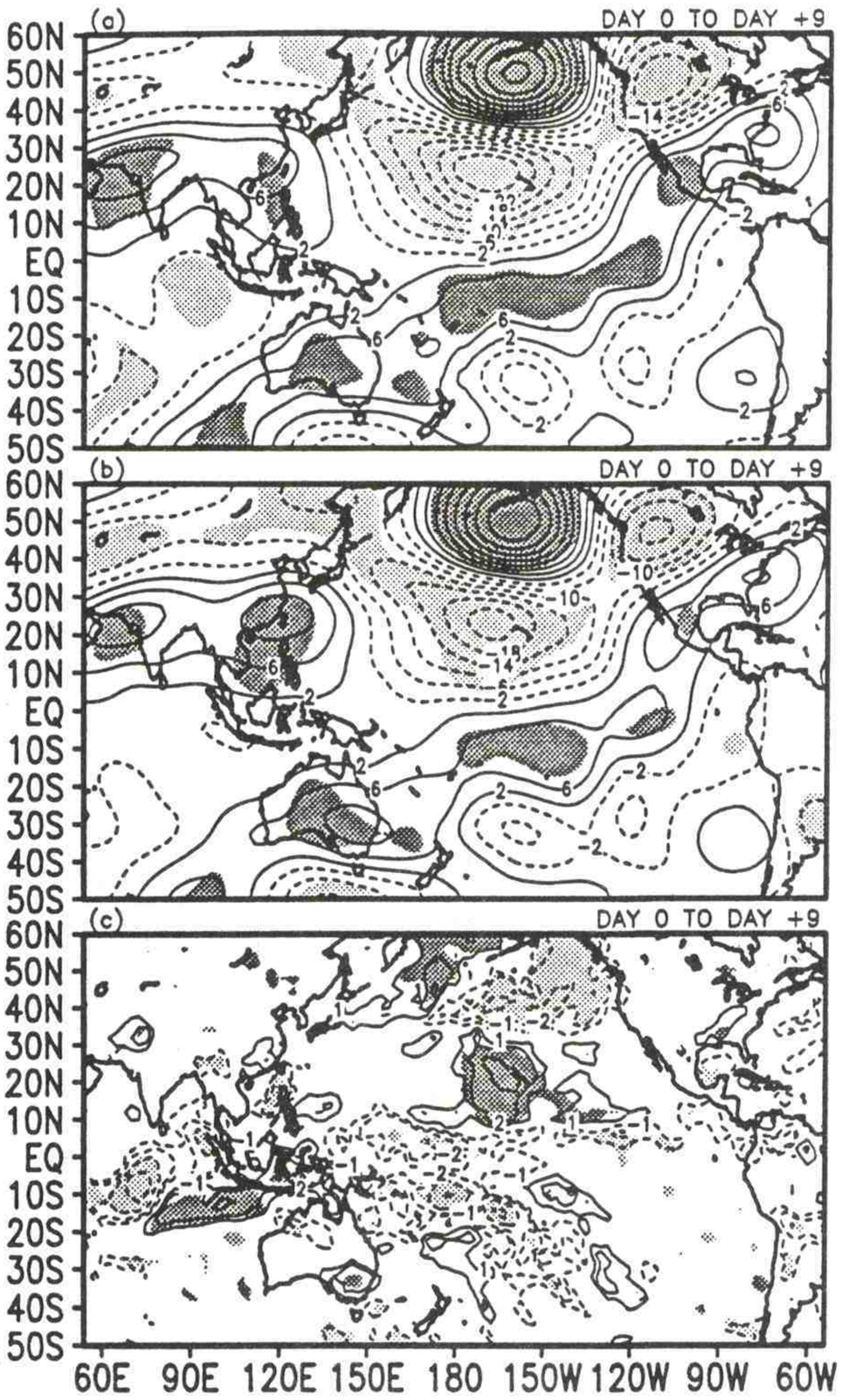

Fig. 1. Composite (days 0-9) 200 mb streamfunction anomalies (Units: 10^{+6} m^2 s^{-1}) in (a) DAO and (b) NMC and precipitation anomalies (Units: mm day^{-1}) in (c) DAO represented as the difference between the 6 PP and 8 PN cases from DJF. Dark (light) shading indicates positive (negative) anomalies significant at the 95% level.

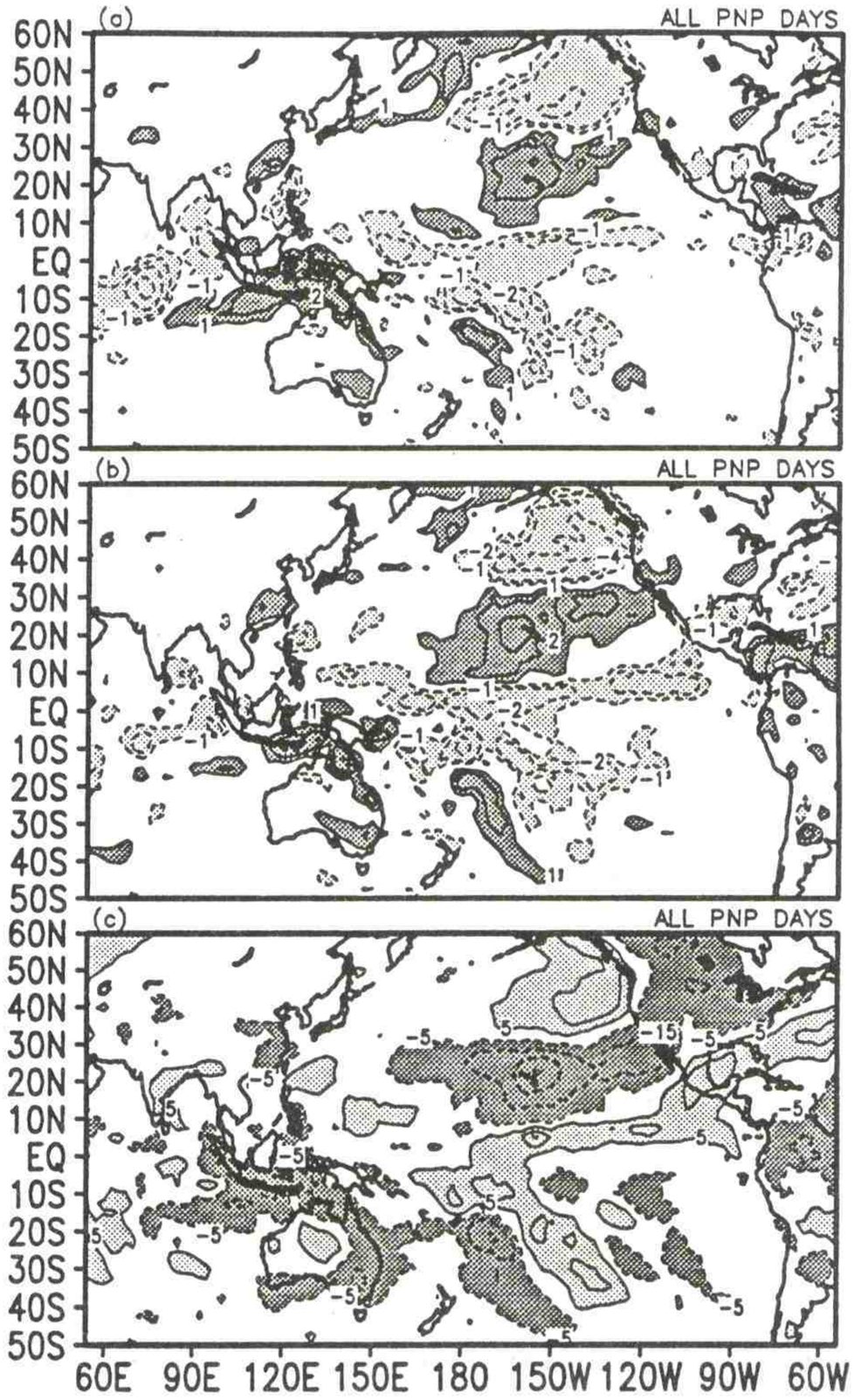

Fig. 2. Composite (all PNP days) precipitation anomalies (Units: mm day^{-1}) in (a) DAO and (b) NMC and (c) NOAA/OLR anomalies (Units: W m^{-2}) represented as the difference between the 6 PP and 8 PN cases from DJF.

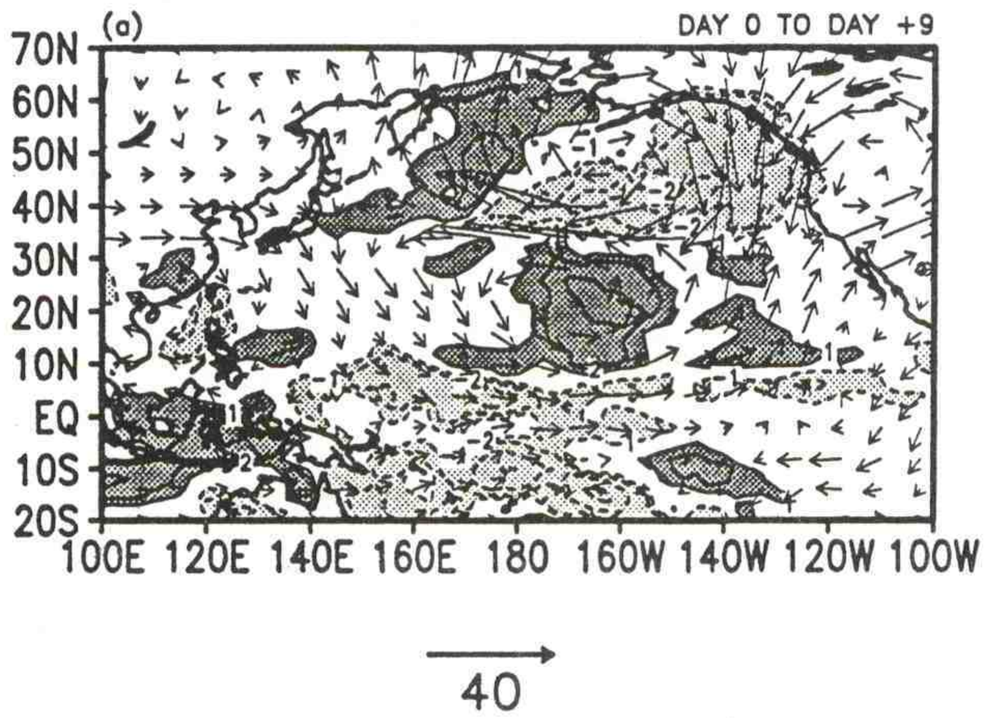

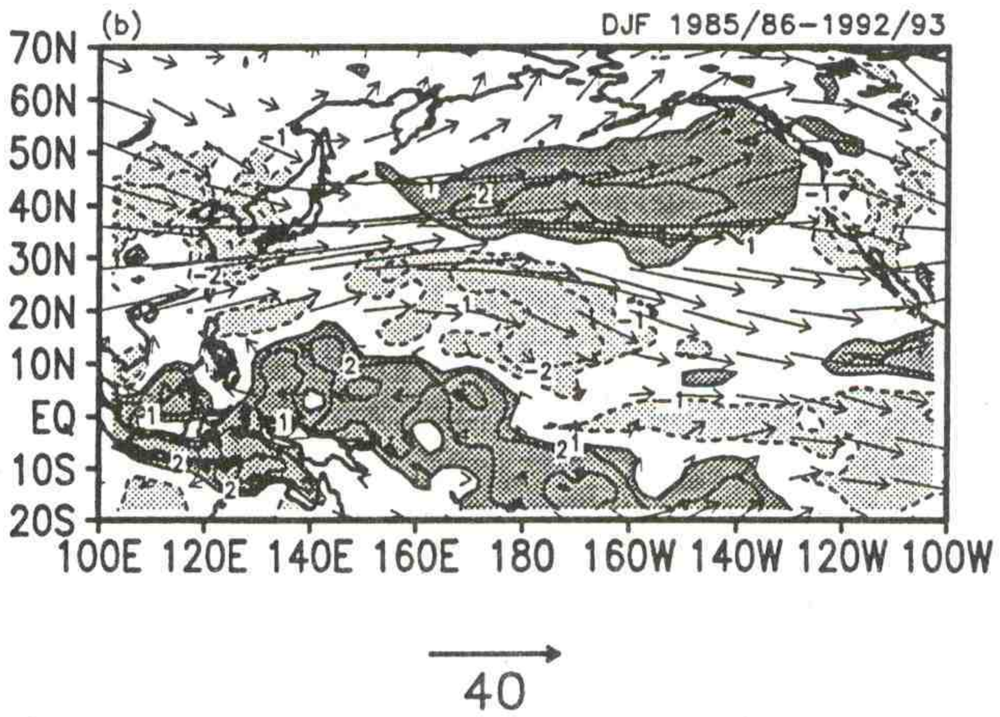

Fig. 3. (a) Composite (days 0- 9) 200 mb vector wind (Units: m s^{-1}) and precipitation anomalies (Units: mm day^{-1}) represented as the difference between the 6 PP and 8 PN cases from DJF in the DAO reanalysis. (b) Time mean (DJF 1985/86-1992/93) 200 mb vector wind and its divergence (Units: 10^{-6} s^{-1}) in the DAO reanalysis.

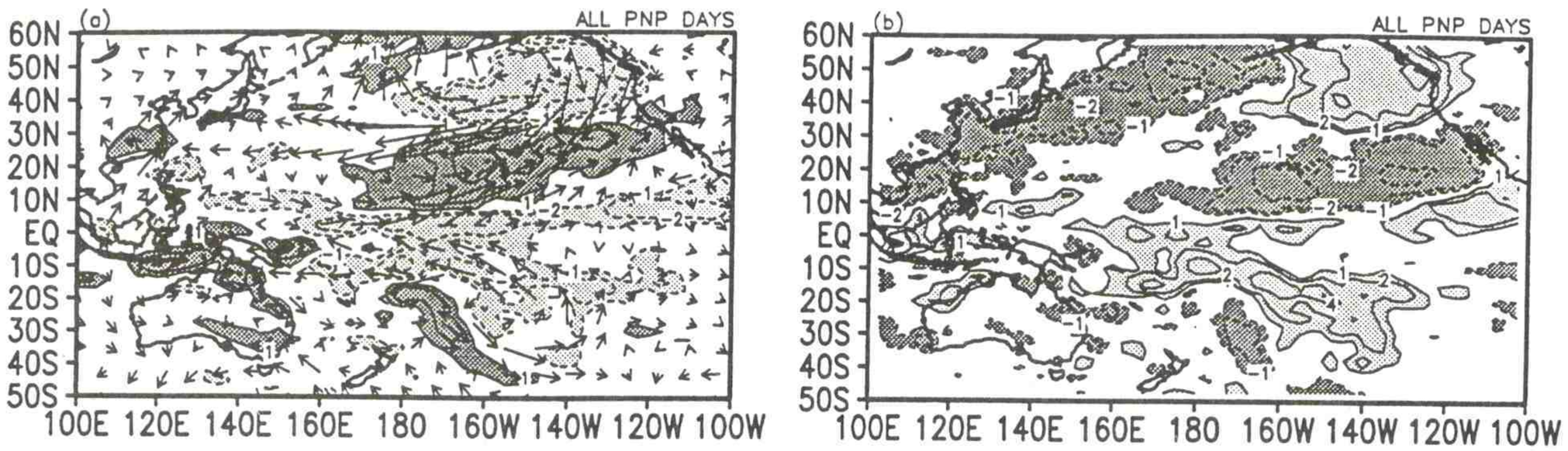

Fig. 4. (a) Composite (all PNP days) vertically integrated moisture flux anomalies (vectors; Units: m s^{-1} g kg^{-1}) and precipitation anomalies (Units: mm day^{-1}) represented as the difference between the 6 PP and 8 PN cases from DJF in the NMC reanalysis. (b) Divergence of the composite moisture flux anomalies (Units: 10^{-6} g kg^{-1} s^{-1}).

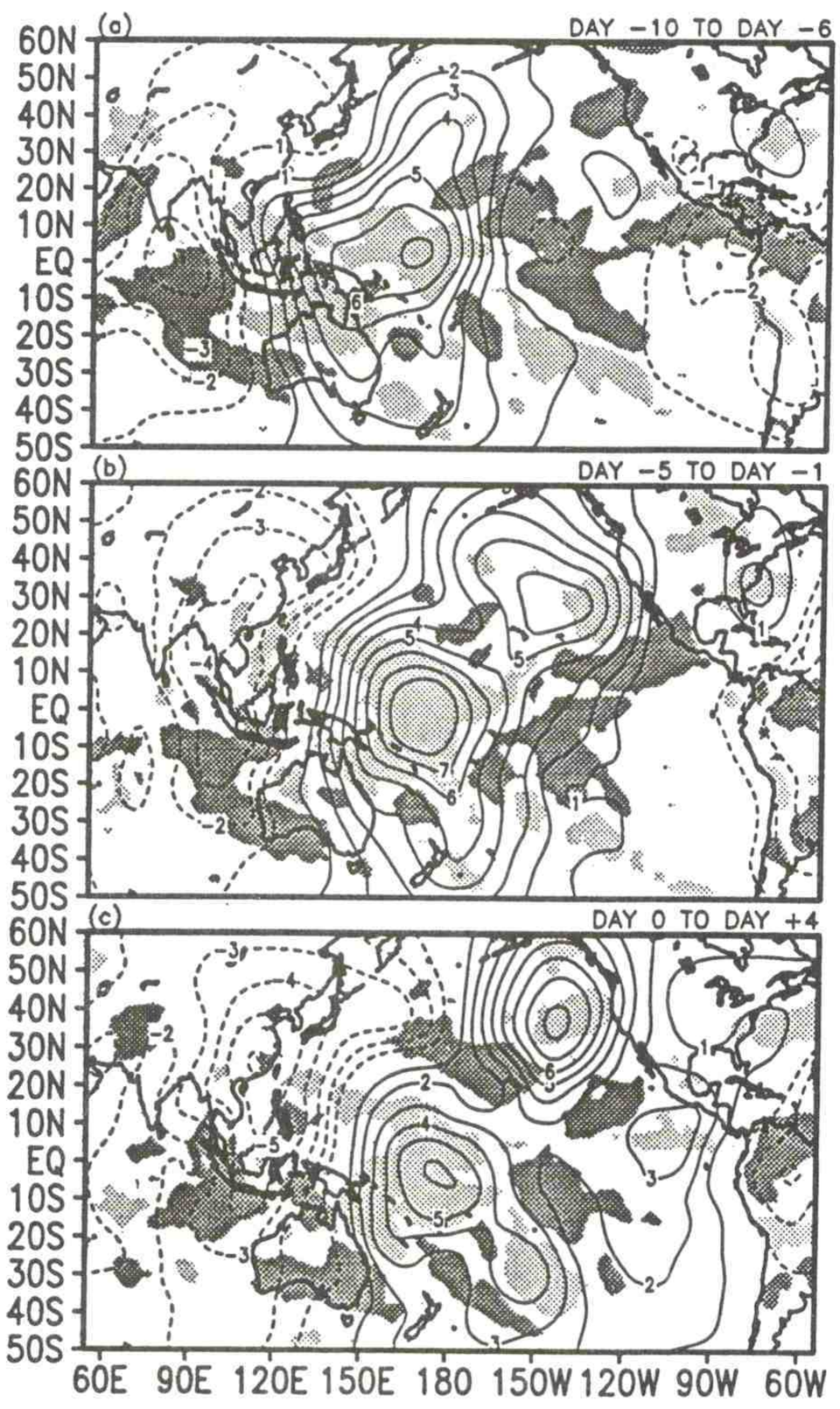

Fig. 5. Map sequence of composite 5-day average 200 mb velocity potential (Units: 10^{+6} m^2 s^{-1}) and NOAA/OLR (shaded; Units: W m^{-2}) anomalies represented as the difference between the 6 PP and 8 PN cases from DJF in the NMC reanalysis. For the NOAA/OLR, the lighter (darker) shades correspond to areas where the values are greater than 5 W m^{-2} (less than -5 W m^{-2}).

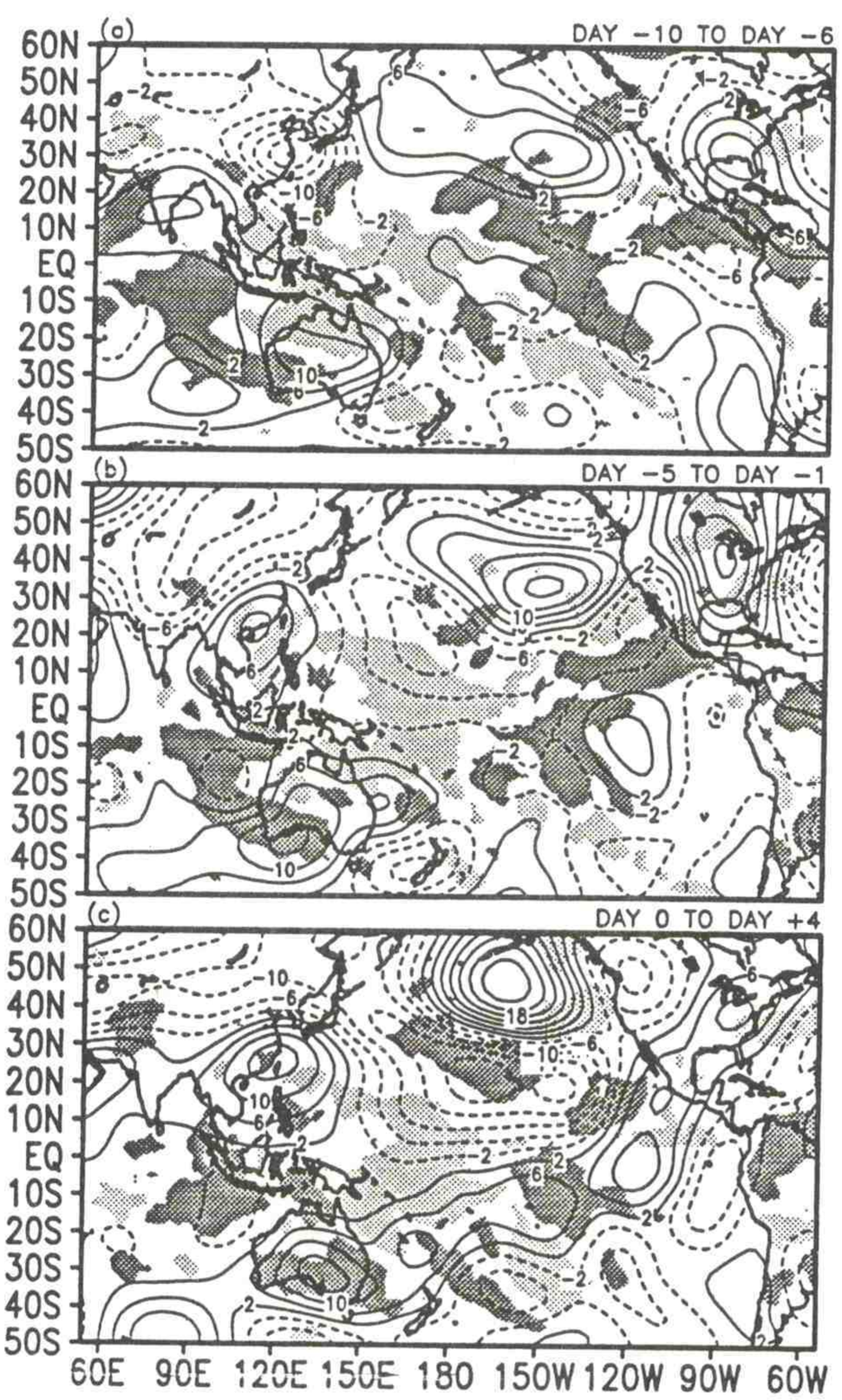

Fig. 6. Map sequences of composite 5-day average 200 mb streamfunction (Units: 10^{+6} m^2 s^{-1}) and NOAA/OLR (shaded; Units: W m^{-2}) anomalies represented as the difference between the 6 PP and 8 PN cases from DJF in the NMC reanalysis. For the NOAA/OLR, the lighter (darker) shades correspond to areas where the values are greater than 5 W m^{-2} (less than -5 W m^{-2}).

TROPICAL-EXTRATROPICAL INTERACTION AS REVEALED BY ANALYSIS OF COMBINED OCEAN-ATMOSPHERE VARIABILITY DURING 1985-1994

Ying Dai and Sumant Nigam

Cooperative Institute for Climate Studies (CICS), Department of Meteorology
University of Maryland, College Park, MD 20742 [Email: ydai@atmos.umd.edu]

1. INTRODUCTION

There is both empirical and modeling evidence that extratropical low-frequency variability is connected to tropical SST (heating) anomalies. The dynamical mechanism underlying this linkage is still being understood. The extratropical wintertime variability is characterized by geographically well-defined patterns such as the Pacific North-American pattern whose forcing and excitation is still a contentious issue. A leading hypothesis posits that Pacific storm-track displacements and attendant transient vorticity-flux modulation significantly impact the quasi-stationary circulation over the Pacific North American region, but the cause(s) of storm-track displacements during El Nino/La Nino episodes itself remain unclear. The recurrent modes of extratropical low-frequency variability during the northern summer season, and their underlying dynamics has also remained largely unexplored.

2. METHODOLOGY

In order to better understand the dynamical mechanism(s) responsible for the generation of various recurrent variability patterns, we have conducted a rotated principal component analysis (RPCA) of combined variability of both the circulation anomalies and their potential forcing functions. The circulation anomalies include the 200 and 850 mb monthly-mean streamfunction anomalies, while the potential forcing functions include sea-surface temperature anomalies, and the residually-diagnosed diabatic heating anomalies in the lower (700–1000 mb) and upper (200–500 mb) troposphere during the 1985-1994 decade. This 10-year period includes two La Nina (1984/85, 1988/89) and, at least, two El Nino (1986/87, 1991/92) events. This combined analysis is restricted to a 10-year long record on account of the availability of residually-diagnosed diabatic heating (from *un*initialized ECMWF analyses) since Jan. 1985.

As the combined covariance matrix in case of 5 variables consists of 5 auto-covariance and 10 cross-covariance submatrices, the extracted rotated loading vectors should represent coupled variability modes. Prior to being put together, these variables were put on par with each other by normalizing each of them by the square-root of their spatially-averaged variance (as discussed in Nigam and Shen, 1993). The rotated loading vectors and principal components were obtained from a singular value decomposition (SVD) of the combined anomaly matrix.

3. WINTERTIME ANALYSIS

The leading mode of wintertime variability in the 1985-1994 decade is connected to El Nino/La Nina related SST variability, but the streamfunction component of this combined mode is not the canonical PNA pattern, in that, the ridge is located almost over Hudson Bay instead of the Pacific Northwest. The canonical PNA circulation pattern is, in fact, part of a higher-order combined variability mode (Fig. 1) whose SST-component bears little resemblance to El Nino/La Nina connected SST anomalies. This PNA mode appears to be related to extratropical SST anomalies in the Pacific basin, and varies in amplitude

on both the intraseasonal as well as decadal time-scales. The relationship of PNA pattern with the extratropical Pacific SSTs has also been noted by Deser and Blackmon (1995). The lower-tropospheric midlatitude diabatic heating anomaly associated with this mode (Fig. 1) indicates a southeastward shift of the Pacific stormtrack and modulation of the Atlantic stormtrack as well. The considerable similarity between the 200mb North Pacific circulation anomalies present in this mode and the leading El Nino-related mode are, perhaps, responsible for their occasional ambiguous identification.

4. SUMMERTIME ANALYSIS

The leading mode of summertime variability in the 1985-1994 decade, like the leading wintertime mode, is linked to El Nino-related SST variability as evident from inspection of the SST component and the coefficient time series in Fig. 2. The northern summer circulation anomalies are only about half as strong as those associated with the leading wintertime mode, but the streamfunction anomalies in Fig. 2, nonetheless, contain an equivalent barotropic wave-pattern that stretches across the Atlantic from eastern United States to Northern Europe. During the summer of a La Nina year, this mode would result in a ridge over the western United States, and a trough over the eastern half of the U.S. at both 200 and 850 mbs--quite reminiscent of the large-scale circulation anomalies over U.S. during the 1988 summer.

The leading summertime variability mode also vividly illustrates the Asian-monsoon--El Nino linkage in which Indian summer-monsoon rainfall is deficient during the El Nino year, as evident from the presence of an upper-level low and a lower tropospheric high, (and weakened onshore monsoonal flow) over the Indian subcontinent. The associated diabatic heating fields confirm this interpretation.

5. DISCUSSION

Our finding regarding the absence of a direct linkage between El Nino SSTs and the PNA pattern is at variance with the findings of Lau and Nath (1994), who find strong linkage between the 500 mb wintertime geopotential height anomalies and El Nino SSTs during the 1946-1988 period from SVD analysis of the cross-correlation matrix between height and SST fields. To understand the reasons for the discrepancy between observation-based results of Lau and Nath and ours, we conducted SVD analysis of the cross-correlation of 500 mb (and 200 mb) height and SST anomalies during the 1982-1994 period. We find that the leading mode obtained from this analysis is rather similar to that found from the combined RPCA analysis. This suggests that the difference between Lau and Nath's and our results may, perhaps, be due to the different periods being analyzed in these studies.

We are presently extracting the combined variability present in Oort's 1958-1989 analyses to check this. To bring out the connection with stormtrack displacements further, we are also repeating our calculations using the transient-eddy heating anomalies in place of the lower tropospheric diabatic heating anomalies.

REFERENCES

Deser, C., and M. L. Blackmon, 1995: On the relationship between tropical and north Pacific sea surface temperature variations. J. Climate, 8, 1677-1680.

Lau, N. C., and M. J. Nath, 1994: A modelling study of the relative roles of tropical and extratropical SST anomalies in the variability of the global atmosphere-ocean system. J. Climate, 7, 1184-1207.

Nigam, S., and H. S. Shen, 1993: Structure of oceanic and atmospheric low-frequency variability over the tropical Pacific and Indian ocean. Part-I: COADS observations. J. Climate, 6, 657-676.

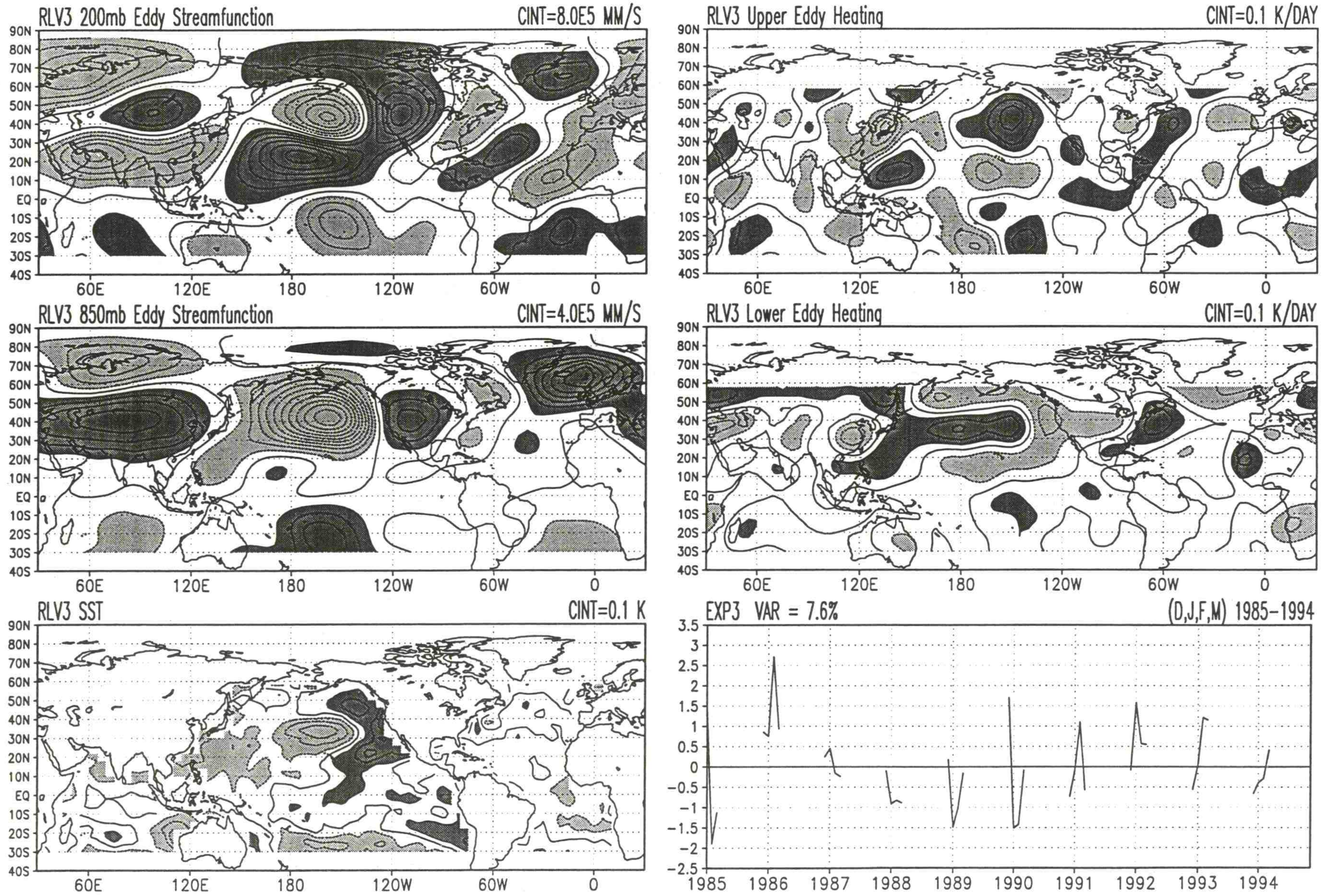

Figure 1. The third leading mode of combined variability of 200mb and 850mb streamfunction, upper-level (200-500mb) and lower-level (700-1000mb) diabatic heating,and SST anomalies during the 1985-94 winter months (Dec, Jan, Feb,& Mar). The contour intervals are shown on top of each panel. Values greater (less) than one contour interval are shaded dark (light) in each panel. This mode explains about 7.6% of the combined domain-averaged variance.

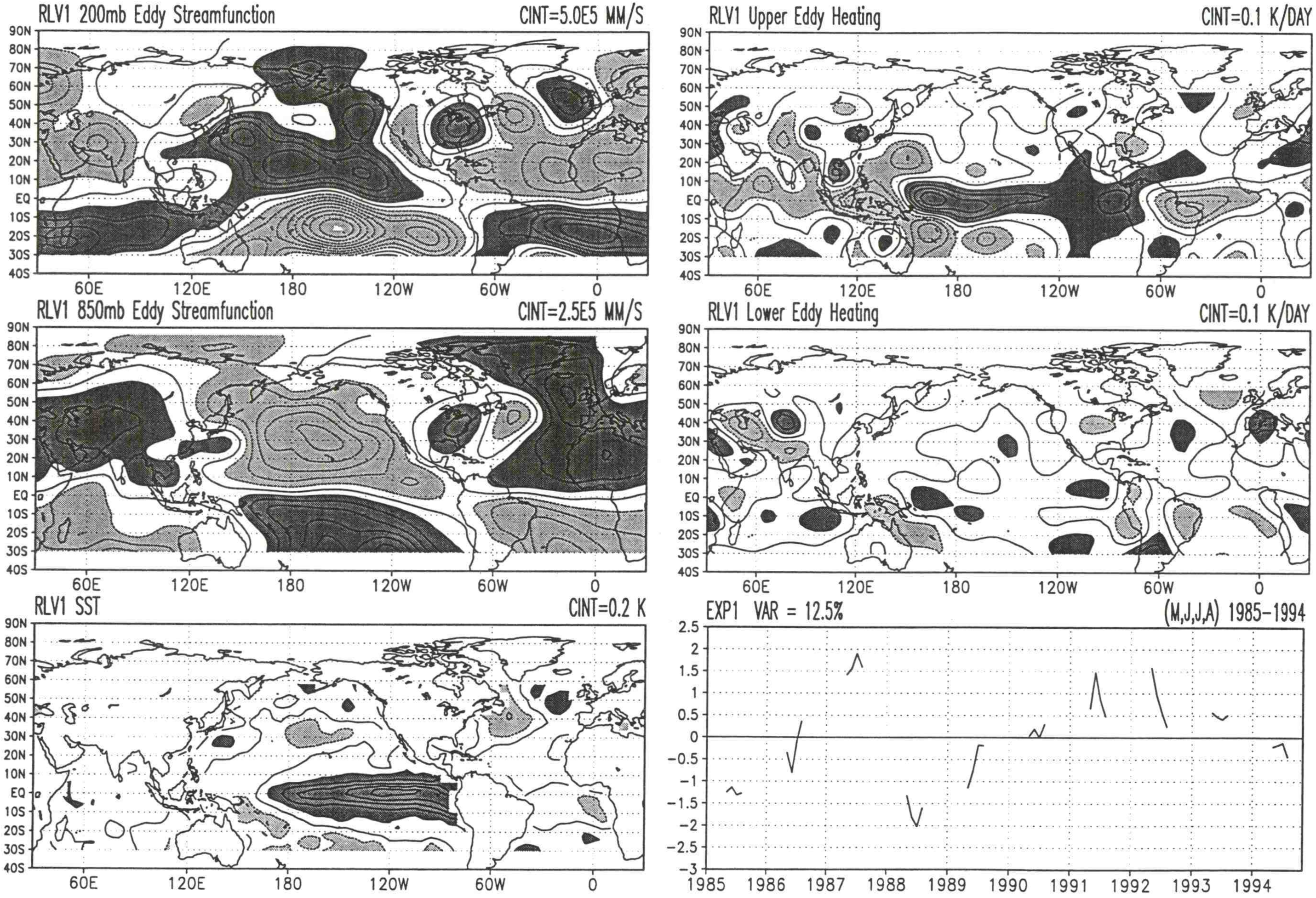

Fig.2. Same ad Fig.1 except for the first leading mode of summer months(May, Jun., Jul., and Aug.). This mode explains about 12.5% combined variance

HADLEY CIRCULATION AS A MODULATOR OF THE WINTER EXTRATROPICAL CLIMATE

Arthur Y. Hou
NASA Goddard Space Flight Center, Greenbelt, Maryland, 20771 USA
(Email: arthur.hou@gsfc.nasa.gov)

SUMMARY

The hypothesis that the Hadley circulation plays an active role in modulating the winter extratropical temperature gradient is investigated using the first five years (1985-1989) of the reanalysis produced by the Goddard Earth Observing System (GEOS-1) Data Assimilation System (DAS) reanalysis and outputs of idealized GCM experiments.

Results from a pair of 1000-day perpetual "northern winter" idealized GCM simulations with no orography show that a stronger cross-equatorial Hadley circulation induced by shifting a prescribed tropical convective heating from the equator to 6°S leads to a statistically significant response in the form of dynamic cooling in the midlatitudes and warming in the high latitudes in the winter hemisphere (Fig. 1). This remote extratropical response reflects a net increase in the poleward heat transport by low-frequency planetary waves and the induced zonal mean circulation in the extratropics, and is associated with an enhanced westerly acceleration of the subtropical jet by the stronger Hadley cell and a poleward shift of the subtropical Rossby-wave source maximum.

The application of the above diagnostics to the GEOS-1 DAS reanalysis reveals that the interannual variation in the zonally-averaged extratropical temperature gradient during the Austral winters from 1985 to 1989 is correlated with the variation in the "Hadley acceleration" (i.e. absolute vorticity flux by the mean meridional circulation) in the subtropics, with correlation coefficients ranging from 0.93 (for Pearson's r) to 1.0 (for Kendall's τ). Shown in Figs. 2a and 2b are June-July-August extratropical temperature anomalies (from the 5-year mean) and the subtropical acceleration and Rossby-wave source anomalies for the Austral winter of 1988. The year-to-year variations in the domain-averaged subtropical acceleration and extratropical temperatures are shown in Fig. 2c.

This study suggests that the extratropical climate depends, in part, upon stochastic generation of low-frequency planetary waves by the divergent circulation in the tropics, whose intensity and structure are sensitive to a small displacement of convective heating from the equator. The implication is that a small change in the land/surface process or forcing by the sea surface temperature could have a significant global impact through an adjustment in the Hadley circulation.

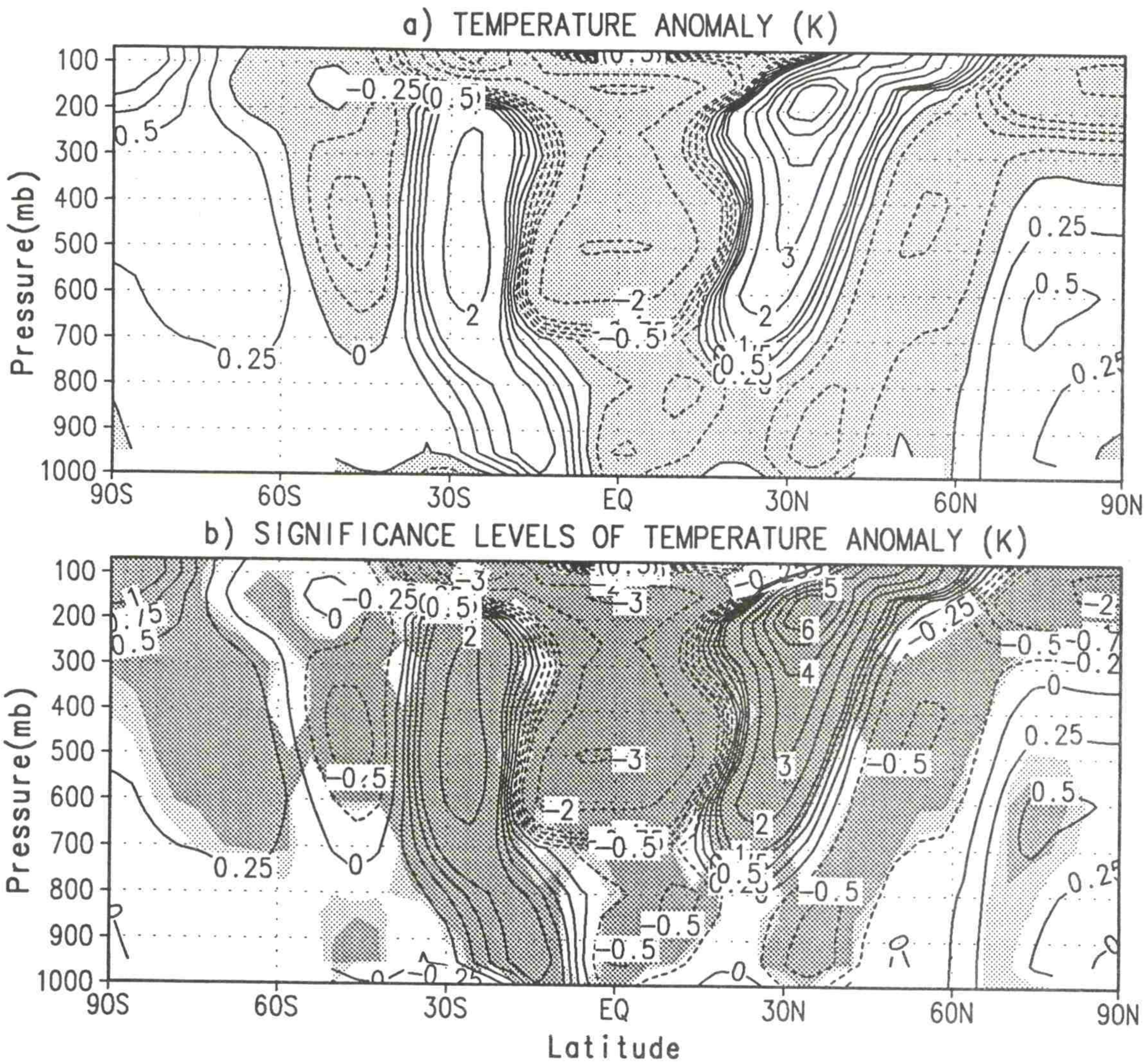

Figure 1. (a) Time-averaged zonal-mean temperature anomaly (in K) associated with a stronger "northern winter" Hadley cell. (b) Significance levels (shaded) of temperature anomalies (contours) according to Student's t-test. Light shade regions exceed 95% and dark shades exceed 99%.

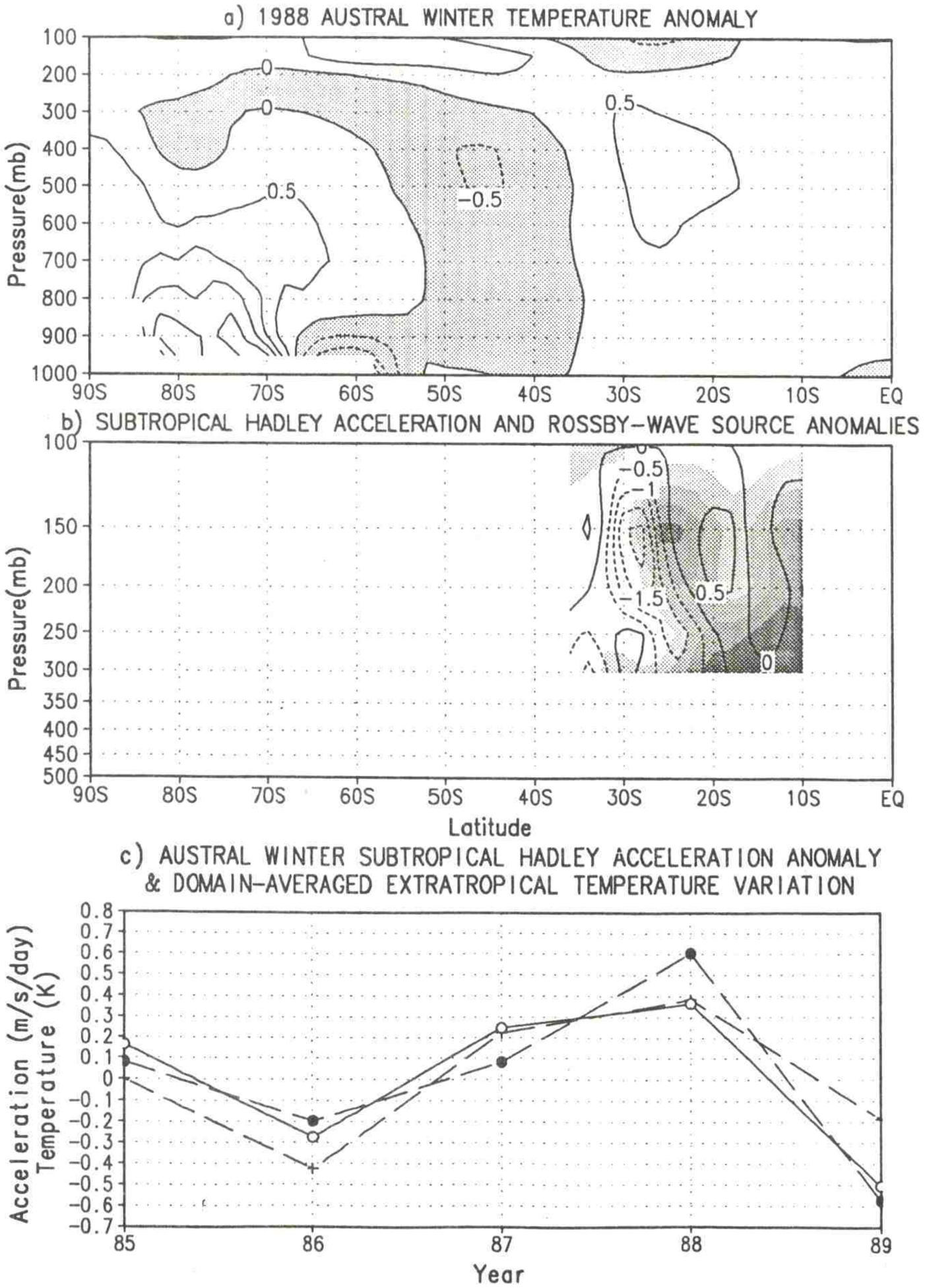

Figure 2. (a) Zonally-averaged temperature anomaly in Kelvin for Austral winter of 1988. (b) Corresponding subtropical Hadley acceleration anomaly (positive values shaded in increments of 0.5 m s^{-1} day^{-1}) and Rossby-wave source anomaly (contours in units of 10^{-11} s^{-2}). (c) Interannual variations in the averaged Hadley acceleration between 150-250 mb and 20°-30°S (open circle), high-latitude temperature anomaly below 400 mb from 60°-90°S ("+"), and a proxy temperature gradient anomaly (closed circle) in terms of the domain-averaged high-latitude temperature anomaly minus the averaged temperature anomaly between 40°-60°S.

The Signature of ENSO in the Midlatitude High-Frequency Variability

Wilhelm May[1] and Lennart Bengtsson[2]

[1]Danish Meteorological Institute, Lyngbyvej 100, 2100 Copenhagen Ø, Denmark
[2]Max-Planck-Institute for Meteorology, Bundesstraße 55, 20146 Hamburg, Germany

In our study we investigate the impact of pronounced Sea Surface Temperature (SST) anomalies in the tropical Pacific linked to the El Niño/Southern Oscillation (ENSO) phenomenon on the atmospheric circulation in the Northern Hemisphere extratropics. We distinguish between various time scales, including changes in the seasonal mean circulation and in the variability on sub-seasonal time scales as well.

The study is based on an ensemble of five individual simulations performed with an atmospheric general circulation model. The model referred to ECHAM3 is a spectral model with triangular truncation at wavenumber 42 (T42) on 19 vertical levels in a hybrid σ-p-coordinate system. A detailed description of the model is given in *Roeckner et al. (1992)*. In each of these simulations a sequence of observed monthly mean SSTs for the period September 1979 through December 1992 is given as lower boundary forcing, but different atmospheric initial conditions are prescribed. This set of simulations has already been used in *May (1994),* where a comprehensive evaluation of ECHAM3 regarding the intra-seasonal variability within the extratropics is given. According to the occurrence of pronounced SST-anomalies in the tropical Pacific, namely the Niño-3 region, we assigned the boreal winters 1982/83, 1986/87 and 1991/92 to be affected by El Niño or warm ENSO-events and the winters 1980/81, 1984/85 and 1988/89 by La Niña or cold ENSO-events. All the other winters were assigned to the control cases.

The anomalous diabatic heating or cooling in the tropical Pacific region linked to the warm and cold ENSO-events, respectively, has a pronounced impact on the time-mean circulation in the Northern Hemisphere extratropics. As an example composites of the seasonal means of the zonal wind component in 300 hPa, indicating the jet streams in the midlatitudes, for the El Niño and the La Niña events are given in Fig. 1.

During the El Niño events the Pacific jet stream is strengthened, and its axis is shifted equatorward. In particular the core of the jet stream, which is located east of Japan, is extending further downstream over the southeastern part of the North Pacific. During the La Niña events the Pacific jet stream is shifted poleward, and relatively strong westerly winds occur over the northeastern part of the North Pacific. In the core of the Pacific jet stream the westerly winds are weaker than during the El Niño events. The Atlantic jet stream, on the other hand, is weakened during the warm ENSO-events and strengthened during the cold ones. Besides, it's axis is shifted equatorward during the El Niño but poleward during the La Niña events. In the European area the distributions reveal relatively strong westerly winds over the northern part of the continent during the cold ENSO-events and further south during the warm ones.

But also the variability on intra-seasonal time scales is affected by the pronounced SST-anomalies in the tropical Pacific related to the ENSO-phenomenon (*May and Bengtsson, 1995*). In particular the activity of the transient fluctuations on synoptic time scales, which are linked to the short baroclinic waves, reveals a marked response. Here, however, we want to describe the interaction between the transient fluctuations on these time scales and the seasonal mean circulation by means of localized Eliassen-Palm-flux diagnostics (*Trenberth, 1986*). This is done in order to investigate, to which extent these transient fluctuations maintain or counteract the anomalous circulation patterns during the ENSO-events. The divergence of the horizontal component of the E-P-flux vectors gives the net forcing of the seasonal mean zonal wind component via barotropic processes, the divergence of their vertical component the forcing via baroclinic processes. These variables derived from the differences of the composites for the El Niño and the La Niña events and the composite for the control cases are shown in Fig. 2.

A comparison of Fig. 2 with the lower panels of Fig. 1 reveals that the transient fluctuations on synoptic time scales tend to maintain the anomalous circulation patterns during the ENSO-events via barotropic processes, but to counteract them via baroclinic processes. That means that during the La Niña events the transient eddies strengthen the westerly winds over the northeastern Pacific via barotropic processes. During the El Niño events, on the other hand, maintain the transients the westerly winds over the southeastern part of the North Pacific. Also over the northern part of North America, which is the entrance region of the Atlantic jet stream, enhance the transient fluctuations the westerly winds during the cold ENSO-events. In the Atlantic/European region maintain the transients the westerly winds over the northeastern Atlantic and northern Europe during the La Niña events, but over the southern part of the continent during the El Niño events. Via baroclinic processes, on the other hand, enhance the transient fluctuations during the El Niño events the westerly winds over the northern Pacific, but also further downstream, in particular over Labrador, where the core of the Atlantic jet stream is located. During the La Niña events weaken the transients the westerly winds in these regions and strengthen them further south. Over central Europe reduce the transient fluctuations the westerly winds during the warm ENSO-events and strengthen them during cold ones.

References:

May, W., 1994: On the intra-seasonal variability within the extratropics in the ECHAM3 general circulation model. *MPI-Report,* **No. 147**, 207 pp.

May, W., Bengtsson, L., 1995: On the extratropical response during El Niño and La Niña in the ECHAM3 general circulation model. Proceedings of the *Nineteenth Annual Climate Diagnostics Workshop in College Park, Maryland*, edited by the National Oceanic and Atmospheric Administration, 59-63.

Roeckner, E., Arpe, K., Bengtsson, L., Brinkop, S., Dümenil, L., Esch, M., Kirk, E., Lunkeit, F., Ponater, M., Rockel, B., Sausen, R., Schlese, U., Schubert, S., Windelband, M., 1992: Simulation of the present-day climate with the ECHAM model: Impact of model physics and resolution. *MPI-Report,* **No. 93**, 172 pp.

Trenberth, K. E., 1986: As assessment of the impact of transient eddies on the zonal flow during a blocking episode using localized Eliassen-Palm flux diagnostics. *J. Atmos. Sci.*, **43**, 2070-2087.

El Niño

La Niña

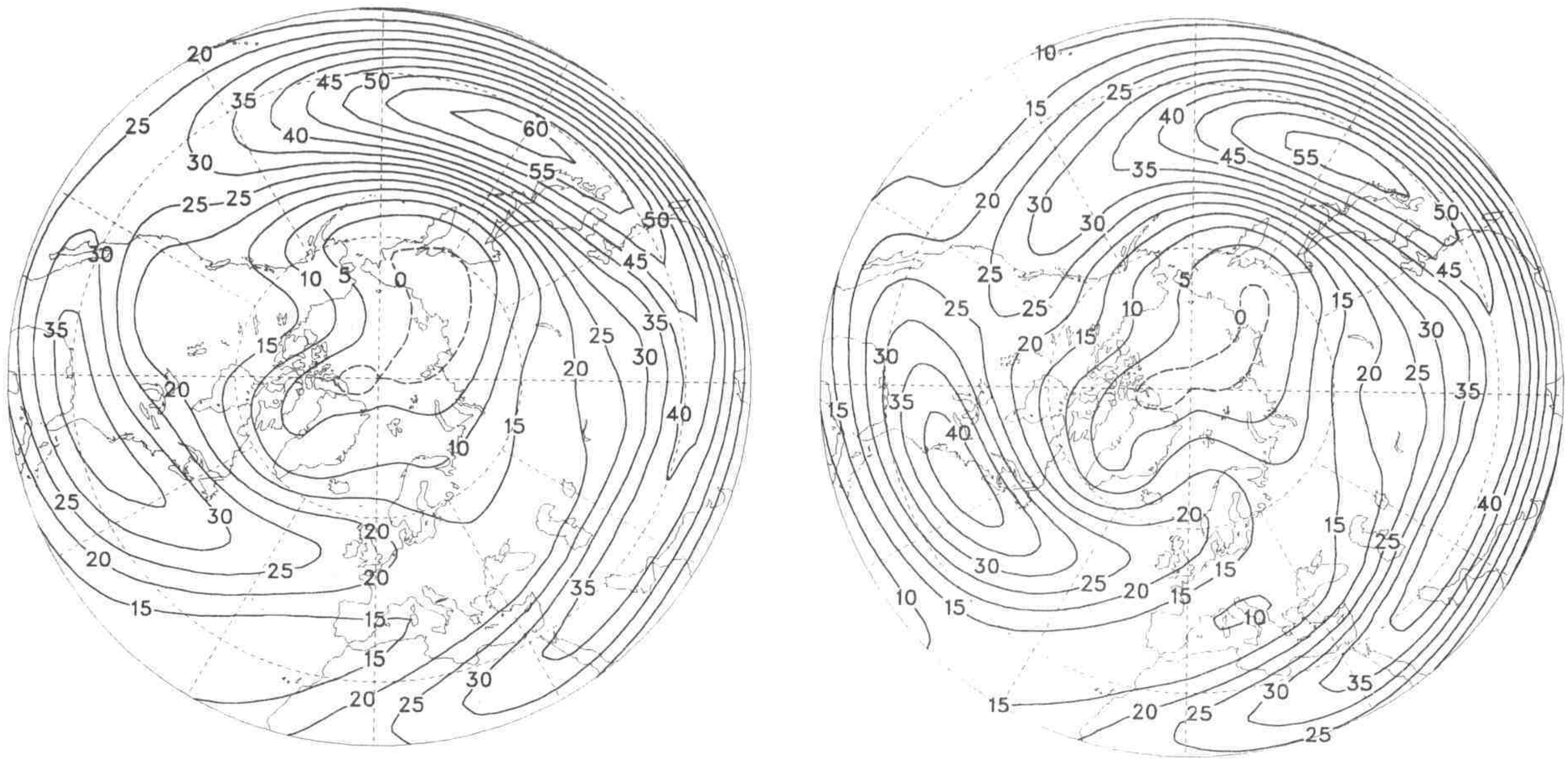

El Niño - Ctrl

La Niña - Ctrl

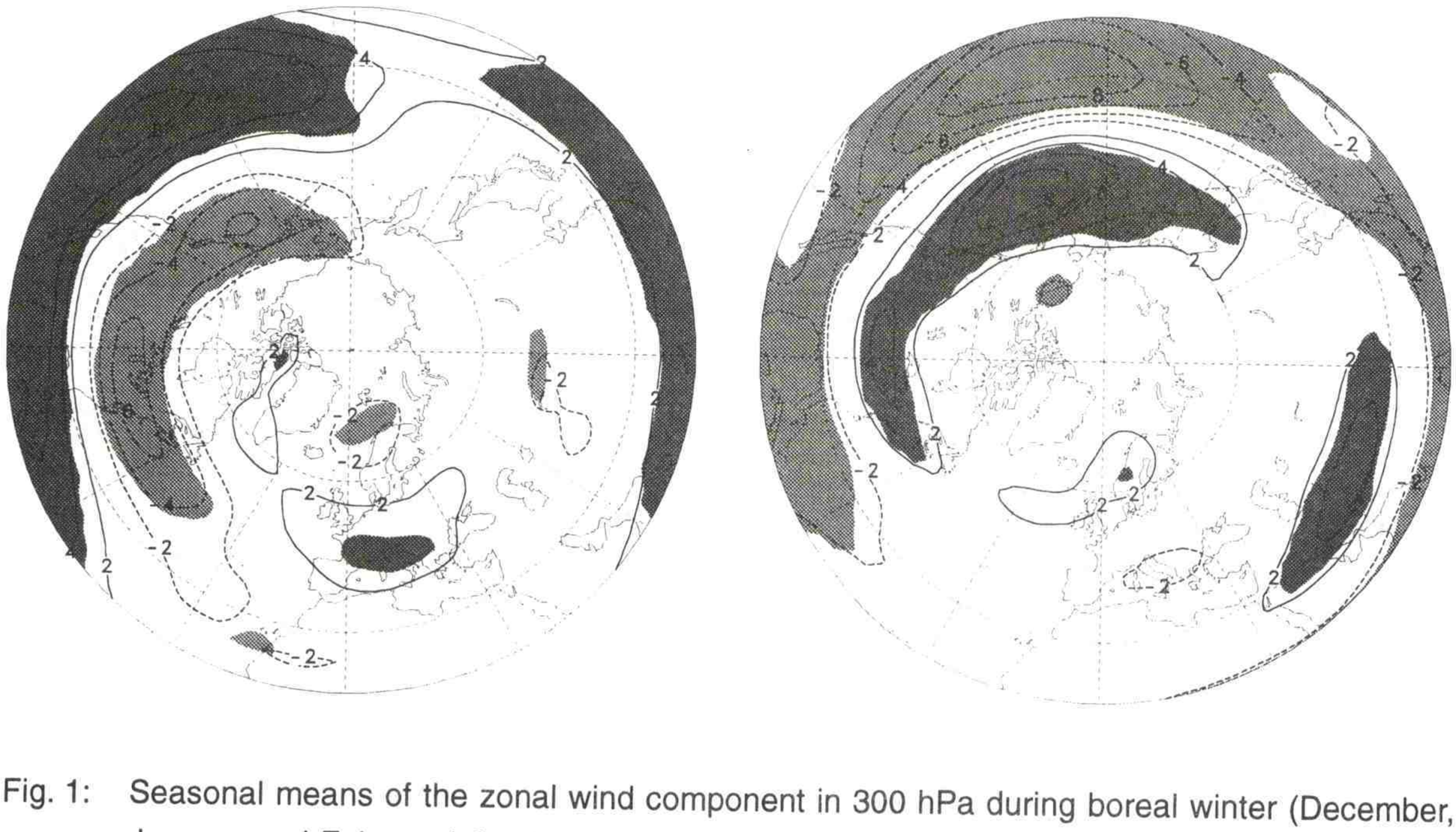

Fig. 1: Seasonal means of the zonal wind component in 300 hPa during boreal winter (December, January and February) for the El Niño and the La Niña events (upper panels). The contour interval is 5 m/s. Further differences between the composites for the El Niño and the La Niña events and the composite for the control cases (lower panels). The contour interval is 2 m/s. Significance at the 97.5%-level according to a two-sided t-test is indicated by the shading. Dark shading indicates positive and light shading negative significant differences.

El Niño - Ctrl horizontal E-P-flux La Niña - Ctrl

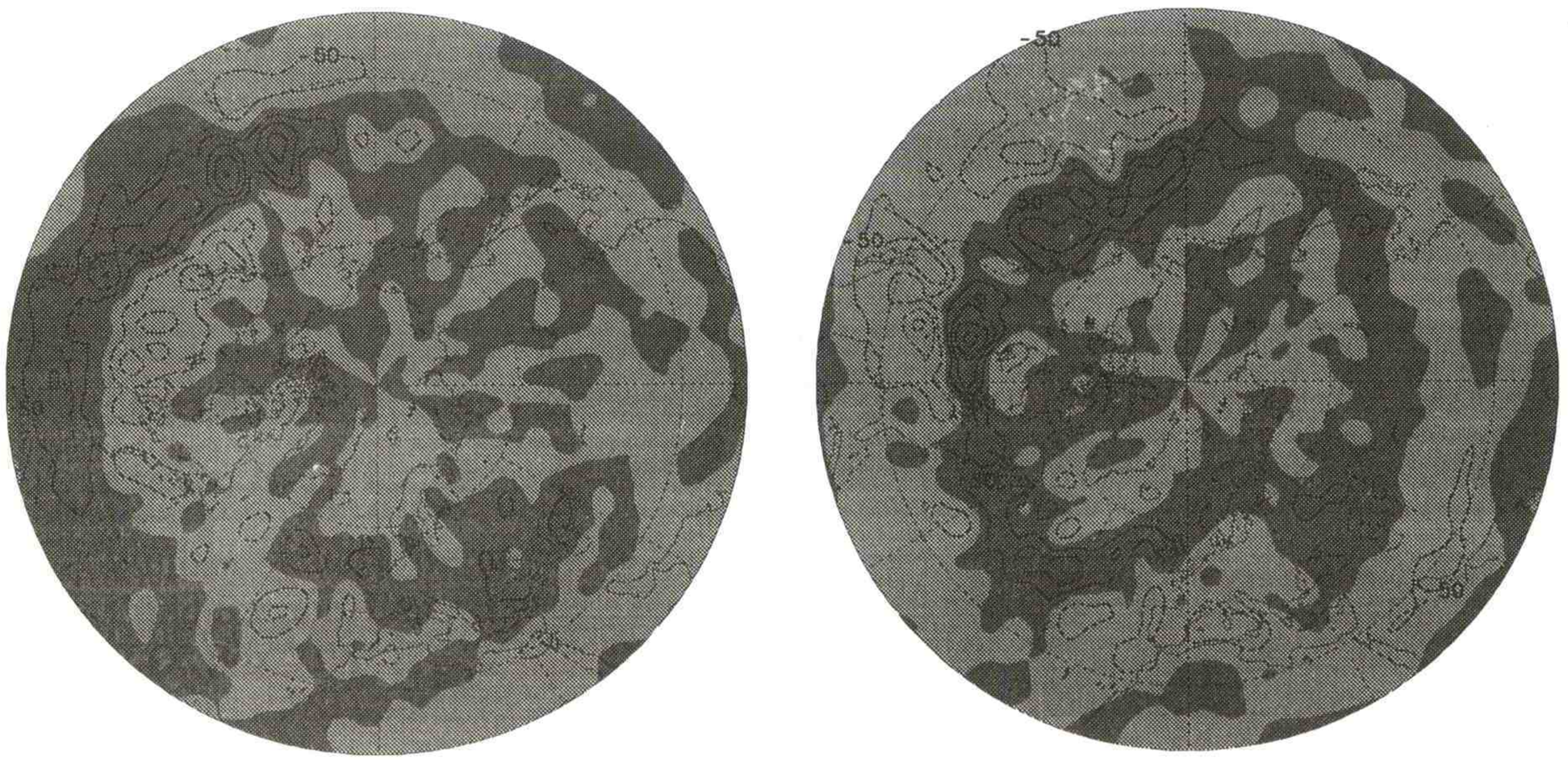

El Niño - Ctrl vertical E-P-flux La Niña - Ctrl

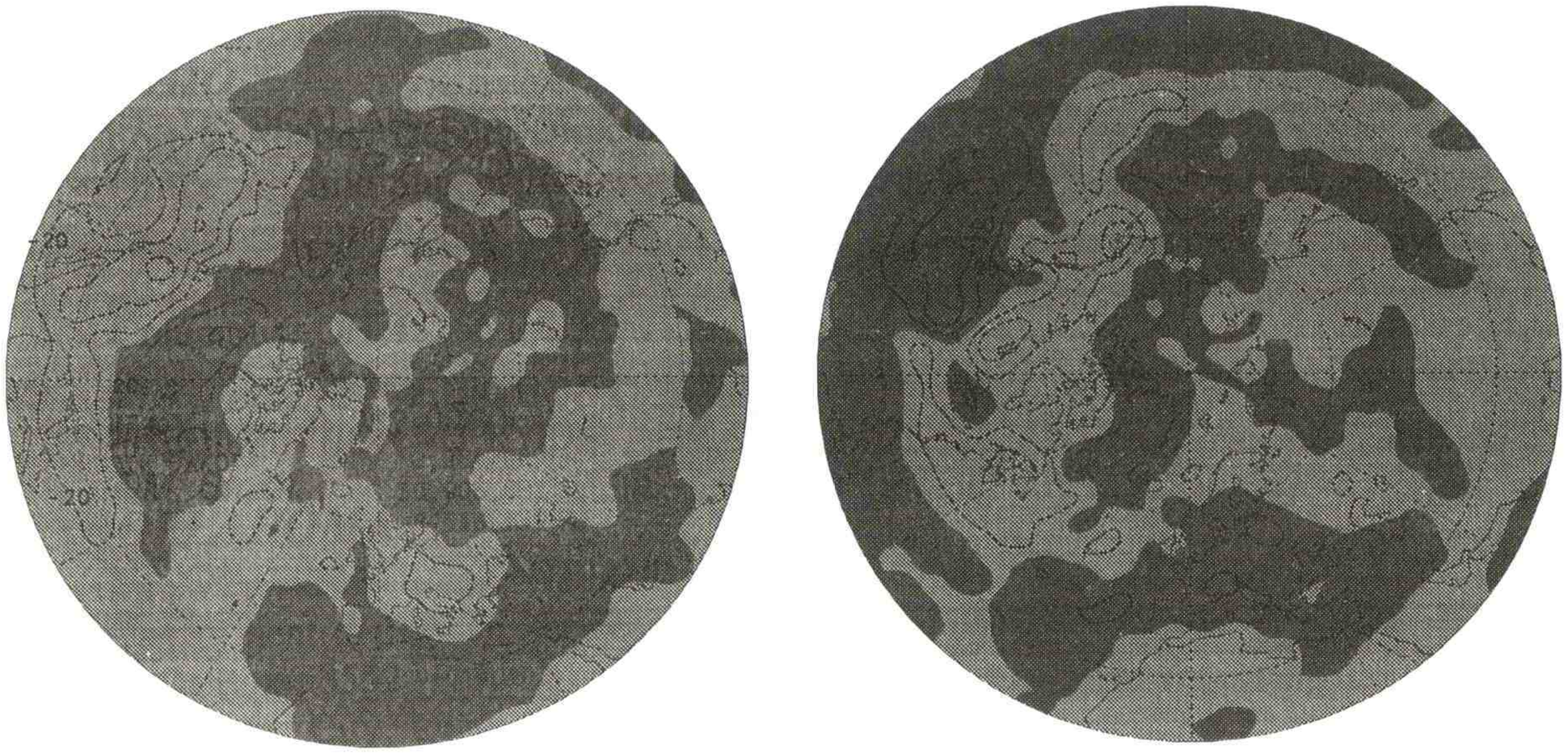

Fig. 2: Divergence of the band-pass filtered horizontal Eliassen-Palm-flux in 300 hPa during boreal winter (December, January and February) derived from the differences between the composites for the El Niño and the La Niña events and the composite for the control cases (upper panels). The contour interval is 0.5 (m/s)/day. Further the divergence of the band-pass filtered vertical Eliassen-Palm-flux between 850 and 300 hPa (lower panels). The contour interval is 0.2 (m/s)/day. Positive values (strengthening of the seasonal mean westerly winds) are indicated by the dark, negative ones (weakening of the westerly winds) by the light shading. The filter retains transient fluctuations at periods between 2.5 and 6 days.

Extratropical Eddy-Mean Flow Interactions Induced by Zonally Symmetrical Heat and Momentum Sources in the Tropics

Edmund K.M. Chang

Center for Meteorology and Physical Oceanography
Massachusetts Institute of Technology

Chang (1995, C95 below) studied the extratropical response to changes in the intensity of the Hadley circulation. The results suggested that in response to an increase in the intensity of the Hadley circulation, the mid-latitude jet will shift equatorward. Associated with that is an increase in temperature in the higher latitudes. In this paper, we will examine the physical mechanism that leads to the equatorward shift in more details.

C95 suggested that the observed shift in the mid-latitude jet in the model simulations could be associated with an anomalous westerly acceleration in the Tropics due to the increase in Hadley intensity. However, an equatorward shift of the jet involves not only acceleration of the jet towards the equatorward flank of the jet, but also deceleration towards the poleward flank of the jet. It is not clear what aspects of the eddy-mean flow interactions lead to the deceleration.

To investigate this further, a series of transient experiments were performed, using the control climate as the initial state. At time zero, the perturbation forcing, equivalent to concentration of heating towards the thermal equator that gives rise to increased intensity in the Hadley circulation, is applied, and the transient development of the flow is examined (Fig. 1). It can be seen that right from the start, apart from the acceleration of the zonal wind seen around 20S due to increased Hadley intensity, there is deceleration seen emanating from around 35S. Integration of a zonal mean version of the model driven by eddy fluxes of the control climate but with the perturbation forcings added (not shown) shows that the forcing already produces an acceleration/deceleration dipole. This is also true if we impose a anomalous momentum source in the Tropics instead of the prescribed heating. It turns out that the imposed forcing drives an indirect mean meridional circulation towards the poleward flank of the forcing that gives rise to zonal wind deceleration over that region. Results of the transient experiments then suggest that the eddies just "diffuse" this deceleration/acceleration dipole poleward.

To examine how the eddies move the zonal wind anomaly poleward, we would like to have a simpler situation in which we only have either an acceleration or deceleration "monopole" instead of a dipole. This can be achieved by appropriate choices of heating perturbations. A positive heat source centered right at the equator will give rise to a direct MMC and zonal wind acceleration around 25S, and a negative heat source placed at 15S gives rise to deceleration around 35S (Fig. 2), and the two together makes up an acceleration/deceleration dipole similar to the concentration of heating prescribed in C95. The response of the zonal mean flow in the full 3-D model to these heating perturbations are shown in Fig. 3. The results suggest that if we just put in an acceleration "monopole" in the Tropics, there will just be an acceleration of the mid-latitude jet. Similarly, with a deceleration forcing in the Tropics, the mid-latitude jet will be decelerated. The eddies mainly act to move the region of acceleration/deceleration poleward. The sum of the results from the two experiments is equivalent to an equatorward shift of the jet, qualitatively similar to that seen in C95.

The case in which we imposed a heating perturbation at the equator is examined in more detail here. To see how the eddies move the region of zonal wind acceleration poleward, we performed the following experiment. The model is initialized using the control climate, but adding in the perturbation forcing *and* the zonal mean climate change induced by that perturbation in the absence of eddy response (which can be obtained by integrating a zonal mean version of the model) over day 1. An ensemble of these transient experiments are performed. In this way, we can isolate the eddy response to the prescribed forcing and zonal mean perturbations. The results show that during the first 20 days or so, the eddies move the zonal

wind anomaly poleward, and the solution approaches the steady state response after about 40 days or so. The anomalous EP cross section averaged over days 6-10 is shown in Fig. 4 (the plotting convention follows those of Edmon et al. 1980). Note that since the prescribed forcing is zonally symmetric, the eddies do not feel the forcings directly, but only feel its effects via changes in the zonal mean state. The anomalous EP vectors and the zonal wind anomaly is shown in the top panel, and the divergence of the anomalous EP fluxes are shown in the bottom panel.

From the EP cross section, we see that associated with the zonal wind anomaly centered around 25S, there is increased penetration of eddies into the Tropics, as indicated by the largely horizontal EP flux anomaly at the upper level. The EP flux divergence anomaly in the upper levels centered around 35S also indicates that some eddies that originally break there can now penetrate further equatorward due to the equatorward displacement of the critical line. There is also an increased baroclinic eddy source, as indicated by the low level divergence centered around 35S. This source is located poleward of the zonal wind (and hence temperature gradient) anomaly, probably due to the rapid increase of the Coriolis parameter with latitude in this latitude range. These two effects together contribute to the divergence/convergence dipole of the EP flux, decelerating the zonal wind over the zonal wind anomaly and accelerating it towards the poleward flank of the zonal wind anomaly, displacing the zonal wind anomaly poleward. Results for the opposite case in which a negative source of heating is imposed is basically a mirror image of the above picture.

The above discussions give us qualitative understanding on how the eddies response to perturbation momentum and heat sources in the Tropics. However, further experiments suggest that this is not the entire story. Fig. 3 shows that the sum of the anomalies driven by a heating anomaly at the equator and a cooling perturbation at 15S resembles the equatorward shift response that C95 observed when the two sources are imposed together. For this case, this response compares well with the response we obtained when we apply the heating and cooling perturbations together. However, when we double the forcing, the amplitude of the sum is much weaker than the response obtained when both sources are imposed together, as shown on Fig. 5, suggesting that the extratropical response is non-linear. Another indication of non-linearity for the case in which heating and cooling perturbations are imposed simultaneously is that the response much more than doubles when the forcing is doubled (not shown here). However, in the case when we only impose a heat source of one sign, the extratropical response appears to be linear. Further work will be done to investigate the physical origin of this non-linearity.

References

Chang, E.K.M., 1995: The influence of Hadley circulation intensity changes on extratropical climate in an idealized model. *J. Atmos. Sci.*, **52**, 2006-2024.

Edmon, H.J., B.J. Hoskins, and M.E. McIntyre, 1980: Eliassen-Palm cross sections for the troposphere. *J. Atmos. Sci.*, **37**, 2600-2616.

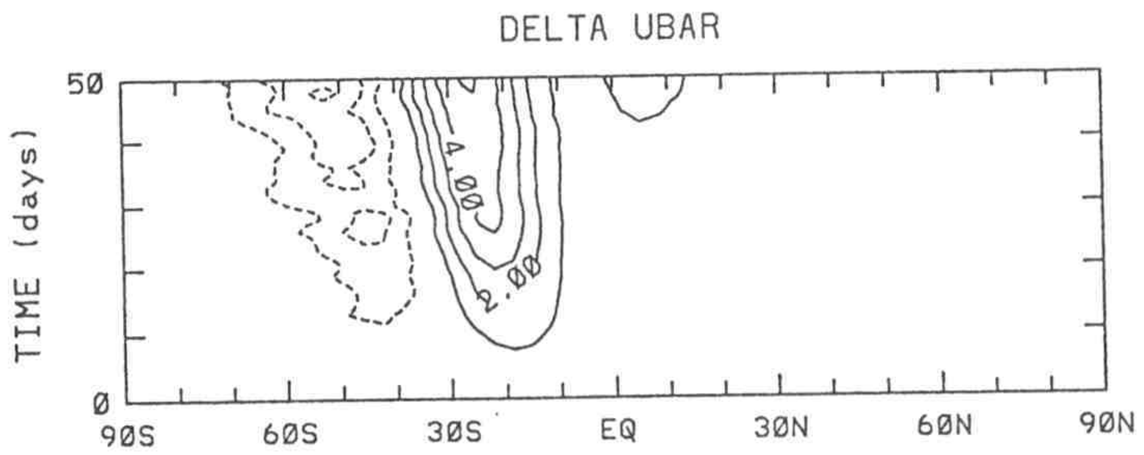

Fig. 1: Evolution of the vertical and zonal mean zonal wind anomaly (m/s) with time after the perturbation forcing is turned on.

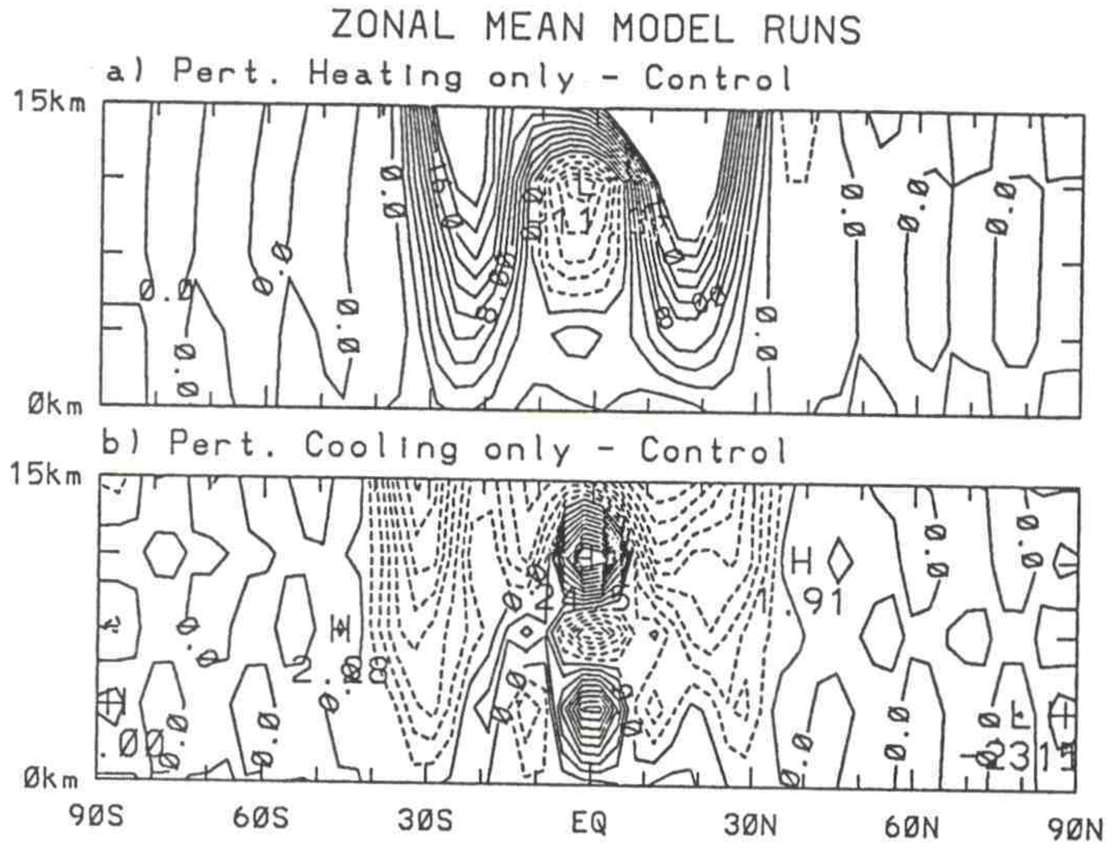

Fig. 2: Response of the zonal mean flow to a) heat source located at equator (upper) and b) cooling source at 15S (lower), contour 2 m/s. This is from a zonal mean model run in which the eddy heat and momentum fluxes have been set constant and equal to those computed from the control experiment.

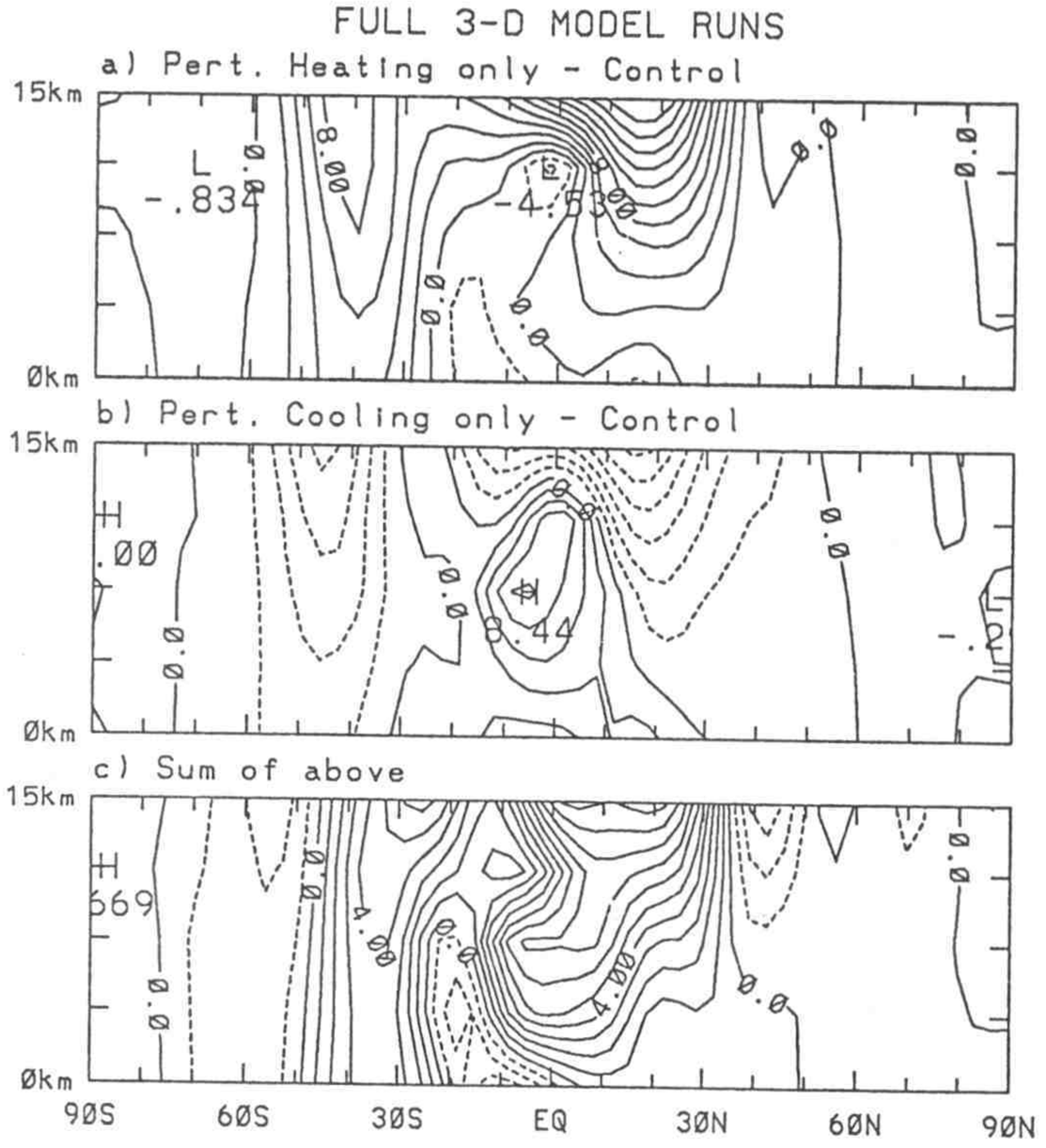

Fig. 3: a) and b) Similar to 2a and 2b except from fully 3-D model runs in which the eddies and their fluxes are allowed to change. c) Sum of a) and b). Contour interval 2m/s for a) and b), and 1 m/s for c).

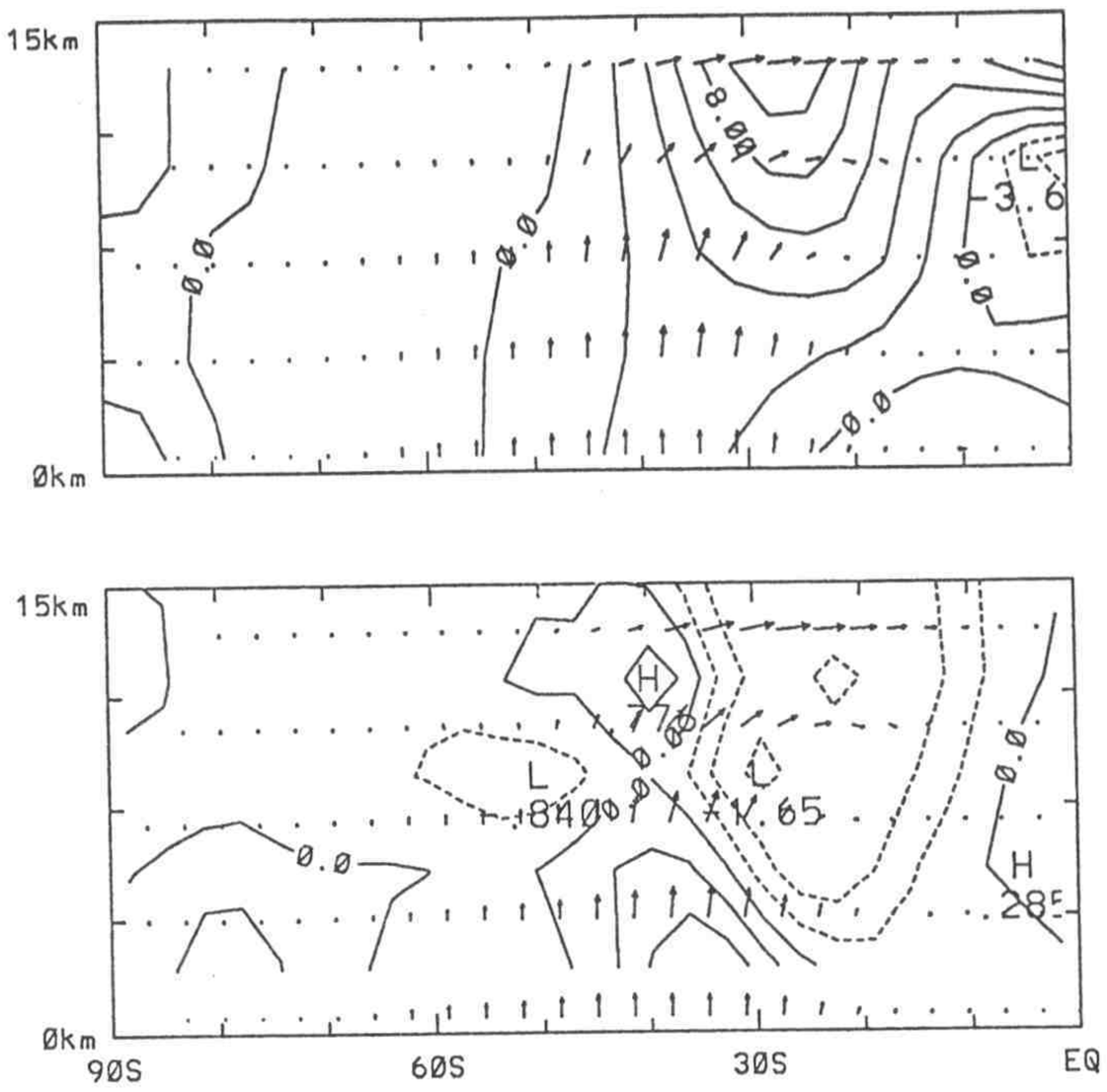

Fig. 4: Upper panel: Zonal wind anomaly (contour 2 m/s) and E-P fluxes from transient ensemble experiments for the case with heating perturbation at the equator, averaged over days 6-10. Lower panel: Divergence of E-P fluxes (contour interval 0.5×10^{15} m^3). Note that a divergence of 10^{15} m^3 roughly corresponds to zonal wind acceleration of about 1m/s/day in the mid-latitudes.

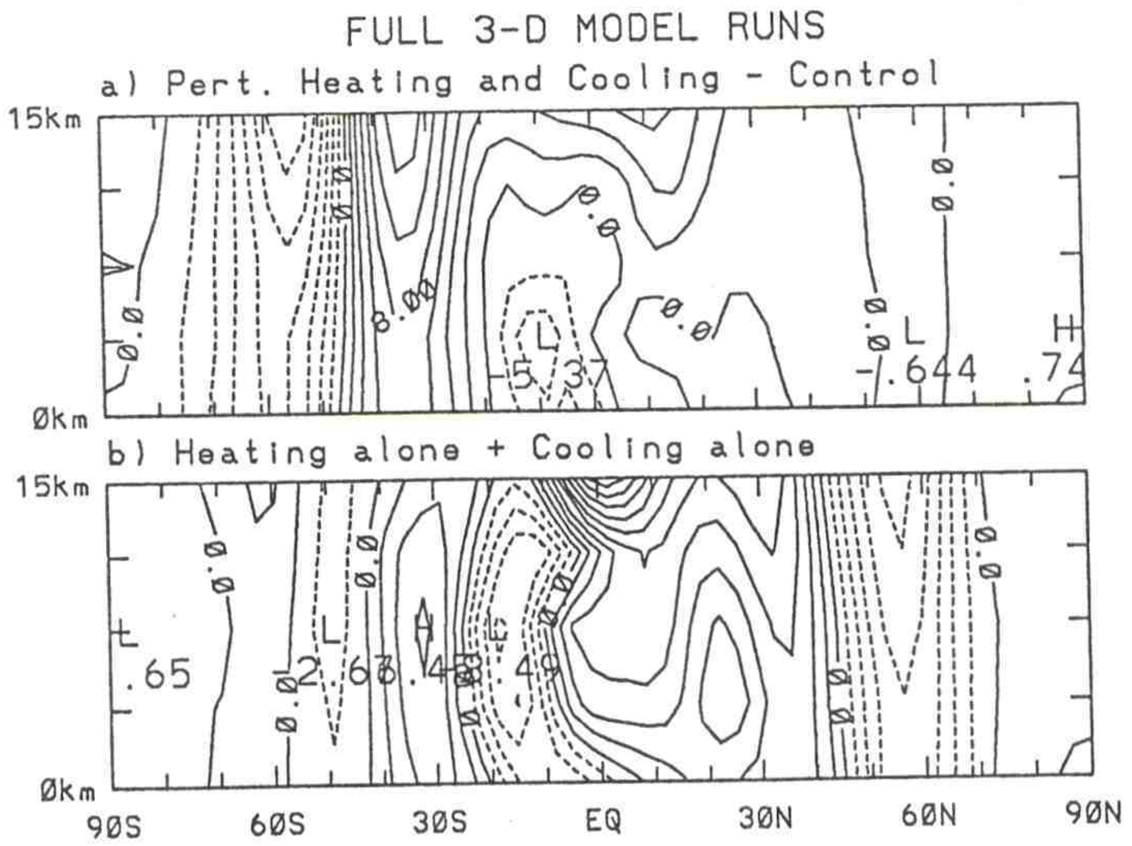

Fig. 5: a) Zonal wind response for the case with perturbation heating at equator and cooling at 15S. b) Sum of responses for the cases with heating and cooling alone (analogous to Fig. 3c). Note that the amplitude of the applied forcing is twice that used in the experiments above. Contour interval 2m/s.

Rapid Development of Upper-Level Anticyclones During the 1988 U.S. Drought

Ping Chen and Matthew Newman
Cooperative Institute for Research in the Environmental Sciences,
University of Colorado, Boulder, CO 80309, U.S.A

1. Introduction

Previous investigations of the 1988 U.S. drought have been primarily focused on monthly and/or seasonal time scales (e.g., Trenberth et al., 1988; Namias, 1991; Lyon and Dole, 1995). The upper-level circulations associated with the drought exhibited large-amplitude variability in shorter time scales, however. In this paper it will be shown that several large-amplitude anomalous cyclones and anticyclones passed through the North American continent between April and July. The strongest anomalous anticyclone developed very rapidly at the end of May and persisted for about two weeks. The rapid development of the anomalous anticyclone will be linked to the downstream energy propagation of Rossby wave packets forced by anomalous divergence/ convergence centers over Southeast Asia and western North Pacific.

2. Results

Figure 1 shows the evolution of the area-averaged[1] ECMWF analyzed streamfunction anomaly from April 1 to July 31, 1988. The transient nature of the circulation is most clearly seen in the 10-day Lanczos low-pass data (solid curve). The streamfunction anomaly was positive during short periods in April and early May and was generally negative in May. It underwent a rapid increase during the last week of May. In mid-June there was a rapid reintensification of the anomalous anticyclone while the streamfunction anomaly was generally positive from late May to early July. Similar behavior is evident in the 30-day Lanczos low-pass data (dashed curve).

In this paper we examine the rapid development of the anomalous upper-level anticyclone over North America near the end of May 1988, which appears to be related to the downstream energy propagation of Rossby waves from Southeast Asia and western North Pacific. Figure 2 shows contour maps of streamfunction anomaly on May 22, 25, 28, 31 and June 3, respectively. On May 22 the streamfunction anomaly was positive over Southeast Asia and quite weak over the North Pacific and North America. In the following four days a strong anomalous anticyclone developed over the central North Pacific

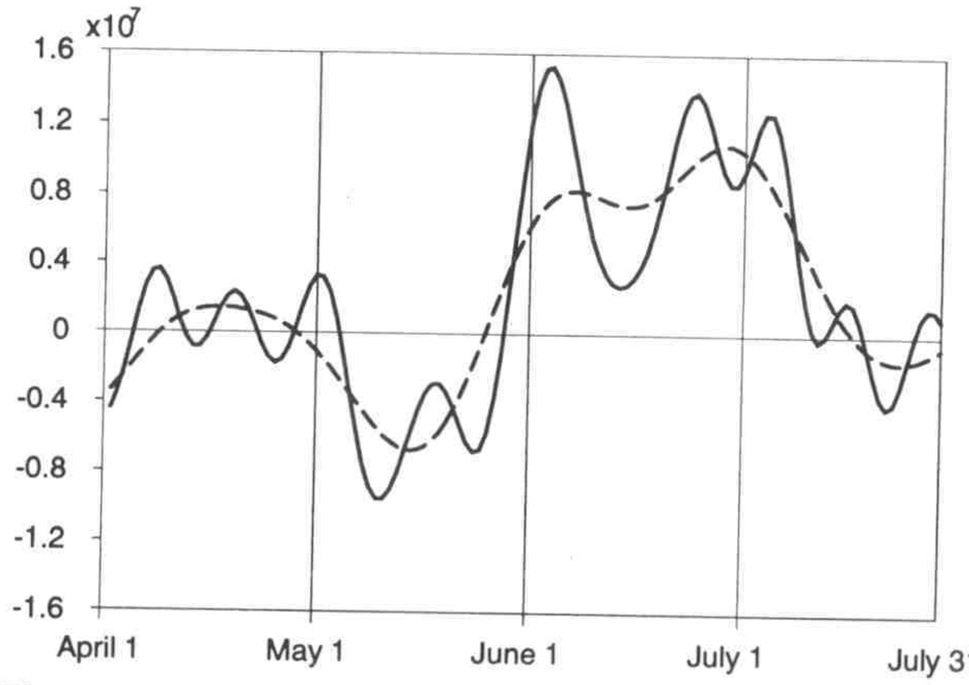

Fig. 1. Area-averaged 10-day low-pass (solid) and 30-day low-pass (dashed) streamfunction anomaly.

while the positive anomaly over Southeast Asia weakened. From May 28 onward the anomalous anticyclone over North America intensified while the anomalous anticyclone over the central North Pacific weakened. The positive anomaly over the Great Plains reached its maximum around June 4 and started to decrease. By June 15 there was no significant streamfunction anomaly over the United States.

Another positive streamfunction anomaly developed over Southeast Asia and western North Pacific between June 2 and June 12 It appears that the downstream propagation of energy associated with this wave packet caused the rapid reintensification of the anomalous anticyclone over North America in late June (see Fig. 1).

Examination of daily low-pass divergence maps (not shown) seems to suggest that the Rossby wave packets shown in Fig. 2 were forced by anomalous divergence/ convergence centers coincident with the anomalously high precipitation over Southeast Asia and western North Pacific in the middle and late May of 1988. A linear barotropic vorticity equation model with spectral truncation T21 was used to test this hypothesis. The base state was determined by computing the first three harmonics of the annual cycle from 14 years (1980-1993) of ECMWF 200 mb winds. (Results are similar if the calculation is made at T42 resolution or at 300 mb.)

The daily divergence anomalies for May 22-June 3 1988 were used as forcing. Only the divergence fields of the Eastern Hemisphere were used to force the model, to test

1. The area, $80^{o}W<\lambda<115^{o}W$; $35^{o}N<\phi<65^{o}N$, covers the region where the anomalous anticyclone in the April-MayJune averaged maps was located (see Trenberth et al 1988).

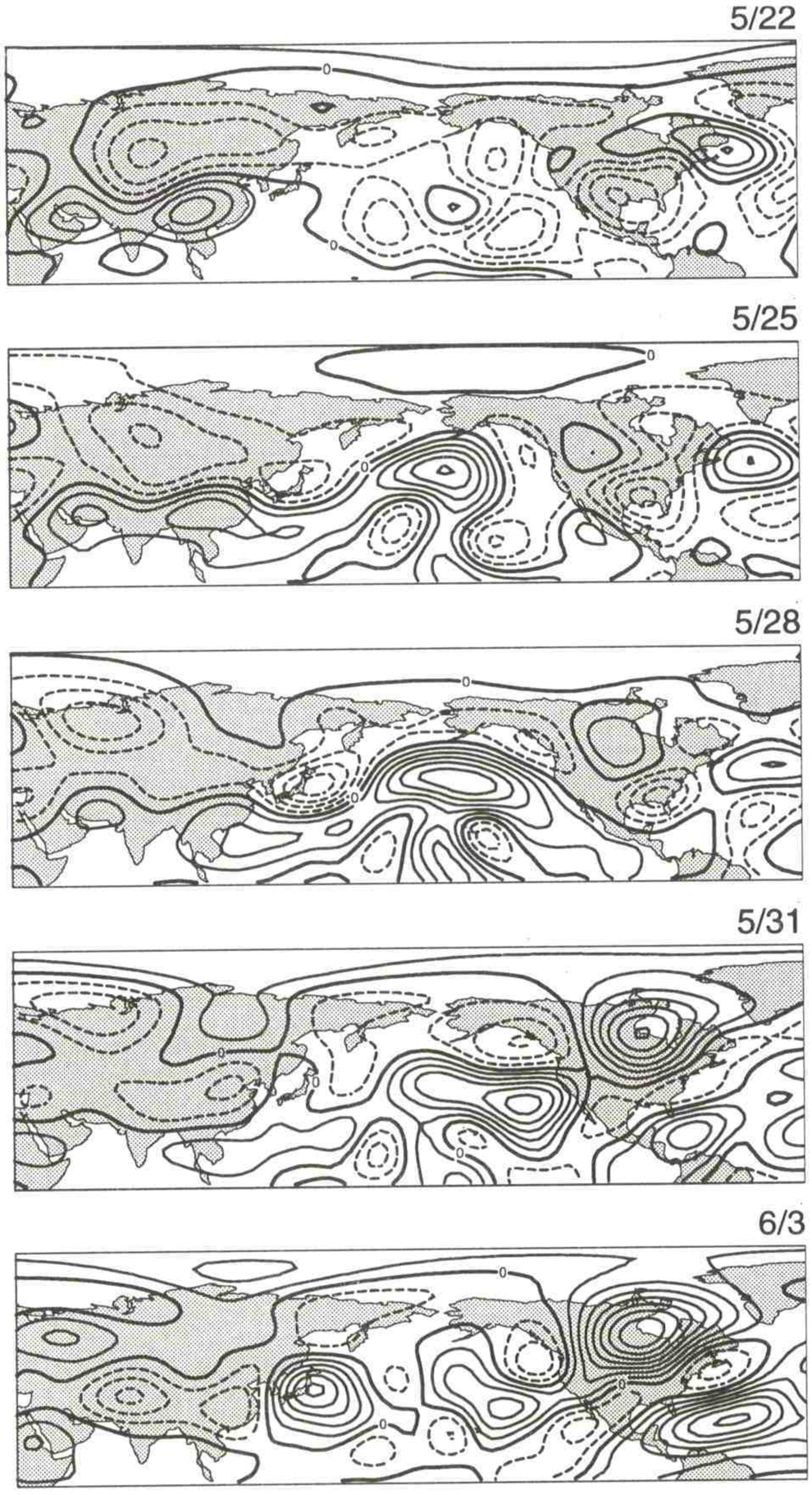

Fig. 2: ECMWF analyzed 200 mb streamfunction anomaly on May 22, 25, 28, 31 and June 3, 1988.

whether the Rossby waves are indeed forced by the divergence anomalies over Southeast Asia and western North Pacific.

Figure 3 shows maps of streamfunction anomalies from the model run initialized on May 22. Comparing Figs. 2 and 3 it is seen that the timing and qualitative location of the observed streamfunction extrema is consistent with Rossby wave energy propagation. On May 25 an anomalous anticyclone appeared over central North Pacific. From May 28 onward an anomalous anticyclone developed very quickly over North America. This anomalous anticyclone reached its maximum around June 4 and persisted for about another week. Detailed comparisons of Figs. 2 and 3 show, however, that the center of the anticyclone in the model is off to the south by 15-20 degrees of latitude and the negative anomaly off the Pacific coast is too strong. Another model run starting June 14 (not shown) produces a similar level of accuracy in the simulation of the late June anticyclone.

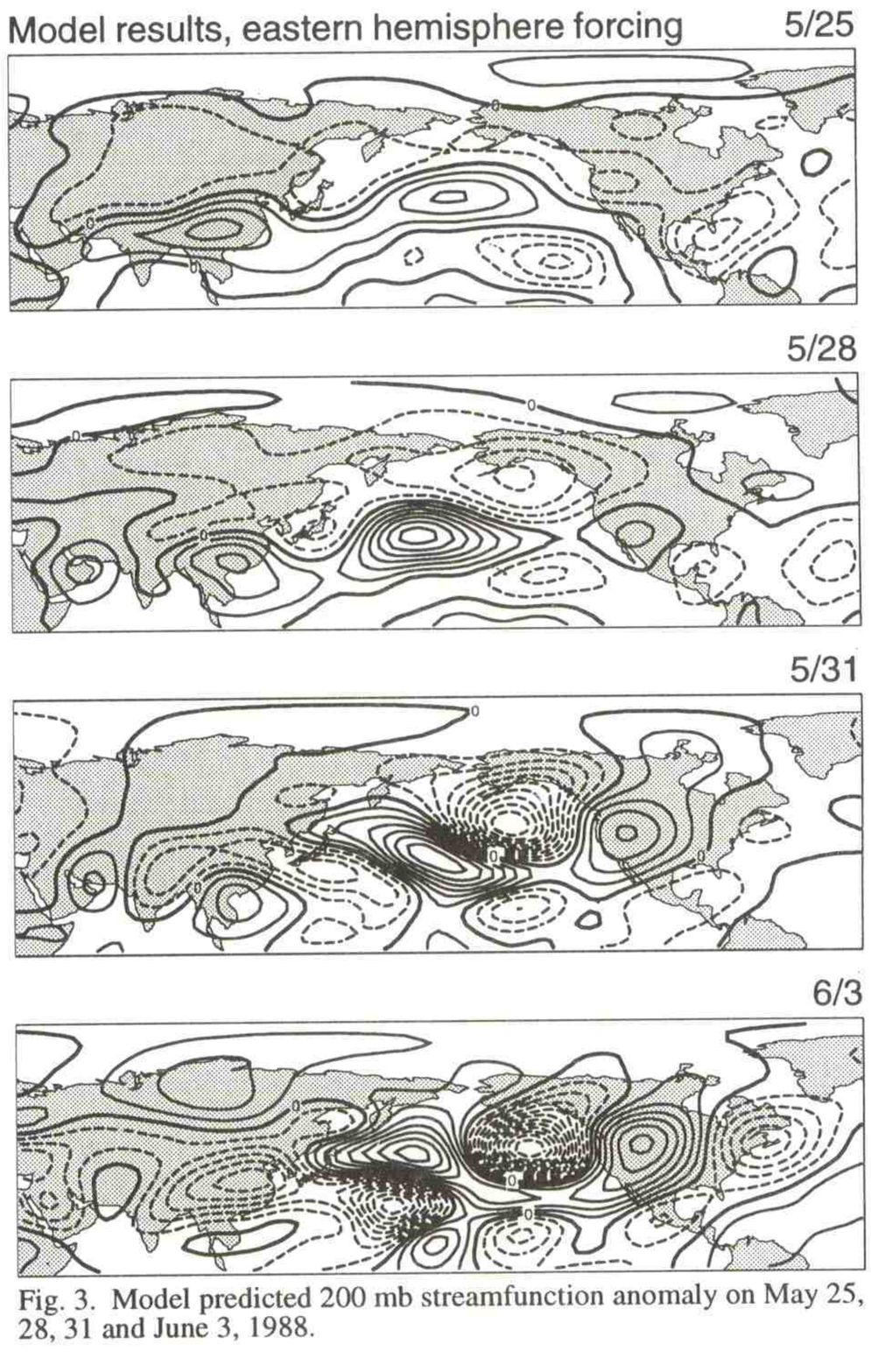

Fig. 3. Model predicted 200 mb streamfunction anomaly on May 25, 28, 31 and June 3, 1988.

3. Summary

The upper-level circulation during the 1988 U.S. drought was quite transient, consisting of several episodes of anomalous anticyclones and cyclones. The strongest anomalous anticyclone developed rapidly within the last week of May and lasted for about two weeks. The observed and modeled daily streamfunction anomaly maps strongly suggest that the rapid development of the anomalous anticyclone at the end of May was due to downstream energy propagation of Rossby wave packets forced by anomalous divergence over Southeast Asia and western North Pacific.

REFERENCES

Lyon, B. and R. M. Dole, 1995: A diagnostic comparison of the 1980 and 1988 U.S. summer heat wave-droughts. *J. Climate*, **8**, 1658-1675.

Namias, J., 1991: Spring and summer 1988 drought over the contiguous United States - causes and prediction. *J. Climate*, **4**, 54-65.

Trenberth, K. E., G. W. Branstator, and P. A. Arkin, 1988: Origins of the 1988 North American drought. *Science*, **242**, 1640-1645.

On the Annual Cycle of Tropospheric Winds Observed Above Christmas Island in the Central Equatorial Pacific

Kenneth S. Gage and John R. McAfee
NOAA Aeronomy Laboratory,
Boulder, CO 80303

and

Christopher R Williams
University of Colorado/CIRES,
Boulder, CO 80309

Introduction

Observations of tropospheric winds have been made nearly continuously since early 1986 in the altitude range 2-18 km using a 50 MHz VHF wind profiler at Christmas Island (2°N, 157°W) (Gage et al., 1994). This paper presents a summary of the annual cycle of zonal winds observed at Christmas Island and interprets the observations in terms of the annual cycle of tropical convection and the Walker circulation.

Annual Cycle of Observed Zonal Winds

Tropospheric zonal winds observed at Christmas Island show a pronounced annual cycle that is present every year in varying degrees. The mean annual cycle of zonal winds is reproduced in Fig 1. The annual cycle is most pronounced during La Niña and weakest during El Niño. The amplitude of the cycle has a broad peak in the upper troposphere. EOF analysis shows that the principal mode (PC#1; Fig 2) explains over 90% of the variance.

We attribute the annual cycle in zonal winds to the annual variation in tropical convection. The annual variation in tropical convection gives rise to an annual cycle in the pressure difference between Darwin and Tahiti. The pressure difference is largest during northern hemisphere winter months. A comparison of the annual cycle in pressure difference with PC#1 is shown in Fig. 3.

Relationship to the Annual Cycle of Convection in the Western Pacific

Other measures of the annual cycle in tropical convection are the OLR, HRC and tropopause height. The tropical tropopause is highest during the northern hemisphere winter months when convection is most active over the maritime continent and lowest when convection is most active over the land masses of the northern hemisphere. The annual migration of the active centers of convection from the northern hemisphere Summer Monsoon to the equatorial Winter Monsoon appears to provide the driving mechanism that is responsible for these annual cycles in the tropical atmosphere. A comparison of PC #1 with the annual variation in tropical tropopause height is shown in Fig 4.

The western Pacific is characterized by the intersection of the South Pacific Convergence Zone (SPCZ) with the northern hemisphere ITCZ. This region is an active center of convection which moves north and south with the sun through the year as shown in Fig 4c of Waliser and Gautier (1993)) . The migration of the equatorial heat sources as evidenced by the climatology of the HRC is an important factor in determining the annual cycle discussed here (c.f. Meehl, 1987). The position of the ITCZ In the western Pacific follows the sun through the annual cycle migrating between about 5°S in northern winter and 12°N in northern summer.

The asymmetry of the ITCZ relative to the equator during the course of its annual migration may be responsible for some of the features of the shape of the annual cycle that is observed in PC#1. Specifically, if the Christmas Island winds are remotely forced from deep convective heating to the west, it is likely that their magnitude will depend on the meridional position of the heat source within the equatorial wave guide. The ITCZ 'crosses' the equator in early April and in late December. If remote tropical convective forcing in the equatorial waveguide is responsible for the Christmas Island winds we would expect to find relative maxima in PC#1 at these times and relative minima in PC#1 at the times when convection is centered farthest from the equator. Consistent with this hypothesis we expect to find relative minima in February and August. Furthermore, since the convective center is much farther removed from the equator in northern summer than northern winter we anticipate that the August minimum will be much deeper than the February minimum. The fact that all of these features are evident in PC#1 lends credibility to the hypothesis that the location of the equatorial heat source within the equatorial waveguide is an important factor in determining the remote forcing of zonal winds at Christmas Island.

Concluding Remarks

We have identified two factors that can explain the observed variability of the Christmas Island winds. These factors are 1) the annual variation of the intensity (or frequency) of deep tropical convection and 2) the migration of the active centers of tropical convection relative to the equatorial waveguide. Both of these factors are likely of major importance in determining the variability of Christmas Island winds. In future work we intend to extend this work to include high frequency, intra-seasonal variability and low frequency interannual variability.

Acknowledgements

The Christmas Island wind profiler was constructed and is being operated with the support of the U.S. TOGA Project Office. It is part of the NOAA/CU Trans Pacific Profiler Network supported by the National Science Foundation under Agreement ATM-87220797 and ATM-9214800. We wish to thank John Bryden for his assistance in the local management of the Christmas Island wind profiler. We also thank Paul Johnston, Warner Ecklund and David Carter for their contributions to the maintenance and upkeep of the Christmas Island profiler and Tony Riddle for his contributions to the archival and quality control of the Christmas Island profiler data. We thank the ECMWF for providing us with monthly reports on the quality of the Christmas Island winds in comparison to their analyses.

References

Gage, K.S. and G.C. Reid, The tropical tropopause and the El Niño of 1982-1983, *J. G. R.*, **91**, 13,315-13,317, 1986.

Gage, K.S., J.R. McAfee, W.L. Ecklund, D.A. Carter, C. Williams, P.E. Johnston and A.C. Riddle, The Christmas Island Wind Profiler: A Prototype VHF Wind-Profiling Doppler Radar for the Tropics, J. Tech., **11**, 22-31, 1994.

Meehl, G.A., The annual cycle and interannual variability in the tropical Pacific and Indian ocean regions, *Mo. Wea. Rev.*, **115**, 27-50, 1987.

Reid, G.C. and K.S. Gage, On the annual variation in height of the tropical tropopause, *J. Atmos. Sci.*, **38**, 1928-1938, 1981.

Waliser, D.E. and C. Gautier, A Satellite-derived climatology of the ITCZ, *J. Climate*, **6**, 2162-2174, 1993.

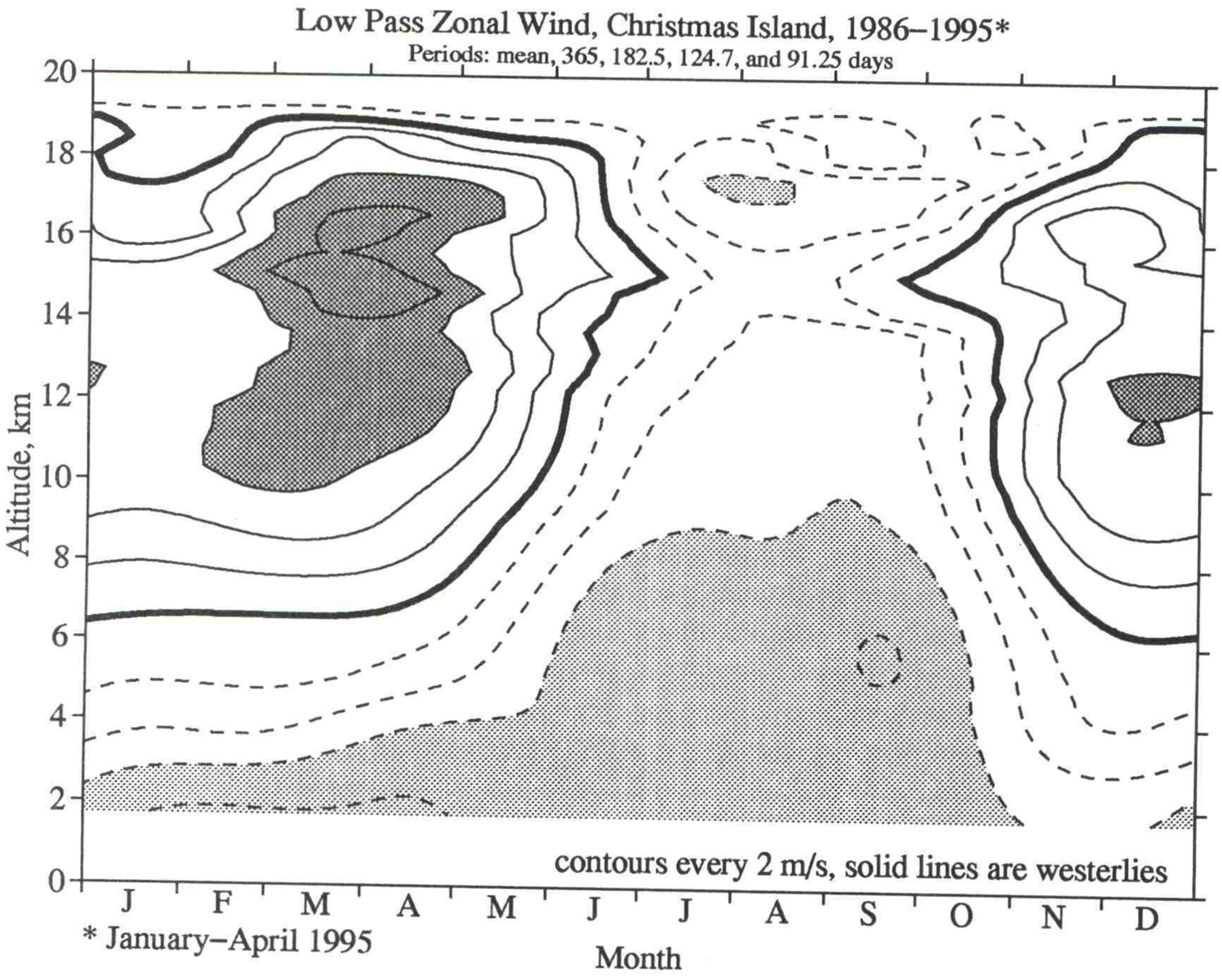

Figure 1. Low-pass filtered composite annual variation of zonal wind observed at Christmas Island. Solid (dashed) contour lines are westerlies (easterlies) and velocities greater than 6 m/s are shaded.

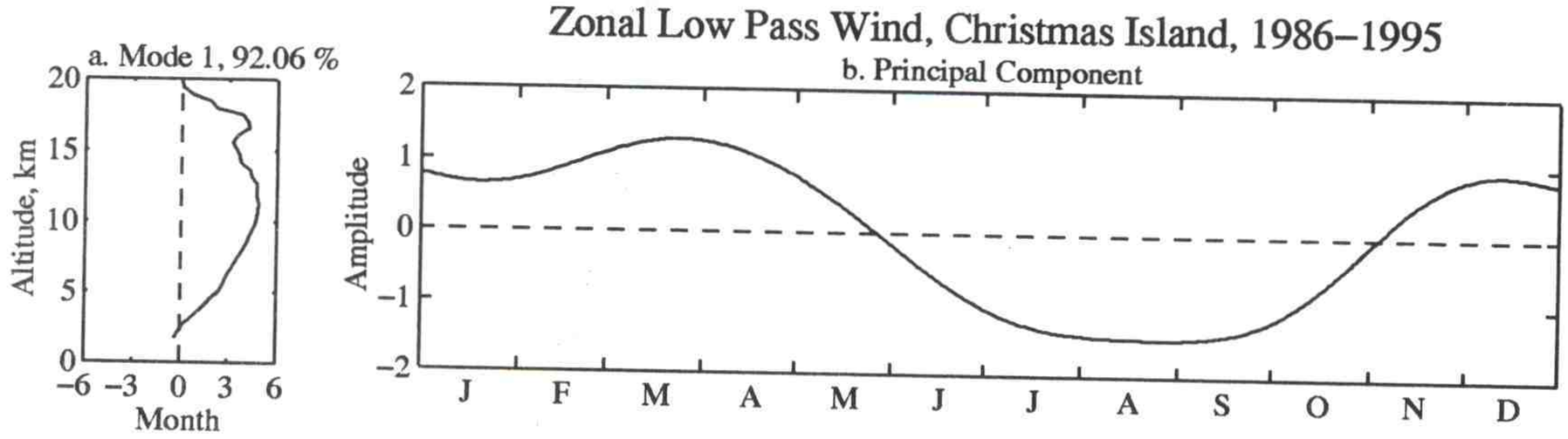

Figure 2. Dominant EOF of the annual variation of zonal winds observed at Christmas Island.

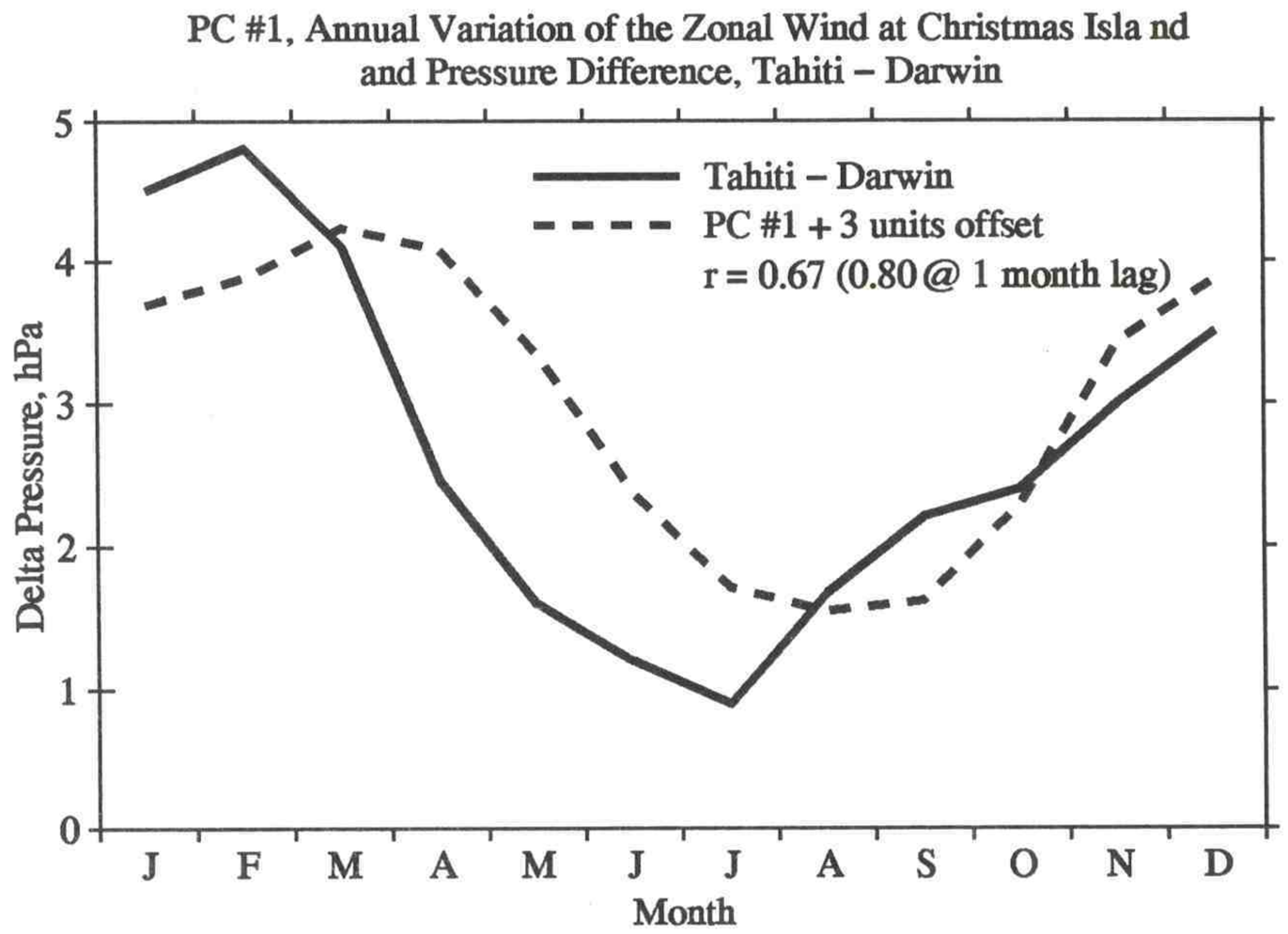

Figure 3. Comparison of the first EOF principal component of the annual variation of Christmas Island zonal winds with the annual variation in Tahiti minus Darwin surface pressure. Note the principal component is offset by 3 units to facilitate the visual comparison.

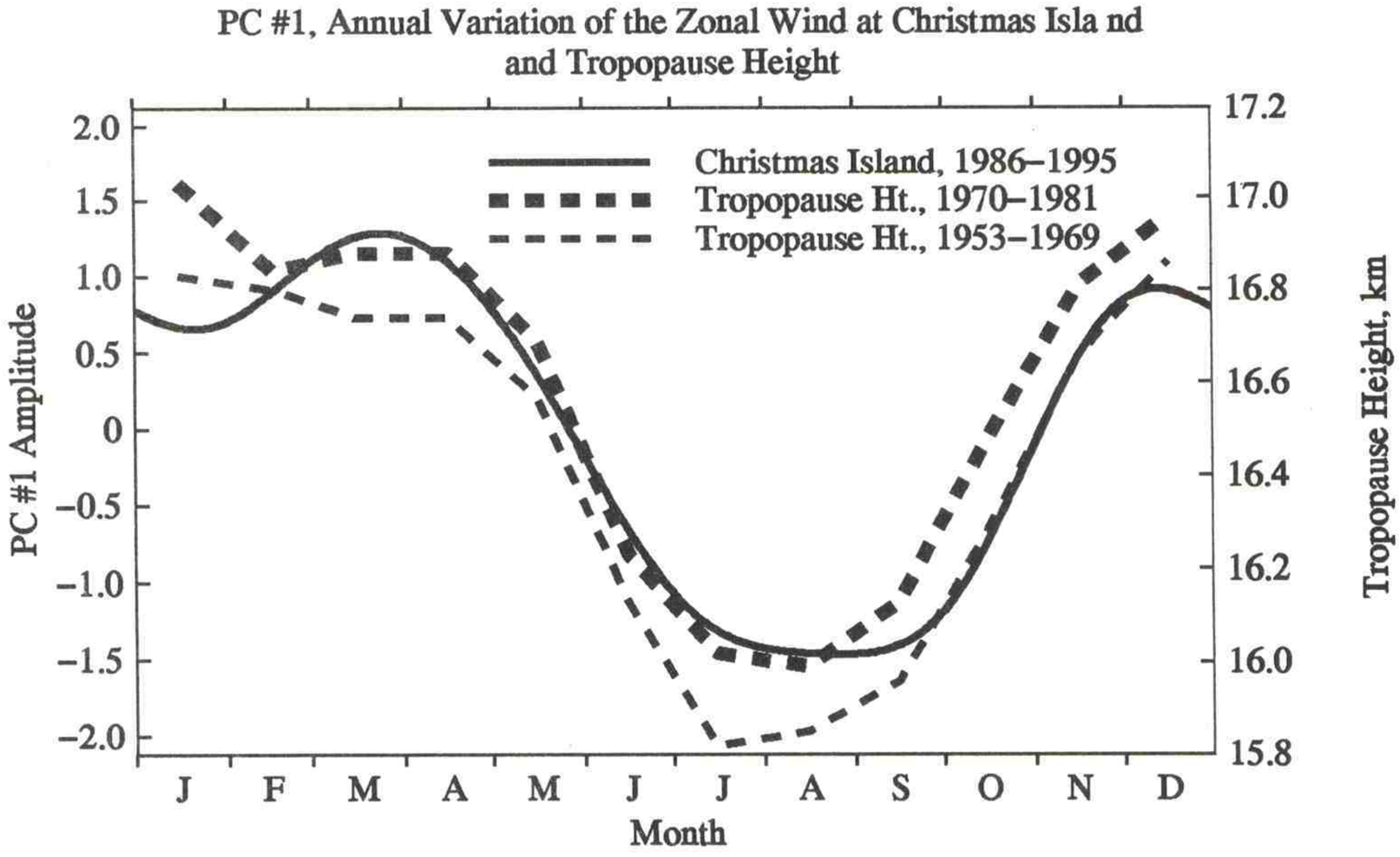

Figure 4. Annual cycle in tropical tropopause height, 1953-1969, and 1970-1981 (Reid and Gage, 1981 and Gage and Reid, 1986). The first EOF principal component of the annual variation of Christmas Island zonal winds is plotted for comparison purposes.

Gauge-Based Analysis of Precipitation During 1971 - 1994

Pingping Xie and Phillip A. Arkin
National Centers for Environmental Prediction
W/NP, NOAA/NWS
Washington, DC 20233

1. Introduction

As part of the Global Precipitation Climatology Project (GPCP), which aims to construct large-scale precipitation datasets for many WCRP scientific activities, a gauge-based monthly analysis of global land precipitation has been created on a 2.5° latitude/longitude grid for the 24-year period from 1971 to 1994. In this paper, its quantitative accuracy and capability in describing large-scale precipitation variations are examined.

2. Gauge Data and Interpolating Scheme

Two sets of gauge observations of monthly precipitation data sets have been collected and used jointly as the input to the analysis. Compiled by the DOE Carbon Dioxide Information Analysis Center (CDIAC), the Global Historical Climatology Network (GHCN) contains quality-controlled monthly precipitation data for over 7500 stations worldwide, among which 4000 - 6000 stations provide precipitation reports each month (Vose et al., 1992). The Climate Anomaly Monitoring System (CAMS), created by the NOAA Climate Prediction Center (CPC), is based on two data sources, one obtained from the historical records collected and edited by NCAR for the period before 1981 and the other accumulated on a real time basis from the Global Telecommunication System (GTS). The number of stations reporting precipitation is roughly 1900 and 3500 for the two periods. The combining of the two datasets improves the gauge network significantly. The total number of gauges is increased, up to over 6000 stations for most months, and the network density is improved for some regions.

The gridded fields of area-mean precipitation for each 2.5° lat/lon grid are defined in three steps. First, monthly precipitation at 0.5° lat/lon grid points is calculated by interpolating the gauge observations over 6000 stations using the algorithm of Shepard (1968), in which the weighting coefficients are inversely proportional to the distance between the grid point and the station. The area-mean value for each 0.5° lat/lon grid box is then computed as the arithmetic average of the point values at its four corners. Finally, the area-mean precipitation for each 2.5° lat/lon box is defined as the areal-weighted average of the 25 0.5° lat/lon boxes inside it.

To investigate the relationship between the analysis accuracy and gauge network density and thereby to get insight into the performance of the gauge-based gridded fields of precipitation, the analysis based on the combined dataset is compared to that based on the CAMS dataset which has fewer gauges than in the combined dataset. The results showed that our gauge-based analysis has good quality in representing large-scale precipitation in general. Its quantitative accuracy increases with local gauge network density, while value-dependent bias exists, particularly over gauge-sparse areas.

3. Applications

The precipitation distributions and their variability as observed in our gauge-based monthly analyses are investigated for the 24-year period over land areas and are compared with those of Jaeger (1976) and Legates and Willmott (1990). Fig.1 presents the spatial distributions of the annual mean precipitation, while fig.2 shows the annual cycles of the mean precipitation averaged over the Southern Hemisphere, Northern Hemisphere and over the entire globe.

In general, the 24-year mean of our gauge-based analysis is in good agreement with those of Jaeger (1976) and Legates and Willmott (1990). The annual mean precipitation over the global land area is 1.88 mm/day in our 24-year analysis, compared to 2.01 / 1.97 mm/day in Jaeger / L-W. All three datasets exhibit similar spatial distributions, characterized by rain-bands associated with the ITCZ and monsoons. Major differences, however, exist in the extension as well as in the amplitude of heavy rainfall, especially over India and South America where gauge networks are relatively poor.

The three datasets contain annual cycles with the same phase and small differences in amplitudes over both hemispheres. The maxima / minima occur in February / August in the Southern Hemisphere and in July - August / January - February in the Northern Hemisphere, in agreement with the seasonal march of the ITCZ and major monsoon systems. The differences in amplitudes occur mainly during the months with large precipitation.

The 24-year monthly analysis is applied to examine the inter-annual variability of the global land precipitation associated with the El Nino / Southern Oscillation (ENSO) phenomenon. Shown in fig.3 is the distribution of precipitation difference between the warm and cold ENSO episodes. In general, cold ENSO episodes bring more precipitation to South Africa, India, Australia and the northern portion of the South America, which are in good agreement with previous studies (Ropelewski and Halpert, 1987, 1989) based on historical station observations but with more details.

4. Summary

1) Monthly analyses of global land precipitation have been constructed for a 2.5° latitude/longitude global grid for the 24-year period from 1971 to 1994 by interpolating gauge observations at over 6000 stations contained in 2 datasets.

2) The gauge-based analysis has good quality in representing large-scale precipitation in general. Its quantitative accuracy increases with local gauge network density, while value-dependent bias exists, particularly over gauge-sparse areas.

3) The 24-year analysis is used to describe the spatial and temporal variations of global land precipitation. The mean distribution and the annual cycles are in good agreement with those of Jaeger (1976) and Legates and Willmott (1990). The inter-annual variability associated with the ENSO is similar to that found by previous studies but with more details.

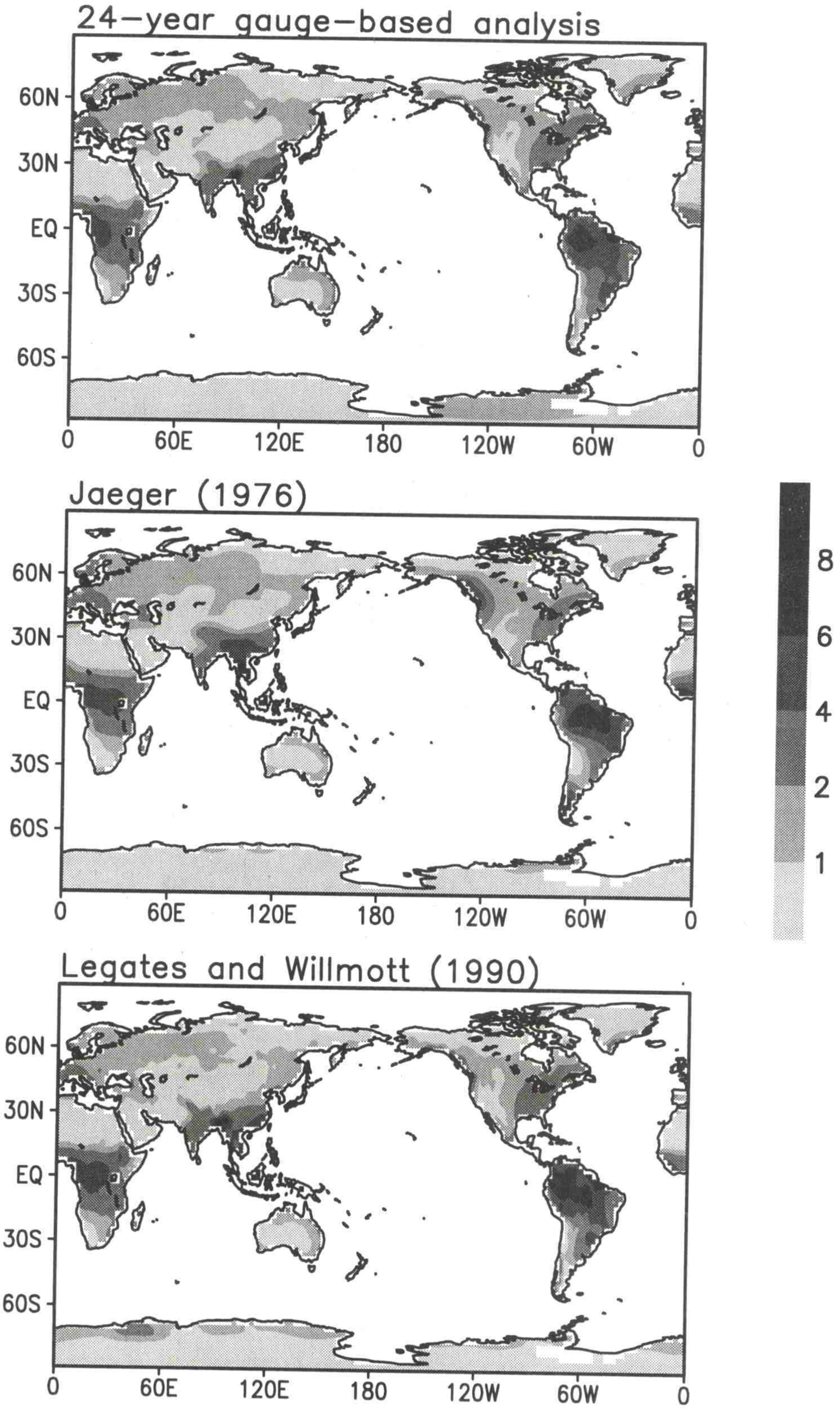

Fig.1 Distributions of annual mean precipitation (mm/day) averaged from the 24–year gauge–based analysis. Long–term means of Jaeger (1976) and Legates and Willmott (1990) are plotted as well for comparison.

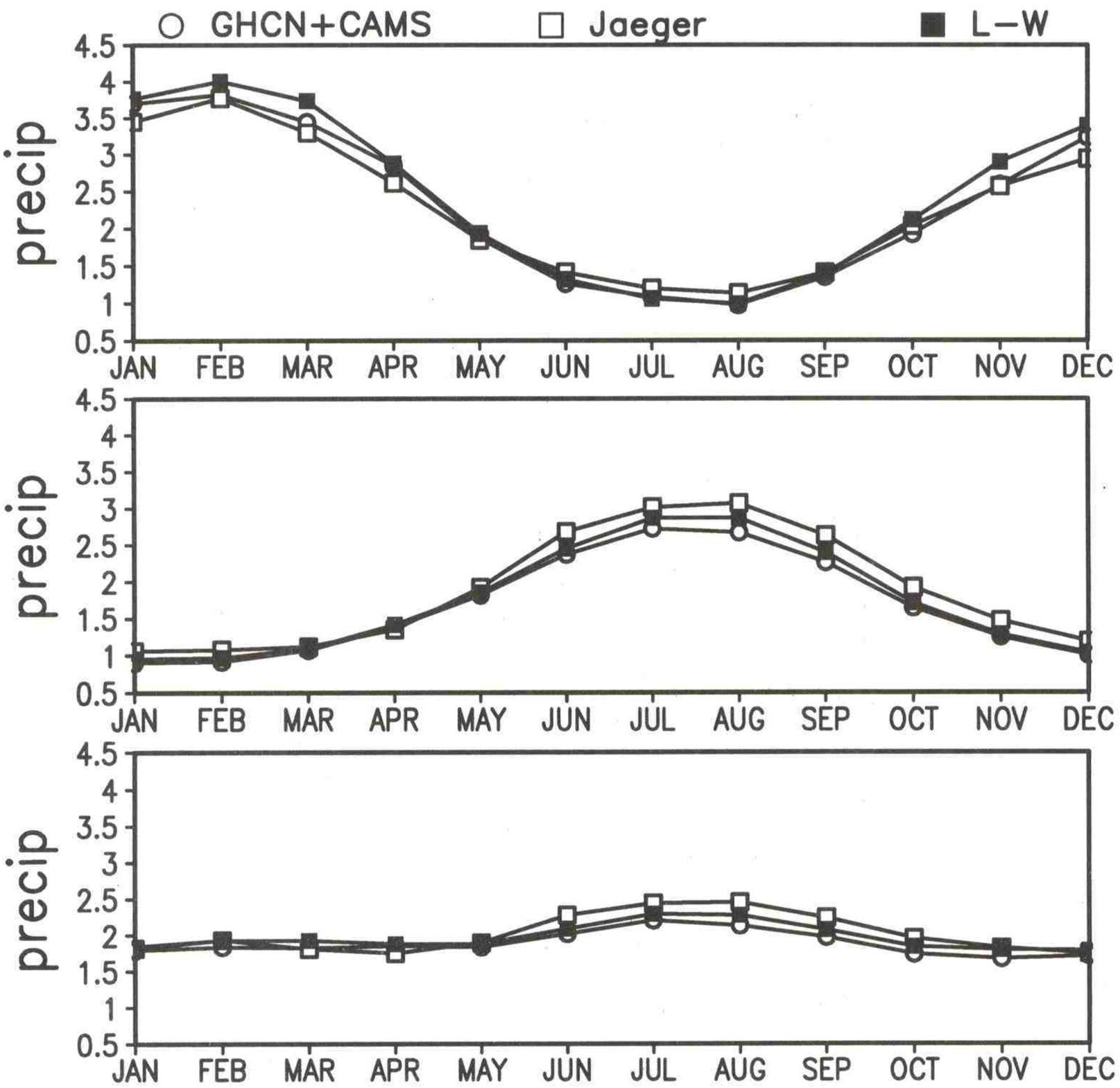

Fig.2 Annual cycles of mean precipitation (mm/day) over grids with at least 50% land over Southern Hemisphere (top), Northern Hemisphere (middle) and the globe (bottom) from the 24–year gauge–based analysis and from the Long–term means of Jaeger (1976) and Legates and Willmott (1990).

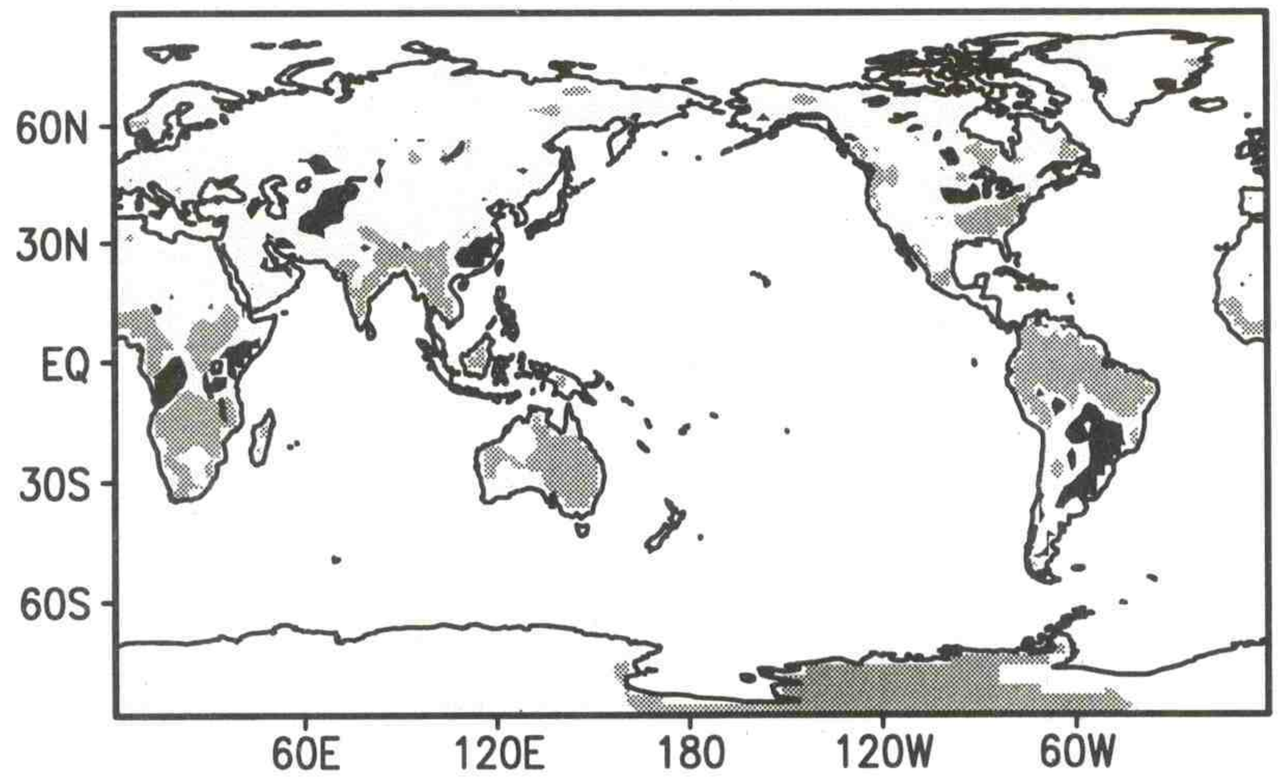

Fig.3 Differences between warm and cold ENSO episodes during the 24–year period for the annual mean precipitation. Areas of wetter (drier) warm ENSO episodes, with difference larger than 0.2 mm/day, are shaded in heavy (light) hatching.

The Diurnal Cycle of Precipitation over the U.S. as Determined from a Comprehensive Hourly Raingauge Dataset

John Janowiak and Wayne Higgins
Climate Prediction Center/NCEP/NWS/NOAA
Camp Springs, MD 20746

I. INTRODUCTION

A dataset containing *hourly* accumulations of precipitation over the period 1963 through 1993 for approximately 2800 cooperative and National Weather Service (NWS) sites were obtained from the Techniques Development Laboratory (TDL) of the NWS. These data, which TDL originally obtained from the National Climatic Data Center in Asheville, NC, were then gridded to a 2.5° longitude by 2.0° latitude grid using a Cressman-type objective analysis procedure. The gridded dataset was then analyzed to determine annual and seasonal precipitation amount and frequency, and the characteristics of the mean diurnal cycle as represented in these data were explored and compared to a similar study performed by Wallace (1975). The results of this simple study suggest that this new dataset is a useful resource from which one can study continental U.S. precipitation on time scales varying from sub-daily to interdecadal.

II. DATA

The ungridded raingauge data are composed primarily of observations from Universal and Fischer/Porter raingauges. The Fischer/Porter instruments, from which, nearly half of the precipitation observations were recorded, record only in increments of 0.1 inch (2.54 mm). Thus, a low bias is inherent in these data, since amounts less than 0.1 inch (2.54 mm) are not recorded. However, the *relative error* decreases proportionally with increasing precipitation amounts.

The station data (approximately 2800 sites) are distributed such that the mean spacing among sites is approximately 70 km (Fig. 1). After gridding to a 2.5° longitude by 2.0° latitude grid, the domain of the dataset (a 33 x 21 array) is bounded in longitude between 140°W-60°W and in latitude by 20°N-60°N. The size of 31-year gridded data set (1963-1993) is 775 MB.

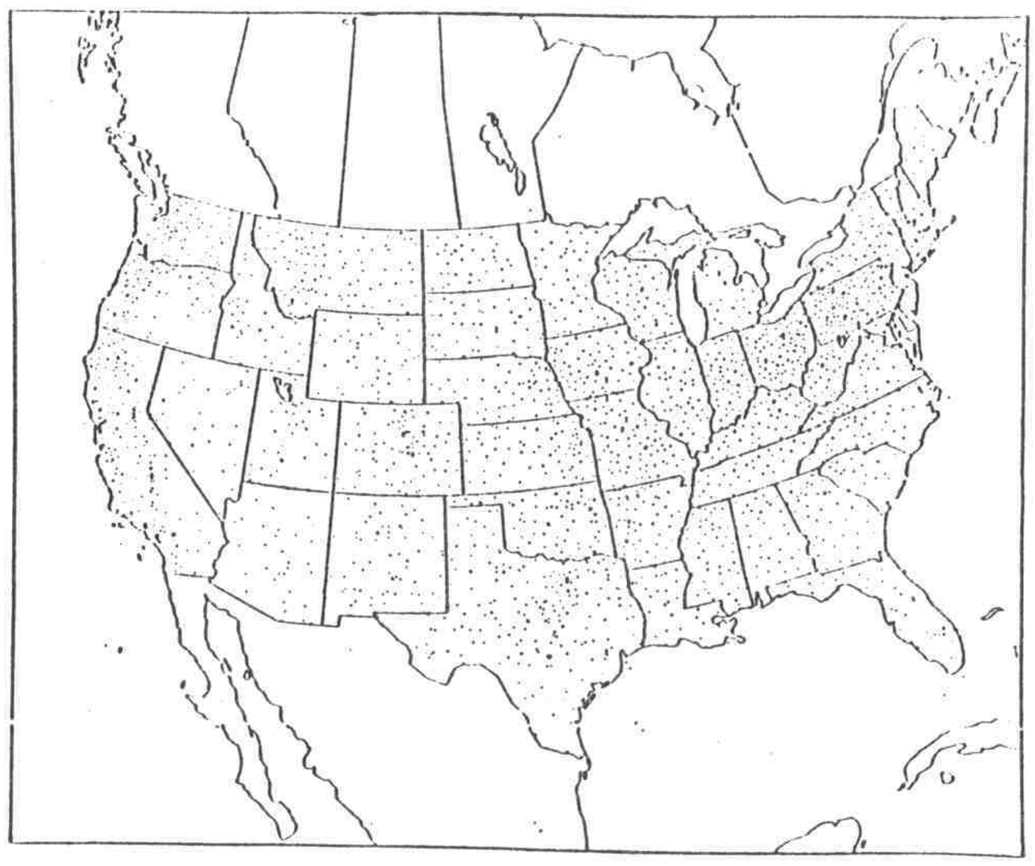

Figure 1. Locations of reporting stations during 1973-1981.

III. DATA ANALYSIS

1. Annual and seasonal

Annual precipitation amounts (Fig.2a) indicate that the Northwest (coastal Oregon and Washington) and Southeast (centered over Alabama and Mississippi) parts of the country

experience the largest precipitation amounts on an annual basis, with amounts exceeding 1250 mm. Precipitation amounts east of the Mississippi River are 3 to 4 times the amounts in the western U.S., exclusive of the Pacific Northwest region. The spatial pattern of annual precipitation frequency (Fig. 2b) is very similar to that of mean annual precipitation amount. The highest frequency of precipitation, on an annual basis, occurs in the Pacific Northwest, despite a pronounced dry season during the summer months in that region. Rainfall occurs more than 20% of the time, on average, over the western third of Oregon and Washington.

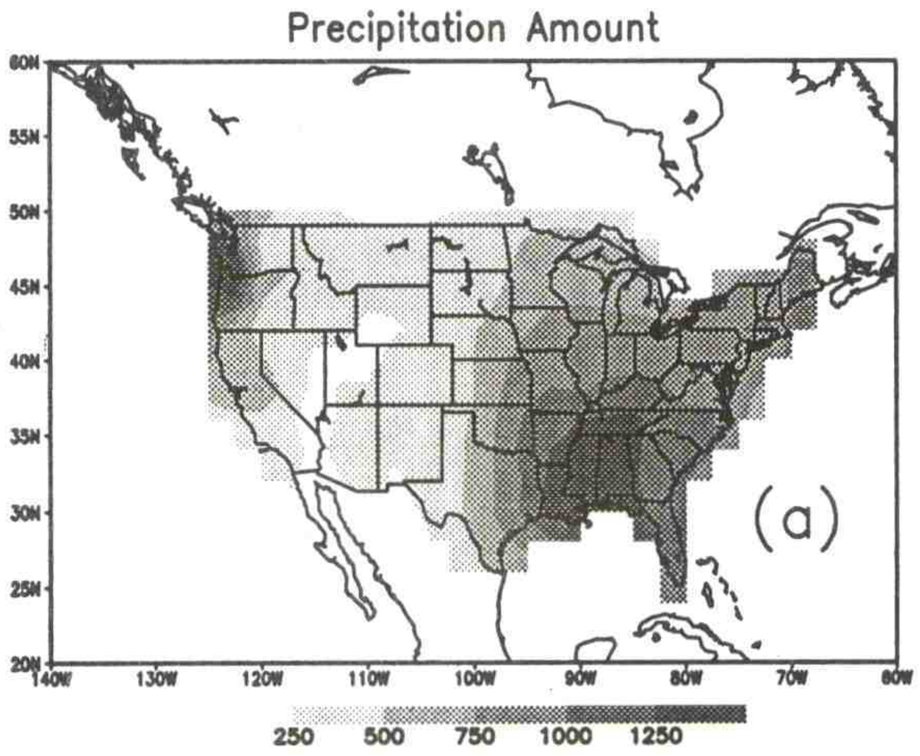

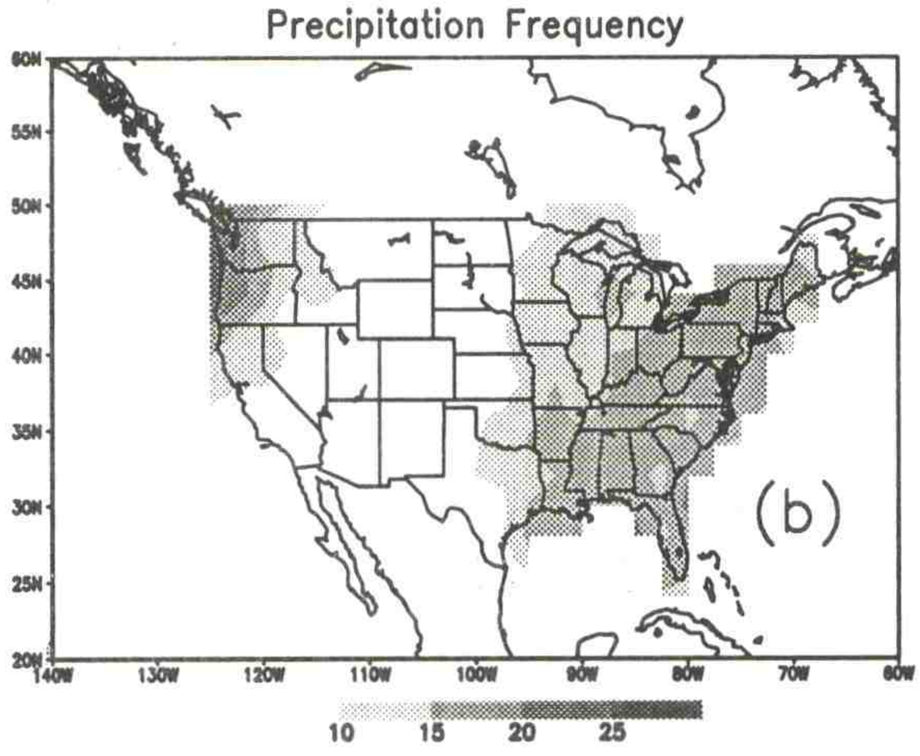

Figure 2. (a) Mean annual precipitation (mm) and (b) mean annual precipitation frequency (percent) during 1963 to 1993.

2. Diurnal variation

An harmonic analysis was performed on the mean hourly precipitation *frequency* over the period 1963-1993 for each grid point in the gridded data set. Separate analyses were performed for the June -August (JJA) and November-March (NDJFM) seasons. These analyses were conducted using the same criteria as imposed by Wallace (1975) which are:

- mid-point in time of the hourly data were used as the reference time

- events at each location had to occur at least 0.9% (0.5%) of the time for the JJA(NDJFM) seasons to be used in the analysis

- amplitudes were normalized by the daily means

The first harmonic of the diurnal cycle of precipitation frequency for JJA (Fig.3a), is in good agreement with Wallace (1975) and indicates a coherent mid-afternoon maximum in precipitation frequency in the Southeast U.S. and the well-documented "midnight" maximum in the central part of the country. Substantially high normalized amplitudes of the first harmonic are also evident in the intermountain states, where an early evening maximum in precipitation frequency is indicated during this season. Relatively small normalized amplitudes extend from the Great Lakes region southwestward to Oklahoma. During the cool season (Fig. 3b), the time of maximum frequency occurs from early to mid-morning east of the Mississippi, except near noon in the extreme Southeast, and near noon as well in most of the western states.

Another depiction of the diurnal cycle of precipitation is presented in Figure 4. In this plot, the percentage of precipitation that is observed during the 3-hour period centered on the time of most frequent occurrence to the mean daily total rainfall for JJA is displayed. A

3-hour period represents about 12% of a day. Thus, if rainfall were equally distributed over the day, one would expect 12% of daily accumulated rainfall to fall over the 3-hour period of maximum frequency. However, in the southeastern U.S., more than one-fourth of the daily rainfall during the summer months falls in the 3-hour period near the time of maximum frequency which is mid-late afternoon in this part of the country (Fig. 3). Similarly, the nocturnal rainfall over much of the Great Plains states accounts for more than 20% of the daily rainfall in that region during JJA. During the cool season, when the amplitude of the diurnal cycle is considerably less, the percentage of precipitation that occurs near the time of maximum precipitation frequency is correspondingly less (Fig. 4b).

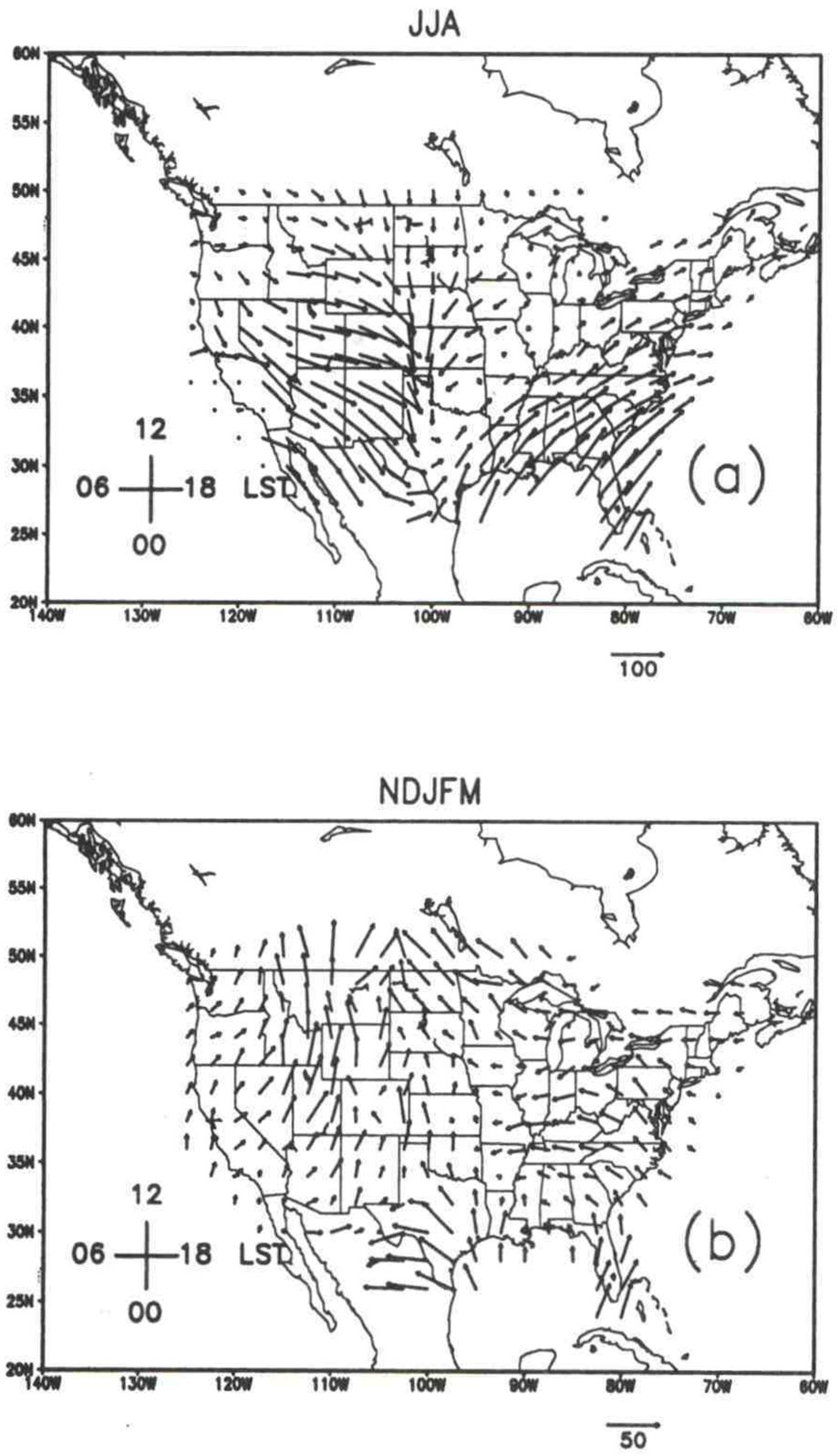

Figure 3. Time of maximum rainfall frequency for (a) JJA and (b) NDJFM determined from harmonic analysis. Time of maximum is represented in harmonic dial form as described in the legend in each figure.

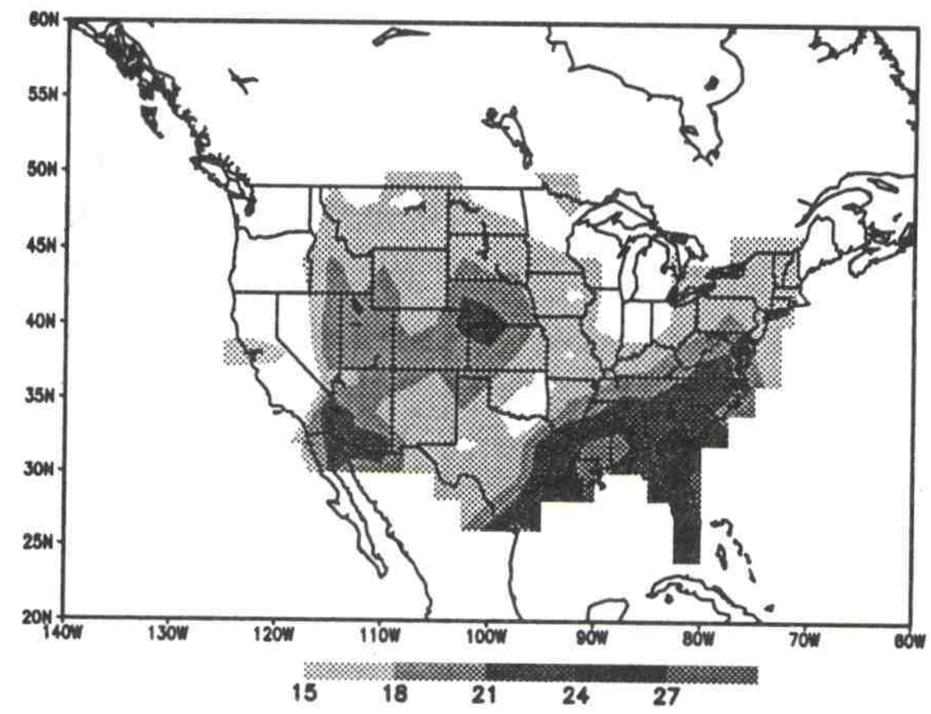

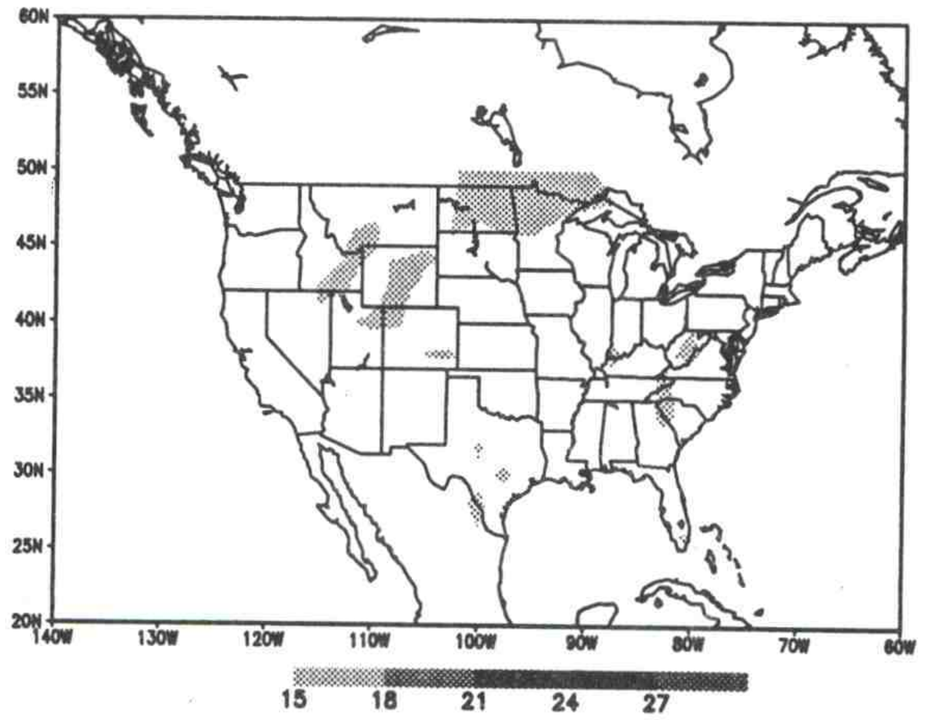

Figure 4. Percent of daily total rainfall contributed by precipitation occurring during 3-hour period centered on hour of maximum precipitation frequency for (a) JJA and (b) NDJFM.

Wallace, J. M, 1975: Diurnal variations in precipitation and thunderstorm frequency over the conterminous United States. *Mon. Wea. Rev.*, **103**, 406-419.

Seasonal Characteristics of Precipitation over the United States in AMIP simulations

James S. Boyle
Program for Climate Model Diagnosis and Intercomparison
Lawrence Livermore National Laboratory
Livermore, CA

Introduction

The seasonal precipitation patterns across the United States represent a broad range of climate types indicative of diverse precipitation mechanisms. These patterns have been documented in many works, e.g. Hsu and Wallace(1976), Horn and Bryson(1960), Kirkyla and Hameed(1989). It is challenge for a climate general circulation model (GCM) to produce precipitation patterns that match those observed over the US. In order to be successful the model must be capable of simulating successfully the proper interaction of a number of precipitation mechanisms, synoptic scale storms, convective complexes, upslope enhancement, even some tropical systems.

Hsu and Wallace (1976) applying a harmonic analysis to 30 years of precipitation observations over the continental US established that there were the following regimes:

(a) An area of pronounced winter maximum in the western states with a Mediterranean regime to the south and west coast regime in the pacific Northwest.

(b) A broad flat area of early summer maxima over the Great plains and Great Lakes, a continental interior regime.

(c) Small areas of late summer maxima over Florida and west Texas which are probably monsoonal in character.

(d) A region of weak spring maxima over the interior of the southeastern states.

(e) A region of weak seasonal variability over the middle and north Atlantic states.

(f) A region of strong semi-annual variability with February and August maxima, centered over Arizona.

These patterns are a result of a subtle blending of a number of physical processes and geographical characteristics. The geographical detail of the above climate regimes should not be expected to be simulated by some of the coarser grid models.

The ability of a model to properly simulate the annual cycle of precipitation would appear to be a necessary precursor to making predictions based on various climate change scenarios. In addition the value of climate predictions to watershed variability depend on an accurate annual cycle. If the precipitation is not distributed correctly through the year then the predictions are not as useful for agricultural or hydrological purposes.

Data sets

The Atmospheric Model Intercomparison Project (AMIP) of the World Climate Research Programme's Working Group on Numerical Experimentation (WGNE) provides a rich data set for model intercomparison. The participants in AMIP simulate the global atmosphere for the decade 1979 to 1988 using a common solar constant, and CO2 concentration, and a common monthly averaged SST. and sea ice data set. An overview of AMIP is provided by Gates (1992).

The observed data used here was blended from two sources. Over the land the data were from Schemm et al. (1992). These data were derived from station data and gridded to a 4 x 5 mesh. Over the ocean the data were from the MSU estimates of Spencer (1993). These observations are taken over the same time period as the AMIP simulations, 1979 to 1988 and consist of monthly mean data.

For the models participating in AMIP, there are available monthly means of precipitation (120 months of data) on the native grid of the model. This is a gaussian grid for the spectral models and usually a regular latitude, longitude grid for the gridpoint models. Monthly data for individual years were averaged together to obtain means for the 12 months of the year.

Figure 1a is a chart of the normalized amplitude and phase of the annual cycle in precipitation over the US using the observed data set described above. Figure 1a compares well with the analogous chart of Hsu and Wallace (1976), their Fig. 8. The data of Hsu and Wallace have considerable more detail than Fig. 1 since they used the individual stations which have a fairly dense distribution over the US. However, since our purpose is to compare against GCM output Fig. a1 is depicting the level of detail appropriate for many of the models participating in AMIP (see Table 1). From the discussion in Hsu and Wallace (1976) quoted in the introduction, it appears reasonable to distinguish three

regimes for the annual cycle over the continental US. A western region, 130W-110W, 30N-50N, which has a winter maximum, a central region, 110W-90W, 30N-50N, with a summer maximum, and an eastern region, 90W-75W, 30N-45N, with a weak annual cycle. One might argue over the individual merits of data sets and analyses techniques but a rough division into these three regions would appear to be robust across all data sets. From a practical standpoint, since there are so many models to be intercompared we must simplify the analysis to a few manageable points of comparison. A presentation of all the model results as in Fig. 1 would be rather overwhelming. Figure 1b presents curves of the observed data set averaged over the regions described above for the 12 months of the year. Subsequent presentations of the models will be deviations from these observed averages.The precipitation is averaged over the area indicated from the native grid of the models.These data represent means over ten seasons and as such should be fairly robust indicators of the model climate.

Results

Figure 2a presents the deviations between the observations and the models for the annual cycle in precipitation over the eastern region of the US, 90W-75W, 30N-45N. The dark shading indicates a model is overestimating the precipitation, the light shading indicates that the model is too dry. The most general observation from Fig. 2a is that the models tend to have a distinct spring or summer surplus and a fall and winter deficit, although there is a considerable amount of variation. This pattern is a consequence of the fact that most of the models have a substantially greater seasonal variation than the observations with a distinct spring/summer maximum and a winter minimum. There are some models that have a relatively subdued seasonal cycle, but virtually all the models have more variation than the observations. As will be shown, this apparent superiority of some models is often the result of compensating errors in the region rather than an overall better simulation.

Figure 2b shows the annual cycle in precipitation for the central US region. Note the presence of a summer maximum and winter minimum in the observed data on the top of the plot. The models tend to capture this seasonal variation but often have much too large an amplitude. There is also a marked tendency to push the maximum to occur too early in the spring. The models in general overestimate the precipitation in this region.

Figure 2c shows the annual cycle in precipitation for the western US region. There is an improvement from the previous two figures in that overall the models have smaller deviations. Once again there is a tendency to overestimate the springtime amounts. The summertime minima appears to be more faithfully simulated than the magnitude of the winter maximum in this region.This could be the result of using common SSTs, so that all the models feel the cold water off the West coast. It is rather remarkable that although the observed climatological phase is reversed in going from the central to the western region, the location of the deviations between Figs. 2b and 2c are quite similar.

The deviations of Fig. 2 are not related in any obvious way to any single property of the model formulation. A model with low resolution such as #11 (GISS) appears to perform better than models with more than double the number of gridpoints. Neither is the type of convective parameterization a robust discriminator. The GLA model, #12, has somewhat different values in Fig. 2 from the UCLA, #26, but both have the same horizontal resolution and both use a version of the Arakawa-Schubert convective scheme. However, an almost all pervasive characteristic is an overestimate of precipitation in the Spring and early Summer. This might indicate a shortcoming in the formulation of almost all the convective parameterizations in dealing with midlatitude convective instability endemic to this season. It might be that parameterizations that are optimized for Tropical convection do not perform as well in the midlatitude regimes.

Table 1 Model identification numbers

model	number	model	number	model	number
BMRC	1	GISS	11	NMC	21
CCC	2	GLA	12	NRL	22
CNRM	3	GSFC	13	RPN	23
COLA	4	IAP	14	SUNY	24
CSIRO	5	JMA	15	SUNY/G	25
CSU	6	LMD	16	UCLA	26
DERF	7	MGO	17	UGAMP	27
DNM	8	MPI	18	UIUC	28
ECMWF	9	MRI	19	UKM	29
GFDL	10	NCAR	20	YON	30

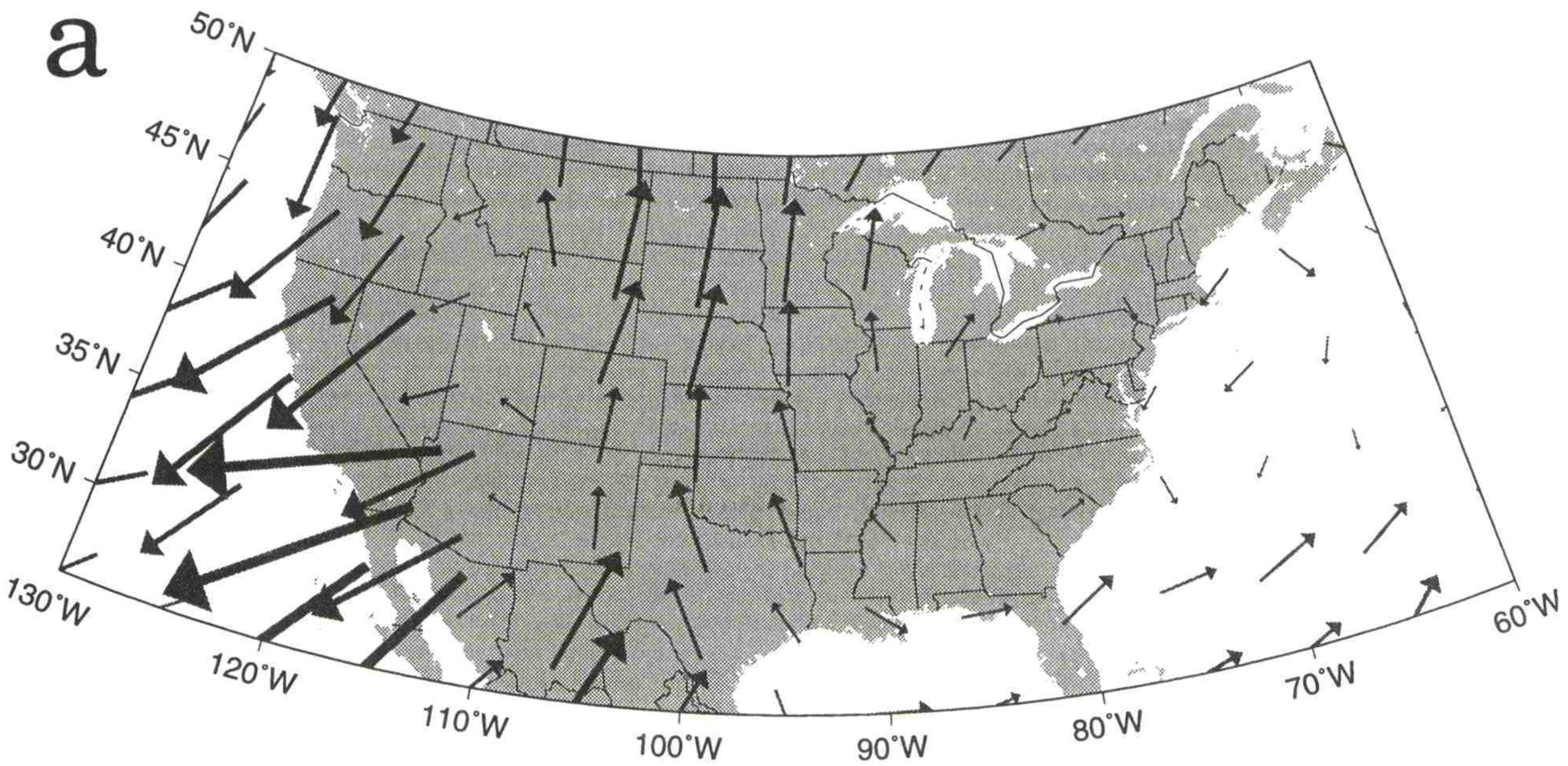

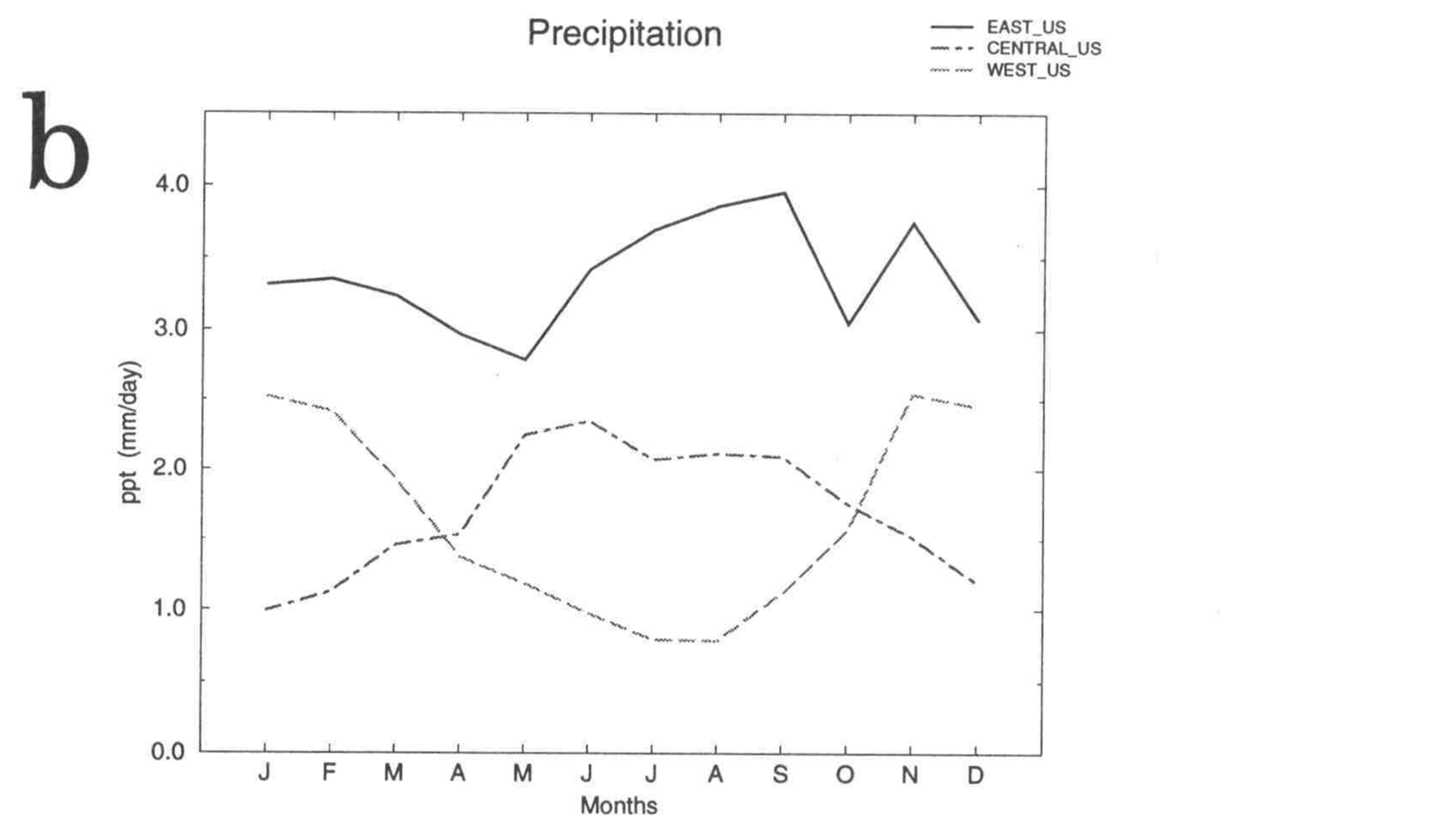

Figure 1. (a) Normalized amplitude and phase of the annual cycle in precipitation over the US. An arrow pointing from north to south indicates a maximum on 1 January, one pointing east indicates a maximum on 1 April and so forth.

(b) The decadal average (1979-1988) seasonal cycle of areal averaged observed precipitation for the three regions mentioned in the text, Eastern, Central and Western United States.

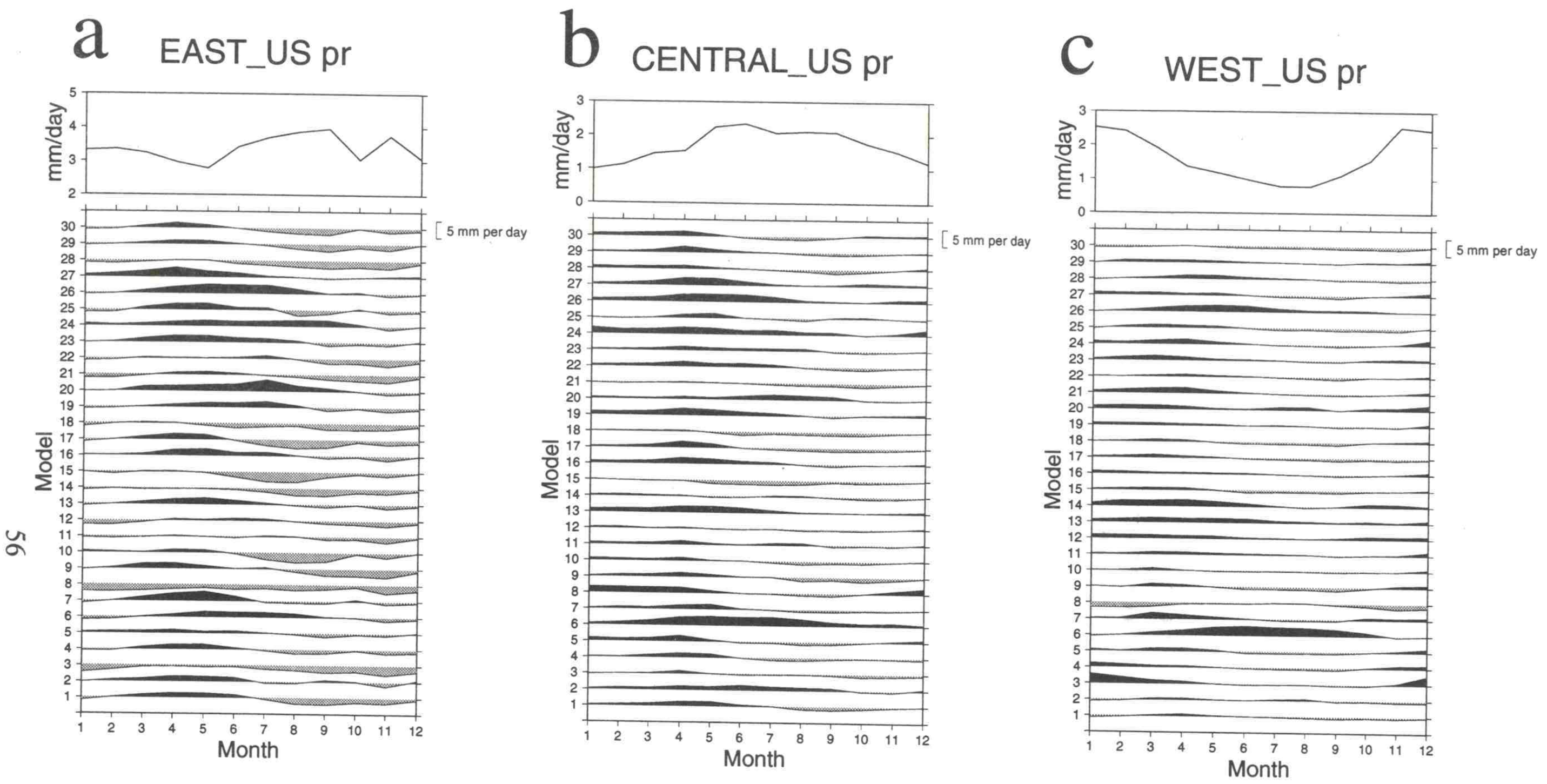

Figure 2. Deviations of the areal averaged precipitation of the AMIP models from the observations over the 10 year (1979 to 1988) mean annual cycle. The precipitation is averaged over the regions (a) Eastern US (90W-75W, 30N-45N), (b) Central US (110W-90W, 30N-50N) , and (c) Western US (130W-110W, 30N-50N). The plot for the observed precipitation is given by the curves at the top of the figures. The models are arranged alphabetically with #1 being the BMRC model and #30 being the YONU model.

SST REGULATION IN THE INDIAN OCEAN: A COUNTERPOINT TO THE PACIFIC WARM POOL

Johannes P. Loschnigg and Peter J. Webster
Program in Atmospheric and Oceanic Sciences
University of Colorado, Boulder, CO. 80309-0311

1. Introduction

A variety of processed exist in the tropical oceans for the limiting of sea-surface temperatures (SST). Recent research has listed many feedbacks which would help to constrain the SSTs in the global ocean to an upper limit near 30°C. Such feedbacks could be a key factor in any predictions of global temperature changes, and examination of these processes in the tropical oceans is particularly important, due to the fact that these areas can have significant effects on the climate of regions spanning the entire globe. For example, the western Pacific "warm pool" has been shown as the area of origin for the "El Nino/Southern Oscillation", and the Indian Ocean is considered to be a key element in the development of the Asian/Indian Monsoon, one of the largest seasonal changes of circulation on the globe.

Much of the recent discussion of SST regulation mechanisms has focused on the Pacific Ocean. During most of the year in this region, SST remains at a temperature greater than 28°C. Observations generally show a maximum in cloudiness and, thus, a minimum in insolation. The juxtaposition of maximum SST with maximum cloudiness led Ramanathan and Collins (1991) to the conclusion that the ocean-atmosphere system self-regulated the SST by a natural thermostat process. In that theory, warm water produces deep convective cloud, with associated cirrus anvils of high albedo. The solar shielding these clouds provide in turn reduces the SST. While the theory has been subject to considerable scrutiny and a number of modifications to include such processes as enhanced evaporation and etc., (e.g., Fu et al, 1992; Hartmann and Michelsen, 1993; Stephens and Slingo, 1992; Wallace, 1992) it is generally recognized that the radiative feedback is at least a component of a system that is in almost local balance.

It does not appear that the mechanisms that regulate SST in the western Pacific Ocean are necessarily dominant in the other tropical oceans. If the theory is ubiquitous then the regions of warmest SSTs in all of the tropical oceans should be collocated with outgoing longwave radiation (OLR) minima. Whereas this is generally true in the western Pacific, it is certainly not the case in the Indian Ocean during large parts of the year, as will be seen in section 3.

2. SST Feedback Processes

The energy balance for a column of the tropical ocean surface can be written as:

$$c_p \, dT_s/dt = SW + LW - LE - SH - \Delta F_o$$

Where T_s is both the temperature of the oceanic mixed layer and the SST, c_p is the heat capacity of the mixed layer, SW and LW are the net solar and longwave radiative heating of the surface, respectively, LE and SH are the latent and sensible turbulent heat fluxes away from the surface, and ΔF_o is the export of heat out of the region by oceanic transport. The term on the left hand side takes into account the the change in heat content, or heat storage, of the uppermost layers of the ocean. On the right hand side, the shortwave term generally varies only with cloudiness, as the surface albedo of the ocean is fairly constant. Longwave heating is more complex, as the amount of blackbody radiation emitted by the ocean surface generally rises with increasing SST, but the downwelling longwave radiation of the atmospheric boundary layer increases as well, due to enhanced atmospheric water vapor. Latent heat flux, or evaporative cooling, generally increases with SST, as evaporation is considered a function of the humidity of the air in contact with the ocean surface.

Most of the discussion of SST regulation mechanisms mentioned in section 1 have focused on those processes which are dominant in the Pacific Ocean, meaning some or all of the terms in the above equation, except for ocean transports. Figure 1 shows the general schematic of the basic combination of processes used in the studies of SST regulation. The first combination represents a system which may remain near local thermodynamic balance or equilibrium such as suggested by the thermostat hypothesis for the western Pacific ocean. The second combination shows a mechanism whereby atmospheric transports can regulate the SST by transporting heat laterally and vertically away from the ocean surface. In this case, evaporative heat loss cools anomolous hot patches of ocean surface, and large-scale dynamical circulation redistributes this heat evenly over the entire tropical troposphere. Finally, ocean transports may be important either

horizontally through ocean currents or vertically through mixing.

If one were to attempt to use similar methods to describe the dominant processes in the northern Indian Ocean, one would note that the first combination does not fully describe the situation, as this region is not in thermal equilibrium with the atmosphere. There is a net flux of greater than 100 $W m^{-2}$ into the ocean. Nor does the second mechanism appear likely. In the Gulf Stream region very large cooling of the SST take place through evaporation and the transport of latent heat away from the region by atmospheric processes. In the North Indian ocean the wind are light and the net flux of heat is into the ocean and not the reverse as would be required for the atmospheric transports to regulate the SST. This leaves ocean transports. At first glance this would seem unlikely as it is generally thought that ocean transports exist on much longer time scales. Furthermore, for the transport to be correct, there would have to be a negative latitudinal flux of heat (i.e., north to south) during the spring and early summer and a reversed flux during the winter.

3. Surface Heat Balances in the Indian and the Pacific Oceans

The major goal of the TOGA COARE experiment (Webster and Lukas, 1992) was to obtain a better estimate of the surface heat balance. From this experiment and the considerable research activity in the Pacific during COARE, the heat balance is fairly well known. Unfortunately, the heat balance is less well known in the Indian Ocean and we have to rely on the gross estimates of Oberhuber (1988) obtained from the long term COADS data set. (Estimates of the surface balances in the western Pacific and the northern Indian Ocean are shown in Figure 2.)

Perhaps one of the more striking differences between these two regions is intense solar radiation received at the ocean surface in the northern Indian ocean for most of the spring and early summer. Figure 3 shows a time-longitude section (time upwards) of the OLR and SST along 12°N. Over the western Pacific Ocean maximum SST matches low OLR for the entire year. However, over the Indian Ocean, during the spring and early summer there is no such relationship. The lack of low OLR here shows an absence of the deep-convective, high albedo clouds that could help in regulating the shortwave radiation received at the surface. In this region, OLR minima do not occur until the onset of the Asian monsoon in June. From Oberhuber (1988), the maxima in OLR corresponds to a maximum in insolation. In fact, the insolation is order 200-250 Wm^{-2} during the spring months compared to 100 Wm^{-2} for the Pacific.

In summary, during the boreal spring and early summer in the Indian Ocean, the warmest sea surface temperatures on the globe are associated with maximum insolation and very light winds. During the summer, after the commencement of the monsoon, the northeastern Indian Ocean remains warm despite a minimum in insolation and much stronger winds. In the northwestern Indian Ocean the SST reduces substantially due to strong upwelling and evaporating.

Using these observations for both the Pacific and Indian Oceans, it is possible to make predictions of how the oceanic mixed layer in each region would respond to such conditions. The heat balance of the Pacific ocean warm pool suggests that the change in SST will be very small. Indeed using the Kantha-Clayson mixed layer model (Kantha and Clayson, 1994), Webster (1994) showed that the temperature increase should be about 0.1°C/month. On the other hand, the same model predicts a temperature increase of 1.5°C/month for the Indian Ocean, or, 6°C during the four months of spring and early summer. However, such an increase is not observed and, in the absence of significant cloud increases, the SST in the North Indian Ocean remains constant. The puzzles are thus:

- Why does the Indian Ocean remain at nearly a constant temperature even though there is a net flux of 100-150 Wm^{-2} into the ocean. Taking into account the area of the North Indian Ocean, this flux results in a gain of 10^{15} W.
- Are there differences between the physical processes that regulate the SST in the Indian and Pacific oceans?

4. The Role of Ocean Transports in the Regulation of SST in the Indian Ocean

During TOGA COARE, a concerted effort by nineteen nations attempted to close the heat balance in the Pacific Ocean. Thus, we have a fair idea of the disposition of energy at the surface of the pacific warm pool. However, no such experiment has taken place in the Indian Ocean and we are forced to use models to test the hypothesis that ocean transports are capable of regulating SST in the Indian Ocean. We choose the dynamic model of McCreary et al, (1993). The model is a two and a half layer intermediate model with full dynamics and thermodynamics. In the upper layers a secondary mixed layer may develop. Although there is little subsurface data in the Indian ocean, the model has been shown to replicate the surface structure of the Indian Ocean as well as its annual cycle. The ocean model is run in stand alone mode. That is, the ocean forcing is prescribed from climatological data sets.

Figure 4 shows the net northward heat transport across the equator as a function of time of year, as well as the net surface heat flux over the ocean basin north of the equator, and the heat storage of the uppermost ocean layers for the same region. The northward heat flux between two positions along a line of constant latitude is defined be:

$$F_Q = \rho_w C_w \int h_i T_i v_i \, dx$$

where h_i, T_i, and v_i are the depth, temperature and meridional velocity component of the i^{th} layer of the model. The figure shows a very strong southward flux of heat during the spring and early summer and a reverse flux during the winter. This net flux is made up of opposing flows in the upper and lower layer of the model and may be thought of as a seasonally reversing meridional circulation (McCreary, et al, 1993). The magnitude of the net southward flux across the equator matches the total flux into the North Indian Ocean quite well at roughly 10^{15} W. Similar values, but of opposite sign, occur during the winter when the North Indian Ocean is losing considerable amounts of heat by evaporation, and strong vertical wind mixing which entrains colder water from below the thermocline.

5. Conclusions and Further Work

The Indian Ocean stands out in quite sharp contrast to the Pacific Ocean. There, warm SSTs are not accompanied by convection and a consequent minima in the insolation. Instead, the warmest SSTs on the globe at that time of the year are accompanied by a maximum in insolation. Yet, the SST does not show appreciable increases. Thus regulation of the SST is not accomplished by radiative effects. Instead, it appears that the ocean transports manage quite well in regulating SST by meridional heat transports.

A number of very basic questions remain to be answered:

- Why doesn't large scale convective cloudiness accompany maxima in SST like in the Pacific Ocean? Is it because the Indian Ocean, until the onset of the monsoon, is strongly subsident thus inhibiting convection?
- What forces the oceanic heat transports? Is it purely oceanic and driven by latitudinal buoyancy gradients? Is it driven by wind stress such that it is a combined ocean-atmosphere phenomenon?

From the perspective of this study:

- The calculations were run with the ocean model in "stand-alone" mode with the driving mechanisms being supplied from climatological atmospheric and flux data. What changes in the results can be expected when the model is run in coupled mode?

We anticipate approaching these questions with a combination of modeling and observational analysis.

6. References

Fu, R., A.D. Del Genio, W. B. Rossow and W.T. Liu, 1992: Cirrus-cloud thermostat for tropical sea surface temperatures tested using satellite data. *Nature*, 358, 394-397

Hartmann, D.L., and M.L. Michelsen, 1993: Large scale effects of tropical sea surface temperature, *J. Clim.*, 6, 2049-2062

Kantha, L.H. and C.A. Clayson, 1994: An improved mixed layer model for geophysical applications, *J. Geophys. Res.*, 99, 25,235-25,266

McCreary, J.P., Kundu, P.K., and Molinari, R.L., 1993: A Numerical Investigation of Dynamics, Thermodynamics and Mixed-layer Processes in the Indian Ocean. *Progress in Oceanography*, 31, 181-244

Oberhuber, J.M., 1988: An atlas based on the COADS data set: The budgets of heat, buoyancy and turbulent kinetic energy at the surface of the global ocean. Rep. 15, 20pp. Max-Plank Inst., Hamburg, Germany

Ramanathan, V., and Collins, W., 1991: Thermodynamic regulation of ocean warming by cirrus clouds deduced from observations of the 1987 El Nino. *Nature* , 351, 27-32

Stephens, G. and T. Slingo, 1992: An air-conditioned greenhouse. *Nature*, 358, 369-370

Wallace, J. M., 1992: Effect of deep convection on the regulation of tropical sea surface temperatures. *Nature*, 357, 230-231

Webster, P.J. and R. Lukas, 1992: TOGA COARE: The Coupled Ocean-Atmosphere Response Experiment, *Bull. Am. Meterorol. Soc.*, 73, 1377-1416

Webster, P.J., 1994: The role of hydrological processes in ocean-atmosphere interactions. *Reviews of Geophysics*. 32, 427-476

7. Acknowledgement

This work is supported by the National Science Foundation under grant no. ATM-9214840.

$$Cp\ dT/dt = SW + LW + LE + SH + \Delta Fo$$

1 ⌊ Ramanathan and Collins

2 ⌊ Wallace, Stephens and Slingo. Fu et al

3 ⌊ Indian Ocean

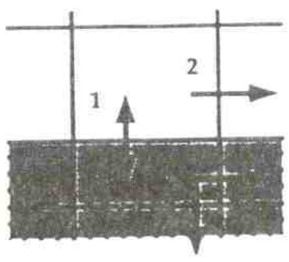

1: Local surface heat balance

2: Atmospheric heat transports (working together with (1))

3: Oceanic heat transports

(or combinations of all three sets of processes)

Figure 1: Schematic of the general processes of how SST may be regulated

Western Pacific Ocean: **Process 1 >> 2,3**

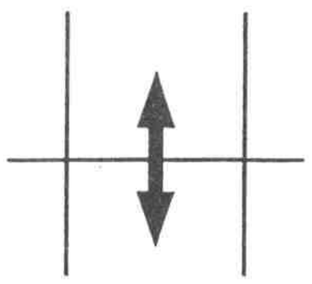

SW = +150
LW = - 50
LE = - 75
SH = - 5
} 10-20 W m^{-2}

North Indian Ocean

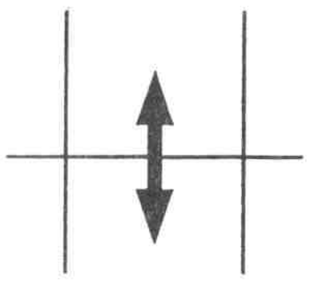

SW = +250
LW = - 50
LE = - 75
SH = - 5
} 100-150 W m^{-2}

Figure 2: Estimates of the general surface heat balance for the Western Pacific and Northern Indian Oceans

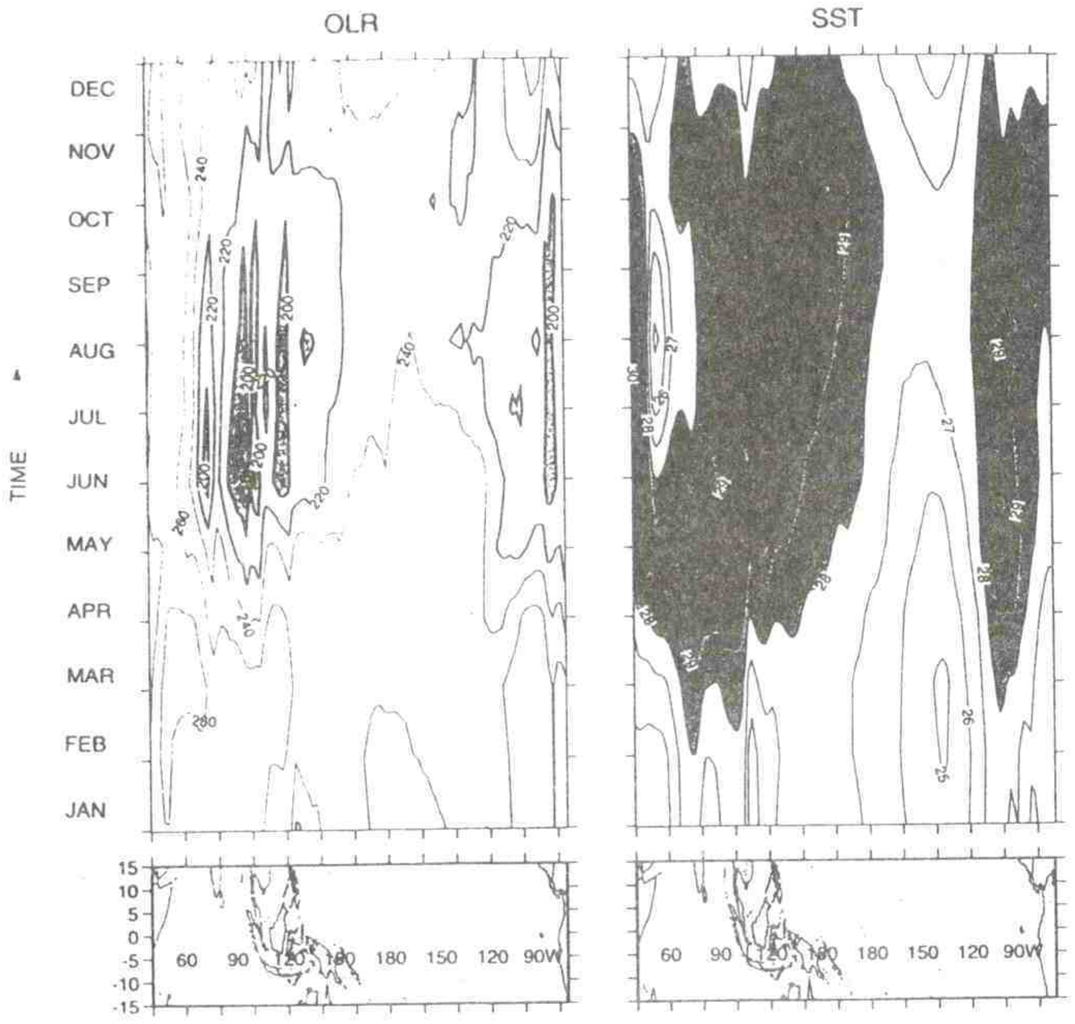

Figure 3: Time-Longitude section of OLR and SST for the Indian and Pacific Oceans along 12°N

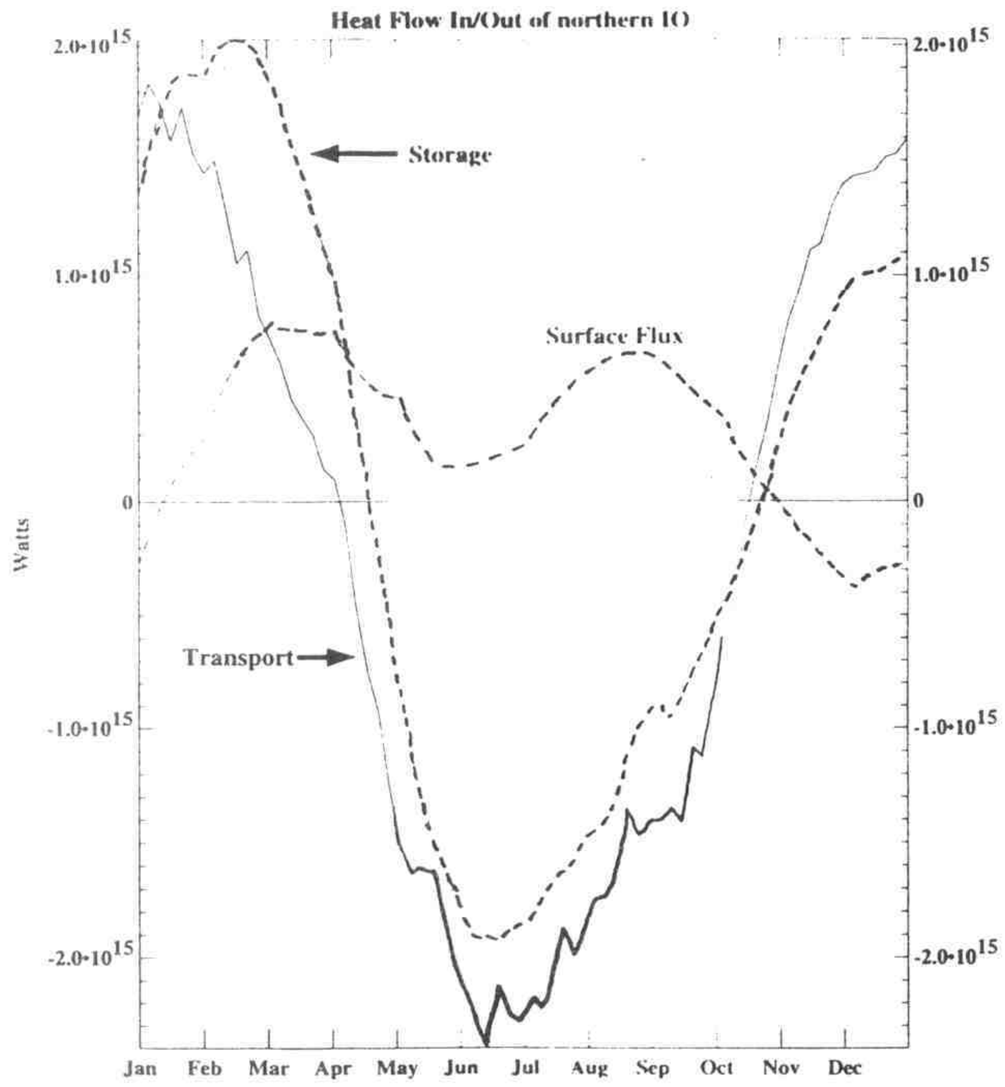

Figure 4: Heat balance of the Indian Ocean north of the equator.

Monsoon Rainfall in the GEOS-1 Assimilation: Sensitivity to Input Data

Chung-Kyu Park
Joint Center for Earth System Science
University of Maryland
College Park, MD 20742-2425

Siegfried D. Schubert, David J. Lamich, and Yelena Kondratyeva
Data Assimilation Office Code 910.3
Goddard Space Flight Center/NASA
Greenbelt, MD 20771

1 Introduction

Operational analyses produced by analysis/forecast systems have become an important tool for climate research. One of the most difficult problems often encountered in using the operational analysis data, however, is the spurious variations in the analysis data introduced by frequent changes and improvement of the NWP systems. Reanalysis, for this reason, has become an important subject with the hope that it will resolve the problems with the operational analyses. The primary objective of reanalysis is to minimize the variability due to algorithm changes and to isolate the climate signals by using a fixed assimilation system. Whereas the signals due to model changes can be successfully eliminated in the reanalyses, changes in the input data are another potential source of spurious climate signals even in the nonvarying analysis system. The changes in input data may result from, for example, increasing the number of observation stations, the introduction of new data types and changes to quality control procedures. The primary interest in this study is to evaluate the sensitivity of monsoon rainfall to the moisture and height reports from the NMC's reject list stations largely distributed in the Indian subcontinent.

2 Sensitivity Experiments

We have performed a series of experiments to evaluate the sensitivity of the analysis to the input data changes. In experiment A, the raw-insonde data purged by the SDM (Senior Duty Meteorologist at NMC) or on the reject list are not used in the assimilation, while the reports from the reject list stations are used in experiment B. In experiment C, only the moisture information from the reject list stations is used, while only the height information from the reject list stations is used in experiment D. The information from the reject list stations used in these experiments are summarized in Table 1.

Table 1. Sensitivity experiments

	$\bar{A}$	$\bar{B}$	$\bar{C}$	$\bar{D}$
Height	$\bar{N}$o	$\bar{Y}$es	$\bar{N}$o	$\bar{Y}$es
Winds	$\bar{N}$o	$\bar{Y}$es	$\bar{N}$o	$\bar{N}$o
Moisture	$\bar{N}$o	$\bar{Y}$es	$\bar{Y}$es	$\bar{N}$o

3 Results

Figure 1 shows the difference between the assimilated precipitations with and without using the rawinsonde reports from the reject list stations for June and July 1994. It is found that the precipitation is substantially increased over the Indian subcontinent region by using the rawinsonde reports from the reject list stations. Increased precipitation is also found over the western Pacific, where the observations are sparse. The precipitation increase over these regions suggests that the reject list station reports have a significant impact on the assimilated rainfall over the data sparse regions, while the impact appears to be insignificant over East Asia where the rawinsonde observation stations are dense.

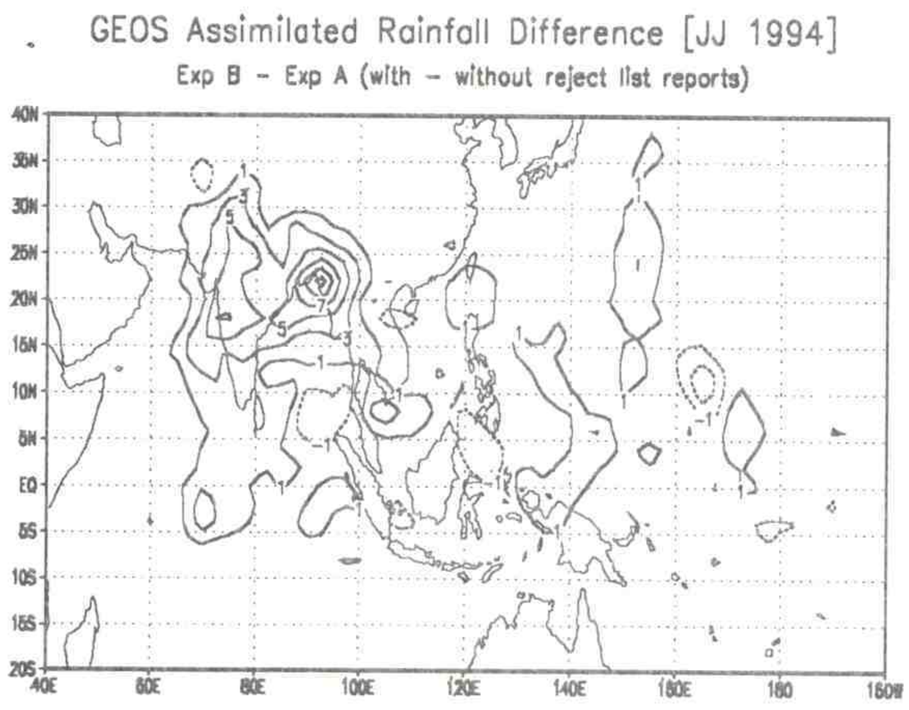

Figure 1. Difference between precipitations assimilated with and without using the reject list reports for June/July 1994. Contour interval is 2 mm/day.

Figure 2 shows the sensitivity of the assimilated precipitation to the moisture and height information separately. As shown in Fig. 2(a), the precipitation difference is mainly due to the moisture reports, while the impact from the height information is much weaker over the Indian monsoon region.

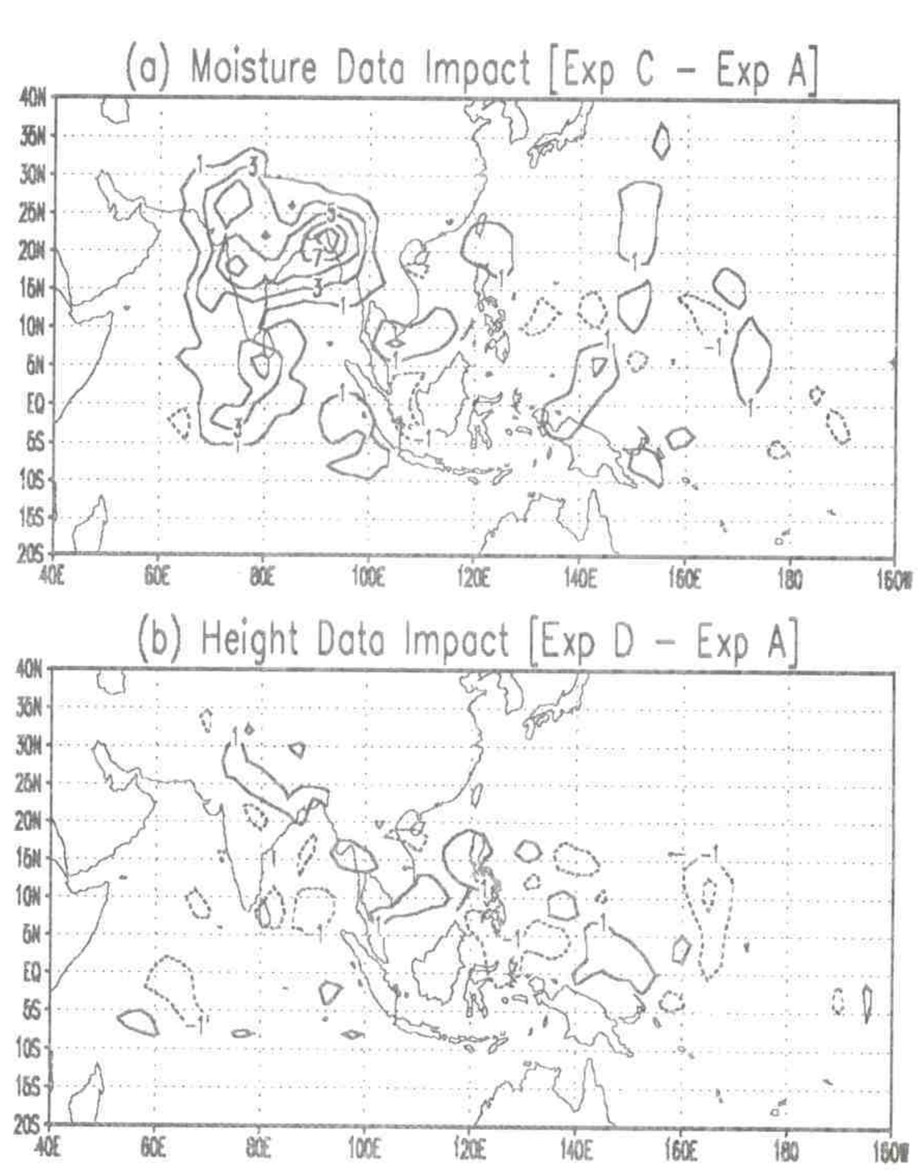

Figure 2. Difference between precipitations assimilated with and without (a) the moisture data and (b) the height data from the reject list stations for June/July 1994. Contour interval is 2 mm/day.

In Figure 3, the latitude-pressure sections over the Indian monsoon region (70E-100E) reveal that both height and moisture fields are substantially modified by the rawinsonde reports from the reject list stations. It is interesting to note that in Fig. 3(a) the height fields increase in the upper troposphere and decrease in the lower troposphere due to moisture information from the reject list stations. Fig. 3(b) shows that the low level moisture is enhanced over the Indian subcontinent region with maximum at the 800 mb level between 10N and 25N. The influence of the moisture increase also extends over the Indian Ocean south of the Equa-

tor. The enhanced convection associated with the moisture changes is likely responsible for the dynamically driven height changes over the Indian monsoon region. The height changes due to moisture data are comparable to the height changes due to height data (Fig. 3c). The moisture changes due to height information in Fig. 3(d) indicate that the moisture changes are induced by the circulation changes associated with the enhanced upper level divergence and low level convergence. The moisture increase south of the high mountains suggests that a part of the moisture increase around 30N in Fig. 3(b) may also be dynamically driven.

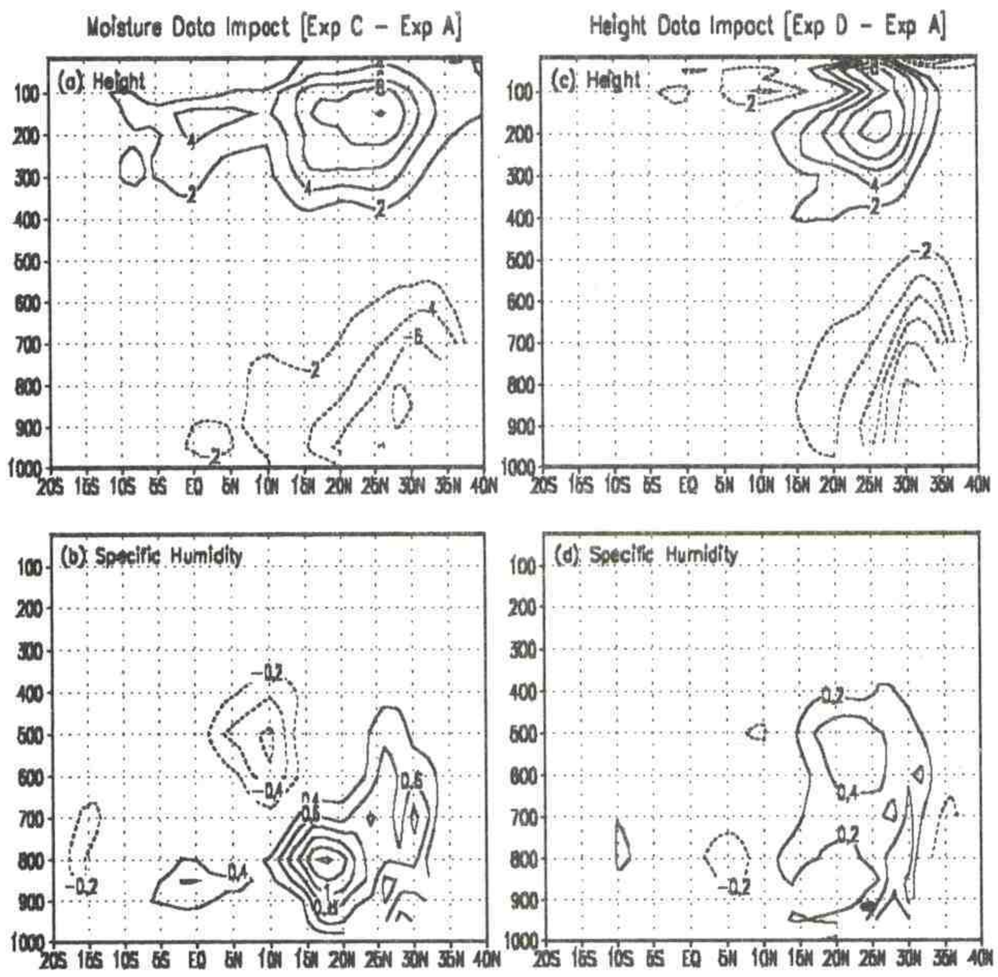

Figure 3. Latitude–pressure section over the Indian monsoon region [70E–100E] of (a) height and (b) moisture difference due to moisture data and (c) height and (d) moisture due to height data from the reject list stations for June/July 1994. Contour intervals are 2 meter for height and 0.2 g/kg for specific humidity.

The temporal variations of the monsoon precipitation in assimilations with and without using the reject list stations show a substantial difference not only in the mean rainfall amount, but also in the low frequency variation (Figure 4). The rainfall variation in Fig. 4b is rather weak (less than 2 mm/day) during the monsoon period except for the variation associated with diurnal cycle, while the difference in Fig. 4c indicates that the reports from the reject list stations introduce substantially stronger rainfall variations with a period of about two weeks.

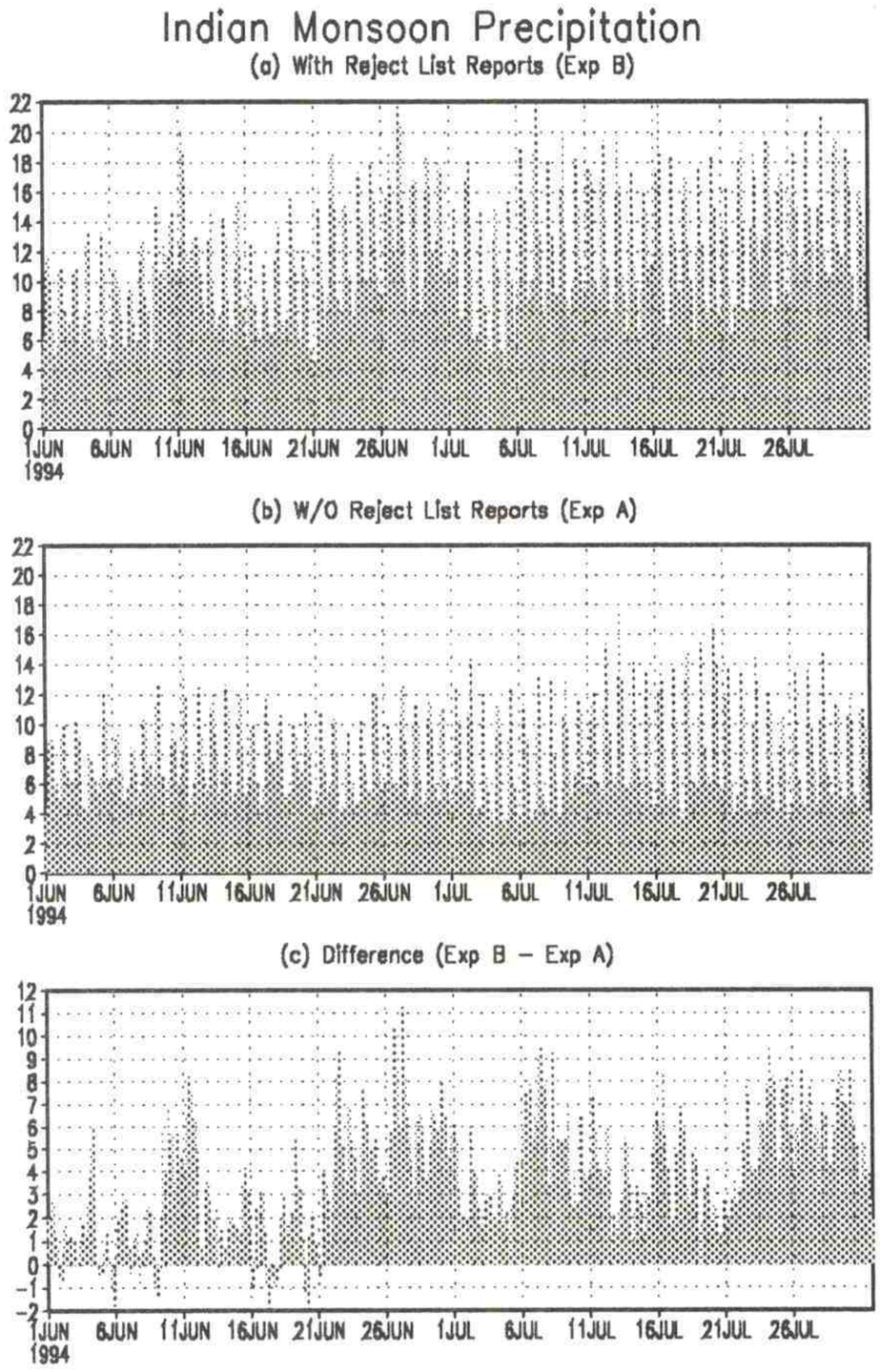

Figure 4. GEOS precipitation over the Indian monsoon region (a) with and (b) without using the reject list reports, and (c) their difference.

The temporal variations of the rainfall, moisture, and the number of reports from the reject list stations are compared in Figure 5 in order to examine whether the low frequency fluctuation is generated by the internal dynamics or forced by the low level moisture fluctuation associated with the observations from the reject list stations. Fig. 5(a) shows the temporal variation of the Indian monsoon precipitation difference due to the reports from the reject list

stations. The temporal variation appears to be similar to the variation of the vertically integrated moisture difference in Figure 5(b). The number of moisture reports from the reject list stations over the Indian monsoon region in Figure 5(c) clearly show a low frequency variation similar to those of the precipitation difference and the moisture variations. These similar variations suggest that at least part of the monsoon rainfall fluctuation is an artifact of the moisture changes associated with uneven forcing from the observations ingested in the data assimilation.

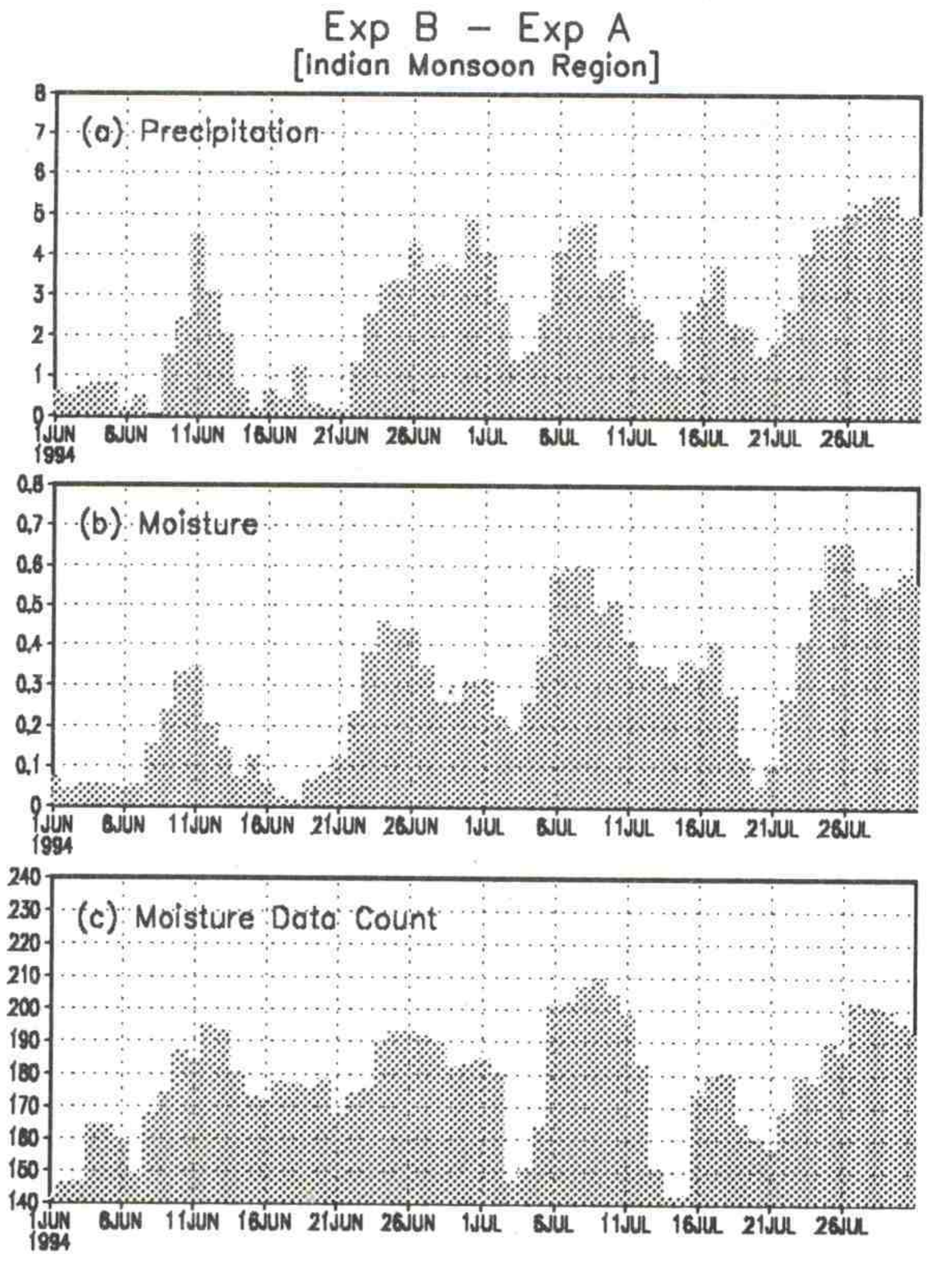

Figure 5. Difference between (a) precipitations, and (b) moisture, assimilated with and without the reports from the reject list stations (with−without), and (c) the number of reports from the reject list stations over the Indian monsoon region (10N−30N;70E−100E).

4 Summary

The Data Assimilation Office at Goddard Space Flight Center is currently producing a multi-year gridded global atmospheric dataset using a fixed assimilation system designed to remove the variability due to algorithm changes. While the signal due to system changes has been eliminated, changes in the input data are another potential source of spurious climate signals. In this study, a set of sensitivity experiments are performed with the GEOS assimilation system to assess the impact of including temperature and moisture information from stations on the NMC reject list that are not used in the GEOS assimilation system.

The results from experiments for the northern summer of 1994 with and without the reject list reports indicate that the data impact on the assimilated rainfall is significant in the tropics. The impact of the input data changes is less dramatic over the "data rich" regions. The most significant difference is found over the Indian summer monsoon region. The precipitation without the reject list reports shows unrealistically dry conditions over the Indian monsoon region. The monsoon precipitation is substantially improved by including the reject list reports, which are mainly located in the Indian subcontinent. The sensitivity experiments indicate that the moisture information from the reject list stations has a significant positive impact on the monsoon precipitation, while the temperature information has a much less impact, although not absent. The low-frequency intraseasonal variations of the monsoon precipitation is enhanced in the experiment that includes the reject list reports. It is found that the enhanced quasi-biweekly oscillation in the monsoon precipitation is not dynamically driven, but forced by the observation data. Whereas the inclusion of the reject list reports has a substantial positive impact on the mean monsoon rainfall, the forcing from the inconsistent data introduces spurious temporal variation in the intraseasonal time-scales.

This study suggests that caution is needed when a new data type is introduced in the reanalysis. It is important, especially for climate data assimilation, to have an unbiased model to minimize the sensitivity to the variations in input data.

Systematic Errors in Phase Speed of Transients and their Interaction with the Mean State

Jianchun Qin and Huug. M. van den Dool
Climate Prediction Center, NCEP/NWS/NOAA
Washington, DC 20233

The systematic forecast error is usually calculated from the time mean forecast and observed flow. In addition to the errors in time means, there exists systematic error in transients. Transients simulated by the model could propagate systematically too fast/slow and add significant errors to the forecast. That is, the mean phase speed of propagating transients may be subject to systematic errors. In this work, the systematic error in phase speed of transients predicted by the NWP model is studied. The idea will be explored by using a simple global model, the so-called "divergent anomaly vorticity advection" (dAVA) model (Qin and Van den Dool, 1996). We first analyze the systematic error in phase speed of transients for forecasts made by the dAVA model without any correction. An interactive approach is then applied to the model forecasts to examine the possibility of error correction and resulting forecast improvement. Finally, the mechanism for the gains from the interactive error correction is investigated by means of the wave-mean flow interaction theory.

The historical data used to calculate the "observed" phase speed of transients consist of NMC's daily global analyses of 500mb geopotential height fields, on a 2.5x2.5 grid. In total, 451 days are selected from 5 successive winters (12/01 - 02/28, DJF) over the period December 1, 1990 - February 28, 1995. The climatology used is derived from 15-year monthly means of the operational NMC analyses, and interpolated to the day in question.

The dAVA model can be described in equation by (applied at 500mb level and run at T30 truncation.):

$$\frac{\partial}{\partial t}(\zeta' - \lambda^2\psi') = -\bar{\mathbf{V}}\cdot\nabla\zeta' - \mathbf{V}'\cdot\nabla(\bar{\zeta} + f + \zeta') - D\nabla^4\zeta' - K\zeta' \qquad (1)$$

where $\overline{(\ )}$ and $(\ )'$ denote climatological mean and anomaly. λ^2, D and K are given constant coefficients. The additional term $-\lambda^2\frac{\partial\psi'}{\partial t}$ on the lhs of Eq. (1) is the anomaly form of the "Bolin-Cressman" correction which represents partly the effect of divergence. It turns out that, by changing λ^2, one is able to adjust systematically the phase speed for propagating transients simulated in Eq. (1).

The mean phase speeds of anomaly waves are computed by using the "phase-shifting" method (Cai and van den Dool, 1991). The systematic error in the phase speed of transients is then formed simply by taking the difference between the ones determined from the model forecasts and the NMC analyses respectively. Fig. 1 shows a comparison of the model ($\lambda^2 = 0$, dotted line) generated phase speeds at 1-day lead with the counterpart calculated from the analysis (full line) at selected latitudes. It is seen that large errors in phase speed exist in long waves, especially at the equator. Errors in shorter waves are also not negligible, as the phase

speed error is a relative quantity with respect to the wave length. Similar results are also obtained for other latitudes.

Correction of the phase speed error is first tried by removing the error from the model forecast a posteriori. The resulting gains in terms of forecast skills are significant but only modest. Taking advantage of the efficiency of the dAVA model, we seek alternative way to improve the forecasts. We attempt to adjust the mean phase speed of transients systematically through changing the "Bolin-Cressman" correction term in Eq. (1). Such an adjustment of the phase speed is interactive, in the sense that all of the intended changes are made during the integration of the model. The impact on the phase speed is shown in Fig. 1 (dashed line). An example of the resulting influence on the 1-10-day forecasts made in dAVA is shown in Fig. 2. The improvement in forecast skills is considerable, not only in the eddy flow (defined as instantaneous departure from zonal mean) but also in the zonal mean.

Efforts are then made to understand why the "interactive" correction of phase speed error benefits forecast more effectively, from the perspective of wave-mean flow interaction theory. We believe that there are strong wave-mean flow interactions through which the systematic errors in phase speed of transients would couple with the systematic errors in the zonal mean flow. The following two equations describe roughly the process of 2-way interaction: a) Equation of zonal mean zonal wind,

$$\frac{\partial [U]}{\partial t} \approx -[V]\frac{\partial [U]}{\partial y} + [V]f - \frac{\partial}{\partial y}[u^* v^*] \qquad (2)$$

and b) Rossby wave equation derived from the dAVA model,

$$C_{Rossby} = [\overline{U}] - \frac{\beta^* + \lambda^2 [\overline{U}]}{k^2 + l^2 + \lambda^2} \qquad (3)$$

where [ ] and * represent the zonal mean and the departure from the zonal mean. It is found that reduction of the systematic errors in the phase speed through changing the intensity of the "Bolin-Cressman" correction also diminish the systematic errors in the zonal mean zonal wind (Fig. 3), which, in turn, regulates the transients as a feedback and benefits the forecast interactively. The mutual relationship between the systematic errors in phase speed of transients and the errors in zonal mean zonal wind can be explained by the classic Rossby wave theory and the wave-mean flow interaction mechanism. In particular, the modulation of the zonal mean flow is mainly accomplished by the systematic eddy momentum flux convergence, and its feedback is simply to reorganize the traveling transients that are superimposed on the basic zonal mean flow.

References

Cai, M., and H. M. van den Dool, 1991: Low frequency waves and traveling storm tracks. Part I: Barotropic component. *J. Atmos. Sci.*, **48**, 1420-1436.

Qin, J., and H. M. van den Dool, 1996: Simple extensions of an NWP model. *Mon. Wea. Rev.*, **124**, 277-287.

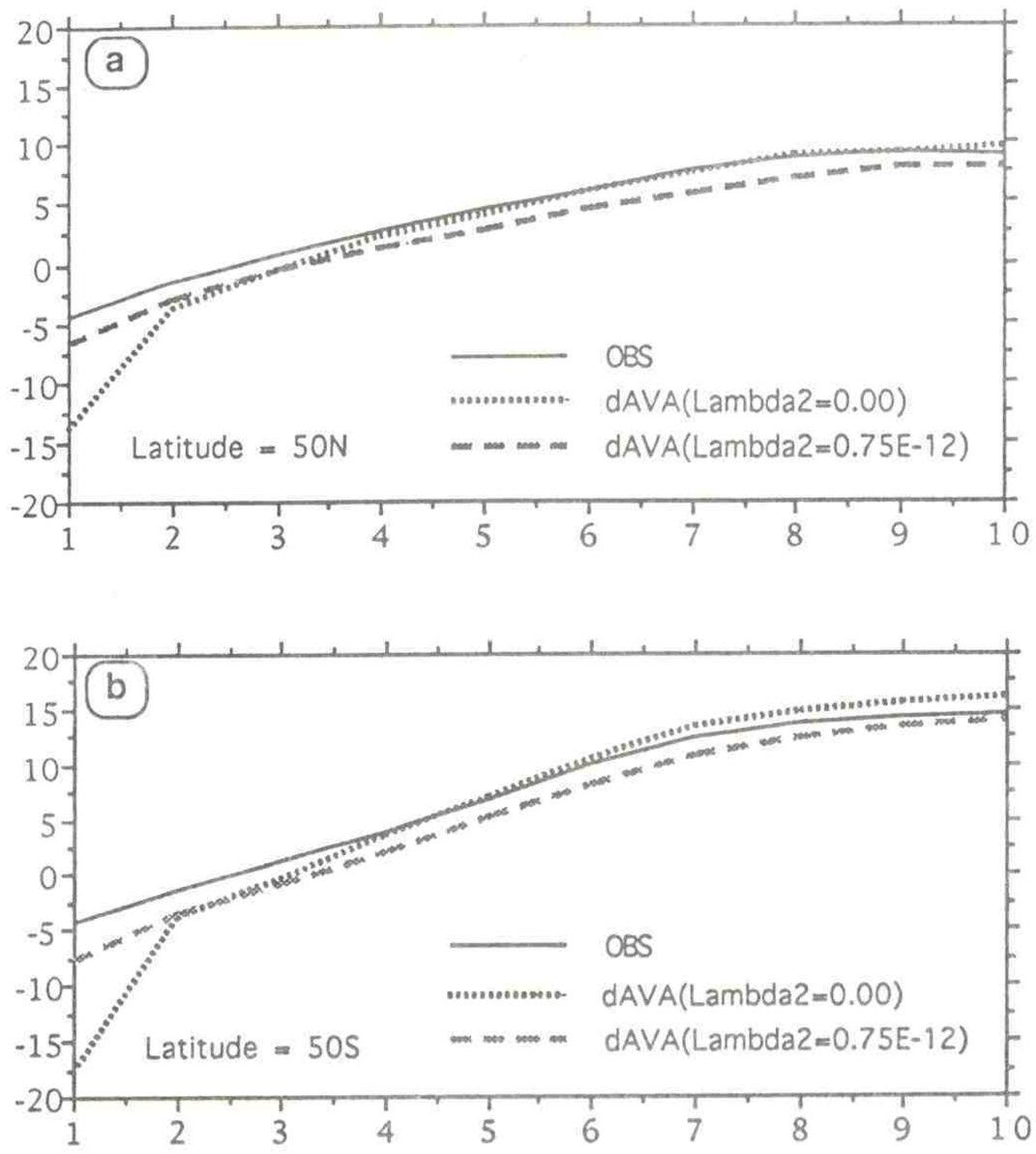

Fig. 1 Phase speed of geopotential height anomaly from dAVA model with different "Bolin-Cressman" parameter (λ^2), as a function of zonal wave number. a) at 50N, b) at 50S, c) at equator. Also shown is the counterpart for NMC analyses.

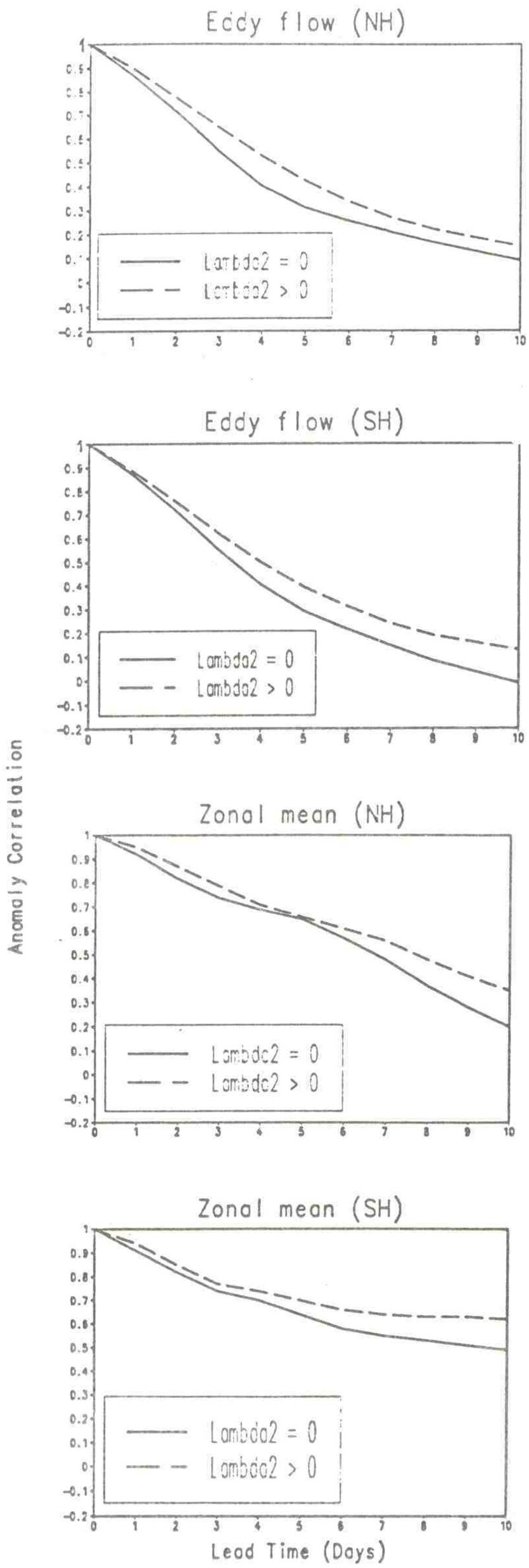

Fig. 2 Anomaly correlation of 1-10 day forecast of geopotential height at 500mb made by dAVA model with (dash line) or without (solid line) the "Bolin-Cressman" correction.

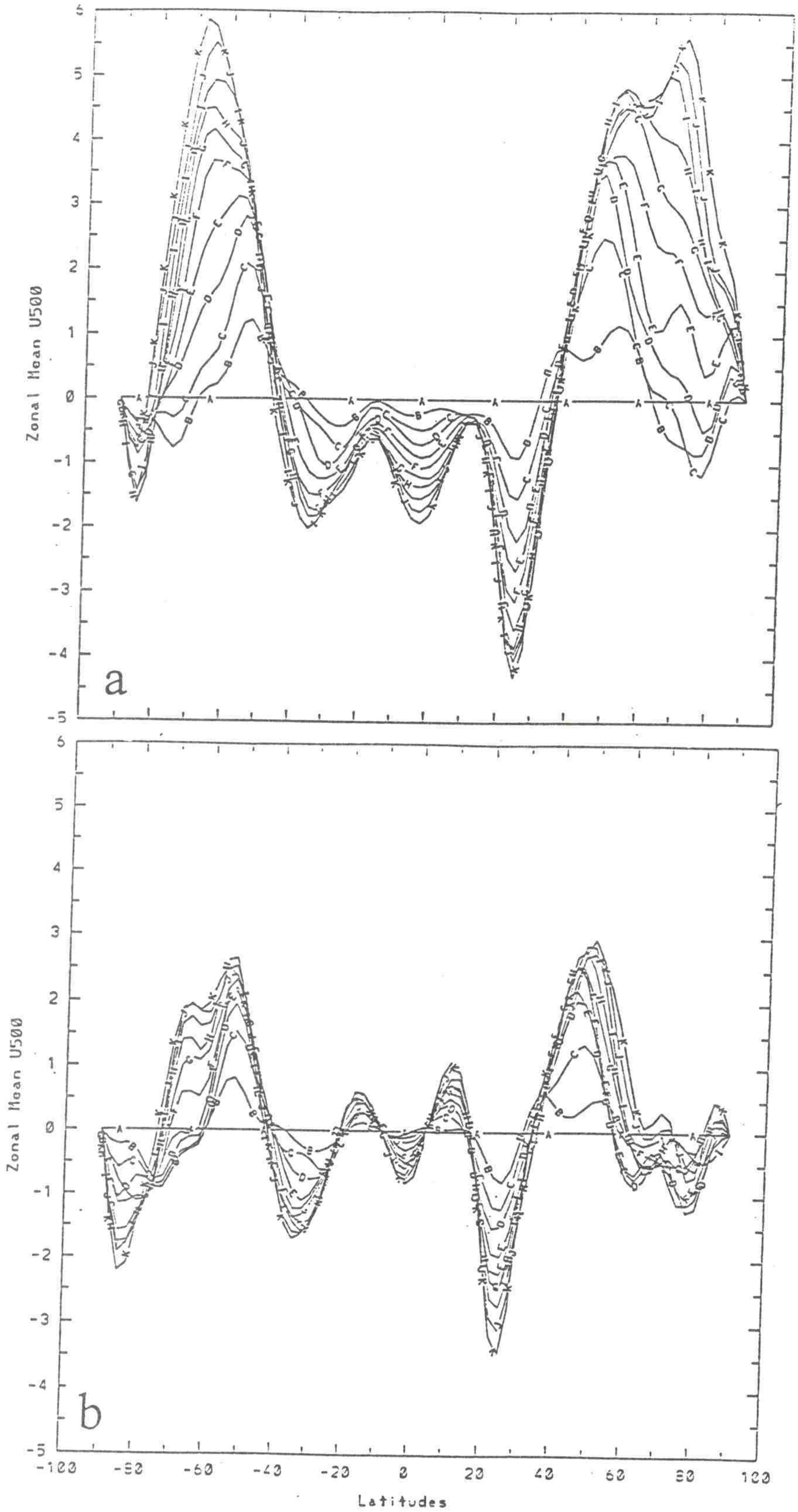

Fig. 3 Systematic error in zonal mean zonal wind $[U]$ of dAVA model's 1-10 day forecasts, without (a) and with (b) "Bolin-Cressman" correction. The alphabet on each curve denotes the lead time: A= 0 day, B=1 day, C=2 day, ... , K=10day, respectively.

A New Global Sea-Ice and Sea Surface Temperature Data Set.

N. A. Rayner and D. E. Parker.
Hadley Centre for Climate Prediction and Research,
Meteorological Office, Bracknell, RG12 2SY. UK.

1 Introduction.

The latest version of the U.K. Meteorological Office (UKMO)'s Global sea-Ice and Sea Surface Temperature data set (GISST2.2) covers the period 1903-1994 and has now been released for use as a prescribed SST field in Atmospheric General Circulation Model (AGCM) integrations of the climate of the 20th century. The product was developed with collaboration from colleagues at NOAA/Climate Prediction Center (CPC) and will form the pre-satellite era SST input fields for the National Center for Environmental Prediction (NCEP) reanalysis project. This is an observations-based product, but has many interpolated data within it and should only be used for observational studies with great care. The Meteorological Office Historical Sea Surface Temperature data set (MOHSST6) is available for anyone who wishes to do a study using purely observed SST.

GISST2.2 has many improvements over the previous version, GISST1.1 [Parker *et al.*], which many groups worldwide have been using in model studies. More *in situ* SST observations have been collected and the Comprehensive Ocean Atmosphere Data Set (COADS) is used to supplement our own historical data base. Other improvements are outlined below.

2 Climatology.

The base of the data set is a new 1^o resolution SST and sea-ice climatology, calculated over 1961-90. This is an improvement over previous climatologies especially in the Southern Ocean and the Arctic, where there had been significant biases. The inclusion of satellite data also results in a better representation of the Gulf Stream and Kuroshio Current areas where SST gradients are tight.

The new climatology builds upon a calendar monthly average of GISST1.1 over 1982-1994, used as a background field. Monthly 1^o latitude by longitude area *in situ* SST superobs for 1961-90 were assembled with ice margin SST estimates (see next section) and expressed as departures from the background field. These monthly departure fields were then linearly interpolated to form global fields. These were then added back to the background field and the 30 monthly fields averaged to a 1961-90 background field, used in a reiteration of the process.

The resulting monthly "GISST2.0" climatology was harmonically synthesized to pentad resolution, from which it was linearly interpolated to produce a daily climatology. This was used in the quality control of *in situ* observations used as a basis for GISST2.2 1949-94.

3 Sea-ice and ice margin SSTs.

The new climatology and the resultant GISST2.2 data set also benefit from newly acquired sea-ice data and the development of a statistically based sea-ice margin SST regression scheme. The new ice data provide an analysis of the concentration of sea-ice within each 1^o grid box in the Arctic (for all months 1903-90) and for the Antarctic (1984-88). When and where observed concentration data were not available, sea-ice concentration was modelled by converting ice edge position data into a linear gradient of concentration. The sea-ice concentration data set is available as a companion data set to GISST2.2.

The sea-ice analysis was used in a regression with available *in situ* SST observations (1961-90) in the Arctic and Advanced Very High Resolution Radiometer (AVHRR) satellite SST measurements (1982-94) in the Antarctic to better determine SST on the ice margins and within the ice pack over the whole of the two regions. All 1^o area monthly SST observations and their surrounding 5^o degree area sea-ice concentrations (observed or derived), within a three month season, within each of a set of 360 running 30^o longitude bands in the Arctic were combined to derive a regression relation of the form:

$$SST = aI^2 + bI + c \tag{1}$$

$I = 1.0$ is equivalent to 10/10 ice concentration, for which SST was constrained to be -1.8^oC. In the geographically simpler Antarctic, one regression relation was developed using monthly data within each season, over the whole region. In both polar regions, 1^o area ice concentrations were then used in the regressions to specify colocated SST: in the Arctic the regression chosen was that for the longitude band centred on the target location. In the development of the GISST2.0 climatology (section 2), however, we used a preliminary version without AVHRR data.

4 Derivation of global SST anomaly fields.

As different periods in the historical SST record have widely varying observed data coverage, we have used three different methods to produce our global SST fields.

2^o area gridded *in situ* SST observations from ships and buoys in 1982-94 were Poisson-blended with satellite measurements. To ensure that this gave globally complete monthly fields, the satellite data themselves had first been Poisson-blended with climatology.

Prior to 1982, however, creation of globally complete fields requires more effort. Two similar methods were used. Monthly fields in 1949-1981 were **reconstructed** using linear combination of 2^o area resolution ocean basin EOFs (see Figure 1 for examples). These EOFs were calculated from a preliminarily filled version of MOHSST6, detrended by taking out values calculated using the first coarse resolution global EOF of a low-pass filtered (> 8 years) version of GISST1.1. This first low frequency EOF is very highly correlated with global mean SST. After reconstruction by the ocean basin EOFs, the trend, was added back to the reconstruction. Fields for 1903-1948 were **interpolated** (ie. in situ observations have been retained and only the data void areas filled with reconstructed values) using coarser resolution ocean basin EOFs. In both cases the underlying theory is the same.

The variance of the fields was first redistributed into ocean basin EOFs. Eigenvectors of the covariance matrix of gridded SST anomaly data were calulated for each of the Atlantic, Indian and Pacific ocean basins (Mediterranean Sea also for 1949-81). In principle, the data from which these were calculated can be reconstructed using:

$$\underline{X} = \underline{ZA} \tag{2}$$

where $\underline{X}$ is the data matrix, $\underline{A}$ the matrix of spatial weights of the whole set of EOFs and $\underline{Z}$ is the set of EOF time series.

The aims of the technique are:

1. To determine Z_{kt} for each EOF,k, at each time,t; given an incomplete data field.
2. To use as many EOFs as will adequately reconstruct the desired SST anomaly field, but minimise the noise contained in the reconstruction. This is necessary as the observed data set from which the EOFs are calculated is inherently noisy.

We are, by definition, reconstructing or interpolating a field where incomplete data coverage exists. This means that any estimate of the time coefficient of the EOFs we make directly from those data will be incorrect as missing data also make a contribution to Z_{kt}. Summation of the products of all pairs of EOF spatial weights at all missing data points provides us with a multiplication factor, which represents the variance

missing from the field. If we define the matrix of this sum to be $\underline{C}'$ and $\underline{Z}_t^*$ to be the coefficients, calculated from the observed data only, of all EOFs used in the reconstruction, the relation:

$$\underline{Z}_t = (\underline{I} - \underline{C}')^{-1} \underline{Z}_t^* \tag{3}$$

allows us to make an unbiased estimate of $\underline{Z}_t$ (Figure 2 demonstrates this graphically), from which we can then reconstruct the whole data field, using Eq. 2.

Between 1903-48, observed data, where available, then replaced reconstructed values, whereas for 1949-81 all the reconstructed data were retained. Because the EOFs were not defined over the whole globe, some data voids still remained. So, some observed data were retained in 1949-81 in Hudson Bay, the Great Lakes and Lake Victoria. Other gaps were filled by Poisson-blending with the climatology. Data available to us for the Caspian Sea were too sparse and too unreliable to include, so all of the Caspian Sea was set to a monthly climatology.

Finally, all monthly 2° area resolution SST anomaly fields were smoothed 1:2:1 east-west then north-south before adding to the GISST2.0 climatology to yield actual values of SST. An example of such an anomaly field, that for July 1988, is shown in Figure 3.

5 Obtaining GISST2.2.

Readers interested in using GISST2.2 should contact D.E.Parker at the above address or by e-mail at deparker@meto.govt.uk. Further details of the processes outlined above can be obtained by writing to the authors.

References

[Parker *et al.*] Parker D.E., C.K.Folland, A.Bevan, M.N.Ward, M.Jackson and K.Maskell. "Marine Surface Data for Analysis of Climatic Fluctuations on Interannual to Century Timescales." National Research Council, 1996. *Natural Climate Variability on Decade-to-Century Time Scales.* Ed. by D.G.Martinson, K.Bryan, M.Ghil, M.M.Hall, T.R Karl, E.S.Sarachik, S.Sorooshian and L.D.Talley. National Academy Press, Washington, DC, *in press.*

Figure 1. Examples of ocean basin EOFs used to reconstruct GISST2.2 1949–81 (EOFs calculated 1951–90). sw/ne shading positive nw/se shading negative.

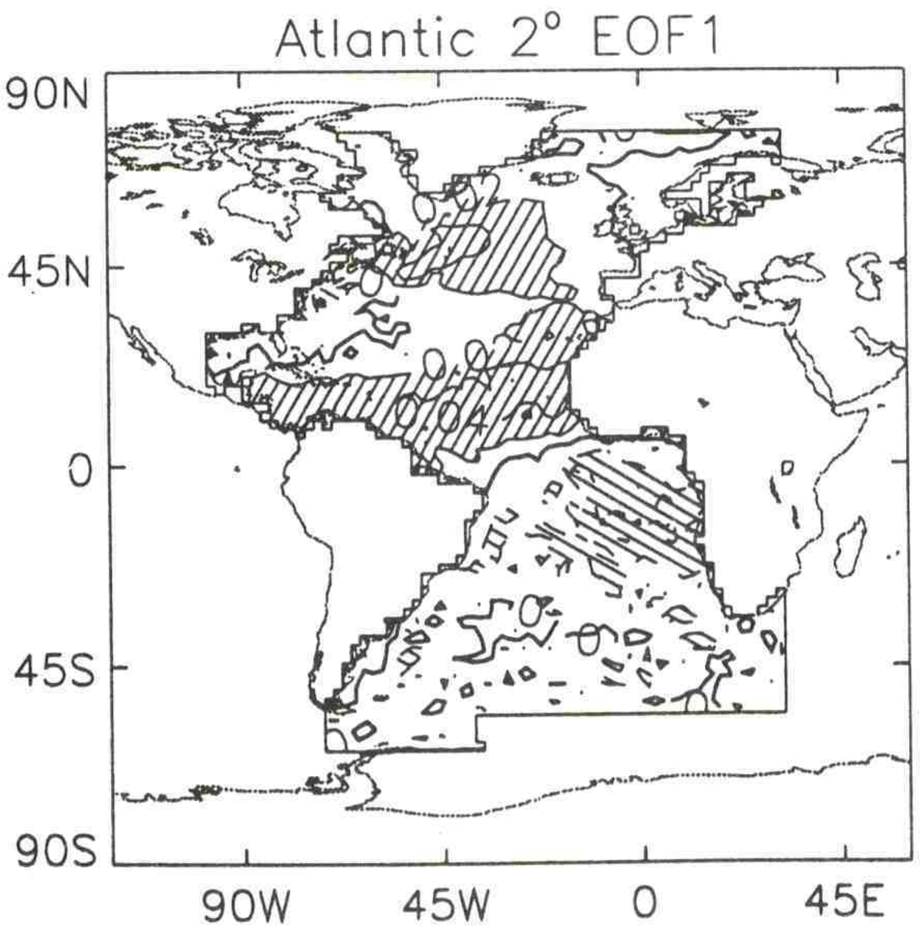

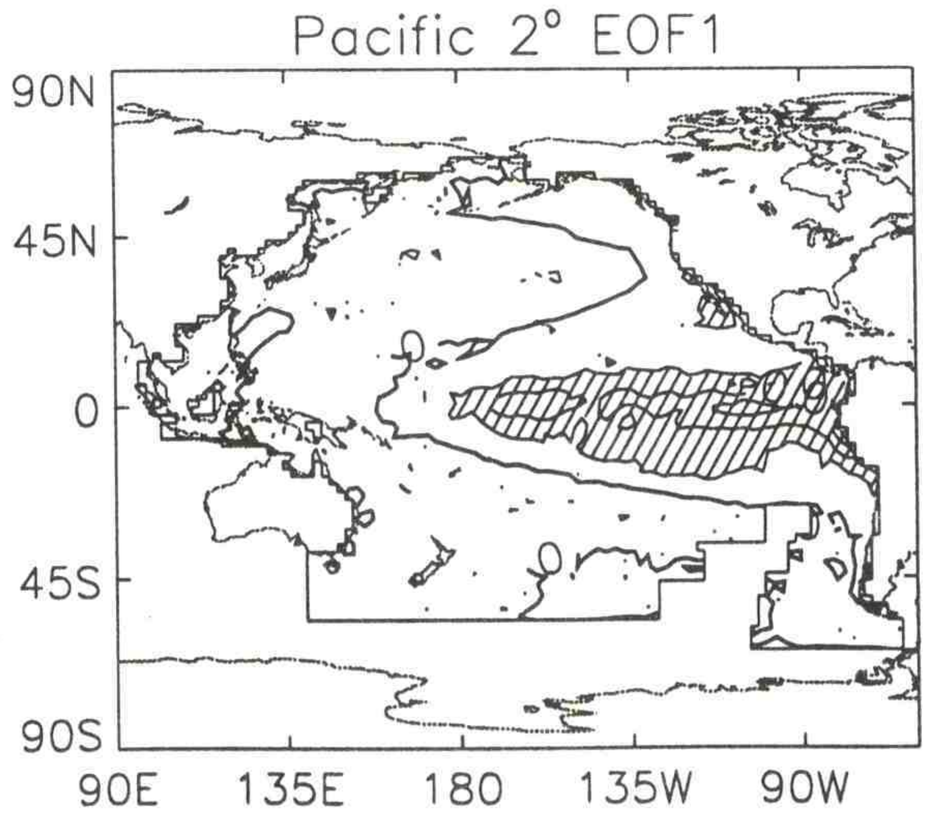

Figure 2. Reconstruction of the leading Pacific Ocean 2° resolution EOF time series 1991–94. Fixed–grid experiment using initial data confined to January 1951 coverage.

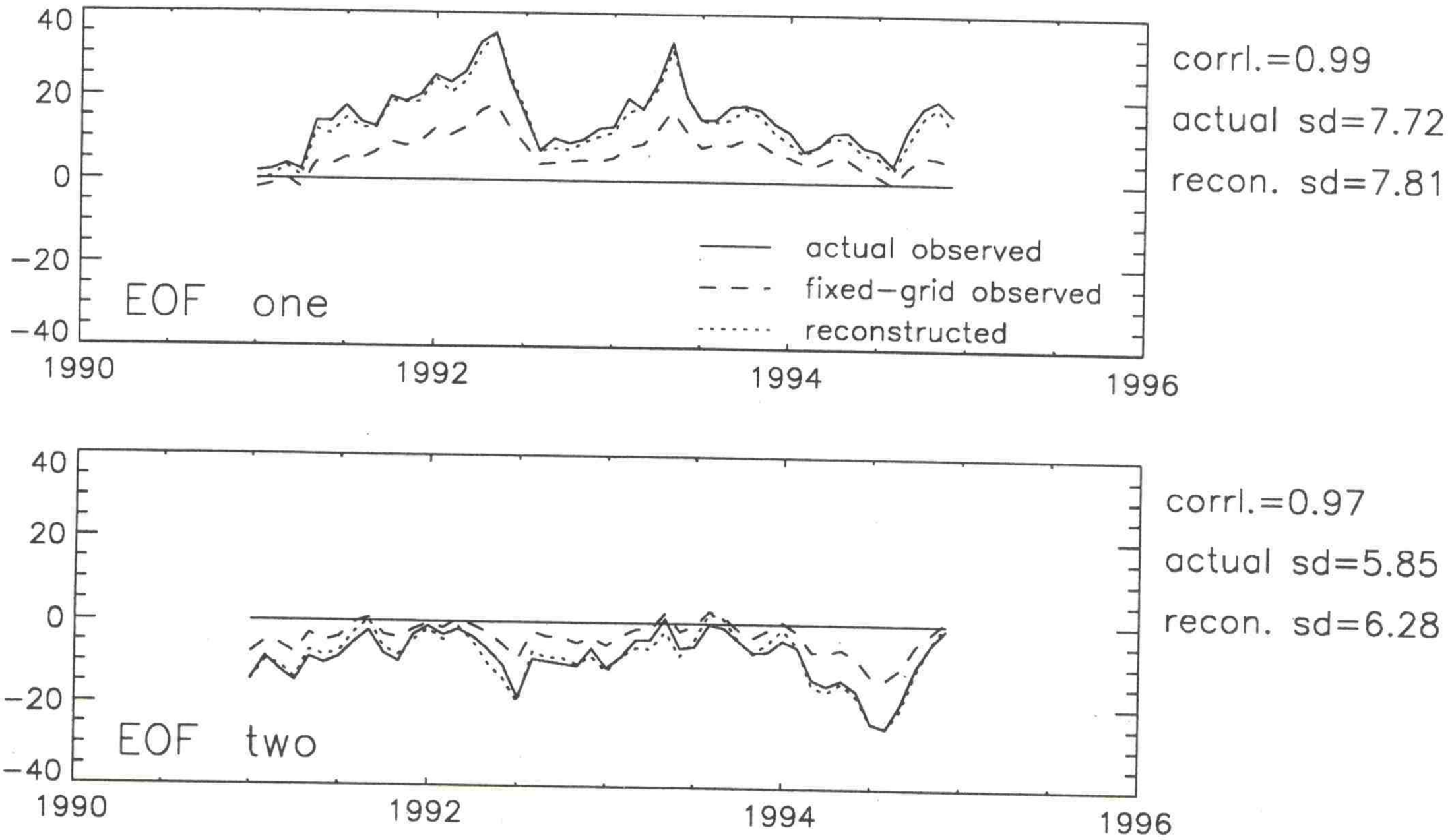

Figure 3. GISST2.2 anomalies wrt 1961–90 for the Pacific La Nina event of July 1988. Values >1°C shaded sw/ne <−1°C shaded nw/se.

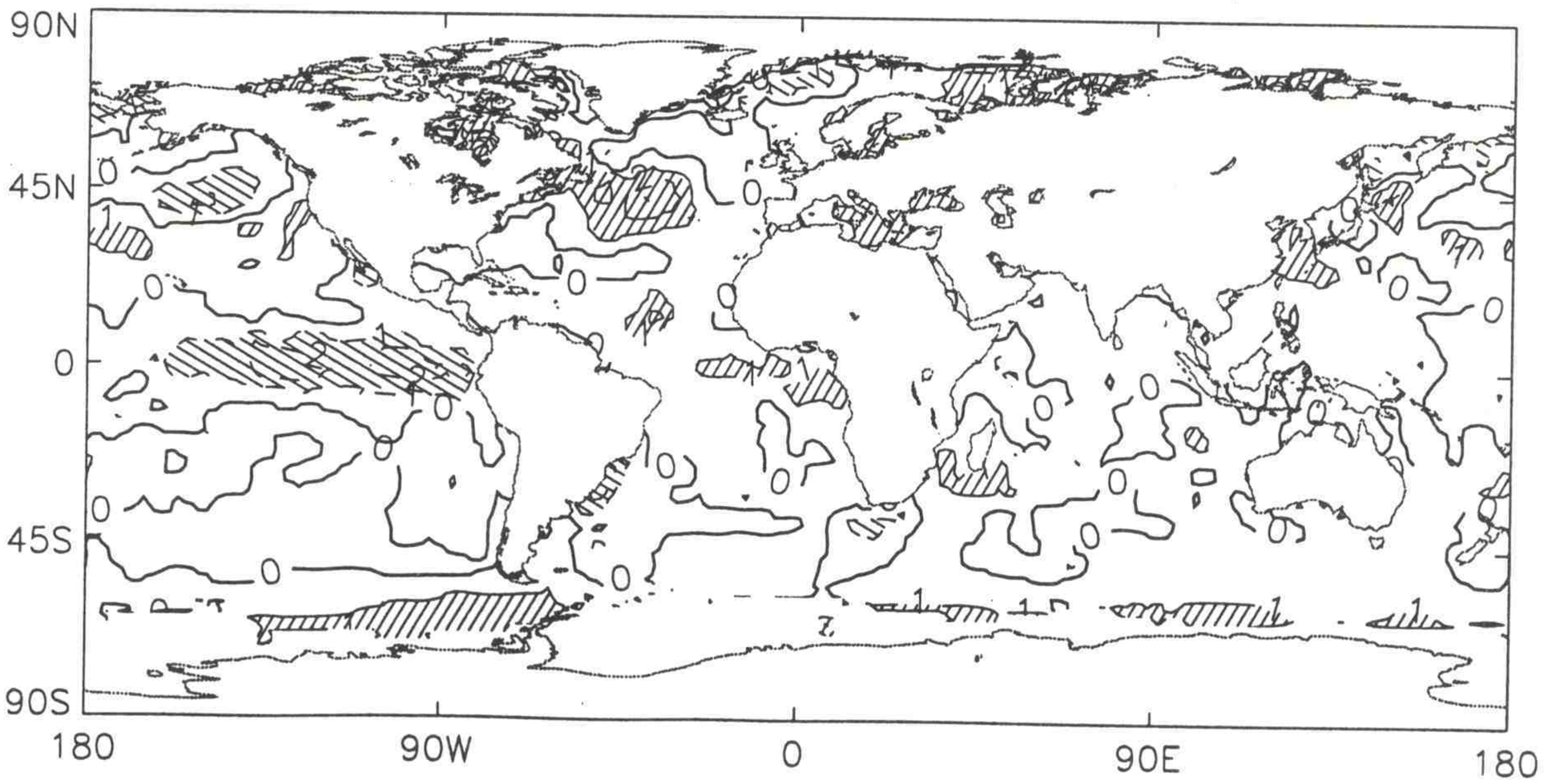

VERTICAL AND HORIZONTAL RESOLUTION COMPARISONS OF CPTEC/COLA GCM

Iracema F.A.Cavalcanti, Paulo Nobre, Magda L.Abreu, Mario Quadro, Luciano P.Pezzi.

CENTRO DE PREVISÃO DE TEMPO E ESTUDOS CLIMÁTICOS / INSTITUTO DE PESQUISAS ESPACIAIS/ BRAZIL.

1-Introduction

The choice of horizontal and vertical resolution for climate studies at Centro de Previsão de Tempo e Estudos Climáticos (CPTEC) has originated this study. Climate prediction has been made in CPTEC since January 1995, using a version of Center for Ocean-Land and Atmosphere (COLA) model, with horizontal truncation of T62 and vertical resolution of 28 levels, until March 1995. T62 L18 was used from April to October.

In order to investigate the performance of the model with different horizontal and vertical resolutions, results using T62 L28, T62 L18, T42 L28 and T42 L18 were analysed and compared to observations. The experiment is made using 4 initial conditions of 14, 15, 16, 17 February 1995 (National Center for Environmental Prediction (NCEP) analyses), observed SST fields and persistent April SST anomalies for the following 6 months. Climatological SST values are used to get the model climatology. Average of May, June and July is used to analyse the results. Observed precipitation data are obtained from Instituto Nacional de Meteorologia (INMET) and global observed OLR and wind fields from NCEP analyses.

2-Results

Precipitation anomalies obtained from different model resolutions are shown in Fig. 1. Observed anomalies can be seen in Fig. 2. T62 L28 shows the main features found in the observed values. Positive anomalies occur at north of Northeast and at South Brazil and close to normal in other regions. Strong negative anomalies are seen at Northeast Brazil in T62 L18 results. The area with positive values is displaced northward and near normal anomalies are seen in other regions. Compared to the other resolutions, this shows the worst result. When the resolution is T42 L28, near normal values are observed at the Northeast and South. T42 L18 shows also negative anomalies at Northeast, but smaller than those showed with T62 L18. Using this resolution, the model tries to represent positive anomaly at the south, but displaced to the east.

The smallest differences between observed and predicted rainfall anomalies occur in T62L28 and the largest in T62 L18.(Figures not shown). The errors at the Northeast are larger using T42L18 than using T42 L28. Although the anomaly precipitation at Northeast and at South Brazil is predicted by T62L28, the anomaly precipitation observed at the east of Northeast is not well predicted by the model. At this time of the year the precipitation there is caused by low level clouds associated with low level easterly flow. Even though the wind field anomaly at 850 mb shows the flow entering perperdicular to the east coast of Northeast (Fig.3), the model does not form the expected clouds.

Differences between observed and predicted OLR anomalies(Figures not shown) exist for all resolutions, but T62 L28 presents the smallest differences mainly over South America and South Atlantic Ocean. The largest errors are found at the Indonesian region for all resolutions. The wind field at 200 hPa is well predicted by T62L28, which presents the main configuration over South America and also the position of the Australian jet. The other resolutions also reproduce the position of this jet, but the configuration over north of South America is displaced to the east. At 850 hPa the global characteristics of the flow are reproduced by all resolutions. The differences between the resolutions are greater at 200 hPa than at 850 hPa. This seems to be related to the number of levels in the stratosphere. L28 has 18 levels in the troposphere and 10 levels in the stratosphere. L18 has 14 levels in the troposphere and 4 levels in the stratosphere.

The model results compared to observed values show that T62 L28 gives the best prediction. When the vertical resolution is reduced (L28 to L18), keeping the horizontal resolution (T62), there is a remarkable change on the results. The increase of horizontal resolution improves the result. Table I shows the rms of rainfall for the area of Brazil, calculated to all resolutions, for the average of May, June and July. Two areas were analysed, the Northeast (50W-30W, 10S-3S) and a large area of Brazil (55W- 35W, 33S-0^0) . The largest error is found in T62L18 and the smallest error in T62L28, for both areas.

3-Conclusion

Changing the vertical resolution implies greater changes on the results than changing the horizontal resolution. The worst combination is found when the highest horizontal resolution and the lowest vertical resolution are used. If the number of levels is reduced, it is necessary to use a compatible horizontal resolution. The increase of horizontal resolution implies in an increase of high frequency waves, which are not well resolved when the vertical resolution is low. The result is improved at some areas if high resolution is used in the vertical, keeping the lowest horizontal resolution. Although T62 L28 showed the best results, the changes reducing the horizontal resolution were not too large. More experiments, including the S.H. summer time, will be performed to decide which resolution should be used in climate experiments to obtain closer realistic simulations/predictions, adequate to our computacional resource.

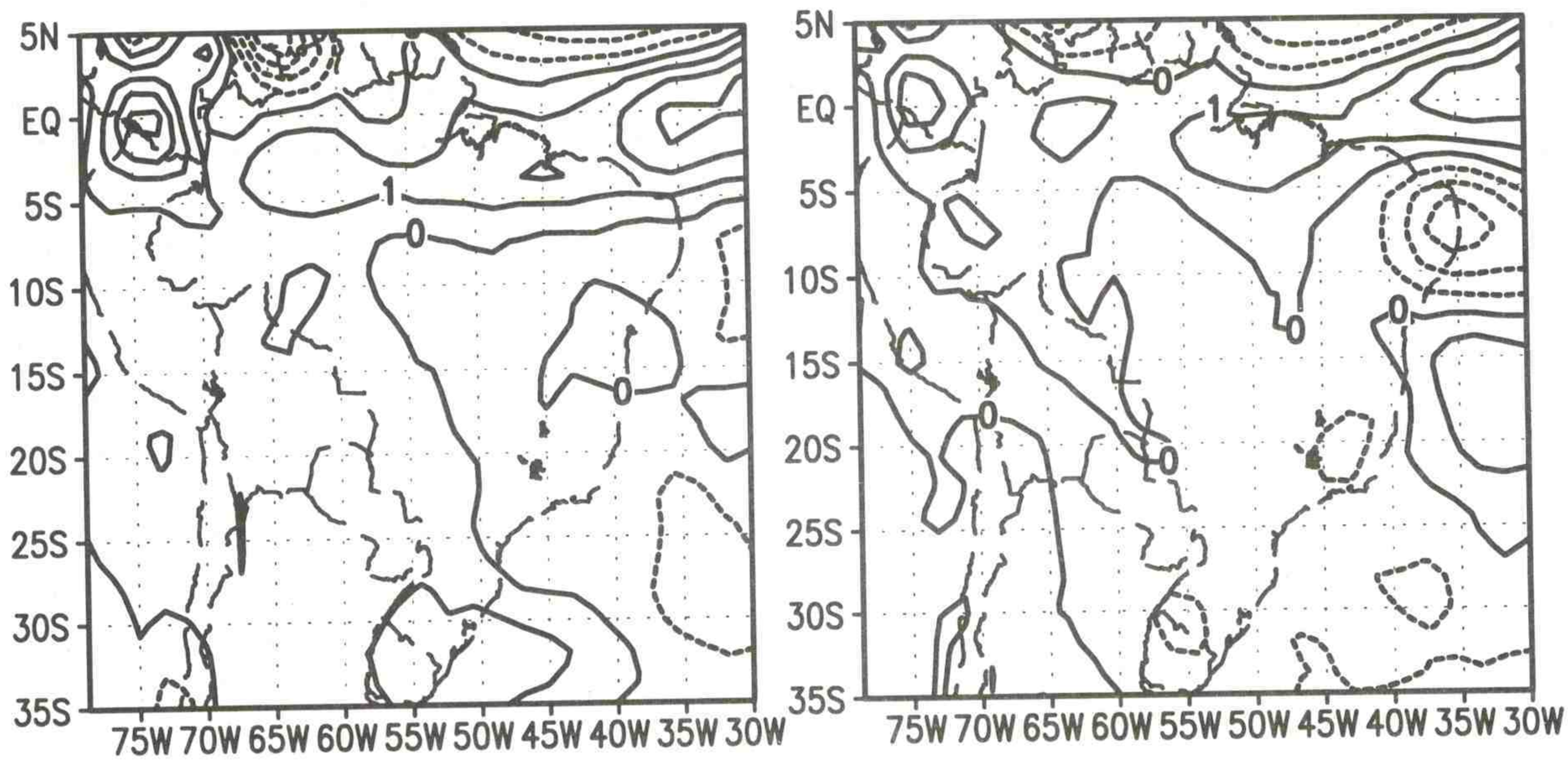

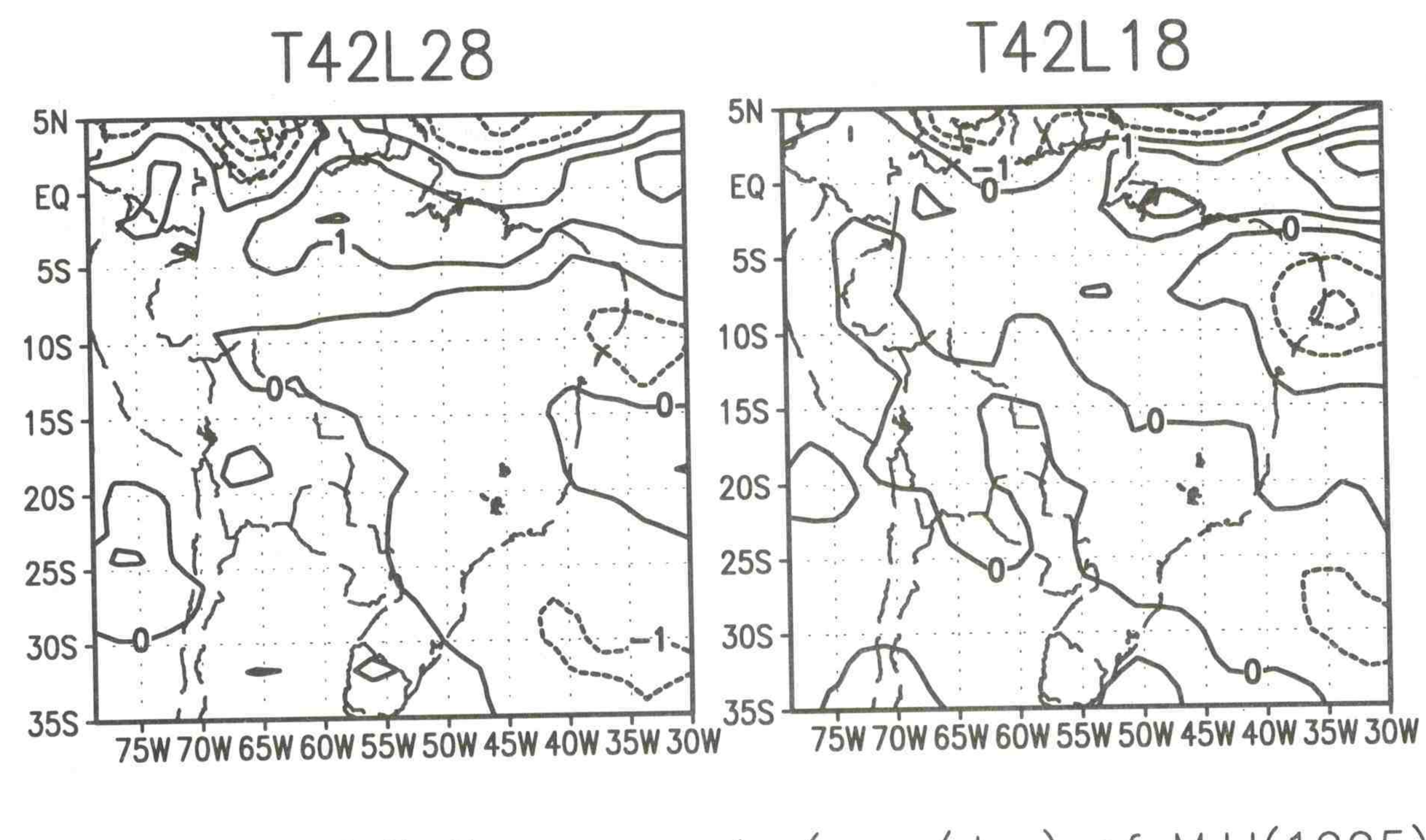

Fig.1— Precipitation anomaly (mm/day) of MJJ(1995)

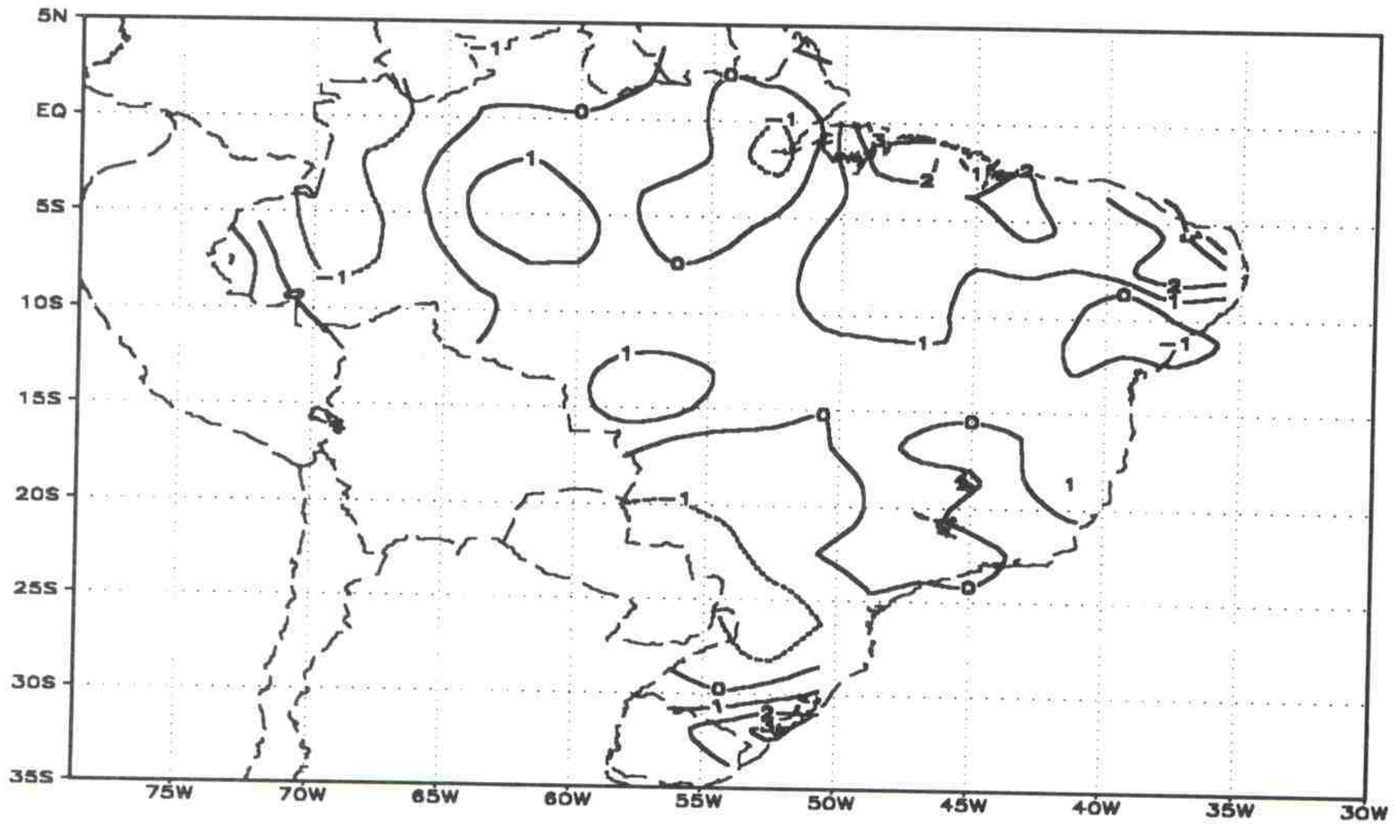

Fig.2—Observed precipitation anomaly(mm/day) (mm/day) for May,June and July 1995.

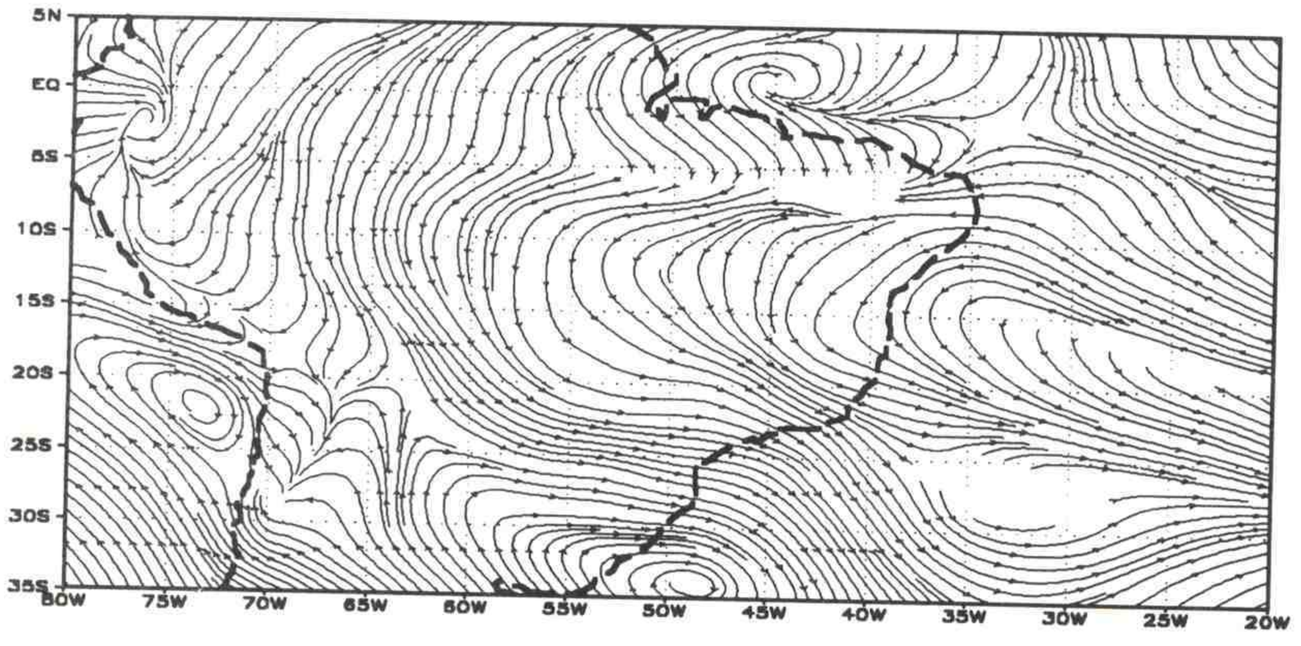

Fig.3—Wind field gnomaly at 850 hPa for May, June and July 1995, using T62L28.

	50W-30W, 10S-3S	55W-35W, 33S-0
T62 L28	1.67	1.08
T42 L28	2.12	1.29
T42 L18	2.45	1.24
T62 L18	2.94	1.55

Table I- Rms(mm/day) calculated from the results with different resolutions .

Relationship Between SST Anomaly Patterns and Atmospheric Flow Patterns in the Northern Hemisphere

Henrik Feddersen and Eigil Kaas
Danish Meteorological Institute
Lyngbyvej 100
DK-2100 Copenhagen
Denmark

Our goal here is (1) to identify dominant coupled patterns of sea surface temperature (SST) and atmospheric flow anomalies on the Northern Hemisphere in the winter months and (2) to study how the atmosphere in an atmospheric GCM responds to selected SST forcings, particularly in extratropical regions.

The dominant coupled patterns are found by applying canonical correlation analysis (CCA) to patterns of SST anomalies and patterns of (1) 500 hPa monthly mean geopotential height anomalies or (2) 500 - 1000 hPa monthly mean thickness anomalies. The SSTs are taken from the GISST1.1 data set; 500 and 1000 hPa heights are (a) NMC analysed observations for DJF 1949-87 and (b) output from a 42 year model experiment with the ECHAM3 atmospheric GCM (T42L19) with prescribed SST for the period 1949-90. Geographically, we consider SST anomalies globally between 10°S and 70°N (on a 64 × 16 point grid) and 500 and 1000 hPa geopotential height anomalies on the Northern Hemisphere north of 20°N (on a reduced, approximately equal area 367-point grid). In the following we shall focus mainly on the combination SST + NMC analysed 500 hPa heights.

The SST anomaly patterns that are identified by the CCA are used as forcing in an atmospheric GCM – in this case Arpege, climate version 1 – which is run in perpetual January mode (with the SST kept fixed). If the model response agrees with the CCA pattern of 500 hPa height anomalies this indicates that the SST pattern in question has a direct influence on the atmospheric flow and consequently the atmospheric pattern in this case is more likely to be predictable on monthly to seasonal time scales on the Northern Hemisphere in the winter season.

Following Barnett and Preisendorfer (1987) the data is prefiltered by applying the CCA only to the first few principal components (explaining about 70% of the total variability) of SST and 500 hPa height anomalies in order to reduce noise that arises due to the relatively short time series considered here.

The leading pair of canonical patterns of SST and 500 hPa height anomalies resemble the leading EOFs of the two fields (EOFs not shown). The SST pattern clearly represents strong ENSO events and the corresponding 500 hPa height anomalies show a PNA-type pattern. This is shown in Fig. 1 (bottom and top left, respectively). Similarly, the second pair of canonical patterns (Fig. 2, bottom and top left) resemble the second EOFs of the two fields. Over the Atlantic the 500 hPa height anomaly shows more of an NAO-type pattern. The second SST pattern is of particular interest to us as it shows large anomalies in the extratropics. The first canonical patterns obtained if ECHAM3 model output is considered instead of NMC analyses agree very well with the canonical patterns shown in Fig. 1. These first canonical patterns are similar, although not identical, to those obtained by Lau and Nath (1994) who used singular value decomposition to identify their patterns.

In order to investigate how the atmosphere responds to the anomalous SST patterns which have been identified with CCA, we force an atmospheric GCM with the SST patterns shown in

Figs. 1 and 2 in perpetual January mode experiments. For each experiment the model is run for 300 days; the figures show the mean response for days 61-300.

The model used is the Arpege climate model (Deque et al., 1994) with a horizontal resolution T21 and 30 vertical levels. The presented response anomalies are relative to a control run where the model was forced with January mean SST.

The two leading canonical SST patterns were scaled in order to make the largest anomalies exceed 2 K. It is these scaled patterns that are shown in Figs. 1 and 2. Curiously, the atmospheric responses (top right figures) to the two forcings seem to be very similar to each other, although the amplitudes are somewhat stronger for the second SST forcing with strong anomalies in the North Atlantic and no ENSO signal. Under the assumption that the relation between SST anomalies and 500 hPa height anomalies is approximately linear this would indicate that a common anomaly in the two SST forcings would dominate the atmospheric response. Likely candidates are the cold anomaly in the Northern Pacific and, possibly, the cold anomaly along the US East coast. Note that the scale of the canonical 500 hPa height patterns does not correspond to the scale of the canonical SST patterns. Thus the absolute amplitudes between the canonical 500 hPa height pattern and the GCM response should not be compared.

The common 500 hPa height anomaly pattern of the GCM response looks more like the pattern of the second pair of canonical patterns (Fig. 2), i.e. it seems that the 500 hPa height pattern of the first pair of canonical patterns (Fig. 1) does not result from a direct forcing by the corresponding SST anomaly pattern. In nature, of course, the oceans and the atmosphere form a complex, coupled system with interactions from ocean to atmosphere as well as from atmosphere to ocean. The latter interactions are not taken into account in a perpetual January mode experiment where the SSTs are kept fixed.

So it appears that if the atmosphere (in a GCM) is forced by the SST anomaly shown in Fig. 2 the response agrees reasonably with the real atmospheric pattern which is dominant when the SST anomaly pattern is like that of Fig. 2 as demonstrated by the CCA. However, if 500 - 1000 hPa thickness is considered instead of 500 hPa geopotential height we find rather poor agreement between the GCM response to an SST forcing of the sort shown in Fig. 2 and the corresponding thickness CCA pattern (not shown).

The results of the experiments presented here – as well as others which are not shown – are ambiguous. We have not found global SST anomaly patterns that controls the state of the atmosphere in a direct way. The patterns shown in Fig. 2 appear to indicate such a direct relationship, but only for 500 hPa height, and probably the entire 500 hPa height anomaly pattern is a response to only part of the global SST forcing.

References

[1] Barnett, T. P., and Preisendorfer, R. Origins and levels of monthly and seasonal forecast skill for United States surface air temperatures determined by canonical correlation analysis. *Mon. Wea. Rev. 115* (1987), 1825–1850.

[2] Deque, M., Dreveton, C., Braun, A., and Cariolle, D. The ARPEGE/IFS atmosphere model: a contribution to the French community climate modelling. *Clim. Dyn. 10* (1994), 249–266.

[3] Lau, N.-C., and Nath, M. J. A modeling study of the relative roles of tropical and extratropical sst anomalies in the variability of the global atmosphere-ocean system. *J. Climate 7* (1994), 1184–1207.

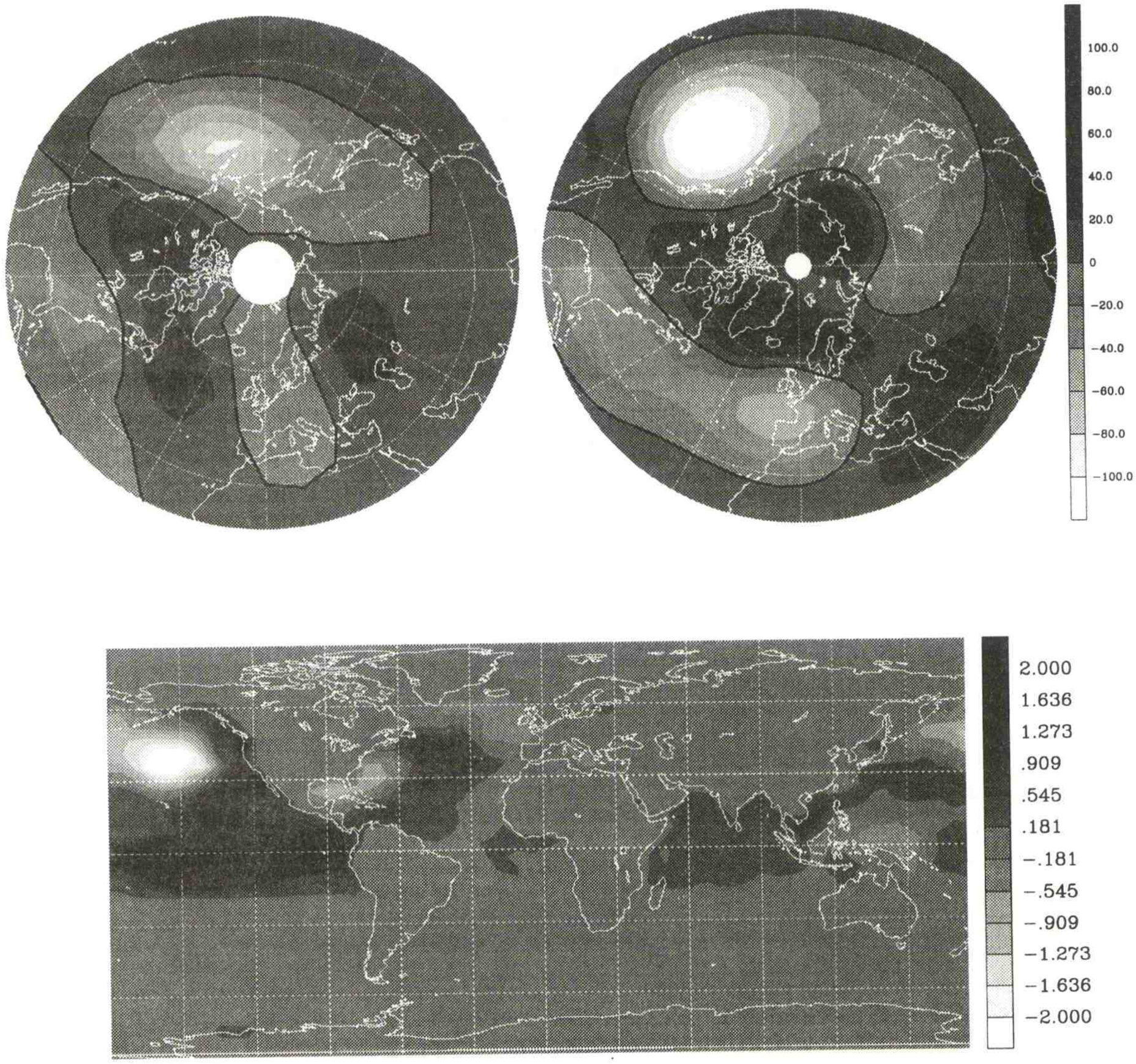

Figure 1. Leading pair of canonical patterns (SST and 500 hPa height anomalies) and GCM mean response (500 hPa height anomaly relative to control run) to forcing with canonical SST pattern in perpetual January mode. Bottom: SST anomaly pattern scaled such that the largest anomalies exceed 2 K. Top left: 500 hPa canonical height anomaly pattern (not scaled accordingly). Top right: GCM response to forcing with shown SST. The SST pattern explains 26% of the total monthly mean SST variability, the 500 hPa height canonical pattern explains 16% of the total monthly mean 500 hPa height and the canonical correlation coefficient is 0.68.

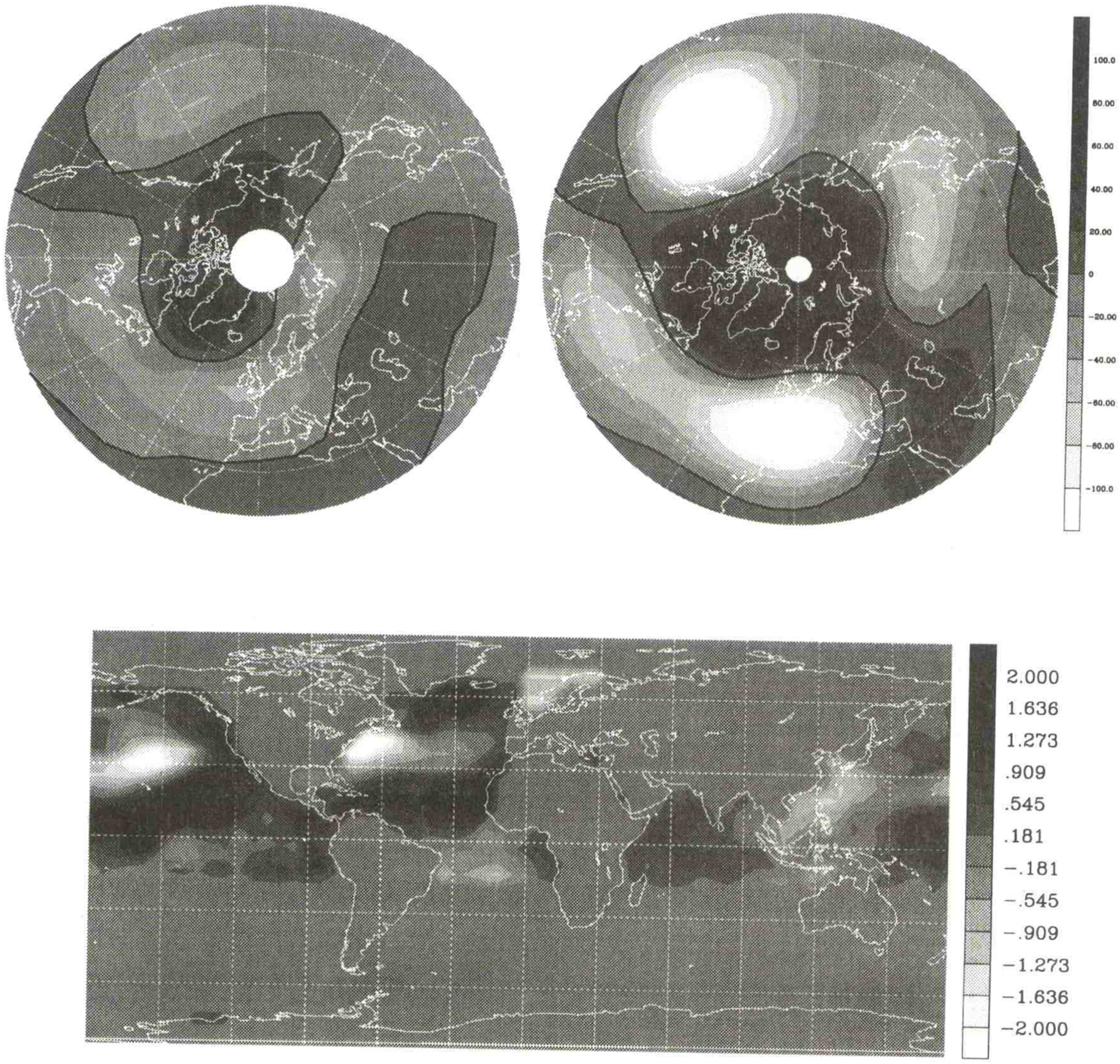

Figure 2. As Fig. 1 but for the second pair of canonical patterns. The SST pattern explains 10.5% of the total monthly mean SST variability, the 500 hPa height canonical pattern explains 13% of the total monthly mean 500 hPa height and the canonical correlation coefficient is 0.66.

WINTERTIME CIRCULATION REGIMES IN THE WESTERN HALF OF THE NORTHERN HEMISPHERE EXTRATROPICS, DEFINED BY H500 DATA IN "KEY REGIONS", AND CLIMATOLOGICAL APPLICATIONS

M.Yu.Bardin
Institute for Global Climate and Ecology
Moscow, Russia

The first step of almost any attempt to classify circulation regimes consists in the diminishing of the phase space dimension. Usual approach at this step is to consider few first principal components of the initial field; this involves estimation of eigenvectors of the large-dimensioned covariation matrix and, besides, may "prescribe" the form of EOFs to the resulting regimes.

Herein, we used the notion of "key regions", containing most characteristic points of the H500 field, such as variance maxima, climatic locations of ridges and troughs, extremums of cyclone frequencies, kinetic energy, relative vorticity, etc. (see Fig.1, right bottom), and consider initial 6-dimensional space of daily mean H500 values within the regions chosen. (Total sample contains daily data for 1951-87.) Note that forms of first EOFs of daily H500 fields [Molteni 1987] and anomaly fields for certain flow regime centroids (e.g., [Mo, Ghil 1988], [Molteni et al., 1990]) are in accordance with this idea and choice of key regions.

Preliminary results of the cluster analysis, using a variant of the "k-means" method for various numbers of classes, ranged from 3 to 15, showed that the principal contribution in the cluster discrimination is that of the pair of key regions over the Aleutian islands (we denote it PAC), and over the eastern Polar Canada region (CAN). The ratio of between-class and within-class variance for these variables is 4 times or more higher, than that for other variables. So we decided to consider classification based on these two variables; naturally enough, in this case we can expect reasonable results mainly for the western half of the Northern Hemisphere.

In Figure 2 one can see the 2-dimensional PDF of H500 in the Pacific (PAC) and Canada (CAN) regions for the subsample of "quasistationary events", defined as central of 3 subsequent dates with the displacement of the point in the (PAC, CAN) phase space between them less then the predefined value (namely, 45 meters, which is the lower tercile of the daily displacement distribution). This PDF has an obviously multimodal nature, and the same (although not that pronounced) is true for the total subsample (not shown). This encourage us to search for clusters in this phase space. A number of experiments, involving various clustering algorithms and clustering parameters, give a reasonable number of 7 clusters. Resulting 7 class centroids in the 2-dimensional phase space (PAC,CAN), obtained for the total sample using the "k-means" method, are shown as black circles (along with corresponding reference numbers we use further). Mean H500 anomaly fields of these clusters are shown in Figure 1. One can see reasonable structure of these classes: the class 6 is that of small anomalies ("climatological class"), and others exhibit various combinations of phases and intensities of the PNA and NAO teleconnection patterns.

In Figure 3, the 1-dimensional PDF of the variable $((PAC-ePAC)^2+(CAN-eCAN)^2)^{1/2}$ is presented, which is apparently multimodal (also shown are the PDF, obtained assuming that PAC and CAN are statistically independent, i.e., conditional probabilities are equal to unconditional, and 5% and 95% percentiles, obtained us-

ing "bootstrap" with 1000 random subsamples). It confirms the existence of (nonlinear) dependency between these two variables, that may be treated as a connection between the PNA and NAO teleconnection systems.

One point of interest in studies of weather regimes concerns the possibility to reconstruct climate anomalies (changes) on the basis of statistics of these regimes (which may enable us to reconstruct regional climate changes from time series of GCM runs - the "downscaling" concept). Figure 4 shows the composite map of SAT anomalies for months with the high (>10 days) vs low (<2 days) frequency of the 4th class, both approximately evenly distributed within the 1951-87 interval. The map exhibits pronounced features corresponding to high frequencies of the 4th class: warming in northwestern parts of the North America (easily interpreted in terms of the warmer air advection from the Pacific in deep Aleutian low conditions), and cooling over the Pacific (caused by heat losses and upwelling by strengthened winds), over the Baffin Land and over the Gulf of Mexico (apparently due to the advection of cold polar air masses by cyclonic circulation centered at southern Greenland, and anticyclonic one over the central parts of the North America). Also of interest the warming over the western parts of Eurasia, which, although, could not be directly explained (but, maybe, connected with higher cyclonic activity over the northern part of Atlantic), and cooling over its eastern and southern parts. This sketch demonstrates potential usefulness of the developed classification for the statistical downscaling applications; more detailed consideration of this topic we plan for near future.

REFERENCES

Mo K. and Ghil M., 1988: Cluster analysis of multiple planetary flow regimes. J. Geoph. Research, 1988, Vol.93, No. D9, pp.10.927-10.952.

Molteni F., 1987: Empirical Orthogonal Function Analysis of the Zonal and Eddy Components of 500 mb Height Fields in the Northern Extratropics. - ECMWF Technical Report 1987, No. 61.

Molteni F., Tibaldi S., and Palmer T.N., 1990: Regimes in the wintertime circulation over northern extratropics. I: Observational evidence. - Q. J. R. Meteorol. Soc., 1990, Vol. 116, pp. 31-67.

FIGURE CAPTIONS

Fig.1 Key regions (right bottom; black circles indicate locations of climatic extremums at 500mb: see the text), and mean H500 anomalies for 7 classes; negative values are dashed.

Fig.2 Probability density function for the subsample of quasistationary ("persistent") events in the phase space (PAC,CAN), and centroids of 7 classes obtained by the total sample.

Fig.3 PDF of the $((PAC-ePAC)^2+(CAN-eCAN)^2)^{1/2}$ function for the subsample of persistent cases; thin line is the "bootstrap" mean, and dashed are 5% and 95% percentiles, given the PAC and CAN variables are statistically independent.

Fig.4 Difference of mean SAT anomaly (x100) for months with high (>10 days) and low (<2 days) class 4 frequency, approximately evenly distributed within 1951-1987 interval.

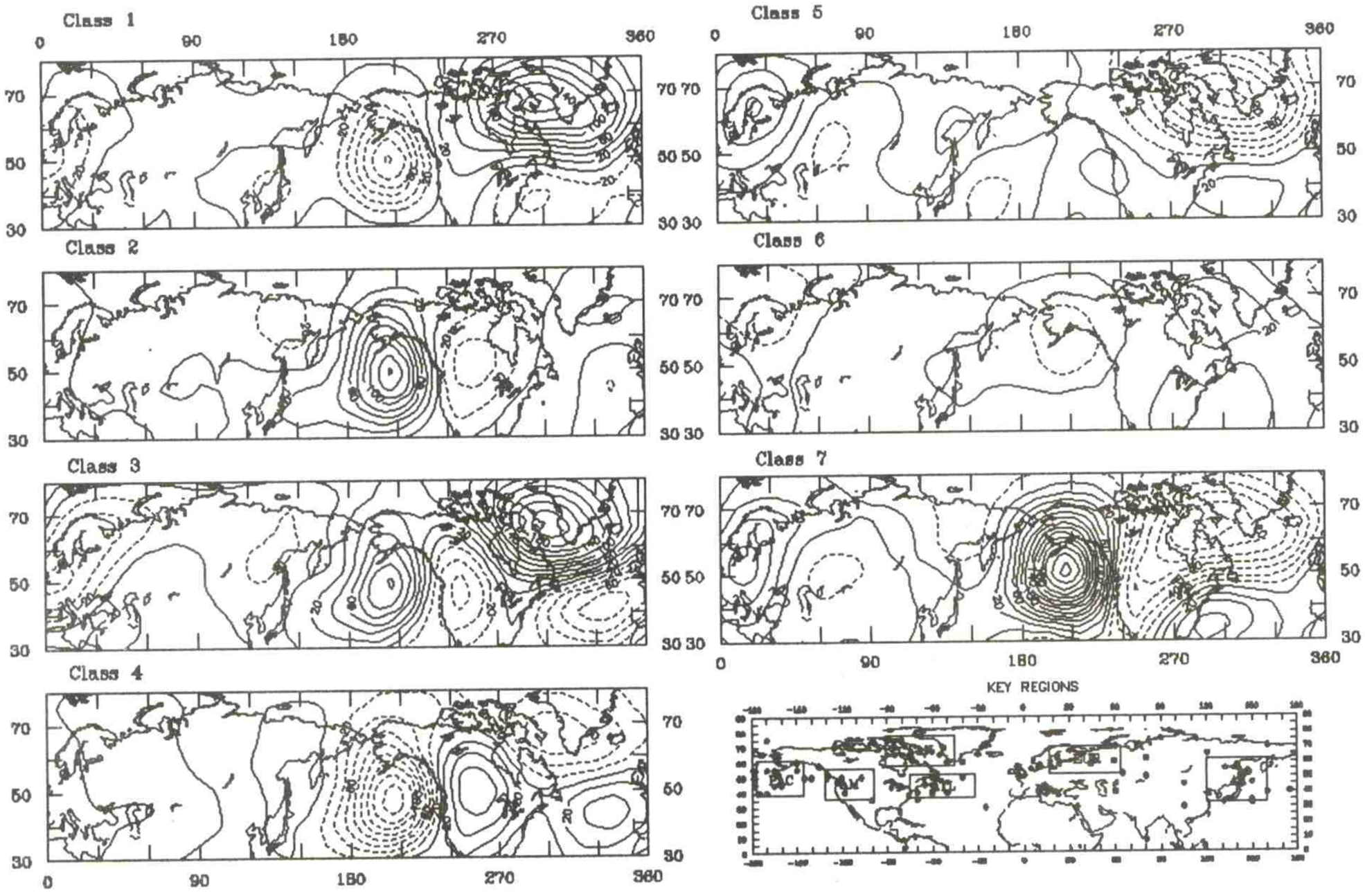

Figure 1

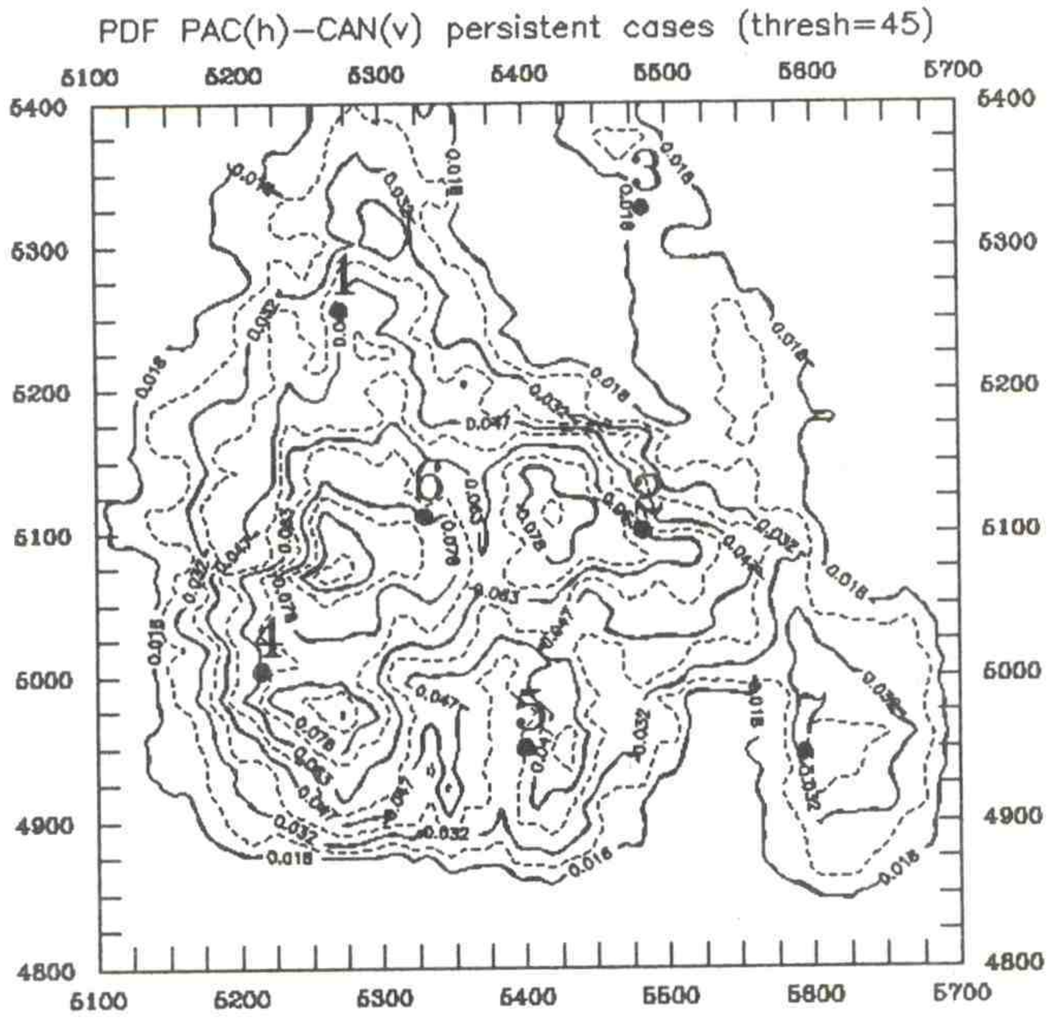

Figure 2

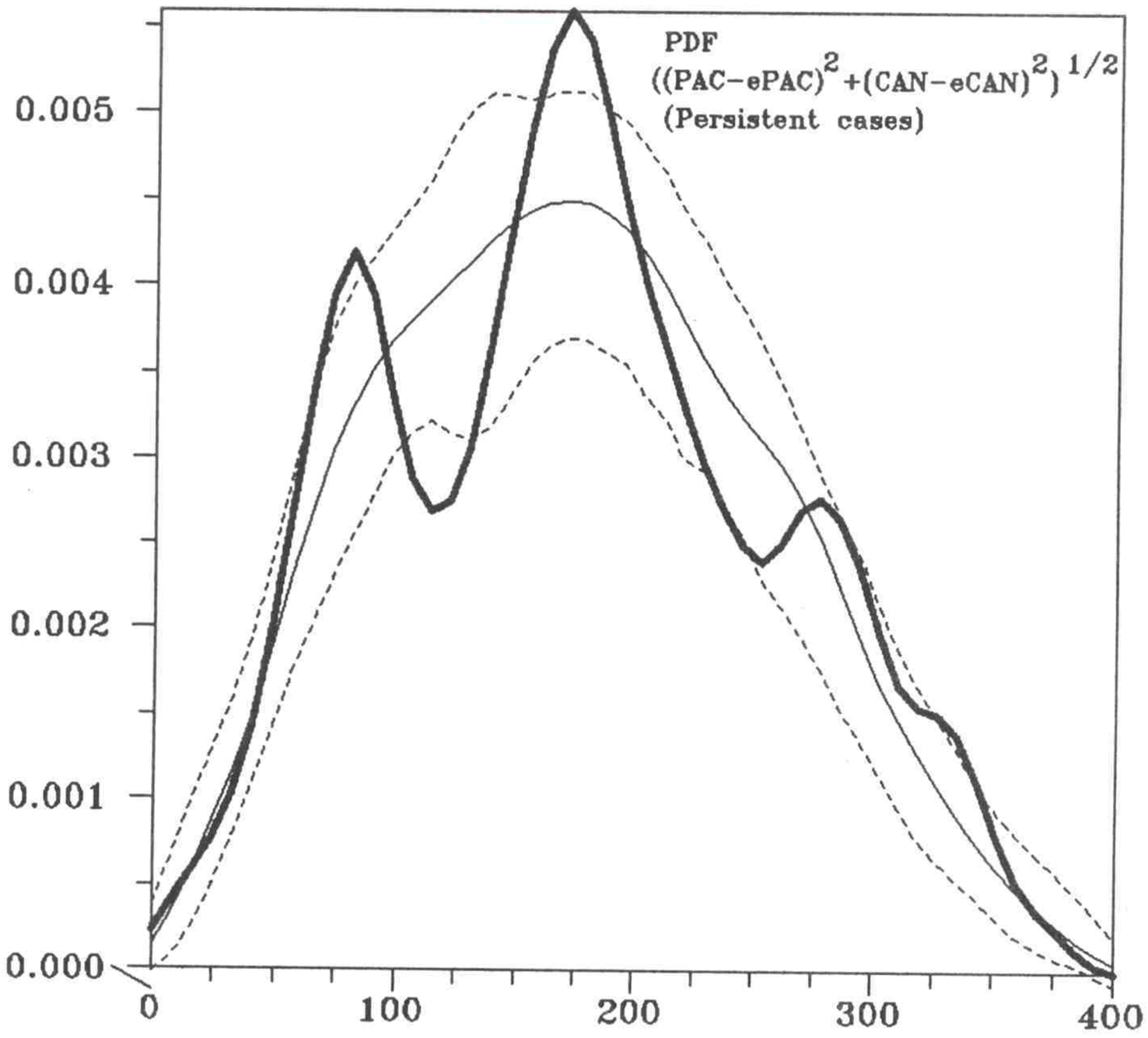

Figure 3

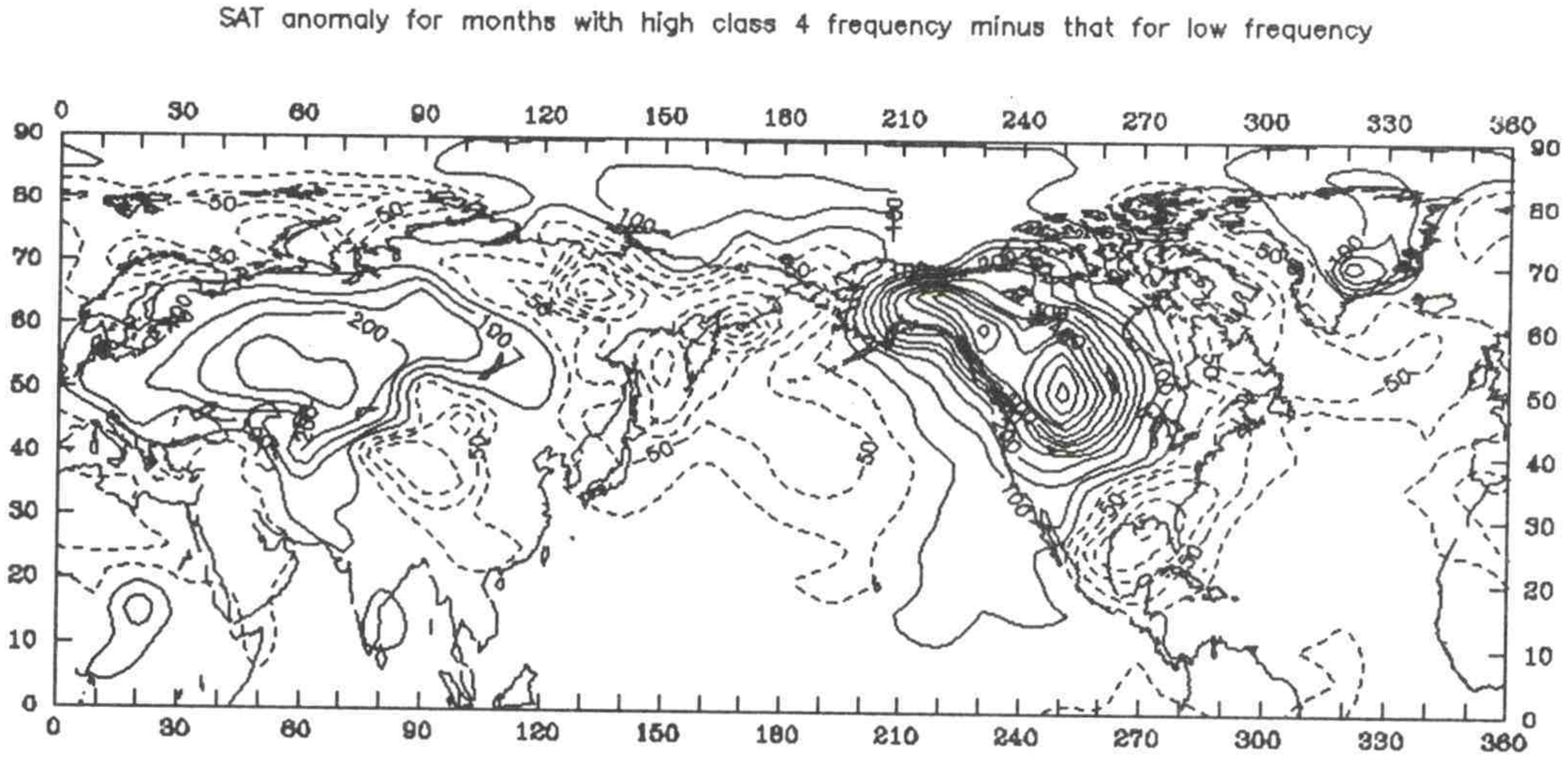

Figure 4

Asymmetric Impact of Tropical SST Anomalies on Atmospheric Internal Variability over the North Pacific

Wilbur Y. Chen and Huug M. Van den Dool

Climate Prediction Center
NOAA/NWS/NCEP
Washington D.C. 20233

A substantial asymmetric impact of the tropical Pacific sea surface temperature (SST) anomalies on the internal variability of the extratropical atmosphere is found. A variety of diagnoses is performed to help reveal the dynamical processes leading to the large impact. Thirty five years of geopotential heights and twenty nine years of wind fields analyzed operationally at the National Meteorological Center (NMC) and three sets of 10-year long perpetual January integrations run with a low resolution NMC global spectral model are investigated in detail for the impact of the SST anomalies on the blocking flows over the north Pacific. The impact on large-scale deep trough flows is also examined.

Both the blocking and deep trough flows develop twice as much over the North Pacific during La Niña than El Niño winters (Fig. 1 and 2). Consequently, the internal dynamics associated low frequency variability (LFV), with time-scales between 7-61 days examined in this study, displays distinct characteristics: much larger magnitude for the La Niña than the El Niño winters over the eastern north Pacific, where the LFV is highest in general (Fig. 3).

The diagnosis of the localized Eliassen-Palm fluxes and their divergence reveals that the high-frequency transient eddies (1-7 days) at high latitudes are effective in forming and maintaining the large-scale blocking blows, while the mid-latitude transients are less effective. The mean deformation field over the north Pacific is much more diffluent for the La Niña than the El Niño winters, resulting in more blocking flows being developed and maintained by the high-frequency transients over the central North Pacific and explains why there are much more blocking flows during the La Niña than the El Niño winters.

In addition to the above dynamical process operating on the high-frequency end of all fluctuations, the local barotropic energy conversion between the LFV components and the time-mean flows is also operating and playing a crucial role. The kinetic energy conversion represented by the scalar product between the **E**-vector of the low frequency components and the deformation **D**-vector of the time-mean flow reveals that, on average, the low frequency components extract energy from the time-mean flow during La Niña winters while they lose energy to the time-mean flow during El Niño winters. This local barotropic energy conversion on the low-frequency end of all fluctuations together with the forcing of the high-frequency transients on blocking flows on the high-frequency end combine to explain why there is a large difference in the low frequency variability magnitude between the La Niña and the El Niño winters.

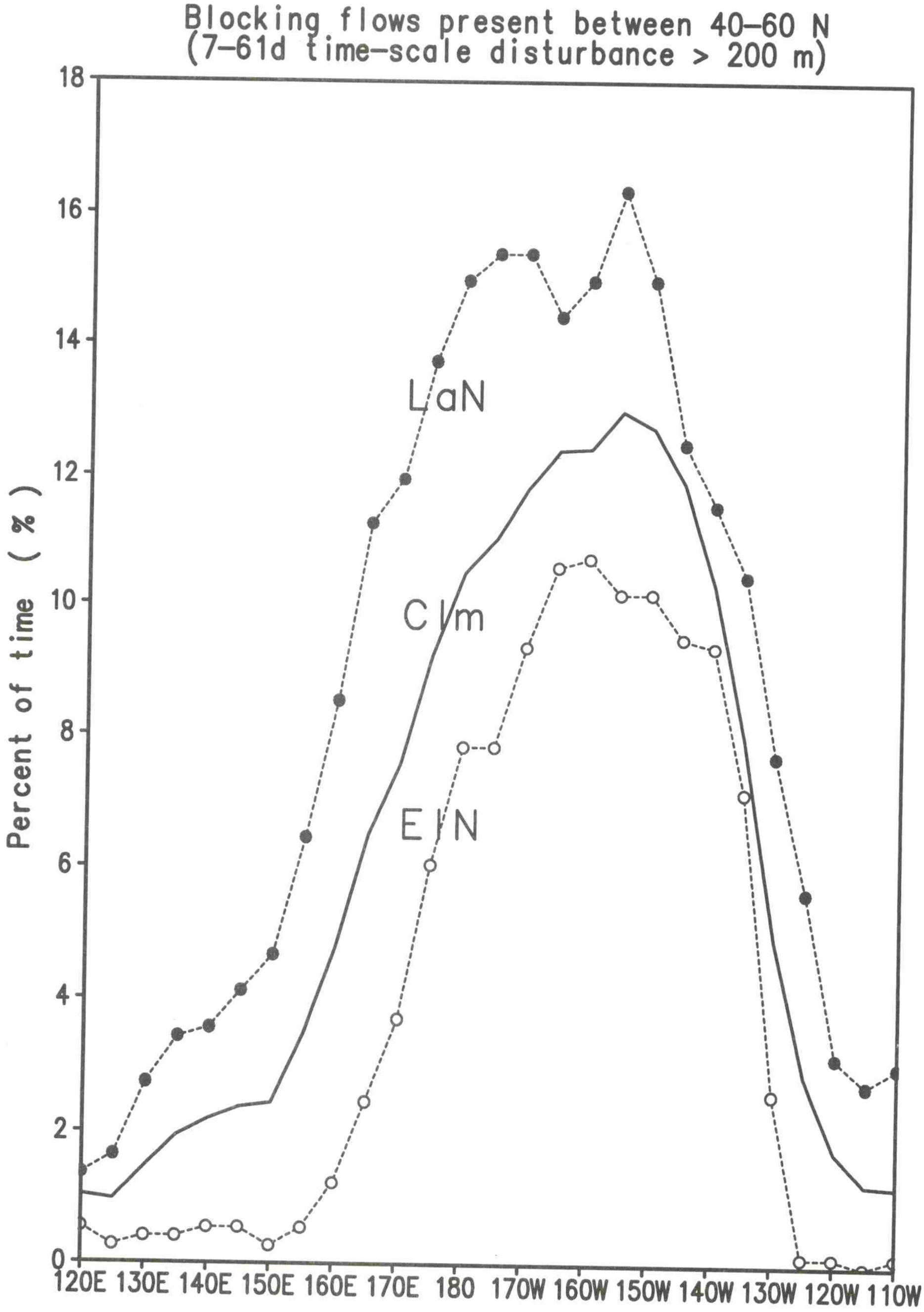
Blocking flows present between 40–60 N
(7–61d time–scale disturbance > 200 m)
Percent of time (%)
18
16
14
12
10
8
6
4
2
0
LaN
Clm
EIN
120E 130E 140E 150E 160E 170E 180 170W 160W 150W 140W 130W 120W 110W
Longitude

Figure 1

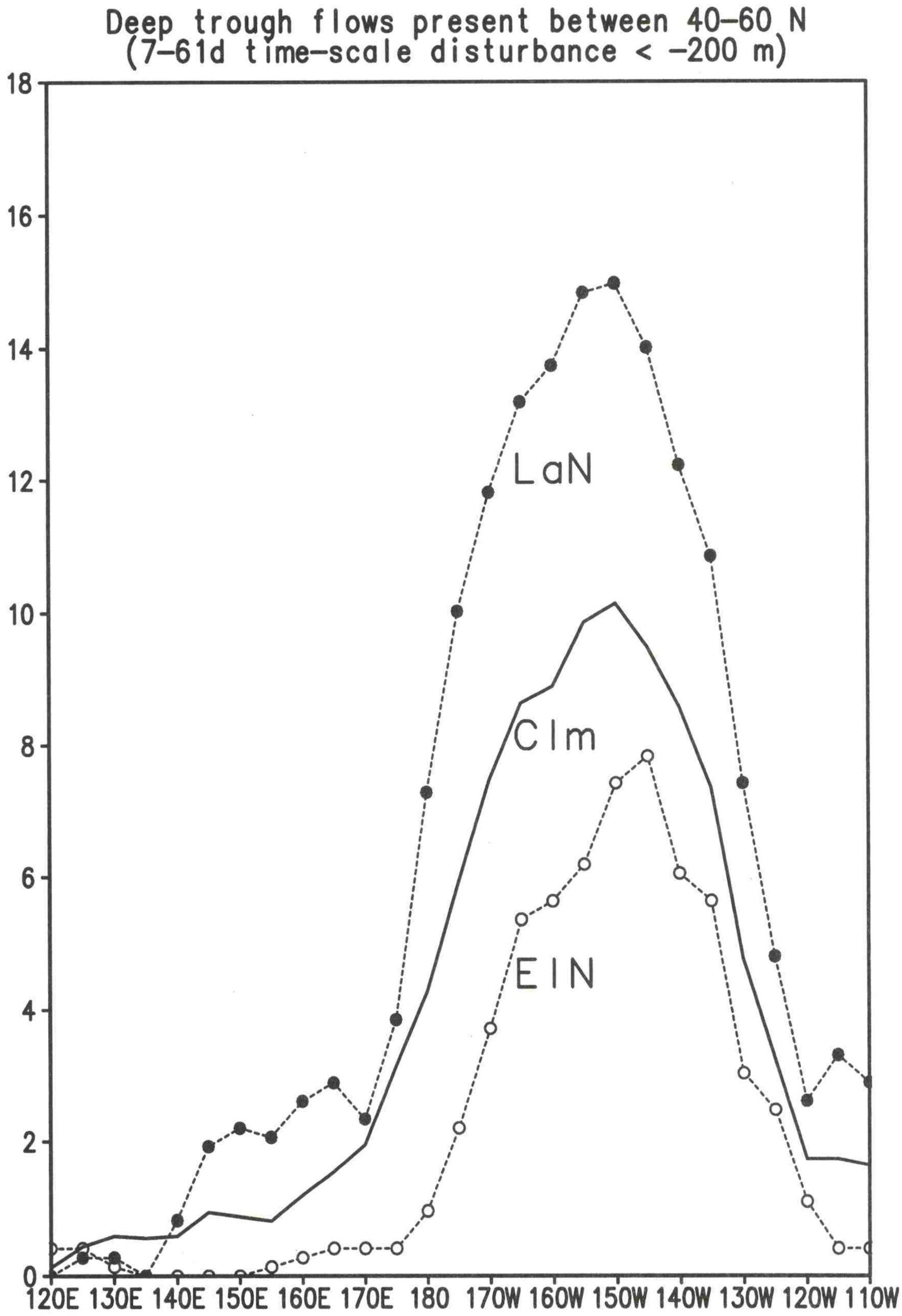
Deep trough flows present between 40–60 N
(7–61d time–scale disturbance < –200 m)
Percent of time (%)
18
16
14
12
10
8
6
4
2
0
LaN
Clm
EIN
120E 130E 140E 150E 160E 170E 180 170W 160W 150W 140W 130W 120W 110W
Longitude

Figure 2

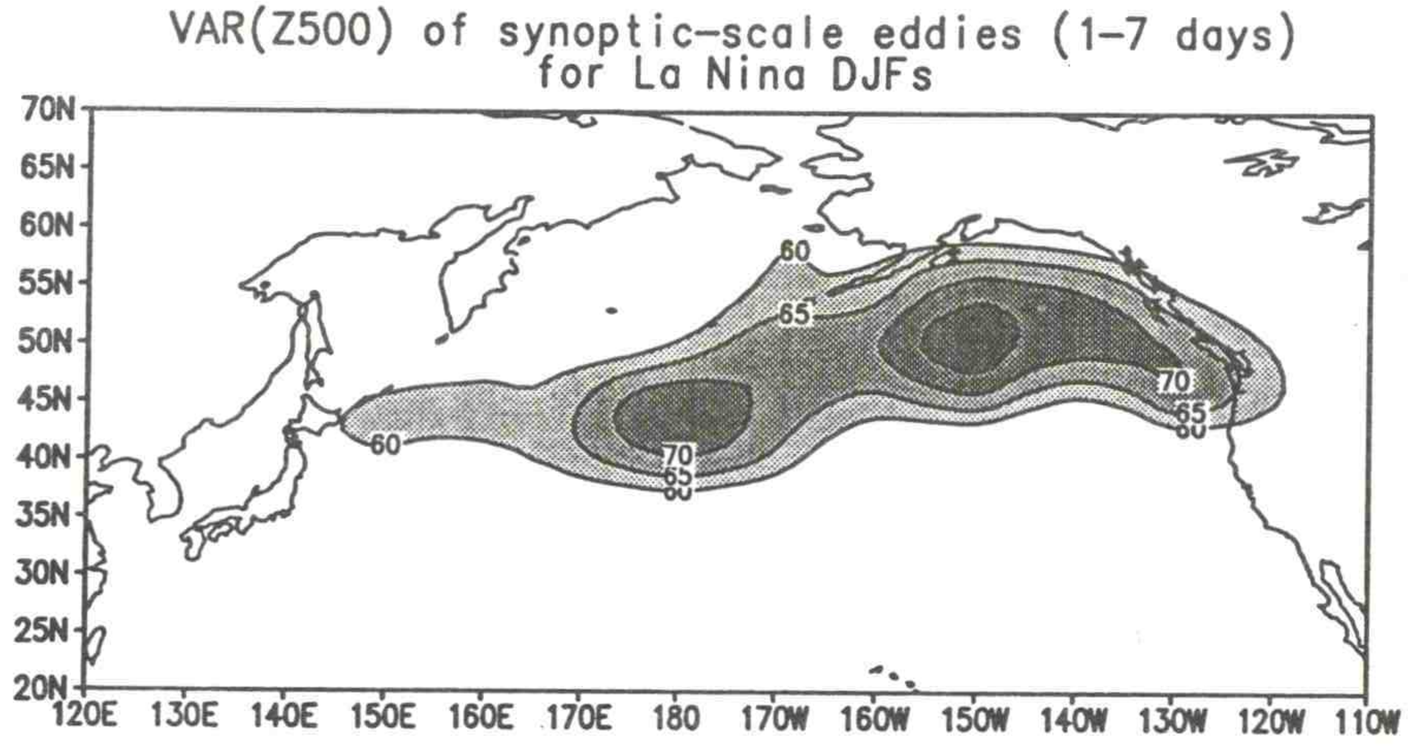
VAR(Z500) of synoptic-scale eddies (1-7 days)
for La Nina DJFs
70N
65N
60N
55N
50N
45N
40N
35N
30N
25N
20N
120E 130E 140E 150E 160E 170E 180 170W 160W 150W 140W 130W 120W 110W
60
65
70
60
65
70
65
60

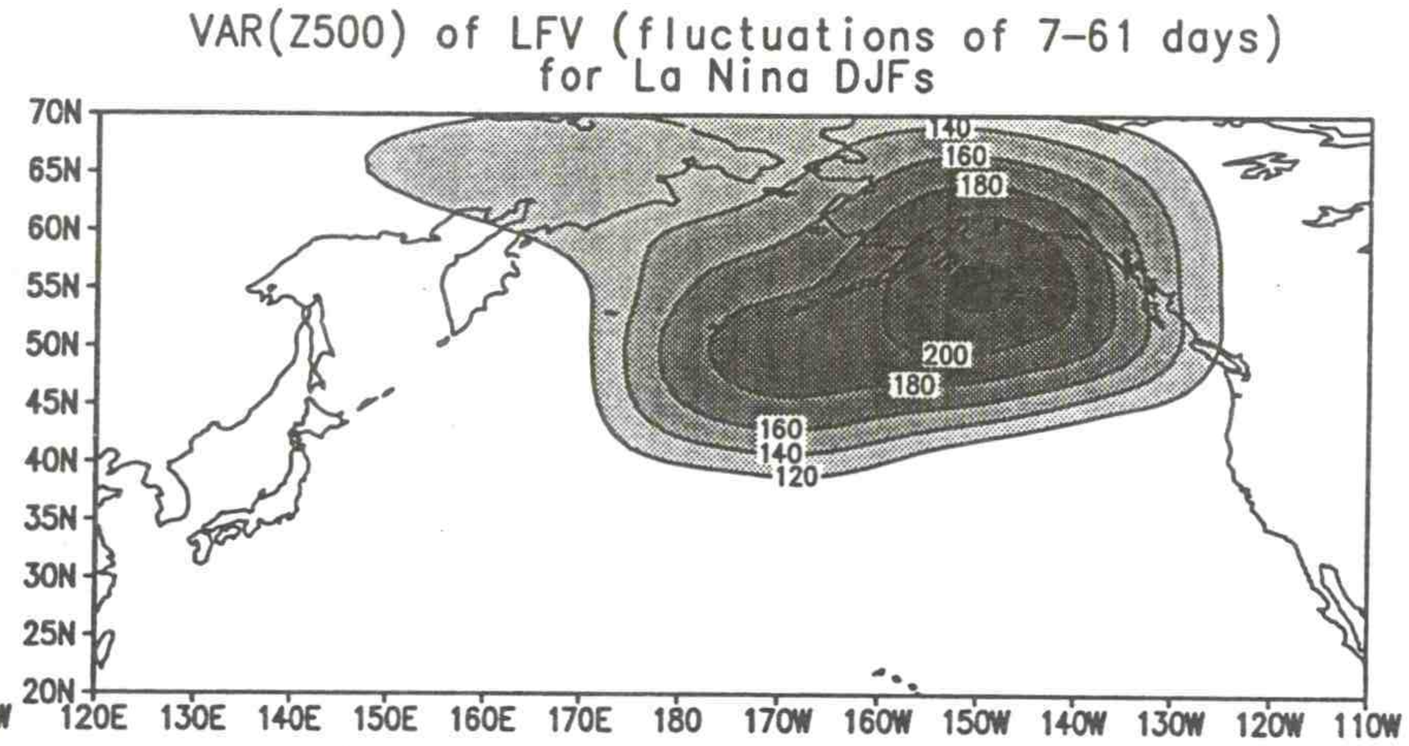
VAR(Z500) of LFV (fluctuations of 7-61 days)
for La Nina DJFs
70N
65N
60N
55N
50N
45N
40N
35N
30N
25N
20N
120E 130E 140E 150E 160E 170E 180 170W 160W 150W 140W 130W 120W 110W
140
160
180
200
180
160
140
120

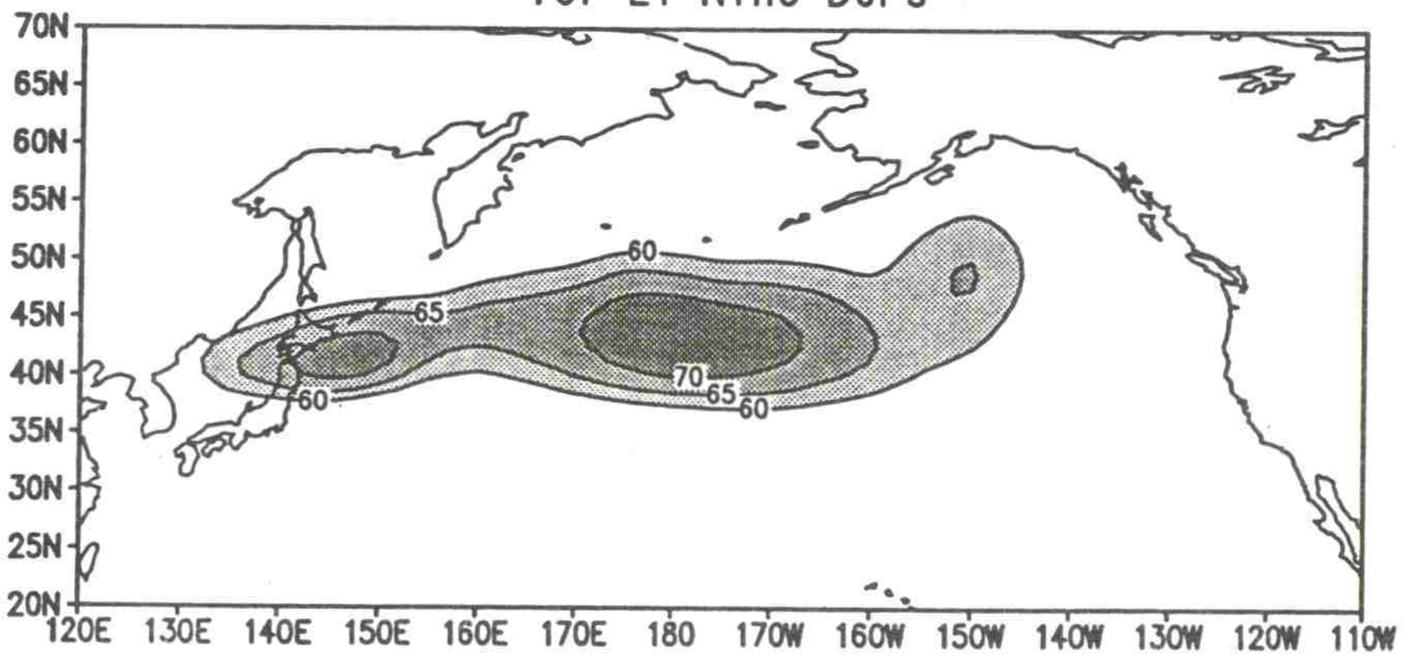
for El Nino DJFs
70N
65N
60N
55N
50N
45N
40N
35N
30N
25N
20N
120E 130E 140E 150E 160E 170E 180 170W 160W 150W 140W 130W 120W 110W
60
65
60
70
65
60

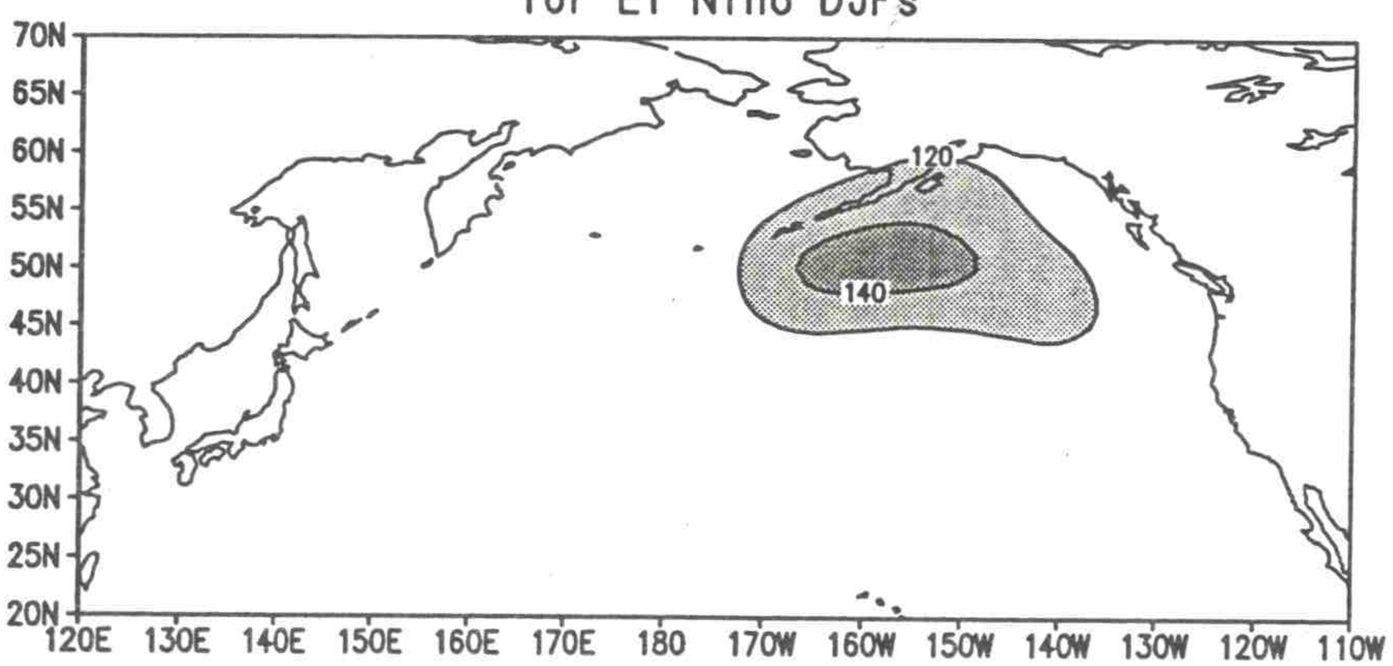
for El Nino DJFs
70N
65N
60N
55N
50N
45N
40N
35N
30N
25N
20N
120E 130E 140E 150E 160E 170E 180 170W 160W 150W 140W 130W 120W 110W
120
140

Figure 3

Prediction of Tropical Pacific SST with the NCEP CCA Model

Anthony G. Barnston and Yuxiang He

NOAA/National Centers for Environmental Prediction/Climate Prediction Center
Washington, DC 20233

The statistical short-term climate predictive skills and their sources for seasonal mean tropical Pacific sea surface temperature (SST) has been estimated at lead times of up to 13 months using CCA in a cross-validation verification design. More detail about CCA as a linear statistical methodology is given in Barnett and Preisendorfer (1987), *Mon. Wea. Rev.*, 1825-1860 and Barnston (1994), *J. Climate*, 1513-1564. Here, the predictor fields include quasi-global sea level pressure (SLP), the SST itself over much of the globe, the depth of the 20°C isotherm in the tropical Pacific, and the dynamical sea level height in the tropical Pacific. Four consecutive 3-month predictor periods are used to detect evolving as well as steady-state conditions over the year prior to the time of the forecast. This study is an extension of that described in Barnston and Ropelewski (1992), *J. Climate*, 1316-1345, in which the SST only in discrete areas was CCA-predicted using quasi-global SLP and the SST in the predictand areas at prior times. By predicting a field of 10°X10° gridded boxes, we hope to forecast different types of ENSO episodes in greater spatial detail.

It is found that use of all four of the predictor fields mentioned above produces the highest skill scores. Sensitivity tests were conducted in which (1) the subsurface sea temperature fields were withheld (i.e. using only SST and SLP), and (2) SLP was withheld (i.e. using only near-global SST, and tropical Pacific depth of the 20°C isotherm and dynamical sea level height). In both cases, skill was diminished noticeably at most seasons and lead times. Figure 1 shows the geographical distribution of the skill using all four predictor fields, expressed as a correlation coefficient between forecasts and observations, for the Jan-Feb-Mar target period; forecast skills are shown for lead times of 0, 1, 2, 3, and 4 seasons. The lead time is defined as the time skipped between the end of the final predictor period and the *beginning* of the 3-month target period. At lead times of 0 and 1 season (forecasts made at the end of September and December, respectively), forecast correlation skill maximizes at values of over 0.9 in the 140-160°W, 0-10°S area. Note that this is well to the west of the Nino 3 region, but does not extend nearly as far west as the Nino 4 region. It is more congruent with the region called Nino 3.4 (Barnston et al. 1994, *Bull. Am. Meteor. Soc.*, 2097-2114), which occupies 120-170°W, 5°N-5°S. For 2 to 4 season lead times skill diminishes to much more modest levels but the forecasts are still usable for some purposes with cognizance of their skills.

Figure 2 shows the seasonal march of correlation skill for SST averaged over the Nino 3.4 region only, for the same five lead times. As has been noted in previous statistical studies, skill is highest from northern late fall through winter, and lowest in summer. The inclusion of the subsurface predictor fields somewhat mitigates the effects of the so-called spring barrier, because subsurface sea temperature anomalies in the west-central and central Pacific tend to be followed by SST anomalies in the eastern and east-central equatorial Pacific 12 to 20 months later (Smith et al. 1996, *Wea. Forecasting*, in press).

To characterize the sources of SST forecast skill for JFM forecasts at 1 month lead (a lead time not shown explicitly in Figs. 1 or 2), we look at the CCA loading patterns and time series associated with the strongest CCA mode for these skillful forecasts. The loading patterns for the SLP fields for the first (DJF) and fourth (SON) of the four predictor periods are shown in Fig. 3. While the DJF field is weak, the field for the latest predictor period shows negative loadings in the eastern equatorial Pacific and positive loadings in the extreme western Pacific and eastern Indian Ocean. The predictand loading pattern (Fig. 4)--the SST loadings for the target period associated with the prior-time predictor loadings--imply positive SST anomalies roughly in the Nino 3.4 region following anomalously low SLP in the eastern tropical Pacific just over one season earlier. This clearly is indicative of the ENSO, as expected. Further confirmation that ENSO is this mode's theme is offered by the canonical component predictor time series (Fig. 5), showing interannual fluctuations closely corresponding to year-to-year changes in the ENSO state.

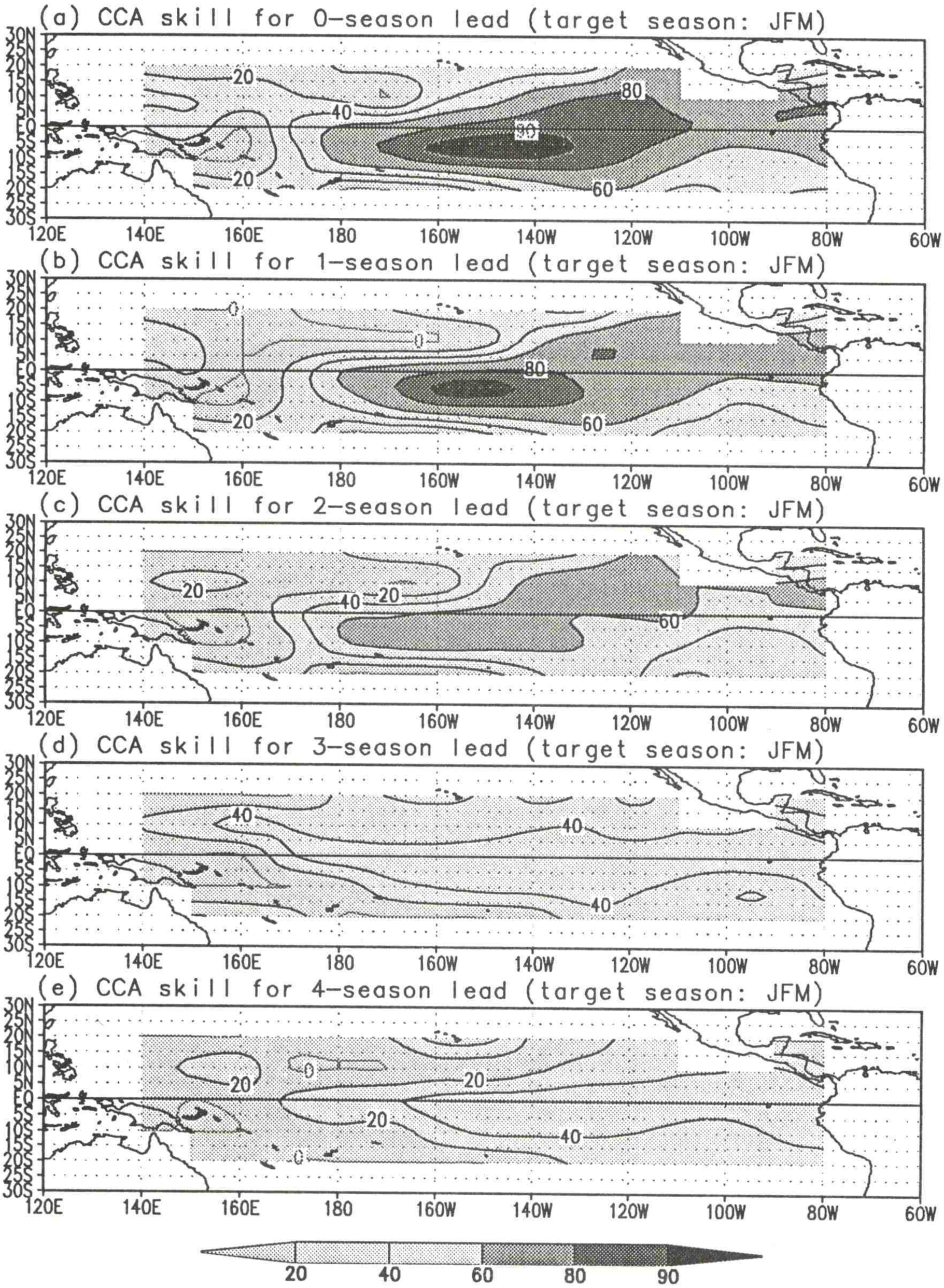

Fig. 1. Canonical correlation analysis (CCA) forecast skill for the tropical Pacific (20°N-20°S, 140°E-80°W) for the Jan-Feb-Mar target season, as estimated using cross-validation. Skill is expressed as a temporal correlation between forecasts and observations. CCA forecasts are based on anomaly patterns of SLP, SST, depth of the 20°C isotherm and dynamic sea level height. Each panel shows skills for forecasts with a different lead time, ranging from no lead time (i.e., made at end of December) to 4 seasons lead time.

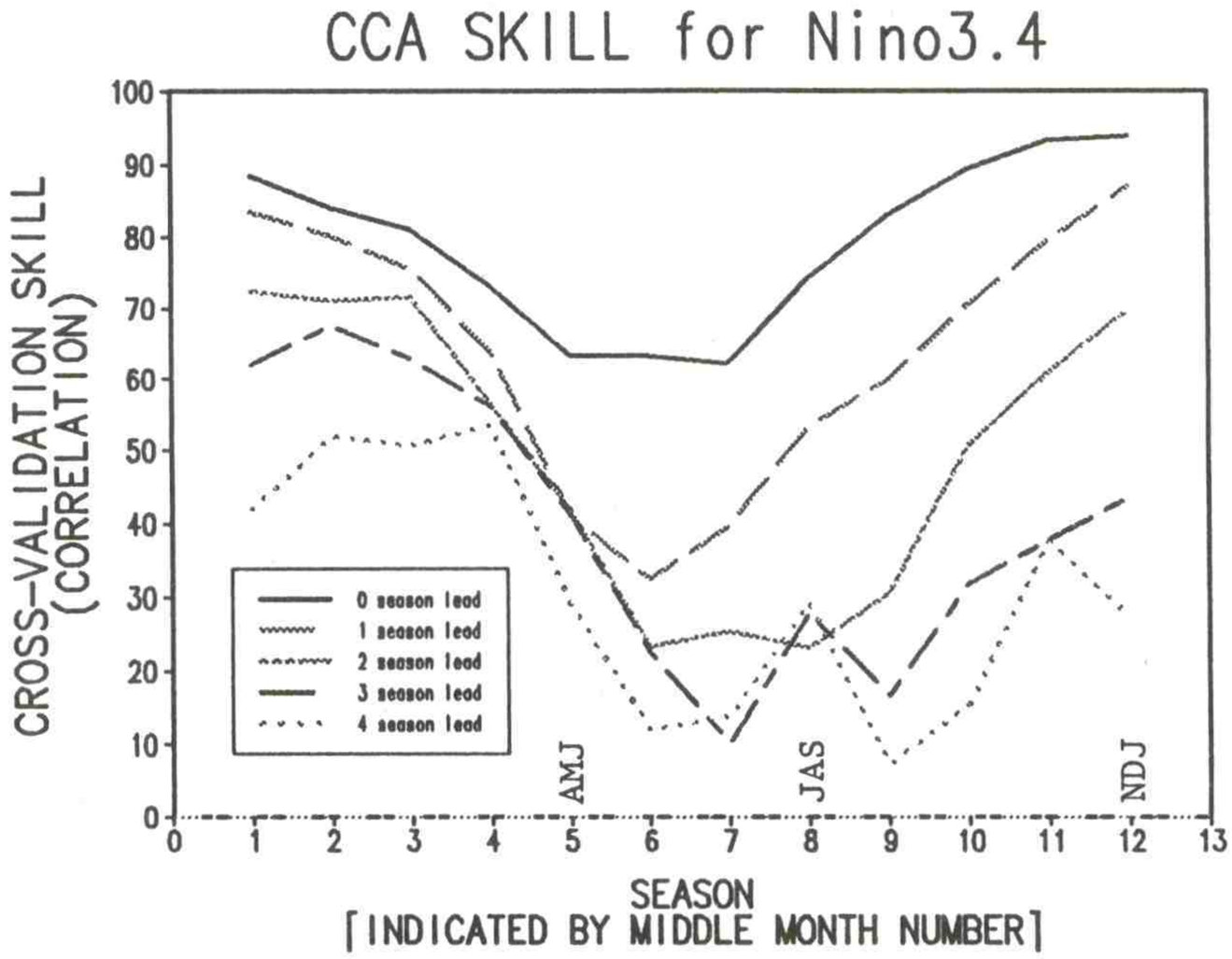

Fig. 2. Seasonal march of cross-validated CCA forecast skill averaged over the Nino 3.4 region (5°N-5°S, 120-170°W) for 3-month mean SST. Each curve shows skill for a different lead time, as indicated in the inset at lower left. The target season, indicated on the x-axis, is indicated by the middle month number (e.g. 2=JFM, 8-JAS, etc.).

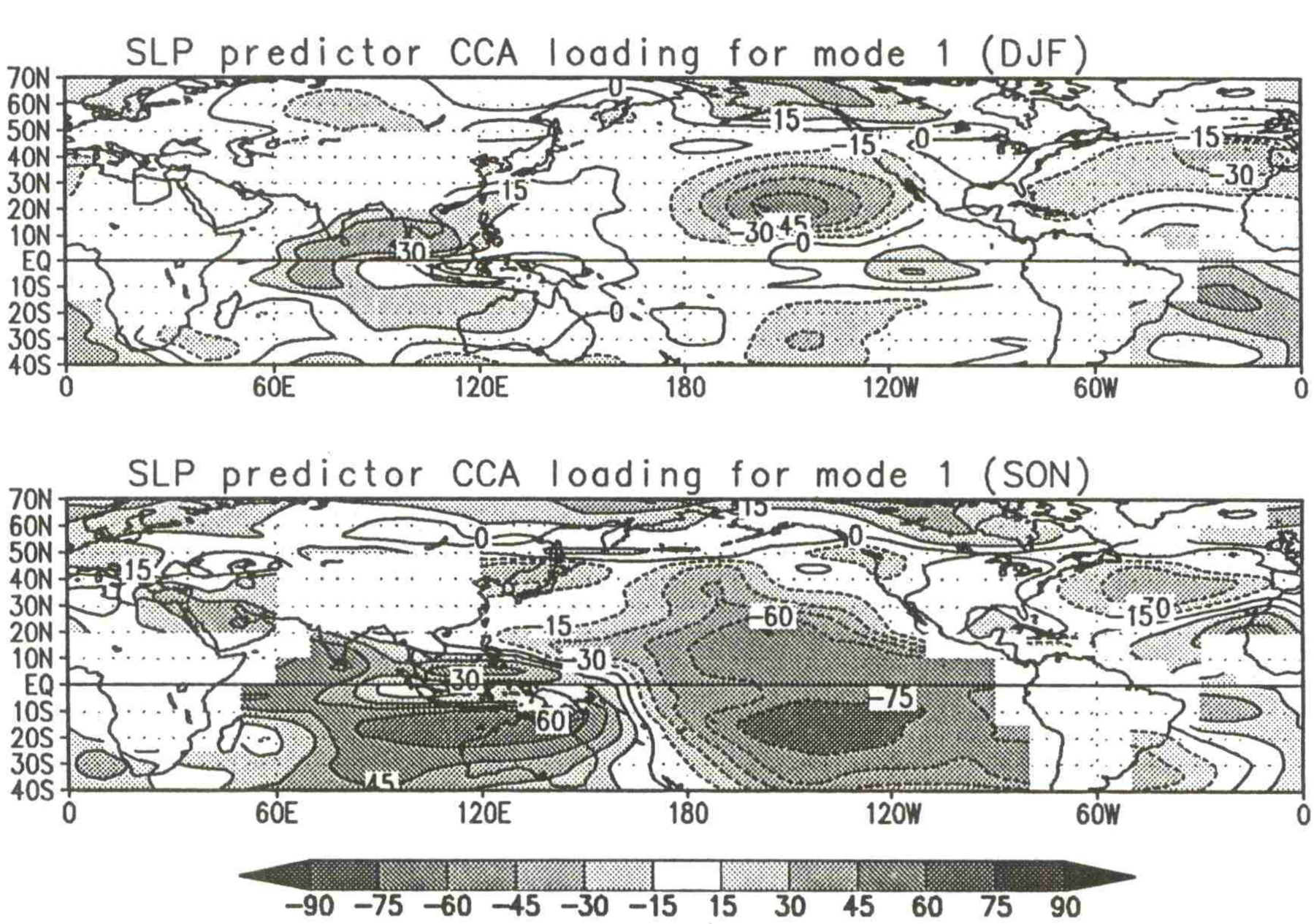

Fig. 3. Sea level pressure (SLP) CCA predictor loading patterns for mode 1 for the first (DJF) and fourth (SON) predictor seasons for prediction of tropical Pacific SST in JFM at one month lead.

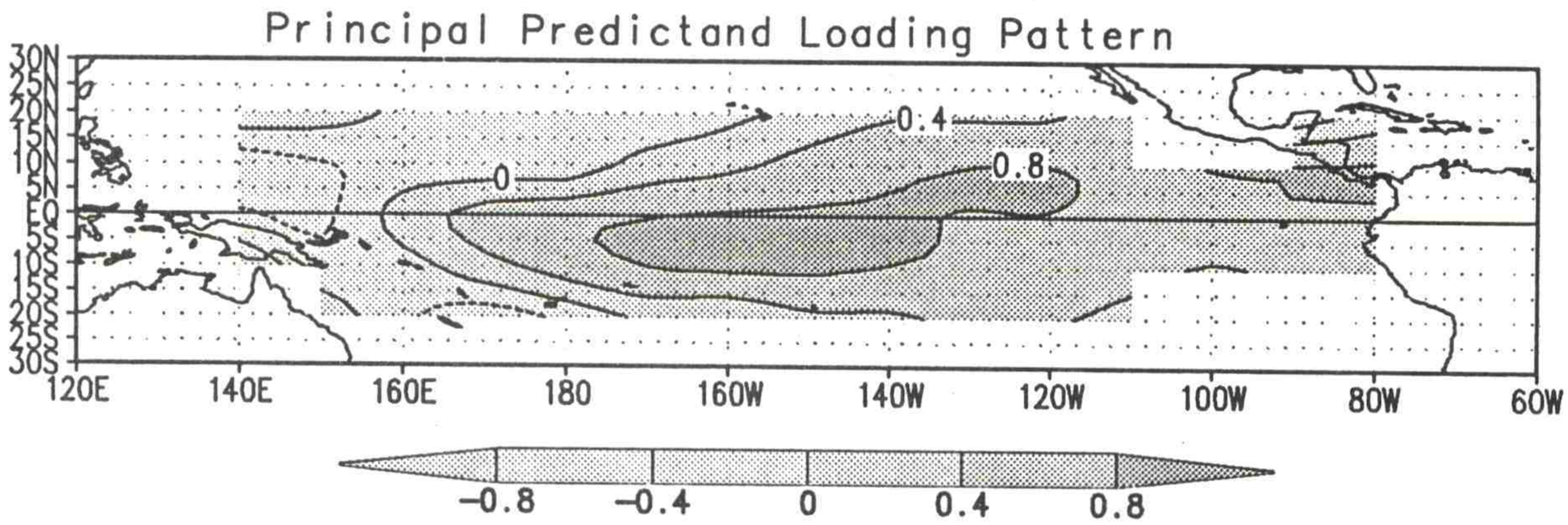

Fig. 4. SST predictand loading pattern for mode 1 for prediction of tropical Pacific SST in JFM at one month lead.

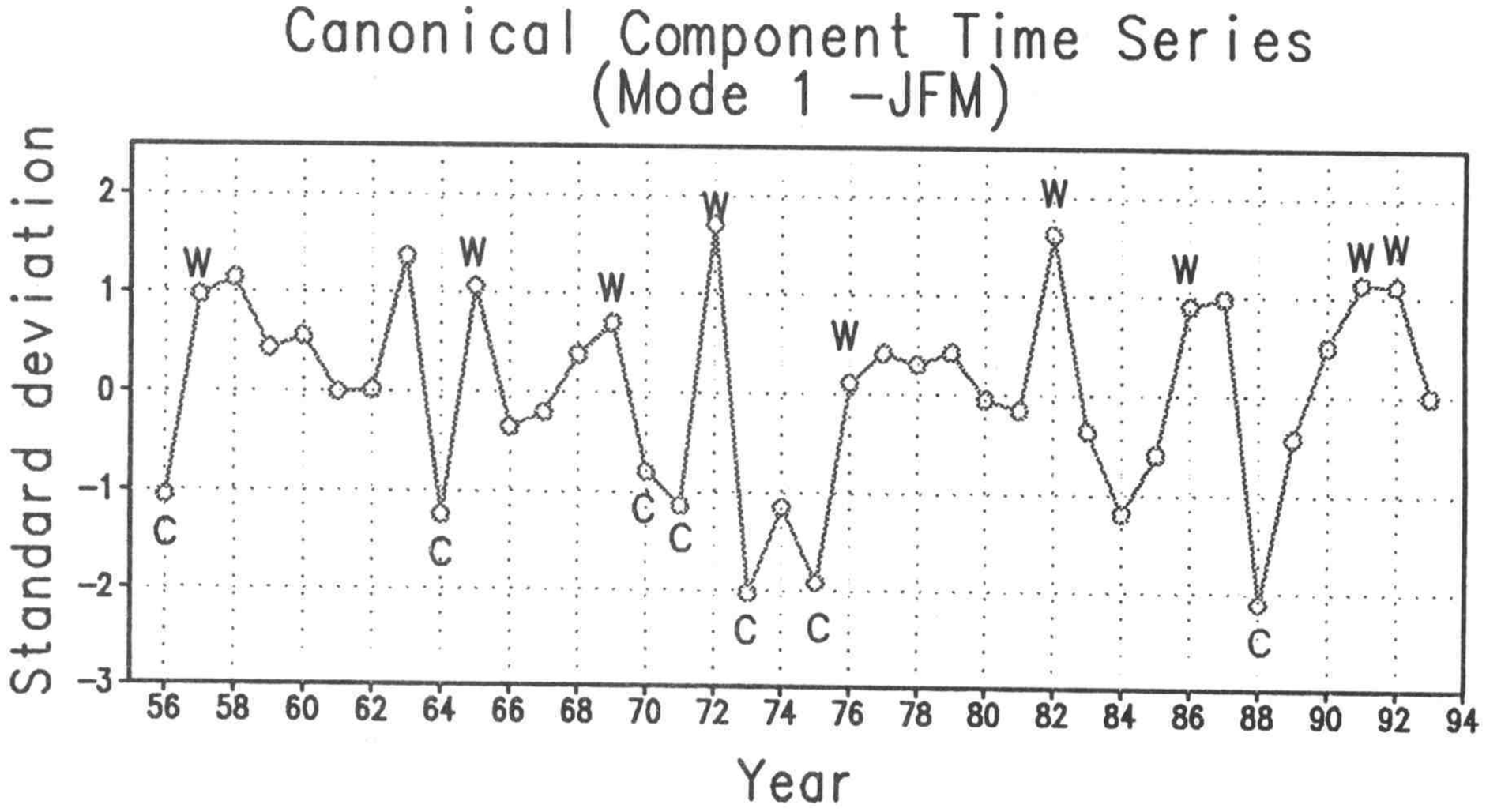

Fig. 5. Canonical component predictor time series for mode 1 for prediction of tropical Pacific SST in JFM at one month lead. The W and C symbols denote warm and cold SO episode years as defined by Ropelewski and Halpert.

THE RELATIONSHIP BETWEEN TROPICAL WESTERN PACIFIC WESTERLY ANOMALIES AND EAST ASIAN PRESSURE SURGES

Gilbert P. Compo[†], Brian E. Mapes[†], George N. Kiladis[*], and Peter J. Webster[†]

[†]Program in Atmospheric and Oceanic Sciences
[*]Cooperative Institute for Research in the Environmental Sciences
University of Colorado at
Boulder, Colorado

1 INTRODUCTION

A tropical response to East Asian pressure surges has been noted in observational case studies. Cold air outbreaks over the eastern coast of Asia produce pressure perturbations, some of which advance equatorward (Williams, 1981; Chang et al, 1982). The response to these perturbations comes in the form of enhanced convection over the Maritime Continent, enhanced Australian monsoonal flow, and westerly wind anomalies in the near equatorial western Pacific (Houze et al, 1981; Kiladis et al, 1994).

The dynamical relationship between penetrating mid-latitude pressure perturbations and tropical convective and circulation anomalies is studied using lagged linear regressions of 14 to 30 day bandpass filtered sea level pressure (SLP), 850 hPa wind, and outgoing longwave radiation (OLR).

2 DATA AND METHOD

Two sources of data are used in this study of northern hemisphere winters 1985–86 through 1993–94. European Center for Medium Range Weather Forecasting (ECMWF) operational analyses of 850 mb wind and sea level pressure provide a self consistent dynamical dataset with twice daily resolution and a 2.5° X 2.5° spatial resolution. As a proxy for convective activity, National Oceanographic and Atmospheric Administration produced twice daily 2.5° X 2.5° gridded outgoing longwave radiation (OLR) is employed.

To remove the annual, seasonal and diurnal cycles from all variables, the first three harmonics of daily averaged timeseries are subtracted from the original. These anomaly timeseries are bandpass filtered into four spectral bands: 2 to 6 day, 6 to 14 day, 14 to 30 day and 30 to 70 day. The bands covering the 2–30 day period capture the majority of intraseasonal variance while the 30–70 day band contains the lower frequency Madden-Julian Oscillation associated variance (Kiladis et al, 1994). The 6 to 14 day and 14 to 30 day bands contain a little more than half of the total anomaly variance for all variables.

To discern regions of activity for westerly anomalies, an objective criterion for westerly wind events is employed. The westerly anomaly element method, similar to that Mapes and Houze (1993) for cloud clusters, uses connected areas of 5 m/s anomalous wind between 20° N and 20° S covering over four grid points in longitude. Once an element is found, a routine calculates its area and center of wind or centroid position. The elements are tracked in time to form westerly anomaly events, where a match in time occurs if two elements are adjacent in time with an overlap of at least 1% with a minimum duration for an event set at 2 days.

Spectral methods are employed to examine the time evolution of those westerly anomalies occurring in the Australian monsoon and western Pacific regions. Cross spectra of sea level pressure and 850mb zonal wind are employed to determine appropriate band pass filters. Lagged linear regressions are used to show the "composite" evolution of circulation and convective anomalies correlated to sea level pressure fluctuations at a chosen base point. In this study, 14–30 day filtered anomaly timeseries SLP at a single point are cross-correlated and linearly regressed against identically filtered 850 hPa wind, SLP, and OLR timeseries at all grid points as in the method of Kiladis and Weickmann (1992). The composite regressions show the dynamical relationships between East Asian pressure surges and the tropical circulation associated with 1 standard deviation pressure anomaly at the base point. All wind vectors and OLR contours correlate with the base point at greater than .22 absolute value of the correlation coefficient.

3 RESULTS

Westerly anomaly events occur ubiquitously around the tropics, with those of longest duration and largest size occurring primarily in the Indian and Pacific Oceans (not shown). Figure 1 shows a map of the centroid of southern hemisphere summer westerly events when each reached maximum size for those events lasting between 2 and 40 days. The locations of

[†] Corr. author address: G. P. Compo, PAOS, CB 311, Univ. of Colorado, Boulder, CO 80309

maxima show regions of preferential activity, particularly the Sahel, southern Indian Ocean, the Australian monsoon region, and the Amazon Basin. The western Pacific shows a wide scatter of maxima location.

As cited by Chu (1988) and shown by Kiladis (1994), one possible cause of westerly wind anomalies in the tropical western Pacific are East Asian pressure surges leading to an equatorial pressure gradient. In the Chu (1988) case studies, anomalous pressure increases along 135°E from 30°N to the equator lead to westerly acceleration, westerly winds, and enhanced convective activity near the equator east of New Guinea. In this study, we show that the pressure surges have an even wider range of influence, being correlated with westerly anomalies and enhanced convection from the Australian monsoon region to the dateline.

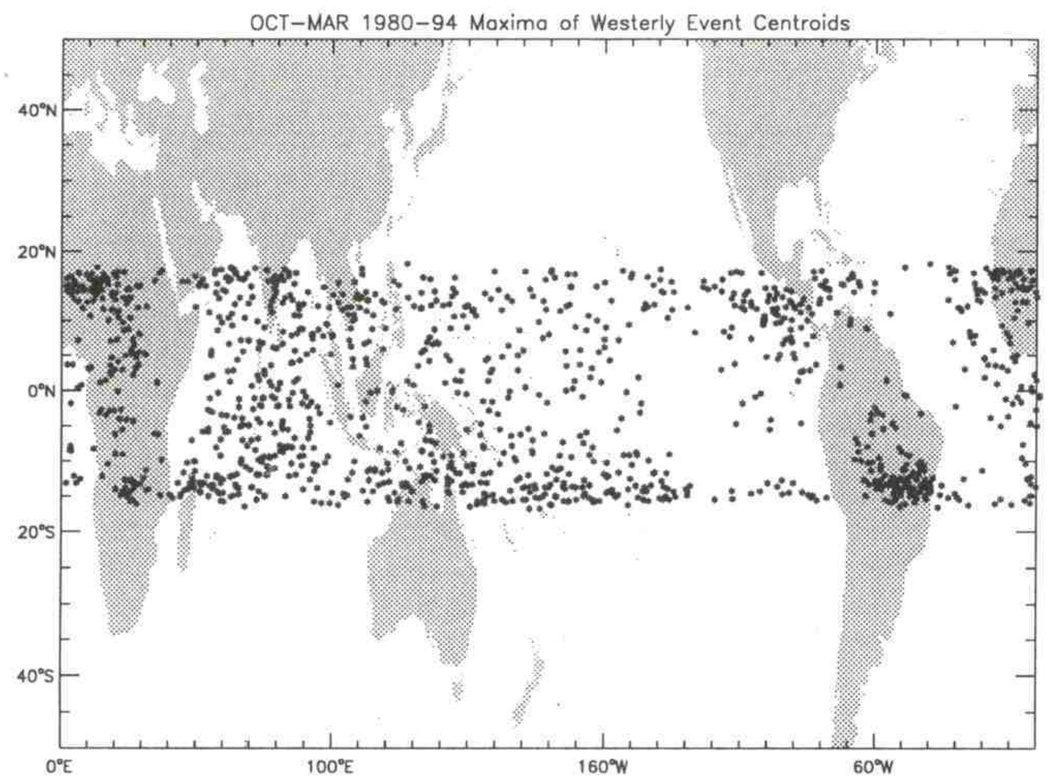

Figure 1. Location of centroid of westerly anomaly events occurring December-February 1980–1994. Events that had durations between 2 and 40 days are included.

To determine preferred timescales of interaction between the surges and westerly anomalies, cross spectra averaged for October– March of 1985–86 to 1993–94 between SLP anomalies in the pressure surge region and 850 hPa zonal wind at the equatorial dateline show a distinct peaks in power around 15 and 20 days. Figure 2 shows the cross spectrum for zonal wind at the equator, 180° with SLP at 20°N, 135°E. Distinct statistically significant peaks near those periods can be seen. Cross-spectra with other points of SLP in the surge region with zonal wind in the Indo-Australian sector show similar features (not shown).

To determine a time lag relationship between the SLP in the East Asian pressure surge region and Indo-Austral westerly anomalies, a lagged linear regression is employed. As noted for the cross-spectra, the relationship between the western Pacific zonal wind and SLP appears to lie in the 15 to 20 day range. The band pass filter chosen for use to highlight this relationship is 14 to 30 days. Multiple base points in the northern Pacific were examined for the pressure surge signal. Results from 20.0N, 135E are shown in figure 3. The point is indicative of the South China cold surges, and the regression of the SLP timeseries at this base point against 850 hPa wind, OLR, and SLP provides a synoptic view qualitatively similar to the known features of South China Sea cold surges but shown in a statistical sense. The regression also contains features correlating the pressure surges to enhanced convection and westerly anomalies in the western Pacific. As shown in figure 3, the regression displays a progression of anomalous high pressure from Siberia, southward parallel to the Himalayan Plateau between Day –7 and Day –4. The positive pressure anomaly over China precedes the strong northerly winds over the South China Sea and enhanced convective activity north of Borneo found in many observational studies (e.g. Ramage, 1971; Chang et al 1983). The form of high SLP contours over China represent an orographically trapped gravity wave as shown in Tilley (1990). A high pressure anomaly is also seen to propagate south and eastward between Day –4 and Day –1. The tropical response to these pressure perturbation manifests itself in three key areas: Australian monsoon, northern Maritime Continent, and the western Pacific.

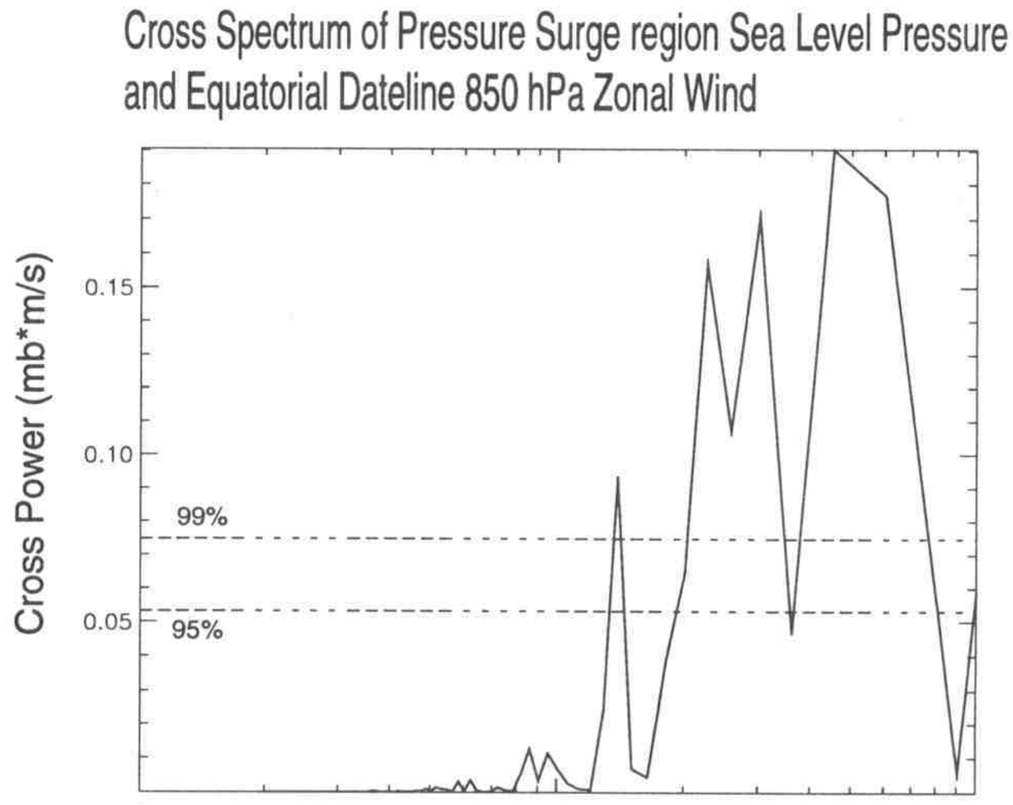

Figure 2. Cross spectrum of SLP at 20°N, 135°E with 850 hPa zonal wind at the equatorial dateline. The 99% and 95% significance levels as determined from Monte Carlo calculations are indicated

The Australian monsoon region receives increased convective activity and enhanced 850 hPa westerly anomalies between Day –7 and Day –4. The westerlies intensify from Day –4 to Day –1 while the convective signal subsides. The timing and form of the Australian monsoon regression response is similar to previous case studies of pressure surges that have a cross hemispheric

effect (Williams, 1981; Love, 1985).

As seen on Day –1, the increased convection north of Borneo and south of the Philippines following the main passage of the northerlies and positive pressure anomaly agrees with results of Houze et al (1981) who found convection in those regions increasing following a pressure surge at Hong Kong from the case studies of the Winter MONEX experiment.

As shown in Day -4 and Day –1, in tandem with the westerly anomaly in the western Pacific, strong northerlies occur between 40°N and the equator along 150°E. Chu (1988) showed cases of SLP perturbations propagating from the mid-latitudes to the equator along 135°E preceding westerly wind bursts east of New Guinea. In the regression of figure 3, a northerly surge and pressure perturbation east of the Philippine Sea accompanying a cyclone-anticyclone pair that moves eastward out of Asia is seen on Day -4. While the cyclone has faded by Day –1, the anti-cyclone is centered over the base point. Also seen is the equatorial pressure gradient resulting from the pressure surge. The signal of resulting westerly winds and convective anomaly east of New Guinea to the dateline indicates that the northerly surges east of the Philippines are probably more closely related to westerly wind bursts than are the cold surges over the South China Sea. Whether pressure surges occur as town distinct phenomena, one over the South China Sean and one east of the Philippines, or if both occur simultaneously, as indicated by the regression is still under investigation.

4 CONCLUSIONS AND FUTURE WORK

The synoptic timescale dynamical relationship between East Asian pressure surges and tropical circulation and convective anomalies has been examined. Lagged linear regression "composites" of South China Sea cold surges and Philippine Sea northerly surges have been presented. The structure of the South China Sea cold surge compares well with previous case studies of cold surges. Enhanced convection north of Borneo and south of the Philippines following passage of a pressure perturbation is shown. The composite also contains the previously observed cross-equatorial influence in the Australian monsoonal flow. The Philippine Sea northerly surges are seen to be more closely tied to westerly anomalies in the tropical western Pacific. The cyclone-anticyclone pair found in the regression resembles that of case studies and small sample composite studies, as does the northerly surge-westerly anomaly relationship. The triggering mechanisms for intra-seasonal westerly anomalies in other Tropical regions will be the aim of future studies.

Acknowledgements This work was supported under the TOGA COARE project grant through NOAA and NSF, ATM-9205914 and the NOAA Ocean-Atmosphere Division, DOC NA56GP0230.

5 REFERENCES

Chang, C. P. and K. M. Lau, 1982: Short-Term Planetary-Scale Interactions over the Tropics and Midlatitudes during Northern Winter. Part I: Contrasts between Active and Inactive Periods. *Mon. Wea. Rev.*, **110**, 933–946.

—, J. E. Millard, and G. T. J. Chen, 1983: Gravitational Character of Cold Surges during Winter MONEX. *Mon. Wea. Rev.*, **111**, 293–307.

Chu, P. S., 1988: Extratropical Forcing and the Burst of Equatorial Westerlies in the Western Pacific: A Synoptic Study. *J. Meteor. Soc. Japan*, **66**, 549–564.

Houze, R. A., S. G. Geotts, F. D. Marks, and A. K. West: Winter Monsoon Convection in the Vicinity of North Borneo. Part I: Structure and Time Variation of the Clouds and Precipitation. *Mon. Wea. Rev.*, **109**, 1595–1614.

Kilidas, G. N. , G. A. Meehl, and K. M. Weickmann, 1994: The Large Scale Circulation Associated with Westerly Wind Bursts and Deep Convection over the Western Equatorial Pacific. *J. of Geophys. Res.*, **99**, 18,527–18,544.

Love, G., 1985: Cross-Equatorial Influence of Winter Hemisphere Subtropical Cold Surges. *Mon. Wea. Rev.*, **113**, 1487–1498.

Madden, R. A. and P. R. Julian, 1994: Observations of the 40–50–Day Tropical Oscillation — A Review. *Mon. Wea. Rev.*, **122**, 814–837.

Mapes, B. E., and R. A. Houze, 1993: Cloud Clusters and Superclusters over the Oceanic Warm Pool. *Mon. Wea. Rev.*, **121**, 1398–1415.

Murakami, T., and W. L. Sumathipala, 1989: Westerly Bursts during the 1982/83 ENSO. *J. of Climate*, **2**, 71–85.

Ramage, C. S., 1971: *Monsoon Meteorology.*, Academic Press, 296 pp.

Tilley, J. S., 1990: On the Application of Edge Wave Theory to Terrain-Bounded Cold Surges: A Numerical Study. Ph. D. Thesis, Department of Meteorology, The Pennsylvania State University, University Park, PA. 353 pp.

Williams, M., 1981: Interhemispheric Interaction During Winter MONEX, *Proc. of the International Conference on Early Results of FGGE and Large Scale Aspects of Its Monsoon Experiment.*, World Meteorological Organization, Geneva.

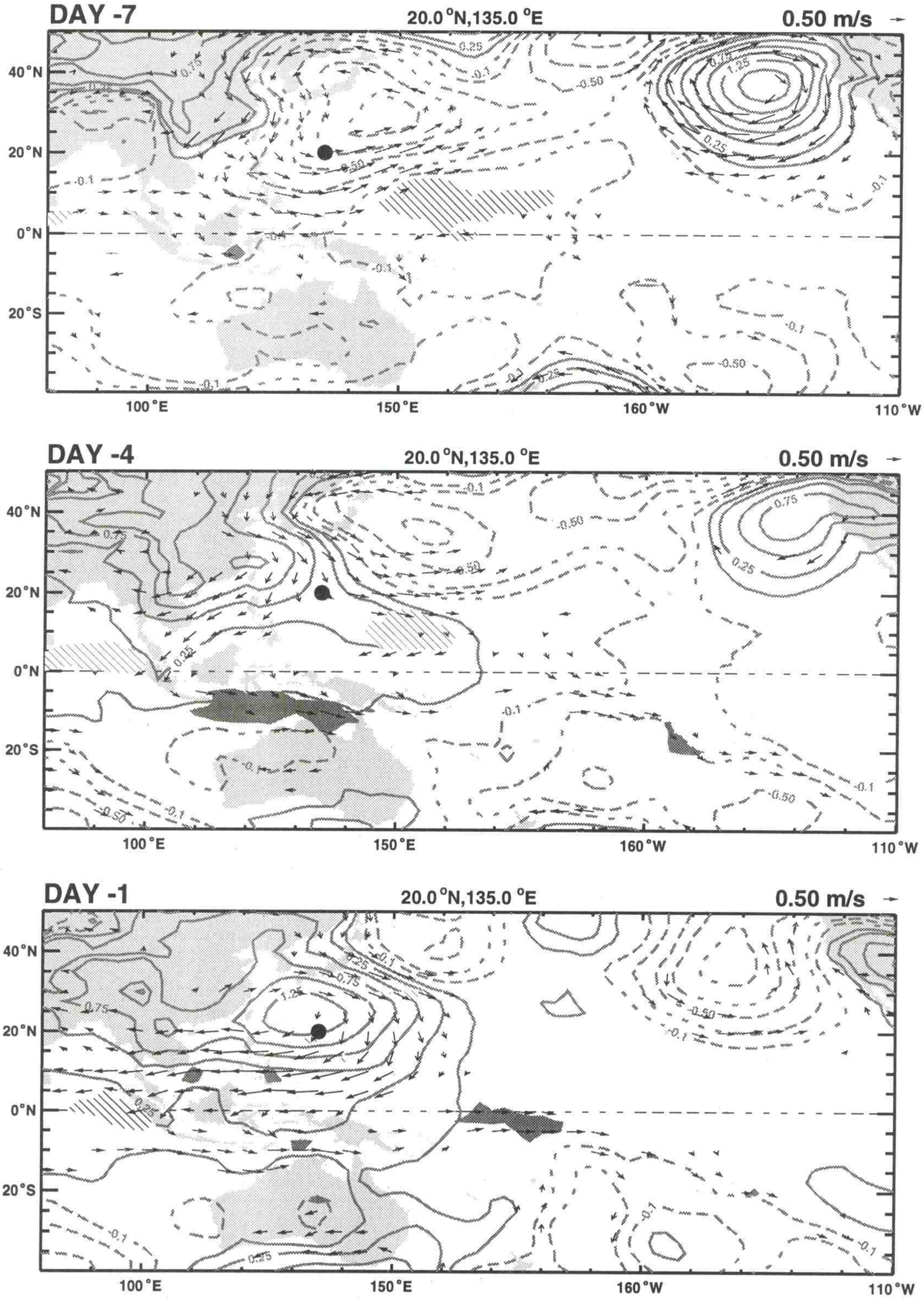

Figure 3. Lagged linear regression of 14–30 day band pass filtered sea level pressure at 20°N, 135°E regressed against identically filtered SLP, OLR, and 850mb wind. Wind vectors and OLR are indicated where the absolute value of the local correlation exceeds .22. The solid (hatched) filled contours indicate negative (positive) OLR anomalies of less (greater) than 5 W/m^2. The contour lines indicate the regressed value of SLP. Dashed contour indicate negative SLP anomalies, while solid contours indicate positive SLP anomalies. Day 0 indicates a simultaneous regression. Days before 0 indicate that the base point lags the field, while days after 0 indicate that the base point leads the field.

On the Relationship Between Sea Surface Temperature, Pressure and Zonal Winds in the Equatorial Pacific

M. J. McPhaden[1], W. Wang[2] and C. Zhang[3]

[1]NOAA/Pacific Marine Environmental Laboratory, Seattle, Washington
[2]School of Oceanography, University of Washington, Seattle, Washington
[3]Joint Institute for the Study of the Atmosphere and Ocean,
University of Washington, Seattle, Washington

INTRODUCTION

In this study, we examine the relationship between sea surface temperature (SST), sea surface pressure (SLP) and surface zonal winds in the equatorial Pacific using the Comprehensive Ocean Atmosphere Data Set (COADS). The work is motivated by the Lindzen and Nigam (1987) hypothesis that atmospheric boundary-layer pressure gradients in thermal equilibrium with the underlying SST field are responsible for driving low-level winds and wind convergence near the equator. The hypothesis figures prominently in theories for the westward progression of the annual cycle in the eastern equatorial Pacific (e.g., Xie, 1994); and in theories of air-sea interaction on interannual time scales associated with ENSO (Neelin, 1991). Lindzen and Nigam (hereafter referred to as LN) argued that boundary-layer pressure gradient forcing was more effective than cumulus heating in driving low-level wind convergence; and furthermore, that this theoretical framework allowed for more physically realistic parameterization of processes involved in ocean-atmosphere coupling.

Various aspects of the LN hypothesis have been examined in previous work focusing on the seasonal and interannual variability in the tropical Pacific (e.g., Wallace *et al.*, 1989; Nigam and Shen, 1993). In general, these studies lend support to the hypothesis of boundary-layer convergence driven by underlying SST gradients, particularly when one takes into account the effects of boundary-layer stability (Nigam and Chao, 1995). However, the relative importance of boundary-layer forcing vs. cumulus heating in driving low-level wind convergence is an issue that is still not yet fully resolved.

In this study we attempt to provide insight into this question through a preliminary analysis of COADS data for the period 1969–91. Results indicate that the strength of ocean-atmosphere interaction is time-scale dependent, with the coupling between zonal winds and SST gradients on interannual time scales about three times stronger than for the mean seasonal cycle. This may indicate that on interannual time scales, boundary-layer zonal winds are responding to cumulus forcing as well as to SST and pressure gradient forcing, consistent with the prevalence of anomalous deep convection in the central Pacific during ENSO.

DATA AND DATA PROCESSING

In this preliminary analysis, we focus on COADS data for the most recent two decades (1969–91) during which data availability is high. A mean seasonal cycle is formed by averaging all years together for each calendar month. Interannual variability is determined as the difference between individual months and the mean seasonal cycle. Pressure and SST zonal gradients are computed over 30° of longitude.

MEAN SEASONAL CYCLE

A well known aspect of the mean seasonal cycle is the westward progression of both winds and SST from near the cost of South America to about 140°W (Horel, 1982; Chang and Philander, 1994). Such a westward progression is evident in our analysis of the COADS data, which also shows the westward progression of both zonal SST gradient and SLP gradient along the equator in the eastern Pacific (Figure 1). Although there are limited degrees of freedom for correlations based on the mean seasonal cycle, analysis on this time scale (Figure 2a) indicates that where the amplitude of the mean seasonal cycle is large (east of 140°W), cross-correlation of zonal wind with zonal SST gradient hovers around 0.8. A similarly high cross-correlation of zonal wind with zonal SLP gradient (but of opposite sign) is evident in this region, consistent with the observation that high SST is associated with low atmospheric pressure and vice versa. A robust relationship between zonal winds, SST and SLP gradients is not so evident in the western Pacific, where SST is characterized by a weak semiannual signal and wind variations are monsoonal (i.e., strongly influenced by continental heat sources and sinks).

Regression analysis in the eastern Pacific indicates that a 1°C per 10° longitude SST gradient will force a 1.3 m s^{-1} zonal wind along the equator (Figure 2b). A similar magnitude relationship (namely, 2 m s^{-1} for the same SST gradient) was used by Xie (1994) in his model of the annual cycle. Assuming that the winds are essentially flowing down a pressure gradient in balance with the SST field, we can estimate a Rayleigh damping coefficient of $(0.34\ \text{day})^{-1}$ for zonal wind variations based on the slope of the regression line between zonal winds and zonal SLP gradient (Figure 2c). This calculation assumes that the zonal momentum balance is linear and that the Coriolis force is small near the equator. Allowing for explicit inclusion of the Coriolis term does not significantly change this estimate (Table 1), which is about half to one-

third the value found by Deser (1993) in an earlier analysis of COADS data. The difference in the two estimates is probably due to the much larger region considered in Deser's analysis (namely, 20°N to 20°S).

INTERANNUAL VARIABILITY

We repeated the above statistical calculations for interannual time scales after first averaging monthly anomalies into 3-month seasonal means. A typical pattern between wind and SST variations associated with ENSO is illustrated in Figure 3 for December 1972 to February 1973. One sees a tendency for surface convergence both meridionally and zonally over warm SST anomalies in the central and eastern Pacific. Specifically, easterly wind anomalies are observed to the east of the maximum SST anomaly and westerly anomalies are observed to the west of the maximum SST anomalies. Correspondingly, along the equator there is high correlation between zonal winds and zonal SST gradients east of 120°W and west of 160°E (Figure 4a). The minimum in correlation between 120°–160°W coincides with the maximum SST anomalies and the weakest wind variability. The correlation between zonal winds and zonal SLP gradient is roughly opposite of that between zonal winds and SST gradient, although there is more small-scale structure in the pressure/wind correlation pattern (e.g., positive values near 150°E, 180°, and 130°W).

Regression analysis in the region of highest correlation between zonal winds, SST, and SLP gradients (155°E to 175°E) indicates that a 1°C per 10° longitude SST gradient will force a 3.6 m s^{-1} zonal wind along the equator, which is about three times larger than the value found for the mean seasonal cycle (Figure 4b; Table 1). Conversely, the estimated Rayleigh drag coefficient of $(0.34\ day)^{-1}$ is identical to that estimated for the mean seasonal cycle (Figure 4c). As for the seasonal cycle, inclusion of the Coriolis term has little impact in this estimate of Rayleigh friction because of proximity to the equator. Repeating these calculations over a broader region (155°E–165°W), where correlation between zonal winds and SST gradient is uniformly high on interannual time scales, leads to essentially identical results (namely, 3.4 m s^{-1} per 1°C over 10° longitude, and a Rayleigh damping time scale of 0.31 days).

DISCUSSION

As expected from the LN hypothesis, there is a consistent relationship between zonal SST gradients and surface zonal winds in the equatorial Pacific on seasonal-to-interannual time scales. However, SST gradients appear to be much more efficient at forcing surface wind variations on interannual time scales compared to the mean seasonal cycle. We interpret this increased efficiency to the effects of cumulus forcing associated with ENSO variability. As LN pointed out, cumulus heating, to the extent that deep convection tends to be colocated with warm tropical SST anomalies, would produce a similar pattern in surface wind convergence as that driven directly by SST gradients. ENSO is characterized by pronounced zonal shifts in deep convection correlated with underlying SST anomalies (e.g., Nigam and Shen, 1993). Conversely, on seasonal time scales, variations in convective activity in the eastern Pacific are more related to meridional displacements and intensification of the ITCZ, whose southern limit is generally located north of 4°N (Wallace *et al.*, 1989). Thus, along the equator in the eastern Pacific there is very little convective activity associated with the mean seasonal cycle.

In the LN formalism, variations in SLP are proportional both to underlying SST and to the height of the boundary layer, the latter of which constitutes a negative feedback on the basic SST forcing of low-level winds. The strength of the boundary-layer "backpressure" effect depends on the efficiency with which mass flux is transferred across the tradewind inversion through cumulus convection. Our results suggest that boundary-layer backpressure is weaker on interannual time scales vis-a-vis the mean seasonal cycle because of the occurrence of pronounced deep convection associated with ENSO. In particular, increased convection is associated with reduced sea level pressure. Thus, for a given zonal SST gradient along the equator, the corresponding zonal SLP gradient would be stronger on interannual time scales. This stronger pressure gradient would lead to larger surface winds because frictional damping is approximately constant across the period band encompassing seasonal-to-interannual time-scale variations in the equatorial Pacific.

REFERENCES

Chang, P., and S.G.H. Philander, 1994: A coupled ocean-atmosphere instability of relevance to the seasonal cycle. *J. Atmos. Sci., 51*, 3627–3648.

Deser, C., 1993: Diagnosis of the surface momentum balance over the Tropical Pacific Ocean. *J. Climate, 6*, 64–74.

Horel, J., 1982: On the annual cycle of the tropical Pacific atmosphere and ocean. *Mon. Wea. Rev., 110*, 1863–1878.

Neelin, D., 1991: The slow sea surface temperature mode and the fast wave limit: analytical theory for tropical interannual oscillations and experiments with a hybrid coupled model. *J. Atmos. Sci., 48*, 584–606.

Lindzen, R.S., and S. Nigam, 1987: On the role of sea surface temperature gradients in forcing low-level winds and convergence in the tropics. *J. Atmos. Sci., 44*, 2418–2436.

Nigam, S., and H.-S. Shen, 1993: The structure of oceanic and atmospheric low-frequency variability over the tropical Pacific and Indian Oceans. Part I: COADS Observations. *J. Climate, 6*, 657–676.

Nigam, S., and Y. Chao, 1995: On the evolution of tropical ocean-atmosphere annual cycle variability. *J. Climate*, submitted.

Wallace, J. M., T. P. Mitchell, and C. Deser, 1989: The influence of sea-surface temperature on surface wind in the eastern equatorial Pacific: Seasonal and interannual variability. *J. Climate, 2*, 1492–1499.

Xie, S.-P., 1994: On the genesis of the equatorial annual cycle. *J. Climate, 12*, 2008–2013.

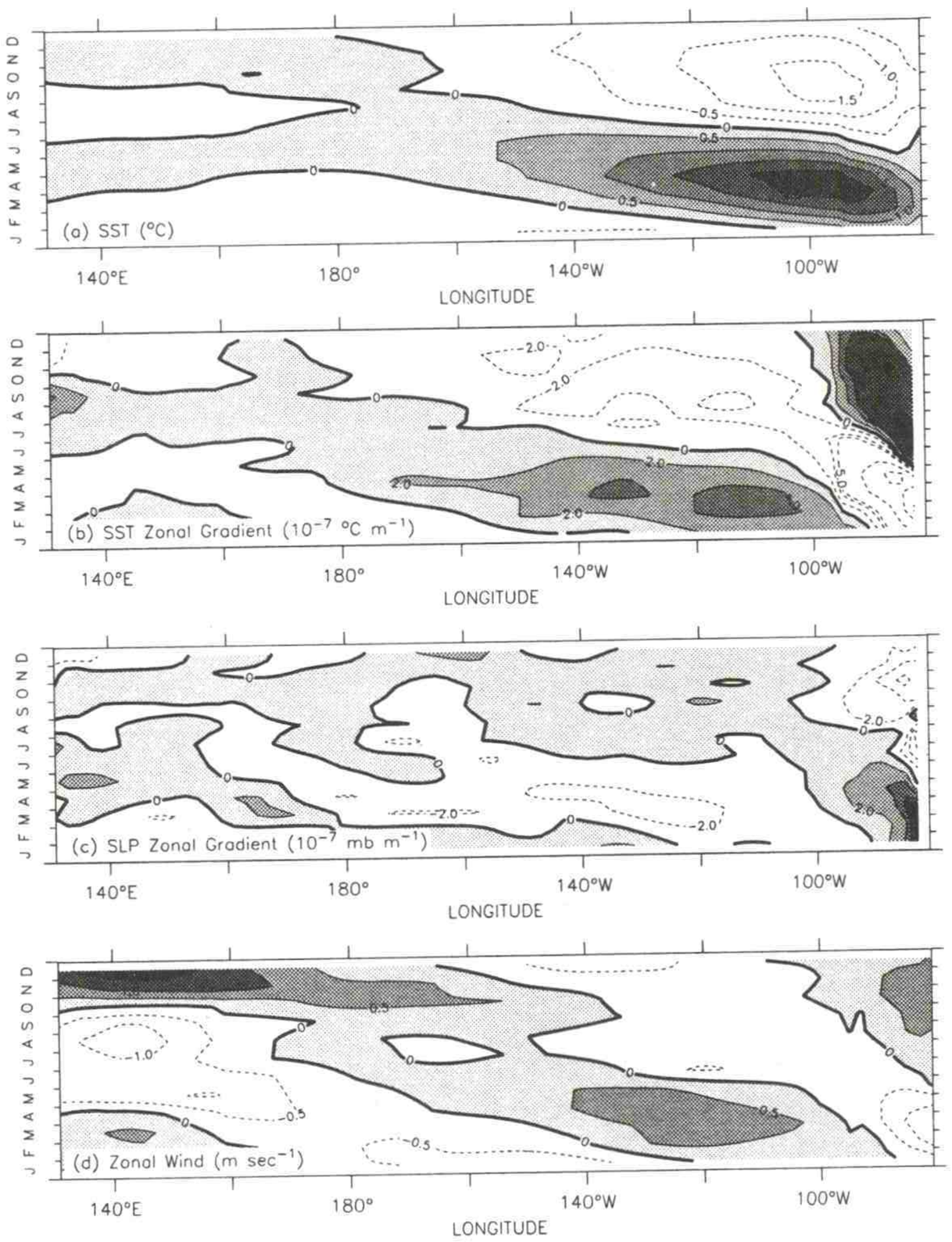

Figure 1. Seasonal cycle in (a) SST, (b) zonal SST gradient, (c) zonal SLP gradient and (d) zonal wind anomalies near the equator (2°N–2°S). Annual means have been subtracted at each longitude.

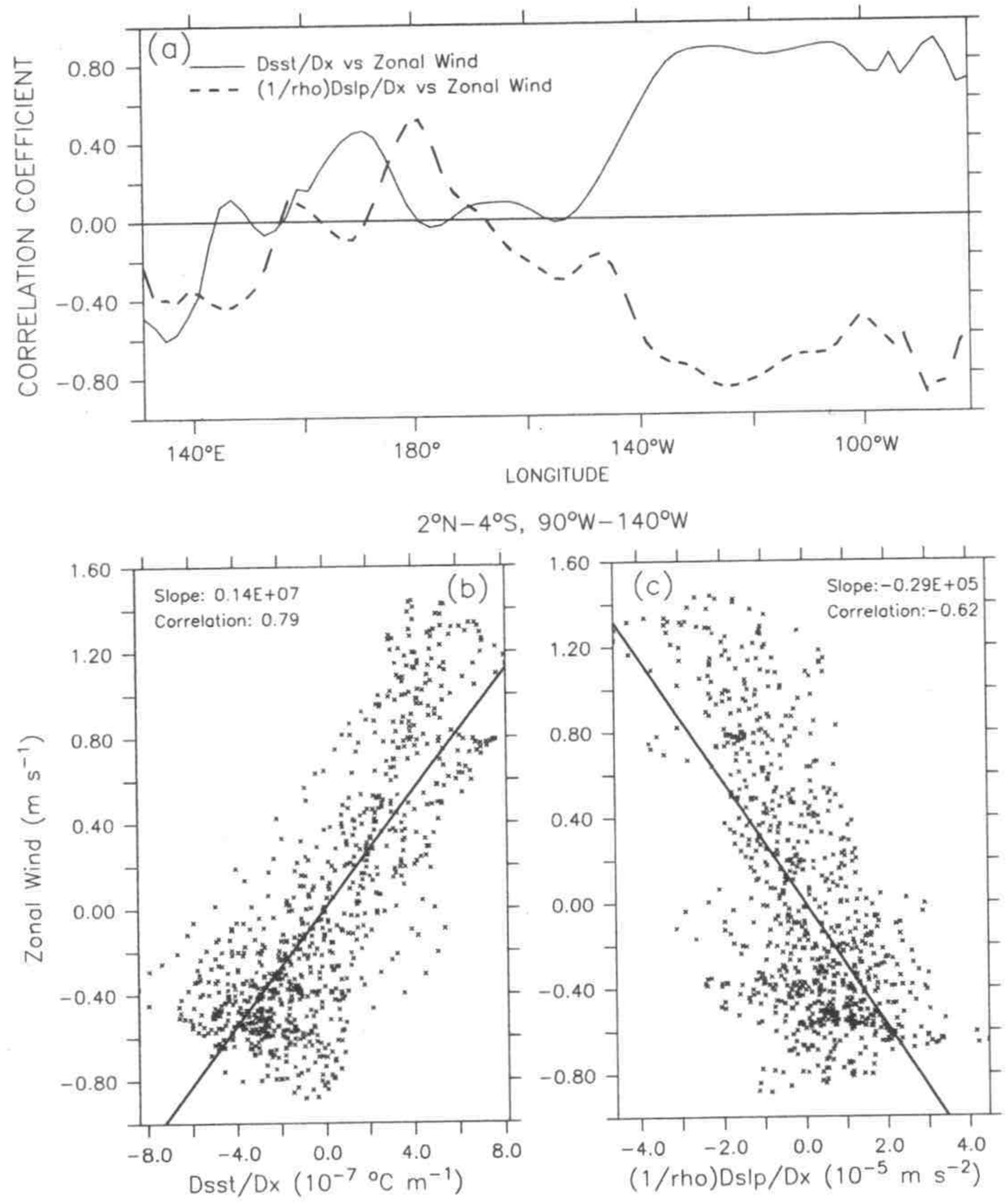

Figure 2. (a) Correlation between the seasonal cycles of zonal SST gradient and zonal wind (solid line); and between seasonal cycles of zonal SLP gradient and zonal wind (dashed line) near the equator (2°N–2°S). (b) Scatter plot for zonal wind and zonal SST gradient in the region 2°N–4°S, 90°–140°W based on the mean seasonal cycle. Solid line is the best fit in a least squares sense using orthogonal regression analysis, and is equivalent to change in the winds of 1.3 m s^{-1} for an SST gradient of 1°C per 10° of longitude. (c) Scatter plot for zonal wind and zonal SLP gradient in the region 2°N–4°S, 90°–140°W based on mean seasonal cycle data. Solid line is the best fit in a least squares sense using orthogonal regression analysis, and is equivalent to Rayleigh drag coeffient with a 0.34-day time constant.

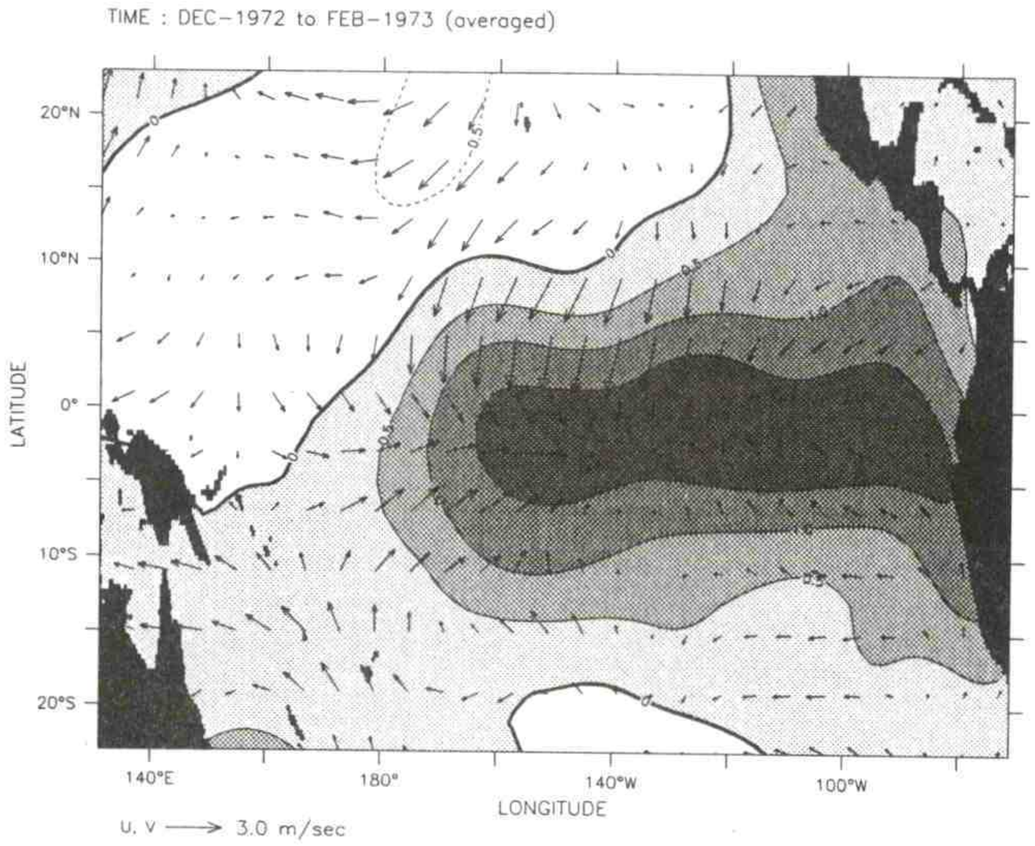

Figure 3. SST anomalies and surface wind anomalies for December 1972 through February 1973, illustrating the relationship between winds and SST on interannual time scales.

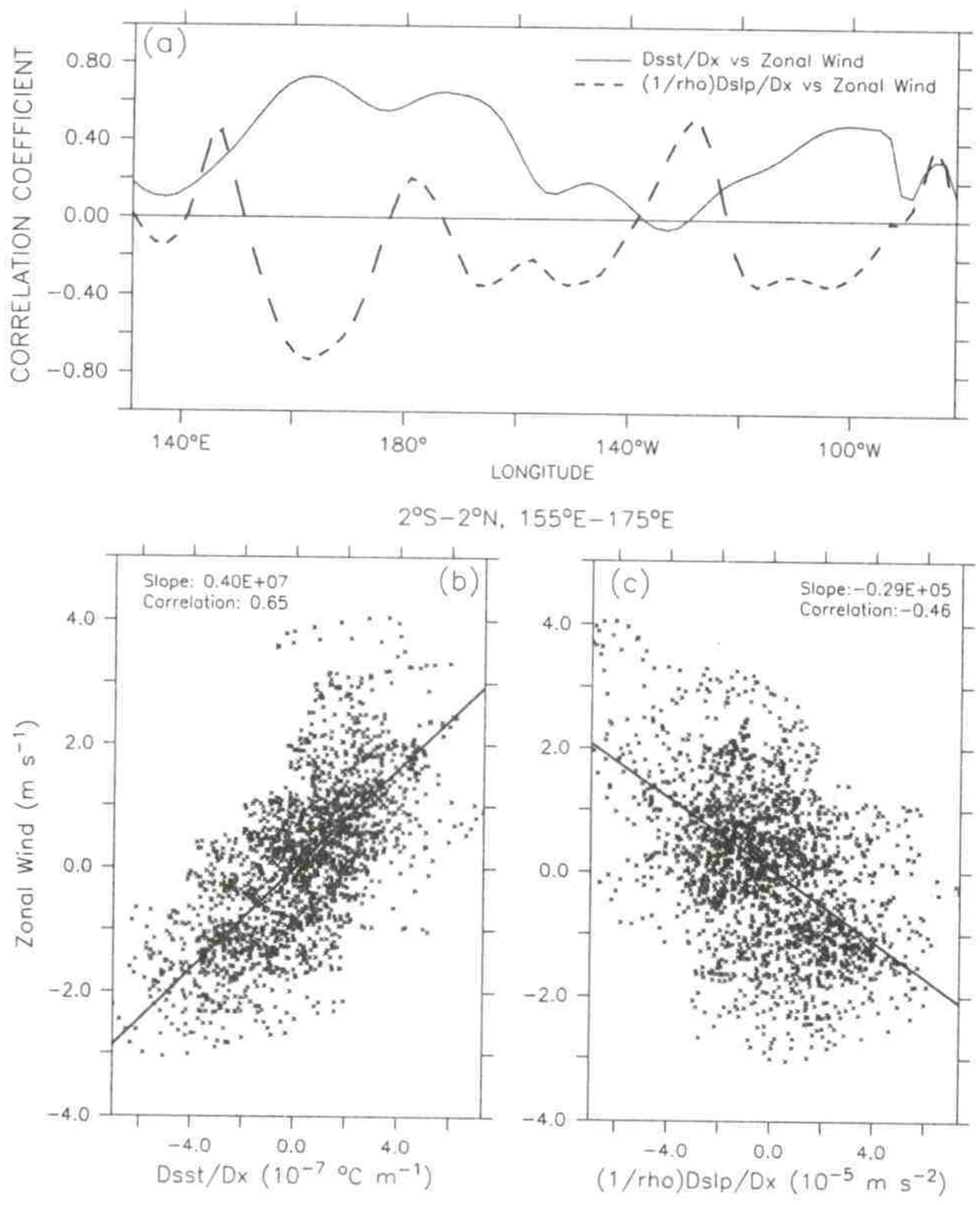

Figure 4. (a) Correlation between interannual anomalies of zonal SST gradient and zonal wind (solid); and between interannual anomalies of zonal SLP gradient and zonal wind (dashed line) near the equator (2°N–2°S). (b) Scatter plot for interannual anomalies of zonal wind and zonal SST gradient in the region 2°N–2°S, 155°E–175°E. Solid line is the best fit in a least squares sense using orthogonal regression analysis, and is equivalent to change in the winds of 3.6 m s^{-1} for an SST gradient of 1°C per 10° of longitude. (c) Scatter plot for interannual anomalies of zonal wind and zonal SLP gradient for the region 2°N–2°S, 155°E–175°E. Solid line is the best fit in a least squares sense using orthogonal regression analysis, and is equivalent to Rayleigh drag coefficient with a 0.34-day time constant.

Table 1. Parameters determined from regression analysis presented in Figures 2 and 4. Numbers in parentheses indicate Rayleigh damping time constant when the Coriolis term is included in the momentum balance (see text for discussion).

	Mean Seasonal Cycle 2°N–4°S, 90°–140°W	**Interannual Variations** 2°N–2°S, 155°–175°E
Zonal Wind (m s^{-1}) per 1°C in 10° longitude	1.3	3.6
Rayleigh Damping Time Constant (days)	0.34 (0.32)	0.34 (0.34)

Climatological Variations of Atlantic Sea Level Pressures

by

John Knaff
Colorado State University
Ft. Collins, CO 80523

1 Introduction

Since the early 1970's the summertime Caribbean sea level pressures have been above normal, the African Sahel region has suffered drought conditions, and Atlantic hurricane activity has been suppressed. This study focuses only on the summertime sea level pressure variations in the Caribbean Sea in order to better understand their evolution and maintenance as well as their impact on the climate and weather. In this endeavor, I attempt to answer two separate yet related questions. The first is "How exactly does the summertime pressure in the Caribbean act to modulate Tropical Storm (TC) activity? " using a combination of surface, upper air, and TC data sets. The answer is found by compositing the ten highest and ten lowest pressure years from 1950 to 1988. The second and more fundamental question I attempt to answer is " What controls variations of the summertime Caribbean pressure?". This was done using a combination of station and COADS data sets.

2 "How does the pressure modulate TC activity?"

Results of the stratification of rawindsonde data by surface pressure conditions yield an adequate explanation of the relationship between Atlantic hurricane activity and Caribbean pressure anomalies. The upper air analysis shows that summertime high pressure conditions in the Caribbean are related to stronger trade winds, stronger 200 mb westerlies, and drier than normal mid-level conditions (Figure 1). All of which are detrimental to the formation and intensification of tropical cyclones, especially the wind fields which result in much greater 850 mb to 200 mb vertical shear (Figure 2). More interesting is the combination of all the upper air results which indicate that during periods of higher Caribbean pressures the strength of the mid-oceanic trough or Tropical Upper Tropospheric Trough (TUTT) is significantly stronger.

3 "What controls the summertime Caribbean pressures?"

The examination of the historical record of surface pressure suggest that the summertime pressures in the Caribbean are somewhat controlled by two factors. These factors have separate time scales. The first which is related to the multi-decadal climate change appears global in nature. It manifest itself as a east west oscillation of pressure with one node in the Caribbean and another in Southeast Asia. I call this the "Wobble". The pressures in Southeast Asia seem to be out of phase

with those of the the Caribbean. An example of the wobble is shown in Figure 3 which shows the annual average of the pressure at Calcutta, India along with the annual average of the pressure at Havana, Cuba. As you can see there appears to be a out of phase relationship, more interesting is the relationship to hurricane activity in the Atlantic and the difference between these two pressure stations shown in Figure 4.

The second of the factors believed involved in the evolution of summertime Caribbean pressure is more year to year in nature. It results simply from a continuation of the conditions of the preceding winter and spring Atlantic subtropical ridge conditions. I find that a large portion of the summertime pressure can be explained (21%) by the strength of the subtropical ridge just off the African coast during the month of March shown in Figure 5. These March conditions are very much related to what happens to the ridge during the winter period. The first detectable precursor to March condition can be found in the early winter conditions of October and November. The relationship between the November ridge and the March ridge is quite good (20% or so). The utility of the November ridge is not to predict the March ridge conditions but to give a early indicator of the strength of the upcoming hurricane season (explaining between 10% and 20% of the variance depending on the measure of activity used). These ridge relationships to pressure in the Caribbean are thought to be a feed back between the wind conditions produced by variations in ridge strength and the pressure field itself. For instance, a stronger ridge in November would produce greater upwelling along the African coast (cold water) this thus affects the March ridge making it stronger. A stronger March ridge results in stronger northeast trade winds which through evaporative and mixing affects tend to cool the SSTs throughout the tropical Atlantic and Caribbean resulting in higher than normal pressures.

4 Conclusions

I started this study with two questions in mind. The analysis and results show that to a large extent my first question concerning pressure hurricane relationships in the Atlantic have been answer. On the other hand, the question concerning the variations of Caribbean sea level pressure has only produced more questions while answering but a few.

The hurricane pressure relationship in the Atlantic seems to be a result of the interaction of the surface pressure and the upper air environment. There is a strong indication that higher pressure conditions result in drier mid-levels and greater subsidence. This affects "I think by radiational processes" the upper level winds on a seasonal time scale. The result of higher pressure seems to affect hurricane activity through two detrimental influences from the environment 1) drier mid-levels and 2) stronger tropospheric shear. This shear is the direct result of a more robust TUTT during years experiencing higher than normal pressures in the Caribbean.

The variation of summertime Caribbean pressure seems to be somewhat controlled by 1) an east–west decadal-scale "wobble" between the Caribbean and South central Asia and 2) a continuation of the preceding winter Atlantic subtropical high conditions. The existence of such a "wobble" suggests that the climate variations which have occured in the North Atlantic could have had a direct impact on decadal scale climate change in South Central and Southeast Asia and visa versa. Furthermore, the combination of the wintertime conditions in South Central Asia and the center of the Atlantic Subtropical high appear to have potential as predictors of summertime Caribbean pressure anomalies. The wintertime conditions associated with the subtropical ridge seem an important aspect of seasonal forecasting. The knowledge of the November conditions of this ridge are very useful in determining

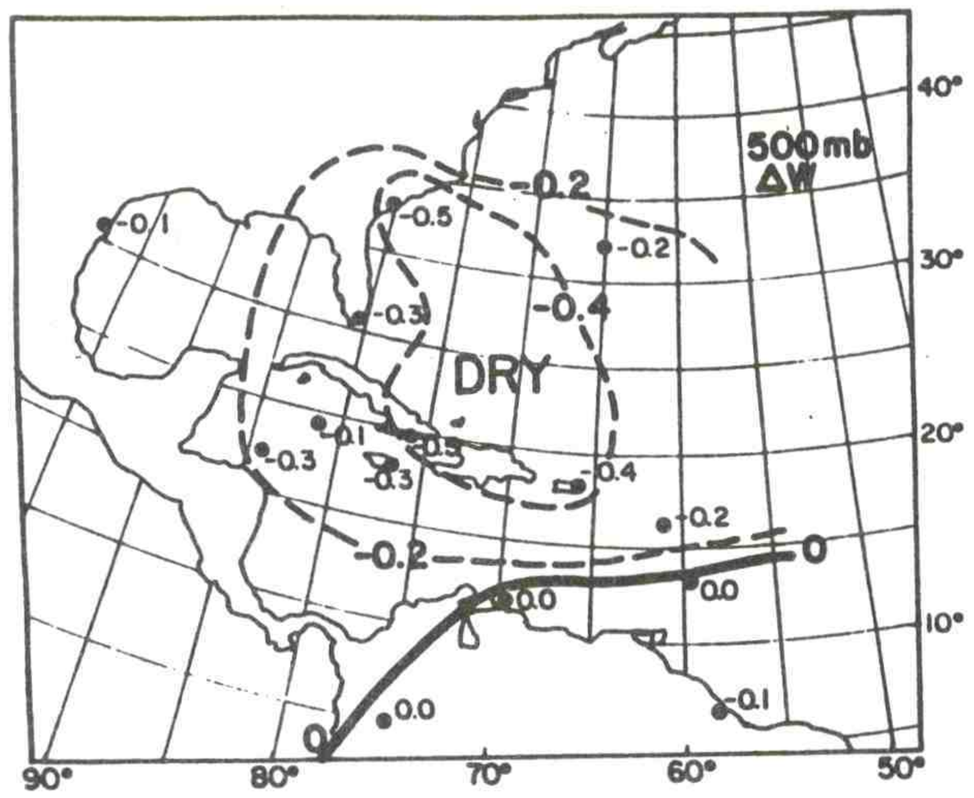

Figure 1: Composite differences of 500 mb mixing ratio obtained from the ten highest pressure minus the ten lowest pressure years in the Caribbean during the months July through September.

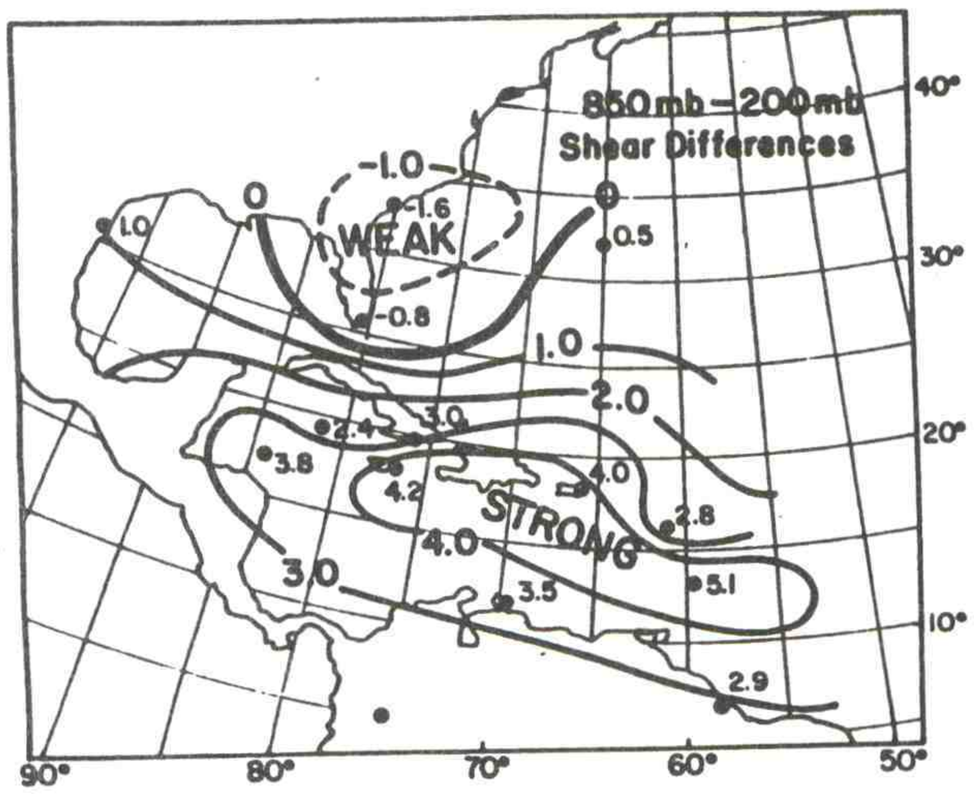

Figure 2: Same as Figure 1 except for the 850 mb to 200 mb vertical wind shear.

the upcoming summertime hurricane activity as well as the March ridge conditions. The March ridge conditions seem useful for not only hurricane activity applications but could be applied to pressure and rainfall predictions which are independent of a hurricane related forecast.

It appears that The Atlantic climate variations are related to not only changes of the North Atlantic sea surface temperatures but to Eastern Hemisphere Parameters. It is this researchers opinion that much of the SST variations on a seasonal basis can be foretold by the monitoring of the strength of the subtropical ridge in the Atlantic ocean through the winter and into the spring and that decadal forecasting of Atlantic Climate change will be possible in the near future. However, many questions remain. This is a very active and interesting area of research.

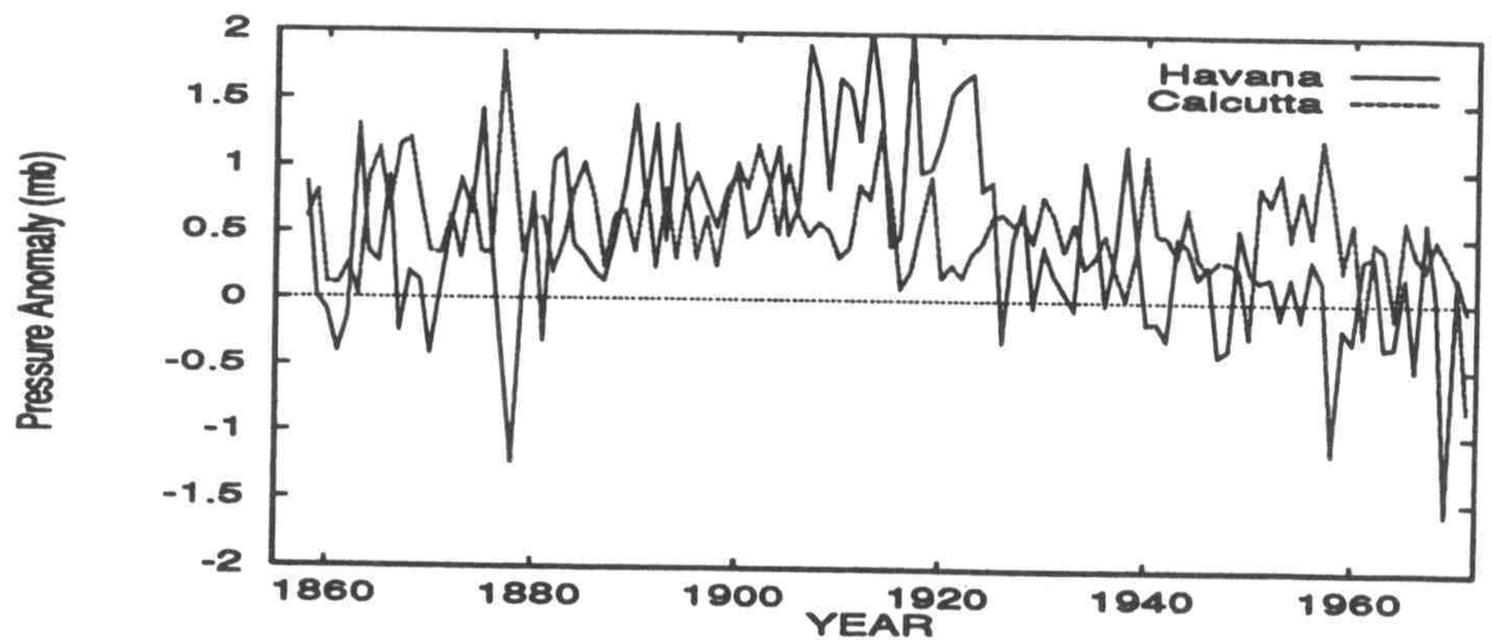

Figure 3: Time series of the annual mean pressure anomaly at Havana and Calcutta.

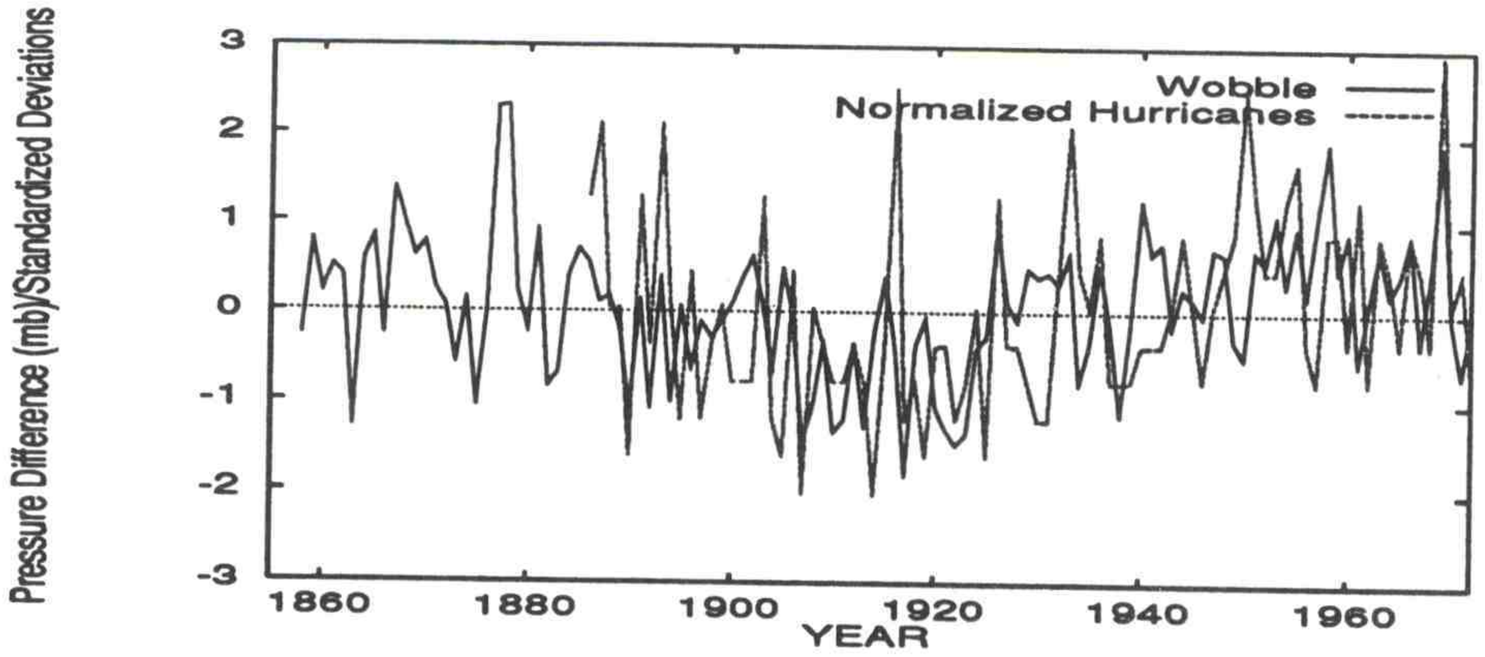

Figure 4: Time series of the "wobble", expressed as the annual Calcutta minus Havana pressure anomaly difference, along with the normalized Atlantic hurricane activity.

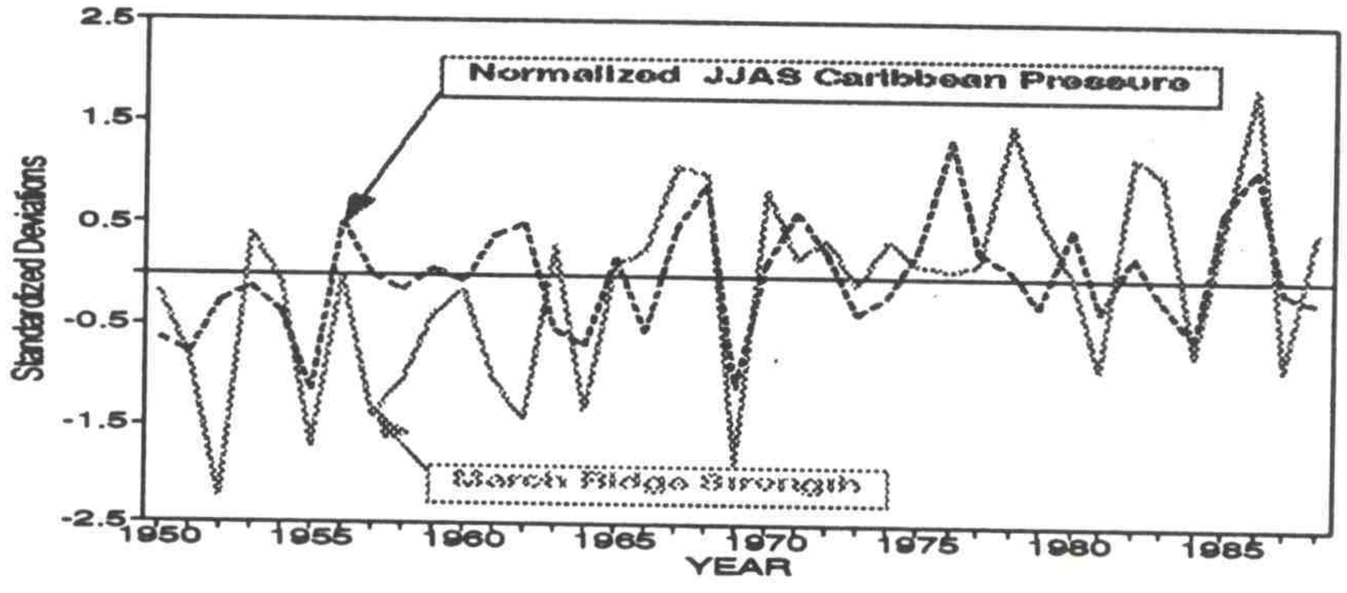

Figure 5: Time series of the normalized strength of the March Atlantic subtropical ridge located in the 20°W to 30°W longitude belt along with a index of normalized Caribbean June through September sea level pressure.

Effects of Various Processing Methods Applied to Ship-Based Surface and Profiler Winds during TOGA COARE

Leslie M. Hartten
Cooperative Institute for Research in Environmental Sciences/NOAA Aeronomy Lab
University of Colorado, Campus Box 216
Boulder CO 80309-0216

1. COARE Integrated Sounding Systems

Integrated Sounding Systems (ISSs) were operated at six locations during TOGA COARE (the Tropical Ocean-Global Atmosphere Coupled Ocean-Atmosphere Response Experiment; Intensive Observing Period (IOP) November 1992 - February 1993). Four were on islands, while two were on the Chinese ships R/V Kexue #1 (RV1) and Shiyan #3 (RV3). Each ISS consisted of an Omega balloon sounding system, a 915 MHz Doppler wind profiler, a Radio Acoustic Sounding System (RASS), and a surface observing station (Parsons et al. 1994). Ship position, speed, and heading information were provided by a Global Positioning System (GPS) receiver, while the direction of the ship's bow was determined by a magnetometer.

Post-processing of the Omega sounding and surface data was handled by NCAR's Atmospheric Technology Division (ATD), while the profiler and RASS data were post-processed by NOAA's Aeronomy Lab (AL) (Miller and Riddle 1994). In the course of this post-processing it became apparent that the magnetometers aboard the two ships had never been calibrated and that the precision of the GPS device was such that unreasonably large 1-minute ship speeds could be recorded. The two processing centers dealt with these facts in two different but reasonable manners (Miller and Riddle 1994; Riddle et al. 1995). As a result, however, intercomparisons between the shipboard low-level omegasonde winds (which are dependent on the surface winds) and the profiler winds are not straightforward (Riddle et al. 1995); neither are attempts to diagnose boundary-layer structure or large-scale profiles of dynamical quantities using both the shipboard surface and profiler winds.

2. Alternate Data Processing

A second set of surface winds has been derived at the AL using the original ship-relative winds and the same methods applied to the shipboard profiler winds. The magnetometer readings from RV3 and RV1 were corrected for apparent biases of 12° and 22°, respectively, before the 1-minute ship-relative wind components were converted into $\vec{V} = (u,v)$. Vector ship motion, computed from cleaned GPS data, was subtracted from that vector wind if the ship speed was greater than 1.0 m s^{-1}. Figures 1 and 2 show timeseries of daily mean wind speeds and directions from RV3, with error bars showing ± 1 standard deviation for each day. The IOP means and standard deviations of the daily-mean values, together with the square root of the IOP-mean variance (root mean variance), are to the right of the plots. The daily standard deviation of the wind direction was computed by summing the squares of the differences, on a 360° dial, between mean and individual directions. The top panel shows the AL-processed winds, while the second panel shows daily means computed from all the original ATD-processed winds which had speeds < 100.0 m s^{-1}. The third panel shows daily means computed from all ATD-processed winds within 5σ of μ, where μ is the IOP-mean and σ the root mean variance from the 2nd panel. The bottom panel shows the differences between the AL-processed and the filtered ATD-processed winds.

3. Results

Applying a 5σ filter to the original ATD-processed winds decreases the speed variance on most days and also decreases the root mean variance over the IOP at both RV3 and RV1 (not shown). However, it does not alter the means or variances of the direction. The AL-processed wind speeds at RV3 and RV1 are similar to the filtered ATD-processed speeds, and the root mean variance at RV3 is smaller. The daily-mean AL-processed wind directions differ from the filtered ATD-processed directions in an irregular manner. The median differences over the IOP, 5° at RV3 and 17° at RV1, are in the correct sense but somewhat smaller than the magnetometer corrections (12° and 22°) applied in the AL method. Timeseries of daily-mean wind speeds and directions at the four land ISS sites (not shown) indicate that the character of the AL-processed ship winds is similar to that of the land stations. The winds over land show signs of frictional slowing and turning, in the IOP-mean, relative to the ship winds. Daily variances at Manus and Kavieng are relatively large; this could be related to the large daily variability of lower-

tropospheric winds at those stations during the IOP (Gutzler and Hartten 1995).

Half-hourly vector-averaged winds have been computed from the 1-minute surface data. Variance-conserving plots of the power spectral density of these surface zonal winds have been constructed for all six ISS sites (not shown). For the two ships, spectra from both the AL and filtered ATD data were constructed. The "filtered ATD" spectrum at RV3 is much whiter than the AL spectrum, consistent with the sense of the plots in Figures 1 and 2. The surface spectra have also been compared to the power spectra of the zonal wind at ~300 m computed from timeseries of half-hourly profiler data. Over the land stations, variances are much higher and the spectra much whiter at ~300 m than at the surface; the differences are smaller at the ship stations. Some of the differences over land could be due to missing profiler data; ship-based profiler and surface observations cover almost identical times, while the land-based profiler data record contains gaps not present in the surface data record. The differences at all stations could reflect the sampling of the variety of turbulent scales prevalent at the two altitudes. Results for meridional winds are similar.

4. Combination of Surface and Profiler ISS Data

Now that a set of ship-based ISS surface winds processed in the same manner as the profiler winds has been developed, work is underway to "merge" all the ISS surface and profiler winds. The plans for this project are as follows. Estimates of boundary-layer depth (z_i) have been made from peaks in the half-hourly range-corrected signal-to-noise ration measured by the profilers (Angevine et al. 1994). Variations in z_i are often visible in the range 0.2 to 1.5 km, as are enhanced reflectivities of undetermined origin at higher altitudes. The estimates of z_i at all 6 stations over the entire IOP indicate that 0.5 km is a reasonable first guess of mean boundary-layer depth; this implies a mean surface-layer depth of 50 m. By assuming that the roughness length $z_0 = 0.01$ m and that both u and v vary logarithmically with height in the surface layer and linearly above that, intermediate-level winds have been constructed. A second merged data set has been created; it has winds at the same intermediate heights, but they are obtained by linear interpolation of each component between the surface and the lowest profiler value. These two data sets are being examined and will be used for high-resolution studies of, for example, the large-scale divergence over the western equatorial Pacific.

Acknowledgments

This research was supported by the US TOGA Project Office through a grant to the NOAA Aeronomy Laboratory. Thanks to Paul Johnston, Tony Riddle, and John Wilson of the Tropical Dynamics and Climate group at the Aeronomy Lab for discussions regarding the 915-MHz profiler data, to Erik Miller and Dave Parsons of NCAR/ATD for information regarding the original surface winds, to Wayne Angevine for comments on determining boundary-layer depth from profiler measurements, and to Dave Gutzler for helpful discussions regarding the research presented.

References

Angevine, W.M., A.B. White, and S.K. Avery, 1994: Boundary-layer depth and entrainment zone characterization with a boundary-layer profiler. *Bound.-Layer Meteor.*, **68**, 375-385.

Gutzler, D.S. and L.M. Hartten, 1995: Daily variability of lower tropospheric winds over the tropical western Pacific. *J. Geophys. Res.*, **100**, 22999-23008.

Miller, E.R. and A.C. Riddle, 1994: TOGA COARE Integrated Sounding Station Data Report - Volume IA Revised Edition, 89 pp.

Parsons, D., W. Dabberdt, H. Cole, T. Hock, C. Martin, A.-L. Barrett, E. Miller, M. Spowart, M. Howard, W. Ecklund, D. Carter, K. Gage, and J. Wilson, 1994: The Integrated Sounding System: Description and Preliminary Observations from TOGA COARE. *Bull. Amer. Meteor. Soc.*, **75**, 553-567.

Riddle, A.C., W.M. Angevine, W.L. Ecklund, E.R. Miller, D.B. Parsons, D.A. Carter, and K.S. Gage, 1995: In situ and remotely sensed horizontal winds and temperature intercomparisons obtained using Integrated Sounding Systems during TOGA COARE. *Contributions of Atmospheric Physics*, in press.

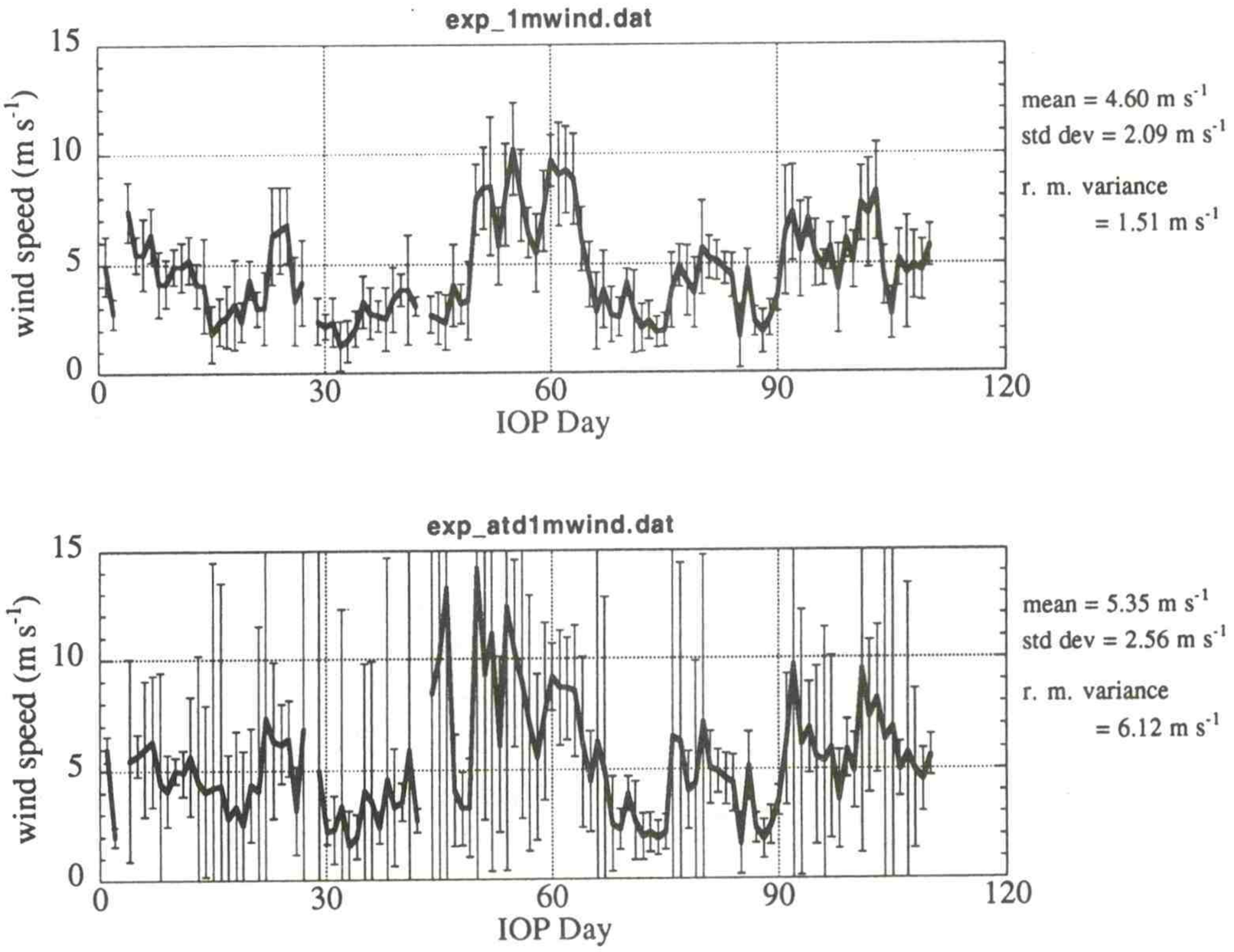

FIGURE 1. Daily means and standard deviations of surface wind speeds at R/V Shiyan #3 (RV3) during the IOP. Statistics are presented to the right of the plots. a) AL winds, b) ATD winds, c) filtered ATD winds, and d) the difference between AL and filtered ATD winds. See text for details of processing methods.

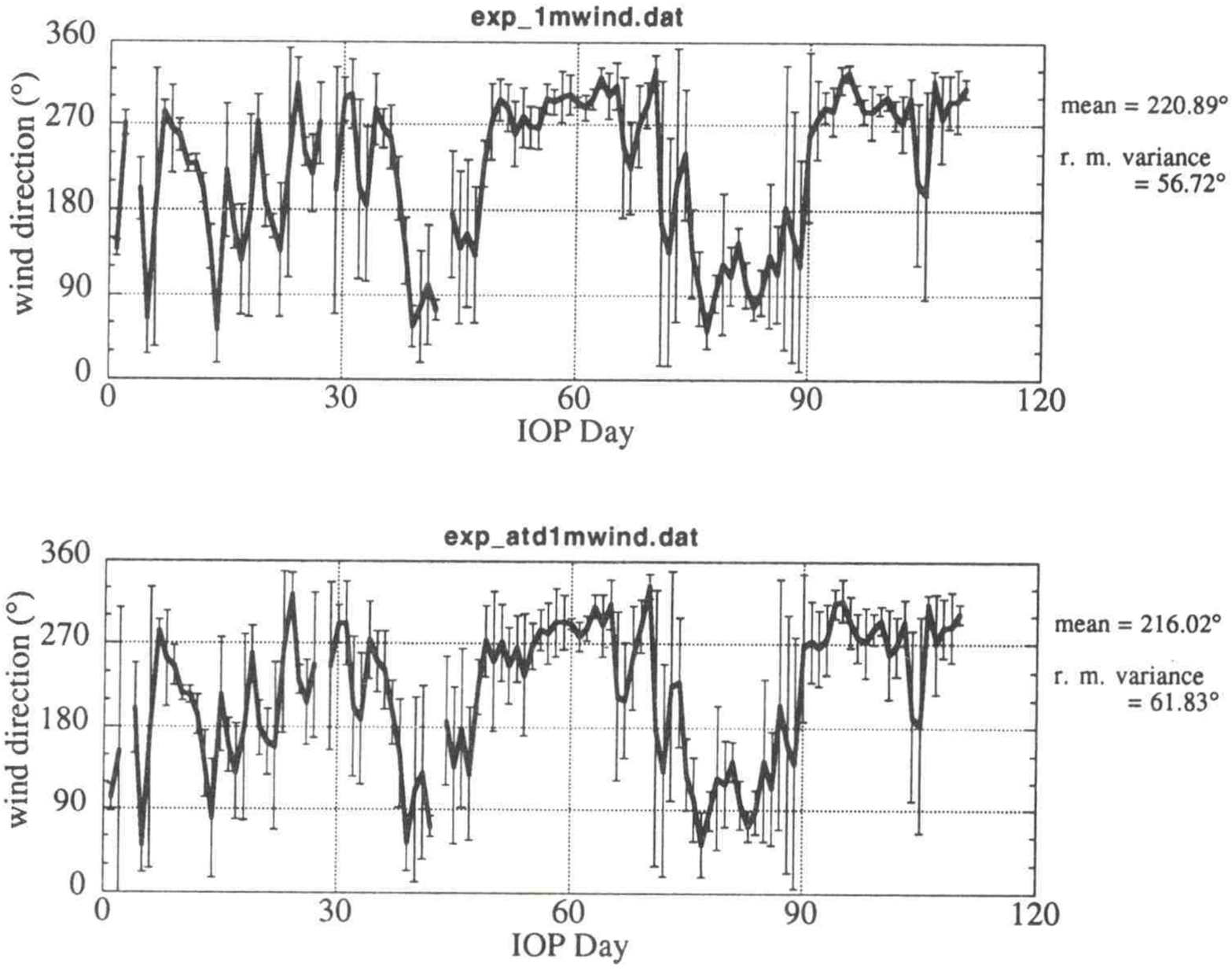

FIGURE 2. Daily means and standard deviations of surface wind directions at R/V Shiyan #3 (RV3) during the IOP. Statistics are presented to the right of the plots. a) AL winds, b) ATD winds, c) filtered ATD winds, and d) the difference between AL and filtered ATD winds. See text for details of processing methods.

ON THE GEOGRAPHICAL DISTRIBUTION OF FORECAST SKILL IN 500 HPA HEIGHT IN THE 6-10 DAY RANGE FOR NH WINTER

Jianfu Pan
(Scientific Management and Applied Research Technologies, Inc. / Climate Prediction Center, NCEP/NWS/NOAA)

Huug van den Dool
(Climate Prediction Center, NCEP/NWS/NOAA)

ABSTRACT

Prediction of low frequency variability in the Northern Hemisphere winter circulation has been assessed with the most recent 7.5 years of 10-day operational forecasts from NCEP's (the National Center for Environmental Prediction) MRF (Medium-Range Forecast) model. This study is based on the daily dataset of 500 hPa heights and for 6-10 day mean forecast.

By analyzing the variability in forecast skill, we have found that the low frequencies are a major contributor to the skill at the extended range of 6-10 days. A geographical distribution of forecast skill shows that the regions of higher skill are broadly consistent with the areas associated with low frequency teleconnection patterns described in Wallace and Gutzler (1981). In particular, most of the PNA region is found to be among the most skillful.

We have explicitly evaluated the model performance on the low frequencies on time scales 7.5-26 days and 30-120 days. Coherence at these scales are estimated between the forecast and analysis anomalies. Results show that large coherence is found in the central North Pacific, eastern North America extending to the eastern Atlantic and some areas in the Eurasian region.

The influence of systematic errors in the low frequency forecast are discussed. Large systematic errors are believed to have a strong negative impact on the forecast skill. These errors could be a manifestation of the model deficiencies in forecasting some of the low frequency regimes.

The geographical distribution of skills

It is common that forecast skills of a model vary significantly from one case to another. In most cases, a medium range forecast is practically useful only when its skill falls into the high phase of the variation. We argue that the skill variability is closely related to the low frequency variations in the circulation.

Fig. 1 shows the geographical distribution of skill of 6-10-day (D+8) mean forecast. The skill is calculated as the time correlation between forecast and analysis anomalies of 500 hPa heights. While a full explanation may be difficult to give, we note the following. High skills (AC > 0.55) are found over the climatological areas of strong low frequency variability, especially over the PNA region.

Low skills are observed over the west coastal area of the North America. Another low skill area is found over southeast Asia, where large mountains may cause the problem. Skills over Europe are quite low as well.

Low frequency forecast in the model

As one method to assess the model performance on forecasting the low frequencies, we estimated in the frequency domain the coherence between the forecast and analysis anomalies.

Fig. 2 presents the coherence at time scales of 30-120 days. The areas of larger coherence are representative of high skill. The distribution is very similar to the one of the skill, suggesting that the 30-120 day time scale is a major contributor to the overall forecast skill in the 6-10 day range.

Fig. 3 is the coherence distribution of frequencies of 7.5-24 days, which cover regimes such as blocking. Large coherence is found over the east coast of Asia, eastern North America and high latitudes of the Eurasian region. We speculate that the high coherence partly reflect the blocking regimes. In general, however, the model has difficulties to forecast a blocking event, particularly when the blocking occurs a few days into the forecast.

Bias in the low frequency predictability

We have demonstrated that the low frequencies are critical to the success of D+8 forecast. In practice, however, the low frequency predictability is limited. One of the problems is the large bias in the forecasts.

Fig. 4 shows the bias in the D+8 forecasts of 500 hPa height. The model has negative biases over most of the northern hemisphere with large negative centers from northern Japan to Alaska and over the high latitudes of western Europe. These large biases can easily contaminate the low frequency signals in the area. Specifically, the negative biases will affect the regimes of positive anomalies. We tested this by making a composite at (15 °E, 55 °N), a location with large negative biases. The positive/negative composites are made out of the cases in which the magnitudes of the observed positive/negative anomalies are larger than one standard deviation. As shown in **Fig. 5**, the model has difficulty forecasting positive anomalies at (15 °E, 55 °N) with associated difficulties upstream. By contrast the biases in the negative composite are much smaller. The results do not exclude that the bias is caused by the model's inability to forecast certain regimes such as the one discussed here.

Reference

Wallace, J. M. and D. S. Gutzler, 1981: Teleconnections in the geopotential height field during the northern hemisphere winter. *Mon. Wea. Rev.*, **109**, 784-812.

Fig.1. D+8 anomaly correlation calculated based on 7.5 winters (16 Nov – 15 Mar) from 1 Jan 1988 to 15 Mar 1995.

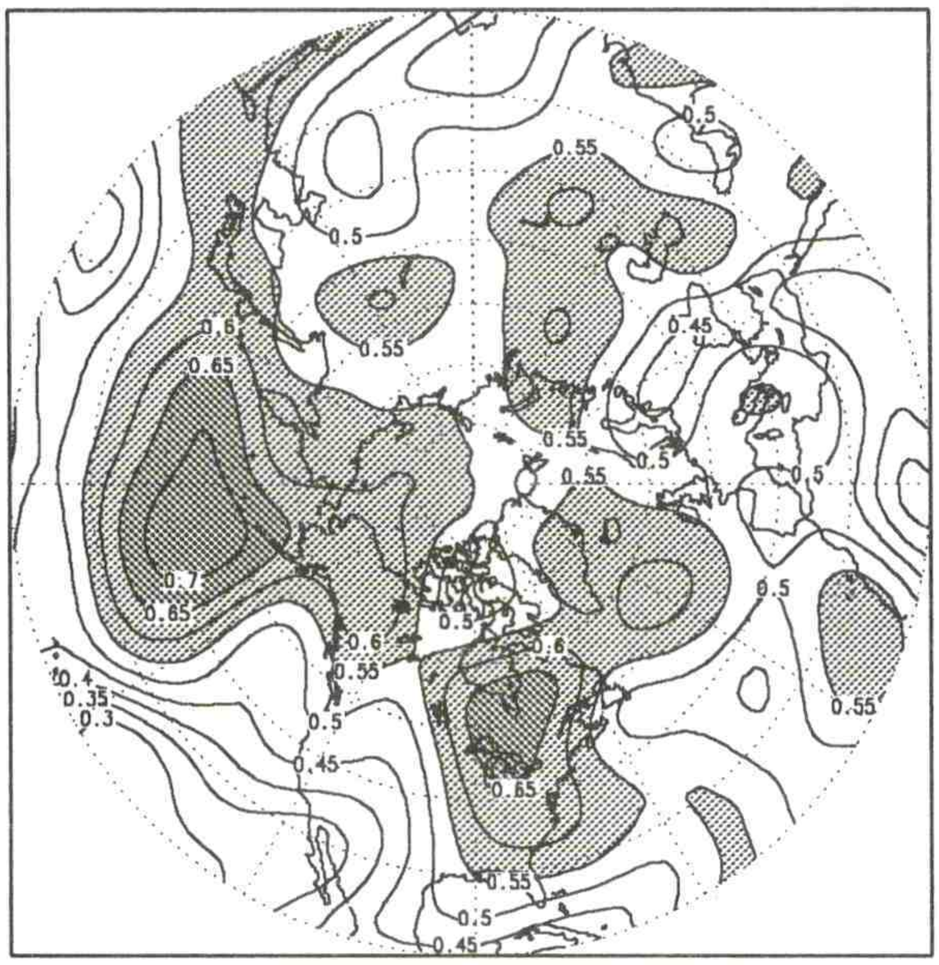

Fig.2. Coherence between D+8 forecast and analysis anomalies at scales of 30–120 days.

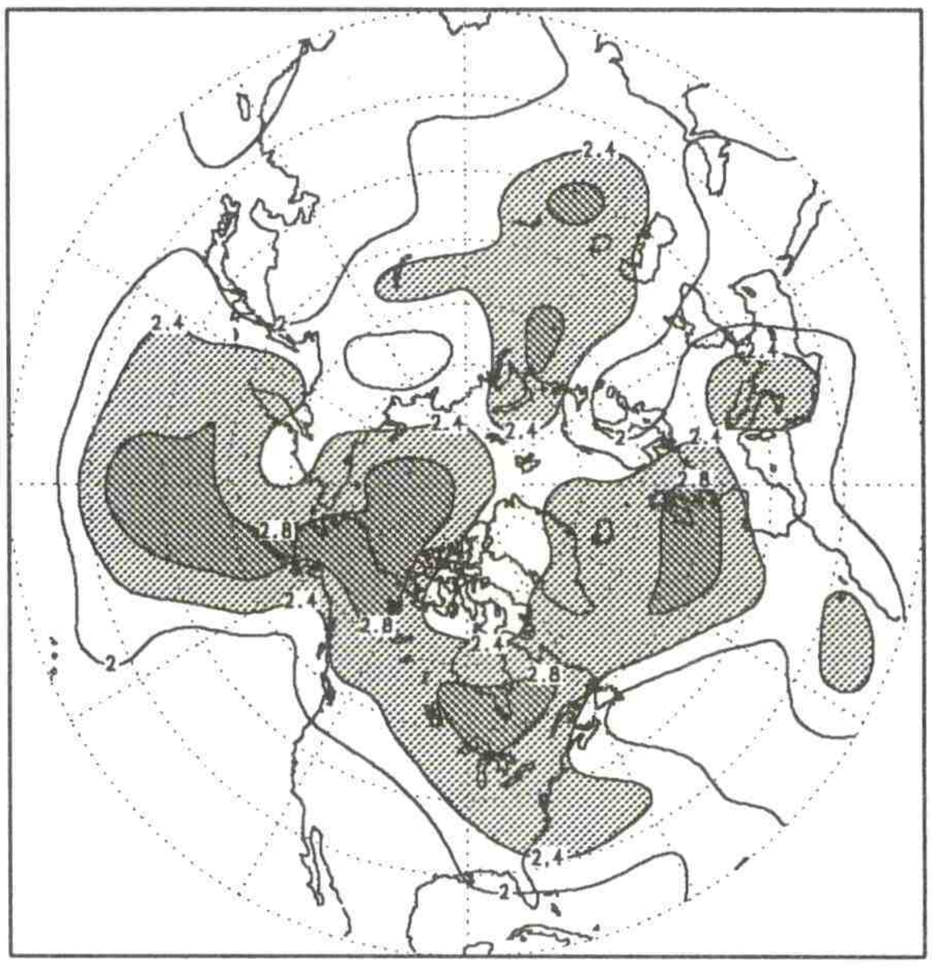

Fig.3. Coherence between D+8 forecast and analysis anomalies at scales of 7.5–24 days.

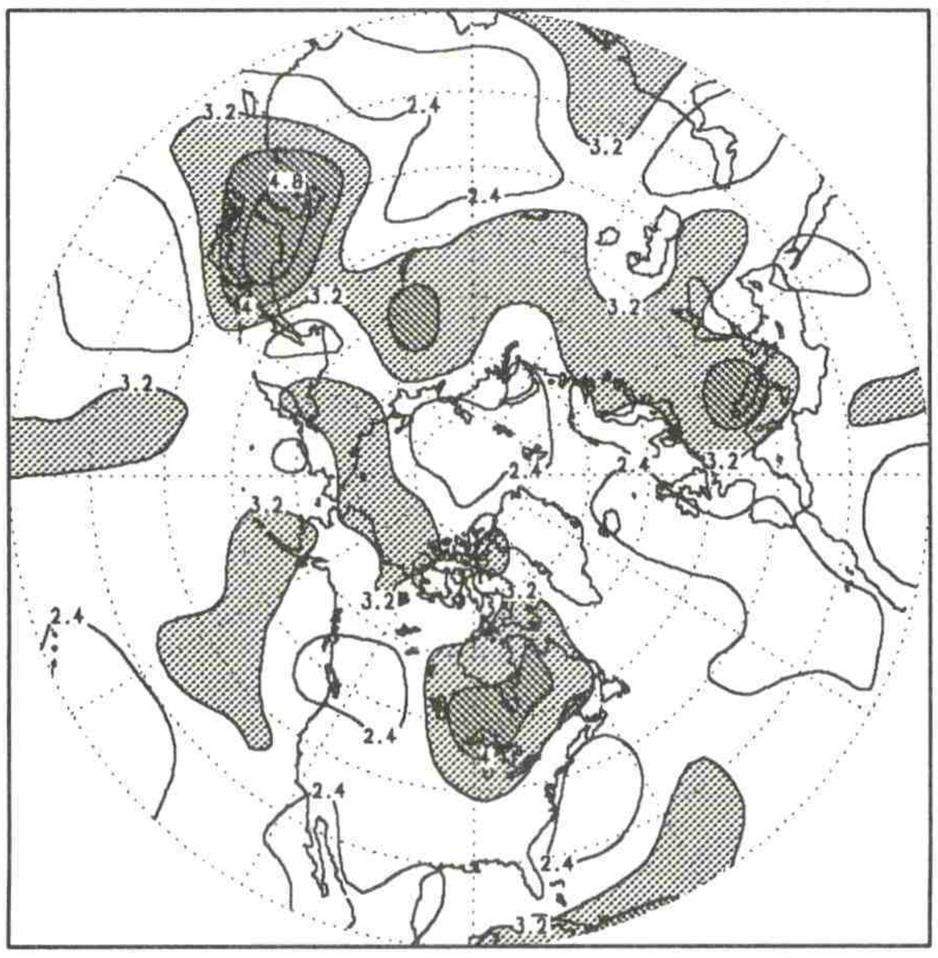

Fig. 4. D+8 systematic error calculated from the 7.5 winters

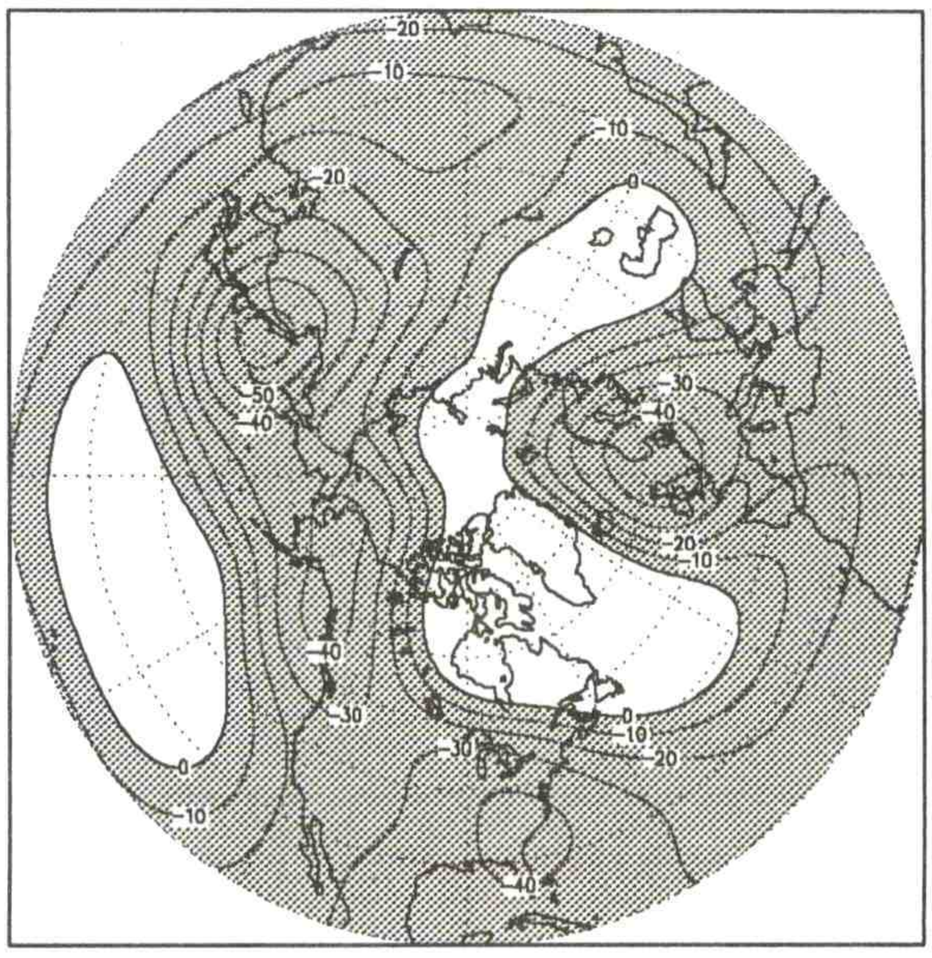

Fig. 5. Anomaly composite map (anomaly magnitudes larger than the standard deviation) over Europe at (15 °E, 55 °N). (Left: positive anomalies; right: negative anomalies)

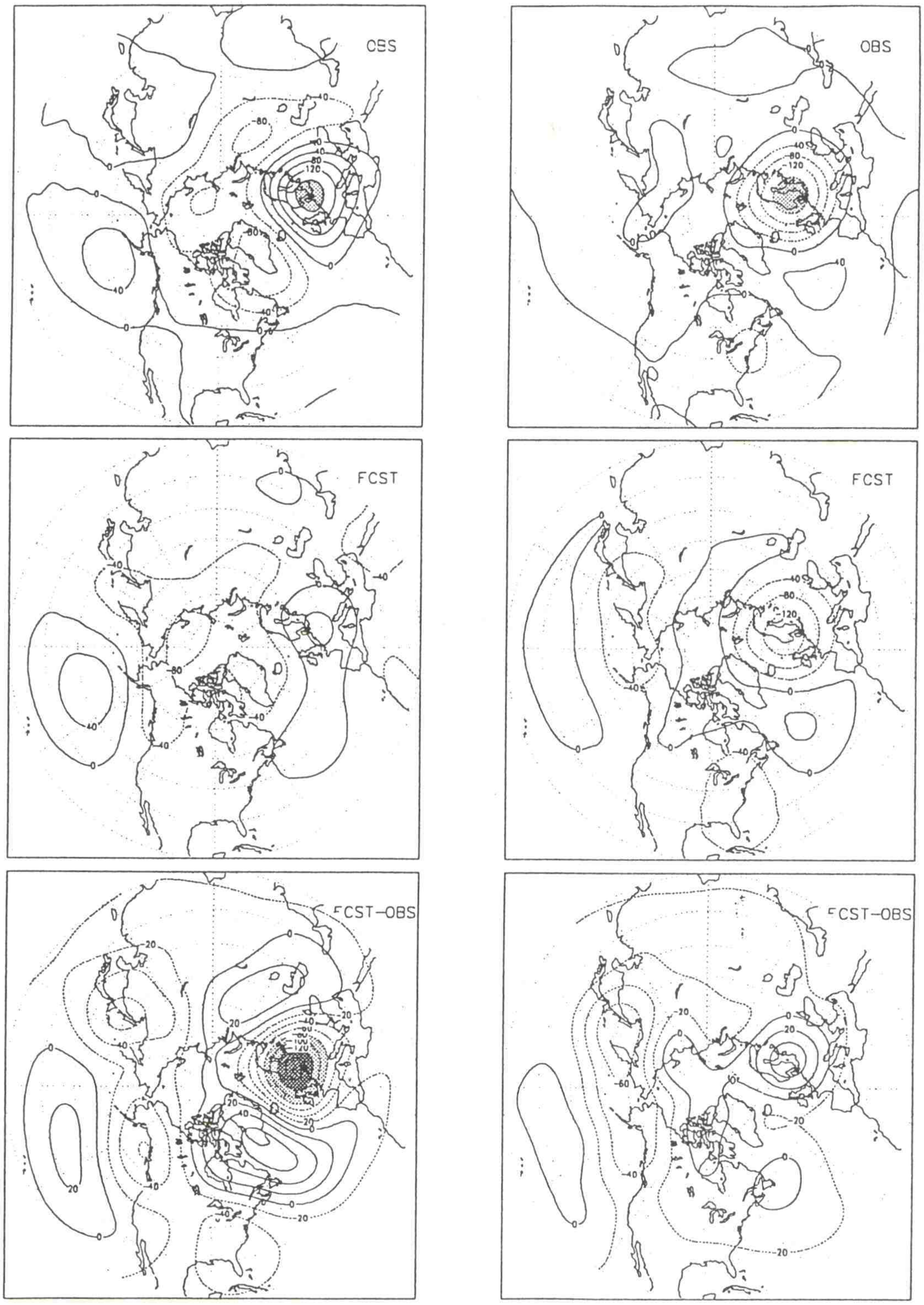

Tropical Cyclone Activity as a Diagnostic Climate Indicator

J. D. Sheaffer
Department of Atmospheric Science
Colorado State University
Fort Collins, CO. 80523

Extensive prior work by W. M. Gray and collaborators has emphasized using global climate data to understand variable modes of tropical cyclone (TC) activity. Newer results suggest that there is sufficient basin-to-basin consistency in most TC - environment associations to recommend variations in TC activity as a basic diagnostic indicator for inferring subtile short and longer-term climate variations which might otherwise pass unnoticed. A compact (data) disc (CD) titled "Global Tropical / Extra-tropical Cyclone Climatic Atlas" was given to W.M. Gray and his research group by M. J. Changery of NOAA, for review and evaluation. In the process of making our review, we found this data disc and self-contained graphics package to be very helpful for making simple test-of-concept studies on both established and potential new associations linking basic climate variations to trends in TC activity. Related work using this same data disc is presented in the paper by R. Quayle (This Volume).

In the work shown here, this TC data disc was used to broaden and refine several prior studies of variable activity in the tropical Atlantic (by Gray) and to extend some of the work to the NW, NE and SW Pacific basins. New results reveal surprisingly strong and diverse variations in the spatial distribution of tropical cyclone tracks in these basins. Notable anomalies of regional ocean (SST) and atmospheric climatic indices appear in composited data for seasons with peculiar trends in TC activity. Similarly, distinct trends in TC activity appear when TC data are carefully stratified for simple indices of insitu basin wide and more localized SST anomalies as well as regional monsoon intensity and other basic ENSO and QBO indices.

Whereas an extensive portfolio of these figures were presented at the Workshop poster session, only a few of these are presented or described here to illustrate how trends in the incidence, intensity and distribution of tropical cyclones are influenced by the regional climate trends which occur to some degree in all tropical cyclone basins. The analyses were loosely classified into four somewhat overlapping groupings as follows: (1)SSTS and Tropical Cyclones,(2) Recent Multi-Year Trends in Tropical Cyclone Activity,(3) QBO / Monsoons and Tropical Cyclones and (4) ENSO and Tropical Cyclones.

Initially, the monthly incidence of TC activity in the deep tropical Atlantic (South of 20 N and East of 60 W) was used to infer months/seasons with comparatively frequent versus infrequent development of hurricanes in this area; presumably as intensifying storm systems associated with easterly wave circulations from Africa. Ten active and ten inactive years were selected and a mean field of SST difference values computed for the Inactive minus Active years, yielding a SST anomaly pattern similar to the one shown in Fig.1. However, the pattern shown in Fig. 1 is for the June-July periods immediately prior to the active/inactive Aug.-Oct. periods, thereby suggesting a

potential predictive association. The distinct cold anomaly of 0.5C between 10-20 N Latitude, extending westward from the African coast in Fig.1 suggests colder SSTS in this area during less active years and (vice versa) warm anomalies prior to (and during owing to persistence for SST) active hurricane seasons in the deep tropics of the Atlantic. Similarly, an index of mean SST anomalies for the area bounded by 20 to 70 W and 10 t0 20 N was used to select ten TC seasons corresponding to warm and cold SST conditions; As in the prior example, the comparative composite plots of intense hurricane activity (TCs with max. winds greater than 100 kn) shown in Fig.2 are obtained by using an index of SST for the just prior June-July periods, thereby again suggesting some predictive association (note that the years selected as active/inactive only partly overlap with the warm/cool selection). A similar analysis but for the tropical Northwest Pacific (not shown) revealed a much higher incidence (ie., more than three -to-one) of late season (Oct. and Nov.) TCs moving westward across the South China Sea to strike the China-Indochina Coast in the region South an West of Hong Kong when SSTs in the Nino-4 region were comparatively cold (ie., lower versus upper quartile Nino-4 SSTS). These same (cold Nino-4) months also had fewer than one third as many recurving TCs which turned eastward and crossed 170 E north of 30N. Even greater bias occurs in the spatial distribution of genesis points which tended to occur much further east and south during the warm Nino-4 periods.

As noted above, many interesting climate and/or TC differences were observed in association with one another. Some of these include fairly remote, apparently teleconnected difference trends. An example of the latter in Fig.3 shows greatly differing intense Atlantic TC activity linked to specific trends in the distribution of intense convection in the Indonesia-Pacific Warm pool region where the latter is inferred from temperature anomalies in the lower stratosphere at Singapore. Important differences were also observed Interannual and longer term multi-year and decadal climate trends affect tropical cyclone activity around the world. All of the work done here expands on earlier work by Gray (and others) to make a further study of the extent to which basic modes of climactic variability can be identified in seasonal and longer term distributions of tropical cyclones of varying intensity in regions where sufficient data exist to allow meaningful analysis.

Acknowledgements: The work summarized above was supported in part by NSF and NOAA climate research grants.

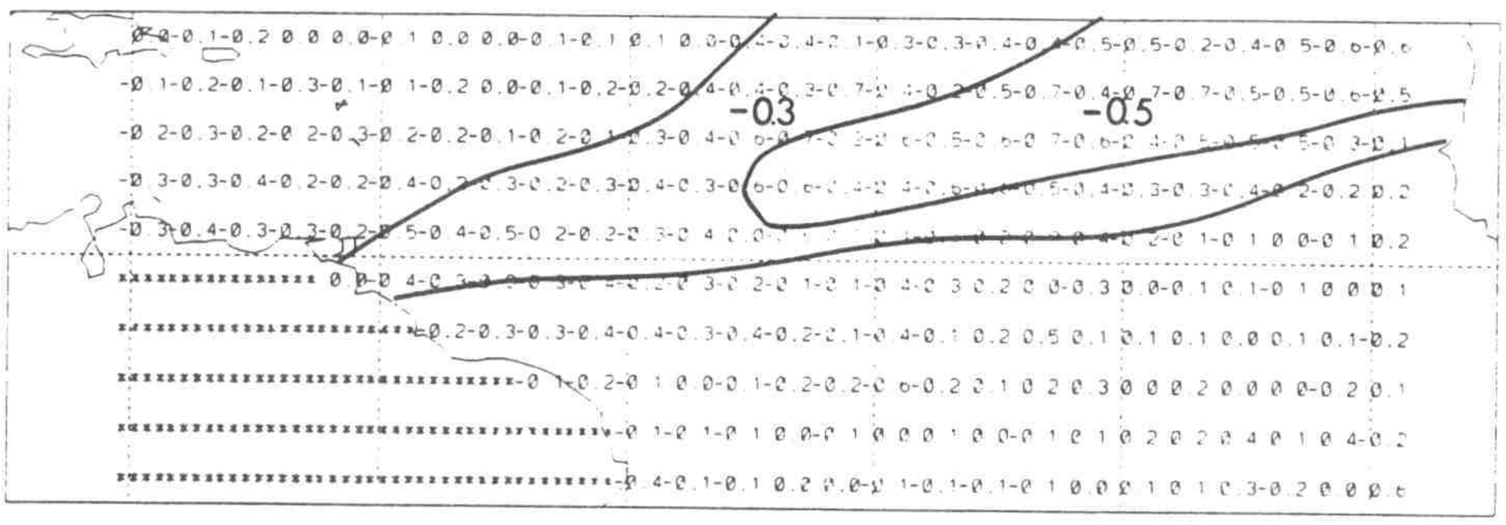

Figure 1: Distribution of mean (COADS) SST anomaly differences obtained as the means during June-Julys prior to ten inactive (minus) and ten active Aug.-Oct. seasons for hurricane development in the tropical Atlantic South of 20N. Temperature contours are at 0.2C intervals.

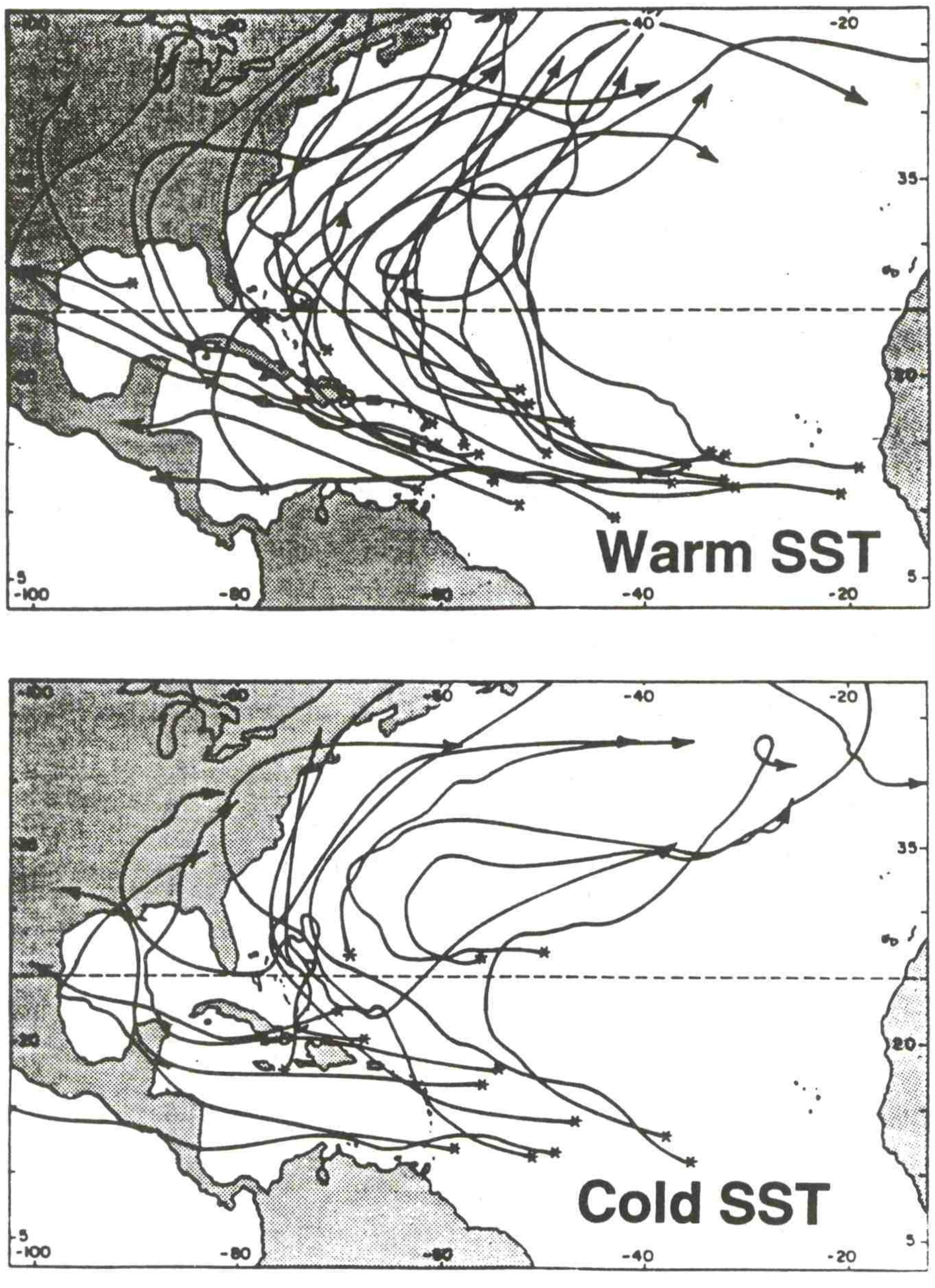

Figure 2: (Top) Distribution of intense hurricanes (Max. winds > 100kn) during ten Aug.-Oct. periods between 1950-1992which were preceded by the ten June-July periods with warmest SSTS in the area bounded by 10-20N, 20-70W. (Bottom) As in the top panel, but for the ten cold June-July SST seasons.

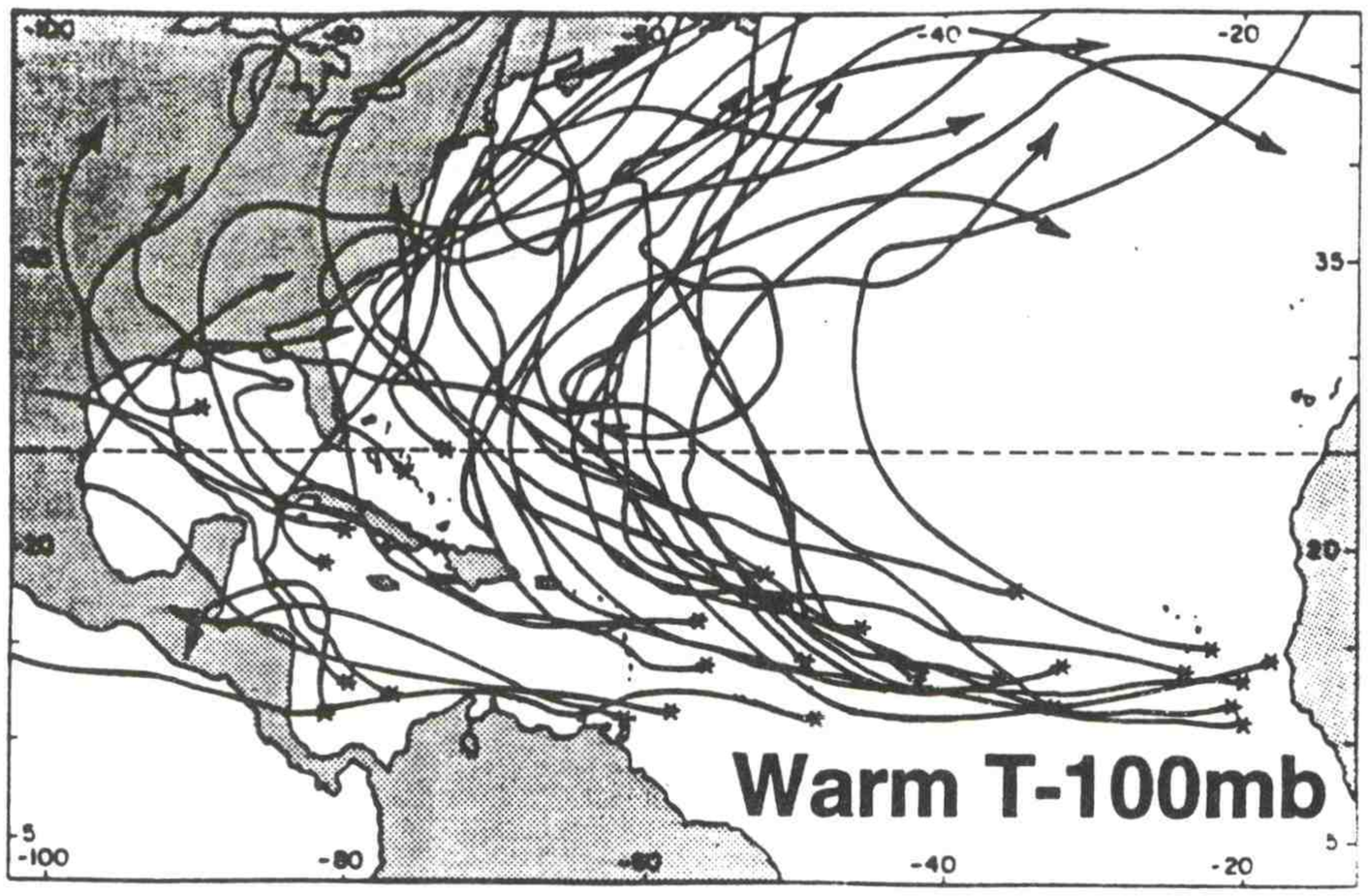

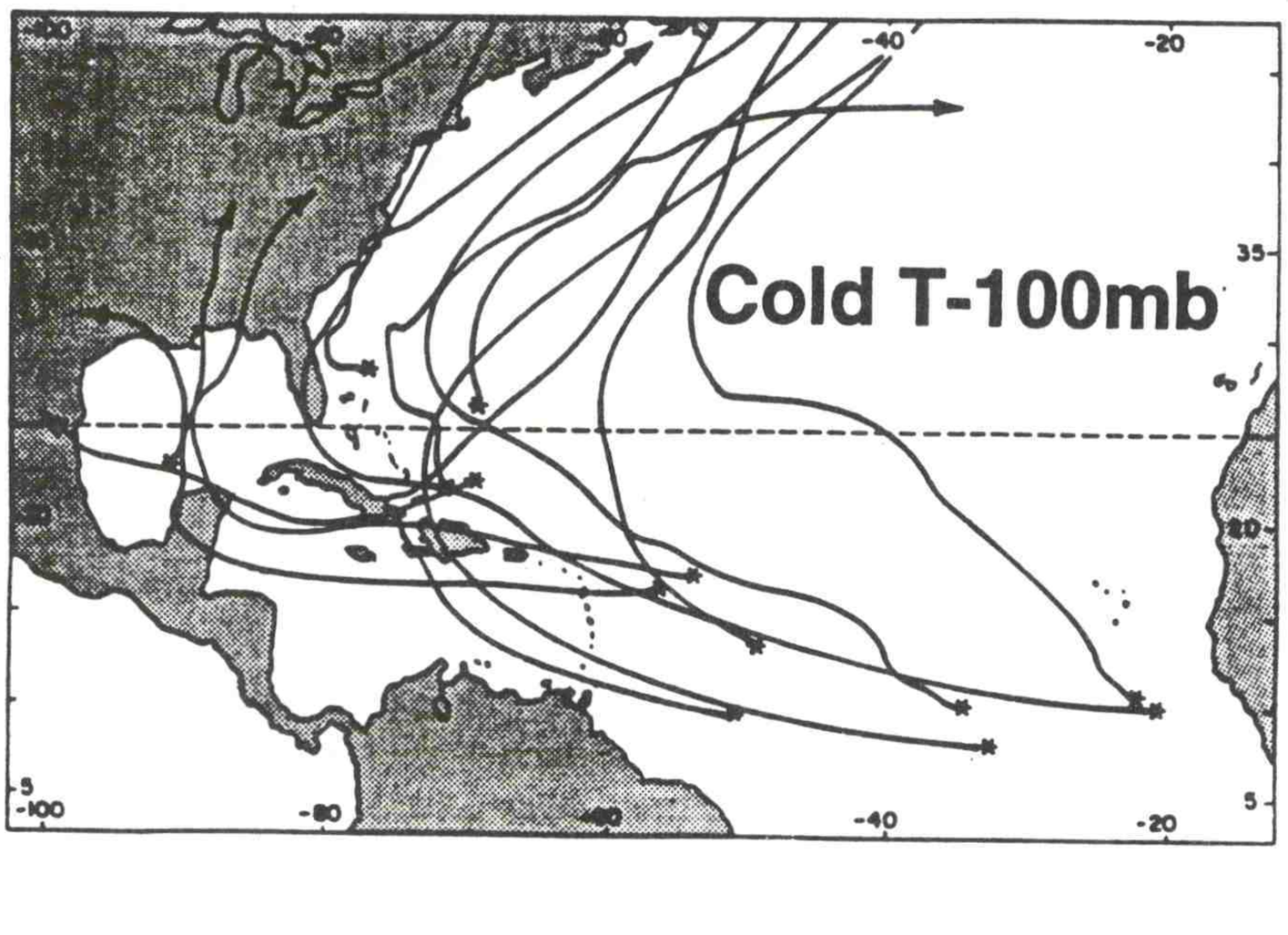

Figure 3: As in Fig.2 but where the Top/Bottom panel is for the ten Aug.-Oct. periods (1957 to 1990) with the warmest/coldest Aug.-Oct. 100 mb temperature values were observed at Singapore.

Temporal and Spatial Variability of the Canadian Polar Trough

John Knox, Amir Shabbar, Walter Skinner, and Kaz Higuchi
Climate Diagnostics Research Group, Atmospheric Environment Service
4905 Dufferin Street, Downsview, Ontario, Canada M3H 5T4

Introduction

Last year it was demonstrated that Canada's east coast experienced a warm winter regime 1951-1960 followed by a cold regime from the early 1970's to the present. This trend, and indeed the interannual variation of winter mean surface temperature, were found to be strongly related to a component of variability in the circulation of the Canadian Polar Trough, similar to, if not identical with the NAO.

The focus in this paper is on the Summer (J,Jy,A,S). The mid-troposphere analyses are based on daily 50kPa data for the 48 years 1946-1993 incl. using a 455-point Lat.-Long. Grid. The surface temperature analyses were derived from Jones et al, 1992, and from the records of Canadian maritime stations.

Definition

By the Canadian Polar Trough (CPT) we mean the large-scale mid-to-upper troposphere cyclonic circulation over eastern North America as shown in standard atlases. The CPT domain is visually enhanced by the eddy component (Z*) which is the departure of Z from the zonal mean [Z], Z*=Z-[Z], as shown in Figures 1(a) and 1(b) for Winter and Summer respectively.

Seasonal Climatological Change of the Eddy Component

Immediately evident is the persistence of the CPT eddy into the warm season, Fig. 1(b). There is a small northward displacement and some attenuation of amplitude of about 4 dams, but this is substantially less than the corresponding seasonal change of its West Pacific Trough (WPT) counterpart, the eddy centre of which has decreased by 15 dams and, though its location is ambiguous, has apparently been displaced eastward some 40 degrees of longitude. Another significant difference between these major troughs of the circum-polar circulation is the meridional orientation of the CPT eddy component compared with the unmistakable E-W orientation of the WPT.

The Baffin Island-West Atlantic Index

Examination of EOF analyses of the 70- and 50-kPa height for the Northern Hemisphere, (Barnston and Livesey, 1987, for all months; Shabbar, 1995 for all months and all seasons; and others) and of teleconnection analyses, (Wallace and Gutzler, 1981, for the winter season; and the atlas by Namias, 1981) strongly suggests that much of the variability of the CPT is accounted for by variations of the north-south anomaly di-pole characteristic of the North Atlantic Oscillation (NAO). A consensus of the above sources indicates that a measure of the sign and intensity of the NAO mode at the mid-troposphere level is given as follows:

WINTER: BWA = 1/2 [Z'(65N,60W) - Z'(30N,60W)]
SUMMER: BWA = 1/2 [Z'(70N,60W) - Z'(45N,50W)]

BWA stands for "Baffin Island-West Atlantic", a designator to emphasize that, for the mid-troposphere, the northern cell is not centred over the North Atlantic Ocean, but close to (actually just east of) Baffin Island. Figure 2(a).

The modification of the index for Summer takes into account the normal northward shift of overall variability during the warm season. The time series of the BWA Index for Summer is shown in Figure 2(b). We now examine the relationship between the BWA di-pole and summer surface temperature anomalies for the eastern Canada coastal region, southwestern Greenland and flanking waters.

Warmest and Coldest Summers, Eastern Canada Coastal Region

The target region for surface temperatures used to select the 5 warmest and 5 coldest summers was originally defined as the area within 45N to 65N and 70W to 40W. This target would provide input from surface data flanking the Labrador Current which has its origin from the Davis Strait. It is known that these waters have cooled during the past 2 decades and the question was whether there has been a preponderance of exceptionally cold summers over the area during that time.

It turned out that the 50kPa composite patterns (not shown) were weakly differentiated, and neither showed evidence of a BWA signal. The reason is that, for summer, the N-S core of the target area along 55W is bisected by the BWA null-point at approximately 55N, Figure 2(a). Consequently, during regimes with a moderate to strong BWA component the surface

temperature and associated 50kPa anomaly over the northern part of the target will be opposite in sign to that over the southern, or, if of the same sign, much reduced in amplitude. In either case the signal will be attenuated. We therefore split the area into two targets, (i) the group of stations N of 55N and (ii) the group to the south, as shown in Figure 3. The dates of the 5 coldest, and 5 warmest summers respectively were obtained for group (i) and the 50kPa composites prepared accordingly. The exercise was repeated using the group (ii) stations.

The results, Table 1, confirmed our hypothesis. The 50-kPa composite Figure 4(a), for the 5 warmest summers at the Northern Stations, featured a strong positive anomaly (4.0 dams) centred very close to the northern pole of the BWA index. The composite for the 5 coldest summers, Figure 4(b) shows a centre of opposite sign but comparable magnitude (-3.0 dams) and located some 5 degrees latitude south of the northern pole.

TABLE 1

	Northern Stations		Southern Stations	
	Warmest	**Coldest**	**Warmest**	**Coldest**
	1957	1972	1967	1986
	1960	1970	1952	1964
	1985	1978	1961	1962
	1948	1983	1960	1963
	1951	1963	1990	1980
Anom. Amp.	4.0dams	-3.0dams	1.8dams	-2.0dams
Location:	70N 60W	65N 60W	45N 50W	43N 65W
BWA Index:	2.3dams	-2.0dams	-0.9dams	0.4dams

For the 6 Southern Stations, the respective composite analyses (not shown) are distinguished by the sign of the anomalous 50-kPa height close to the location of the southern pole of the summer BWA. The positive centre (1.8 dams) for the warm composite is almost coincident with that pole, while the cold composite features a negative centre (-2.0 dams) just south of Nova Scotia.

EOFs of the Summer Surface Temperature over Eastern N. America, the North Atlantic and Western Europe

A PCA of the summer surface temperature was carried out over the domain extending from 20N to 85N and from 100W to 20E. The amplitude of the second EOF, designated EOF-TMP #2, (Figure not shown), correlated strongly (0.80) with the northern component of the BWA Index, but less so with the Index itself (0.56).

EOFs of the Summer (Jun-Sep) 50kPa height over the Northern Hemisphere

EOFs (EOF-Z) were also prepared for the Summer 50kPa height field over the Northern Hemisphere for the 48-year period 1946-1993. The summer BWA is immediately recognizable in both the first and third EOFs, and particularly the latter, Figure 4(c). The correlation between EOF-TMP #2 and EOF-Z #3 is particularly strong, (0.70) in spite of the much larger domain of the latter field.

These PCAs reinforce our confidence in the usefulness of the BWA Index (defined for summer) as a measure of a characteristic mode of the variability of the CPT.

Trends

For the Winter seasons, 1946-1989, there was a downward trend of the BWA Index during the past two decades. This probably indicated a higher incidence of above normal intensity of the CPT in its normal location. This is consistent with a contemporaneous decrease of winter surface temperature over Canada's east coast and flanking waters. There is a similar trend for Spring and Fall and for the Year as a whole.

For Summer, there was a very slight warming trend over land and no perceptible trend over the coastal waters. This is somewhat surprising because, for both groups of surface stations, it is evident from Table 1 that the majority of years for the coldest summers occurred after 1962, and for the warmest summers before.

Concluding Comments

An effective measure of the variability of the Canadian Polar Trough for Summer is the seasonally adjusted BWA Index as defined in this paper. However, to determine the salient features of the CPT 50-kPa circulation associated with ranking warm/cold seasons for eastern Canada the geography of the targeted areas must be taken into account. By so doing the composite charts reveal a strong relationship between surface temperature anomaly and the 50-kPa anomaly as measured at one or the other of the BWA di-poles.

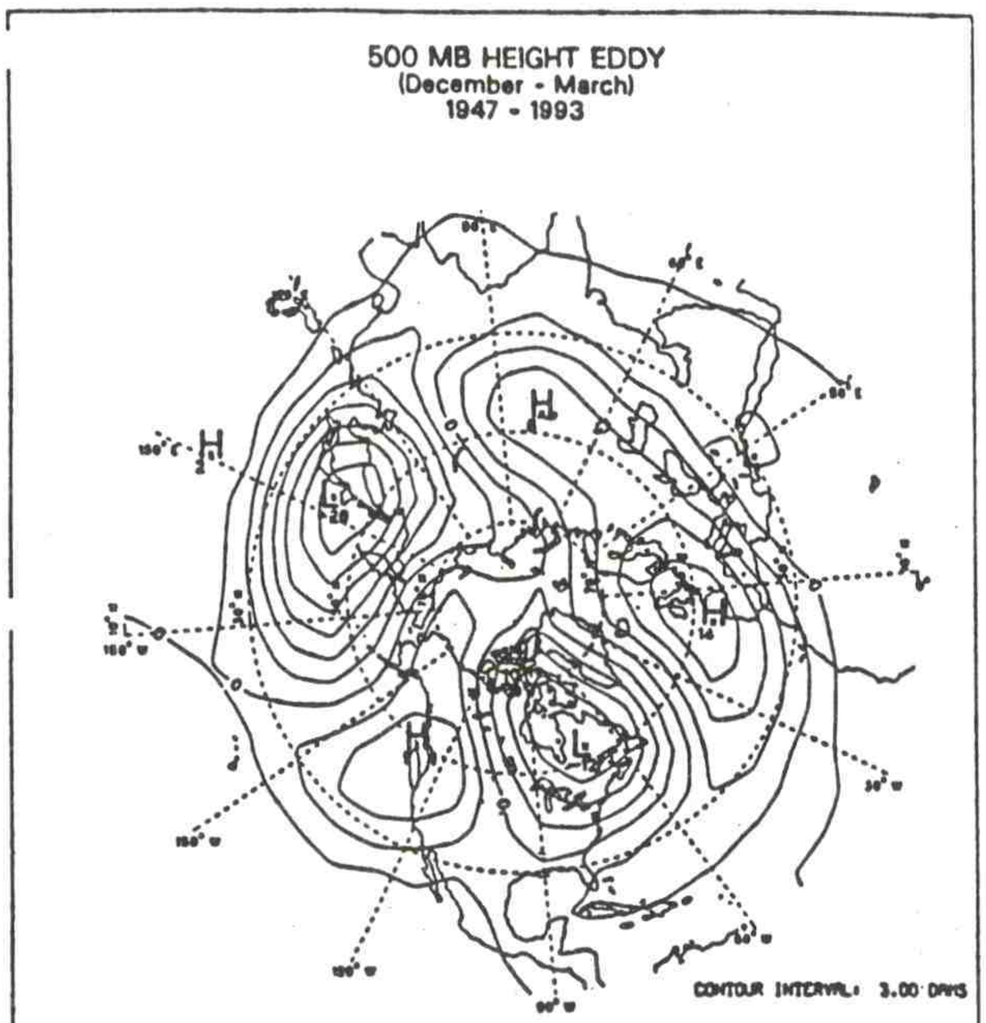

Fig 1(a)

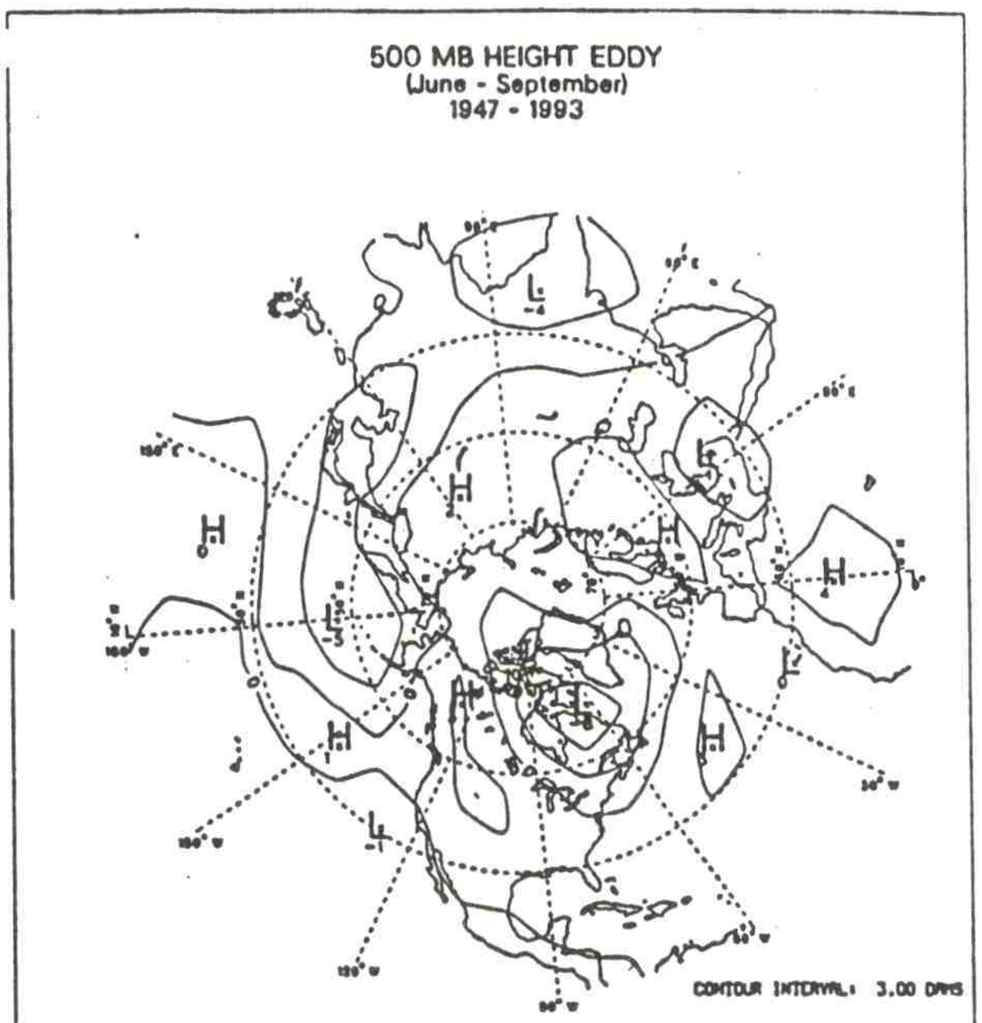

Fig 1(b)

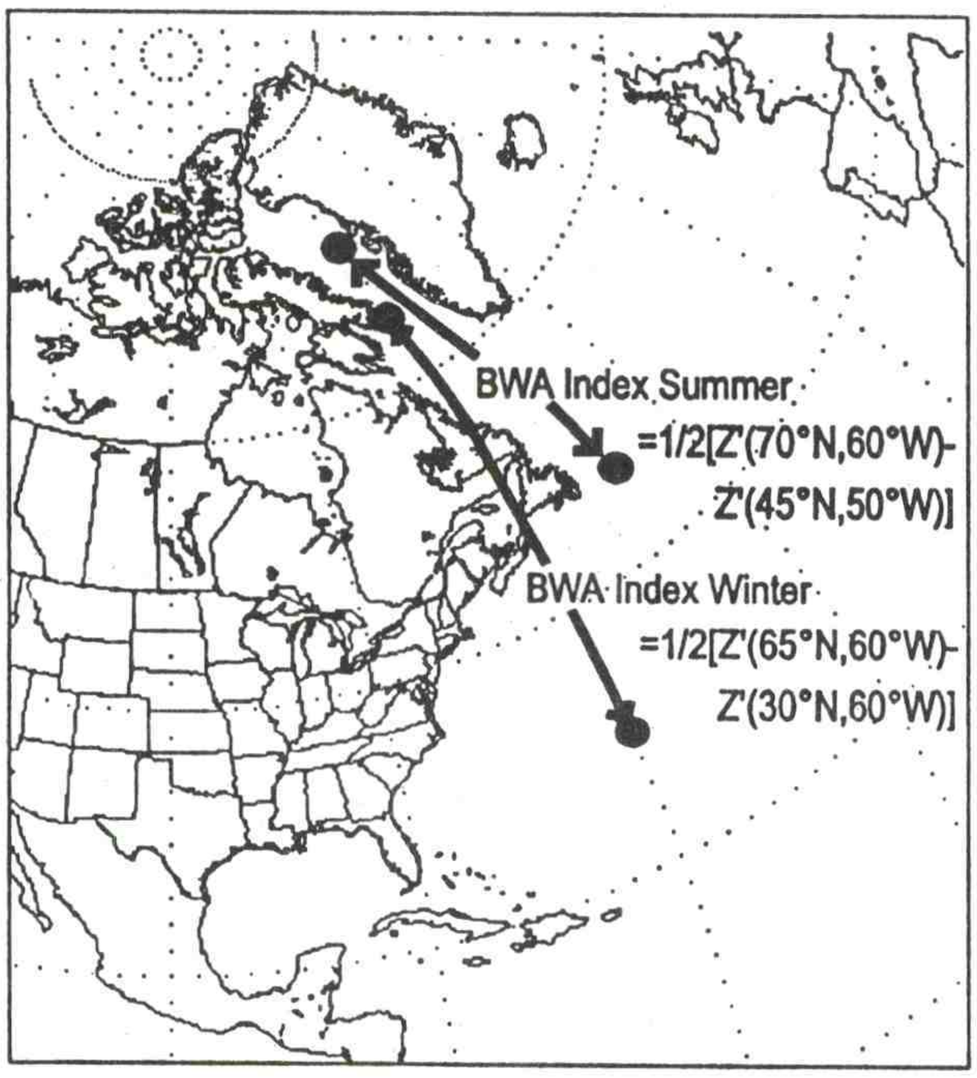

Figure 2(a). The Baffin Island-West Atlantic (BWA) teleconnection in winter (DJFM) and in summer (JJAS).

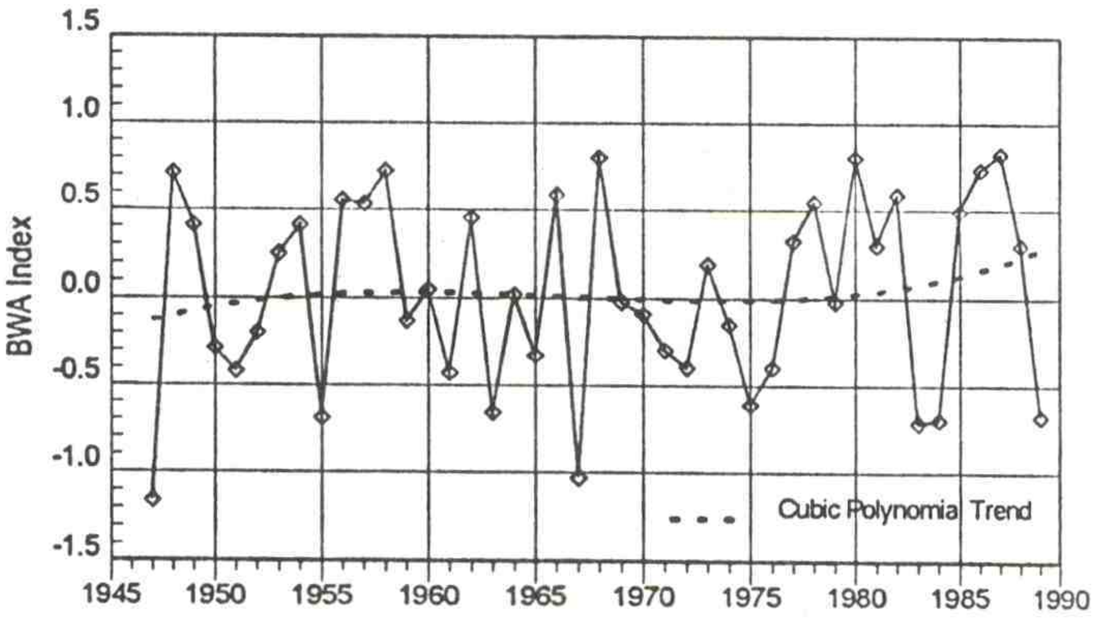

Figure 2(b). Time series of Baffin Island-West Atlantic in summer (JJAS). Index is calculated from 50 kPa heights from 1947 to 1989.

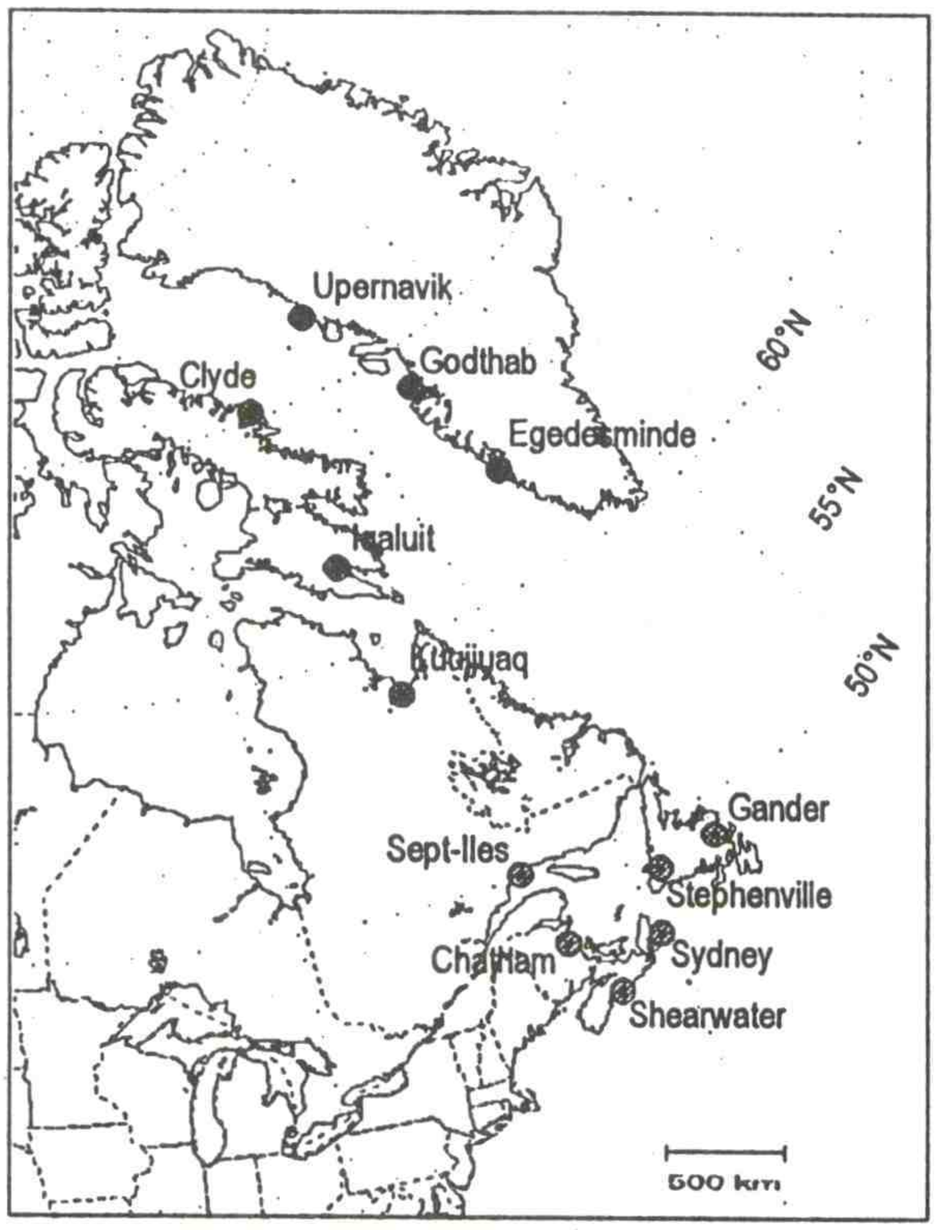

Figure 3. Climate stations used for summer (JJAS) surface air temperaure analysis. Entire region is split into two targets for summer analysis, station groups both north and south of 55°N.

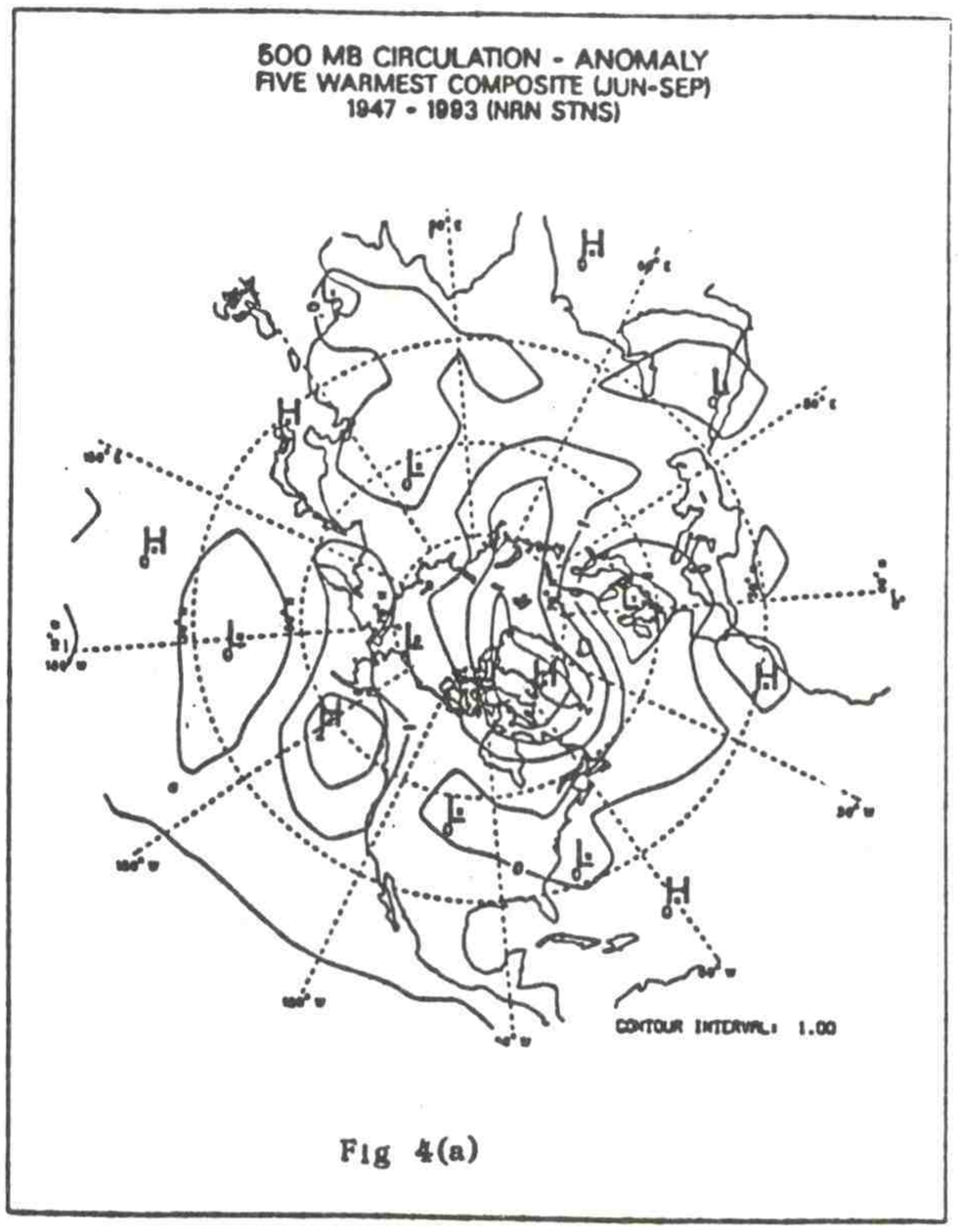

Fig 4(a)

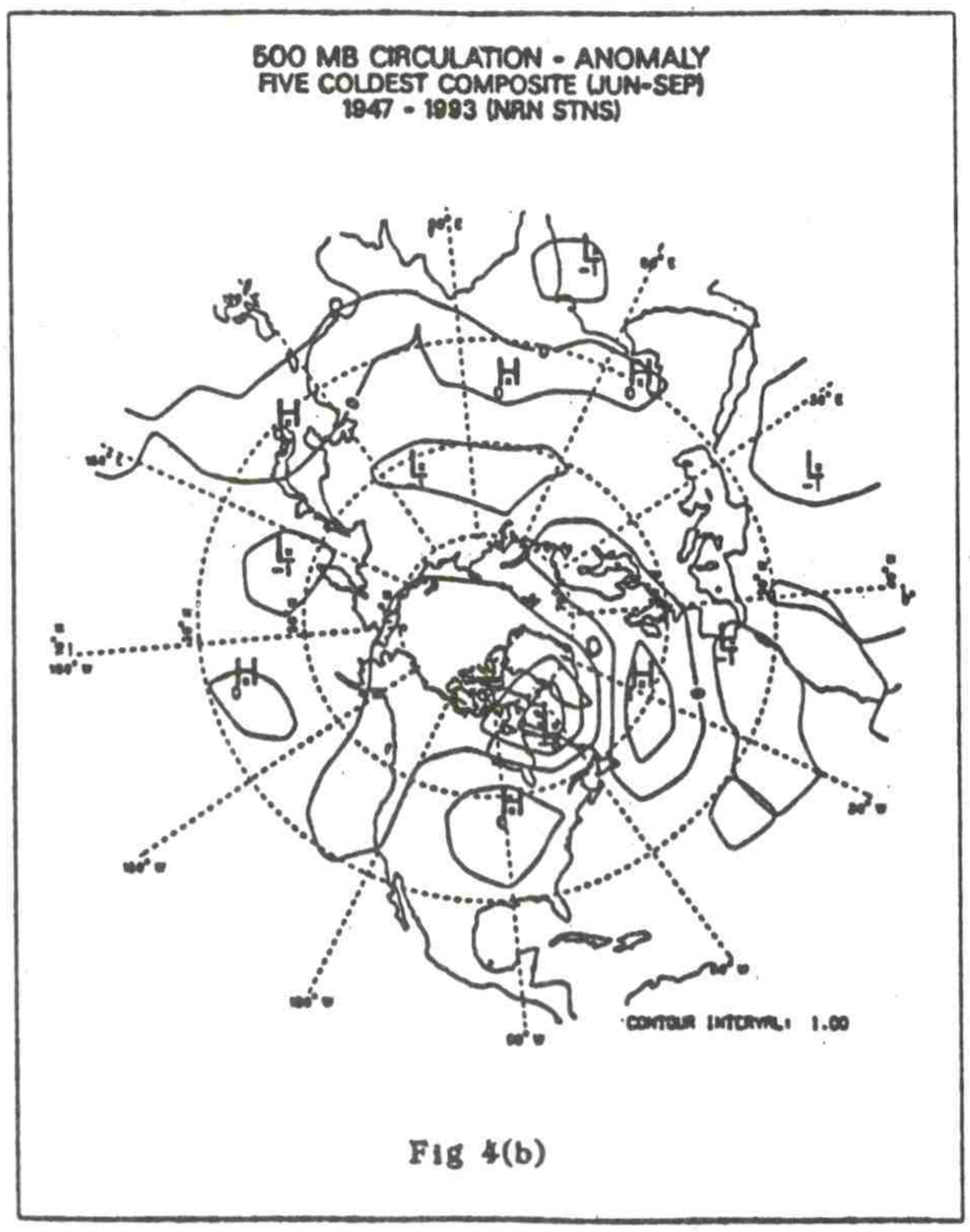

Fig 4(b)

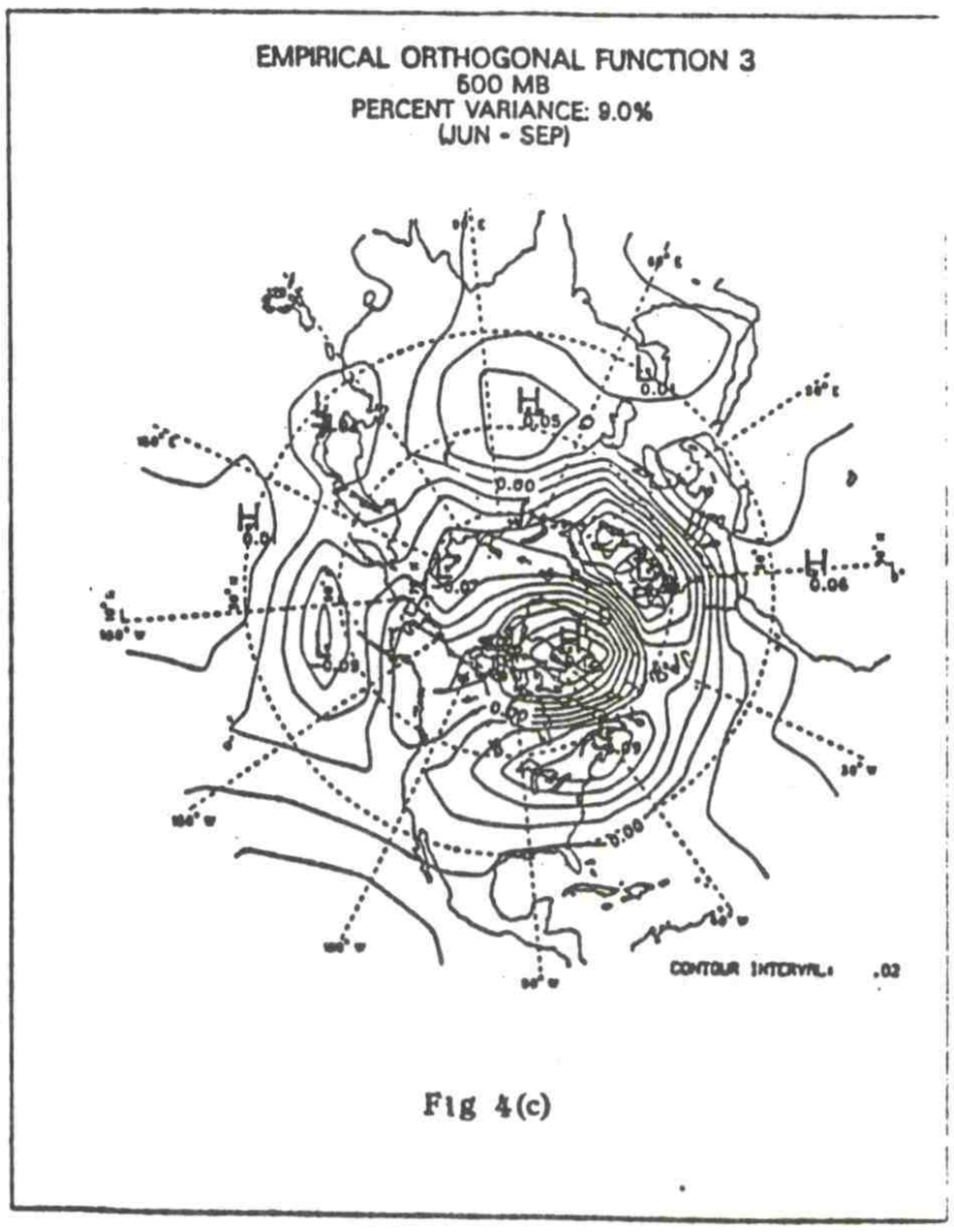

Fig 4(c)

Revised Atlantic basin seasonal tropical cyclone prediction methods for 1 June and 1 August forecast dates

Christopher W. Landsea[1], William M. Gray,
Department of Atmospheric Science, Colorado State University, Fort Collins, CO 80523, USA

Paul W. Mielke, Jr. and Kenneth J. Berry
Department of Statistics, Colorado State University, Fort Collins, CO 80523, USA

This paper describes recent advances regarding seasonal forecasting of Atlantic basin tropical cyclone activity. Previous analyses (Gray et al. 1992, 1993, 1994) had utilized a grouped cross–validation to estimate forecast skill from hindcast Least Absolute Deviations (LAD) regressions. Elsner and Schmertmann (1993, 1994) demonstrated that this grouping methodology does not produce a fully cross–validated result. Therefore, the grouped cross–validation LAD regression has been replaced by simply performing a non cross–validated LAD regression and estimating the amount of future skill reduction from experiments in Mielke et al. (1995). Mielke et al. provide suggested forecast skill based upon the hindcast skill (measured by ρ – the measure of agreement), the number of predictors, and the number of datapoints available. In general, the amount of degradation between hindcast sample skill and forecast skill (i.e. "shrinkage") is high when the ratio of the number of predictors to datapoints is large.

For the 1 June forecasts of tropical cyclone activity, the same thirteen predictors as in Gray et al. (1994) are available for the regressions. In an effort to reduce shrinkage of skill, the regression equation only accepts a predictor if it is able to increase the expected forecast skill (not the hindcast skill) by at least 0.01. With this restriction, we are able to choose between five and nine predictors and, for the most part, provide hindcast skill that is nearly equal to that shown in Gray et al. (1994). This earlier work utilized all thirteen predictors for each tropical cyclone parameter being forecast. The following lists the predictors available by 1 June and the tropical cyclone parameters to be forecast (all anomalies and standardized deviations are based upon mean 1950–1990 conditions):

PREDICTORS

U50: 50 mb zonal winds over the Caribbean Sea extrapolated from May to September in ms^{-1}.

U30: 30 mb zonal winds over the Caribbean Sea extrapolated from May to September in ms^{-1}.

Shear: Absolute zonal wind shear between extrapolated 30 and 50 mb values in ms^{-1}.

R_S: August to September rainfall in North Africa's Western Sahel from the previous year in standardized deviations.

R_G: August through November rainfall along North Africa's Gulf of Guinea from the previous year in standardized deviations.

ΔP_x: North African interior to coastal sea level pressure gradient anomalies from February through May in standardized deviations.

[1]Corresponding author address: Christopher W. Landsea, NOAA AOML/Hurricane Research Division, 4301 Rickenbacker Causeway, Miami, Florida 33149 (landsea@aoml.noaa.gov)

ΔT_x: North African coastal to interior surface temperature gradient anomalies from February through May in standardized deviations.

SLPA: April to May sea level pressure anomalies in mb around the Caribbean Sea.

ZWA: April to May 200 mb zonal wind anomalies in ms^{-1} around the Caribbean Sea.

SST: April to May NINO–3 sea surface temperature anomalies in °C.

ΔSST_t: April to May minus January to February NINO–3 sea surface temperature anomalies in °C.

SOI: April to May Southern Oscillation Index values in standardized deviations.

ΔSOI_t: April to May minus January to February Southern Oscillation Index values in standardized deviations.

TROPICAL CYCLONE PARAMETERS

NS: Named storms (i.e. tropical storms and hurricanes).

NSD: Named storm days.

H: Hurricanes.

HD: Hurricane days.

IH: Intense hurricanes.

IHD: Intense hurricane days.

HDP: Hurricane destruction potential.

NTC: Net tropical cyclone activity.

Table 1 presents estimated forecast skill available for each tropical cyclone parameter and the predictors chosen.

Table 1: 1 June measures of agreement (ρ) for the original hindcasts shown in Gray et al. (1994) based upon the years 1950 to 1991 and 13 predictors, the current hindcast skill based upon the years 1950 to 1994, the expected forecast skill estimated by results from Mielke et al. (1995), and the predictors chosen for current methodology (number in parentheses).

Tropical Cyclone Type	Original Hindcast Skill	Current Hindcast Skill	Expected Forecast Skill	Predictors Chosen
NS	0.514	0.500	0.296	(6) U50, Shear, R_S, R_G, ΔT_x, SLPA
NSD	0.660	0.630	0.476	(8) U50, Shear, R_S, R_G, ΔT_x, SLPA, SST, ΔSOI_t
H	0.617	0.530	0.349	(5) Shear, R_S, R_G, SLPA, SST
HD	0.703	0.644	0.494	(8) U50, Shear, ΔT_x, SLPA, ZWA, ΔSST_t, SOI, ΔSOI_t
IH	0.637	0.598	0.442	(6) U50, R_G, ΔP_x, ZWA, ΔSST_t, SOI
IHD	0.614	0.543	0.363	(6) R_S, ΔP_x, ΔT_x, SLPA, SOI, ΔSOI_t
HDP	0.709	0.662	0.517	(8) U50, Shear, R_G, ΔT_x, SLPA, ΔSST_t, SOI, ΔSOI_t
NTC	0.718	0.696	0.556	(9) U50, Shear, R_G, ΔP_x, ΔT_x, SLPA, ΔSST_t, SOI,ΔSOI_t

Note that the amount of skill estimated to remain in forecasts of future activity ranges from nearly one–third to over one–half of the variability. While quite high, these values are somewhat reduced from what we had originally suggested in Gray et al. (1994).

For the 1 August forecasts, two items have been substantially changed in addition to the new methodology of predictor choice selection and estimations of forecast skill. We have removed any pre–1 August tropical cyclones and have included an additional four possible predictors to be selected.

From the dependent data set (i.e. the tropical cyclone parameters), we removed the tropical cyclone activity which occurred before 1 August of that particular year. For example, if a hurricane became so designated on, say, the 29th of July and continued as a hurricane until the 3rd of August, then that hurricane and those six hurricane days would be excluded from the seasonal H and HD calculations for the 1 August forecasts. The reason for doing so is to only predict activity that occurred after the forecast date. Typically, around 90% of the tropical cyclone activity (less for named storms, more for intense hurricanes) are observed from August through November (Landsea 1993).

In addition to the nine predictors for the 1 August forecast described in Gray et al. (1993), four more potential predictors are also introduced. Two (ΔT_x and ΔP_x) are identical to those being utilized in the 1 June forecasts. The other two (ΔSST_t and ΔSOI_t) are updates from information available at 1 June to include El Niño–Southern Oscillation trends through June and July. The thirteen predictors are as follows:

PREDICTORS

U50: 50 mb zonal winds over the Caribbean Sea extrapolated from July to September in ms^{-1}.

U30: 30 mb zonal winds over the Caribbean Sea extrapolated from July to September in ms^{-1}.

Shear: Absolute zonal wind shear between extrapolated 30 and 50 mb values in ms^{-1}.

R_S: June to July rainfall in North Africa's Western Sahel in standardized deviations.

R_G: August through November rainfall along North Africa's Gulf of Guinea from the previous year in standardized deviations.

ΔP_x: North African interior to coastal sea level pressure gradient anomalies from February through May in standardized deviations.

ΔT_x: North African coastal to interior surface temperature gradient anomalies from February through May in standardized deviations.

SLPA: June to July sea level pressure anomalies in mb around the Caribbean Sea.

ZWA: June to July 200 mb zonal wind anomalies in ms^{-1} around the Caribbean Sea.

SST: June to July NINO–3 sea surface temperature anomalies in °C.

ΔSST_t: June to July minus April to May NINO–3 sea surface temperature anomalies in °C.

SOI: June to July Southern Oscillation Index values in standardized deviations.

ΔSOI_t: June to July minus April to May Southern Oscillation Index values in standardized deviations.

Note that the 1 August NTC is computed for each year based upon the activity from August onward compared with climatology for August onward. Thus 1 August NTC can be either higher or lower than the NTC utilized for the 1 June forecast, which is based upon all season activity.

As described above for the 1 June forecast, the 1 August LAD regression is then selected based upon whether the last predictor added contributes at least 0.01 in the estimated forecast skill. Table 2 details the predictors chosen and what the expected forecast skill is estimated to be.

Expected forecast skill varies from near 30% of the variability for the frequency of NS to over 50% for NTC. Most of these parameters seem to indicate less skill available at the 1 August forecast time than at 1 June. However, the expected forecast skill is not directly comparable between the two forecast times because of the elimination of the pre–August cyclones from the 1 August forecasts. The two that can be directly compared – the IH and

Table 2: 1 August measures of agreement (ρ) for the original hindcasts shown in Gray et al. (1994) based upon the years 1950 to 1991 and 9 predictors, the current hindcast skill based upon the years 1950 to 1994, the expected forecast skill estimated by results from Mielke et al. (1995), and the predictors chosen for current methodology (number in parentheses).

Tropical Cyclone Type	Original Hindcast Skill	Current Hindcast Skill	Expected Forecast Skill	Predictors Chosen
NS	0.477	0.484	0.275	(5) U50, Shear, R_G, ΔP_x, SLPA
NSD	0.608	0.580	0.417	(6) U50, U30, R_S, R_G, ΔP_x, ΔT_x
H	0.472	0.488	0.288	(5) U50, U30, R_G, ΔT_x, SLPA
HD	0.505	0.624	0.481	(5) U50, U30, R_G, ZWA, ΔSST_t
IH	0.586	0.610	0.458	(6) U30, R_S, R_G, ΔT_x, SLPA, SOI
IHD	0.540	0.566	0.392	(7) U50, Shear, R_S, R_G, ΔT_x, SST, SOI
HDP	0.549	0.639	0.492	(7) U30, Shear, R_S, R_G, ΔT_x, ZWA, ΔSST_t
NTC	0.581	0.651	0.511	(6) U50, U30, R_S, R_G, ΔT_x, ΔSOI_t

IHD categories due to virtually no occurrences before 1 August – show substantial improvements in skill at the 1 August forecast time over what is available at 1 June.

ACKNOWLEDGMENTS: Support for this research has been provided by a NASA Global Change Fellowship to the lead author.

REFERENCES

Elsner, J. B., and C. P. Schmertmann, 1993: Improving extended–range seasonal predictions of intense Atlantic hurricane activity. *Wea.Forecasting*, **8**, 345–351.

Elsner, J. B., and C. P. Schmertmann, 1994: Assessing forecast skill through cross validation. *Wea.Forecasting*, **9**, 619–624.

Gray, W. M., 1984a: Atlantic seasonal hurricane frequency. Part I: El Niño and 30 mb quasi-biennial oscillation influences. *Mon.Wea.Rev.*, **112**, 1649–1668.

Gray, W. M., 1984b: Atlantic seasonal hurricane frequency. Part II: Forecasting its variability. *Mon.Wea.Rev.*, **112**, 1669–1683.

Gray, W. M., C. W. Landsea, P. W. Mielke, Jr., and K. J. Berry, 1992: Predicting Atlantic seasonal hurricane activity 6–11 months in advance. *Wea.Forecasting*, **7**, 440–455.

Gray, W. M., C. W. Landsea, P. W. Mielke, Jr., and K. J. Berry, 1993: Predicting Atlantic basin seasonal tropical cyclone activity by 1 August. *Wea.Forecasting*, **8**, 73–86.

Gray, W. M., C. W. Landsea, P. W. Mielke, Jr., and K. J. Berry, 1994: Predicting Atlantic basin seasonal tropical cyclone activity by 1 June. *Wea.Forecasting*, **9**, 103–115.

Landsea, C. W., 1993: A climatology of intense (or major) Atlantic hurricanes. *Mon.Wea.Rev.*, **121**, 1703–1713.

Mielke, P. W., Jr., K. J. Berry, C. W. Landsea, and W. M. Gray, 1995: Artificial skill and validation in meteorological forecasting. Accepted to *Wea.Forecasting*, 47 pp.

A West-Pacific Upper Tropospheric Westerly Wind Surge during TOGA-COARE

Haig Iskenderian and Lance F. Bosart
Department of Atmospheric Science
SUNY/Albany
1400 Washington Avenue
Albany, New York 12222

The purpose of this work is to document the occurrence of unusually strong upper-level westerlies across the Tropical Ocean Global Atmosphere-Coupled Ocean Atmosphere Research Experiment (TOGA-COARE) region from 30 December 1992 to 30 January 1993, with westerly shear over the eastern portion of the TOGA-COARE network between 850 hPa and 200 hPa exceeding 24 m s^{-1}. This episode of strong upper-level westerlies and associated large vertical wind shear has been previously documented by McBride et al. (1995, their Fig. 4). The large scale and synoptic scale contributions to this event will be illustrated. The possible role of cross-equatorial flow, as well as the possible contributions from inertial and barotropic instability to the acceleration of the upper-level westerlies will be discussed.

The data sources used in the study are the European Centre for Medium Range Forecasts (ECMWF) 2.5° X 2.5° uninitialized gridded fields available very 12 hours from the National Center for Atmospheric Research (NCAR). The TOGA-COARE radiosonde archive available from the University Corporation for Atmospheric Research Office of Field Project Support (UCAR/OFPS) Cooperative Distributed Interactive Atmospheric Catalog System (CODIAC) archives are also used.

The ECMWF gridded fields were used to evaluate the low-frequency variability associated with the onset of the major Near-Equatorial Westerly Trough (NEWT) in the upper troposphere. Daily maps of the wind and streamfunction were also inspected to assess the role of the synoptic-scale features of both hemispheres to the formation of the NEWT. These analyses were verified against available aircraft, satellite winds, and radiosondes for accuracy.

Fig. 1a shows 200 hPa ECMWF winds for 00 UTC 30 December 1992. The TOGA-COARE region is dominated by easterlies at 200 hPa averaging 10-20 m s^{-1}. These easterlies are on the equatorward side of a large anticyclone situated near 140°E. Poleward of this anticyclone, a strong westerly jet is situated across southern Japan. In the Southern Hemisphere, an anticyclonic circulation is situated near southeast Australia, with a confluent westerly jet entrance region located downstream in the vicinity of New Zealand. In the lower troposphere (not shown) at this time, a previously-documented equatorial westerly wind burst (Kiladis et al. 1994) is moving through the TOGA-COARE region. By 00 UTC 17 January 1993, 200 hPa easterlies have been replaced by 200 hPa westerlies in the TOGA-COARE region (Fig. 1b). These westerlies arise in conjunction with the development of a NEWT west of the Date Line. The NEWT is defined by a northeast-southwest oriented trough line, implying poleward eddy angular momentum flux. The NEWT forms equatorward of the exit region of the Asian jet, and within the entrance region of the subtropical jet. The westerlies of the subtropical jet extend from near 140°E (west of Kwajalein), east-northeastward across the Pacific to the west coast of Mexico. Simultaneously, in the Southern Hemisphere, a deep, positively-tilted trough has formed downstream of a sharp ridge that is situated northwest of New Zealand. Both of these NEWTs show evidence for the configuration of a breaking Rossby wave, with relatively strong westerlies along the equator between them.

The time-dependent behavior of the 200 hPa zonal winds for the month of January 1993 along 170°E is shown in Fig. 2. Climatologically favored easterlies along the equator are evident

throughout most of the month. These easterlies are interrupted by westerlies during 14-21 January, which peak around 17 January, when westerly zonal winds approach 10-20 m s^{-1}. The onset of the near-equatorial westerlies occurs in association with the equatorward movement of westerly wind perturbations from both hemispheres. A double westerly jet structure is observed in both hemispheres at the time of maximum equatorial westerlies. The polar jets of the Northern and Southern Hemisphere are situated near 40°N and 50°S respectively. Simultaneously, the subtropical jet entrance regions are located near 10°-15°N and 10°-15°S respectively.

The previous discussion has illustrated a shift in the large-scale circulation regime over the Pacific on a time scale of 2-3 weeks. Further evidence of the changes in the wind regime over the TOGA-COARE region can be seen in time series of twice-daily radiosonde winds from Kwajalein (Fig. 3a). Upper level easterlies in the beginning of January become westerly above 400 hPa by the middle of the month. The westerlies at 100 hPa on 8 January gradually shift downward to 300 hPa by 13 January, providing the impression of a downward progression of the westerlies. At their peak, the westerlies extend down to 400 hPa, with maximum winds near 30 m s^{-1} on 16-17 January. The easterly winds in the lower troposphere appear to be generally unaffected by the sequence of events in the middle and upper troposphere.

The presence of a double jet shown in Fig. 1b and Fig. 2 suggests the possibility that the barotropic instability may play a role in formation of the NEWT. The presence of twin breaking Rossby waves with their associated ridges hints at a possible role for inertial instability. The existence of large-scale confluent flow in the entrance region of both NEWTs suggests the possible role of large-scale deformation in the NEWT in the entrance region of both jet entrance regions. In an effort to test these possibilities, we present 200 hPa maps at 00 UTC 17 January of absolute vorticity (Fig. 3b), and the meridional gradient of time-mean absolute vorticity $\left(\beta - \partial^2\bar{u}/\partial y^2\right)$ (Fig. 3c) where $\bar{u}$ is the time-mean zonal wind from 15-23 January. This period corresponds to the time of peak upper-tropospheric westerlies in the TOGA-COARE region shown in McBride et al. (1995). Lastly, we show the 200 hPa resultant deformation and dilatation axis for 00 UTC 17 January in Fig. 3d.

Comparison of Fig. 3b and Fig. 1b reveals that areas of near-zero absolute vorticity lie equatorward both of the polar front jet across the western Pacific and the subtropical jet extending eastward from 160°E. In particular, we find a large area of low values of absolute vorticity in the Rossby wave breaking region defined by the equatorward polar front jet exit regions and poleward subtropical jet entrance region. Coincident with this apparent breaking Rossby wave is a region where the meridional gradient of absolute vorticity changes sign (Fig. 3c), suggestive of a possible role of barotropic instability in the formation of the NEWT. This region of meridional gradient of absolute vorticity reversal extends mostly east-west across the Pacific between 20° and 30°N latitude, and is situated between the polar front and subtropical jets. Finally, from Fig. 3d, we see that large-scale deformation processes must play an important role in the formation and westward extension of the subtropical jet (Compare Fig. 3d with Fig. 1b).

Acknowledgment. Support for this work by NSF grant ATM-9114598 and NOAA grant NA56GP0197 is appreciated.

1a.

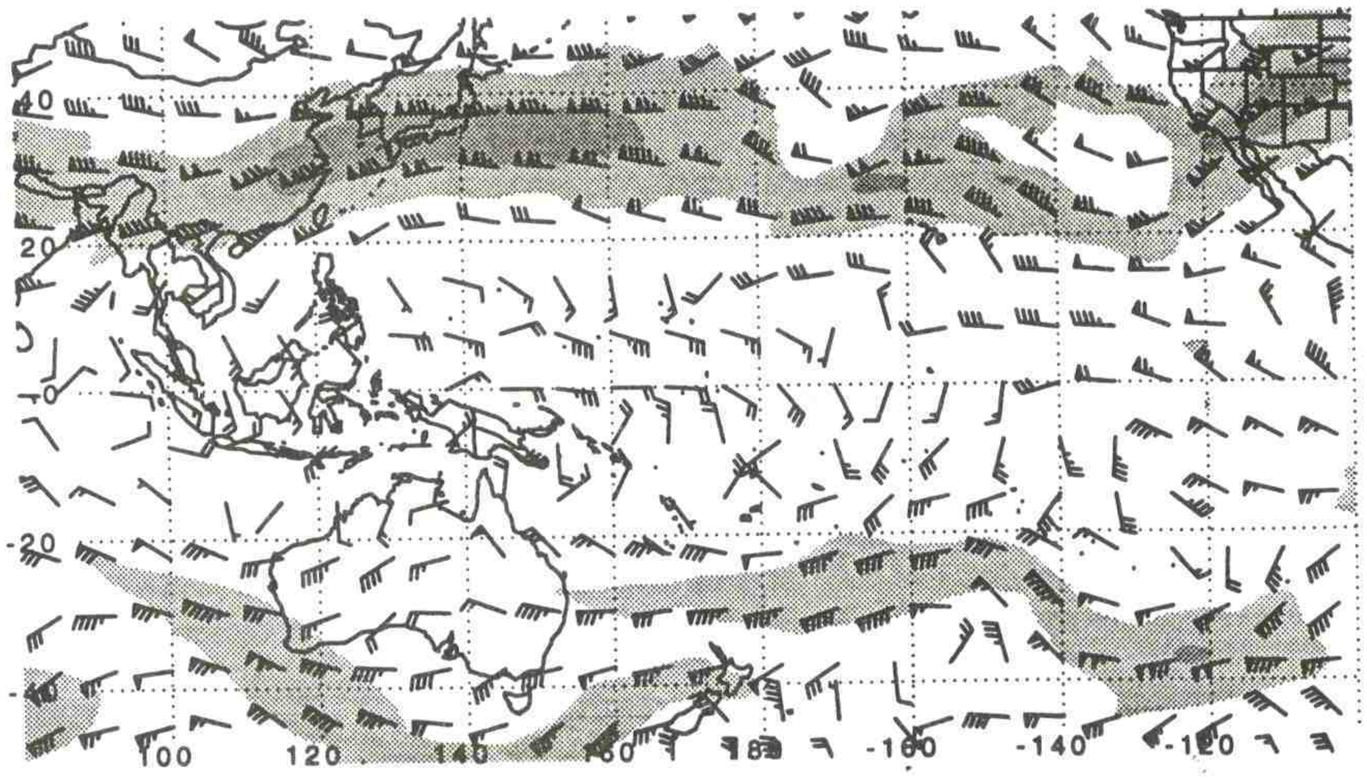

921230/0000 200 MB ECMWF Winds (m/s)

1b.

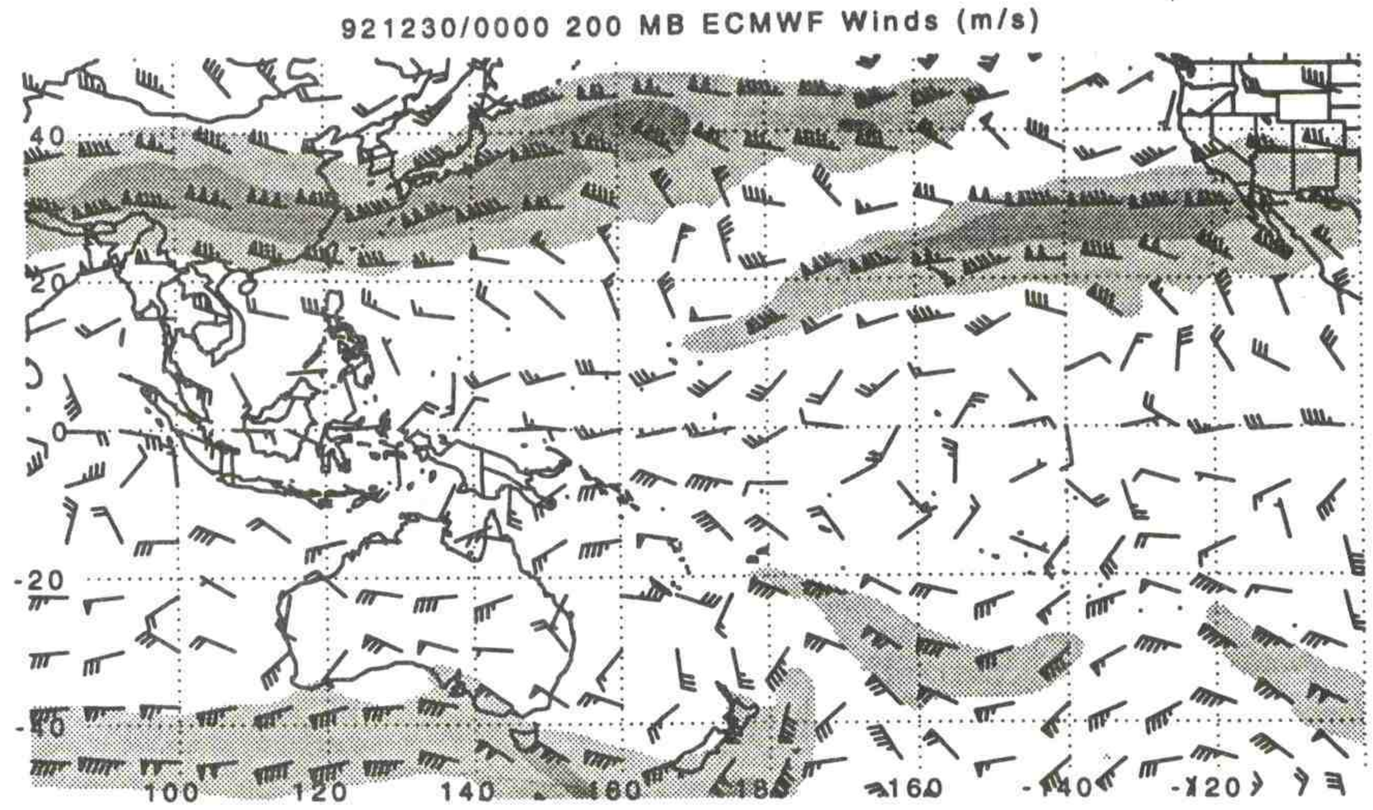

930117/0000 200 MB ECMWF Winds (m/s)

FIG. 1. ECMWF 200 hPa gridded winds for 0000 UTC 30 December 1992. Winds plotted in m s^{-1} with one pennant, barb and half barb denoting 25, 5 and 2.5 m s^{-1}, respectively. Light (dark) shaded areas denote wind speeds > 35 (60) m s^{-1}. (b) ECMWF 200 hPa gridded winds for 0000 UTC 17 January 1993. Winds plotted as in (a).

2.

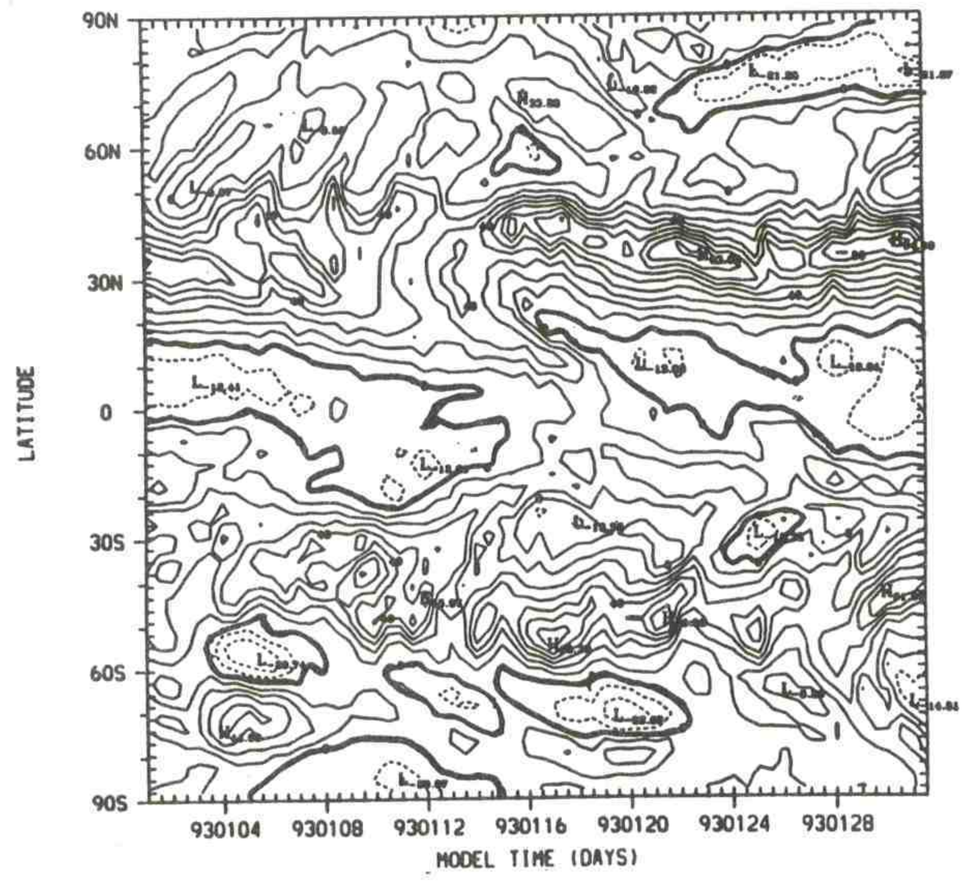

FIG. 2. Time series of 200 hPa zonal wind along 170°E for January 1993. Contours every 10 m s^{-1} with solid (dashed) contours denoting westerly (easterly) winds.

3a.

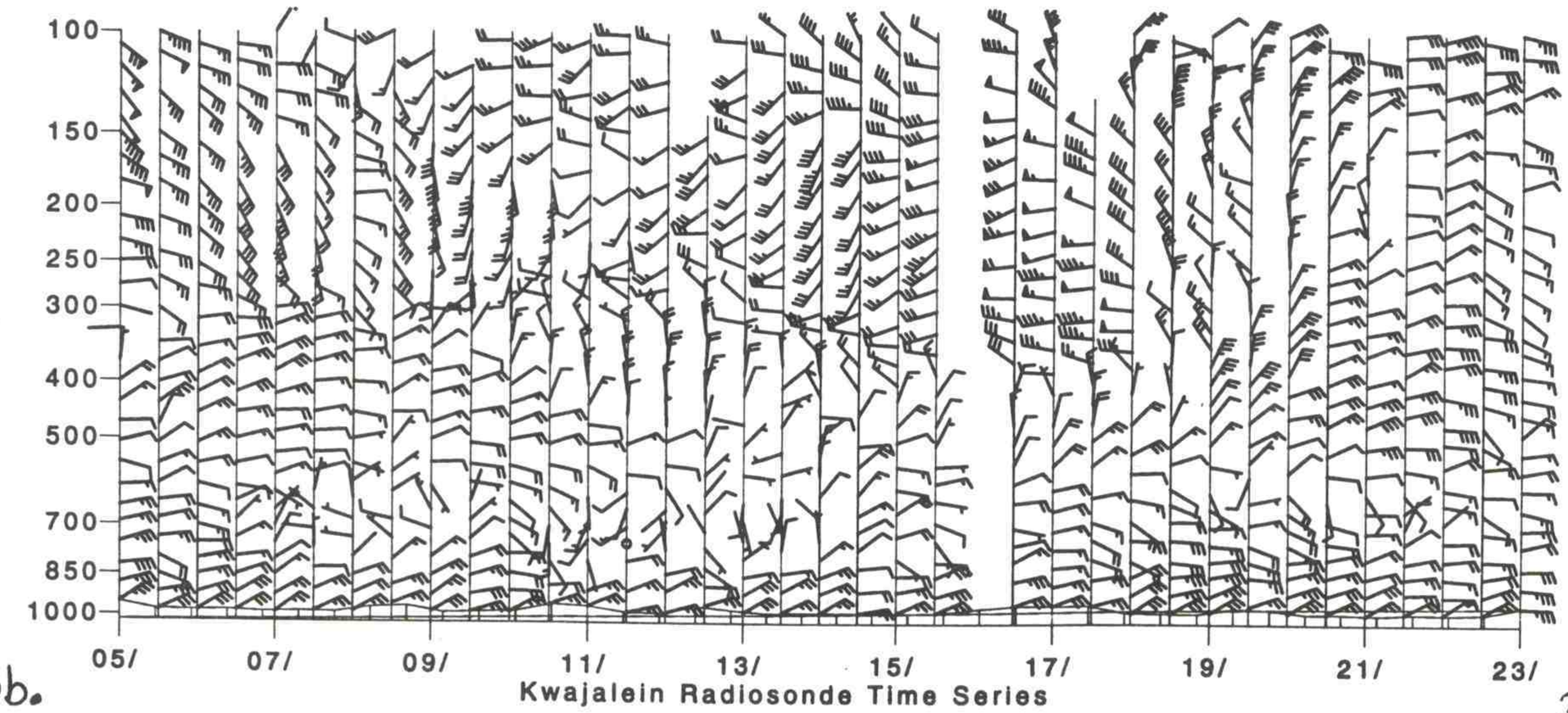

Kwajalein Radiosonde Time Series

3b.

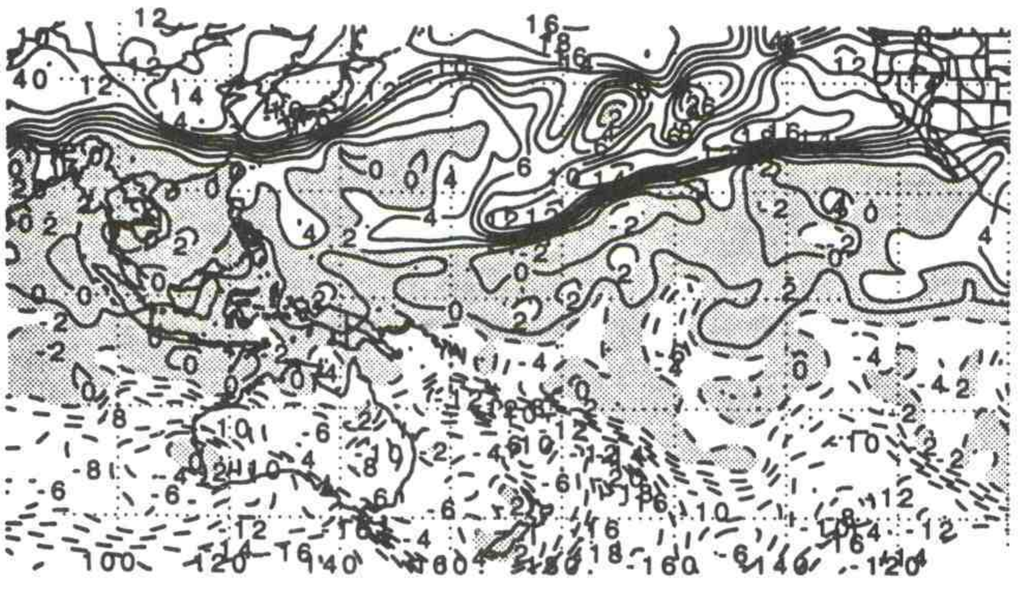

930117/0000 200 MB Absolute Vorticity

3c.

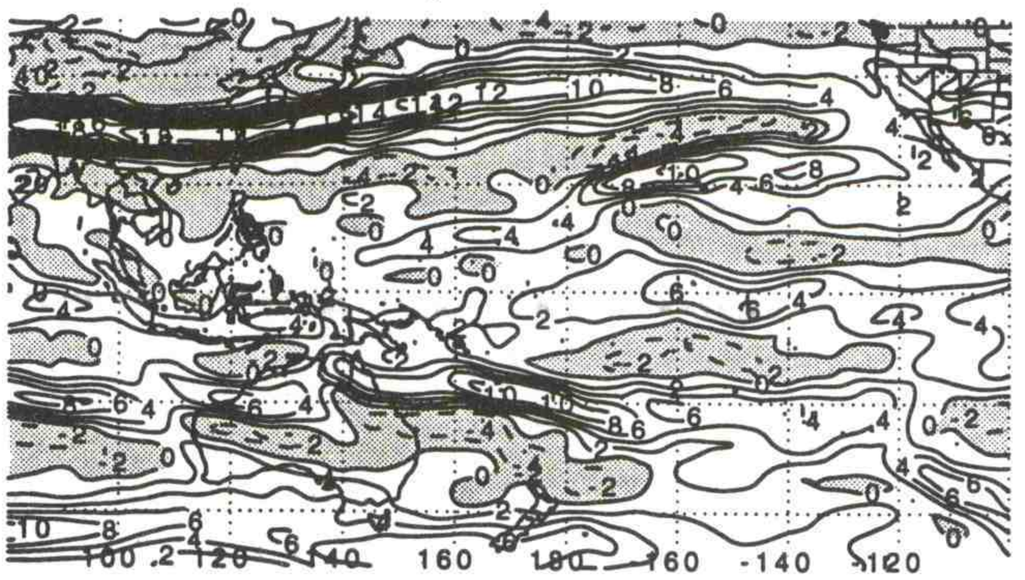

15-23 Jan 200 MB Merid. Gradient Abs. Vort.

3d.

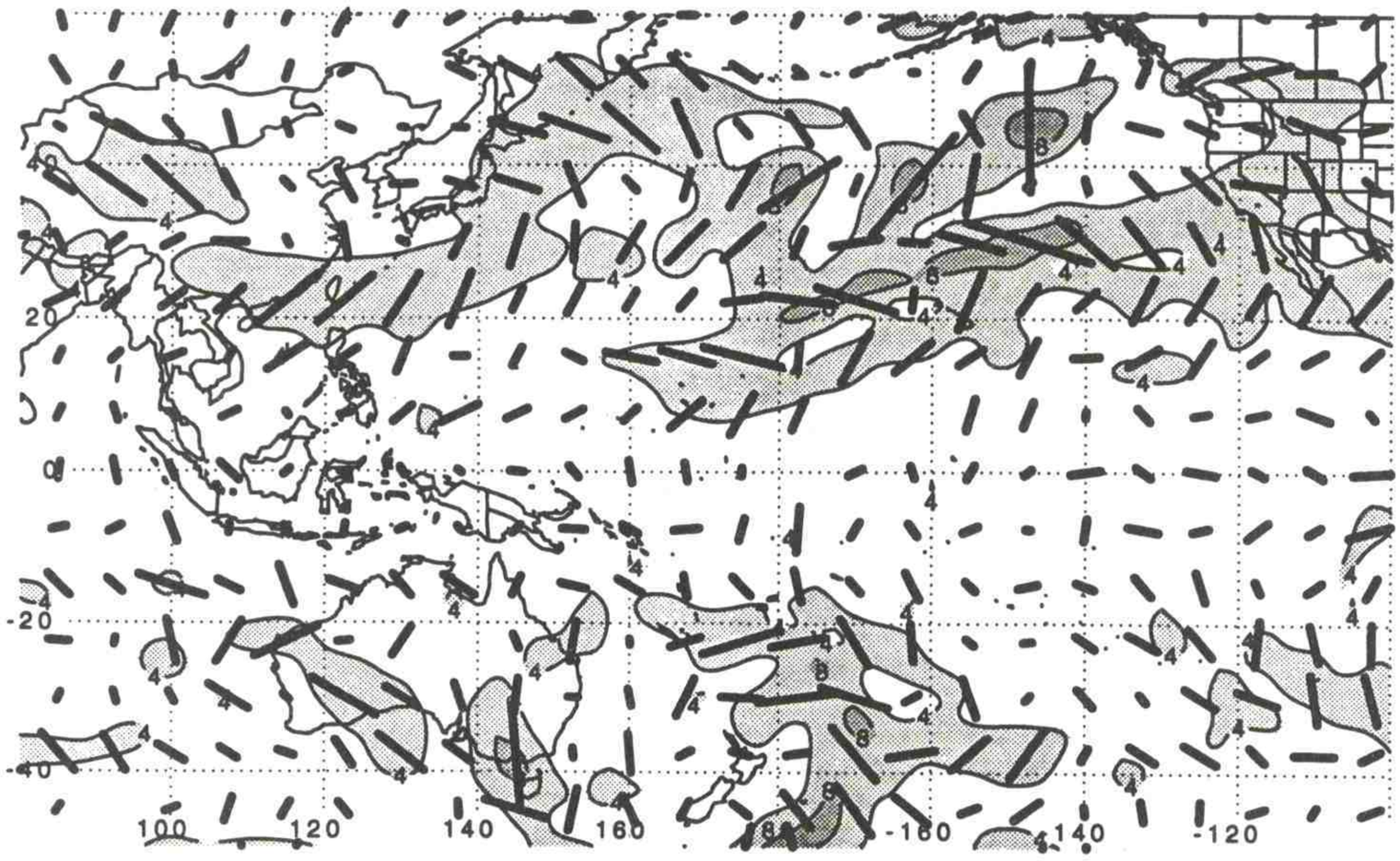

930117/0000 200 MB Total Deformation
and 200 MB dilatation axis

FIG. 3. (a) Kwajalein Island time series of twice-daily radiosonde winds for 5-23 January 1993. Units: m s^{-1} with winds plotted as in Fig. 1. (b) 200 hPa absolute vorticity for 0000 UTC 17 January 1993. Contours every 2 x 10^{-5} s^{-1} with solid (dashed) contours denoting positive (negative) values. Values between 2 and -2 are shaded. (c) Time-mean 200 hPa map of $\left(\beta - \partial^2\bar{u}/\partial y^2\right)$ for the period 15-23 January 1993. Units: 10^{-11} m^{-1} s^{-1}. Negative values are shaded. (d) 200 hPa total deformation (x 10^{-5} s^{-1}) for 0000 UTC 17 January 1993. Contours every 4, with values greater than 4 lightly shaded, greater than 8 darker shaded.

Application of EOF Analysis to Tropical Wind Profiler Data

Christopher R. Williams
Cooperative Institute for Research in Environmental Sciences (CIRES)
University of Colorado, Boulder, CO 80309
in cooperation with the
National Oceanic and Atmospheric Administration (NOAA)
Aeronomy Laboratory, Boulder, CO 80303

Introduction

Empirical Orthogonal Function (EOF) analysis is applied to wind profiler data so that the orthogonal functions describe the vertical structure of the observed winds and the corresponding principal components describe the temporal evolution of these structures. This paper presents the EOF analysis technique applied to the annual and interannual variability of zonal winds observed during 9 years of observations at Christmas Island, Kiribati (2°N, 157°W).

Annual Variation of Zonal Wind

The annual variation of zonal wind from Christmas Island was determined by constructing an ensemble year using daily mean winds observed from April 1986 to April 1995. The ensemble year was low pass filtered to retain the mean wind and the first four annual harmonics. An EOF analysis was performed on this filtered data set with the first two modes representing 92% and 5% of the variance. The time-mean removed zonal mean wind is shown in Figure 1 along with the eigenvectors describing the vertical structure and the corresponding principal components from the first two modes. Gage et al. (1995) has related the temporal evolution of EOF #1 to the annual variation of tropical convection and the annual variation in the Walker circulation.

Zonal Wind Anomalies

The zonal wind anomalies from Christmas Island were constructed by removing the annual variation of zonal wind (calculated above) from the original daily zonal wind. The resulting zonal wind anomalies were filtered with a 3 day running mean and an EOF analysis was performed. The first three EOF's are shown in Figure 2 and represent 54%, 12% and 9% of the variance associated with the zonal wind anomalies. The eigenvector of EOF #1 is similar to the annual variation of zonal wind EOF #1 eigenvector shown in Figure 1. The Southern Oscillation Index (SOI) is shown with PC #1 in Figure 2. The PC #1 was filtered to produce monthly values which are correlated with the monthly SOI ($r = 0.67$) and suggest EOF #1 results from the interannual variation of convection across the Pacific associated with ENSO.

Concluding Remarks

Empirical Orthogonal Function (EOF) analysis describes the structure of observations using the fewest possible number of orthogonal functions and also describes the time evolution of these

structures. EOF analysis is a common mathematical tool used to describe two-dimensional structures and their evolution in global climate models (GCMs) and numerical weather prediction (NWP) models. The EOF analysis applied to wind profiler data is novel and results in orthogonal functions describing the vertical structure of the observed winds with the corresponding principal components describing the temporal evolution of these structures. The examples shown in this paper relate the time evolution of the dominant zonal wind mode with tropical convection at both the annual and interannual time scales.

References

Gage, K.S., J.R. McAfee, and C.R. Williams, On the annual variation of tropospheric zonal winds observed above Christmas Island in the central equatorial Pacific, accepted, J. Geophy. Res., 1995.

Acknowledgments. The Christmas Island wind profiler was constructed and is being operated with the support of the U.S. TOGA Project Office. The NOAA/CU Trans Pacific Profiler Network is supported by the National Science Foundation under Agreement ATM-87220797 and ATM-9214800.

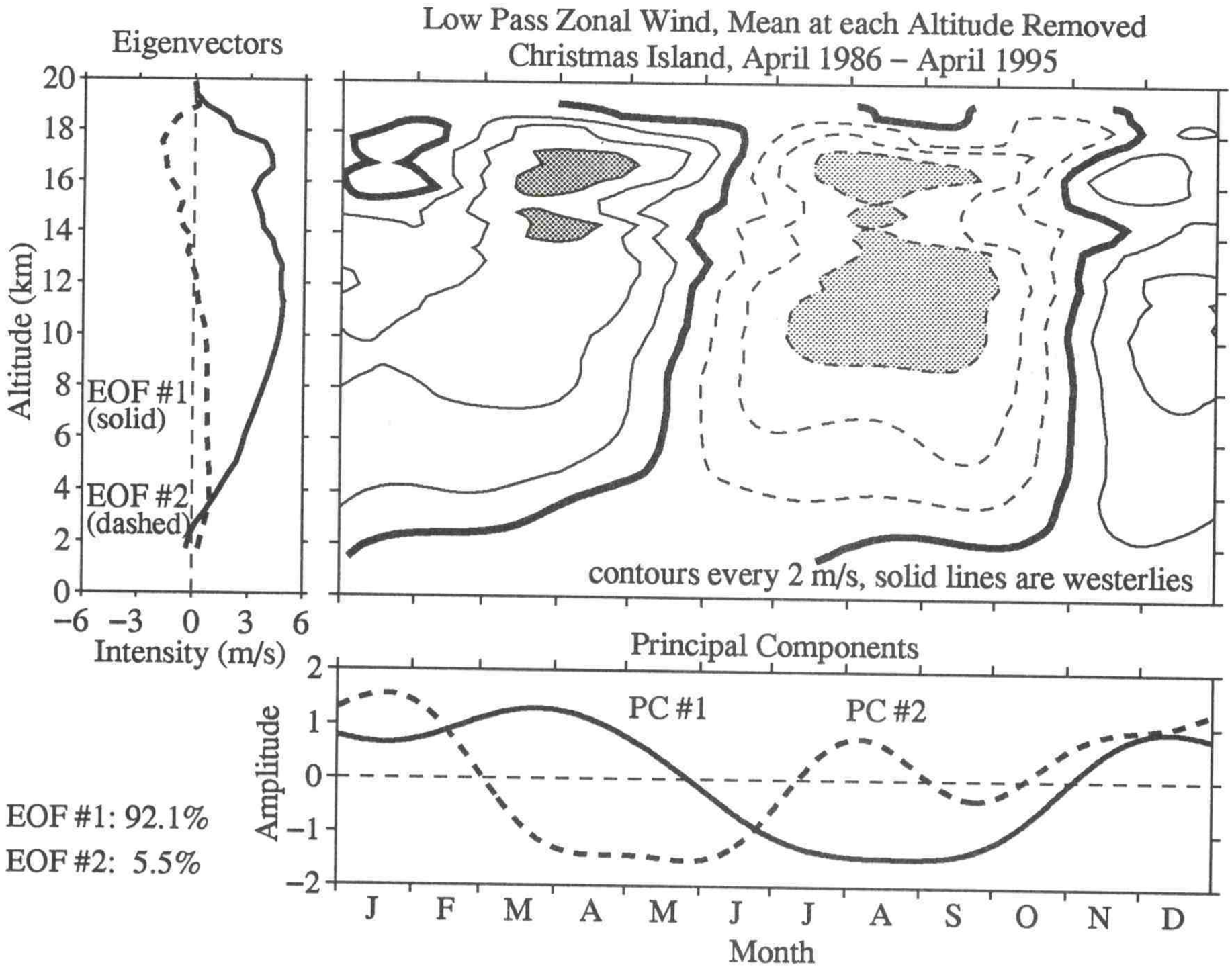

Figure 1. Time-mean removed low pass zonal wind along with the eigenvectors and prinicipal components from the first two EOF modes.

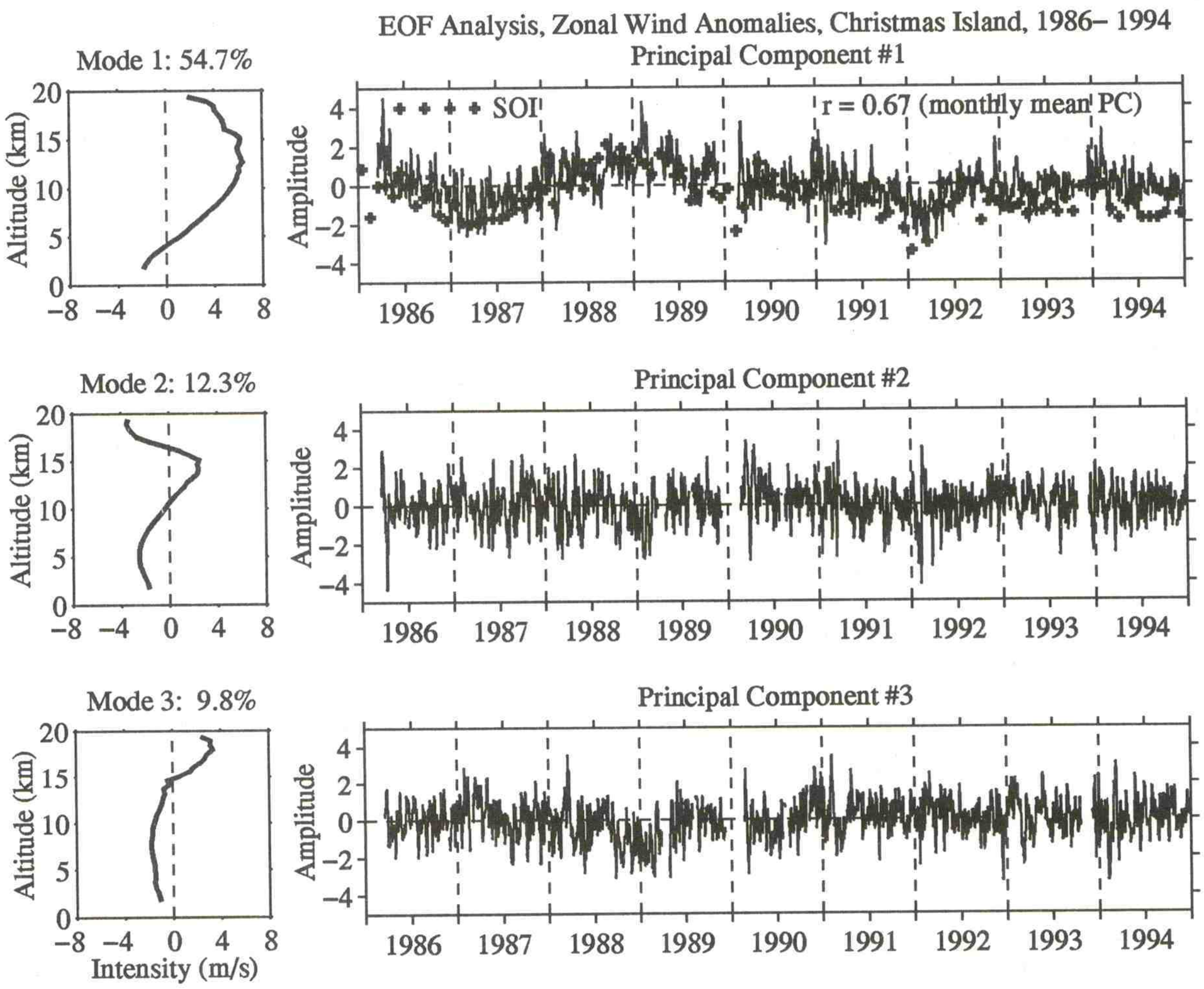

Figure 2. First three EOF's from the zonal wind anomalies at Christmas Island. The left column contains the eigenvectors and the right column contains the prinicipal components. EOF #1 (top) represents 54%, EOF #2 (middle) represents 12% and EOF #3 (bottom) represents 9% of the variance associated with the zonal wind anomalies. The SOI is shown with PC #1 and has a correlation coefficient of r = 0.67.

Impact of Slowly-Varying Boundary Forcings on the Broad-Scale Asian Summer Monsoon

SONG YANG AND K.-M. LAU

Laboratory for Atmospheres, Code 913
NASA-Goddard Space Flight Center
Greenbelt, Maryland 20771

1. INTRODUCTION

Accumulated evidence has indicated that sea surface temperature (SST) variations and land surface processes (LSPs) are two important factors in the variability of the Asian summer monsoon (Shukla 1975; Palmer *et al.* 1992; Webster and Yang 1992; Chen and Yen 1994; Meehl 1994; Ju and Slingo 1995; Vernekar *et al.* 1995; Li and Yanai 1996; Yang *et al.* 1996). However, to what an extent these boundary conditions influence the monsoon is uncertain. What is the relative importance of SST variations and LSPs on the interannual variability of the monsoon? This work is conducted to answer this question by carrying out a number of experiments with the Goddard Laboratory for Atmospheres (GLA) GCM.

The GLA GCM used in this study is an AMIP-version model which has 17 sigma levels with a horizontal resolution of 5°x4°. Recent studies (Lau and Yang 1996; Yang *et al.* 1996) have indicated that the model simulates the Asian summer monsoon and its variability reasonably well. The first experiment with the model is AMIP experiment in which the model is forced by observed monthly SST while the atmosphere and land surface are fully interactive. The second experiment (CLSST) is different from AMIP only in that the forcing for CLSST is a 12-month SST climatology calculated from the observed SST used in AMIP. In the third experiment (CLGW), the model soil moisture and snowfall are specified to a 12-month climatology calculated from the output of AMIP while SST forcing remains the same as that used in AMIP. In all three experiments, the climate decade of 1979-1988 is simulated.

2. RESULTS

Figure 1 shows the climatology of May-September (MJJAS) averaged rainfall and its difference (AMIP-CLSST). Clearly, the Asian summer monsoon is weaker in AMIP than in CLSST. This feature can also be seen in the changes of atmospheric circulation (Yang and Lau 1996). The strongest signals occur over the central Pacific and the Asian monsoon region. It can be seen from Fig. 2, which shows time evolution of monsoon rainfall and its change due to the impact of SST, that the monsoon is weaker in AMIP during the entire summer season. The variability of SST exerts its strongest influence during the period of monsoon transition in May.

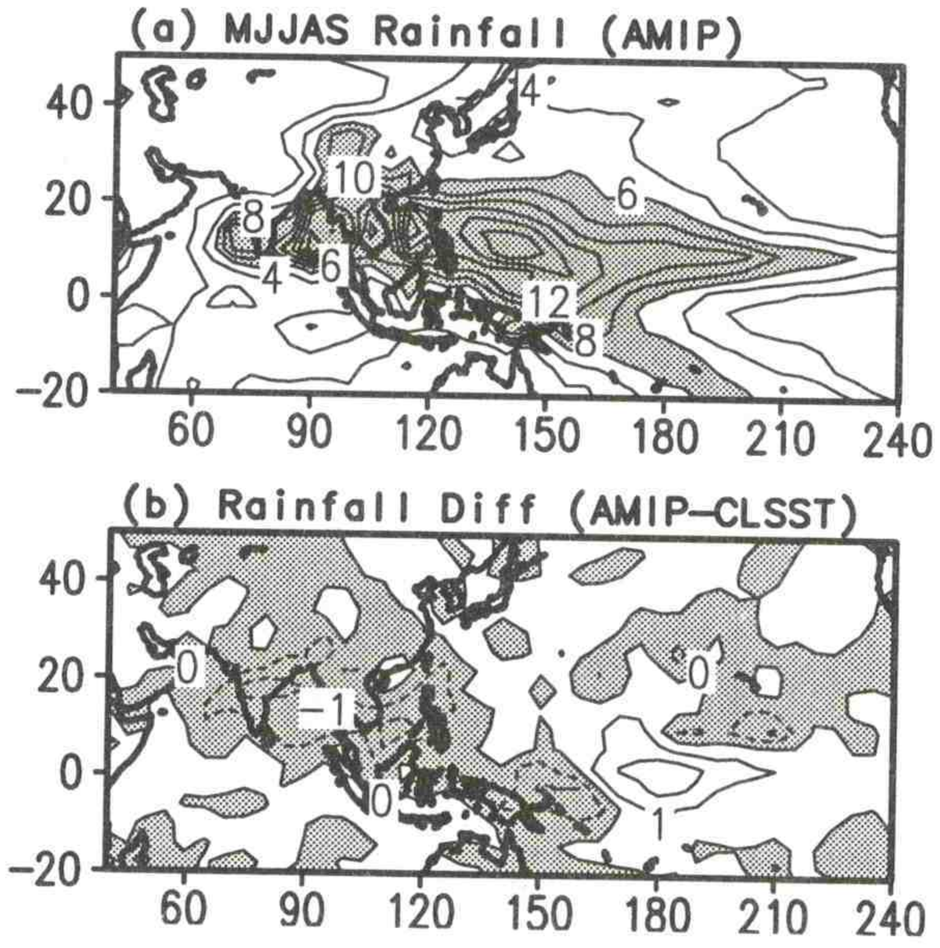

Fig. 1. MJJAS averaged rainfall climatology of AMIP (a) and rainfall difference (AMIP-CLSST; b).

The response of the Asian monsoon to SST variations does not show a two-sided feature. While the monsoon becomes remarkably weaker during the warm events, no indication of monsoon intensification is found during the cold events (Fig. 3). A clear out-of-phase change between the warm and cold events occurs

over the central Pacific: a well-known ENSO feature.

The impact of warm SST on the monsoon is both direct and indirect. The warming of SST in the eastern-central Pacific reduces directly the zonal gradient of sea level pressure across the Pacific which causes weaker trade winds (Fig. 4). The changes in wind regimes lead to changes in atmospheric divergence, diabatic heating and rainfall (see Fig. 3). Results show that the Walker circulation and local Hadley cell become significantly weaker during the warm SST events (not shown).

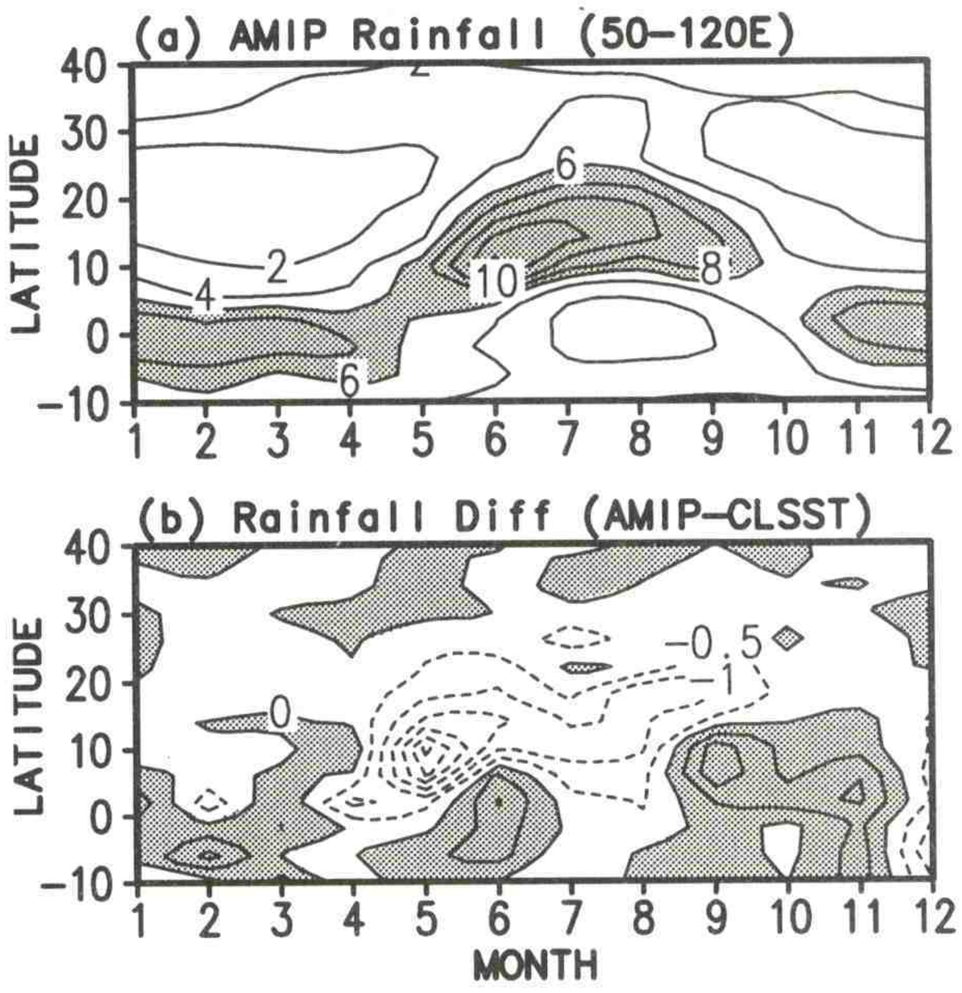

Fig. 2. Time-latitude sections of AMIP rainfall averaged for the Asian monsoon region (a) and difference of the monsoon rainfall (AMIP-CLSST; b).

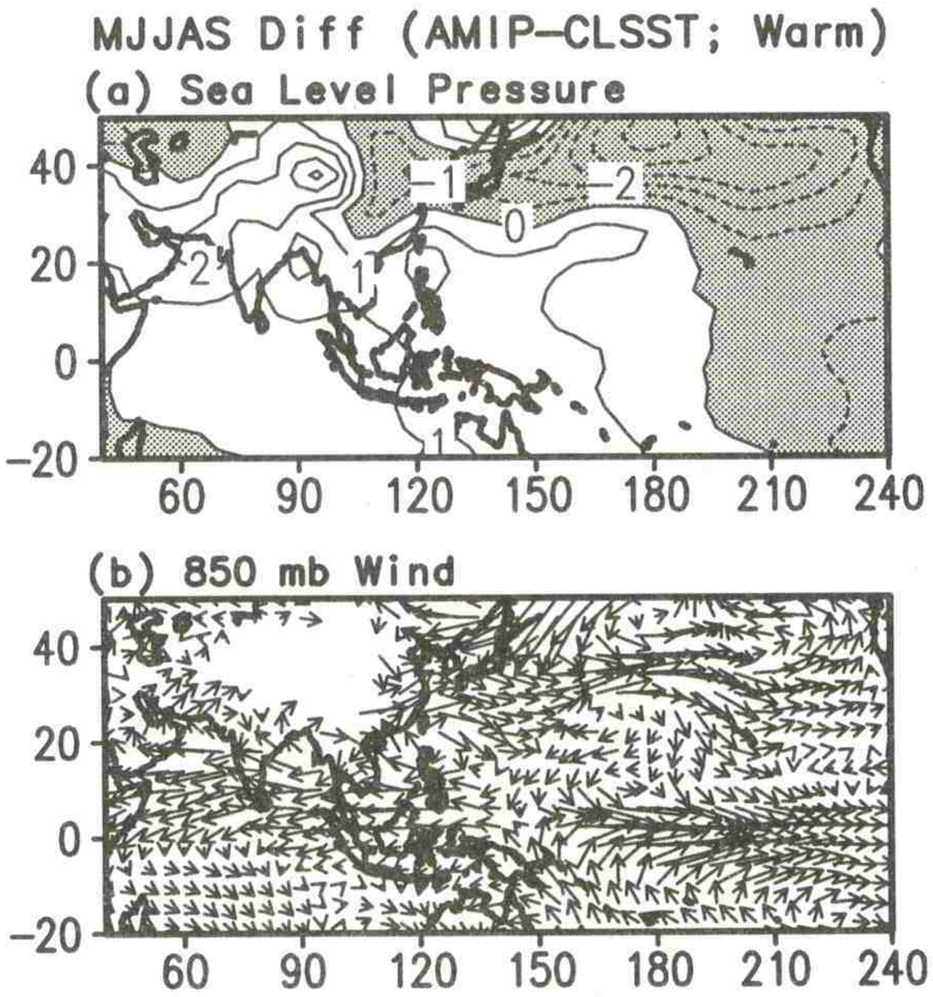

Fig. 4. MJJAS averaged fields of differences (AMIP-CLSST) in sea level pressure (a), 850 mb winds (b) and 200 mb velocity potential (c) for warm SST events.

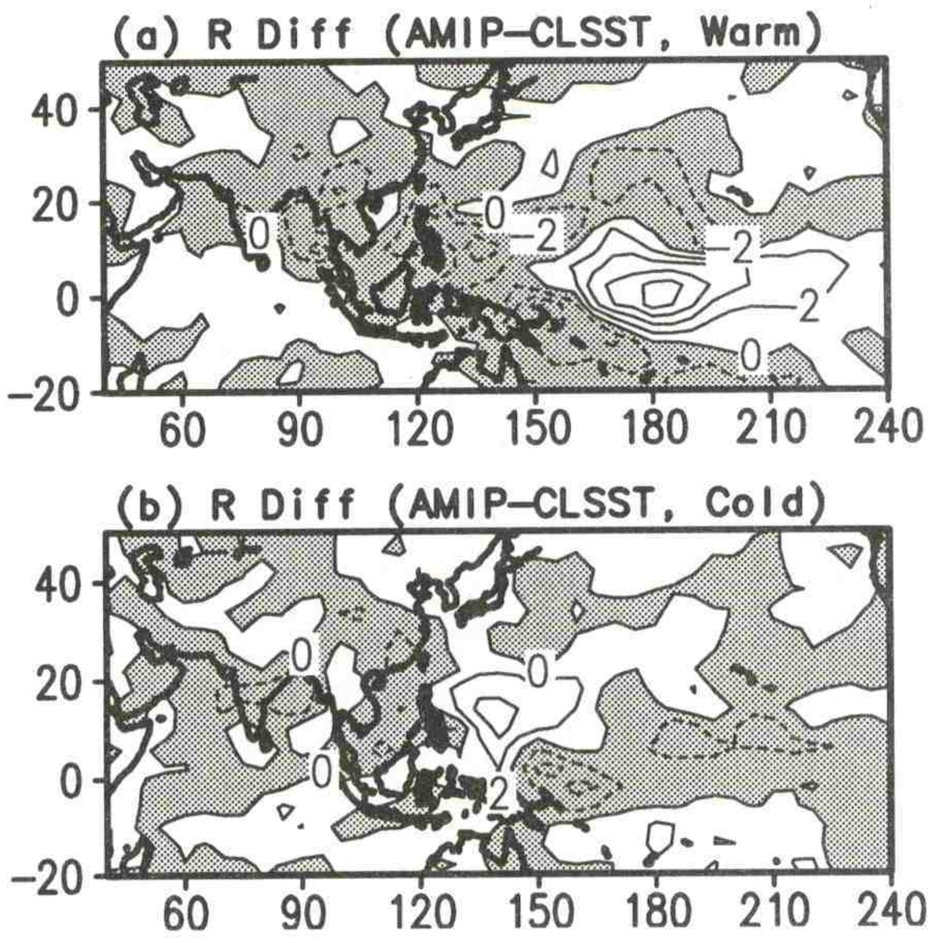

Fig. 3. MJJAS averaged rainfall difference (AMIP-CLSST) for warm (a; 1982, 1983 and 1987) and cold (b; 1984, 1985 and 1988) SST events.

SST's indirect impact on the Asian summer monsoon is through its antecedent influence on the LSPs of the Asian continent. Associated with the warm events, lower surface temperature and higher sea level pressure appear over subtropical Asia during the winter and spring prior to the monsoon season (Fig. 5). This causes an unfavorable change in the driving force (land-sea thermal contrast) for the development of a strong monsoon. The

change in temperature and pressure fields also gives rise to stronger cold-season westerlies over subtropical Asia (not shown), precursory signals of a weak summer monsoon (Yang *et al.* 1996).

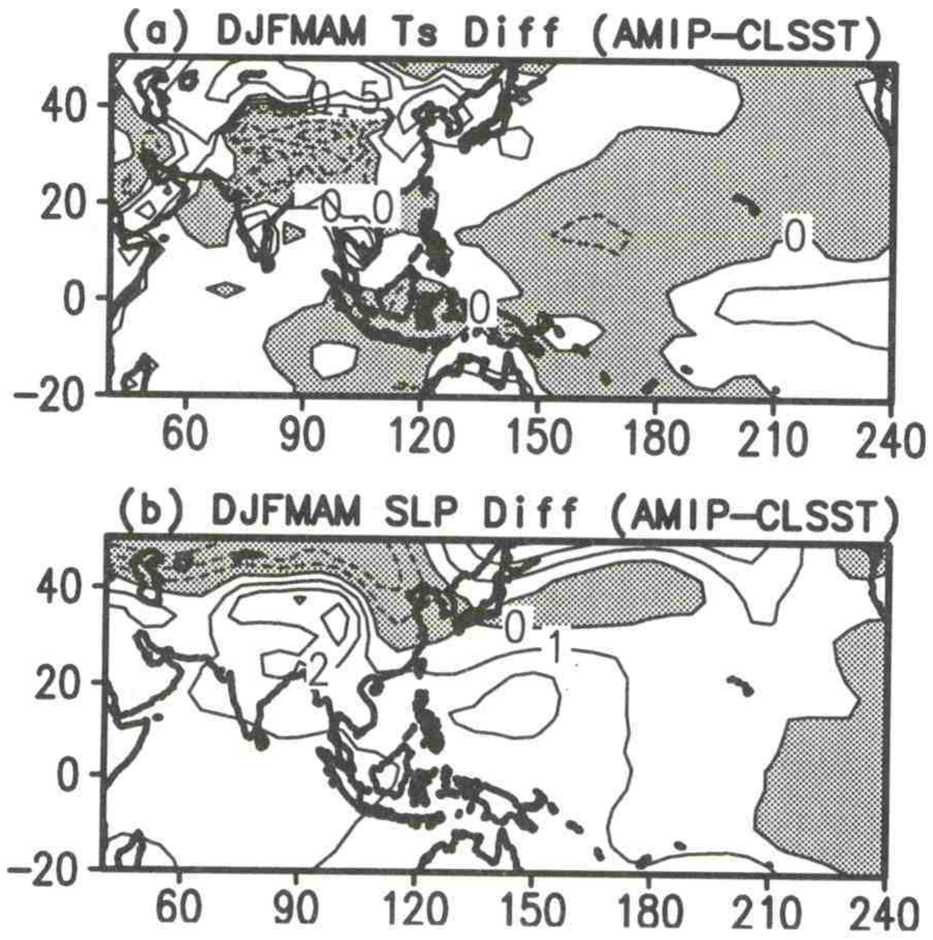

Fig. 5. December-May (DJFMAM) averaged differences (AMIP-CLSST) in surface temperature (a) and sea level pressure (b) for warm SST events.

SST variations play a more dominant role than LSPs in influencing the interannual variability of the Asian monsoon. This is consistent with the observational studies of Yang (1996) and Sankar-Rao *et al.* (1996) and the model results of Lau and Bua (1996) from a different GCM. For CLSST in which the interannual variations of SST forcing are excluded, the Asian monsoon possesses little interannual variability although LSPs change from year to year (Fig. 6). In fact, the interannual variability of the monsoon flow in CLSST is very different from that in AMIP. The monsoon flow in CLSST exhibits a larger mean value and a much smaller standard deviation. On the other hand, the interannual variations of the monsoon flow are more similar to each other in AMIP and CLGW experiments where SST forcing is the same but LSPs are treated in different ways.

Figure 6 also shows that the intensity of the upper tropospheric mean monsoon is reduced significantly from AMIP to CLGW. This change is associated with changes in surface fields and lower tropospheric atmospheric circulation. Figure 7 indicates that compared with CLGW higher land surface temperature and lower sea level pressure occur in a broad region in AMIP. This causes a large-scale change in atmospheric circulation including a stronger monsoon in AMIP than in CLGW. The reason of the continental-scale surface cooling in CLGW is under investigation.

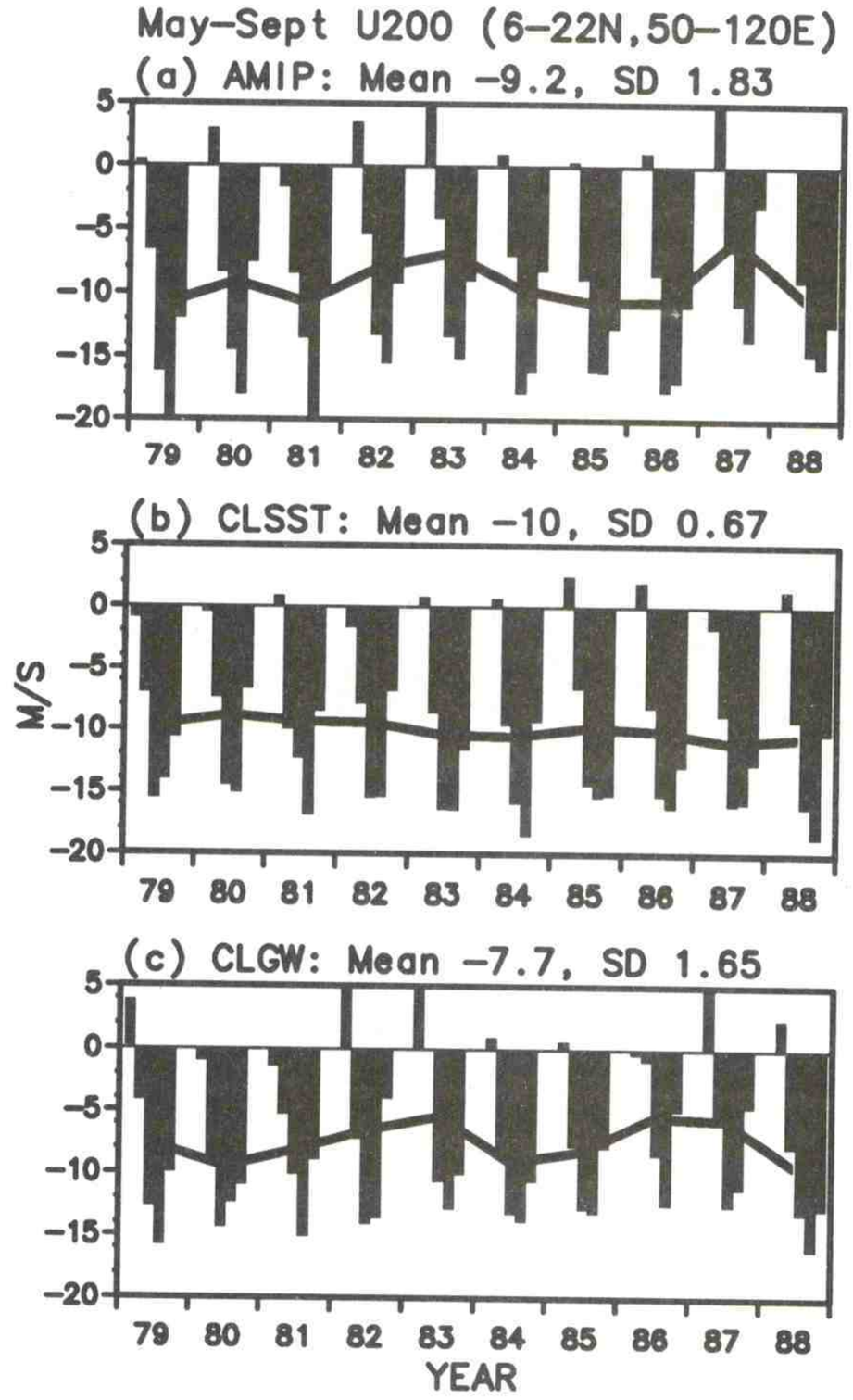

Fig. 6. Monthly values (bars) of May-September 200 mb zonal winds averaged over 6°N-22°N, 50°E-120°E for various experiments. The curves show the MJJAS averaged values of the winds.

3. REFERENCES

Chen, C.-T., and M.-C. Yen, 1994: Interannual variation of the Indian monsoon simulated by the NCAR Community Climate Model: Effect of the tropical Pacific SST. *J. Climate*, **7**, 1403-1415.

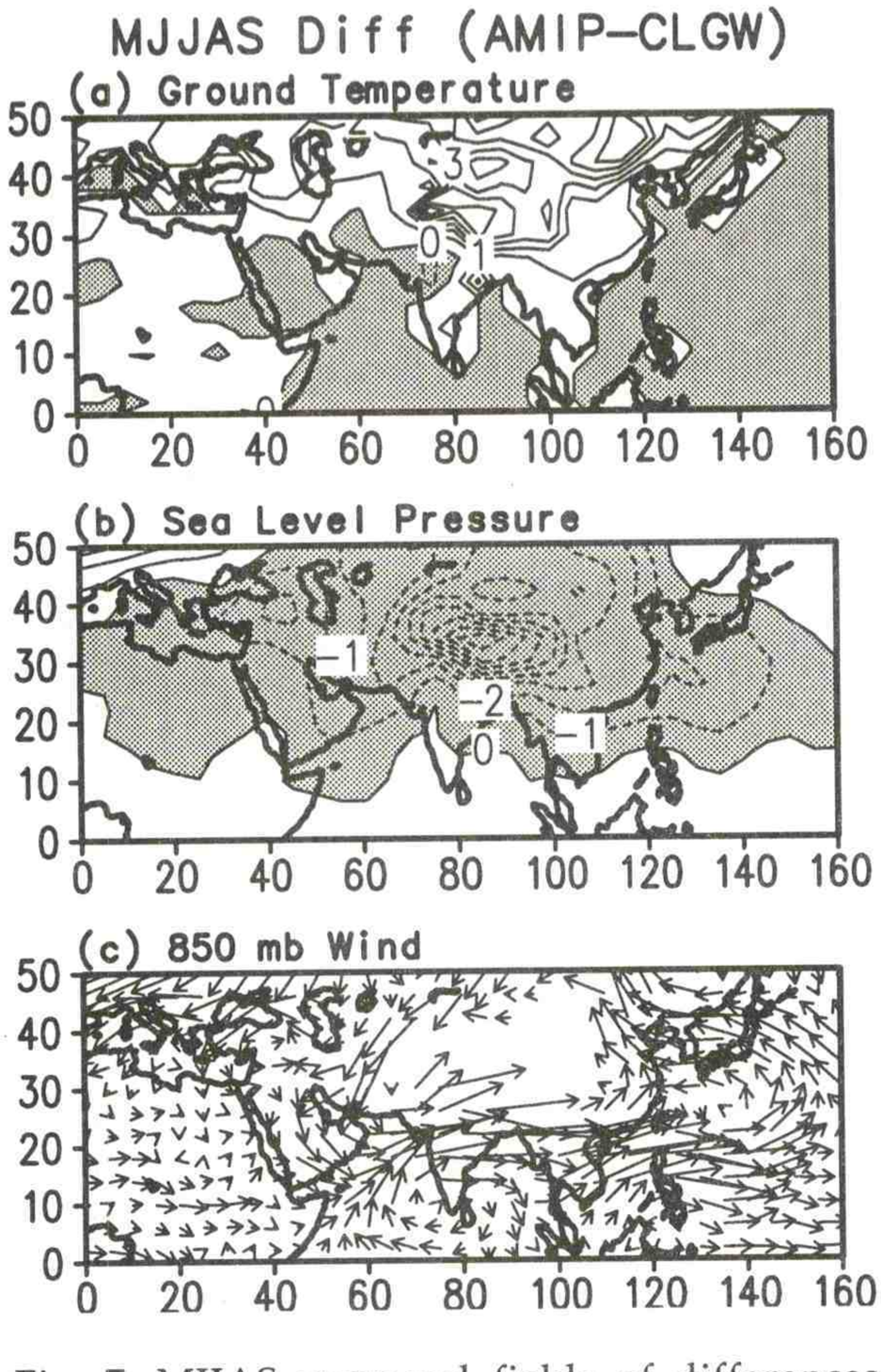

Fig. 7. MJJAS averaged fields of differences, between AMIP and CLGW, in ground temperature (a), sea level pressure (b) and 850 mb winds (c).

Ju, J., and J. Slingo, 1995: The Asian summer monsoon and ENSO. *Quart. J. Roy. Meteor. Soc.*, **121,** 1133-1168.

Lau, K.-M., and W. R. Bua, 1996: The relative impact of SST and land surface anomalies on tropical circulations. AMS Preprints, *76th AMS Annual Meeting/GOALS,* 28 January - 2 February 1996, Atlanta, Georgia.

Lau, K.-M., and S. Yang, 1996: Seasonal variation, abrupt transition and intraseasonal variability associated with the Asian summer monsoon in the GLA GCM. *J. Climate.* (in press)

Li, C., and M. Yanai, 1996: The onset and interannual variability of the Asian summer monsoon and relation to land-sea thermal contrast. *J. Climate.* (in press)

Meehl, G. A., 1994: Influence of the land surface in the Asian summer monsoon: External conditions versus internal feedbacks. *J. Climate,* **7,** 1033-1049.

Palmer, T. N., C. Brankovic, P. Viterbo and M. J. Miller, 1992: Modeling interannual variations of summer monsoons. *J. Climate,* **5,** 399-417.

Sankar-Rao, M., K.-M. Lau and S. Yang, 1996: On the relationship between Eurasian snow cover and the Asian summer monsoon. *Int. J. Climatol.* (in press)

Shukla, J., 1975: Effect of the Arabian Sea surface temperature anomaly on Indian summer monsoon: A numerical experiment with the GFDL model. *J. Atmos. Sci.,* **32,** 503-511.

Vernekar, A. D., J. Zhou and J. Shukla, 1995: The effect of Eurasian snow cover on the Indian monsoon. *J. Climate,* **8,** 248-266.

Webster, P. J., and S. Yang, 1992: Monsoon and ENSO: Selectively interactive systems. *Quart. J. Roy. Meteor. Soc.,* **118,** 877-926.

Yang, S., 1996: ENSO-snow-monsoon associations and seasonal-interannual predictions. *Int. J. Climatol.* (in press)

Yang, S., and K.-M. Lau, 1996: Impact of SST variability and land surface processes on the Asian summer monsoon. AMS Preprints, *76th AMS Annual Meeting/GOALS,* 28 January - 2 February 1996, Atlanta, Georgia.

Yang, S., K.-M. Lau and M. Sankar-Rao, 1996: Precursory signals associated with the interannual variability of the Asian summer monsoon. *J. Climate.* (in press)

Coherent 3-d-Propagation-Patterns in the Energetic Exchange between Tropo- and Stratosphere

Gerhard Schmitz and Norbert Grieger

Institut für Atmosphärenphysik
an der Universität Rostock, Kuehlungsborn, 18221
Germany

Introduction

The dynamical coupling between troposphere and stratosphere is determined by vertical energy propagation of both stationary and transient large scale waves which depends on zonal stratospheric mean wind and temperature fields.
In the following travelling waves and wavepackets in the troposphere and stratosphere have been analysed and an interpretation with wavepattern resulting from baroclinic instability is given. Travelling waves and wavepackets have been detected by application of the method of Principal Oscillation Pattern (POP) to daily geopotential fields. The POP method (Hasselmann 1988, v. Storch et al. 1988) is based on the assumption that the dominant process can be described by a linear equation disturbed by a small noisy forcing. The characteristic matrix can be derived from covariance matrices, and it yields the period of a travelling structure and the e-folding time. The data-base is the geopotential of the winters 1982-93 from the ECMWF-analyses and a data set up to 1 hPa made available to us by W. J. Randel. The POP analyses is compared with a quasi-geostrophic stability calculation, using the zonal mean wind- and temperature-fields of the respective winter seasons. POP analyses in the troposphere and a comparison with quasi-geostrophic-stability theory have been done by Schnur (1993) and Schnur et al. (1993).

Results

a) Single Wavecomponents

The POP analyses for the Southern hemispheric winter data (J J A) yields significant structures with periods between 16 and 8 days for the first three wavenumbers. The comparison with the solutions of the eigenvalue-problem shows a good agreement as well in the spatial pattern as for periods, Tab. 1.

Method	POP-Analyses	Stability Analyses
wave number	period [day]	period [day]
1	16.53	21.1
2	10.03	10.5
3	8.43	8.1

Tab.1 The periods of selected wavenumbers from POP - and linear stability-analyses.

The POP-amplitude and -phase (real part) and the result of the stability calculation are shown in Fig. 1 for the wavenumber 2.
The good agreement of analyses and model indicates that travelling waves in the southern stratosphere are caused by baroclinic energy conversion in the lower troposphere. The phase tilts show vertical energy propagation up to stratospheric heights.

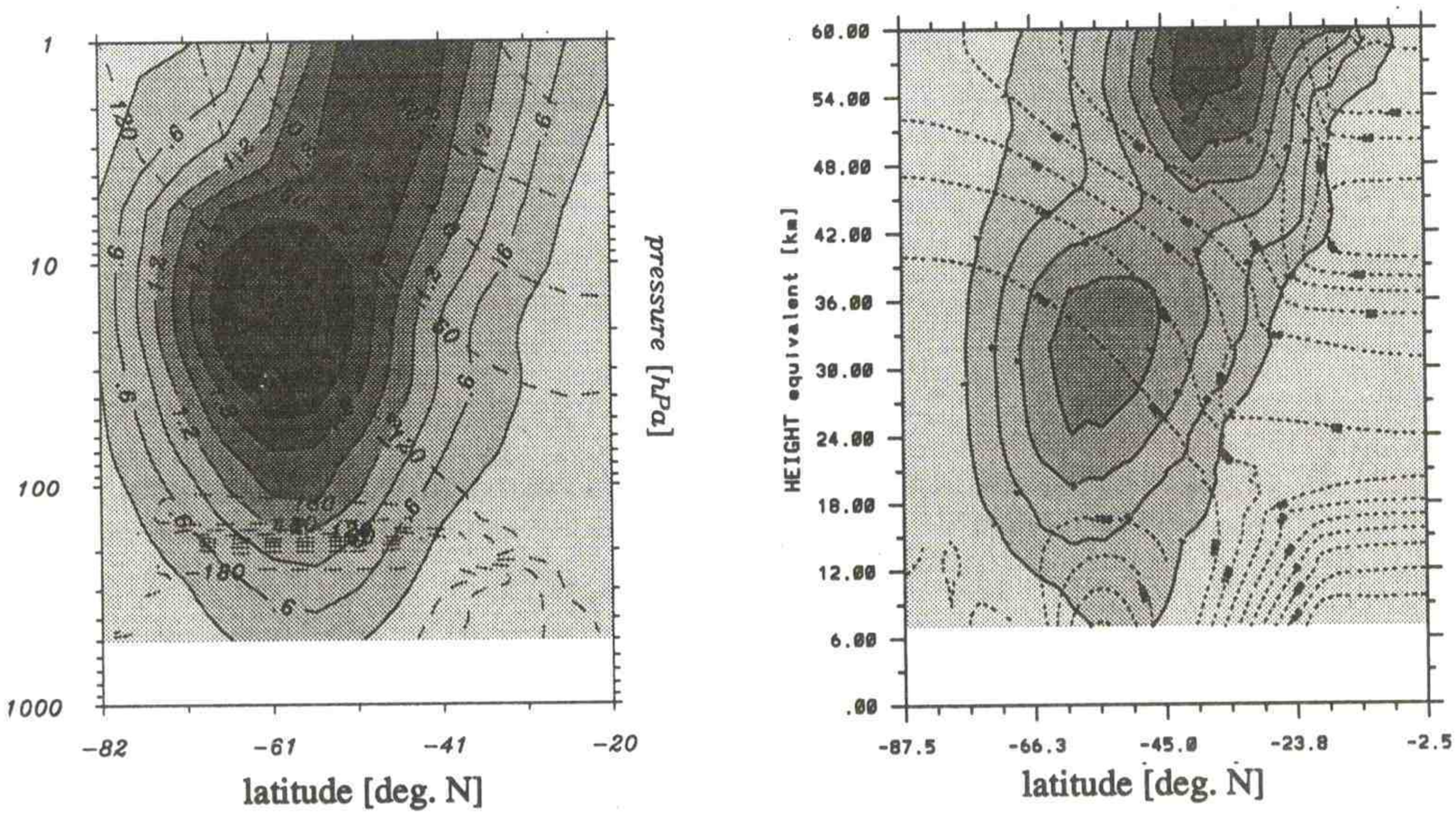

Fig.1 The relative amplitudes (solid lines) and phases (dashed lines) of the POP (lhs) and linear stability analyses (rhs) for wavenumber 2 and JJA Southern hemispheric winter conditions. The oscillation periods are 10.03 days and 10.5 days, respectively.

b) Wavepackets

Two different types of patterns have been detected. The first one (not shown) is domi-

nated by wavenumber 6 in the troposphere, and the structures are located around the stormtrack region of the Northern Hemisphere. This wavepackets have a period of 4-5 days with maximum amplitudes in the lower troposphere, and the growing and decaying phases in the lifecycle of the packet are discernible.

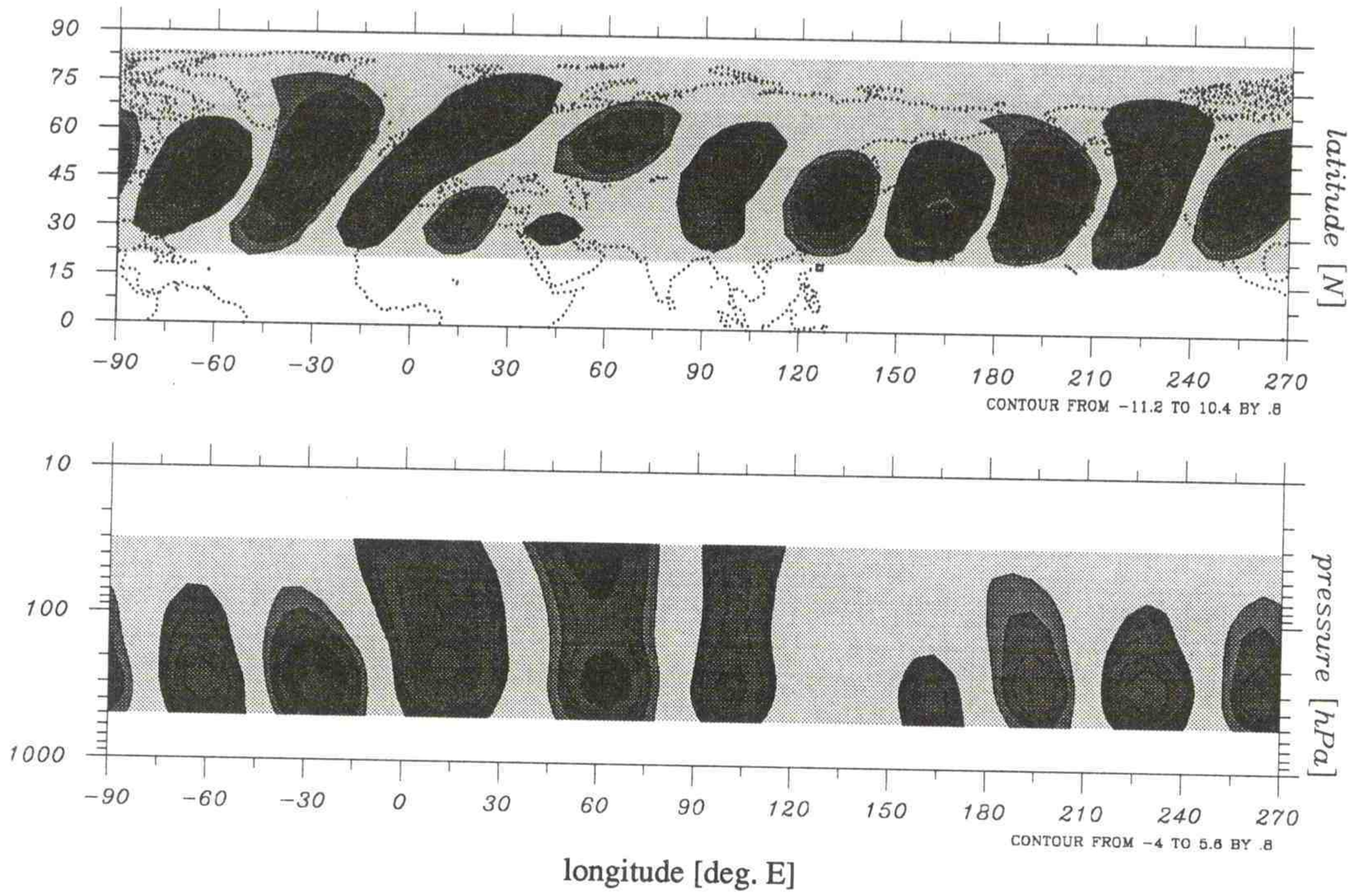

Fig. 2 A horizontal- (upper part) and vertical-cross section (lower part) of a 3-dimensional POP structure (imaginary part), period 7.87 days, at 250 hPa and at 57 °N, respectively. (ECMWF analyses)

The POP, shown in Fig. 2, has a period of 7.87 days and propagates up to stratospheric heights. This vertical wave propagation is discernible downstream of the Atlantik stormtrack region from the westwards phase inclination with height. The horizontal cross-section of the pattern shows a strong south-west - north-east tilt over the Atlantik region and seems to be connected with the decay phase of a baroclinic wavepacket lifecycle.

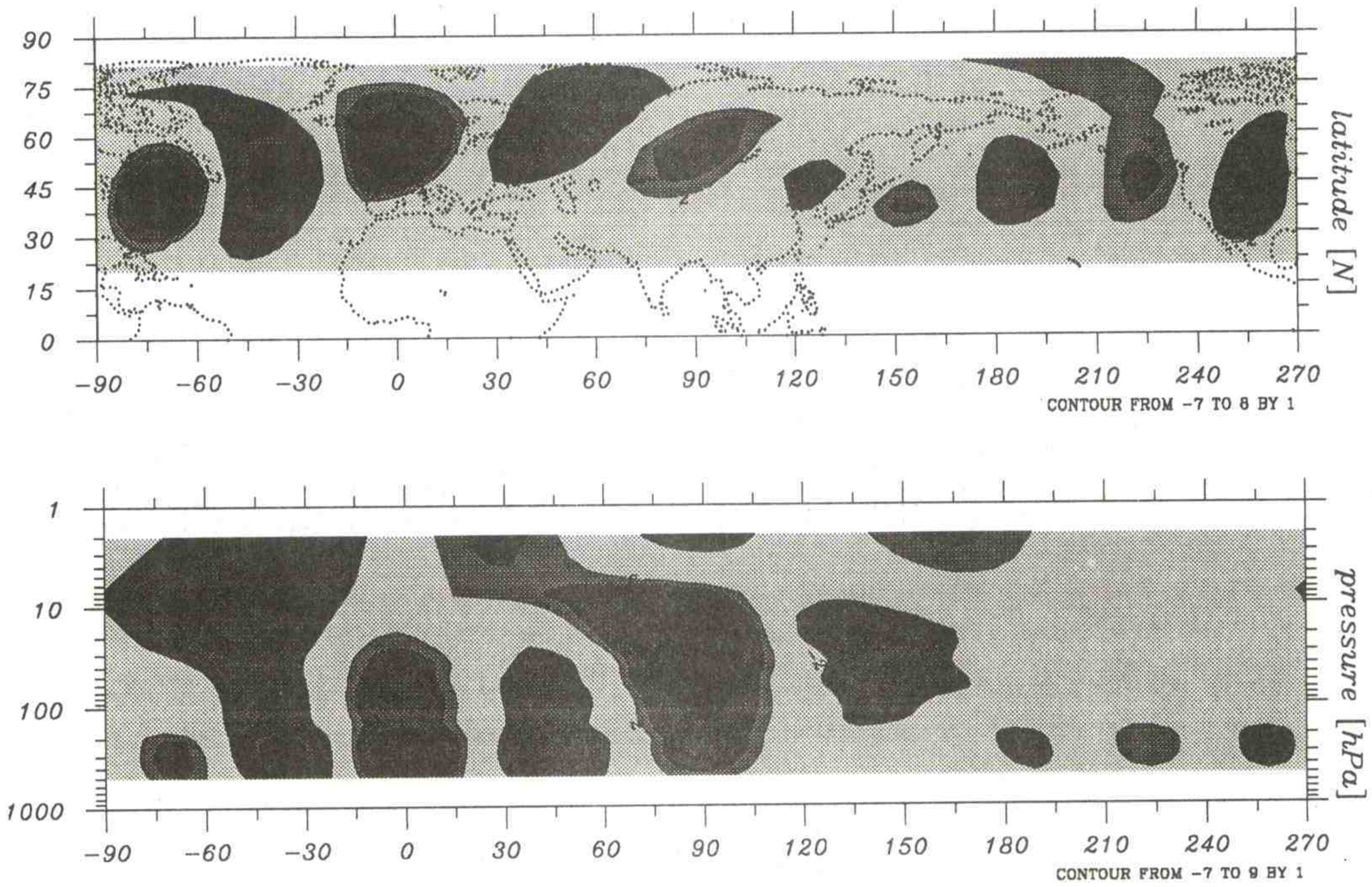

Fig. 3 A horizontal- (upper part) and vertical-cross section (lower part) from a 3-dimensional POP structure (imaginary part), period 9.01 days, at 250 hPa and 55.6 °N, respectively. (data from W. J. Randel)

In Fig. 3 is shown a POP with a period of 9.01 days and it is clear to see the filtering of shorter waves during its propagation to stratospheric levels.
Summarizing, the results show that the POP-method well identifies travelling wavepackets which propagate into stratospheric heights and are connected with the baroclinic energy conversion process.

Acknowledgement

We are grateful to W. J. Randel for the permission of using the NCAR geostrophical height fields up to 1 hPa and copying the data sets.

Literature

Hasselmann, K., 1988, J. Geophys. Res., 93, 11015-11021.
v. Storch, H., T. Bruns, I. Fischer-Bruns, K. Hasselmann, 1988, J. Geophys. Res., 93, 11022-11036.
Randel, W. J., 1987, NCAR Technical Notes, NCAR/TN-295+STR.
Schnur, R., G. Schmitz, N. Grieger, H. v. Storch, 1993, J. Atmos. Sci., 50, 2386-2400.
Schnur, R. 1993, Examensarbeit, 16, Max-Planck-Institut für Meteorologie, Hamburg.

LAND SURFACE TEMPERATURES

Alan Basist* and Tom Peterson**

*Climate Prediction Center, NWS/NCEP/CPC, Washington, DC 20233
**Global Climate Lab, NCDC, NOAA, Asheville, NC 28801

Introduction

A global network of shelter-height temperatures, composed of in-situ and satellite data, has never been operationally available. The potential benefits from such a data set are invaluable, monitoring: the effect of temperature on crop development, snow melt over remote mountains, model validation, and climate variability, to name a few. A technique of blending in-situ and satellite measurements has been very successful over the ocean. We are developing a similar product over land.

Unfortunately, land surfaces are highly irregular, compared to ocean surfaces, and these gradients are significantly more difficult to resolve. Since in-situ measurements are very limited over many areas, it is necessary to use satellite observations to identify the temperatures gradients. However, filters and corrections must be applied to satellite measurements before they can be accurately related to shelter height temperatures. The biggest noise in visible and infrared observations is clouds; whereas, in the microwave spectrum it is the surface emissivity. Many attempts to remove these features have achieved various grades of success. However, none of them have been deemed successful enough to run in an operational mode.

Our approach to the problem is to blend in-situ shelter, and satellite microwave measurements. We use observations from the network of stations reporting over the Global Telecommunication system and the Special Sensor Microwave Imager SSM/I on DMSP satellites. The in-situ measurements serve as an anchor to the satellites derive temperatures. We also correct for surface emissivity effects associated with surface wetness, snow cover, bare soil, rain, etc. Preliminary results show that reasonable adjustments can be achieved, and that a blended product could provide a useful field of global land surface temperatures.

Data Sets

The SSM/I instrument has unique microwave signatures for various land surfaces. These signatures are used to identify the shelter height temperature over around the globe. For instance, a vegetated surface has a emissivity near 0.95 in the 19 GHz wavelength, and temperature rises slightly as frequency increases. Snow has a slightly lower emissivity, and temperature goes down with frequency. Wet ground has a low emissivity at 19 GHz, the temperature rises with frequency. These relationship between the channel measurements serve as the basis in

discriminating the different surfaces.

The global network of stations that report shelter height temperatures is used to anchor satellite gradients. Approximately 1700 stations currently report on a regular basis to the near real-time data base, and a larger network is available a month later. These stations will be quality controlled by various filter, in order to screen out questionable data. The good values are earth located, and the shelter height coordinates will be run through a Digital Elevation Model (DEM), which will translate the specific elevation to a mean pixel elevation of the satellite observation. A lapse rates derived from the *in situ* measurements at various elevations will serve as a first guess to the vertical temperature gradients in an area. We will also explore additional information to translate the *in situ* temperatures to mean pixel temperatures.

Proof of Concept

The afternoon passes of the SSM/I instrument were processed for July 1992. The combination of channels measurements were passed through a preliminary decision tree, which associates a surface type and a dynamic surface emissivity adjustment to each pixel. The derived shelter height temperature was calculated at 1/3° resolution for this month (Fig. 1a). Then monthly, mean maximum temperature from the 5000 *in situ* observations (the U. S. cooperative network) were used as ground truth in the study (Fig. 1b). Note the smooth nature of the satellite data, compared to the *in situ* observations. Also note the satellite gradients over regions of high terrain: i.e. the Sierra Nevada and Appalachian Range. Over much of the country difference between these two temperature fields are less than 1° K, and many of the larger differences occur over regions of high terrain (Fig 2a). Therefore they be reduced when the lapse rate between shelter and mean pixel elevation is removed. (This will be implemented when a more sophisticated blending technique is used.). Finally, the smoothed difference fields (using a 2° resolution smoother) is added back to the satellite temperature. Fig. 2 shows how the two fields can be blended together into a single product.

We must still spend a considerable amount of work refining the algorithm, and merging the two data sets together. We will improve the current algorithm by investigating numerous schemes to derive shelter height temperature from the satellite channel measurements. We must also find an effective procedure to merge *in situ* point observations to spatially integrated measurements from the satellite, realizing there can be considerable variability within a pixel. It appears that we can extract quality information from each data set, and produce a superior analysis of land surface temperatures. The in-situ measurements will provide the anchor, while the satellite observations will identify the spatial temperature gradients around the world.

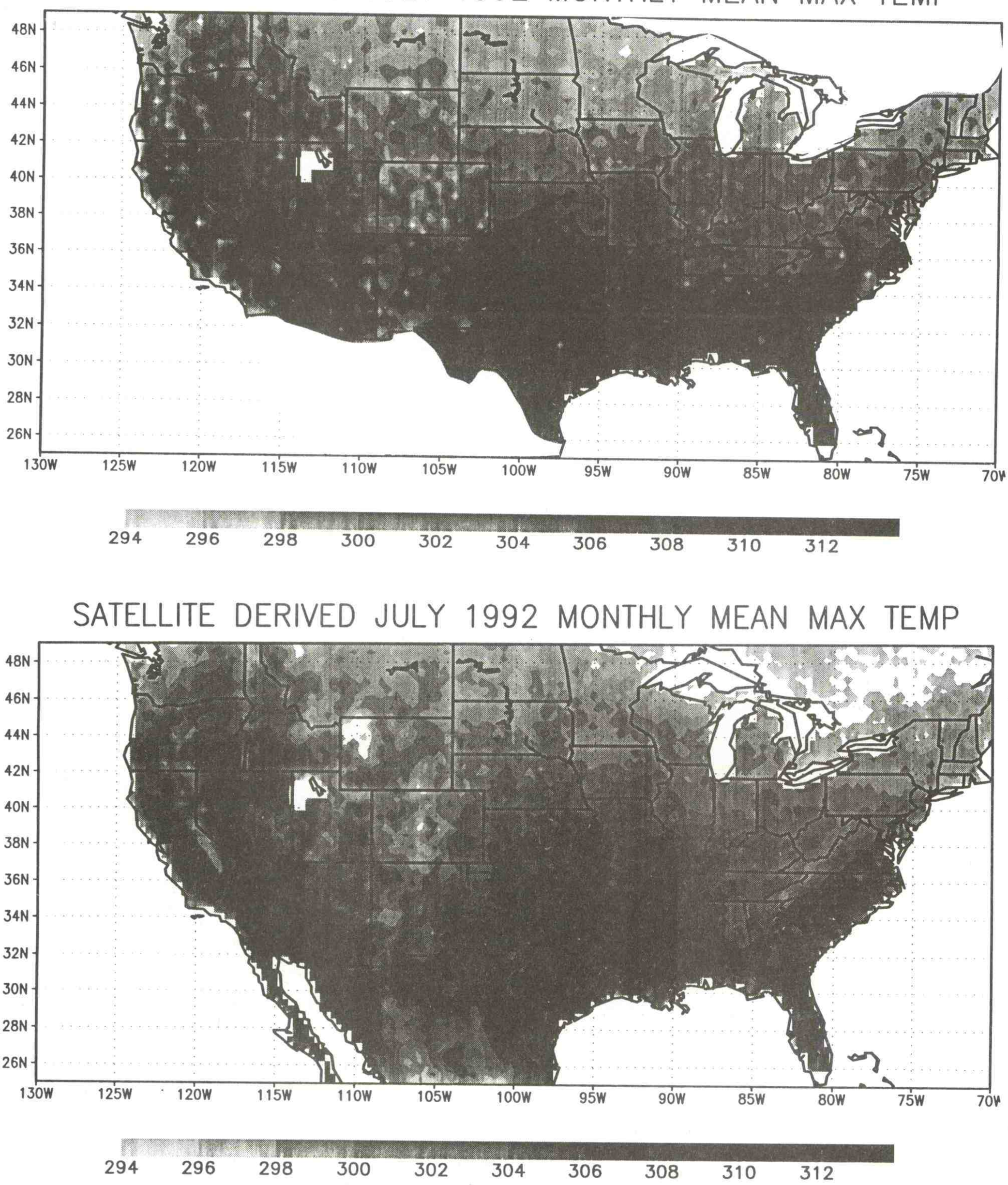

Figure 1. A. *In situ* shelter height temperatures from the U.S. cooperative network gridded at 1/3° resolution. B. Shelter height temperatures, simulated from the SSM/I channel measurements, are also gridded to 1/3° resolution. Note the smooth structure of the satellite grid and the gradients over the Appalachian, Sierra Nevada and Rocky mountains.

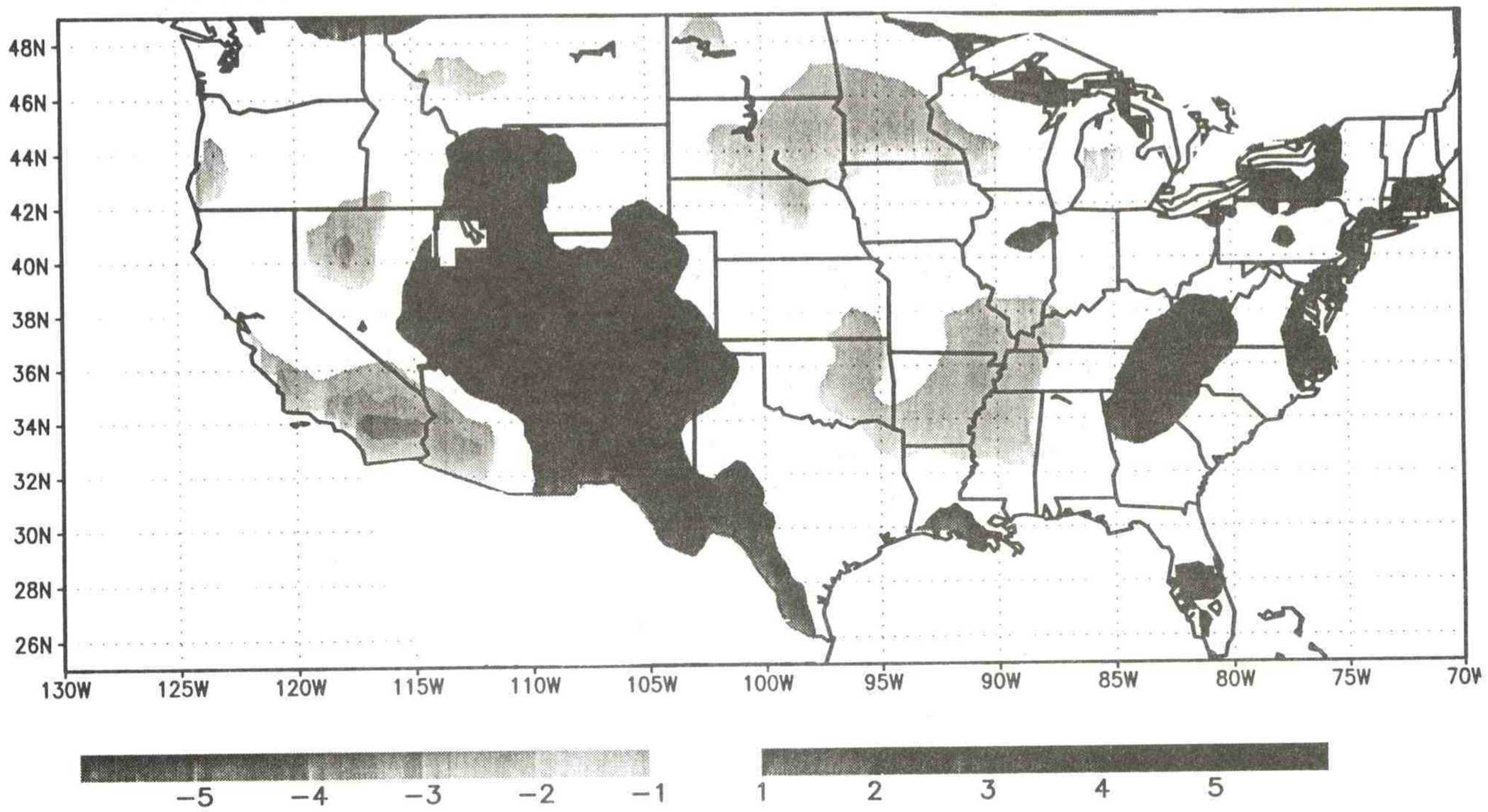

Figure 2. A. Spatially smoothed difference fields between *in situ* and satellite derived, shelter height temperatures. The differences are less than 1° K over much of the country. Ignore territory outside of the U.S. border, since no *in situ* observations were used from these areas. B. The difference field has been added back to the satellite measurements. The final temperatures are anchored on the *in situ* observations, while satellite provides the gradients.

Early Comparisons of the GPCP Combined Data Set Suite with Individual Estimates and Climatology

George J. Huffman[1], Robert F. Adler[2]
1: SSAI, Laboratory for Atmospheres, NASA/GSFC
2: Laboratory for Atmospheres, NASA/GSFC

The Global Precipitation Climatology Project (GPCP) is almost ready to release the first sample (covering July 1987 to December 1992) of a set of precipitation estimates obtained by combining several independent global precipitation data sets:

- The microwave estimate is computed with the Chang-Wilheit emission-based technique over water and the NOAA scattering-based technique over land, both applied to Special Sensor Microwave/Images (SSM/I) data.
- The infrared estimate is computed with the GOES Precipitation Index technique from three-hourly geosynchronous IR images, with gaps in coverage filled by low-orbit IR data.
- The raingauge analysis is computed with the SPHEREMAP procedure from an error-checked collection of about 6500 gauges.
- The four-dimensional data assimilation (4DDA) estimate is taken from the Goddard EOS assimilation system, version 1.

Error

The computation and presentation of precipitation error is a thorny problem due to the wide variation of climatic regimes and lack of verification data.

We make the assumption that sampling error dominates the total error in most places. We are working to develop a better theory-based functional form for sampling error. On the presentation side, displays of both absolute and relative error are unsatisfactory for comparing the skill of the various techniques because global fluctuations in precipitation dominate the fields. Instead, we estimate the "equivalent number of gauges" it takes to give the error attributed to each grid box. This is done by inverting the appropriate expression for gauge error to get "equivalent gauges" as a function of error variance and other parameters. [This computation can be reversed to recover error, if desired.]

Combination Procedure

The combination procedure sequentially combines the data sources listed above, shown in Fig. 1. It closely follows Huffman et al. (1995), who provide more details. Philosophically, bias errors are corrected where possible (in the AGPI

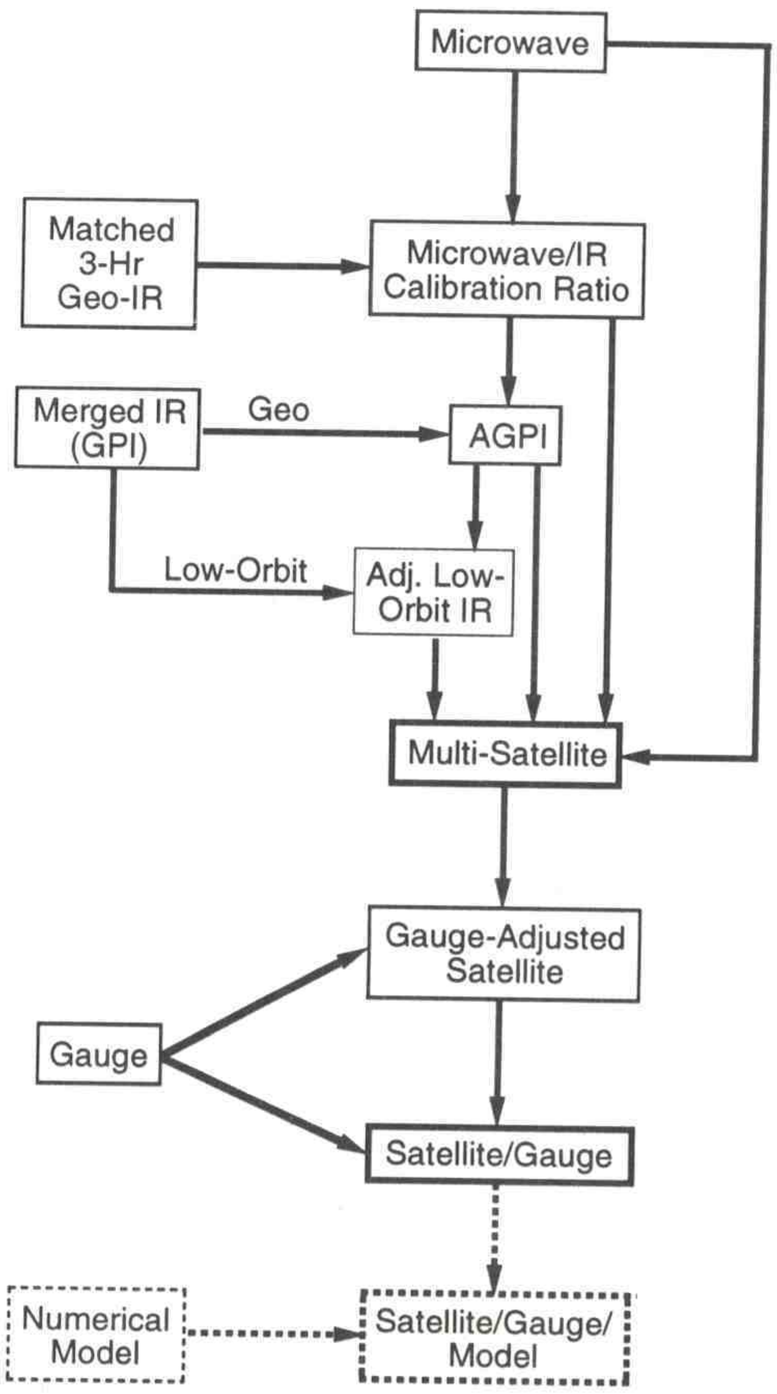

Fig 1. SGM Method for estimating global precipitation by combining several independent estimates.

step, described in Adler et al., 1994), and in the Gauge-Adjusted Satellite step), and independent estimates are combined using the inverse of the (spatially varying) error variance for weighting. The results of the combination are a set of products:

- multi-satellite (S, includes microwave and IR),
- satellite-gauge (SG, includes S and gauge), and
- an experimental satellite-gauge-model (SGM, includes SG and 4DDA).

Examples

A few quick comments are presented here to highlight particular features in the figures. Fig. 2 shows reasonable continuity in the precipitation field for an individual month despite significant changes in data source (marked by jumps in estimated error). The general pattern of average SG precipitation in Fig. 3 compares favorably with the average Jaeger precipitation, although closer inspection reveals regional differences. The boreal summer-winter difference and the boreal-winter (1992 El Niño) — (1989 La Niña) difference shown in Fig. 4 show important regional differences from other methods (not shown), particularly in the maritime continent and eastern tropical Pacific. Fig. 5 shows no strong reaction to changes in SSM/I data availability, although interseasonal and interannual variations are noticeable. Overall, the SGM and Jaeger means differ by only 0.08 mm/day (2.6 vs. 2.7) and the difference in typically largest in boreal summer.

Final Note

Information on the status of the GPCP version 1 combined datasets may be obtained by contacting Dr. George J. Huffman, (301) 286-9785 or huffman@agnes.gsfc.nasa.gov .

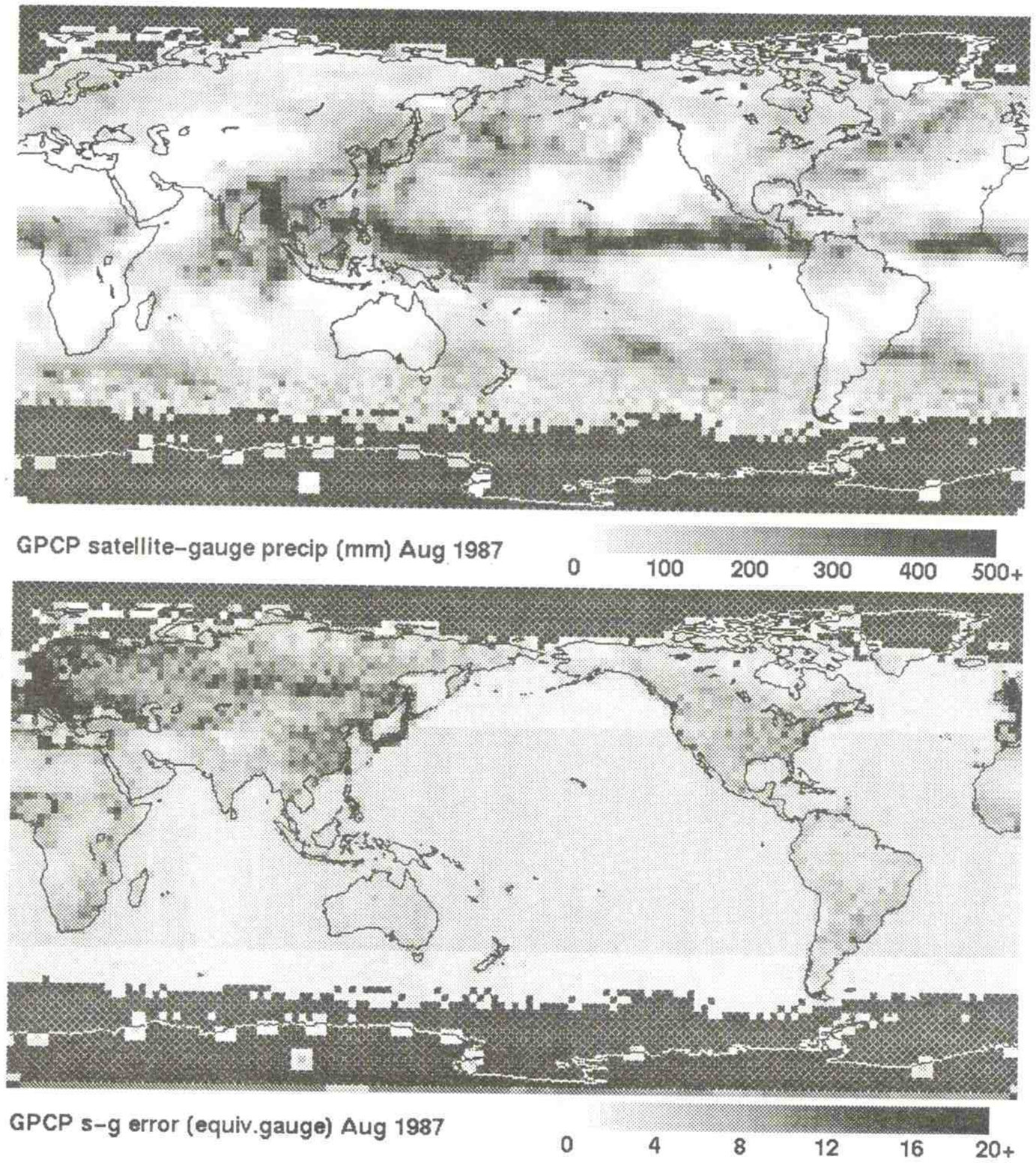

Fig. 2 Precipitation (top, in mm/mo) and error (bottom, in number of equivalent gauges) estimated in the SG product for August 1987.

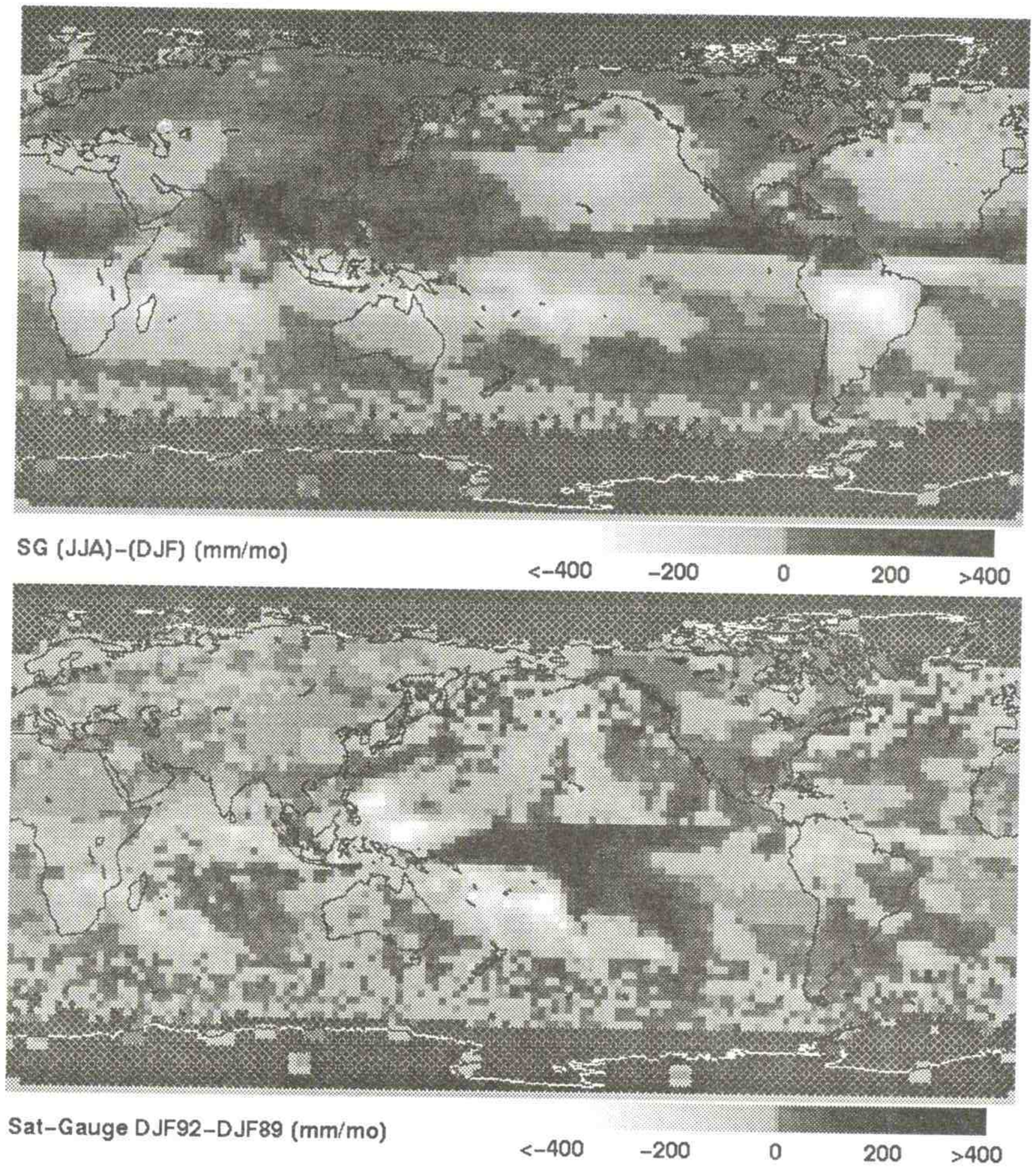

Fig. 3 Average precipitation for the SG product over 1988 through 1992 (top), and "matched" average precipitation for the Jaeger climatology (bottom), in mm/mo.

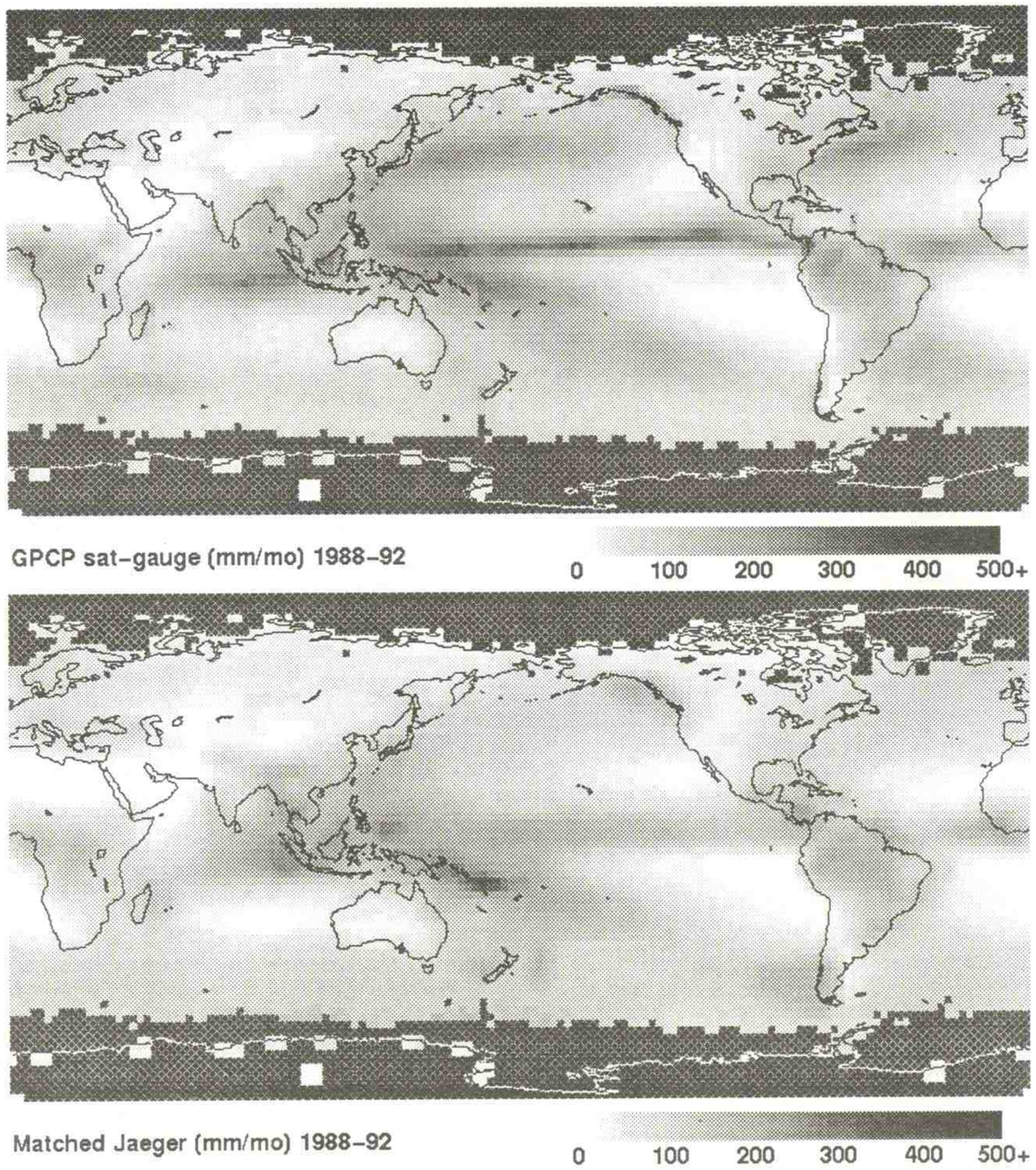

Fig. 4 Difference between JJA and DJF in the 1988-1992 average SG precipitation (top), and difference between DJF 1991-92 and -DJF 1988-89 SG precipitation averages (bottom), in mm/mo.

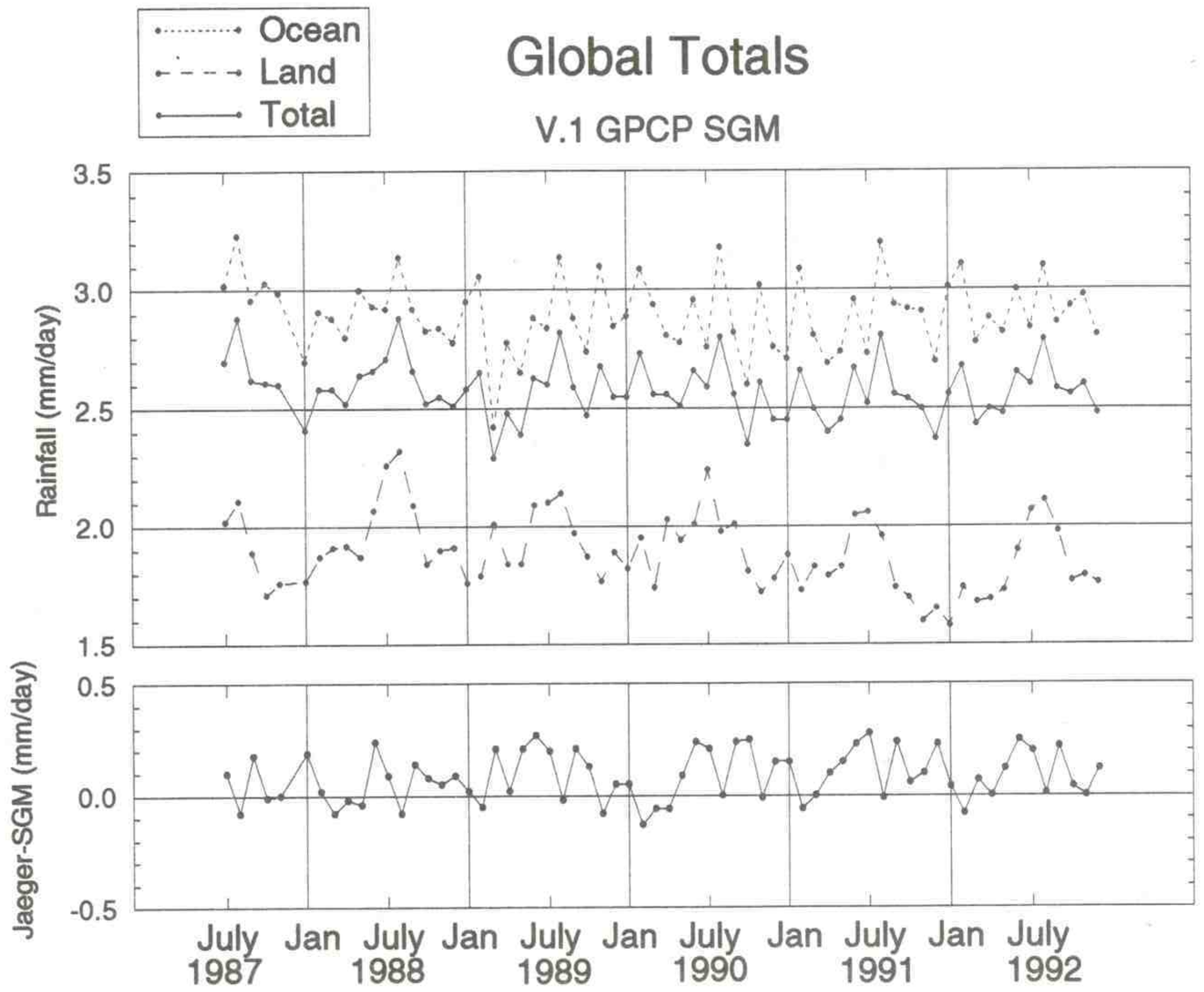

Fig. 5 Time series of global-average SGM precipitation for ocean (dotted), land (dashed), and all (solid) areas (top), and of the difference between the global totals from the Jaeger climatology and the SGM (bottom), all in mm/day.

NASA Reanalysis: An Overview of Results and Future Plans

S. Schubert, H.M. Helfand and C.-Y. Wu
Data Assimilation Office
NASA/GSFC
Greenbelt, MD 20771

1) Status of GEOS-1 Reanalysis

Version 1 of the Goddard Earth Observing System (GEOS-1) Data Assimilation System (Takacs et al. 1994; Suarez and Takacs 1995; Pfaendtner et al. 1995) was "frozen" in March of 1993. This version of the GEOS system was established by the Data Assimilation Office (DAO) to provide a benchmark for further development, and to provide a stable system for generating assimilated data sets for use by the research community. One of the immediate applications of the GEOS-1 system was to generate a long-term reanalysis of historical data (Schubert et al. 1993). The first five years (3/85-2/90) were completed in May of 1994 (Schubert et al. 1995), and a workshop was held at Goddard in March of 1995 to obtain user feedback, both on the quality of the assimilated data and on the method of distribution. The results of the workshop, including a summary of known problems and development efforts to address them, are described in Schubert and Rood (1995). The assimilation has now been extended through 1993. Current plans are to continue the assimilation with GEOS-1 to cover the period 1979 - 94. It is anticipated that this project will be completed sometime during the summer of 1996.

The next section presents an example of an application of the GEOS-1 assimilation to study the hydrological cycle over the United States. The focus is on the moisture transport associated with the Great Plains low level jet. The final section summarizes the anticipated changes that will be incorporated into the next (intermediate) version of the GEOS system.

2) U.S. Moisture Transport

This study examines the dominant time scales and structures of the low level winds responsible for transporting moisture from the Gulf of Mexico into the central U.S. during spring and summer. The approach is based on a compositing technique which employs a wavelet analysis (Weng and Lau 1994) to isolate the dominant time scales of the low level flow.

The top panel in Figure 1 shows, as an example, the time series of the northward boundary layer moisture transport during the spring and summer of 1994 at a grid point near Ft. Worth, Texas. The wavelet decomposition is shown in the bottom panel. The results of the wavelet analysis shows a number of distinct time scales in the low level moisture transport. The strong signature of the spring storms is clearly evident (synoptic time scales, 2-8 days) During June longer intraseasonal time scales appear to replace the synoptic signal. During summer a very strong and regular diurnal cycle dominates the spectrum. July is also marked by a general enhancement of the seasonal cycle characterized by an overall increase in the northward moisture transport, presumably in association with the flood conditions that prevailed over the midwest during much of that summer.

In order to better understand the nature of the fluctuations, the time series of the wavelet coefficients were used to composite the extreme (+/- 1 standard deviation) occurrences of moisture fluctuations at Ft. Worth on diurnal, synoptic (2-8 days) and low frequency intraseasonal (8-32 days) time scales. The results are based on the 9 years of assimilation (1985-93) currently available for the spring and summer months (May - August). Figure 2 shows an example of various composite fields on the synoptic time scales computed as the difference between periods with enhanced and suppressed northward transport. The upper left panel shows the low level moisture transport anomaly superimposed on the precipitation anomaly obtained from the GEOS-1 assimilation. The midwest shows positive precipitation anomalies greater than 2 mm/day, while much of the east coast has reduced precipitation of more than 1 mm/day. The lower left panel is the same as the upper left, except that the precipitation is from station observations. The similarity with the GEOS precipitation suggests the assimilation is providing a reasonable picture of the synoptic fluctuations. The upper right panel shows the winds at approximately 300mb. The enhanced low level moisture transport is coupled with a well-defined upper level wave train characterized by cyclonic flow over the western United States and anticyclonic flow over the eastern half of the country. The vertical cross section at 36N (lower right panel), shows the synoptic signal is characterized by a vertically extensive moisture and wind anomaly.

Current efforts are devoted to comparing the synoptic signature of the low level winds to the diurnal and longer time scales, as well as, determining the time evolution (or life cycle) of these composite structures.

3) The Next GEOS System

Development efforts are currently aimed at providing an intermediate "frozen" system to be ready by sometime early 1996. This system is considered intermediate with respect to the 1998 GEOS system which will be used to assimilate the wide array of EOS and other satellite and in situ observations that will become available at that time. The anticipated changes to the GEOS-1 GCM include a gravity wave drag parameterization, substantially increased vertical resolution (70 levels) with a model top at 0.01mb, a new radiation code consistent with the higher model top, the ability to rotate the computational pole, and substantial retuning of the clouds and the convective parameterization (Relaxed Arakawa Schubert). The optimal interpolation (OI) analysis system will be replaced by the new Physical-Space Statistical Analysis System (PSAS) developed at the DAO. This scheme avoids the data selection problem inherent in the current OI scheme by solving the system globally. The system also provides greater flexibility in the specification of the error covariances, and the incorporation of new data types. Other on-going developments (which may or may not get into this version of the system) are the incorporation of a land surface model and a prognostic cloud water/ice scheme. Current plans are to reanalyze 1979 with this system.

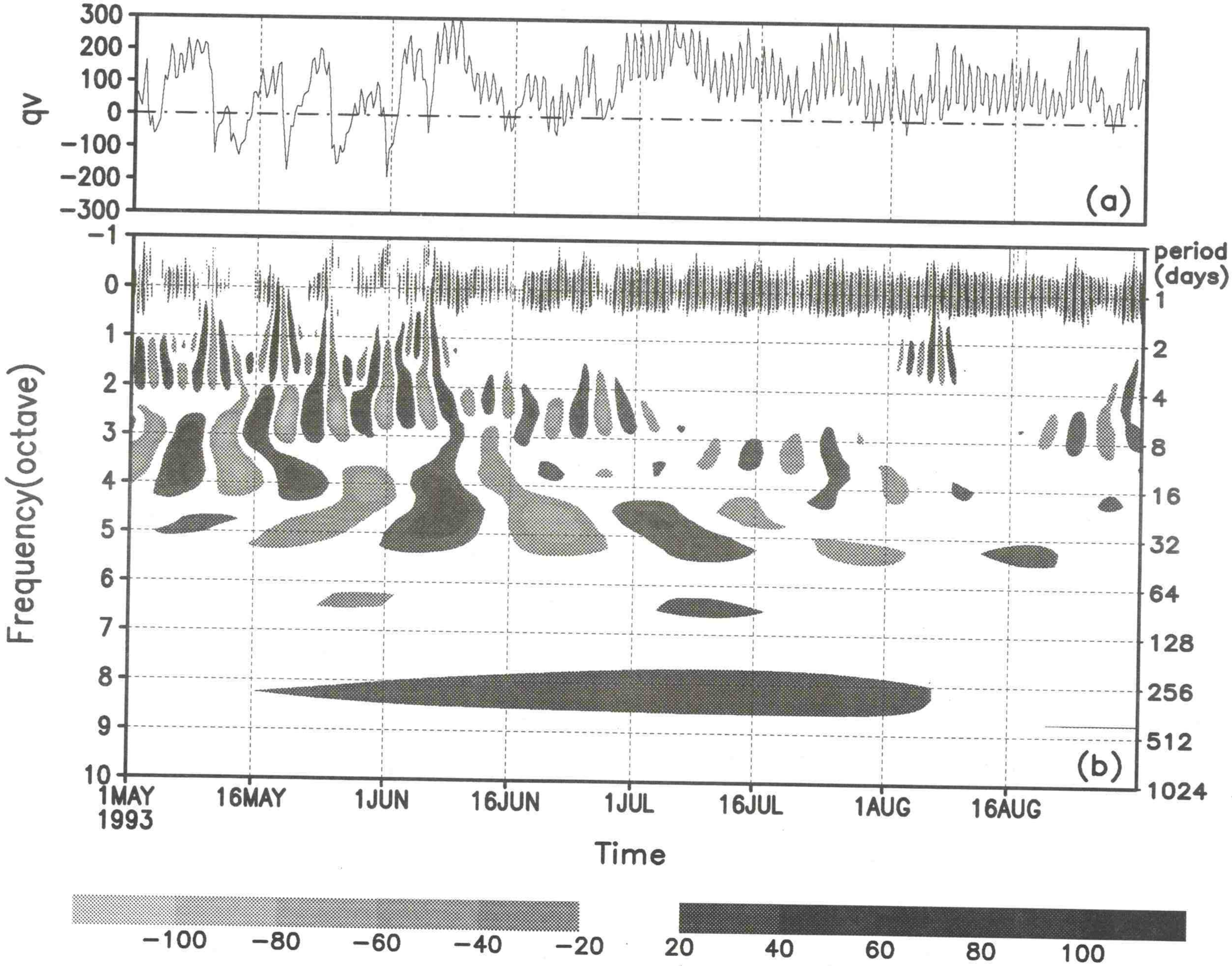

Figure 1: Wavelet analysis of vq at 32N, 97.5W shown for the period May - August of 1993. The top panel shows the time series of *vq* . The bottom panel shows the real part of the wavelet transform. Units are $(m/s\ g/kg)^2$. The wavelet analysis was perform on the entire 9 year record.

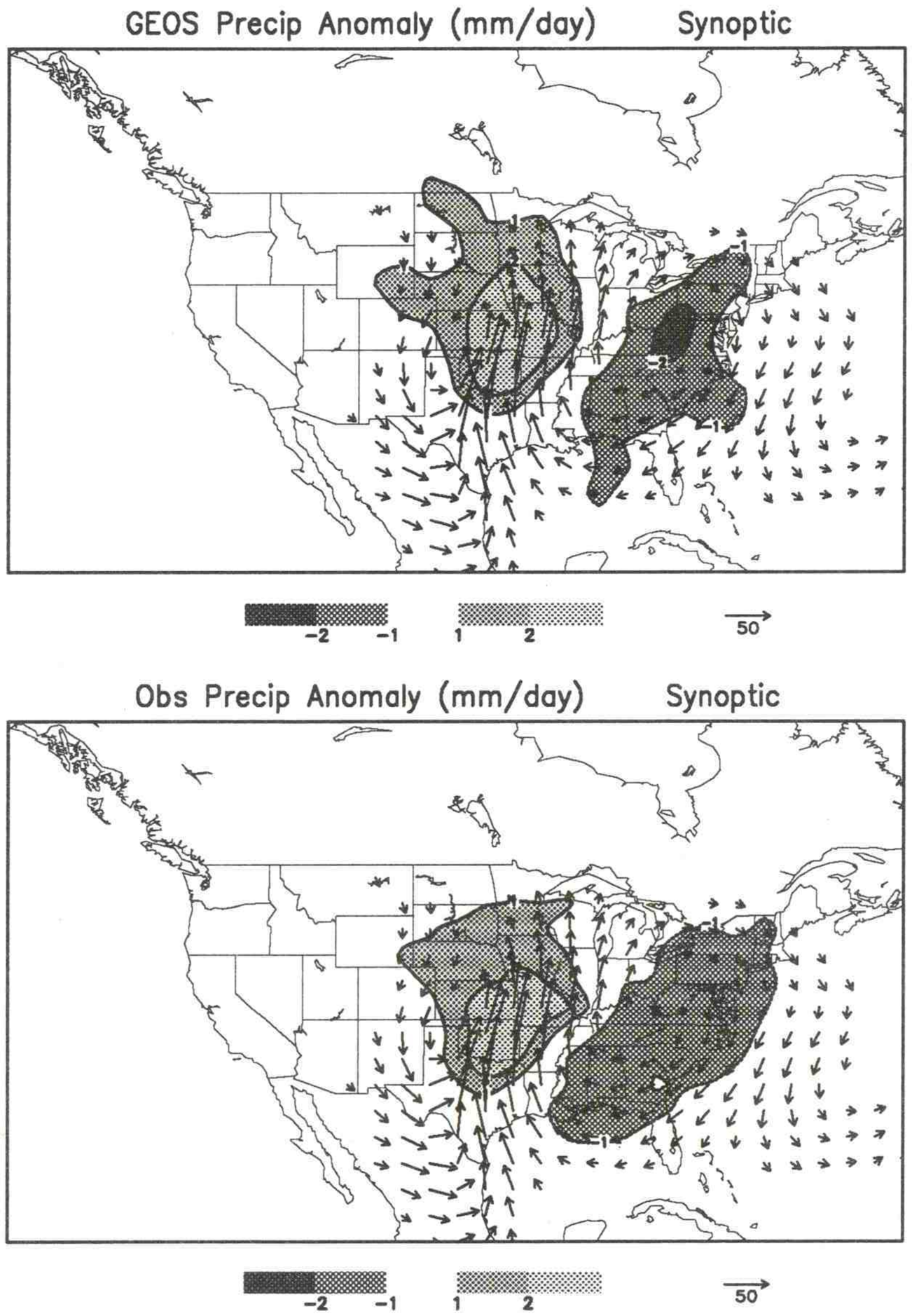

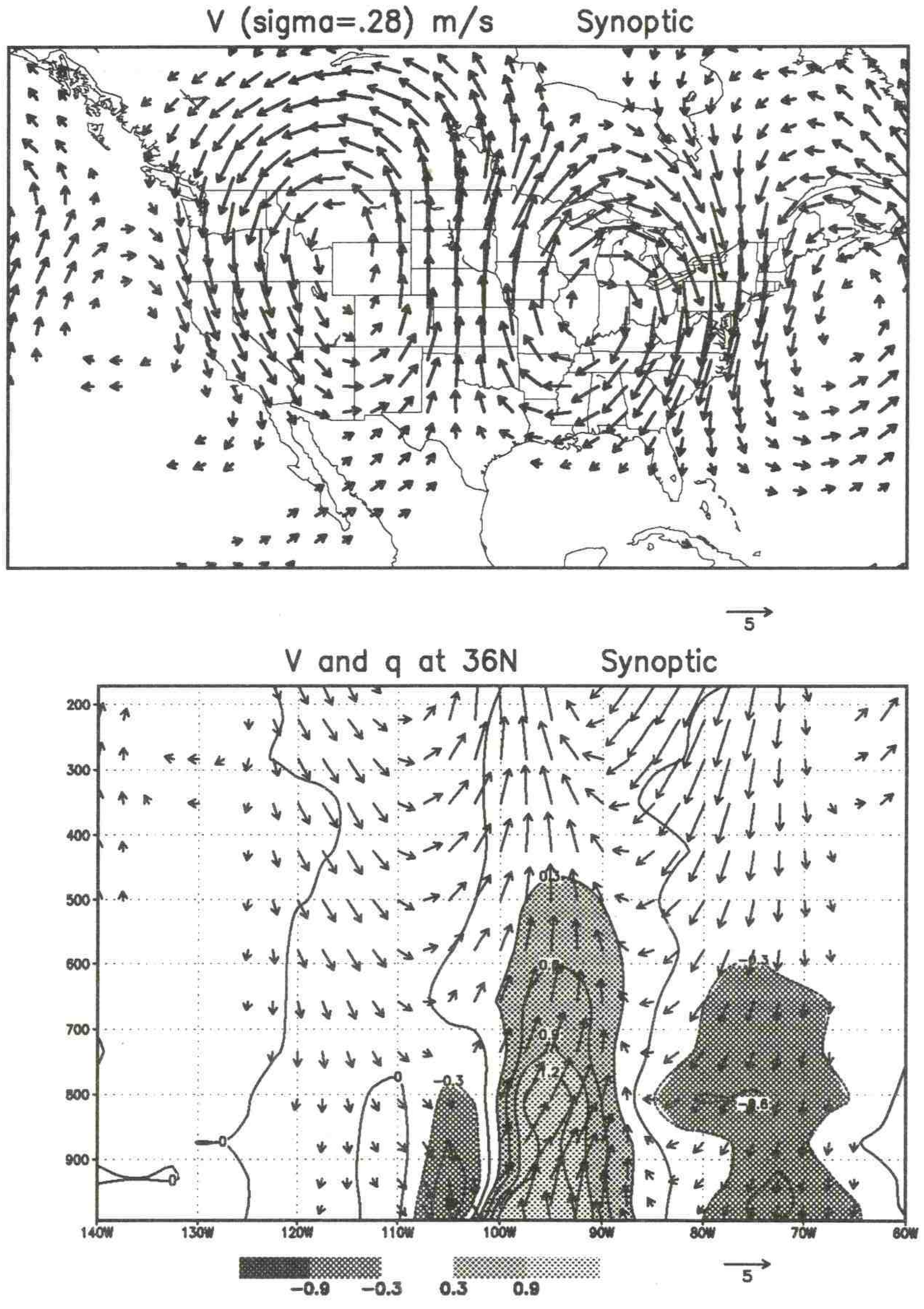

Figure 2: The high transport minus low transport composite anomalies for the synoptic (2-8 day) time scales. See text for criteria used to form the composites. a) The moisture flux (m/s g/kg) at $\sigma = 0.97$, and the precipitation (mm/day). b) The same as a) except for the observed precipitation. c) The winds at σ=0.28. d) The profile of the horizonal winds and moisture (g/kg) at 36N.

Evaluation of the ECMWF re-analysis with emphasis on the precipitation.

Klaus Arpe and Martin Stendel
Max-Planck-Institut for Meteorology
Bundesstr.55, D-20146 Hamburg, Germany
This study has been carried out within the ECMWF re-analysis validation project which is supported by the EC project No. EV5V-CT93-0286

1. Introduction

Operational analyses are often not suitable for the detection of climate variability because of numerous changes in the analysis/forecasting schemes. These changes may lead to variations of some sensitive variables which are larger than the signal of climate variability itself. Several centres are therefore creating analyses with a frozen scheme. These schemes are then applied to historical data (ECMWF from 1979 onward). A most important variable for climatological studies is the precipitation and this is unfortunately also a most difficult quantity to analyse or simulate. A key question is therefore, how realistic are precipitation estimates created with the analysis scheme. The precipitation is not analysed but it is gained from the atmospheric forecast model which is providing the first guess field or which is run every day. A comparison of different analysis schemes can help to identify sensitive areas and in areas with a good observational data coverage one can compare the estimated precipitation with observations. Precipitation is closely related to the divergent wind and a comparison of wind observations with the analyses may help to gain or lose confidence in the analysis data. Also the degree of adjustment between the analysis and short range forecasts (spin-up) gives some measure for the quality of the analysis data. The available data cover different periods and in the moment there is only a short overlap in time. Therefore the study is restricted to the months July 1985 and January 1986. The results can only be indicative and further investigations are needed.

2. Hadley circulation

Fig. 1 shows the zonal mean meridional wind for July 1985 and January 1986. The left panels display the Hadley circulation in the ECMWF re-analysis (ERA) while the other panels show differences to ERA. In July the differences between the analyses are quite small while they are large for January. Therefore the following discussion will be restricted to the January 1986 data. In the NASA analysis the January Hadley circulation is much weaker than in the other analyses. The lower branch at 850 hPa is much stronger in the ERA analysis than in the other two. From the +/- pattern in the upper troposphere in the difference between ERA and NMC one can infer that the northward flow occurs at a higher level in the NMC analysis. Of course one would like to know which of the three analyses is most realistic in representing the Hadley circulation. The best observational data for comparison are radiosonde and pilot observations. There are not many in the area of concern but one would expect the analyses to honour these important observations. We have compared the observations with analyses at the two areas with strong local Hadley circulations, i.e. over the western Pacific and north of Brazil. Fig. 2 shows the composite meridional wind of 4 radiosonde observation in an area over the western Pacific (134°-159°E, 6°-14°N) in comparison with the area means from the three analyses. It reflects our finding from the zonal means in Fig. 1, i.e. NASA has the weakest circulation, NMC has an upper branch which is higher than ERA and at 850 hPa ERA has the strongest southward flow. The comparison with the observations reveals that the NASA analysis is unrealistic while there is no clear cut preference between ERA and NMC. It is interesting to note that the ERA and NMC analyses suggest an unrealistic small secondary circulation with southward flow at 300 hPa and northward flow at 700 hPa, a feature which was very strong in the ECMWF FGGE

main analysis.

3. Precipitation distribution

The Global Precipitation Climate Project (GPCP) needs to use model output data from analysis cycles to complement their precipitation analysis in areas without any observational data and it has to be decided which of these three re-analysis data sets should be used. The main areas for which observational precipitation data are not available are the polar caps. Therefore we compare in Fig. 3 the three re-analyses fields for January 1986 in the northern polar region. All three re-analysis data sets are quite similar except that NMC displays unrealistic noise although the data have already been smoothed to a T21 resolution. This noise makes the NMC product very unattractive for the use in

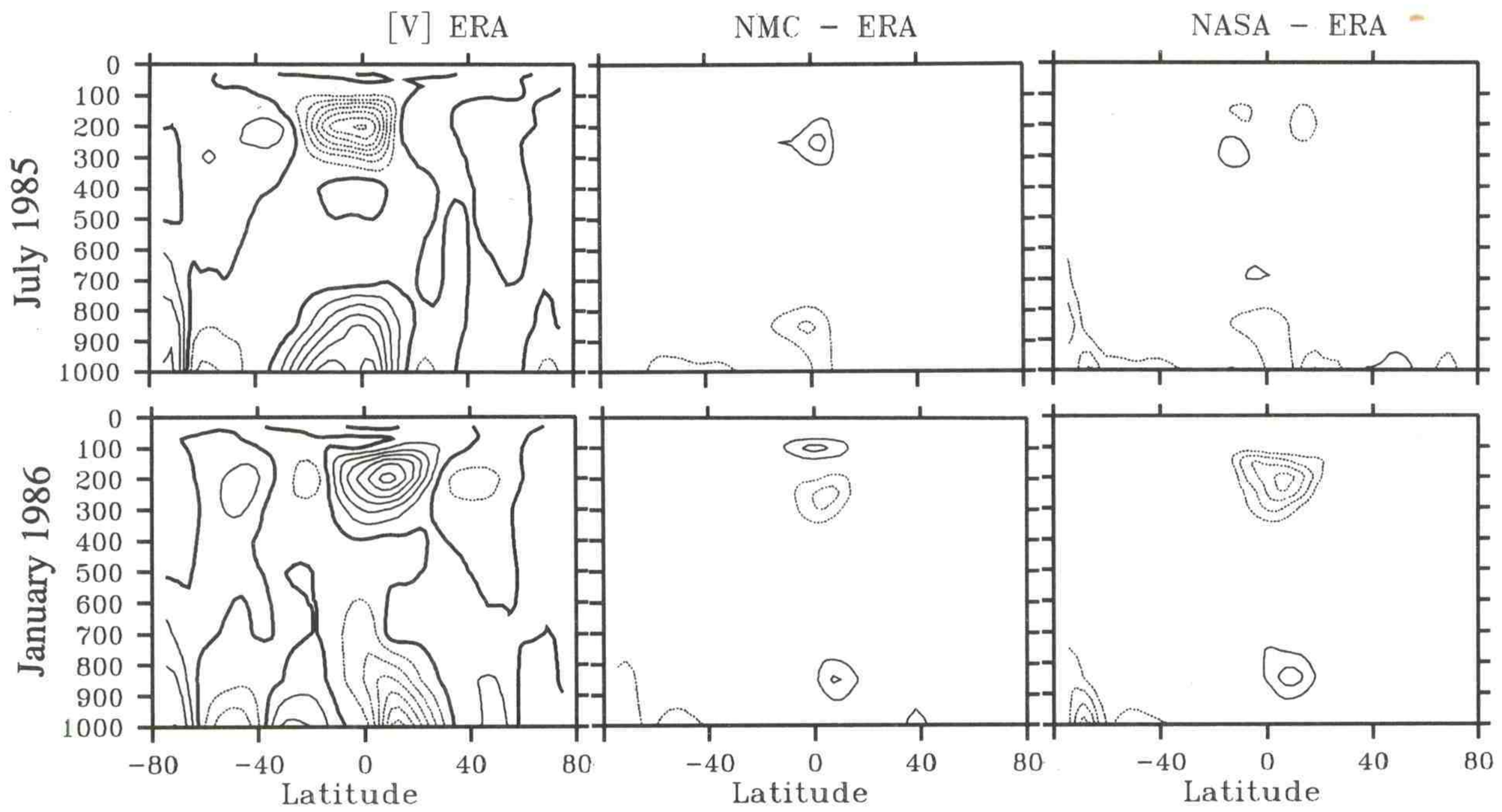

Fig. 1: Zonal mean meridional wind. Contours every 0.5 m/s, negative values are dotted. Left panels: ECMWF analysis (ERA), other panels: differences to ERA.

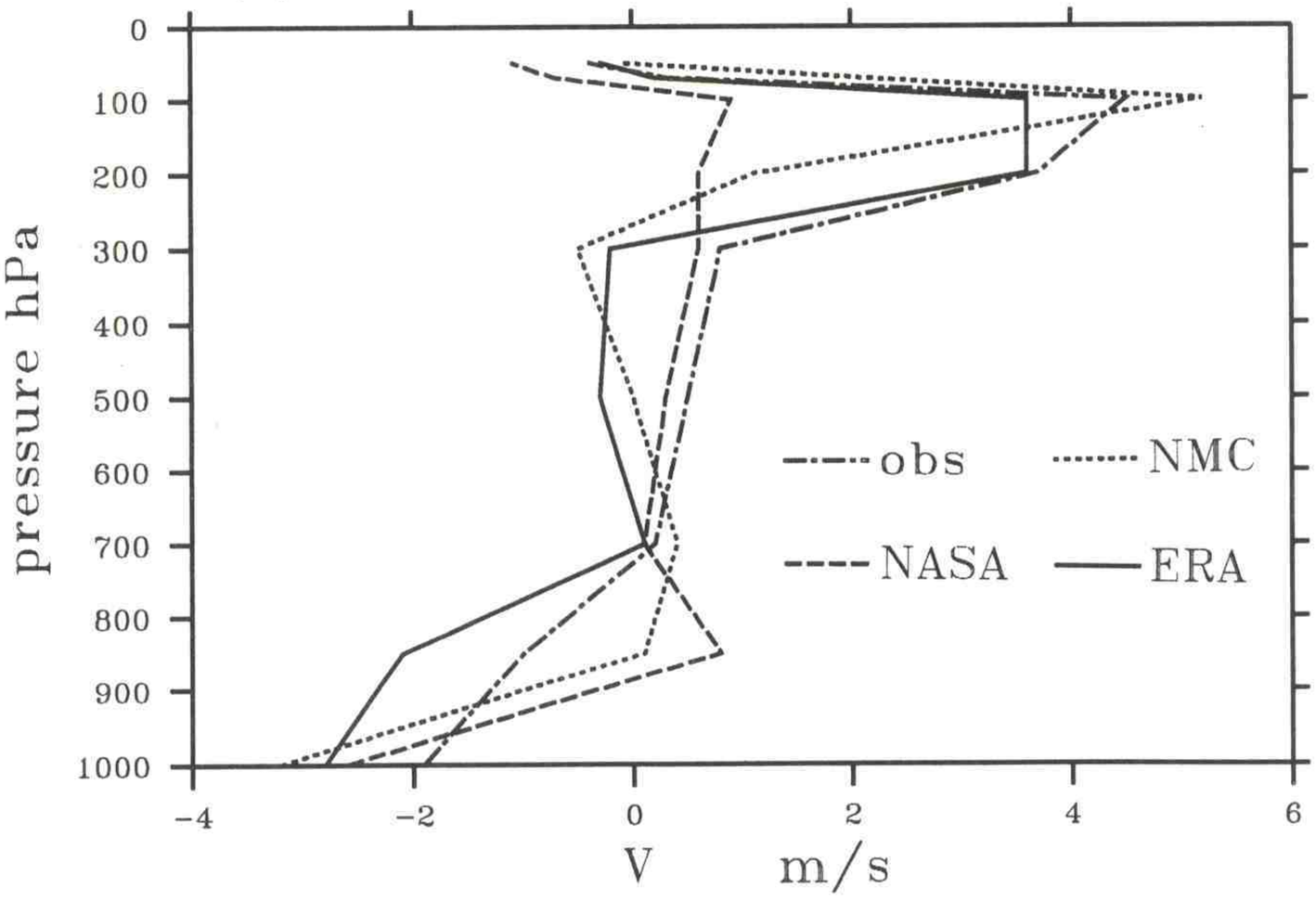

Fig. 2: Vertical sounding of the meridional wind for the western Pacific (134°-159°E, 6°-14°N) during January 1986.

GPCP while there is no clear cut advantage for the ERA or NASA data set when comparing them with analysed data from precipitation observations. We looked as well in other areas, e.g. the tropical Africa. ERA provides there too much precipitation compared to the GPCP analysis. All provide too much precipitation north of the equator. Differences between the re-analyses can reach 4 mm/d but over all none can be judged to be superior for this area.

4. Spin-up in the ECMWF re-analysis

Models as well as the data assimilation schemes are still not perfect and adding observational data during the analysis cycle can lead to imbalances which might lead to gravity waves or to initial overreactions or damping of precipitation in the short-range forecasts, commonly named spin-up. From ECMWF we had available extra to the 6h forecasts 4 times a day also 24 hour forecasts 2 times a day. In Fig. 4 we demonstrate two different behaviours of spin-up of precipitation for two areas, northern Europe and northern Australia. Two diurnal cycles are displayed because a 24h forecast starting at 12GMT reaches into the next day. Precipitation values from the forecasts for the first guess (6hour) is an average which is plotted at 3 GMT, 9 GMT and so on. The 24 hour forecast starting at 00GMT gives 4 values, i.e. at 3,9,15, and 21 GMT and that starting at 12 GMT gives values for 15, 21 GMT and 3, 9 GMT of the next day. For northern Europe there is only a small diurnal cycle in the 6h forecasts and in both 24 h forecasts one finds a strong increase during the

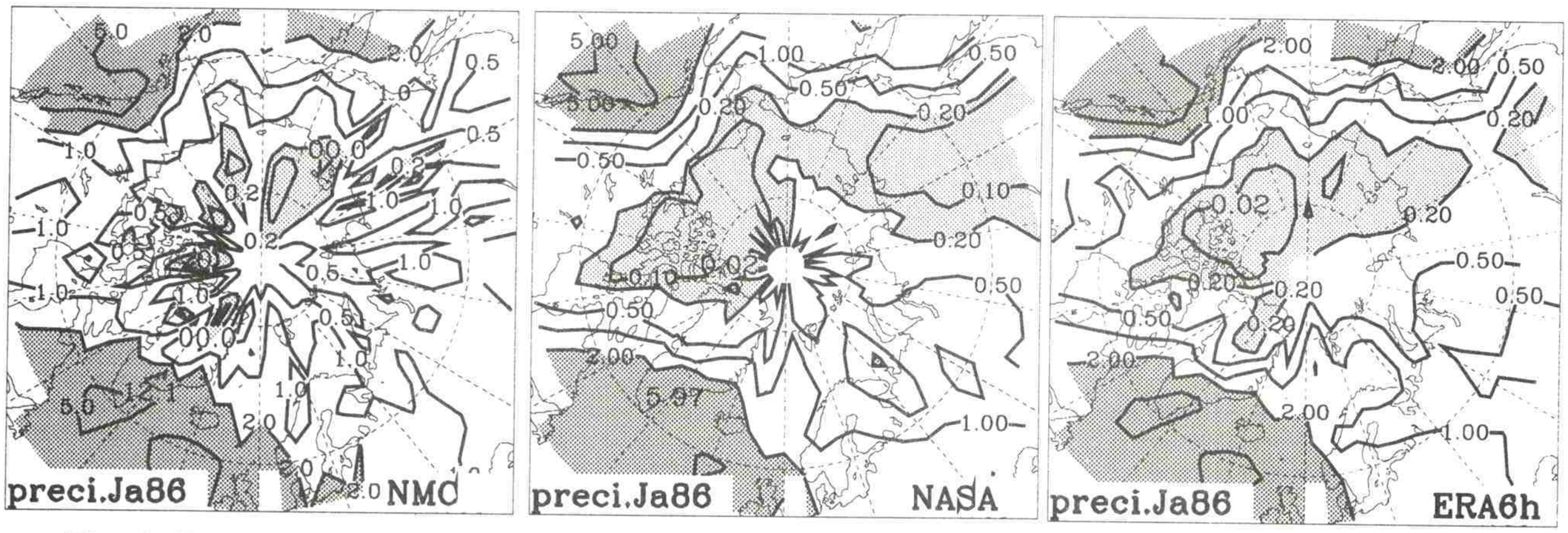

Fig. 3: Precipitation in northern polar regions by different analysis schemes for January 1986. Contours at 0.1, 0.2, 0.5, 1, 2, 5, 10 mm/d, shading for < 0.2 and > 2 mm/d.

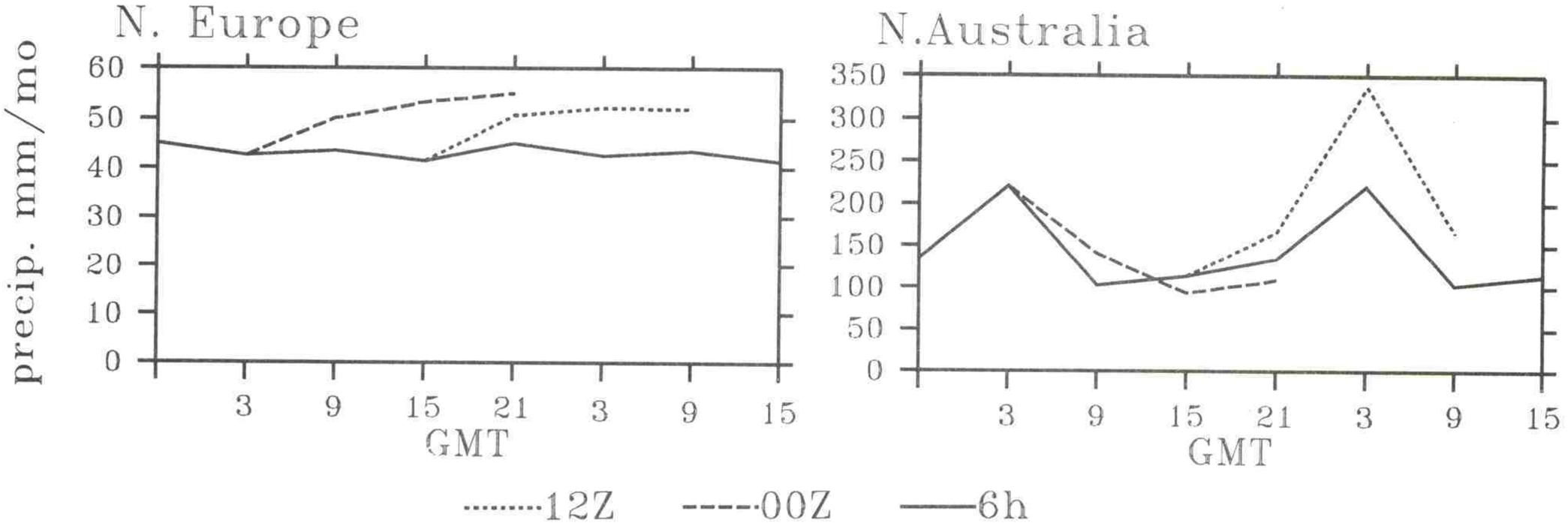

Fig. 4: Precipitation during January 1986 in the 6 hour forecasts (solid line), during the 24 hour forecast starting at 00 GMT (dashed line) and starting at 12 GMT (dotted line).

course of the forecasts. For northern Australia there is a strong diurnal cycle and the spin-up is prominent only in the forecast starting at 12 GMT. Further investigations show that the spin-up differences between 00 and 12 GMT are quite large scaled and that there is always a larger spin-up over land at locations where the corresponding initial analysis is valid for late evening or night, also for the extra tropics in summer. For daily averages the 12-24h forecast range provides nearly everywhere larger values than the 0-6h forecast range of about 10% and it is the question which of these two forecast ranges gives the more realistic estimate of the truth. A clear-cut decision cannot be made but comparisons with GPCP analyses and subjective judgement suggests that in extra tropical winter the 12-24 hour forecasts are more realistic while in the tropics the 6 hour forecasts may be marginally better. Global means (in brackets land only) give the following values for Jan86: ERA6h: 2.90 (1.85) ERA24h: 3.03 (1.98) NASA 2.49 (1.74) NMC: 2.66 (1.94) GPCP: 2.93 (1.89). Also these global means do not give a clear picture except that NASA is on the low side.

5. Diurnal cycle

Already in Fig. 4 the diurnal cycle of precipitation in the ERA scheme was shown. Also the NASA data resolve the diurnal cycle. By Fig. 5 we want to compare this cycle in both analyses and also want to compare these values with daily means by NMC, GPCP and an analysis by Schemm et al. Two areas with strong diurnal cycle are selected, i. e. Northern Australia (115°-155°E, 15°-21°S, land only) and central Africa (14°-31°E, 10°N-10°S). In both cases the ECMWF analysis has a maximum of precipitation at noon while the NASA analysis has a more realistic maximum a few hours later. For summer we have found that NASA provides unrealistically high amplitudes of the diurnal cycle in the extra tropics (not shown). In Fig. 5 daily means from NMC, GPCP and Schemm et al. are presented as well. For central Africa all re-analysis schemes give too large amounts especially ERA. For northern Australia the values are very similar in all analyses except NASA which has low values.

6. River runoff in the ERA data

For long time averages one can validate the difference between precipitation and evaporation with river runoff data. This is a study we intend to do, first we did only a simple test by checking seven year means of this quantity for negative values over land (not shown). There are quite large areas where the evaporation exceeds the precipitation by more than 0.2 mm/d, almost over all arid areas. The ERA soil moisture scheme does not conserve water at the ground and therefore such an unrealistic feature can happen.

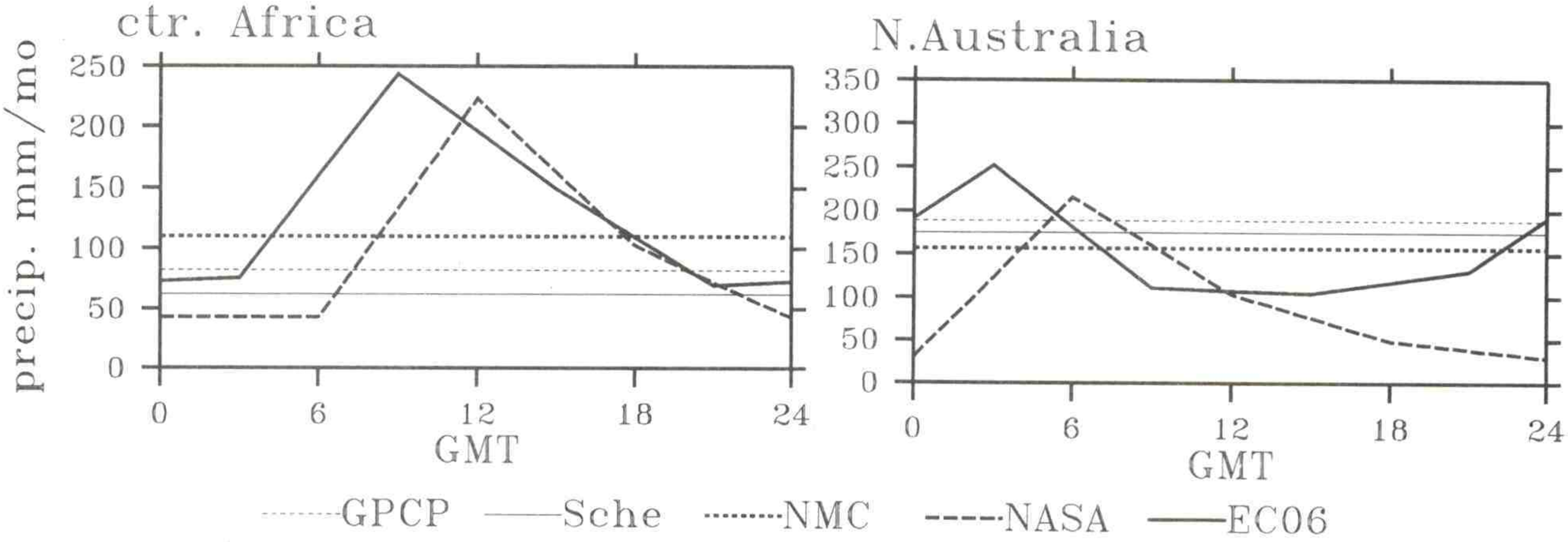

Fig. 5: Diurnal cycle of precipitation for two areas in the 6 hour forecasts by ECMWF and in the NASA scheme as well as daily means by NMC, GPCP and Schemm et al.

An evaluation of the surface fluxes in the NMC/NCAR reanalysis

S. Saha, G. White and R. Reynolds
Environmental Modeling Center
National Centers for Environmental Prediction
NOAA/NWS
Washington, DC 20233
wd23gw@sun27.wwb.noaa.gov

The NCEP/NCAR reanalysis project has completed several years of data analysis using a frozen, state-of-the-art global atmospheric data assimilation system. As part of the 6-hour first guess for each analysis time, the model physics produces estimates of the surface energy fluxes. These fluxes are saved in the reanalysis archive, are available from NCAR and other centers and will be available on CD-ROMS. This paper examines the surface fluxes from reanalysis for the period 1982-93.

D. Cayan of Scripps calculated surface fluxes from several years of COADS data (Cayan, 1992) and then calculated anomalies for each month. Fig. 1 shows the temporal correlation over the period 1982-92 of his latent heat anomalies with latent heat anomalies frrom reanalysis (which includes COADS data). Fig. 2 compares the times series of monthly latent heat anomalies from Cayan and from reanalysis averaged over the northeast Pacific. Regions of high correlations tend to occur where ship observations are most abundant. This indicates that reanalysis produces very similar results to independent calculations based on COADS data where COADS is most abundant.

Fig. 3 displays the annual mean net surface heat flux over the ocean from reanalysis for 1982-93. The pattern appears to be fairly realistic, with heat flux into the ocean at the equator, particularly in the eastern oceans where cold sea surface temperatures cause clear skies and strong net solar radiation. Over the Gulf Stream and Kuroshio, the warm waters produce net upward heat fluxes. Somewhat surprisingly, high latitudes in the Southern Hemisphere are dominated by net heat flux into the ocean.

Fig. 4 compares zonal mean net heat flux into the ocean from the reanalysis climatology to climatological estimates made by da Silva *et al.* (1995). da Silva *et al.* (1995) calculated a careful surface flux climatology from several years of COADS data; the curve labelled UWM shows their initial result. It is largely into the ocean, implying an unrealistic net heat transport by the ocean. da Silva *et al.* (1995) then adjusted their fluxes, decreasing solar radiation and increasing latent heat, to obtain more reasonable patterns of net heat flux (labelled UWMcon) and the implied oceanic heat transport. In the tropics the reanalysis which has not been adjusted shows much better agreement with the adjusted da Silva *et al.* (1995) estimate than with the unadjusted estimate, indicating that the net heat flux from reanalysis, which has not been adjusted, gives a more reasonable zonal mean pattern than the unadjusted COADS climatology. In higher latitudes the reanalysis net heat flux tends to be more positive than the adjusted da Silva estimate.

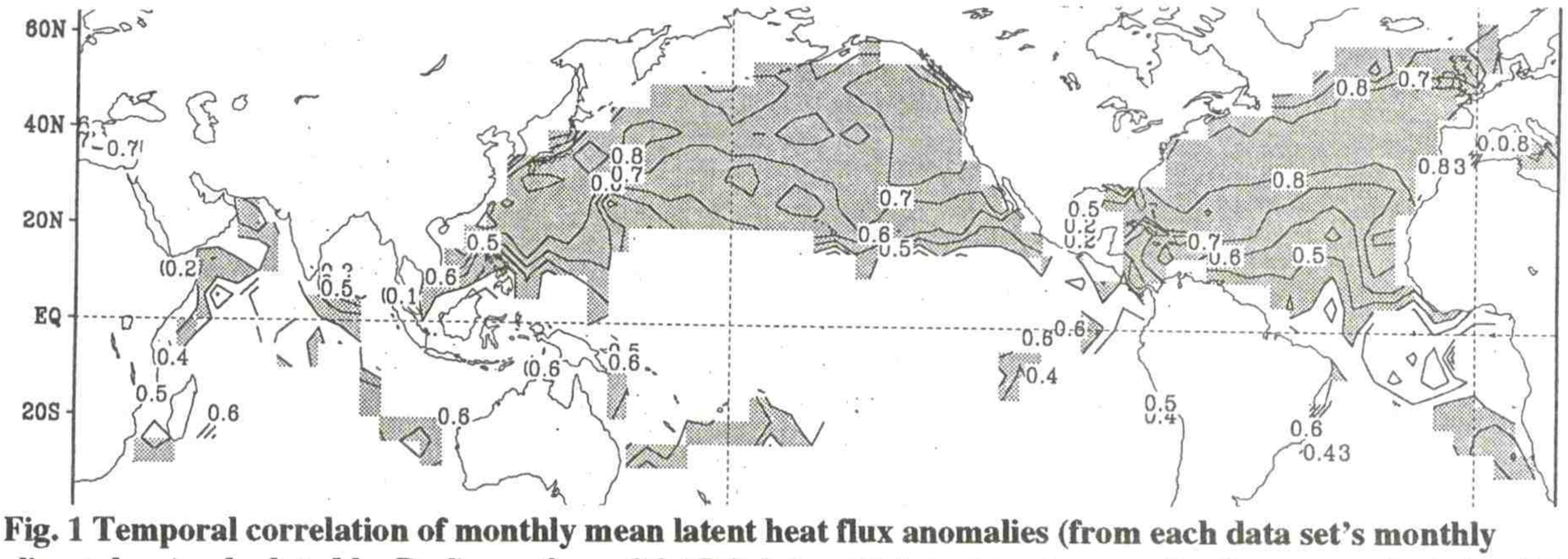

Fig. 1 Temporal correlation of monthly mean latent heat flux anomalies (from each data set's monthly climatology) calculated by D. Cayan from COADS data with latent heat anomalies from reanalysis for 1982-92.

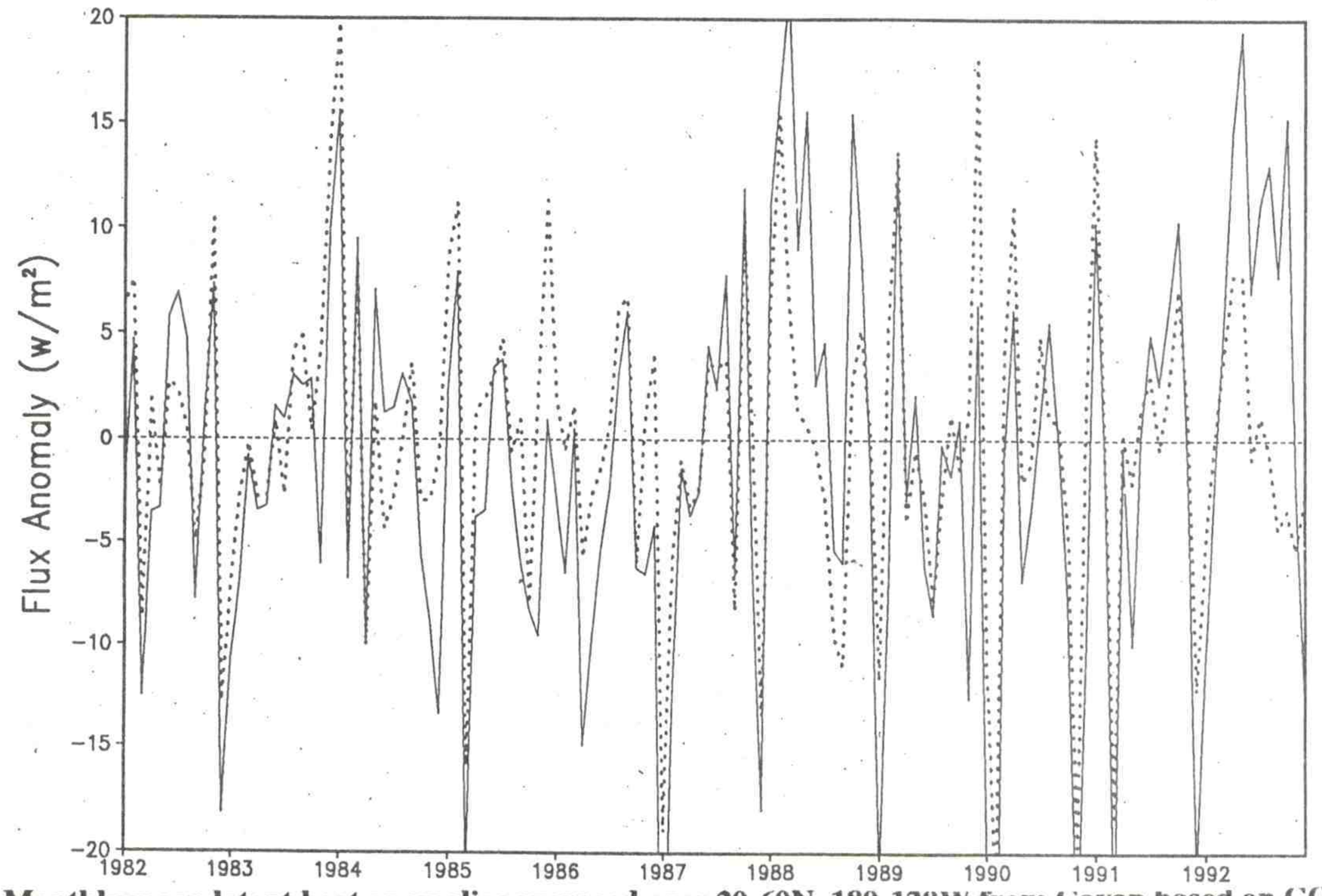

Fig. 2 Monthly mean latent heat anomalies averaged over 20-60N, 180-120W from Cayan based on COADS data (solid) and from reanalysis for 1982-92 (dashed).

Fig. 5 displays the zonal mean oceanic heat transport implied by the net heat flux from reanalysis. The pattern shows heat transport away from the equator, with maxima in the subtropics; however, the heat transport fails to go to zero at the South Pole. This reflects a time-averaged global mean net heat flux into the ocean of slightly less than 6 W/m² in reanalysis. Replacing the net shortwave from reanalysis with a satellite-derived shortwave radiation (Pinker *et al.*, 1995) yields a more realistic net heat flux (da Silva and White, 1995). Reanalysis cloudiness in Southern Hemisphere midlatitudes is lower than ISCCP estimates. The reanalysis appears to have too high oceanic surface albedo. A new short wave radiation code with a corrected surface albedo is being tested at NCEP.

Fig. 6 compares longitude-time crosssections of monthly sea surface anomalies and net surface heat flux anomalies from reanalysis in the equatorial Pacific (120E-80W). The net heat flux anomalies show a good correspondence to SST anomalies, generally displaying

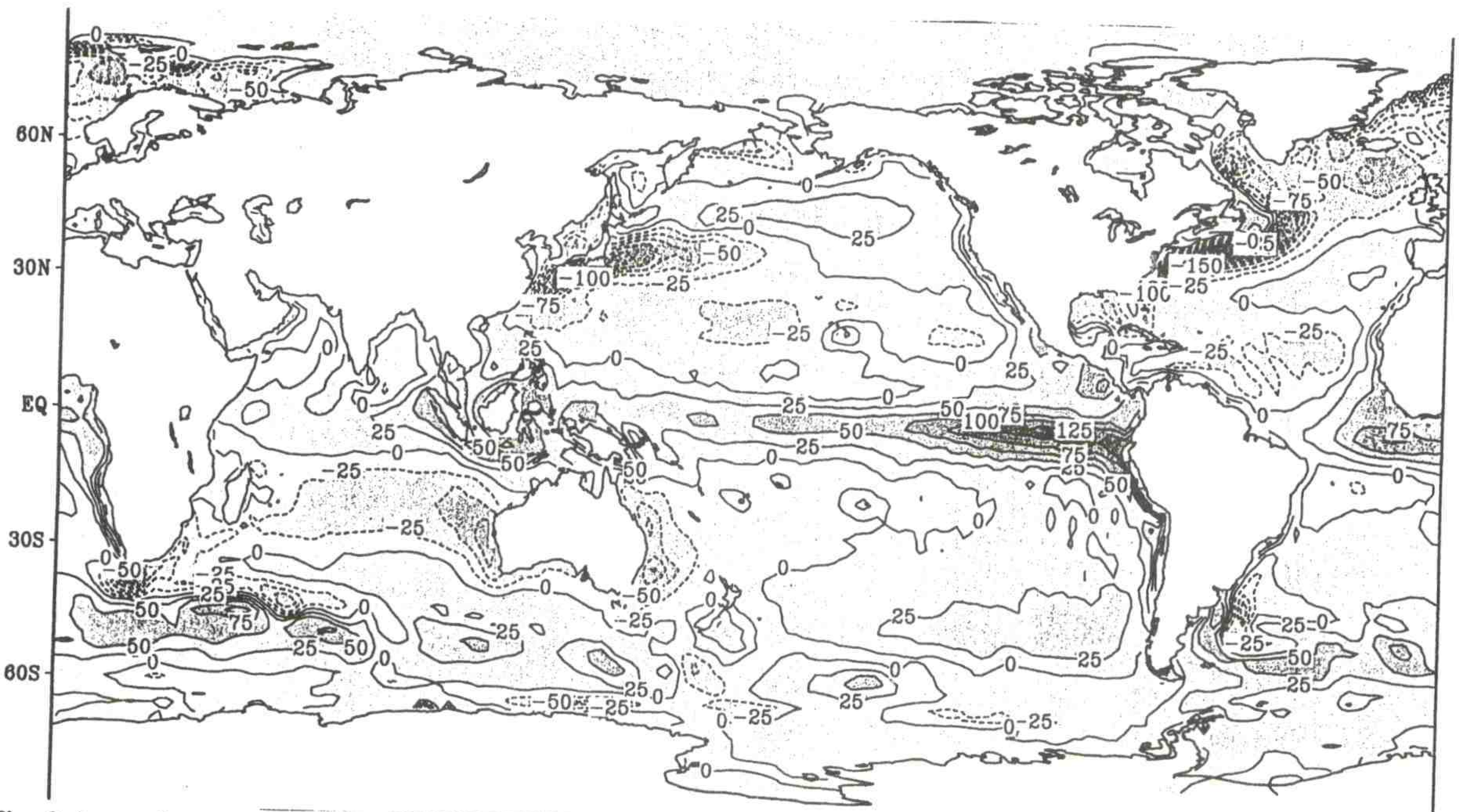

Fig. 3 Annual mean surface net heat flux (ocean only) from reanalysis for 1982-93. Contour interval 25 W/m²; upward (negative) flux dashed.

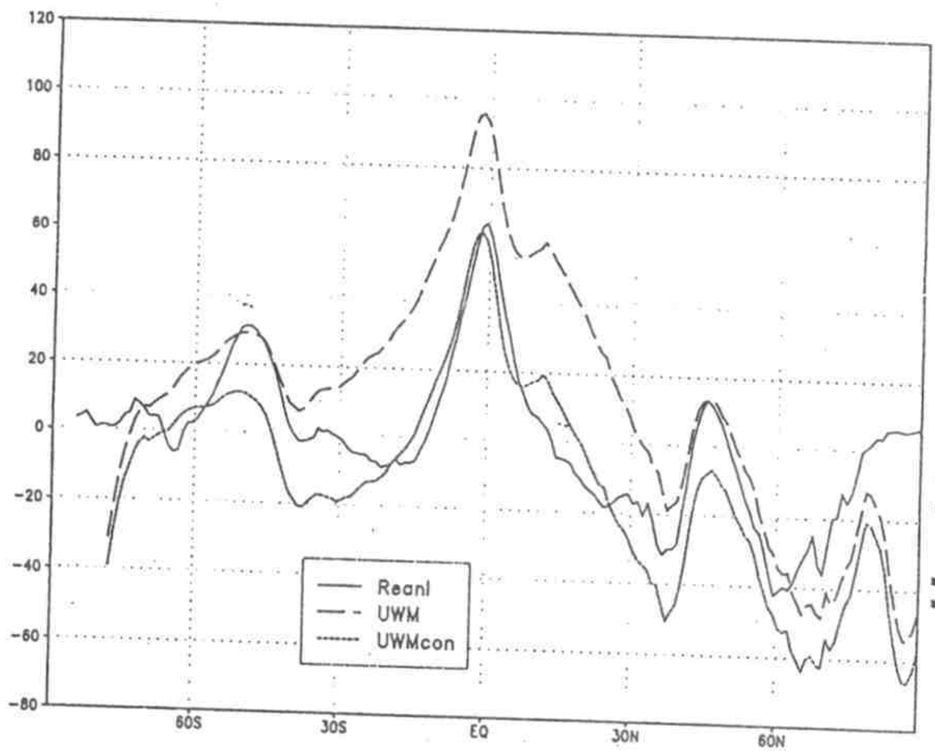

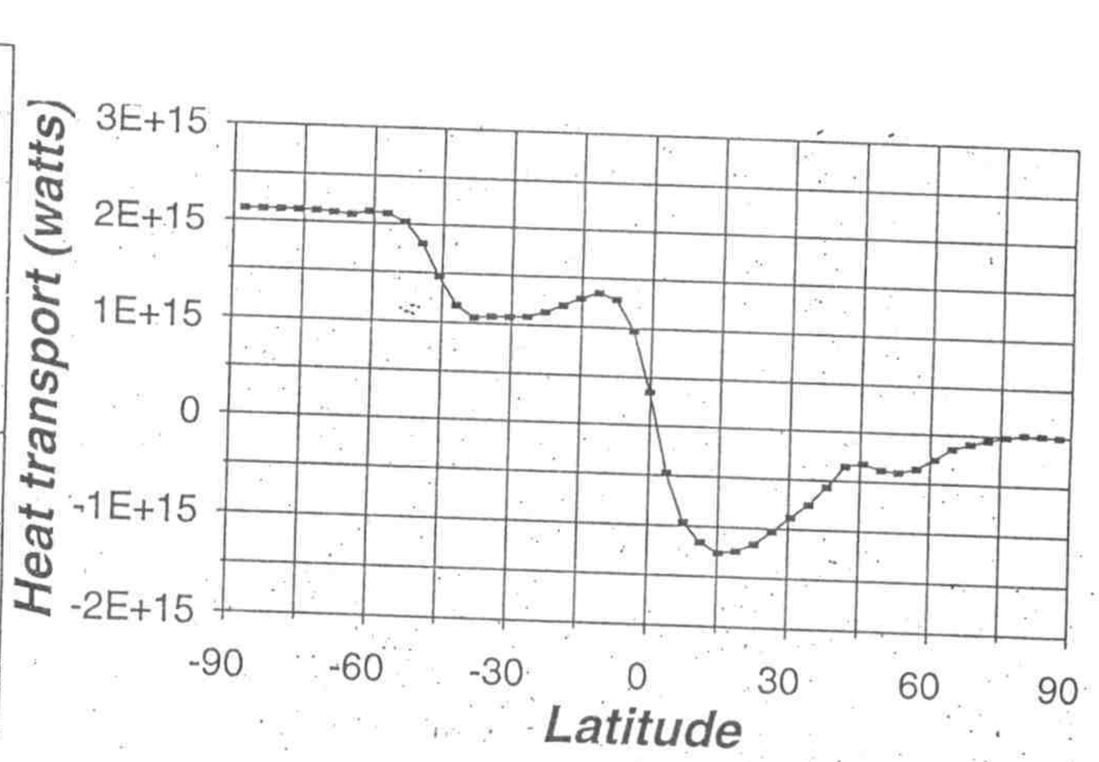

(Left) Fig. 4 Zonally averaged annual mean net surface heat flux into ocean from 1982-93 reanalysis (solid line), da Silva *et al.* (1995)'s unadjusted climatology (long dashes) and da Silva *et al.* (1995)'s *con*strained climatology (short dashes). Positive implies downward flux, units W/m². (Right)Fig. 5 Zonal mean oceanic heat transport calculated by integrating zonally averaged annual mean net surface heat flux from reanalysis into ocean from North Pole. Positive implies southward transport.

more upward (negative) net heat flux when warm SST anomalies occur and more downward (positive) net heat flux with cold SST anomalies. This indicates that the surface fluxes display a realistic pattern of interannual variability in the tropical Pacific.

Surface fluxes from reanalysis agree well with surface fluxes derived independently from COADS data in regions where the COADS data are better sampled. They appear to be generally reasonable in both their climatology and in interannual variability, although the short wave radiation appears to contain some errors. They offer a much more complete and consistent record of the surface energy budget than previously available.

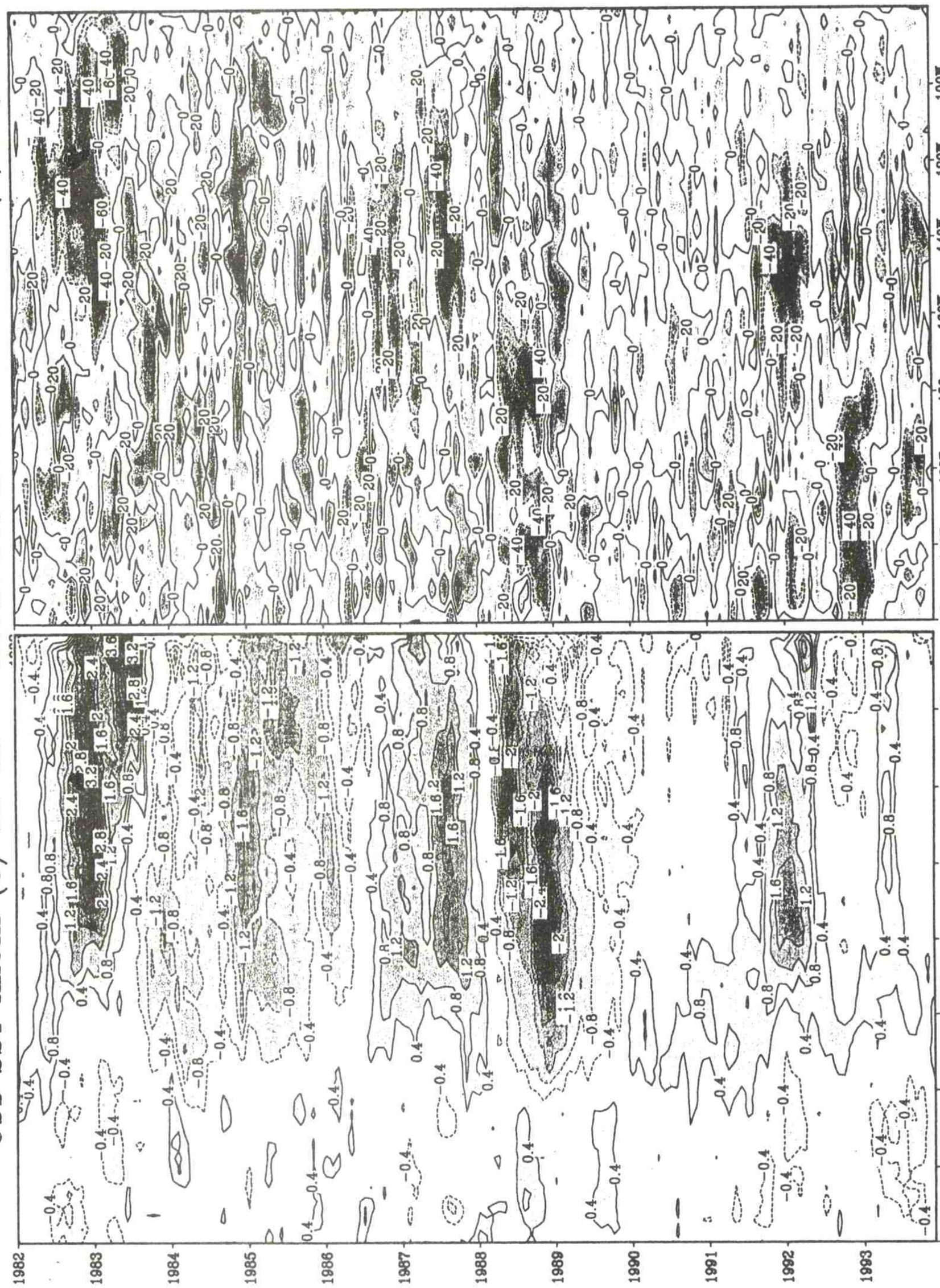

Fig. 6 Logitude-time distribution of (left) SST anomalies and (right) net heat flux anomalies in the Pacific (120E-80W) for 1982-93 averaged over 5N-5S from reanalysis. Contour interval (left) .4 C, cold anomalies dashed, zero omitted; (right) 20 W/m^2, negative (upward) anomalies dashed, zero included.

References

Cayan, D.R., 1992: Latent and sensible heat flux anomalies over the northern ocean: Driving the sea surface temperature. *J. Phys. Oceanography*, *22*, **859-891.**

da Silva, A., and G. White, 1995: Intercomparison of surface marine fluxes from GEOS-1/DAS and NCEP/NCAR reanalyses. WCRP Workshop on Air-Sea Fluxes for Forcing Ocean Models and Validating GCMs. ECMWF, Reading, England, Oct. 24-27, 1995. World Meteorological Organization, Geneva, Switzerland, in press.

da Silva, A., C.C. Young and S. Levitus, 1995: *Atlas of Surface Marine Data 1994 Vol.1: Alogrithms and Procedures.* **NOAA Atlas NESDIS 6, U.S. Dept. Of Commerce, NOAA, NESDIS, Washington, DC**

Pinker, R.T., I. Laszlo, C.H. Whitlock and T.P. Charlock, 1995: Radiative flux opens new window on climate research. *EOS Trans., 76*, **145-158.**

A Comparison of Monthly Precipitation among the NCEP/NCAR and NASA/DAO Reanalyses and a Satellite-Raingauge Merged Analysis

John Janowiak, Pingping Xie, and Phillip Arkin
National Centers for Environmental Prediction/NWS/NOAA
Camp Springs, MD 20746

I. INTRODUCTION

A recently developed satellite-raingauge merged dataset (Xie and Arkin, 1995) is compared with monthly accumulated precipitation from the NCEP/NCAR and NASA/DAO reanalyses over the period 1988 through 1993. In addition, daily outgoing longwave radiation (OLR) data are used to examine precipitation frequency in the reanalyses, and *hourly* raingauge data over the U. S. are used to examine the diurnal cycle of precipitation in the NCEP/NCAR reanalysis data.

II. DATA

The satellite-raingauge analysis (hereafter referred to as *merged analysis*) is comprised of raingauge data from the Climate Prediction Center 'CAMS' station data, the Pacific atoll data set (Morrissey and Greene), and satellite-derived estimates from IR and SSM/I. The satellite estimates were linearly combined using a maximum likelihood estimation (MLE) approach in which the weighting coefficients are functions of the random errors in the measurements, which are determined from comparisons with raingauge data. The results of the MLE step are then blended with the gauge data in a manner similar to the Reynolds SST blending scheme, where the satellite data define the shape of the field, and the gauges determine the amplitude.

Daily OLR that are collected at the Climate Prediction Center are used in a qualitative sense to validate, as best as possible, the frequency of precipitation in the reanalyses. The frequency of occurrence of mean daily OLR observations less than 240 W m^{-2} (which corresponds to a sensor "window" temperature of approximately 276 K) are compared with frequency of precipitation in the NASA/DAO and NCEP/NCAR reanalyses during 1992. The comparisons with the OLR data are qualitative since the 240 W m^{-2} threshold to define precipitation occurrence is subjective, and because the daily mean OLR is determined from merely 2 observations per day, 12 hours apart.

Hourly raingauge data for approximately 2800 sites were gridded (see paper by Janowiak and Higgins in this volume) and used to examine the diurnal cycle in NCEP/NCAR reanalysis precipitation over the U.S..

III. COMPARISONS

1. Monthly Mean

A time series of *global* mean monthly precipitation during 1988 through 1993 for the merged analysis and reanalysis datasets (Fig. 1) depicts a consistent annual cycle in the reanalyses, with maximum precipitation during northern summer and minimum in northern winter that is not indicated in the merged analysis. The amplitude of the annual cycle is considerably stronger in the NASA/DAO precipitation, particularly in the northern winter season. During the northern warm season, both the NASA/DAO and NCEP/NCAR precipitation peak near 3 mm day^{-1}, but during the northern cool season, the minima average about 2.35 mm day^{-1} for NASA/DAO and about 2.60 mm day^{-1} for NCEP/NCAR.

The correlations of the monthly time series between the merged analysis and the NASA/DAO and NCEP/NCAR are 0.47 for each, and the anomaly correlation is 0.19 and 0.02, respectively. The global mean annual rainfall is 2.62 mm day^{-1} for the merged analysis and NASA/DAO, and 2.72 mm day^{-1} for the NCEP/NCAR reanalysis.

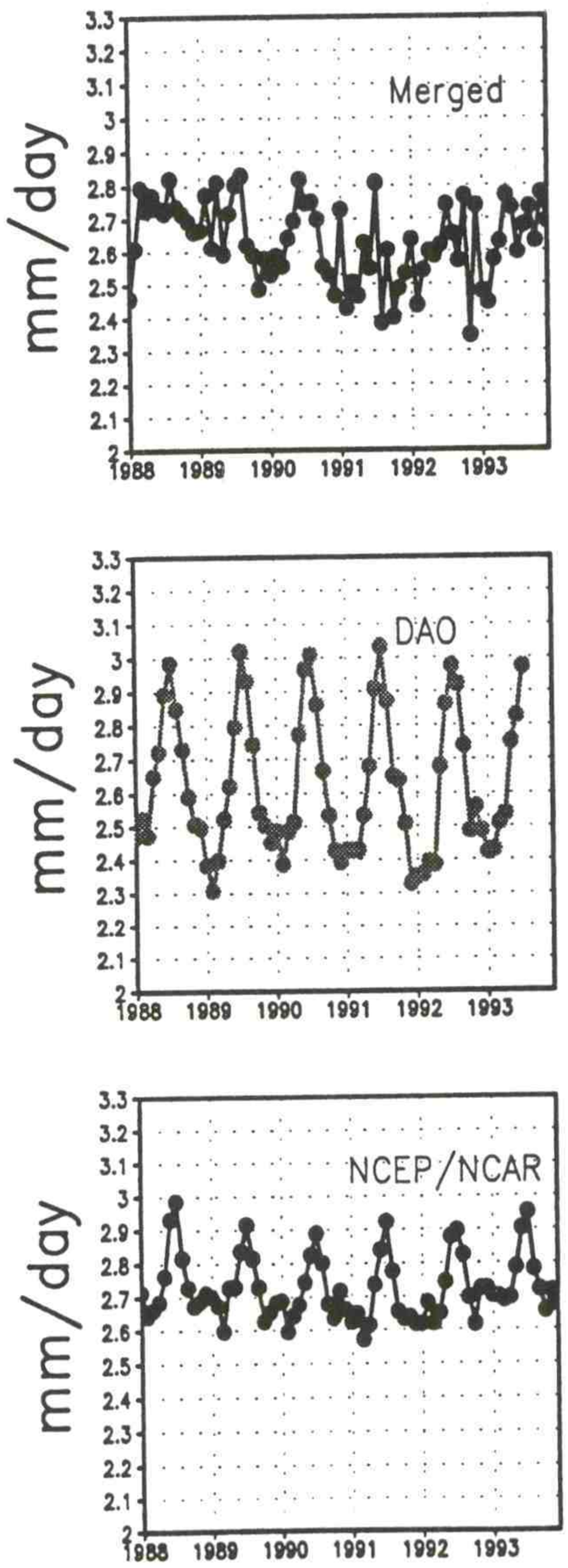

Figure 1. Mean monthly global precipitation (mm day^{-1}) for the satellite-raingauge merged analysis (top), NASA/DAO reanalysis (middle), and NCEP/NCAR reanalysis (bottom).

Mean annual precipitation (1988 -1993) in the merged analysis is considerably more intense than in either reanalysis product (Fig. 2) in the oceanic ITCZ regions (especially the Pacific), the SPCZ, SACZ, and in the North Pacific and North Atlantic storm tracks. Conversely, both reanalyses indicate heavier precipitation in equatorial South America that extends northward into the Caribbean, and over Southeast Asia and extreme western equatorial Africa. The NCEP/NCAR reanalysis shifts the SPCZ farther east relative to the merged analysis, as indicated in the difference map (Fig. 2) by positive differences to the east and negative differences to the west.

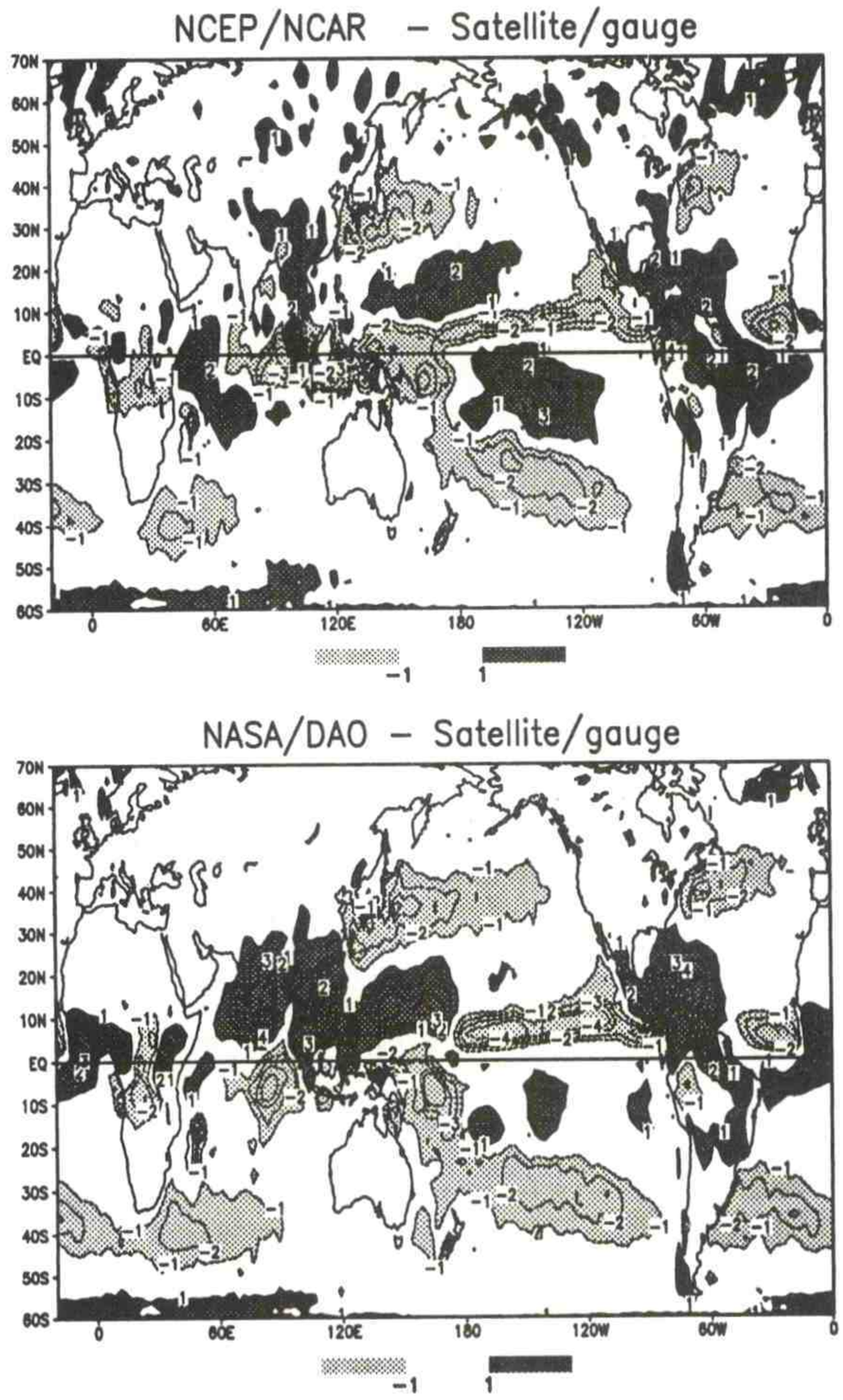

Figure 2. Difference in annual mean precipitation during 1988 through 1993 (mm day^{-1}) between reanalyses and the satellite-raingauge merged analysis.

2. Daily Frequency

Rainfall frequency in the global Tropics, as depicted by the frequency of mean daily OLR below 240 w m^{-2} (276 K) is in qualitative agreement with the reanalyses (Fig. 3) when considering only rainfall amounts greater than 1 mm day^{-1}. If all rainfall amounts are used, the NASA/DAO precipitation frequency is much greater (in excess of 90% in most regions - not shown).

The peculiar "spotty" pattern of precipitation frequency in the NCEP/NCAR reanalysis data is a reflection of the "Gibbs effect", which is caused by an interaction with orography that is represented in a spectral domain.

3. Diurnal Cycle

The diurnal cycle in the NCEP/NCAR reanalysis precipitation is now compared with that observed from hourly raingauge data over the conterminous U. S. The hourly raingauge data were summed to 6-hour totals to match the NCEP/NCAR reanalysis precipitation short-range forecast accumulations for JJA 1985. To portray the diurnal cycle, the percent departures from the daily mean rainfall for the four 6-hour periods (averaged over the JJA 1995 season) were computed and displayed (Fig. 4) for both the observations and the model forecasts.

The observations indicate a diurnal cycle that is consistent with the notion of continental heating during the day which leads to rising motion and a maximum of convection in the mid-afternoon to early evening over most land surfaces, with corresponding subsiding vertical motions and convective minima during the nighttime hours. The exception is the well-documented nocturnal precipitation maximum in the Great Plains.

The NCEP/NCAR reanalysis precipitation forecasts indicate a much higher amplitude diurnal cycle than the observations. The phase of the diurnal cycle as represented in the model forecasts is also different from the observations. The most convective times of day in the model are morning to early afternoon.

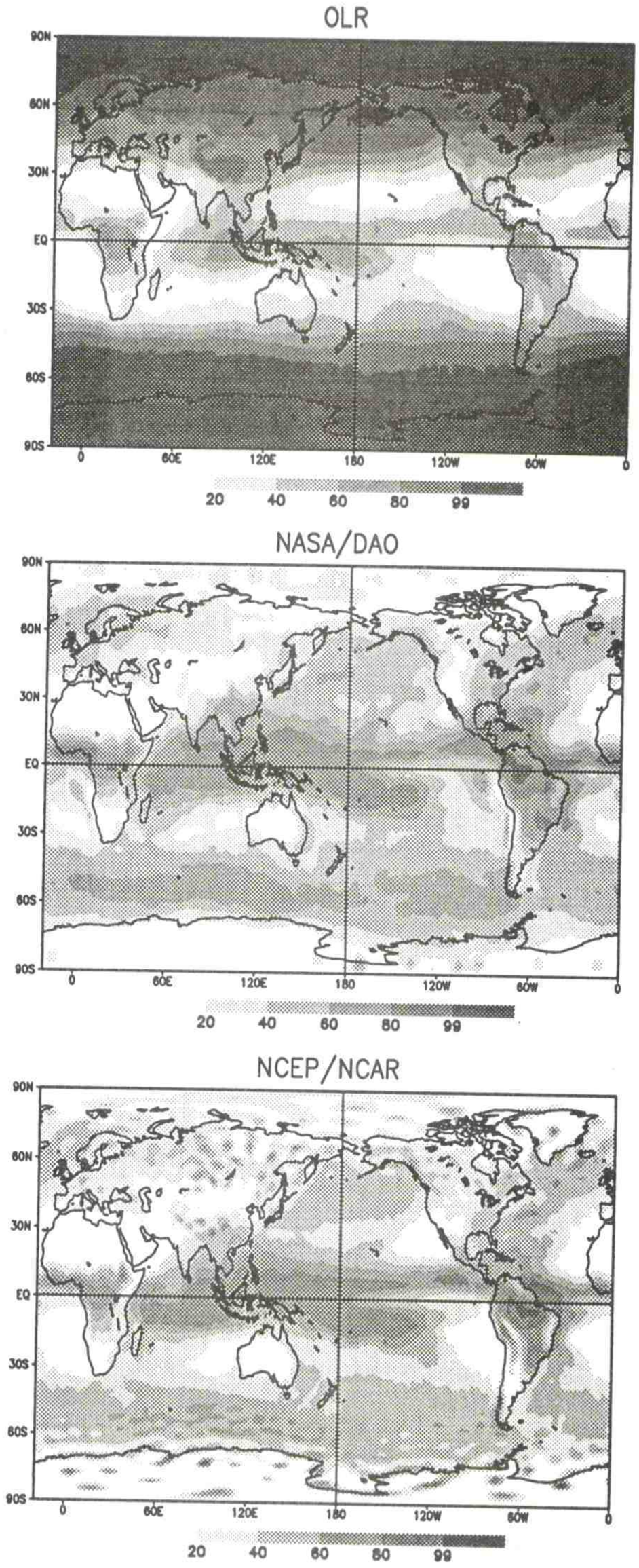

Figure 3. Frequency of occurrence (%) of (top) OLR < 240 w m^{-2} (top), (middle) precipitation (> 1 mm day^{-1}) for NASA/DAO, and (bottom) precipitation (> 1 mm day^{-1}) for NCEP/NCAR.

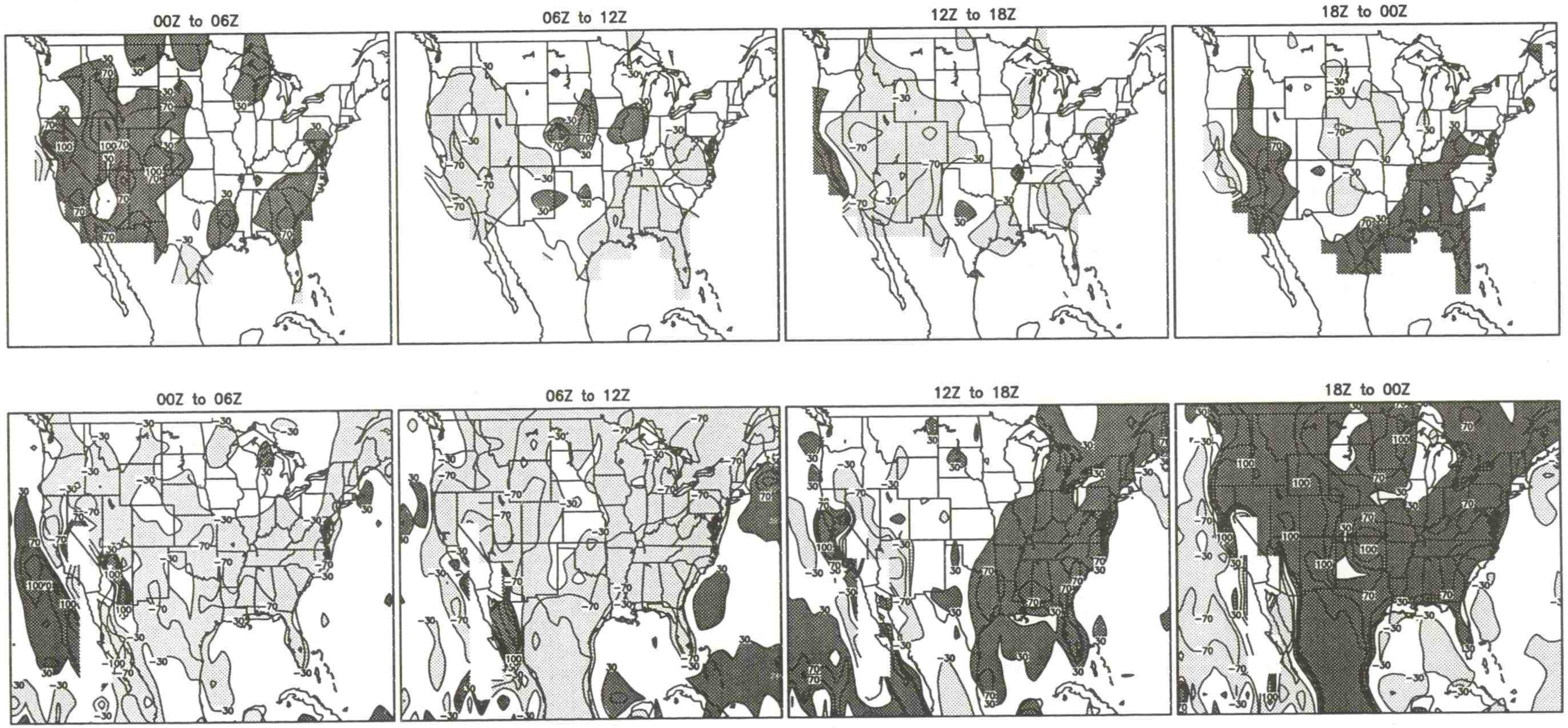

Figure 4. Percent departures from the daily mean of precipitation for 6-hour rainfall, averaged over JJA 1985. Top row is for raingauge observations; bottom row is for the NCEP/NCAR reanalysis precipitation forecasts.

On the annual cycle of the Mean Meridional and East-West Circulations from the NMC/NCAR reanalyzed fields during 1985-94

Muthuvel Chelliah
Climate Prediction Center, NMC/NWS/NOAA, Washington DC

It has been well known that the analyses of wind, particularly its meridional/divergent components, and vertical pressure velocity fields in the tropics which characterize the major aspects of the Mean Meridional Circulation (MMC) and the East-West Circulation (EWC) of the tropical atmosphere have only slowly been improving over the course of the last few years at many operational meteorological centers around the world. These MMC and EWC related fields along with the diabatic heating field, have been considered the least well known (and studied) of the atmospheric variables/quantities, since these are highly sensitive to constant changes in a) analysis system, b) convective parameterization scheme, c) observational network in the tropics, and so on.

Now that ten (1985-94) years of reanalysis data from the NMC/NCAR Reanalysis project have become available (30 more years of data will be available in the next couple of years), it is about time to begin to examine the MMC and EWC in more detail. A study of the mean annual cycle is essential before any attempt to investigate interannual or ENSO time-scale variability. In this preliminary study only DJF and JJA mean (based on 1985-94) zonal, meridional, vertical velocity fields from NMC Reanalysis and GDAS (NMC operational analysis, traditionally known as CDDB at the Climate Prediction Center) are computed and compared. We have examined zonal means (for the MMC) at all latitudes and averages over the latitude domain 5°N-5°S at all longitudes (for EWC). Furthermore, we also looked at the mean annual march of some these quantities through time-longitude plots. When relevant, comparisons of some of these fields are also made against corresponding fields from NASA Reanalysis and also against other independent observations such as outgoing longwave radiation.

In this write-up, due to space limitations only limited plots such as longitude-pressure sections near the equator are shown. Zonal mean meridional wind for DJF season is shown in Fig.1. For the same season, 5°N-5°S averaged zonal wind is shown in Figure 2. A similar cross section is shown in Fig.3 for vertical velocity omega for Jun-Jul-Aug season in Fig. 3. Also shown here for comparison are the means from NMC operational analysis in all figures, and from NASA's reanalysis in Fig. 3. Note from Figure 1 that, besides the 0.25-0.50 m/sec difference in the in the upper troposphere and stratosphere, even the correct direction of the vertical tilt of the meridional wind is different between reanalysis and operational analysis. In Figure 2, which shows the zonal component of wind in the equatorial atmosphere, large difference are seen over the Indian Ocean, eastern Pacific Ocean, and Atlantic Ocean. Improved stratospheric resolution in the reanalysis model able to nicely close off the vertical circulations. It is clear from Figure 3 that the mean vertical motion field from both reanalyses agree better with each other than with NMC's operational analysis. In general , the equatorial east-west circulation is stronger in the reanalysis. Figures not shown, also indicate that the march of the annual cycle in the deep tropics in fields such as 500 mb omega from reanalysis, agrees much better with similar plot of OLR in both spatial and temporal details. Finally it should be noted that time series (figures not shown) of any of the mean quantities mentioned above from reanalysis, represents and is more consistent with "actual climate signal" variation much better than was possible from any operational analyses that is available today.

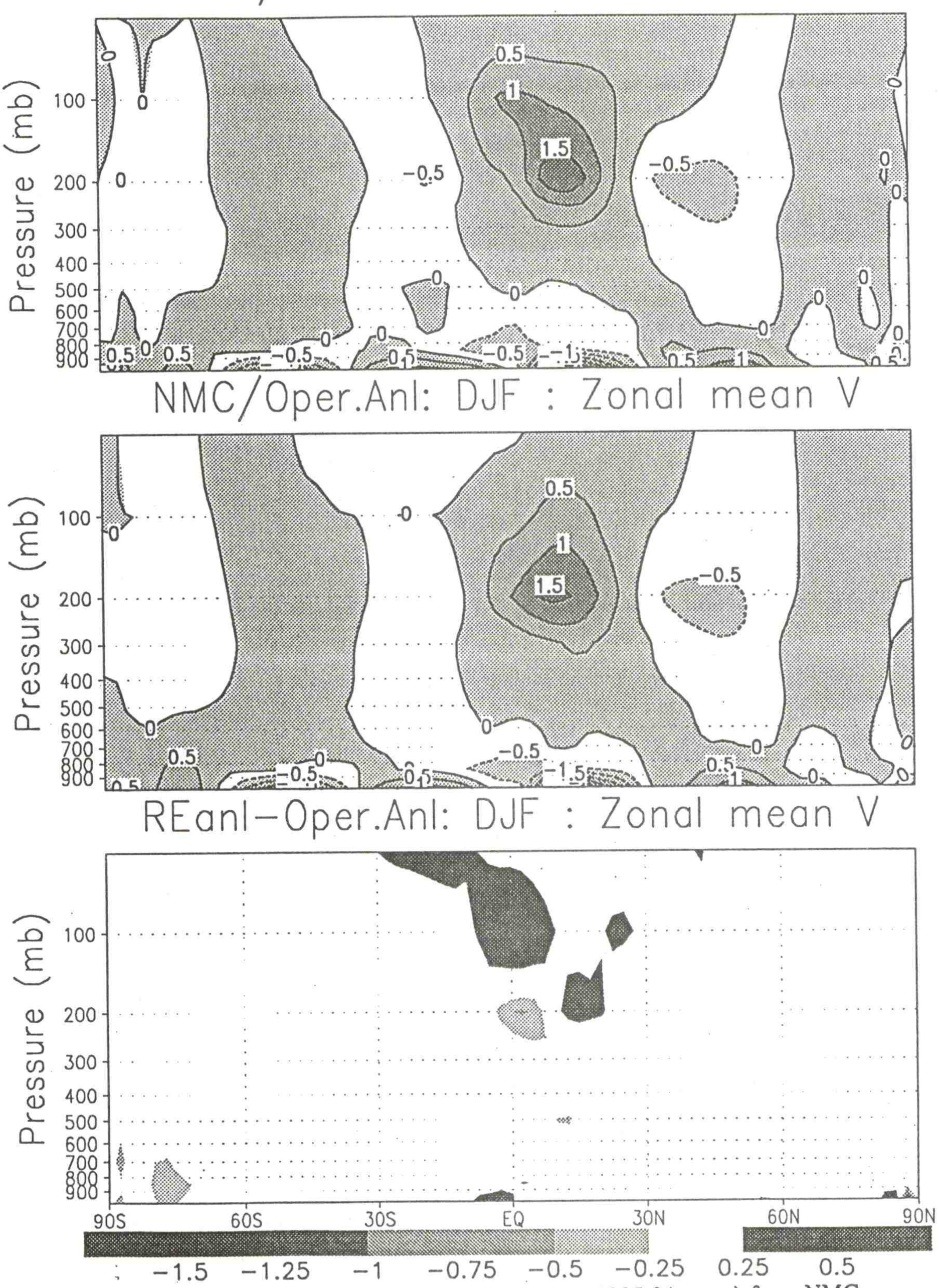

Figure 1: Zonal mean meridional wind for DJF season (1985-94 mean) from NMC reanalysis (top), NMC operational analysis (middle) and difference (bottom).

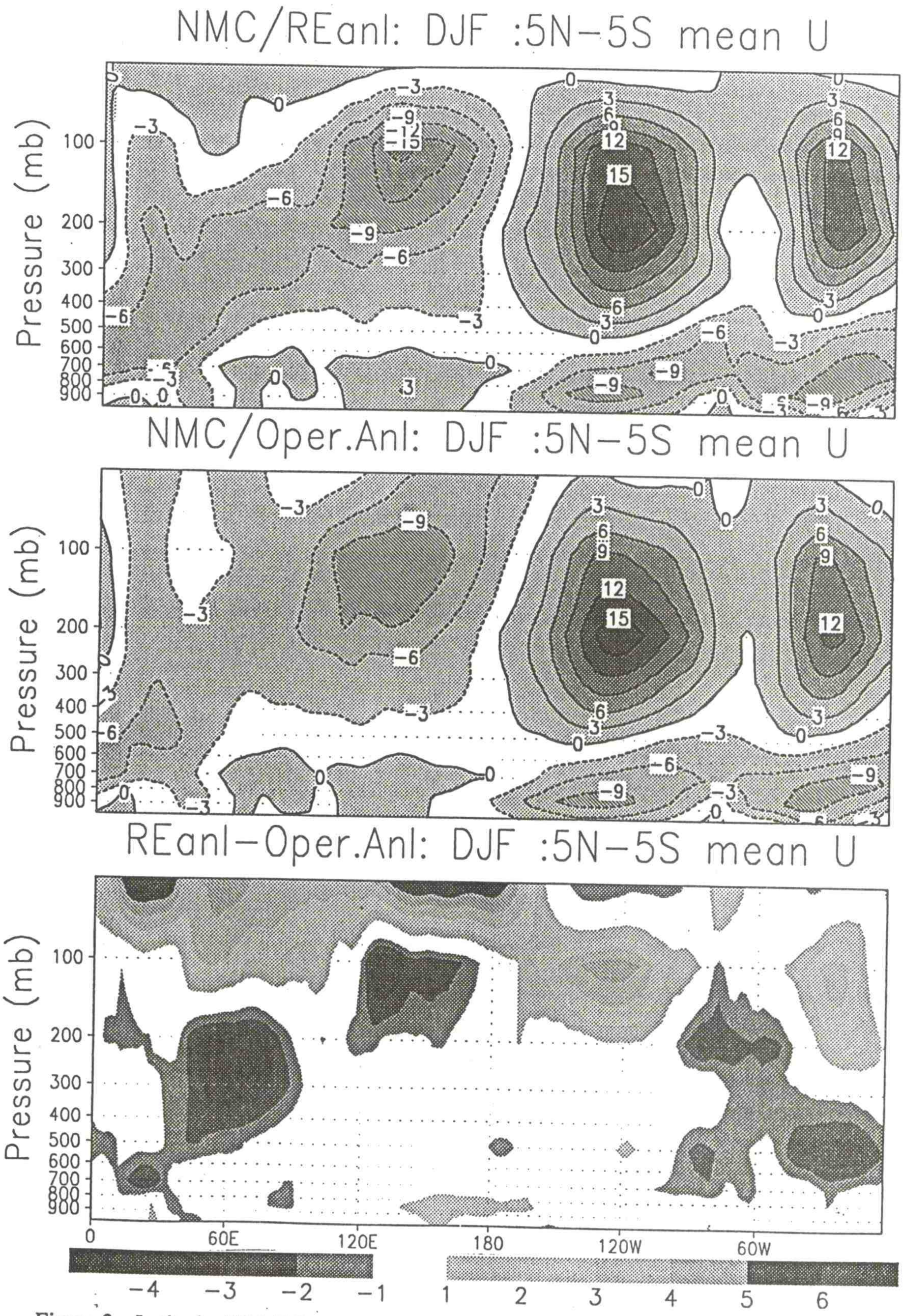

Figure 2: Latitude (5°N-5°S) mean Zonal wind for DJF season (1985-94 mean) from NMC reanalysis(top), NMC operational analysis (middle) and difference (bottom).

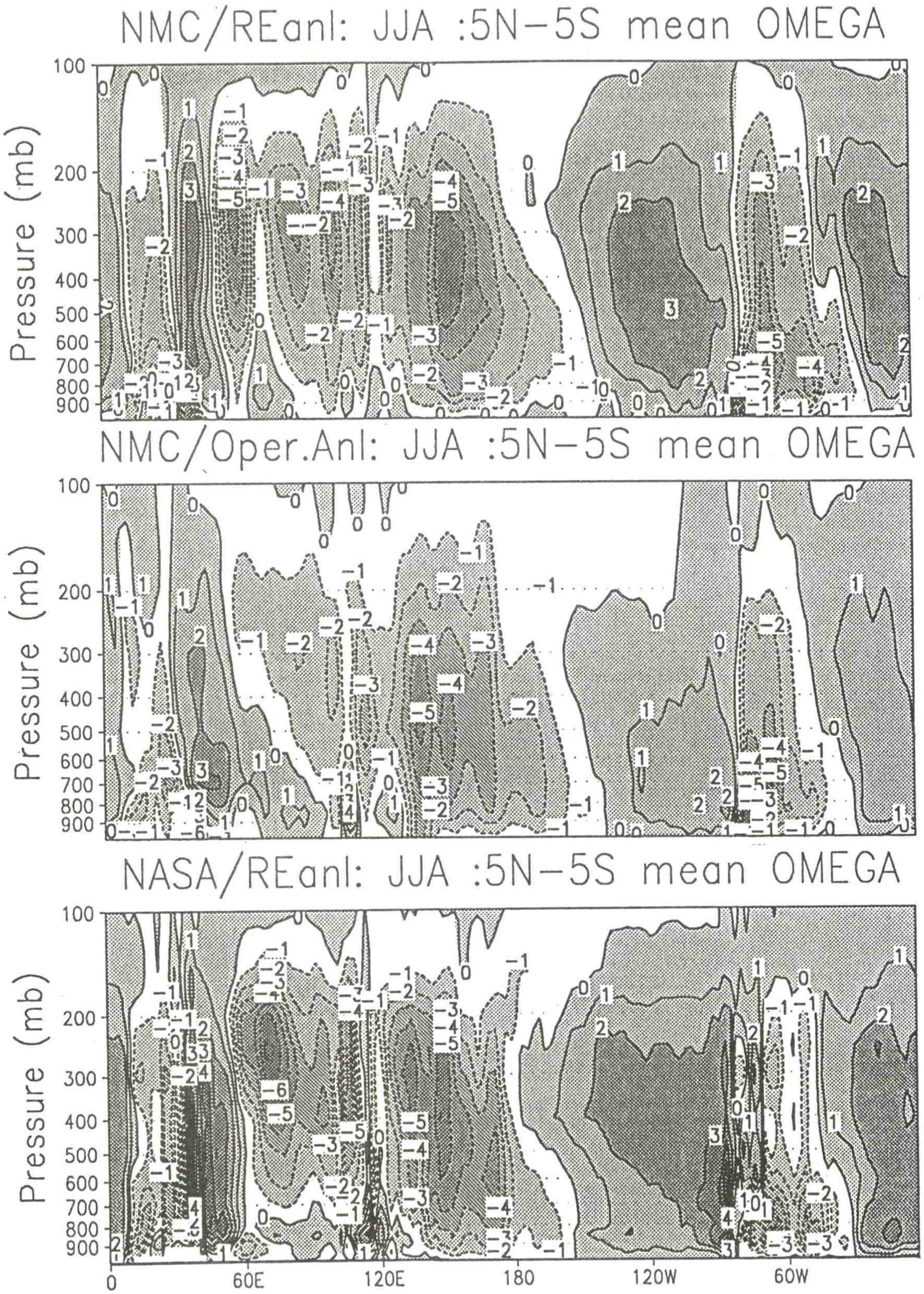

Figure 3: Latitude (5°N-5°S) mean Omega for JJA (1985-94 mean) season from NMC reanalysis (top), NMC operational analysis (middle) and from NASA reanalysis (bottom).

The Annual Cyle of Low-frequency Storm Track as Revealed in NCEP/NCAR Reanalysis

X.L. Wang

Climate Prediction Center, W/NCEP52
NCEP/NWS/NOAA, Washington, DC 20233

1. Introduction

Storm tracks, i.e., transient fluctuations on subweekly time scales, and their relationship with the midlatitude tropospheric stationary waves during the northern hemisphere winter have been documented in a series of observational studies by Blackmon et al. (1977, 1984a, 1984b) and Lau (1978). The climatological positions of the storm tracks are intimately related to the configuration of the time-mean flow, i.e., stationary troughs and quasi-permanent jet streams (Wallace and Gutzler, 1981; Lau, 1988).

Observational studies of low-frequency atmospheric variability have mostly seen concerned with *first*-moment quantities such as geopotential height, temperature or wind. This is particularly true when refer to climatology. In view of close relationship between seasonal mean circulation (*first*-moment) and low-frequency storm tracks activity (*second*-moment), it would be of interest to explore the variability of second moment statistics as well. Since stable estimates of these higher statistical moments often require long and homogenous data records, some limitations of previous attempts to study the storm track and its relationship with circulations include 1) the reliance of the height field in most observational studies, 2) a focus on a particular season such as northern winter which is just a portion of seasonal cycle. Those limitations, together with the lack of sufficient and homogenous data, have made it difficult to study relationship between the storm-track and circulation in a time continuous fashion. The current study uses a recent 9-year (1985-1993) global reanalysis datasets produced by NMC/NCAR (Kalnay et al. 1995), to re-examine the relationship between the storm track and circulation. This report focuses on identification of dominant patterns of climatological storm track and their association with climatological mean circulations in the global domain and in a time continuous frame.

2. Data and Analysis

The dataset used are daily averages of 200 mb stream function field of the NCEP/NCAR reanalysis from January 1, 1985 to December 31, 1993. Data has a resolution of 2.5° x 2.5° and spans globally. Detailed descriptions of the assimilation systems and output are found in the reference above, therefore, will not be discussed here.

In order to accentuate the synoptic scale disturbances with characteristic periods of several days, the daily stream functions are high-pass filtered to only retain those signals with temporal scale less than 6 days. A twenty day running variance of the high-passed stream functions are then calculated on daily base. This quantity is defined to approx the storm track activity.

Since the primary focus is on low-frequency climatology with period from sub-monthly to annual, pentad mean datasets are computed from both daily stream function and daily storm track activity for entire 9 years to reduce high frequency signal. The pentad climatologies are then subsequently formed for both variables. Results shown here are all based on these two pentad climatologies.

Extended Empirical Ortho-gonal Function analysis (EEOF) is used to further smooth the datasets and to identify dominant patterns of the low-frequency climatologies. For both datasets, a pair of annual cycle modes and a pair semi-annual cycle modes are obtained. The explained variance of these modes are shown in Table 1.

Table I Percentage Variance of EEOFs

	Mode 1 (AC-1)	Mode 2 (AC-2)	Mode 3 (SA-1)	Mode 4 (SA-2)
S.T.	46%	32%	10%	8%
S.F.	57%	34%	5%	4%

By identification of those modes, the stream function and storm track activity are then reconstructed with respect to the annual modes and semi-annual modes. From the reconstructed stream function, zonal wind and tendency of the zonal wind are calculated. Following discussion will be mainly based on these reconstructed quantities.

3. Time Asymmetry of Annual Cycle

Shown in Fig. 1 are principal components corresponding to the first four eigen modes of the stream function. It is clear that the first two modes, as a pair, describe the annual cycle, while the second pair (modes 3 and 4) captures the semi-annual variation. These modes constitute to the climatology of the stream function. Similar characteristics are seen in analysis of the storm track (Figures not shown). It is interested to note time asymmetry for the annual cycle modes (modes 1 and 2) in Fig. 1.

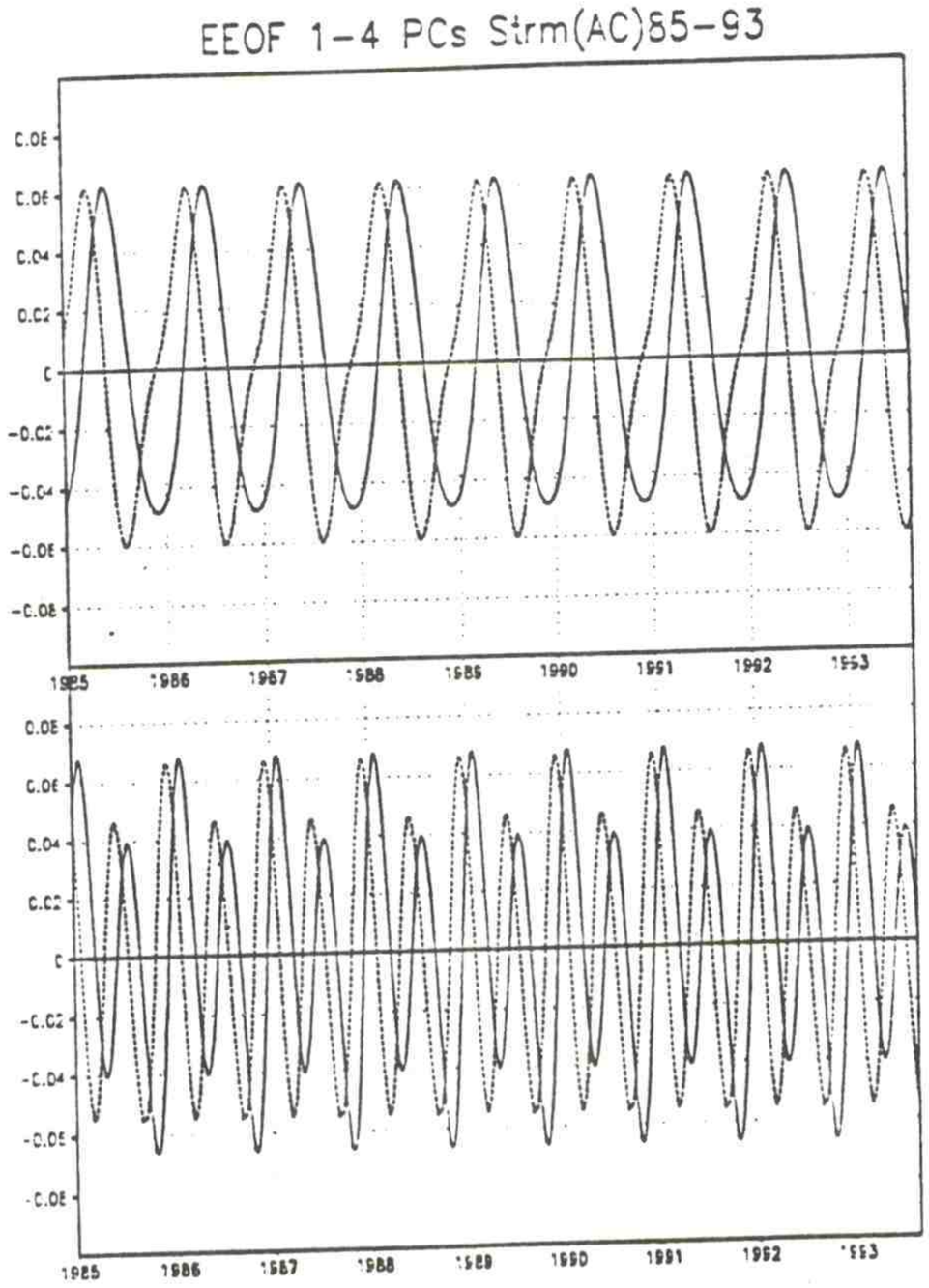

Fig.1. The first four principal components of the EEOF analysis for the pentad mean climatology of the 200 mb stream function.

After the reconstruction with these two modes, one point time series at location of 30°N and 160°E, where the climatological jet core is located, is plotted in Fig. 2. Each open circle in the diagram represents a pentad. It is very obvious that changes of the stream function in annual cycle are not sinusoidal. In the Fig. 2, it takes only 26 pentads changing from minimum to maximum and about 47 pentads on reverse course. Corresponding to annual evolution of the jet stream, this feature tells that jet acceleration from early Summer to late Fall is much faster than its weakening process. More discussion on this aspect will be furnished later.

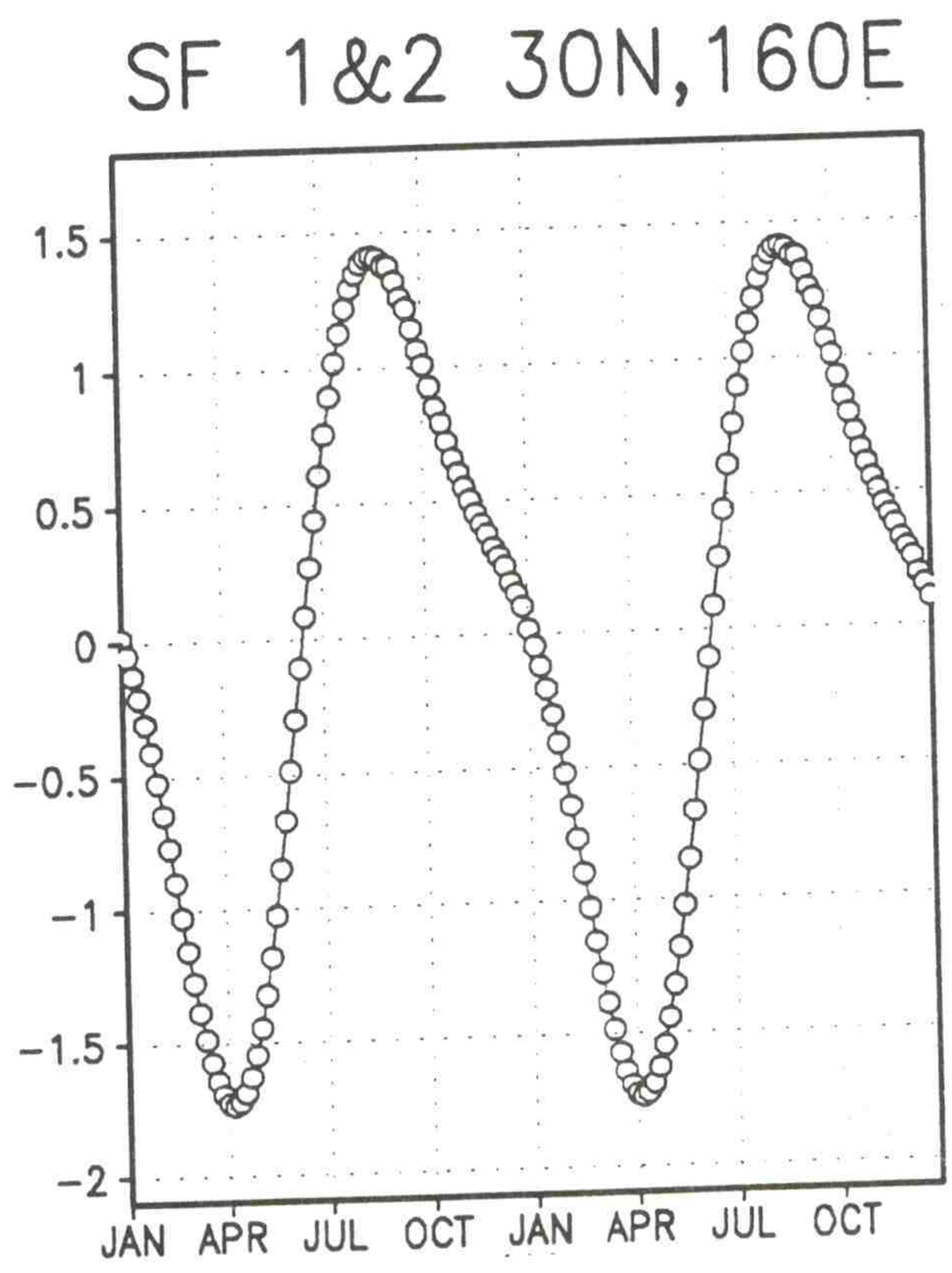

Fig.2. Re-constructed stream function using the first two EEOF modes at 30°N and 160°E. Each open circle represents a single pentad. Unit is 10^7 m^2/s

4. Relationship between Storm Track and Circulation

As mentioned earlier, the zonal wind and its acceleration are computed using reconstructed stream function

field in order to discuss relationship between jet stream evolution and storm track activity. In the following discussion, long term mean of the stream function and the storm tracks are excluded to highlight evolution of climatology.

a) Annual Cycle

Shown in Fig. 3 are a time-longitude section of zonal wind tendency (du/dt) along with storm track activity at 30°N where the Asian-Pacific jet core is located. For the du/dt, the minimum (the jet de-acceleration is the largest) and the maximum (the largest acceleration of jet) occur around 140°E at early June and later September, respectively. From the largest de-acceleration to the largest acceleration of the jet, it takes less than four months. This suggests once again the time asymmetry

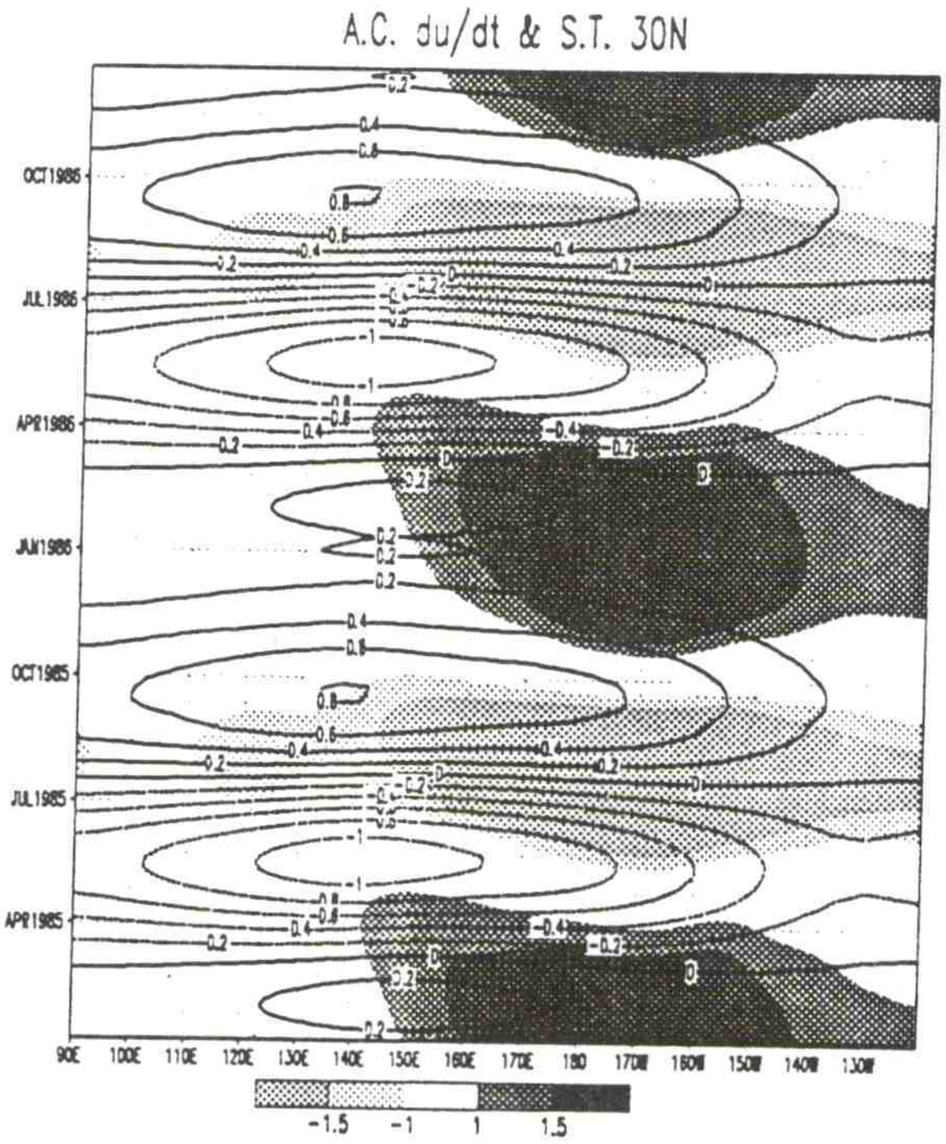

Fig.3. Time-longitude section of the zonal wind tendency (contour) from re-constructed stream function using first two EEOF modes at 30°N. Re-constructed storm tracks from the first two EEOFs are also shown as the shading. Units are 10^{-5} m/s² for du/dt and 10^{13} m⁴/s² for storm track activity. The contour intervals are 0.2 units and shading levels are as shown.

of the evolution of the jet in annual cycle. The largest changes of the storm tracks can be seen in the downstream from 160°E to 150°W.

b) Semi-Annual cycle

Similarly, semi-annual cycle of the zonal wind tendency and the storm track are shown in Fig. 4. Noticeably, the maximum or minimum du/dt occurs around 160°E, and corresponding storm track changes appear in further downstream. The time asymmetry is not evident in the semi-annual cycle.

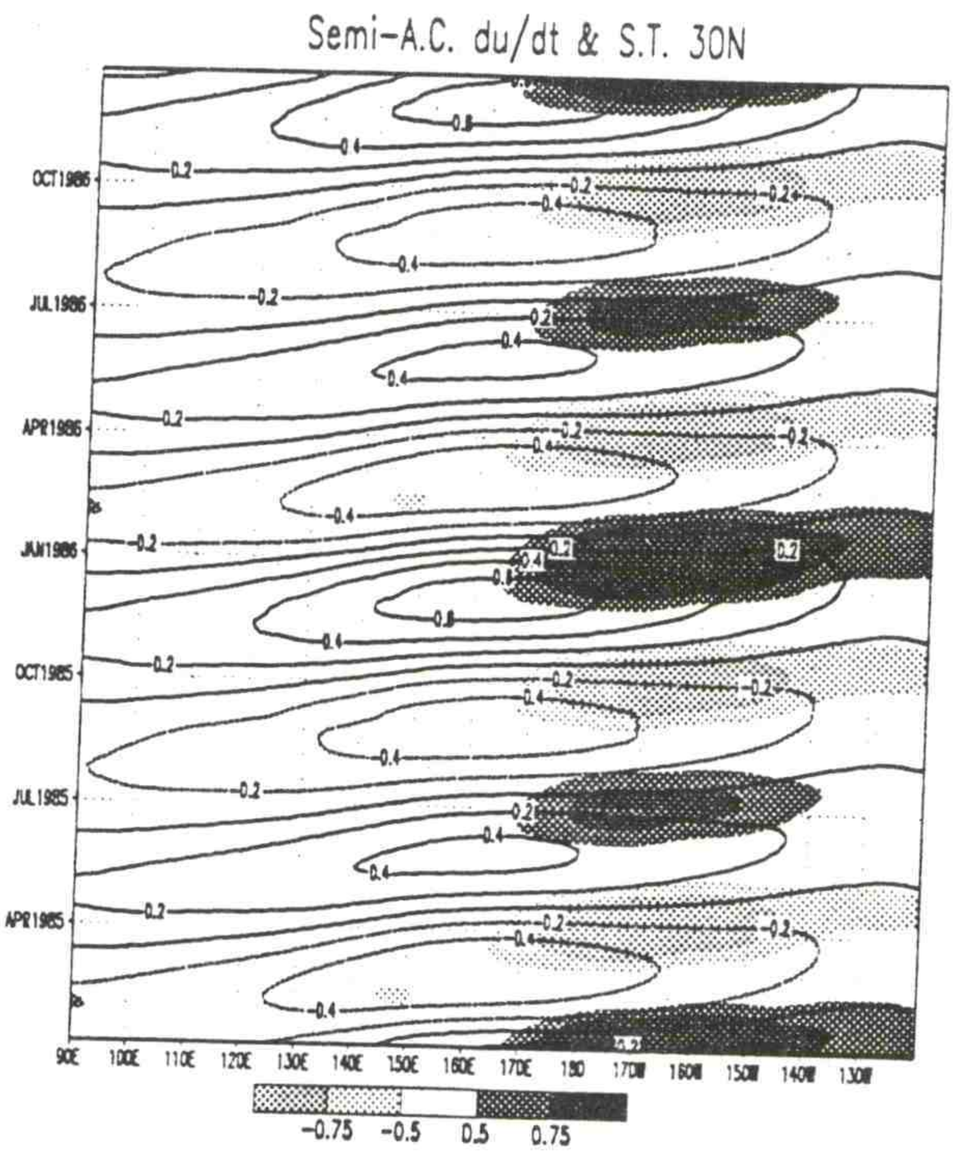

Fig.4. The same as in Fig. 3, except for the re-construction are made from the third and the fourth EEOF modes.

c) Climatology

With inclusion of both the annual cycle and the semi-annual cycle, climatologies of the zonal wind tendency and the storm tracks are shown in Fig. 5. It is quite clear that acceleration of the jet stream occurs first at west around 120°E-130°E and progresses toward east to about 160°E-170°E. However, The de-acceleration of the jet occurs first at east around dateline and retreat back to climatological jet core position south of Japan. Climatological evolution of the storm tracks are corresponding

very well to the jet change.

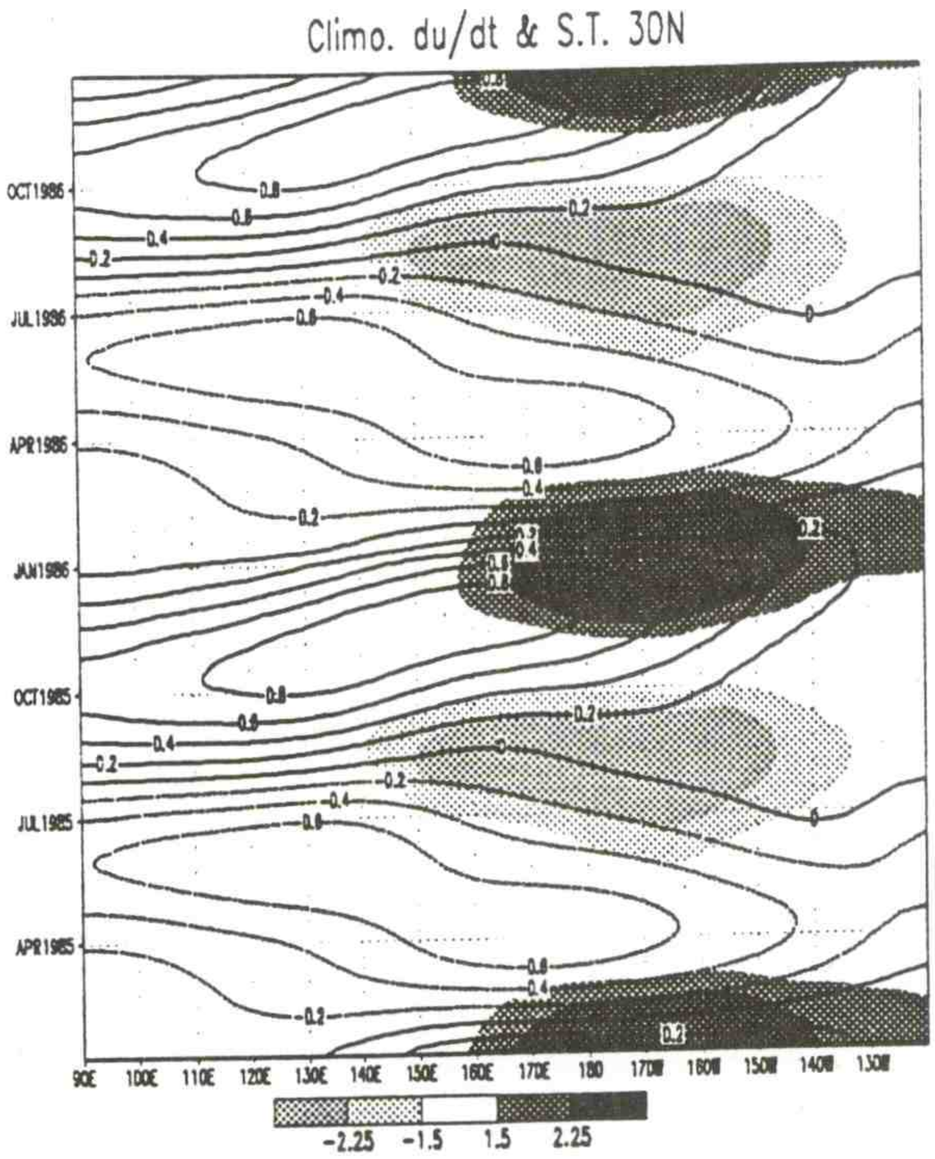

Fig.5. The same as in Fig..3, except for the re-construction made from the first four EEOF modes including both annual cycle modes and semi-annual cycle modes. This re-construction is nearly identical to the original pentad mean climatologies.

5. References

Blackmon, M.L., J.M. Wallace, N.-C. Lau, and S.L. Mullen, 1977: An observational study of the Northern Hemisphere wintertime circulation. *J. Atmos. Sci.*, 33, 1607-1623.

------, Y.-H. Lee, and J.M. Wallace, 1984a: Horizontal structure of 500 mb height fluctuations with long, intermediate and short time scales. *J. Atmos. Sci.*, 41, 961-979.

------,------,------, and H.-H. Hsu, 1984b: Time variation of 500 mb height fluctuations with long, intermediate and short time scales as deduced from log-correlation statistics. *J. Atmos. Sci.*, 41, 981-991.

Kalnay, E.M. et al., 1995: The NMC/NCAR Reanalysis Project. *Bull. Amer. Meteor. Soc.*, (in press).

Lau, N.-C., 1978: On the three-dimensional structure of the observed transient eddy statistics of the Northern Hemisphere wintertime circulation. *J. Atmos. Sci.*, 35, 1900-1923.

------, 1988: variability of the observed midlatitude storm tracks in relation to low-frequency changes in the circulation pattern. *J. Atmos. Sci.*, 45, 2718-2743.

Wallace, J.M. and D.S. Gutzler, 1981: Teleconnections in the geopotential height field during the Northern Hemisphere winter. *Mon. Wea. rev.*, 109, 784-812.

Components of the Earth Radiation Budget in NCEP/NCAR Reanalysis

Shi-Keng Yang [1], Alvin J. Miller[2] ,Yu-Tai Hou [3], and Chet Ropelewski[2]
[1] Research and Data Systems, Corp/Climate Prediction Center/NCEP
[2] Climate Prediction Center/NCEP
[3] General Science Corp/Environmental Modeling Center/NCEP

Introduction

The NCEP/NCAR Reanalysis (Kalnay et al., 1995) project is providing a long history of meteorological data that is processed from a single global data assimilation system (GDAS). This process has ensured a consistent homogeneous, high quality data set that contains the coherent dynamical-physical states. The data, thus, give the opportunity for understanding the characteristics of GDAS in energy exchanges among the space, the earth and the atmosphere. It would also provide the basis for further refinements in clouds and radiative transfer parameterizations in GDAS and the operational weather prediction models.

In this study, the components of the Earth Radiation Budget from NCEP/NCAR Reanalysis, including outgoing longwave radiation (OLR), reflected solar radiations (in both total sky and clear sky conditions), net surface shortwave radiation, surface albedo, compared with various satellite data sets, either measured, or inferred from ERBE. The performance of physical parameterizations in GDAS are analyzed.

Data

The components of Earth Radiation Budget in NCEP/NCAR Reanalysis are utilized for the study. Two years' data, 1985-1986, are taken from the monthly mean archive and translated from Gaussian grids to a 2.5° x 2.5° lat/lon grid.

Top-of-the-Atmosphere (TOA) fluxes measured by NASA Earth Radiation Budget Experiment (ERBE) (Barkstrom, et al., 1989) are used for comparison. During the two-year period studied here, the monthly mean data are derived from the measurements sampled by two satellites, the sun-synchroneous NOAA-9 and ERBS (Earth Radiation Budget Satellite).

For the current study, the scanner data are used for their higher spatial resolution, 40 Km at nadir, and mapped to a 2.5° x 2.5° lat/lon grid. For the instantaneous irradiance, the uncertainties are about 1% for longwave and 2~3% for shortwave. These translate to the uncertainties of $\pm$ 5 W/M^2 for the monthly averages of both shortwave and longwave. A comparison of ERBE and NOAA Advanced Very High Resolution Radiometer (AVHRR) longwave flux (Gruber et al. 1994) indicates that the global bias between the two data sets is between -1 and 2 W/M^2.

Surface net shortwave flux is from Li et al. (1993) algorithm estimates the net shortwave radiation at the surface from the TOA reflected shortwave flux. The algorithm is a parameterization of radiative transfer calculation that takes the effect of precipitable water into account. Combined with the humidity data of European Center for Medium Range Weather Forecasts and ERBE, Li and Leighton (1993) have thus derived a five-year global climatology of Solar Radiation Budget at the surface which are used in the current study.

ERBE provides a global coverage for the clear sky fluxes, which makes it all possible to estimate the broadband surface albedo. Staylor and Wilber's (1990) estimates of the surface albedo

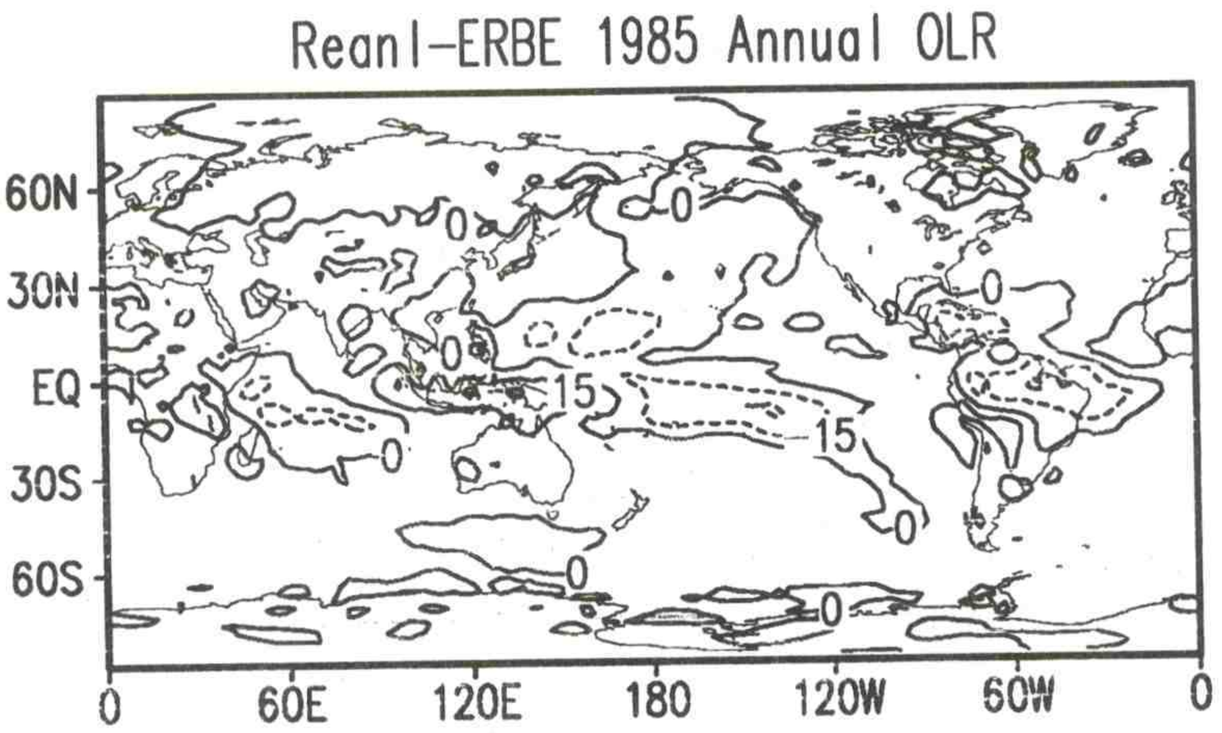

fig.1

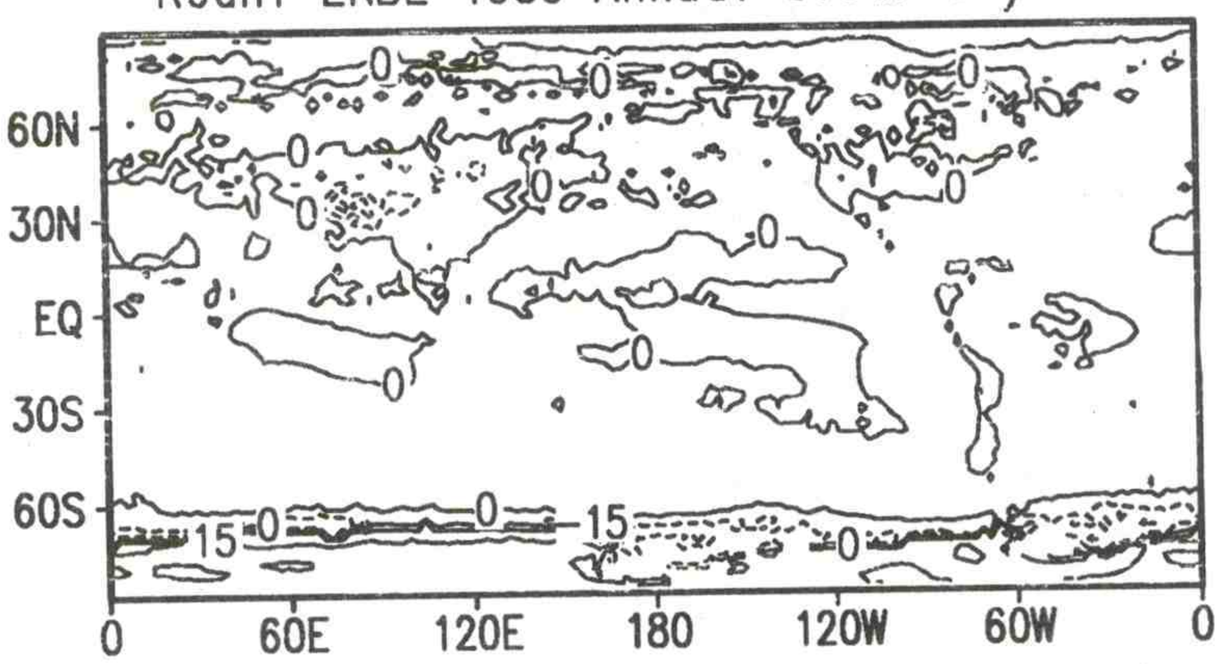

fig.2

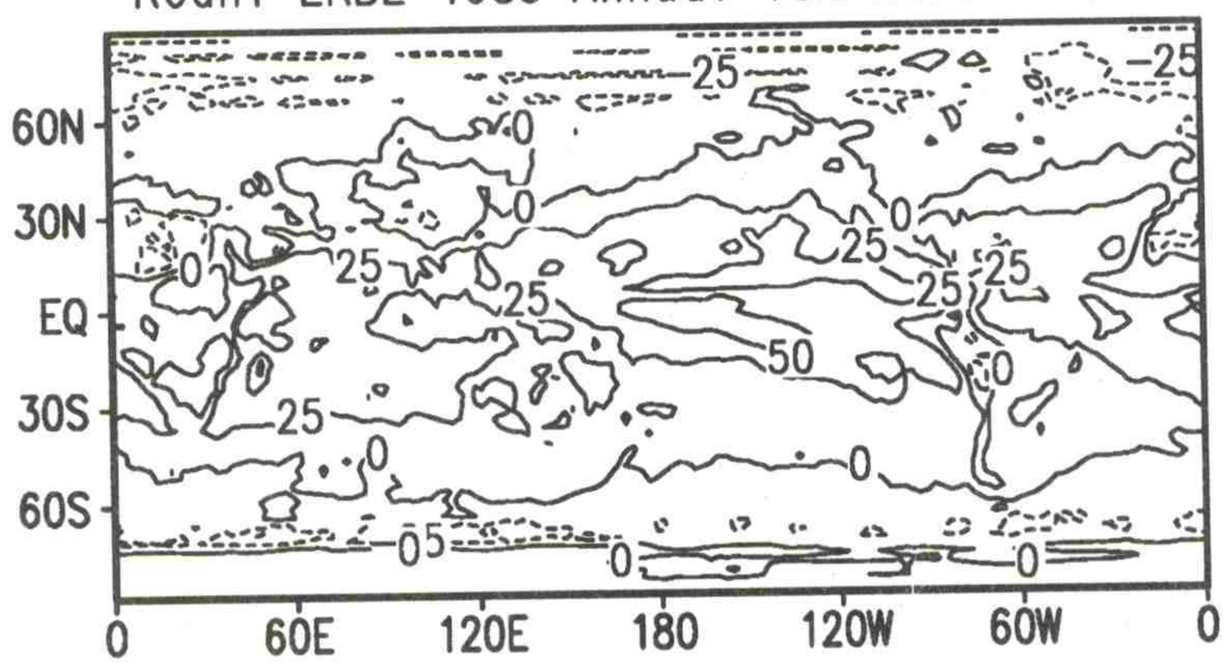

fig.3

are based on the TOA-to-Surface conversions of Koepke and Kriebel (1987), with the effect of solar zenith angle, water vapor, and aerosol absorption and scattering taken into account. Ozone absorption above the stratosphere is treated as well. In compiling this surface albedo data set, ancillary water vapor and ozone data are taken from TOVS observations, and aerosol data are from World Climate Programme reports (WCRP, 1993)

Results

Compared to the broadband measurements from Earth Radiation Budget Experiment (ERBE), shows that the global annual mean OLR difference is only about 1.5% with Reanalysis slightly higher than ERBE (237 W/M^2 vs. 233.7 W/M^2). Annual mean correlation coefficient for OLR is .81; while clear sky OLR is .76. Synoptic patterns in the Reanalysis are well defined, however. Systematic biases over Amazon basin and Indonesia are larger than 20 W/m^2, see Fig.1. Since both regions compare well with ERBE in clear sky condition, shown on Fig.2, both are active convection regions, but show opposite signs of differences in total sky conditions, it suggests that GDAS cloud formation mechanisms over land may be different from that over ocean.

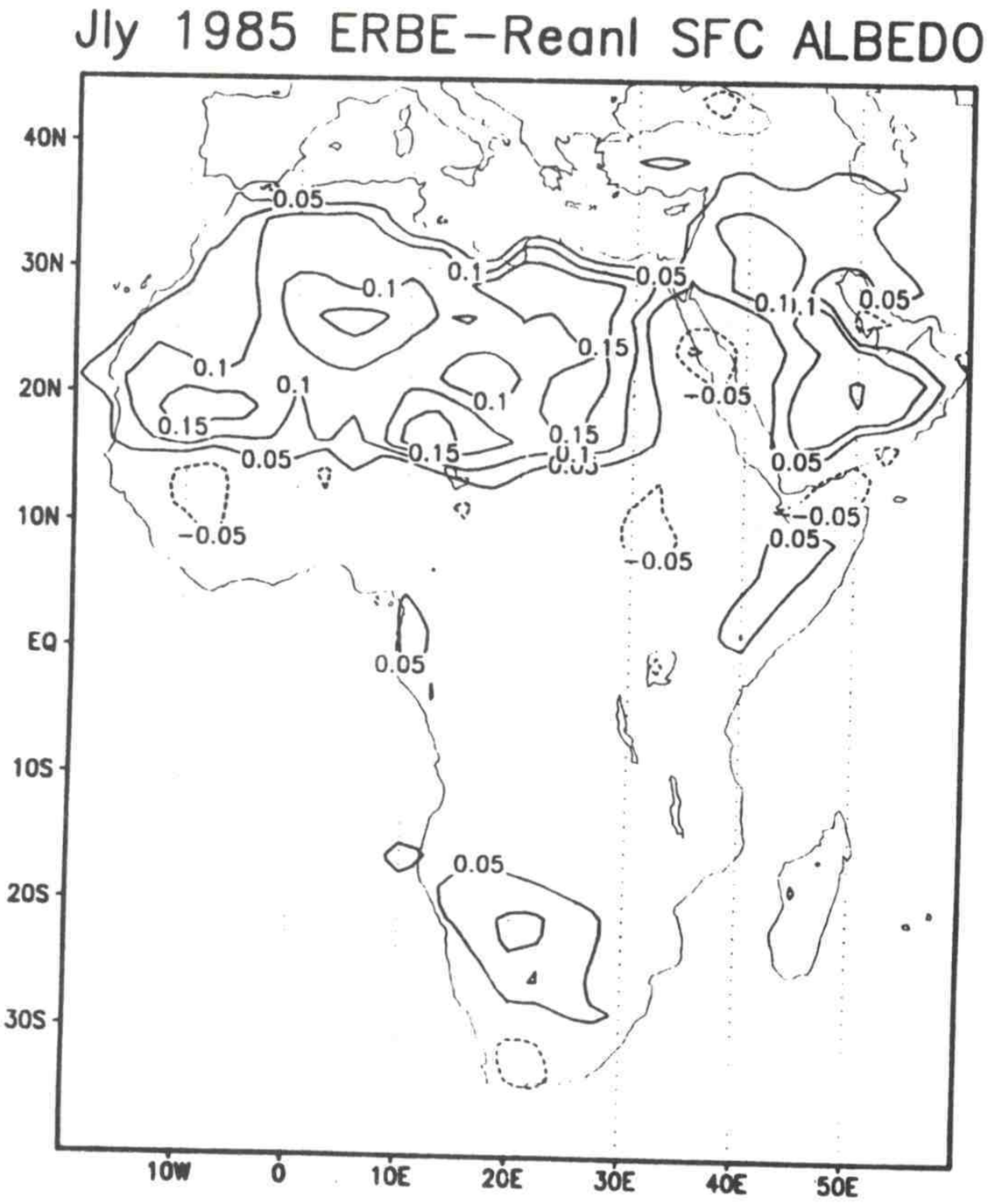

Fig.4

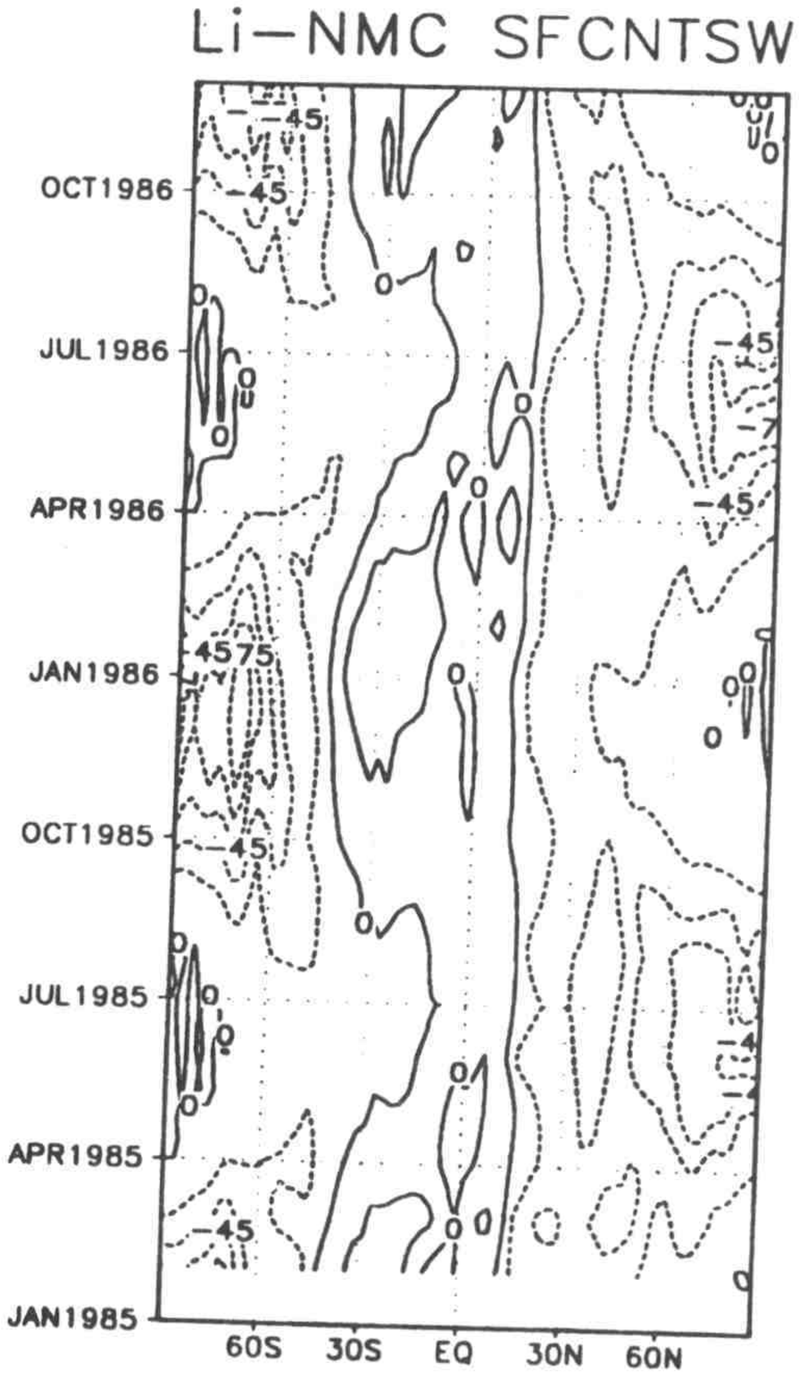

Fig.5

Over the Sahara Desert, the Reanalysis underestimates the reflected shortwave (Fig.3), and overestimates OLR, both in the clear sky and total sky conditions, indicating that the prescription of the surface albedo in the Reanalysis is too high. This result is confirmed by comparing to Staylor and Wilber (1990) surface albedo, shown on Fig.4. It is suggested that surface albedo prescription in GDAS can be increased by up to 20%.

The comparison on the reflected shortwave radiation at TOA also reveals differences as a function of latitude in the mid-high latitudes (Fig.3), indicating that the error may be related to solar angles in the radiative transfer calculations. The annual mean correlation coefficient is .58 for total sky; and .77 for clear sky.

Surface net shortwave radiation from the Reanalysis is compared with the estimates of Li and Leighton (1993), shown on Fig.5. As in the case of OLR, the results show very good agreement in the synoptic patterns. However, the results also indicate a larger annual global mean bias of 4% for Reanalysis, (155.4 w/m^2 for Li vs. 162.3 w/m^2 for the Reanalysis).

In spite of the cited differences, the Reanalysis data can contain signals for climate variations, if one compares the patterns of the interannual variabilities. Continual improvement on the cloud/radiation parameterizations, are necessary for improving future analyses and numerical forecasts. This validation suggests that the reanalysis data are useful in diagnosing climate variabilities, However, also indicate the deficiencies of the NMC global forecast model, such that a long integration of the model could possibly lead to a cooler model climatology.

Acknowledgment:

We appreciate Dr. Z Lee of Canadian Remote Sensing Center for providing the surface net sw radiation data. Also, extend our thanks to Dr, Charlie Woodlock and Ms. Nancy Rich of LaRC for the Surface Albedo info. This work is supported by a NASA Grant L 90988C.

References

Barkstrom, B., E. Harrison, G. Smith, R. Green, J. Kibler, R. Cess, and ERBE Science Team, 1989: Earth Radiation Budget Experiment (ERBE) Archival and April 1985 Results. Bull. Amer. Meteor. Soc, V70, pp 1254-1262.

Gruber, A., R. Ellingson, P. Ardanuy, M. Weiss, S.-K. Yang, and S. N. Oh, 1994: A Comparison of ERBE and AVHRR Longwave Flux Estimates. Bull. Amer. Meteo. V75. No. 11, pp 2115-2130

Kalnay, E., et al., The NMC/NCAR Reanalysis Project. To appear in Bull. AMS., 1995.

Kalnay, E., G. DiMego, S. Lord, M. Kanamitsu, A. Leetmaa, and D. B. Rao, NMC Modeling and Data Assimilation plans for 1994-1998. 1994: Proc. 10th AMS Conf . on Numerical Weather Prediction, Portland OR, July 18-22.

Koepke, P., and K. T. Kriebel, 1987: Improvements in the shortwave cloud-free radiation budget accuracy, Part I: Numerical study including surface anisotropy. J. Cli. App. Met., V26 pp 374-395.

Li, Z., H.G. Leighton, K. Masuda, and T. Takashima, Estimation of SW flux absorbed at the surface from TOA reflected flux, J. Clim., V6, pp317-330

Li, Z., and H. G. Leighton, 1993: Global climatology of the solar radiation budget at surface and in the atmosphere from 5 years of ERBE data. J. Geo. Res. V98, pp 4919-4930

Staylor, W. F., and A. C. Wilber, 1990: Global Surface Albedos Estimated from ERBE Data, pp. 231-236. Proc. 7th AMS Conf. on Atmos. Radiation, San Francisco, CA July 23-27, 1990

WCRP, 1993: Experts meeting on aerosols and their climate effects. A. Deepak and H. E. Gerber editors, WCP-55 107 pp.

THE MAINTENANCE OF INTRASEASONAL TRANSIENT EDDY ACTIVITY IN THE GEOS-1 ASSIMILATED DATASET

Robert X. Black
School of Earth and Atmospheric Sciences
Georgia Institute of Technology, Atlanta, GA 30332-0340

1. Introduction

A fundamental question in climate dynamics is precisely how the observed spectrum of intraseasonal transient wave activity is maintained. Although past observational studies clearly illustrate the importance of processes such as heat and momentum fluxes, scale interaction, and diabatic heating, the limitations of observational datasets have made it difficult to quantify the contributions of physical processes such as diabatic heating and frictional dissipation. Furthermore, in traditional approaches to eddy budgets (e.g., energetics analyses) regional budgets are difficult to implement. Adopting a potential vorticity framework in conjunction with the multi-year GEOS-1 assimilated dataset (GEOS-1 DAS) we perform local, quantitative assessments of the role of specific dynamical and physical processes in maintaining intraseasonal eddy variability.

2. Methods

We diagnose winter-averaged potential enstrophy analyses for distinct classes of intraseasonal transient eddies. Eddy potential enstrophy budgets are constructed from the conservation relation governing the time evolution of quasigeostrophic (QG) pseudopotential vorticity on a sphere. Separate budgets are formulated for bandpass (2.5-6 days) and lowpass (10-90 days) transient eddies. Dividing dependent variables into time-average (overbar) and perturbation (primes) components, the general form of these budgets is given by:

$$\left(\frac{\partial}{\partial t} + \bar{\mathbf{v}} \cdot \nabla\right)\left(\frac{\overline{q'^2}}{2}\right) = -\overline{\mathbf{v}'q'} \cdot \nabla\bar{q} - \overline{q'(\mathbf{v}' \cdot \nabla q')} + \overline{q'S_H'} + \overline{q'S_F'} \qquad (1)$$

Where q is the QG pseudopotential vorticity, $\mathbf{v}$ is the geostrophic velocity, and S_H and S_F are diabatic and frictional sources of q, respectively. For seasonal averages (zero tendency) there is a balance among horizontal advection by the mean flow, cross-gradient eddy fluxes of q, nonlinear eddy interactions, and diabatic and frictional sources/sinks of enstrophy. Following Illari and Marshall (1983), if $\bar{q} = \bar{q}(\bar{\Psi})$, then part of the cross-gradient eddy flux term simply acts to balance enstrophy advection by the mean flow. Subtracting this component results in an equation that is now localized both horizontally and vertically (see Black and Dole 1993 for details):

$$\frac{\partial}{\partial t}\left(\frac{\overline{q'^2}}{2}\right) = -\overline{(\mathbf{v}'q')}_* \cdot \nabla\bar{q} - \overline{q'(\mathbf{v}' \cdot \nabla q')} + \overline{q'S_H'} + \overline{q'S_F'} \qquad (2)$$

(A) (B) (C) (D)

The new residual cross-gradient eddy flux term (A) represents local conversions from the climatological-mean flow into the eddies. In applying (2) to particular frequency bands, interactions among different frequencies will be manifested by local nonlinear sources or sinks (B). Term (C) includes separate contributions from latent heating, radiation, and turbulent dissipation of heat. We apply (2) to 8 winters of the GEOS-1 DAS produced by the Data Assimilation Office at NASA/GSFC. The GEOS-1 DAS provides dynamically consistent estimates of diabatic heating and frictional dissipation (e.g., Schubert et al. 1993). Using the assimilated data we calculate the contributions of the individual terms in (2). This provides a quantitative assessment of the roles of nonlinear and nonconservative processes in maintaining the intraseasonal transient eddy activity. Uncertainties in individual budget terms, particularly contributions from diabatic and frictional processes, will be analyzed by comparing our results to similar estimates derived from NCEP/NCAR reanalyses. By contrasting Ertel and QG formulations, we also aim to assess the adequacy of the QG approach.

3. Results

Fig. 1 displays vertical profiles of eddy potential enstrophy for both bandpass (BP) and lowpass (LP) eddies averaged over the North Atlantic storm track region. Above the boundary layer, both profiles are observed to peak in the upper troposphere. Thus, we focus on enstrophy budgets performed at the 400 mb level. The results are not sensitive to the exact level chosen. In Fig. 2, contours of eddy potential enstrophy are superposed upon vectors of the total eddy flux of q for each frequency band. Over the storm track regions, BP eddies are characterized by local maxima in eddy enstrophy and southwestward eddy fluxes of q (Fig. 2a). On the other hand, LP eddies (Fig. 2b) exhibit local enstrophy maxima near the end of the storm tracks with associated eastward and southward eddy fluxes of q. There is a component of the LP eddy flux that appears to rotate cyclonically around the enstrophy contours. This is the part of the flux acting to balance enstrophy advection by the climatological-mean flow.

The residual cross-gradient eddy flux is plotted in Fig. 3 along with contours of climatological-mean q. For BP eddies we note distinct downgradient residual fluxes in the storm track regions over the North Pacific and North Atlantic. This implies a local conversion of enstrophy from the winter-mean flow into the BP eddies. Similarly, for the LP eddies there are prominent downgradient residual fluxes located near the two primary local maxima in LP eddy enstrophy (compare Figs. 2b and 3b). Therefore, there are substantial positive conversions from the winter-mean flow into the eddies for both BP and LP frequencies.

This is quantified by calculating term A in (2), displayed in Fig. 4a for the BP eddies. As expected, significant positive conversions are found in the storm track regions. The conversions are primarily offset by nonlinear interactions with eddies in other frequency bands (term B - not shown), which act mainly as an enstrophy sink. Conversely, latent heat release (included in term C) provides an additional positive enstrophy source over the storm tracks (Fig. 4b). Over the North Pacific this contribution is of the same order as the conversion from the mean flow. This is consistent with the notion that latent heat release plays an important role in synoptic-scale processes such as cyclogenesis. Radiative processes (not shown) are weakly dissipative of BP eddy potential enstrophy. Turbulent dissipation of heat and momentum is very weak at the 400 mb level.

Terms A and B of (2) are shown for LP eddies in Fig. 5. As for the BP eddies, we note prominent positive conversions over the two local maxima in LP eddy activity (see Fig. 2b). A comparison of the conversions (Fig. 5a) with the nonlinear term (Fig. 5b) suggests that the conversions are largely balanced by a nonlinear sink of eddy potential enstrophy. Unlike for BP eddies, however, latent heating plays a weaker and less coherent role in the LP budget. Both latent heat release and radiative processes are, on average, weakly dissipative of LP eddy enstrophy.

Acknowledgments. This research is supported by NASA grant NAG 5-2919.

References.

Black, R. X. and R. M. Dole, 1993: The dynamics of large-scale cyclogenesis over the North Pacific Ocean. *J. Atmos. Sci.,* **50,** 421-442.

Illari, L., and J. C. Marshall, 1983: On the interpretation of eddy fluxes during a blocking episode. *J. Atmos. Sci.,* **40,** 2232-2242.

Schubert, S. D., R. B. Rood and J. Pfaendtner, 1993: An assimilated dataset for Earth science applications. *Bull. Amer. Meteor. Soc.,* **74,** 2331-2342.

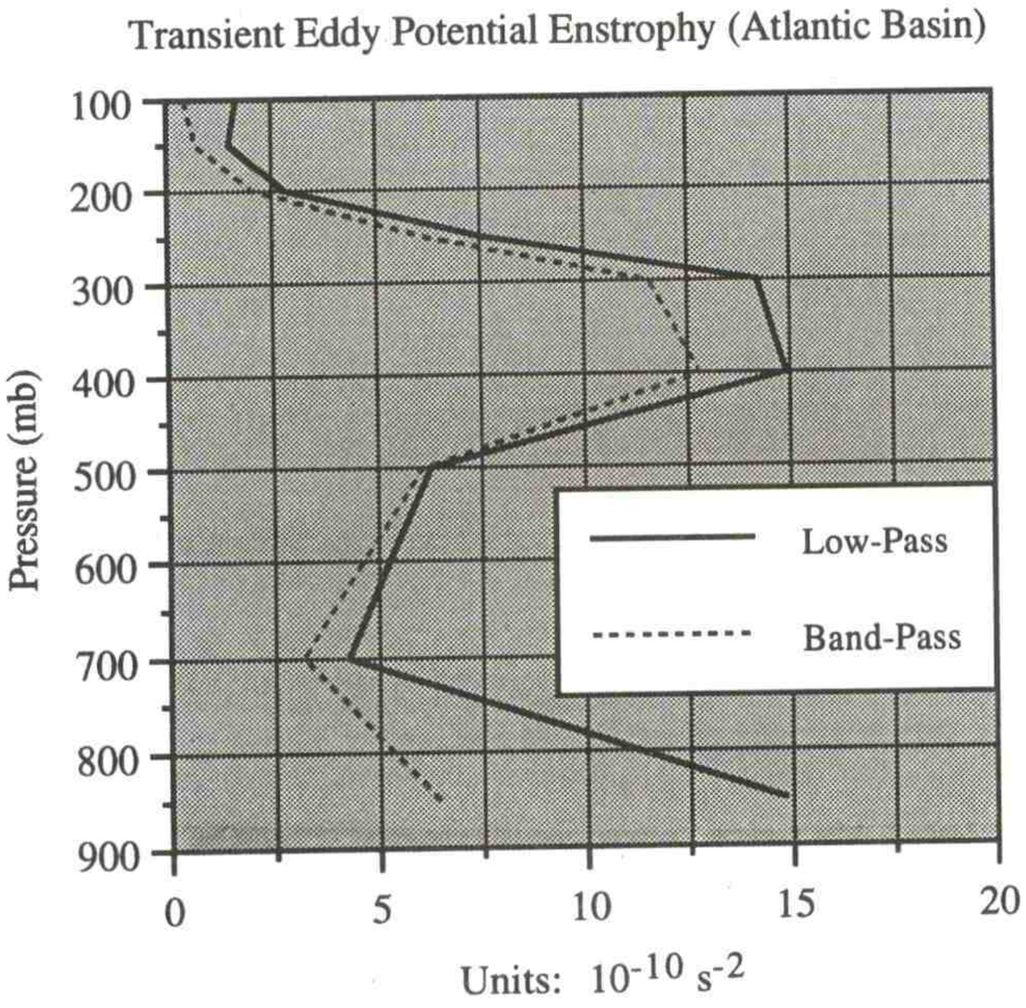

Fig. 1. A vertical profile of the winter-mean transient eddy potential enstrophy averaged over the North Atlantic basin for LP and BP eddies. Units: 1×10^{-10} s^{-2}.

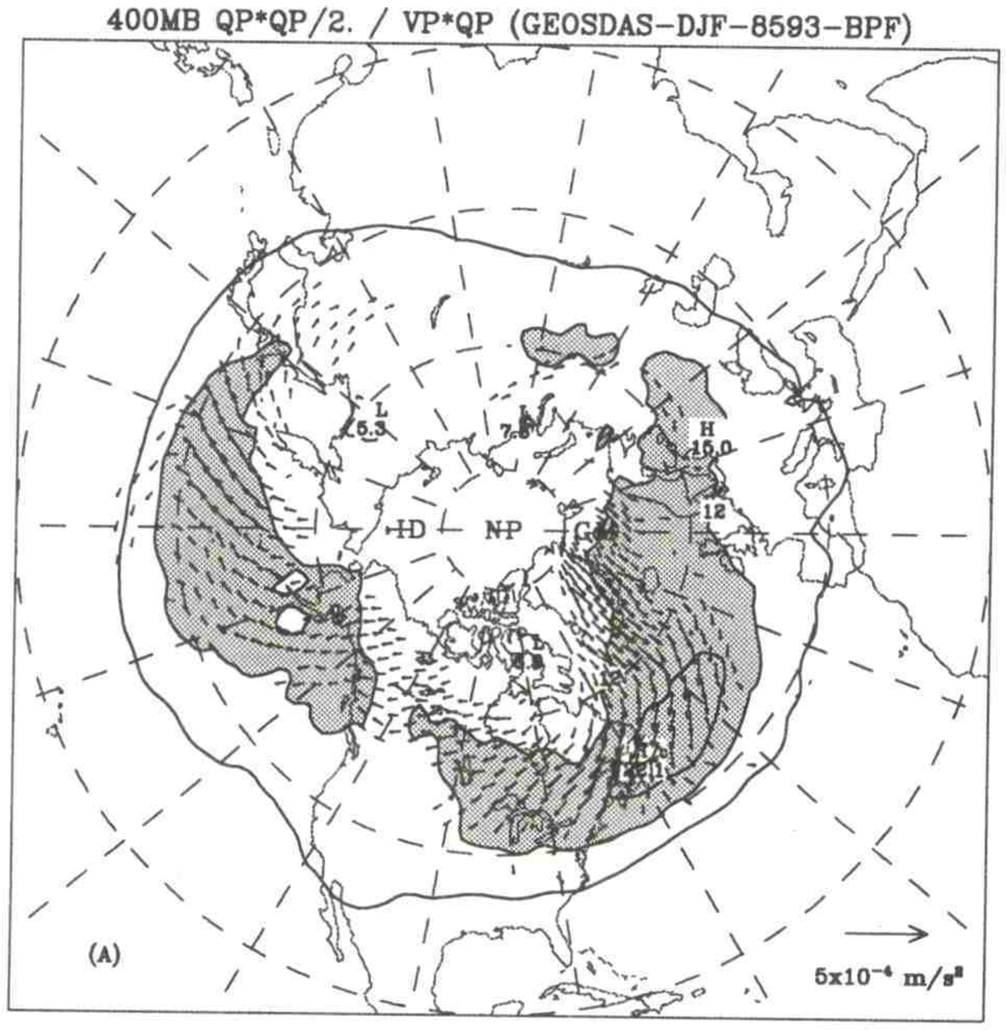

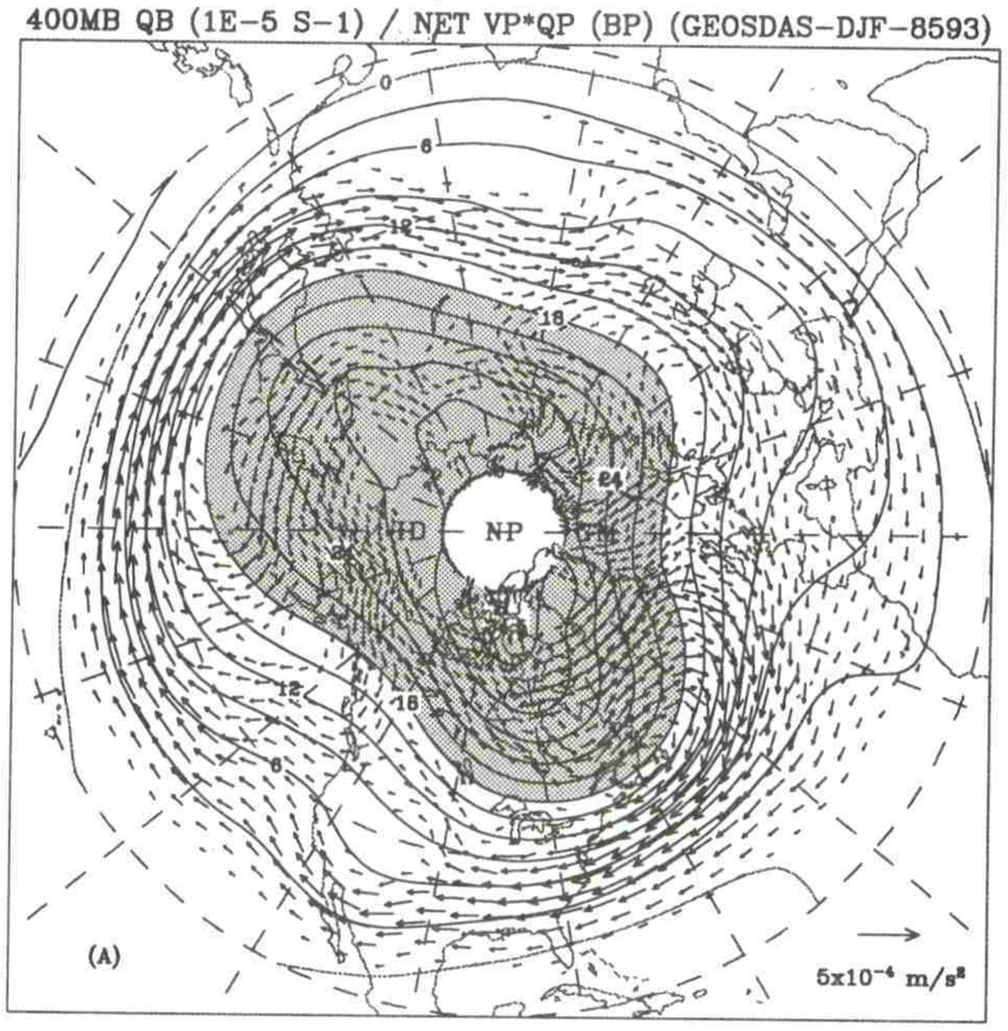

Fig. 2. Wintertime-mean 400-mb eddy potential enstrophy (Contour interval: $6x10^{-10}$ s^{-2}) and vectors of the total eddy flux of pseudopotential vorticity for (a) BP and (b) LP transient eddies. Enstrophy magnitudes greater than 12 (18) units are shaded lightly in a (b).

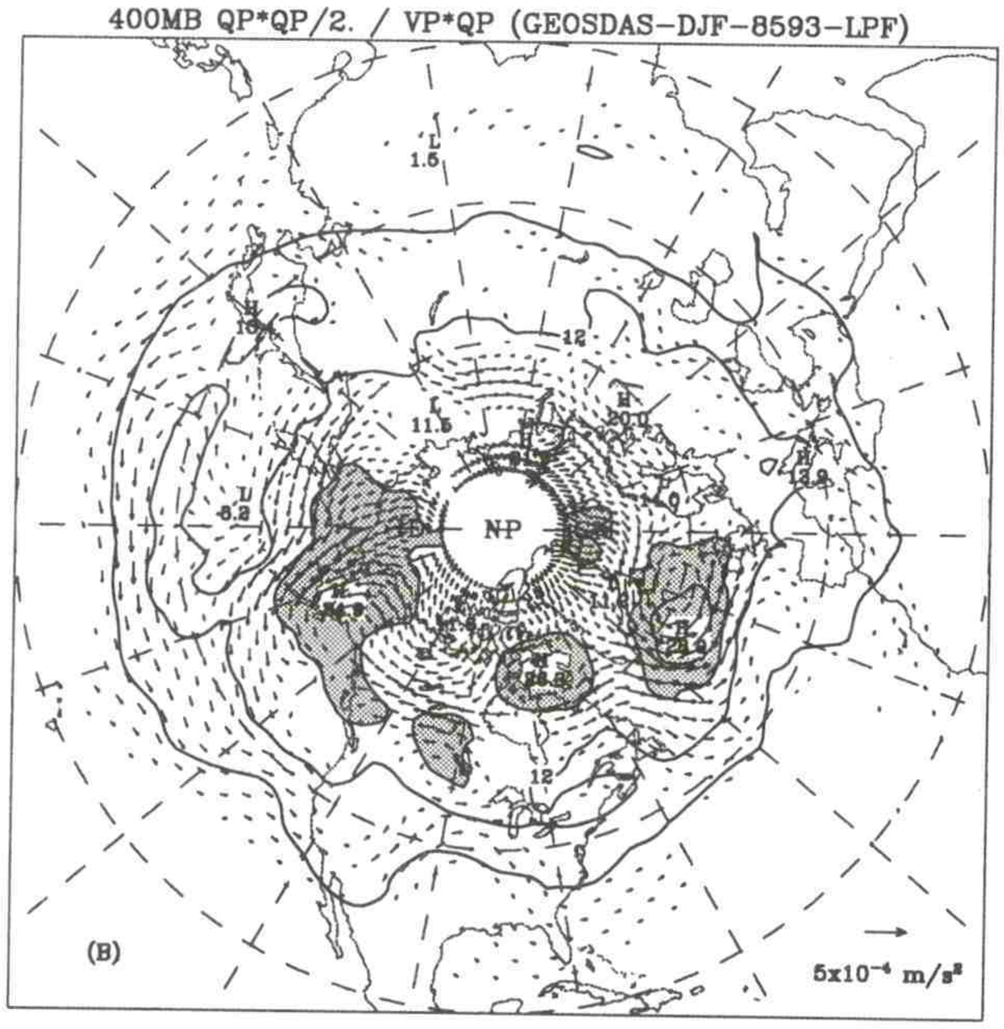

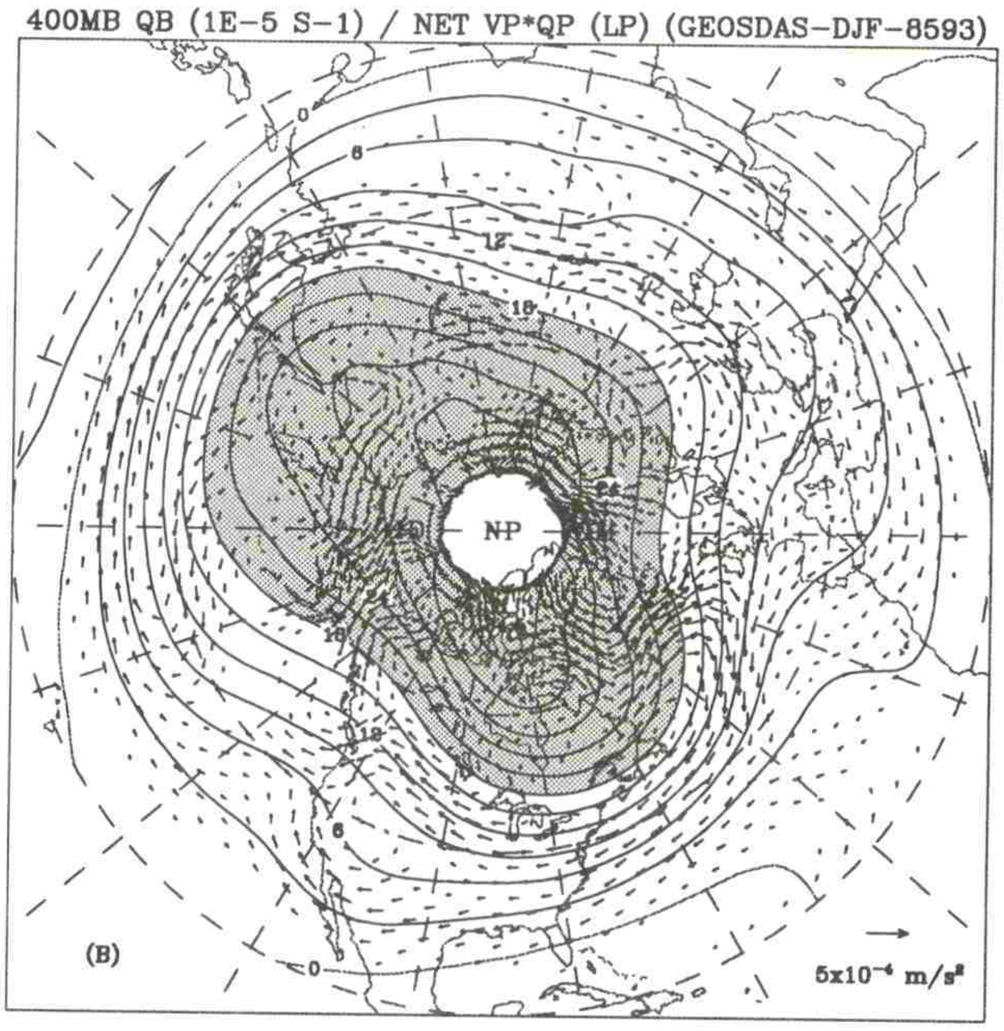

Fig. 3. Wintertime-mean 400-mb pseudopotential vorticity (Contour interval: $3x10^{-5}$ s^{-1}) and the residual eddy flux of pseudopotential vorticity for (a) BP and (b) LP transient eddies. Pseudopotential vorticity magnitudes greater than 18 units are shaded lightly.

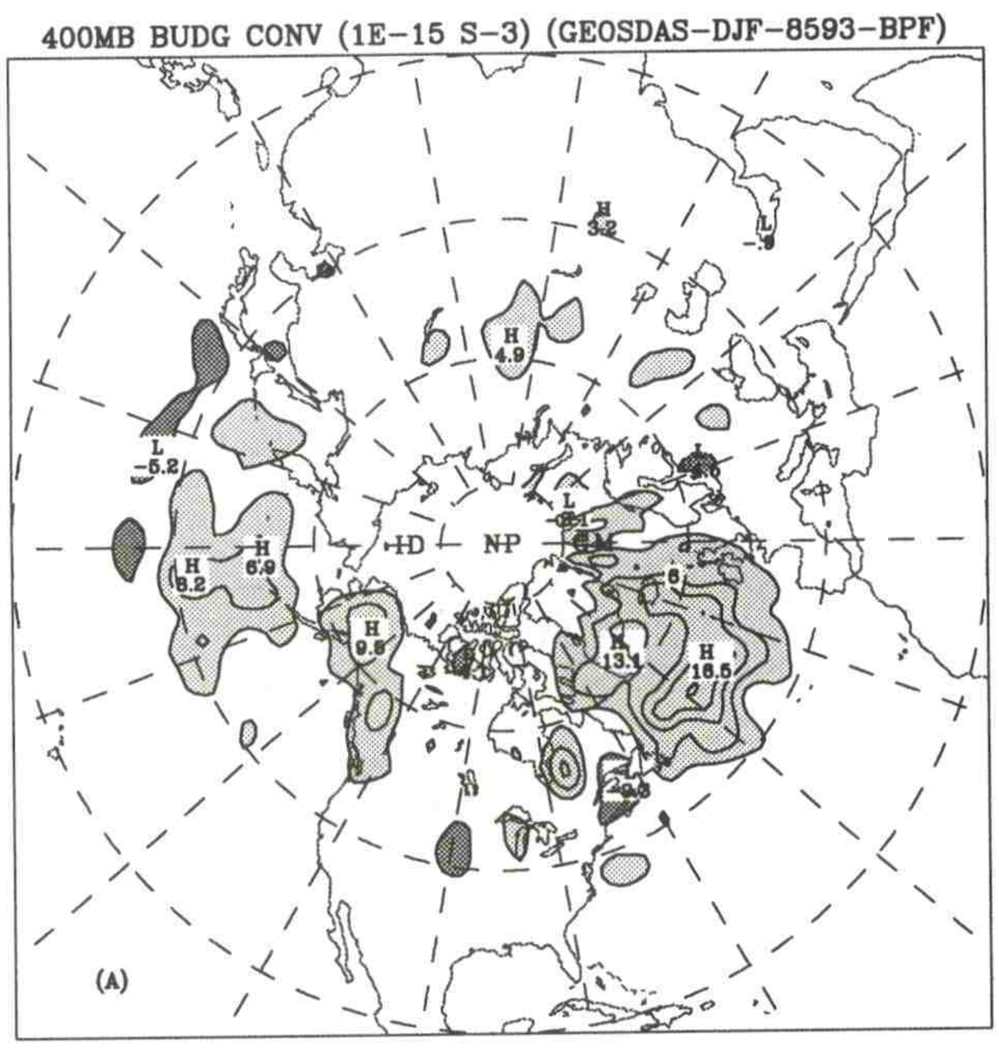

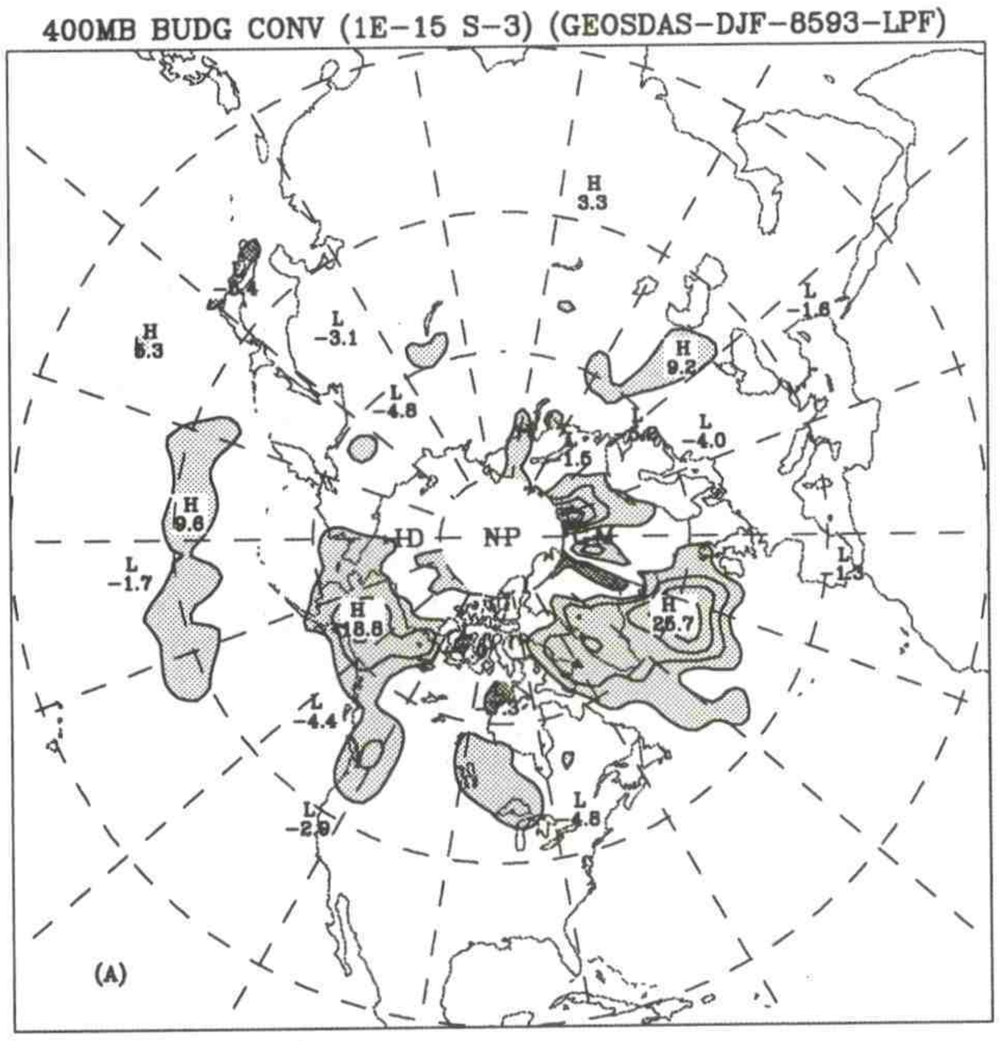

Fig. 4. Potential enstrophy budget components for BP transient eddies. (a) Potential enstrophy conversions. (b) Latent heating contributions (Contour interval: $3x10^{-15}$ s^{-3}).

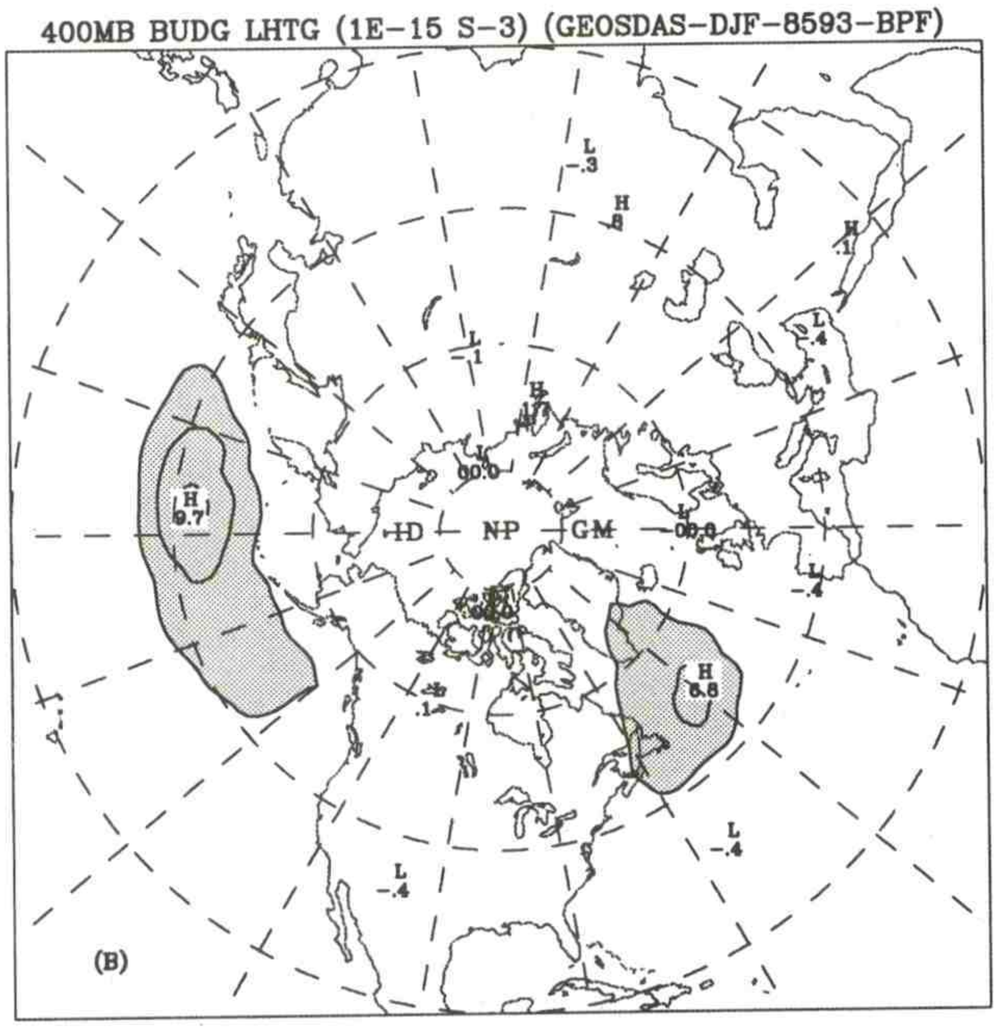

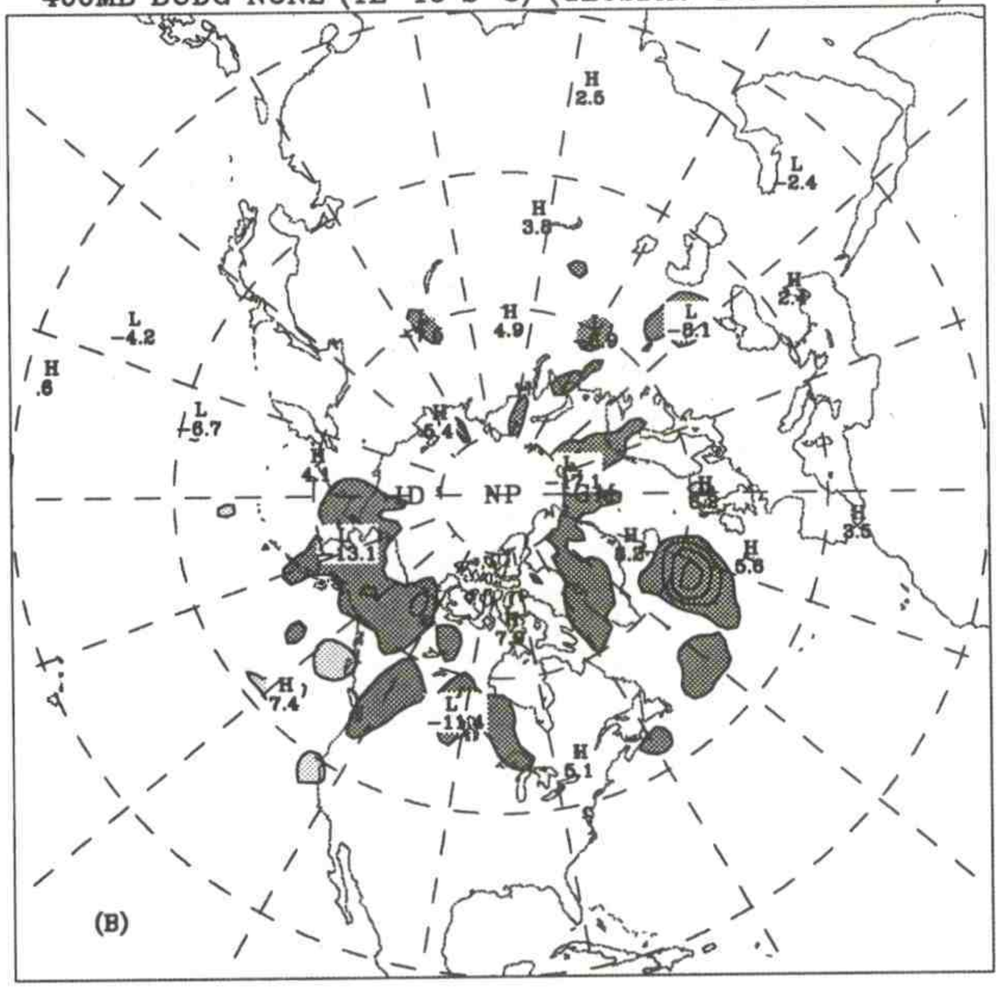

Fig. 5. Potential enstrophy budget components for LP transient eddies. (a) Potential enstrophy conversions. (b) Nonlinear interactions (Contour interval: $5x10^{-15}$ s^{-3}).

The Mean Annual Cycle of Water Vapor Over the Mississippi River Basin (1973-1992)

E. S. Yarosh
Research and Data System Corporation, Greenbelt, MD, 20770
and
C. F. Ropelewski
Climate Prediction Center, NCEP/NWS, NOAA, Washington DC, 20233

Introduction

Lack of reliable radiosonde data has previously limited the number of observational water vapor related studies. Release of the "Radiosonde Data of North America, 1946 - 1992" (1993), to a great extent, fills this data void. Here we describe the first of a series of GEWEX Continental-scale International Project (GCIP) related studies being performed at the CPC using this data set. We describe the data and analysis techniques and present the mean annual cycle of integrated flux divergence, mean monthly changes in total atmospheric water vapor and estimates of evaporation minus precipitation (E-P) over the Central United States.

Data and Initial Data Processing

Though the dataset covers the period 1946 - 1992, we work with the data for 1973 - 1992 period to avoid most of known instrumental problems with humidity sensors and because the network was more stable over that period.

Individual radiosonde observations in the data set were processed by month. Monthly "inquiry" files were constructed containing, with the total number of soundings, WBAN and WMO numbers, latitude, longitude, and "warning" files with the list of repeated reports for the month. Since the stations of interest to our study generally contained records every 50 hPa the resulting monthly products contained averages not only for mandatory levels but for the surface and every 50 hPa from 1000 hPa to 200 hPa. Also a number of vertically integrated water budget quantities were calculated for the following layers: surface - 200 hPa; surface - 950 hPa, surface - 850 hPa, 850 hPa - 700 hPa, 700 hPa - 500 hPa, 500 hPa - 200 hPa; every 50 hPa interval from 950 hPa to 200 hPa. For each individual sounding, at least 5 levels of data were required to estimate the surface to 200 hPa integral quantities and at least 2 levels of data for each of the layer means. Vertically integrated quantities were computed using every point of the vertical profiles.

Procedures for averaging included search and analysis to avoid double averaging of the points (same pressure data) and to pick up the most complete data. Monthly averages for particular station were computed irrespective of the number of soundings in a month.

Separate files of monthly means were created for 00Z and 12Z, as well as for all times of observations (since some stations reported not only at 00Z or 12Z). Monthly mean for each parameter was accompanied by its standard deviation for each month and by the number of observations. Every vertically integrated mean includes the standard deviation and number of points in the integration providing estimates of the reliability for monthly stations products. Data were stored by station for each month of the record. In addition to the derived

water budget quantities, the monthly mean surface pressure, height, temperature, specific humidity, wind components and vapor flux components, along with their standard deviations were computed for the surface and every 50 hPa level from 1000 hPa to 200 hPa.

As part of the quality control, nine test maps were examined to identify gross errors. Regional precipitation estimates were made on the basis of gridded dataset (Janowiak and Higgins, 1996).

Discussion

The radiosonde analysis shows that, in the mean, precipitable water increases from winter to summer. In all seasons the smallest values are over north-eastern Canada while the largest values are over the areas adjacent to the Gulf of Mexico. The amplitude of annual cycle over northern regions is about two twice the amplitude over the southern areas. Precipitable water amount increases from about 2-4 mm in winter to about 8-16 mm in summer in the northern regions, and from 20-24 mm to almost 50 mm over the Gulf coast. Standard deviation (SD) fields generally follows the mean fields for the cold season with the typical values of SD from less than 2 mm in the north to 8-10 mm in the south. During the warm season the area of the maximum variability in precipitable water (over 8 mm) is shifted from the southern regions to the north-east.

Most of North America experiences westerly vertically integrated vapor flux with a summer maximum of about 200 kg/(m sec) over the mid-latitude eastern coast. Strong easterly fluxes are typical for the Gulf of Mexico, and there is a weak easterly component over Alaska in all seasons. Standard deviation of zonal component of vertically integrated flux generally follows the mean flux. We note fact that even in the regions with strong westerly flux the variability is of the same order as the flux itself.

The most notable feature of the meridional component of the vertically integrated vapor flux is the "tongue" of the meridional flux (with values of up to 160 kg/(m sec)) from the Gulf of Mexico northward. While this feature is generally associated with the low level jet, prominent in spring, it can be seen on the winter and fall maps as well. Its magnitude during these seasons is less (up to 120 kg/(m sec)) and with less deep penetration over the continent. This "tongue" of meridional transport, defined here by the isoline of 40 kg/(m sec) is concentrated in a comparatively narrow band between 90-105W in August while it is much wider in other seasons e.g., between 80W and 110W in May and over the whole south-eastern U.S. in February and November. We also note that weak southerly flux dominates most of North America during the cold season while southerly flux is restricted to the north-eastern part of the continent during the warm season. Even though the zonal component of the flux dominates the meridional flux their respective standard deviations are of the same magnitude.

Our radiosonde-based water balance consists of the sum of atmospheric vapor storage change and the vertically integrated flux divergence, to yield a residual. This residual is taken to equal to the evaporation minus precipitation (E-P). We computed the water balance for a region, here called the Central U.S., defined by 15 upper-air stations (Fig. 1). This regions was chosen because a) there were very few changes in the station locations and most stations reported all 240 months during the 1973 to 1992 period, b) it avoids regions with

extreme changes in topography and thus avoids uncertainties in atmospheric budget computations associated with high terrain, c) the regular shape allows the precipitation estimates from a gridded precipitation dataset d) the area covers most of the GCIP region.

Our estimates of the atmospheric water balance, Fig. 2, are in general agreement with Rasmusson (1968), who looked at slightly different area for a period in the 1960's and are of larger amplitude than the NMC-model-based estimates by Roads et al. (1995). According to our computations, in the mean, precipitation exceeds evaporation during the summer. The changes in atmospheric storage are largest in spring and fall when vapor flux divergence term is changing its sign. This suggests that estimates of atmospheric water budgets during transition seasons may critically depend on accurate estimates of the monthly atmospheric storage terms and may be especially difficult to perform.

Area averaged evaporation (E) can be obtained from the budget estimates of E-P in conjunction with estimates of precipitation (P). Here we use precipitation from the hourly gridded dataset described by Janowiak and Higgins (1996). The twenty year average precipitation and evaporation, Fig. 3, show that for December and January the estimate of E is very close to zero. An examination of the 20 year monthly time series, Fig. 4, shows some negative estimates of evaporation during several winter months. We do not have any reason to expect biases in atmospheric vapor balance terms but there were several studies indicating that gauge-measured precipitation is underestimated. Groisman and Legates (1994) estimate that measured climatological precipitation over the U.S. is underestimated 5% to 40%. They found that underestimation is especially significant in cold season when at least part of precipitation is coming in solid form. Thus, the uncertainty in precipitation establishes one severe limit on validation of the water balance over North America.

References

Groisman, P. Ya., and D. R. Legates, 1994. The Accuracy of the United States Precipitation Data. *Bull. of the Amer. Met. Soc.*, **75**, No. 3, 215-227.

Janowiak, J., and W. Higgins, 1996. The diurnal cycle of precipitation over the U.S. as determined from a comprehensive hourly raingage dataset. *Proc. of the 20th Annual Climate Diagnostics Workshop*, October 23 - 27, Seattle, WA, (this volume).

Radiosonde Data of North America, 1946 - 1992, Version 1.0, 1993. NOAA, Forecast Systems Laboratory, Boulder, CO - National Climatic Data Center, Asheville, NC. Volumes I - IV.

Rasmusson, E. M., 1968: Atmospheric water vapor transport and the water balance of North America. Part II. Large scale water balance investigations. *Mon. Wea. Rev.*, **96**, 720-734.

Roads, J. O., S.-C. Chen, A. K. Guetter and K. P. Georgakakos, 1994: Large-scale aspects of the United States Hydrologic Cycle. *Bull. Amer. Met. Soc*, **75**, 1589-1610.

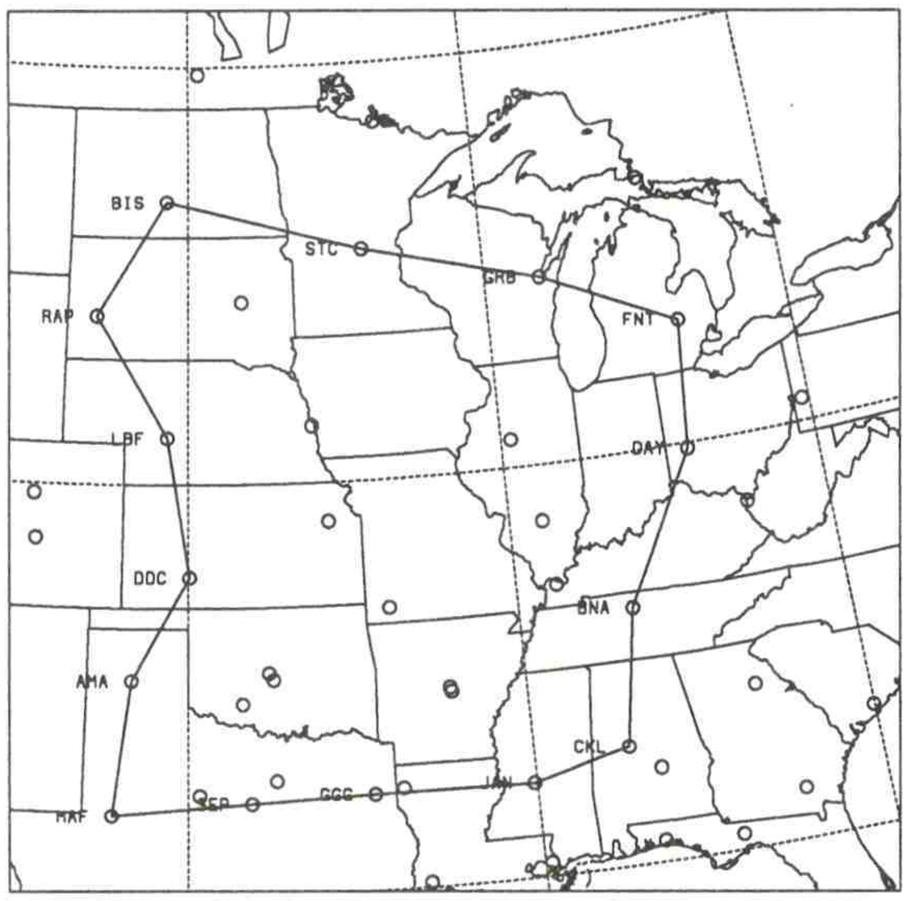

Fig. 1. Stations locations and contour over the Central U.S. used in atmospheric water balance computations.

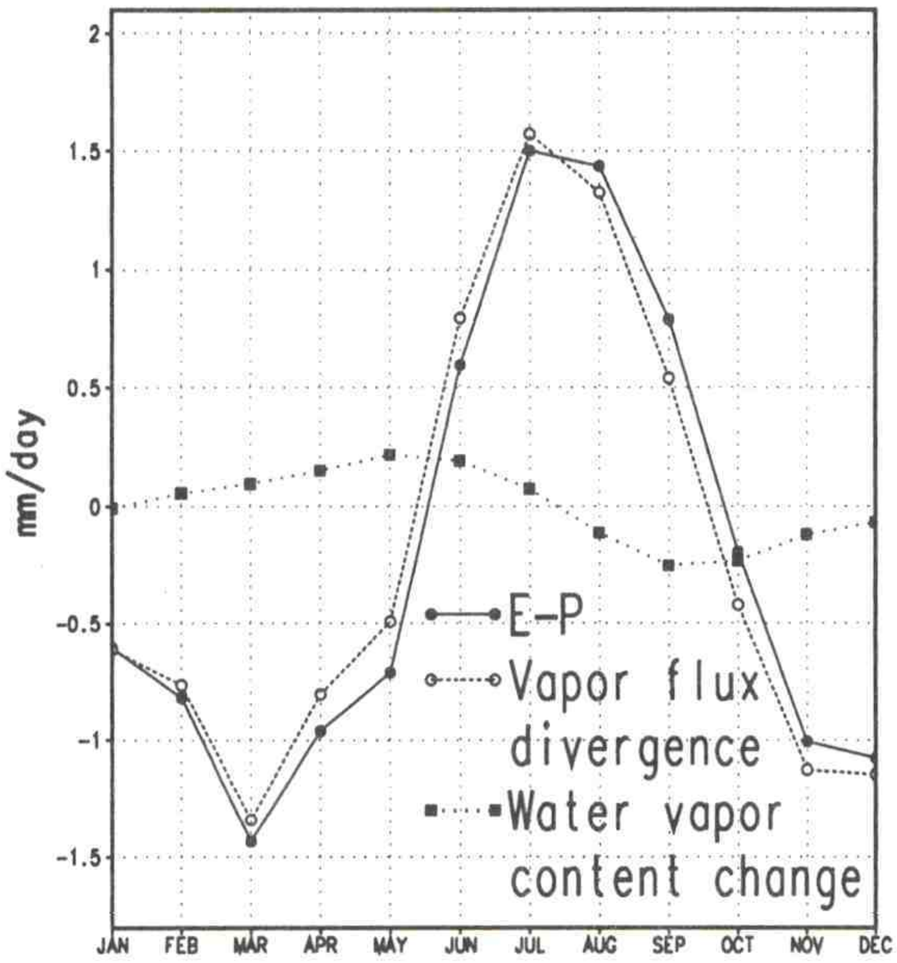

Fig. 2. Twenty-year average atmospheric water balance components over the Central U.S.

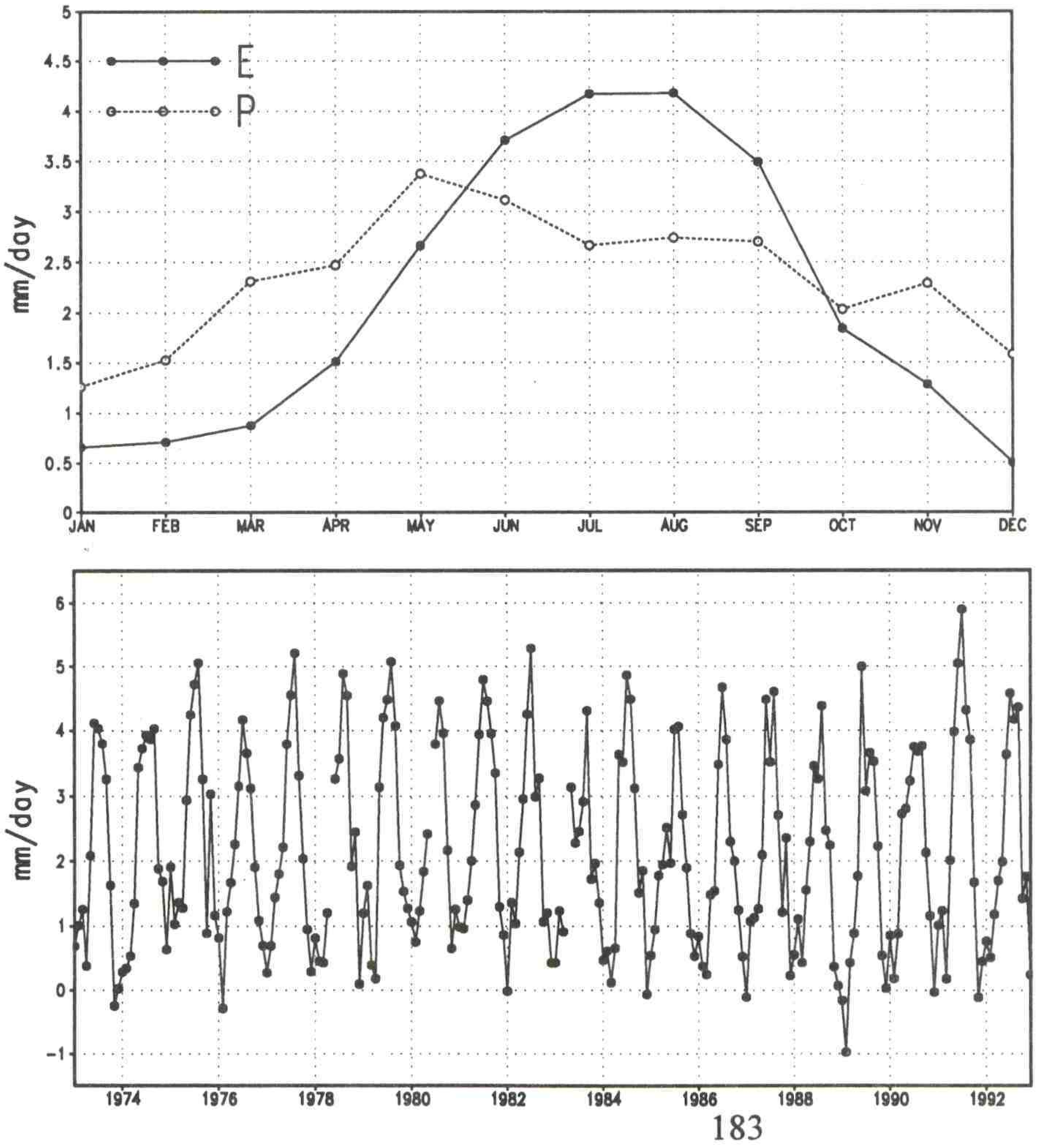

Fig. 3. Twenty-year averaged evaporation evaluated from the atmospheric water balance and gauge-measured precipitation for the Central U.S.

Fig. 4. 1973 - 1992 monthly evaporation evaluated from the atmospheric water balance and gauge-measured precipitation for the Central U.S.

GCIP Energy and Moisture Budgets

J. Roads, S. Chen, S. Yang
M. Kanamitsu, H. Juang

Climate Research Division
Scripps Institution of Oceanography
University of California, San Diego
La Jolla, CA 92093-0224
Phone: (619)534-2099
Fax: (619)534-8561
e-mail: jroads@ucsd.edu

1. Background

The Global Energy and Water Cycle Experiment (GEWEX) continental international project (GCIP) is underway in the Mississippi river basin. The Mississippi was chosen as the site for the first GCIP experiment because it is one of the world's largest river basins and covers most of the interior of as well as contributing the dominant streamflow from the continental United States. The Mississippi also has a wealth of observations. Basic observing systems include satellite measurements, radiosondes, surface weather stations, and stream-gauges. New climatic information from the NEXRAD Doppler radars, wind profilers, and automatic weather stations being developed as part of the weather modernization are a key part of this experiment. New surface hydrologic measurements measuring snow and soil moisture are being developed and will become part of our nations climatic information system during this experiment. NMC's operational prediction models are already making more use of some of this new data. In addition, the ETA operational prediction model is also being upgraded to include more of this data at higher and higher resolution. One of the purposes of this multi-national and multi-agency experiment, being led by NOAA, is to develop a better understanding of the processes controlling continental energy and hydrologic cycles. From this understanding we hope to be able to provide increased capabilities for predicting our water resources on short to long time scales.

2. Problem

How can we evaluate the energy and moisture budgets for the GCIP region? GCMs have been traditionally used for budget studies in the past, but they are unsatisfactory because they usually have fairly coarse resolution and can have climates that may not be sufficiently realistic. Calculating budgets directly from observations is incredibly difficult and not really attempted anymore because modern analysis systems, which attempt to grid the observational data, are now providing more reasonable output.

Analysis systems are not a panacea. For example, not all terms are archived. In particular, since every time step cannot be archived, snapshots and accumulations of some of the data are archived every few hours. From these snapshots, and limited data we attempt to develop budgets and find that there is not a balance, which is pretty irritating since we might have thought we are really dealing with model data. Another irritating feature discovered by Kanamitsu and Saha (1995) is that there are invisible tendency terms that are not small.

3. Model

One potential solution for alleviating these analysis problems is to develop a forecast system which can be initialized with the basic analysis data and can be modified to provide new diagnostics. We believe such a system might be a useful diagnostic supplement to standard analyses. We are using the NMC reanalysis model described in this proceedings

by Saha and White (1995) and Janowiak et al. (1995). This model uses the NMC reanalysis or operational analyses as initial conditions. The model has a complete physics package, including surface hydrologic parameterizations, radiation, gravity wave drag. Simplified Arakawa Schubert convective parameterizations as well as shallow cumulus effects in the planetary boundary layer are also present. The model provides all the standard output present in the archives. In addition, a complete diagnostic package was developed. All terms are accumulated every time step and perfect model budgets can be developed. The initial goal of our research is to develop an annual cycle from available analysis data 4 times a day and 1 day forecasts.

The model's vertical domain is kept the same as the initial conditions. For the operational analysis, this means 18 sigma layers (19 levels, which includes the surface and the model top at 0 pressure) for the period prior to August 1993. Thereafter as well as for the reanalysis data, the number of model layers is 28 (29 levels). There are a fair number of levels in the boundary layer. In the previous pressure analysis system, only 1000 and 850 mb could be used to define the planetary boundary layer. A T62 (192x94) 2° grid is always used in the horizontal. This grid has about 100 grid points within the entire basin. There are also a sufficient number of grid points to cover the 4 large-scale sub-basins of the GCIP experiment which are: (1) the Oklahoma southwest Arkansas-Red river region, the site of the ARM experiment and the GCIP warm season emphasis; (2) the north central Minnesota-Illinois region which emphasizes cold season processes; (3) the Appalachian Ohio river valley to the east; and (4) the Missouri river basins to the northwest and in the lee of the Rocky mountains.

4. Budget equations

The moisture equation is the simplest budget to consider

$$\pi \frac{\partial q}{\partial t} = -(\pi v \bullet \nabla q + \pi \dot{\sigma} \frac{\partial q}{\partial \sigma} - \pi K \nabla^n q) + \frac{\partial F_q}{\partial \sigma} - \pi C_1 .$$

π represents the surface pressure divided by gravity; thus vertical integrals need only include the layer sigma thickness. The terms inside the parentheses represent the 3 dimensional moisture advection as well as horizontal diffusion. Planetary boundary layer vertical diffusion, with the bottom boundary condition being the surface evaporation, is also important. Condensation acts to remove moisture from the atmosphere. This term is denoted C_1 here.

The atmospheric thermodynamic energy can be written in a number of ways. Here we write it in the virtual temperature form used in the model.

$$\pi \frac{\partial T}{\partial t} = -(\pi \vec{v} \bullet \nabla T + \pi \dot{\sigma} \frac{\partial T}{\partial \sigma} - \omega \alpha / C_p - \pi K \nabla^n T - F_v) + (\frac{\partial F_H}{\partial \sigma} + \frac{\partial F_R}{\partial \sigma} + \pi L C_2) / C_P$$

The terms inside the first set of parenthesis represent the advection of temperature, including horizontal temperature diffusion. Two additional terms are present, one involving the work done by the pressure on the surrounding volume, the $\omega\alpha$ term, as well as a strange term that takes into account that this is a virtual temperature equation and that a moisture forcing must also be included in this equation. The terms inside the second set of parentheses represent the vertical diffusion of sensible heat in the boundary layer, with the bottom boundary condition being the surface sensible heat, the radiation, and the latent heat released by condensation. . This term is denoted C_2 here because the condensation acts

differently in this equation. Although the vertically integrated condensation is the same in the moisture and temperature equations, the vertical distribution is different because convection acts to redistribute the heat and moisture in the vertical. This is not a small distinction.

5. Vertical variations

In the moisture equation, water vapor is increased by boundary layer moisture diffusion from the surface, E, and decreased by condensation, C_1. The net transport from planetary boundary layer cumulus as well as large-scale motions, D_q acts to take this surface moisture further up into the troposphere.

In the virtual temperature equation, virtual temperature is increased by latent heat released by condensation, LC_2, as well as by the boundary layer diffusion of sensible heat, SH. This heating is balanced in part by the planetary boundary layer and large-scale heat transports, D_T, as well as the net radiative cooling, which is dominated by long-wave cooling.

Latent heat of condensation does not follow the profile of condensation shown in the moisture equation. Latent heating peaks near the top of the atmosphere. Clearly there are substantial transports by the subgrid scale motions that need to be better understood before we understand the large-scale energy and hydrologic cycles.

The residual term is an important contributor to the budget, especially during the first 6 hour forecast and especially in the moisture equation. Not shown is the seasonal dependence of this term, acts differently in the winter and seasons.

6. Summary

We believe that the methodology of short term forecasts proposed here is an important augmentation to modern analysis systems since these forecasts can reduce the tendency terms and can provide additional variables and complete diagnostic budgets. We need to better understand the nature of the errors in these kinds of forecasts by comparing the various terms with available and soon to be available observations. GCM simulations will also be useful, given that the tendency terms are zero in GCM simulations.

Further details about the vertical as well as geographical seasonal, diurnal and spectral climatological budgets are provided in Roads et al. (1995).

7. References

Kanamitsu, M. and S. Saha, 1995: Systematic tendency error in budget calculations. Proceedings, 20th annual climate diagnostics workshop. Seattle, WA

Roads, J., S. Chen, S., Yang, M. Kanamitsu, H. Juang, 1995: GCIP moisture and virtual temperature budgets. (To be submitted)

Saha, S. and G. White, 1995: An evaluation of the water budget and surface fluxes in the NMC/NCAR reanalysis. Proceedings, 20th annual climate diagnostics workshop. Seattle, WA.

Janowiak, J., P. Xie, and P. Arkin, 1995: A comparison of monthly precipitation among the NMC/NCAR and NASA/DAO reanalyses and a satellite-rain-gauge merged analysis. Proceedings, 20th annual climate diagnostics workshop. Seattle, WA.

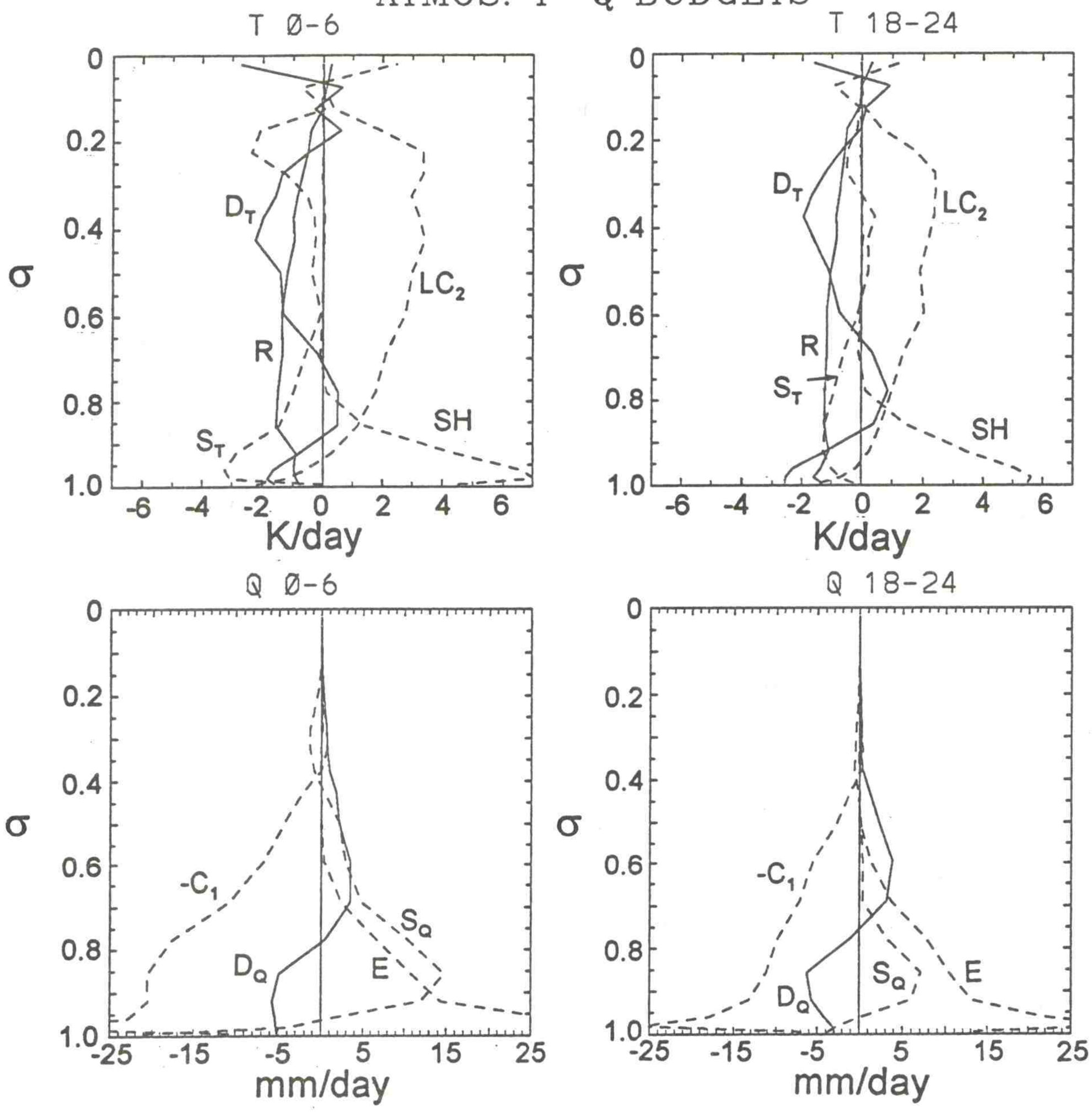

Fig. 1 Vertical profiles of various budget terms averaged over the GCIP region. The budgets for the first 0-6 hour forecast are shown in the left hand panels, the budget for the 18-24 hour forecasts are shown in the right hand panels. Budgets for the virtual temperature are shown in the upper panels. Vertical profiles of latent heat of condensation, LC_2 , boundary layer diffusion and cloud transport of sensible heat, SH, large-scale heat transports, D_T, net radiative cooling, R, and the residual, S_T, are shown. Budgets for the moisture equation are shown in the lower panels. Vertical profiles of condensation, C_1, boundary layer diffusion and cloud transport of moisture, E, large-scale moisture transports, D_q, and the residual, S_q, are shown.

Recent progress in the study of water vapor budgets using EDAS analyses.

Ernesto H. Berbery and Eugene M. Rasmusson

Cooperative Institute for Climate Studies
Department of Meteorology
University of Maryland
College Park, MD 20742

Adequate estimates of water budgets require an accurate resolution of the vapor flux fields in the lower troposphere (Rasmusson 1967, 1968). Rasmusson noted that in order to produce reliable budgets, it is necessary to have at least: (a) high vertical resolution in the planetary boundary layer, (b) resolution of systematic diurnal variability in the lower troposphere flux field, and (c) adequate resolution of topographic variations, i.e., the elevation of the land surface. Traditionally, the convergence of water vapor fluxes was computed from radiosonde data, but in recent years the use of 4DDA has proved to be an alternative tool. This is the case of the Eta model, the new regional model used at the National Centers for Environmental Prediction (formerly National Meteorological Center) . This model, and its associated assimilation system, the Eta model Data Assimilation System (EDAS), have been selected to meet the near-term GEWEX Continental-Scale International Project (GCIP) needs for model output data (International GEWEX Project Office 1995).

In a recent paper, Berbery et al. (1995) studied the ability of the Eta model forecast products to reproduce known features of the atmospheric branch of the hydrologic cycle. To achieve this, they used observed precipitation in conjunction with the forecast water vapor fluxes. They found that over an idealized Mississippi basin (a square region of about the same size) estimates of evaporation obtained as a residual of the water vapor budget equation ranged from a maximum of 2.5 mm/day during August to a minimum of 0.1 mm/day during February. This range and values are in general agreement with earlier estimates from radiosonde information (Rasmusson 1968). In this note we report early results for the First Enhanced Seasonal Observing Period of GCIP, that extended from April 1995 to September 1995. Computations of the water cycle components from EDAS are done in the model native grid, which is an Arakawa E grid with a horizontal resolution of about 48 km. There are 38 levels in the vertical, with as many as 18 of them below the 700 hPa level when the terrain is near sea level. EDAS analyses every three hours and forecast products at selected times were used to compute monthly values of a number of terms related to the water and energy cycles.

The areas of interest are the Mississippi basin and the so-called GCIP Large Scale Areas that cover the following drainage basins: (a) Arkansas-Red River, (b) Upper and Lower Missouri River, (c) Upper Mississippi River and (d) Ohio River. Fig. 1a depicts the basins as represented by the Eta model grid points. Fig. 1b presents a second region of interest, the "Central United States", selected for future comparison to radiosonde estimates of the water budget. Finally, the hexagon in Fig. 1b represents the Clouds and Radiation Testbed/Atmospheric Radiation Measurement (CART/ARM) array, that will also be used for comparisons.

The atmospheric branch of the hydrologic cycle can be written as

$$P - E = -\frac{\partial W}{\partial t} + \frac{1}{A} \oint (\overline{Q}.\overline{n})\, d\gamma \qquad (1)$$

where P is the precipitation, E is the evaporation, the first term in the RHS is the change in precipitable water and the last term on the RHS is the convergence of water vapor fluxes. All terms are area averaged over the basin of interest. EDAS estimates of P-E for the Mississippi River basin are presented in Fig. 2. There is a maximum of 2.5 mm/day during May and a decay to a minimum of -1.5 mm/day during August. Radiosonde estimates of P-E over the Central United States for a 20 year period (1973-1992), kindly provided by Evgeney Yarosh, display a similar seasonal evolution (see also Yarosh and Ropelewski 1995). The larger values of P-E observed during the spring of 1995 are possibly the result of the Midwest flooding that occurred at that time.

Our research will focus on the impact of spatial and temporal resolution in the estimates of the water budgets. To have a complete view of the hydrologic cycle, we plan to complement our 4DDA model based estimates with observed variables, such as precipitation and stream discharge.

References

Berbery, E. H., E. M. Rasmusson and K. E. Mitchell, 1995: Studies of North American continental scale hydrology using Eta model forecast products. *J. Geoph. Res.* in press.

International GEWEX Project Office, 1995: Major Activities Plan for 1996, 1997 & Outlook for 1998 for GCIP. *IGPO Publication Series No. 16*, International GEWEX Project Office, Washington, D.C.

Rasmusson, E. M., 1967: Atmospheric water vapor transport and the water balance of North America: Part I. Characteristics of the water vapor flux field. *Mon. Wea. Rev.*, **95,** 403-426.

Rasmusson, E. M., 1968: Atmospheric water vapor transport and the water balance of North America: Part II. Large-scale water balance investigations. *Mon. Wea. Rev.*, **96,** 720-734.

Yarosh, E. S., and C. F. Ropelewski, 1995: The Mean Annual Cycle of Water Vapor Over the Mississippi River Basin (1973-1992). *Proc. of the 20th Annual Climate Diagnostics Workshop*, October 23 - 27, Seattle, WA, (this volume).

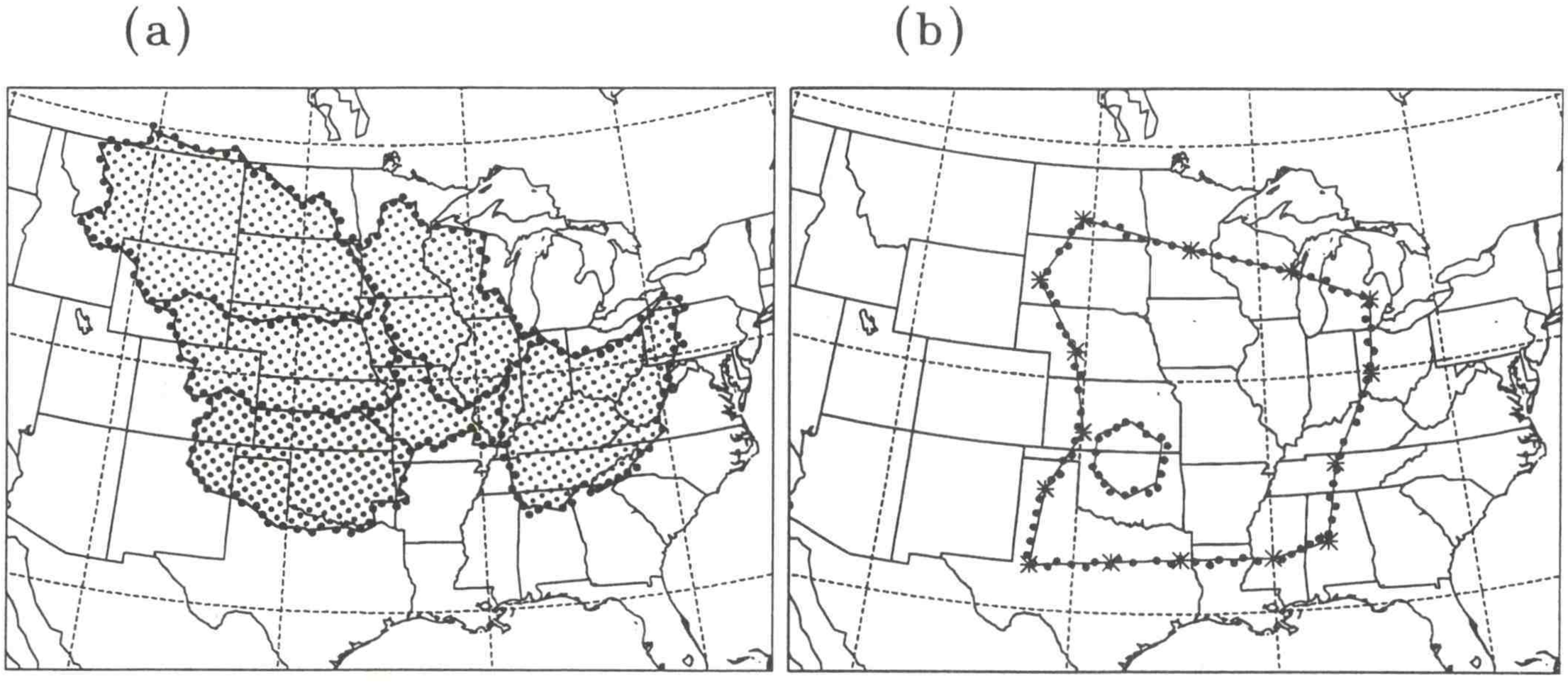

Figure 1. (a) Mississippi basin and subbasins as represented by the model grid points. (b) Perimeters of the Central United States and CART/ARM array. Dots represent Eta model grid points and asterisks are radiosonde stations.

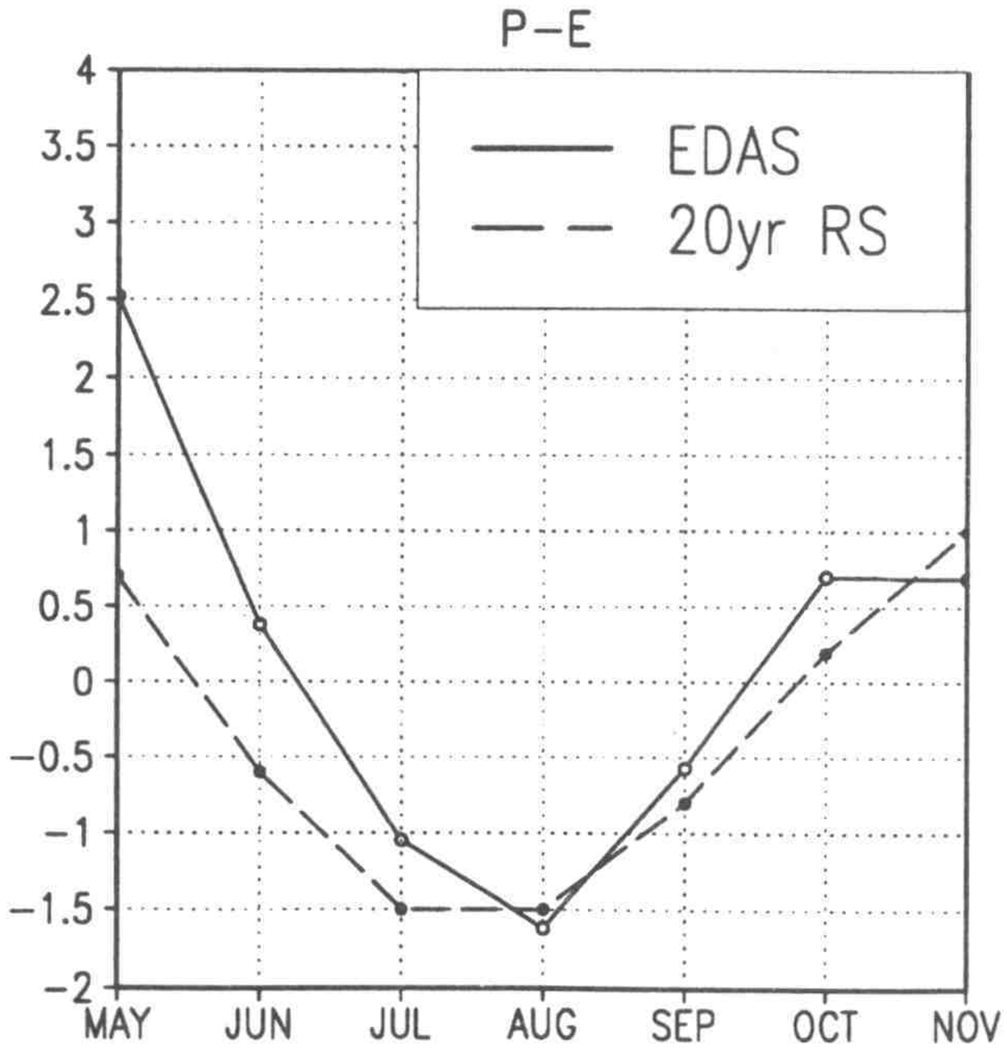

Figure 2. Precipitation minus Evaporation estimated from EDAS analyses (continuous line) and from radiosonde data for a 20 year period (dashed line).

New Results on the Hydrology of the North African Desert, Based on the NMC Reanalyses

Frederic Vitart
Atmospheric and Oceanic Sciences Program, Princeton University, P.O. Box CN710, Princeton, NJ 08544

Abraham H. Oort
Geophysical Fluid Dynamics Laboratory/NOAA, P.O. Box 308, Princeton, NJ 08542

Kingtse Mo
Climate Prediction Center/NCEP/NOAA, 5200 Auth Road, WWB, Room 605, Camp Springs, MD 20746

1. Introduction. In a well-known paper on the hydrology of deserts, Starr and Peixoto (1958, Tellus, 10, 188-194) showed a net divergence of water vapor over the major desert regions of the subtropical continents. The divergence of the vertically integrated flux of water is connected with the evaporation-minus-precipitation rate (E-P) through the relation:

$$\partial W/\partial t = -div\left(\vec{Q} + \vec{Q}_C\right) + (E - P)\,, \tag{1}$$

where W is the precipitable water, $\vec{Q}$ is the vertically integrated flux of water vapor, and $\vec{Q}_C$ is the corresponding flux of condensed water. Using the common assumption that the $\vec{Q}_C$ flux is very small compared to the $\vec{Q}$ flux, Starr and Peixoto concluded that there had to be an excess of E over P over the major deserts.

Ground hydrologists have questioned these results, since E > P would require either depletion of subterranean fossil water reservoirs or an inflow of water by surface and subsurface flows into the desert. However, the early results of Starr and Peixoto have been confirmed by many later studies with an improved radiosonde network. Nevertheless, there are possible biases in the observations. Notably, the diurnal variation in land-sea breezes around the periphery of the continents may not be sampled adequately by twice-a-day radiosonde observations, and could thereby lead to fictitious $div\vec{Q}$ values over the region.

The historical reanalyses now being made at the National Centers for Environmental Prediction (NCEP) use all available observations (radiosonde, surface, satellite, etc.) in one of the best data-assimilation models, that includes a diurnal cycle (Kalnay et al., 1996, Bull. Am. Meteor. Soc., in press). In the present study we make use of this unique set of analyses for the period January 1985-December 1993 to "revisit" the above controversy and to study in more detail the atmospheric branch of the hydrological cycle over North Africa. The four-times-a-day NCEP reanalyses enable us to remove some of the possible biases, and estimate their possible impact on the earlier results.

2. Results. In Fig. 1 we show, for reference, the 9-year annual mean precipitable water over North Africa. Major dryness is found around an east-west axis located at about 24°N with minimum values of less than 11 kg/m^2. The wet zone associated with the ITCZ is found south of 10°N with

values over 40 kg/m^2. Of course, these zones shift equatorward in winter and poleward in summer.

To show the prevailing flow patterns of moisture, streamlines of the vertically integrated flux of water vapor, $\vec{Q}$, are presented in Fig. 2. The figure shows general eastward flow north of about 20°N, and westward flow to the south. Clearly water vapor is transported into the North African region from both the North Atlantic Ocean and the Mediterranean. On this figure, we also indicate three latitudinal boxes between 15°N and 30°N latitude, and 10°W and 30°E longitude, that we will use later in studying the temporal variations of the hydrological cycle.

The actual source and sink regions for water vapor, as computed from the $div\vec{Q}$ and $\partial W/\partial t$ fields using (1), are shown in Fig. 3. Basically this figure represents the annual-mean field of (E-P). It shows an almost continuous belt of strong excess of evaporation over precipitation of 2-5 mm/day (or about 1 m/yr) over practically all the waters surrounding North Africa, i.e., the eastern North Atlantic Ocean, Mediterranean Sea, Red Sea and Gulf of Aden. Over the Atlas mountains in Algeria, the Ethiopian highlands, and south of about 10°N near the ITCZ region, we find as expected an excess of precipitation of 1-4 mm/day. On the other hand, over the North African desert areas we find a rather weak field of alternating negative and positive (E-P) regions but, on the average there is E > P. Some of the (E-P) maxima can be identified with oases. The overall excess of E over P is shown perhaps more clearly in Fig. 4 where a time series is plotted for the monthly-mean values of (E-P), averaged over the 15-30°N, 10°W-30°E zone. We note a strong seasonal variation with maxima of about 0.25 mm/day in summer, and close-to-zero minima in early winter.

The diurnal variation in the averages for the three 5° wide boxes (see Fig. 2) is presented in Table 1. The estimates show a predominant excess of evaporation in the 25-30°N and 20-25°N boxes throughout the day. However, in the southern box of 15-20°N, the sign seems to depend strongly on the time of day, showing only an excess of evaporation at local noon and during the afternoon.

Some words of caution are warranted. First, the distribution of the input data over Africa is still rather sparse, and therefore some of the results may be biased by the NCEP data-assimilation procedure and model used. Second, as kindly pointed out to us by Prof. Pinhas Alpert of Tel Aviv University, there is some recent work that suggests that the term $div\vec{Q}_C$ in (1) may not be negligible over desert regions (Alpert and Shay-El, 1993, Ann. Geophysicae, 11, 190-194). Unfortunately, the actual magnitude of this term is very difficult to estimate and, as far as we know, has not been measured directly.

In conclusion, we can tentatively say that the NCEP reanalyses over the North African dry regions confirm Starr and Peixoto's (1958) result of an excess of evaporation over precipitation, even when diurnal variations are taken into account. However, more research is clearly needed to investigate the effects of gaps in the upper air data, and possible contributions due to inflow or outflow of condensed water in clouds into the desert regions.

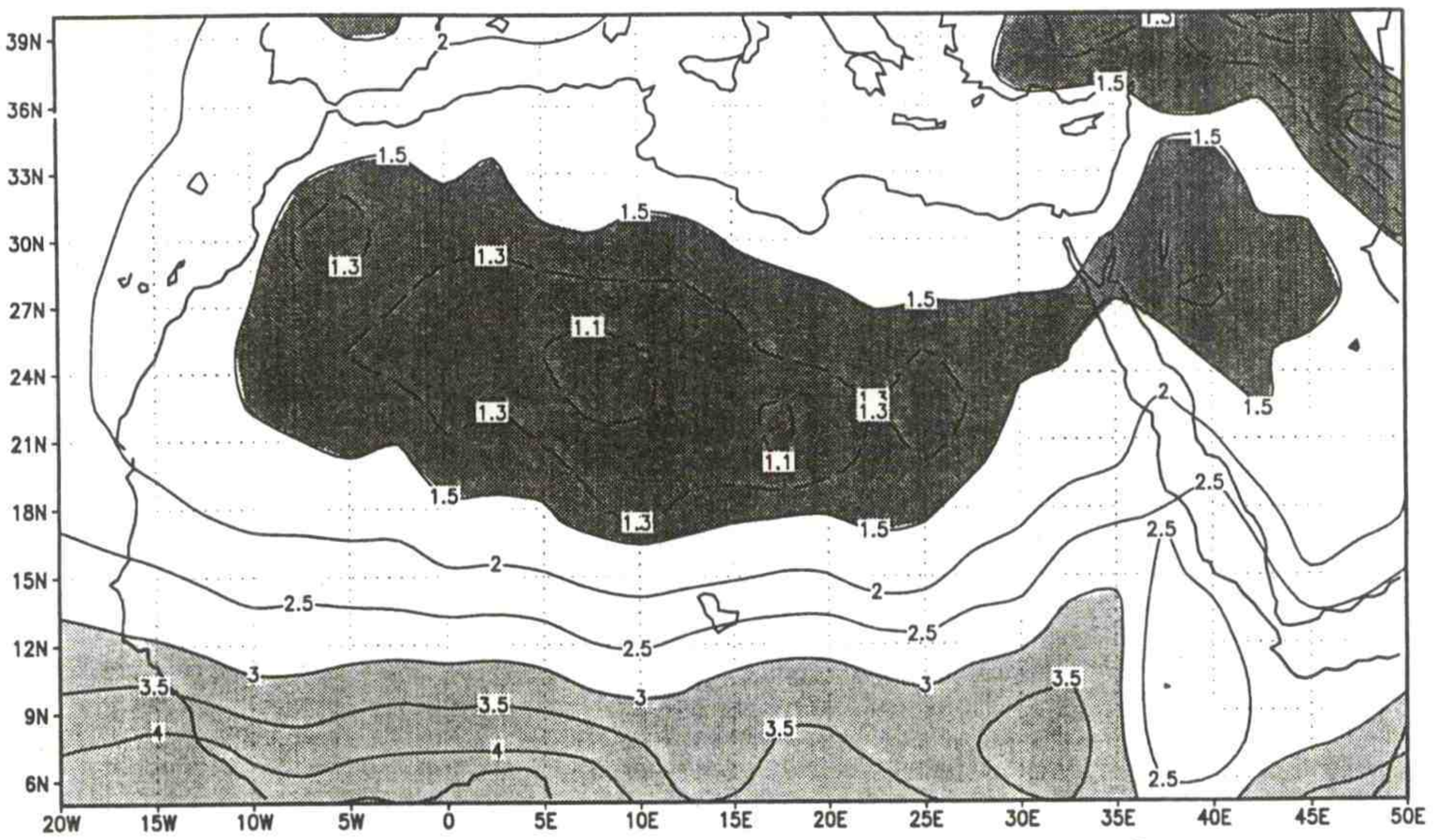

Fig. 1. Horizontal distribution of the precipitable water W (in 10 kg/m^2) over North Africa for annual-mean conditions based on 4-times daily NCEP reanalyses for the period January 1985-December 1993. Solid isolines are drawn for every 5 kg/m^2, and dashed lines for 11 and 13 kg/ m^2.

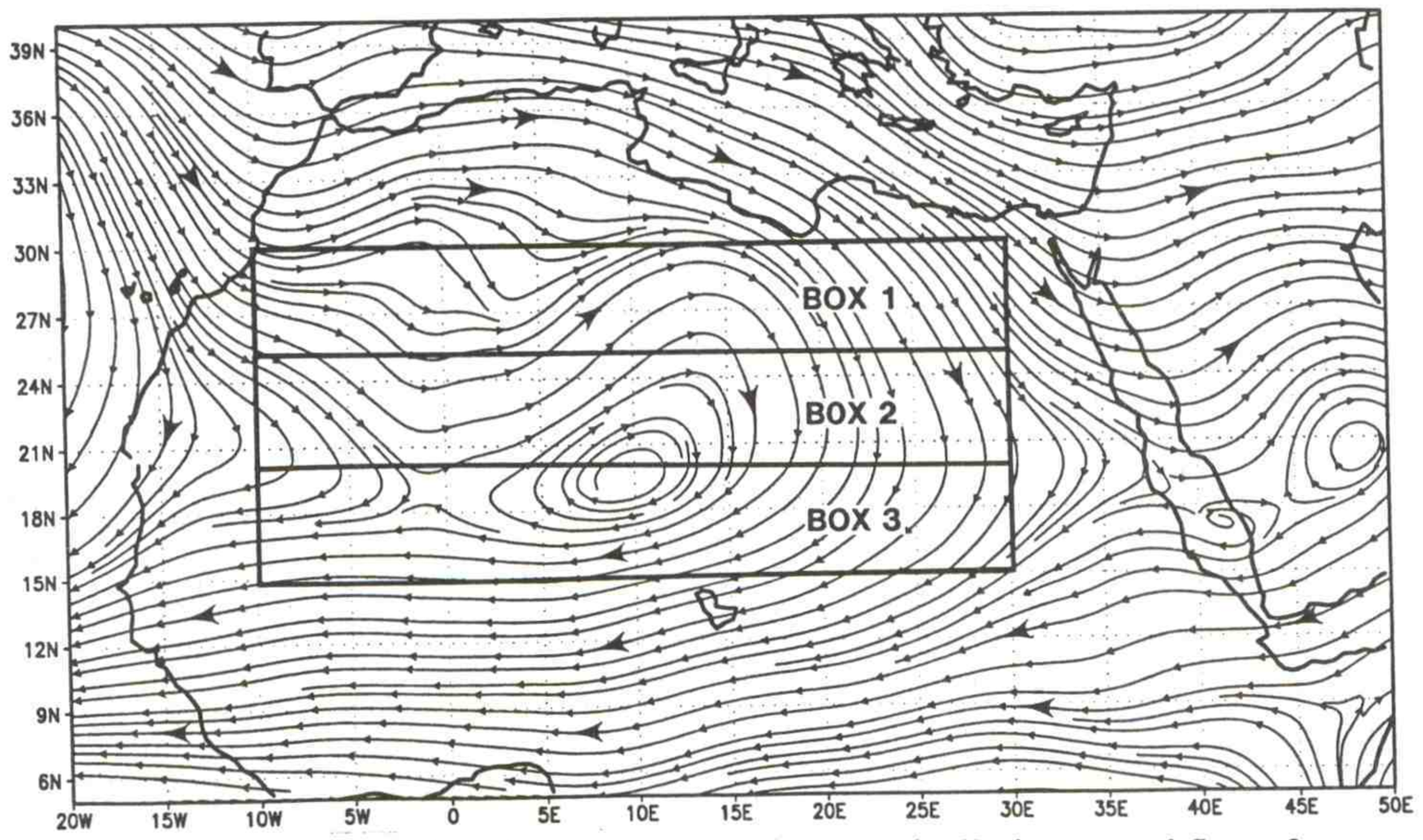

Fig. 2. Same as in Fig. 1, but for streamlines of the vertically integrated flux of water vapor $\vec{Q}$. Also shown are three latitudinal boxes between 15 and 30°N latitude, and 10°W and 30°E longitude for which the hydrological budgets are studied.

Table 1: Mean (E-P) based on the NCEP reanalyses for the period January 1985-December 1993 for four times a day in different latitudinal zones over North Africa (in units of mm/day).

	00 GMT (~ midnight)	06 GMT	12 GMT (~ noon)	18 GMT	Diurnal Mean
Box 3 (25-30°N)	0.80	0.02	0.38	0.26	0.37
Box 2 (20-25°N)	0.08	-0.06	0.32	0.32	0.16
Box 1 (15-20°N)	-0.35	-0.60	0.85	0.35	0.06
Box 1+2+3 (15-30°N)	0.20	-0.30	0.62	0.30	0.20

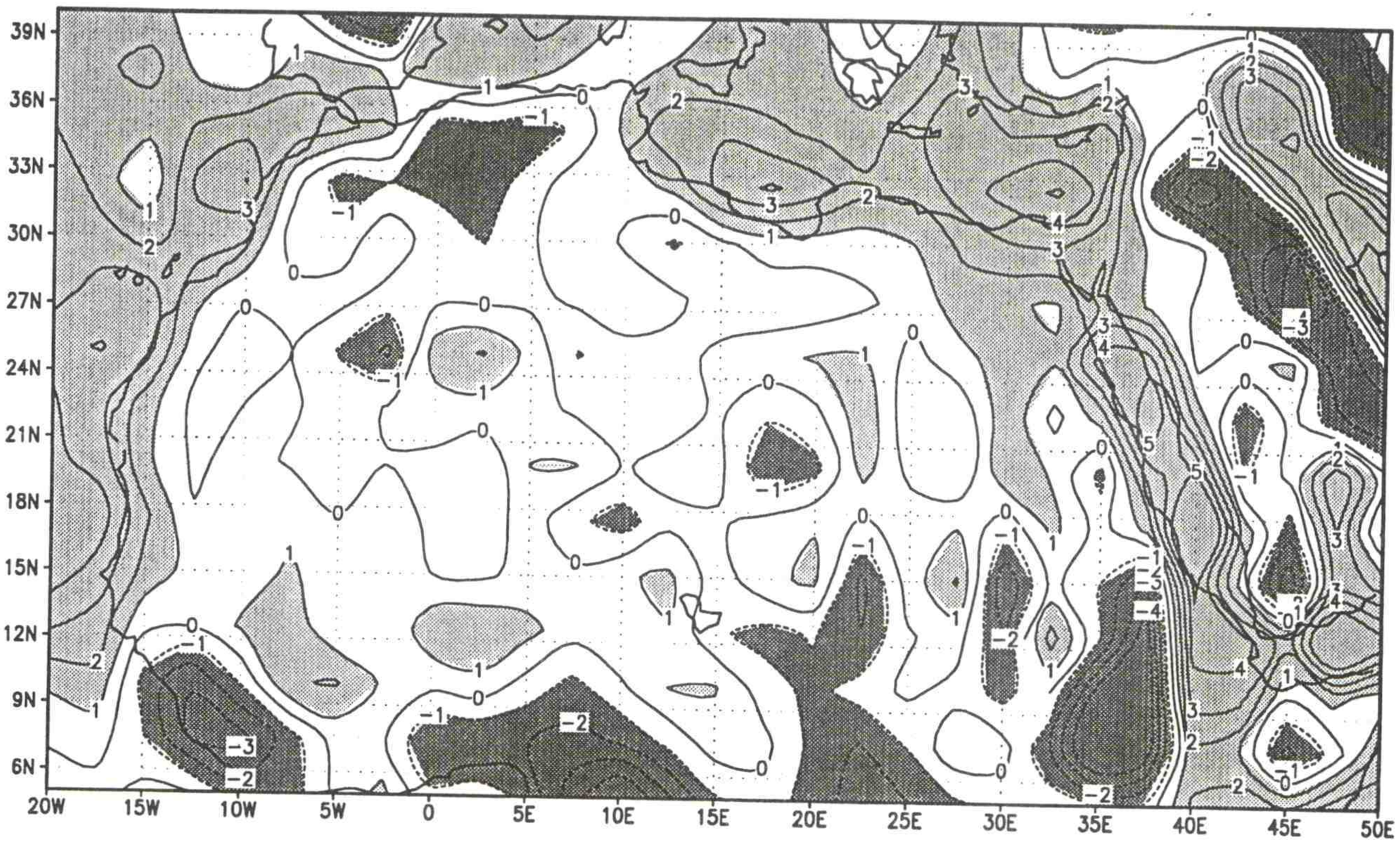

Fig. 3. Horizontal distribution of the evaporation-minus-precipitation, E-P (in mm/day), over North Africa for annual-mean conditions based on four-times-a-day NCEP reanalyses. Isolines are drawn every 1 mm/day.

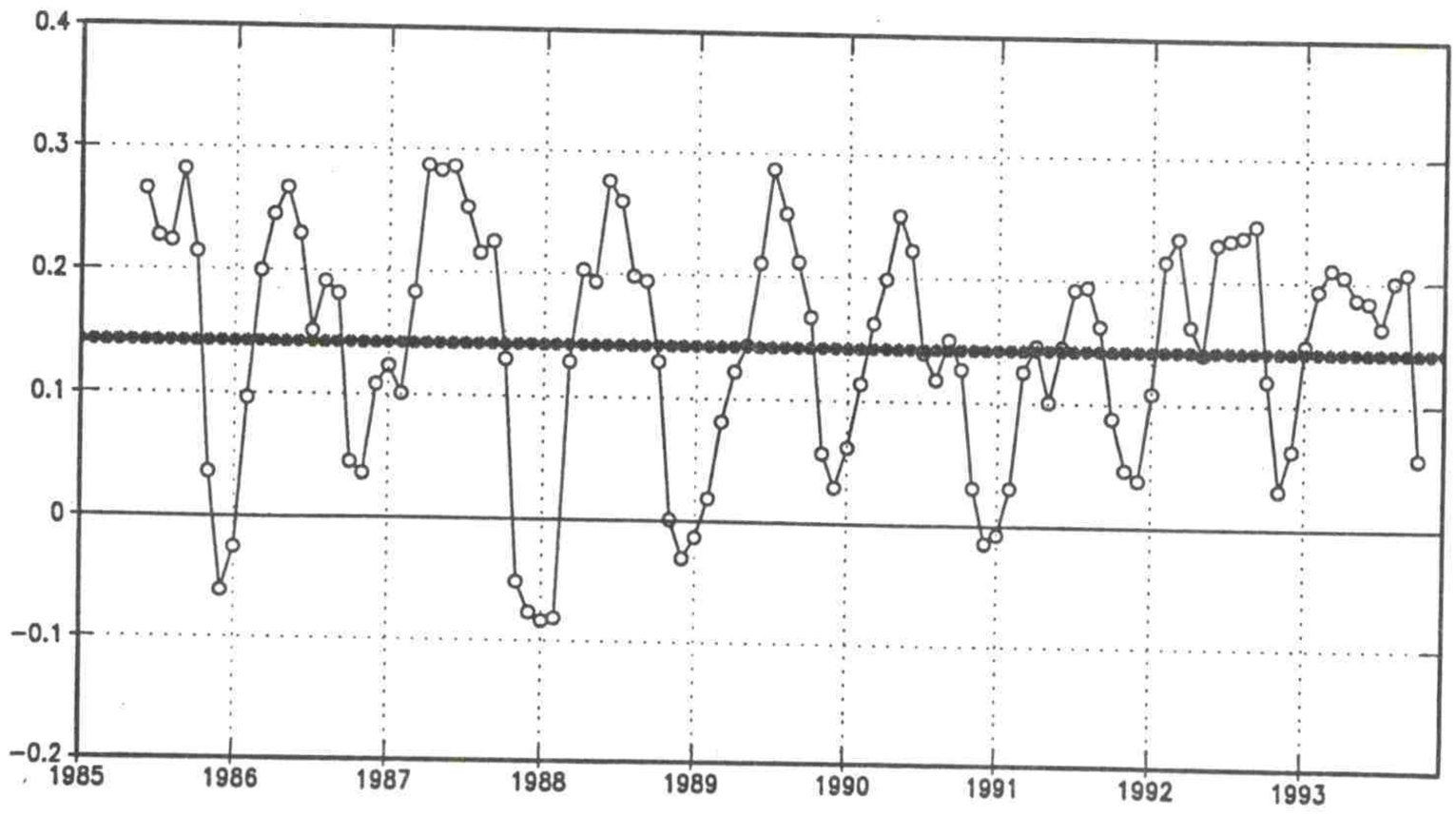

Fig. 4. Time series of monthly-mean E-P (in mm/day) averaged over the entire region 15-30°N, 10°W-30°E. The original monthly values were smoothed using a 15-point Gaussian-type filter with weights 0.012, 0.025, 0.040, 0.060, 0.083, 0.101, 0.117, and 0.122 at the central point.

ENSO-like Decade-to-Century Scale Variability: 1900-93

Yuan Zhang, John M. Wallace and David S. Battisti
University of Washington, Seattle, WA 98195

A number of recent studies have reported an ENSO-like EOF mode in the global sea surface temperature (SST) field, whose time variability is marked by an abrupt change to a warmer tropical eastern Pacific and a colder extratropical North Pacific in 1976-77. The present study compares this pattern with the structure of the interannual variability associated with the ENSO cycle, and documents its time history back to 1900. The analysis is primarily based on the leading EOFs of the SST field in various domains and the associated expansion coefficient time series, which are used to construct global regression maps of SST, sea-level pressure (SLP), and a number of related variables.

The time variability of the leading EOF of the global SST field is separated into two components: one identified with the "ENSO cycle-related" variability on the interannual time scale, and the other a linearly independent "residual" that comprises all the decadal-to-century scale variability in the record and some of the interannual variability as well (Fig. 1). The two components exhibit remarkable similar spatial signatures in the global SST, SLP, surface windstress and 500-mb heigh fields (Figs. 2, 3 and 4). The SST signature in the residual variability is less equatorially confined in the eastern Pacific and it exhibits larger amplitude over the extratropical North Pacific. The corresponding SLP signature is also stronger over the extratropical North Pacific, and its counterpart in the cold season 500-mb height field more closely resembles the PNA pattern. Qualitatively similar distinctions are also evident between regression patterns based on 5-year high-pass versus low-pass filtered time series of ENSO indices. The time variability of the ENSO-like pattern in the residual variability reflects the above mentioned shift in 1976-77, as well as a prior shift, of opposite polarity, during the 1940s.

Reference

Zhang, Y., J. M. Wallace, and D. S. Battisti, 1996: ENSO-like decadal-to-century scale variability: 1900-93. Submitted to *J. of Climate*.

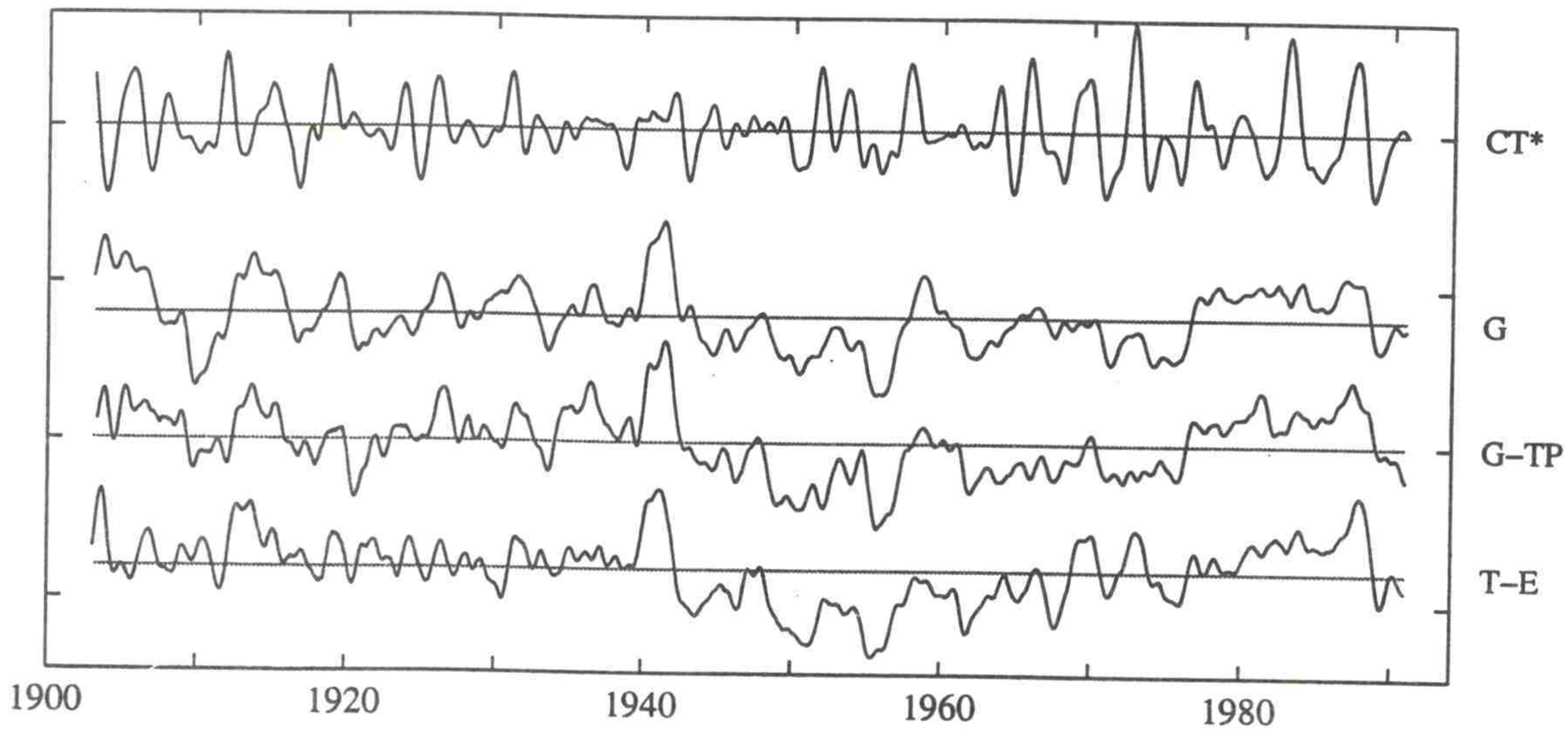

Figure 1: Normalized time series. CT* is the 5-year high-pass filtered cold tongue index. G and G-TP are expansion coefficients of the leading EOFs of the SST anomaly field over the global domain and the global domain excluding the tropical Pacific, respectively. The bottom curve (T–E) is the normalized difference between spatially averaged SST anomalies over the tropical and extratropical oceans (equatorward and poleward of 20° latitude). The least-squares best fits of the last three time series to the CT* time series are removed. For display purposes all time series have been smoothed with successive 9-month and 5-month running-mean filters. The interval between tick-marks on the vertical axis is 1.0 standard deviation. The spacing between the curves is arbitrary.

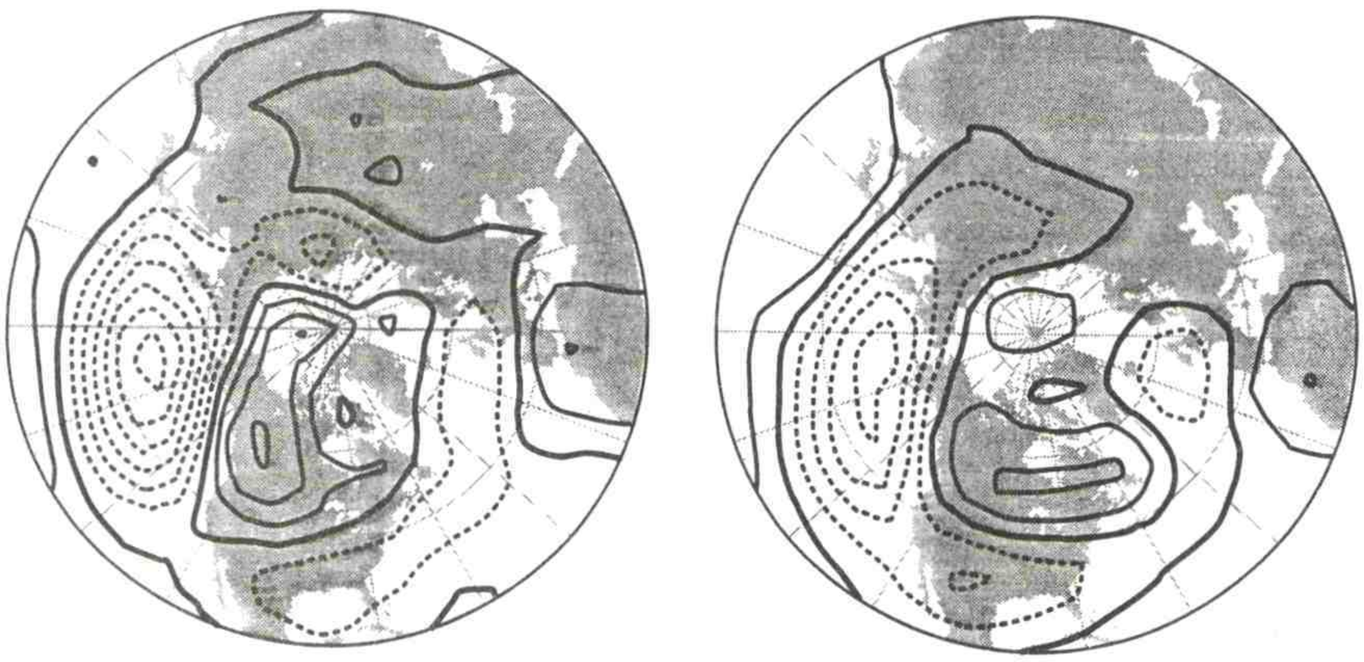

Figure 4: As in Fig. 2 (*left*) and Fig. 3 (*right*) for the cold season (November through April) 500-mb height field; based on the period of record 1946-93. Contour interval 5 m per standard deviation: negative contours are dashed; the zero contour is thickened.

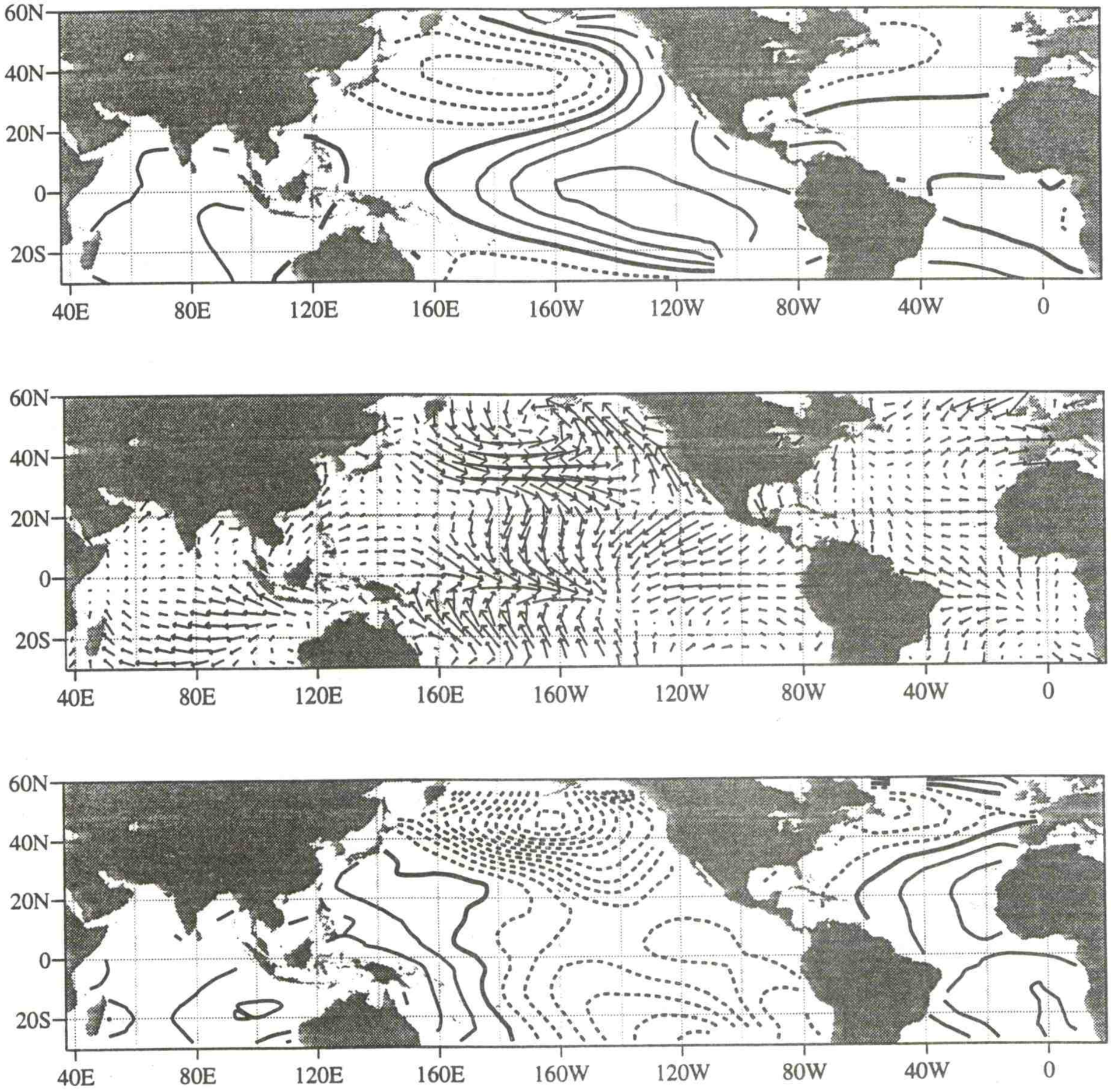

Figure 2: Global fields regressed upon the normalized expansion coefficient time series of the leading EOF of the global residual SST anomaly field (the time series labeled G in Fig. 1): (*top*) SST, contour interval 0.1 K per standard deviation (std); (*middle*) wind stress, the longest vectors represent a value of 8.3 m^2s^{-2} per std; (*bottom*) SLP; contour interval 0.1 mb per std. The negative extremum in the vicinity of the Aleutian Low corresponds to 1.3 mb per standard deviation. Negative contours are dashed; the zero contour is thickened.

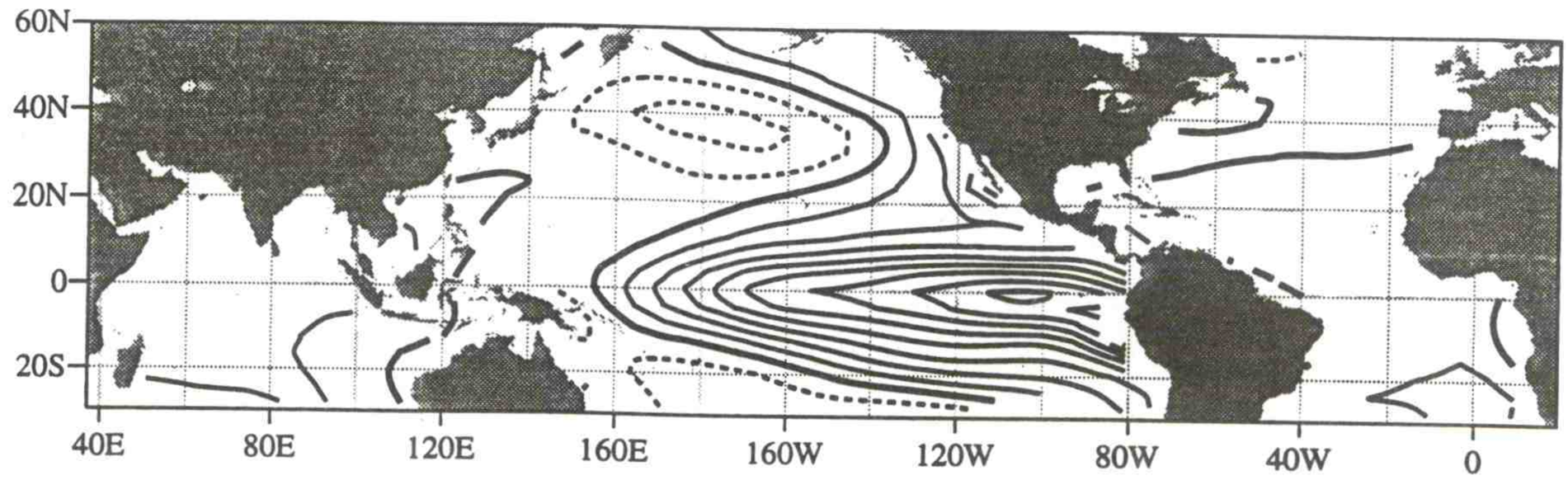

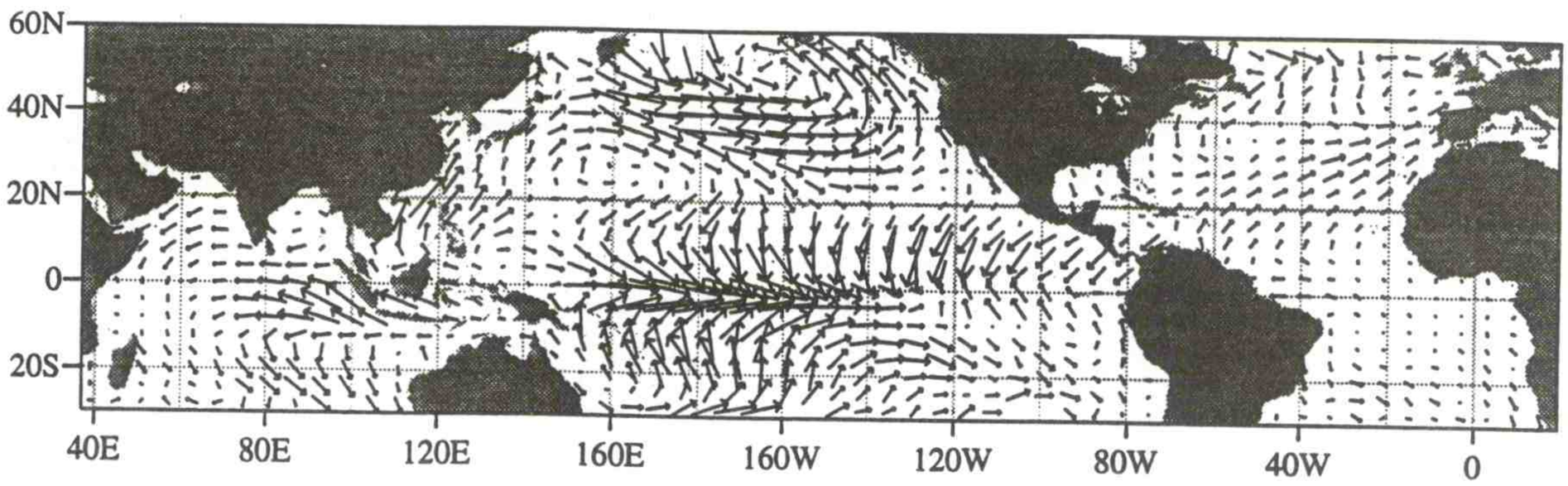

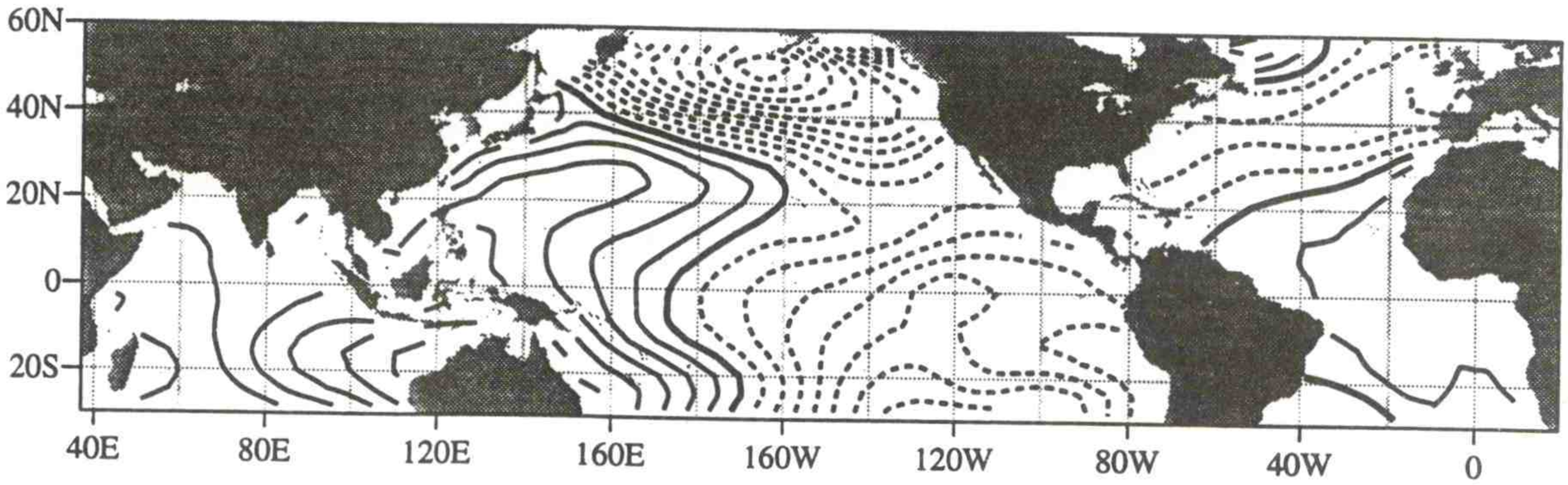

Figure 3: As in Fig. 2, but based on the normalized 5-year high-pass filtered time series of the cold tongue index (the time series labeled CT* in Fig. 1).

Decadal and Interannual Variability in the Tropical Western Pacific

David S. Gutzler

Depts. of Earth & Planetary Sciences and Geography
University of New Mexico, Albuquerque

This paper describes an examination of tropical western Pacific radiosonde data for decadal trends of tropospheric specific humidity (*q*) and equivalent potential temperature (θ_e). These trends are compared with trends for the same period derived from analyzed SST. The western Pacific signature of ENSO-related interannual variability is compared with longer-term variability in order to assess whether decade-scale changes could be interpreted simply in terms of aggregated ENSO fluctuations.

Western Pacific (WP) averages of *q* and θ_e are derived from daily (0000UTC) radiosonde ascents for the period April 1973–December 1993 at four U.S.-operated stations: Koror (7.3°N,134.5°E), Truk [now Chuuk] (7.4°N,151.8°E), and Pohnpei (6.9°N,158.3°E), all part of the Federated States of Micronesia, and Majuro, Marshall Islands (7.1°N,171.4°E). The locations of the stations are shown in Fig. 1a. Monthly means are derived from daily humidity and temperature values and then averaged over the four stations.

Gridded monthly mean SST analyses from the NOAA Climate Prediction Center (CPC) for the period January 1970–December 1994 are used to define spatial averages over four near-equatorial regions (Fig. 1a). Three of these averaging regions (Niño1+2, Niño3, and Niño4) are very similar to those used operationally by the CPC to monitor near-equatorial variability in the central and eastern Pacific associated with El Niño-Southern Oscillation (ENSO). A fourth region, dubbed 'Niño5', is derived in this study to describe monthly mean SST fluctuations in the tropical warm pool region west of the dateline, covering the range of longitudes of the stations from which the WP averages are derived. The eastern part of the Niño5 region overlaps the western part of the Niño4 region, so these two SST indices are not completely independent, but it will be shown that the Niño5 and Niño4 SST time series exhibit quite distinct temporal fluctuations. In this short paper results will be presented just for the Niño4 and Niño5 regions.

Figure 1 shows monthly mean time series of SST since 1970 in the Niño4 and Niño5 regions. Each of these time series exhibits a statistically significant upward trend over the period, shown by the dashed linear regression line in each panel. Except for a few months in early 1994, Niño4 SST has remained above its 1973-1993 climatological value of 28.4°C continuously since the beginning of 1990. The amplitude of variability of Niño5 SST is small relative to SST farther east. Both annual and semiannual harmonics are prominent in the seasonal cycle: minimum temperature is reached in boreal winter with a secondary minimum in late boreal summer. The decade-scale trend is 0.25°C/decade, less than half as large as exhibited in Niño4. Statistically, however, this trend is as significant as the Niño4 trend because the variability on shorter time scales is so much smaller.

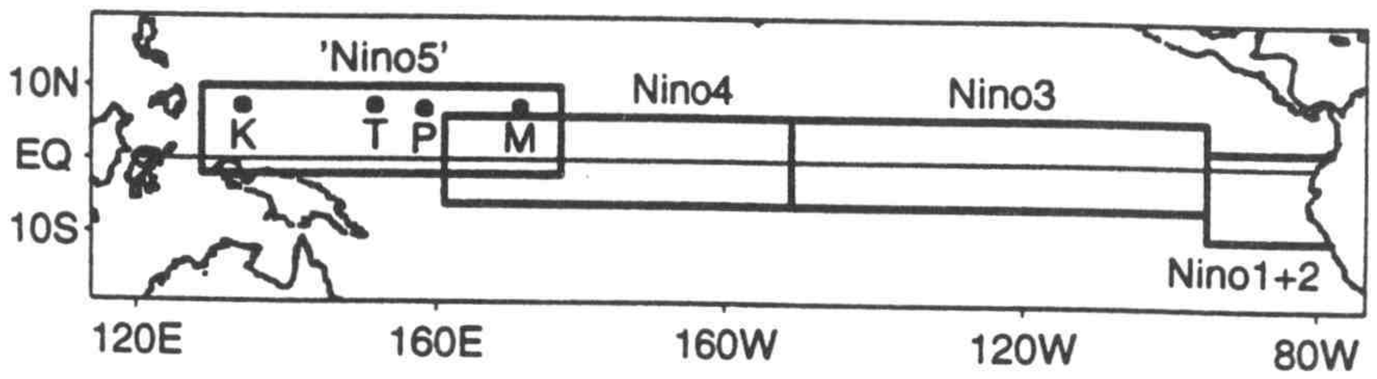

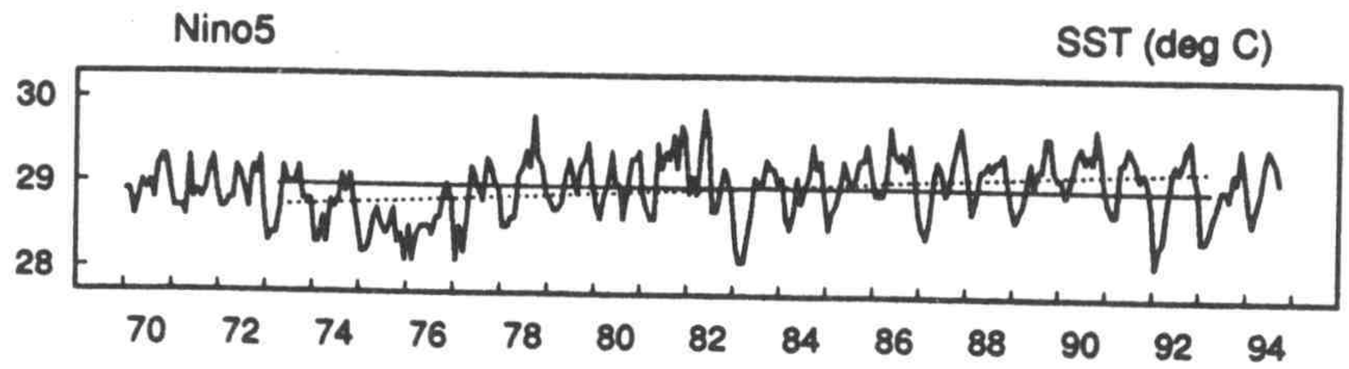

Figure 1: (a) Areas used to define the SST spatial averages from NOAA gridded analyses. The Niño4, Niño3, and Niño1+2 areas are very similar to areas with the same names defined by the NOAA Climate Prediction Center. The locations of radiosonde stations used to define Western Pacific averages of temperature and humidity are shown within the Niño5 box (K=Koror, P=Pohnpei, T=Truk, M=Majuro).

(b,c) Time series of monthly mean SST (°C), averaged over the Niño5 and Niño4 regions delineated in (a). The climatological average for the 1973-1993 period is shown in each panel by the horizontal solid line, and the linear trend fit to each time series is shown by the dashed line (climatological monthly means are retained in the plot but were removed before calculating the regression coefficients).

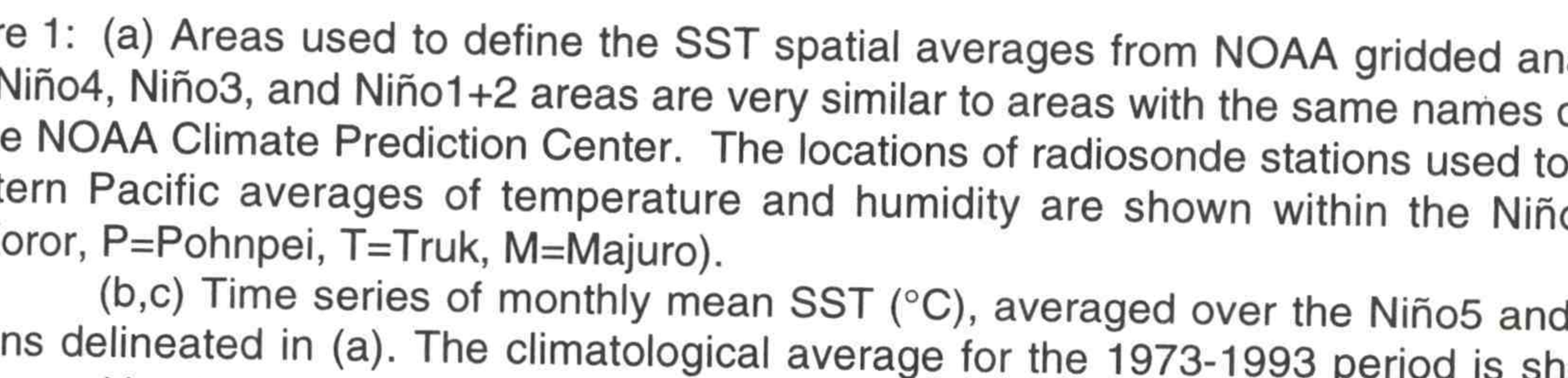

Figure 2: WP-average specific humidity (gm/kg) at 1000 hPa. The climatological average and linear trend are shown by solid and dashed lines, respectively, as in Fig. 1.

Figure 2 shows WP-average time series of q at 1000 hPa. The upward trend is statistically significant, with unprecedented moistening in recent years (the q_{1000} time series reached its highest values in the data record in 1993). The recent moistening is even more pronounced in relative humidity (given the interruption of the low-level warming trend), and the difference between q_{1000} and the saturation value associated with Niño5 SST is also decreasing with time (these results not shown).

The significant upward trends in the time series shown in Figs. 1 and 2 are occurring year-round. For example, the 1973-1993 linear regression for Niño4 SST based on just January-March months (the coldest months of the year in the Niño4 region) is 0.53°/decade, while the regression based on just May-July (the warmest months of the year) is 0.49°/decade. The WP q_{1000} trend shows a similar insensitivity to season. The Niño5 SST trend is largest in the boreal summer, but all seasons show an upward tendency over the 1973-1993 period.

Figure 3a shows time series of θ_e at 300 hPa and 1000 hPa. Both time series show upward trends, due principally to warming at 300 hPa and moistening at 1000 hPa. Figure 3b shows the difference θ_{e300}-θ_{e1000}, denoted $\Delta\theta_e$, which is a measure of convective instability in the tropospheric column ($\Delta\theta_e$<0 defines convectively unstable conditions). The $\Delta\theta_e$ trace shows that the WP region is almost always convectively unstable, the only exception being the mature phase of the 1982/83 warm event. The amplitude of convective instability is increasing in this period by more than 1°/decade, i.e. the increased instability due to boundary layer moistening more than counteracts the stabilizing effect of upper tropospheric warming. During El Niño events $\Delta\theta_e$ decreases in amplitude (the troposphere becomes less unstable), as observed in early 1983 and 1992, and less prominently in 1976/77 and 1987. Thus the $\Delta\theta_e$ curve provides clear evidence that the decade-scale variability in the western Pacific is not merely a reflection of more frequent ENSO warm episodes.

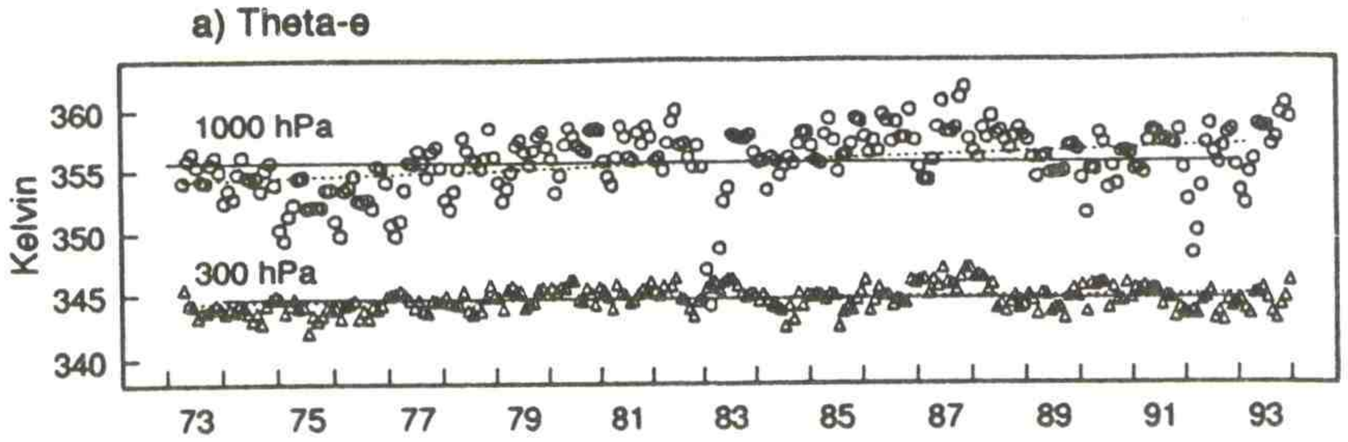

Figure 3: (a) WP-average equivalent potential temperature θ_e (K) at 1000 hPa (circles) and 300 hPa (triangles).
(b) θ_e difference between 300 hPa and 1000 hPa, denoted $\Delta\theta_e$.

To summarize, the principal findings are:

(1) The tropical Pacific ocean and atmosphere exhibit both long-term (decadal) and shorter-term, interannual variability. Regional indices of western and central equatorial Pacific SST exhibit significant upward trends in recent decades. Specific humidity in the warm pool boundary layer exhibits a statistically significant upward trend and $\Delta\theta_e$ shows a downward trend indicating increased levels of convective instability.

(2) In several respects the tropical western Pacific response to El Niño events is opposite the recent decade-scale trends, suggesting that the decade-scale variability cannot be considered simply an aggregate of the effects of more frequent ENSO warm events. On decadal scales, Niño4 and Niño5 SST, western Pacific boundary layer humidity, and the magnitude of western Pacific convective instability are all increasing. El Niño is associated with warm anomalous SST in Niño4, but decreased boundary layer humidity and convective instability over the western Pacific.

(3) Recent multidecadal variability in the tropical Pacific is large enough relative to ENSO-related variability to affect monitoring of ENSO by standardized anomaly indices. The Niño4 SST index is particularly sensitive to the choice of a base period, because recent lower-frequency variability in the central equatorial Pacific is similar in amplitude to the ENSO signal there.

On the Phase-Locking between El Niño and the Annual Cycle

Cécile Penland

Coöperative Institute for Research in the Environmental Sciences,
University of Colorado, Boulder, CO 80309-0449

The tendency of the mature phase of El Niño events to occur in the late boreal fall or winter is well known. It is also well known that this phase-locking is not absolute; for example, the large 1987 warm event peaked in July and the smaller 1993 event peaked in May. Nevertheless, pattern correlations between sea surface temperature anomaly (SSTA) maps and the leading empirical orthogonal function (EOF), which is dominated by the SSTA pattern associated with a mature warm event, are more likely to be large during the late boreal fall or winter than during the rest of the year (Fig. 1).

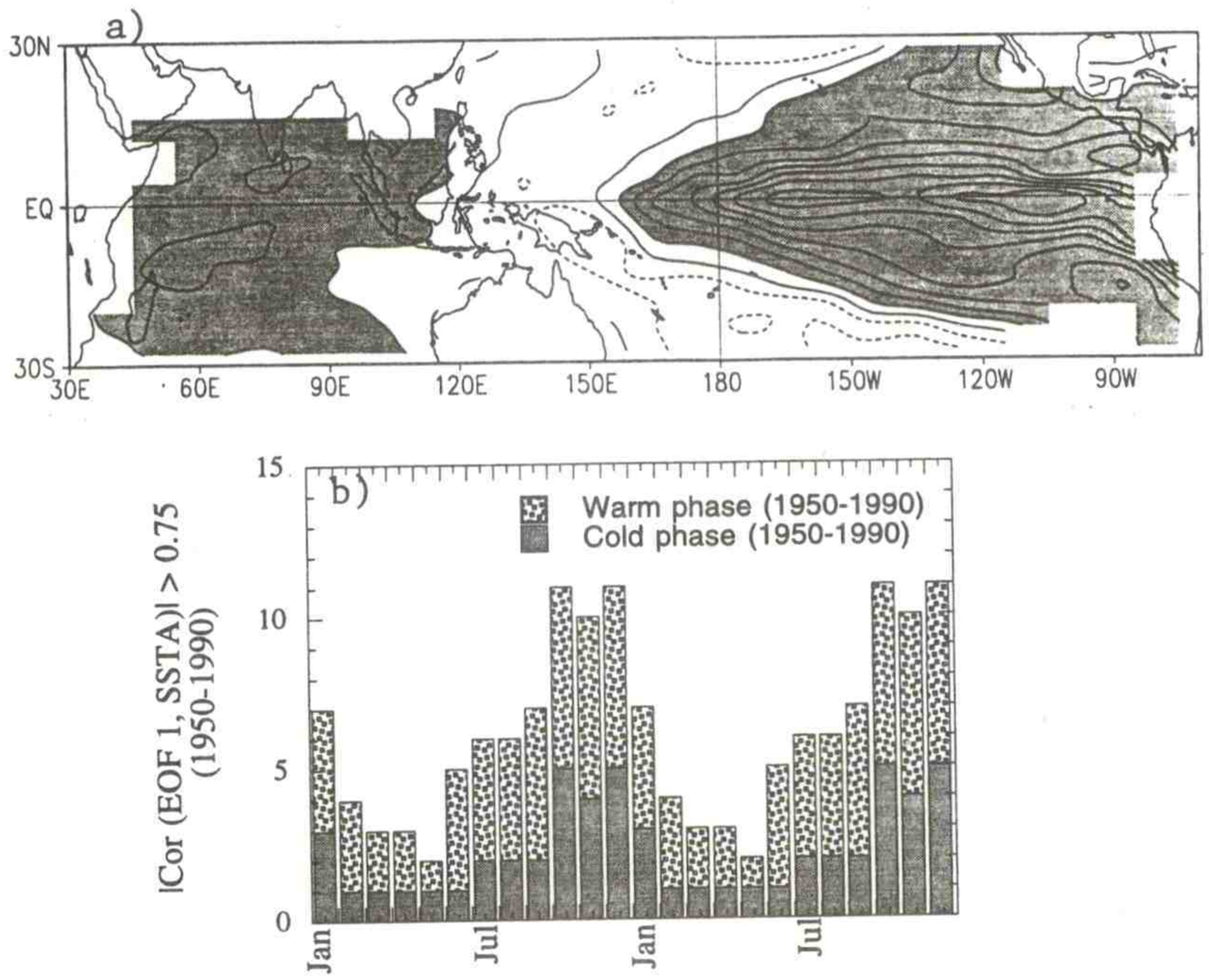

Fig. 1: a) Leading EOF of COADS IndoPacific SSTA explaining about 28% of the variance in the 1950-1990 record. SSTs were subjected to a three-month running mean and anomalies were calculated relative to the standard 1950-1979 climatology. b) Number of times the size of the pattern correlation between Fig. 1a and SSTA exceeded 0.75, stratified by month. Two cycles are shown for clarity.

Given the phase-locking between El Niño and the annual cycle, it has been puzzling to some researchers that skillful predictions of IndoPacific SSTAs are made routinely using a statistical technique, Linear Inverse Modeling, which apparently does not consider the annual cycle at all (e.g., Penland and Sardeshmukh, 1995, *J. Climate* **8**, 1999-2024, PS95 hereafter; see also the *Climate Diagnostics Bulletin*). Further, an optimal initial SSTA structure (Fig. 2), obtained using stationary statistics, is found to precede nearly every mature warm event by a lead time of four to ten months (Fig. 3). This implies that the optimal structure itself is phase-locked to the annual cycle, occurring predominantly in the boreal spring, and this has been found to be the case (PS95,

their Fig. 18). Finally, PS95 have shown that SSTAs pass a sensitive test for linear dynamics (the "tau-test": see the extensive discussion in PS95), and one can easily show that nonstationarity (such as an annual cycle) in the deterministic dynamics will in general cause a failure of that test.

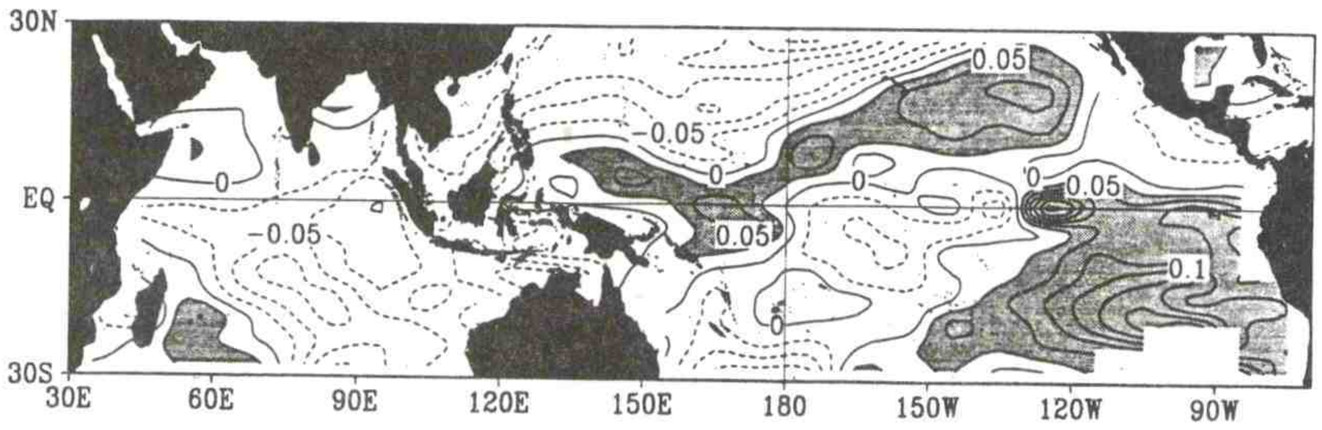

Fig. 2: Optimal initial structure which precedes the mature El Niño pattern by four to ten months.

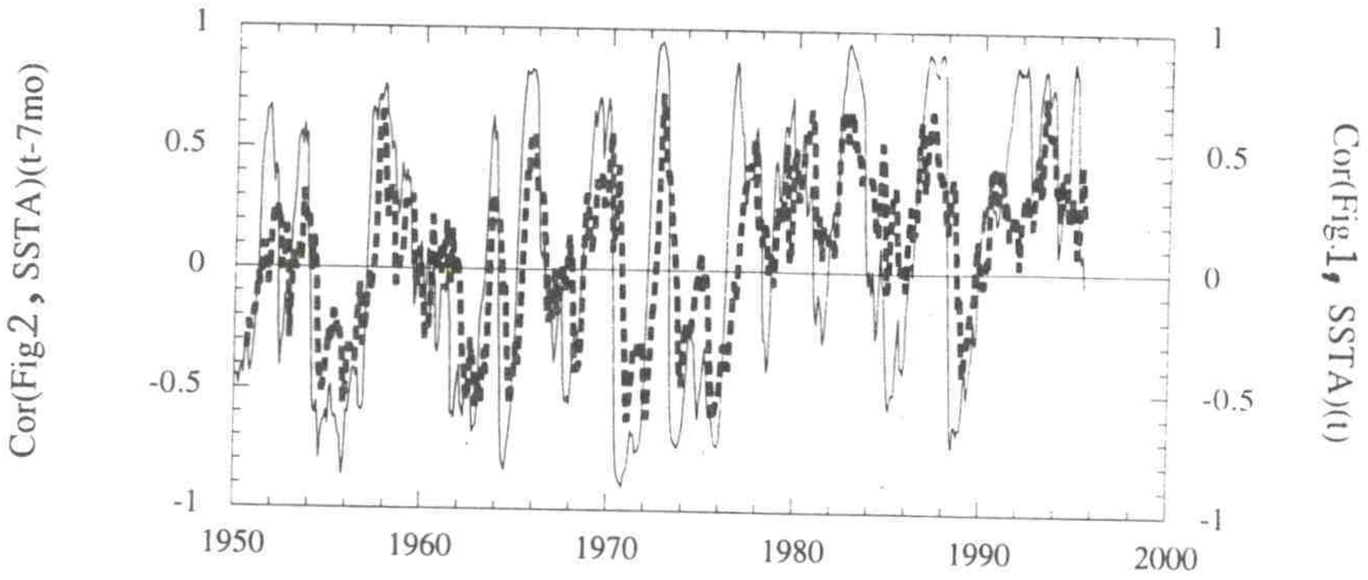

Fig 3: Time series of pattern correlation between Fig. 1 and SSTA (light solid line) along with the time pattern correlation between Fig. 2 and SSTA 7 months earlier (heavy broken line). The correlation between the two is 0.67.

It is shown here that there is no contradiction between the rough phase-locking of El Niño and the basic dynamical assumption behind Linear Inverse Modeling that SSTAs on the seasonal timescale may be described as a stable linear process driven by spatially-coherent white noise. Recall that predictions are made by operating an empirically-derived Green function on an initial condition representing the current state of the system. The Green function depends only upon the deterministic dynamics; the stochastic forcing does not enter into the prediction process. Still, the stochastic forcing does play a role in setting up the initial conditions upon which the Green function operates. Whether the stochastic forcing has stationary or periodic (cyclostationary) statistics is irrelevant to the prediction process; however, cyclostationary stochastic forcing allows the observed phase-locking between El Niño and the annual cycle.

To see this, let $\boldsymbol{x}$ be the vector each component of which is the SST anomaly at a particular location. Assume that $\boldsymbol{x}$ is described by the following linear stochastic differential equation

$$\frac{d\boldsymbol{x}}{dt} = \mathbf{B}\boldsymbol{x} + \xi, \tag{1}$$

where **B** is a constant matrix and where ξ is multivariate white noise with $\langle\xi(t+\tau)\xi^{T}(t)\rangle = \mathbf{Q}(t)\delta(\tau)$, and with $\mathbf{Q}(t)$ periodic. We solve the Fokker-Planck equation appropriate to Eq. (1) and find that the conditional probability density $p(\boldsymbol{x},t+\tau \mid \boldsymbol{x}_0,t)$ that the anomaly vector of SSTA will have value between $\boldsymbol{x}$ and $\boldsymbol{x}+d\boldsymbol{x}$ at time $t+\tau$ given anomaly vector $\boldsymbol{x}_0$ at time t is a multivariate Gaussian centered on $exp(\mathbf{B}\tau)\boldsymbol{x}_0$. That is, the predictions are made exactly as in the stationary case. Also, the method of estimating the multivariate Green function $\mathbf{G}(\tau)\equiv exp(\mathbf{B}\tau)$ is the same as in the stationary case (see, e.g., PS95), as long as the statistics are accumulated over an integral number of periods. The error covariance matrix Σ for the predictions is given by

$$\Sigma(t,\tau) = \langle\boldsymbol{x}(t+\tau)\boldsymbol{x}^{T}(t+\tau)\rangle - \mathbf{G}(\tau)\langle\boldsymbol{x}(t)\boldsymbol{x}^{T}(t)\rangle\mathbf{G}^{T}(\tau), \tag{2}$$

which allows a cycle in the prediction error, but reduces to the error covariance matrix for the stationary system (**Q** constant) when $\langle\boldsymbol{x}(t+\tau)\boldsymbol{x}^{T}(t+\tau)\rangle = \langle\boldsymbol{x}(t)\boldsymbol{x}^{T}(t)\rangle$ for all τ. The time-dependent Fluctuation-Dissipation Relation (FDR: Penland and Matrosova 1994) between the stochastic forcing and the deterministic dynamics is

$$\frac{d\langle\boldsymbol{x}(t)\boldsymbol{x}^{T}(t)\rangle}{dt} = \mathbf{B}\,\langle\boldsymbol{x}(t)\boldsymbol{x}^{T}(t)\rangle + \langle\boldsymbol{x}(t)\boldsymbol{x}^{T}(t)\rangle\,\mathbf{B}^{T} + \mathbf{Q}(t) \tag{3}$$

and reduces to the stationary FDR when integrated over a period of $\mathbf{Q}(t)$, which is equal to one year in this study.

The data used to confront this explanation were monthly-averaged SSTAs between Jan 1950 and Feb 1985 from the Comprehensive Ocean-Atmosphere Data Set (Slutz et al. 1985). The standard 1950-1979 COADS climatology was removed from the data, which were then subjected to a three-month running mean and projected onto 15 EOFs containing about two-thirds of the variance. We were left with 420 maps corresponding to 35 years. We obtained **B** as in PS95, but with $\tau_0 = 4$ months (see PS95 for details; they used $\tau_0 = 7$ months). As in PS95, one optimal initial structure ϕ_1 for SST variance growth was found (see Fig. 2) to precede the mature phase of El Niño by about 7 months; the correlation between this optimal structure and the one found by PS95 is higher than 0.9. After estimating $\langle\boldsymbol{x}(t)\boldsymbol{x}^{T}(t)\rangle$ and $d\langle\boldsymbol{x}(t)\boldsymbol{x}^{T}(t)\rangle/dt$ for each month from the data,

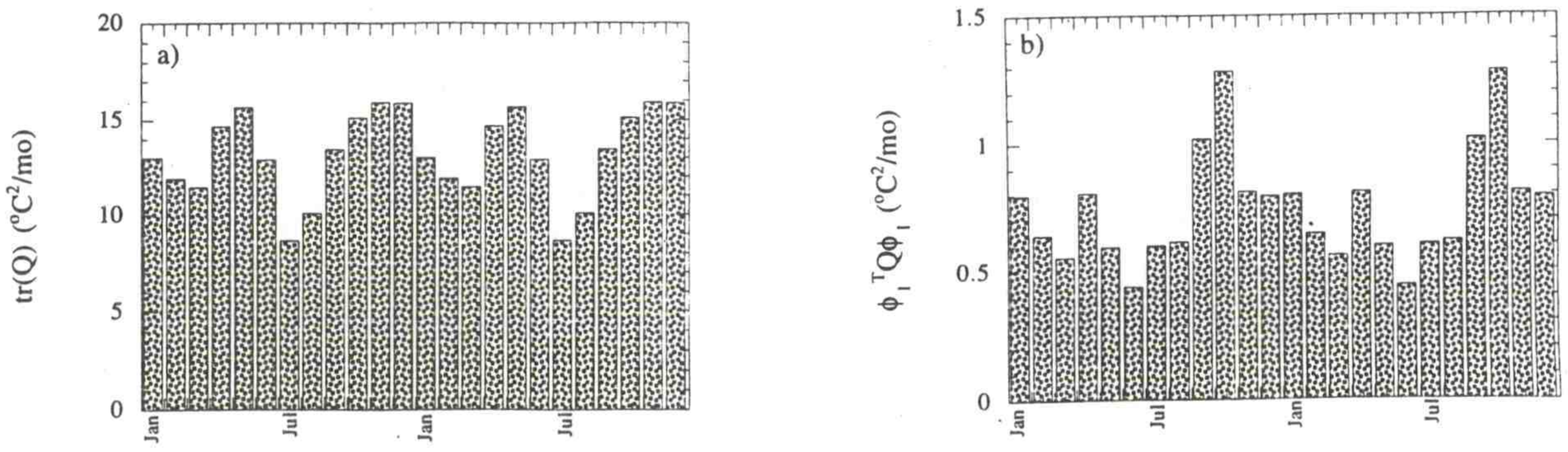

Fig. 4 a) The annual cycle of the total variance of stochastic forcing. b) The annual cycle of the amount of stochastic forcing which excites the optimal structure.

$\mathbf{Q}(t)$ was estimated for each month from Eq. (3). Obviously, given the paucity of data, the errors in the estimations of $<\boldsymbol{x}(t)\boldsymbol{x}^{\mathrm{T}}(t)>$ and $d<\boldsymbol{x}(t)\boldsymbol{x}^{\mathrm{T}}(t)>/dt$ are large, and $\mathbf{Q}(t)$ is proportionally uncertain. The variation of the variance of the stochastic forcing (tr $\mathbf{Q}(t)$) with the time of year is not a simple cycle. Neither does the amount of variance of stochastic forcing which directly excites the optimal structure ($\phi_1{}^{\mathrm{T}}\mathbf{Q}(t)\phi_1$) peak in the boreal spring as one would expect if the stochastic forcing were the primary source of ϕ_1 (Fig. 4); in fact, the stochastic forcing appears to be most efficient in exciting ϕ_1 at the time of year when the projection of the SSTA onto ϕ_1 is least likely to be large. Therefore, if the dynamic scenario suggested here is valid, the deterministic dynamics must process the annual cycle provided by the stochastic forcing in order to set up the optimal structure in the spring; the optimal initial structure for growth is not directly forced stochastically. If the deterministic dynamics *do* process the annual cycle this way, we should be able to reproduce the phase-locking between the annual cycle and El Niño in a numerical model of Eq. (1) driven by cyclostationary stochastic forcing with periodic variance as in Fig. 4.

Given the empricially-derived deterministic dynamics $\mathbf{B}$ and the statistics of the stochastic forcing $\mathbf{Q}(t)$, the stable linear model Eq. (1) was generated. The procedure for generating the stationary system is explained in detail in Penland and Matrosova (1994) and is easily extended to the case with time-dependent $\mathbf{Q}(t)$. A time step of six hours was used to generate the output time series. The initial values of SSTA were set at the peak of the stationary probability distribution ($\boldsymbol{x} = \boldsymbol{0}$) and the system was exercised for 100 years in order to lose memory of the initial condition. Output was recorded once per month (every 120 time steps) thereafter, for a total time series length of 2000 years. The output was examined for phase-locking between El Niño and the annual cycle. Fig. 5 shows that the observed phase-locking is reproduced, even with the large uncertainties in $\mathbf{Q}(t)$. These results indicate that the deterministic dynamics play a large role in setting up the optimal structure in the boreal spring, followed by a mature El Niño event in the late fall or winter, even though the ultimate source of the phase-locking between El Niño and the annual cycle is in the stochastic forcing.

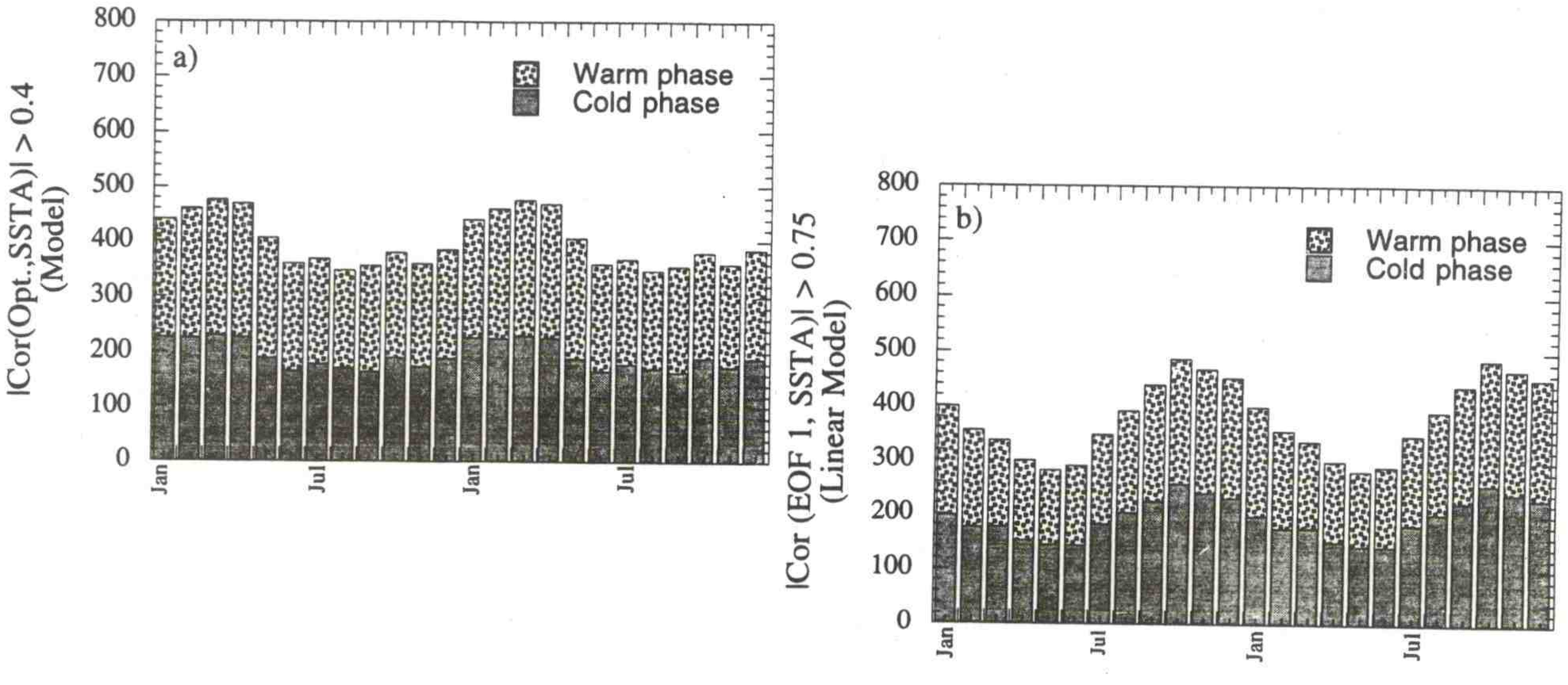

Fig. 5: a) Number of times the size of the pattern correlation between Fig. 2 and model output SSTA exceeded 0.4, stratified by month. Two cycles are shown for clarity. b) Number of times the size of the pattern correlation between Fig. 1 and model output SSTA exceeded 0.75, stratified by month.

AN ANALYSIS OF THE STARTING DATE FOR THE SUMMER MONSOON IN WESTERN MEXICO AND SOUTHEAST ARIZONA

Arthur V. Douglas and Phillip J. Englehart
Atmospheric Sciences - Creighton University
Omaha, Nebraska 68005

INTRODUCTION

The summer monsoon in Central America shifts northward into southeast Mexico in late April and early May. By June the monsoon has spread through much of the country, with northwest Mexico on the northern edge of the rains. In early July the monsoon has typically extended into the southwestern United States. Past studies of the North America monsoon have been limited to analyses of monthly precipitation data sets. In previous work we have shown the relationships between the monsoon and various atmospheric and oceanic variables (e.g. 700mb height anomalies, continental 700mb ridge position over North America, sea surface temperature anomalies and various tropical indices). Detailed diagnostic studies of the monsoon have been hindered by a lack of daily precipitation data for Mexico. Through NOAA's Pan American Climate Studies Program, we have initiated a comprehensive collection of daily data for 18 climate divisions in Mexico (Figure 1). Preliminary results are presented here which characterize the annual variability in the starting date of the monsoon in three synoptically distinct regions of Mexico and the United States: Oaxaca (Region 16), Sinaloa and Sonora (Regions 4 and 3), and Southeast Arizona.

DATA AND DEFINITIONS

In this preliminary analysis, we have focused on three main areas of the summer monsoon in western North America. Oaxaca is the Mexican state closest to convection associated with the ITCZ and this region displays a typical double peak in summer precipitation (May-June and again in September-October, with a pronounced dry period in July and August). Data from three long-term stations have been collected in this state: Salina Cruz, Ostuta and Tehuantepec. The western Mexican states of Sinaloa and Sonora are typically the wettest region of Mexico during the months of July and August. The summer monsoon in these states is not characterized by the mid-summer dry regime noted in Oaxaca. Three stations in each state have been selected: Badiraguato, Choix, and Huites in Sinaloa; and Minas Nuevas, Quiriego, and San Bernardo in Sonora. The northern edge of the monsoon is found in Southeast Arizona were summer rainfall is typified by greater interannual variability compared to that of Sonora and Sinaloa. More than 20 stations in the NCDC climate division for Southeast Arizona have been used to determine the starting date of the summer rains in this peripheral region of the summer monsoon.

In our analysis a Julian date was assigned for the start of the rainy season at each station for each year of record. The summer rainy season in these three sections of North America typically commences after a long period of spring dryness in which one or more months receive no rainfall. We have defined the starting date for the monsoon to be the first date of measurable rainfall at each station. An additional condition (suggested by WMO research) was that additional rainfall must occur within 7 days of the initial rains for the first date of rainfall to be declared the official starting date of the monsoon. Between 10% and 20% of the initial rains failed to be followed by additional rains within a 7 day period. These early dates were then classified as false starts and the next period of rainfall was then analyzed using the same criteria for obtaining the starting date for the rainy season.

In Arizona, all stations were considered collectively to determine the starting date of the monsoon within the climate division. For Mexico, an index of the starting date for the summer monsoon was constructed. This index is expressed as the average Z-score for the normalized starting date of the monsoon derived for each station in the division. Histograms for the starting dates of the monsoon are presented in Figure 2. Time series are shown in Figures 3-6. A graph relating Julian start dates to each year is shown in Figure 7. An index of the starting date

for the monsoon in the combined region of Northwest Mexico and Southeast Arizona is presented in Figure 8. This index was calculated by averaging the Z-scores for the starting dates in Southeast Arizona, Sonora and Sinaloa.

RESULTS

Statistics associated with the initiation of the summer monsoon in western Mexico and southeast Arizona are presented in the following table.

REGION	MONSOON START DATE MEAN	MEDIAN	STANDARD DEVIATION OF THE START DATE	RANGE OF THE START DATE (Julian Date)
Oaxaca	147	147	11.1 days	122 to 186
Sinaloa	174	174	6.9 days	155 to 191
Sonora	179	180	6.4 days	163 to 196
SE Arizona	182	182	7.8 days	164 to 196

The mean and median dates for the start of the summer monsoon are very close in each respective region. Greatest variability in the start date of the monsoon is noted in the far south and north (Oaxaca and Southeast Arizona, respectively). In the case of Oaxaca the time span between the earliest and latest start dates is 64 days---almost two months. In the far north, the range between the earliest and latest start dates is closer to one month.

The time series for the start date in Arizona was correlated with that for Sonora and Sinaloa. For the 65 year period the correlations were +0.411 and +0.416 (Sonora and Sinaloa, respectively and significant at the 99% level). Based on this relatively high correlation, we combined the normalized time series of each region and then created a mean start date for the northwest region of the monsoon (Figure 8, see Data section above).

In order to understand the conditions leading up to the initiation of the monsoon, we developed composite maps of the 700mb circulation prior to and during the month of initiation (Figures 9-14). Those years in which the start date was more than one standard deviation from the mean were used in the composites. For the early start dates the evolution of height anomalies during the spring are shown in Figures 9-11. Below normal heights are noted off the southwest coast of Mexico throughout the period. In the North Pacific and the eastern United States, deep troughs are noted to retreat northward prior to the onset of the monsoon. By June, an enhanced Bermuda high with an inverted trough to the southwest of Mexico is observed in the composite map. Anomalous flow at 700mb in the target region is from the southeast during early onset years (Figure 12).

Late starting monsoons were found to be associated with two distinct height anomaly patterns (Figures 13-14). In about half of the years a late start is associated with a strong negative height field over the continental United States with anomalous strong westerlies across the target region: a condition inhibiting the northward migration of the monsoon. This pattern is common following a late ending ENSO event. In the other years associated with a late start date, failure of the rains to move north appears to be connected to the development of higher than normal heights directly over the monsoon region. In many respects the two circulation patterns are almost opposite each other (comparison of Figures 13 and 14). This suggests that simple correlation analysis would not be useful in diagnosing factors associated with the onset of the monsoon in Southeast Arizona and Northwest Mexico.

In the next year additional daily data will be collected and analyzed. A more detailed study of the northward migration of the monsoon will be possible with this expanded data base. Once developed, the time series for each region in Mexico will then be related to daily 700mb heights and various tropical indices in order to complete a thorough analysis of the factors controlling the onset of the summer monsoon in North America.

FIGURE CAPTIONS

Figure 1. Location of climate divisions in Mexico and along the southern border of the United States.

Figure 2. Histograms depicting the starting date for the summer monsoon in western Mexico and Southeast Arizona. Julian dates are used throughout the paper (e.g. June 15 = Julian day 166; and July 1 = 182).

Figures 3-6. Time series of the starting date for the summer monsoon in western Mexico and Southeast Arizona.

Figure 7. Histogram demonstrating the relationship between the starting date of the monsoon in Southeast Arizona and associated year(s) of occurrence for each Julian date. Earliest recorded start date is 1936 (bottom left on graph) while latest start date is 1948 (upper right). Multiple year occurrences are centered to the right of each date.

Figure 8. Normalized starting date (Julian) for the summer monsoon in the combined region of Southeast Arizona, Sonora, and Sinaloa. See text for details regarding this index.

Figures 9-12. Composite maps showing the evolution of 700mb height anomalies (meters) leading up to an early start of the monsoon in the combined region of Southeast Arizona, Sonora, and Sinaloa. The specific years used in the composites are indicated below the figures. See text for selection process of years used in the composites.

Figures 13-14. Composite maps showing 700mb height anomalies associated with two distinct circulation types associated with a late arrival date for the summer monsoon. Late starts associated with Figure 13 are common following late ending ENSO events, while late starts under the circulation in Figure 14 are associated with drought development in the Southwest.

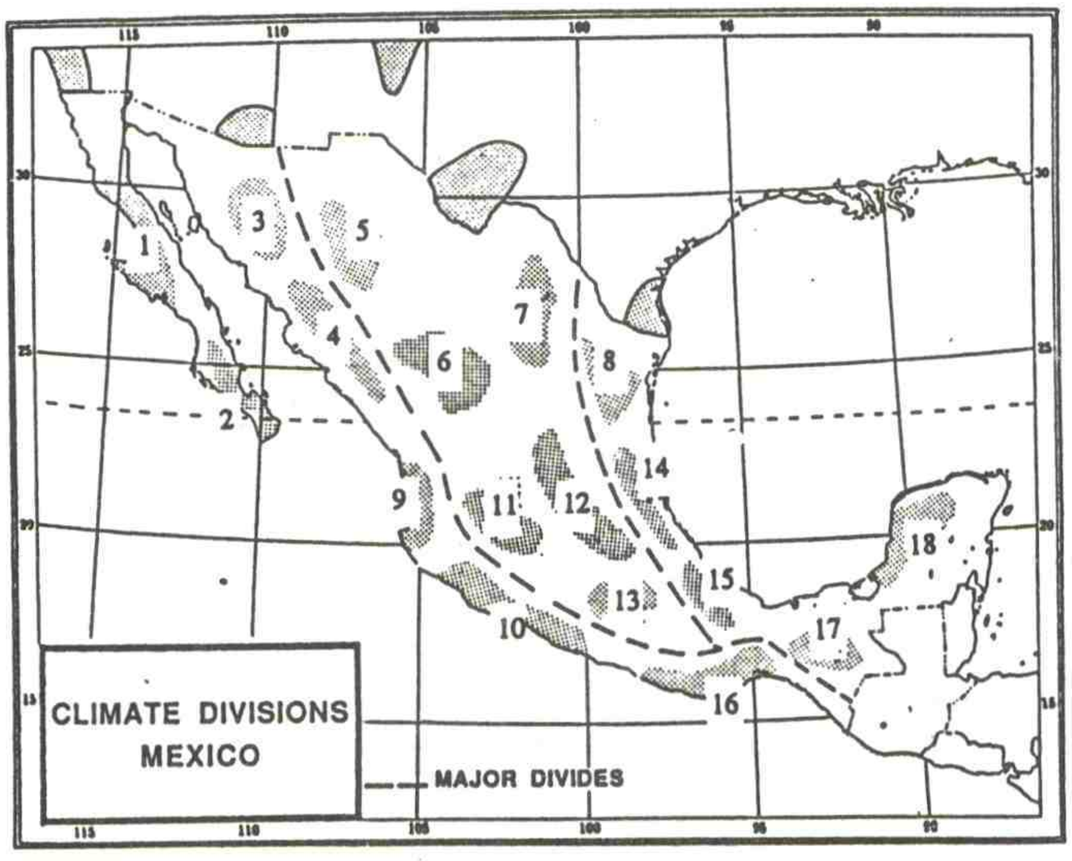

FIGURE 1

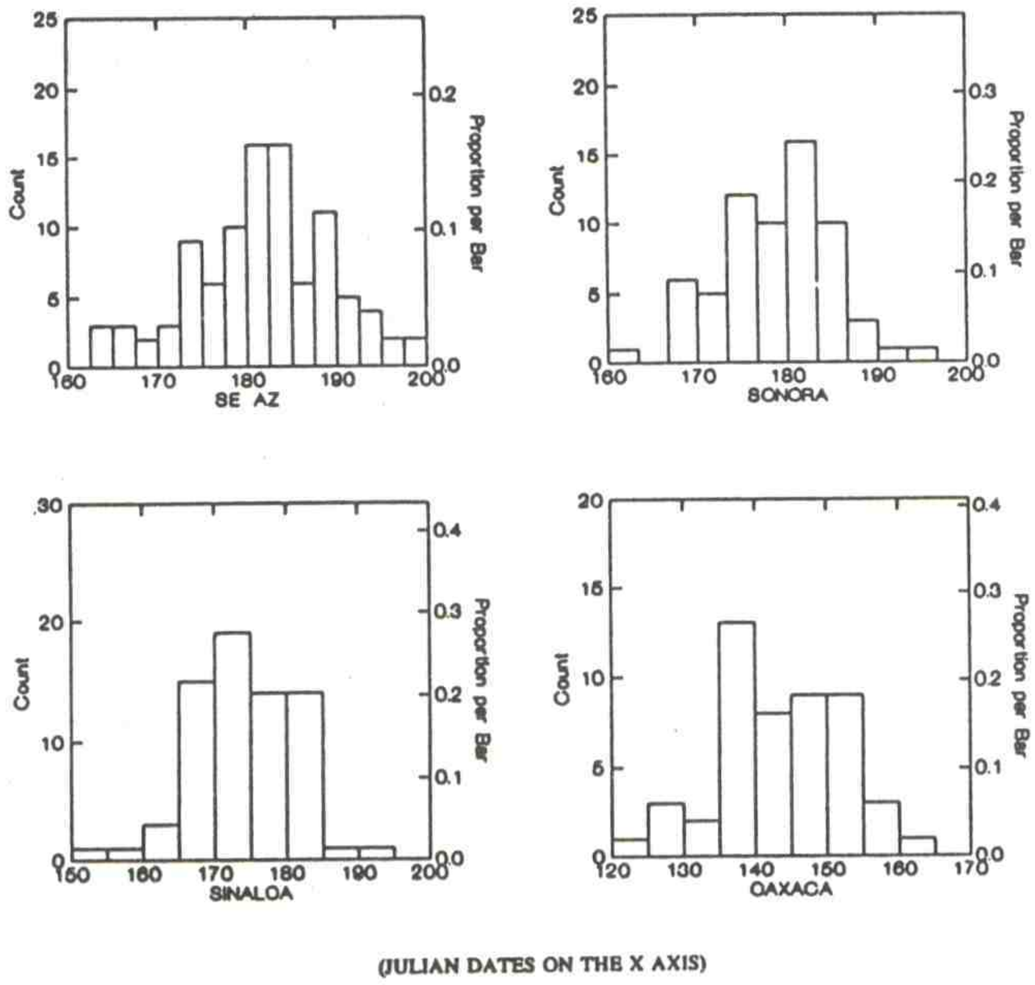

FIGURE 2

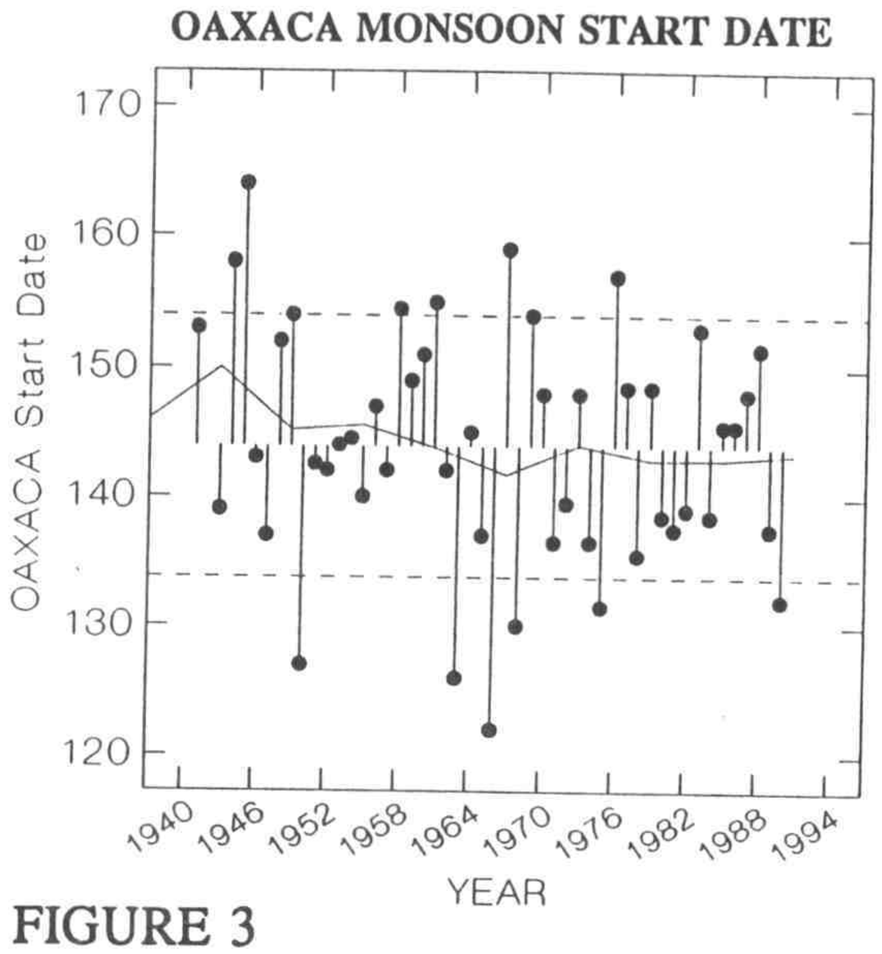

FIGURE 3

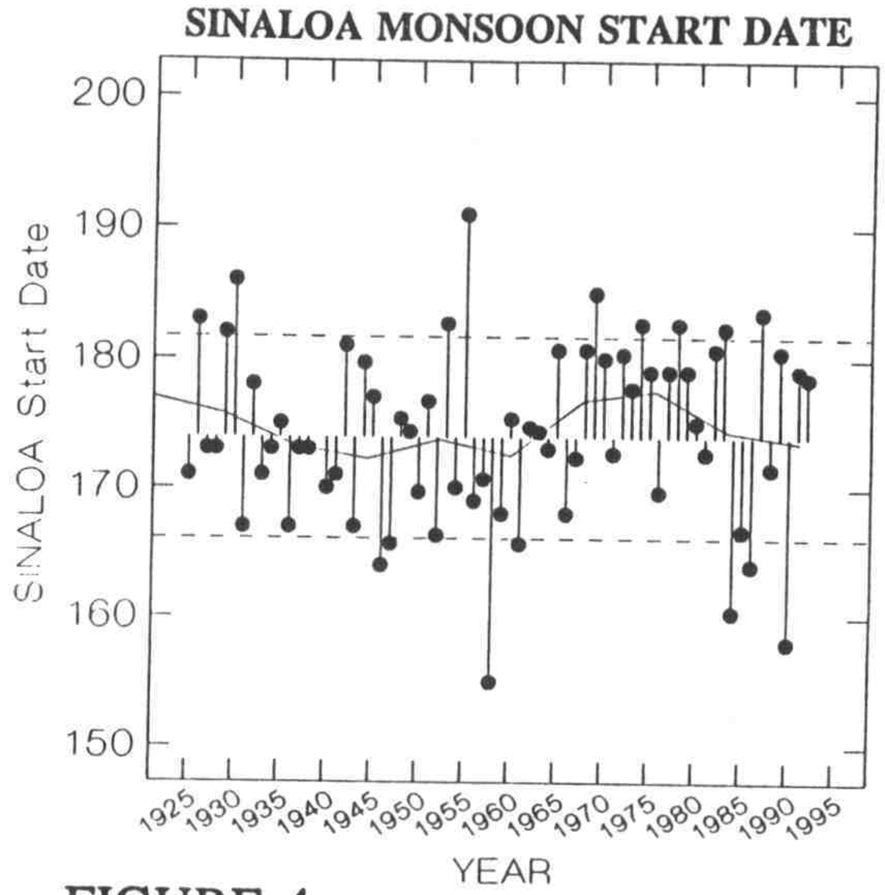

FIGURE 4

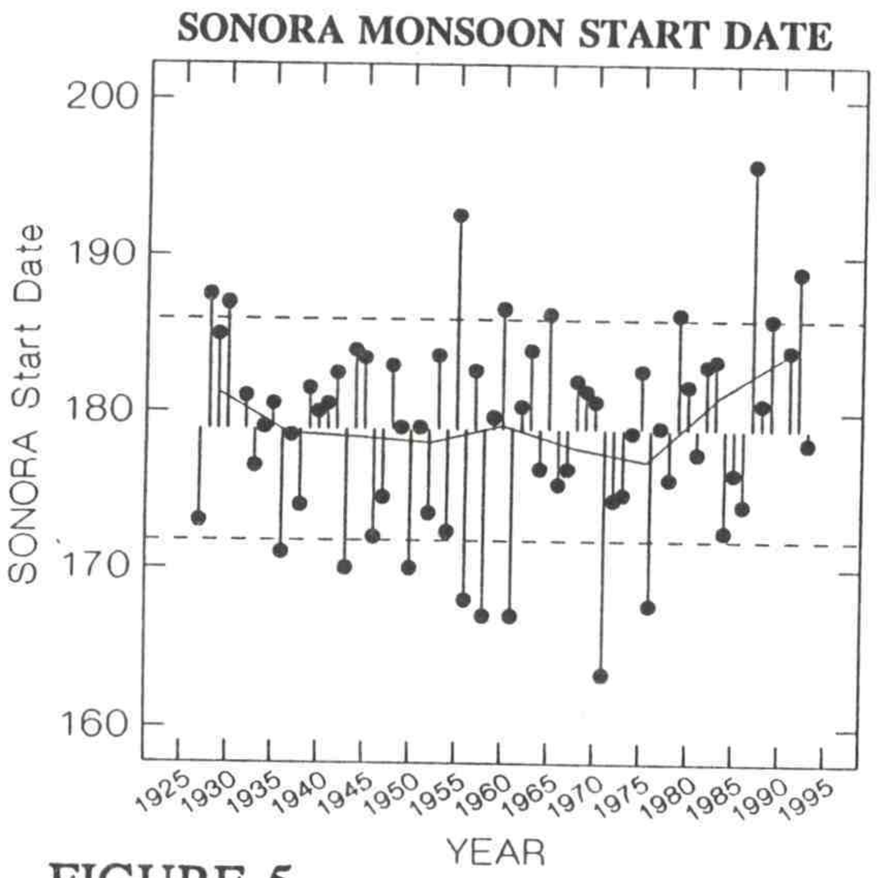

FIGURE 5

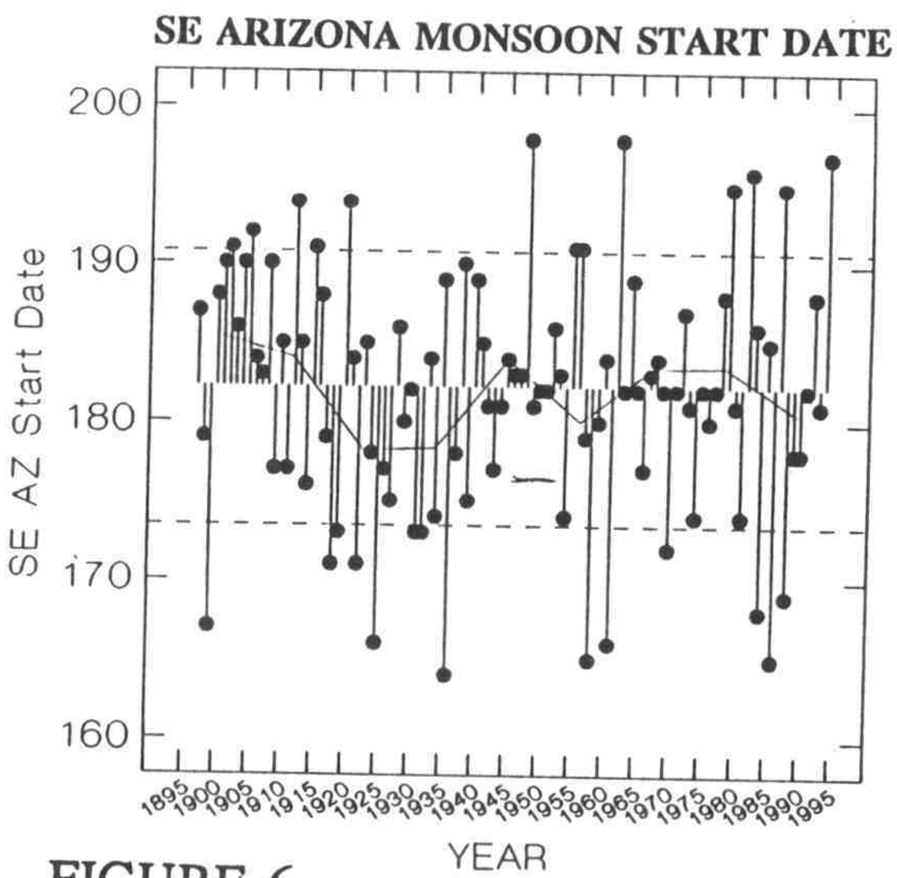

FIGURE 6

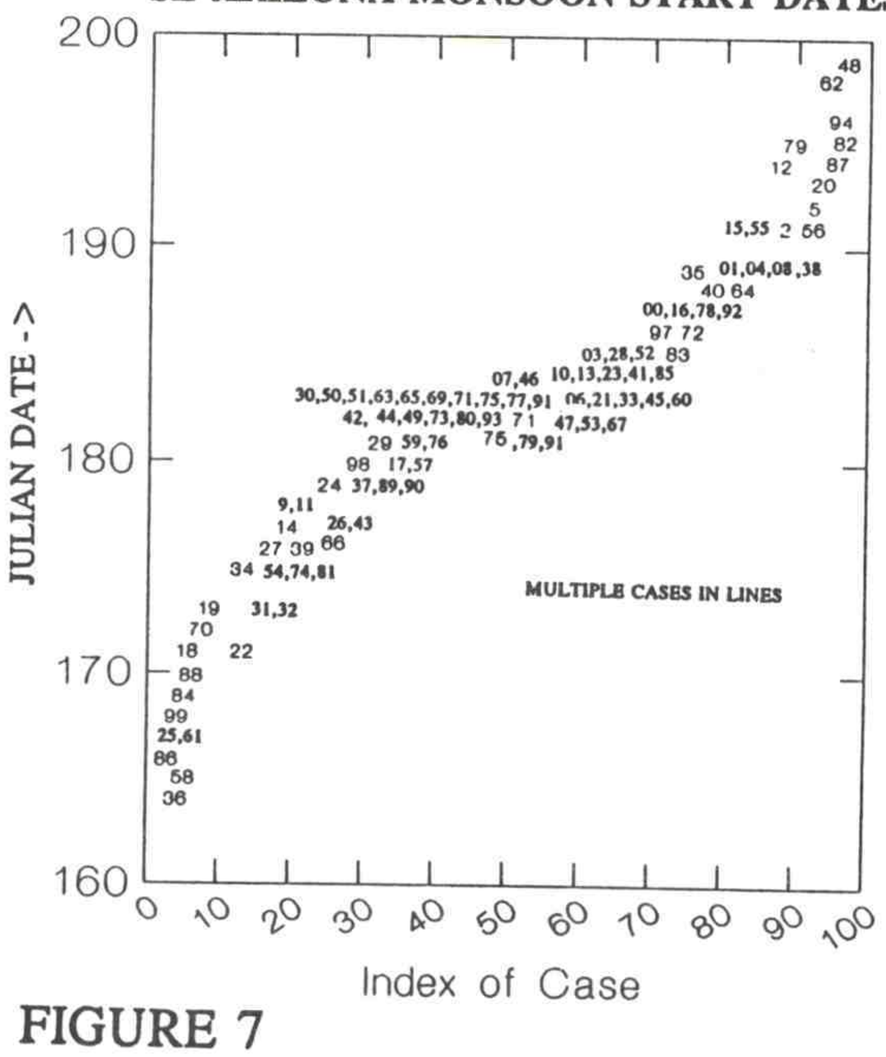

FIGURE 7

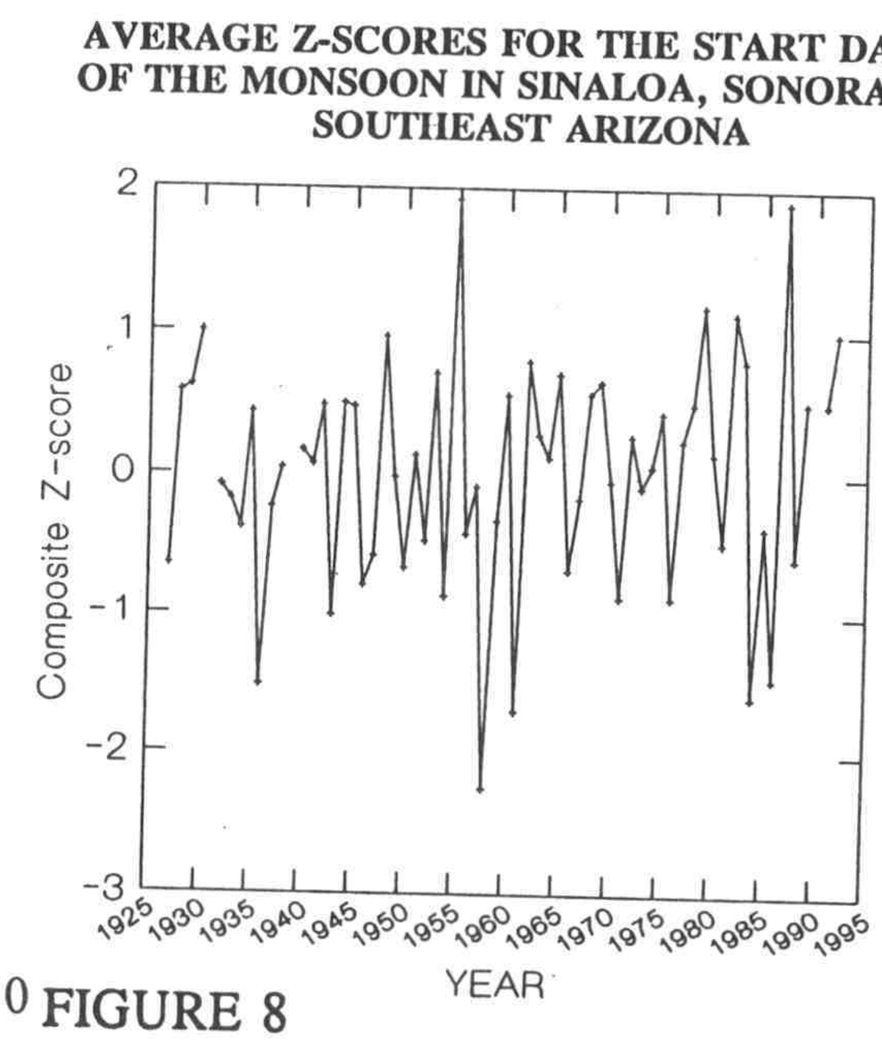

 FIGURE 8

MARCH COMPOSITE 700 MB HEIGHT ANOMALIES PRIOR TO EARLY STARTING MONSOONS

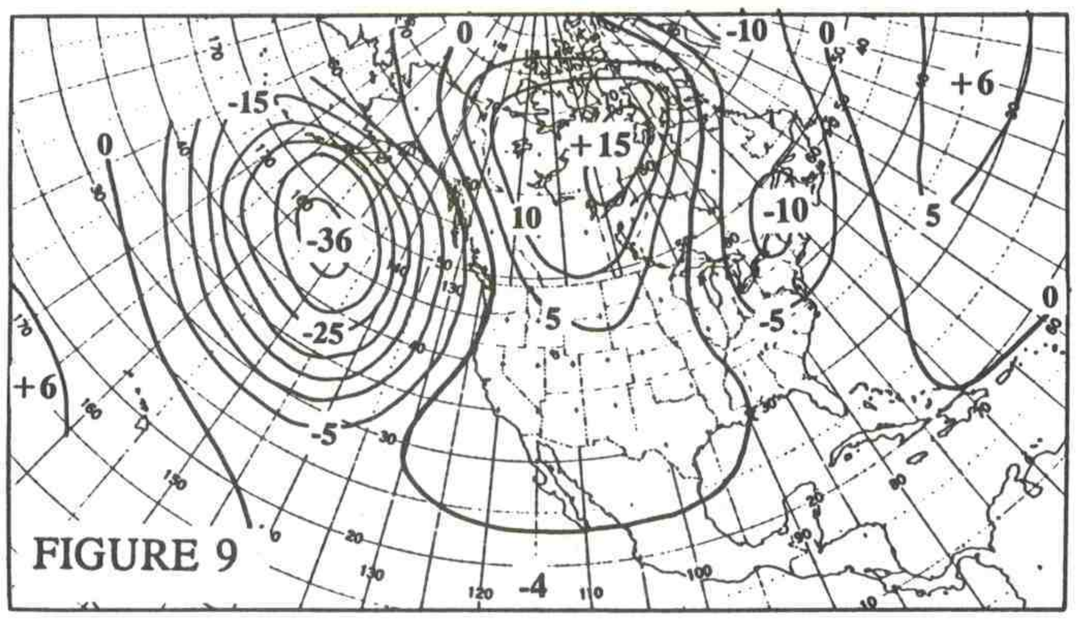

FIGURE 9

EARLY START DATE YEARS: 1958, 61, 84, 86, 90, 54, 76, 66, 50, 71, 81

APRIL COMPOSITE 700 MB HEIGHT ANOMALIES PRIOR TO EARLY STARTING MONSOONS

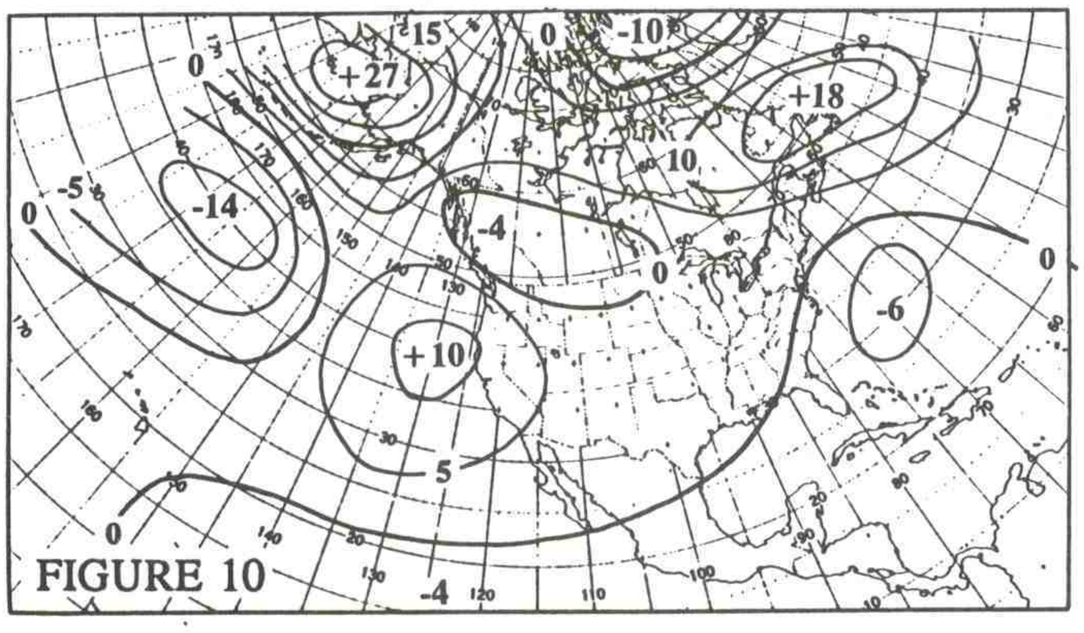

FIGURE 10

EARLY START DATE YEARS: 1958, 61, 84, 86, 90, 54, 76, 66, 50, 71, 81

MAY COMPOSITE 700 MB HEIGHT ANOMALIES PRIOR TO EARLY STARTING MONSOONS

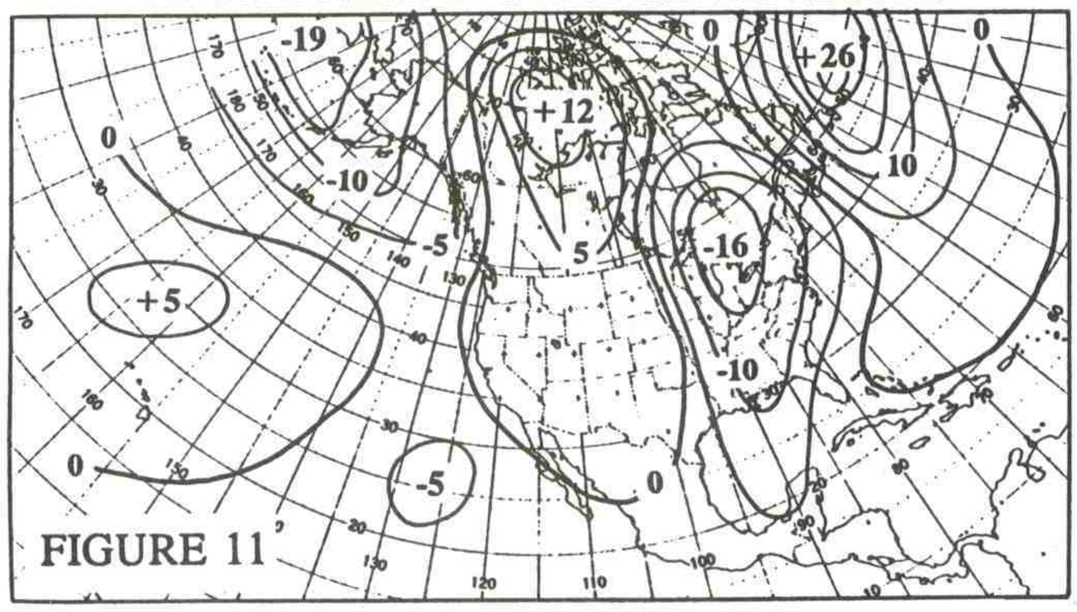

FIGURE 11

EARLY START DATE YEARS: 1958, 61, 84, 86, 90, 54, 76, 66, 50, 71, 81

JUNE COMPOSITE 700 MB HEIGHT ANOMALIES EARLY STARTING MONSOONS

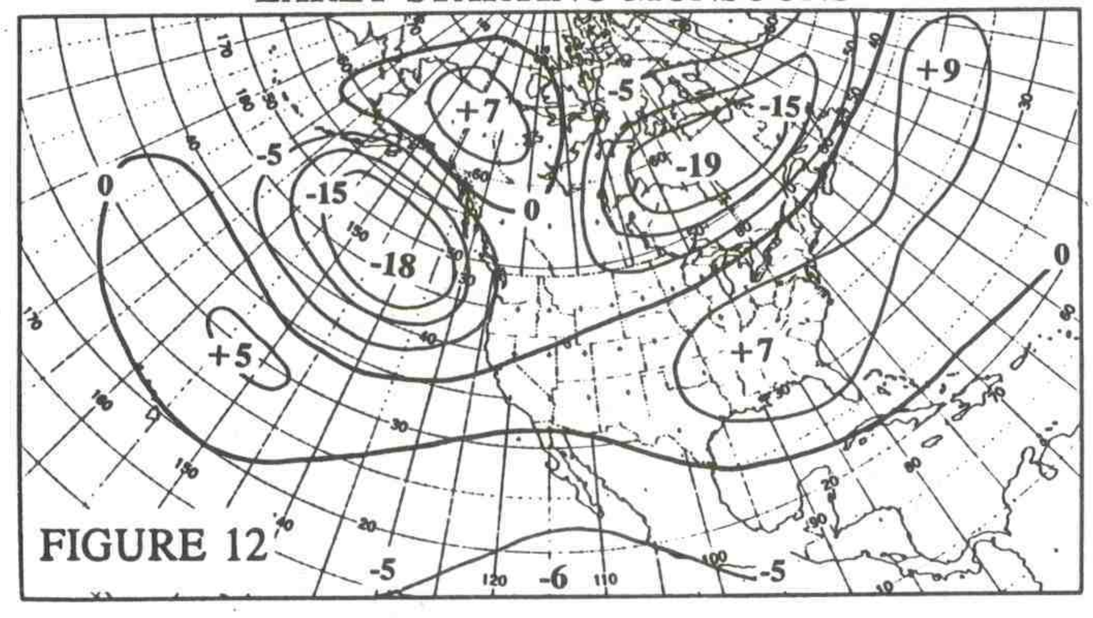

FIGURE 12

EARLY START DATE YEARS: 1958, 61, 84, 86, 90, 54, 76, 66, 50, 71, 81

JUNE COMPOSITE 700 MB HEIGHT ANOMALIES LATE STARTING MONSOONS---STRONG WESTERLIES

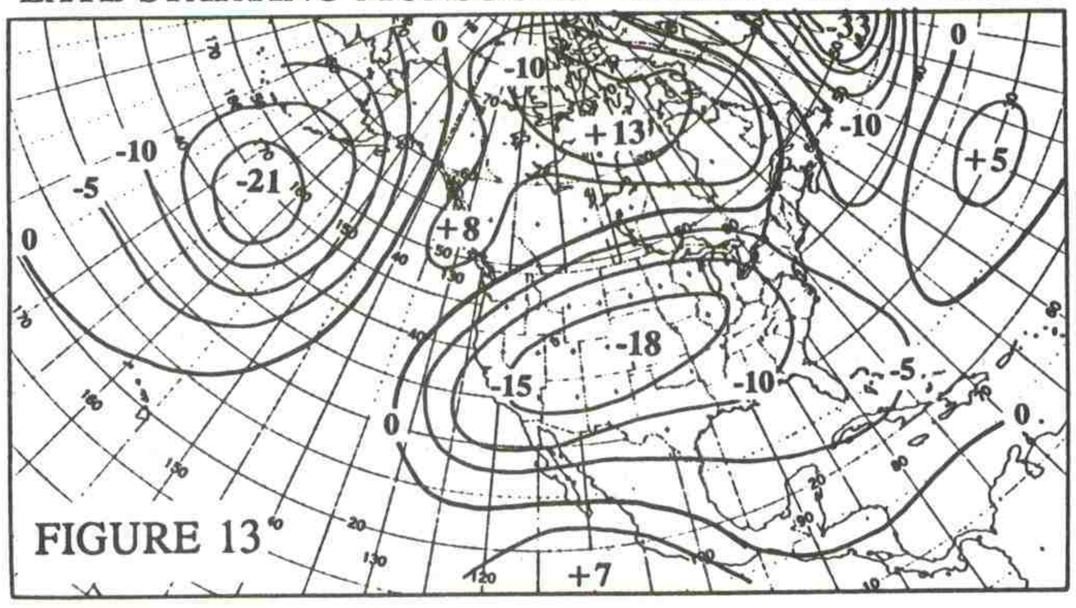

FIGURE 13

LATE START DATE YEARS: 1955, 1982, 1983, 1965, 1968, 1969, 1962

JUNE COMPOSITE 700 MB HEIGHT ANOMALIES LATE STARTING MONSOONS---STRONG RIDGING

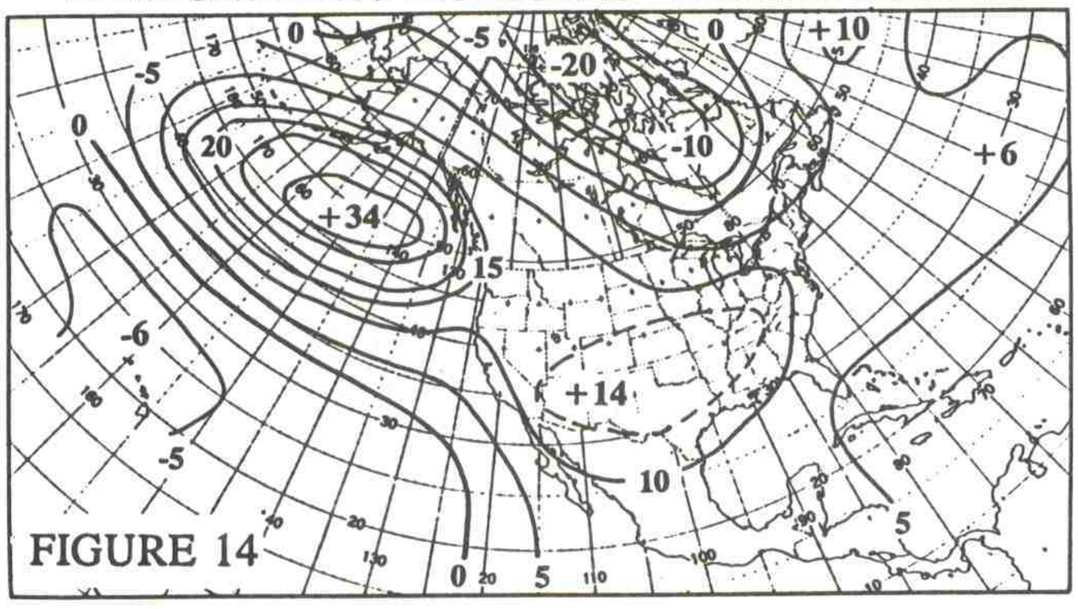

FIGURE 14

LATE START DATE YEARS: 1987, 1979, 1953, 1948, 1960, 1978

The Extratropical Response of the Atmosphere to Tropical Intraseasonal Heating in a Simple GCM: Implications for Detection and Forecasting.

Ileana Bladé and Dennis L. Hartmann

Department of Atmospheric Sciences
Box 351640, University of Washington
Seattle, Washington 98195

This study examines the dynamical nature of the nonlinear extratropical response to tropical intraseasonal heating with various temporal and spatial structures in a simple nonlinear model of the atmosphere, in an attempt to identify the conditions under which the heating is able to excite a significant response in midlatitudes and, by extension, what aspects of the Madden-Julian oscillation (MJO) are crucial to the manner it may influence the extratropics. A second goal is to investigate the role of zonal asymmetries in the time-mean flow in modulating the midlatitude response to tropical intraseasonal heating.

The model used is a global, two-level, nonlinear, spectral model, rhomboidally truncated at total wavenumber 21, and thermally driven by Newtonian relaxation of the temperature to a zonally symmetric radiative equilibrium profile, representative of mean NH winter conditions. All experiments were run for 1200 days. A linear version of the model was also used to conduct preliminary tests on the sensitivity of the response and to assess the degree to which the full response can be explained through linear dynamics.

We find that the extratropical response is extremely sensitive to the phase speed of the forcing. Eastward moving heating such as that associated with the MJO induces a weaker response than a stationary source. The response diminishes rapidly in amplitude as well as in spatial scale as the eastward phase speed increases. The reduced response arises from the fact that a substantial portion of the equatorial divergence and associated Rossby wave source are effectively embedded in strong easterly flow, which traps the excited waves in the tropics.

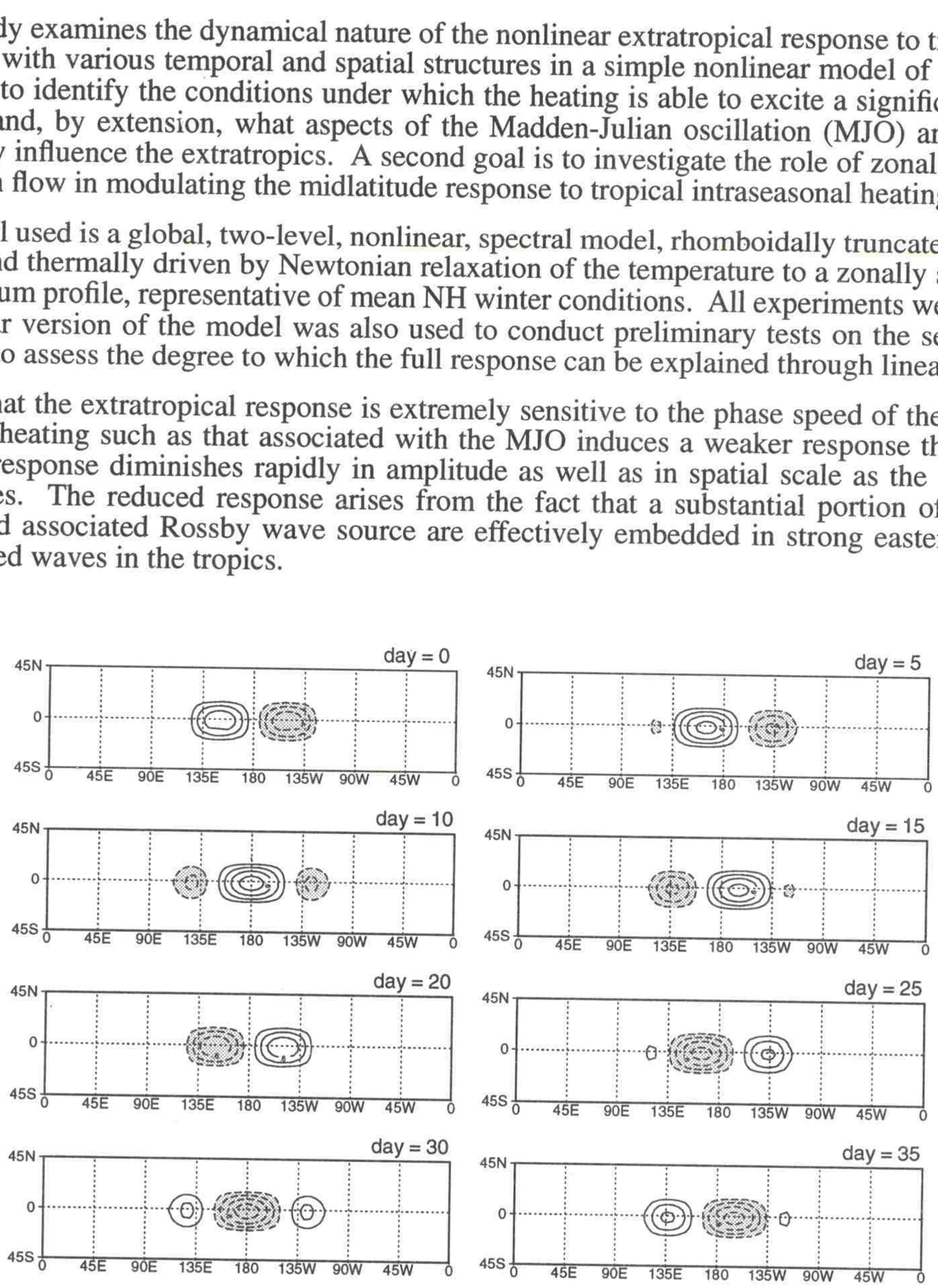

FIG. 1. The localized, k=3, T=40 days, eastward propagating dipolar heating field used in the experiments described in this paper. The contour interval is 2×10^{-5} K/s.

Proper simulation of the observed phase speed of the MJO heating is therefore essential for purposes of investigating the tropical/extratropical interactions. A monopole source traveling eastward uniformly with an *around-the-world* period near 40 days — characteristic of the MJO-like disturbances simulated by most GCMs, which systematically overestimate the phase speed of the heating by a factor of 2 or more — is thus not a good approximation to the forcing associated with large-scale MJO convection. It will result in weak and bland extratropical patterns even for strong heating amplitudes.

The slowly moving, large-scale, periodic, eastward propagating heat source used in our study (c~4 ms^{-1}, k=2-3, T=40 days, see Fig. 1) is, in addition, dipolar in nature, meridionally extensive, and longitudinally confined. It was designed to mimic the temporal and spatial structure of MJO convection, as depicted by the first two EOFs of observed intraseasonal OLR. The extratropical response in this case (Fig. 2) is strong and well-defined and stands significantly above the background variability. The heating and cooling parts of the source each excite time-dependent wavetrains which interfere with each other, so that the evolution of the combined response depends on the relative phases of the individual responses.

The *nonlinear* response to this oscillatory dipolar heating is very asymmetric: the wavetrain is strong when heating is located to the west of cooling (days 0-10), but propagation into the extratropics is suppressed during the reverse phase (days 20-25). The wavetrain forced by the new cooling region to the west of 180° does not begin to form until day 30, even though the cooling has been strong since day 20; in fact even the development of the local (near equatorial) response seems delayed. Yet, except for this interval of time in which propagation to the extratropics is inhibited, the evolution of the response is similar, qualitatively speaking, to that predicted by the linear model.

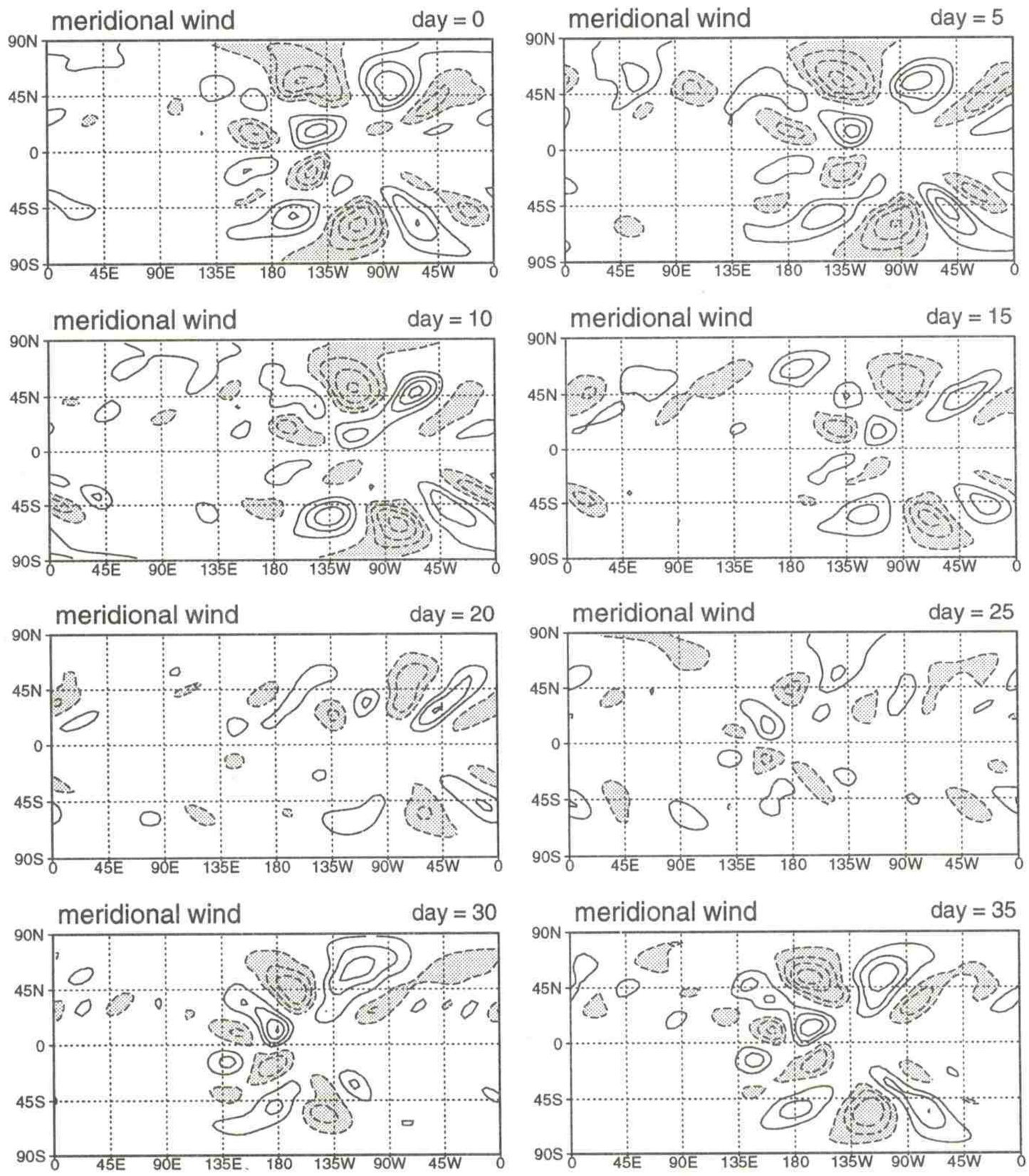

FIG. 2. The 30-sample composite of the nonlinear response in meridional wind to the eastward propagating heating dipole in Fig. 1 (shown is a complete composited 40-day cycle). The contour interval is 3 ms^{-1}.

The explanation for the temporal asymmetry in the response and the breakup of the linear solution lies in the distribution of perturbation zonal wind, presented in Fig. 3. When the mass distribution is driven by cooling located to the west of heating (day 20) the resulting zonal flow at the equator has to be easterly (i.e. directed from mass source to mass sink), which inhibits wave propagation into the extratropics. It is not until the average flow in the region of the forcing becomes more westerly (day 30) that the development of the new wavetrain can begin. During the reverse phase (days 0 and 5), strong westerly winds prevail around the forcing region, which induces an amplified local Rossby wave response and favors propagation into midlatitudes. Although the tropical zonal winds tend to be too strong, experiments with steady dipolar forcing indicate that the temporal asymmetries persist even when the perturbation winds are of reasonable magnitude. Thus, this nonlinear effect is apt to be at least somewhat important in the real world.

The nonlinear response to the heating is not substantially modified in the presence of an orographically induced wavy background flow, regardless of the longitudinal position of the diabatic source relative to the climatological jetstream (Fig. 4). In all cases examined but one (expt. DIP-M2), the wavetrains are generally less persistent and coherent than in the presence of a zonally symmetric time-mean flow, although they can be stronger on particular days. In the zonally asymmetric case, too, the nonlinear response is similar to the linear response on those days when it is strong. Our results therefore indicate that time-mean longitudinal asymmetries in midlatitudes are not necessary to excite a pronounced response. The lack of interaction between the tropical heating and the extratropical stationary waves, however, is likely to be the most model sensitive of our results. On the other hand, the presence of a realistic midlatitude flow, with its evolving planetary wave pattern, may add enough complexity and sensitivity to the way the extratropical circulation responds to individual MJO events to invalidate the idea of an "average", or a potentially predictable response.

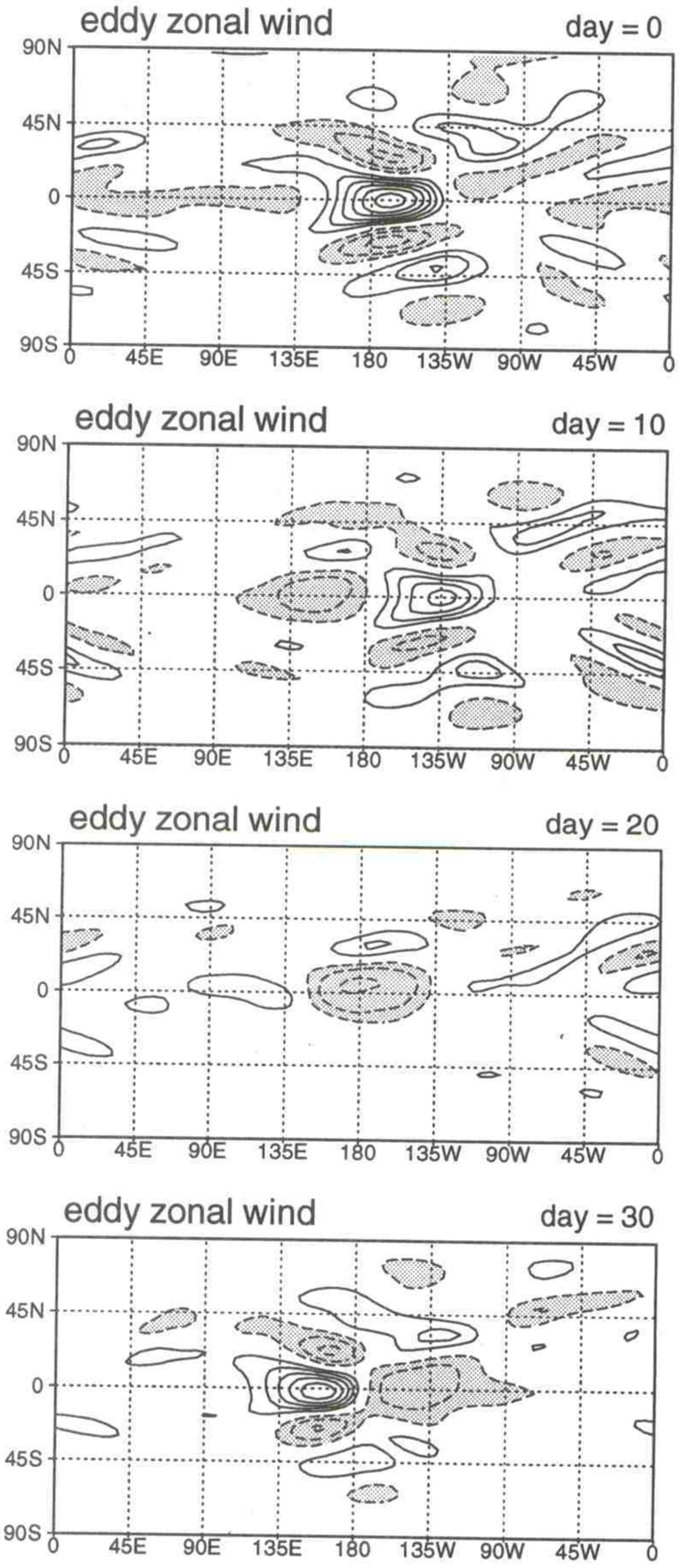

FIG. 3. The 30-sample composite of the nonlinear eddy zonal wind response to the eastward propagating heating dipole in Fig 1. The contour interval is 5 ms^{-1}.

The potential nonlinear temporal asymmetries in the response to dipolar heating should be kept in mind when attempting to detect the remote response to the MJO from observations. Compositing for selected phases of the heating might be the best solution if enough strong events are available. Indeed the response might only be manifest during a discrete part of the cycle, as evidenced by the composites from the zonally asymmetric experiments. It also appears from this study that in order to correctly simulate the extratropical response to the MJO it is crucial to reproduce exactly the temporal variability, magnitude and geographical distribution of the heating associated with the MJO. It is important to note that the midlatitude manifestation of the real oscillation might still be too weak or too flow-sensitive to be of any use for prediction purposes. Our point here is that GCMs that produce MJO-like disturbances with much faster phase speeds than observed (like most current GCMs) cannot be expected to excite much of a response in the extratropics. Moreover, if weather prediction models are to exploit potential extratropical extended-range forecast skill associated with the MJO, they must simulate the phase speed and structure of the MJO very accurately.

Note: Full details of this study can be found in Bladé and Hartmann, 1995: "The linear and nonlinear extratropical response of the atmosphere to tropical intraseasonal heating". *J. Atmos. Sci.* **52**, 4448-4471.

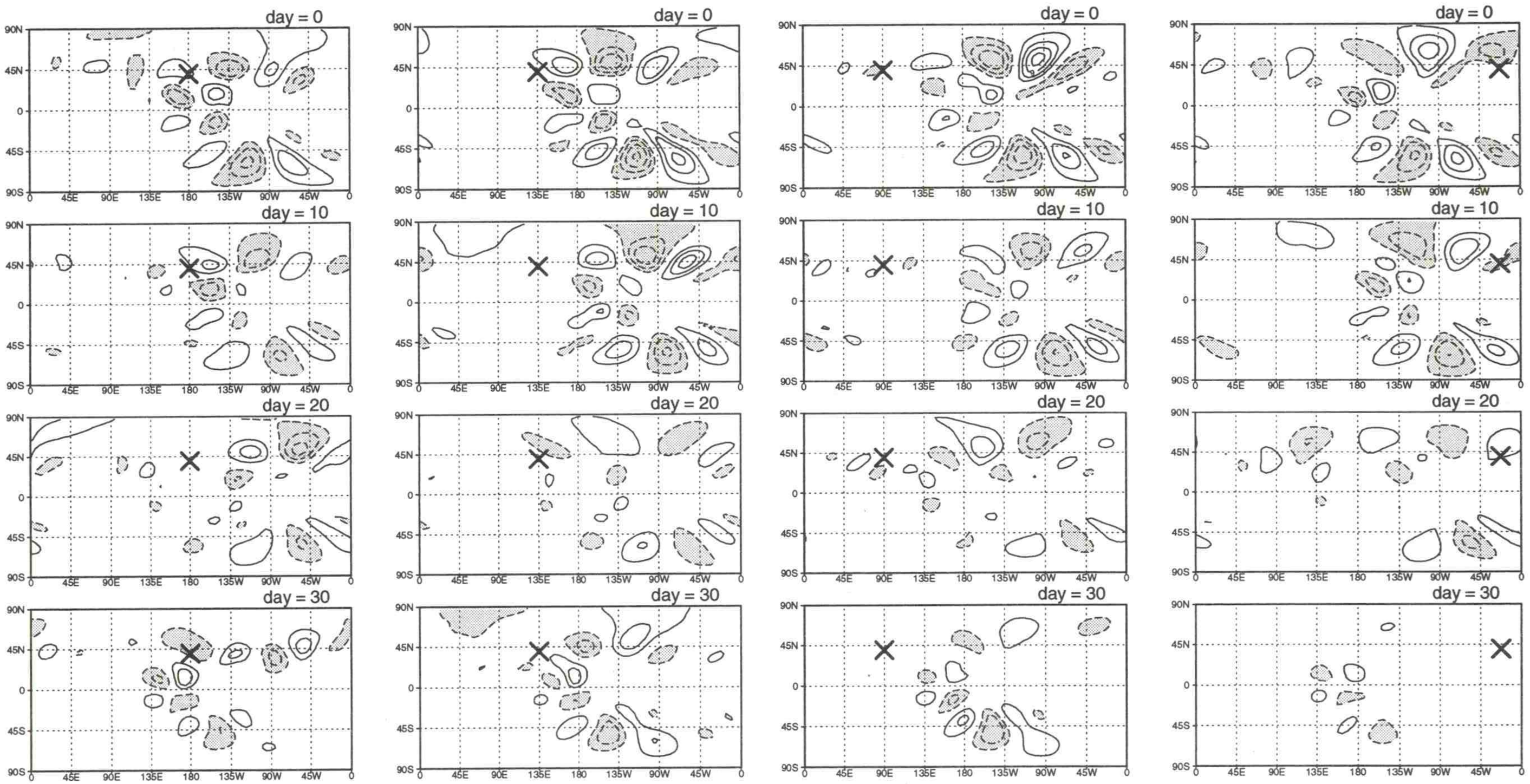

FIG. 4. The 30-sample composite of the nonlinear meridional wind response to the localized eastward propagating heating dipole in Fig. 1, for four experiments with topography (a gaussian mountain at 40°N, indicated by a thick cross). Data have been low-pass filtered (T>10 days) and the time-mean has been removed. Contour interval is 3 ms^{-1}. The time-mean flow in each case is characterized by a zonally localized jet stream about 75° downstream of the orography, which is associated with a topographically forced stationary wave.

Zonal Mean Flow/Eddy Relationship In A Perpetual January GCM Experiment

Peitao Peng
AOS Program, Princeton University
and
Ngar-Cheung Lau
GFDL/NOAA, Princeton University

1. Introduction

It has been suggested that fluctuation of zonal mean flow (i.e., zonal mean zonal wind) is an important contributing factor to stationary eddy variability. The zonal mean flow/eddy relationship was first discussed by Rossby (1939). His well-known dispersion relationship for one-dimensional eddies in a barotropic atmosphere suggests a link between the zonal wave length and the speed of the zonal mean flow. Recent studies with wintertime monthly mean data from observations and GCM experiments have shown that zonal mean flow and eddy do have significant correlations in some regions, although only a small fraction of total eddy variance can be explained by this relationship (Branstator 1984, Kang and Lau 1986). Experiments with linear barotropic models have some success in simulating the anomalous stationary waves associated with the change of the observed zonal mean flow, thus indicating that this relationship can be explained by two-dimensional Rossby wave dynamics (Branstator 1984). Kang (1990) demonstrated that the change in turning latitude due to zonal flow fluctuations plays an important role in altering the stationary wave pattern. In this study, we would like to focus on the following issues:

1) Would data with higher temporal resolution than monthly means provide more information on the zonal mean flow/eddy relationship?

2) If we are given a prediction of the zonal flow change, how well can we predict the associated eddy change?

1. Data

The data used in this study are Northern Hemisphere 200hPa wind from a 100,000-day perpetual January integration of GFDL GCM with rhomboidal truncation at 15 wavenumber and with 9 vertical levels. The model is forced with climatological SST. In this preliminary study, only data from the first 20,000 days of this integration has been used. The once-daily model output has been subjected to a low-pass filter retaining fluctuations with period longer than 10 days.

2. Results

a) Statistical relationship

We first performed an EOF analysis for the zonal mean zonal wind. The three leading EOFs explain 34%, 21% and 15% of the total variance, respectively (Figure 1). The first EOF mode represents the out-of-phase fluctuations of the zonal wind speed at 35°N and 55°N. The second EOF depicts opposite perturbations at 45°N and 65°N. The third EOF is associated with wind variations near the equator. We then correlated the temporal coefficients of individual EOFs with the eddy stream function at each grid point. The charts thus obtained are shown in Fig. 2. Assuming that the time series contains 2000 degrees of freedom, correlation coefficients with absolute value larger than 0.05 would excess the 95% significant level. The most significant features associated with the first two EOFs are in the middle latitudes; whereas the third EOF is related to stream function changes in western and central Pacific. We have also examined the corresponding lagged correlations between the EOF coefficients and eddy streamfunction, but did not find any correlations stronger than those shown in Fig. 2. The zonal/eddy adjustment is hence seen to be almost simultaneous. It is also possible that the time scale of this adjustment is too short to be resolved by the low-pass filtered data.

b) Linear model simulation

Starting from the steady nondivergent barotropic vorticity equation, we can derive a linear model to diag-

nose the relationship between the zonal mean wind anomaly ($\Delta\bar{u}$) and the associated eddy streamfunction anomaly (ψ'). In the Mercator projection of the sphere, the model equation is as follows:

$$\bar{u}\frac{\partial}{\partial x}\nabla^2\psi' + \frac{\partial}{\partial x}\psi'\frac{d}{dy}\left(f - \frac{d}{dy}\bar{u}\right) = -\Delta\bar{u}\frac{\partial}{\partial x}\nabla^2\psi + \frac{\partial\psi}{\partial x}\frac{d^2}{dy^2}\Delta\bar{u}$$

where $\bar{u}$ denotes the climatological zonal mean flow, ψ the climatological eddy stream function. The first forcing term in the right hand side can be interpreted as the advection of climatological vorticity by the anomalous zonal wind, the second term is the advection of anomalous vorticity by the climatological meridinal wind. For a given $\Delta\bar{u}$, one can obtain the corresponding eddy streamfunction anomaly by solving this equation. Figure 3a presents the composite of the GCM-generated eddy stream function anomaly based on the time coefficients of the first zonal flow EOF. The pattern is very similar to that displayed in the correlation map in Fig. 2a except that Fig. 3a provides additional information on the actual wave amplitude. The magnitude of the corresponding zonal mean wind anomaly is about 6 ms^{-1}. Fig. 3b shows the eddy response to total forcing as computed using the linear barotropic model discussed above. Despite the simplicity of this model, most of the features in the full GCM pattern (Fig. 3a) are captured in Fig. 3b. Further experiments, however, have shown that for some other zonal/eddy correlation patterns, the linear model simulations are not as successful as this one. It is thus suggested that in those cases, some other processes not included in this linear model, like transient eddy feedback and diabatic heating, may be important.

c) Eddy prediction

For a predicted zonal flow change, its profile would be usually a linear combination of all the zonal flow EOFs. According to the above discussion, the prediction of the corresponding quasi-stationary eddy need to take into account of the possible influences from transients and diabatic heating. This can be accomplished by using an empirical method. Projecting the historical zonal flow anomalies onto the predicted zonal flow change, one would obtain a time series. The composite of historical eddies based on this time series would be the empirically predicted eddy associated with that zonal flow. Our experiments have shown that for zonal flow anomalies confined in mid-latitude, the corresponding eddy anomalies predicted by the empirical method are very close to those predicted by the linear model in pattern; while for the zonal flow anomalies in lower or higher latitudes, the results from the two approaches are quite different. Fig. 4 gives an example of the eddy prediction for a mid-latitude zonal flow change. The zonal flow change represents the southward shifting of the subtropical jet (Fig. 4a).

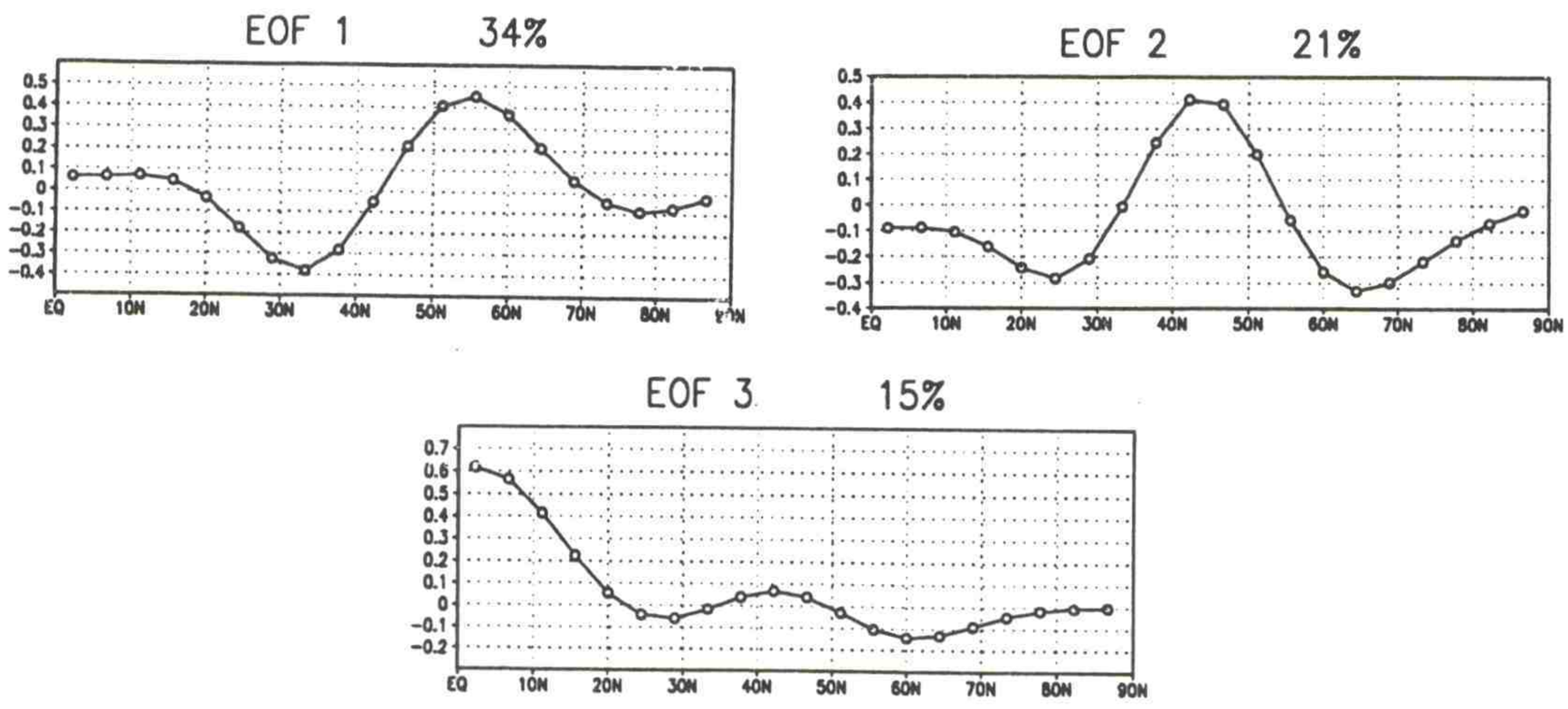

Fig. 1 The three leading EOFs of the low-passed zonal mean zonal flow.

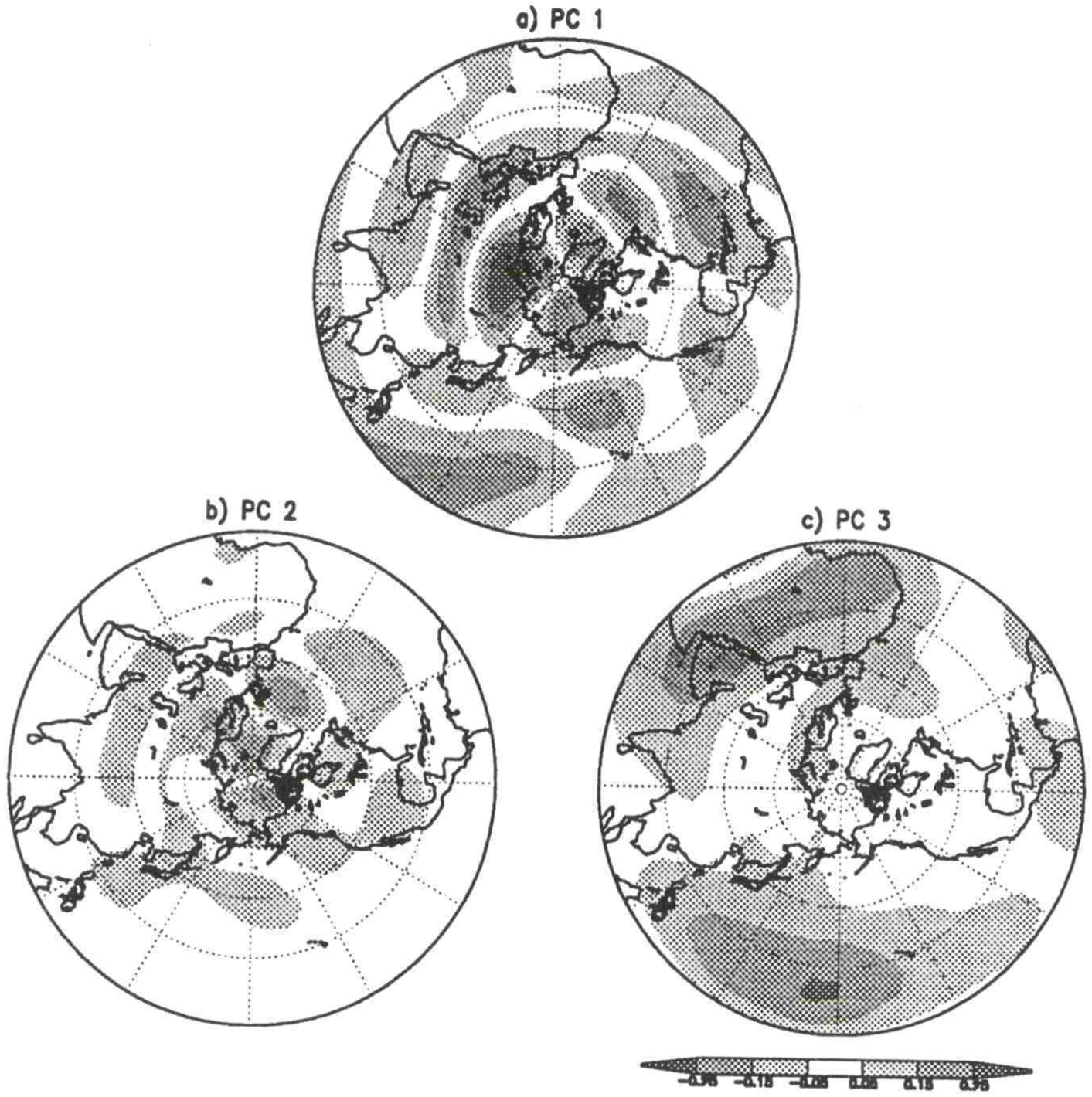

Fig. 2. The correlations between temporal coefficient of zonal-flow EOFs (shown in Fig. 1) and the NH eddy streamfunction for a)EOF1, b) EOF2 and c) EOF3.

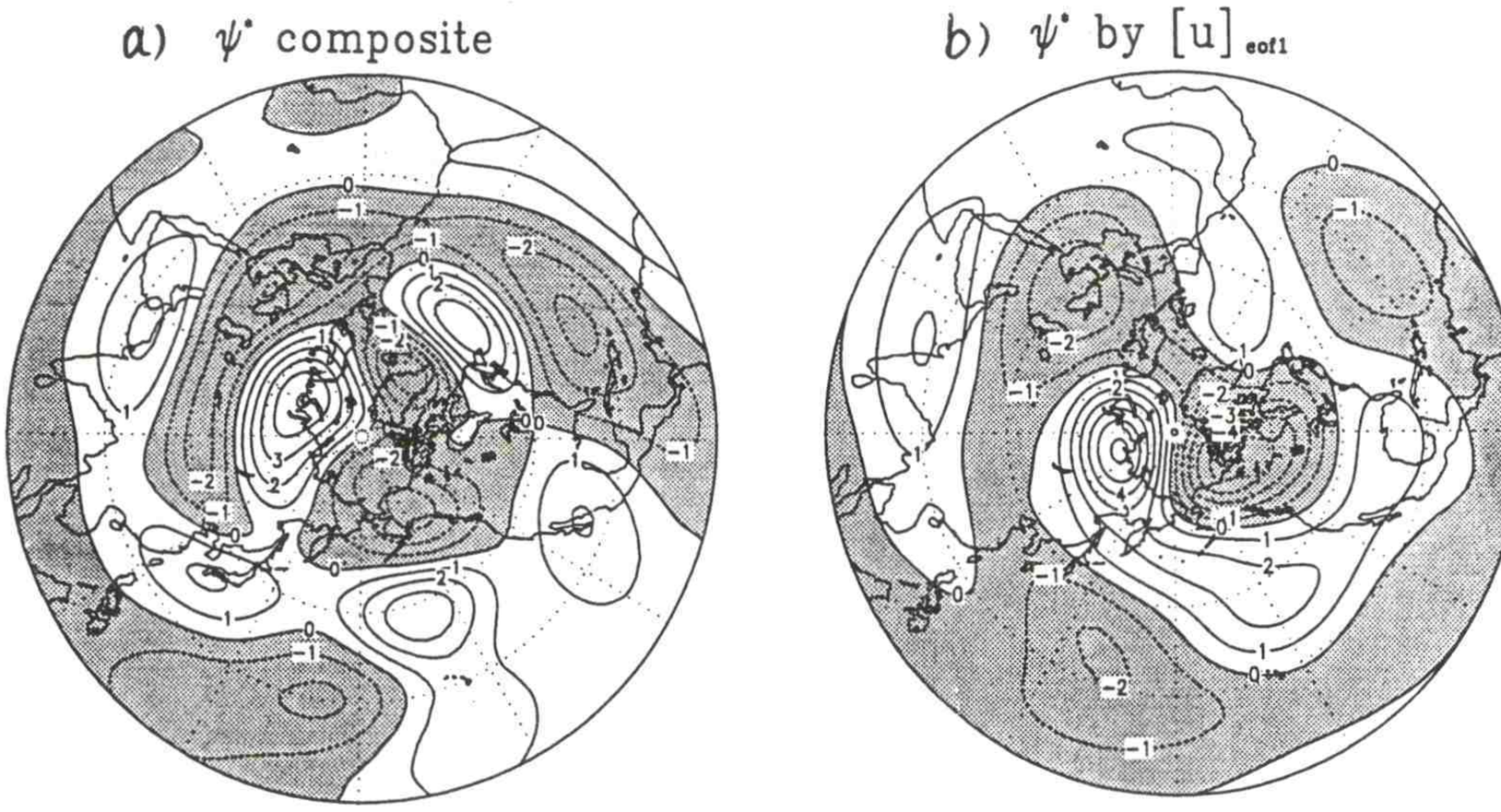

Fig. 3. a) The eddy streamfunction composite based on the temporal coefficient of zonal flow EOF1. b) The linear model simulation. Contour interval is $10^6\ m^2s^{-1}$. Negative values are shaded..

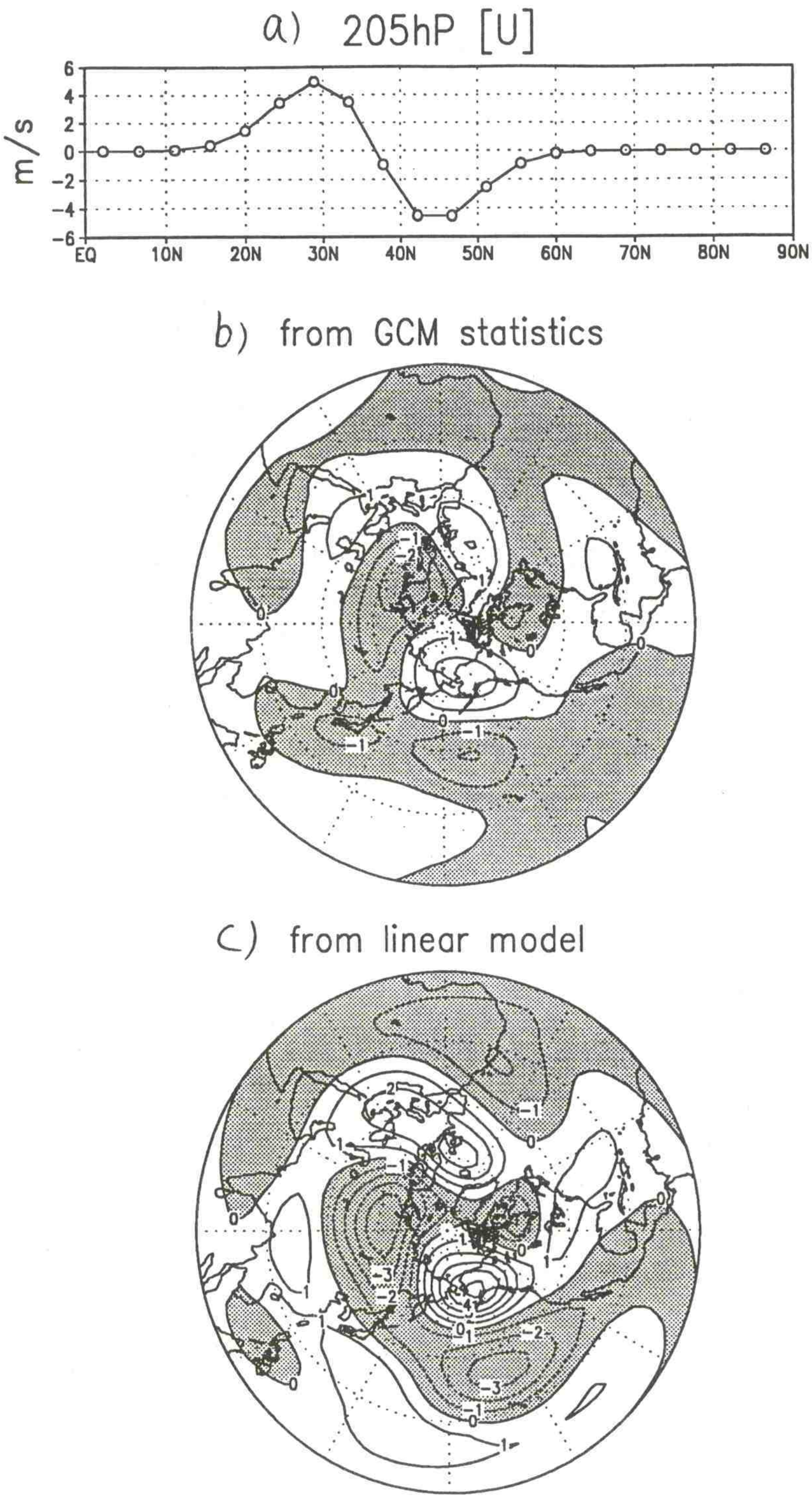

Fig. 4. a) A given zonal wind anomaly representing the southward shift of the subtropical jet. b) empirically predicted eddy anomaly. c) the linear model predicted eddy anomaly. Contour interval is 10^6 m^2s^{-1}. Negative values are shaded.

On the Forcing of the March-to-May Circulation-change over the Eastern Equatorial Pacific

Sumant Nigam
Department of Meteorology/CICS, University of Maryland, College Park, MD 20742-2425
(Email: nigam@cola.umd.edu)

1. INTRODUCTION

The ocean-atmosphere seasonal cycle in the eastern equatorial Pacific is remarkable because its predominantly annual period is twice that of the solar forcing. Its warm and cold SST phases moreover occur when the semiannual solar forcing is at a maximum, i.e., at the time of the vernal and autumnal equinoxes, respectively. Although the phasing of the SST annual-cycle in the central/eastern equatorial Pacific suggests that it is linked to the equatorward (and cross-equatorial) penetration of the Southern Hemisphere's extratropical SST-annual cycle, diagnostic analysis of Mitchell and Wallace (1992) and stability analysis of Chang and Philander (1994) indicate that positive feedback between meridional (and zonal) winds and SST-gradients near the equator/coastline are central to the rapid meridional (and zonal) expansion of the SST cold-tongue during the northern summer season.

While processes governing the expansion and growth of SST annual-cycle amplitudes involve local coupled air-sea interaction, those governing the transition of the coupled system from extreme SST annual-cycle phases are reckoned to involve interaction with the adjoining land-masses as well. Mitchell and Wallace, in fact, argue for the importance of meridional windstress variability, driven by the evolving Central American monsoons, in initiating the SST-cooling tendency in early April, and the warming tendency in October.

2. METHODOLOGY

In an effort to further understand the role of developing continental monsoons in initiating SST-cooling in April, we have diagnostically modeled the change in the climatological 3-D circulation from March to May. This modeling was undertaken with a steady global primitive-equation model that is linearized about a zonally-symmetric climatological March or May basic state, and that has 18 sigma levels of which 6 are below the 700 mb level. This diagnostic model is forced by the 3-D distribution of residually-diagnosed diabatic heating, and momentum and thermal transients, all of which are obtained from the twice-daily high-resolution ECMWF analyses covering the decade 1985–1994. [For an assessment of the quality of the residually-diagnosed 3-D diabatic heating fields, and for diagnostic modeling details, see Nigam (1994)].

When forced by global forcing functions, the modeled March-to-May circulation change bears a striking resemblance to the corresponding ECMWF-analyzed circulation change in both the near-surface and upper-tropospheric winds. This allowed us to diagnostically assess the importance of various components of forcing.

3. RESULTS

The undertaken modeling experiments indicate that the southerly surface-wind tendency, and the surface-divergence tendency during April in the near-coastal equatorial Pacific (110°W–80°W) is forced largely by the diabatic heating of the planetary boundary layer ($p \geq 775$ mb). The interaction of orography with the specified zonally-symmetric circulation, on the other hand, generates, opposing northerly surface-wind tendency in April.

Modeling experiments designed to assess the relative impact of continental .vs. oceanic heating will also be discussed.

REFERENCES

Chang, P., and S. G. H. Philander, 1994: A coupled ocean-atmosphere instability of relevance to the seasonal cycle. *J. Atmos. Sci.*, **51**, 3627-3648.

Mitchell, T.P., and J.M. Wallace, 1992: The annual cycle in equatorial convection and sea surface temperature. *J. Climate*, **5**, 1140-1156.

Nigam, S., 1994: On the dynamical basis for the 'Asian summer-monsoon rainfall—El Niño' relationship. *J. Climate*, 7, 1750–1771.

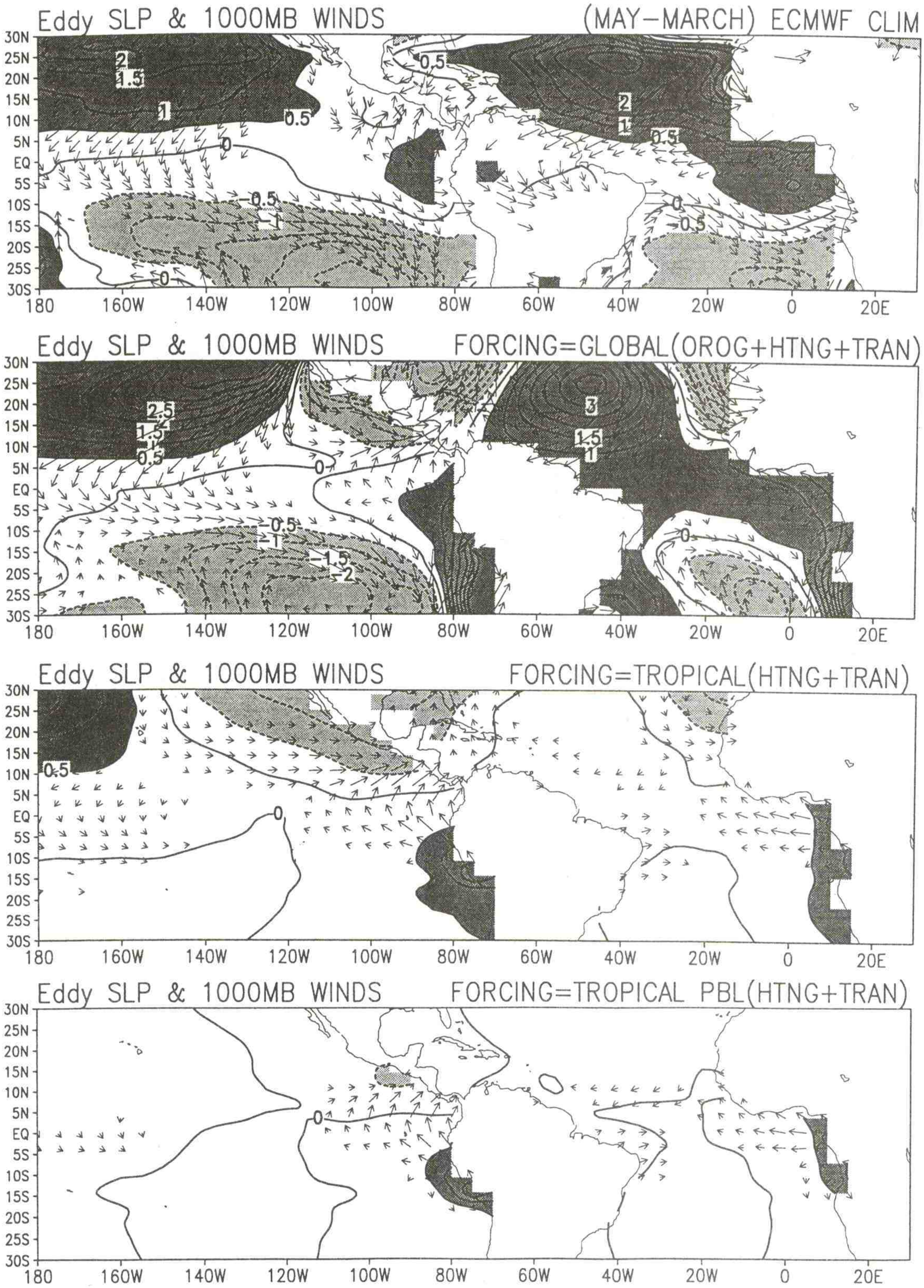

Figure 1. The March-to-May change in eddy sea-level pressure and 1000 mb winds. The top panel shows these fields from a ten-year long (1985–94) ECMWF climatology. The next panel shows the simulation from a steady primitive-equation model (having 18 σ-levels, 21 zonal waves, and $\Delta\theta$=1.8°) forced by global orography, residually-diagnosed diabatic heating, and momentum and thermal transient-eddy fluxes (all from ECMWF analyses). The third panel shows this diagnostic model's response to only tropical (15°S–15°N) diabatic heating and transient eddies, whereas the bottom panel shows the model's response to only the PBL part ($p \geq 775$ mb) of this tropical forcing. Sea-level pressure is contoured with a 0.5 mb interval in all panels.

Surface Flux Variability Over the North Pacific in a GCM

Michael A. Alexander
James D. Scott
CIRES, University of Colorado

1. Introduction

Cayan (1992a,b,&c) performed a detailed analysis of the observed surface flux variability over the Northern Hemisphere oceans. He used monthly averaged data to investigate the spatial variability of the fluxes, and their relationship to the atmospheric circulation and sea surface temperature (SST) anomalies. In this study, we examine the surface fluxes and their relation to the atmospheric circulation over the North Pacific Ocean in the Geophysical Fluid Dynamics Laboratory (GFDL) General Circulation Model (GCM). We expand on Cayan's work by: i) examining variability at periods less than a month; ii) isolating the variability in the fluxes solely due to atmospheric fluctuations; and iii) comparing the model results with observations.

2. GFDL Model Simulation

The atmospheric GCM used in this study is a global spectral model with rhomboidal truncation at wave number 30, which is approximately 2.25° latitude by 3.75° longitude. The model has 14 sigma levels in the vertical, with the lowest level at ~30 m above the surface. The model was integrated for 17 years in which the mean seasonal cycle of SST was repeated each year. The net radiative flux at the surface depends on interactions with predicted clouds. The surface sensible heat flux is given by:

$$Q_{sh} = c_H c_p \rho U (SST - T_{air}) \qquad (1)$$

where c_H is the heat flux coefficient assigned a constant value of 1×10^{-3}, c_p and ρ are the specific heat and density of air, U is the wind speed, and T_{air} is the air temperature. The latent heat flux (Q_{lh}) is computed from a similar bulk formula.

3. Results

Our analyses primarily focus on the sensible and latent heat fluxes which are the dominate fluxes over the North Pacific during winter (DJF), the period when atmosphere-ocean interaction is strongest. The mean $Q_{sh}+Q_{lh}$ from the GFDL GCM and from the National Meteorological Center (NMC) reanalysis are shown in Fig. 1. The NMC Reanalysis provides an estimate of the observed flux fields for the years 1985-91.

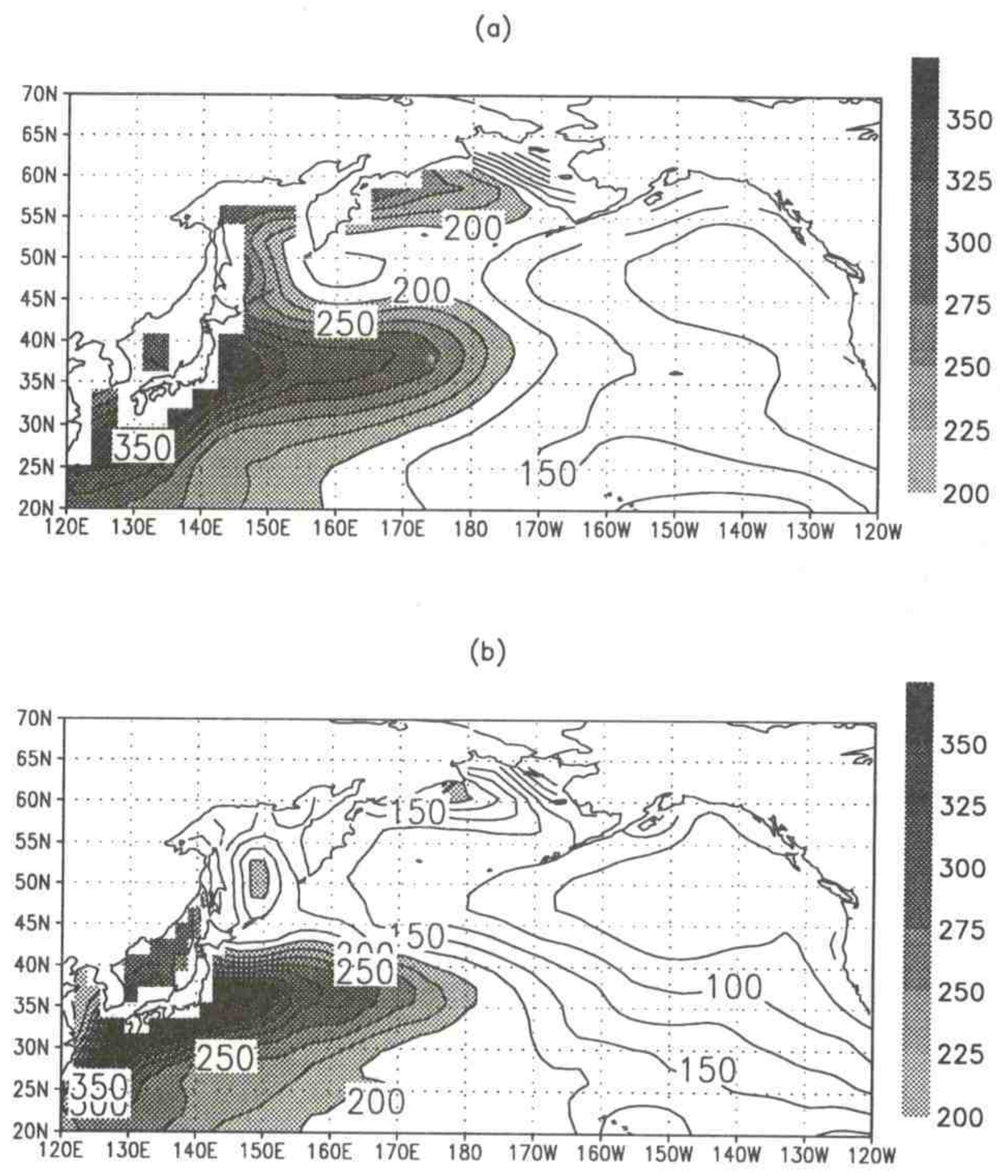

FIG. 1. Mean $Q_{sh}+Q_{lh}$ (W m^{-2}) in the (a) GFDL GCM and (b) NMC Reanalysis. Ocean-to-atmosphere fluxes are positive.

Overall, the GFDL GCM and the NMC Reanalysis are similar with ocean-to-atmo-

sphere fluxes exceeding 350 W m^{-2} in the vicinity of Japan. These strong fluxes occur as cold dry air flows out over the ocean. As the air moves eastward its characteristics are modified by the ocean below, Q_{sh} and Q_{lh} decrease, and their sum drops below 150 Wm^{-2} in the northeast corner of the basin. The primary difference between $Q_{sh}+Q_{lh}$ in the GCM and the NMC Reanalysis is that the former indicates more ocean heat loss north of ~45°N.

The intraseasonal and interannual standard deviation of $Q_{sh}+Q_{lh}$ are shown in Fig. 2. The intraseasonal deviations are based on daily departures from individual seaonal means. The standard deviations on both intraseasonal and interannual time scales are maximized in the western North Pacific. Variability on the sub-seasonal time scale exceeds the interannual variability over the entire domain.

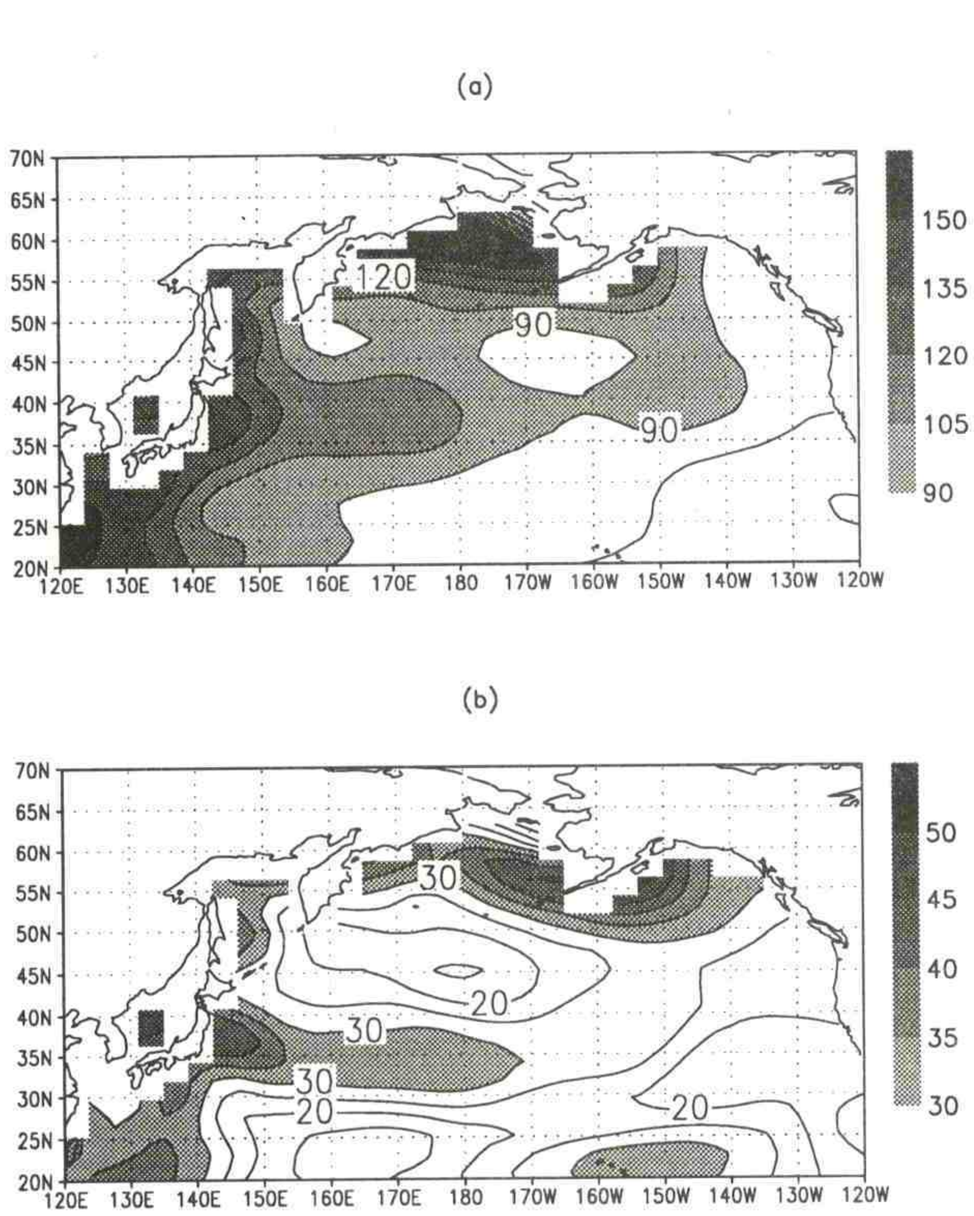

FIG. 2. The (a) intraseasonal and (b) interannual standard deviation of $Q_{sh}+Q_{lh}$ ($W\ m^{-2}$).

The surface flux variability depends directly on the relationship between the wind speed and air temperature, as indicated by Eq. 1, and indirectly on the near surface atmospheric circulation. Correlations between daily anomalies (indicated by a prime) of air temperature and both wind speed and direction are shown in Fig. 3.

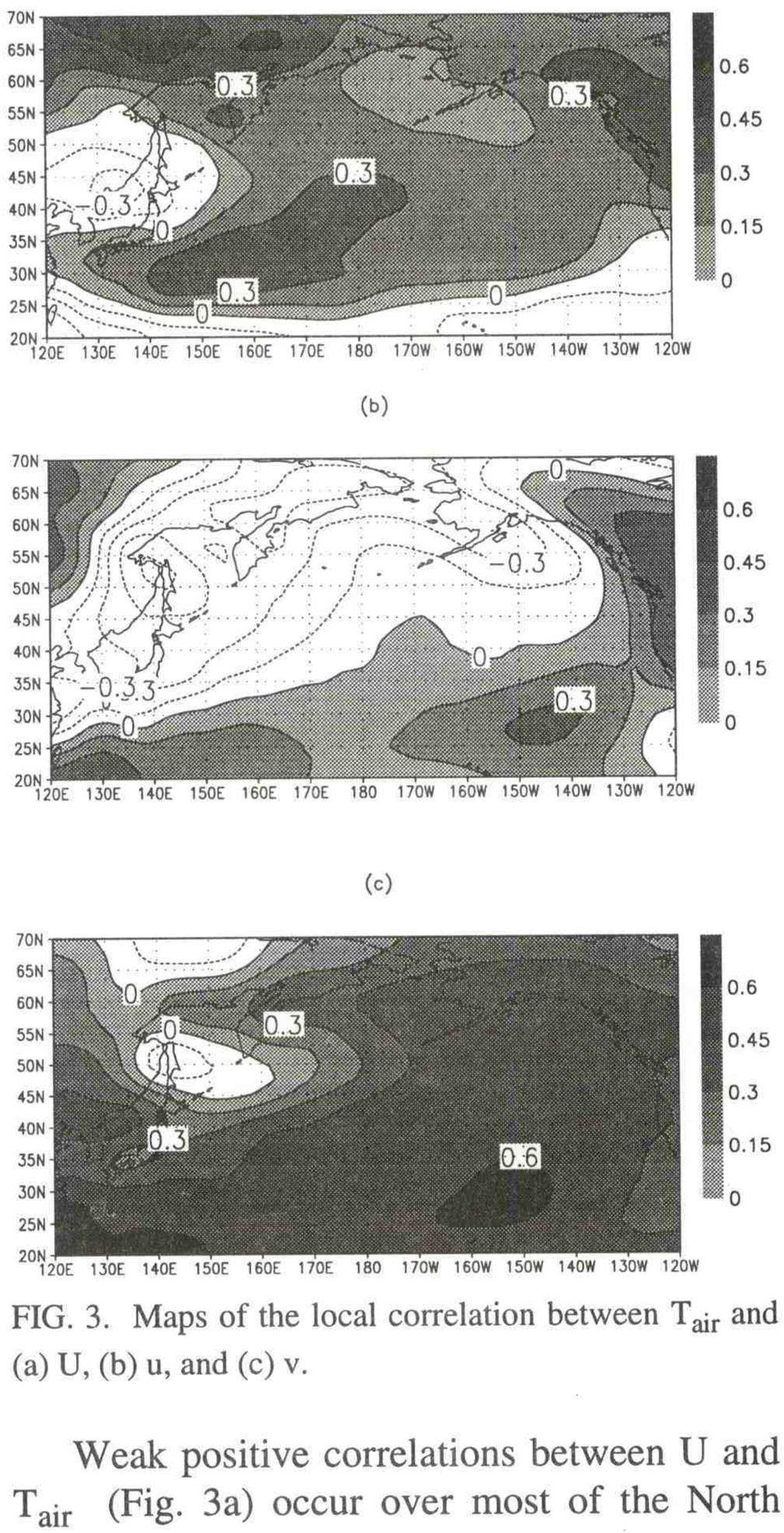

FIG. 3. Maps of the local correlation between T_{air} and (a) U, (b) u, and (c) v.

Weak positive correlations between U and T_{air} (Fig. 3a) occur over most of the North Pacific. The two fields are linked via the surface heat flux: stronger than normal winds enhance Q_{sh} which in turn leads to an increase

in T_{air}; likewise Q_{sh}' and $T_{air}' < 0$ when $U' < 0$. Correlations between the zonal wind (u) and T_{air} (Fig. 3b) are positive (negative) south (north) of ~35°N, the latitude separating the Trade Winds from the mean westerlies. North of 35°N enhanced westerlies ($u' > 0$) are associated with more cold air advection over the ocean ($T_{air}' < 0$) resulting in negative correlations between u and T_{air}. The impact of advection on T_{air} diminishes with distance from the Asian continent. Poleward advection of warm air results in positive correlations between the meridional wind (v) and T_{air} (Fig. 3c) over most of the North Pacific. Similar relationships exists between the wind and atmospheric moisture.

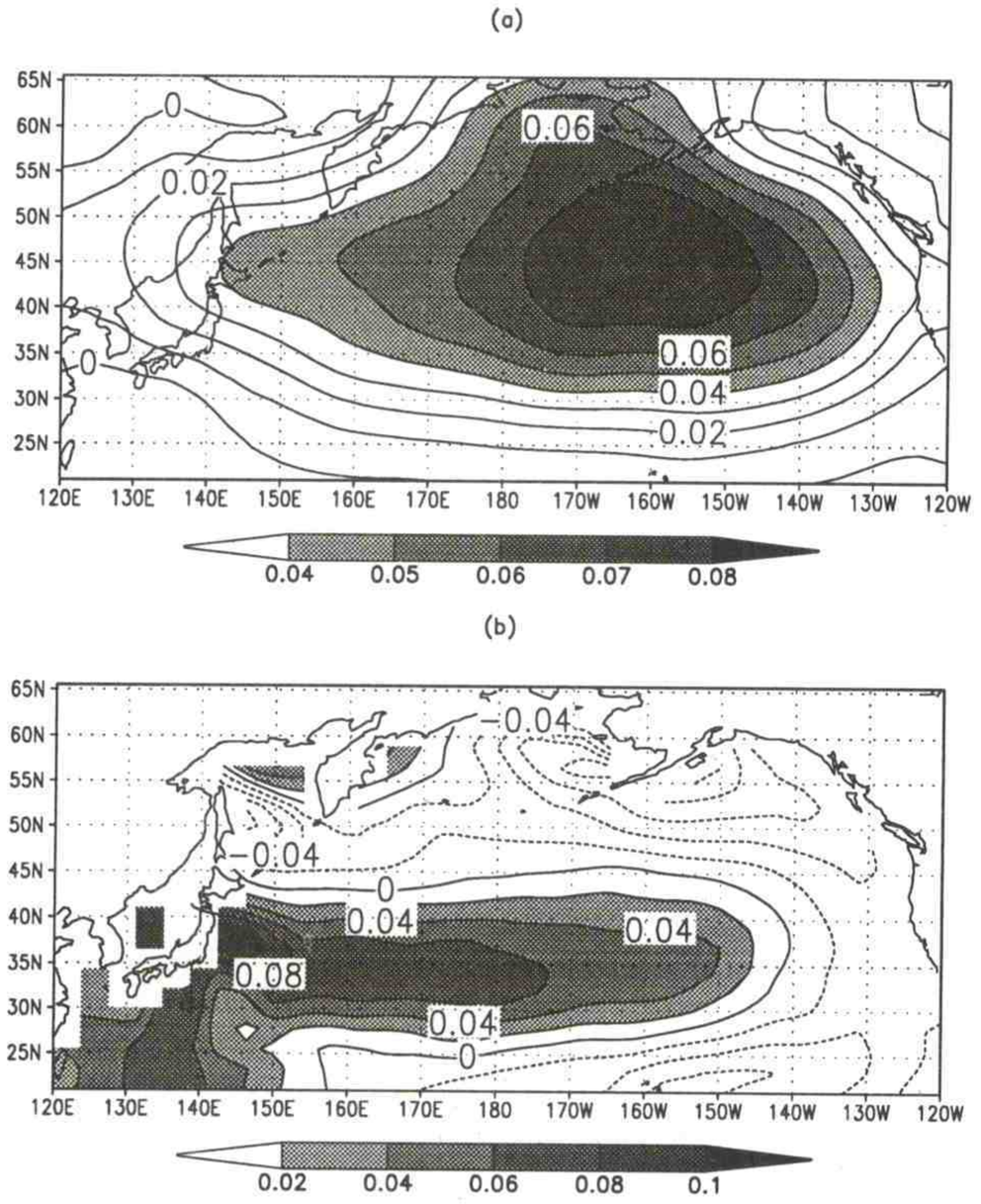

FIG. 4. The first EOF of (a) SLP and (b) $Q_{sh}+Q_{lh}$ computed from the covariance matrix.

The relationship between the atmospheric circulation and the surface energy flux is examined further using the leading Empirical Orthogonal Functions (EOFs) of Sea Level Pressure (SLP) and $Q_{sh}+Q_{lh}$ (Fig. 4). The dominant mode of SLP variability is associated with fluctuations in the strength and position of the Aleutian Low. A deeper low, the negative phase of EOF 1, is associated with enhanced westerlies south of 45°N and southerly winds in the eastern part of the basin. This circulation pattern would result in anomalous upward heat fluxes in the west central part of the basin and downward fluxes to the north and east. This is the pattern indicated by EOF 1 of $Q_{sh}+Q_{lh}$, and by the correlation between the time series (principle component) of SLP EOF 1 and the time series of $Q_{sh}+Q_{lh}$ at the individual grid points over the North Pacific (not shown). In addition, the time series (principle components) of the two EOFs are highly correlated (-0.885). All of these factors suggests that the surface energy fluxes during winter are strongly controlled by the atmospheric circulation.

To address the question of whether it is the windspeed or air-sea temperature difference which controls the sensible heat flux anomalies we have performed a decomposition of Eq. 1:

$$Q_{sh}' = \underbrace{c_H c_p \rho \bar{U} (SST - T_{air})'}_{a} + \underbrace{c_H c_p \rho U' \overline{(SST - T_{air})}}_{b} + \underbrace{c_H c_p \rho U' (SST - T_{air})' - \overline{U' (SST - T_{air})'}}_{c} \quad (2)$$

The three terms in Eq. 2 represent the impact of anomalies in (a) SST-T_{air}, (b) U, and (c) the covariance between the two, on Q_{sh}'. Fig. 5 shows the local correlations between each of

the three terms and Q_{sh}'. The correlation between Term a and Q_{sh}' exceeds 0.6 over most of the basin, Term b shows high correlations (> 0.6) with Q_{sh}' in the vicinity of Japan and south of 25°N, while Term c is of less importance. The spatial patterns of the correlations are related to the strength of the mean fields, i.e. Term a is dominant in the northeast Pacific where $\overline{U}$ is largest (not shown), likewise Term b is most important in the west where $\overline{(SST - T_{air})}$ is largest. Since SSTs repeat the same seasonal cycle, Fig. 5 suggests that Q_{sh}' is most strongly influenced by T_{air}'.

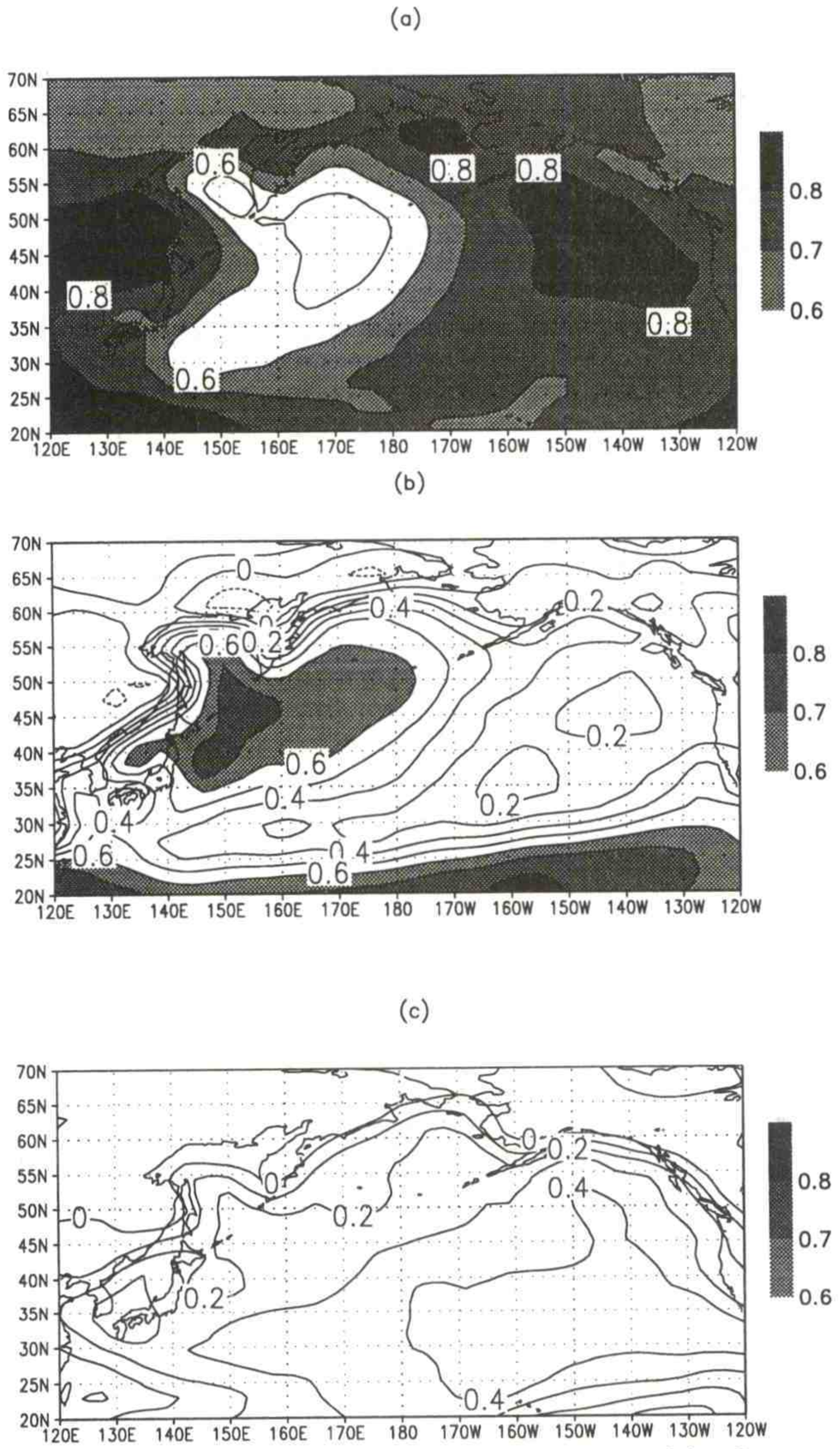

FIG. 5. Local correlations between Qsh and its 3 components: $(c_H c_p \rho)$ (a) $\overline{U}\,(SST - T_{air})'$, (b) $U'\left(\overline{SST - T_{air}}\right)$, (c) $U'\,(SST - T_{air})' - \overline{U'\,(SST - T_{air})'}$

REFERENCES

Cayan, D. R., 1992a: Variability of latent and sensible heat fluxes estimated using bulk formulae. *Atmosphere-Ocean*, **30**, 1-42.

___, 1992b: Latent and sensible heat flux anomalies over the northern oceans: the connection to monthly atmospheric circulation. *J. Climate*, **5**, 354-369.

___, 1992c: Latent and sensible heat flux anomalies over the northern oceans: driving the sea surface temperature. *J. Phys. Oceanogr.*, **22**, 859-881.

SPATIAL PATTERN OF TENDENCIES IN SURFACE AIR TEMPERATURE CHANGE OVER THE LAST DECADES

V.N. RAZUVAEV, E.G. APASOVA, O.N. BULYGINA, N.N. KORSHUNOVA, R.A. MARTUGANOV
All-Russian Research Institute of Hydrometeorological Information
- World Data Center
(RIHMI - WDC)
6, Korolyov str., Obninsk, 249020 Kaluga region, RUSSIA

An increase of mean minimum (MIN) and maximum (MAX) air temperature and decrease of the diurnal temperature range (DTR) is reported for the European part of the former USSR in the cold period (Razuvaev et al.,1995).

On the average, for the European part of the country, positive tendencies were found to be observed in a long-term trend of the two extreme temperatures, with MIN growing much more rapidly than MAX, which results in the DTR decrease.

For individual regions, however, a MAX drop is the major factor in the DTR decrease, which suggests different causes of extreme temperature variations (and correspondingly DTR) even over one of the regions of the Northern Hemisphere.

This work presents the results of analysing long-term tendencies in MIN, MAX and DTR during calendar winter (December - February) for the whole of the former USSR using long-term data for 1951-1993.

The original data set was prepared at the All-Russian Research Institute of Hydrometeorological Information - World Data Center (RIHMI-WDC) and the first version issued in 1993 as Numerical Data Package-040 "Daily Temperature and Precipitation Data for 223 USSR Stations" by the Carbon Dioxide Information Analysis Center (Razuvaev et al.,1993). An improved version of this dataset was prepared in RIHMI-WDC. Temperature observation for 1990-1993 were added and the missing data were included where possible.

The daily maximum and minimum temperatures were taken from measurements of the maximum/minimum thermometers. The diurnal temperature range is defined as the difference between MAX and MIN. Monthly means calculated as the average of daily values for each calendar month. All characteristics expressed as anomalies of the 1961-90 averages for winter (December-February) for 223 stations.

Figure 1 shows a map of linear trend coefficients ß(°C/10 yr) for DTR in conventional symbols appropriate to four ranges. The coefficients are negative for the most of the territory and their absolute value is generally no more than 0.5 °C/10 yr. The amplitude decreases most appreciably in Central Kazakhstan and Eastern Siberia where ß reaches 0.7 °C/10 yr at individual stations. The largest source of positive tendencies is in the north of the European part and in the Western Siberia. Moreover, the values of ß>0 are typical for Ukraine, Transcaucasia and Southern Siberia. Positive coefficients do not often exceed 0.5 °C/10 yr.

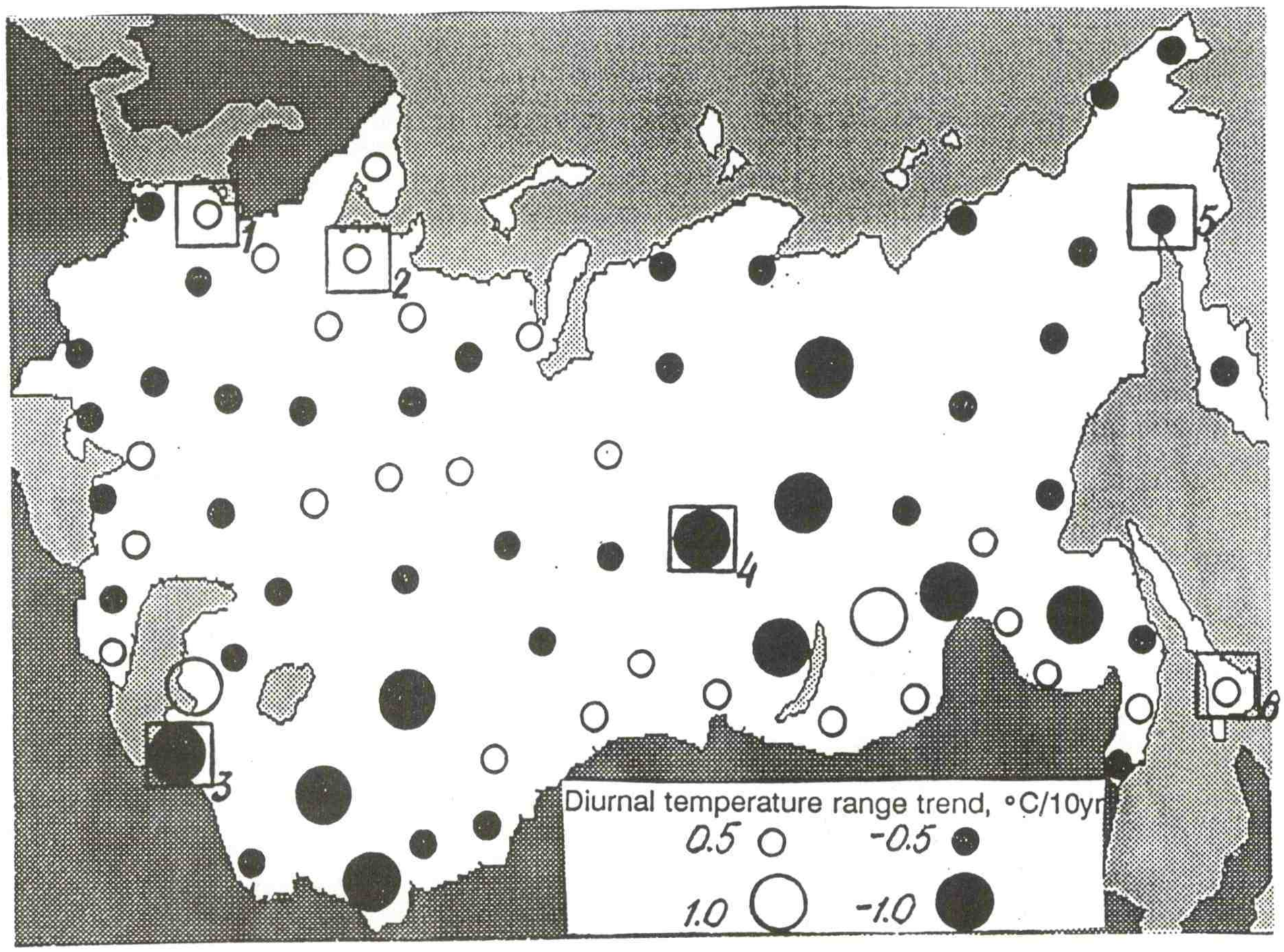

Figure 1. Linear trend coefficients of the diurnal temperature range, °C/10 year, December-February, 1951-1993.

The amplitude is an integrated index and its change is caused either by a prevailing effect of one of the extremes or by the joint unidirectional impact of the two extremes. With the known long-term tendencies in DTR components, it is possible to establish an impact factor. The factor causing a particular tendency in the long-term DTR trend is established for each station.

This may consist in a simultaneous drop in the two extremes giving rise to a smaller amplitude owing to the fact that the MAX linear trend coefficient is lower in magnitude than the similar characteristic of MIN. In this situation the amplitude can increase if MIN drops more rapidly than MAX.

With a simultaneous growth in the two extremes, the amplitude decreases if MIN grows more intensively than MAX and increases with MAX growing more intensively than MIN. The two other combinations of extreme's tendencies consist in the fact that one of the extremes grows and the other drops, then both of them contribute to the amplitude's increase or decrease.

When considering the tendencies in the DTR variation and extreme temperature variations over the whole territory, it can be seen that nearly everywhere the factor of the amplitude drop is the MIN growth which is more intensive than the MAX growth. The amplitude decrease at the expense of the MAX drop is much less frequent (the Black Sea

cost of the Caucasus, the Crimea, and Kamchatka). The joint unidirectional impact of the two extremes causes the DTR drop largely in the south, i.e. the Causasus and Central Asia. At the sites of the DTR growth, the MIN drop is as frequent as the MAX growth. It is rare for the DTR growth to be caused by their joint impact. To illustrate the established types of variability over the territory in question, we selected six points with different combinations of tendencies. They are indicated by numbered squares on the map. Numerical estimates are given in Table 1.

Table 1. Trends of diurnal temperature range on some stations over the former USSR. 1951-1993.

Number on map (see Fig.1)	Station's name and WMO index	Linear trend coefficients, °C/10yr			Notes
		MIN	MAX	DTR	
1.	TALLINN (26038)	-0.08	0.14	0.22	MAX(+), MIN(-)
2.	ARHANGE.(22550)	-0.32	-0.01	0.30	MIN(-)
3.	GASAN-K.(38750)	0.24	-0.44	-0.67	MIN(+), MAX(-)
4.	ENISEJS.(29263)	1.23	0.71	-0.52	MIN(+)
5.	KAMENSK.(25744)	-0.25	-0.42	-0.30	MAX(-)
6.	PORONAJ.(32098)	0.06	0.48	0.44	MAX(+)

DTR drops in Enisejsk (4), which is attributed to the fact that MIN growth is much more intensive than MAX. MAX drops more rapidly than MIN on Kamenskoe (5), which is likely to cause the DTR decrease. In Gasan-Kuli (3), the DTR decrease is due to the MIN increase and MAX decrease. DTR grows in Tallinn (1) due to the MIN drop and MAX growth. The same is for Arhangel'sk (2), but here the DTR growth is largely due to the MIN drop. In Poronajsk (6), the DTR growth is prevented by the MIN growth and promoted by the MAX growth.

Thus, the amplitude decreases over the most of the former USSR, which is largely due to the minimum temperature increase. However, the maximum temperature decrease or the joint variation of the two temperatures can be the factor of the amplitude increase in individual regions. In the zones of the amplitude increase, the MIN drop and the MAX growth act as impact factors.

The results obtained make it possible to suggest a substantial impact of local climate-forming factors on the extreme temperature variability. These factors should be established and taken into account when trying to attribute the MIN growth and the DTR decrease over the region to the impact of different global causes.

References

Razuvaev V.N., Apasova E.G., Martuganov R.A., Vose R.S., Steurer P.M.(1993). "Daily temperature and precipitation data for 223 USSR stations". ORNL/CDIAC-56, NDP-40. Oak Ridge, Tennessee. 127 p.

Razuvaev V.N., Apasova E.G., Bulygina O.N., Martuganov R.A.(1995). Variations in the diurnal temperature range in the European region of the former USSR during the cold season. Atm. Res. Vol.37, pp. 45-51.

Decadal Variations of the Annual Cycle

H.L. Rui[1] and X.L. Wang[2]

[1]Environmental Modeling Center
[2]Climate Prediction Center
NCEP/NWS/NOAA
Washington, DC 20233

1. Introduction

There is convincing evidence that the annual cycle interacts nonlinearly with interannual variability, i.e., El-Nino/Southern Oscillation (ENSO) cycle. While the ENSO exhibits large secular variability, secular changes of the mean annual cycle have also been reported from both coral data and sea surface observations. However, those reports used mostly indices and showed no spatial structures due to data constraint. This work is an attempt to document spatial structures for decadal changes of the mean annual cycle using global sea surface temperature (SST) field.

2. Data and Analysis

The data used is the month mean of global SST from 1950 to 1995. According to the five-year running mean of global mean SST time series (figure not shown), the period of 1950-1995 is divided into three roughly equal segments as: 1950-1962, 1963-1979, and 1980-1995. These three segments are identified as S1, S2, and S3, respectively.

The annual cycles are computed for entire 45 years (1950-1995), and for the three segments. Decadal changes will be shown as differences between the annual cycle of the three segments and the grand mean annual cycle for entire 45 years.

3. Results

Shown in Fig. 1 are the ranges (the maximum minus minimum) of the annual cycle difference as defined above. The largest changes in the annual cycle are over north Pacific, north Atlantic, central-eastern tropical Pacific, south Pacific, and south Indian Ocean. Considering relatively poor data quality in Southern Hemisphere, rest of discussion will focus on the first three regions. To see detailed structures of Fig. 1, the time-longitude sections of the difference annual cycle are shown in Fig. 2 (for tropical section) and 3 (for North Hemisphere midlatitude section).

Over the equatorial central-eastern Pacific (Fig. 2), the Spring SST warm up is much quicker and stronger and the Autumn cooling is prolonged and stronger during 50's and early 60's (period S1, top panel of Fig. 2). Therefore, the SST annual cycle is stronger in general. However, the Spring warming is delayed and

the Autumn cooling is earlier during 80's and 90's (period S3, bottom panel of Fig. 2). This suggests that the warming up phase of the eastern Pacific cold tougne has fast paced and is relatively weaker. Decadal changes in the annual cycle of SST is generally weak during late 60's and 70's (period S2, mid panel of Fig. 2).

Over the northern Pacific (Fig. 3), the annual cycle is much stronger during 50's and early 60's, i.e., winter is colder and summer is warmer. The annual cycle is weaker during 80's and 90's, indicated by warmer and prolonged winter and colder summer. During late 60's and 70's, decadal changes are weaker.

However, secular change of the annual cycle in SST is completely reversal in northern Atlantic. A warmer winter and colder summer indicate the weaker annual cycle in period S1, and a colder winter and warmer summer show the stronger annual cycle in period S3. Once again, decadal change of the annual cycle in SST is relatively weak in period S2.

The secular changes of the annual

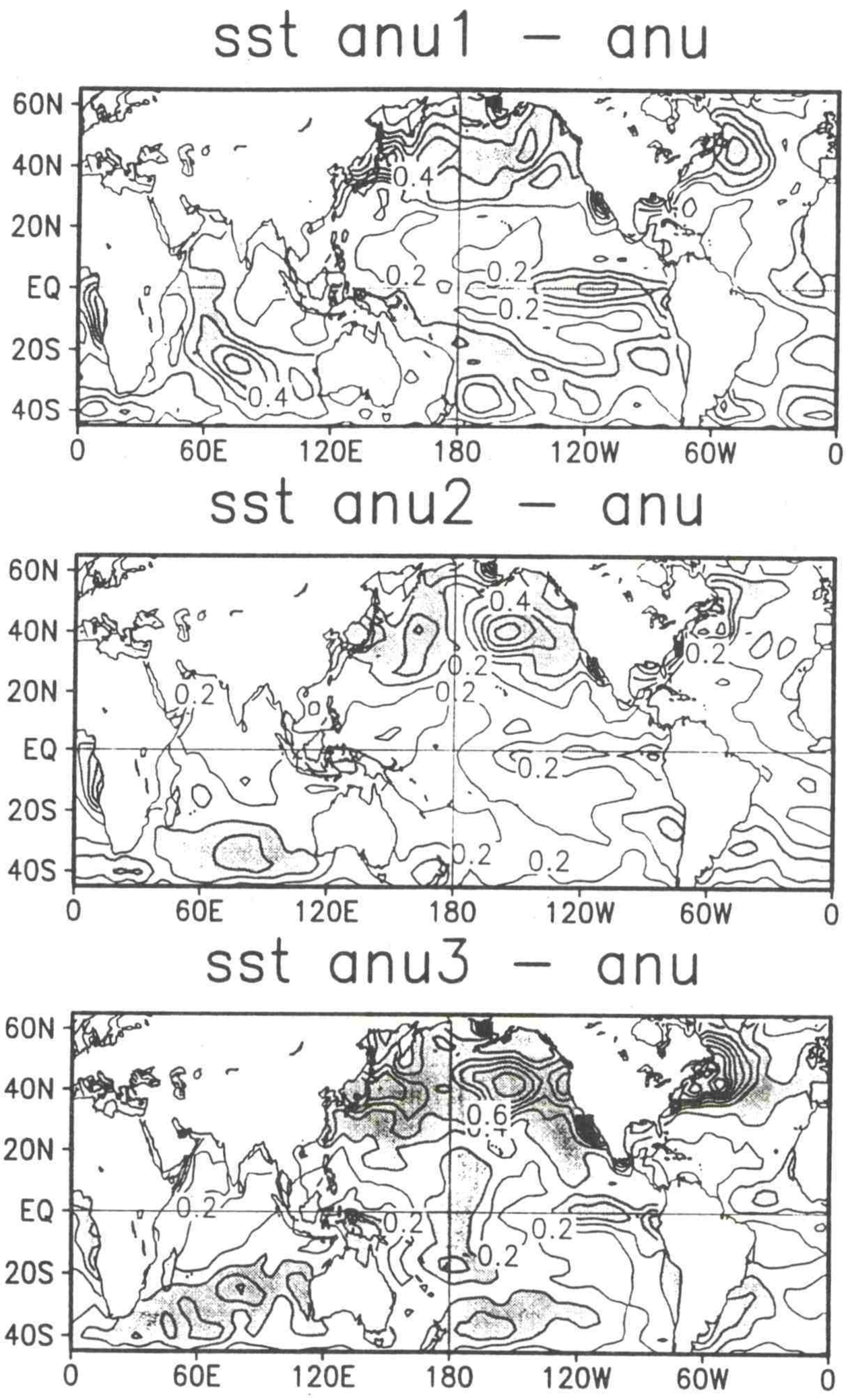

Fig. 1, The maximum range (max.-min.) of the annual cycle differences of SST between the annual cycle of three segments (S1, S2, and S3) and 45 year grand mean annual cycle. Intervals are 0.1°C and shaded area is greater than 0.3°C.

cycle in SST are as high as 0.6°C in north Atlantic, 0.5°C in north Pacific, and 0.4°C in equatorial central-eastern pacific. These magnitudes are comparable to secular changes or long term trend of SST.

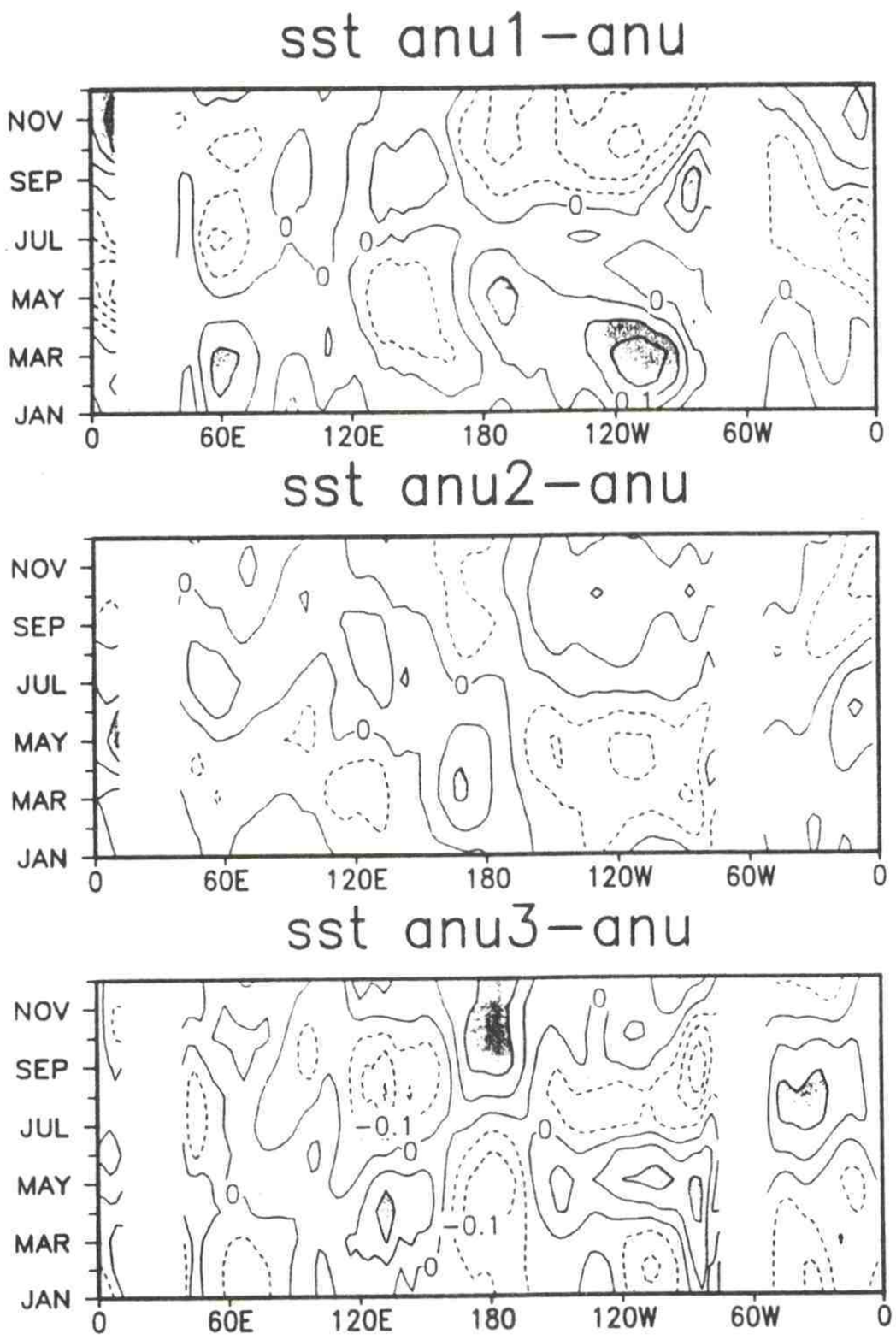

Fig. 2, Time-longitude sections averaged from 5°N-5°S of the annual cycle differences of SST for the S1(top), S2(middle), and S3(bottom). Intervals are 0.1°C and heavy (light) shading indicates SST greater (less) than 0.2°C (-0.2°C).

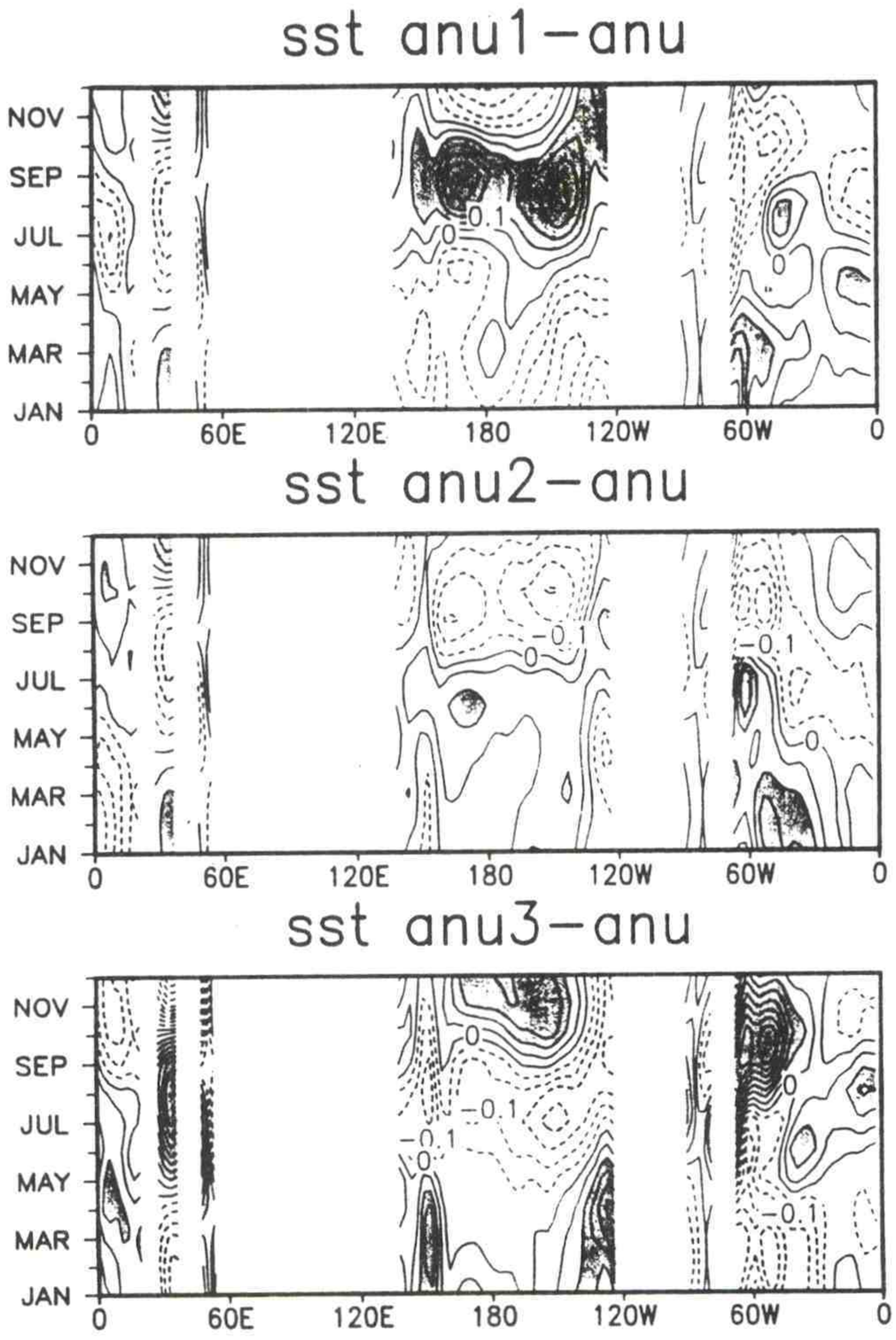

Fig. 3, Time-longitude sections averaged from 45°N-55°N of the annual cycle differences of SST for the S1(top), S2(middle), and S3(bottom). Intervals are 0.1°C and heavy (light) shading indicates SST greater (less) than 0.2°C (-0.2°C).

Consistency of the diabatic heating in the NMC/NCAR Reanalysis

Wesley Ebisuzaki
Climate Prediction Center
NCEP
Washington, DC

1. Introduction

The quality of atmospheric data assimilation systems has improved over the last two decades. For example, Fig. 1 shows the observed outgoing long-wave radiation (OLR) for January 1993. The OLR is a rough guide to the tropical convection. The 500 mb diabatic heating (Fig. 1) from the NMC/NCAR Reanalysis shows a strong spatial similarity to the tropical OLR. For comparison, the ITCZ cannot be clearly seen in calculations using the earlier FGGE analysis (e.g., Holopainen's 1988 review).

The Reanalysis estimates of the diabatic heating were produced by averaging the simulated diabatic heating from many 6-hour forecasts; consequently these estimates are very dependent the model's physical parameterizations. This study will try to quantify the accuracy of the diabatic heating estimates. Since this study is still in a preliminary stage, only one month (January 1993) was examined.

2. Method

Two common methods to estimate the diabatic heating are to use the simulated diabatic heating (Q_{mod}) from short model simulations (e.g. Reanalysis) or to compute the diabatic heating as a residual; i.e.,

$$\frac{\partial T}{\partial t} + \nabla(V \cdot T) + \frac{\partial \omega T}{\partial p} - \frac{R\omega T}{pC_p} = Q_{res}. \tag{1}$$

As a practical matter, Eq. 1 is usually integrated over a time period. Since the analyzed fields are usually only available once every 6 hours, the analyzed fields are assumed to be valid for the following 6-hour interval. Time averaging Eq. 1 gives,

$$\frac{T(t_n) - T(t_0)}{t_n - t_0} + \nabla(\overline{V \cdot T}) + \frac{\partial \overline{\omega T}}{\partial p} - \frac{R\overline{\omega T}}{pC_p} = \overline{Q}_{res} \tag{2}$$

where $\overline{F} = \int_{t_0}^{t_n} F dt$.

Q_{mod} depends on the accuracy of the physical parameterizations (and the analysis). Q_{res}, on the other hand, is less dependent on the physical parameterizations. In regions of moderate to high data density, Q_{res} is insensitive to the parameterizations as the final analysis is much more dependent on the observations than the details in the first guess. Q_{mod} and Q_{res} can be tied together by the heat budget of the data assimilation system. The Reanalysis data-assimilation system first makes a 6-hour forecast starting from the previous analysis. (Q_{mod} comes from this step.) This 6-hour forecast is called the "first guess." Then data from a 6-hour window (± 3 hours) is "merged" with the first guess. The "merging" consists of finding finding the solution (final analysis) which minimizes the error with the first guess and the observations. The difference between the final analysis and the first guess is called the "increment." The heat budget for the data assimilation system can be written as

$$\frac{\partial T}{\partial t} + \nabla(V \cdot T) + \frac{\partial \omega T}{\partial p} - \frac{R\omega T}{pC_p} = Q_{mod} + \sum_i Q^i_{inc} \delta(t - i\Delta t) \tag{3}$$

The major difference between the thermodynamic equation for the atmosphere and Eq. 3 is the last term, the effects of the temperature increments. The temperature increments are the result of the imbalance between the advective and "model diabatic heating" terms. While we can not say that the temperature increment is solely the result of inaccuracies in Q_{mod}, we can use the temperature increment to obtain an idea about the accuracy of the Q_{mod}.

In theory, we could evaluate all the terms in Eq. 3. However, this would be difficult. Problems include: (1) calculating the divergence of the heat flux requires information at every time step (not

saved), (2) the horizontal diffusion of the heat was not saved, (3) the effects of time filtering and time integration have to included, and (4) one would have do the computations pseudo-spectrally on sigma surfaces. The approach used here is to (1) approximate the time integral of the heat-flux divergence by the divergence at the analysis times, (2) compute the thermodynamic equation on pressure surfaces, (3) compute the derivatives using centered finite differences and (4) put the unsaved terms into the residual. Time averaging the resulting equation yields,

$$\overline{Q}_{res} = \overline{Q}_{mod} + \overline{Q}_{inc} + \overline{R}. \tag{4}$$

The above equation relates the two common estimates of the diabatic heating. In previous equation, $\overline{Q}_{res}$, $\overline{Q}_{mod}$, and $\overline{Q}_{inc}$ can be obtained or calculated which then allows us to determine the residual, $\overline{R}$. If $\overline{R} \ll \overline{Q}_{res}$, we have some confidence that the method used to compute $\overline{Q}_{res}$ only introduced small errors. If $|\overline{R}| \geq O(\overline{Q}_{res})$, then either the "unsaved" diabatic heating terms are large (unlikely) or that calculation of Q_{res} is sensitive to the procedure.

Q_{inc} is imbalance between Q_{mod} and advective and time-rate-of-change terms. In regions of very good analyses (i.e., the Q_{res} estimate is good) , this term is the error in Q_{mod}. In regions of moderate quality, Q_{inc} maybe considered an estimate of the accuracy of Q_{mod}, and in regions of no observations, Q_{inc} would be zero. Since most regions have some observations, Q_{inc} should provide an order of magnitude estimate of the error in Q_{mod}.

3. Results

Eq. 4 was evaluated for 17 pressure levels for the month of January 1993. However, only the 700, 250, and 100 mb levels will be discussed. The results for the 700 mb level were quite good. The term $\overline{R}$ was small ($|\overline{R}| < 0.2$ K/day for 50% of the globe, and $|\overline{R}| < 0.4$ K/day for 90% of the globe). The small values of $\overline{R}$ indicate that the approximations introduced relatively small errors into the $\overline{Q}_{res}$ estimate. The spatial patterns of $\overline{Q}_{res}$ and $\overline{Q}_{mod}$ were very strongly correlated (see Fig. 2). The only problem was that $\overline{Q}_{inc}$ and $(\overline{Q}_{res} - \overline{Q}_{mod})$ were uniformly 0.5 K/day. While it is possible that some unusual set of analysis errors could produce a uniform 0.5 K/day error in $\overline{Q}_{res}$, it is more plausible that this is an indication of a problem with the physical parameterizations and that $\overline{Q}_{mod}$ has too little heating.

At 250 mb, $\overline{R}$ was small over the tropical oceans; however, it has values of 1 K/day over the mid-latitudes. $\overline{Q}_{inc}$ has typical values of -0.5 K/day over the tropical oceans, -1K/day over the mid-latitude continents, and 1.4 K/day over the mid-latitude oceans. If we can trust the analyzed winds and temperatures, $\overline{Q}_{inc}$ is the biases in $\overline{Q}_{mod}$, otherwise $\overline{Q}_{inc}$ provides an error estimate.

At 100 mb, $\overline{Q}_{inc}$ had values greater than 2.5 K/day. This large increment was confirmed using an independent calculation. Peak values of $\overline{R}$ and $\overline{Q}_{res}$ were over 4 K/day. $\overline{Q}_{mod}$, on the other hand, had values that only ranged from -1 to 0.7 K/day. The moderate values of $\overline{Q}_{mod}$ were plausible as most clouds are below 100 mb. Thus it appears that Reanalysis can not be used to calculate $\overline{Q}_{res}$ at 100 mb. This conclusion was also shared by J. Whitaker (CDC, personal communication) and P. Peng (GFDL, personal communication) who both tried to calculate Q_{res} on sigma surfaces. Consequently one must conclude that the stratospheric winds and temperatures analyses have some defect which fouls up the Q_{res} calculation.

4. References

E. Holopainen, 1988: Recent estimates of diabatic forcing on the planetary scale: a review, ECMWF Workshop on Diabatic Forcing. [Available from ECMWF, Reading, U.K.]

5. Figures

Fig. 1: Outgoing Long-Wave Radiation (OLR) for January 1993 from satellites (W/m^2, shaded), model simulated 500 mb diabatic heating Q_{mod} for the same time period (K/day, contour).

Fig. 2: 700 mb diabatic heating from residual calculation (W/m^2, shaded) and model simulated Q_{mod} (K/day, contour) both for January 1993.

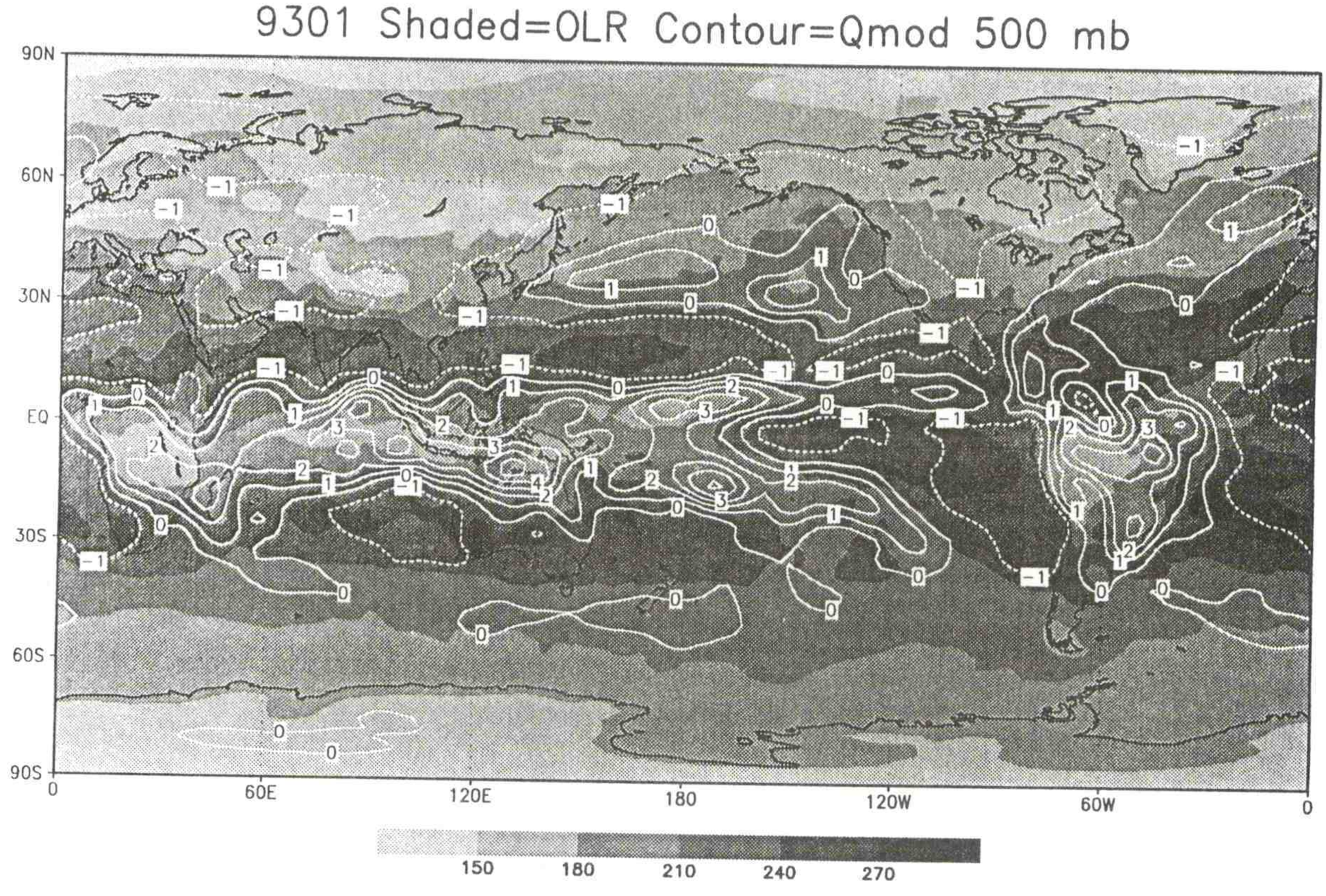
9301 Shaded=OLR Contour=Qmod 500 mb
90N
60N
30N
EQ
30S
60S
90S
0
60E
120E
180
120W
60W
0
150
180
210
240
270
GrADS: COLA/IGES

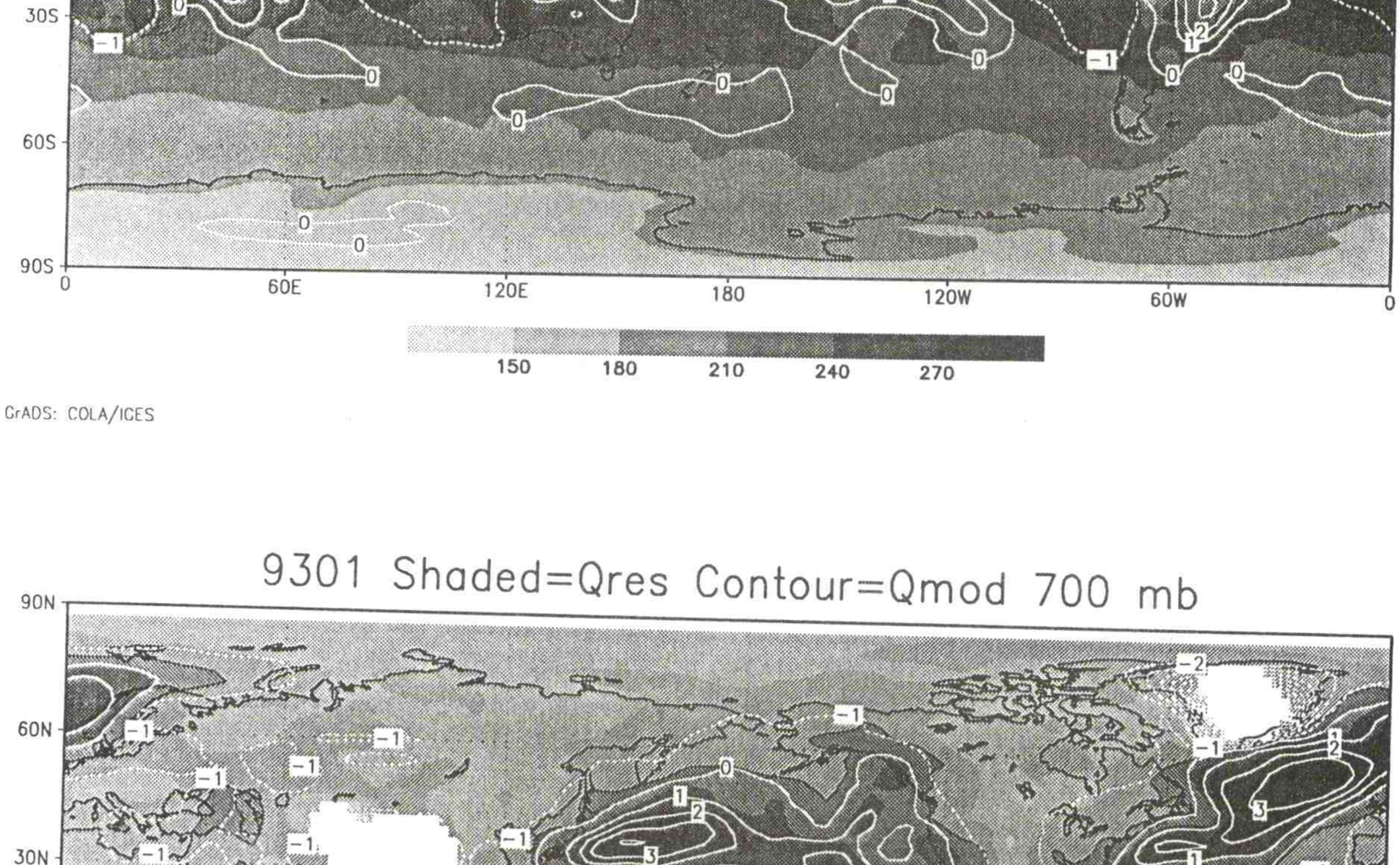
9301 Shaded=Qres Contour=Qmod 700 mb
90N
60N
30N
EQ
30S
60S
90S
0
60E
120E
180
120W
60W
0
−3
−2
−1
0
1
2
3
4
GrADS: COLA/IGES

The Influence of ENSO on the Temperature Field over Canada

Amir Shabbar and Madhav Khandekar
Atmospheric Environment Service
Environment Canada, Downsview, Canada

1. Introduction

The purpose of this investigation is to make a comprehensive analysis of the impact of the extreme phases of El Niño-Southern Oscillation (ENSO) namely El Niño and La Niña on the surface temperatures over various regions of Canada. Additionally, the response of the tropical forcing on the lower tropospheric air temperatures over Canada is examined. This study focuses on the winter-time temperature response of ENSO events over various regions of Canada. ENSO-related variability as it affects Canadian surface temperatures is also highlighted.

2. Data

The data set used in this study is the combined land and marine gridded monthly surface air temperature anomalies (departure from a 1951-1979 mean) for the years 1900-1990. This data set is an updated version of Jones et. al (1986a) surface temperature data. Homogeneity of the data was checked by comparison with data from adjacent stations. The data set suffers from poor spatial coverage prior to 1900 particularly in the high latitudes and the eastern Canadian Arctic. Data coverage is fairly good after 1900 from the Yukon through western Canada and the Great Lakes basin into the Maritimes. In order to remove bias in the data set, a linear trend is removed at each grid point for each month separately. The upper air data for this investigation consist of monthly (1200 UTC) 500 and 1000 hPa height analysis of the Northern Hemisphere (10^{o}N to 80^{o}N) on a 455 grid point network of 5^{o} latitude by 10^{o} longitude for the period 1946 to 1990.

3. Results and Discussion

An ENSO event has been shown to have some well-known atmospheric teleconnective patterns with middle latitudes of North and South America (e.g., Horel and Wallace, 1981). Since the central Pacific SSTs and the Southern Oscillation index are highly correlated, ENSO years have been defined as those years in which the Southern Oscillation index remained in the lower 25% (El Niño) or upper 25% (La Niña) of the distribution for 5 months or longer. Using this definition, we identified 23 moderate to strong El Niño and 13 La Niña events between 1900-1990. In this study we examine the effect of these events on the surface and lower tropospheric temperatures over Canada from the ENSO onset year to the spring of the following year. The definition of ENSO years is the same as those choosen by Ropelweski aned Jones (1987).

(i) El Niño and Canadian Temperature

The composites of the Canadian surface temperature anomaly pattern for the three-month average Dec-Feb is shown in Fig. 1a. Similar composite of thickness (500-1000) hPa anomaly for three-month average is presented in Fig. 1b. The November-January composite (not shown) shows the emergence of above normal temperature over western Canada. Positive anomalies over British Columbia, as well as negative anomalies east of Baffin Island, are statistically significant at the 5% level. The corresponding 500-1000 hPa thickness map (not shown) for the same period shows a pattern which resembles the Pacific North American (PNA) oscillation pattern. The positive anomaly centre over western Canada is indicative of the amplification of the western Canadian ridge; as well, the negative anomaly centre over northeastern Pacific ocean signifies deepening of the Aleutian Low. The combination of these two features gives rise to a strong southwesterly flow along the west coast of Canada and, consequently, positive surface temperature anomalies in British Columbia. For the Dec-Feb time period, significant positive surface temperature anomalies strengthen. Two distinct centers of positive anomalies can be identified, one over the Mackenzie Valley and the other over a region just west of Hudson Bay. The corresponding composites of 500-1000 hPa thickness (Fig. 1b) show the strengthening of the positive anomalies and reveals the tropospheric PNA-like thickness pattern.

ii) La Niña and Canadian Temperature

The composites of the Canadian temperature pattern based on 17 cold phases of ENSO for the Dec-Feb average of the La Niña onset year are shown in Fig. 2a. The Nov-Jan composite, (not shown) shows significantly below normal temperature anomalies from the Yukon to the northwestern Canadian prairies. Compared to the warm phase, the cold phase surface temperature anomalies are stronger. The 500-1000 hPa map, Fig. 2b, for the same period shows again a PNA oscillation pattern over the North American sector. The combination of a negative anomaly centre over the Canadian Rockies and a positive anomaly centre over northeastern Pacific ocean is conducive to northwesterly cold air advection over western Canada.

During the La Niña phase, two separate areas of strong negative anomaly centers could be identified in Dec-Feb, one over the Mackenzie Valley and the other over the regions just west of Hudson Bay. In contrast to the warm phase composite however, negative surface temperature anomalies remain confined mainly to western Canada during winter. These anomalies reach their farthest eastward extent, north of the Great Lakes, in the Dec-Feb period. The corresponding 500-1000 hPa maps show a PNA oscillation pattern which weakens considerably by spring. Both surface and 500-1000 hPa negative anomalies weaken considerably during the Mar-May period and by early summer no ENSO related anomalies are found over Canada (Shabbar and Khandekar 1995). Western Canada exhibits ENSO-temperature relationships during both phases of ENSO and is opposite in sign. Eastern Canada, however, shows the ENSO influence only in the warm phase of ENSO.

iii) Variability in Relationship

The distribution of El Niño, La Niña and normal temperatures in western Canada is shown in Fig. 3. The values shown are the average of all the grid points in the boxed area as shown in Fig. 1a during the Dec-Feb period. A guassian curve is fitted to the three distribution separately. It is clear that the mean of the distribution of the El Niño temperatures is shifted towards the warmer temperatures relative to the normal temperature distribution and the distribution of the La Niña temperatures is shifted towards the colder temperatures relative to the normal temperature distribution. Even though the means of the El Niño and La Niña temperature distribution is statistically different from the normal distribution at the 5% level, there is considerable overlap among the three distribution.

In summary, we find that for the warm phase significant positive temperature anomalies first appear in western Canada and then expand eastward during the winter months. The lower tropospheric temperature response is consistent with the presence of the PNA and TNH pattern. While western regions of Canada exhibit temperature relationships during both phases of ENSO, eastern Canada shows temperature changes only during the warm phase of ENSO. The largest positive (negative) anomalies are found to be centered over two separate regions, one over the Yukon and the other just west of Hudson Bay in the El Niño (La Niña) years. The range of temperature response among the El Niño and La Niña cases is large particularly where the anomalies are significant.

References

Horel, J.D., and J.M. Wallace, 1981: Planetary scale atmospheric phenomena associated with the Southern Oscillation. *Mon. Wea. Rev.*, **109**, 813-829.

Jones, P.D., S.C.B. Raper, R.S. Bradley, H.F. Diaz, P.M. Kelly and T.M.L. Wigley, 1986a: Northern Hemisphere surface air temperature variations, 1851-1984. *J. Clim. Appl. Met.*, **25**, 161-179.

Ropelewski, C.F., and P.D. Jones, 1987: An extension of the Tahiti - Darwin Southern Oscillation index. *Mon. Wea. Rev.*, **115**, 2161-2165.

Shabbar, A., and M. Khandekar, 1995: The impact of ENSO on the temperature field over Canada. Submitted to *Atmosphere-Ocean.*

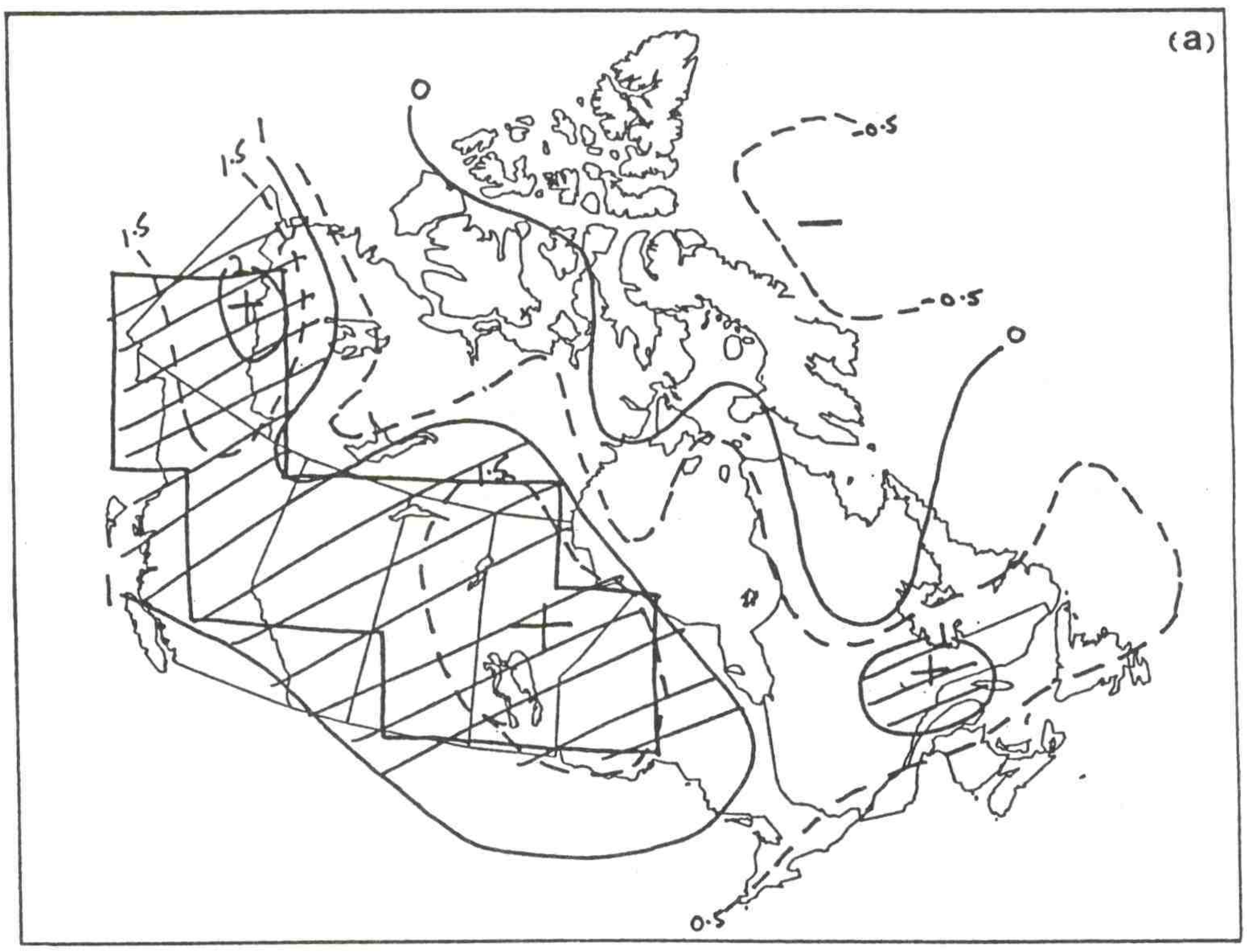

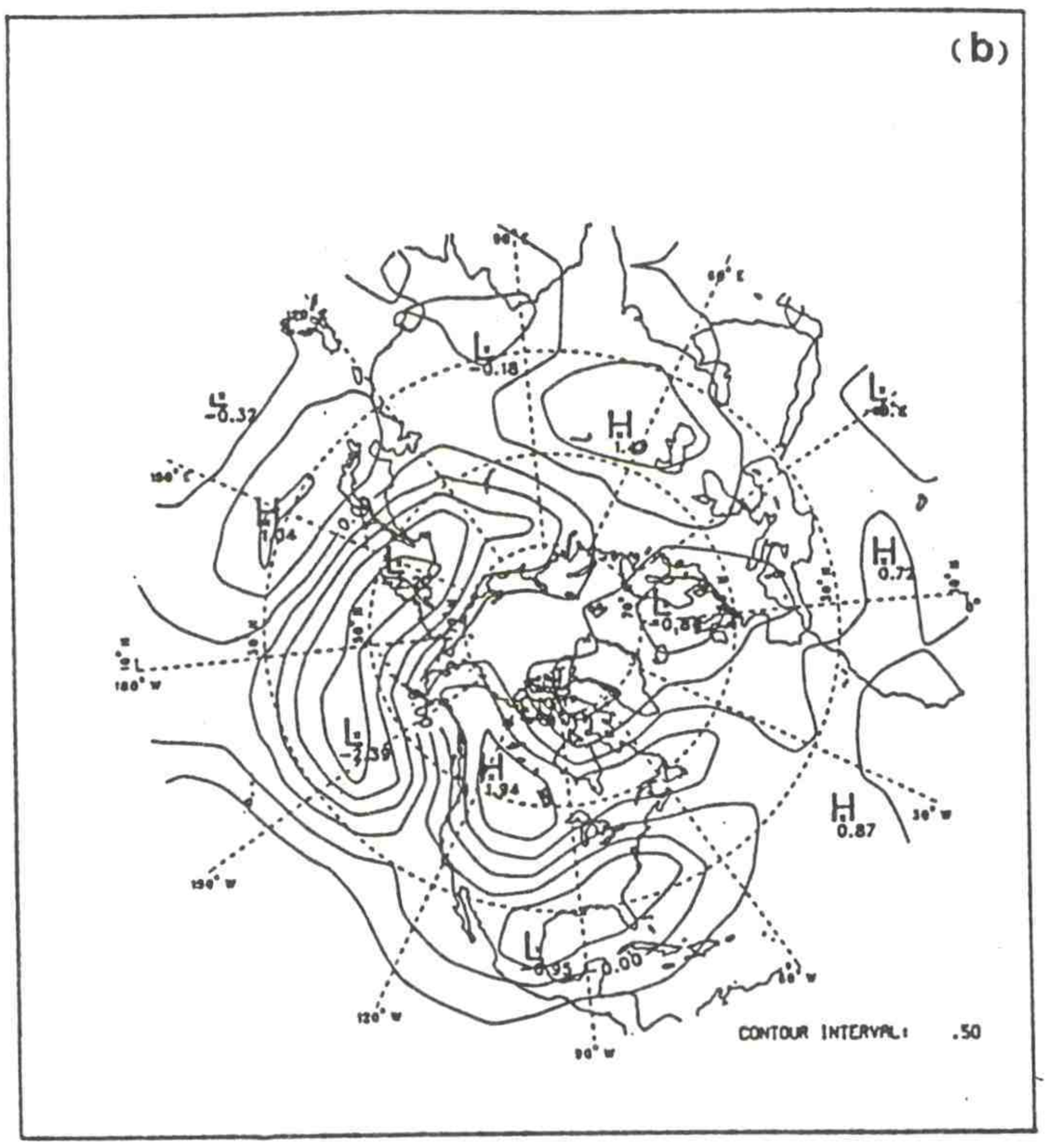

Figure 1. (a) Mean temperature anomaly composite (degree celsius) of 23 strong to moderate El Nino episodes during Dec-Feb period. Values in the shaded areas are statistically significant at the 5% level. Values in the boxed area are used to calculate temperature distribution shown in Fig. 3.
(b) Mean 500-1000 hPa thickness anomaly composite (dam) of 23 strong to moderate El Nino episodes during Dec-Feb period.

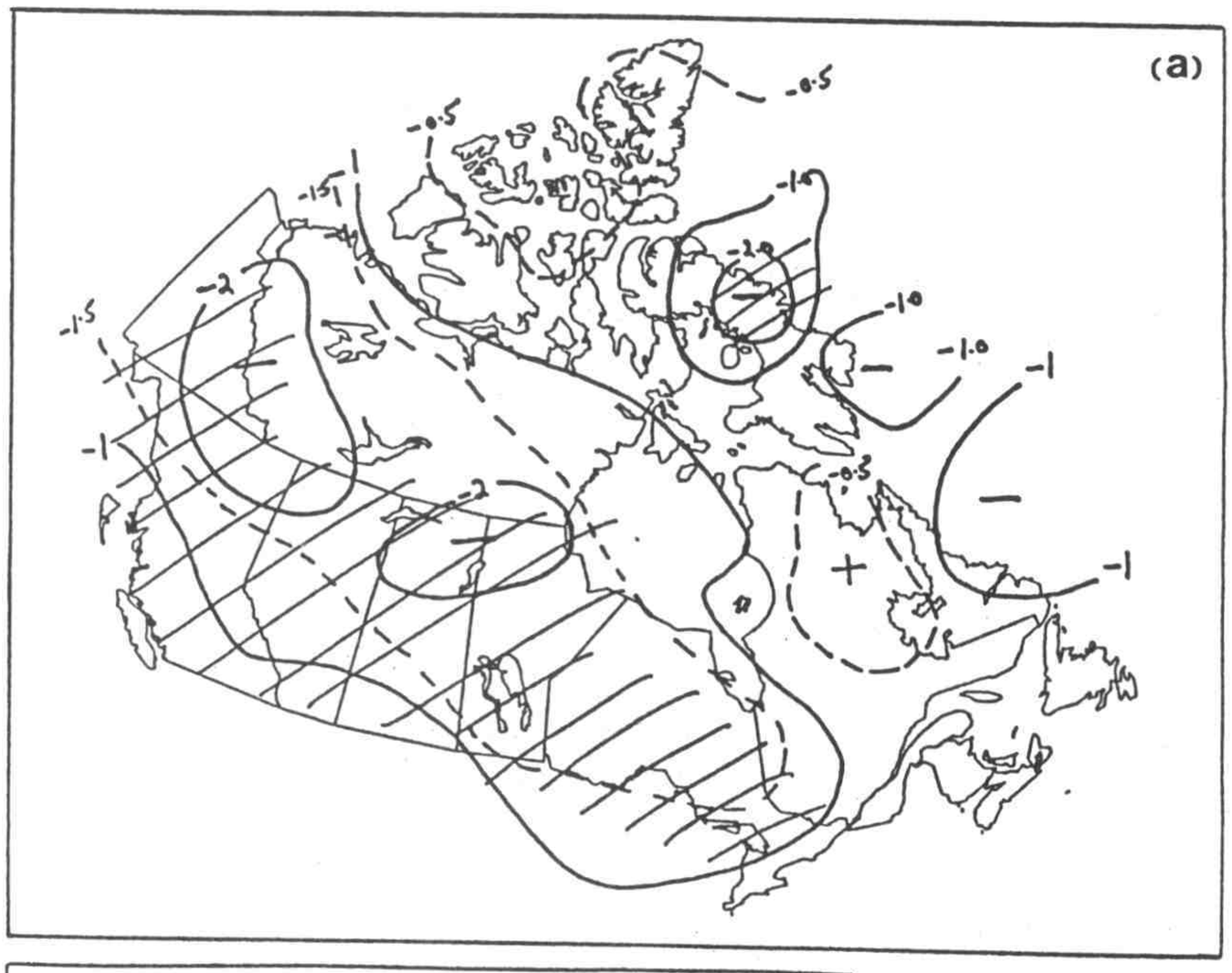

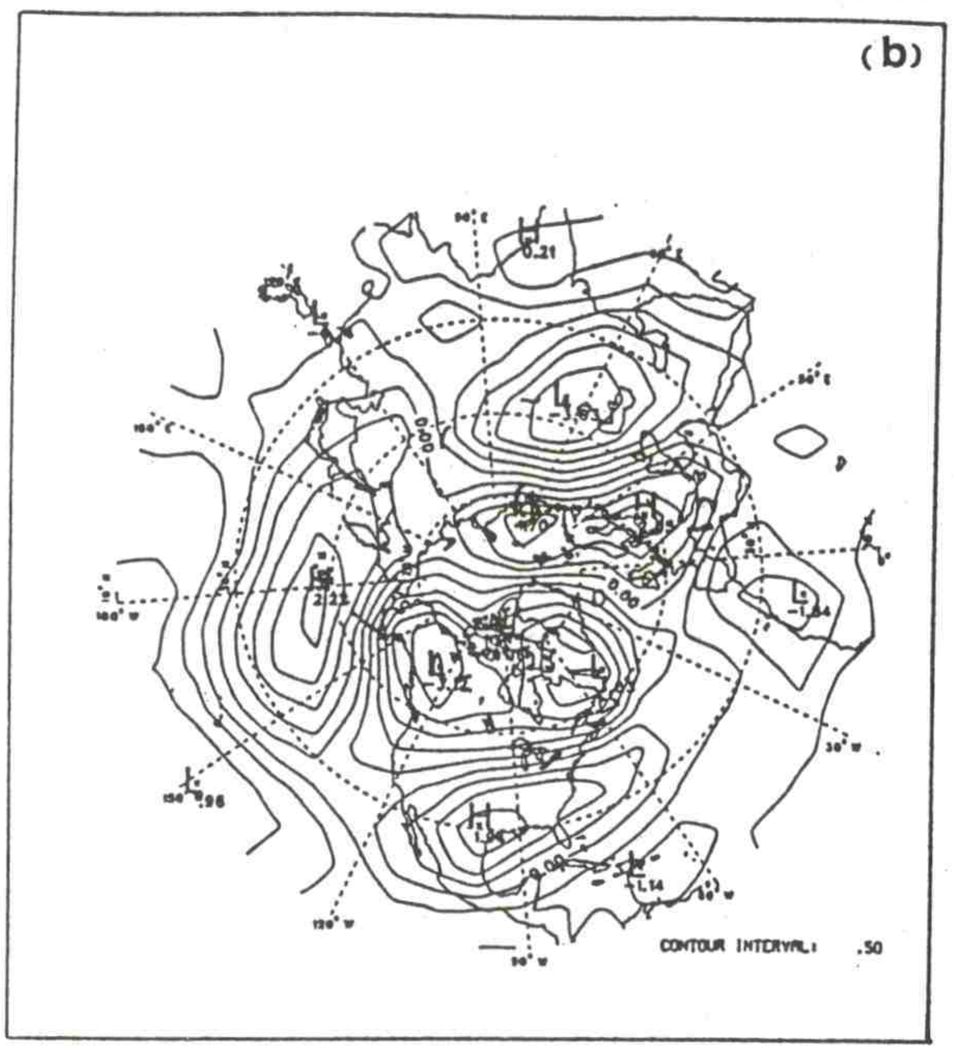

Figure 2. (a) Mean temperature anomaly composite (degree celsius) of 17 strong to moderate La Nina episodes during Dec-Feb period. Values in the shaded areas are statistically significantat the 5% level. (b) Mean 500-1000 hPa thickness anomaly composite (dam) of 17 strong to moderate La Nina episodes during Dec-Feb period.

Figure 3. Mean temperature anomaly distribution for El Nino (solid), La Nina (hatched) and normal (open) years for the boxed area shown in Fig. 1. A guassian curve is fitted to the three distribution separately.

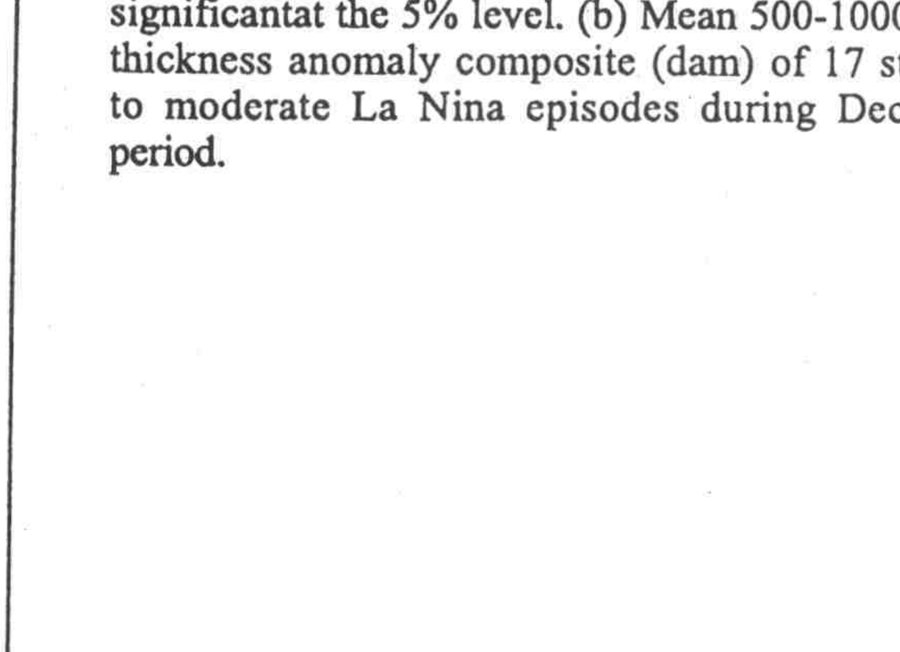

The Prediction of Seasonal Wildfire Severity in the Western USA

John W. Benoit, Francis M. Fujioka and Morris H. McCutchan
Pacific Southwest Research Station
USDA Forest Service
Riverside, CA 92507

1. Introduction

The 1994 wildfire season was one of the busiest on record in the Western USA, overtaxing even the combined firefighting resources of the National Interagency Fire Center (NIFC). Located in Boise, Idaho, NIFC provides logistical and technical support for wildfire suppression throughout the nation, when local and regional forces are inadequate for a fire emergency.

Weather is critical to fire planning, because it significantly influences the short- and long-term potential of forest fires. On a seasonal to multiyear scale, droughts increase wildfire potential by desiccating vegetation, particularly brush and trees. If long-term weather effects can be predicted sufficiently, fire agencies can formulate more cost-effective presuppression strategies (Meisner et al., 1994). Previous studies have examined the correlation between climate and wildfire, for example, fire statistics in El Niño vs non-El Niño years (Simard, Haines and Main, 1985). Others have investigated the potential predictability of weather-dependent seasonal fire indices (Meisner and McCutchan, 1994). Our objective is to examine the correlations between fire activity and surface weather in the June to August time frame, in the western USA. The months chosen for the study correspond, with some exceptions, to the western fire season. If significant correlations exist between weather and fire activity on the seasonal scale, the Climate Prediction Center's long-lead outlooks of mean temperature and precipitation (O'Lenic, 1994) may be useful for seasonal fire activity prediction.

2. Data and Methods

The basic unit of data in this study is a three-month mean (e.g., temperature) or a three-month total (e.g., number of fires). We computed the correlations between the weather variables and fire variables, and the corresponding significance probabilities under the null hypothesis that the correlation is zero. We also examined the normality of the data, to determine the validity of applying inference methods based on normal theory.

The fire weather network for this study has 126 stations, each associated with a dominant fuel type represented by a letter code (Fig. 1). The length of record of the stations varied, but all data came from the period 1970 to 1994. The weather stations, serving national forests within six Forest Service regions (Fig. 2), reported daily mid-afternoon temperature, dew point, relative humidity, wind speed, and 24-hour precipitation amount. We required a minimum of 15 observations in a month to compute a monthly mean, which we used, in turn, to compute the three-month mean. We computed total precipitation by summing the daily values over the three months.

We further limited this study to areas with fuel type C: open canopy pine stands with perennial grasses and forbs. This vegetation complex is found in all regions of the study area. We selected five locations per region. The criteria imposed upon the data reduced the number of qualifying stations to 21.

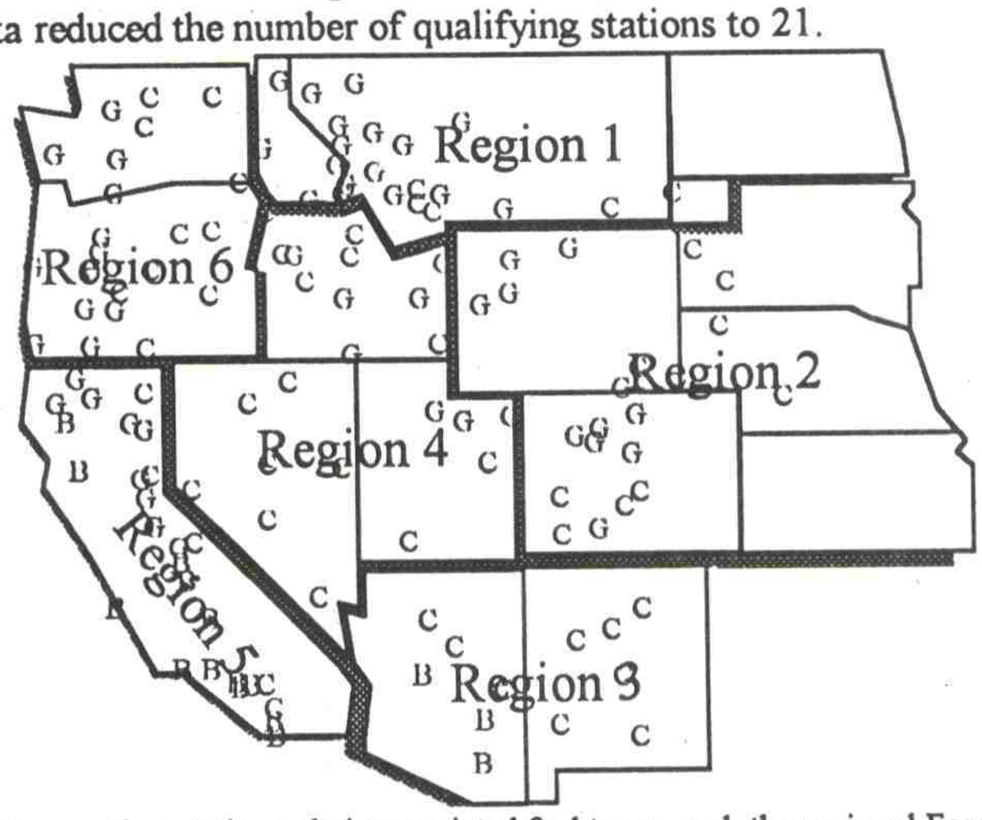

Figure 1: Locations of fire weather stations, their associated fuel types, and the regional Forest Service boundaries in the western USA.

Table 1: Some common fuel types in the western USA.

Fuel Type	Description
B	Dense fields of brush, such as chaparral.
C	Open pine stands with perennial grasses and forbs.
G	Dense conifer stands with heavy accumulation of litter.

Table 1 describes the fuels represented by the letter codes in Fig. 1. The fire data consisted of the district number in which the fire occurred, the discovery time, containment time, number of acres burned, and fire size class.

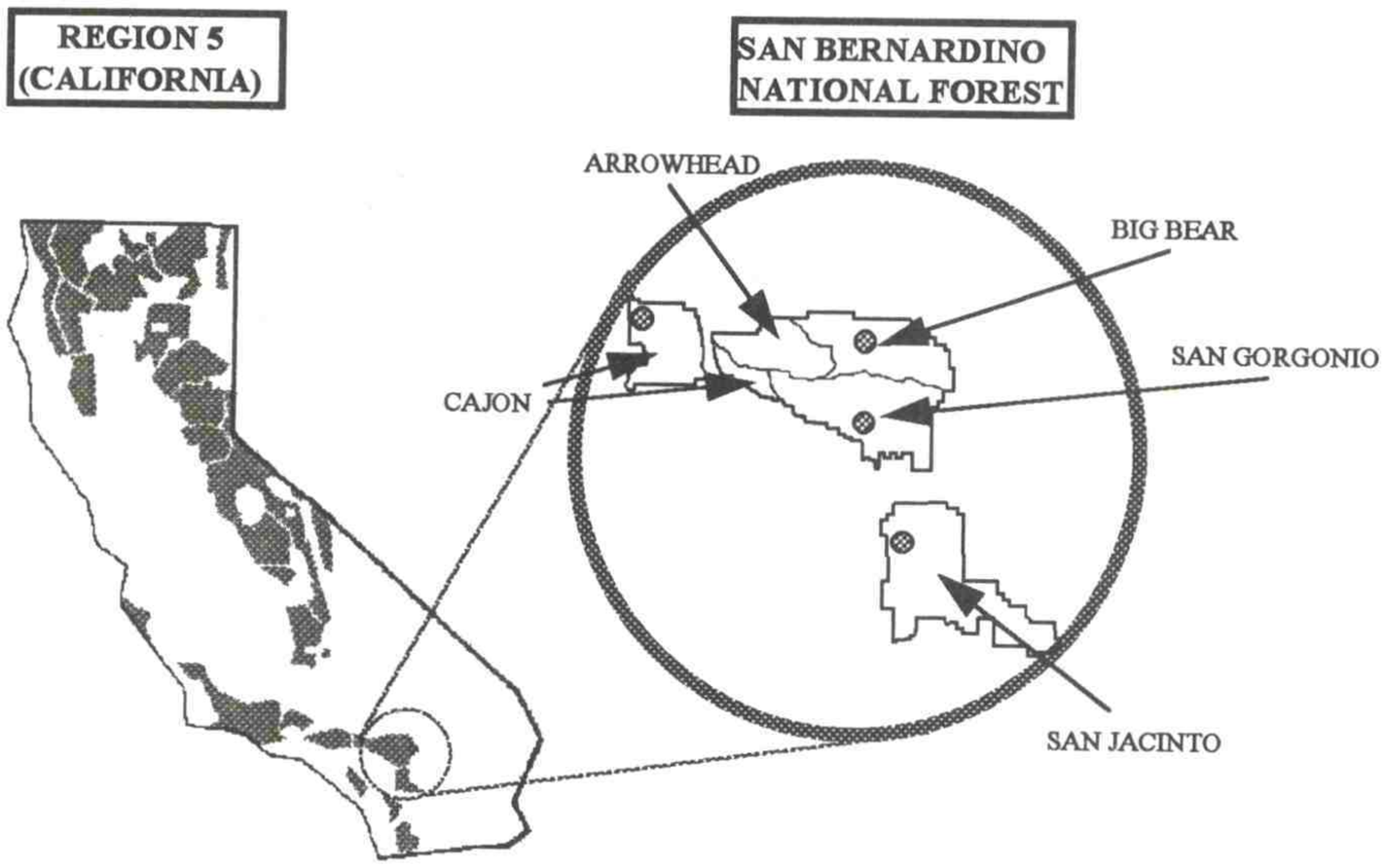

Figure 2: This example of the Forest Service administrative region, forest, and district breakdown shows the national forests in Region 5,California. Each forest (e.g., the San Bernardino National Forest) consists of districts (e.g., Cajon, Arrowhead, etc.), and each district may have a number of fire weather stations (represented by the dots), or none.

Each of the fire variables is a sum over June to August of each year. For this three-month period, we considered number of fires, number of C+ fires (fires that burn 10 or more acres), number of days on which a fire occurred, number of days on which a C+ fire occurred, number of acres burned, and number of acres burned by C+ fires.

3. Results

Work on this study is still in progress, but the limited results we already have are indicative of the complexity of the climate/fire relationship. We examined the correlations between seasonal weather and fire at five locations in Montana. The magnitude of the correlations ranged from 0.044 to 0.798. The climate variable that correlated significantly with most of the fire statistics was temperature. To a lesser extent, precipitation and relative humidity were also significantly correlated with fire. Dew point and wind speed, on the other hand, seldom correlated significantly with fire.

Note that significant correlations at Jefferson occur row-wise across all climate variables except wind speed, for number of fires and number of fire days. At Ennis, on the other hand, significant correlations occur column-wise across fire variables, for temperature, relative humidity, and precipitation. Yet these two locations are among the closest of all pairs.

Helena

	Temperature	Dew Point	Relative Humidity	Wind Speed	Total Precipitation
Total Acres Burned	0.149	0.055	-0.085	0.229	-0.197
C+ Acres Burned	0.134	0.061	-0.072	0.229	-0.182
Number Of Fires	0.630	-0.221	-0.558	0.462	-0.569
Number Of C+ Fires	0.330	-0.044	-0.271	0.129	-0.315
Number Of Fire Days	0.580	-0.312	-0.527	0.532	-0.467
Number Of C+ Fire Days	0.409	-0.242	-0.381	0.378	-0.325

Jefferson

	Temperature	Dew Point	Relative Humidity	Wind Speed	Total Precipitation
Total Acres Burned	0.460	-0.361	-0.441	-0.060	-0.433
C+ Acres Burned	0.438	-0.340	-0.416	-0.068	-0.421
Number Of Fires	0.665	-0.716	-0.737	0.282	-0.543
Number Of C+ Fires	0.446	-0.345	-0.424	-0.075	-0.421
Number Of Fire Days	0.798	-0.612	-0.738	0.168	-0.646
Number Of C+ Fire Days	0.473	-0.353	-0.450	-0.134	-0.358

Ennis

	Temperature	Dew Point	Relative Humidity	Wind Speed	Total Precipitation
Total Acres Burned	0.656	-0.200	-0.535	-0.258	-0.438
C+ Acres Burned	0.647	-0.196	-0.526	-0.256	-0.432
Number Of Fires	0.715	-0.167	-0.571	-0.069	-0.393
Number Of C+ Fires	0.720	-0.279	-0.597	-0.304	-0.444
Number Of Fire Days	0.770	-0.303	-0.667	-0.189	-0.494
Number Of C+ Fire Days	0.713	-0.357	-0.637	-0.390	-0.504

Fort Howes

	Temperature	Dew Point	Relative Humidity	Wind Speed	Total Precipitation
Total Acres Burned	0.582	-0.097	-0.389	0.264	-0.382
C+ Acres Burned	0.569	-0.110	-0.386	0.261	-0.369
Number Of Fires	0.555	0.144	-0.283	0.173	-0.408
Number Of C+ Fires	0.559	-0.115	-0.387	0.323	-0.425
Number Of Fire Days	0.451	0.073	-0.268	0.109	-0.457
Number Of C+ Fire Days	0.594	-0.083	-0.396	0.313	-0.485

Camp Crook

	Temperature	Dew Point	Relative Humidity	Wind Speed	Total Precipitation
Total Acres Burned	0.294	-0.261	-0.316	0.393	-0.217
C+ Acres Burned	0.297	-0.269	-0.319	0.388	-0.220
Number Of Fires	0.227	-0.230	-0.312	0.294	-0.181
Number Of C+ Fires	0.433	-0.227	-0.384	0.358	-0.309
Number Of Fire Days	0.349	-0.236	-0.360	0.319	-0.143
Number Of C+ Fire Days	0.588	-0.472	-0.562	0.206	-0.372

Table 2: Five fuel-type C stations for Region 1. The shaded cells represent correlations significant at the 95% level, under the hypothesis of zero correlation.

Encouraged by the relatively high correlation coefficients at Ennis, we regressed number of C+ fires on temperature. This model is interesting as a potential tool for predicting the number of large fires from summer temperature.

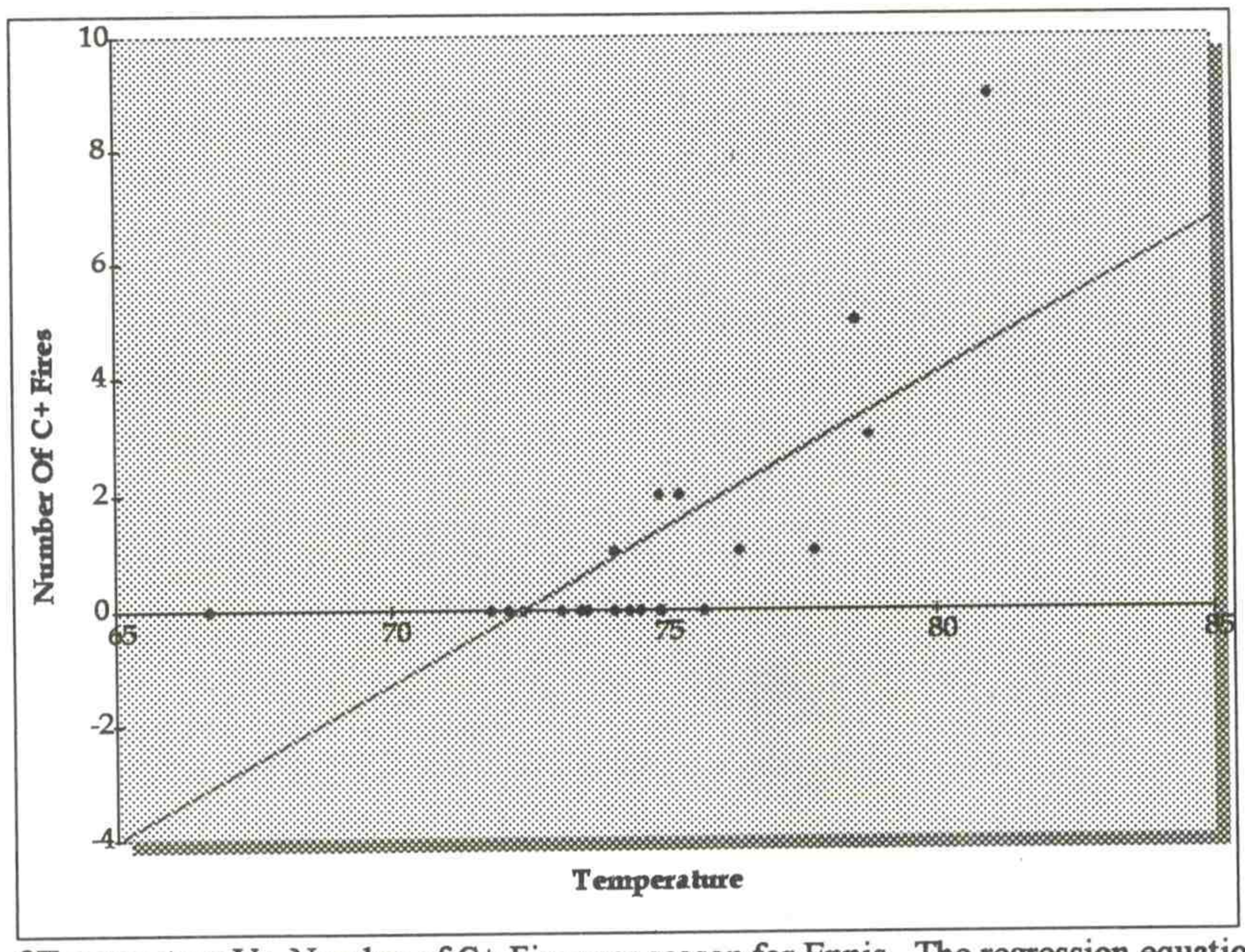

Figure 3: Plot of Temperature Vs. Number of C+ Fires per season for Ennis. The regression equation has the form: `Predicted Number Of C+ Fires = -38.97326 + 0.537855 * Temperature`.

Care is required, however, in drawing the usual type of statistical inferences from the regression results, because normal probability plots of the number of C+ fires at each of the stations revealed that they were nonnormal. In particular, the plots were convex, indicating a leftward skew in the distribution of the number of fires per fire season. The leftward skew indicates that many seasons have few or no fires, but occasionally, there is a season with relatively many fires.

4. Conclusions and Recommendations

Reasonable correlations exist between seasonal weather variables and fire activity statistics, but the relationship depends heavily on location. In Montana, seasonal fire forecast equations would have to be based on data collected at least at the forest level. The large differences in correlations between forests preclude a simple regional fire forecasting scheme.

Non-normality of the data suggests that other analytical methods should be used. Rank correlation statistics, for example, do not depend on the distributional assumptions that we used here. Similarly, a generalized linear model may be more appropriate than the simple linear regression of this study. One suggested form would be

$$\log y = \beta_0 + \beta_1 x + \varepsilon$$

where the betas are parameters to be estimated, and ε is a non-normal error.

The fact that seasonal temperature and precipitation correlate with fire statistics relatively frequently, compared to the other climate variables, bodes well for the prospects of fire forecasting. Fortunately, these are the two climate variables for which seasonal forecasts are made. We cannot preclude, however, the importance of intraseasonal variability. It may be advantageous also to examine information in yearly trends, because one might expect consecutive drought years, for example, to increase the flammability of vegetation.

REFERENCES

Meisner, B. N., R. A. Chase, F. M. Fujioka, M. H. McCutchan, and J. W. Benoit, 1994: WxPlan: a weather-related strategic planning tool for fire managers and planners. Proceedings of the 12th Conference on Fire and Forest Meteorology, Jekyll Island, GA, Soc. Amer. Foresters, 383-390.

Meisner, B. N. and M. H. McCutchan, 1994: Potential predictability of seasonal fire danger indices in the western U.S. Proceedings of the 18th Annual Climate Diagnostics Workshop, Boulder, CO, National Technical Information Service, Springfield, VA, 256-259.

O'Lenic, Edward A. 1994. Operational Long-Lead Outlooks of Seasonal Mean Temperature and Precipitation. Technical Procedure Bulletin Series No. 418. National Weather Service Office of Meteorology. 30 p. (Draft).

Simard, Albert J., Donald A. Haines and William A. Main, 1985: El Niño and wildland fire: an exploratory study. Proceedings of the 8th Conference on Fire and Forest Meteorology, Detroit, MI, Soc. Amer. Foresters, 88-95.

The 1992-95 rainy seasons in Northeast Brazil: real-time forecasts and verification

by

Lawrence Greischar

and

Stefan Hastenrath

Department of Atmospheric and Oceanic Sciences, University of Wisconsin, Madison

A real-time forecast has again been issued for the 1995 rainy season in Northeast Brazil. This is summarized here along with a verification. The forecasts for the three previous years are also reviewed. The method is presented in Hastenrath and Greischar (1993a).

The description of characteristic precursors of anomalous rainy seasons is in the following repeated from Hastenrath and Greischar (1993b). Deficient March-June Nordeste rainfall is heralded by (a) deficient October-January (ONDJ) precipitation, (b) enhanced southerly wind component and (c) weakened northward SST gradient in the Atlantic, and (d) warm Pacific waters in January. Forecast models use stepwise multiple regression (SMR), neural networking (N), and linear discriminate analysis (LDA). The training period is 1921-57 and verification period is 1958-89. The forecast is made from information through January, and predictors used are included in Tables 1 and 2. The rainfall indices ONDJ and MAMJ were compiled from a network of 27 raingauges in the Nordeste. From COADS we constructed the index V of southerly wind component over the tropical Atlantic (30N-30S), and of SST in the equatorial Pacific, PAC. From the UKMO SST set (Bottomley et al., 1990) the indices ST29, ST31 and T31-NDJ of the southward SST gradient in the Atlantic were compiled.

In the 1995 pre-season ONDJ was barely positive, V slightly positive (southerly departures), ST29, ST31 and T31-NDJ negative (enhanced northward SST gradient), and PAC positive (warm anomaly in equatorial Pacific). A map of outgoing longwave radiation, OLR, indicates intense convection over the equatorial Atlantic (Climate Analysis Center, 1995). Note that OLR is not among the inputs to the quantitative prediction models.

The quantitative results from the prediction models are summarized in Tables 1 and 2. All SMR models and model N point to above average rainfall conditions while both LDA models indicate very wet conditions. Regarding the conversion from index values to absolute rainfall amounts, a MAMJ index of unity corresponds approximately to 200 mm (27-station average of standard deviation; Table 3).

The seasonal evolution of the fields of anomalous V, SST, and OLR, was studied from maps of the months January through June 1995. The slight southerly wind departures of January become northerly departures in March and April before returning to southerly departures in June. Negative SST departures in the tropical North Atlantic and warm anomalies to the South of the Equator persisted. The equatorial Pacific waters became less warm as the rainy season progressed (Table 3). Maps of OLR showed an intensified near-equatorial convection belt particularly in April and May (Climate Analysis Center, 1995).

The rainfall in Northeast Brazil stayed close to the long-term mean during January through March with strong positive departures in April and May (Table 3), and the index of the

accumulated March-June rainfall was positive. Table 3 indicates that the 1995 Nordeste rainy season was somewhat wetter than predicted.

Table 4 summarizes the past four years of Nordeste rainy season forecasts (Greischar and Hastenrath, 1994, 1995; Hastenrath and Greischar, 1993b, 1994, 1995). Overall the method performs well, and the forecasts have served as input to the agricultural planning of the State of Ceará. Prior to the 1994 rainy season the method was transferred to INPE, and duplicate calculations have been carried out there for the 1994 and 1995 seasons. The up to date maintenance and generous sharing of key datasets by the colleagues of FUNCEME, UKMO, CIRES, and CPC, was essential to the real-time application of our climate prediction methods.

Acknowledgements: This study was supported by NSF Grant ATM-9101097. For the data acquisition for the real-time forecast we thank again the staff of FUNCEME, David Cullum, and Vernon Kousky.

References

Bottomley, M., Folland, C. K., Hsiung, J., Newell, R. E., Parker, D. E., 1990: *Global ocean surface temperature atlas.* Meteorological Office, Bracknell, UK, 313 pp.

Climate Analysis Center, NOAA, 1995: Climate Diagnostics Bulletin, January to June 1995. NOAA, Washington, D.C.

Greischar, L., Hastenrath, S., 1994: Multiple Regression and Discriminant Analysis to Predict Mar-Apr-May-Jun 1994 Rainfall in Northeast Brazil, NOAA Experimental Long-Lead Forecast Bulletin, Vol. 3 No. 1, pp. 19-20.

Greischar, L., Hastenrath, S., 1995: Multiple Regression and Discriminant Analysis to Predict Mar-Apr-May-Jun 1995 Rainfall in Northeast Brazil, NOAA Experimental Long-Lead Forecast Bulletin, Vol. 4 No. 1, pp. 32-33.

Hastenrath, S., Greischar, L., 1993a: Further work on the prediction of Northeast Brazil rainfall anomalies. J. Climate, 6, 743-758.

Hastenrath, S., Greischar, L., 1993b: The 1992 rainy season in Northeast Brazil: real-time forecast and verification. pp. 438-444 in Proceedings of Seventeenth Annual NOAA Climate Diagnostics Workshop, Norman, OK, Mar. 1993, Washington, D.C., 444 pp.

Hastenrath, S., Greischar, L., 1994: The 1993 rainy season in Northeast Brazil: real-time forecast and verification. pp. 382-385 in Proceedings of Eighteenth Annual NOAA Climate Diagnostics Workshop, Boulder, CO, Feb. 1994, Washington, D.C., 397 pp.

Hastenrath, S., Greischar, L., 1995: The 1994 rainy season in Northeast Brazil: real-time forecast and verification. pp. 160-163 in Proceedings of Nineteenth Annual NOAA Climate Diagnostics Workshop, College Park, MD, Feb. 1995, Washington, D.C., 497 pp.

Table 1. Results for 1995 from stepwise multiple regression SMR and neural networking N (ref. Hastenrath and Greischar, 1993a).

Model	predictors	predicted MJ index
1	OJ	+0.20
4	OJ, V	+0.16
10	OJ, ST29	+0.51
18	OJ, V, ST31	+0.23
25	OJ, V, ST29, PAC	+0.35
29	OJ, T31-NDJ, PAC	+0.30
32	T31-NDJ, PAC	+0.21
N	OJ, V, ST29, PAC	+0.38

Table 2. Results for 1995 from linear discriminant analysis LDA (ref, Hastenrath and Greischar, 1993a; quint boundaries for index MJ are approximately -0.56, -0.28, +0.05, +0.66).

LDA Model	predictors	predicted quint	
25	OJ, V, ST29, PAC	V	very wet
32	T31-NDJ, PAC	V	very wet

Table 3. Seasonal evolution of 1995 Nordeste rainy season. INDEX95 is rainfall index of indicated months in 1995. *x* and s are means and standard deviations, in mm with 1921-57 reference period. PAC95 denotes the equatorial Pacific SST anmoalies (°C) in 1995.

	ONDJ	J	F	M	A	M	J	MAMJ
INDEX95	+0.03	-0.12	+0.10	-0.02	+0.92	+1.75	+0.20	+0.92
x [mm]	132	75	139	202	166	84	35	486
s [mm]	98	70	104	117	100	66	28	229
PAC95 [°C]		+1.1	+0.8	+0.4	+0.3	+0.2	+0.3	

Table 4. Summary of 1992-95 Nordeste rainy season forecasts and verification.

Year	SMR and N forecasts range			LDA25	LDA32	Observed rainfall MAMJ	Quint
1995	+0.10	to	+0.51	V	V	+0.92	V
1994	+0.48	to	+1.06	V	V	+0.64	IV
1993	-0.50	to	-1.01	I	I	-1.24	I
1992	-0.62	to	+0.76	V	I	-0.83	I

A Review of SSM/I Derived Climate Products

Ralph Ferraro, Fuzhong Weng, Norman Grody, Arnold Gruber
NOAA/NESDIS/Office of Research and Applications
5200 Auth Road, Room 712
Camp Springs, MD 20746
rferraro@orbit.nesdis.noaa.gov

Alan Basist, John Janowiak
NOAA/Climate Prediction Center
Camp Springs, MD

C. Kondragunta
CICS/University of Maryland
College Park, MD

1. Introduction

Beginning in 1994, Special Sensor Microwave/Imager (SSM/I) derived products of monthly rainfall and snowcover were included in the Climate Prediction Center, monthly "Climate Diagnostics Bulletin" (CDB). Then, in early 1995, the product list was expanded to include oceanic cloud liquid water (CLW) and total precipitable water (TPW). These products are routinely generated by the NOAA/NESDIS/Office of Research and Applications, and an archive of these global monthly fields extends back to mid-1987. Because of the high stability of the SSM/I sensors, this eight-year data set provides invaluable information on the seasonal, annual, and interannual variability of these parameters.

Since these products are relatively new, it is the purpose of this paper to familiarize the workshop participants with the products and how they may be useful in climate applications. Examples will be shown to demonstrate the robustness of these products.

2. Data and Products

The first SSM/I instrument was launched on June 19, 1987 aboard the DMSP Block 5D-2 F-8 satellite. Other instruments have been launched into orbit aboard the F-10 (December 1990), F-11 (November 1991), F-12 (August 1994), and F-13 (March 1995) satellites,with the F-10 and F-13 currently operational. The SSM/I is a seven channel radiometer measuring earth emitted radiation at 19.35, 22.235, 37.0, and 85.5 GHz. All of the measurements are dual-polarization except at 22.235 GHz, where only vertical polarization is measured. The DMSP satellites operate in a sun-synchronous orbit with an orbital period of about 102 minutes and has an orbital swath width of 1400 km. More detail about the SSM/I can be found in Hollinger, et. al (1987).

The table below summarizes the monthly mean products that are presented in the CDB, while more details can be found in Ferraro et al (1996) and the algorithm references.

Product	Surface	Accuracy/Units	Reference
Rainfall	Land/Ocean	± 25 % (mm/mon)	Ferraro and Marks (1995)
Snow Cover	Land	± 10 % (frequency/mon)	Grody and Basist (1996)
Cloud Liquid Water	Ocean	± 20 % (mm)	Weng and Grody (1994)
Total Precipitable Water	Ocean	± 10 % (mm)	Alishouse et al, (1990)

The entire time series of the products are archived at the National Climatic Data Center (NCDC) and can be accessed via the world wide web at http://www.ncdc.noaa.gov.

3. Examples

Shown in Figure 1 is the December-February mean of each parameter calculated from the 1988 to 1994 base period. These "climatological" fields can be used to examine the temporal and spatial variability associated with the annual cycle. In addition, they can be used to examine interannual variability. For example, Figure 2 shows the rainfall and TPW anomalies (from the 1988-94 base period) for January 1989 (cold SST episode) and January 1992 (warm SST episode). Note the changes in the tropical and sub-tropical Pacific ocean in both the rainfall and TPW fields.

A more detailed analysis of the interannual variability of the entire time series is ongoing, as well as investigations on the relationship of the various parameters to one another and the underlying SST. We hope to present these findings at the next workshop.

4. References

Alishouse, J.C., S.A. Snyder, J. Vongsathorn, and R.R. Ferraro, Determination of oceanic total precipitable water from the SSM/I, *IEEE Tran. Geo. Rem. Sens.*, ***28***, 811-186, 1990.

Ferraro, R.R. and G.F. Marks, 1995: The development of SSM/I rain rate retrieval algorithms using ground based radar measurements. *J. Atmos. Oceanic Tech.*, ***12,*** 755-770.

Ferraro, R.R., F. Weng, N.C. Grody, and A. Basist, 1996: An eight year (1987-1994) time series of rainfall, clouds, water vapor, snow-cover, and sea-ice derived from SSM/I measurements. *In Press, Bull. Amer. Meteor. Soc.*

Grody, N.C. and A. Basist, 1996: Global identification of snow cover using SSM/I measurements. *In Press, IEEE Trans. Geo. Rem. Sens.*

Hollinger, J., R. Lo, G. Poe, R. Savage, and J. Pierce, 1987: Special Sensor Microwave/Imager User's Guide, Naval Research Laboratory, Washington, DC, 120 pp.

Weng, F. and N.C. Grody, 1994: Retrieval of cloud liquid water using the special sensor microwave imager (SSM/I). *J. Geophys. Res.*, **99**, 25535-25551.

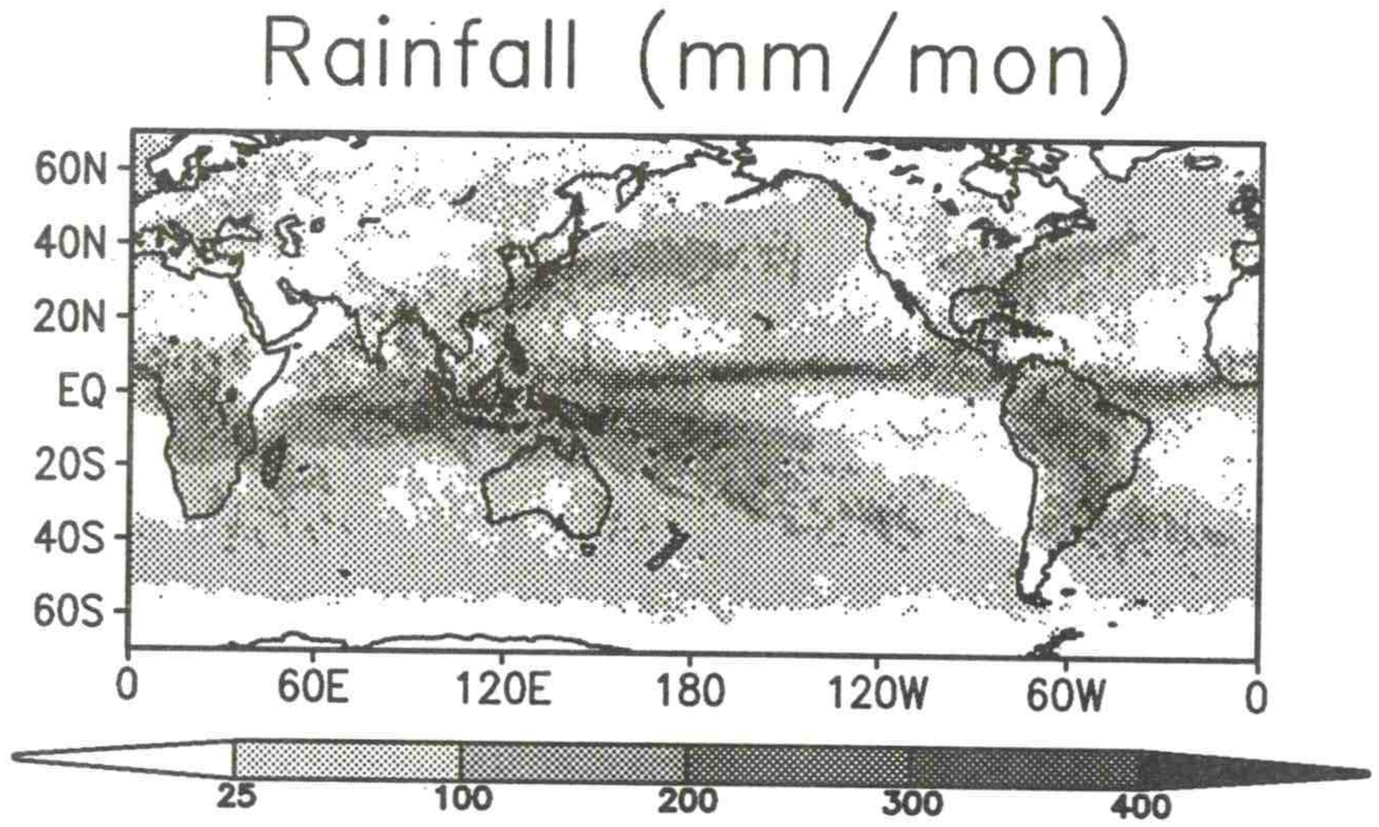

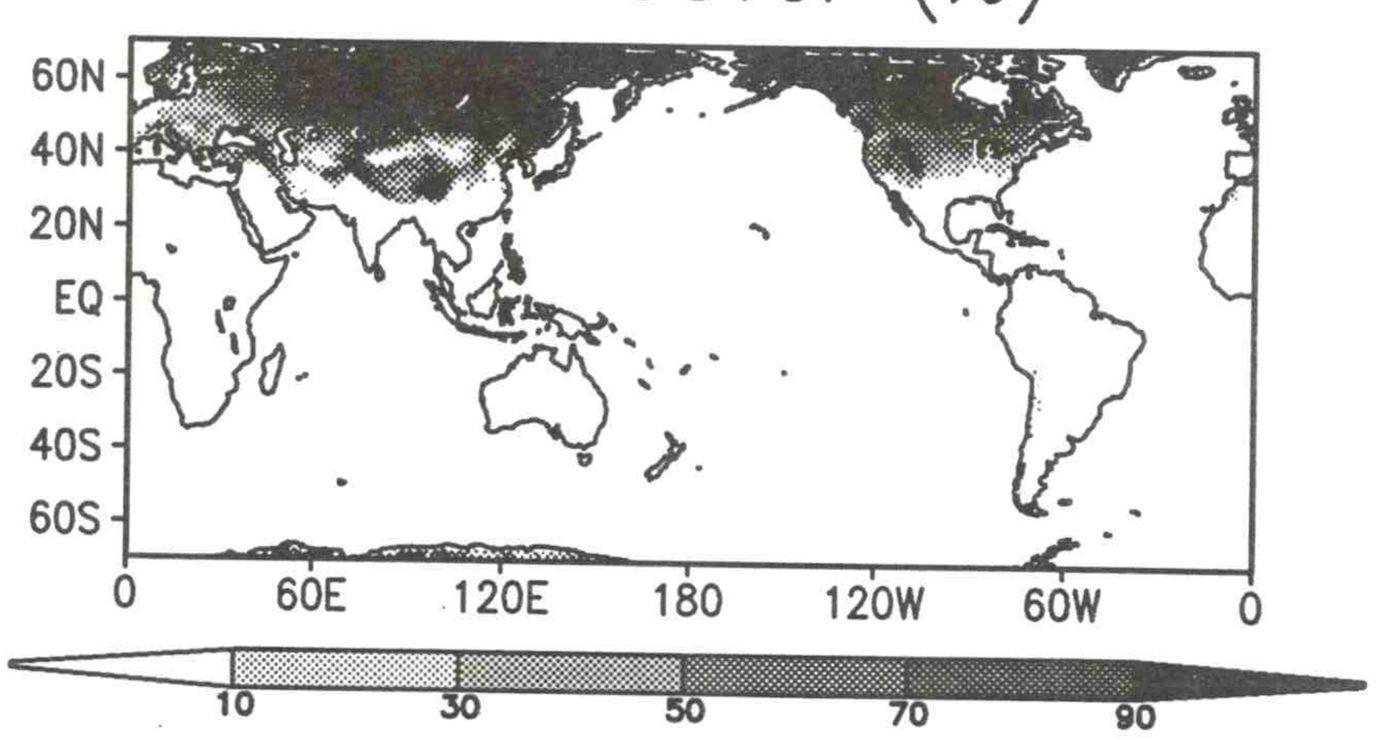

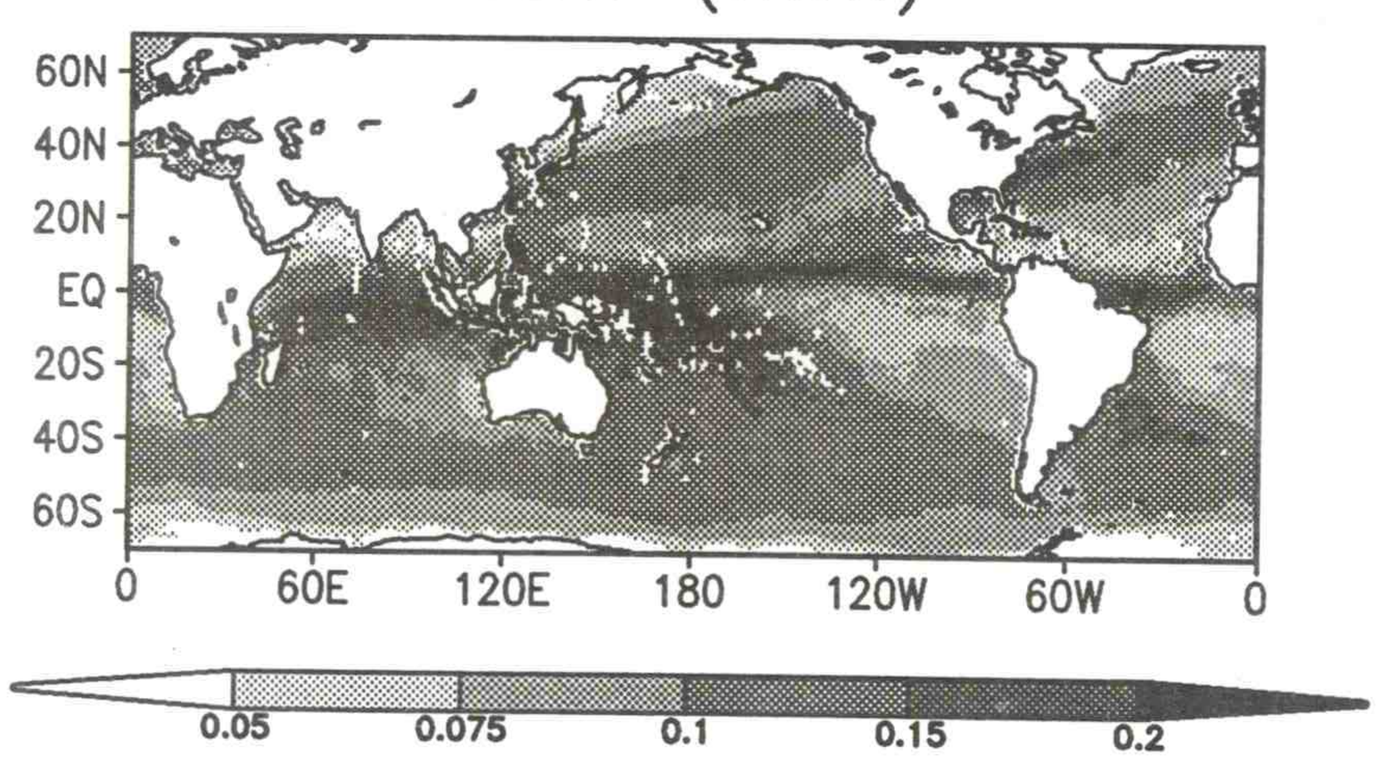

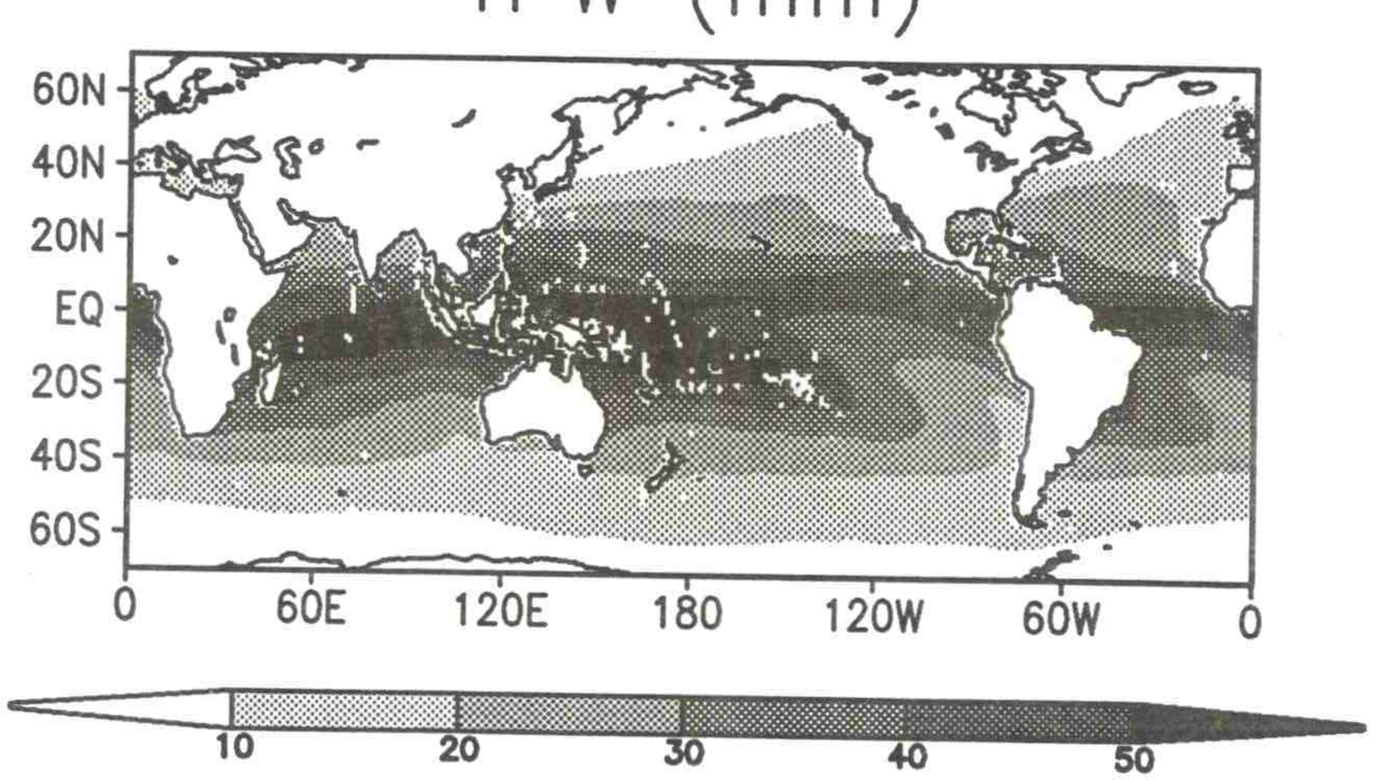

Fig. 1 SSM/I DJF Seasonal Climatologies

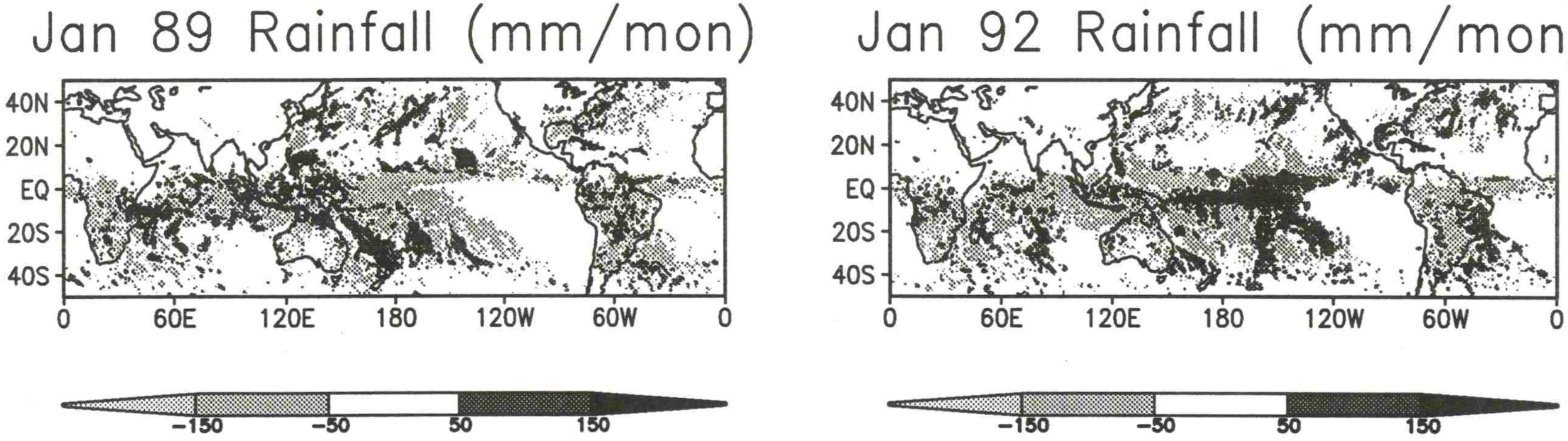

Fig. 2 SSM/I Rainfall and TPW anomalies

AN INFLUENCE OF THE 11-YEAR SUNSPOT CYCLE IN THE LOWER STRATOSPHERE-UPPER TROPOSPHERE ON THE NORTHERN HEMISPHERE

H. van Loon and K. Labitzke[1]
NCAR[2], Boulder, CO

1. The Annual Mean

A 10–12 year component in the interannual variation of the subtropical and tropical geopotential heights of the lower stratosphere and in the temperature of the upper troposphere has been in phase with the 11-year sunspot cycle (SSC) since the early 1950s when the observations began (e.g., van Loon and Labitzke, 1994; Labitzke and van Loon, 1995). The association between the SSC and the atmosphere is exemplified in Fig. 1 by lines of equal correlation between the annual mean 30-hPa geopotential height and the 10.7cm solar flux, which is a measure of the solar cycle. The 1% local significance level for the 37-year sample is 0.44 (shaded regions). Since we began analyzing this association in 1987, each additional year has strengthened the shape of the pattern and increased the significance of the correlations.

There is no significant correlation with the SSC in the arctic and subarctic; but the high correlations over large areas of the subtropics and tropics indicate that as much as 25% to 50% of the interannual variance of the heights in these regions was associated with the solar cycle during the years 1958–1994.

The time series in Fig. 2 — from a point near the Hawaiian Islands — consists of annual mean 30-hPa heights from the historical analyses made in the Stratospheric Research Group at the Freie Universität, Berlin. The figure shows the number of realizations in the series, and it illustrates the fact that the annual-mean heights were in phase with the sunspot cycle during the four maxima and minima of the cycle. The correlation at the point is 0.74. It is noteworthy that the 30-hPa heights returned to the same low level in each of the four solar minima, because it suggests that *there is zero forcing in the minima.*

The high values in 1982 and 1983 are owing to the warming of the lower tropical-subtropical stratosphere by the eruption of El Chichón (Labitzke *et al.*, 1983). They are not associated with the warm event in the Southern Oscillation which occurred in the same years: the signal of a warm event is to warm the tropical troposphere and cool the stratosphere above (van Loon and Labitzke, 1987; Hamilton, 1993).

The 10-12 year oscillation in the 30-hPa heights in Figs. 1 and 2 requires variability on the same time scale in the temperature below this level, or in the sea level pressure, or both. We have shown (Labitzke and van Loon, 1992) that the 30-hPa height oscillation is linked mainly to corresponding temperature variability in the middle and upper troposphere; below the crescent-shaped area of highest correlations in Fig. 1 the troposphere is thus warmer at the peaks than in the valleys of the SSC. This is demonstrated in Fig. 3 by means of the observations at two

---

[1] Affiliate Scientist. Permanent affiliation: Freie Universität, Berlin, Germany.
[2] The National Center for Atmospheric Research is sponsored by the National Science Foundation.

stations: The temperatures at Lihue and Truk Island have been divided into the extremes of the SSC — two years in each peak and valley of three solar cycles. At Truk the positive difference in the annual mean temperature (that is, higher temperature at the peaks than in the valleys of the SSC) is quite evenly distributed in the troposphere, though from May to October the highest values are in the upper troposphere. Since the station lies in an area with convection during most of the year, with the ITCZ nearest the island between May and October, we suggest that the temperature difference between the extremes of the SSC is due to a larger release of latent heat — and thus a stronger rising branch of the Hadley circulation — in the peaks than in the valleys of the cycle. At the levels about the tropopause the difference between maxima and minima of the SSC is negative because the dry air at these levels cools adiabatically when lifted in the convection, and the cooling is stronger in the presumably stronger convection at solar maxima.

The Hawaiian station lies in the subtropical high pressure belt where subsidence predominates; and the large positive difference between the extremes of the SSC is likely due to stronger downward motion in the sinking branch of the Hadley circulation at the peaks of the solar cycle than in the valleys.

2. Two-Month Averages

The high and statistically significant correlations between the SSC and the 30-hPa heights in Fig. 1 are owing to the fact that the pattern is the same in all months of the year (Fig. 4). The correlations are weakest in January-February, wax through spring to the highest values in July-August, and wane from summer to autumn.

References

Hamilton, K., 1993: An examination of observed Southern Oscillation effects in the northern hemisphere stratosphere. *J.Atmos.Sci.*, **50**, 3468–3473.

Labitzke, K., Naujokat, B., and M.P. McCormick, 1983: Temperature effects on the stratosphere of the April 4, 1982 eruption of El Chichón, Mexico. *Geophys.Res.Lett.*, **10**, 877–880.

Labitzke, K., and H. van Loon, 1992: Association between the 11-year solar cycle and the atmosphere. Part V: Summer. *J.Clim.*, **5**, 240–251.

Labitzke, K., and H. van Loon, 1995: Connection between the troposphere and stratosphere on a decadal time scale. *Tellus*, **47A**, 275–286.

van Loon, H., and K. Labitzke, 1987: The Southern Oscillation. Part V: The anomalies in the lower stratosphere of the Northern Hemisphere in winter and a comparison with the Quasi-Biennial Oscillation. *Mon.Wea.Rev.*, **115**, 357–369.

van Loon, H., and K. Labitzke, 1994: The 10--12 year Oscillation. *Meteorol.Zeitschr.*, **3**, 259–266.

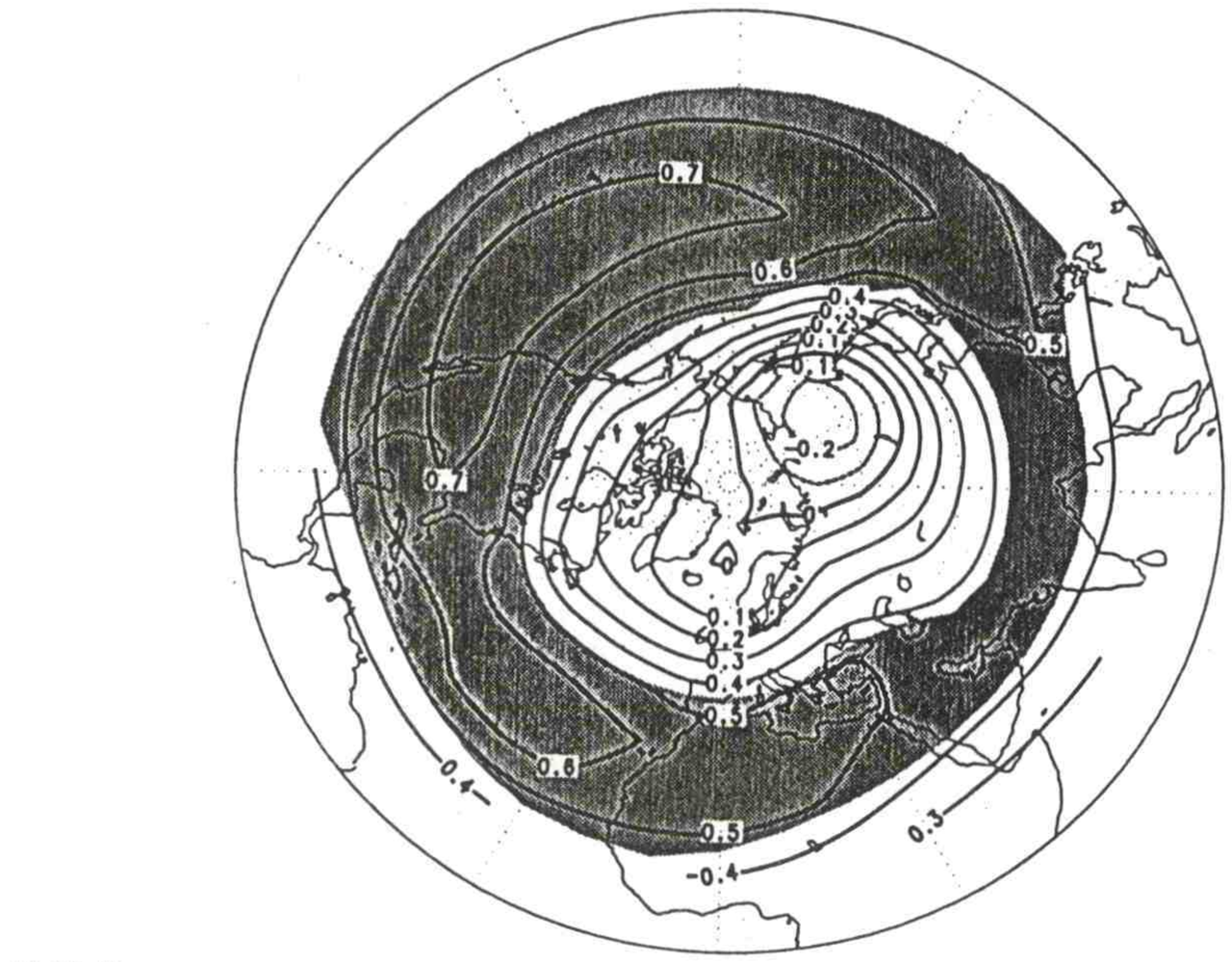

Figure 1. Correlation of the annual mean 30-hPa height, 1958--1994, with the 10.7cm solar flux. Shading denotes local significance at the 1% level. From van Loon and Labitzke, 1994, updated.

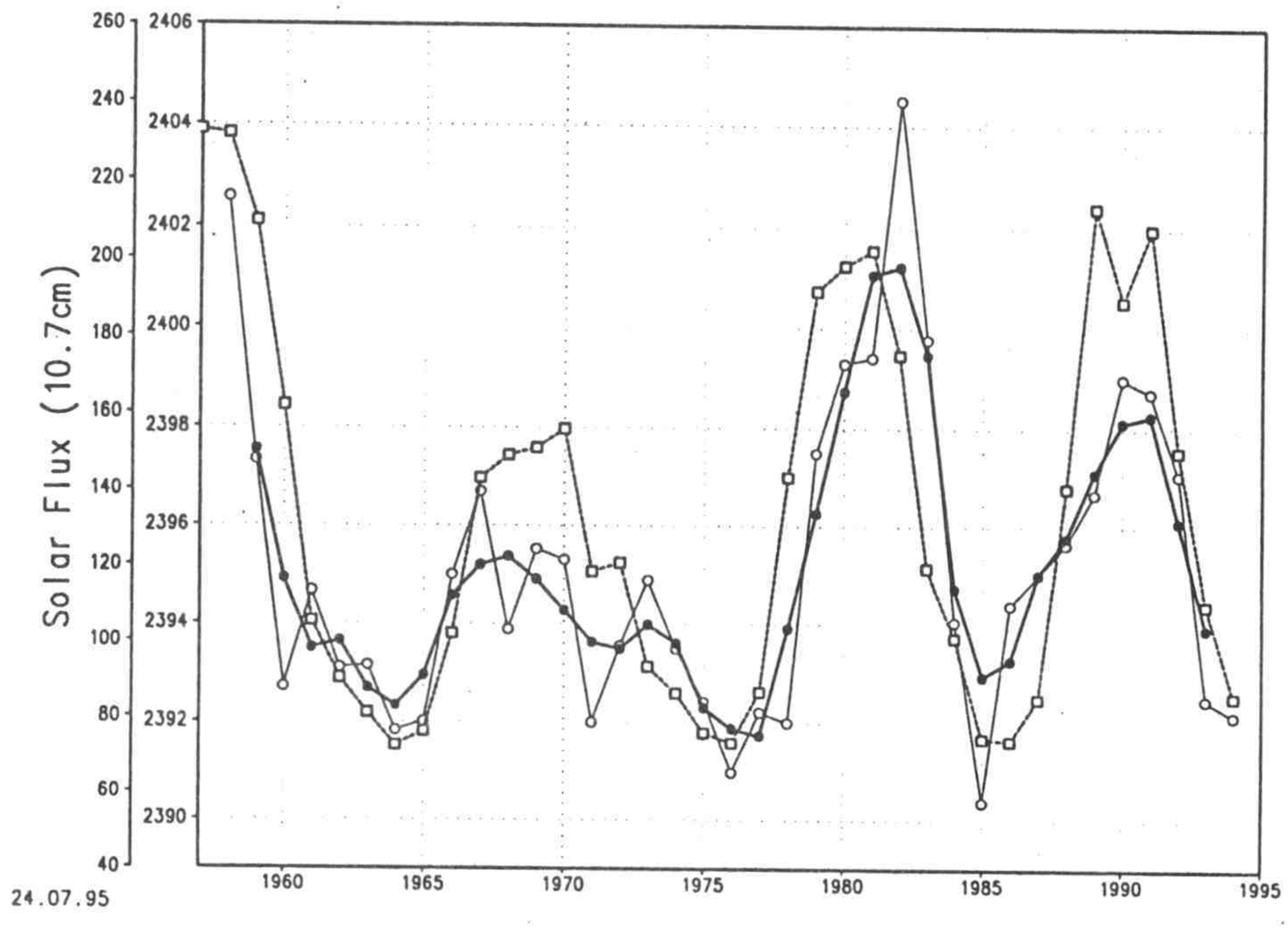

Figure 2. Time series of the 10.7cm solar flux (dotted line), the annual mean 30-hPa height at 30°N 150°W (thin solid line), and the three-year running means of this 30-hPa height (heavy solid line). The correlation (30-hPa height, 10.7cm flux) is 0.74; the 0.1% significance level is 0.56. From van Loon and Labitzke, 1994, updated.

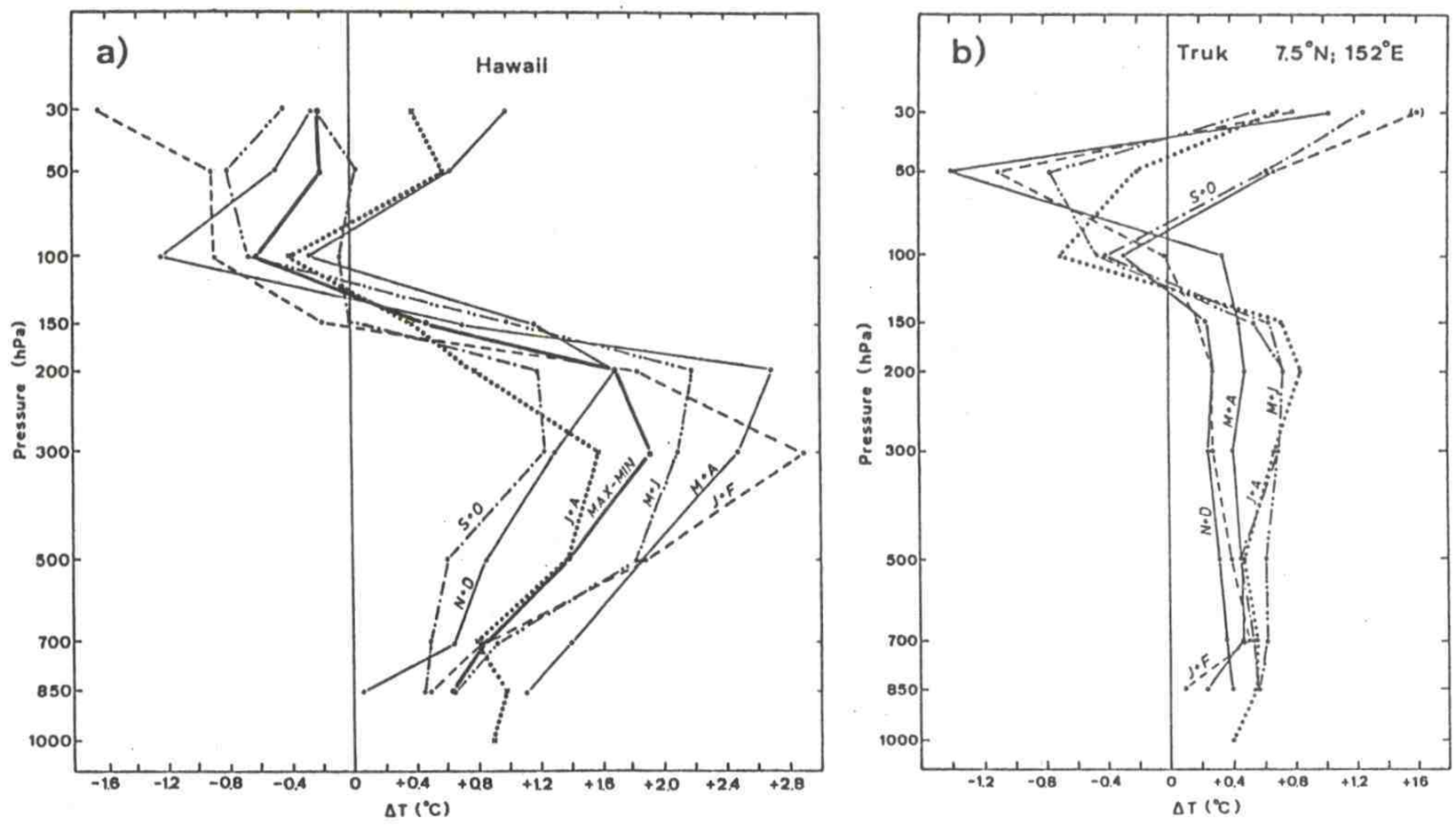

Figure 3. Two-month temperature differences (°C) between three maxima and minima in the 11-year solar cycle, at Lihue, Hawaii (left) and Truk. The heavy solid line at Lihue is the annual mean difference. From Labitzke and van Loon, 1995.

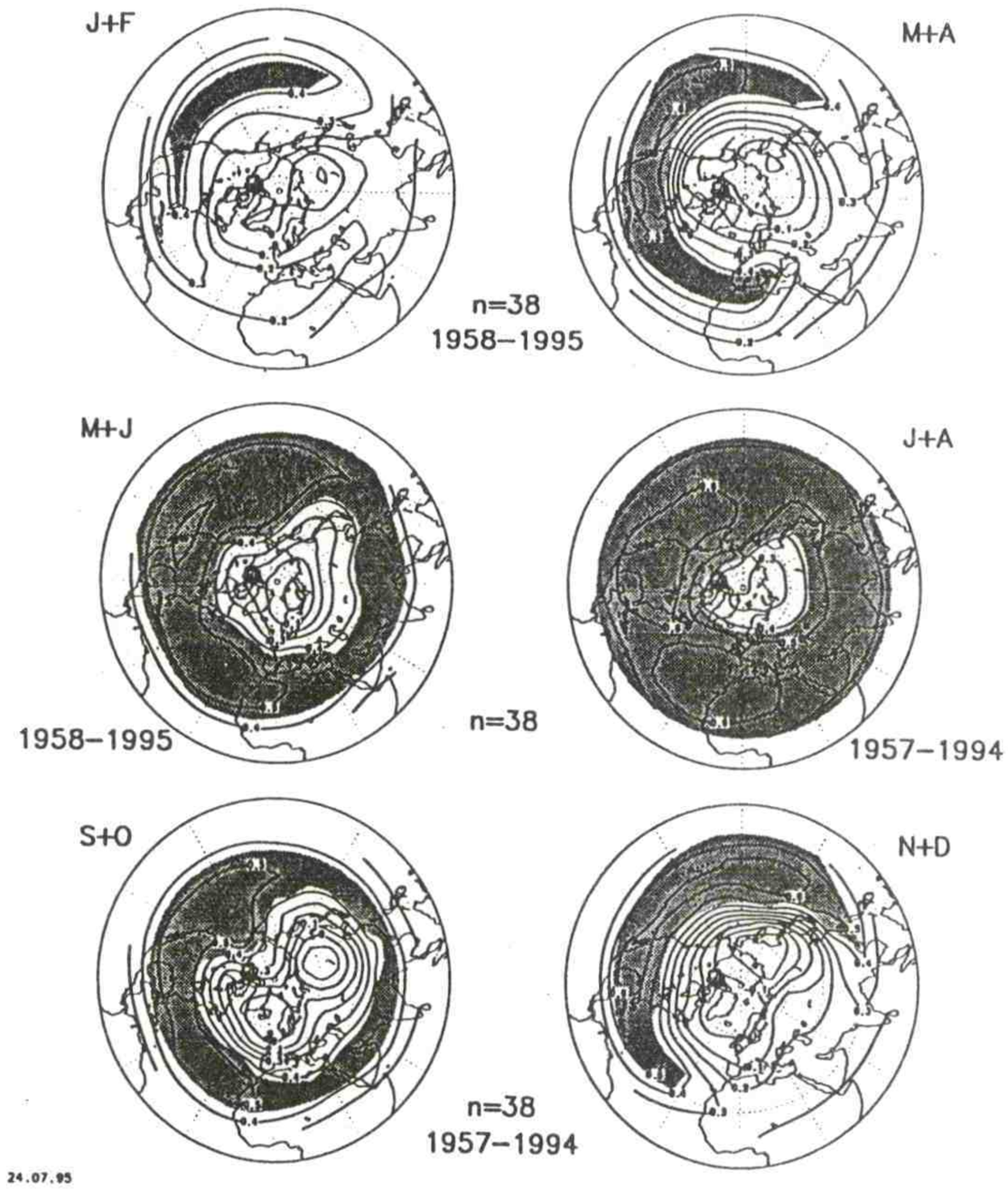

Figure 4. Correlations between the 10.7cm solar flux and two-month means of 30-hPa heights. Shading denotes local significance at the 1% level. From Labitzke and van Loon, 1995, updated.

A SPECTRAL ANALYSIS OF THE GEOS-1 ASSIMILATION AND SIMULATION

Wei Min, Siegfried D. Schubert and Chung-Kyu Park
Data Assimilation Office
Goddard Space Flight Center/NASA
Greenbelt, MD 20771

1. Introduction

A comparison is made of atmospheric variance fields for a five-year (March 1985 - February 1990) period based on 1) a reanalysis datasets produced with version 1 of the Goddard Earth Observing System (GEOS-1) data assimilation system, 2) a parallel five-year simulation with the GEOS-1 general circulation model (GCM) forced by the observed surface boundary conditions, and 3) the corresponding European Center for Medium Range Weather Forecasts (ECMWF) operational analyses. Our focus is to examine and compare the variability of the atmospheric circulation produced by the GEOS-1 DAS, the parallel GEOS-1 GCM simulation, and the ECMWF operational analysis. Comparison between assimilation and simulation enables us to evaluate the impact of the GCM on the assimilation products, to understand and to identify uncertainties associated with model bias and poor observational coverage.

2. Results

2.1. Kinetic energy spectra

Generally, the kinetic energy spectra show two maxima in the Northern Hemisphere, which correspond respectively to the eddy planetary-scale waves (n=1-3) and baroclinic waves (n=5-6), and one in the Southern Hemisphere (n=3-6). Large seasonal variations are evident in both hemispheres. In the tropic region, n=1 is dominant, which may be associated with the Madden-Julian oscillation (MJO). The differences between GEOS-1 assimilation and ECMWF analysis are comparably small. The ECMWF analyses generally have less kinetic energy than the GEOS-1 assimilation. The differences between the simulation and the assimilation are significant. For the GCM simulation, the kinetic energy at n=2-4 is larger than the assimilation while the synoptic-scale waves (n>4) have less energy than the assimilation.

2.2. Variance Analysis

The computation of the variance is based on the time Fourier analysis for each one-year period starting from March 1. The wind fields shows larger seasonal variations in both hemispheres. The centers of low-frequency oscillation and the storm tracks are evident in the GEOS-1 assimilation. The strong monsoonal variation of the total precipitation is clearly shown for the GEOS-1 assimilation. The seasonal variability of the outgoing longwave radiation (OLR) is comparatively strong

in the GEOS-1 assimilation, which is about twice as much as in the NOAA satellite measurements. This may indicate the effect of the model physics on the atmospheric variability.

For the GCM simulation, the variance of the 200 mb wind fields differs significantly from the assimilation. The dipole structure of the variance differences suggests a northward shift of the circulation system in the Northern Hemisphere. The differences between ECMWF analyses and the GEOS-1 assimilation are small except for the polar regions. It is also noted that in the midlatitudes of both hemispheres the ECMWF analyses constantly show smaller variance than the GEOS-1 assimilation, especially in the Southern Hemisphere.

2.3. Space-time Spectral Analysis

In this study, the space-time spectral analysis is adopted (Hayashi 1972). The datasets were broken up into warm seasons and cold seasons for both hemisphere. Each season consists of 180 days. The northern warm (southern cold) season start at April 1, and the northern cold (southern warm) season at October 1. We first apply the zonal Fourier transform to the data, and the resulting time series of the sine and cosine coefficients are utilized to estimate the power spectrum, quadrature spectrum and the co-spectrum.

The power spectra of 200 mb wind field show strong seasonal variations for both hemispheres. In the northern cold season, the westward traveling variance at n=1-3 is dominant with period larger than 20 days, and the eastward propagation is dominant for the synoptic-scale waves (n>3). In the southern hemisphere, both seasons show the dominance of the eastward propagation.

The differences of spectra density between hemispheres are also evident between datasets. The GCM simulation shows a shifting of variances in the wavenumber-frequency domain, which is mainly reflected in the eastward traveling variance. For the ECMWF analyses, the differences from the GEOS-1 assimilation is comparably small except for the Southern Hemisphere cold season. In the tropical region, the eastward traveling waves with a 40-60 day period (Madden-Julian Oscillation) are well presented in the ECMWF analyses and the GEOS-1 assimilation although there are some differences.

The impact of a gravity-wave drag parameterization was tested with the GEOS-1 GCM. It is found that the GCM bias can be significantly reduced with the gravity-wave drag parameterization.

DAILY CYCLES OF SSTS AND SURFACE WINDS OVER THE TROPICAL PACIFIC FROM THE TAO MOORED BUOY ARRAY

CLARA DESER AND CATHERINE SMITH

CIRES
University of Colorado
Boulder, CO 80309
e-mail : cxd@cdc.noaa.gov, cas@cdc.noaa.gov

Recently, Deser (JGR, 1994) documented the diurnal cycle in surface winds over the equatorial Pacific during June-August 1992 using hourly data from 14 moored buoys. The purpose of this study is to extend the results of Deser (1994) to a larger area of the tropical Pacific using a more extensive network of buoys from the Tropical Ocean Atmosphere (TAO) moored array, maintained by the Pacific Marine Environmental Laboratory. We also examine the spatial pattern of diurnal SST variability.

Figure 1a shows the average daily march of the zonal wind component during May-October 1994 at 37 buoys east of the dateline within 8° of the equator. The daily march is dominated by the semi-diurnal component (amplitude ~ 0.2 m/s), with maxima at ~ 3 and 15 hrs local time, and minima ~ 9 and 21 hrs local time. Figure 1b shows the average daily march of the meridional wind component during May-October 1994, east of the dateline. In contrast to the zonal wind component, the meridional wind exhibits a predominantly diurnal component, with amplitude ~ 1 m/s. The phase of the meridional wind diurnal cycle is variable, but with a general tendency for the strongest southerlies around midday north of the equator and in the late afternoon south of the equator.

Figure 2 shows the mean surface wind vectors at 00, 06, 12, and 18 hrs local time for May - October 1994. The winds were reconstructed from the first harmonic of the average daily marches shown in Fig. 1. The mean daily winds have been removed. Strong equatorial divergence is apparent at 06 hrs local time, with strong convergence 12 hrs later. The daily cycle in equatorial divergence is ~ 30% of the daily mean (not shown). The plausible association of the diurnal cycle in surface wind divergence and the diurnal cycle of deep convection in the ITCZ to the north remains to be investigated.

The theory of thermal tides in the atmosphere, driven by the absorption of solar radiation by ozone and water vapor, predicts a semi-diurnal surface pressure wave in the tropics (amplitude ~ 1 mb) that migrates westward with the Sun (c.f. Chapman and Lindzen, 1970). A simple linear inviscid zonal momentum balance using the observed globally-averaged semi-diurnal pressure wave along the equator yields a zonal wind semi-diurnal cycle that is in excellent agreement with observations (not shown).

The shape of the daily march of SST in the tropical Pacific is similar at all locations, with a minimum ~ 7 am and a maximum ~ 3 pm local time (not shown). Figure 3a shows the spatial distribution of the average daily SST range (defined as the maximum minus the minimum) during May - October 1994. The daily SST range is ~ 0.25 - 0.65 °C, with the larger values in the western Pacific and along the equator in the eastern Pacific.

The daily range of SST is determined primarily from a balance between incoming solar radiation and wind-stirring (c.f. Bond and McPhadden, 1995). The larger the insolation, the larger the daily SST range; the stronger the wind speed, the smaller the daily SST range due to the enhanced downward mixing of heat. Figure 3b shows the distribution of surface wind speed cubed (mechanical wind mixing is proportional to the cube of the wind speed) during May - October 1994. In general, there is an inverse

relationship between the daily SST range and the mean wind speed, with weaker winds and larger SST ranges in the western Pacific and in a narrow band along the equator in the eastern Pacific. The spatial correlation between the SST daily range and mean wind speed cubed is -0.81.

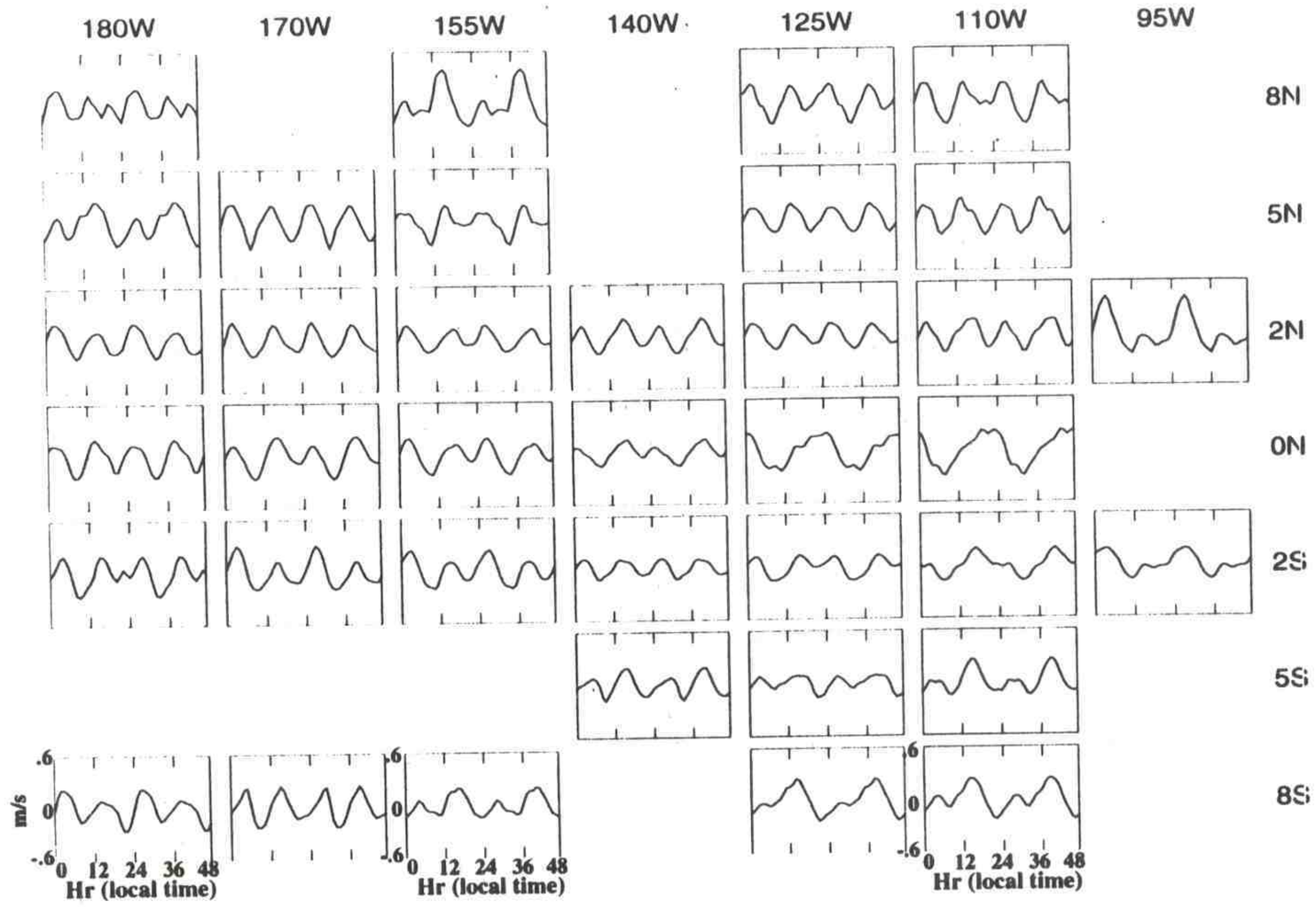

Figure 1 (a). Average daily march of the zonal wind component during May–October 1994. All boxes are drawn to the same scale, with local time on the abscissa (0–48 hrs; the 24 hr period is repeated for clarity) and wind speed on the ordinate (-0.6 to 0.6 m/s). The daily mean winds have been removed. Positive (negative) values indicate westerly (easterly) winds relative to the daily mean.

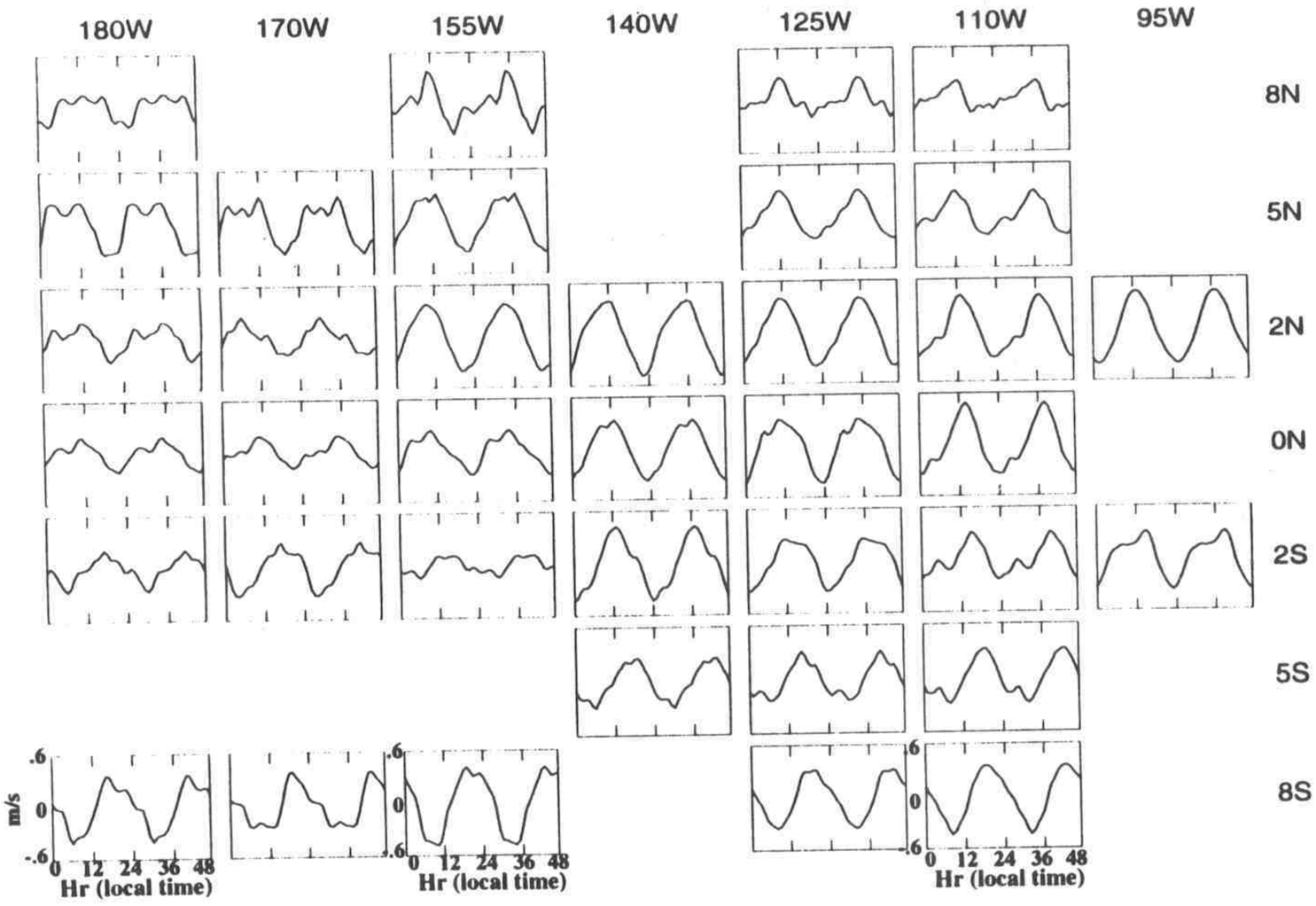

Figure 1 (b). As in (a) but for the meridional wind component. Positive (negative) values indicate southerly (northerly) winds relative to the daily mean.

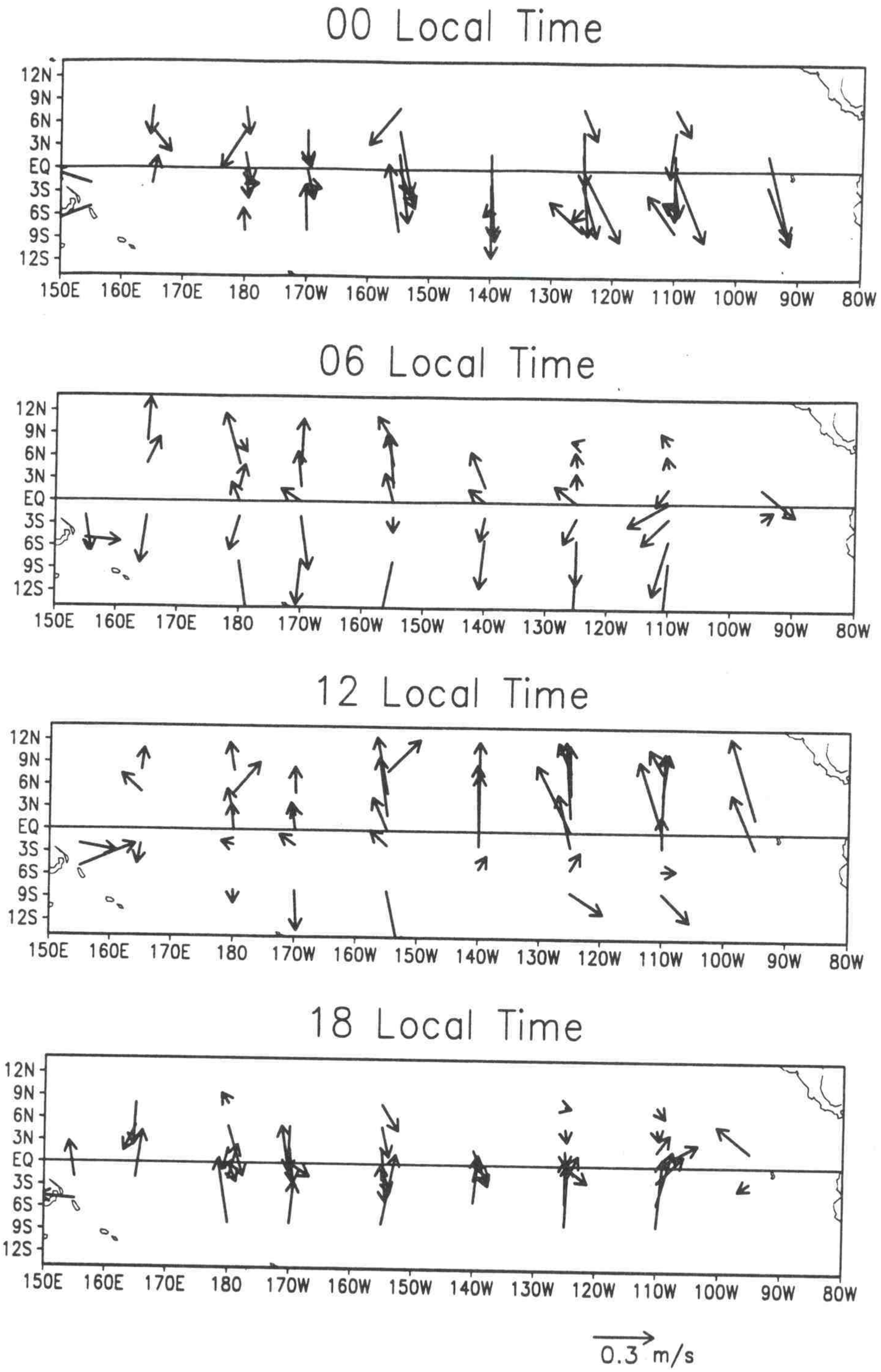

Figure 2. Mean surface wind vectors at 00, 06, 12, and 18 hrs local time for May–October 1994. Winds were reconstructed from the first harmonic of the average daily marches shown in Fig. 1. The mean daily winds have been removed.

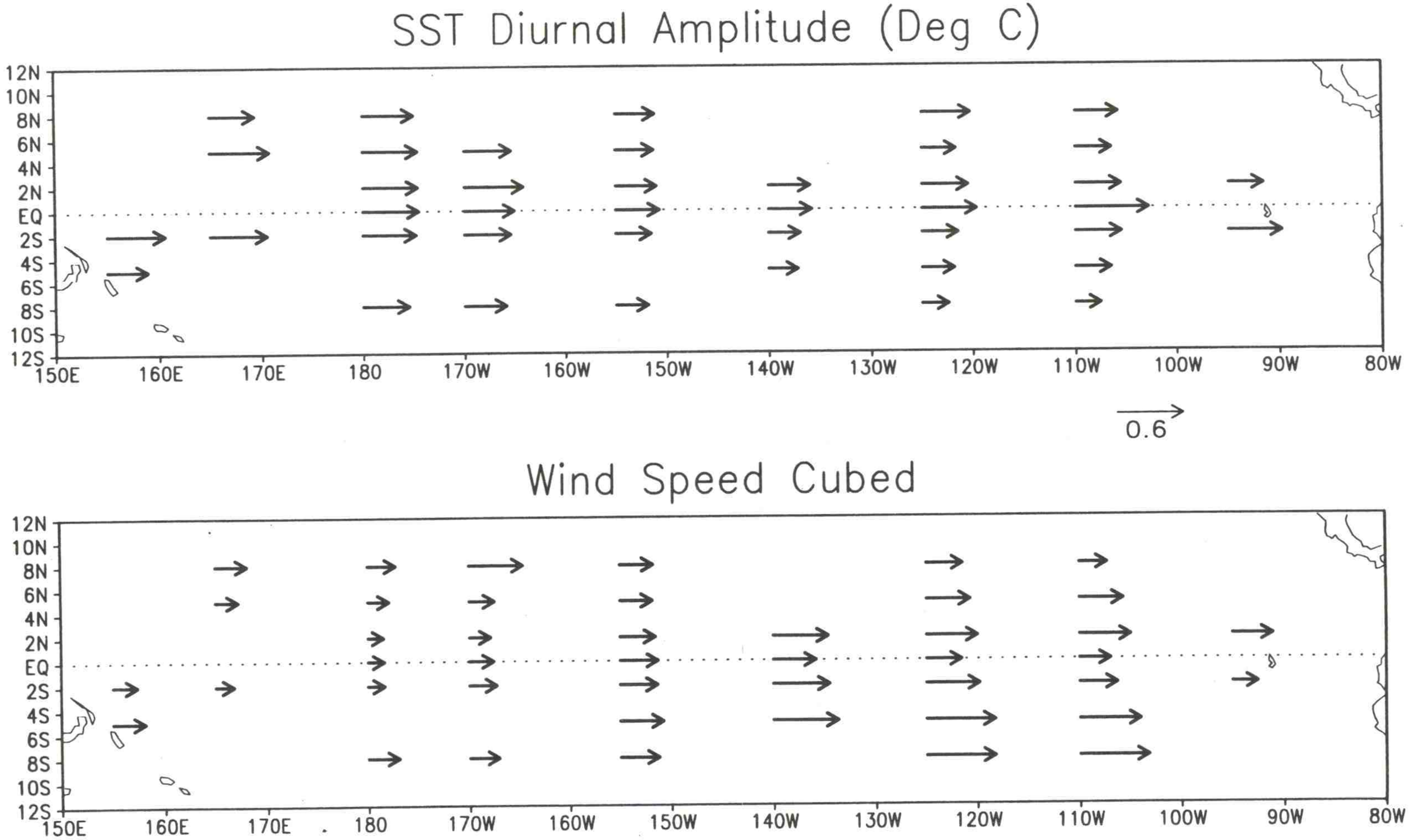

Figure 3. (Top) Mean daily SST range (°C) during May-October 1994. The length of each arrow is proportional to the daily SST range (see scale at lower right). (Bottom) Mean wind speed cubed during May-October 1994.

ASSIMILATION VARIABILITY IN THE GEOS–1 DATA ASSIMILATION SYSTEM

Meta Sienkiewicz
Data Assimilation Office
NASA/Goddard Space Flight Center
Greenbelt, MD, 20771

The Data Assimilation Office (DAO) at NASA/Goddard Space Flight Center has used the Goddard Earth Observing System–Version 1 Data Assimilation System (GEOS–1 DAS) to produce a multi-year assimilated dataset for climate research. Our use of a single assimilation system to analyze the the entire period is intended to reduce spurious variability due to system changes. Other sources of variability are possible, however. Changes in data coverage and gaps in the data record will allow assimilation fields to drift in areas where little or no data is being assimilated. Also, since we have had to perform the assimilation in separate segments rather than in one continuous block, there will be periods where (in effect) differing initial conditions are used. This research addresses how changes such as these could affect assimilations produced by the system.

The sensitivity of the GEOS–1 DAS to data gaps and changes in initial conditions was assessed using an ensemble of assimilation runs. The purpose is to see how quickly and to what extent differences between the assimilations are reduced by assimilation of observational data. A 'control' assimilation and eight perturbed assimilations with varying length of initial data gaps, using a lower resolution ($4° \times 5°$) version of the GEOS system, were run for a 1-month period and compared. The variation in height fields between ensemble members decreased quickly in the Northern Hemisphere mid-latitudes and tropics, but differences in height fields persisted through the assimilation period in polar regions and in the Southern Hemisphere south of 30°S. Monthly mean fields of height showed persistent differences between the assimilations in the polar regions; monthly mean upper-tropospheric u-component fields also showed variations in the tropics. Figure 1 shows the mean precipitation rate (mm/day) for the one-month integration, and standard deviation of precipitation calculated across the nine-member ensemble. In the tropics and Southern Hemisphere the standard deviation is 5–10% of the monthly mean value.

One factor contributing to assimilation variability is the difference in quality-control decisions between assimilations. Three perturbed assimilations were run using quality control decisions forced by the 'control' assimilation; Fig. 2 demonstrates the effects of quality-control decisions. In Fig. 2(a) zonal RMS differences in estimated 300 mb height analysis errors between two assimilations are plotted; these differences indicate where different quality-control decisions were made. The corresponding zonal RMS differences in 500 mb height are plotted in Fig. 2(b). Fig. 2(c) shows RMS differences between the 'control' assimilation and a perturbed assimilation forced to use the same data as the 'control'. The height differences were smaller for the runs with forced quality-control but still remained significant after two weeks of assimilation.

Development of the GEOS system has continued since the version used for the DAO reanalysis. A later system, GEOS–1.2, includes fourth-order differencing in the momentum equations and reduced filtering at the poles. Three assimilations were performed using this later version of the GEOS system; these assimilations demonstrated improvements in assimilation convergence in the polar regions and in the Southern Hemisphere. Fig. 3 shows zonal RMS height differences at 300 mb for assimilations with the new system. Comparing Fig. 3(a) with Fig. 2(b) and (c) we see that the reduced polar filtering has enabled the data influence to be much more effective at bringing the 'control' and perturbed assimilations together. Even with a 96–hour initial data gap (Fig. 3(b)) the GEOS 1.2 assimilation converges fairly quickly.

These experiments show (as has our experience) that differences between assimilations in polar regions (particularly 'noisiness') in the GEOS–1 DAS can persist for relatively long periods. The newer assimilation system (GEOS–1.2) is much improved over the previous version. Performing parallel assimilations in this fashion can be useful in determining the effectiveness of future improvements in our data assimilation system.

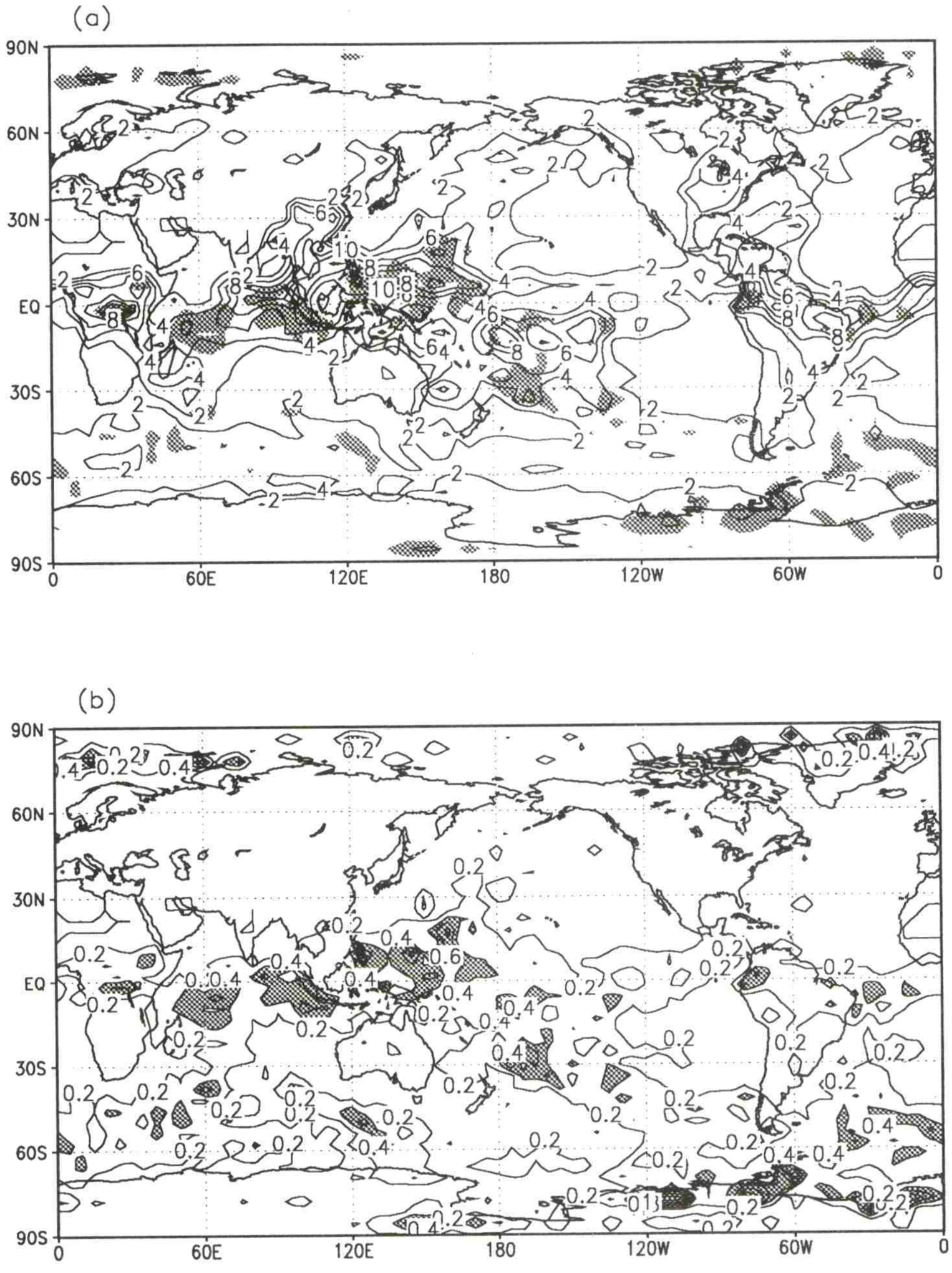

Figure 1: (a) Ensemble average of mean total precipitation (contour interval 2 mm day^{-1}) and (b) standard deviation of mean total precipitation (contour interval 0.1 mm day^{-1}) for mean total precipitation calculated over the one-month period 8 Apr 1985 – 7 May 1985. Standard deviations greater than 0.4 mm day^{-1} are shaded.

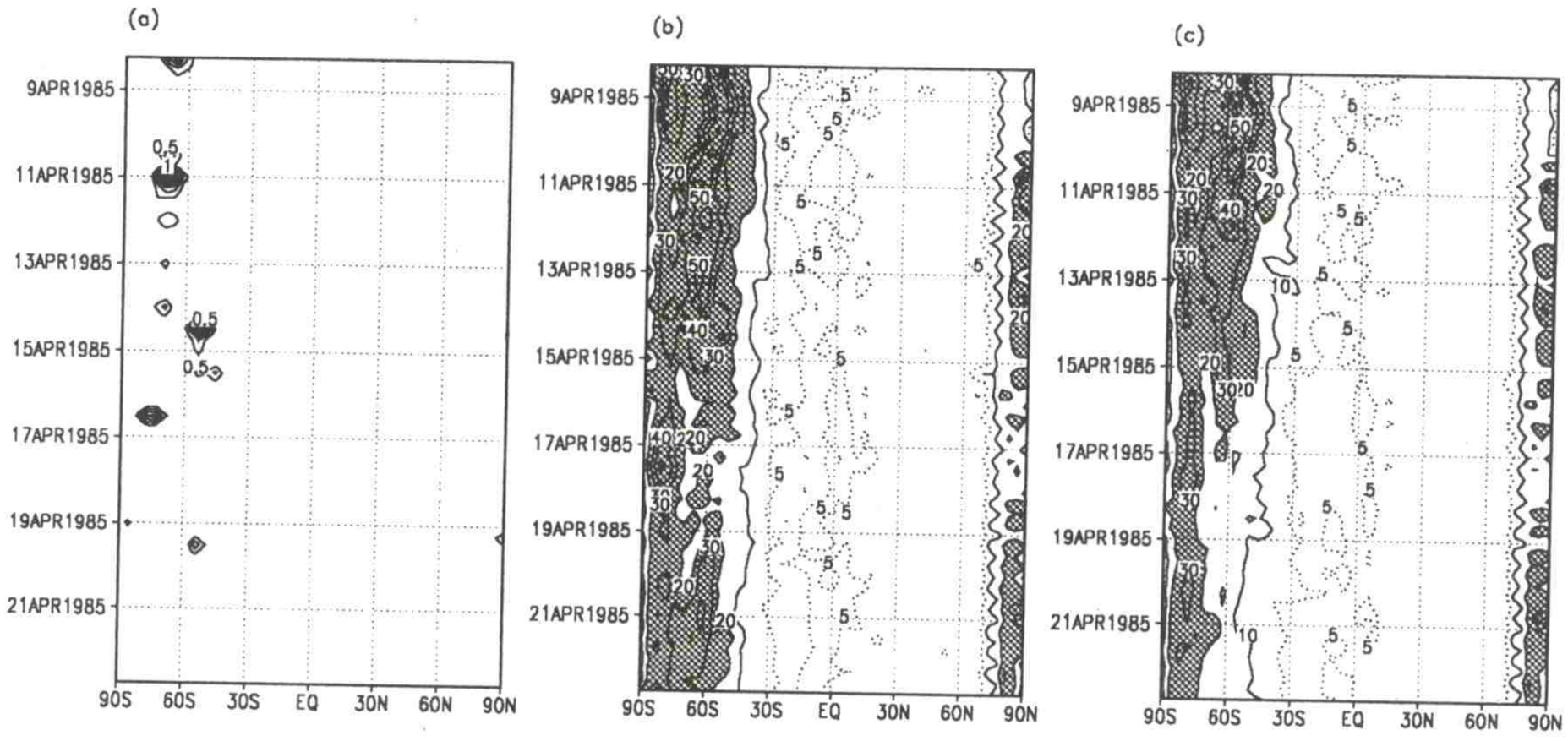

Figure 2: Time series of zonal root-mean-square differences of 300 mb analysis fields between the control run and perturbed runs with 48-hr initial data gap for assimilations with independent and forced quality control. (a) Rms differences in height analysis error (square root of average error variance). Contour interval is 0.5 m. (b) Rms height differences with independent quality control. Contour interval is 10 m. (c) Rms height differences with forced quality control. Contour interval is 10 m. Rms height differences greater than 20 m are shaded.

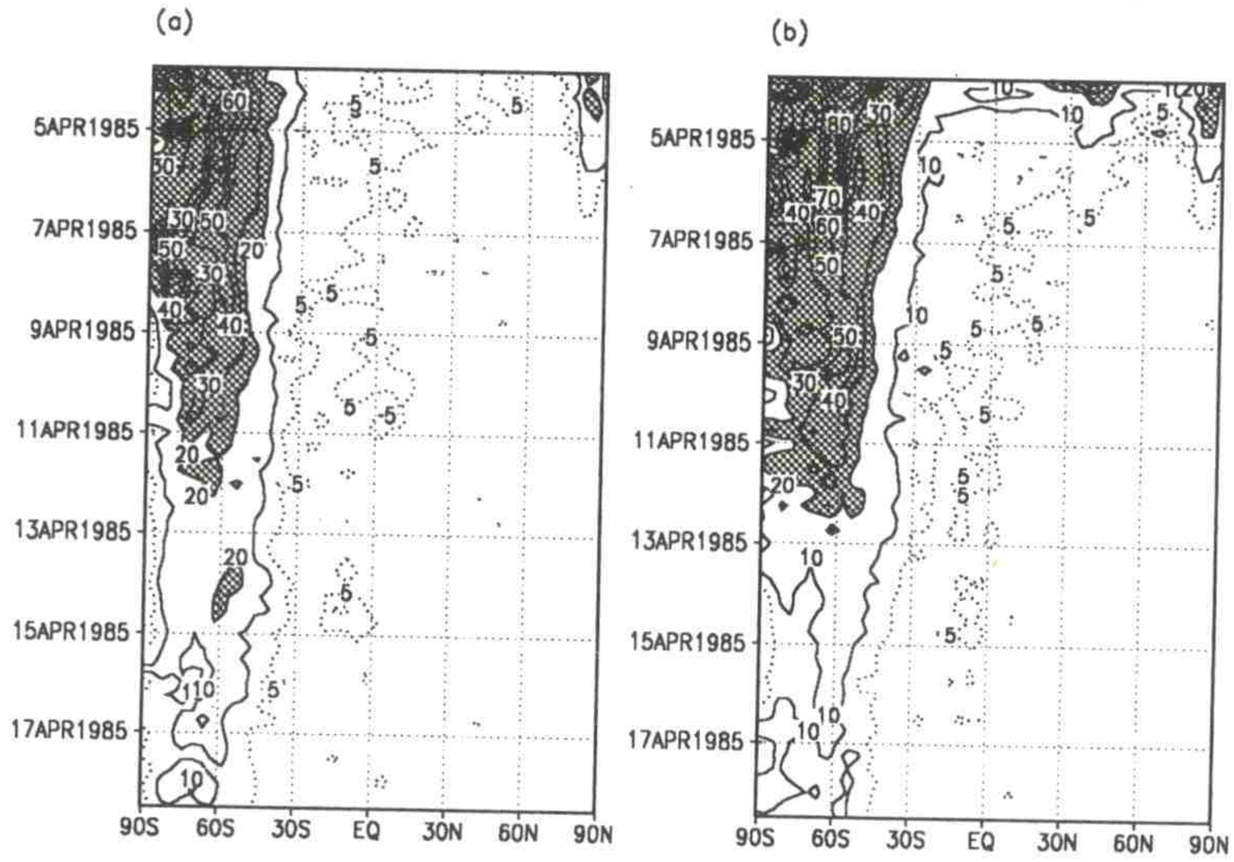

Figure 3: Time series of zonal root-mean-square differences of 300 mb height between the control run analysis field and the analysis fields from (a) a perturbed assimilation with 48-hr initial data gap and (b) a perturbed assimilation with 96-hr initial data gap, for assimilations using GEOS-1.2. Contour interval is 10 m. Rms differences greater than 20 m are shaded.

Potential predictability of tropical storms in an ensemble of forecasts

F. Vitart, J.L Anderson, W.F Stern
GFDL/NOAA

1 Introduction

S. Manabe described for the first time in 1970 the presence of disturbances reminiscent of observed tropical storms in a very low resolution GCM. Since that time, numerous studies have examined these model tropical disturbances in a variety of GCMs. Some of these studies have argued that the model disturbances are dynamically consistent with observed tropical storms, although this remains a point of active debate.

In the present study, a 9-member ensemble of 10-year integrations (1979-1989, the AMIP period) of a T42 atmospheric model forced by observed SSTs has been produced. The potential predictability of the tropical storms produced by this ensemble has been examined for each ocean.

2 Automatic procedure for tracking model tropical storms

An automatic procedure for tracking model tropical storms has been developed using data for 1980 from the first member of the ensemble. The criteria defining this automatic procedure have been chosen and adjusted to give the most realistic tracks from this data set. The main problem was to eliminate extratropical disturbances without eliminating tropical disturbances. The required presence of a warm core was used in this automatic procedure as the principal way to eliminate extratropical disturbances.

When 'tropical' storms have been located for each day, an automatic procedure is applied to find their trajectories. For a given storm, we examine the position of the closest storm which appeared the following day. If the distance between their centers is less than 800 Km they are considered to belong to the same trajectory. Finally, we consider only the trajectories that last more than two days and that have a velocity at 850 MB within a 7x7 grid box centered on the maximum vorticity point larger than 17 m/s during at least two days.

3 Tropical storm distribution in the T42 model ensemble

The automatic procedure for tracking tropical storms has been applied to a 9-member ensemble of a t42 atmospheric model with 18 vertical levels forced by monthly SSTs.

Figure 1 depicts the tropical storm trajectories for the first experiment of the year 1980. The large majority of them form in the same regions and at the same perioad as real tropical storms, but in the model, some tropical disturbances are created : in the southern Atlantic (about 1 per year), in the Eastern Atlantic (it happened only twice during the 81 years), over land (about twice per year) and too far eastward in the south Pacific.

The chi-square test was used to define if the distribution of the 9 members for a particular year was statistically different from the climitological distribution. The results for each basin are presented in table 1. If we consider that there is potential predictability for a significance larger than 95%, then the years 1982, 1986, 1987 and 1988 display for most of the basins the strongest potential predictability while the years 1983 and 1984 display less potential predictability. The Eastern Pacific and Western Pacific have a very strong potential predictability for most of the years, but the Northern and Southern Indian basins have a very poor potential predictability.

Figure 2 shows the ensemble forecasts of the number of tropical storms

over the western Atlantic. Table 2 displays the correlation between the observations and the mean of the 9-member ensemble. Over the Western Atlantic and Western Pacific, the model simulates realistic interannual variations of number of tropical storms. These variations have the incorrect sign over Southern India and South Pacific basins.

4 Conclusion

This experiment showed that the model we used had some skill in simulating interannual variability of the number of tropical storms since their potential predictability is particularly strong during these events. Over the Western Atlantic and Western Pacific, this interannual variability is very close to that observed. This model may have some skill in predicting interannual variations of tropical storms over these two basins.

Table 1 : Significance of Chi-Square test between one year and the climatology

	1980	1981	1982	1983	1984	1985	1986	1987	1988
Atlan	**0.94**	**0.992**	**0.996**	**0.26**	**0.36**	**0.95**	**0.92**	**0.91**	**0.76**
W Pac	**0.14**	**0.992**	**0.996**	**0.999**	**0.915**	**0.85**	**0.987**	**0.991**	**0.999**
N Ind	**1.0**	**0.84**	**0.39**	**0.24**	**0.77**	**0.88**	**0.07**	**0.93**	**0.21**
E Pac	**0.36**	**0.57**	**1.**	**0.999**	**0.94**	**0.996**	**0.999**	**0.999**	**0.999**
S Ind	-	**0.34**	**0.44**	**0.89**	**0.83**	**0.91**	**0.90**	**0.98**	**0.37**
Aus	-	**0.98**	**0.99**	**0.87**	**0.28**	**0.04**	**0.56**	**0.26**	**0.99**
S Pac	-	**0.02**	**0.16**	**0.75**	**0.57**	**0.97**	**0.91**	**0.999**	**0.995**
World	-	**0.17**	**0.23**	**0.87**	**0.29**	**0.60**	**0.97**	**0.84**	**0.994**

Table 2 : Linear correlations between model tropical storm and observed tropical storm number

	WORLD	*West Atlantic*	*East Pacific*	*West Pacific*	*North India*	*South India*	*Austral. Basin*	*South Pacific*
CORRELATION	**0.41**	**0.53**	**0.545**	**0.66**	**-0.63**	**-0.66**	**0.57**	**-0.775**
SIGNIFICANCE (Student's test)	**0.69**	**0.86**	**0.88**	**0.945**	**0.93**	**0.93**	**0.87**	**0.977**

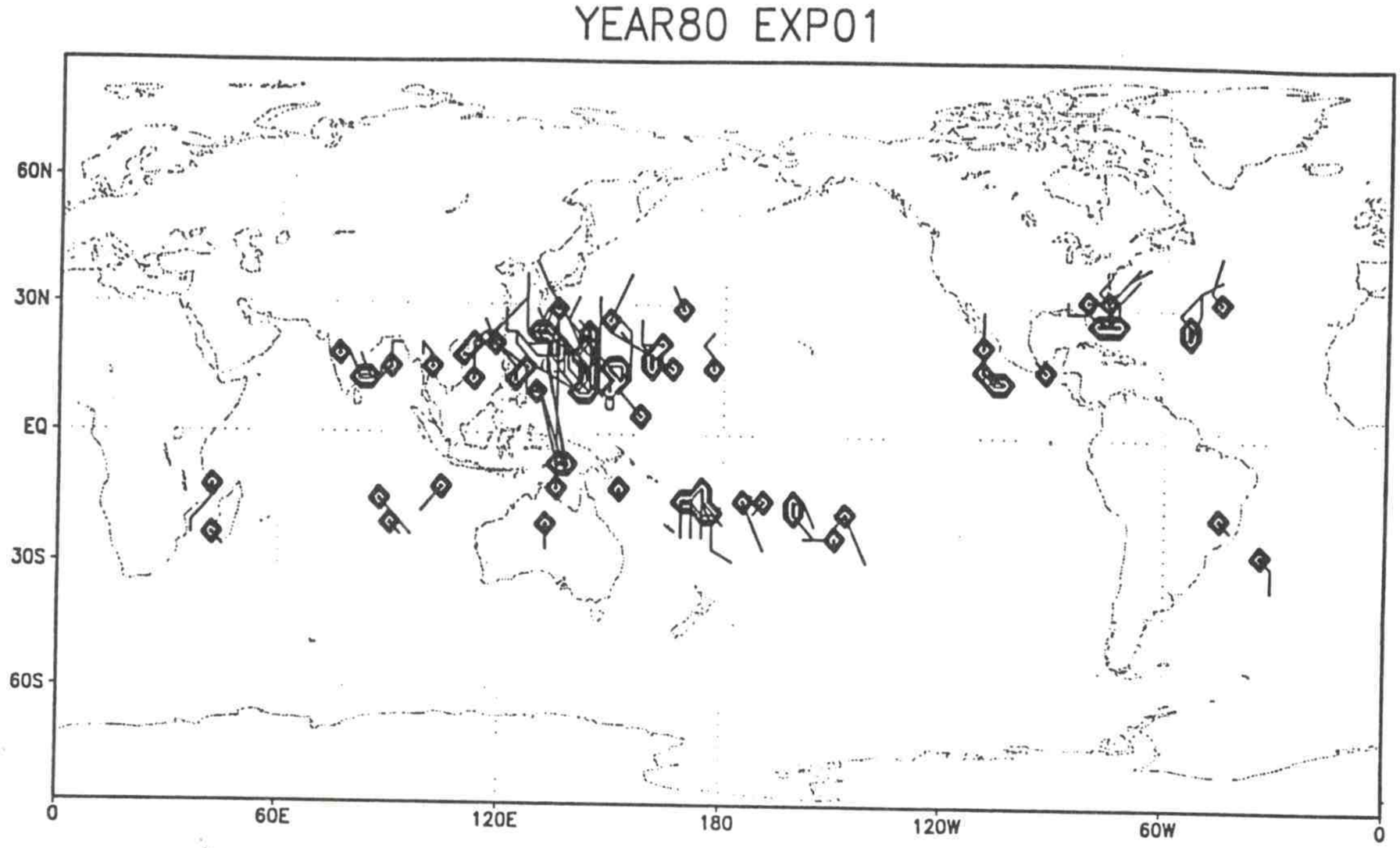

Fig1 : Tropical storm origines and trajectories for the year 1980 of the first element of the ensemble

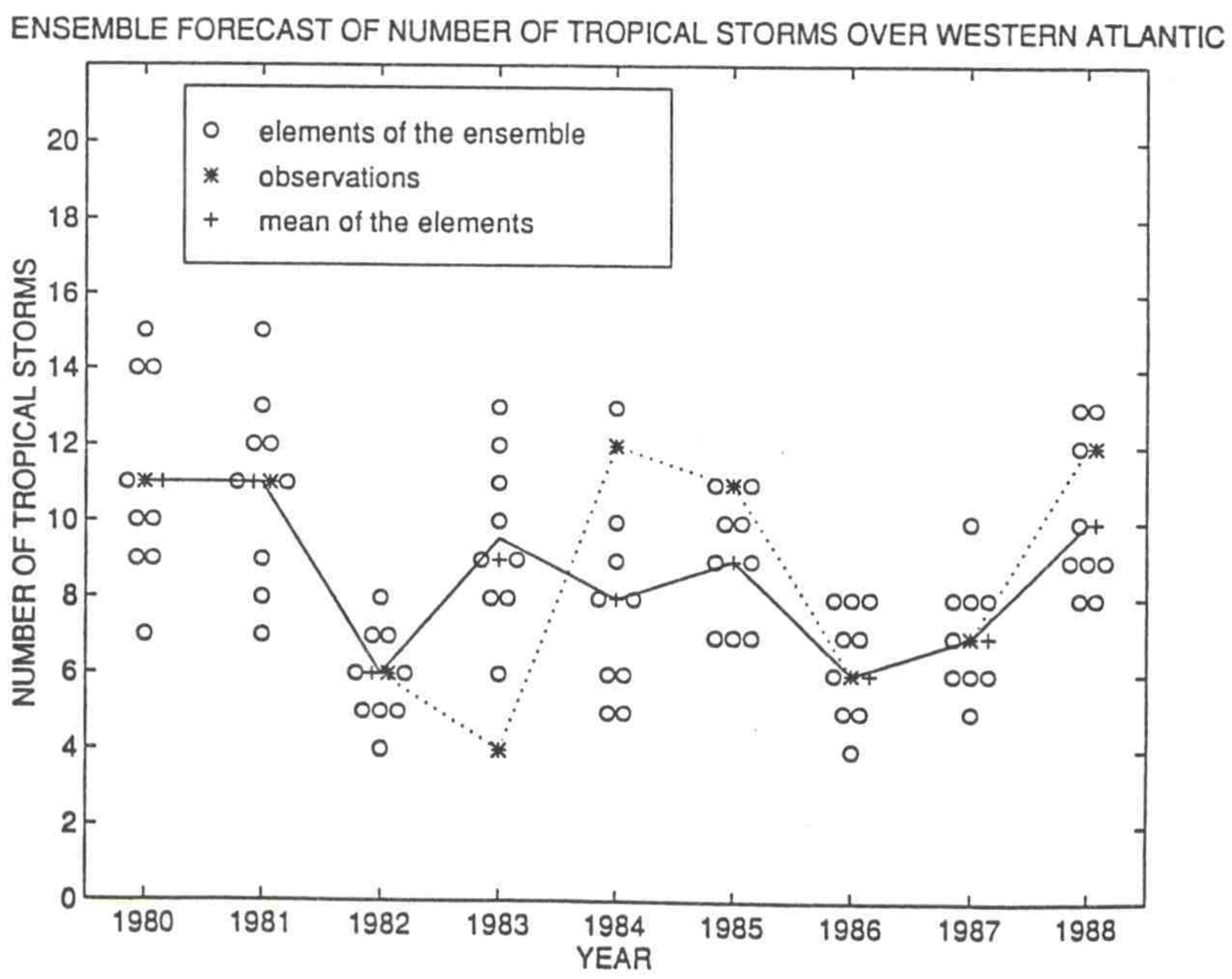

Fig2 : Number of tropical storms over western Atlantic per year for all the elements of the ensemble, their mean and the observations

Statistical Analysis of Chilean Precipitation Anomalies associated with ENSO

Rodrigo H. Nuñez, Todd S. Richards and James J. O'Brien
Center for Ocean-Atmospheric Prediction Studies 020 Love Bldg.
The Florida State University
Tallahassee, FL 32306 - 3041, U.S.A.

1.0.- INTRODUCTION

The purpose of this study is to analyze the seasonal and interannual effect of ENSO on rainfall in Chile by means of multiple statistical techniques. An Empirical Orthogonal Function analysis, complemented by a Bootstrap analysis (Efron, 1993), will be used to obtain a better understanding of the interannual and seasonal precipitation anomalies associated with ENSO.

2.0.- DESCRIPTION OF DATA AND STATISTICAL ANALYSIS

2.1.- Description of Data

The precipitation data was obtained from the Dirección Meteorológica de Chile in Santiago, Chile. Monthly precipitation anomalies were calculated for nine stations covering the Central (Subtropical) and Southern (Temperate Oceanic) regions of the country, for the 34-year period from 1961 to 1994.

The Sea Surface Temperature Anomalies (SST) data was obtained from the Japanese Meteorological Agency (JMA) and represents a region located between 4° N and 4° S and between 150° W and 90° W (figure 2). The SST anomalies for the period 1949-1994 were filtered using a five-month running average to calculate the JMA - SST anomaly Index, later used to classified the precipitation data (conceptually similar to the Southern Oscillation Index published by the U.S. - National Meteorological Center).

2.2.- Empirical Orthogonal Function (EOF) Analysis

In order to obtain the spatial and temporal patterns of the precipitation anomalies, an EOF analysis was performed on the nine stations. The result of the analysis was a set of nine rainfall-anomaly spatial patterns (eigenvectors), each associated with a rainfall-anomaly time series. Each eigenvector is modulated by its corresponding time series. Physical patterns are then assigned to particular eigenvectors that account for a large fraction of the variance.

The first 2 EOF modes account for 79.35 percent of the variance (first mode 61.09 percent and second mode 18.26 percent, respectively). It is very unusual for a data set to be dominated by two patterns accounting for 80 percent of the variance.

2.3.- Bootstrap Technique "Margin Probability Analysis"

The second aspect of this study involves investigation into the seasonal impact of ENSO on precipitation in Chile. The technique used is based on Richards (1995) and Sittel (1994). In order to complete such an analysis, the data are first separated into ENSO categories based on the Japanese Meteorological Agency index (JMA Atlas, 1991). This index defines ENSO years based on sea surface temperature anomalies in the previously defined JMA region. According to the index, an El Niño event occurs when the five month running average of SST anomalies is greater than 0.5°C for at least six consecutive months. In addition, the series of six consecutive months must begin before October, and

must include October, November, and December. A similar definition is applied to El Viejo years denoted by SST anomalies less than -0.5°C for at least six consecutive months. Further, years that fail to fit into one of the categories are defined as Neutral years. The resulting categorized years are listed in Table 1. For the purpose of this study, an ENSO year is defined from October to September so as to include the entire event.

In order to determine the seasonal impact of ENSO on Chilean rainfall, each of the years of this study are subdivided into three-month seasons. For each of these seasons, three-month means of the data are calculated. Next, a statistical resampling technique known as bootstrapping is applied to the seasonal means to compensate for the small number of years within each ENSO category. That is, the bootstrap technique involves repeated sampling with replacement of the existing nine El Niño years within the period of study, to provide a more robust estimate of the population statistics for those ENSO years.

The bootstrapping process is completed for the ten three-month seasons from October-November-December (OND) through July-August-September (JAS) within each of the three ENSO categories at all nine stations. The means which are produced are based on one million samples. By comparing the means from each ENSO category, during each of the ten seasons, the seasonal effects on ENSO are determined for the individual stations (figure 3, a and b).

Comparing the means from each ENSO category provides insight into the relationship between ENSO and Chilean precipitation, however, this study goes a step further. Probability estimates of above or below average precipitation associated with ENSO years are computed by calculating marginal probabilities.

Because precipitation is not normally distributed, and is in fact more log-normal in shape, a more easily defined and variable distribution is used to estimate the continuous probability distributions of the data. This study utilizes a least squares approximation to fit Weibull distributions as detailed by Pavia and O'Brien (1986). The Weibull curves were chosen because they are easy to define and can approximate the curve for the precipitation data. Each Weibull curve is defined by two parameters, a shape parameter, and a scaling factor. By least squares fitting these Weibull parameters to the precipitation data, continuous distribution curves result for each station, three-month period, and ENSO category. The area under these curves is then utilized to calculate probability estimates. By computing such probabilities, the variability of the data is accounted for, and more insight into the magnitude and timing of precipitation anomalies in Chile associated with each ENSO category is provided (figure 4, a and b)

3.0.- CONCLUSIONS

The EOF analysis gives us temporal patterns (figure 2, a and b) that are easily recognized as being modulated by an ENSO signal. The spatial pattern of EOF-1 (figure 1a) indicates that all stations will behave in the same way for any specific given temporal perturbation. In contrast, the spatial pattern of EOF-2 (figure 1b) indicates that the four southern most stations will behave oppositely as compared with the stations located in the Central region of the country. The spatial pattern of EOF-2 is supported by the results of previous studies (Pittock, 1980; Rutllant and Fuenzalida, 1991) and it is interpreted as the geographic separation of two well defined climatic regions. As a result, the impact of ENSO on the Southern region is less severe than in the Central region. The spatial distribution of EOF-2 shows that EL Niño event will produce a negative precipitation anomaly that tends to cancel a portion of the positive precipitation anomaly of EOF-1, resulting in a less severe positive anomaly. During El Viejo years, the effect will be opposite, keeping the resulting negative precipitation anomaly smaller.

As a result of applying bootstrap analysis, we discovered definite temporal (seasonal) patterns within the data that can be related to ENSO. Stations in the Central region experienced an increase in precipitation during El Niño winter and spring seasons. Conversely, the Southern region experienced an increase in precipitation during El Viejo summers.

5.0.- ACKNOWLEDGMENTS

Support for this research through the following agencies and their grants is gratefully acknowledged: 1) Chilean Navy - Hydrographic and Oceanographic Service, 2) Department of Defense grants N00014-85-J-1240 and N00014-93-1-1132.

El Niño (09)	Neutral (18)	El Viejo (07)
1963	1961	1964
1965	1962	1967
1969	1966	1970
1972	1968	1971
1976	1974	1973
1982	1977	1975
1986	1978	1988
1987	1979	
1991	1980	
	1981	
	1983	
	1984	
	1985	
	1989	
	1990	
	1992	
	1993	
	1994	

Table 1: List of ENSO years.

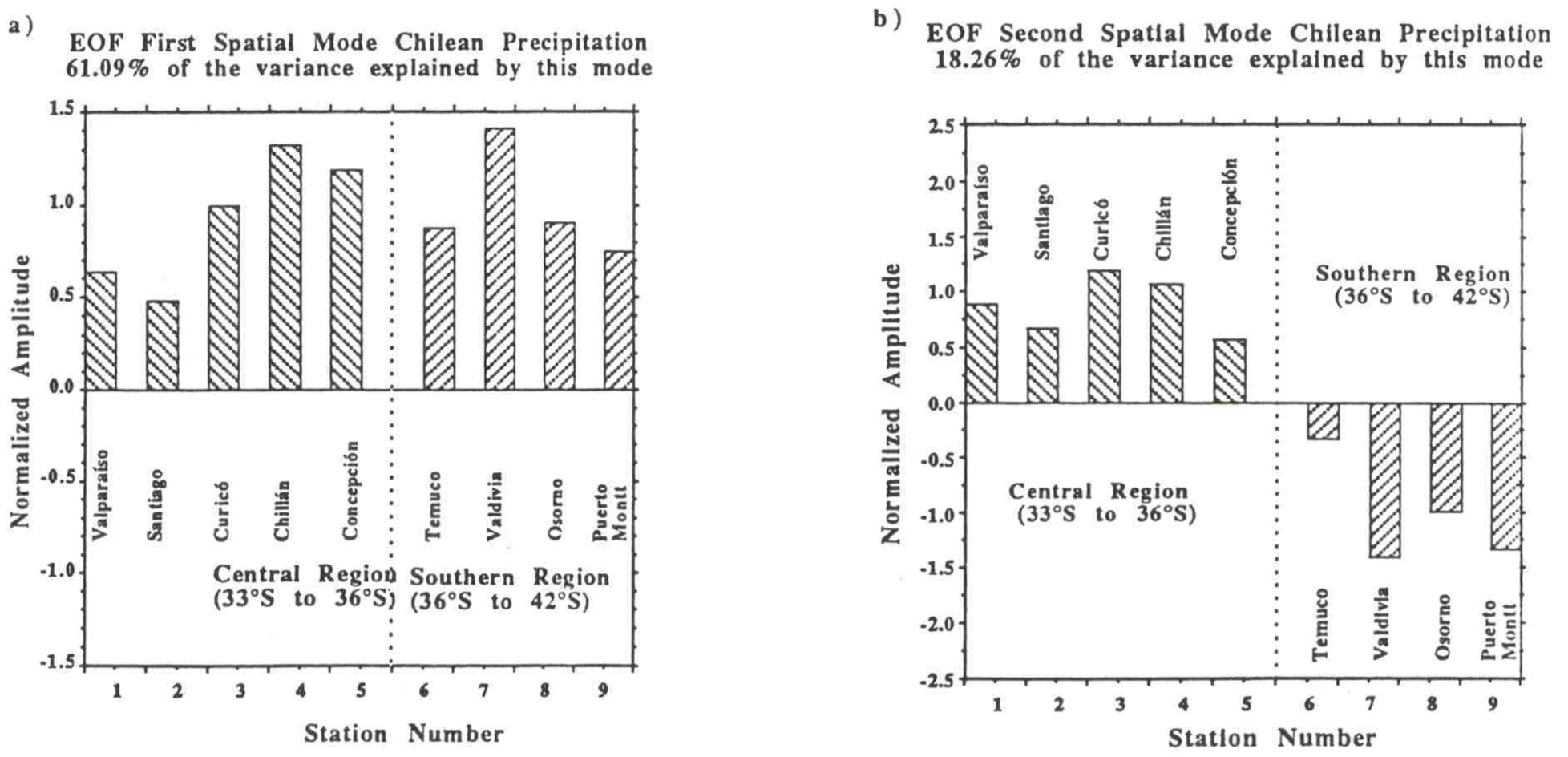

Figure 1 : Spatial Pattern for a) First and b) Second EOF Mode.

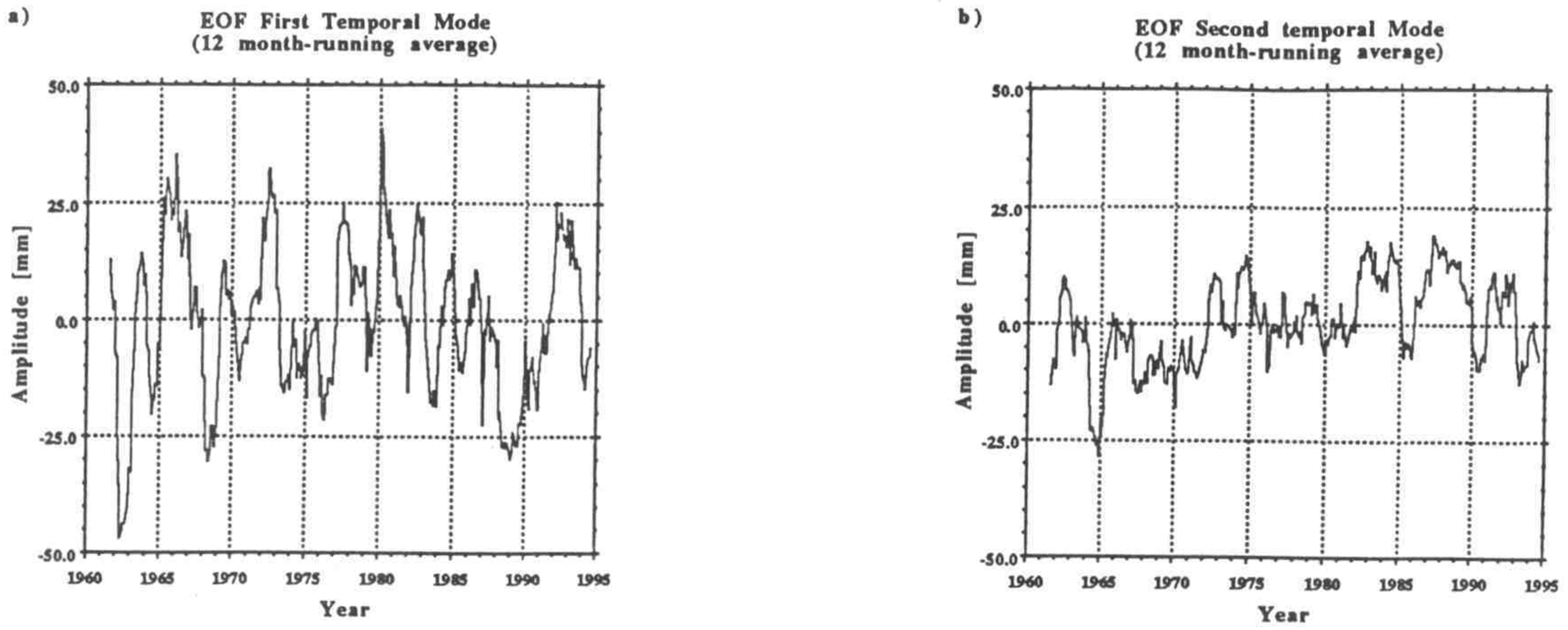

Figure 2 : Time Series for a) First ans b) Second EOF Mode.

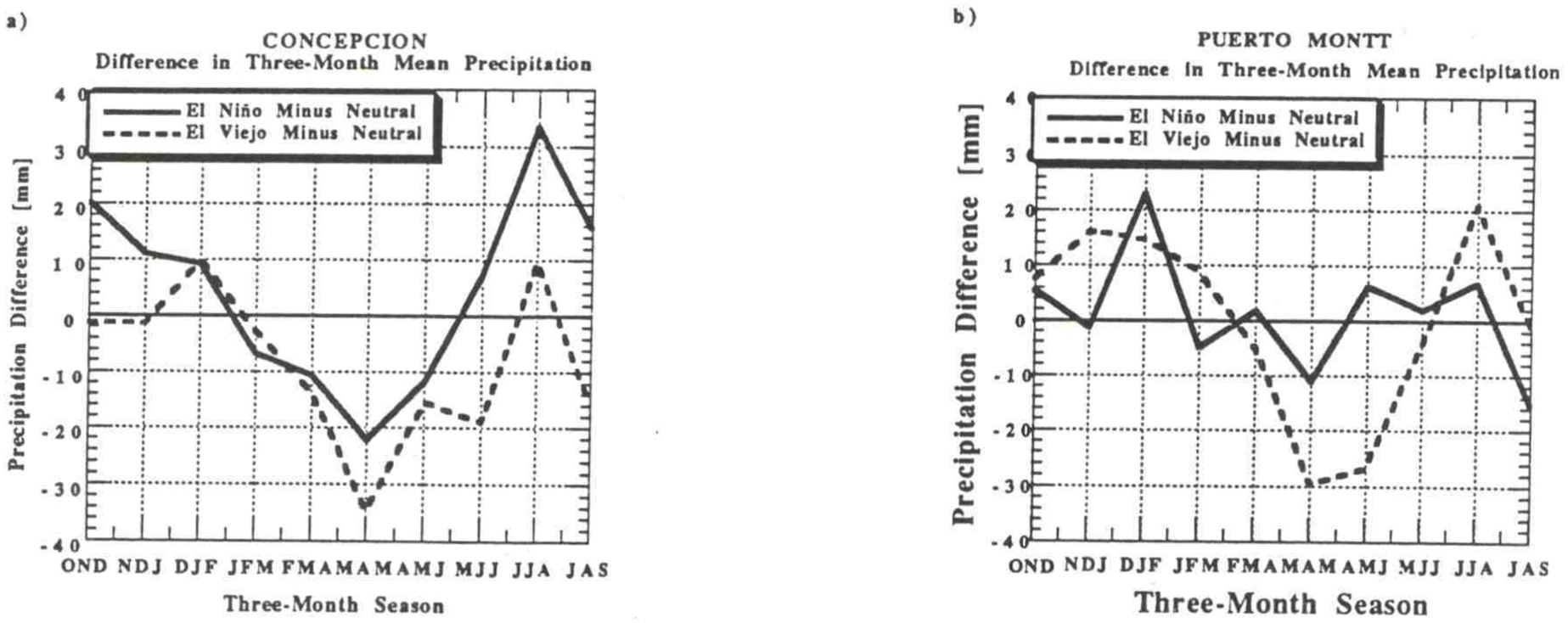

Figure 3 : Differences in three-month mean precipitation for a) Concepción and b) Puerto Montt.

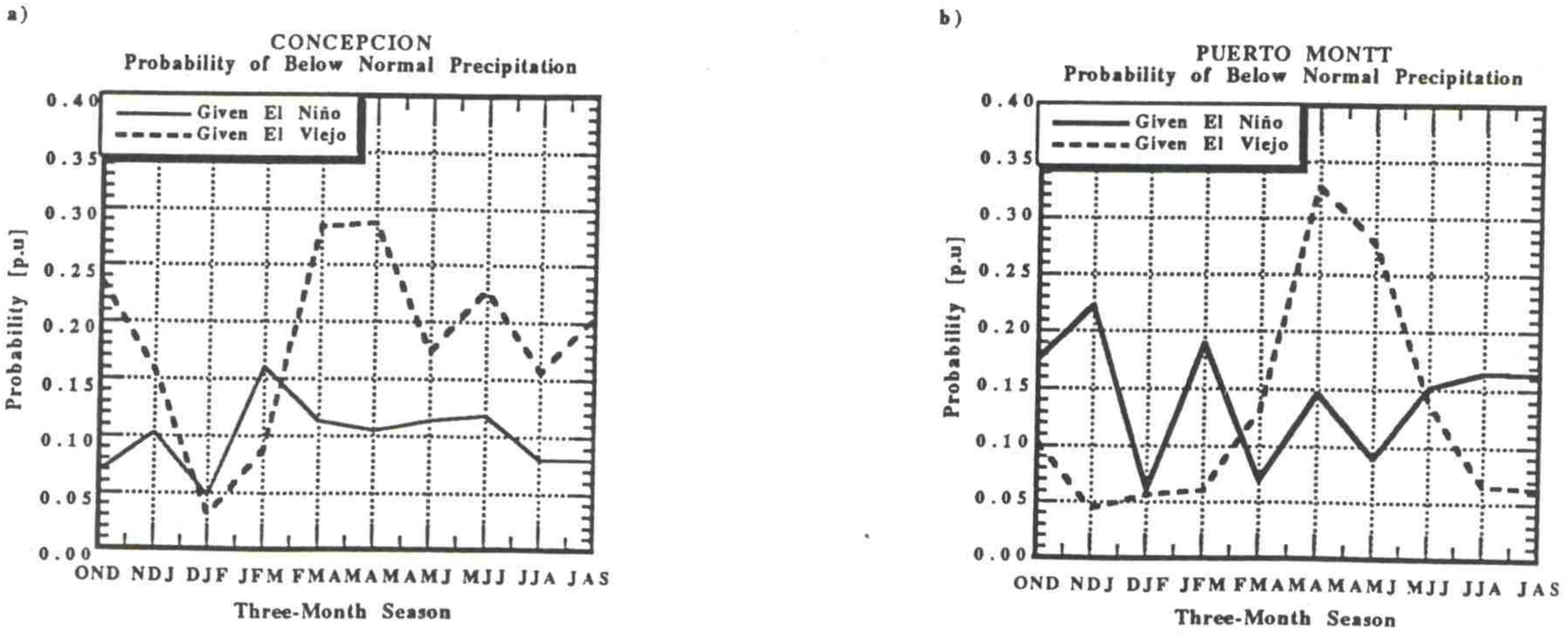

Figure 4 : Probability of below normal precipitation for a) Concepción and b) Puerto Montt

First Year of Observations from the Galápagos Utilizing a 915 MHz Wind Profiler

KS Gage
NOAA Aeronomy Laboratory,
Boulder, CO 80303

and

CR Williams
University of Colorado/CIRES,
Boulder, CO 80309

Introduction

UHF profiler observations of lower tropospheric winds and precipitating clouds have been made nearly continuously since early October 1994 from San Cristóbal Island in the Galápagos Islands of Ecuador. Figure 1 shows a map of the Galápagos Islands that extend along the equator off the coast of Ecuador. The profiler is maintained by the Aeronomy Laboratory in cooperation with the National Institute of Meteorology and Hydrology of Ecuador (INAMHI). It is located at the INAMHI meteorological observing station (Fig. 2) at Puerto Baquerizo Moreno near the commercial airport on the southwestern end of the island of San Cristóbal. The profiler is operated in two modes: a low mode that extends from about 100 m to 5 km with 100 m vertical resolution and a high mode that covers the altitude range from about 500 meters to 12 km with 400 m vertical resolution. In the absence of precipitation the altitude coverage in the low mode typically extends to 2 km and to 4 - 5 km in the high mode. The altitude coverage is somewhat less than similar profilers obtain in the western Pacific.

Lower Tropospheric Winds

Time-height contour plots of the lower tropospheric winds observed at San Cristóbal are shown in Fig 3. Typically winds at this location are southeasterly trades. The trade winds are strongest in the marine boundary layer below about 1 km. During the 'cold season' trade winds are strong, 8-12 ms^{-1}. During the 'warm season' that begins in December and extends through May, the trades are greatly reduced in magnitude and occasionally northerlies are observed. Zonal winds are easterly throughout the year with occasional episodes of lower tropospheric westerlies. The occasional westerlies are less than 5 ms^{-1} and confined below about 3 km. Above 3 km the zonal winds are typically strong easterlies with rare episodes of midtropospheric westerlies. These episodes of midtropospheric westerlies appear independent of the episodes of lower tropospheric westerlies. Unlike the zonal winds the meridional winds show a strong gradient near 1 km. This marks the upper limit of the trade winds that blow primarily from the south. The trade wind circulation appears quite steady through the cold season but is markedly reduced during the warm season. In addition, northerlies are often present above the marine boundary layer especially during the cold season but may extend down to the surface during the warm season. Northerlies evidence considerable vertical and temporal variability.

Precipitating Clouds

The 915 MHz profilers are excellent tools for diagnosing and classifying convective cloud systems (Gage et al, 1994; Williams et al., 1995). Substantial differences were seen in the vertical structure of precipitating clouds during the cold and warm seasons over San Cristóbal. During the cold season precipitation (at the surface) is rare but 'precipitating clouds' are not. It is not unusual to have light precipitation falling from low clouds that evaporates before reaching the surface. An example of a warm rain episode during the cold season is shown in Fig. 4. The occurrence of rain is documented by the rain gauge located at the profiler site and by the vertical Doppler velocity observed by the profiler. Vertical velocities of a few ms^{-1} are seen below 2 km at the same time that

rain is being recorded at the surface. The occurrence of fairly steady light rain is very different from what is observed in the western Pacific (Ecklund et al, 1995, Williams et al, 1995). During the warm season precipitation is observed to be more similar to what is observed over the western Pacific. The primary difference observed at San Cristóbal is that heavy rain associated with deep convection is much more likely to occur during the warm season. Fig 5 contains the time-height cross section of vertical Doppler velocities associated with a deep convective storm observed at San Cristóbal on 31 January-1 February. Unlike the example in Fig 4, the precipitating cloud structure in Fig. 5 contains a pronounced enhancement above the melting level (near 5 km). The deep convection produces frozen hydrometeors in the upper troposphere. As these ice/snow hydrometeors fall to the surface they melt and accelerate as liquid raindrops. The melting layer structure is clearly evident in Fig. 5 and persists for much of the period of light rain that occurs on 1 February. Heavier rain can be seen on 31 January associated with the strong updraft above 6 km.

During 1994-95 there were indications of a warm episode in the Pacific. It is impossible to conclude how much of the changes observed during 1994-95 are typical of the usual seasonal cycle or how many can be attributed to the occurrence of El Niño. Many years of observations will be needed to before we can clearly define the annual cycle of the lower troposphere at the Galápagos.

Acknowledgements

The San Cristóbal profiler was constructed and is being operated with the support of the U.S. TOGA Project Office. We thank Paul Johnston, John Wilson and Mark Haeg for their contributions to the deployment and maintenance of the San Cristóbal profiler and Tony Riddle for his contributions to the archival and quality control of the profiler data. We also thank INAMHI for their cooperation.

References

Ecklund, W.L., K.S. Gage, and C.R. Williams, 1995: Tropical precipitation studies using 915 MHz wind profilers, Radio Sci., 30, 1055-1064.

Gage, K.S., C.R. Williams, and W.L. Ecklund, 1994: UHF profilers: A new tool for diagnosing tropical convective cloud systems, Bull. Amer. Meteor. Soc., 75, 2289-2294.

Williams, C.R., W.L. Ecklund, and K.S. Gage, 1995: Classification of precipitating clouds in the tropics using 915 MHz wind profilers, J. Atmos. and Oceanic Technol., 12, 996-1012.

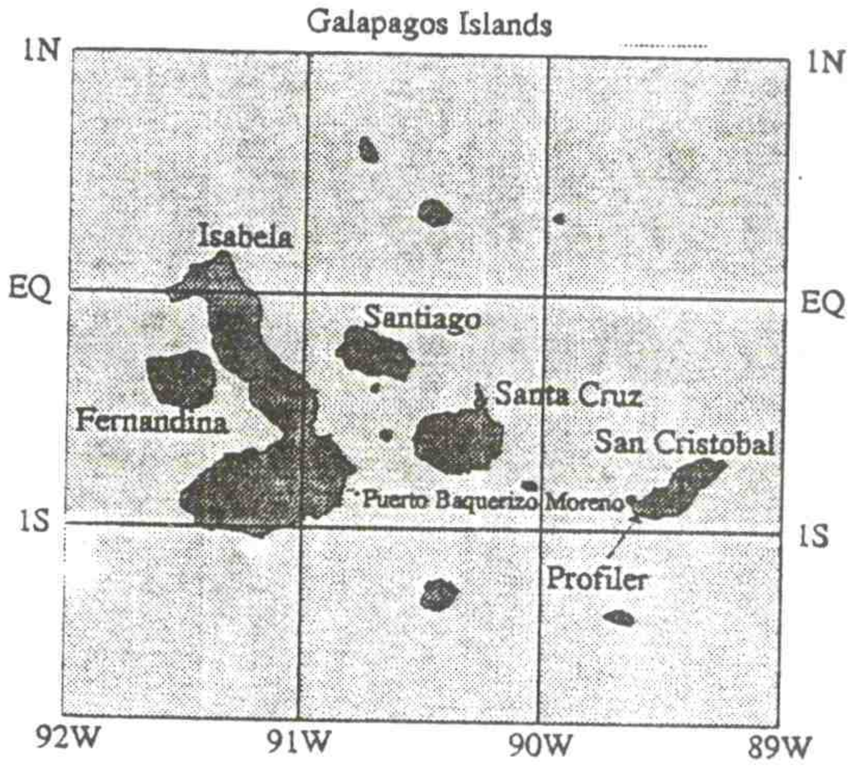

Fig. 1 Map showing the Galápagos Islands.

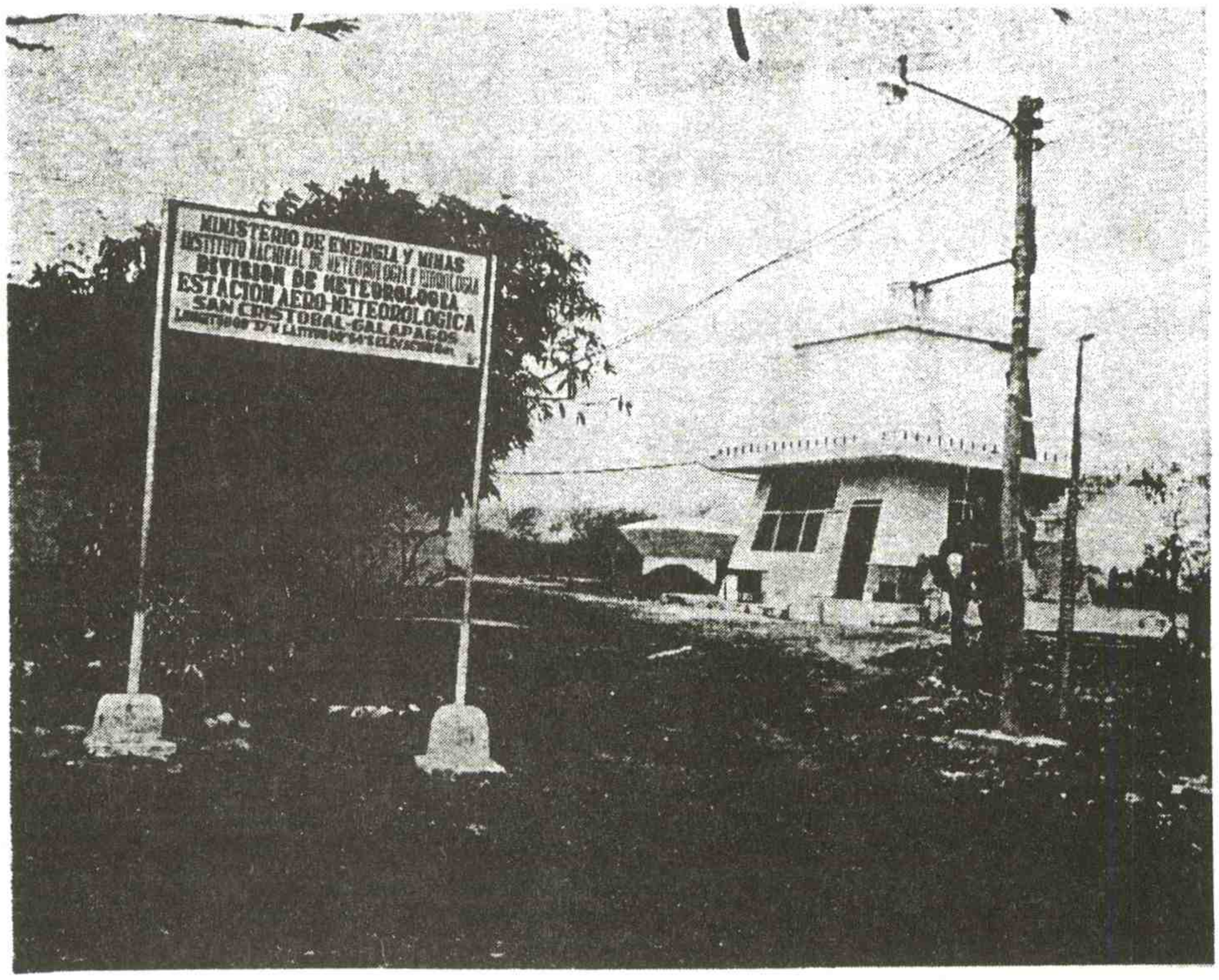

Figure 2. 915 MHz profiler at San Cristobal.

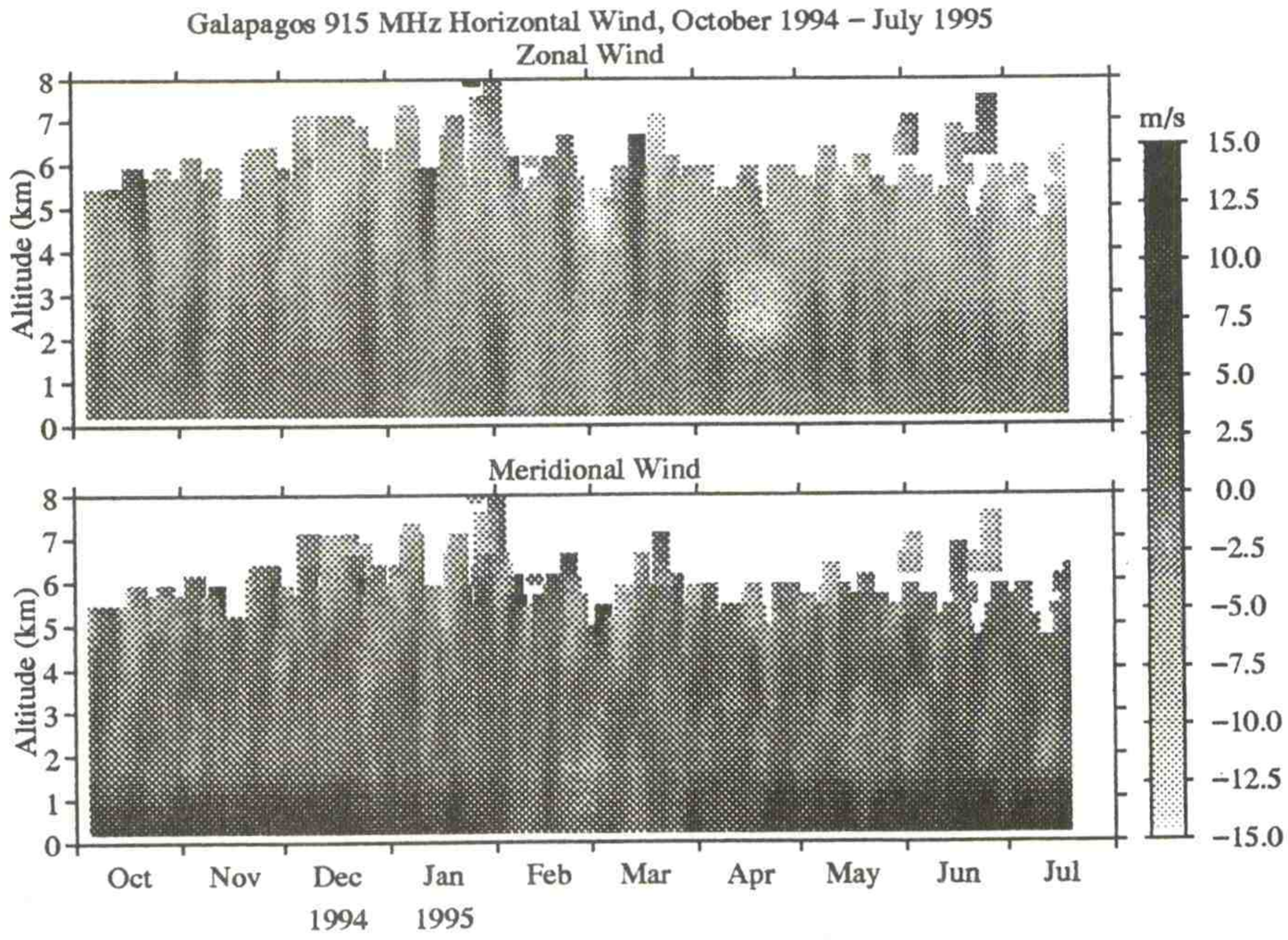

Figure 3. Lower tropospheric winds observed at San Cristobal, Octover 1994 - July 1995.

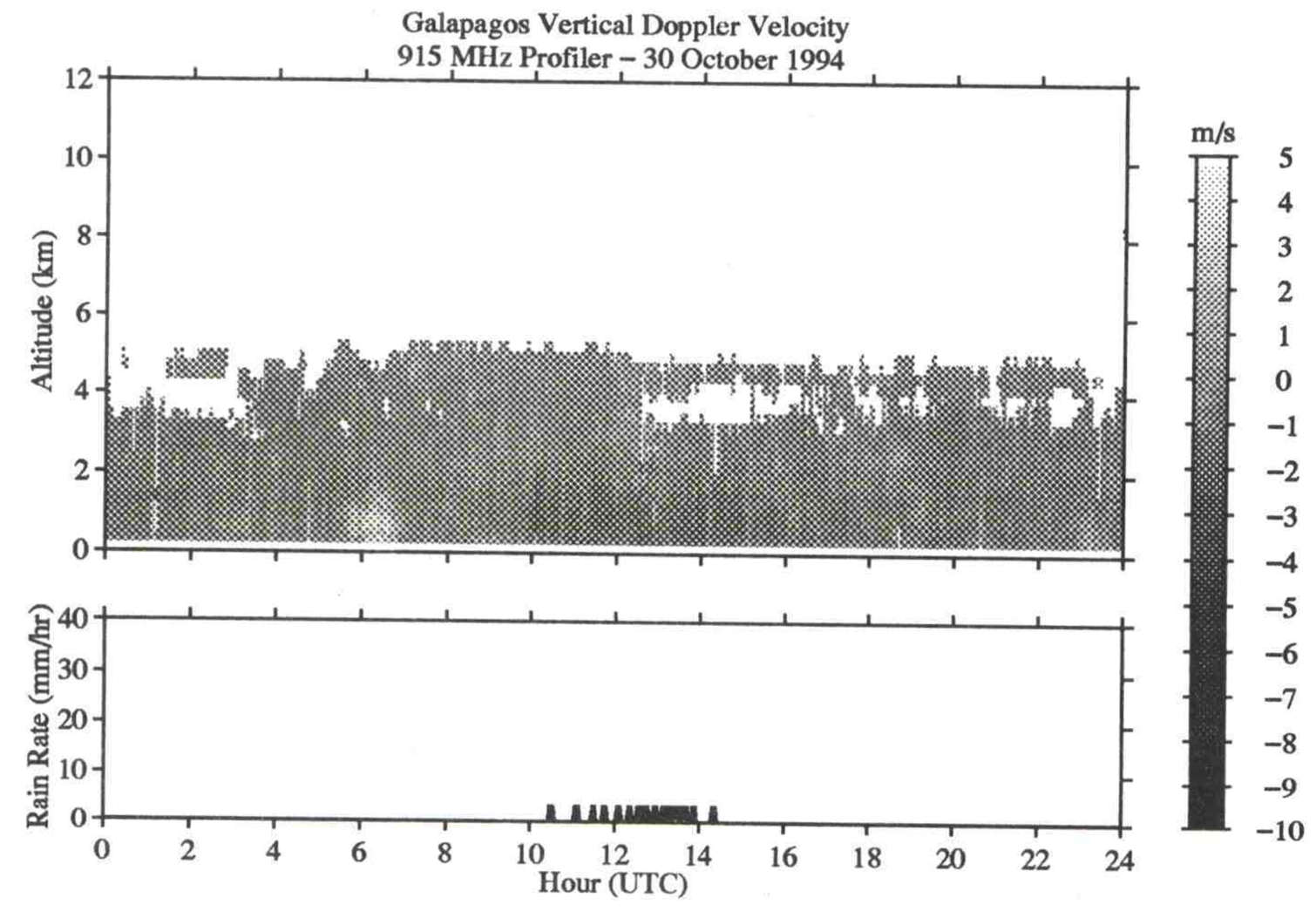

Figure 4. Observations of precipitating clouds at San Cristobal in the cold season.

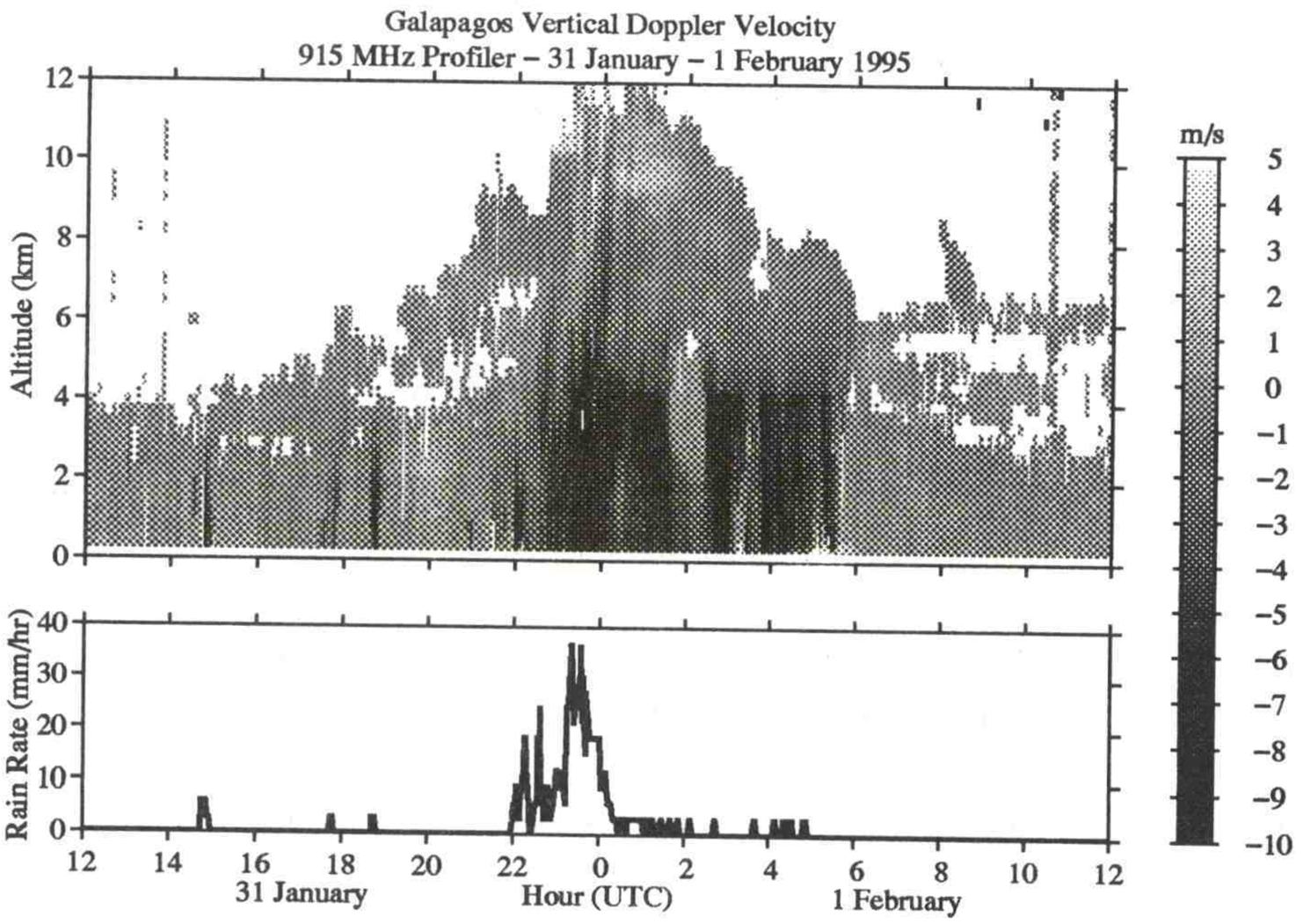

Figure 5. Observations of precipitating clouds at San Cristobal in the warm season.

Statistical Prediction of Global Continental Temperature and Precipitation to 1 Year in Advance Using Global SST

Anthony G. Barnston and Thomas M. Smith

NOAA/National Centers for Environmental Prediction/Climate Prediction Center
Washington, DC 20233

A reconstructed global sea surface temperature (SST) data set is used to examine predictive relationships between SST and seasonal mean surface temperature (T) and total precipitation (P) over most of the global continents for the 1950-92 period. The SSTs are reconstructed using COADS observations coupled with the spatial covariance relationships based on EOFs computed from the 1980s high resolution SST analyses. Land T and P data are gridded irregularly, due to the spatial variance of the density of the constituent stations. Canonical correlation analysis (CCA) is used to describe the relationships and to provide information aiding in physical interpretation of the findings. A sequence of four consecutive three-month periods of global SST anomalies is related to T and P anomalies during three-month periods ranging from one to four seasons later. Skill is evaluated using the temporal correlation between the observations and the forecasts for a given location and season.

Predictive skill is modest except for certain regions and/or times of the year having correlations of 0.5 and greater. The seasonal cycles of skill for T and P in North and South America, Africa and Australia are shown in Fig. 1 for lead times of 1, 2, 3 and 4 seasons, where lead time is defined as the time between the center of the latest predictor period and the center of the target period. Seasonal T is generally predicted with greater skill than P. Some regions have well defined seasonalities in their predictability, where skill varies more strongly as a function of the target season than lead time. Two such cases are P in Africa in northern summer and T in summer and winter in the U.S. The geographical distributions of correlation skill in northern late winter and late summer at a lead time of 2 seasons are shown for T and P in Figs. 2 and 3, respectively.

The CCA loading patterns for the strongest modes (not shown here) indicate that predictions are most skillful in areas affected by the ENSO, including the global Tropics during all seasons, and during specific seasons in northern and eastern Australia, northern tropical Africa, and parts of North and South America. Skill is weakest in Europe and mid-latitude Asia where ENSO's direct influence is lacking. However, non-ENSO skill sources also contribute substantially to final skill; these exist both in regions strongly and minimally influenced by ENSO. The most important of these is an interdecadal trend from the 1950s to the 1980s-90s defined by a warming in the Indian and South Atlantic oceans paralleling a cooling in the North Pacific and Atlantic basins. Another controlling SST dipole with a less obvious trend includes mainly the tropical SST of all three ocean basins versus the extratropical (especially Northern Hemisphere) SST.

Some of the regions that have modest but usable seasonal predictive potential have no predictive history because they are not directly influenced by ENSO and/or have only marginal data quality or density. This is encouraging, since the statistical skill realized here should be reproducible, and hopefully surpassable, using dynamical prediction models.

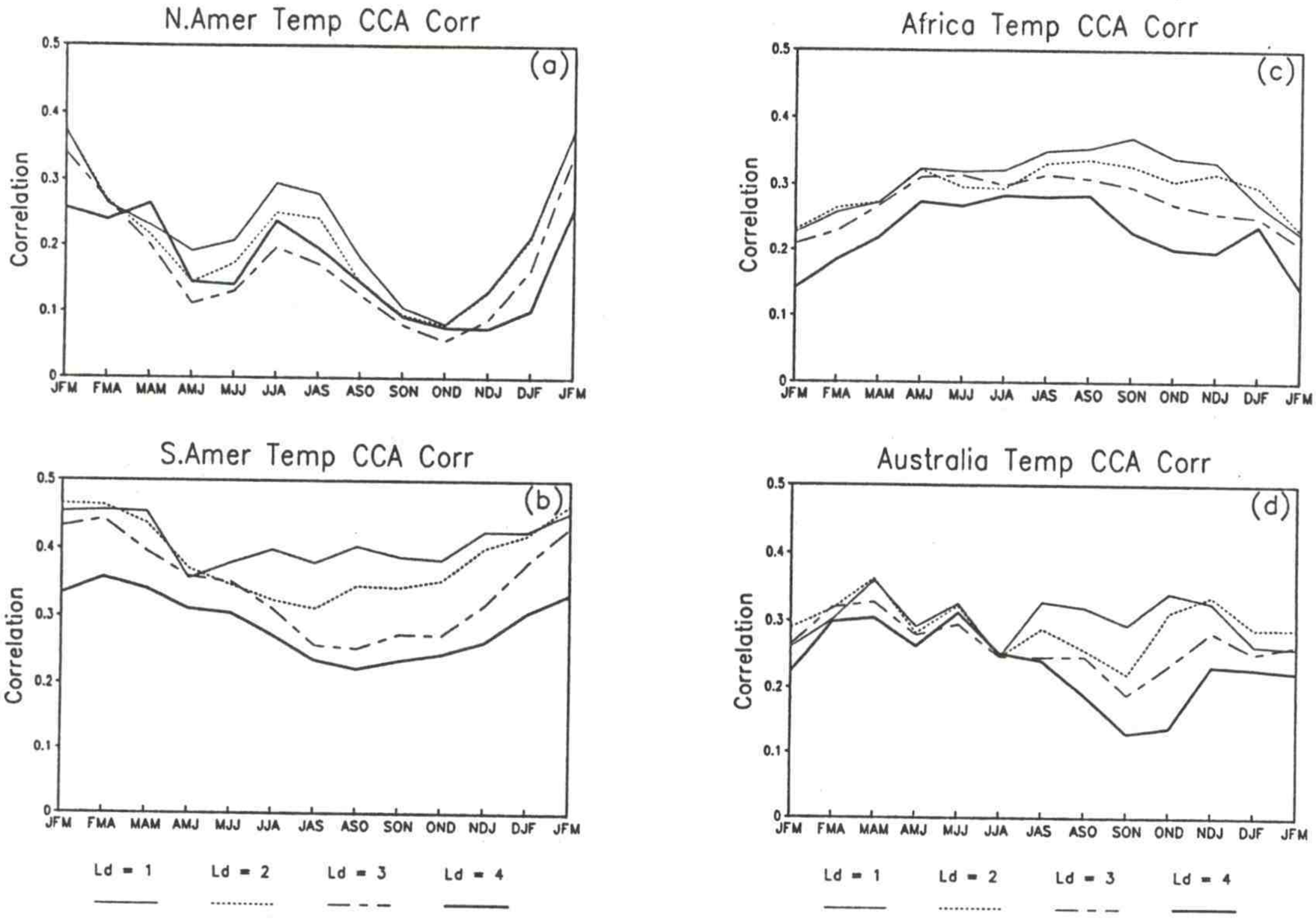

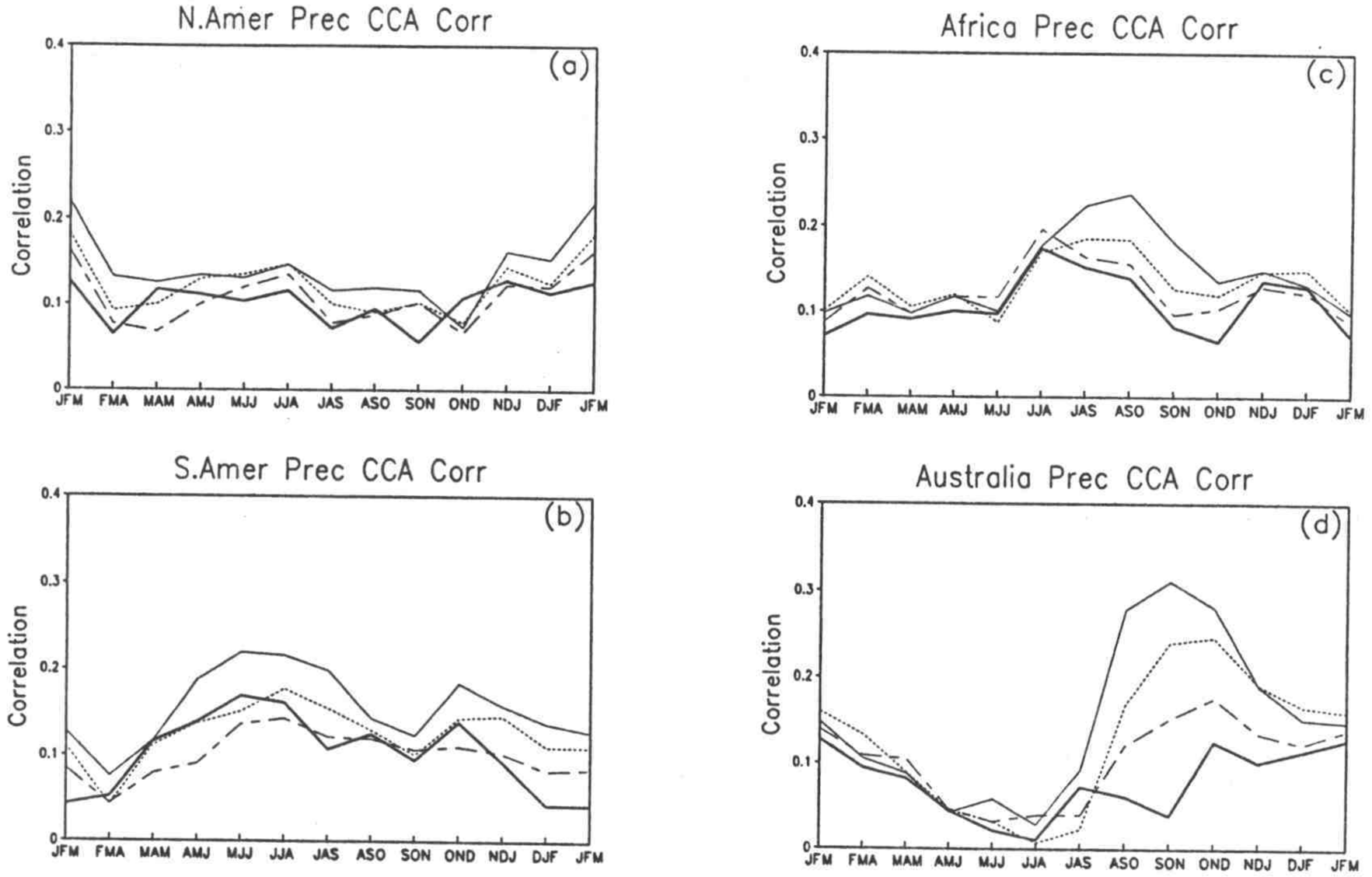

Fig. 1. Seasonal cycle of cross-validated CCA skill in forecasting seasonal mean surface temperature (top 4 panels) and precipitation (bottom 4 panels) in four continents. Skills for four lead times ranging from 1 to 4 seasons lead are shown. The 1 season lead time is defined for a forecast whose 3-month target period begins at the time of the latest available data--i.e., the time of forecast.

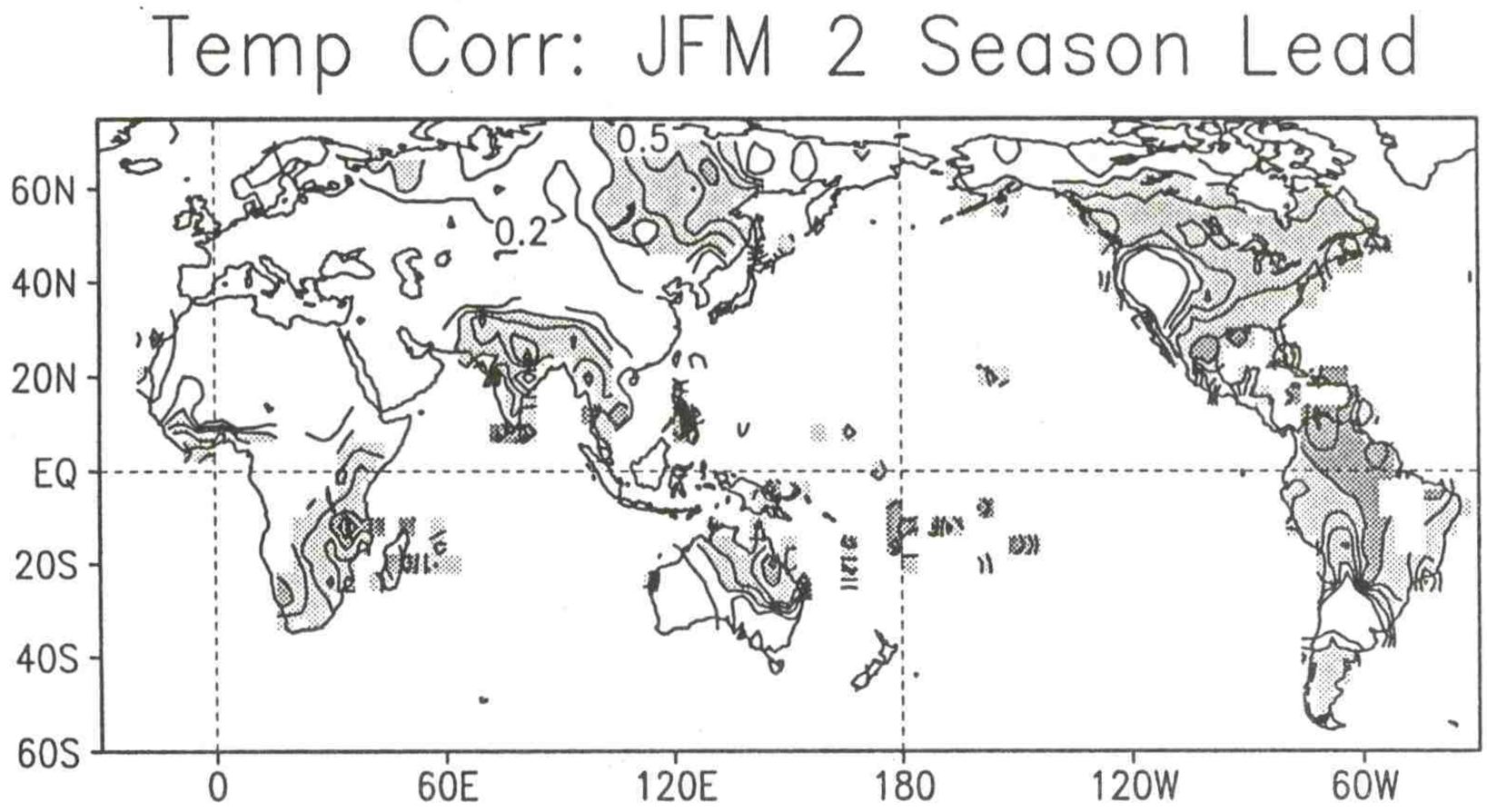

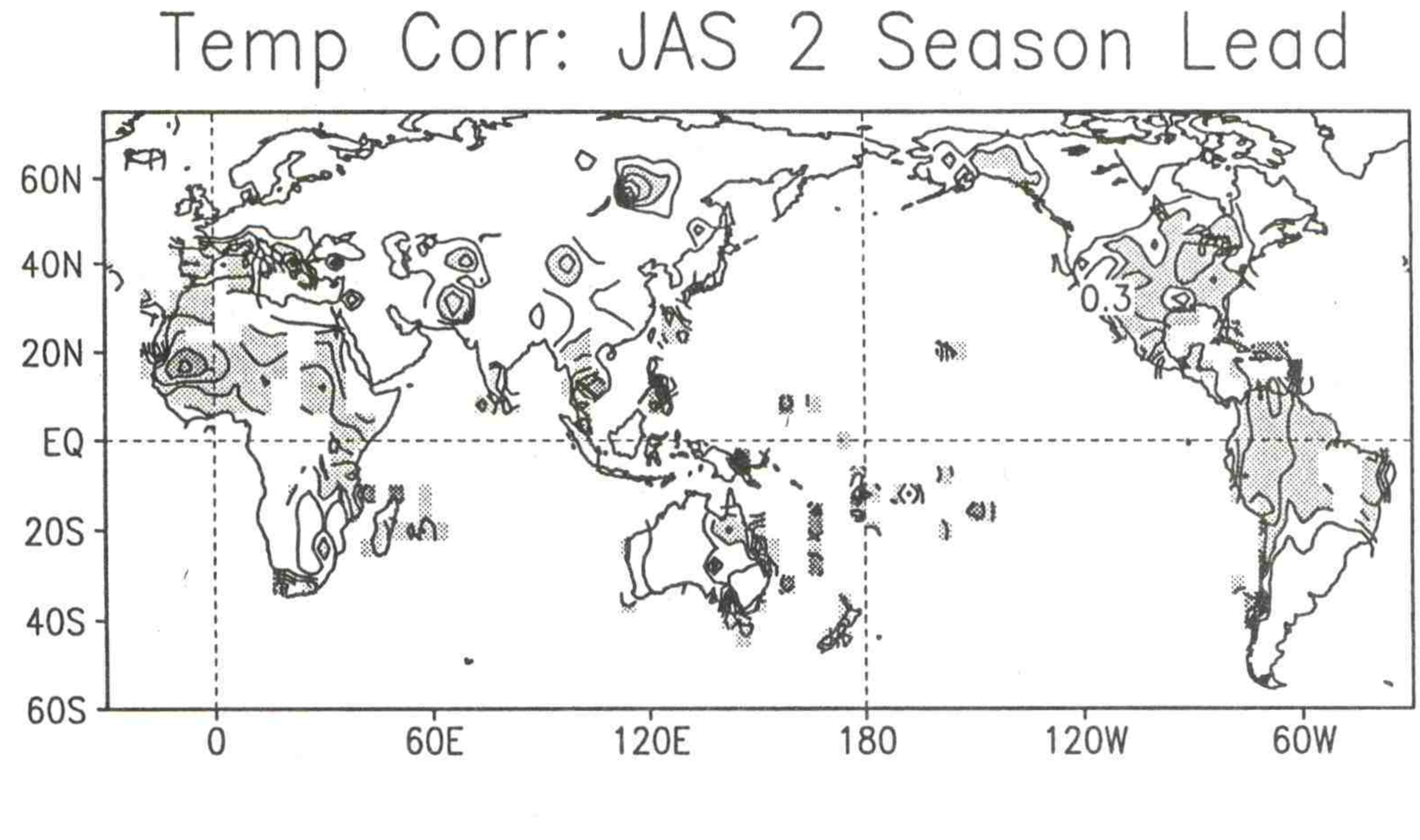

Fig. 2. Global geographical distribution of cross-validated CCA correlation skill for seasonal temperature forecasts in northern late winter (top) and late summer (bottom) at a lead time of 2 seasons. Contour interval is 0.1 for |skill| >0.2. Light shading denotes skill >0.3, dark shading >0.6.

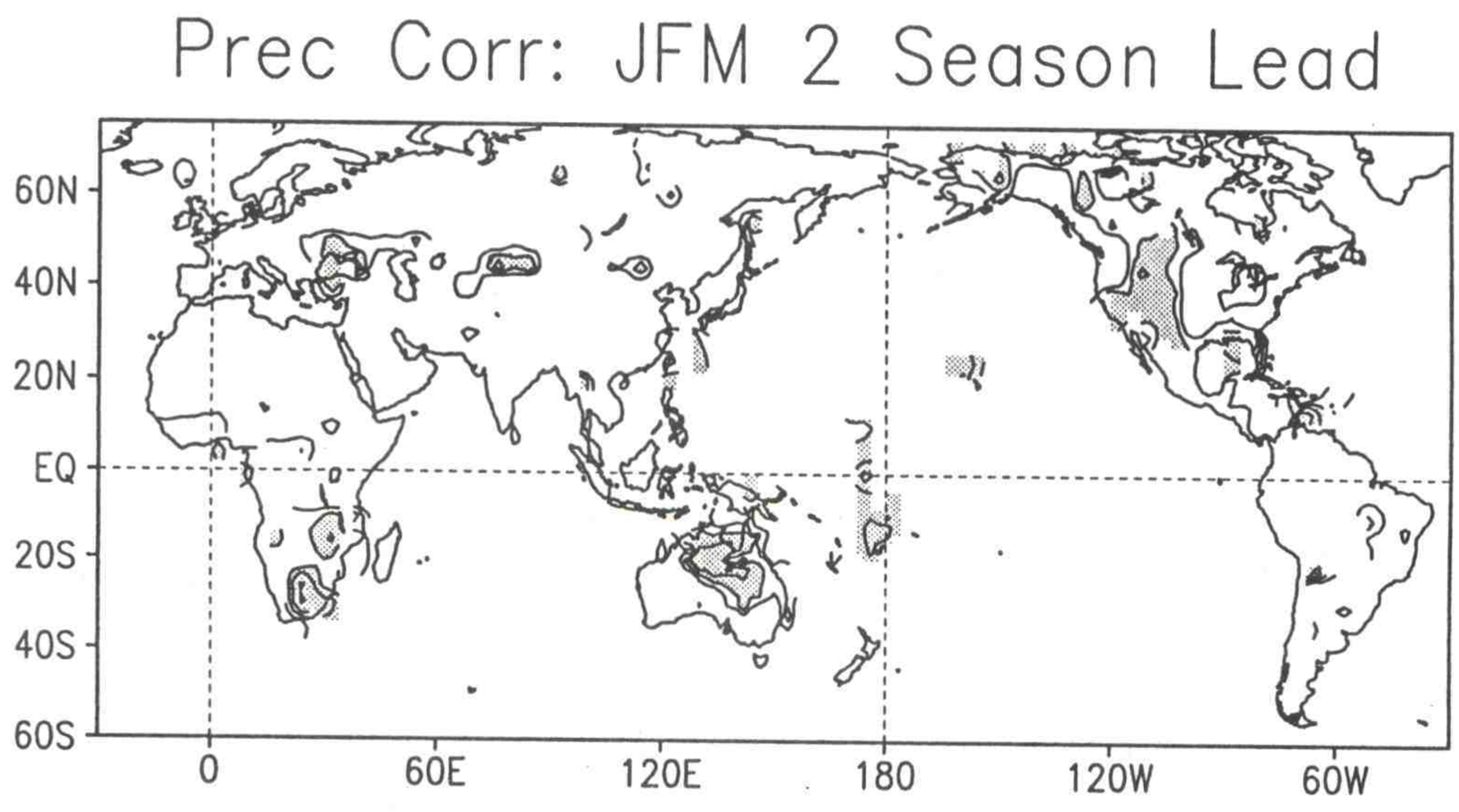

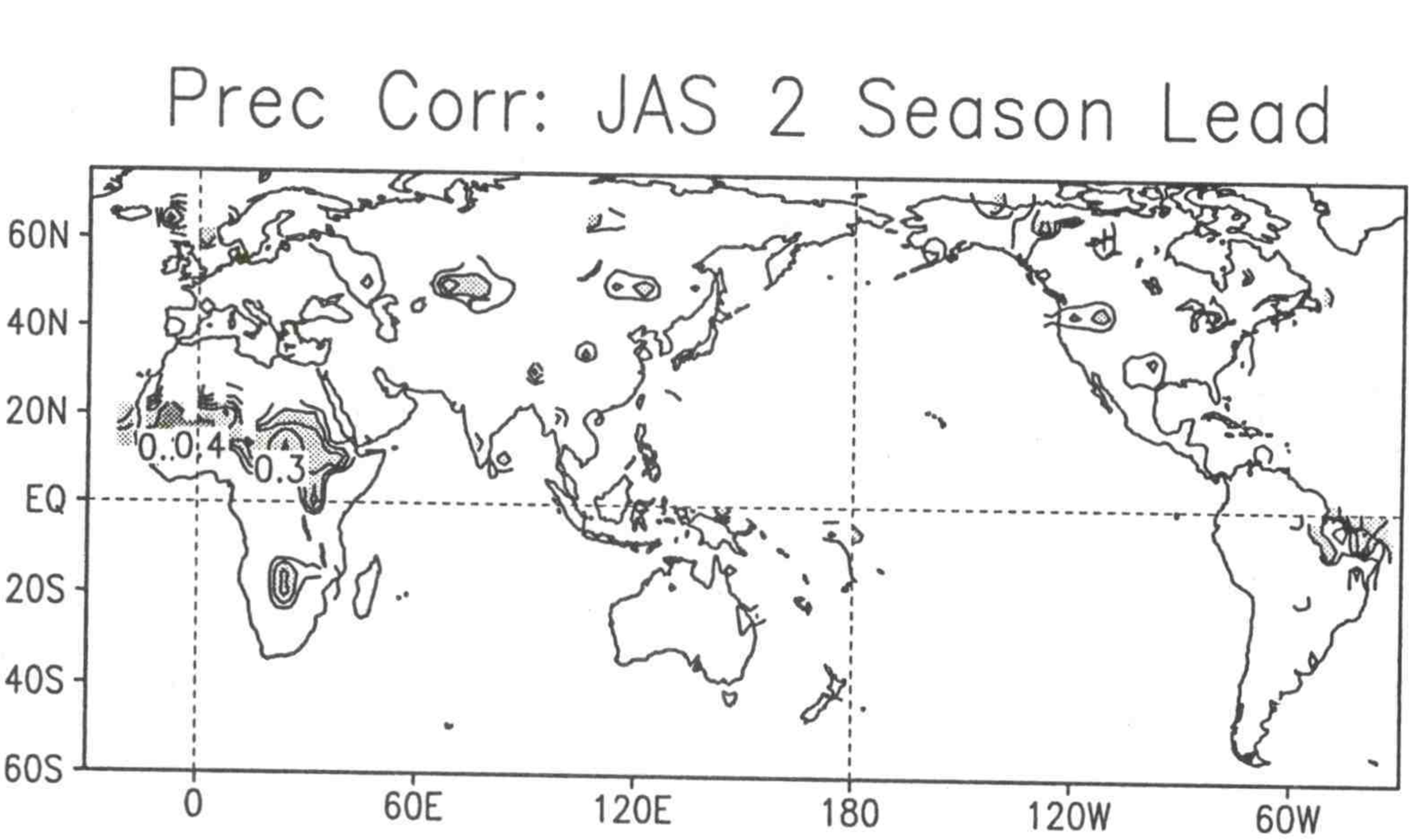

Fig. 3. Global geographical distribution of cross-validated CCA correlation skill for seasonal precipitation forecasts in northern late winter (top) and late summer (bottom) at a lead time of 2 seasons. Contour interval is 0.1 for |skill| >0.2. Light shading denotes skill >0.3, dark shading >0.6.

MAJOR CLIMATIC EVENTS AND ANOMALIES AROUND THE WORLD DURING 1995

by

Richard Tinker of the Climate Prediction Center, NCEP, National Weather Service, NOAA

1. The Western Atlantic Basin and Eastern North America:

SECOND-MOST ACTIVE HURRICANE SEASON ON RECORD.

The 1995 Atlantic hurricane season featured 19 tropical storms, 11 of which became hurricanes. This was the second largest number of storms (21 in 1933) observed in any season since records began in 1871, and the second greatest number of hurricanes (12 in 1969) in one season since hurricane statistics began in 1886, according to the National Hurricane Center (NHC).

The season began early as Hurricane Allison became the region's first June hurricane since Bonnie in 1986. The storm dumped between 100 and 250 mm of rain on western Cuba and the Southeast. Localized flash flooding and strong, gusty winds affected much of the area, but the rains were largely beneficial to the Southeast.

In early August, Tropical Storm Dean dumped heavy rains (100 to 375 mm) on the central and west-central Gulf Coast region, eastern and north-central Texas, and central Oklahoma. Then, Hurricane Erin dumped 100 to 250 mm of rain on central and extreme northwestern Florida.

By mid-month, heavy showers from Tropical Storm Gabrielle drenched northeastern Mexico and extreme southern Texas with 100 to 330 mm of rain. As August finished, Tropical Storm Jerry slowly tracked through Florida and south Atlantic states, dropping 100 to 400 mm of rain on much of Florida and western South Carolina, causing flash flooding.

During September, Hurricanes Luis and Marilyn, following similar tracks, causing extensive damage on some Leeward Islands. In early October, Hurricane Opal became the fourth tropical system to affect Florida in 1995. Torrential rains (300 to 430 mm), a 5 to 6 meter storm surge, and devastating winds (gusting to 230 kph) buffeted the western Florida Panhandle and adjacent Alabama, causing considerable property damage and disrupting electrical power in many areas.

In Opal's wake, Hurricane Roxanne became the second hurricane in 10 days to buffet the Yucatan and Cuba. In southeastern Mexico, where precipitation data are sparse, 200 to 600 mm of rain may have fallen on some locations.

2. Western United States:

1994-95 WET SEASON CHARACTERIZED BY HEAVY PRECIPITATION AND SEVERE FLOODING.

Locally heavy precipitation fell on much of the Far West during the 1994-95 wet season, but conditions were particularly severe in California. The year began with heavy precipitation (up to 559 mm on January 1-9) deluging much of California. The Office of Hydrology reported widespread flash flooding and mudslides across central and southern California, and major river flooding in northern parts of the state. As the month progressed, lesser but still surplus precipitation was recorded. By the end of January, seasonal precipitation was near or above normal throughout the West, with amounts at least twice the October - January normal across southern California.

February brought tranquil conditions to the western tier of states, allowing flood-plagued regions to recover. As March began, however, renewed flooding hit much of California, and abundant precipitation prevailed across most areas from the Rockies westward. By month's end, precipitation totals since October 1994 ranged between 2160 and 2775 mm in parts of the northern Sierra Nevada. The 243-day season (October 1994 - May 1995) was the wettest on record across California, and was above normal in most areas from the Rockies westward. Between 200% to 275% of normal was measured in parts of southwestern California.

3. Central and Eastern United States:

SHORT BUT INTENSE MID- JULY HEAT WAVE.

In mid-July, dangerously hot and humid conditions spread across most of the central and eastern United States, with highs soaring above 40°C as far north as South Dakota and western Wisconsin. Few locations reported all-time record highs, but many recorded their highest temperatures of the past few years, or in some cases, over a decade. Furthermore, the heat combined with dew points of up to 29°C to yield dangerous apparent temperatures of 46°C to 49°C in parts of the central Great Plains, Great Lakes states, mid-Atlantic, and southern New England. Media and local government sources indicated that the heat took many hundreds of lives, forced local utilities to impose controlled localized power outages, and caused a shortage of available water and localized water-pressure reductions. All-time highs were recorded at La Crosse, WI (42°C, July 13), Danbury, CT (41°C, July 15), Chicago/Midway, IL (41°C, July 13), Chicago/O'Hare, IL (40°C, July 13), and Flint, MI (38°C, July 14).

4. Northeastern United States:

DROUGHT CONDITIONS PREVAIL FROM JUNE THROUGH SEPTEMBER.

During August, most of the Northeast and mid-Atlantic received little rain, including several locations that experienced a record or near-record consecutive number of days without measurable rain (33 days at Washington, DC; 25 days at Raleigh-Durham, NC). This exacerbated longer-term deficits that had been accumulating since at least mid-March, and in some areas, since October 1994. From March through August, less than 75% of normal precipitation fell on a large area from eastern North Carolina northward through the mid-Atlantic and Northeast, with several areas along the East Coast Megalopolis registering less than half of normal precipitation.

Late-August rains from the remnants of Tropical Storm Jerry alleviated the dryness across Georgia and the Carolinas, but farther north, the remnants of eastern Pacific Hurricane Ismael fueled rains across the eastern United States in mid-September that provided only slight relief from the drought. By early October, the remnants of Hurricane Opal spread moderate to heavy rains over a large part of the Northeast, and subsequent heavy precipitation over the next six weeks categorically ended moisture shortages.

5. Central United States:

HEAVY PRECIPITATION ENGENDERS FLOODING FROM APRIL THROUGH JUNE.

From early April through early June, many areas of the central United States received more than twice their normal precipitation. This resulted in flooding along the lower and middle Missouri, middle and lower Mississippi, and lower Ohio Rivers and many of their tributaries, affecting some of the same areas that were inundated by the "Great Flood of 1993." The largest precipitation totals (450 to 765 mm) were observed in eastern Oklahoma and Kansas, southwestern and central Missouri, southern Illinois and Indiana, and central Kentucky. The flooding prevented crop planting near the affected rivers and delayed field operations elsewhere.

6. Northwestern United States:

HEAVY PRECIPITATION AND FLOODING BATTER REGION DURING NOVEMBER AND DECEMBER.

A series of disturbances dumped heavy precipitation on the region late in the year, generating severe river flooding, especially west of the Cascades. Most of the storms were accompanied by well above normal temperatures, allowing rain to fall on all but the highest elevations of the Cascades, which further added to runoff. From mid-November through mid-December, 200 to 500 mm of rain fell on parts of western Washington and northwestern Oregon. Numerous schools, businesses, and roads were forced to close by the flooding, which approached but generally did not exceed the severity of the "Hundred-Year Flood" of November 1990.

7. Southeastern Asia and the Philippines:

TYPHOONS AND HEAVY RAINS SOAK REGION THROUGH MUCH OF THE YEAR.

Tropical Storms Gary, Helen, and Irving brought heavy tropical showers to southeastern and southern China during late July and August. All three storms dropped daily rainfall totals of 90 to 130 mm near the landfall sites. In addition, over 300 mm of rain fell on much of central and southeastern Taiwan, south-central and coastal southeastern China, and portions of Vietnam and Thailand from July 23 through August 21. Exceptionally heavy rains (750 to 950 mm) inundated parts of coastal southeastern China.

In late August and early September, the remnants of Typhoon Lois dumped 100 to 400 mm of rain on north-central Vietnam, south-central China, and northern Thailand while Typhoon Kent, packing wind gusts to 295 kph, yielded similar amounts in Hong Kong and adjacent sections of China. Farther east, Typhoons Kent and Nina drenched Luzon Island of the Philippines with up to 400 mm of rain.

Typhoon Nina subsequently dumped up to 130 mm of rain on parts of southern China in early September. Heavy rains continued throughout September and into early October, when Typhoon Sibyl delivered up to 350 mm of rain to the central and northern Philippines, Hong Kong, and southern China. Typhoon Ted made landfall in Guangxi province of southern China in mid-October, accompanied by 100 to 230 mm of rain. In late October, Tropical Storm Yvette and Typhoon Zack brought more heavy rain to the Philippines, then proceeded westward to drop 200 to 300 mm of rain on the southern coast of Vietnam.

Super Typhoon Angela, the strongest typhoon to hit the Philippines since 1987, struck the central Philippines on November 3 with gusts to 315 kph and more heavy rain, claiming over 500 lives and disrupting electrical power for one-third of the country's inhabitants. Copious rains continued across portions of the Philippines through December. During the last seven months of the year, as much as 4225 mm of rain doused parts of southern Luzon.

8. Indian Subcontinent:

PRE-MONSOONAL HEAT WAVE FOLLOWED BY EXCESSIVE MONSOON RAINS.

Exceptionally hot weather enveloped most of the Indian Subcontinent during the first two-thirds of June, with temperatures soaring to 50°C in some places. The initial monsoon showers provided relief from the heat wave in late June, but subnormal rains were reported in most areas until mid-July.

Following the hot and dry start to the monsoon season, rains increased sharply across the Subcontinent, with some areas of coastal southwestern India receiving over 1200 mm of rain in the next 25 days, at least twice normal for the period. By early September, much of the Indian states of Tamil Nadu, Andhra Pradesh, Haryana, northern Rajasthan, and Punjab, as well as extreme eastern India and northeastern Pakistan, had received 125% to 175% of normal rainfall for the season. Parts of southeastern Andhra Pradesh measured more than twice normal. The copious rains generally benefited crops, but also contributed to several episodes of flooding. For the 1995 monsoon season as a whole (June - September), areally-averaged precipitation for the Indian Subcontinent was the heaviest since 1988 and the 7th heaviest since 1918.

9. Western Europe:

HOT AND DRY WEATHER DOMINATES NORTHERN HEMISPHERE SUMMER.

Significant moisture shortages began affecting the region in early June and persisted into September. In addition, abnormally high temperatures affected much of western Europe, with the mercury soaring to 44°C in southern France in mid-July. Conditions were particularly severe across the British Isles, where June 5 - September 4 rainfall totaled less than 100 mm of rain in most of eastern Ireland, central Northern Ireland, and most of England and Wales. At a few locations across northeastern, central, and southern England, totals of only 15 to 50 mm represented just 15% to 35% of normal for the period. Unofficial statistics from the British Meteorological Office indicated that Great Britain probably endured its driest summer (June through August) in more than 3 centuries of record. Furthermore, temperatures averaged 2°C to 4°C above normal throughout the islands from late June through late August, with the largest departures reported in central Ireland and western England.

10. Australia:

UNUSUALLY WET IN THE WEST AND DRY IN THE EAST DURING OCTOBER 1994 - MAY 1995.

The first three months of the wet season (October - December 1994) featured well below normal precipitation across much of the eastern half of Australia. In January, subnormal rains were again reported along the eastern Australian coastline, but surplus rains from central Queensland southward through eastern Tasmania allowed moisture shortages to decline. January totals were at least twice normal over most of the southeastern third of Australia while torrential rains (over 500 mm at a few locations) deluged Arnhem Land. Favorable precipitation continued through late February across the eastern half of the continent, dramatically improving crop and pasture conditions across eastern Australia.

Subnormal rainfall returned to much of eastern Australia during March and April, with under half of normal March totals measured across central and southern Queensland, most of New South Wales, much of South Australia, southern sections of the Northern Territory, and northern portions of Western Australia. The first week of May brought late-season rains to the eastern half of Australia, including the first significant precipitation to fall on parts of New South Wales since February. As May progressed, seasonable dryness overspread most of the continent.

For the wet season as a whole (October 1994 through April 1995), subnormal precipitation covered much of the eastern half of the country, with parts of east-central Queensland and southern South Australia receiving under half of normal.

Farther west, Cyclone Bobby brought rare heavy rains to much of northern and central Western Australia. Five-day (February 22-26) totals of 100 to 320 mm were common over the region, where *annual* normals are only 215 to 285 mm.

11. Southern Africa:

PROLONGED DRYNESS THROUGHOUT MOST OF YEAR FOLLOWED BY HEAVY LATE-YEAR RAINS.

The 1994-95 wet season (October - April) was slow to commence across much of Botswana and northern and central South Africa. Dry conditions spread across most of the region in November, then December brought significant rains to the northern and eastern sections of southern Africa, but subnormal monthly totals were again reported over much of central South Africa and western Botswana.

Heavy January rains (100 to 250 mm) fell on several previously dry areas, including the eastern half of South Africa, southern Botswana, most of Zimbabwe, and central Mozambique. Dry weather, however, continued in the Northern Transvaal, eastern Kwazulu-Natal, southern Zimbabwe, Zambia, and southern Mozambique. Below normal rainfall once again dominated most of southern Africa from late January through February, with totals among the lowest 10% of climatological occurrences over southern Botswana, northern Zimbabwe, and central Mozambique. Dryness persisted into March, but heavy late-month rains (100 to 250 mm) provided much-needed moisture to many areas from Botswana and central Zimbabwe southward.

For the 1994-1995 wet season as a whole, subnormal rains were reported over the vast majority of southern Africa, with parts of Namibia, northern Zimbabwe, and northwestern Mozambique reporting less than half of normal.

Following a seasonably dry austral Winter and early Spring, the 1995-1996 wet season began slowly, exacerbating the long-term moisture shortages from last wet season. In late November, however, heavy rains (50 to 250 mm) fell on southwestern Zimbabwe, eastern Botswana, and northeastern South Africa. Surplus December rains were reported in much of South Africa, but seasonal deficits remained across most areas into mid-December. Shortly thereafter, torrential rains (75 to 240 mm in one week) drenched northern and eastern South Africa as well as Swaziland, Lesotho, southern Botswana, and central Zimbabwe. Locally severe river flooding plagued central Kwazulu-Natal province.

12. East-Central Asia:

PERIODS OF HEAVY PRECIPITATION INTERSPERSED WITH ABNORMAL DRYNESS.

From mid-April through June, 500 to 1400 mm of rain fell on the northern sections of Hunan and Jiangxi provinces of northeastern China, leading to locally severe flooding. Parts of the Yangtze River Valley received 300 to 500 mm more rain than normal during this period. In sharp contrast, less than half of normal precipitation was recorded during the same period across large sections of north-central China and along the southeastern coastline.

In Japan, most of Honshu southwestward across Shikoku and Kyushu were inundated by over 750 mm of rain from early April through early July, with several locations reporting 1000 to 2000 mm. At the end of July, Typhoon Faye brought winds gusts of 160 kph and 100 - 210 mm of rain over Kyushu, extreme southwestward Honshu, and southern South Korea.

Shortly thereafter, two weeks of intense rainfall induced severe flooding across northeastern China and North Korea. Totals exceeded 350 mm east of Beijing and approached 610 mm in northwestern North Korea. These rains engendered severe river flooding, and the Chinese Government indicated that a few rivers in northeastern China reached their highest levels on record. During the 77-day period ending September 2, more than 500 mm of rain soaked most of Korea and adjacent China, with totals of 1000 to 1360 mm reported across the central tier of the Korean peninsula, northwestern North Korea, and adjacent southern Manchuria.

In stark contrast, much of southern Japan and the Yangtze River Valley of China experienced deficient rains during July and August. In mid-September, weakening Typhoon Oscar spread heavy rains, gusty winds, and localized flooding across Tokyo and neighboring areas, ending the dry spell. Late in the month, Typhoon Ryan dumped 50 to 270 mm of rain on most of Taiwan and on Kyushu, Shikoku, and eastern Honshu Islands. In addition, rainfall from the remnants of Typhoon Sibyl dropped 80 to 150 mm on east-central China in early October, but subnormal precipitation returned after the storm and persisted through the end of the year.

13. Central South America:

OVER SEVEN MONTHS OF SUBNORMAL PRECIPITATION RECORDED.

Persistently below normal precipitation began over parts of South America in early May and continued into mid-December. Large sections of central and southern Brazil, southern Paraguay, and central and northeastern Argentina received less than 75% of normal precipitation during May 1 - December 19, with under half normal totals recorded in parts of northern Rio Grande do Sul state in Brazil, southeastern Paraguay, and the Argentine provinces of Corrientes, northern Santa Fe, and a few other areas along the western tier of the region.

14. Russia and Adjacent Central Asia:

RECORD WARM YEAR.

An upper-level ridge brought unseasonably mild weather to much of Siberia early in the year, with weekly departures reaching or exceeding +15°C at times in mid-February, early March, and most of April. Temperatures returned to near normal in most areas during early May, but warm conditions again covered most of Russia in early June as highs reached 32°C at Moscow, the highest June temperature in 100 years, according to local meteorological officials

Through the last four months of 1995, near to somewhat above normal temperatures dominated the region. For 1995 as a whole, most of Russia and parts of neighboring Asian countries reported annual mean temperatures among the warmest 10% of the 1961-1990 distribution, averaging 2°C to 4°C above normal at many locations. The former Soviet Union as a whole averaged 2.1°C above normal - the warmest year since records began in 1891, according to the Institute for Global Climate and Ecology in Russia.

15. Northern and Central Europe:

VERY WET CONDITIONS PREVAIL JANUARY - MAY.

Beginning in mid-January, a series of powerful Atlantic storms brought heavy precipitation and severe flooding to central and northwestern Europe. Some rivers rose to levels rivaling those recorded during the December 1993 "Flood of the Century," according to local hydrometeorological officials. Parts of northwestern Spain, northwestern France, and southern Belgium received 200 to 290 mm of rain during January 17 - 29.

In the long-term, surplus precipitation dominated much of Europe from the Alps and Slovakia northward to northern Scandinavia from early December 1994 through early April. During December 4, 1994 - April 8, 1995, between 800 and 1340 mm deluged part of central Germany, a few locations in Switzerland and Austria, southwestern Norway, and portions of north-central Norway.

Above normal precipitation (100 to 200 mm) drenched much of southern and western Scandinavia from March 12 through June 3. Up to 100 mm of rain in south-central Norway in one week combined with rapid snowmelt to generate severe river flooding in portions of southern Norway.

MAJOR GLOBAL CLIMATE ANOMALIES AND EPISODIC EVENTS IN 1995

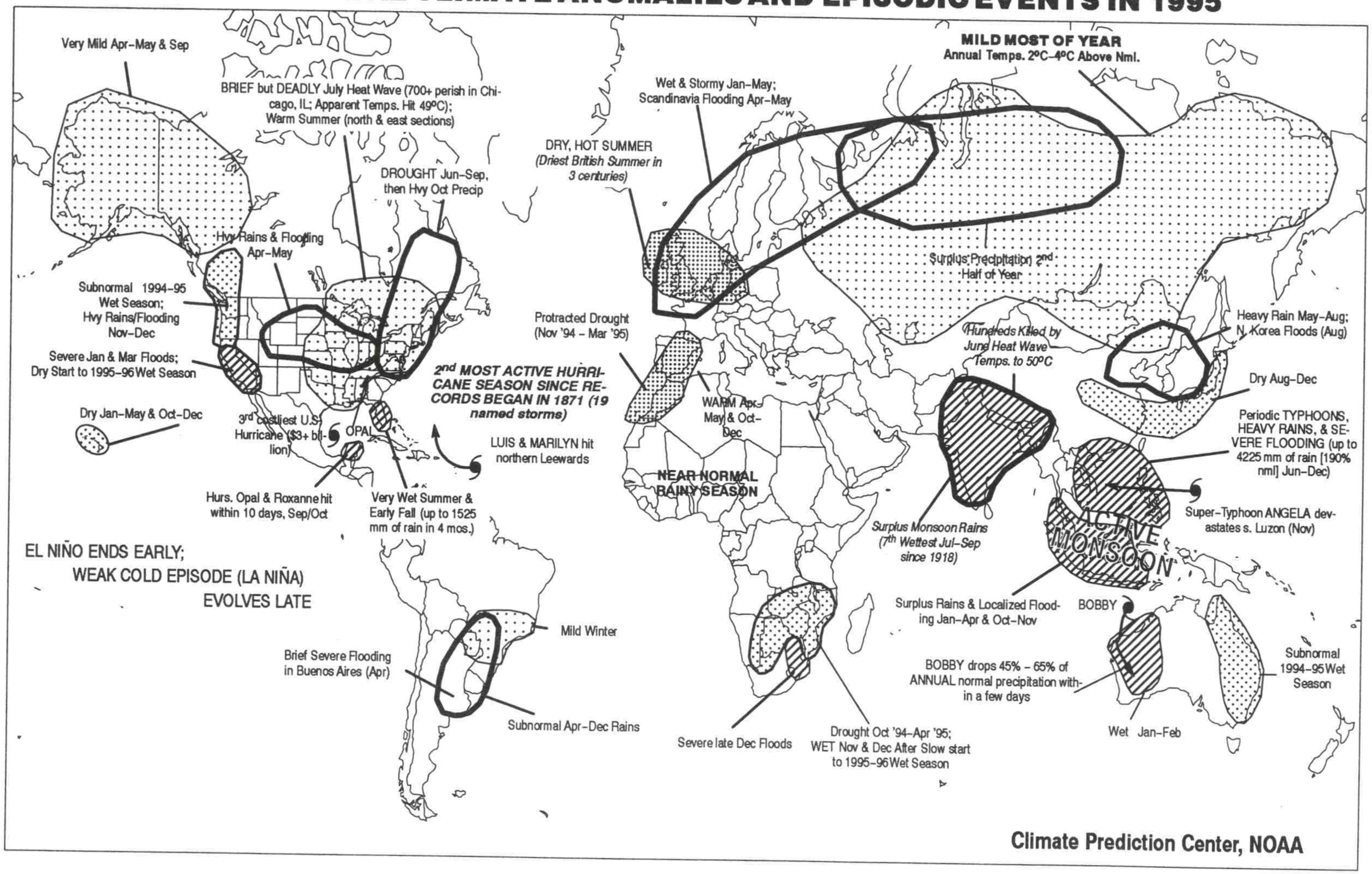

Decadal Variability of Snow in the Western United States

Dan Cayan[1,2] and Larry Riddle[1]
[1]Scripps Institution of Oceanography [2]U.S. Geological Survey

From records over several decades of high elevation snow courses over the western conterminous United States, we consider the following issues:

1. What is the space/time structure of decadal (>7 *yr* period) variability at high elevation snow accumulation as revealed by mountain snow course snow water equivalent (SWE) records (1930-1989)?
2. Is SWE variability consistent with that of other hydrological measures (*e.g.*, temperature, precipitation and streamflow)?
3. How is SWE variability related to large scale fields of atmospheric circulation and SST?
4. How does decadal SWE variability compare with that on the ENSO time scale?

By relating the SWE fluctuations to observed historical variations of other hydroclimate measures, atmospheric circulation, and SST, we conclude that:

1. A major portion (about 55%) of the decadal SWE variability is expressed in two EOF's (Fig. 1): a "northwest" pattern (Washington, Oregon, Idaho, Montana and western Wyoming), and a southwest/northwest opposition pattern (California, Nevada, Utah, and southwestern Colorado out-of phase with northern Idaho and Montana). The northwest pattern has had 3 or 4 major rhythms since 1930, while the opposition pattern has had two broad maxima in the late 1930's—early 1940's and in the early 1980's. Interestingly, the decadal spatial patterns of EOFs 1 and 2 have very strong resemblance to the spatial patterns of EOFs 1 and 2 of ENSO filtered SWE.

2. SWE decadal variability is strongly related to decadal streamflow and at least modestly related to regional precipitation. Thus, heavy high elevation snow is partially reflected in traditional rain gage (lower elevation) measures, and is strongly related to stream discharge (water supply). The northwestern pattern has high snow coincident with cooler temperatures, but the opposition pattern has high snow in the California-through-Utah sector coincident with warmer temperatures over most of the West. The disparity between the Northwest and Southwest snow vs. temperature relationship suggests that temperature is not a major cause of snow variability, but rather the two are associated variables that are both driven by the atmospheric circulation and other aspects of the large scale climate system.

References

Cayan, D.R., 1995: Interannual climate variability and snowpack in the western United States. Accepted for publication in *J. of Climate.*

Changnon, D., McKee, T.B., and N.J. Doesken, 1993: Annual snowpack patterns across the Rockies: long-term trends and associated 500-*mb* snynoptic patterns. *Monthly Weather Review*, **121**, 633-647.

Dettinger, M.D. and D.R. Cayan, 1995: Large-scale atmospheric forcing of recent trends toward early snowmelt runoff in California. *J. of Climate*, **8**, 606-623.

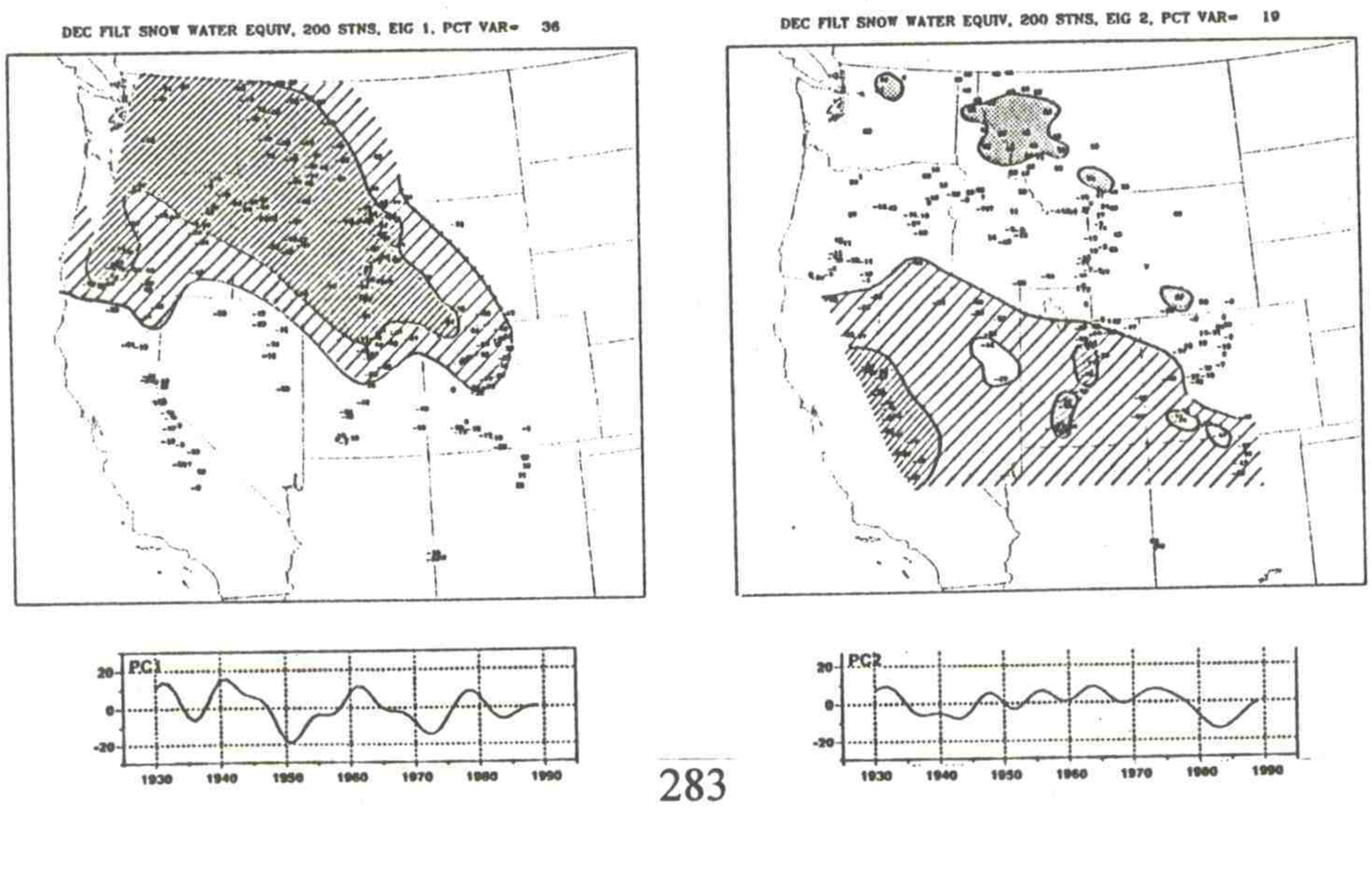

Three-dimensional diabatic heating fields from the NCEP/NCAR reanalysis

G. White and S. Saha
Enviromental Modeling Center
National Centers for Environmental Prediction
Washington, DC 20233
wd23gw@sun27.wwb.noaa.gov

For thirty years estimates of atmospheric diabatic heating have been calculated from data assimilation analyses, usually by solving the thermodynamic equation using analyses of winds of temperatures (Lau, 1979; Hoskins *et al.*, 1989). Ebisuzaki (1995) calculated diabatic heating from the NCEP/NCAR reanalysis using this approach. This paper studies diabatic heating from the NCEP global model's physical parameterizations during the 6-hour forecasts used as the first guess for the analysis. The components of diabatic heating are on a 192 by 94 Gaussian grid and on 28 sigma levels. Monthly mean diabatic heating components are available at NCAR and other sites. A monthly mean climatology of diabatic heating components from reanalysis for 1982-94 will be on a CD-ROM in the *Bulletin of the American Meteorological Society* (Kalnay *et al.*, 1996).

Fig. 1 shows zonal mean cross-sections in sigma of heating components from the model parameterizations for June-Aug. (JJA) 1982-93. Outside the boundary layer deep convective heating and long-wave cooling dominate. Fig. 2 compares zonal mean diabatic heating in sigma from the reanalysis model's parameterizations for JJA 1982-93 to zonal mean diabatic heating calculated from the thermodynamic equation from ECMWF operational analyses for JJA 1983-88 (Hoskins *et al.*, 1989). The two have many common features; reanalysis has more cooling near 800 mb and more heating in the upper tropical tropo-sphere. Hoskins *et al.* (1989) was calculated on pressure levels at lower resolution.

Fig. 3 displays longitudinal cross-sections of heating from reanalysis for JJA 82-93. At 52N heating extends throughout the troposphere over the continents while cooling occurs over the oceans. At 20N upper tropospheric heating occurs in the monsoons, while cooling appears in the eastern oceans. Over the Sahara low-level heating and upper level cooling can be seen. At 7N localized maxima extend throughout the troposphere.

Fig. 4 compares interannual variability in satellite-observed outgoing long wave (OLR) radiation at the top of the atmosphere and in mid-tropospheric deep convective heating from reanalysis over the Pacific between 5N and 5S. Negative anomalies of OLR indicate more deep cloudiness than normal and show good agreement with positive anomalies in mid-tropospheric deep convective heating.

The vertical and horizontal patterns of diabatic heating from reanalysis are generally quite reasonable in climatology and in interannual variability. Reanalysis offers a much more complete, consistent and longer record of atmospheric forcing than previously available. However, model limitations in resolution and in model physics affect the heating, especially near the surface and near tropical orography, and need to be considered. Considerable uncertainty still remains as to the distribution, especially on smaller scales, and the magnitude of divergent motion in the atmosphere, especially in the tropics. This affects the analysis of vertical motion, precipitation and diabatic heating. However, the spatial pattern of these fields are quite reasonable on larger scales.

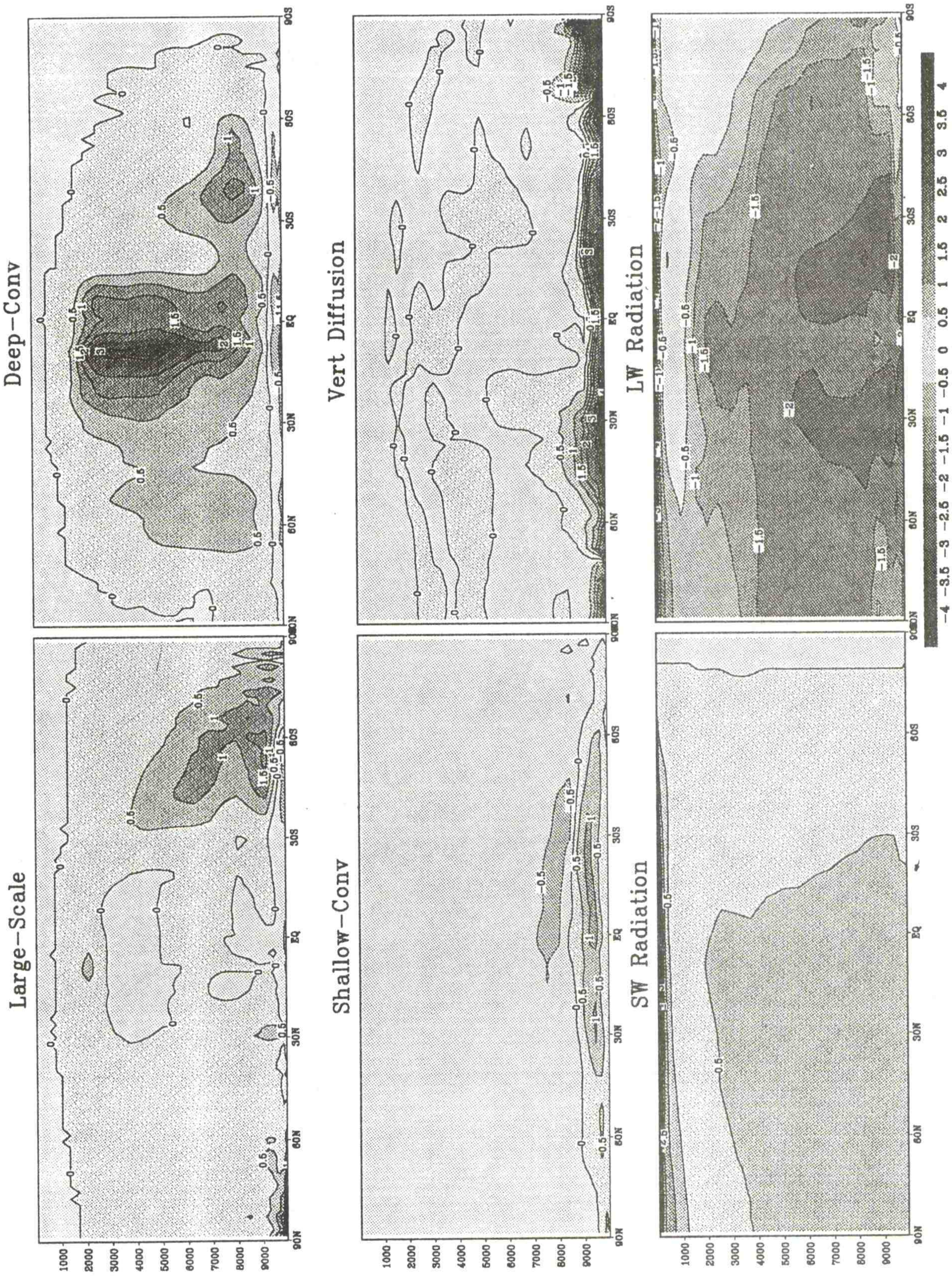

Fig. 1 Zonal mean components of diabatic heating from reanalysis model physics for June-Aug. 1982-93 in sigma. Units K/day.

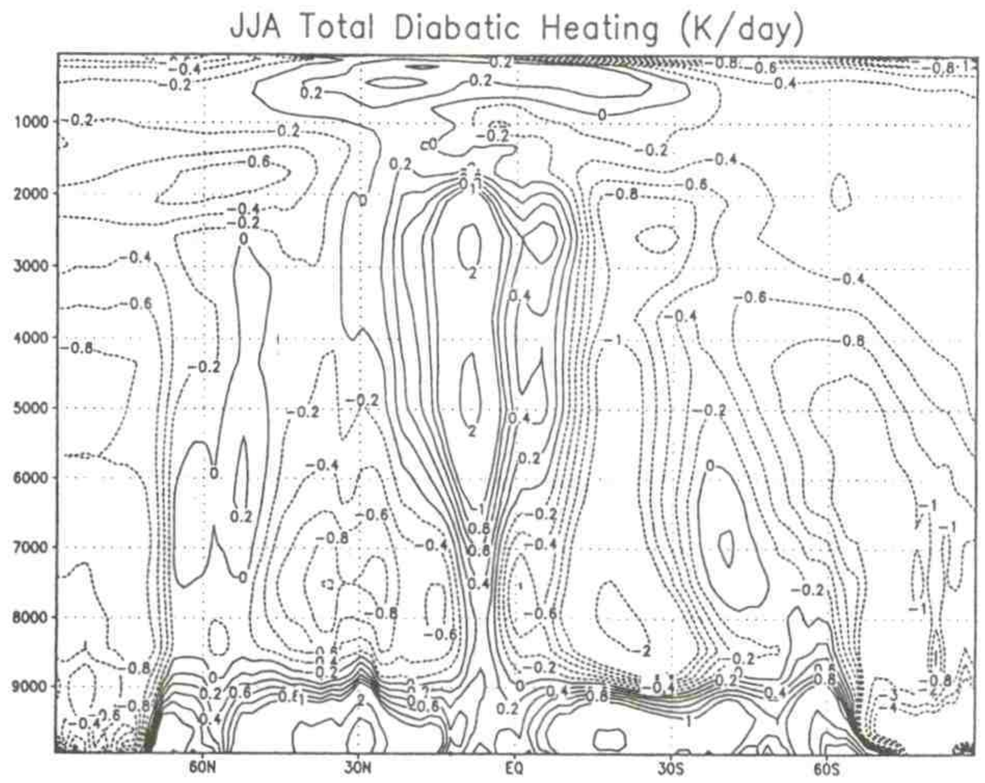

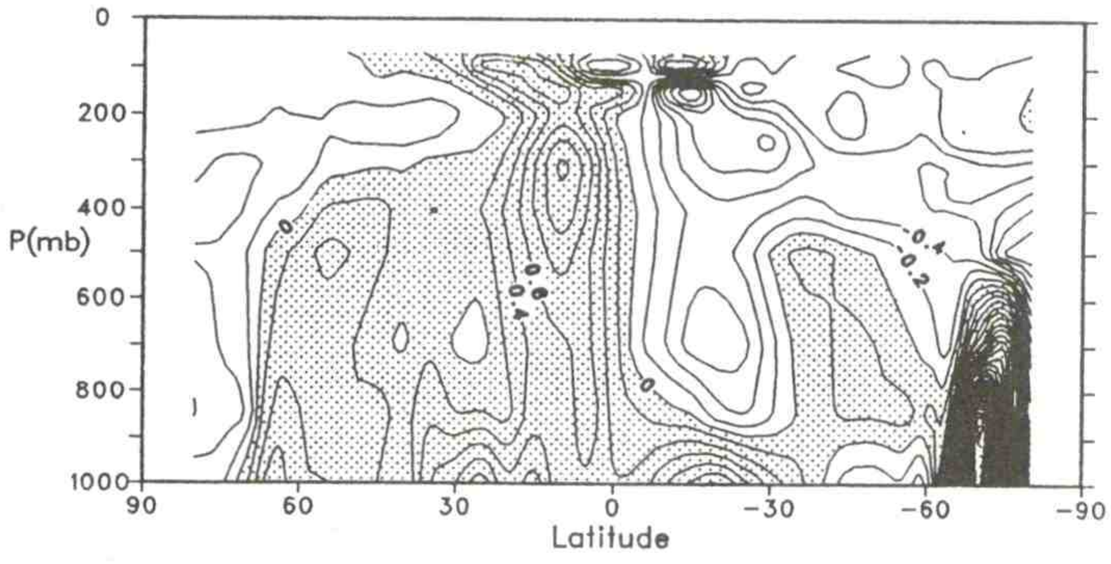

Fig. 2 Zonal mean diabatic heating a) in sigma from reanalysis model physics for June-Aug. 82-93, b) in pressure from thermodynamic equation from ECMWF operational analyses for JJA 83-88 (Hoskins *et al.*, 1989).

Ebisuzaki, W. ,1995: An examination of the diabatic heating and temperature increments from the NMC/NCAR reanalysis. This volume.

Hoskins, B.J., H.H. Hsu, I.N. James, M. Masutani, P. Sardeshmukh, and G.H. White, 1989. *Diagnostics of the Global Atmospheric Circulation Based on ECMWFAnalyses 1979-89.* WMO/TD 326, World Meteorol. Organization, Geneva, Switzerland, 217 pp.

Kalnay, E., M. Kanamitus, R. Kistler, W. Collins, D. Deaven, L. Gandin, M. Iredell, S. Saha, G. White, J. Woollen, Y. Zhu, M. Chelliah, W. Higgins, J. Janowiak, K.C. Mo, C. Ropelewski, J. Wang, A. Leetma, R. Reynolds, R. Jenne, and D. Joseph, 1996: The NMC/NCAR 40-year reanalysis project. *Bull. Amer. Meteorol. Soc.*, in press.

Lau, N.C., 1979: The observed structure of tropospheric stationary waves and the local balances of vorticity and heat. *J. Atmos. Sci.*, 36, 996-1016.

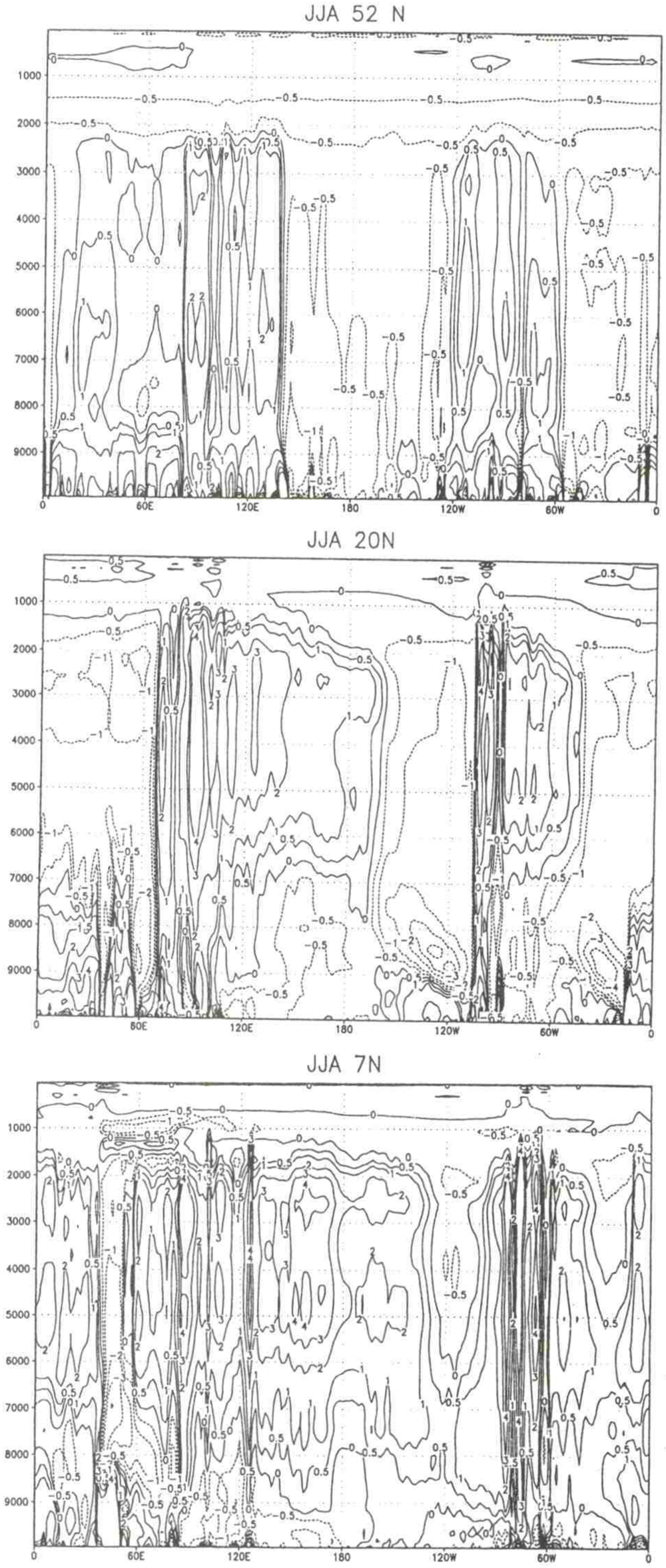

Fig. 3 Longitudinal-sigma cross-sections of diabatic heating from reanalysis for JJA82-93 for (top) 52N, (middle) 20N and (bottom) 7N.

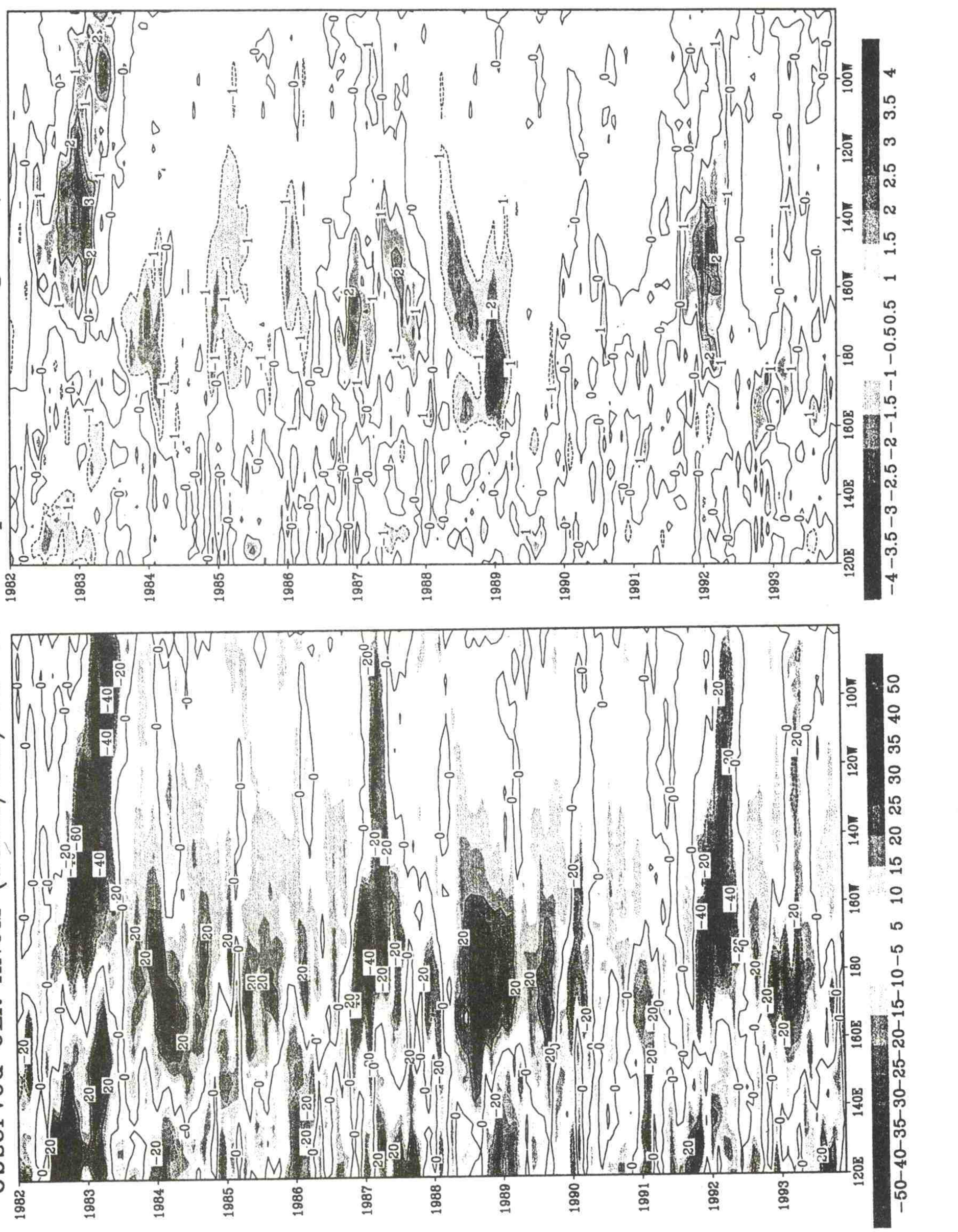

Fig. 4 Longitude-time cross-sections of top of the atmosphere outgoing longwave radiation anomalies from satellite observations and of mid-tropospheric deep convective heating anomalies from reanalysis for 1982-93. Cross-section from 120E to 80W (Pacific) averaged from 5N to 5S.

Dynamical Impact of Localized GWD Forcing in GCM

by JIAYU ZHOU*, Y.C. SUD and K.-M. LAU

Climate and Radiation Branch
Laboratory for Atmospheres, NASA/GSFC, Greenbelt, Maryland, USA

Orographically induced gravity wave drag (GWD) is invoked in general circulation models (GCMs) to relieve the systematic westerly bias over midlatitudes of the winter hemisphere. Though the Eulerian mean analysis shows improvement following a better description of the zonally-averaged flow, the question keeps open that whether the GWD is a physical process or the parameterization a remedy for the model weakness. The dynamical connection between the localized GWD forcing and the geographical influence needs to be further explored.

The impact of GWD parameterization has been investigated in the Goddard Laboratory for Atmosphere (GLA) GCM. The GWD scheme used is a modified version of Vernekar *et al.* (1992), which was based on Alpert *et al.* (1988). After showing large beneficial effect on the systematic errors in the extended range prediction, a set of winter and summer simulations is performed to study the cause and effect between the GWD forcing and the simulated circulation and rainfall. We have isolated three major influences of GWD on the simulations.

(i) The correction of the excessive westerly bias, that is asymmetric about the equator between two hemisphere winters, has been linked to the GWD forcing (Fig.1). This affirms the importance of GWD parameterization for GCMs in which subgrid scale orography is not resolved. As a result of the correction of the wind field, the systematic bias of the sea level pressure particularly over the winter polar regions has been greatly reduced.

(ii) The role of GWD forcing is clearly demonstrated in establishing southward transport of westerly momentum by improved stationary wave in high latitudes (Fig.2 and 3). Dynamical analysis reveals that a Rossby wave source can be created by gravity wave breaking at high altitude. Moreover, it also can be the result of local enhancement of baroclinicity due to the planetary wave response to the remote GWD forcing in the lower atmosphere. Overall, the correction in the stationary wave field can be produced by the GWD induced anomalous Rossby wave propagation in three dimensional space, that has been demonstrated by the analysis of anomalous stationary wave activity flux (Fig.4). Significant improvement of the circulation over northern Pacific leads to a better simulation of the storm track hence the precipitation distribution (Fig.5).

(iii) The adjustment of the secondary circulation to the correction of local zonal mean zonal wind has been examined for the summer Asian monsoon region (Fig.6). The corrections in the fields of vertical motion and horizontal divergence are found to be dynamically related to the local zonal mean GWD forcing (Fig.7). The GWD induced correction of the local secondary circulation produces the required northward shift of the Asian summer monsoon precipitation belt (Fig.8).

An open upper model boundary condition has been applied in this study. The result shows that during summer the orographically excited gravity waves are weak and mainly broken below

---

* Applied Research Corporation

the lower stratosphere. In winter a nonnegligible part of drag momentum flux can pass through the model top (10 mb) in the mid-latitudes. This is especially the case in northern winter hemisphere, where strong westerlies extend from the surface to the upper model atmosphere in addition to large topographic variance over Eurasian and North American continents. All these results are consistent with the observations. Overall, an elimination of spurious GWD forcing at the model top layer was found, contributing to a better vertical distribution of the momentum deposition. As discussed by Holton (1982) the drag force created by the gravity wave breaking at mesospheric height is an important part of the momentum budget in the middle atmosphere since it nearly balances the Coriolis torque due to the mean meridional circulation which is locally forced by radiative heating.

The current scheme has also been implemented in the Data Assimilation Office (DAO) GCM at Goddard Space Flight Center. Almost all of the improvements found with the GLA GCM are refirmed in DAO-simulations. This indicates that the GWD mechanism is model independent.

REFERENCES

[1] Alpert, J.C., M. Kanamitsu, P.M. Caplan, J.G. Sela, G.H. White and E. Kalnay, 1988 : Mountain induced gravity wave drag parameterization in the NMC medium-range forecast model. *Proceedings of the Eighth Conference on Numerical Weather Prediction*, Baltimore, Maryland, February 22–26, 1988, 726 –733.

[2] Holton, J.R., 1982: The role of gravity wave-induced drag and diffusion in the momentum budget of the mesosphere. *J. Atmos. Sci.*, **39**, 791–799.

[3] Vernekar, A.D., B. Kirtman, J. Zhou and D. DeWitt, 1992 : Orographic gravity-wave drag effects on medium-range forecasts with a general circulation model. *Physical Processes in Atmospheric Models.* Edited by D.R. Sikka and S.S. Singh. Wiley Eastern Limited, 295-307.

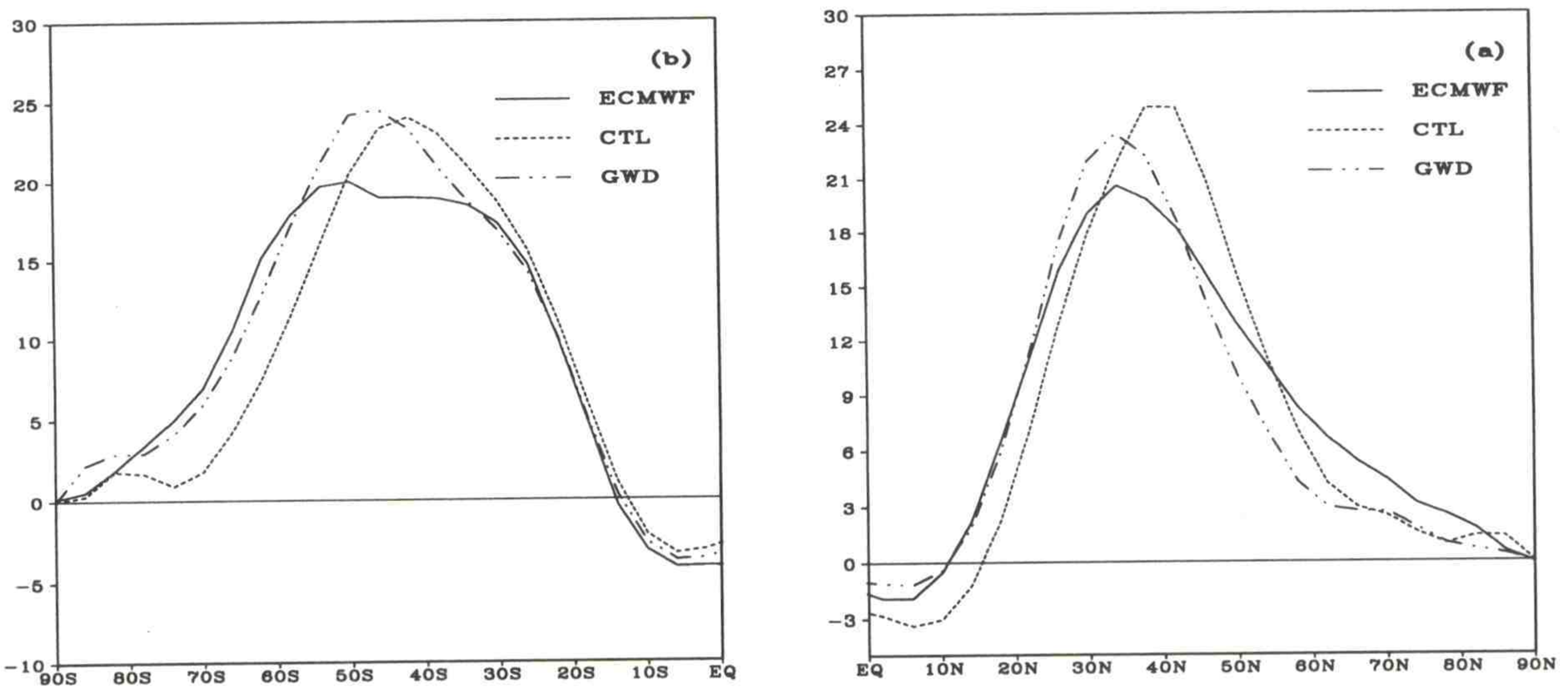

Figure 1 Zonally averaged zonal wind (m/s), for a mass-weighted average over a layer between the surface and 30 mb. (a) 1988 JJA and (b) 1987 $\sim$ 1988 DJF.

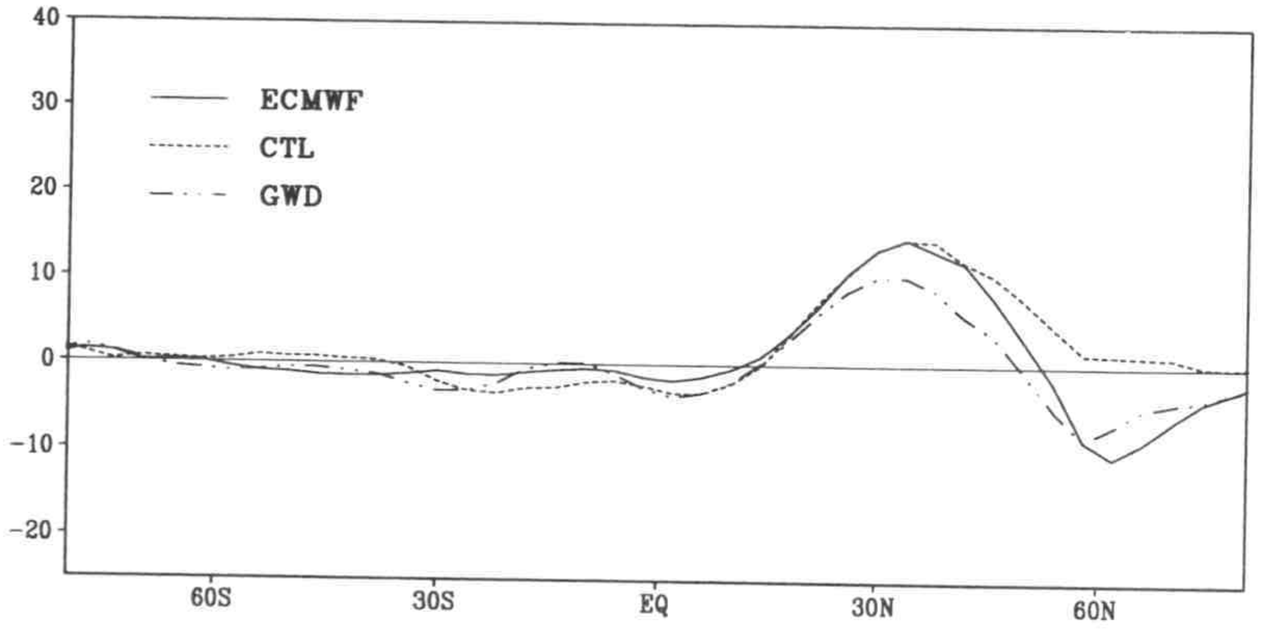

Figure 2 1987 ~ 1988 DJF surface ~ 30 mb averaged zonal mean meridional transport of zonal momentum (m^2/s^2) by stationary eddies.

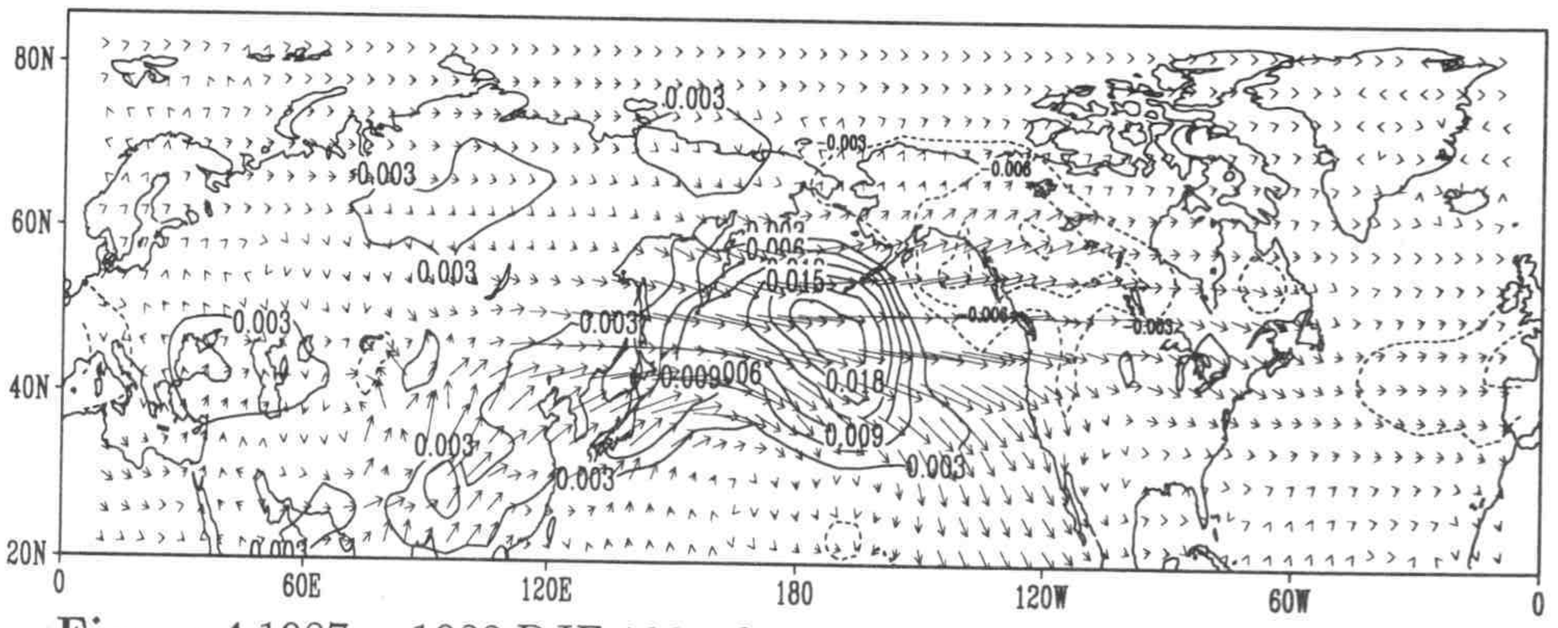

Figure 4 1987 ~ 1988 DJF 100 mb anomalous stationary wave activity flux (GWD - CTL, m^2/s^2). The arrows indicate the horizontal direction of the anomalous wave energy propagation; the contours show the magnitude of the vertical component of the anomalous wave activity flux.

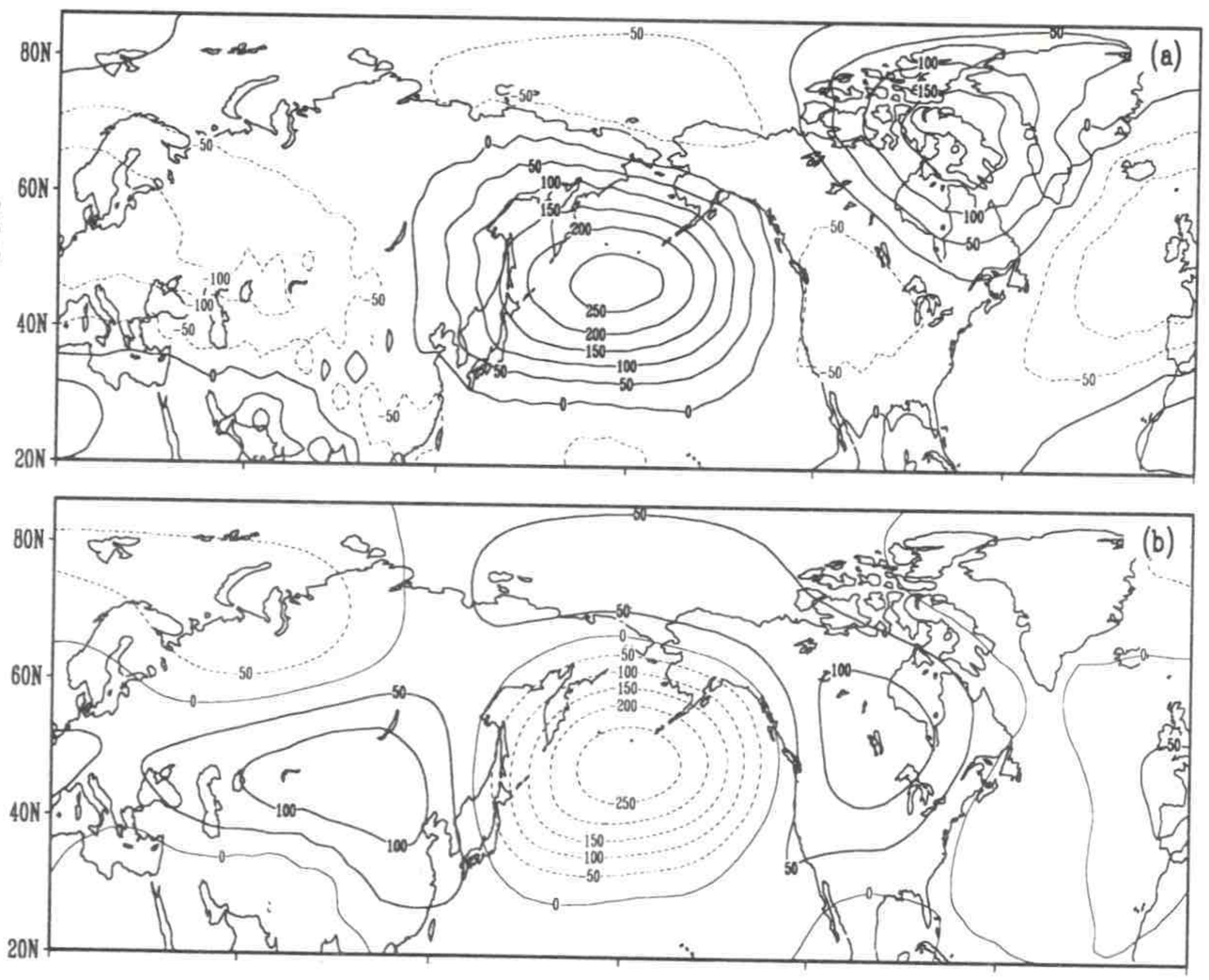

Figure 3 1987 ~ 1988 DJF 100 mb geopotential height stationary wave difference (m) of (a) CTL - ECMWF and (b) GWD - CTL.

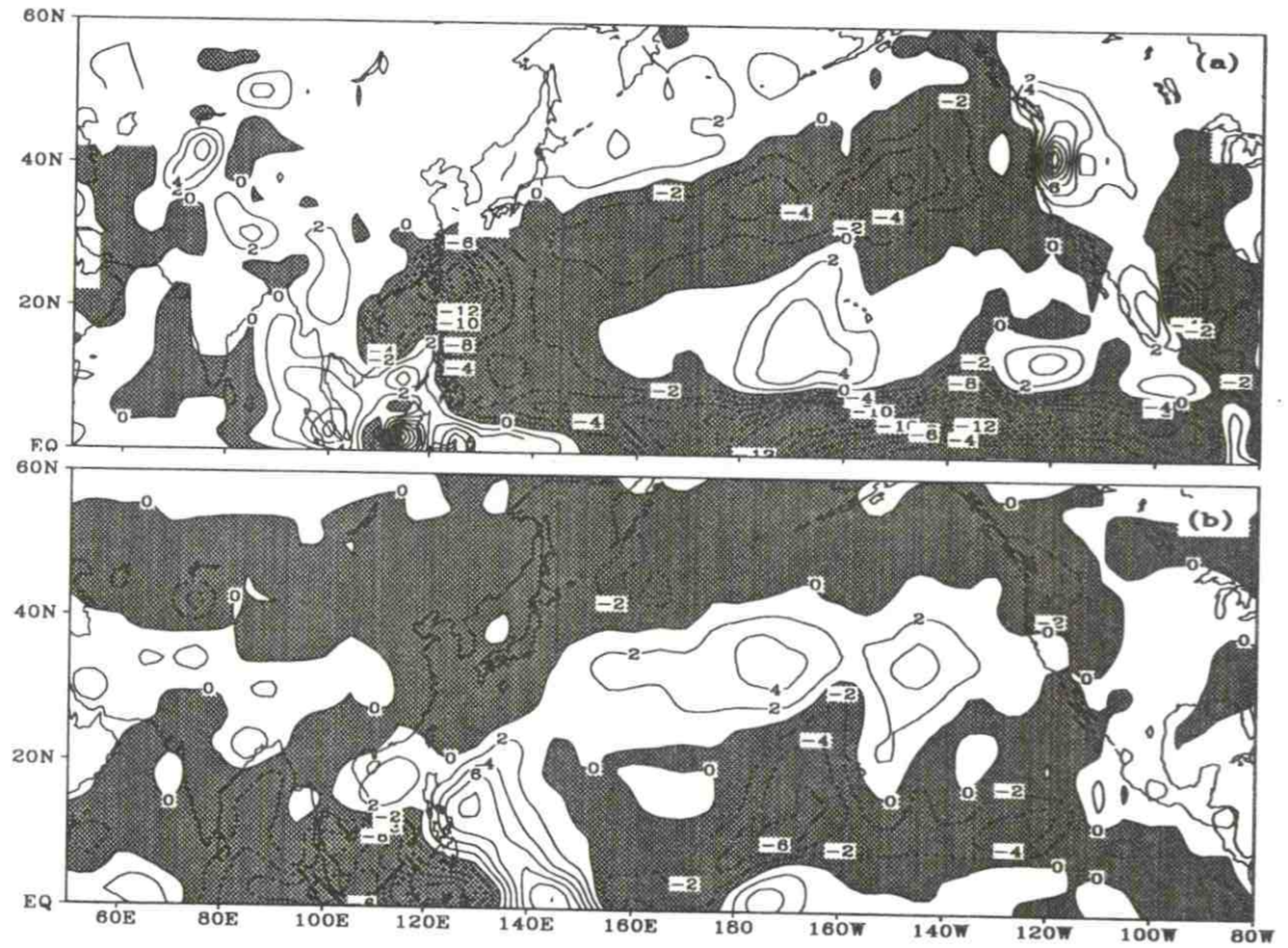

Figure 5 1987 ~ 1988 DJF precipitation difference (mm/day) of (a) CTL - OBS and (b) GWD - CTL, where OBS is the data observed by MSU over ocean and rain gauge over land.

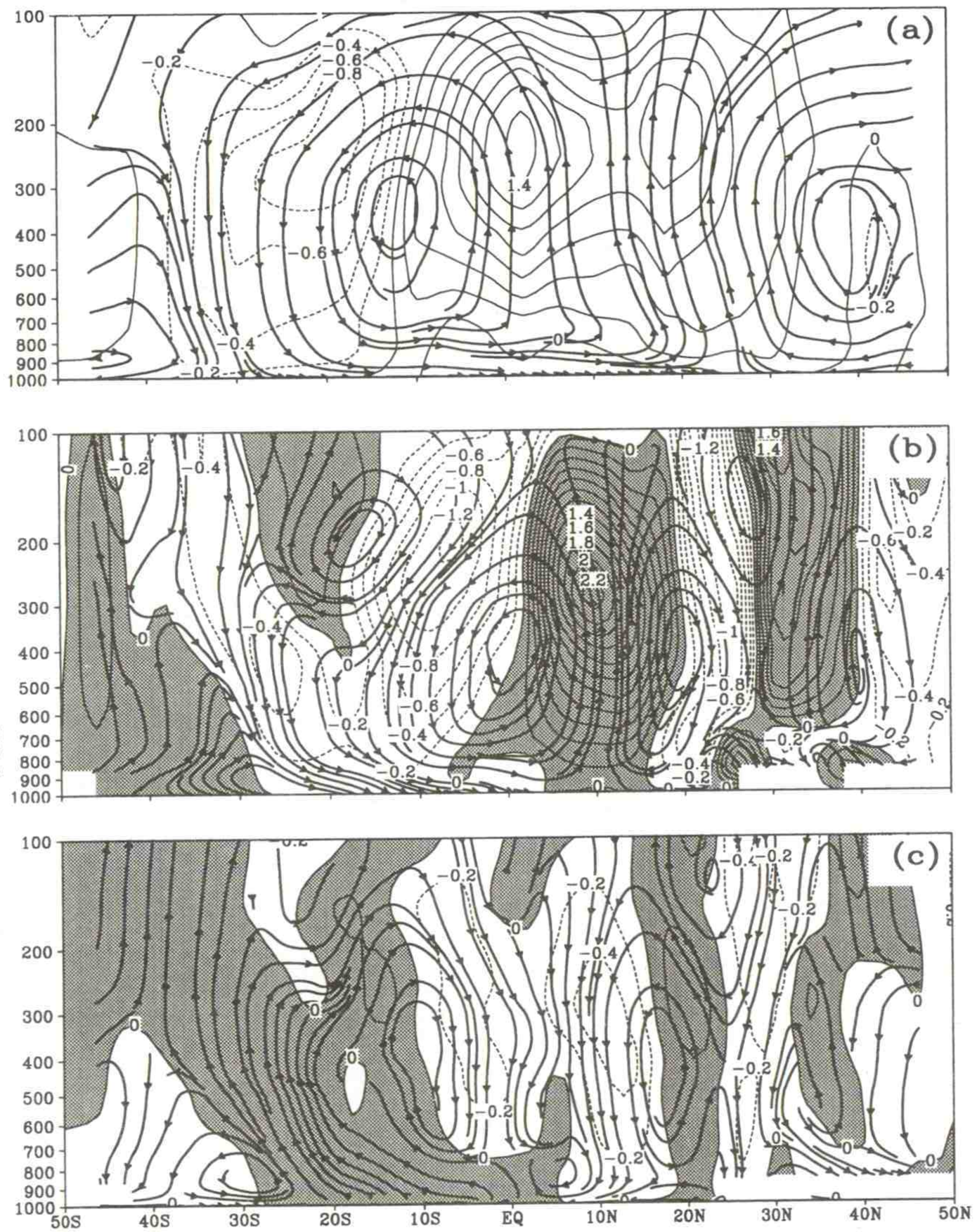

Figure 6 1988 JJA 60° ~ 120°E averaged meridional circulation. Contours indicate vertical velocity (cm/s) and vectors the stream lines. (a) ECMWF analysis, (b) CTL - ECMWF and (c) GWD - CTL.

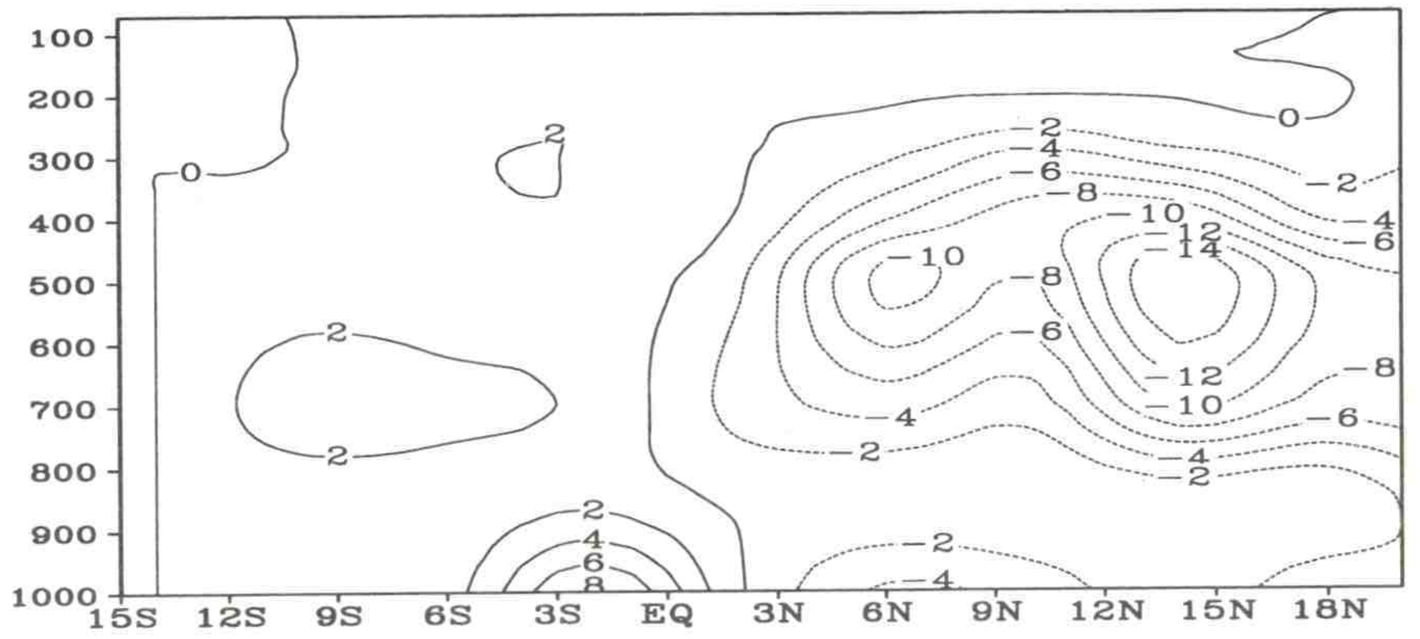

Figure 7 1988 JJA 60° ~ 120°E zonally averaged GWD acceleration. Units:$10^{-6}m/s$.

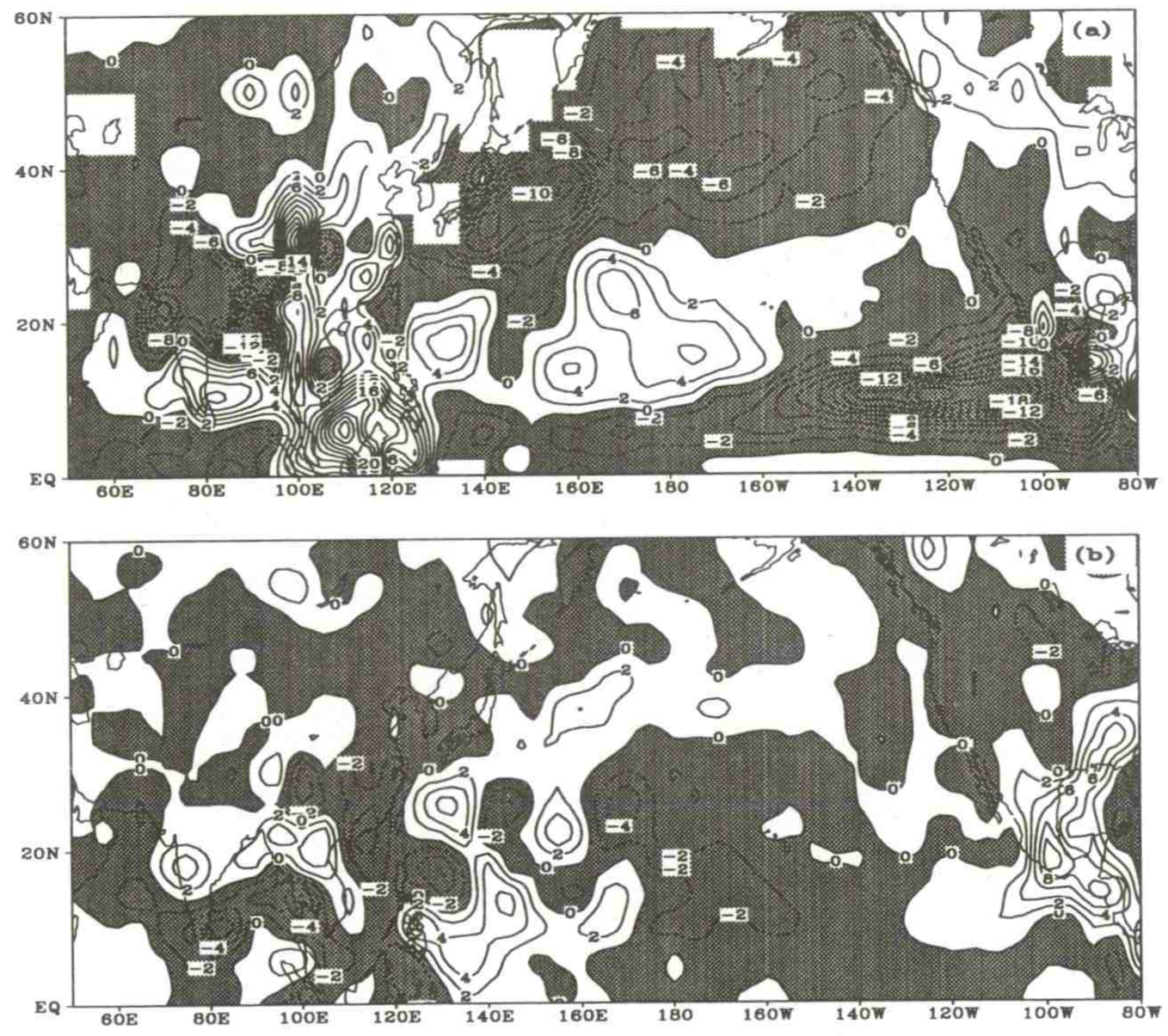

Figure 8 Same as Figure 5 except for 1988 JJA.

Decadal Changes in the Circulation of the Northern Hemisphere: Relation to Surface Temperature

James W. Hurrell and Harry van Loon

National Center for Atmospheric Research[1]
Boulder, CO 80307

Introduction

At the core of the debate of anthropogenic climate change is the observation that global mean surface temperatures have increased to record levels during the past decade. The warming has been largest during the winter and spring seasons over the continents between 40°N and 70°N, while weak cooling has occurred over the northern oceans (Fig. 1). The pattern of temperature change is related to observed decade-long changes in the circulation of the atmosphere and ocean. It is the purpose of this paper to illustrate and quantify the relationship between the circulation changes and surface temperature anomalies in the NH during winter using multivariate linear regression.

Circulation Indices

A large amount of evidence has emerged of a substantial change in the wintertime atmospheric circulation over the North Pacific that began in the mid-1970s and lasted throughout the 1980s. The changes involved the Pacific-North American teleconnection pattern and corresponded to a deeper and eastward shifted Aleutian low pressure system which advected warmer and moister air along the west coast of North America and cooler and drier air over the central North Pacific. A simple index used to measure the variations over the North Pacific (NP) is the area-weighted mean sea level pressure over the region 30°to 65°N, 160°E to 140°W. The NP index, averaged over the winter months from December through March, is shown in Fig. 2 since 1934-35. Pressures from 1976-77 to 1987-88 were lower by 2.2 mb relative to the 60-winter NP-area mean.

The decadal changes over the North Pacific have been linked to variations in the tropics, and several modeling studies have confirmed that North Pacific atmospheric variability is controlled in part by anomalous tropical Pacific SST forcing. Fluctuations in tropical SSTs are related to changes in the Southern Oscillation (SO) and the occurrence of the El Niño–Southern Oscillation (ENSO) phenomenon. Variations in the SO can be measured through an index defined by the normalized Tahiti minus Darwin SLP anomalies. The SO index for the winter months clearly illustrates a change toward more negative values and thus warmer tropical conditions since the mid-1970s (Fig. 2), including the prolonged warm conditions since 1990.

Another teleconnection that has played a major role in the pattern of regional temperature change over the past two decades is the North Atlantic Oscillation (NAO). A simple index of the NAO (Fig. 2) is defined as the difference of normalized pressures between Lisbon, Portugal and Stykkisholmur, Iceland, which are near the centers of the teleconnection during winter. Positive values of the index indicate stronger-than-average westerlies over the middle latitudes associated with low pressure anomalies in the region

[1] The National Center for Atmospheric Research is sponsored by the National Science Foundation

of the Icelandic low and anomalously high pressures across the subtropical Atlantic. A striking feature of the NAO index (Fig. 2) has been the reversal from the weak meridional pressure gradient of the 1960s to strongly positive index values since 1980.

The changes in local surface temperatures and SSTs based on linear regression with the NAO, the NP and the SO indices are presented in Fig. 3. It is evident that the changes in circulation over the Atlantic have contributed much to the recent wintertime warmth across Europe, the coolness over the eastern Mediterranean, and to the very cold conditions over the northwest Atlantic. The pattern of temperature change associated with the NP index shows that the North Pacific basin anomalies since the mid-1970s are consistent with the longer record: below normal NP values are associated with below-normal temperatures over the North Pacific and above normal surface temperatures along the west coast of North America extending into Alaska and across most of Canada. Also, it is clear that the NP and the SO indices explain much of the same surface temperature variance.

Regression Analysis

The effect of the circulation changes on temperature can be quantified through multivariate linear regression. The indices in Fig. 2 were regressed upon the NH extratropical (20°N to 90°N) temperature anomalies for each winter since 1934-35. The results can be extended farther back in time, but only with the tradeoff of less reliable circulation indices and less reliable estimates of surface temperature and SST.

The regression model using all three indices explains 47% of the NH extratropical surface temperature variance, and the leading regression coefficient is associated with the NAO index. The strong relation between the NP and the SO indices (the two are correlated at 0.51) contributes to relatively high standard errors of the regression coefficients associated with these two indices. When only the NAO and the SO indices are used in the regression more confidence can be placed in the estimated coefficients, and 44% of the variance of the extratropical NH temperatures is explained. Shown in Fig. 4 are the temperature changes since 1934-35 associated with the NAO, the SO and their sum. Also shown are the mean NH temperature anomalies relative to the 60-winter mean and the residual time series after the removal of the temperature contributions by the two circulation indices. Over the entire period, variations of temperature associated with the NAO account for 31% of the hemispheric interannual variance, while the SO accounts for 16% of the interannual variance. Both the NAO and the SO indices can account linearly for much, but not all, of the hemispheric warming over the past two decades. Over the period 1976-77 to 1993-94, the NH extratropical temperature anomaly relative to the 60-winter mean was 0.21°C, while the anomaly of the residual series was 0.06°C. Of the 0.15°C difference, the NAO-related warming was 0.10°C.

Regression was also performed locally using the NAO and the SO indices as the independent variables. The anomalies of the residual temperatures averaged over the winters since 1976-77, recomputed relative to a 1951-1980 base period, reveal that the distinctive regional features evident in Fig. 1 are linearly related to variations in these two indices (Fig. 5). Most notable is the reduction of the warm anomalies over the NH extratropical landmasses and the elimination of the strong cooling over the northwest Atlantic. The residual coolness over the North Pacific, the warmth over Alaska and the coolness over

the southeast United States is related to the exclusion of the NP index from the regression. It must also be recognized that the residual anomalies in Figs. 4 and 5 probably reflect the exclusion of other teleconnection indices that affect patterns of interannual temperature variability in the NH, and that linear regression techniques do not account for feedback (nonlinear) effects.

Elements of the temperature anomaly pattern since the mid-1970s (Fig. 1) resemble the greenhouse warming fingerprint predicted by some general circulation models. However, it is difficult to assess whether the observed changes are in response to greenhouse gas forcing, or whether the changes are part of a natural decadal-timescale variation in the circulation. Regardless of cause, the changes in circulation since the mid-1970s have resulted in a particular surface temperature anomaly pattern that has amplified the hemispheric-averaged warming because of its interaction with land and ocean. Because anomalies over oceans are more subdued due to the large heat capacity of water, the hemispheric mean surface air temperature is largely determined by the temperature of the continents.

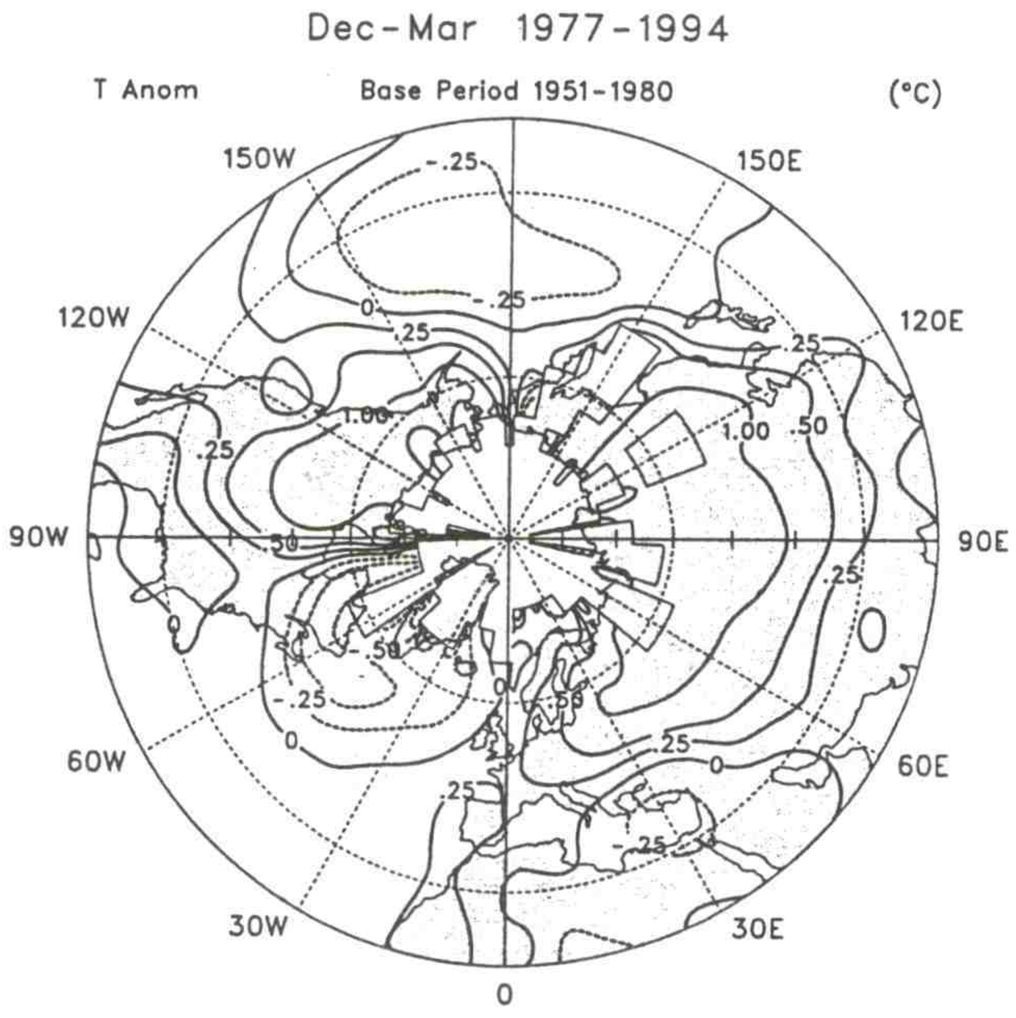

Fig. 1. Eighteen winter average surface temperature and SST anomalies expressed as departures from the 1950-51 to 1979-80 mean. Negative anomalies are dashed, and regions of insufficient data coverage are not contoured.

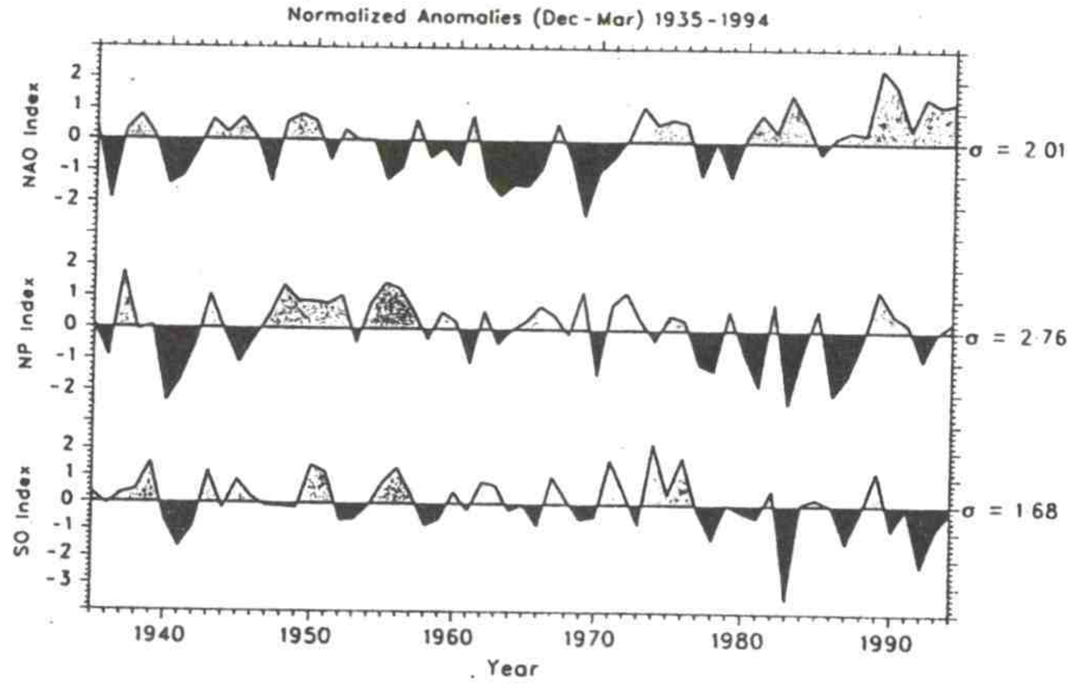

Fig. 2. Time series of winter values of the NAO, the NP and the SO indices as defined in the text. Values are normalized relative to the mean from 1934-35 to 1993-94, and the standard deviations are plotted on right axis.

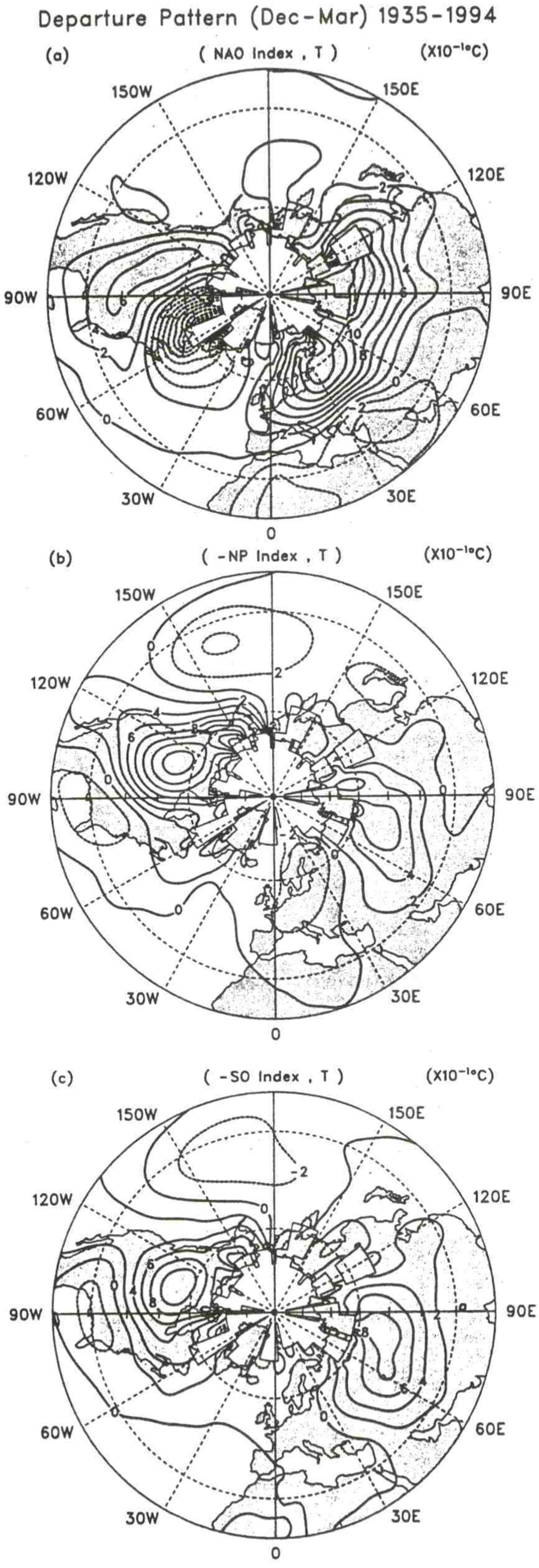

Fig. 3. Changes in temperatures (x 10^{-1}°C) corresponding to unit deviations of the (a) NAO index, (b) NP index, and (c) SO index computed over the winters from 1934-35 to 1993-94. The NP and the SO indices were multiplied by minus one. Regions of insufficient data are not contoured.

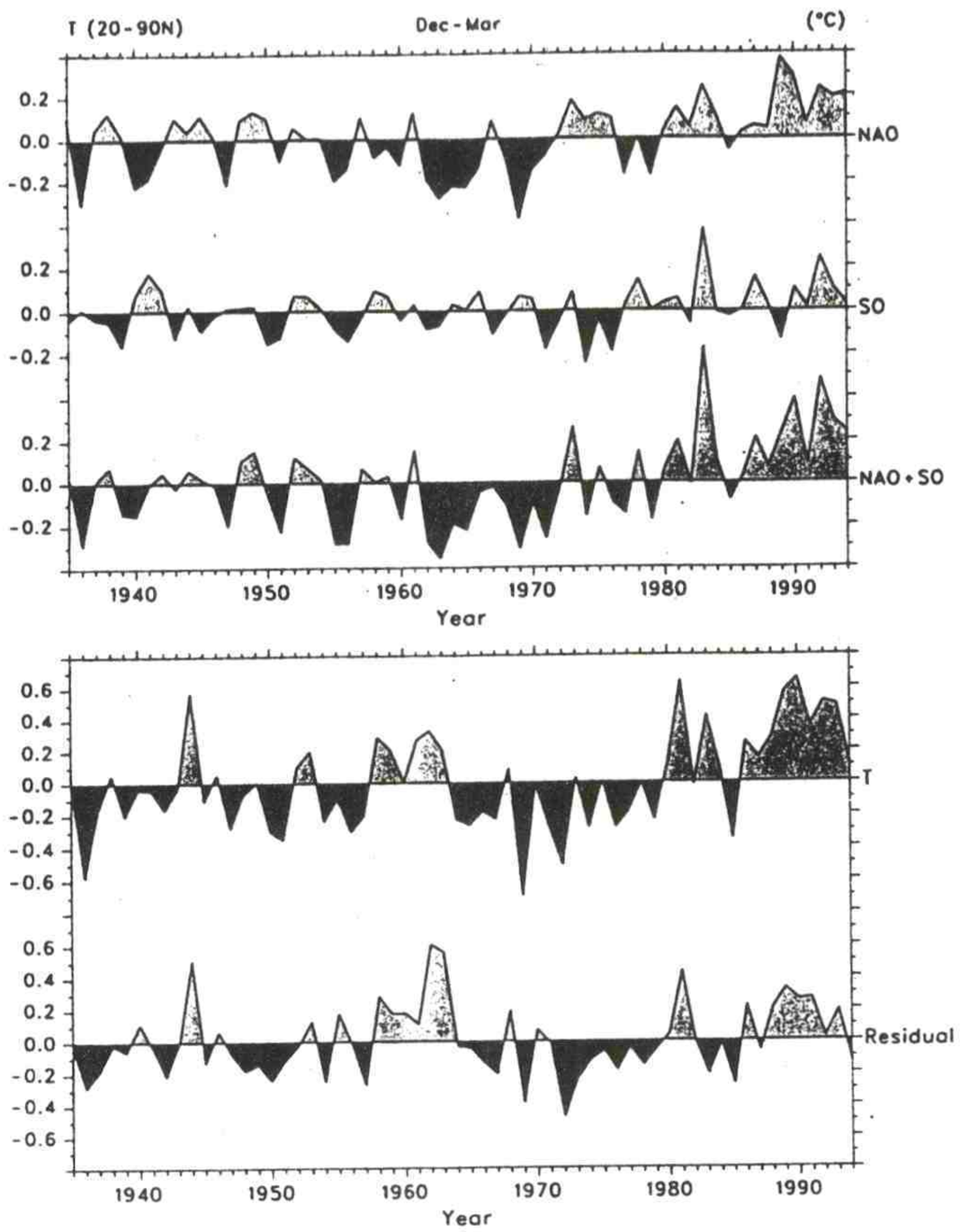

Fig. 4. Temperature changes associated with the NAO, the SO and their sum averaged from 20°N to 90°N. The NH extratropical temperature anomalies relative to the 1934-35 to 1993-94 mean, and the residual after removing the linear effects of the NAO and SO are shown in the lower panel.

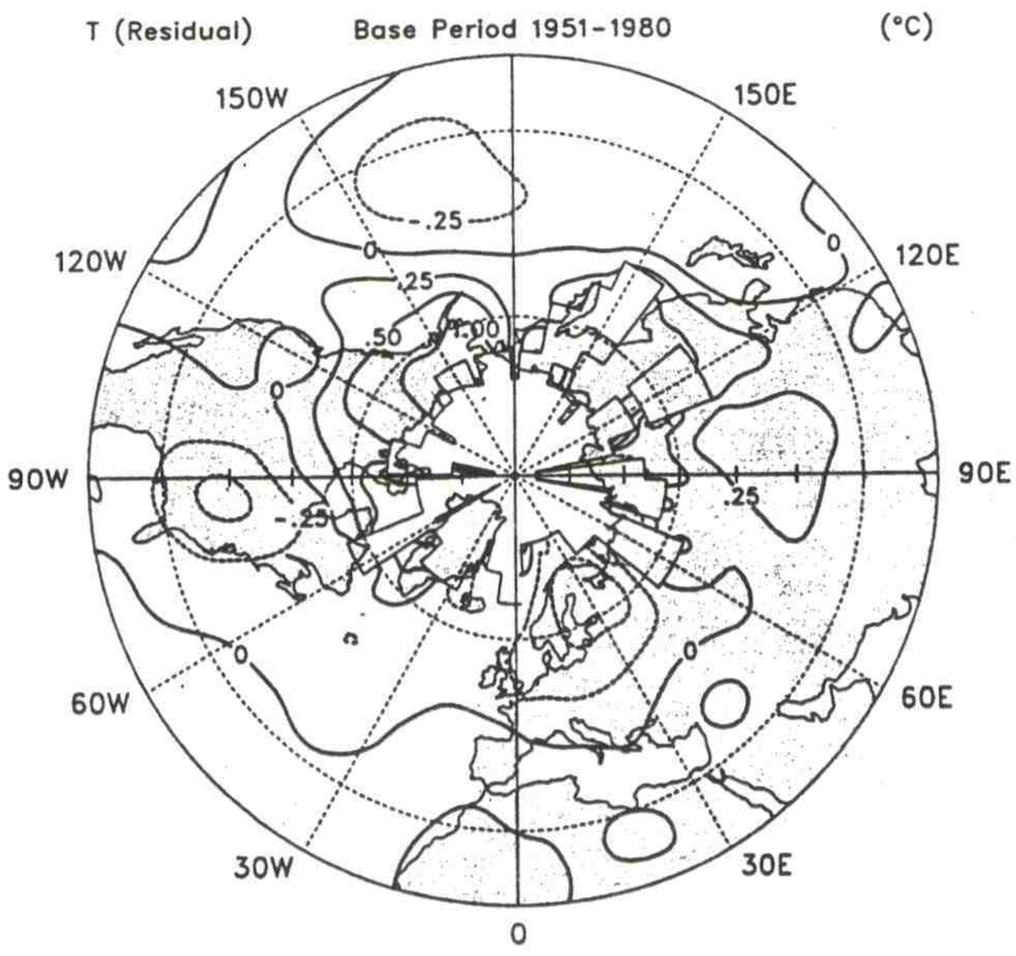

Fig. 5. Same as Fig. 1, but for the surface temperature and SST anomalies after the linear effects of the NAO and the SO have been removed.

El Niño Predictions by the NCEP Coupled Ocean-Atmosphere Model: A View from the Ocean Subsurface Thermal Variability

Deng-Hua Wu, Ming Ji and Ants Leetmaa

National Centers for Environmental Prediction/NWS/NOAA
Camp Springs, Maryland 20746

1. Introduction

It is now well established that the El Niño and the Southern Oscillation (ENSO) in the tropics is the result of the large scale ocean-atmosphere interactions. The memory of the coupled oscillations is mainly in the ocean through the slow evolution of the ocean subsurface variability induced by the large scale, low-frequency oceanic waves. To predict successfully the El Niño events, a model needs to capture the evolution of not only sea surface temperature (SST), but also of the subsurface variability such as the thermocline depth anomalies which have significant impact on the SST variations on the ENSO time scales. For longer prediction lead times, the key to a better prediction of El Niño may rely on a correct prediction of the thermocline depth anomalies, since it is these anomalies that are most likely linked to the future evolution of El Niño. The success of simple or intermediate coupled ocean-atmosphere models for ENSO predictions has in fact appeared to suggest the importance of correctly simulating the subsurface variations. Though with simplified physics, the evolution of the thermocline depth anomalies are presumably captured well in these models, thus leading to the significant skill of predicting ENSO events at lead time of several seasons.

The NCEP (National Centers for Environmental Prediction) coupled model and prediction of SST anomalies associated with the El Niño by this model have been described in Ji et al (1994). In this paper, we report on a study of the prediction skill of the model for the ocean subsurface variations, specifically thermocline depth anomalies. The data for the present analysis are from a large set of forecast experiments carried out to evaluate the skill of the coupled model for predictions of ENSO. The forecasts were initiated one month apart for the period from April 1982 through September 1994 from initial conditions taken from an ocean reanalysis . Each forecast is performed for one year. Although the coupled model produces a climatology which differs from that observed, i.e. significant systematic errors arise, the anomalies are captured fairly well.

2. Results

Systematic errors are also present in the forecasted thermocline depth anomalies; here we will focus on the examinations of the anomalies that remain after these errors have been removed in the remainder of this paper. Because of the lack of observed subsurface data with the appropriate spatial and temporal coverage, the results of the predictions will be compared against the ocean reanalysis. Anomalies of the depth of 20°C isotherm will be used as a proxy for the thermocline depth anomalies, since this isotherm lies in the middle of thermocline in the tropics.

Fig.1 shows the correlation and rms (root mean square) error of the depth of the forecast 20°C anomalies averaged over the Nino-3 region (150°W-90°W and 5°S-5°N) as a function of lead time. In these calculations, the predictions regardless of starting time were used. For reference, the skill for persistence of the reanalysis is also shown in the figure. It is seen that except for the first season, the

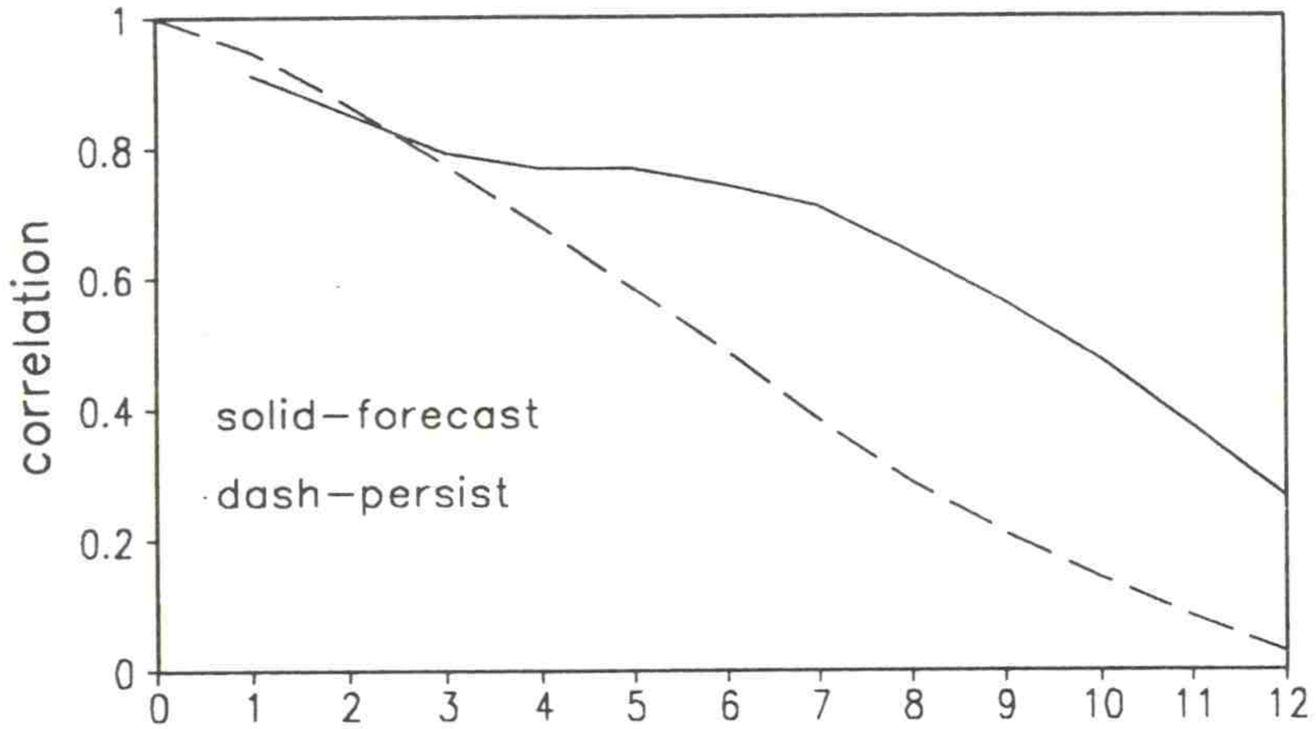

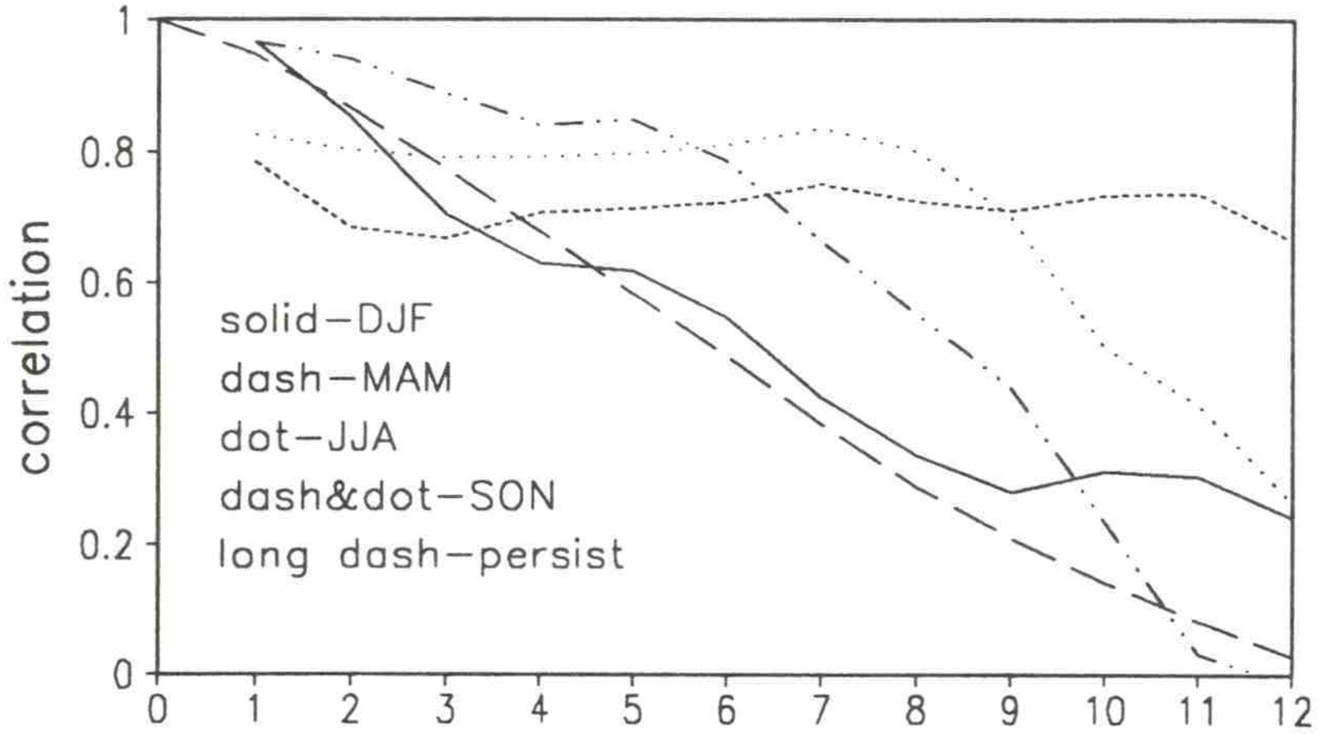

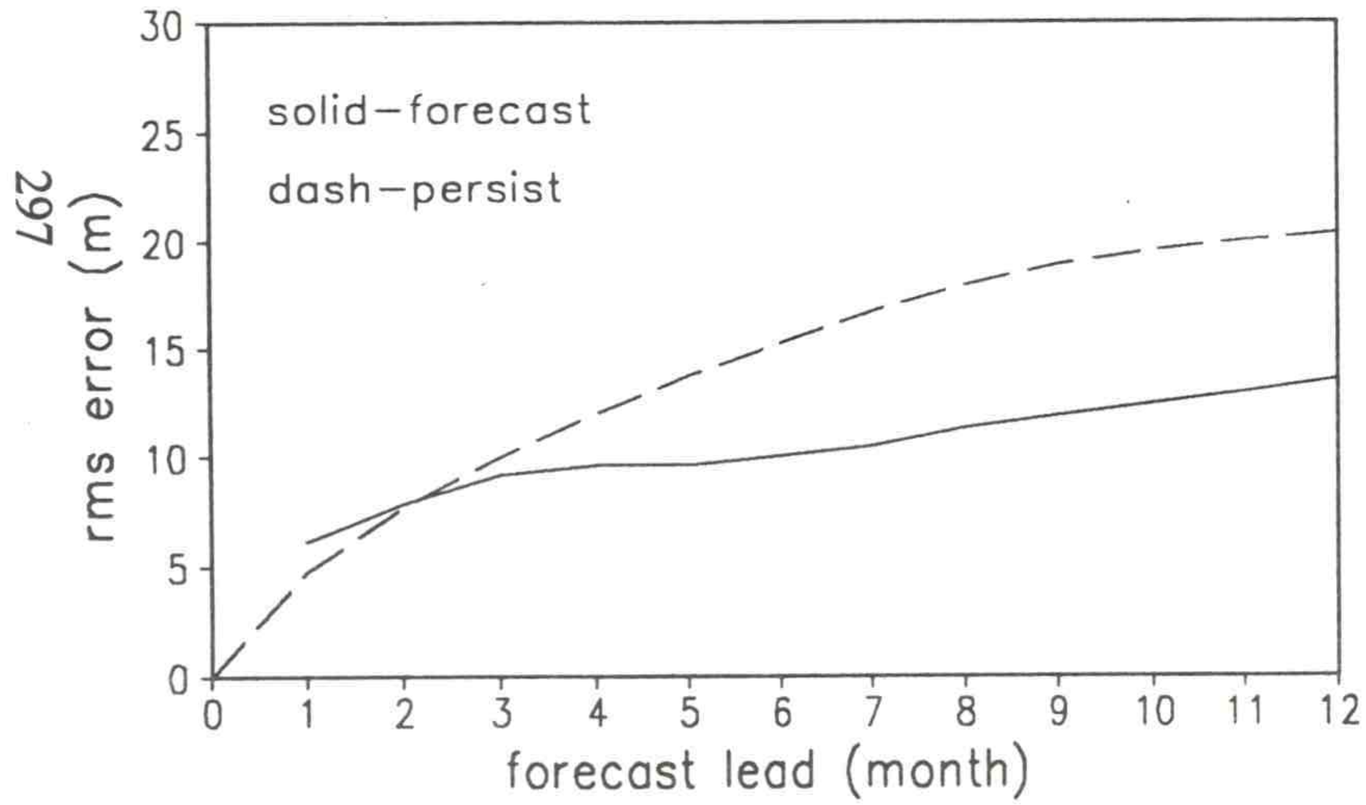

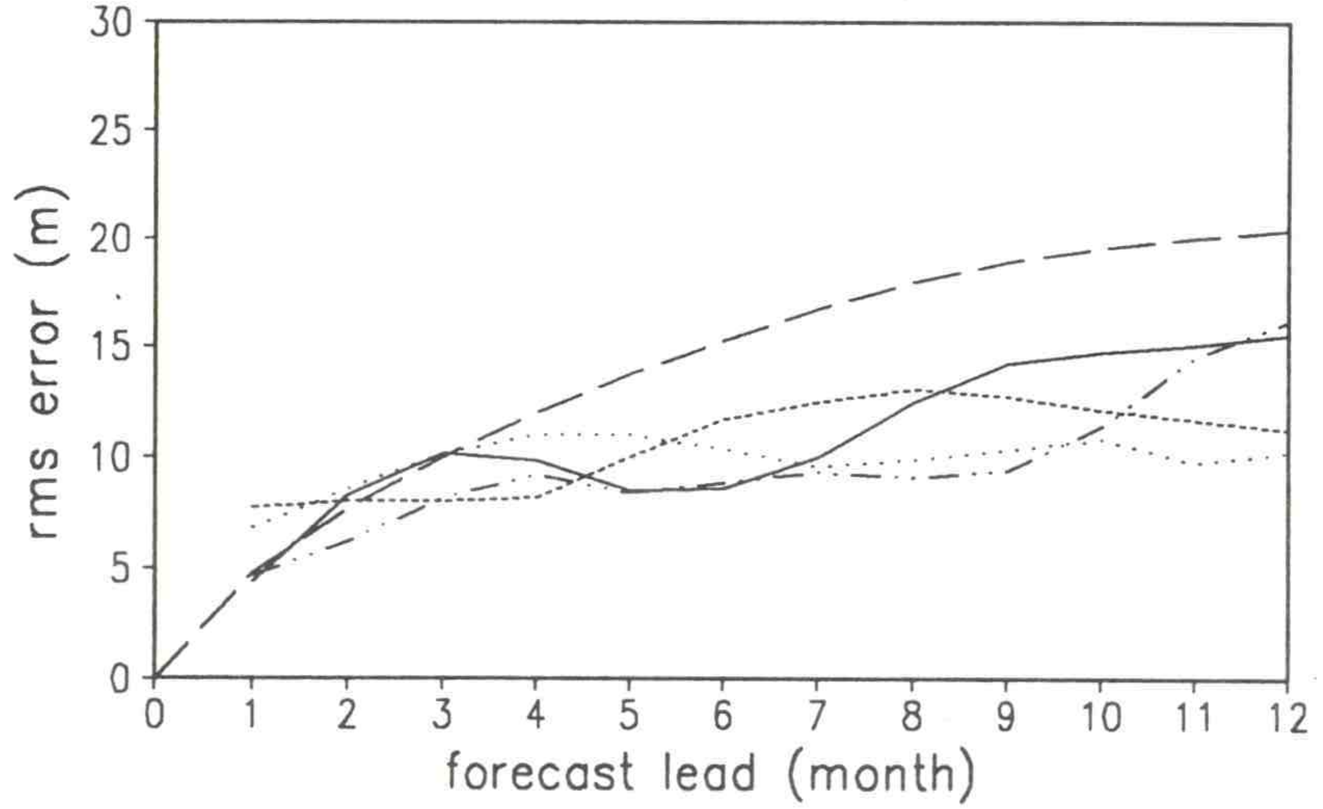

Fig.1: *Correlations (top), and rms errors (bottom) of the depth of 20°C anomalies between the predictions and the reanalysis. The anomalies are averaged over the Nino-3 region (150°W-90°W and 5°S-5°N). The dashed lines are for the persistence of the reanalysis.*

Fig.2: *The same as Fig.1, but for predictions starting from different seasons.*

forecasts outperform persistence for all the lead time considered here. The predictions have significant skill with the correlations above 0.7 up to a lead time of about 7 months, after which the skill drops relatively quickly. The temporal skill in the forecast of SST was very similar.

To examine the seasonal dependence of the prediction skill, the correlations were calculated by using forecasts which are grouped according to their starting time. Fig.2 shows the prediction skills for different starting times; however the persistence curve is the same as in Fig.1. A strong seasonal dependence of the skill is apparent; predictions starting from summer are much better than that starting from winter. The model loses skill most rapidly in the March, April, May period. It is of interest to note that although forecasts starting in MAM initially have the lowest skill, they retain this initial level of skill up to a lead time of about a year. While predictions initiated after the MAM season have higher correlations, the timing of the significant decline of the skill comes earlier. For example, the skill starts to drop quickly at lead time of about 8 months for predictions starting from JJA, while it begins the decline at a lead time of about 5 months for predictions starting from SON which however have the highest skill for the first 5 lead months among the different starts. In contrast, predictions initiated in the DJF season virtually have no plateau in the correlation as is seen in other starting seasons and start to lose skill almost immediately. Although the sharp declines of the prediction skill occur at varying lead times, they all appear to occur when the predictions are made across the spring season. This finding appears to suggest that the "spring barrier" for predicting SST encountered by a number of coupled models (Latif et al, 1994) may be related to a seasonality in the skill in the prediction of thermocline depth anomalies. Of course, the cause-effect relation needs further investigations as the seasonality in SST anomalies, by inducing wind stress anomalies, could also be responsible for the seasonality of predicting the thermocline depth anomalies in the coupled system. By using a coupled model of intermediate complexity, Chen et al (1995) recently suggested that the "spring barrier" may result from the inappropriate initialization procedures which did not produce sufficiently balanced initial conditions for the coupled system. Further efforts are needed to elucidate the impact of the initialization on the skill of El Niño predictions by coupled GCMs, especially for the spring season.

To further illustrate the seasonal dependence of the prediction skill, Fig.3 shows horizontal maps of correlations of the depth of 20°C anomalies between the predictions and the reanalysis. For prediction for the DJF season (initiated in JJA), the 6-month lead correlations of greater than 0.6 are mainly confined in the eastern equatorial Pacific, and in a small off-equatorial region in the western Pacific. For prediction for the JJA season, however, the regions of correlations above 0.6 are less well organized.

3. Summary

The performance of the El Niño predictions by the NCEP coupled ocean-atmosphere model was examined from a view of the skill of forecasting the thermocline depth anomalies. These anomalies contribute significantly to causing SST changes and contain the potential link to a future El Niño as has been demonstrated in a number of simple or intermediate coupled models.

The results show that the thermocline depth anomalies (represented by the depth of 20°C anomalies here) are well predicted by the coupled model with significant skill up to a lead time of several seasons with a skill that is comparable to that for the SST prediction by this model. The prediction skill, as for SST, has a strong seasonal dependence. Predictions starting from summer have higher skill than that starting from winter, and the skill drops significantly when the prediction is made across the spring season. This result appears to suggest a connection to the "spring barrier" of SST predictions encountered by a number of coupled models. The origins of the barrier, however, remain

unclear at present. Efforts will be devoted to improvement of the coupling between the air-sea interface, in order to take the advantage of the longer predictable memory carried by the ocean subsurface variability.

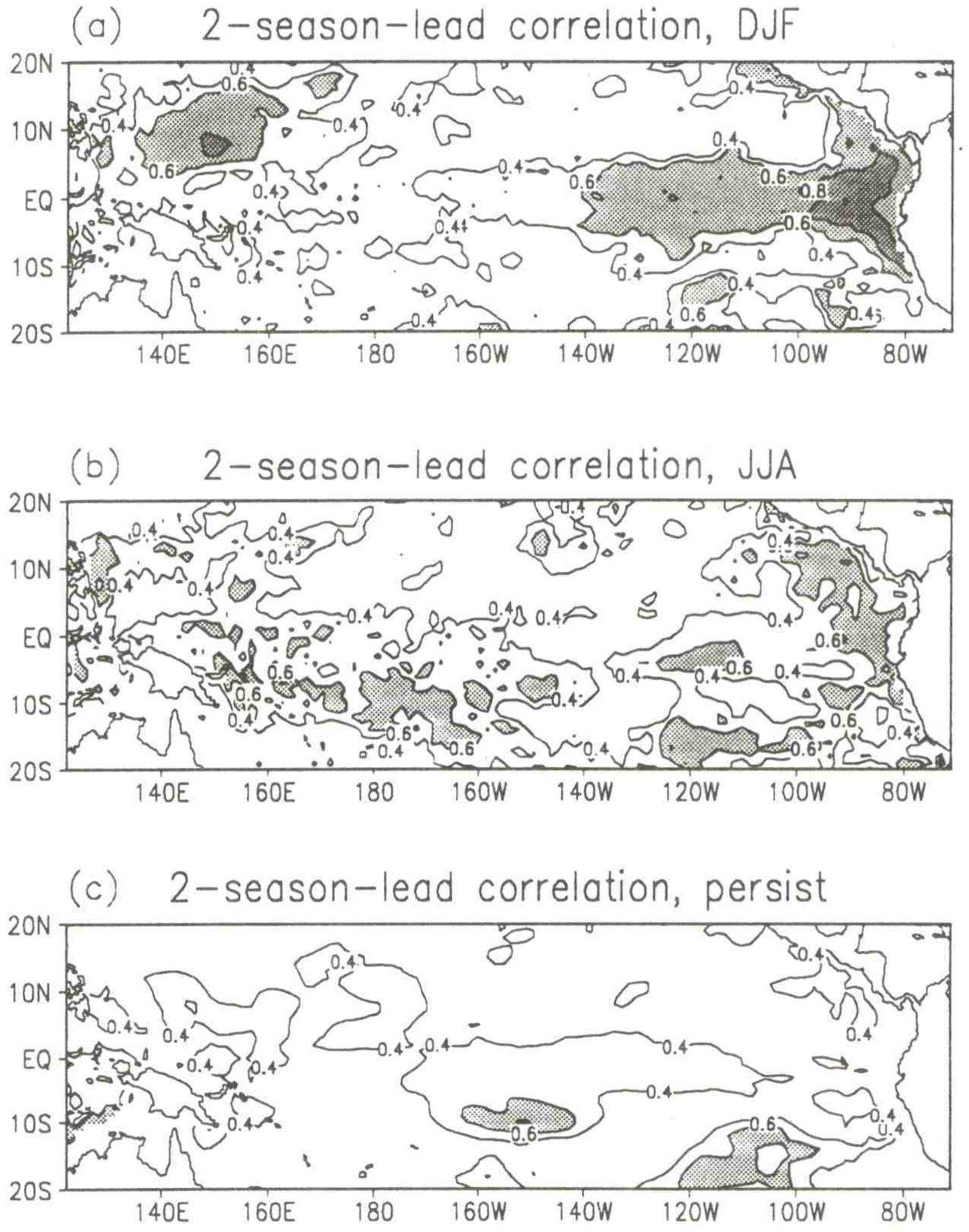

Fig.3: *Horizontal maps of correlations of the depth of 20°C anomalies between the reanalysis and predictions at 6-month lead. The persistence for the reanalysis is also shown in (c) for comparison.*

References:

Chen, D., S.E. Zebiak, A.J. Busalacchi, and M.A. Cane, 1995: An improved procedure for El Niño forecasting: Implications for predictability. *Science*, **269**, 1699-1702.

Ji, M., A. Kumar and A. Leetmaa, 1994: An experimental coupled forecast system at the National Meteorological Center: Some early results. *Tellus*, **46A**, 398-418.

Latif, M., T.P. Barnett, M.A. Cane, M. Flugel, and N.E. Graham, 1994: A review on ENSO prediction studies. *Climate Dyn.*, **9**, 167-179.

EXTRATROPICAL AIR-SEA INTERACTION ON WEEKLY TIME SCALES

CLARA DESER AND MICHAEL TIMLIN

CIRES
University of Colorado
Boulder, CO 80309
e-mail : cxd@cdc.noaa.gov

Many studies have examined the lead/lag relationships between extratropical atmospheric circulation anomalies and sea surface temperature (SST) anomalies on monthly time scales as a means of ascertaining cause and effect (c.f. Davis, 1978; Wallace and Jiang, 1987). A typical result of these studies is the comparable strength of the relationships at zero and one-month lag (atmosphere leading SST), indicative of the atmosphere forcing SST. In this study, we seek to sharpen the lead/lag relationships using weekly data.

We use weekly-averaged SSTs from the high-resolution (1° lat/lon) optimum interpolation analysis of Reynolds and Smith (1995), based on a blend of satellite and in situ data, and weekly-averaged 500 mb heights from twice-daily data archived at NMC. We examine the ocean/atmosphere relationships during 14 winters (1981/82 - 1994/95), with winter defined as the 27 weeks from November - March.

Table 1 shows the total temporal squared covariance between SST and 500 mb height anomalies over the North Atlantic during winter as a function of lag. Negative (positive) lags indicate SST leads (lags) the atmosphere. Units are non-dimensional as each grid point has been normalized by its respective temporal standard deviation. The simultaneous covariance has been arbitrarily assigned a value of 100 units. The total covariance shows a strong asymmetry with respect to lag, with a minimum (50 units) at lag -2 weeks and a maximum (158 units) at lag +2 weeks.

The covariability between the SST and 500 mb height fields can be partitioned into dominant patterns or "modes" using the technique of Singular Value Decomposition (SVD). SVD seeks pairs of spatial patterns (i.e., an SST anomaly pattern and a 500 mb height anomaly pattern) which explain a large fraction of the total squared covariance and whose temporal correlation is high. Table 2 shows the squared covariance associated with the dominant SVD mode between SST and 500 mb height anomalies over the North Atlantic during winter at lags -4 to +4 weeks. The individual winter means were removed before applying SVD analysis to sharpen the asymmetry of the lag-covariance statistics (however, the results are very similar when the winter-means are included; not shown) The squared covariance for SVD 1 varies from a minimum of 47 units at lags -2 weeks to a maximum of 206 units at lag +2 weeks, more than a four-fold increase. The covariance doubles between lag 0 and lag +2 weeks. Mode 1 accounts for 60-80 % of the total squared covariance, depending on lag.

The spatial patterns of normalized 500 mb height (left) and SST (right) anomalies for the leading SVD mode at lag +2 weeks are shown in Fig. 1. Each pair of patterns was formed from the so-called "heterogeneous" correlations: e.g., the expansion coefficient (time series) of the SST SVD pattern was correlated with the time series of 500 mb height anomalies at each grid point to form the 500 mb height anomaly pattern, and the expansion coefficient of the 500 mb height SVD pattern was correlated with the time series of SST anomalies at each grid point to form the SST anomaly pattern. Correlation coefficients exceeding 0.4 in absolute magnitude are shaded. Note the different map projections for the 500 mb height and SST fields.

The 500 mb height pattern features a north-south oriented dipole with centers over southern Greenland and along 35 °N in the central Atlantic, as well as a downstream center over western Russia. The SST pattern is organized into zonal bands of alternating polarity, with an additional center over the Norwegian and Baltic Seas. These structures are similar to those obtained in numerous previous studies based on monthly and seasonal data (c.f. Wallace and Jiang, 1987).

The time series of the 500 mb height and SST anomaly patterns of the leading SVD mode at lag +2 weeks are shown in Fig. 2. Each winter is represented by a continuous curve, with breaks between winters. The 2-3 week lag between 500 mb height and SST is visually apparent, even for the lower amplitude fluctuations of the last 4 winters. The correlation coefficient between the two curves is 0.75 at a lag of +2 weeks.

Similar lag-covariance results are found for the lower-order SVD modes in the North Atlantic, and for SVD modes in the North Pacific (not shown).

As a tentative explanation for the 2-3 week lag, we appeal to the stochastic forcing model of Frankignoul and Hasselmann (1977). In this model, the atmosphere is treated as a temporal white-noise process which forces an oceanic mixed layer. The resulting SST response is 'red' due to the integrating effect of the ocean mixed layer. Using typical e-folding time scales for the atmosphere (~ 1 week) and ocean mixed layer (~ 4 - 6 months), this model predicts a maximum correlation between the atmosphere and SST at a lag of 16-23 days. Thus, the observed 2-3 week lag between the SST and atmospheric circulation fields is consistent with the idea of stochastic atmospheric forcing of the ocean mixed layer.

Table 1. Total temporal squared covariance between SST and 500 mb height anomalies over the North Atlantic during winter as a function of lag in weeks. Negative (positive) lags indicate SST leads (lags) the atmosphere. Units are non-dimensional. The simultaneous covariance has been arbitrarily assigned a value of 100 units.

Lag in Weeks								
-4	*-3*	*-2*	*-1*	*0*	*1*	*2*	*3*	*4*
53	51	50	64	100	141	158	154	140

Table 2. As in Table 1 but for the leading SVD mode at the lag indicated. The SVD modes explain 60-80% of the total squared-covariance, depending upon lag. Individual winter means were removed from the data prior to the SVD analysis.

Lag in Weeks								
-4	*-3*	*-2*	*-1*	*0*	*1*	*2*	*3*	*4*
52	56	47	54	100	170	206	205	173

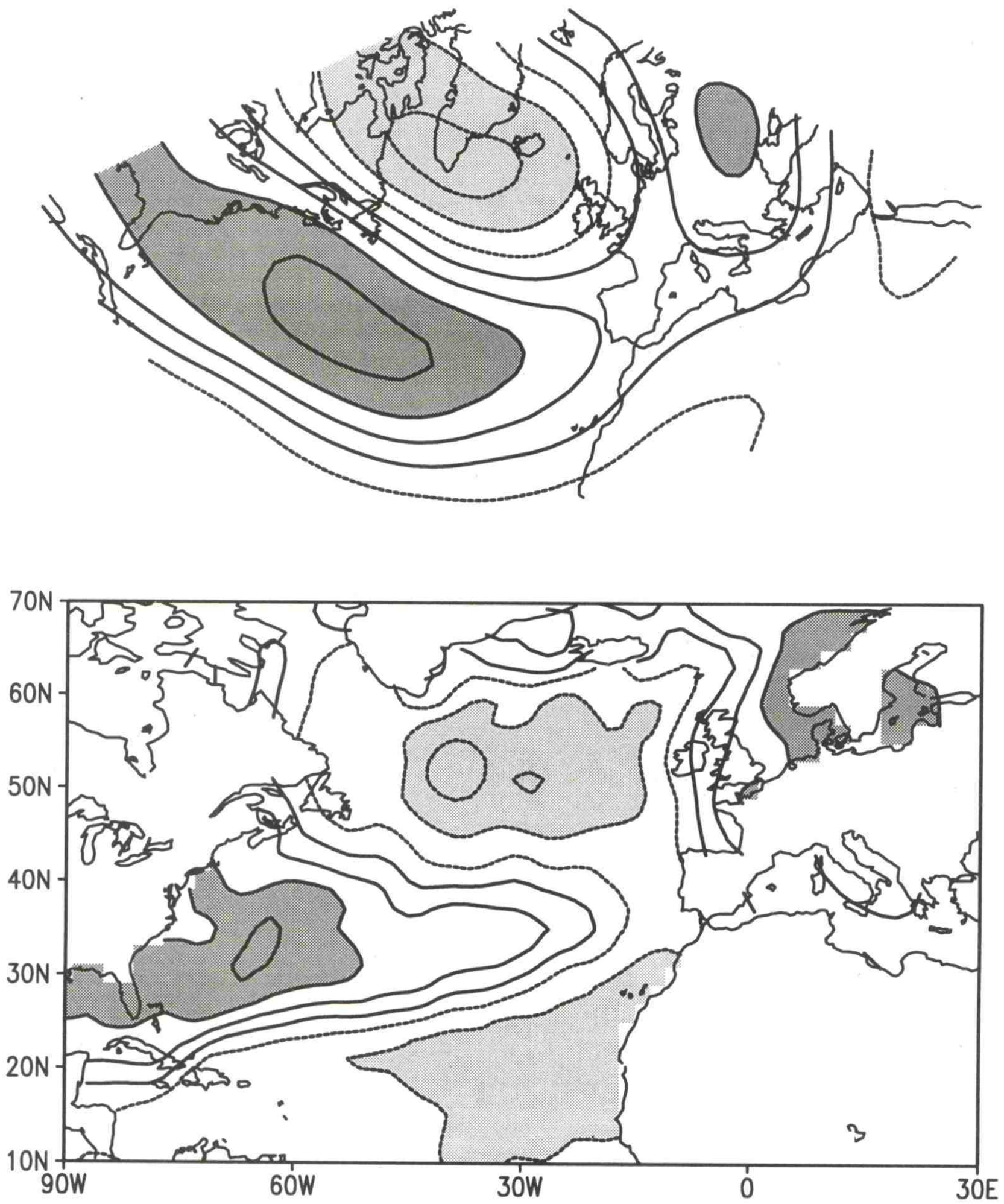

Figure 1. The leading SVD mode between normalized anomalies of 500 mb height (top) and SST (bottom) over the North Atlantic during winter. The SSTs have been lagged by 2 weeks relative to the 500 mb height field. Contour interval = 0.2, with shading above 0.4 and below -0.4.. Negative correlations are dashed. The SVD mode accounts for 73% of the total squared covariance between 500 mb height and SST.

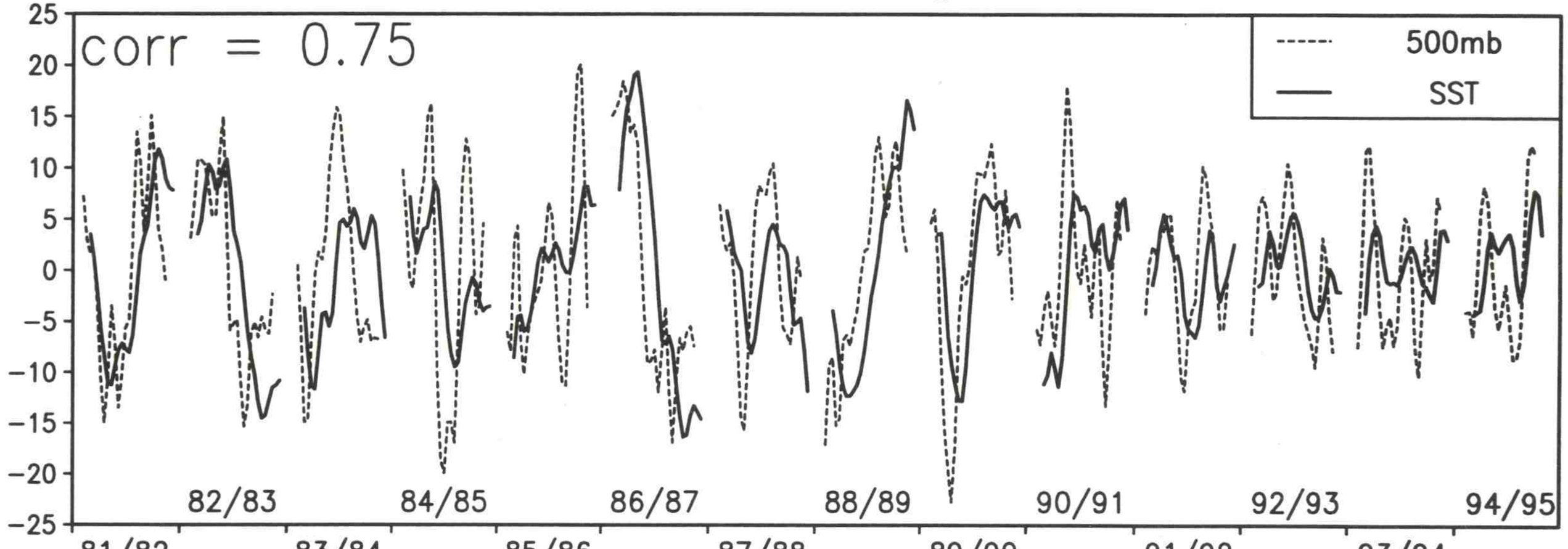

Figure 2. Weekly time series of the 500 mb height (dashed) and SST (solid) patterns shown in Fig. 1. Each continuous curve shows the amplitude of the patterns during the 27 weeks in a given winter (starting with the winter of 1981/82), with breaks between winters. The correlation coefficient between the two records is 0.75 at a lag of 2 weeks.

Coupled Predictions at COLA

Ben P. Kirtman

Center for Ocean-Land-Atmosphere Studies
4041 Powder Mill Road, Suite 302, Calverton, MD 20705

The Center for Ocean-Land-Atmosphere studies (COLA) has recently developed an anomaly coupled prediction system, using sophisticated dynamical ocean and atmosphere models, that produces skillful forecasts of tropical Pacific sea surface temperature anomaly (SSTA) up to 1½ years in advance. The atmospheric component is the COLA atmospheric general circulation model (AGCM) that includes a state-of-the-art land surface model and physical parameterizations. The AGCM is a global spectral model that is horizontally truncated at triangular wavnumber 30 and has 18 unevenly spaced σ levels in the vertical. The oceanic component is a Pacific basin version of the Geophysical Fluid Dynamics Laboratory (GFDL) ocean model. In the ocean model there are 20 levels in the vertical with 16 levels in the upper 400 m. The zonal resolution is 1.5° of longitude and 0.5° of latitude between 10°N and 10°S. Further details of the ocean model are described in Huang and Schneider (1995).

The atmosphere and ocean models have been tested separately in order to evaluate their performance when forced by observed boundary conditions. In the case of the atmosphere, the prescribed boundary condition is the observed monthly mean SST for 1948-present (personal communication C. K. Folland and Reynolds, 1988) and, in the case of the ocean, several multi-year simulations were carried out forced by observed surface wind stress from ECMWF (1985-92) and FSU (1964-Present) analyses and parameterized surface heat fluxes (Huang and Schneider, 1995; Huang and Shukla, 1995). The ocean model does fairly well in reproducing observed interannual equatorial Pacific SST variability when forced by the observed wind stress.

When the atmospheric model was forced with observed SST and the resulting model output wind stress was used to force the ocean model, serious errors were found in the ocean model simulation (Huang and Schneider, 1995; Huang and Shukla, 1995). The errors in the atmospheric model wind stress appear to be most severe during boreal spring when the anomaly becomes extremely weak and far too confined to the western part of the Pacific basin. We have found that these atmospheric wind stress errors are confined to the boundary layer and that the winds at the top of the boundary layer (approximately 850 mb) can be effectively converted into a surface stress that yields a substantially improved ocean simulation and coupled predictions (Huang and Shukla, 1995 and Kirtman et al., 1995b).

Figure 1 shows the ocean model simulated SSTA along the equator for three experiments with prescribed wind stress forcing along with the Reynolds (1988) observed anomaly (far left). The far right panel shows the ocean simulation where the prescribed wind stress forcing is determined directly from the AGCM without the statistical correction. The right middle panel shows the simulation with the FSU wind

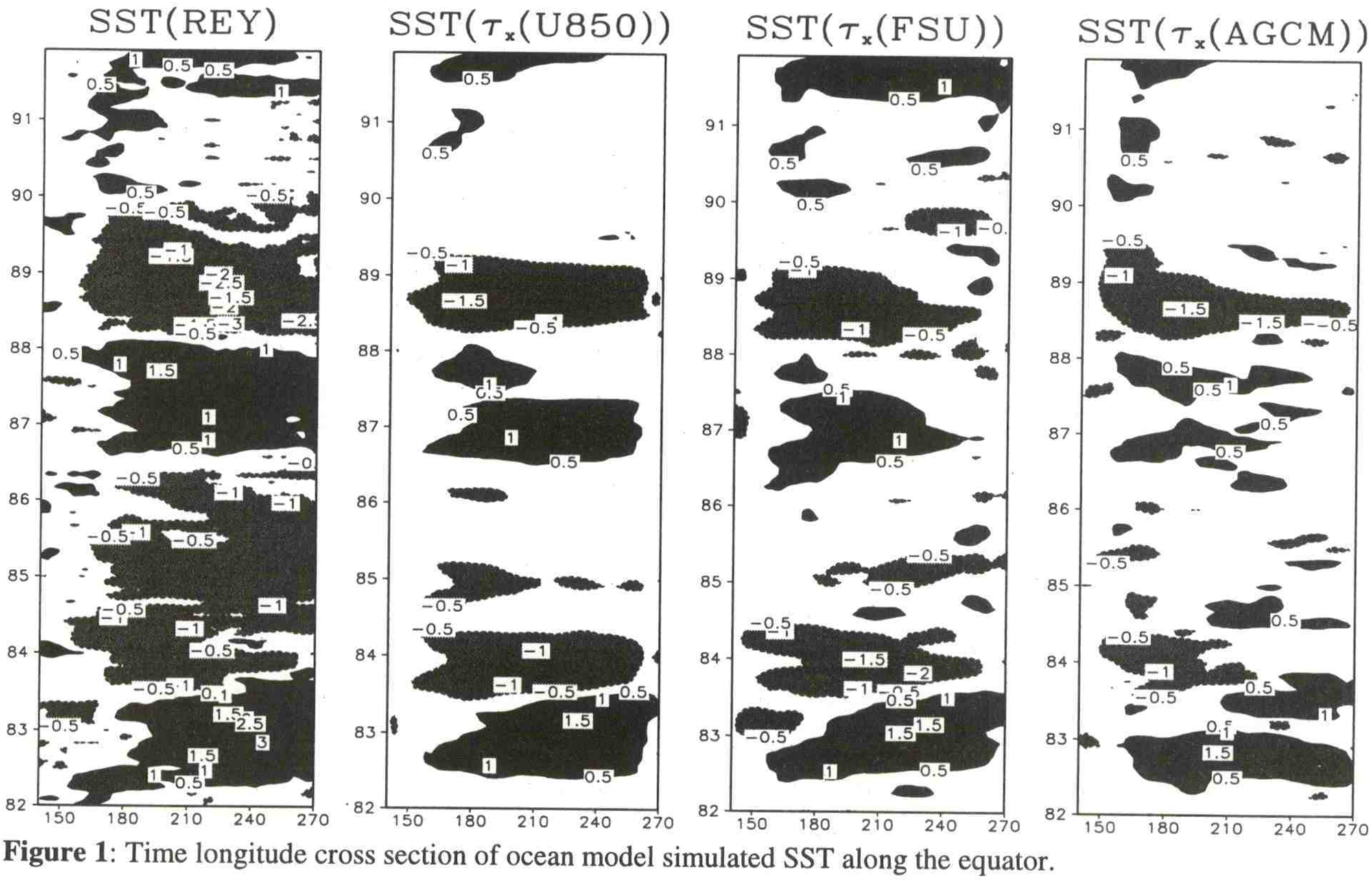

Figure 1: Time longitude cross section of ocean model simulated SST along the equator.

converted into a zonal wind stress. The AGCM data is calculated from extended uncoupled simulations with observed SST from 1949-1994. The simulation becomes progressively better in going from right to left, but all three simulations do not completely capture the strength of the SST variations, particularly in the eastern Pacific. The erroneous cold interruptions of the warm ENSO events are less severe when the zonal wind stress is calculated from the 850 mb zonal winds. Temporal correlations and root mean square errors of simulated SST indicate that the simulation with the 850 mb zonal wind converted into a zonal wind stress gives the best simulation of the three.

In order to improve the ocean simulation and initial states for coupled predictions, we have developed an iterative procedure, based on the SSTA error, for adjusting the observed wind stress that reduces the ocean model simulated SSTA error especially in the eastern Pacific and possibly gives a superior wind stress field (Kirtman et al., 1995a). After this iterative procedure is applied the ocean simulation is used to initialize the coupled forecasts. Figure 2 shows the correlation of the observed and simulated SSTA before and after the iteration is applied. The zonal wind stress before the iteration is determind from the AGCM 850 mb zonal wind as described above. After the iteration there is an increase in the correlation with a larger region where the observed SSTA and the simulated SSTA have a correlation coefficient greater than 0.6. There are also notable increases in the correlation in the eastern Pacific and portions of the sub-tropical Pacific. Since the iteration procedure defines the ocean model initial conditions, Fig. 2 can also be interpreted as the zero lead time correlation of the forecasts.

The primary difference between the prediction system described here and that used by the coupled model project at the National Meteorological Center (NMC) is in the coupling strategy and the development of initial conditions. Where NMC uses a state-of-the-art ocean data assimilation system to initialize the predictions (Ji et al., 1994) we use the iterative wind stress assimilation scheme described above (Kirtman et al., 1995a) which does not include any observed sub-surface or satellite data. In addition to using the 850 mb zonal wind to define the zonal wind stress anomaly the COLA coupled prediction model exchanges 30 day running

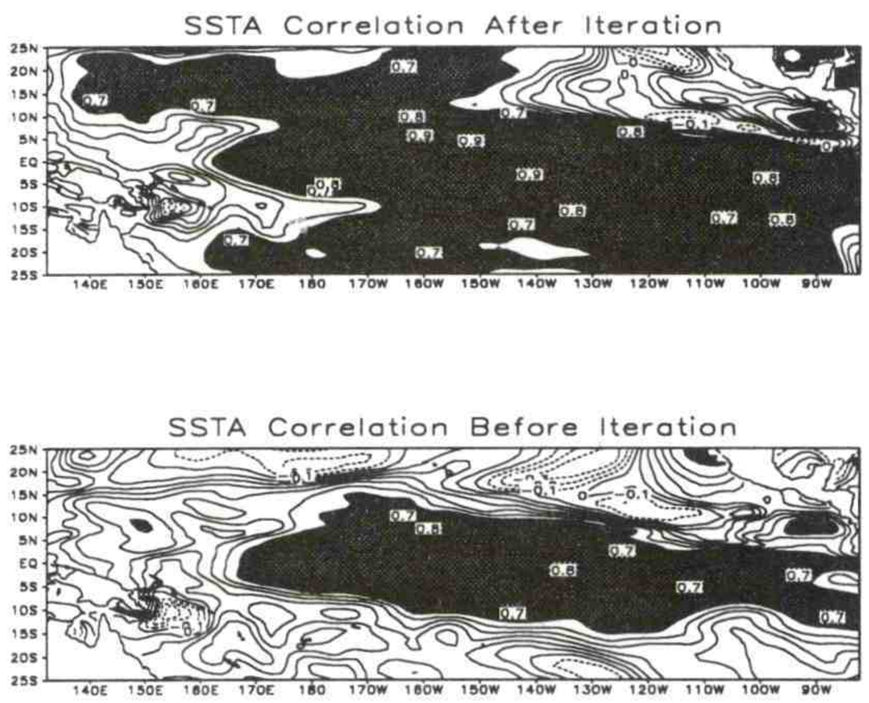

Figure 2: Temporal correlation of the observed and simulated SSTA before (lower) and after (upper) iteration.

means of wind stress and SST anomaly once a day. In contrast, at NMC a model output statistical correction based on a singular value decomposition is applied to the wind stress anomaly every time step and the coupled model exchanges fluxes of heat and momentum once every five days (Ji personal communication). Details of this coupled model described in Kirtman et al., (1995b).

We have completed a set of hindcast predictions for the period 1964-1994 using the dynamical ocean-land-atmosphere general circulation model described above. To date, a hindcast was initialized for each January, April, July and October of 1965, 1966, 1970, 1972, 1973, 1974, 1975, 1982, 1983, 1984, 1986, 1987, 1988, 1989 and 1991. These dates where chosen to sample warm, cold and normal years. The ocean initial conditions for all of these predictions were taken from an uncoupled simulation in which the 850 mb zonal wind was converted into a surface stress and then the iterative wind stress correction was applied so that both the ocean and atmosphere model are close to equilibrium with the wind stress anomaly and the SSTA respectively.

Figure 3 shows the 18 month evolution of the NINO3 SSTA for all the hindcasts. The systematic error in the predicted SSTA has been removed and the observed NINO3 SST is indicated by the bold solid line. For the most part, the predictions track the observed anomaly for the first 12 months although there are some notable exceptions. The forecasts

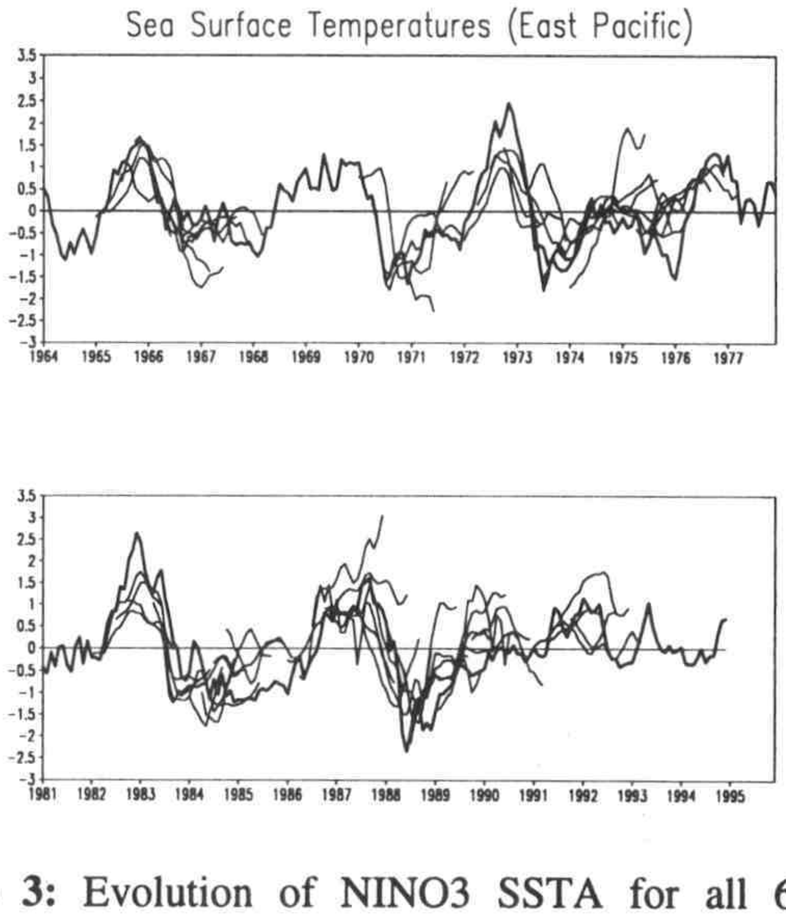

Figure 3: Evolution of NINO3 SSTA for all 60 hindcasts. Thick curve denotes the observed SSTA.

initialized in January 1974, 1989 and July

1988, relatively cold initial states, produced erroneous warm anomalies approximately 9-12 months later when the observed conditions were near normal.

Figure 4 provides an overall assessment of the performance of the anomaly coupled model based on all 60 forecasts. The top panel of Fig. 4 shows the SSTA correlation in the NINO3 region and the middle panel shows the root mean square error (RMSE). For comparison we show the skill of persistence. It is clear that the COLA coupled prediction model is more skillful than persistence and, by these simple metrics, is competitive with other coupled model currently used for prediction experiments. The bottom panel of Fig. 4 shows the anomaly correlation based on a subset of 10 cases (January and July 1986,87,88,89,91). The "COLA" curve corresponds to the complete prediction system as described above. The "No iteration" curve is calculated from the same 10 cases but without the iteration procedure for the ocean initial conditions. In the "No iteration" case, however, the 850 mb zonal wind to wind stress correction remains as the predictions evolve. For the final curve, "No U850," neither the iteration procedure nor the statistically formulated wind stress are used. With both the statistical correction to the wind stress and the iteration procedure the anomaly correlation is significantly improved. In addition, the iteration procedure improves the correlation for all lead times suggesting that improvements in the ocean initial state will lead to further enhancements of forecast skill.

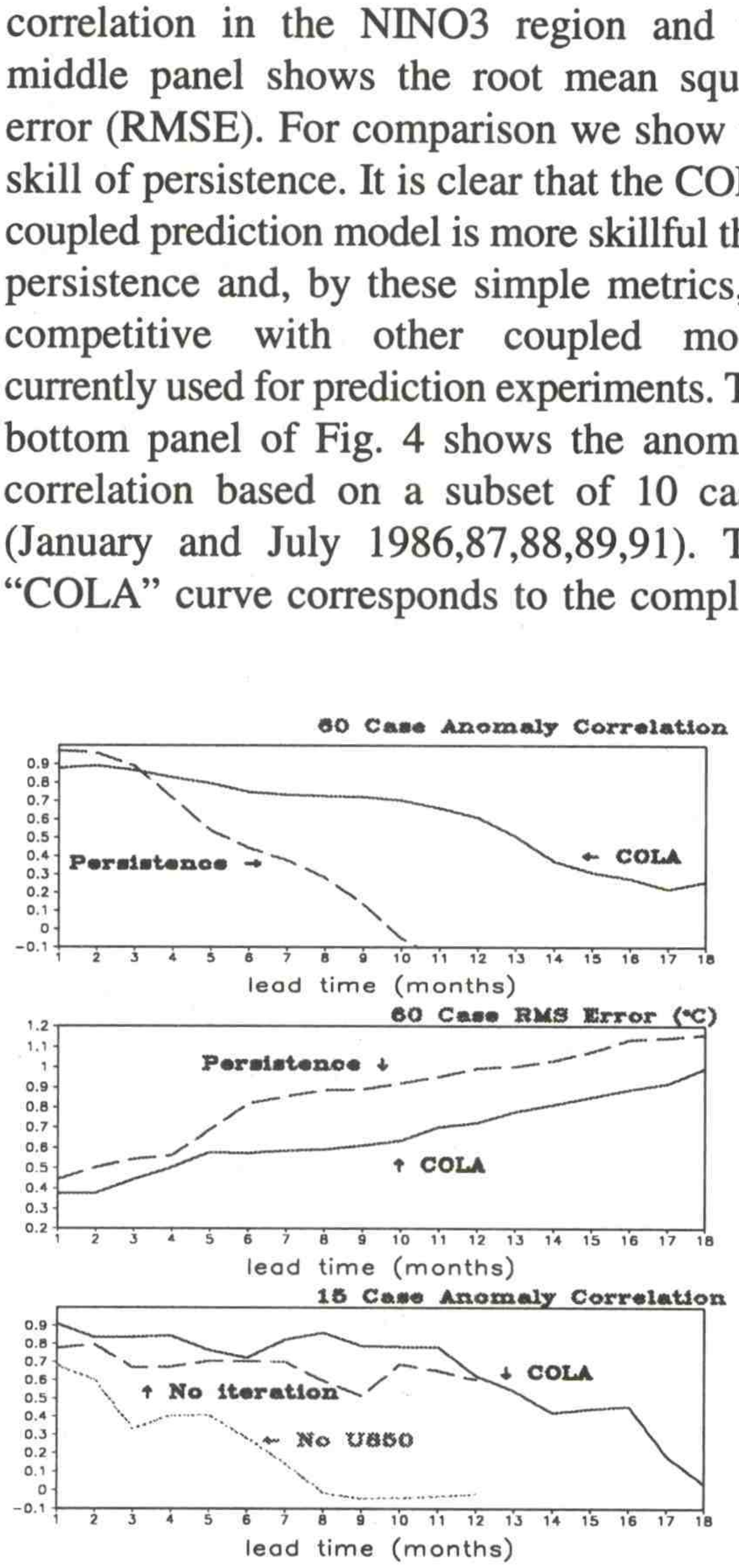

Figure 4: Anomaly correlation for NINO3 (top) and RMSE (middle) based on all 60 cases. The bottom panel shows the anomaly correlation based on 10 cases (January and July 1986,87,88,89,91) without the iteration procedure and the statistically derived wind stress (see text for details).

Acknowledgments: This work was supported under NOAA grant NA26-GP0149 and NA46-GP0217 and NSF grant ATM-93-21354.

References

Huang, B., and J. Shukla, 1995: Surface wind stress based on AGCM simulated low level winds over the tropical Pacific ocean. *Mon. Wea. Rev.*, (in press).

Huang, B., and E. K. Schneider, 1995: The response of an ocean general circulation model to surface wind stress produced by an atmospheric general circulation model. *Mon. Wea. Rev.*, (in press).

Ji, M., A. Kumar, A. Leetmaa, 1994: An experimental coupled forecast system at the National Meteorlogical Center: Some early results. *Tellus*, **46A**, 398-418.

Kirtman, B. P., E. K. Schneider, B. Kirtman, 1995a: Model based estimates of equatorial Pacific wind stress. *J. Climate,*(accepted).

Kirtman, B. P., J. Shukla, B. Huang, Z. Zhu, E. K. Schneider, 1995b: Multiseason predictions with a coupled tropical ocean global atmosphere system. *Mon. Wea. Rev.*, (accepted).

Reynolds, R.W., 1988: A real time global sea surface temperature analysis. *J. Climate,* **1,** 75-86.

INTERDECADAL RELATIONS AMONG ANOMALOUS 400M OCEAN CURRENTS, TEMPERATURE AND ATMOSPHERIC FORCING IN THE NORTH PACIFIC

Arthur J. Miller, Daniel R. Cayan and Warren B. White

Scripps Institution of Oceanography, La Jolla CA 92093-0224

1. Introduction

In previous work, we have diagnosed the ocean dynamics and thermodynamics which prevailed in causing the ocean to shift from a warm SST state in the central North Pacific to a cold state after the 1976-77 winter (and vice versa for the eastern North Pacific) by studying a numerical simulation (Miller et al., 1994, *Clim. Dyn.*). Anomalously strong horizontal advection teamed with surface heat flux forcing to install the new regime in the surface mixed layer.

In this study, we inspect the ocean beneath the mixed layer (the thermocline) in order to dissociate the response from direct contact with the atmosphere which coaxes mixed layer variables to bear spatial scales commensurate with the large-scale atmospheric forcing which predominantly drives them (Cayan, 1992, *JPO*). In the thermocline, one instead anticipates that ocean dynamics will succeed in establishing the spatial structures and temporal variations which occur.

2. Observations

We have carried out an extended empirical orthogonal function (EEOF) analysis of observed seasonal anomalies of 400m temperature from XBTs for the period 1970-1988. We included zero through 12-season lags of seasonal anomalies although only a subset of the phase-lag maps is shown. We use extended EOFs because it strongly aids in separating the propagating from the stationary signals in the analyses. (Indeed, the second strongest signal in all that follows is a pair of propagating modes with ENSO time scales which will not be further discussed here.) Fig. 1 (left) shows the first EEOF (23% of the variance) which is dominated by a stationary pattern between 30 and 40N which increases in amplitude towards the western part of the analysis domain (155E). The second EEOF (Fig. 1, right) also reveals a nearly stationary signal which grows in time, spreads westward and is centered around 150W-160W and 25N though it explains only 8% of the variance. The time variation of EEOF-1 is also shown in Fig. 1 (bottom) where it can be seen that it has a decadal scale. Commencing in the early 1970s, it represents an anomalously warm thermocline (temperature at 400m) and reverses sign around 1980 before entering a cool regime in the early 1980s.

Although the time variations of these two modes appear to be 90 degrees out of phase, the spatial patterns and variance mismatch do not suggest that they represent a propagating wavelike feature. Instead they represent a dominant stationary feature (a western intensified hump at 38N) which flips sign from the 1970s to the 1980s concurrently with the growth/decay of spreading features separate from the hump.

3. Model and observations comparison

A primitive equation ocean model was applied by Miller et al. (1994) to study monthly-mean through decadal-scale variations over the Pacific basin (60N to 76S). The surface forcing consists of a monthly-mean seasonal cycle climatology of wind stress, total surface heat flux and turbulent kinetic energy input to the mixed layer, to which are respectively added the specified observed monthly mean anomalies derived from COADS observations for the period 1970-1988.

We seek to identify what features of the observations the model is able to capture by using a combined EEOF analysis. Since the model 400m temperature variations are somewhat weaker than those observed, we normalize the time series with the rms value of the fields averaged over the entire analysis subdomain (rms T_m=0.13C, rms T_o=0.25C). The first combined EEOF of 400m temperature explains 29% of the combined variance and is shown in Fig. 2 (top), plotted as an average of all 13 lags. Comparison with Fig. 1 (left) reveals that the observed portion is essentially the same pattern as the first EEOF of the observations alone. The decadal time variation (Fig. 2, left) also compares well with that of the observations alone (Fig. 1, bottom). Thus, we have found that the model has fidelitously captured the stationary feature which occured in nature, viz., the western intensified decadal-scale cooling of the thermocline (400m temperature) between 30N and 50N.

4. Model velocity, temperature and forcing relations

Since the decadal feature is the dominant signal we seek to explain its dynamics by analyzing the model version of this signal by computing combined EEOFs of model 400m temperature and velocity field together (normalized by rms: $T = 0.2°$ and $\mathbf{u}$= 0.05 cm/s). The first EEOF explains 21% of the combined variance and again corresponds to the decadal signal previously identified. Fig. 2 (middle) shows the first combined EEOF in which one can see that the velocity field associated with the changes in the thermocline is nearly geostrophically adjusted. It is evident that the Kuroshio extension (along 35N) the subpolar gyre return flow (along 50N) and the subtropical gyre return flow (along 20N) were all strengthened by about 10% from the early 1970s to the early 1980s (cf. Sekine, 1991, *JGR*; Trenberth and Hurrell, 1994, *Clim. Dyn.*). Also an anomalously northward flow into the central part of the Gulf of Alaska developed in the model over this time interval (cf. Lagerloef, 1995, *JPO*). Little change in velocity occurs near the west coast of North America.

A candidate mechanism for driving the modeled decadal change in gyre-scale circulation is the increase in wind stress which was observed to occur over the North Pacific in the mid-1970s. We therefore test the hypothesis that anomalous wind stress curl drives the anomalous model decadal temperature and velocity patterns by computing the Sverdrup relation $\rho H \bar{v} = (\text{curl } \tau)/\beta$, at each grid point. The overbar indicates integration from the the surface to our selected reference depth of 1500m, curl τ is computed on the model grid from the input wind stress components (derived from observations) and β is the latitudinally dependent gradient of the local Coriolis parameter.

Combined extended EOFs of annual averages of the two sides of (1) were computed in order to identify the relationship between the two fields on the decadal timescale. The basin-scale decadal signal associated with our identified change in temperature appears as the third EEOF which explain 9% of the combined annual anomaly variance. The EEOF patterns (Fig. 2) reveal that the eastern portion of the north Pacific (east of 170W) is nearly in a local Sverdrup balance (within a factor of two) on this decadal time scale (10-year trough to peak change; Fig. 2, left). The model has a very deep lower isopycnal layer (typically 3000m) which can be influenced strongly by the variable topography in the North Pacific resulting in non-negligible vertical velocity fields at the top of that lowest layer which defeats the quantitative Sverdrup balance. Nonetheless the similarity between the wind stress curl patterns and the north-south transport supports the idea that the surface fields are driven by the decadal-scale wind-stress curl change.

5. Summary

Our analyses have revealed that 400m temperature (thermocline) anomalies have a decadal signal which is western intensified in the North Pacific. The signal appears in both observations of upper ocean temperature and in a model simulation forced by observed wind stresses and heat flux anomalies over the period 1970-1988. The western intensified structure of the temperature change is due to ocean dynamics as the gyre scale circulation strengthens by 10% to adjust to the increasing wind stress curl. This is in contrast to the well known pattern of SST change which occurs in the mixed layer where atmospheric forcing imposes spatial structures commensurate with the atmospheric patterns which drive it (Cayan, 1992; Miller et al., 1994). The time variation of the deep temperature change is also more gradual than the step-like change that occurred during the 1976-77 winter in the surface temperature, surface mixed layer and other surface variables.

Deser et al. (1995) also noted the decreasing temperatures at 250-400m in the western North Pacific in this XBT dataset and additionally discovered that in the interior portion of the North Pacific a cold anomaly that was formed in the mixed layer around 1977-79 between 140W and 170W and which migrated southward from 35N to 25N and downward to 300-400m depth in the water column along isopycnals ten years thereafter. This subduction was not captured by the numerical model but it does appear in our analysis of the observations (Fig. 1, left). It is interesting to note that the decadal signal discussed by us here appears to be dynamically distinct from the signal of Deser et al. in that the signal discussed here is driven by wind stress curl forcing as opposed to being generated by surface processes (likely diabatic) and advected downwards. We plan to continue to study the model to attempt to understand this deficiency and to remedy it in future hindcasts.

Acknowledgments. Funding was provided by NOAA under the Scripps ECPC (NA36GPO372) and the Lamont/Scripps Consortium for Climate Research (NA47GPO188) and (to AJM) by the G. Unger Vetlesen Foundation. AJM thanks Weimin Xu, Mike Alexander, Clara Deser and Jeff Polovina for discussions.

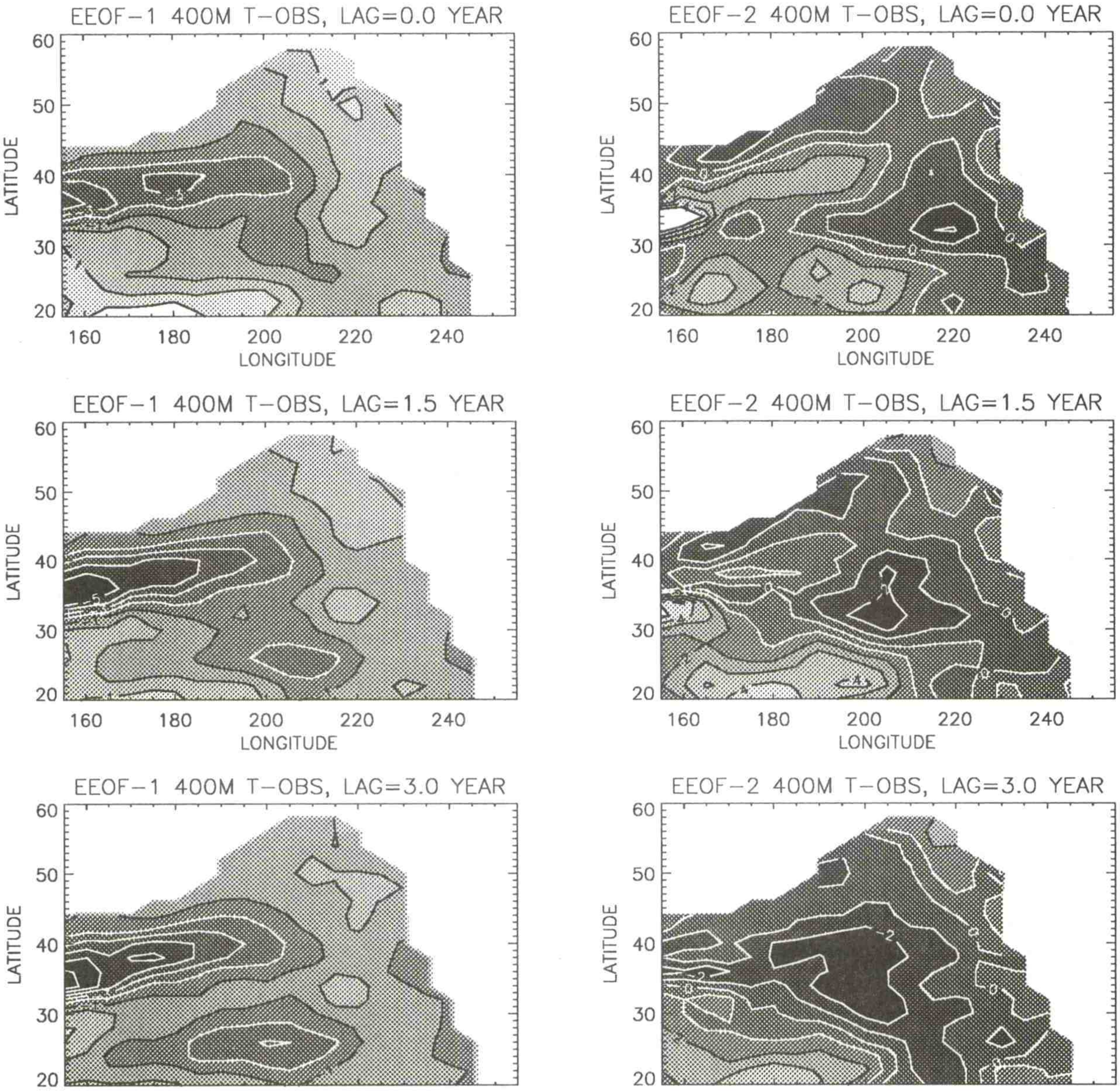

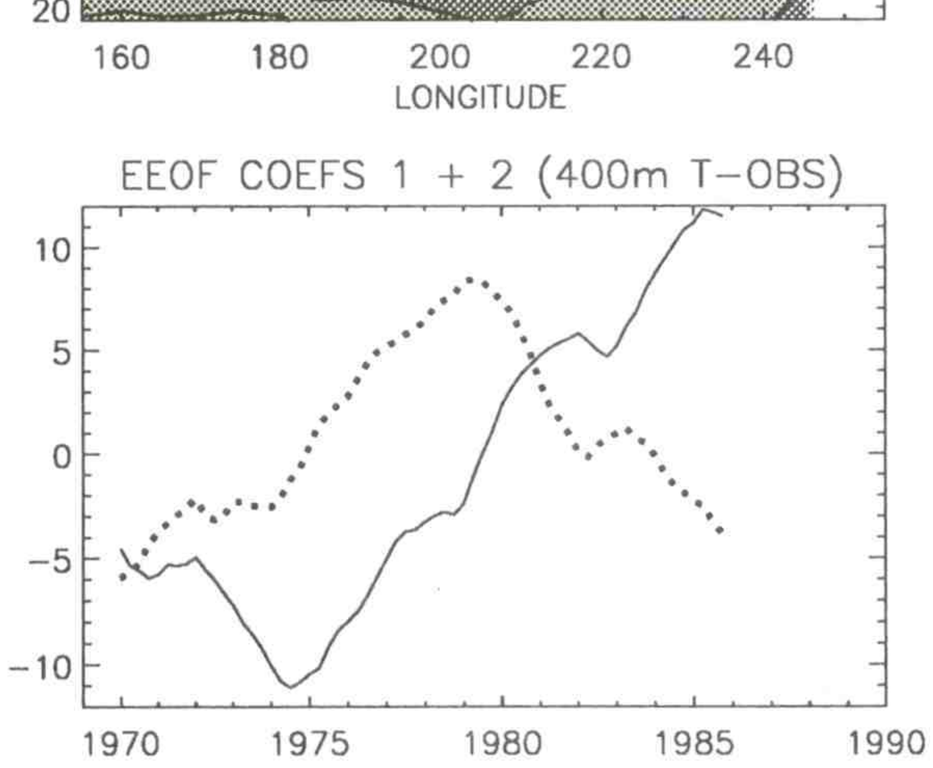

Figure 1. Maps of extended EOF-1 (left) and extended EOF-2 (right) of seasonal anomalies of observed 400m temperature in the North Pacific for (from top) 0-year, 1.5-year and 3-year lags (complete lags include 0 through 12 seasons). (bottom) Time series of the principal components of EEOF-1 (solid, 23% of total variance) and EEOF-2 (dotted, 8% of total variance).

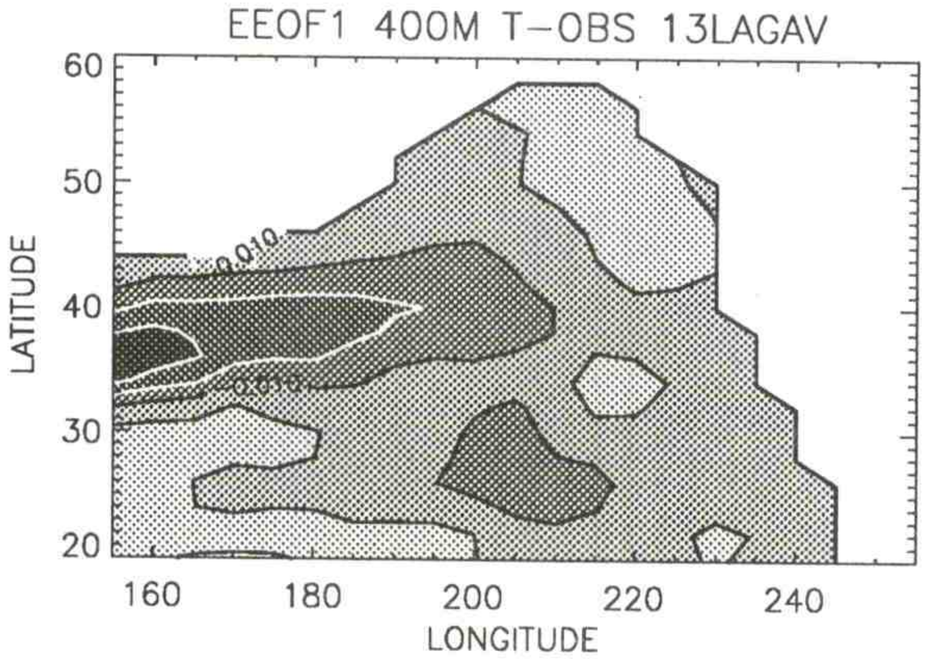

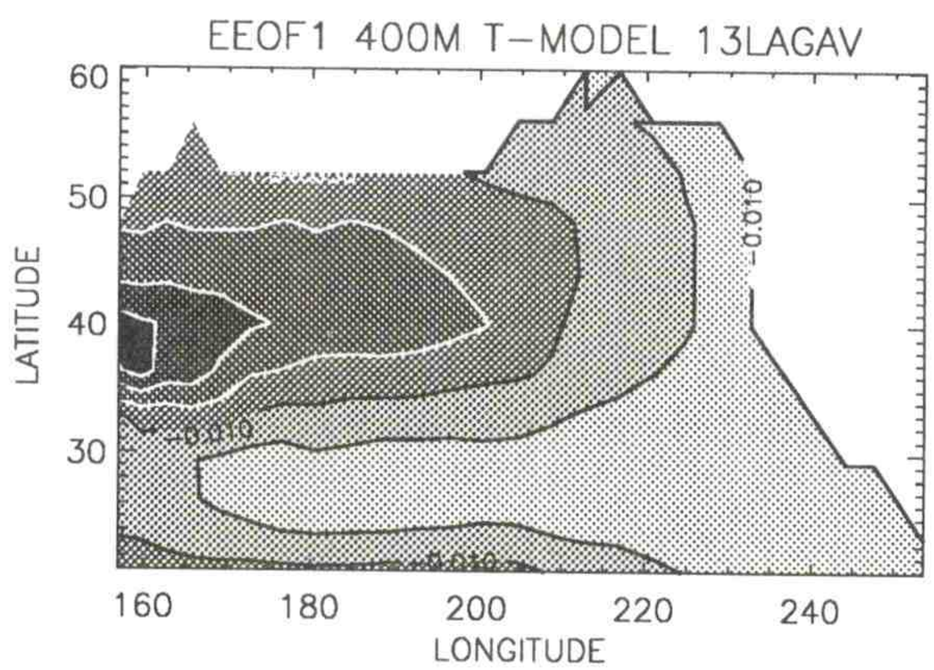

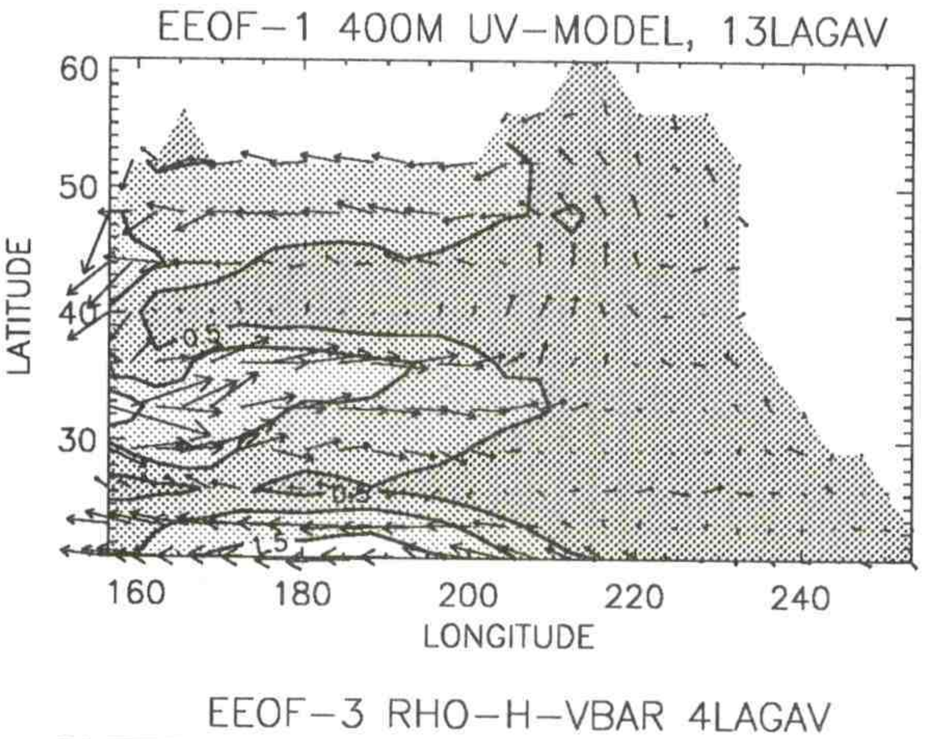

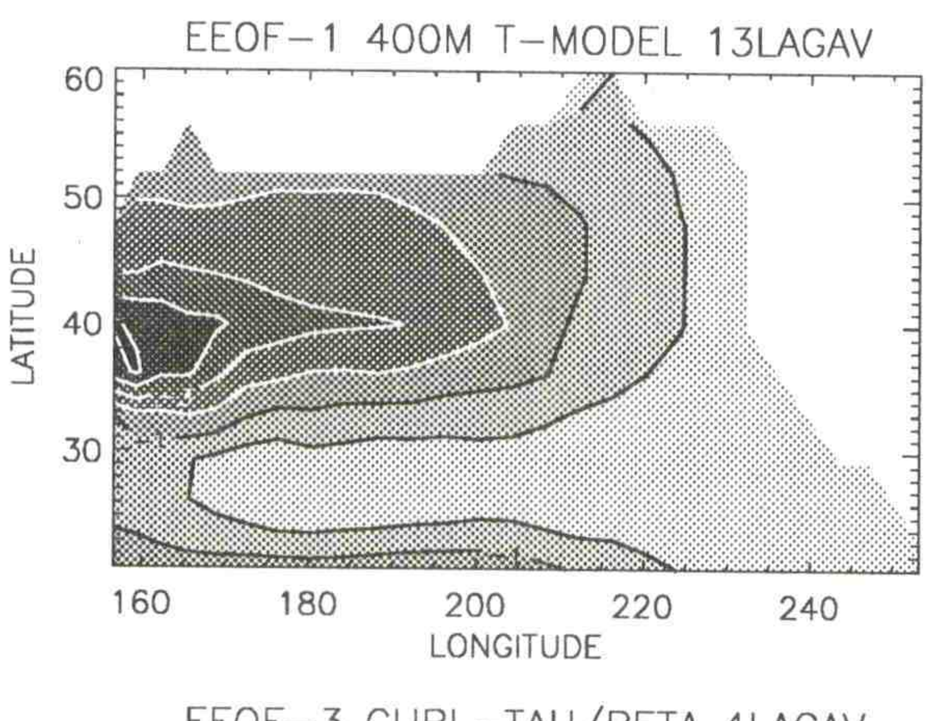

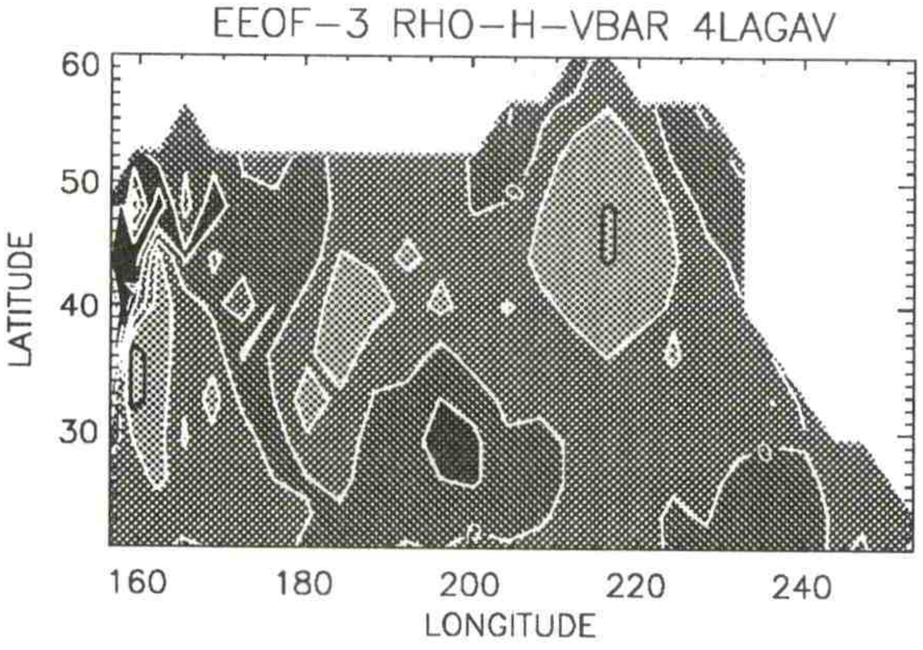

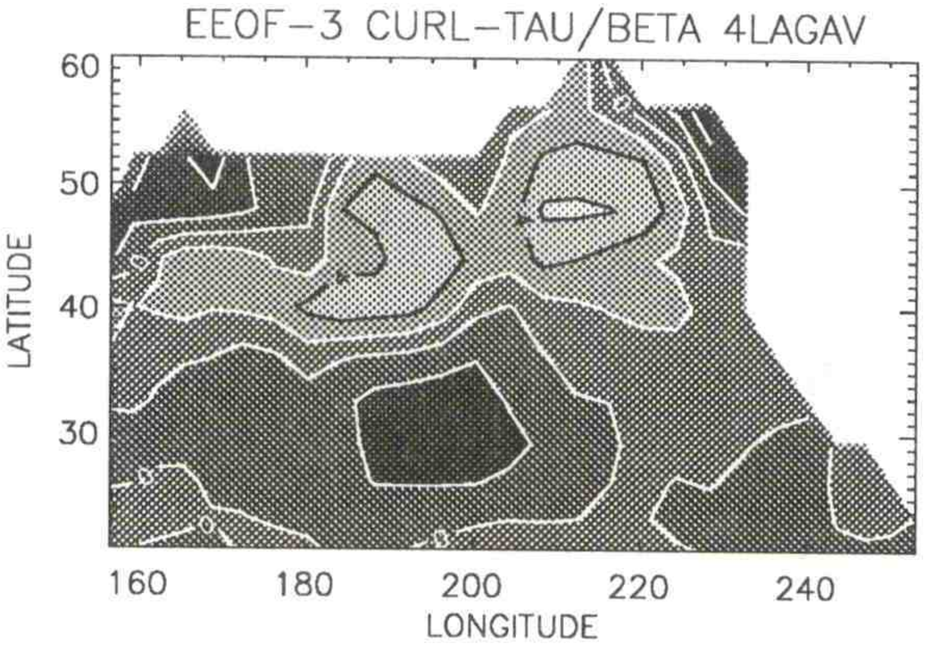

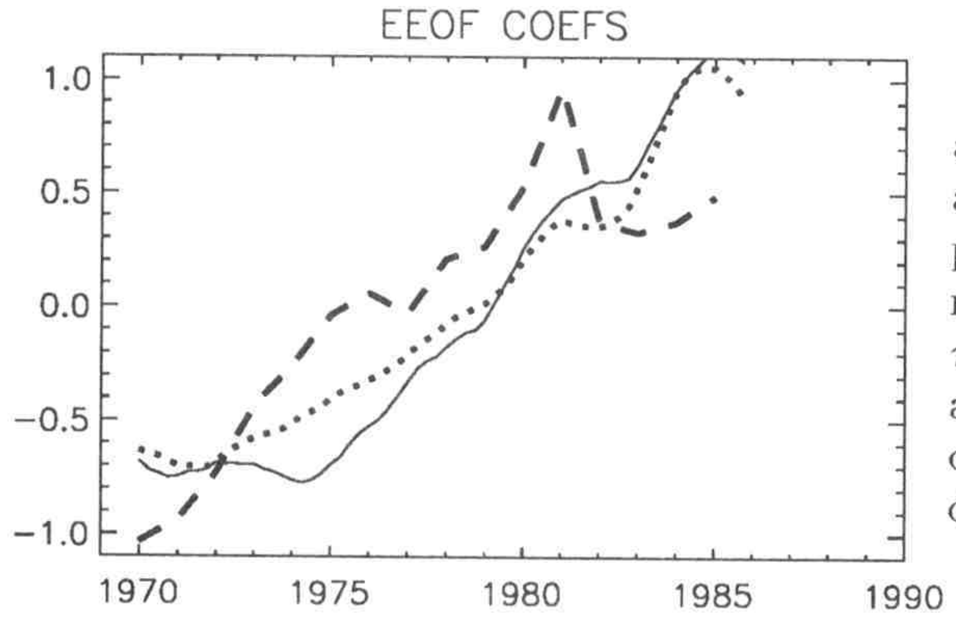

Figure 2. Maps of combined EEOF-1 of seasonal anomalies of (top) observed and modeled 400m temperature (29%), (middle) modeled 400m velocity and temperature (21%) and (bottom) combined EEOF-3 of annual anoms of modeled north-south transport and curl τ, scaled to Sverdrup relation (9%). Plotted are averages over all the included lags. (left) Time series of the combined EEOFs solid for top, dotted for middle and dashed for bottom, scaled to fit on same plot.

Modeling Intraseasonal Thermocline Variations in the Eastern Pacific

Brant Liebmann, Harry Hendon, and John Glick

Cooperative Institute for Research in Environmental Sciences
Campus Box 449
University of Colorado
Boulder, Colorado 80309-0449

This project is an attempt to understand intraseasonal variations of the oceanic thermocline in the central and eastern Pacific Ocean. We compare observations with results obtained by forcing a linear, shallow-water model containing a single mode with phase speed 2.3 m/s and no mean current, with European Centre winds. Thermocline fluctuations are approximated by variations of the depth of the 20C isotherm (Z20) obtained from the TOGA-TAO array, which extends from 165°E - 110°W, and from July 1986 through June 1993. All data are pre-filtered to include intraseasonal periods 26-100 days.

We first extract the dominant mode of Z20 variability by performing an empirical orthogonal function (EOF) analysis. The first two EOFs explain 80% of the intraseasonal variability and combine to form a propagating mode. We then regress the Z20 and zonal stress fields onto the 2 leading principal components (PCs) of the EOF analysis, shown in Fig. 1. The dominant mode in Z20 is consistent with a Kelvin wave as described by Kessler et al. (1995 JGR). It moves eastward at about 2.4 m/s.

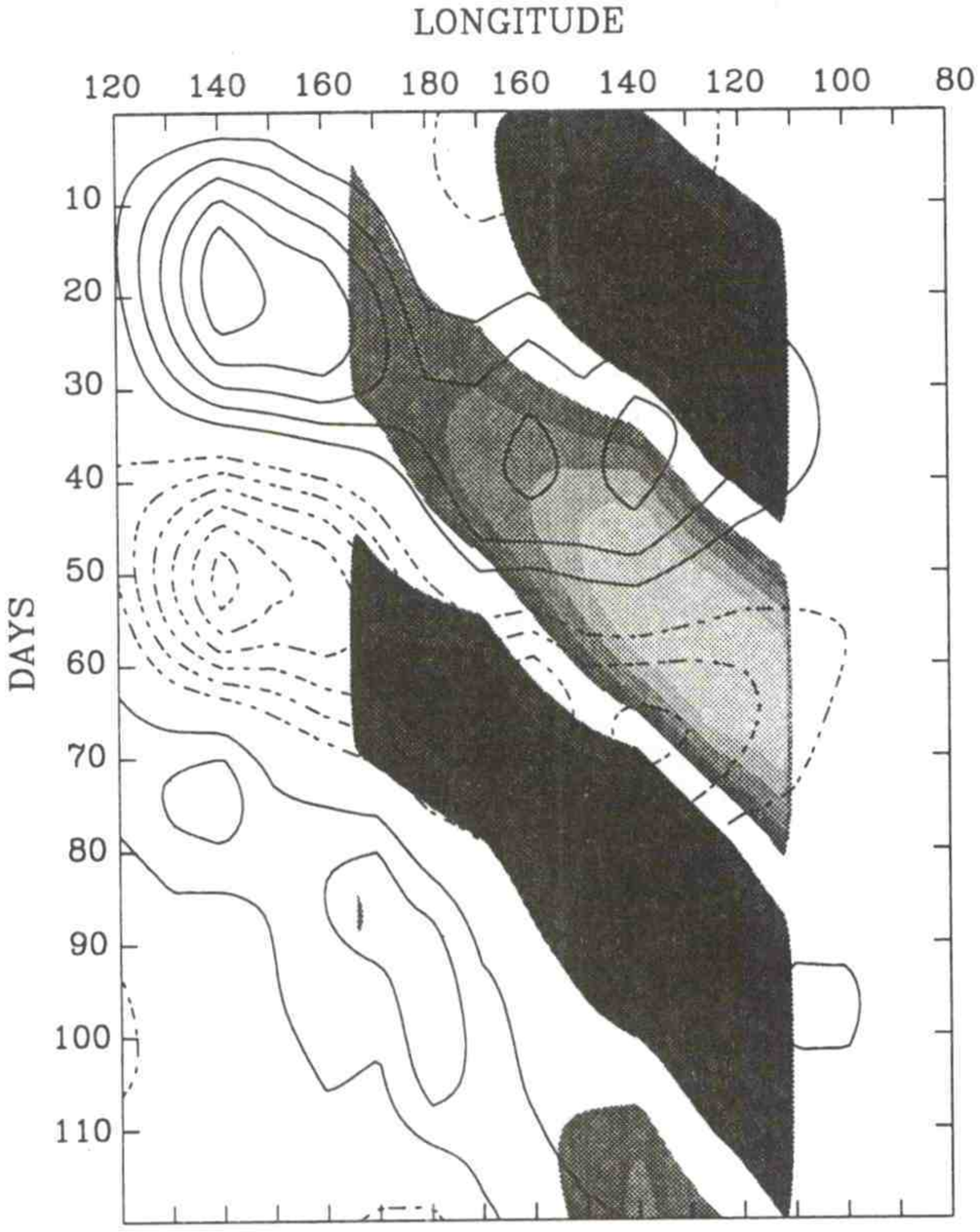

Fig. 1) Multiple linear lag-regression of Z20 (shading) and zonal stress onto 2 leading PCs of Z20 from EOF analysis for 1 standard deviation PC anomaly. Shading starts at 3m, with interval of 3; contours start at .0025 N/m^2, with interval of .0025.

The associated stress shows the signature of the Madden-Julian oscillation (MJO); west of the dateline the stress anomalies move eastward at 3-4 m/s, while east of the dateline they move rapidly eastward (~20 m/s). However, the stress anomalies exhibit periods of about 60 days, which is at the lower end of the spectrum of the dynamical behavior associated with the MJO. The stress anomalies associated with the dominant 40-50 day period of the MJO do not strongly project onto the oceanic Kelvin wave because of their higher phase speeds.

We then attempt to reproduce observed intraseasonal variability of Z20 by forcing the model with intraseasonal stress. In the first experiment we force the model with full 26-100 day stress. The correlation between Z20 and model depth perturbation (h') across the TAO domain varies from around 0.6 to 0.4 (Fig. 2).

Next, we force the model with the stress obtained from the regression onto the

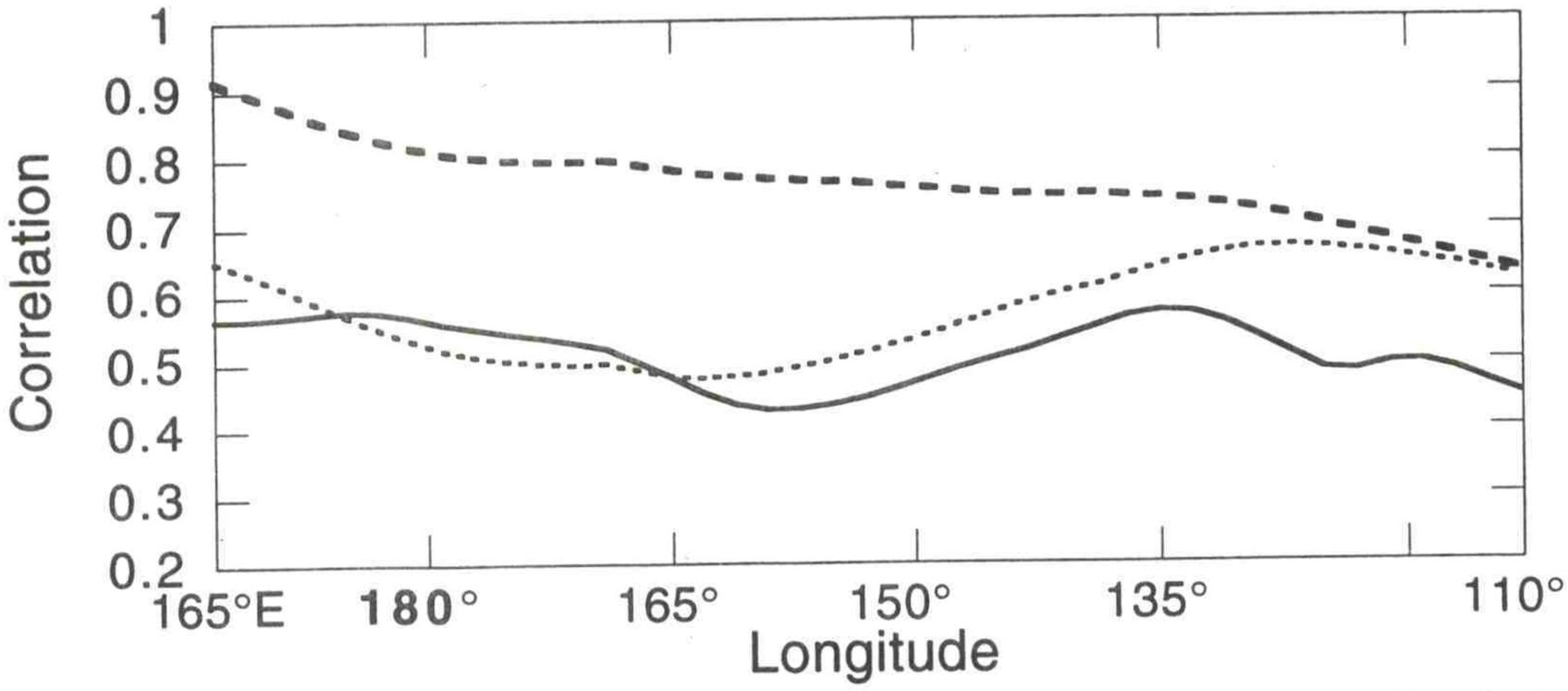

Fig. 2. Temporal correlation of model h' versus observed Z20 as function of longitude for: solid curve, 26-100 day data; dashed curve, dominant mode of Z20 (see text) versus model h' forced with dominant stress; dotted curve, dominant mode of Z20 versus dominant mode of model run forced with 26-100 day winds.

Z20 PCs. We correlate h' from that run with the Z20 data regressed onto its own PCs (Fig. 2). The result is a large improvement over the first result (although the degrees of freedom are less).

Finally, we integrate the model with the 26-100 day filtered winds, and then compute the EOFs of h' (over the TAO domain). The two leading PCs explain 76% of the h' variance. The correlations of the model h' regressed onto the leading h' EOFs versus the dominant mode from the observations (Fig. 2), however, reveal that the correlations are little better than the correlations with the 26-200 day filtered data. Thus, while the model can produce a reasonable result when forced with the observed wind stress that is coherent with observed Z20 variability, it fails to select the observed dominant mode of variability when forced by complete intraseasonal stress.

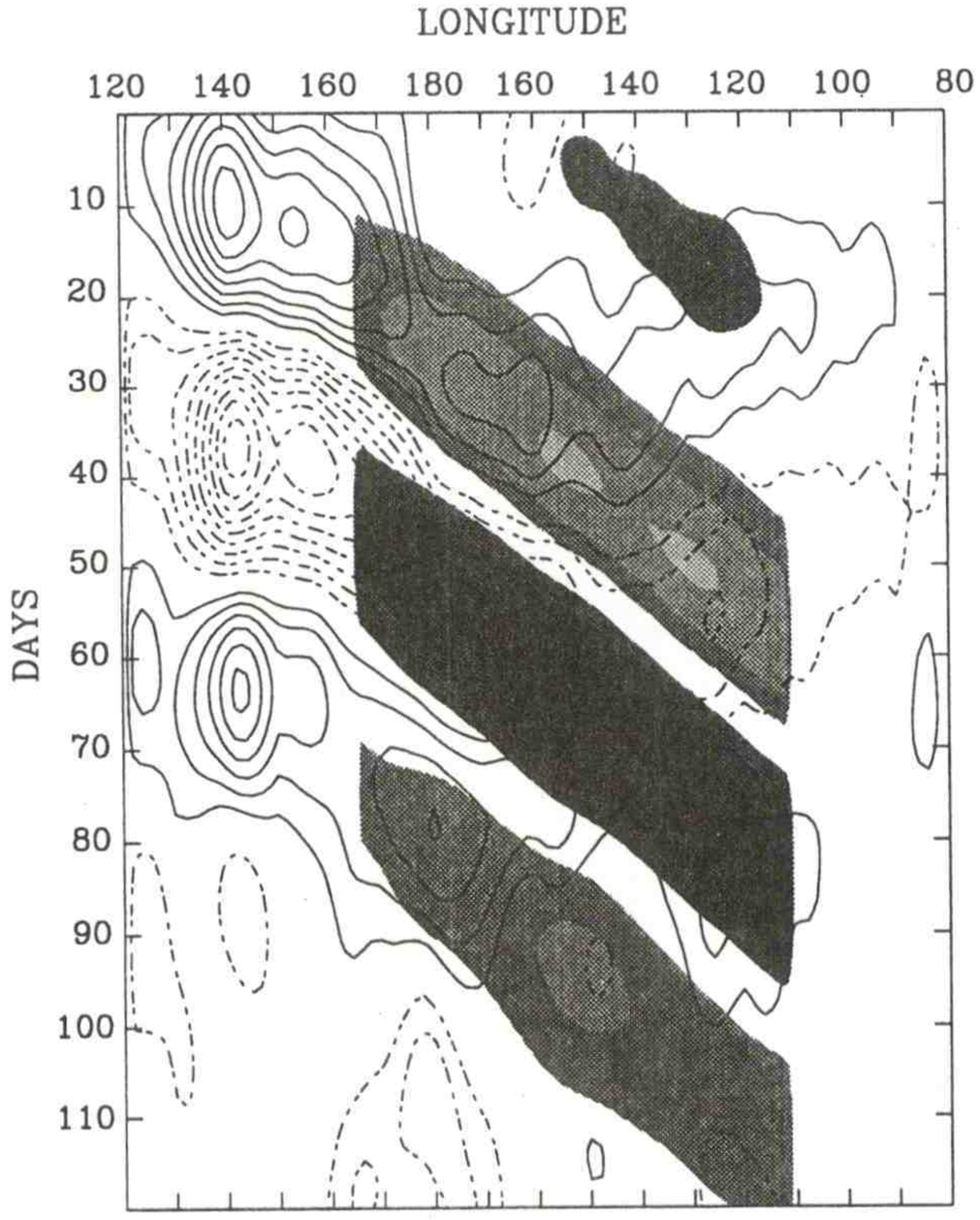

Fig. 3) Multiple linear lag-regression of 26-100 day model h' (shading) and zonal stress (contours) onto 2 leading PCs of h'. Shading and contours as in Fig. 1.

Although the correlations between the dominant Z20 and dominant h' from the model run forced with the full intraseasonal wind stress are small, if we now regress stress and h' onto the h' PCs (Fig. 3), we observe that the structure of the response and of the associated stress field is quite similar to the observed response and its associated stress (Fig. 1).

Comparison of the power spectra of the h' and observed Z20 PCs, however, reveals the model to respond at higher frequencies than is observed. While the model is able to selectively filter for lower frequencies than the dominant forcing, the 'red-shift' is less than observed in the real ocean.

A Simple Model for the Climatology and ENSO of Equatorial Pacific Ocean–atmosphere System

Ming Cai

Cooperative Institute for Climate Studies,
Department of Meteorology, University of Maryland
College Park, MD 20742

1. Introduction

The hypothesis of Bjerknes (1969) that views El Niño–Southern Oscillation (ENSO) as a "never–ending succession of alternative trends by air–sea interaction in the equatorial belt" has been a doctrine that guides our efforts of understanding the underlying mechanisms for ENSO. Despite that the Bjerknes's hypothesis is about the mechanism for both the mean equatorial circulation (Walker circulation) and its basin–wide variability (Southern Oscillation), our current understanding of ENSO hinges heavily upon the success of anomaly coupling approaches (especially Zebiak and Cane 1987; and Battisti 1988). The studies with fully coupled air–sea models (e.g., Schopf and Suraez 1988; Philander et al. 1992; Nagai et al. 1992) do suggest that the coupled air–sea mechanisms are important not only for ENSO but also for the equatorial ocean–atmosphere climatology, in consistency with the Bjerknes's original postulate.

Two simple mechanisms have been proposed to account for ENSO variabilities (see Neelin et al. 1994 for a comprehensive review): (i) instability of the climatological state of the equatorial ocean–atmosphere system and (ii) delayed oscillation. The early instability analyses focused on temporal growing behaviors of the coupled system (Lau, 1981; Philander et al. 1984; Hirst 1986, 1988). The instability analyses derived from intermediate coupled models (e.g., Zebiak and Cane 1987) further explain some prominent features of equatorial interannual variabilities, including oscillatory behaviors with a multi–year time scale, realistic spatial structure of SST, surface wind, and thermocline depth anomalies, and the temporal relationship among these anomalous fields (Neelin 1991; Wakata and Sarachik 1991; Hao et al. 1993; Jin and Neelin 1993a,b; Neelin and Jin 1993). The delayed oscillation theory, first proposed by Suarez and Schopf (1988) and refined later by Battisti and Hirst (1989), Schopf and Suarez (1990), Cane et al. (1990), and Münnich et al. (1991), views oscillatory behaviors of the intermediate coupled models as a collective result of a local growing of coupled Kelvin waves in the eastern basin and a delayed negative feedback of Kelvin waves due to refection of uncoupled Rossby waves at the western boundary. The time scale of delayed oscillation depends heavily on the time scale of oceanic waves.

This paper attempts to illustrate that the equatorial Pacific air–sea interaction system works as a basin–wide nonlinear oscillator that not only produces ENSO oscillation but also gives rise to a new equilibrium state of the coupled system from initially zonally leveled themocline. In the equilibrium state, the equatorial ocean has a deep–in–west/shallow–in–east sloped thermocline and the equatorial atmosphere has prevailing surface easterlies.

2. Model

We begin our model derivation from shallow water equations with longwave approximation on an equatorial beta plane:

$$\frac{\partial u}{\partial t} - \beta y v + g' \frac{\partial h}{\partial x} = \frac{\tau}{\rho H}\,; \quad \beta y u + g' \frac{\partial h}{\partial y} = 0\,; \quad \frac{\partial h}{\partial t} + H\left(\frac{\partial u}{\partial x} + \frac{\partial u}{\partial y}\right) = 0 \tag{1}$$

Following Battisti (1988), we obtain the non-dimensional equations for the first two ocean modes

$$\frac{\partial K}{\partial t} + \frac{\partial K}{\partial x} = \tau_0 \quad \text{and} \quad \frac{\partial R}{\partial t} - \frac{1}{3}\frac{\partial R}{\partial x} = -\frac{\sqrt{2}}{3}\tau_0\,. \tag{2}$$

where, "K" and "R" , respectively, stand for the Kelvin wave and the first Rossby mode, and τ_0 is the projection of the zonal wind stress onto the first normalized Hermite polynomial function. The boundary conditions are:

$$K_{west} = (\sqrt{2} - \frac{1}{\sqrt{2}})\, R_{west} \text{ and } R_{east} = \frac{K_{east}}{(\sqrt{2} - \frac{\delta}{\sqrt{2}})}, \text{ where } \delta = 1 \text{ or } \delta = 0. \quad (3)$$

We shall refer to (2) and (3) as the basin–mode model. The case that $\delta = 0$ corresponds to the traditional eastern boundary condition for the Rossby waves, namely, no zonal current at the eastern boundary ($u^E = 0$). Under this boundary condition, the eastern boundary is not a perfect reflector (i.e., only part of the Kelvin wave is reflected back to the system as the Rossby modes) and thereby there is net loss of kinetic energy of the basin–mode model at the eastern boundary as what occurs in the nature. The case that $\delta = 1$ would make the eastern boundary condition be the same as the western boundary condition ($\int_{-\infty}^{\infty} u^W dy = 0$ and $\int_{-\infty}^{\infty} u^E dy = 0$), which obviously would make the eastern boundary be a perfect reflector for this basin–mode model. Without this modification in the eastern boundary condition, the solution of the basin–mode model is a damped oscillator. Under this modified eastern boundary condition, the oscillator is no longer a damped oscillator but the oscillating time scale of the oscillator remains unchanged. It is of importance to point out this modification only works for the two–mode system. When higher modes are allowed in the model, the reflection of the Kelvin wave at the eastern boundary would generate other Rossby modes and the loss of kinetic energy of the basin–mode oscillation is inevitable. The reason we invoke this modification on the eastern boundary condition is for the sake of mathematical convenience so that we could obtain an analytical solution for the period of the basin–mode oscillation in the coupled air–sea system.

The zonal wind stress is decomposed into two component. The first one is the zonal wind stress (denoted as τ^H) produced by the trade wind associated with the zonally uniform Hadley circulation induced by a zonally **leveled** thermocline. This zonal wind stress is assumed to be very small compared to observed annual mean total zonal wind stress because it is determined by the zonally symmetric circulation. As a zeroth–order approximation, we can simply regard it as a constant. The second component is the zonal wind stress associated with the Walker circulation (denoted as τ^w). The Walker circulation, a product of basin–wide atmospheric thermo-convection in the tropics, is driven by a west–east sea surface temperature contrast. To a zeroth–order approximation, the basin–wide SST differences in the zonal direction can be assumed to be proportional to the basin–wide zonal gradient of the thermocline depth, $(h_{EAST} - h_{WEST})$. Because of the dynamical/physical constraints of the equatorial atmospheric system (such as the availability of moisture in the atmosphere, finite amount of the total air mass, and the nonlinearities of the system), it is reasonable to assume that τ^w is a nonlinear function of $(h_{EAST} - h_{WEST})$ such that the amplification of τ_W becomes slower and slower as the basin–wide slope of the thermocline increases. In short, the total zonal wind stress in this simple equatorial air–sea system is represented by

$$\tau_0 = (\tau^H + \tau^w)\sin(\frac{\pi x}{x_e}) = \{\tau^H + \alpha \tanh(\frac{h_{west} - h_{east}}{H})\}\sin(\frac{\pi x}{x_e}), \quad (4)$$

where, τ^H is a small negative constant (e.g., corresponding to a westward zonal wind tress of 0.005 dyne/cm^2), α is the coupling coefficient, x_e is the non–dimensional length of the equatorial basin, H is the mean thermocline depth, h_{west} and h_{east} are the thermocline depth evaluated at the western and eastern boundaries, respectively. (2)–(4) are the elements of the simple equatorial air–sea system used in this study.

There are two free parameters that determine the equilibrium state and the period of the coupled system: τ^H and α. The physical interpretation for τ_0 has been discussed previously. The coupling parameter α determines the linear stability of the zonally leveled thermocline state.

3. Solutions

In this short paper, we only present an approximated analytical solution for the equilibrium state of the coupled system (i.e., the annual mean climatology) and the oscillation period of the coupled system about the equilibrium state. We have compared the approximated analytical solution with the numerical solutions of the coupled system using an initial–value approach and found high accurancy of approximated analytical solution.

The equilibrium solution of (2)–(4) can be obtained by letting the tendency terms in (2) be zero. Using the relation between the thermocline depth at the equator and the unknowns K and R (e.g., Battisti, 1988),

$$h = \frac{1}{2\pi^{1/4}}(K + R/\sqrt{2}), \tag{5}$$

and the boundary conditions (3) with $\delta = 1$, and then approximating $\frac{\partial K}{\partial x}$ and $\frac{\partial R}{\partial x}$ with their finite differences, we obtain

$$\frac{\pi}{2x_e}\frac{\Delta h}{H} = \alpha \tanh(\frac{\Delta h}{H}) - \tau^H, \tag{6}$$

where, $\Delta h = (h_{west} - h_{east})$. (6) enables us to calculate the equilibrium state of the coupled system as a function of the two free parameters of the model in terms of the thermocline depth difference across the basin, Δh. Then the zonal wind stress in the equilibrium state can be determined from (4).

The period of the coupled oscillation can be determined by linearizing (2) about the equilibrium state. This yields

$$\frac{\partial K'}{\partial t} + \Big(1 - \frac{\alpha(2x_e/\pi)}{\cosh^2(\Delta h/H)}\Big)\frac{\partial K'}{\partial x} = 0 \text{ and } \frac{\partial R'}{\partial t} - \frac{1}{3}\Big(1 - \frac{\alpha(2x_e/\pi)}{\cosh^2(\Delta h/H)}\Big)\frac{\partial R'}{\partial x} = 0, \tag{7}$$

where, the prime stands for the perturbation about the equilibrium state. In deriving (7), we have used (5) and boundary conditions (3) with $\delta = 1$, and have approximated $(q'_{west} - q'_{east})\sin(\pi x/x_e)$ with $(2x_e/\pi)\frac{\partial q'}{\partial x}$, where q' can be either K' or R'. It follows that the period of the coupled oscillation is

$$T = \frac{T_0}{1 - \frac{\alpha(2x_e/\pi)}{\cosh^2(\Delta h/H)}}, \tag{8}$$

where T_0 is the period of the uncoupled oscillation equal to $4x_e$ in non–dimensional unit.

Now let us evaluate the dependence of the equilibrium solution and the oscillating period of the coupled system upon these two free parameters. The suitable numerical values of the model parameters for the equatorial Pacific basin are: $\frac{\Delta\rho}{\rho} = 0.003$, $L = 1.7\text{x}10^7$ meters, $H = 180$ meters. One unit of the non–dimensional time then corresponds to approximately 1.59 day. The period of the uncoupled ocean, T_0, is about 348 days.

Presented in Figure 1 are the equilibrium solutions and their corresponding oscillating periods obtained from (6) and (8) as a function of the coupling coefficient for $\tau^H = 0$ in the panel on the left and $\tau^H \neq 0$ (corresponding to a dimensional wind stress –0.005 dyne/cm^2) in the panel on the right. Let us first discuss the case that $\tau^H = 0$. When the coupling coefficient is smaller than a critical value (about 0.65 for this set of model parameters), the zonally leveled thermocline is stable whereas the oscillating period of the coupled system increases as the coupling coefficient increases. After α exceeds the critical value, the zonally leveled thermocline becomes unstable and two equilibrium solutions are bifurcated from the zonally leveled thermocline

state: One corresponds to a normal climatology that has a deeper thermocline in the west and a shallower thermocline in the east (the solution in which $\Delta h > 0$) and the other corresponds to an anti–climate state in which the thermocline depth is deeper in the east. In this scenario, it is equally plausible for an initially zonally leveled thermocline plus a random perturbation to oscillate about one of the two equilibrium states. These two equilibrium solutions have identical oscillating period. When a very small negative (westward wind stress) τ^H is included in the system, the anti–climate state is separated from the normal climate state by an unstable equilibrium state that has a weakly tilted thermocline. Because the unstable equilibrium state also has an anti–climate configuration, an initially leveled thermocline plus a random perturbation would preferentially oscillate about the normal climate state. In the other word, the normal climate state is much more favored than the anti–climate equilibrium state. Other than this major difference, the behaviors of the coupled system with the presence of τ^H are very similar to those for $\tau^H = 0$. Not shown here is the total zonal wind stress in the equilibrium states which can readily determined from (4). The wind stress produced by the air–sea interaction is much larger than the imposed pre–existed wind stress τ^H. The oscillating time scale of the coupled mode about the new equilibrium state is much longer than the uncoupled period but would decrease as the coupling coefficient further increases. For example, for $\Delta h \approx 100$ meters, the total zonal wind stress is about 0.4 dyne/cm^2 and the oscillating period is about 600 days. Therefore, we in this study have demonstrated that this coupled system not only can produce a oscillating time scale much longer than the uncoupled time scale but also produces a much more favored equilibrium state in which the equatorial ocean has a deep–in–west/shallow–in–east thermocline and the atmosphere has prevailing easterlies.

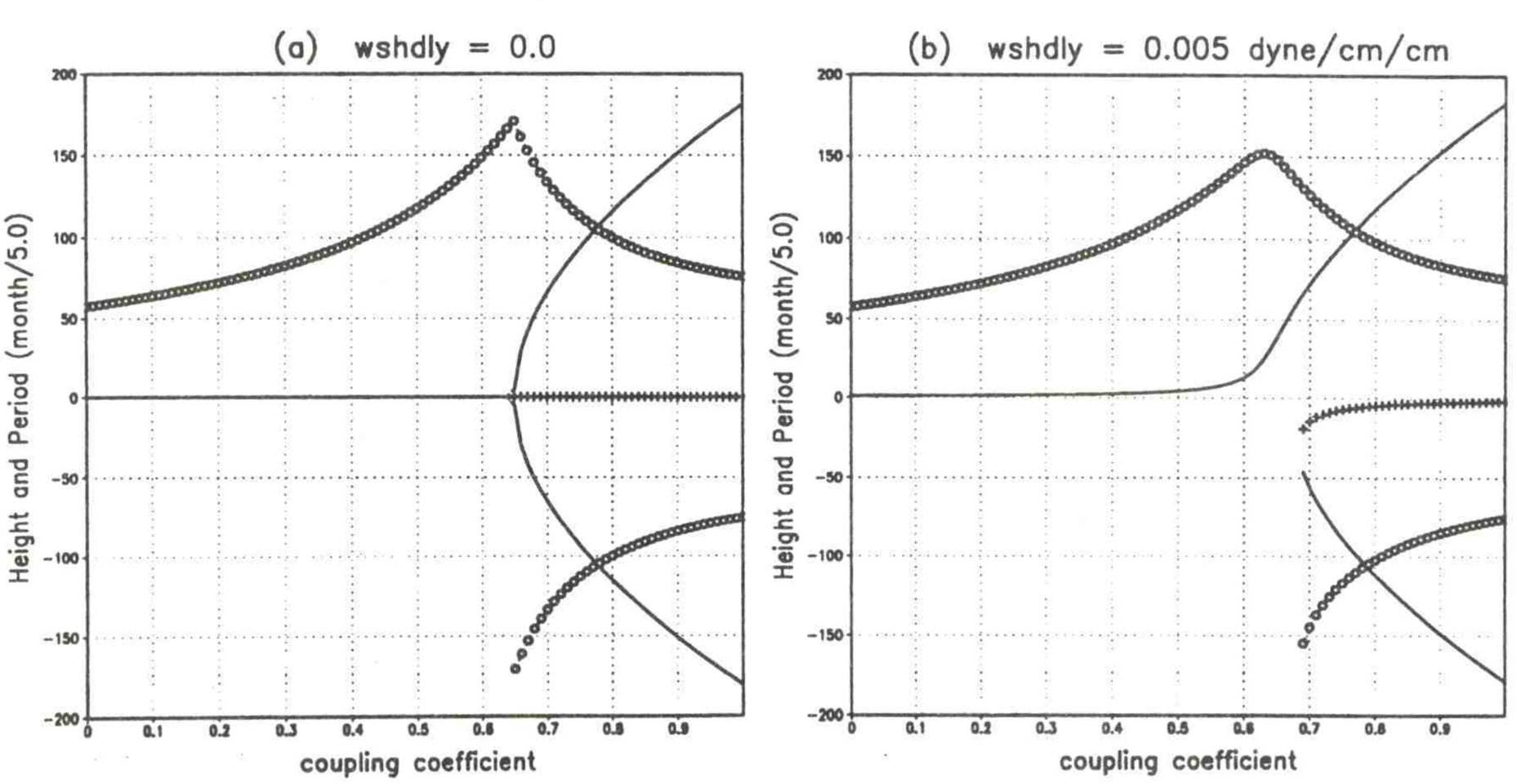

Figure 1 Equilibrium solutions and oscillating period of the simple coupled equatorial Pacific ocean–atmosphere system. Panel on the left: $\tau^H = 0$; Panel on the right: τ^H corresponds to a westward wind stress of 0.005 dyne/cm^2. The solid curves are for the stable equilibrium states, the crossed–curve represents the unstable equilibrium state. The equilibrium solutions are represented in terms of the thermocline depth difference between the western boundary and the eastern boundary (unit: meters). The curve with open–circle represents the oscillating period of the stable equilibrium solution (unit: 0.2 months and the negative values are used to present the period of the stable equilibrium state that has negative Δh).

Tropical Convection Low Frequency Variations over the Americas and associated boundary layer currents

Julia Nogués-Paegle and Kingtse C. Mo*
Department of Meteorology, University of Utah

*Climate Prediction Center, NCEP/NOAA, Washington, D.C., 20233

1. INTRODUCTION

A well defined north-west to south-east arc of convection extending from the Amazon basin to about 30 W and 30 S is often found in satellite observations. This is referred to as the South Atlantic Convergence Zone. Its intraseasonal variations have been associated with the 30-60 day (Madden-Julian) oscillation by Kousky and Kayano (1994), Park and Schubert (1993). Additionally, Kousky and Casarin (1986), used half- monthly means of outgoing longwave radiation (OLR) anomalies and 200 mb winds to relate deficient rainfall over Southern Brazil with an enhancement of the SACZ. These studies are extended here using daily OLR values filtered to retain 10-90 day periodicities. NCEP reanalyses (Kalnay et al., 1996) are used to describe the three dimensional structure of atmospheric motions associated with dry and wet periods over Southern Brazil and central Argentina. In particular, low level jets (LLJs) east of the Andes and their role in transporting moisture from the Amazon basin into the South American subtropical plains is discussed. These topographically bound currents are compared with similar LLJs found east of the Rocky Mountains.

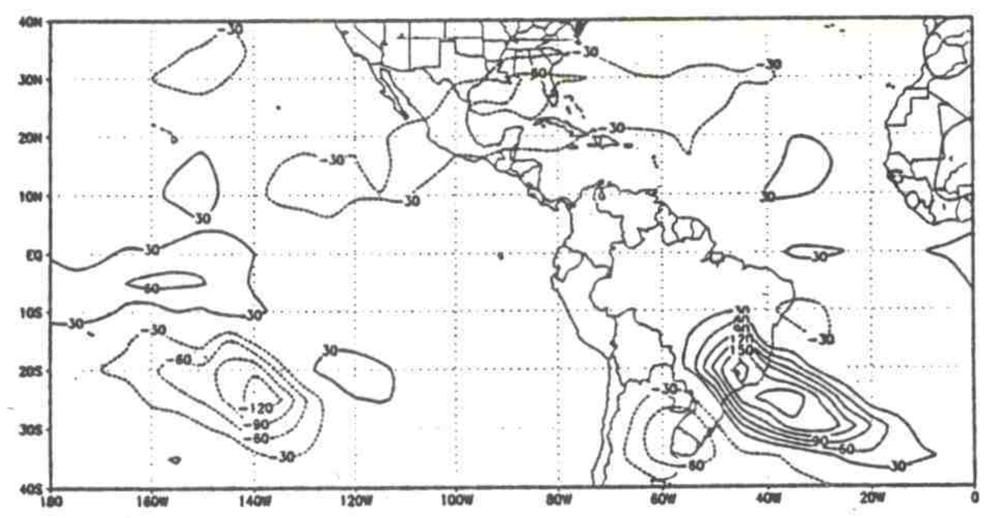

Fig 1. REOF 5.

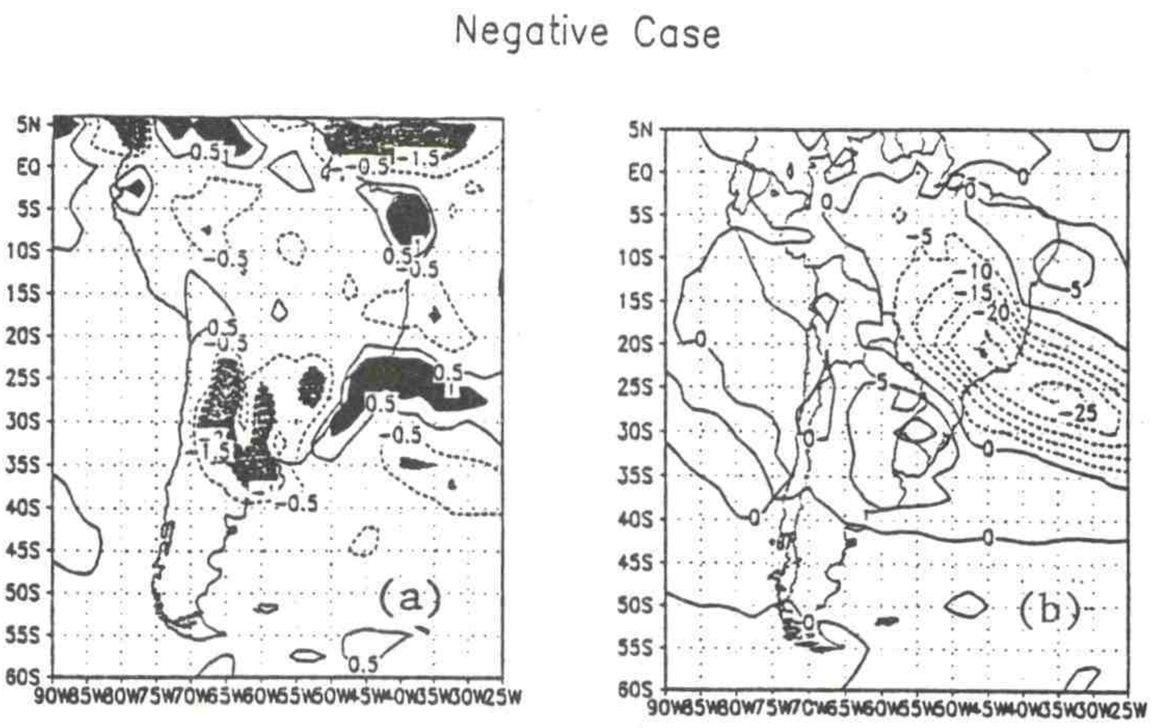

Fig 2. Composites of rainfall anomalies (a, c, light shades less than -1 mm/day, dark shades more than 1 mm/day) and OLR anomalies (b, d, contoured every 5 W/m^2).

2. DATA and METHODOLOGY

(I) Data

Daily outgoing long wave radiation (OLR) data from 1 June 1974 to 31 June

1993 with 10 months missing in 1978 are used as proxies of tropical convection. Archives available in a 2.5 by 2.5 deg latitude-longitude grid and every 6 hours from the NCEP/NCAR reanalyses from 1983-1993 are used to represent atmospheric conditions and to quantify diurnal variations. Data from 15 November to 15 March are used as representative of austral summer. The seasonal cycle is defined as the sum of annual and semiannual cycles and grand mean. Anomalies are defined as differences between daily values and the seasonal cycle. OLR anomalies were filtered to retain fluctuations with periods between 10-90 days.

(II) METHODOLOGY

Empirical orthogonal function analysis was performed on the filtered OLR anomalies from 1974/75 summer to 1992/93. The domain covers the study area identified by the PanAmerican Climate Studies (PACS) program (40 S - 40 N, 180 W -20 E). Rotated EOFs (REOF) were obtained using the varimax rotation method. The number of eigenmodes to be rotated was based on the criterion given by O'Lenic and Livezey (1988). Subsequently, the filtered OLR anomalies were projected onto the REOF 5 pattern, which depicted a well marked SACZ, to obtain principal components (PC). This REOF explains 3.8% of the variance. The standard deviation of PC 5 was computed using all 18 summer seasons. Events are chosen based on PC 5 magnitude (greater than 1.2 or less than -1.2 of the standard deviation) and duration (at least 5 consecutive days). A positive event indicates positive OLR anomalies for the SACZ as shown in Fig 1. From 1974-1993, there are 28 positive and 34 negative events.

3. DISCUSSION

Figure 2 shows the total OLR and rainfall anomaly composites for positive and negative events. Rainfall estimates are those produced by the NCEP/NCAR Reanalysis in the course of the reanalysis. The southward extension and strengthening of the SACZ for the negative composite is associated with suppressed rainfall from 40 to 20 S and 70 to 50 W. The opposite is true

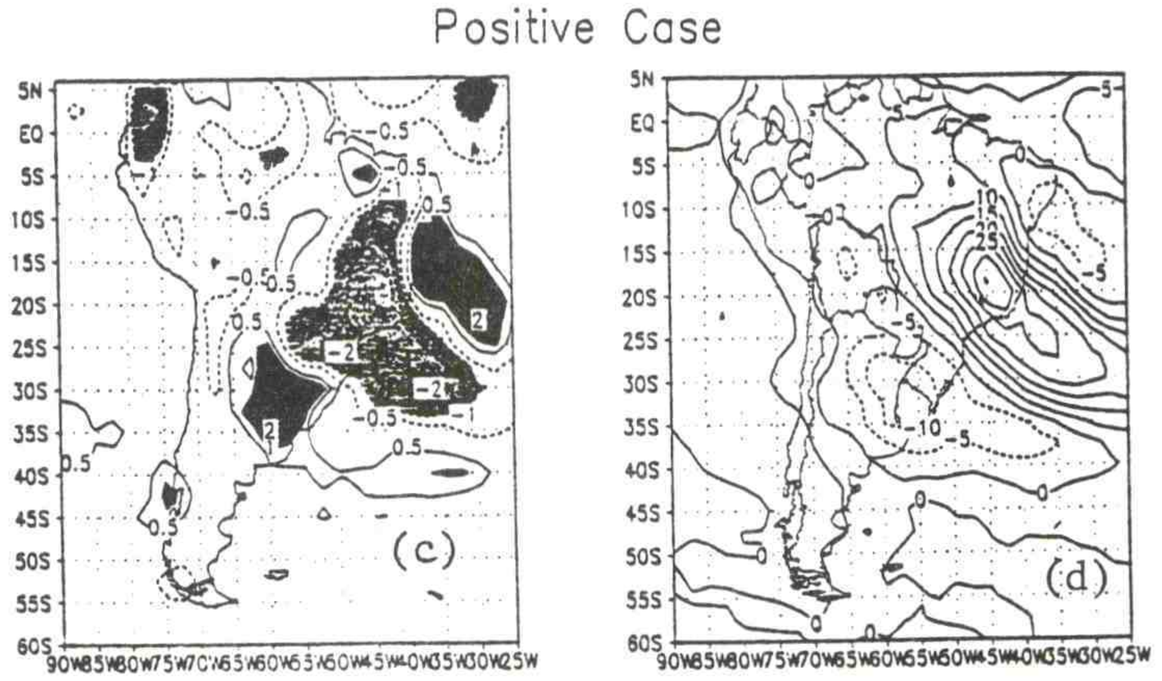

Fig 2. (continued)

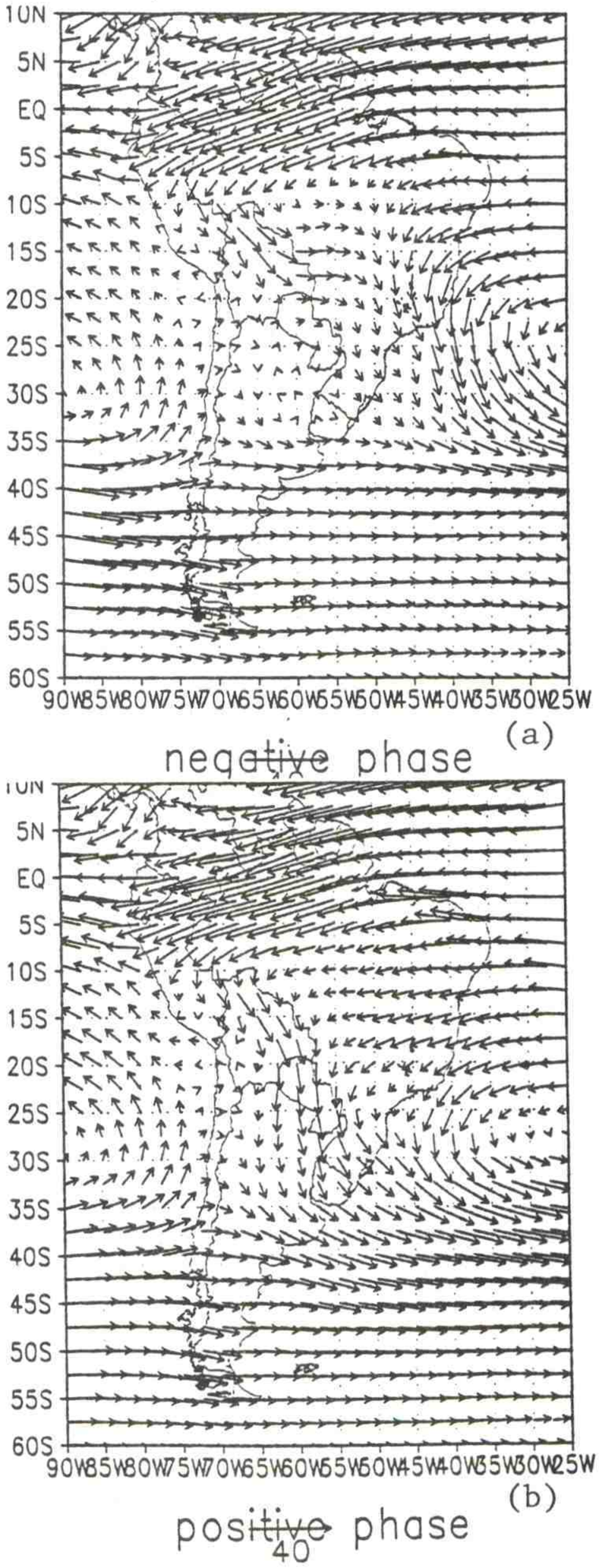

for the positive composite which shows enhanced rainfall over the subtropical plains of South America. These rainfall anomalies are associated with convergence/divergence of the vertically integrated moisture flux over this region for the positive/negative event respectively (Fig 3). The moisture flux was computed in sigma coordinates. There are 28 sigma levels in the assimilation model with 8 levels at 800 mb and below (.80, .84, .88, .915, .942, .964, .982, and .995), this gives a very good resolution of moisture transport within the lower atmospheric levels. Cases with plentiful rainfall over the subtropical plains are associated with northerlies just east of the Andes. Such wind motions are not observed during cases of enhanced convection in the SACZ.

Figure 4 shows a vertical time diagram of the meridional wind component for the 21 February 1987 through 13 March 1987 period. The PC time series (not shown) reveals the existence of a positive event that lasted from 21 February through 2 March 1987 and a negative event for 7-14 March 1987. The positive case has a well defined LLJ with a strong diurnal oscillation.

4. CONCLUSIONS

The study shows oscillation in the SACZ with changes from enhanced to diminished convections within two week periods. Events associated with strong convective activity over the SACZ are associated with rainfall deficits over the subtropical plains of South America. In contrast, when th SACZ weakens, precipitation over these plains is abundant. These results are in agreement with those of Kousky and Casarin (1986). Additionally, we have found that the influx of moisture over central Argentina and southern Brazil is caused by a strong low level jet which displays marked diurnal oscillations. This jet appears to have similar characteristics to the well documented LLJs over the great plains of North America (see e.g Paegle et al., 1996). Both the North and South American LLJs play similar roles in estbalishing moisture corridors that produce rainfall in subtropical and mid latitudes of both continents during the summer.

Acknowledgements

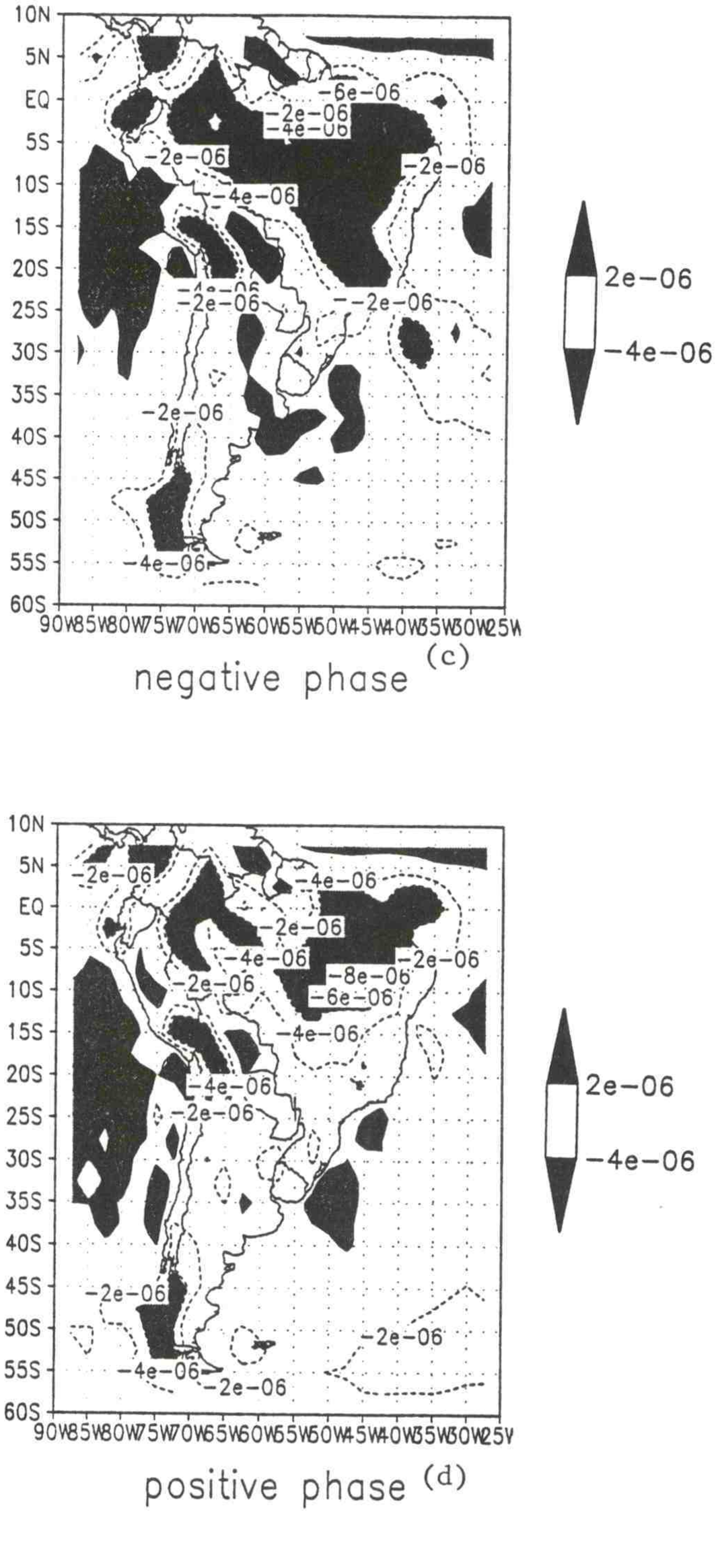

Fig. 3. Vertically integrated moisture flux (a, b, in units of 100 g/(cm s)) and divergence of this moisture flux (c and d).

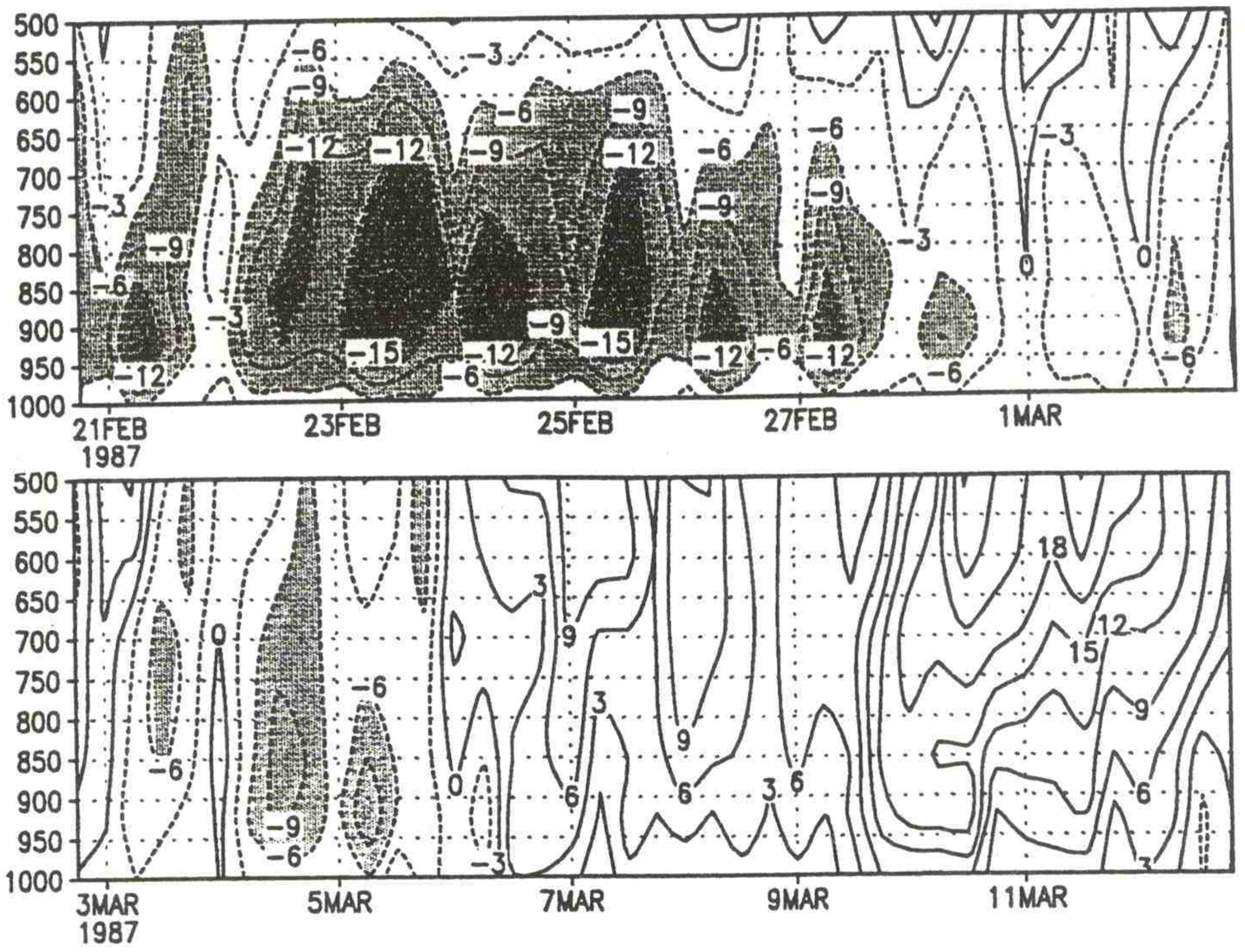

Fig. 4. Vertical time diagram of the meridional wind at 57.5 W and 25.5 S.

This investigation was supported by NOAA grants GC95-013 and GC95-833 to the University of Utah. The OLR data was kindly provided by Liebmann and Smith, 1996

References

Kalnay, E., M. Kanamitsu, R. Kistler, W. Collins, D. Deavan, L. Gandin, M. Iredell, S. Saha, G. White, J. Woollen, Y Zhu, M. Chelliah, W. Ebisuzaki, W. Higgins, J. Janowiak, K. C. Mo, C. Ropelewski, J. Wang, A. Leetma, R. Reynolds R. Jenne and D. Joseph, 1996: The NCEP/NCAR 40 year reanalysis project. *Bull. Amer. Met. Soc.*, in print.

Kousky, V. and D.P. Casarin, 1986: Rainfall anomalies in southern Brazil and related atmospheric circulation features. Extended Abstracts: Second International Conference on Southern Hemisphere Meteorology, Wellington, New Zealand, December 1-5, 1986.

Kousky, V. and M. T. Kayano, 1994: Principal modes of outgoing long wave radiation and 250 mb circulation for the South American sector. *J. of Climate*, 7, 1131-1143.

Liebmann, B. and C. A. Smith, 1996: Description of a complete (interpolated) outgoing long wave radiation data set. Submitted to *Bull. Amer. Met. Soc.*

O'lenic, E. A. and R. L. Livezey 1988: Practical considerations in the use of rotated principal component analysis (RPCA) in diagnostic studies of upper air heigth fields. *Mon. Wea. Rev.*, 106, 1682-1689.

Paegle, J., K.C. Mo and J Nogués-Paegle, 1996: Dependence of simulated precipitation to surface evaporation during the 1993 U.S. summer floods. *Mon. Wea. Rev.*, in press

Park, C-K and S. D. Schubert, 1993: Remotely forced intraseasonal oscillations over the tropical Atlantic. *J. Atmos.Sci.*, 50, 89-103.

A Comparison of Equatorial Pacific Winds Observed by Wind Profilers and Modeled by Numerical Weather Prediction Analyses

Christopher R. Williams
Cooperative Institute for Research in Environmental Sciences (CIRES)
University of Colorado, Boulder, CO 80309

Kenneth S. Gage
National Atmospheric and Oceanic Administration (NOAA)
Aeronomy Laboratory, Boulder, CO 80303

Introduction

The NOAA Aeronomy Laboratory in cooperation with the University of Colorado has installed several 50 MHz wind profilers across the tropical Pacific to measure the tropospheric and lower stratospheric winds. The wind profiler at Christmas Island, Kiribati (2 N, 157 W) has been operational since April 1986 and has been in near continuous operation ever since. Hourly profiler winds are available four times daily for incorporation into numerical model analyses via the Global Telecommunication System (GTS) since early 1987. These transmitted winds are encoded to look like a pilot balloon sounding (PIBAL) with winds recorded at mandatory pressure levels above 850 hPa and are available in archived data sets as WMO site number 91492.

Due to changes in software during December 1993, observed winds were transmitted to the GOES satellite but were not accepted by the GTS and the winds were not available for assimilation into numerical models for about six months during 1994. This interval of non-assimilation provides an excellent opportunity to evaluate the impact of wind observations in the remote areas of the tropics on numerical models. In this study, we compare the transmitted PIBAL winds from Christmas Island with the ECMWF and NMC analyses at the closest 2.5° x 2.5° (2.5°N, 157.5°W) grid point. The monthly differences and monthly standard deviations increase when the observations are not available for assimilation, which is to be expected. But surprisingly, there is an increase in zonal wind difference at 850 hPa during the boreal winter of 1991-1992 as the observed easterly winds decrease in strength and become westerly winds during January 1992. This El Niño signature of winds observed by the wind profiler was underestimated by the numerical model analyses.

Observations vs. Model Analyses

Before the observed winds can be compared with the modeled winds, the inherent differences between these two products must be understood. The transmitted PIBAL report from the Christmas Island wind profiler represents a single point observation of the winds one hour before transmission. The analysis winds represent one component of the state of a finite grid box. Due to these different spatial scales the observations and modeled winds are not expected to agree perfectly.

To evaluate the impact of the observations on the analyses, the difference (analysis - PIBAL) was calculated for each available analysis/PIBAL pair from 1987 to 1995 (March 1995 for ECMWF and June 1995 for NMC). The calculated differences are shown in Figure 1. The ECMWF - PIBAL

difference shows a decrease in scatter between the first three years (1987-1989) and the next four years (1990-1993) probably due to improvements in analysis procedures. The increase in scatter during the first half of 1994 due to the unavailable observations is clear in the ECMWF - PIBAL difference. The NMC - PIBAL difference shows more scatter compared to the ECMWF - PIBAL difference. There is also an increase in scatter during the first half of 1994 when observations were not available.

Westerly Winds at 850 hPa

From Figure 1, it can be seen that both analyses exhibit an increased difference during the boreal winter of 1991-1992, which was during a warm phase of the Southern Oscillation (El Niño). Figure 2 shows the twice daily analyses (00Z and 12Z) and PIBAL observations from November 1991 through February 1992. During the month of January 1992, the observed winds become actual westerlies at the 850 hPa level. These low level westerlies result from the convection east of Christmas Island associated with the El Niño. The ECMWF analyses agree with the observations with more consistency than the NMC analyses during this westerly wind event. The difference is only at the lowest level and reflects the unwillingness of the modeled boundary layer to accept the observed westerly winds which are in contrast to the climatological easterlies.

Concluding Remarks

Complete statistical analysis of the differences between the observations and analyses can not be performed without the knowledge of when the observations are being utilized by the models. A request for the time series indicating if and when the Christmas Island observations were used by the analyses was made publicly. With that data set, the complete statistical impact of providing observations in the remote tropical Pacific can be performed.

In the interest of improving numerical weather prediction models the NOAA Aeronomy Laboratory plans to install satellite communication equipment at all of the wind profiler sites. When the data communication system is complete, this data will be available four times daily and provide wind observations from remote tropical Pacific locations.

Acknowledgments. The Christmas Island wind profiler was constructed and is being operated with the support of the U.S. TOGA Project Office. The NOAA/CU Trans Pacific Profiler Network is supported by the National Science Foundation under Agreement ATM-87220797 and ATM-9214800. We wish to thank John Bryden for his assistance in the local management of the Christmas Island wind profiler. We also thank Paul Johnston, Warner Ecklund and David Carter for their contributions to the maintenance and upkeep of the Christmas Island wind profiler and Tony Riddle for his contributions to the archival and quality control of the Christmas Island profiler data. We thank the ECMWF for providing us with monthly reports on the quality of the Christmas Island winds in comparison to their analyses.

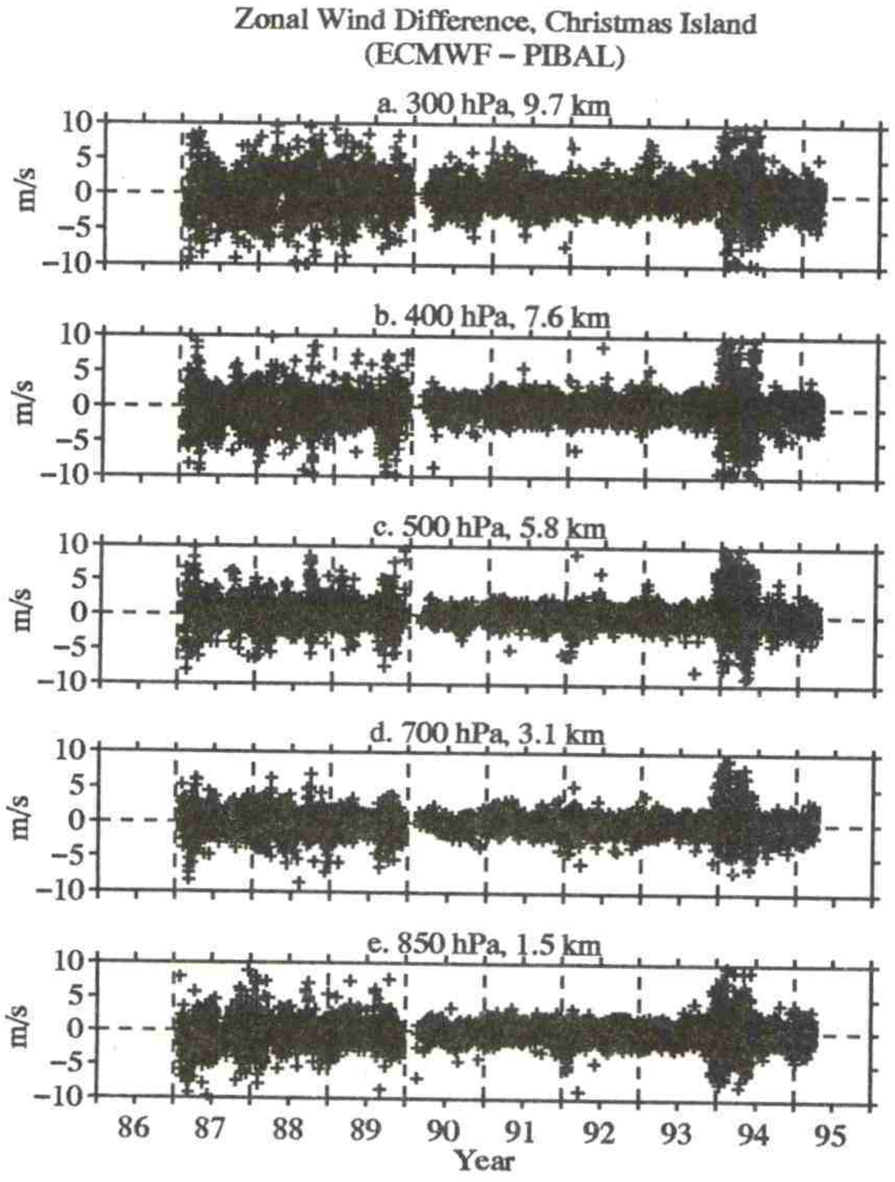

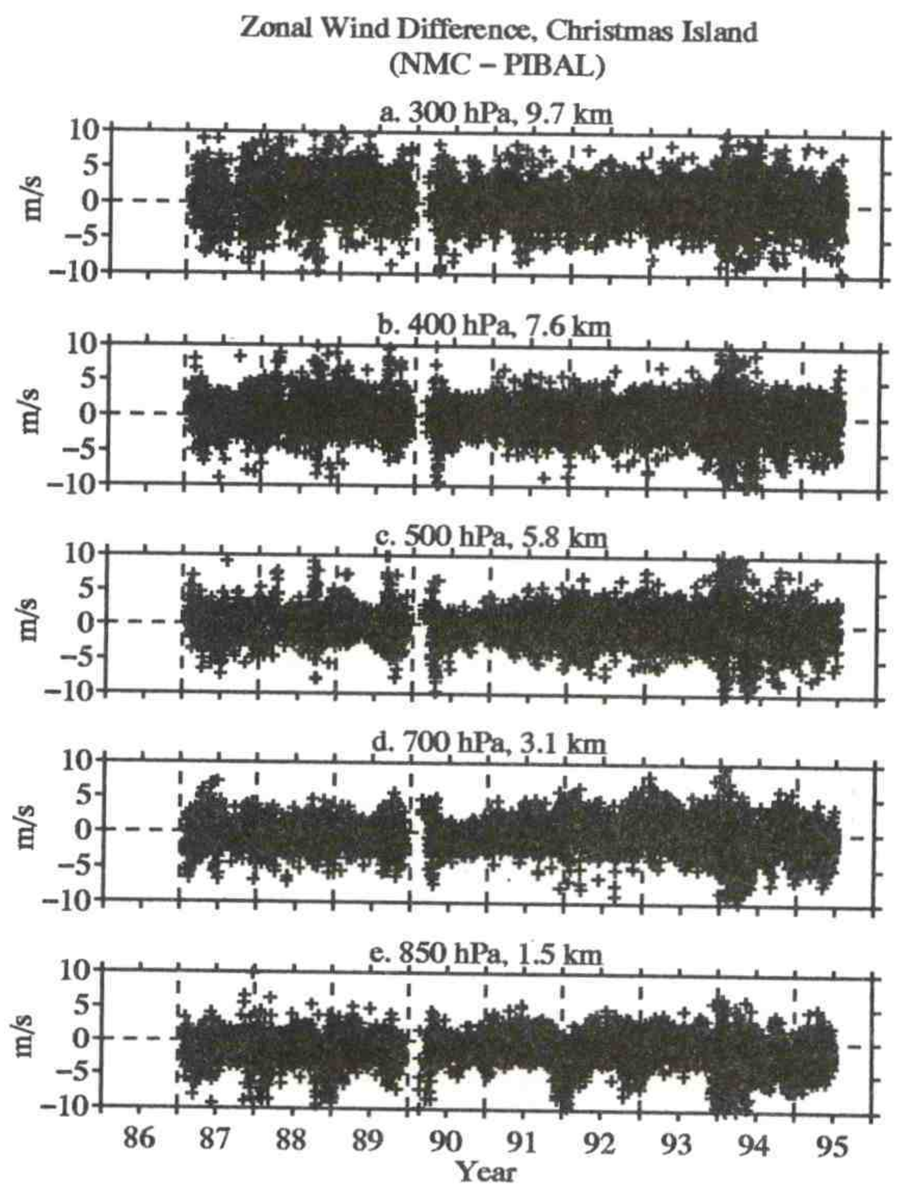

Figure 1. Calculated difference between twice daily (00Z and 12Z) zonal wind from 1987 to 1995, (left column) ECMWF - PIBAL, (right column) NMC - PIBAL.

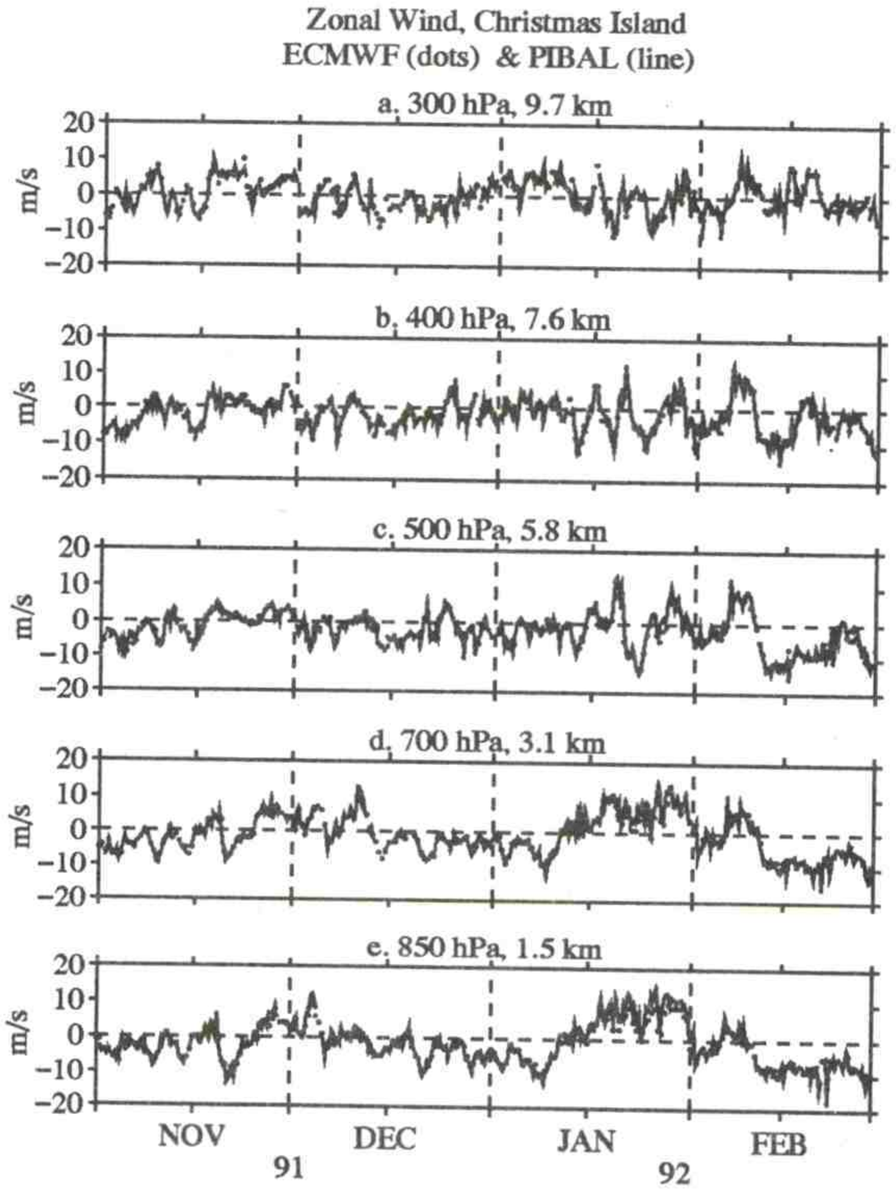

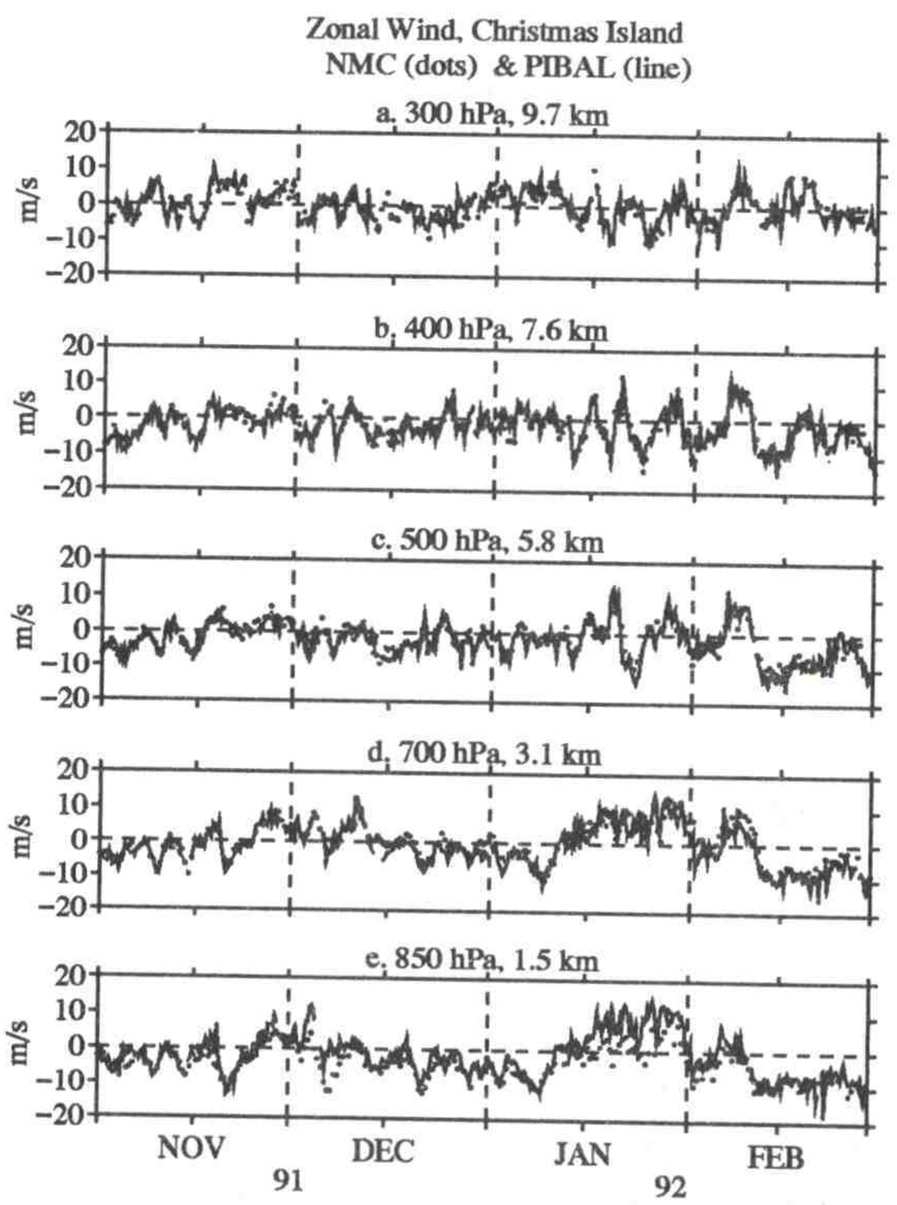

Figure 2. Twice daily (00Z and 12Z) zonal wind analyses and observations from November 1991 through February 1992, (left column) ECMWF analyses and PIBAL observations, (right column) NMC and PIBAL observations.

A Vorticity Budget of Tropical-Extratropical Interaction

George N. Kiladis
NOAA/ERL R/E/AL3
325 Broadway
Boulder, Colorado 80303

This study is an outgrowth of some recent work concerned with identifying the seasonality and vertical structure of large-scale circulation associated with tropical convection. The methodology follows the approach outlined in Kiladis and Weickmann (1992), whereby filtered circulation data is regressed against identically filtered Outgoing Longwave Radiation (OLR) data in order to isolate the "preferred" circulation accompanying tropical convection. During of course of this investigation, highly significant relationships were obtained between OLR fluctuations in the ITCZ to the east of the Philippines and upper level circulation over Australia during southern winter.

Several papers have addressed the relationship between the Australian circulation and ITCZ convection north of the equator on intraseasonal time scales (Berbery and Nogués-Paegle, 1993; Nogués-Paegle and Zhen, 1987; Nogués-Paegle and Mo, 1988). These studies have emphasized the role of meridional overturning, as evidenced by an apparent enhancement of the local Hadley circulation, in forcing a strengthening of the jet. These observations also support the idea that advection of vorticity by the divergent wind associated with tropical heating can lead to the generation of anticyclonic relative vorticity in the subtropics on the time scale of a few days, as described by Sardeshmukh and Hoskins (1988).

Here we concentrate on fluctuations at the 6-30 day time scale, which removes variability due to the 30-60 day Madden-Julian Oscillation, as well as much of the baroclinic wave activity on time scales less than 6 days. The band is still very broad, and contains roughly half the intraseasonal variance in both OLR and circulation once the seasonal cycle is removed.

OLR derived from satellite is used as a proxy for deep tropical convection, and NMC global analyses at 200 mb are used for circulation data. The OLR, and u and v components of the wind are first filtered to retain fluctuations in the 6-30 day band. Filtered OLR in a 10 degree box base region is then regressed separately against filtered u and v and OLR itself at each global grid point. The regression equations are then applied for a -1 standard deviation in OLR at the base region. Negative anomalies in OLR generally occur during periods of deep convection, thus the reconstructed circulations are meant to represent those associated with deep convection at the base region. This procedure is applied to data during June-August for nine years of data from 1985 through 1993. Statistical significance has been estimated locally using a t-test, and all of the fields shown here are highly significant when a Monte Carlo field significance test is applied. More details are given in Kiladis and Weickmann (1992).

Fig. 1a shows the results for 200 mb wind leading negative OLR in the region 5°N-15°N, 150°E-160°E by two days. Regressed u and v anomalies are computed for a -1 standard deviation in OLR at the base point (-17.1 Wm^{-2}), and thus represent the circulation anomaly two days prior to the peak in active convection in the shaded region. As convection increases in the base region, the anticyclone initially over central Australia strengthens and moves toward the east coast (Fig. 1b). At this point strong outflow into the Southern Hemisphere is evident from the region of the OLR perturbation, the bulk of which is divergent flow. The anticyclone continues to strengthen over the next couple of days (Fig. 1c), with the flow evolution suggestive of forcing by the mass circulation associated with the convection.

A barotropic vorticity budget for the regressed wind perturbations was computed in order to determine the importance of various terms associated with the tropical heating. This budget was obtained by calculating for Day 0 the terms:

$$\frac{\partial \zeta}{\partial t} = - v_\psi \bullet \nabla\zeta - v_\chi \bullet \nabla\zeta - \zeta D$$

where $\frac{\partial \zeta}{\partial t}$ = the absolute vorticity tendency, $v_\psi \bullet \nabla\zeta$ = advection of vorticity by the rotational wind, $v_\chi \bullet \nabla\zeta$ = advection of vorticity by the divergent wind, and ζD = stretching, neglecting dissipation, the vertical advection and twisting terms, and also neglecting the cross terms involving interactions between the 6-30 day fluctuations and other frequencies. Despite the fact that the budget is incomplete, the budget residual (not shown) is almost everywhere less than 20% of the tendency, so an approximate assessment of the relative importance of the leading terms can be obtained.

A comparison of the terms indicates that, in the extratropics, the large term due to the advection of vorticity by the rotational wind (Fig. 2, middle) is approximately balanced by stretching (Fig. 2, bottom). In the subtropics, however, vorticity advection by the divergent wind (Fig. 2, top) is dominant and is responsible for an anticyclonic tendency which would act to retrogade the anticyclone in Fig. 1b, offsetting the strong advection of this feature by the rotational westerlies within the Australian jet. Since the subtropical divergent wind in this case is directly connected to the convection north of the equator, this is consistent with the notion of tropical diabatic heating leading to a subtropical Rossby wave source as the divergent wind blows through a region of strong potential vorticity gradient along the jet (Sardeshmukh and Hoskins, 1988).

CONCLUSIONS

We conclude that tropical heating north of the equator is important in the forcing of the extratropical circulation over Australia on the sub-monthly time scale through the divergent circulation. Upper level anticyclonic perturbations in the subtropics and a strengthening of the Australian jet follow peaks in convective activity in the ITCZ over the western Pacific. This lag relationship, along with the apparent importance of vorticity advection by the divergent wind, suggest a strong dependence of transient wave activity over this region on tropical heat sources.

REFERENCES

Berbery, E.H., and J. Nogués-Paegle, 1993: Intraseasonal interactions between the tropics and extratropics in the Southern Hemisphere. *J. Atmos. Sci.*, **50**, 1950-1965.

Kiladis, G.N., and K.M. Weickmann, 1992: Circulation anomalies associated with tropical convection during northern winter. *Mon. Wea. Rev.*, **120**, 1900-1923.

Nogués-Paegle, J., and K.C. Mo, 1988: Transient response of the Southern Hemisphere subtropical jet to tropical forcing. *J. Atmos. Sci.*, **45**, 1493-1508.

Nogués-Paegle, J., and Z. Zhen, 1987: The Australian subtropical jet during the second observing period of the Global Weather Experiment. *J. Atmos. Sci.*, **44**, 2277-2289.

Sardeshmukh P.D. and B.J. Hoskins, 1988: The generation of global rotational flow by steady idealized tropical divergence. *J. Atmos. Sci.*, **45**, 1228-1251.

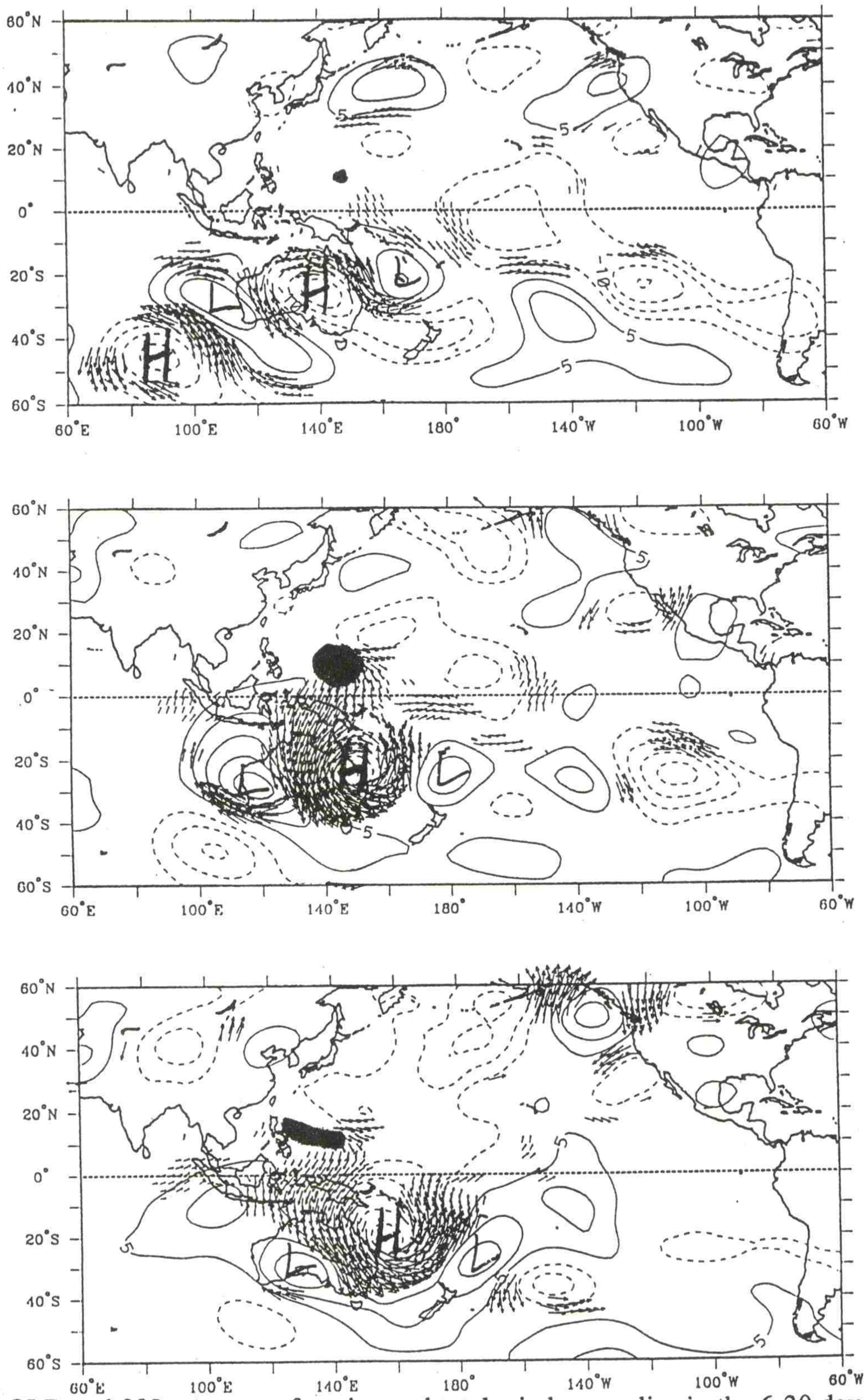

Fig. 1: OLR and 200 mb streamfunction and total wind anomalies in the 6-30 day band associated with an area-averaged OLR of -1 standard deviation in the base region (-17.1 Wm^{-1}, shown by the shading). Only statistically significant wind vectors are shown. Calculations are done using June through August data for the 1985-93 period. The largest vectors are about 5 ms^{-1}, Top: Two days prior to the peak in convection (Day-2). Middle: Day 0. Bottom: Day+2.

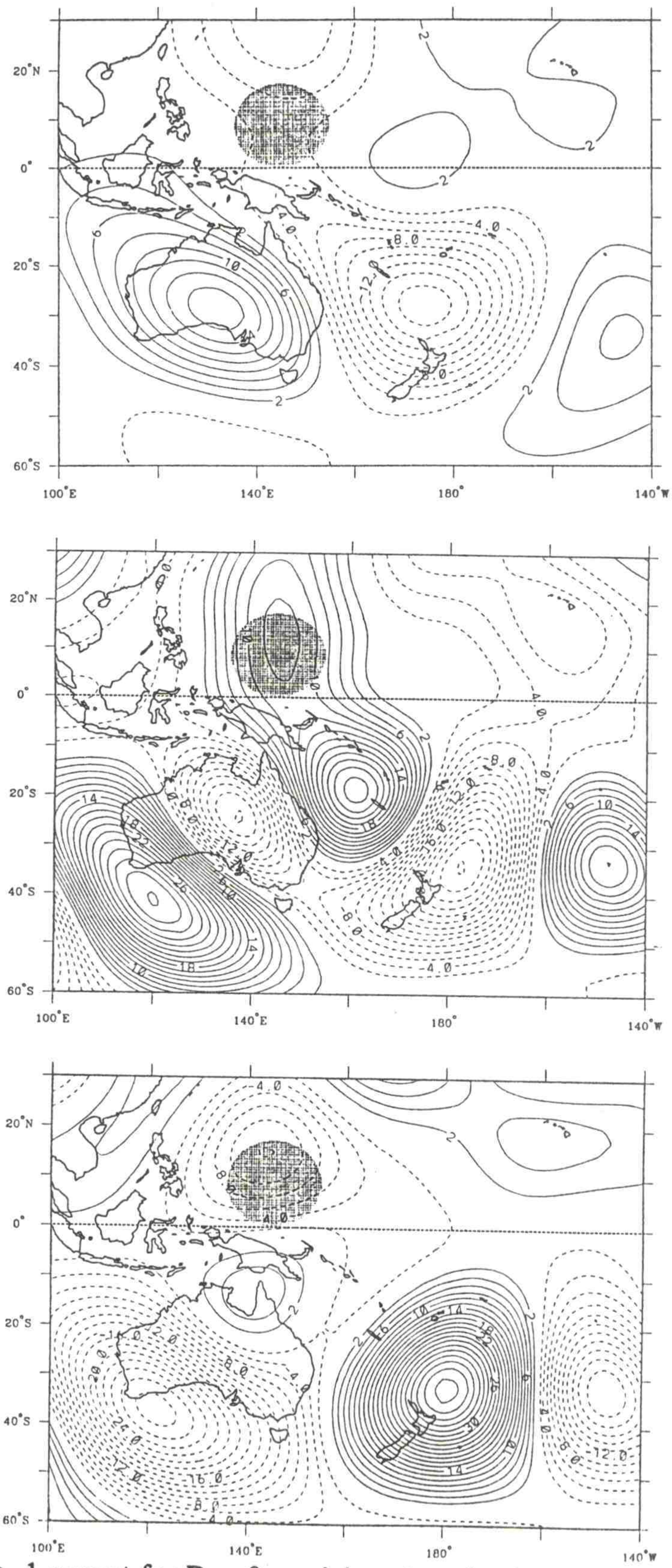

Fig. 2: As in Fig. 1 except for Day 0 vorticity advection by the divergent wind (top), vorticity advection by the rotational wind (middle), and stretching (bottom). Contour interval is X $10^{-12}s^{-1}$.

The role of large scale atmospheric circulation in the relationship between tropical convection and sea surface temperature

K.-M. Lau

Laboratory for Atmospheres, NASA/GSFC, Greenbelt, MD 20771

H.-T. Wu
Applied Research Corporation, Landover, MD 20785

1. Introduction

Despite many previous studies of the relationship between tropical convection and sea surface temperature (SST), the basic mechanisms underlying the observed relationship remain somewhat enigmatic. In terms of climate feedback mechanisms, tropical convection-SST relationship has been given renewed interpretations (Waliser and Graham 1993). It is clear that a better understanding of radiation-clouds-dynamics feedback will require a more in-depth knowledge of the physical underpinnings of the observed convection-SST relationship. This is the motivation of the present study.

2. Data

We use three datasets for this study: SST, outgoing longwave radiation (OLR), and 200 mb wind divergence (DIV). The SST data are grid-point analysis from the Climate Analysis Center (Reynolds 1988). The OLR data, which will be used as a proxy for tropical convection, are from the Advanced Very High Resolution Radiometer (AVHRR) of NOAA operational polar orbiting satellites. The DIV data are derived from the European Centre for Medium-Range Weather Forecasts (ECMWF) analysis and are used as a measure of the dynamical state of the tropical atmosphere. All three datasets have been processed to provide monthly mean values on the same $5^o \times 5^o$ latitude-longitude grid between 40^oS to 40^oN for the period from June, 1985 through December 1989. All climatologies of SST, OLR and DIV are computed for this period. Anomalies are defined as deviations from the climatological seasonal cycle.

3. Results

A commonly used representation of the relationship between OLR and SST is a scatter plot of collocated SST and OLR grid-point values as shown in Fig. 1. This plot is comprised of a total of over 40 thousand data points. Three apparent SST-OLR regimes can be identified:

Regime I: an increasing OLR with increasing SST from 18^oC to 26^oC ,
Regime II: a decreasing OLR with SST from 26.5^oC to 29.5^oC and
Regime III: a steep increasing OLR with increasing SST for SST $>29.5^oC$.

The increase in OLR with SST in Regime I is primarily due to the increase in water vapor and SST under clear sky conditions (e.g., Zhang 1993). From the scatter of the data points with OLR < 240 $Wm^{-2}/^oC$, it is clear that deep convection, though with much less frequency compared to the higher SST regimes, can occur even in this low SST regime. Regime II is ascribed to the rapidly increased frequency of occurrence of deep convection over warm water. The large scatter in the low OLR values signals the inherent temporal and spatial variabilities of deep convection which are not matched by the SST variation, but may be related to the large scale moisture convergence (Gadgil et al. 1984; Graham and Barnett 1987). Waliser (1995) attributed Regime III to the presence of hot-spots in isolated regions of forced subsidence within the western Pacific warm pool. From Fig. 1, we note that

the statistics of Regime III at extreme high SST's (> 30.5^{o}C) is contributed by relatively small number of data points outside the data envelope and therefore may be affected by sampling errors.

To examine the SST-OLR relationship as a function of the large scale motion, we divide the circulation regimes of the tropical atmosphere into seven categories according to the strength of the upper level divergence. The definition of the categories and the total number of data points in each category are shown in Table 1. The large number of data points in each category ensures that statistically robust SST distribution can be obtained from each category.

Before discussing the circulation-stratified OLR-SST relationships, it is helpful to illustrate the frequency distribution of the SST as a function of the circulation regimes (Fig. 2). Of particular interest is Category IV, which represents conditions of vanishing upper level divergence. This category has maximum frequency of occurrence of SST at 27.5^{o}C. The spatial distribution of the DIV categories (not shown) also indicates that Category IV represents a large number of SST occurrence over a large portion of the tropical ocean under conditions in which the large scale dynamical control is weakest. Therefore, Category IV should provide an estimate of an intrinsic OLR-SST relationship when influence from the large scale circulation is minimal, i.e., this relationship should be closer to the true thermodynamical sensitivity of OLR due to local SST.

The OLR-SST relationships for the different DIV categories are shown in Fig. 3. The functional relationships, including the aforementioned SST regimes are quite well defined and well separated for each large scale circulation category. The "clear-sky" portion (Regime I) of each SST-OLR relationship appears to be quite similar for each DIV category. The difference in the back ground OLR for different DIV is due to the different probability of deep convection under different atmospheric large scale circulation forcings, when the SST remains constant. This is supported by separate calculations which show that the dependence of OLR on DIV is quite linear and is nearly independent of SST (not shown).

While, the increase in convection with SST (Regime II) can be found in all DIV categories, the range of SST (25.5-27.5^{o}C) at which deep convection starts to increase is quite broad, i.e., there is no obvious sharp SST threshold beyond which convection increases drastically. Most importantly, the rate of increase of convection (decrease of OLR) with respect to SST is substantially different for different DIV categories. For the positive DIV categories (I, II and III), increase in deep convection rises steeply with increasing SST, but as can be seen from the increasing separation between the family of curves, much of the rise is also due to the increase in the rising motion. Referring to Table 1, for Category I, $\frac{\partial(OLR)}{\partial(SST)}$ at 27^{o}-28^{o}C is -15.2 Wm^{-2}/^{o}C, much steeper than that for Category IV which only has a slope of - 4.5 Wm^{-2}/^{o}C . The sensitivity is reduced further for the stronger subsidence categories (V and VI). The strongest subsidence Categories VII shows increased sensitivity of OLR to SST, but because of the smaller sample of SST > 27^{o}C for this category, the result is almost certainly affected by sampling errors.

For SST Regime III, Fig. 3 shows that in the strong ascending region (Categories I and II), the increase in deep convection with SST is monotonic with no significant decrease beyond 29.5^{o}C. With the increasing proportion of upper level convergence (subsidence), a reversal in OLR-SST gradient appear to be present at higher SST, but not necessarily at 29.5^{o}C. For Category III, the peak convection appears to occur at 30^{o}C; for Category IV and V it occurs near 29.5^{o}-30^{o}C. In general, there is a tendency for the OLR peak to occur at lower SST's for increasing subsidence categories. The statistics of the SST Regimes III for Categories III through V are quite robust because of the relatively large number of data points in the SST range from 29-30^{o}C in these categories. This is also evident from the clear separations among the different OLR-SST relationships. On the other hand, because the occurrence of

relatively higher SST's (>29.5^{o}C) for the strongest subsidence categories (VI and VII) is scarce and sporadic, the presence of Regime III in these categories may be questionable. The above results show that there is no magic to the 29.5^{o}C isotherm for maximum convection, but its existence or lack thereof, is strongly tied to the large scale circulation over the entire tropics.

As an alternate but complementary methodology, linear regression analysis provides an estimate of the intrinsic OLR-SST relationship when the influence of atmospheric circulation is "removed" in a statistically sense. Results from linear regression analysis (see Lau and Wu, 1995) are consistent with those from the categorization procedure discussed above.

4. Concluding remarks

The results of this paper show an intrinsic OLR-SST sensitivity of approximately -4 to -5 $Wm^{-2}/^{o}C$, considerably weaker than the bulk sensitivity found in previous studies (-15 to -20 $Wm^{-2}/^{o}C$). The latter is presumably due to the juxtaposition of different circulation regimes of diverse spatial and temporal scales. The present results also point to multiple causes, that underpin a given bi-variate relationship. As such, a bi-variate relationship involving co-located tropical convection and SST does not imply and should not be used to infer local causality, without fully understanding the influence of other critical factors. We also note that while the lower sensitivity in the intrinsic OLR-SST relationship found here may better reflect the underlying thermodynamical control i.e., that arising from the Clausius-Clapyeron relationship governing water vapor and convection by temperature change, the effect of large scale circulation feedback on shorter time scales unresolvable by monthly averages is still present in the intrinsic relationship found here. Hence the underlying thermodynamical sensitivity due to one-dimensional radiative convective processes (when the effect of subseasonal scale large scale circulation is also taken out) may be even weaker. The present results should serve as a reminder of the need to view critically any generalized interpretations on climate change feedback processes such as the super-greenhouse or thermostat processes based on climate surrogates such as seasonal and interannual variability.

Table 1. Classification of circulation regimes according to the strength of the upper level divergence (DIV) and total number of data points in each category. $\frac{\partial OLR}{\partial SST}$ denotes the partial rate of change of OLR w.r.t. SST at constant DIV for SST between 27^{o}C to 28^{o}C in unit of $Wm^{-2}/^{o}C$.

DIV(10^{-6} s^{-1})	> 2.5	[1.5,2.5]	[0.5,1.5]	[-0.5, 0.5]	[-1.5,-0.5]	[-2.5,-1.5]	< -2.5
Category	I	II	III	IV	V	VI	VII
Total number	3791	4407	7065	9401	8989	5347	3718
$\frac{\partial OLR}{\partial SST}$	-15.17	-10.66	-8.96	-4.55	-3.12	-3.26	-6.24

Reference

Lau, K.-M., and H.-T. Wu, 1995: The role of large scale atmospheric circulation in the relationship between tropical convection and sea surface temperature, *J. Cimate,* **submitted**.

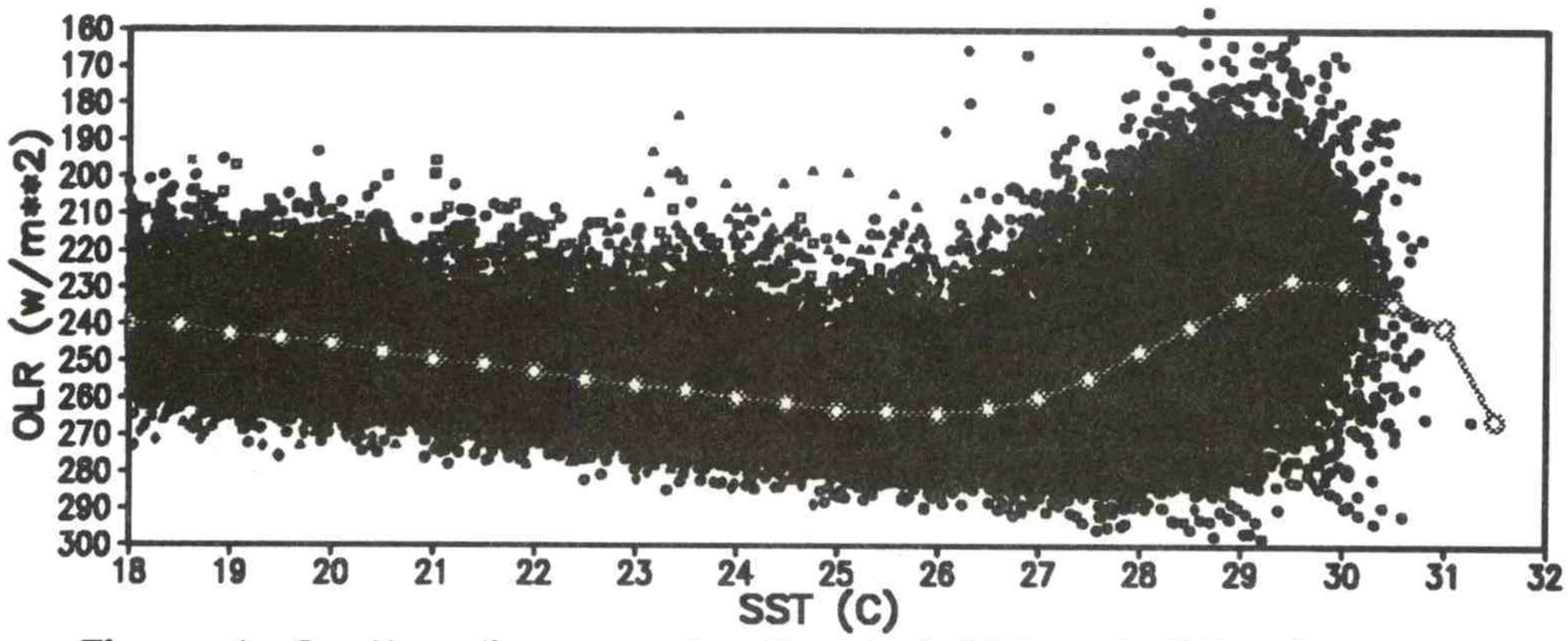

Figure 1. Scatter diagram of collocated SST and OLR grid-values for the global tropical oceans. Superimposed is the mean OLR values as a function of every 0.5 C SST bin.

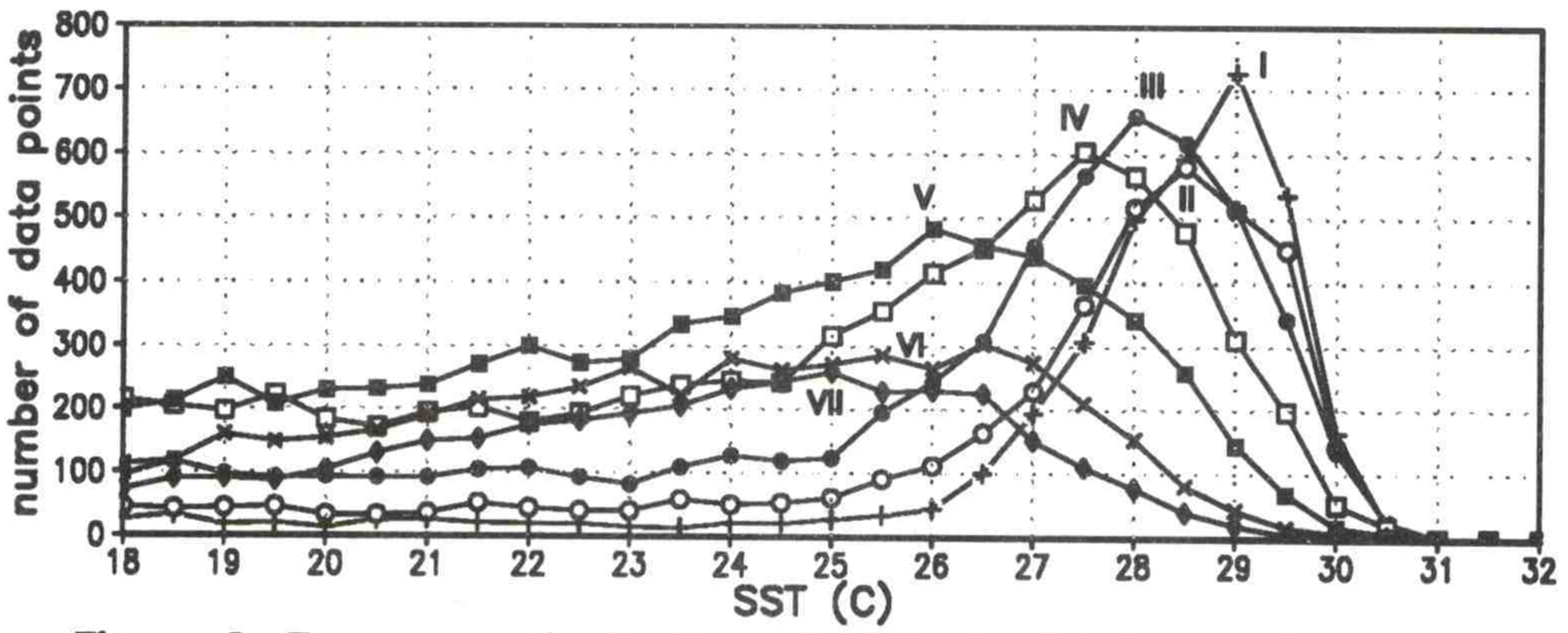

Figure 2. Frequency distribution of SST, stratified according to the DIV categories (see Table 1 for definition of category).

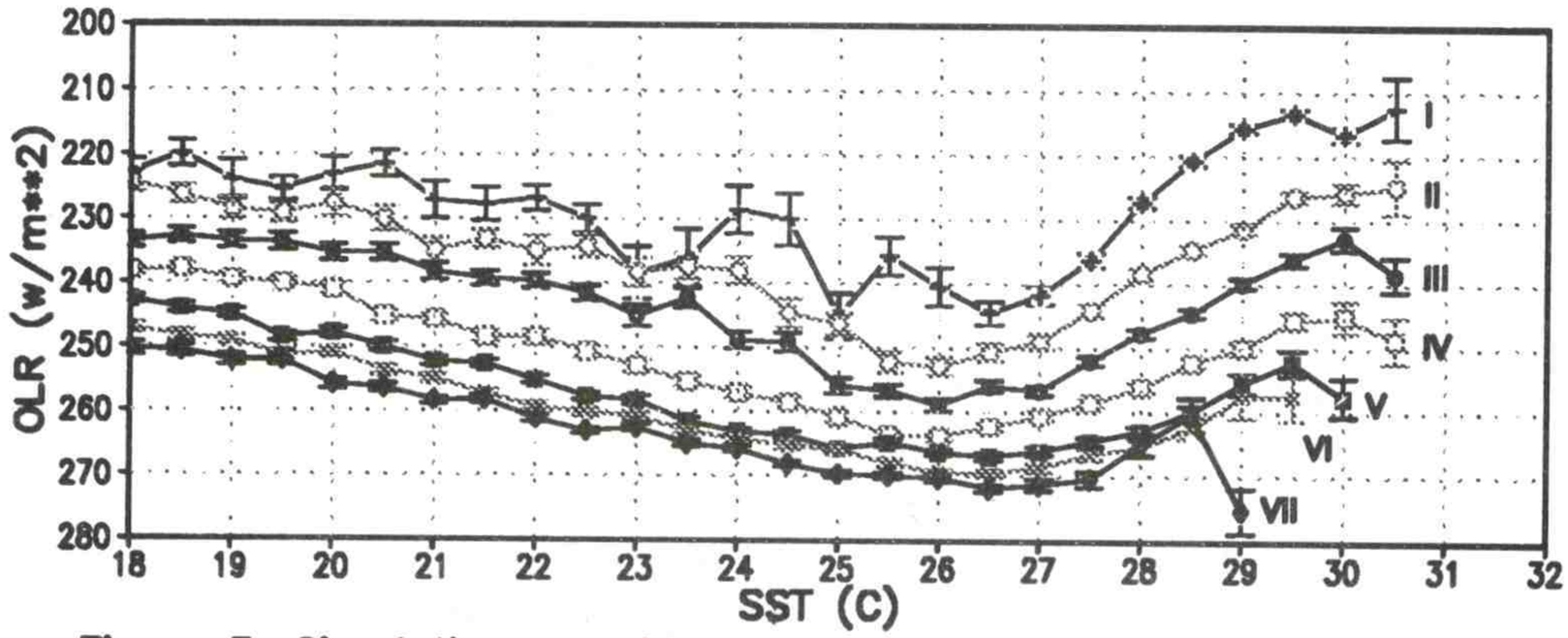

Figure 3. Circulation-stratified OLR-SST relationship expressed as mean OLR values for every 0.5 C SST bin. Error bars indicate standard error.

SCATTEROMETER WINDS COMPOSITED ACCORDING TO THE PHASE OF THE TROPICAL INTRASEASONAL OSCILLATIONS

Roland A. Madden, Timothy J. Hoar, and Ralph F. Milliff

1. INTRODUCTION

Scatterometer wind data from the European Remote-Sensing Satellite (ERS-1) provide an unprecedented opportunity to study surface winds over the world's oceans. Here we try to learn more about the behavior of the surface winds over the equatorial Pacific associated with large-scale, eastward propagating, Tropical Intraseasonal Oscillations. ERS-1 was launched in the summer of 1991. We restrict our study to the two-year period 1992-1993. Our area of interest extends from 140E eastward to 80W longitude and from 20S to 20N.

The satellite scatterometer is a microwave radar (C-band) designed to measure return from the sea surface. The return varies with surface geometry which, in turn, is a function of surface wind velocity. Data used in this study are wind vectors determined from algorithms developed at the Jet Propulsion Laboratory in Pasadena.

Figure 1 shows data swaths available in our area of interest on 18 June 1993. Five hundred km wide swaths running from southeast to northwest are ascending, orbits of ERS-1. Each swath is separated by about 100 minutes and 2800km (progressively westward). Descending orbits (from northeast to southwest) pass over the same area of an ascending orbit about 11 hours later. Data are sampled within the swath at a 25km spacing although the true resolution of the instrument is nearer 50km.

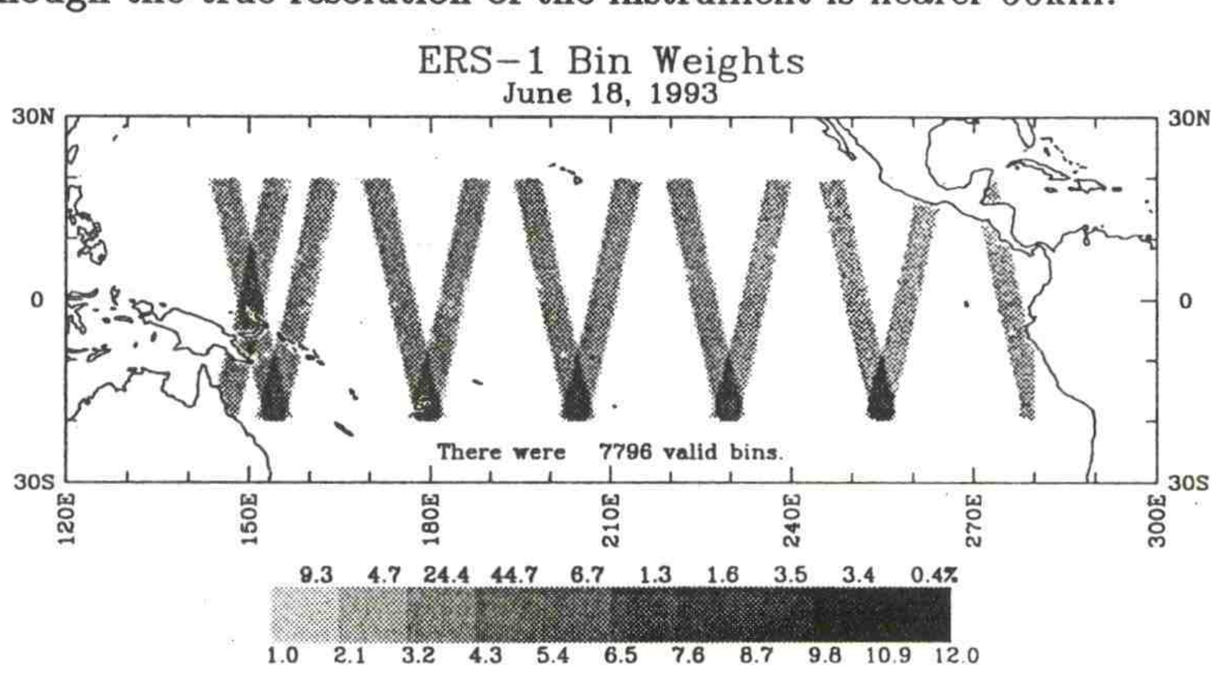

Figure 1. Number of observations (Bin Weights) in each 1/2 degree lat/lon square from ESR-1 on 18 June 1993.

2. COMPOSITING

Large-scale convective regions move from the Indian Ocean to the west Pacific on a fairly regular basis with a typical time scale near 45 days for a complete oscillation. They can easily be identified in time-longitude sections of satellite cloud measurements or in the upper tropospheric velocity potential (χ). We used the latter at 200hPa to identify the longitude of upper level divergence associated with the oscillation. Interested readers can see examples of the oscillation manifested in χ in the Climate Diagnostics Bulletin. Dates were subjectively selected when the eastward propagating minima in χ was at 0E, 45, 90, 135, 180, 135W, 90W, 45W. During the two-year period 65 total dates were selected. They were approximately distributed throughout the calendar year. Most of these 65 dates corresponded to χ minima at 90E(11), 135E(10), and 180E(11), where the oscillation is most frequently observed. The fewest dates (3) were recorded when the χ minima were at 45W.

The scatterometer winds were first binned into two-degree lat/lon squares. The binned winds were then averaged over five-days centered on the dates according to the longitude of the upper-level χ minima. Figure 2 shows the surface divergence determined from all the wind data regardless of longitude of the χ minima. The total number of days averaged is slightly less than 65*5 because of occasional overlaps in the five days centered on a selected date. Shaded areas in Fig. 2 represent regions of convergence. These regions compare well with known locations of the Intertropical and South-Pacific Convergence Zones. This comparison gives us confidence in the accuracy of the winds.

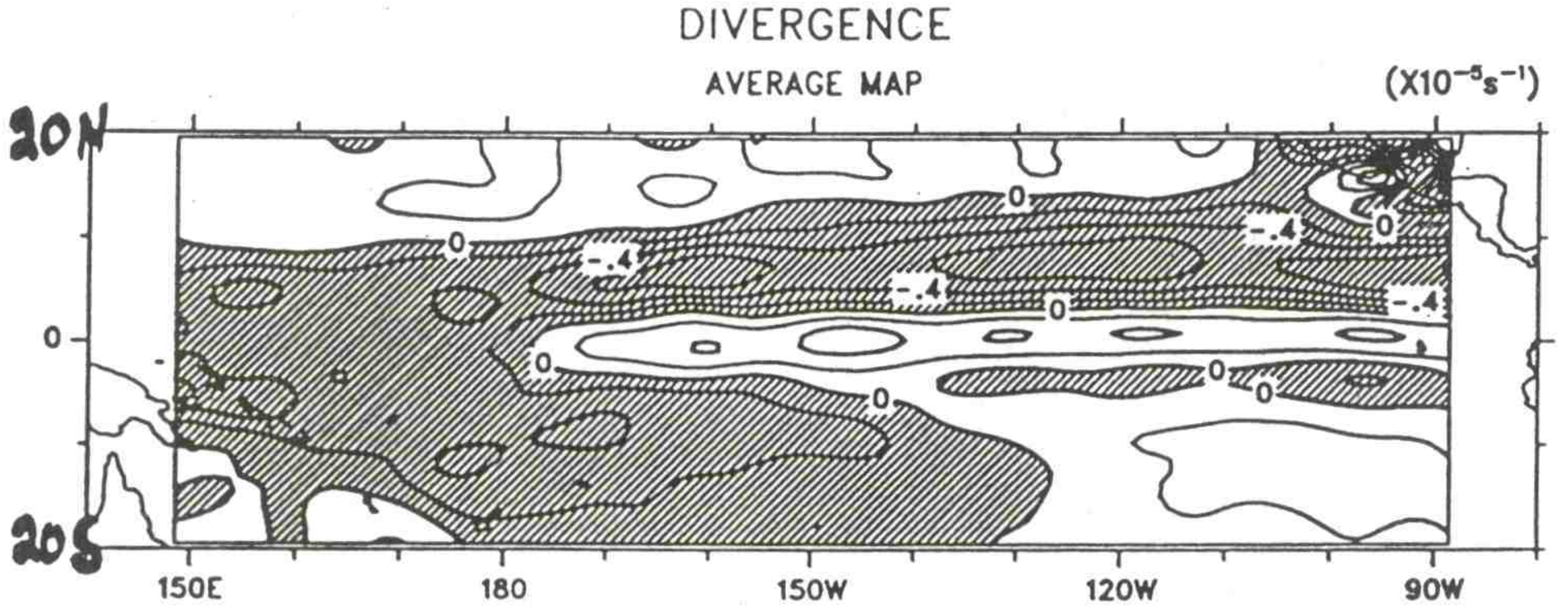

Figure 2. The divergence of the scatterometer determined winds averaged over all dates (shaded regions represent convergence) contour labels are in units of $10^{-5}s^{-1}$. Blank areas at the right and left of the figure result from a seven-point filter used to smooth data in the east-west direction.

3. SURFACE WIND STRESS VARIATIONS

Figure 3a shows the grand average wind vectors used in computing the divergence of Fig. 2. The contours in the figure represent the zonal wind stress on the atmosphere determined from the equation

$$\tau_x = -\rho C_D u|V|$$

The density, ρ was taken to be $1.2\frac{kg}{m^3}$; the drag coefficient C_d was 1.14×10^{-3} for winds less than 10m/s, and $(0.49+0.065 \times |V|) \times 10^{-3}$ for wind speeds over 10m/s (only one of our five-day averaged winds exceeded 10m/s); u is the zonal wind speed and $|V|$ is the total wind speed. Shaded regions in Fig. 3a represent westerly u-winds.

Figures 3b and 3c present the anomaly wind vectors (that is the difference from the grand average) for the time when the traveling χ minimum was at 90E and 135W (225E) respectively. There is a clear change from dominant easterlies and positive wind stress when the χ minimum, and presumably convection of the Intraseasonal Oscillation, are at 90E to the dominant westerly anomalies and negative wind stress when it is at 135W.

Figure 4 is presented to summarize the zonally averaged anomaly stress from 140E to 80W for each of the eight categories defined by the longitude of the eastward traveling χ minimum. The anomalies are mostly positive as the convection moves from the Indian Ocean to the central Pacific (45E, 90E, 135E, and 180E), and mostly negative during other times of the oscillation. Integrating these stresses over the entire area and multiplying by the moment arm gives the contribution to the anomalies in frictional torque on the atmosphere. They turn out to explain about one half of variations in total torque thought to be associated with the oscillation.

4. SUMMARY

The Scatterometer provides an excellent source of surface winds over the oceans. We hope to learn more about the surface wind variations associated with the Tropical Intraseasonal Oscillation from the scatterometer data. The current results focus on anomalies in wind stress. They reveal positive anomalies in equatorial easterlies, u-wind stress, and frictional torque as the traveling χ minimum moves from the Indian to Pacific Ocean.

Here we have included all data regardless of season in our composite anomalies. There are seasonal variations, and we hope to add more data to our base so that composites can be seasonally stratified. The outlook for this is good since ERS-1 scatterometer data are now available for 1994 and part of 1995. In addition the NASA designed NSCAT instrument is scheduled for launch in the summer of 1996.

3a

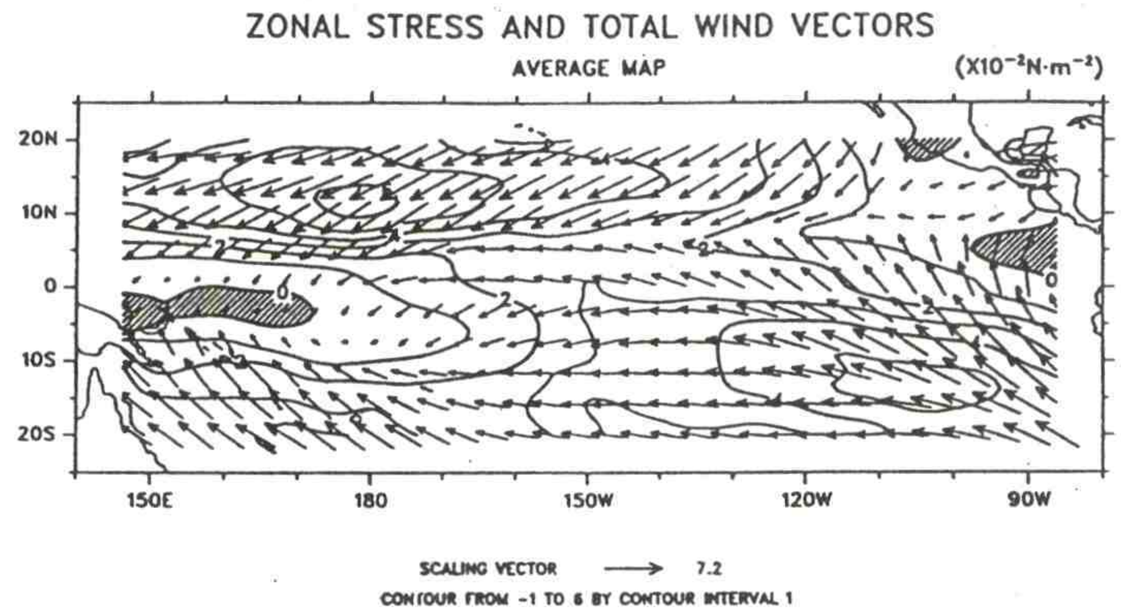

3b

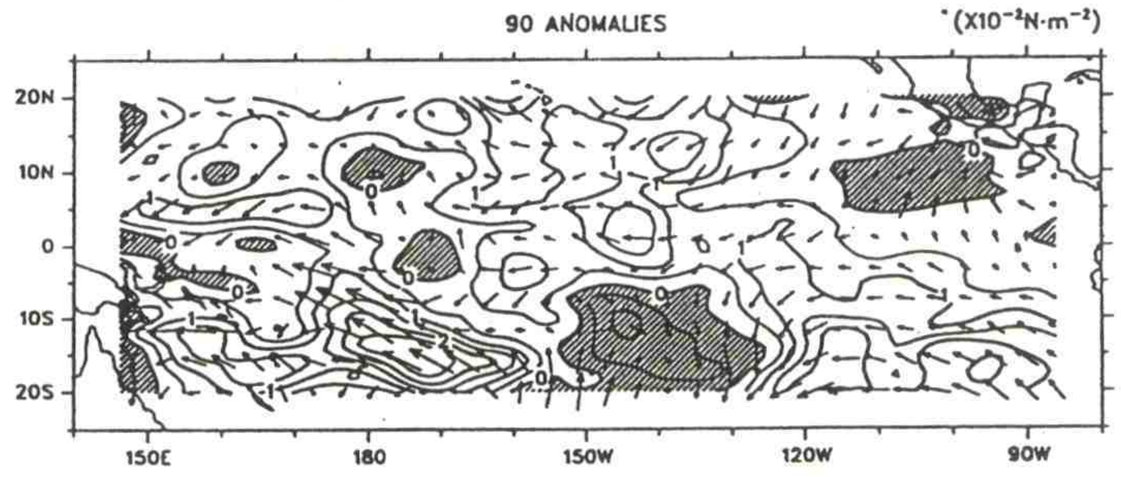

3c

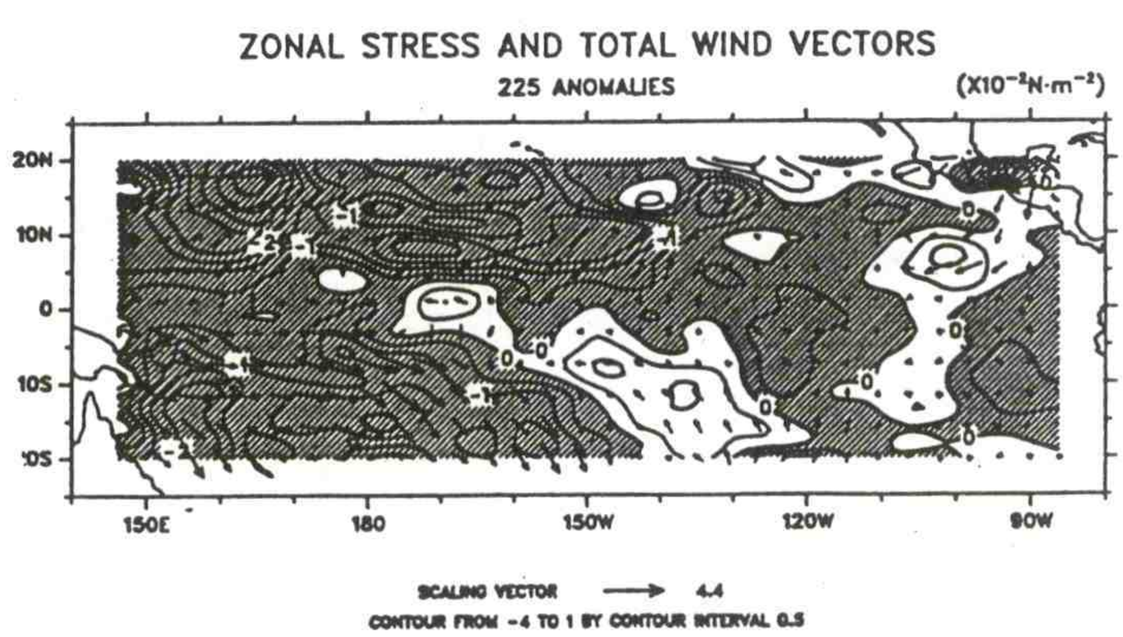

Figure 3. a) The wind vectors (m/s) averaged over all dates and contours of resulting u-wind stress. Shaded areas represent negative stress and westerly winds. b) Anomalies from a) when upper level χ minima were at 90E and c) 225E (135W).

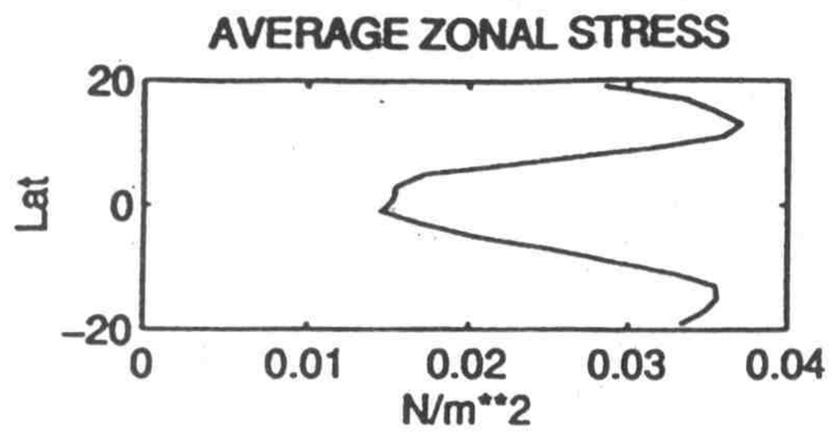

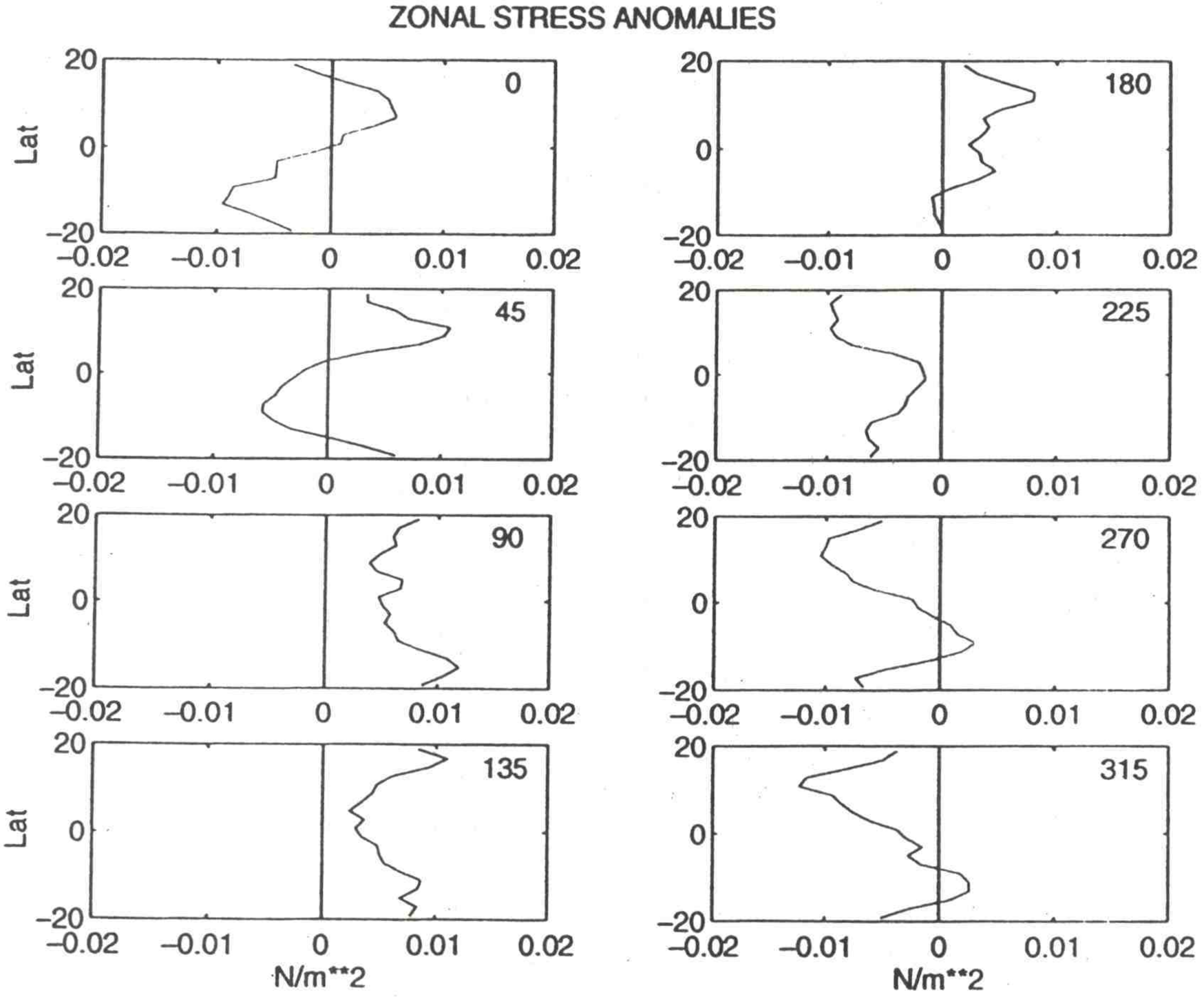

Figure 4. top) The zonally averaged (140E-80W) u-wind stress averaged over all dates. Other eight panels represent the anomalies from the top panel for dates when the χ minima were at the indicated (upper right of each panel) longitude (degrees east).

Angular momentum and energetics in reanalysis products

David A. Salstein and Richard D. Rosen
Atmospheric and Environmental Research, Inc., Cambridge, MA 02139

1. ***Introduction.*** Questions about climate variability demonstrate the need to reanalyze the historical state of the atmosphere using a modern analysis system applied to as consistent a set of observational data as possible. Two such reanalysis sets are now being prepared: one by NCEP/NCAR, eventually spanning several decades (Kalnay and Jenne 1991); and one using the NASA Goddard Earth Observing System Data Assimilation System (GEOS-1 DAS), being run for about a decade but developed with future inputs of space-based data in mind (Schubert et al. 1991).

The currently available pilot series from these reanalyses span more than five years. Here we examine the potential for these data to contribute to climate studies by considering aspects of the planetary budgets of atmospheric angular momentum and energetics.

2. ***Angular momentum diagnostics.*** Atmospheric angular momentum (AAM) about Earth's axis is a well-determined quantity, which has been shown to be remarkably consistent with measurements of the Earth's rotation rate in that its variations are proportional to those in the length of day (l.o.d.) on timescales between several days and years. In addition, AAM is being used as a verification tool for atmospheric models (Salstein and Rosen 1994) such as those contributing to the Atmospheric Model Intercomparison Project. Estimates of this quantity have been made from several weather centers (Salstein et al. 1993), and although values produced by different centers had moderate differences a decade or more ago, they are in better agreement today. New estimates of AAM based on reanalyses have the potential to reduce the errors that existed in earlier years.

The difference between AAM and equivalent values of l.o.d. for individual years is typically smaller when the AAM value is based on NCEP/NCAR reanalysis than when it is derived from operational analyses. Indeed, a seven-year set (1985-91) of values shows the reduction in rms to be about 30%; this result (Fig. 1) was determined using the full vertical extent of the analysis domains and after removing a low-order signal not related to atmosphere-solid Earth momentum exchange.

The differences in AAM between reanalyses and operational analyses appear to derive from zonal winds in the tropics and southern hemisphere mid to high latitudes. Reanalysis appears to have stronger easterly momentum than do operational values, in general. Interestingly also, reanalysis-based AAM values are temporally smoother than their operational counterparts, as a spectral analysis of such values over the five years demonstrates (Fig. 2).

An advantage of reanalysis data derives from the inclusion of higher levels than was the case heretofore. Use of such levels is typically required for momentum balances on seasonal scales (Rosen and Salstein 1991). For example, the semiannual amplitude in l.o.d. of 0.173 milliseconds during 1985-91 is not matched by the troposphere alone (amplitude equivalent to 0.116 ms), but including of the stratosphere up to the 20 millibar level reduces the difference with the l.o.d.-derived value by about one half (amplitude equivalent to 0.144 ms).

Values of AAM, when distributed into zonal belts, can be used to study the structure of climate anomalies. The GEOS-1 system, for example, shows the 1987 El Niño maximum and 1988 La Niña minimum in the subtropics, each signal with a precursor near the equator one year earlier.

Such a result, first noted by Dickey et al. (1991), may eventually be generalized over many decades with the reanalysis-based values.

NCEP/NCAR and NASA GEOS-1-based values of AAM are in rather close agreement with each other, with the two sets showing a strong coherence on intraseasonal time scales that remains statistically significant down to about three days (Fig. 3). From this result, we may infer that the reanalysis sets have consistent zonal wind fields.

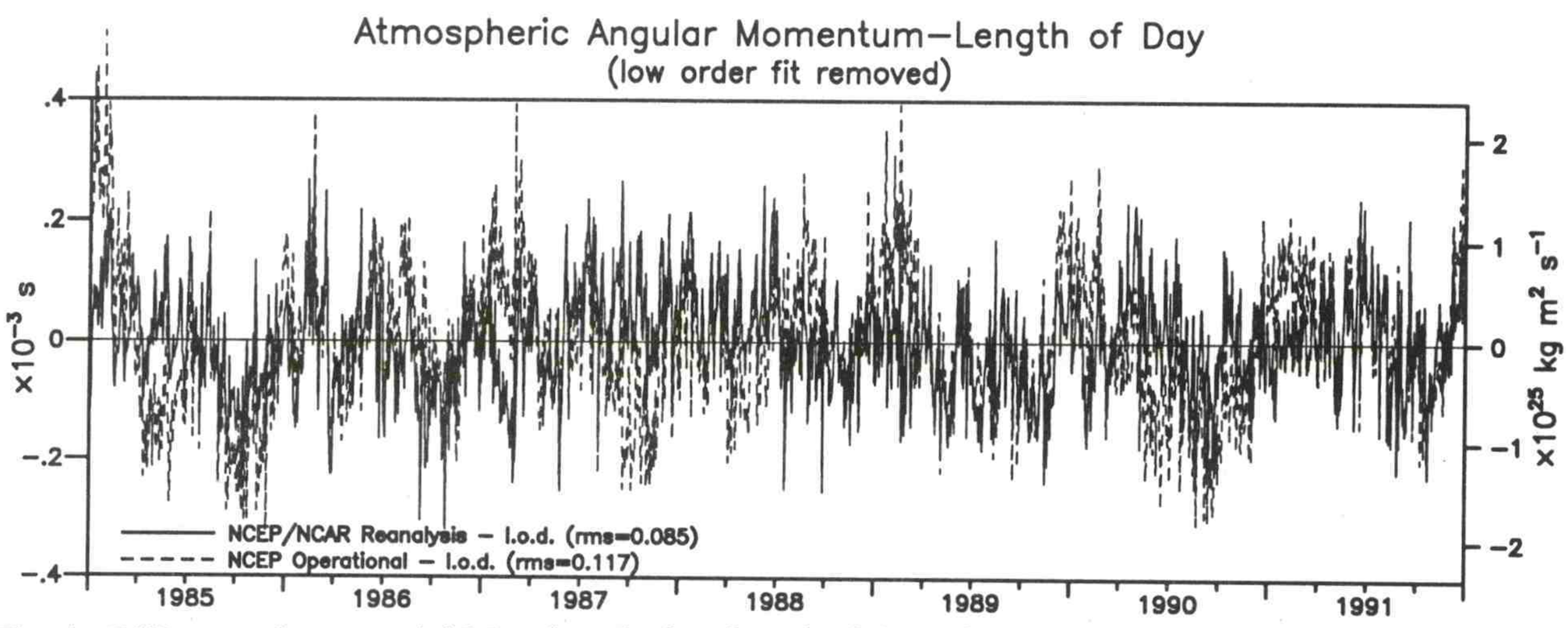

Fig. 1. Difference between AAM and equivalent length of day values, given in two proportional scales, l.o.d. on left and AAM on right. AAM is derived from NCEP/NCAR reanalyses and NCEP operational analyses. A low-order fit, representing non-atmospheric effects, is removed from the difference series.

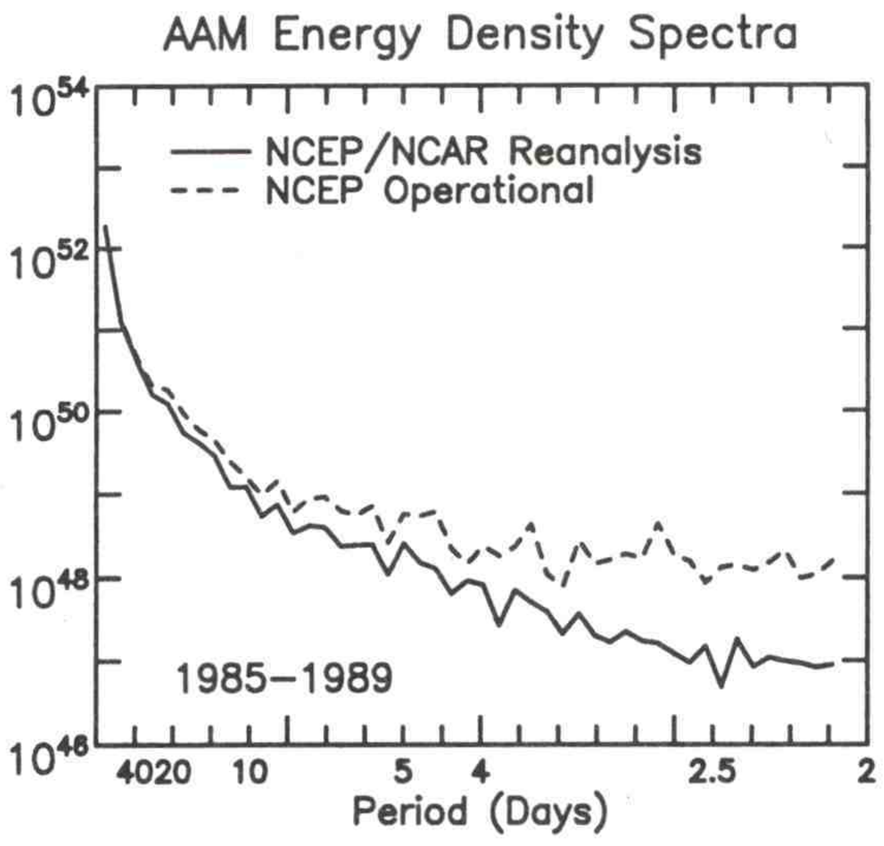

Fig. 2. Energy density spectra of AAM from NCEP/NCAR reanalyses and NCEP operational analyses for 1985-1989, based on once-daily values. Units are (kg m^2 s^{-1})^2 x day.

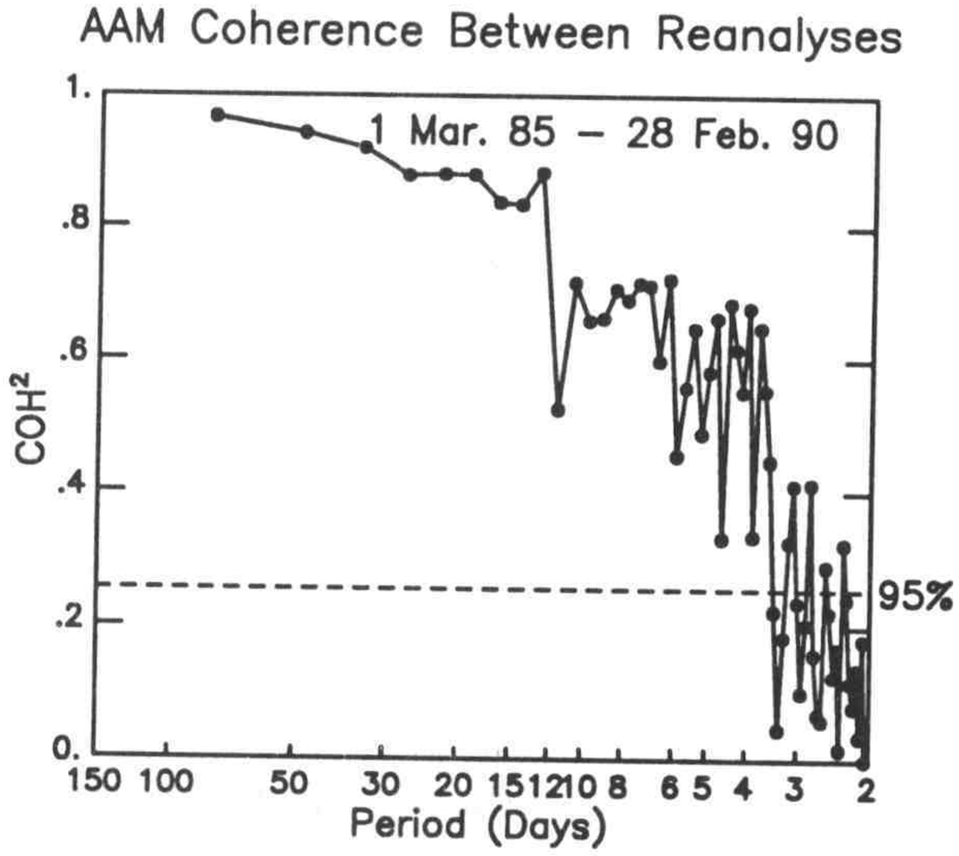

Fig. 3. Square of coherence between AAM values (to 20 millibars) from the NCEP/NCAR and NASA GEOS-1 DAS reanalyses over five years,and an estimate of the 95% level of significance.

3. ***Energy diagnostics***. The atmosphere may be considered as a heat engine in which potential energy is converted into kinetic energy (Peixoto and Oort 1992). Moreover, these energy forms may be partitioned into their zonal mean and eddy components, with conversions taking place between such components by actions of meridional eddy transports. Potential energy is generated through differential heating of the atmosphere through diabatic processes; the generation of its zonal mean form, for example, requires a positive correlation of heating rate and temperature across the (hemispheric or global) domain. The diabatic processes involved are those of sensible, latent, longwave radiational, and shortwave radiational heating.

Signals in the strength of atmospheric energy forms, conversions, and generation can be indicative of important interannual variations. We used the first five years of the NASA GEOS-1 analysis to analyze atmospheric energetics in monthly periods. Potential and kinetic energy contents of each hemisphere display strong annual signals, with all zonal mean and eddy components strongest during a hemisphere's winter. Furthermore, the northern hemisphere signal dominates the seasonal signal. When the mean seasonal cycle is removed, the transition from 1987 El Niño maximum to 1988/1989 La Niña minimum is clearly visible in the energy signals in both hemispheres (Fig. 4). The time series of zonal mean available potential energy generation displays a signal in which the portion associated with latent heat explains much of the character of total energy generation (Salstein and Sud 1994). Moreover, interannual signals in anomaly generation terms also indicate an impact of the ENSO cycle.

We have also made a preliminary estimate of the differences in the energetics between the NCEP/NCAR and GEOS-1 DAS reanalyses during the 1987-1988 period, which are relatively small (only 5% or less of the typical values). Some of the larger differences are in the zonal mean available potential energy in the southern hemisphere and eddy kinetic energy in both hemispheres, in which the NCEP/NCAR values tend to be less than those of GEOS-1 DAS. After examining zonal-mean zonal wind values, we find, for March 1988, the month with the largest difference in mean kinetic energy, that such a difference is related to the strength and position of the jets, which tend to be stronger and placed more equatorward in the NCEP/NCAR analysis. As for eddy kinetic energy, the two-year mean conditions show that the zonal mean variance in the winds in NCEP/NCAR is less than that of GEOS-1 throughout much of the globe, but in particular in the southern hemisphere jet, which is centered near 50S and 250 millibars (Fig. 5).

4. ***Acknowledgments***. Support for this study came from NOAA Climate and Global Change Program grant NA46GP0212, and from NASA EOS Program grant NAGW-2615 and Global Modeling and Analysis Program contract NAS5-32861.

5. References

Dickey, J. O., S. L. Marcus, and R. Hide, 1992: Global propagation of interannual fluctuations in atmospheric angular momentum. *Nature*, **357**, 484-488.

Kalnay, E. and R. Jenne, Summary of the NMC/NCAR reanalysis workshop of April 1991. *Bull. Amer. Metoeorol. Soc.*, **72**, 1897-1904.

Peixoto, J.P., and A.H. Oort, 1992: *Physics of Climate*, Amer. Inst. Phys., New York, 520 pp.

Rosen, R.D., and D.A. Salstein, 1991: Comment on "A seasonal budget of the Earth's axial angular momentum" by Naito and Kikuchi. *Geophys. Res. Lett.*, 18, 1925-1926

Salstein, D.A., D.M. Kann, A.J. Miller, and R.D. Rosen, 1993: The Sub-bureau for Atmospheric Angular Momentum of the International Earth Rotation Service: A meteorological data center with geodetic applications. *Bull. Amer. Meteorol. Soc.*, **74**, 67-80.

Salstein, D.A., and R.D. Rosen, 1994: Validation of model-based and analyzed momentum and moisture diagnostics. *Proc. 19th NOAA Climate Diagnostics Workshop,* College Park, MD.

Salstein,D.A., and Y. Sud.1994: Large-scale diabatic heating in a model with downdrafts. *Proc. 10th Conf. on Numerical Weather Prediction*, Amer. Meteror. Soc., 72-74.

Schubert, S. D., R.B. Rood, and J. Pfaendtner, 1993: An assimilated dataset for Earth science applications. *Bull. Amer. Meteorol. Soc.*, **74**, 2331-2342.

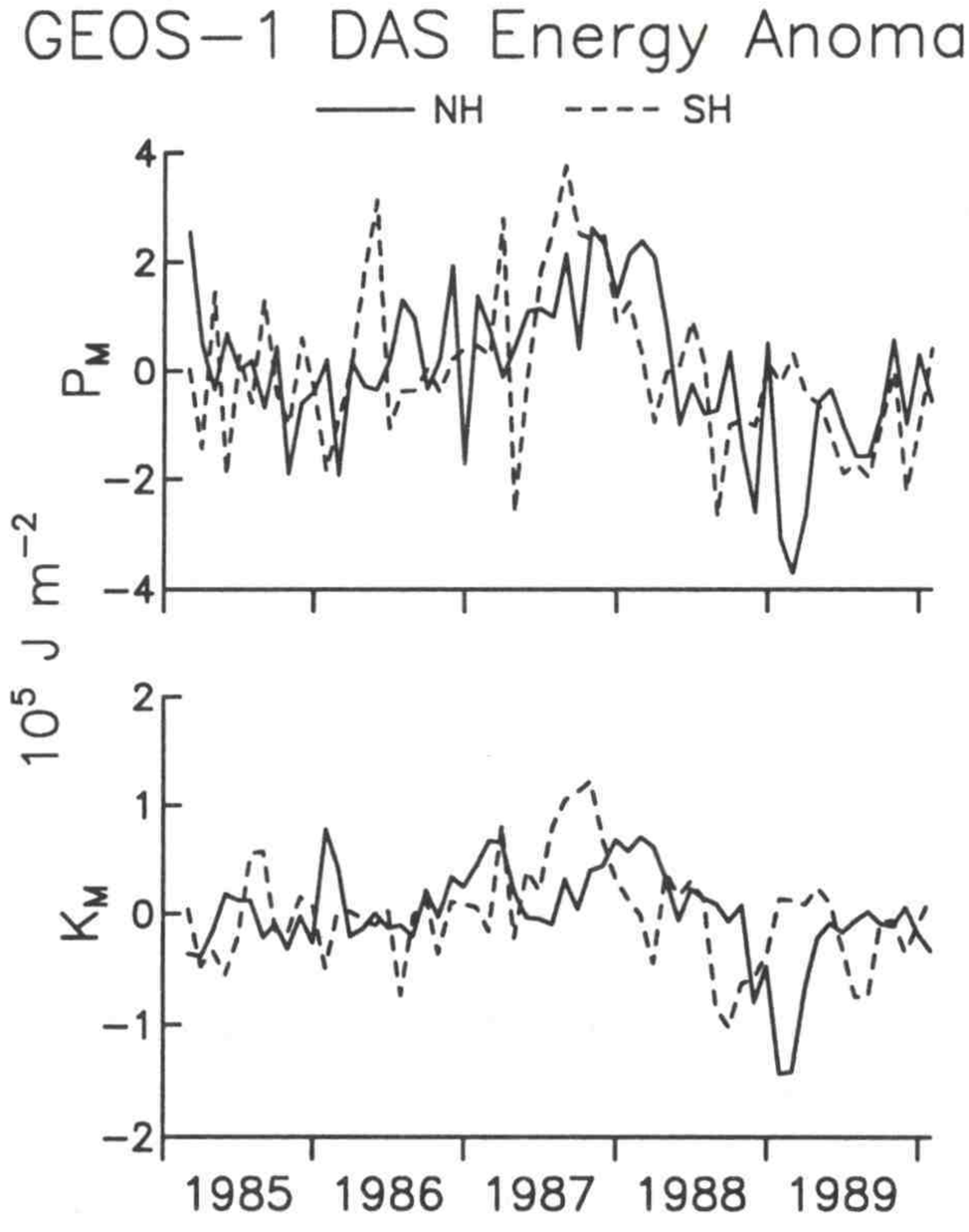

Fig. 4. Hemispheric anomaly values from five-year calendar-monthly means for zonal mean potential and zonal mean kinetic energies, based on the NASA GEOS-1 DAS system.

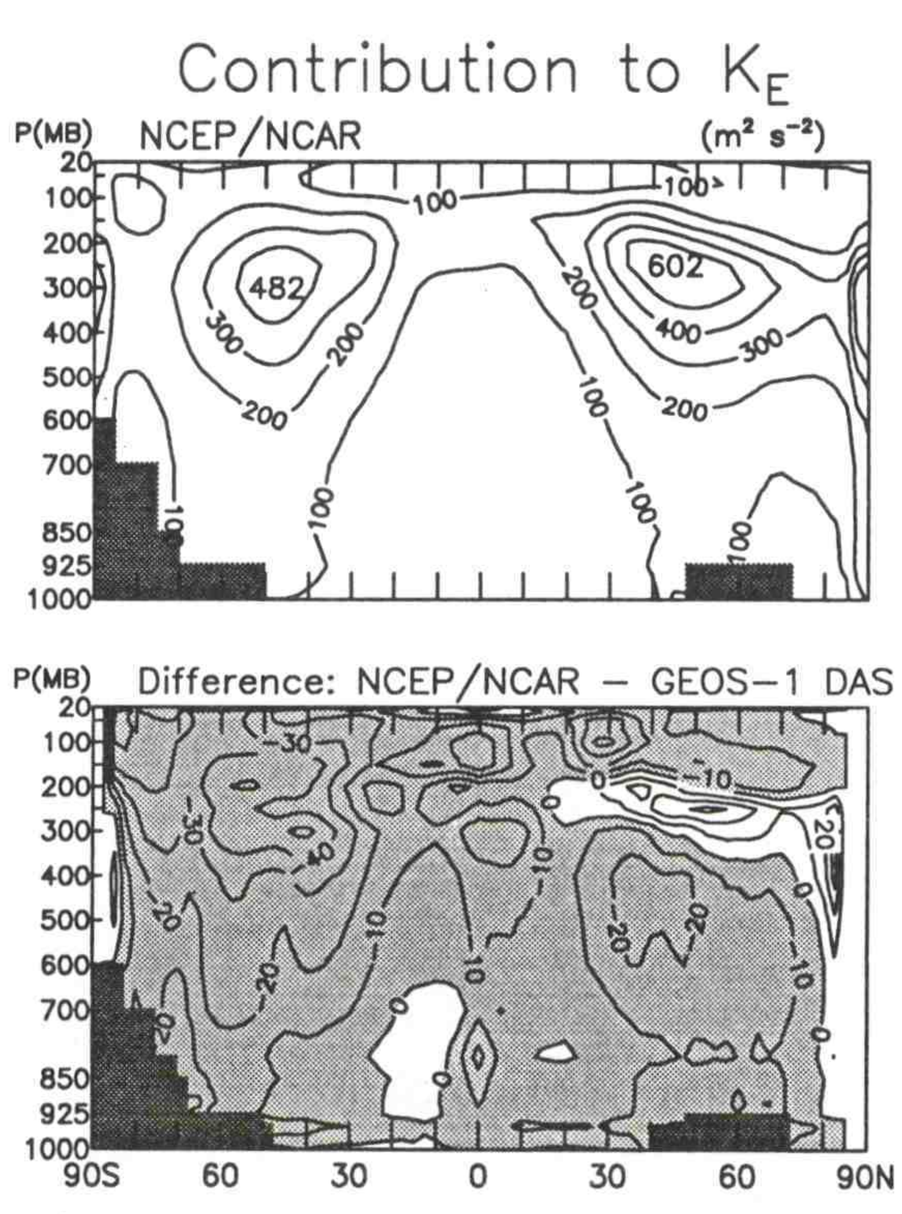

Fig. 5. Pressure-latitude distribution, 1987/88 of the mean square transient and standing eddy wind components from one reanalysis and from the difference between two reanalyses. Values are proportional to eddy kinetic energy. Light and dark shading represent negative values and high topography regions respectively.

Detecting Greenhouse Climate Change During the 20th Century

D.M.H. Sexton, D.J. Karoly, C.K. Folland, J.F.B. Mitchell and D.P. Rowell
Hadley Centre for Climate Prediction and Research
Meteorological Office
Bracknell, U.K.

Three ensembles of extended simulations with the Hadley Centre atmospheric general circulation model (HADAM2a) have been carried out for the period 1948-1994 with different specified forcing factor distributions. These simulations are being used to understand the role of different processes in determining the observed climate variations during the second half of the twentieth century. All of the ensembles involve four independent runs of the model with different initial atmosphere conditions. They have been forced with a common specified global observed monthly sea ice and sea surface temperature distributions (GISST1.1). The first ensemble has fixed CO_2 concentrations at 321 ppmv. The second ensemble starts in October 1903 and runs until December 1994 with best-estimate increasing equivalent CO_2 concentrations, starting from observed 1903 CO_2 ppmv (IPCC, 1990). The third ensemble has the same CO_2 forcing as the second ensemble, but also includes a simple representation of the direct radiative effects of increasing anthropogenic sulphate aerosols. This is achieved by increasing the surface albedo over time in regions with high sulphate aerosol emissions in the way carried out by Mitchell *et al* (1995, Nature vol.376, p501-504).

We are using these simulations to try to identify climate signals associated with SST alone and the additional direct radiative effects of anthropogenic forcing. Variations between runs within an ensemble provide an estimate of the internal climate variability. Here, we concentrate on temperature variations at the surface and in the upper air.

A first view of the relative effects of the different forcings and internal variability on the simulated climate can be seen in timeseries of area-averaged temperatures from different model levels (as shown in Figure 1a). We first consider surface temperatures averaged over land only, as the additional influences of CO_2 forcing etc. should be clearly visible. The data have been low-pass filtered to emphasise variations on decadal and longer timescales, such as might be expected from the effects of slowly-increasing CO_2 and sulphate aerosols. Fig. 1a shows a clear separation between the ensemble of runs with fixed $CO_2$and the ensembles with increasing CO_2, which show greater warming. However, Fig. 1a shows that the model's simulated warming trend over the period 1949-94 due to increasing SST and increasing CO_2 of about 0.4°C is slightly less than the observed warming, and the warming when both increasing CO_2 and sulphate aerosols are included is reduced to about 0.35°C, but still larger than the warming (0.2°C) due to SST effects alone.

Fig. 1a. Land Surface Temperature anomalies (wrt 1950–59)
Filtered annual mean over land.

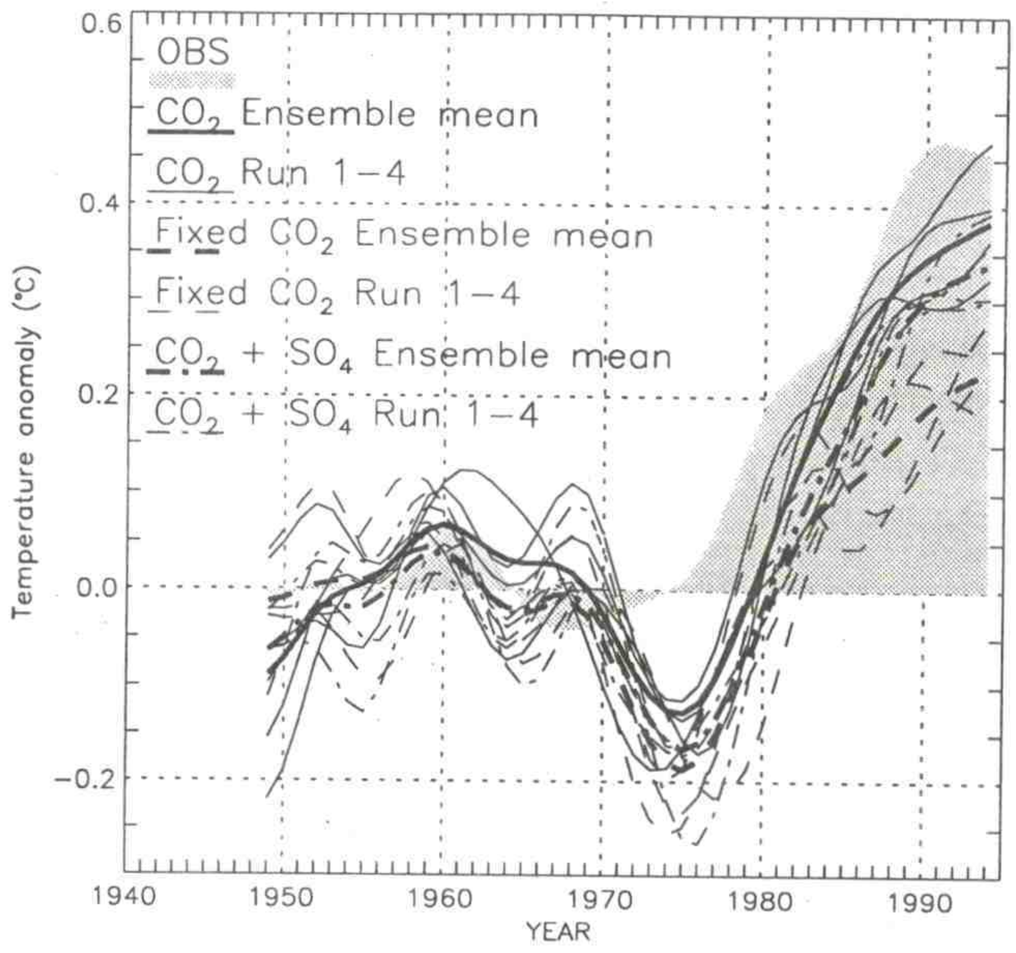

Fig. 1b. 50hPa Temperature anomalies (wrt 1963–72)
Low pass filtered Annual Ensemble mean over globe.

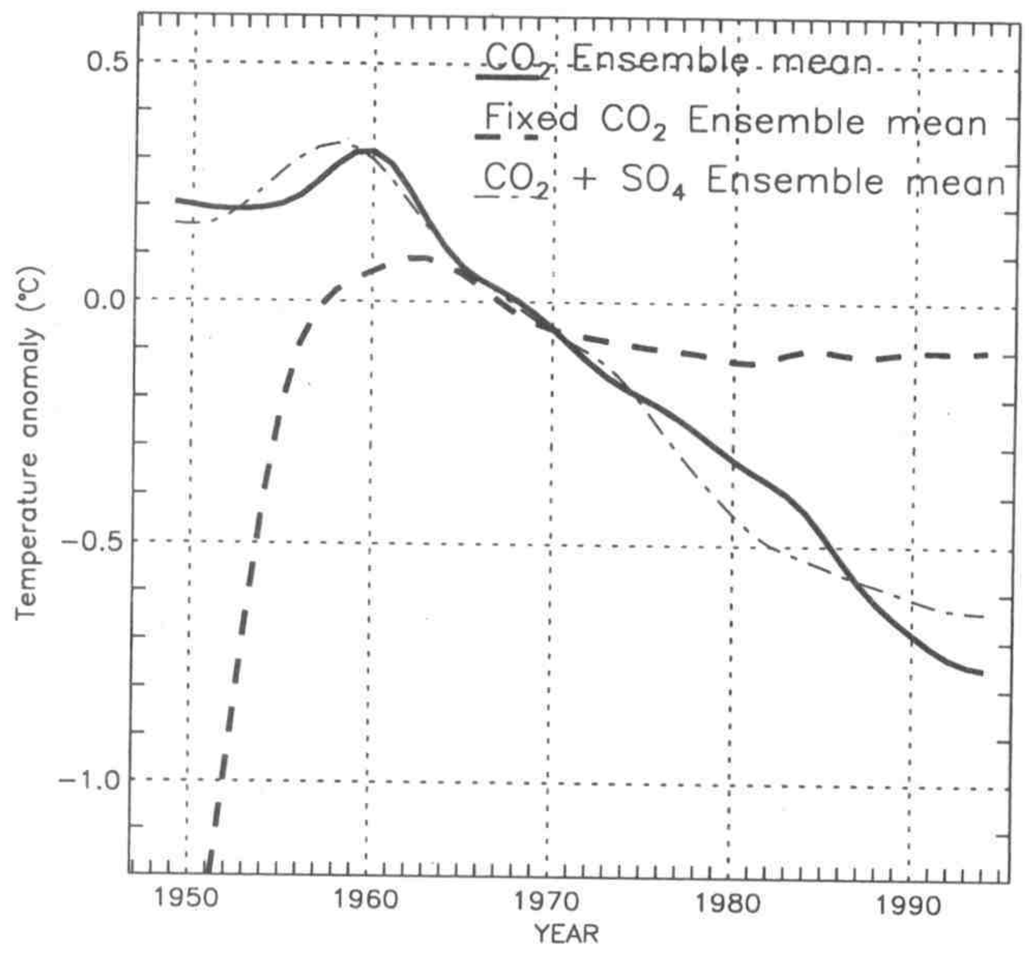

To identify the spatial structure of the changes in the mean fields due to the different forcings, maps of the differences of near surface air temperature between the last decade (1984-93) and the first decade (1950-59) of the simulations are compared (not shown). Differences between the ensembles which are large relative to the internal variability are considered to be significant. Over the oceans, the decadal differences of surface air temperature are very similar, showing the expected dominant effect of SST forcing. There is a significantly greater warming (up to 0.5°C) over north Eurasia and eastern North America due to CO_2. The observed anomalies are around 1.5°C in these same two regions, a major reason for the underestimation of the warming of land surface temperature when compared with the observed trend. This is partly attributed to the model not reproducing a strong enough westerly winter circulation over the North Atlantic and Eurasia that has been observed since the mid-'70s, but may also be due to the incorrect representation of feedback processes in the model. The addition of sulphate aerosols produces significant additional cooling over the Middle East and China.

For upper air temperatures, first global mean temperatures are considered (averaged over land and sea points). In the troposphere, the interannual variations of simulated global mean temperature are almost identical between the three ensembles, showing the dominant effect of the SST forcing. In the lower stratosphere however (Fig. 1b), there are large differences between the ensembles, which show the effects of the increasing CO_2. For the fixed CO_2 ensemble, there is a rapid increase in lower stratospheric temperature in the first few years following a model adjustment to the initial conditions. This involves a loss of water vapour from the model stratosphere, leading to an essentially dry stratosphere for the remainder of each run. Water vapour is an efficient long-wave radiative emitter to space in the stratosphere so the loss of water vapour leads to increasing stratospheric temperatures. For the runs with increasing CO_2, there is a steady

cooling of stratospheric temperatures, as CO_2 is also an efficient long-wave radiative emitter to space. Even without low-pass filtering, the stratospheric cooling trend in the ensembles with increasing CO_2 is larger than the interannual variations in any of the ensembles or the differences between individual runs in any one ensemble. This cooling trend in the lower stratosphere due to increasing CO_2 can be regarded as part of a fingerprint of greenhouse climate change for detecting the greenhouse effect in observations.

Hence, there has been a warming in the troposphere and a cooling in the stratosphere over the last thirty years. This can be seen in the observed decadal difference of zonal mean upper air temperatures in Fig. 2a. Fig 2b-d also show warming in the troposphere, mainly in the tropics and Southern Hemisphere, in all three experiments, showing the dominant effect that SST forcing has on the zonally-averaged temperature in the troposphere. However, a pronounced cooling in the lower stratosphere at all latitudes is only seen when increasing CO_2 is included, although not to the extent observed. This is due to inhomogeneities in the observed data and the fact that there is no depletion of stratospheric ozone in the model. The modelled warming at the tropopause is due to an error in the numerical scheme, whereby moisture is transported poleward at the tropopause, leading to an erroneous temperature response at that level.

To provide a quantitative measure of the similarity between the simulated patterns of decadal temperature change with different forcings and the observed temperature changes, we use the centred pattern correlation between the modelled and observed decadal mean temperature changes from some reference period. The pattern correlations have been calculated from the ensemble means of the simulations, as well as from the individual runs.

Fig. 3 shows centred correlations for modelled and observed zonal mean upper air temperatures sampled every 5° of latitude, over the period 1963-1988. Even without changing CO_2 forcing, the correlations are significant relative to zero change owing to the similarity between the modelled and observed patterns of change in the troposphere due to SST forcing, despite the unrealistic warming at 100mb in the model. When CO_2 forcing is included, the correlations increase with the additional cooling in the model stratosphere while the tropospheric pattern stays much the same. Therefore, we have detected a significant change in the climate but in order to attribute this climate change to increasing CO_2, we would have to demonstrate that the difference between the pattern correlations of the fixed CO_2 and transient CO_2 experiments is significant. Future work will use Monte Carlo methods to determine the significance levels of the difference between the pattern correlations and EOF techniques to analyse these signals in more detail.

Fig. 2a. Oort Data.Zonal mean temperature
Annual 1978–87 minus 1963–72.

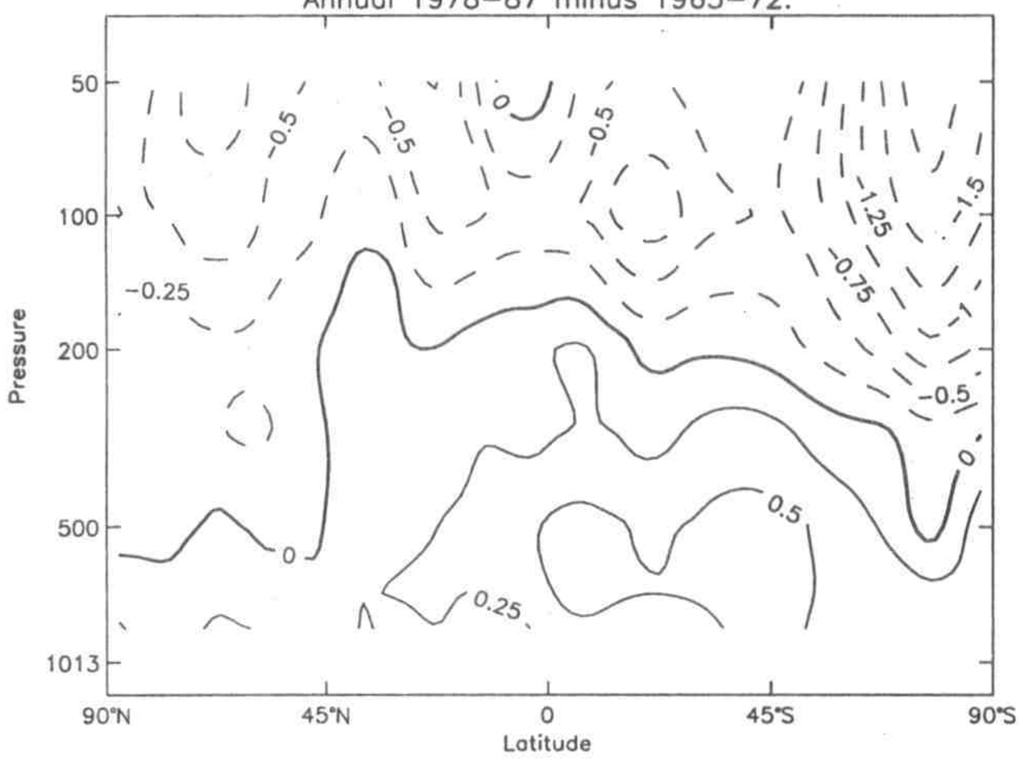

Fig. 2b. Fixed CO2. Zonal mean temperature
Annual 1978–87 minus 1963–72.

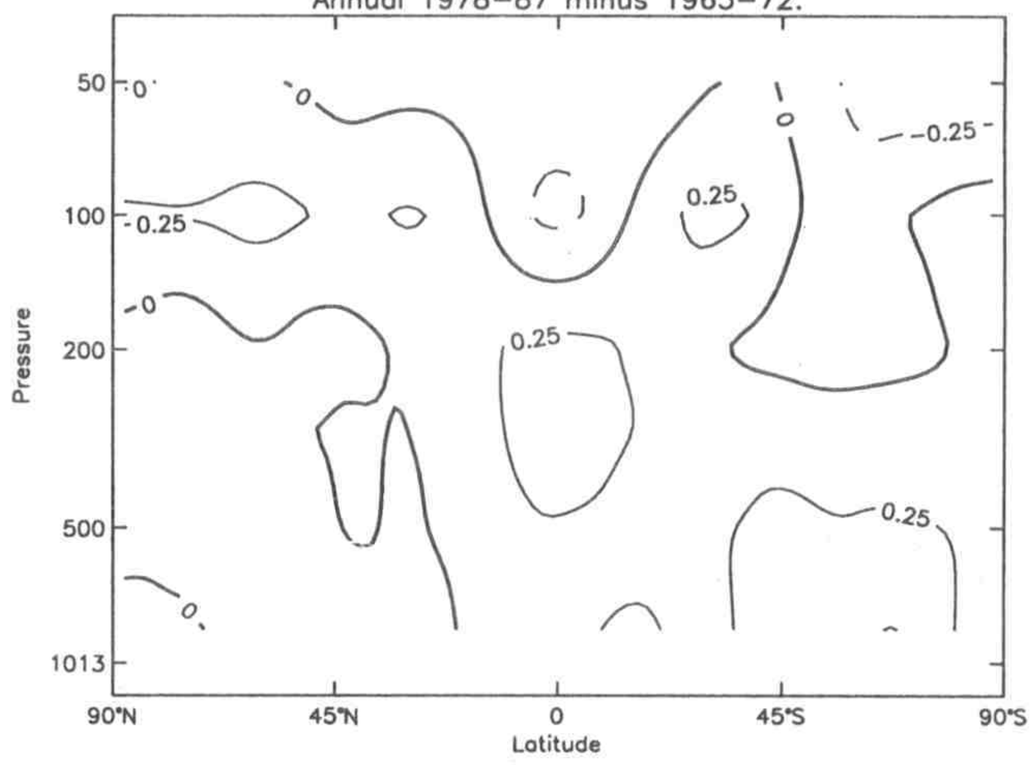

Fig. 2c. Changing CO2. Zonal mean temperature
Annual 1978–87 minus 1963–72.

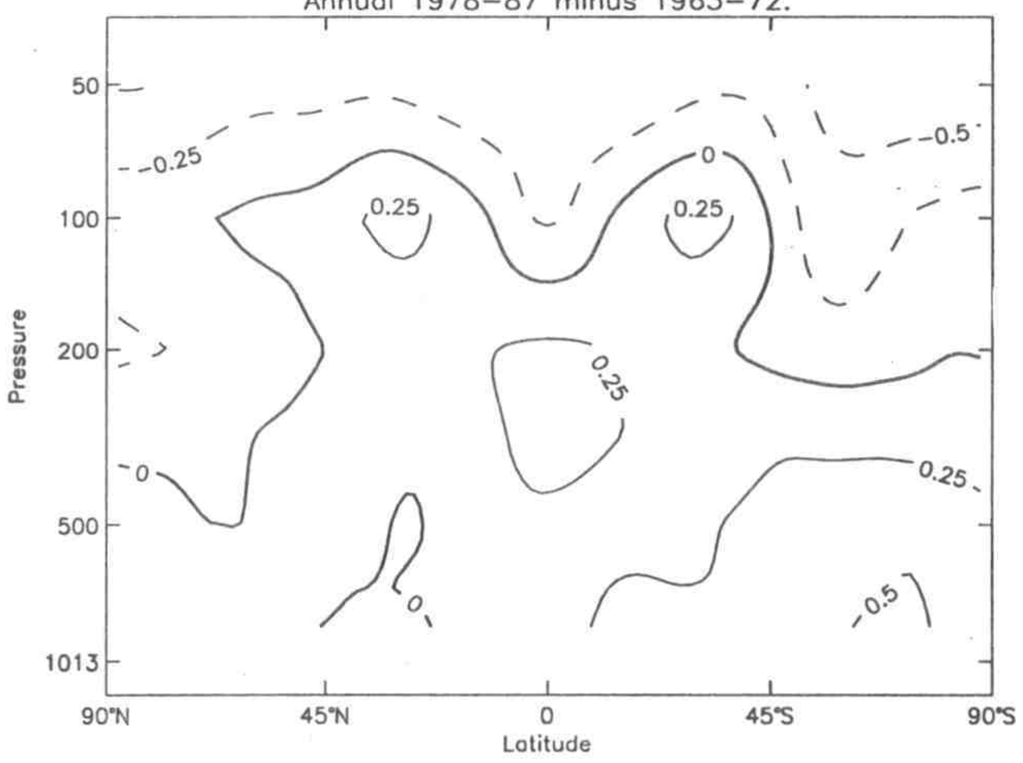

Fig. 2d. Changing CO2+SO4. Zonal mean temperature
Annual 1978–87 minus 1963–72.

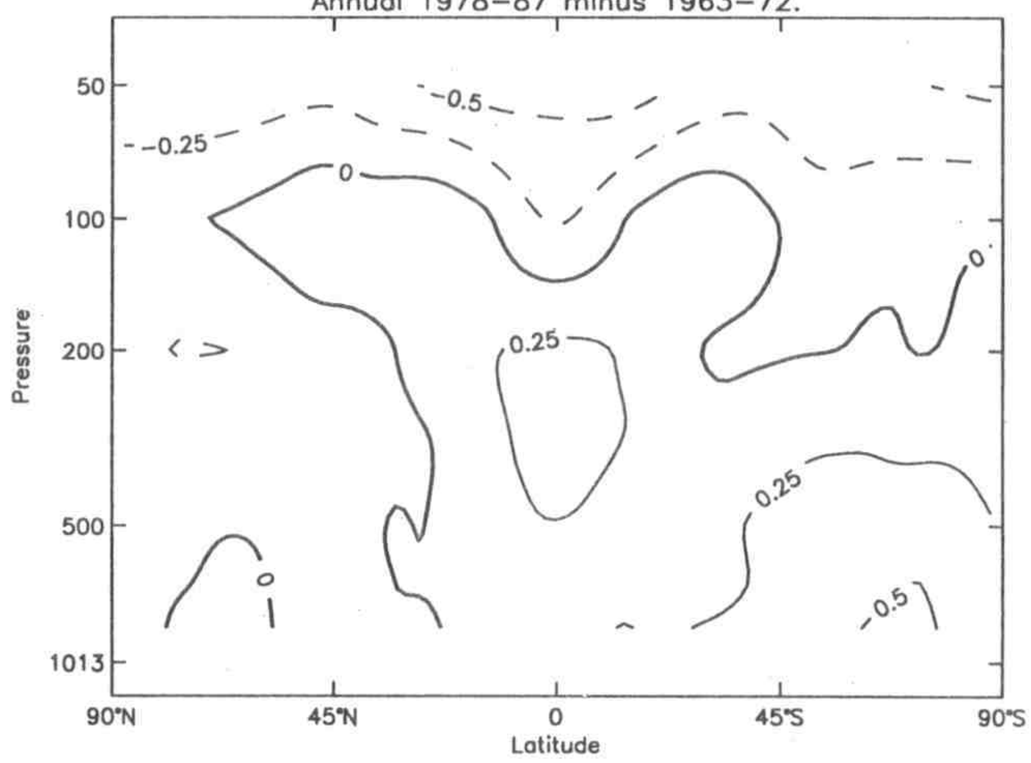

Fig. 3.

2. Decadal difference of zonal mean cross–section of upper air temperature wrt 1963–72 for observed and model data.

3. Pattern Correlation of Decadal Differences wrt 1963–72. Observed versus Modelled Zonal–Mean Cross–sections of temperatures.
(Thin lines=examples of individual members.)

NOAA's MSU Time Series for Detecting Climate Change

Mitchell D. Goldberg and David S. Crosby
NOAA/NESDIS/Satellite Research Laboratory
Camp Springs, MD

Wenchi Chung
SMSRC
Bowie, MD

1. INTRODUCTION

The measurements from the Microwave Sounding Unit (MSU), on board NOAA's operational polar orbiting satellites, have gained recognition during the past few years as a measure of deep layer mean temperature for long term monitoring of climate change (Spencer and Christy (1992a, 1992b, 1993), Spencer, et al. (1990)). The MSU has 4 channels measuring outgoing radiation at 50.31, 53.73, 54.96 and 57.95 GHz. Channel 1 (50.31 GHz) has a large surface component and is generally not used for deriving temperature due to uncertainty in the surface emissivity. The first MSU was launched in 1979 and to date its replacements have provided nearly complete daily coverage of the earth by scanning across the orbital track at +/- 47.35 degrees about nadir at approximately 9.47 degree increments. The MSU's 6 view angles results in the projection on the earth of 11 fields of view (FOV) for each scanline. The weighting functions for channels 2 through 4 at each of the 6 view angles are given in Fig. 1. The highest peaking group of weighting functions is for MSU channel 4, followed by MSU channels 3 and 2. The higher peaking weighting functions in each channel grouping are associated with larger off-nadir angles. Because radiance in the 50 - 60 GHz spectral region is extremely linear with temperature, the observations can be interpreted as deep layer mean temperatures for the layer defined by the weighting function. This is not true for infrared spectral region, where the relationship between temperature and radiance can be very nonlinear. Microwave observations are usually expressed in units of temperature (brightness temperature), which can be obtained from radiance using the inverse form of the Planck function.

A deep layer mean temperature from a single microwave observation has the equivalent vertical resolution of the channel. Improved vertical resolution can be obtained by combining different channels. NOAA has developed its own algorithm for deriving MSU deep layer mean temperatures (Goldberg and Fleming, 1995). The algorithm has been used to generate time series of MSU deep layer mean temperatures associated with the 7 averaging kernels given in Fig. 2. Briefly, the algorithm determines the coefficients needed to combine a set of weighting functions in order to best fit a specified averaging kernel. The best fit averaging kernels in Fig. 2. were constrained to look like Gaussian functions. The Goldberg and Fleming paper provides in great detail the mathematical development and application for deriving these averaging kernels. The purpose of this paper is to show some preliminary results and to advertise the availability of the data for climate studies.

2. DATASET AVAILABILITY

NOAA's MSU time series are available for NOAA-10 and NOAA-12. NOAA-12 is adjusted to "look like" NOAA-10. The NOAA-10 data period is from 12/86 - 08/91, whereas the period for NOAA-12 is 6/91 - present. The NOAA-10 and -12 overlap period of three months (6/91 - 8/91) was used to derive a look-up table for adjusting each observation and product from NOAA-12 to look like NOAA-10.

An example of a time series for +/- 10 degrees latitude is shown in Fig 3. The

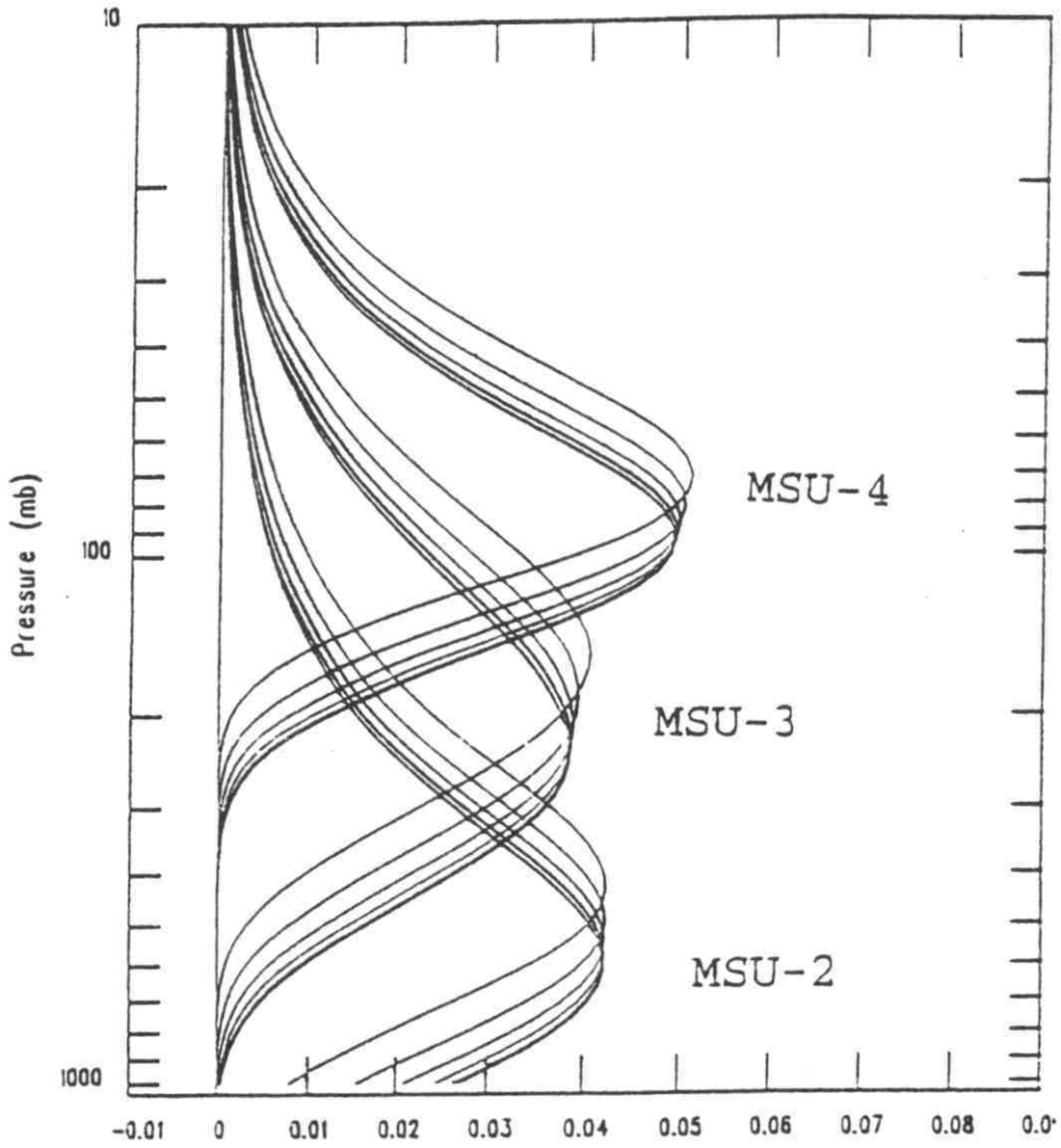

Fig. 1 MSU channels 2, 3 & 4 weighting functions.

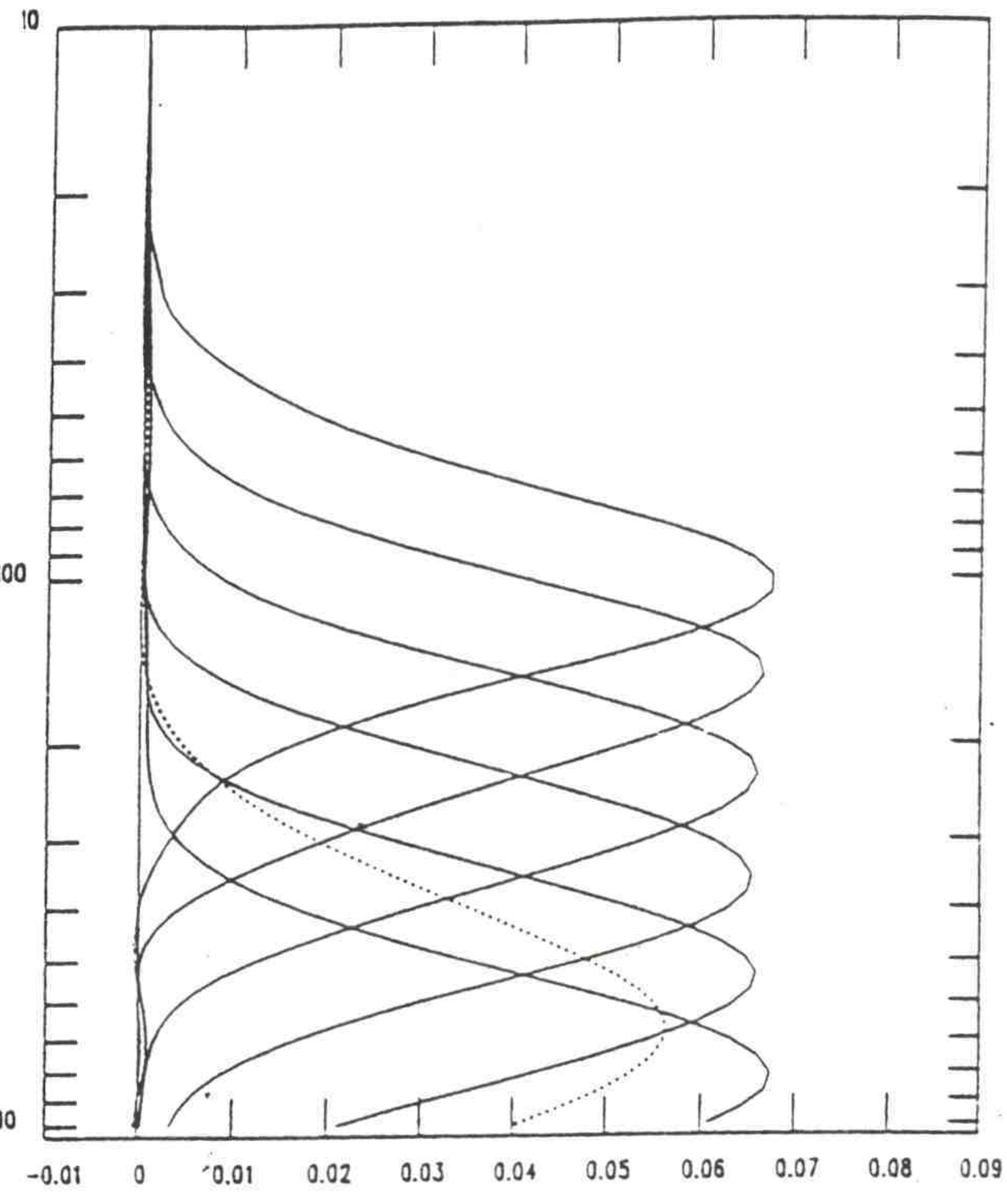

Fig. 2 NOAA's MSU averaging kernels.

first 7 time series are associated with averaging kernels in the upper right of the figure. The dashed averaging kernel is for the 7th time series. The peak of each is given in the time series heading. In addition to the 7 deep layer mean temperatures, time series are also given for MSU channels 2, 3 and 4 (the weighting functions are in the upper left). The additional NOAA layers have been found to be quite useful. For example in the La Nina period of early 1989, it can be observed that maximum cooling occurs at about 225 mb. This is undetectable in the current Spencer and Christy time series, which consists of two layers (MSU channel 4 and MSU-2R, which looks like SDLMT-6).

3. VALIDATION

The NOAA MSU products have been validated with radiosonde data. The NOAA-10 derived products were collocated to radiosonde reports with a time and space window of 2 hours and 150 km. The radiosonde (raob) temperature profiles were weighted by the deep layer mean temperature averaging kernels to yield raob calculated deep layer mean temperatures. Time series for each season from the fall of 1987 to summer of 1991 were derived for the raob computed and the actual MSU deep layer mean temperatures. The correlation between the two time series was found to be quite high at .98 with a standard error of the anomalies of .11 K. The other layers have similar standard errors with the exception of the layer centered about 800 mb. The error for the 800 mb layer was 0.25 K, which can be attributed to the lack of ground truth skin temperature; instead the first significant level temperature was used.

NESDIS/ORA/Satellite Research Laboratory (SRL)

NOAA-10/12 MSU PATH-C2 TIME SERIES

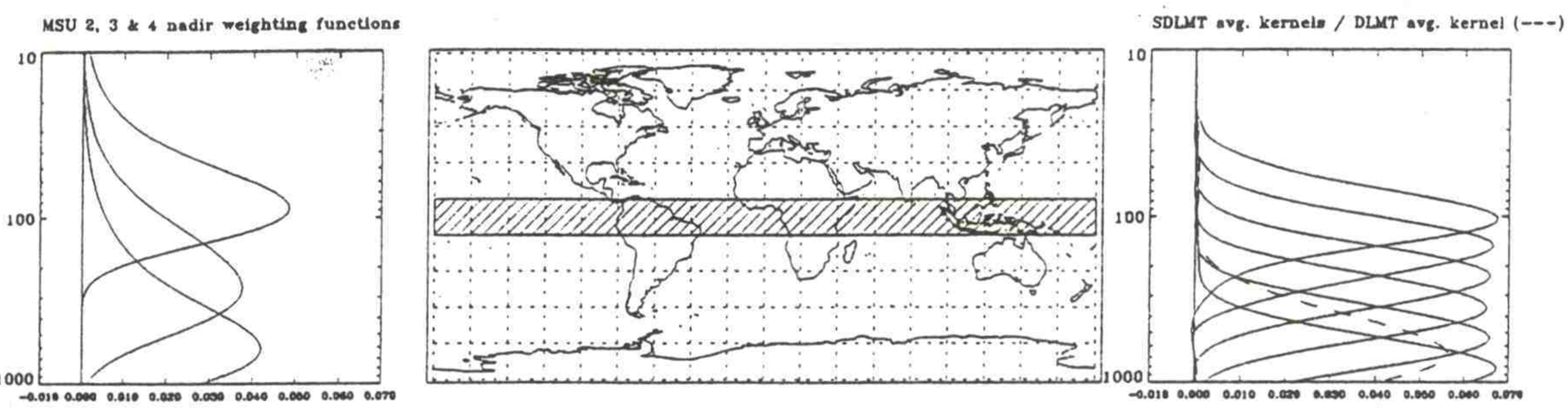

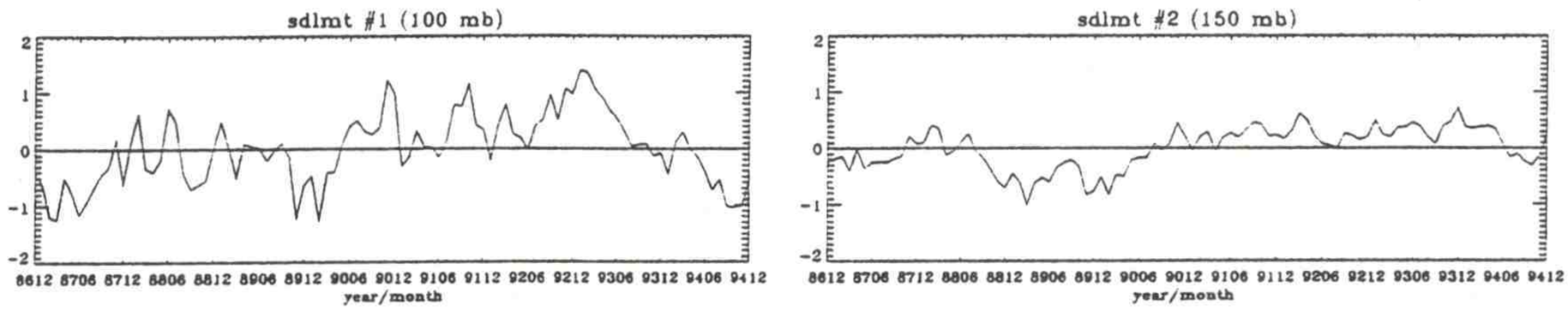

Fig. 3. MSU time series for +/- 10 degrees latitude from 1987 through 1994.

4. CONCLUDING REMARKS

Monthly datasets of NOAA-10 and -12 MSU derived deep layer mean temperature for the period from 12/86 to present (as long as NOAA-12 survives) are available for monitoring interannual temperature trends. The data can also be used to verify other observing/assimilation systems. Validation with radiosonde data show good agreement.

Both NOAA-10 and -12 are morning satellites. There are some advantages of having a time series based only on morning satellites. For example, the certainty of adjusting morning satellites is probably greater than adjusting afternoon satellites, since the equator crossing time (ECT) for morning satellites does not change nearly as much as it does for afternoon satellites (e.g. NOAA-11 ECT has varied by 11 hours over 4 years, NOAA-10 has varied by less than 1 hour). The same argument is true for adjusting a combination of afternoon and morning satellites. The next generation microwave sounder - Advanced MSU which will begin to replace MSU in 1996. The first AMSU will also be a morning satellite (the Goldberg and Fleming paper also discusses how we plan to continue MSU with AMSU). For this reason, we plan to maintain a separate "morning only" time series. Our goal is to adjust all the MSU data, which will require more sophisticated procedures for removing diurnal changes between morning and afternoon satellities. We also need to determine the uncertainties in the time series associated with these empirical adjustment procedures.

The processing of the MSU data was funded by NOAA's Climate and Global Change/Pathfinder program.

5. REFERENCES

Goldberg, M.D. and H.E. Fleming, 1995 An algorithm to generate deep-layer mean temperatures from microwave satellite observations for the purpose of monitoring climate change. *J. Climate*, **8**, 993 - 1004.

Spencer, R.W., J.R. Christy, and N.C. Grody,1990: Global atmospheric temperature monitoring with satellite microwave measurements: method and results 1979-84. *J. Climate*, **3**,1111-1128.

Spencer, R.W. and J.R. Christy, 1992a: Precision and radiosonde validation of satellite gridpoint temperature anomalies, part 1: MSU channel 2. *J. Climate*, **5**, 847-857.

Spencer, R.W. and J.R. Christy, 1992b: Precision and radiosonde validation of satellite gridpoint temperature anomalies, part 2: a tropospheric retrieval and trends during 1979-90. *J. Climate*, **5**, 858-866.

Spencer, R.W. and J.R. Christy, 1993: Precision lower stratospheric temperature monitoring with the MSU: technique, validation, and results 1979-1991. *J. Climate*, **6**, 1194-1204.

Variations in central and eastern North American precipitation teleconnections during warm and cold tropical Pacific SSTA events

David L. Montroy and Michael B. Richman

School of Meteorology and Cooperative Institute for Mesoscale Meteorological Studies
The University of Oklahoma

1. Introduction

The associations between tropical Pacific sea-surface temperature anomaly (SSTA) events and North American climate have been investigated by a number of authors. These include Ropelewski and Halpert (1986, *Mon. Wea. Rev.*: **114**, 2352-2362; 1989, *J. Climate*: **2**, 268-284), and Kiladis and Diaz (1989, *J. Climate*: **2**, 1069-1090), all of which described seasonal precipitation relations, in addition to Montroy (1995, *J. Climate*: submitted), which has outlined monthly linear SSTA-precipitation relationships. While much research (including Kiladis and Diaz 1989; Montroy 1995) has assumed a linear relationship between tropical Pacific SSTA and global climate patterns, the works by Ropelewski and Halpert suggest such an assumption may not be appropriate. Ropelewski and Halpert (1986) examined North American precipitation patterns linked with the low-index phase of the Southern Oscillation (i.e., warm SSTA events), while Ropelewski and Halpert (1989) considered only high-index Southern Oscillation events (i.e., cold SSTA events). Their results indicate that not all regions with a consistent warm event signal had a counterpart for cold events. Using this motivation, this study separately examines monthly North American precipitation patterns associated with each type of event.

A number of studies have also documented an observed shift in atmospheric and oceanic conditions around 1976/77. This shift is characterized by a deepening of the Aleutian Low in November-March (Trenberth and Hurrell 1994, *Clim. Dyn.*: **9**, 303-319) and a warming of winter SST in the central and eastern tropical Pacific by nearly 1°C (Graham 1994, *Clim. Dyn.*: **10**, 135-162). Richman (1994, Unpublished PhD thesis, University of Illinois, 321pp) also showed that the most important geopotential height circulation mode since 1970 has a tropical and subtropical tropospheric response in both summer and winter which is highly related to SSTA in all tropical oceans and has a sharp discontinuity around 1976/77. To determine if this 1976/77 climate shift affected the typical warm event precipitation response over North America, the present study will separately examine the associations in each of two time periods (1950-76 and 1977-92).

2. Data

2.1 Sea-surface temperature

The sea-surface temperature data used consisted of 2°x2° gridded data extracted from the reconstructed set available from the Climate Prediction Center between 19° N/S and stretching from 140°E to the American coasts. These data were created by computing the empirical orthogonal functions (EOFs) of SSTA in different oceanic regions from the 1982-93 optimal interpolation data of Reynolds and Smith (1994, *J. Climate*: **7**, 929-948) and then fitting these EOFs to COADS observations in a least squares sense. Smith *et al.* (1995, *J. Climate*: in press) gives full details on the construction of these data. The anomalies used here were computed relative to 1950-92.

2.2 Precipitation

The monthly North American precipitation data used were totaled from a set of daily precipitation observations for 766 stations located east of the Rocky Mountains in the United States and some Canadian provinces. The daily values spanned the period 1 January 1949 to 31 December 1992, with the monthly totals from January 1950 through December 1992 used here. The 766 stations were selected to approximate a 1° latitude-longitude grid over the domain, as shown in Fig. 1. A unique characteristic of this dataset is the lack of any missing or objectively-analyzed data values due to the substitution of observations from one of a number of secondary stations when data from a primary station were unavailable. Additionally, these data have been thoroughly quality-controlled, with gross outliers identified and verified with printed records. Full details on the

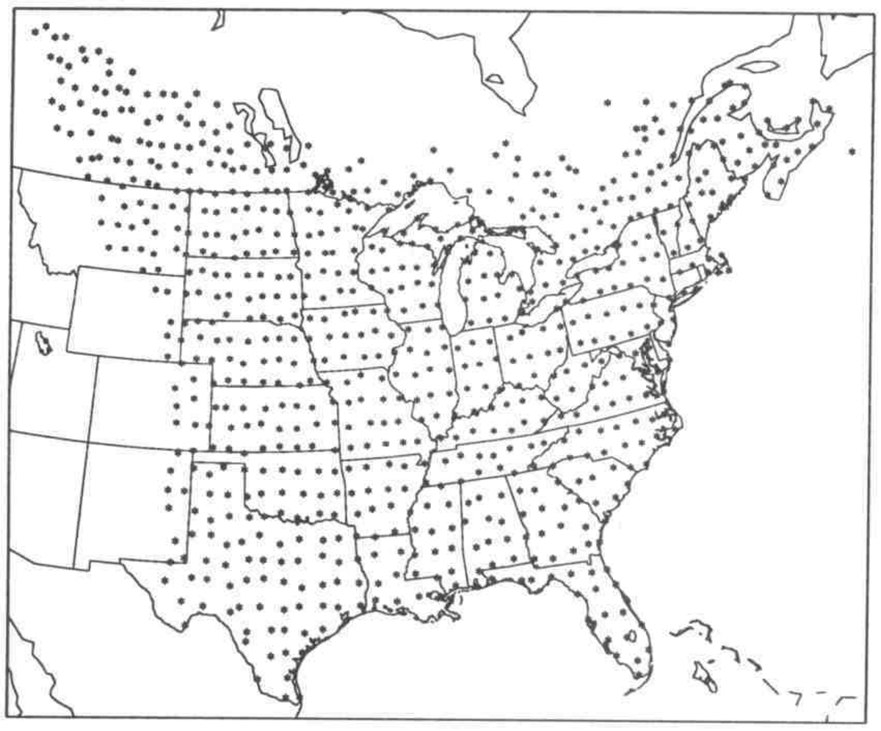

Figure 1: Primary precipitation station network.

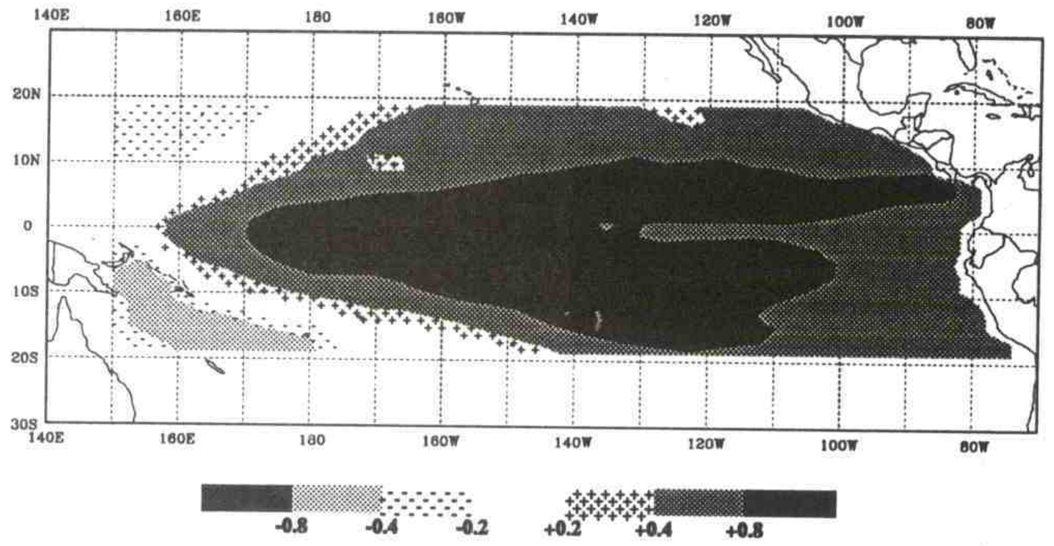

Figure 2: Spatial loading pattern associated with first unrotated principal component of tropical Pacific SSTA. Shading is according to given legend.

construction of the dataset may be found in Richman and Lamb (1985, *J. Climate Appl. Meteor.*: **24,** 1325-1343; 1987, *Atmosphere-Ocean*: **25**, 137-158).

3. Methodology

3.1 Selection of warm and cold events

Warm and cold event months were identified for different regions of the tropical Pacific using the results of a principal component (PC) analysis performed on all months of the SSTA dataset for 1950-92 similar to that in Montroy (1995). Unrotated and Varimax-rotated analyses were performed, with the first 6 unrotated PCs used in the rotation. The PCs explaining the most variance in the SSTA domain were the first unrotated PC (UPC1), and the first and second rotated PCs (VPC1 and VPC2) representing variability in the central tropical Pacific (see Fig. 2), eastern tropical Pacific, and the western tropical-to-north-mid Pacific, respectively (last two not shown). The associated PC score time series were used to designate warm and cold events, with a threshold of +0.97 (-0.97) used to indicate the occurrence of a warm (cold) event. With the normalized nature of the PC score time series, the threshold of 0.97 designates the upper (lower) sextile of SSTA as warm (cold).

3.2 Compositing

For each set of warm and cold events identified in section 3.1, the composite precipitation calendar monthly anomaly field was computed by simply averaging the station data over all eligible months. The monthly means used to compute the anomalies were the calendar monthly average over the corresponding time period (i.e., different climatology fields were used for 1950-76 and 1977-92).

4. Results

The analyses described in section 3 were performed separately for all 12 calendar months for warm and cold events during 1950-76 and 1977-92. Fig. 3 shows the composite precipitation anomalies for November, December, and January events, respectively, based on warm 1950-76, cold 1950-76, and warm 1977-92 central tropical Pacific SSTA events as represented by UPC1. The following discussion will focus on the linearity of patterns associated with warm and cold events during 1950-76 and the differences in the patterns associated with warm events for 1950-76 and 1977-92.

4.1 November

Figs. 3a-b indicate that the sign of the observed November precipitation anomaly along the Atlantic and Gulf of Mexico coast was linearly related to that of tropical Pacific SSTA during 1950-76, but that the cold event relations had a smaller magnitude and extended farther up the Atlantic coast than the warm event associations. The composite precipitation anomaly for six warm Novembers (Fig. 3a) shows a large coherency of composite precipitation values (CPVs) $\geq$ +0.5 inches southeast of a line from northern Texas to Maine and New Brunswick, with sizable embedded regions of CPVs exceeding +1.0 inches. This pattern was observed in five of the six composite members, with November 1965 characterized by dry conditions from Oklahoma to the mid-Atlantic

states instead (not shown). The composite 1950-76 cold event anomaly pattern is characterized by small coherencies of negative CPVs ≤ -0.5 in southeastern Texas and in Florida and adjoining coasts, with smaller regions along the Atlantic coast (Fig. 3b). The small magnitudes result from the presence of two primary observed precipitation anomaly patterns (not shown) during the ten cold 1950-76 Novembers. November 1950, 1954, 1955, 1970, and 1971 were all characterized by dry conditions in the lower Mississippi River Valley and some wet conditions along the Atlantic coast, while November 1964, 1973, and 1974 exhibited wet conditions from Oklahoma-Alabama and dry along the Atlantic coast. Combining these patterns results in small CPVs in the south and along the Atlantic coast.

The composite November precipitation anomalies for warm events were also found to extend farther up the Atlantic coast during warm 1950-76 events than for warm 1977-92 events. Fig. 3c shows a coherency of positive CPVs ≥ +0.5 from Texas to Alabama in the precipitation anomaly composite of four warm Novembers during 1977-92. Positive anomalies were observed over this region in each composite member except November 1991 (not shown). This region is substantially smaller than that in the warm 1950-76 composite (Fig. 3a), particularly in that it does not extend up the Atlantic coast, and, in fact, some scattered negative 1977-92 coherencies replace parts of the positive 1950-76 region.

4.2 December

Figs. 3d-e do not support a linear relationship between December precipitation and tropical Pacific SSTA. The composite anomaly for four warm Decembers in 1950-76 (Fig. 3d) primarily consists of two CPV coherencies, one positive and centered near Illinois-Michigan, and another negative and stretching from Arkansas to the Carolinas. The observed anomaly patterns (not shown) for all four composited months were characterized by wet conditions near Lake Michigan, but only two (1957 and 1965) presented dry anomalies in the southern states. In the corresponding cold event composite (Fig. 3e), however, only a small negative coherency is present over Louisiana and Mississippi, in the same region as the negative coherency in the warm composite.

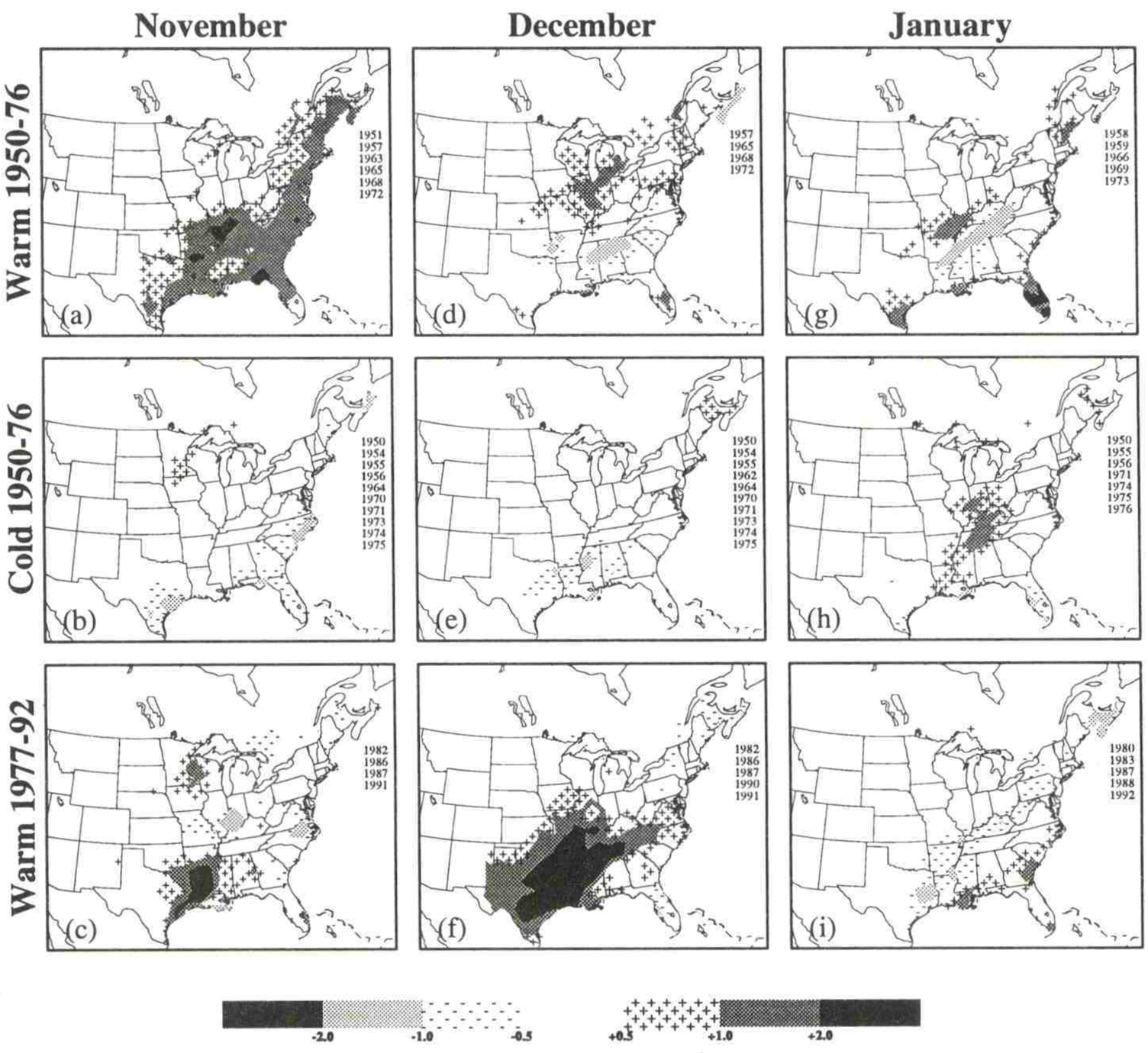

Figure 3: Precipitation anomaly composite for November, December, and January for 1950-76 warm events, 1950-76 cold events, and 1977-92 warm events. Events are defined based on central tropical Pacific variability represented by SSTA UPC1.

Furthermore, the lack of a sizable coherency in the cold 1950-76 composite once again results from the variability of the observed precipitation anomaly fields during these cold months, as in November (see section 4.1). In December 1950, 1955, 1962, 1970, and 1975, the Ohio River Valley and lower Mississippi River Valley region experienced abnormally dry conditions, while in December 1954, 1964, and 1973, the Ohio River Valley and Nova Scotia/New Brunswick had wet conditions, with the others (1971 and 1974) falling into neither category. The lack of a linear SSTA-precipitation relation in December may be a reason why the response to tropical Pacific SSTA in this month is generally not considered to be the same as that in November and January (Ropelewski 1995, personal communication).

Additionally, Figs. 3d,f show that the composite December precipitation anomaly for warm SSTA events in 1950-76 differs substantially from that for 1977-92 events. An extensive positive coherency from Texas to Virginia in the warm 1977-92 precipitation anomaly composite (Fig. 3f) is not suggested in the warm 1950-76 composite (Fig. 3d). Furthermore, a negative CPV coherency replaces the positive one in New Brunswick/Nova Scotia. The observed precipitation anomalies for December 1982, 1986, 1987, 1990, and 1992 (not shown) exhibit a structure similar to the 1977-92 composite, although wet conditions from Texas to Virginia are not present in December 1986, nor are dry conditions over New Brunswick and Nova Scotia in December 1990.

4.3 January

Figs. 3g-h suggest a linear relationship between the signs of tropical Pacific SSTA and January precipitation anomalies in Florida. The composite precipitation anomaly for five warm 1950-76 January's (Fig. 3g) possesses a dipole structure in the southeastern United States, with a positive (negative) coherency over Florida (west of the Appalachian Mountains). The observed anomaly patterns for the five months support this structure, although Florida precipitation in January 1969 was near, not above, normal and precipitation in Louisiana-Mississippi was above, not below, normal in January 1973. The cold 1950-76 composite (Fig. 3h) also displays a weak dipole structure with polarity reversed. However, the observed anomaly patterns indicate that the positive CPV coherency from Louisiana to Ohio is largely a result of January 1950 and 1974, as precipitation anomalies exceeding +3.0 inches were observed in that region. But Florida did experience dry conditions in every cold January except 1955.

Figs. 3g,i suggest that the January precipitation response to warm tropical Pacific SSTA events appears to have changed in Florida and Nova Scotia/New Brunswick. Similar to warm 1950-76 events (Fig. 3g), the warm 1977-92 (Fig. 3i) precipitation composite reveals a dipole pattern, with negative coherencies west of the Appalachians and positive regions centered near northern Florida. However, in 1977-92, the negative Appalachian region extends into New England and Nova Scotia/New Brunswick, while the positive coherency over Florida seemingly lifts to the north, leaving no relationship in Florida. The observed precipitation anomalies generally support this structure, although dry conditions spanned southern Georgia and Alabama in January 1980, and wet conditions prevailed in New Brunswick/Nova Scotia in January 1992.

5. Summary

Using precipitation anomaly composites with support from the observed anomaly patterns, this study has proposed regions in which the sign of the observed monthly precipitation anomaly associated with cold tropical Pacific SSTA events is not the opposite of that linked to warm events. Linear SSTA-precipitation relationships during 1950-76 were only supported along parts of the Atlantic and Gulf of Mexico coast in November and over Florida in January. The lack of linearity in other regions was largely due to the presence of two different precipitation patterns during cold 1950-76 events. Additionally, the observed 1976/77 climate shift was shown to be associated with a change in the observed precipitation response during warm events in November and January along the Atlantic coast and in December from Texas to Virginia to Wisconsin. Future research will focus on the meteorological factors associated with these relations and the individuality of each warm or cold event.

Acknowledgments. This work was funded in part by NSF grant ATM 92-96119 and USEPA Cooperative Agreement CR-819646010. The computing was done on the CRAY Y-MP at the National Center for Supercomputing Applications, the CRAY C-90 at the Pittsburgh Supercomputing Center, and the workstations at the Climate Diagnostics Center. The authors would like to thank Peter Lamb for his continuous support of this research, and Chet Ropelewski, Thomas Smith, and Richard Reynolds for assistance in obtaining the reconstructed SST data.

Annual and Interannual variability in Large-Scale Precipitation During 1987 - 1994

Pingping Xie and Phillip A. Arkin
National Centers for Environmental Prediction
National Oceanic and Atmospheric Administration
Washington, DC 20233

1. Introduction

The annual and inter-annual variability in global precipitation are not well documented because of the lack of a comprehensive observing system. The principal existing sources of large-scale precipitation can be divided into 5 categories, including gauge observations, estimates inferred from satellite observations of IR, microwave (MW) scattering and MW emission, and numerical model predictions. Xie and Arkin (1995) examined several datasets and found that at least three major deficiencies exist in these individual data sources; 1) incomplete global coverage, 2) significant random error, and 3) non-negligible bias. Based on this result, Xie and Arkin (1996) developed a new algorithm to construct a gridded field (analysis) of global monthly precipitation by merging several kinds of individual data sources so as to ensure complete coverage and reasonable quality. Using this algorithm, we have recently produced global monthly precipitation analyses for the 7-year period from July 1987 to June 1994. In this paper, we will describe the annual and inter-annual variability in large-scale precipitation as observed in the 7-year merged analysis.

2. Methodology

One example is selected from each of the 5 categories and used to construct the merged analysis of global monthly precipitation. In this study, a monthly analysis based on gauge observations of the Climate Anomaly Monitoring System (CAMS) of NOAA/CPC and the Global Historical Climatology Network (GHCN) of DOE/CDIAC (Xie et al., 1996), three satellite-based estimates - the IR-based GPI (Arkin and Meisner, 1987), SSM/I scattering (Grody, 1991) and SSM/I emission (Wilheit et al., 1991), and model predictions of the ECMWF (Arpe, 1991) are selected to represent each category. A two-step algorithm is applied to first reduce the random error and then to remove the bias. First, the 3 satellite estimates and the model predictions are combined linearly through the Maximum Likelihood Estimation Method to reduce the random error. Since the output of the first step contains bias passed through from the input, the second step is included to remove it. For that purpose, the output of the first step is blended with the gauge observations, in which the first-step-output is used to define the shape while the gauge data is used to define the amplitude of the precipitation field. Simulation and verification tests showed that the quality of the merged analysis is significantly better than its components. Its random error has been reduced substantially and its bias has been removed almost completely.

3. Results

The algorithm is applied to create the global monthly precipitation analysis on a 2.5° latitude/longitude grid for a 7-year period from July 1987 to June 1994. Fig.1 shows the

distribution of mean precipitation from our 7-year merged analysis and from long-term means of Jaeger (1976) and Legates and Willmott (1990). Generally speaking, all of them present similar large-scale distribution patterns, with rainbands associated with the ITCZ, SPCZ and storm tracks. A split in the ITCZ is observed over the central Pacific in our merged analysis and in the Legates and Willmott climatology, while the Jaeger climatology exhibits wider and smoother distributions for the rainbands. Heavy rainfall is observed in the Legates and Willmott climatology over the eastern Pacific ocean, but there is no corresponding feature in our merged analysis and in the Jaeger climatology.

Fig.2 shows the annual cycles of mean precipitation for the Southern Hemisphere, Northern Hemisphere and for the whole globe as obtained from the merged analysis. Significant annual cycles are observed for each of the hemispheres, while the annual cycles are quite modest for the global mean, with a peak in July-August. The Jeager climatology exhibits annual cycles with similar phase and over-all amplitude to our merged analysis, although its amplitude over land is somewhat larger. The Legates and Willmott climatology, meanwhile, shows quite different phases and amplitudes for the annual cycles, particularly over ocean.

We also applied our merged analysis to examine the inter-annual variability associated with the ENSO. Shown in fig.3 are the time series of SST anomaly over the Nino3 area and the Hovermoller diagram for the precipitation averaged over the Pacific. The annual cycle of the precipitation is quite significant and it is apparently modified by the SST anomaly which is related to the ENSO cycles. When the SST exhibits positive anomalies, the magnitude of the precipitation becomes larger and its distribution extends farther south, while the precipitation becomes weak in general when the SST is colder.

4. Summary

1) A 7-year analysis of global monthly precipitation has been constructed by merging 5 kinds of individual data sources, including gauge observations, estimates inferred from satellite observations, and numerical model predictions.

2) The 7-year analysis has been used to examine the annual and inter-annual variability of global precipitation and the results showed that the annual cycles resembles existing climatologies but with some differences.

3) The dataset succeeded in capturing the inter-annual variability associated with the ENSO signal.

4) Further work is under way to improve the algorithm and to extend the analysis for a longer period from 1979 to present.

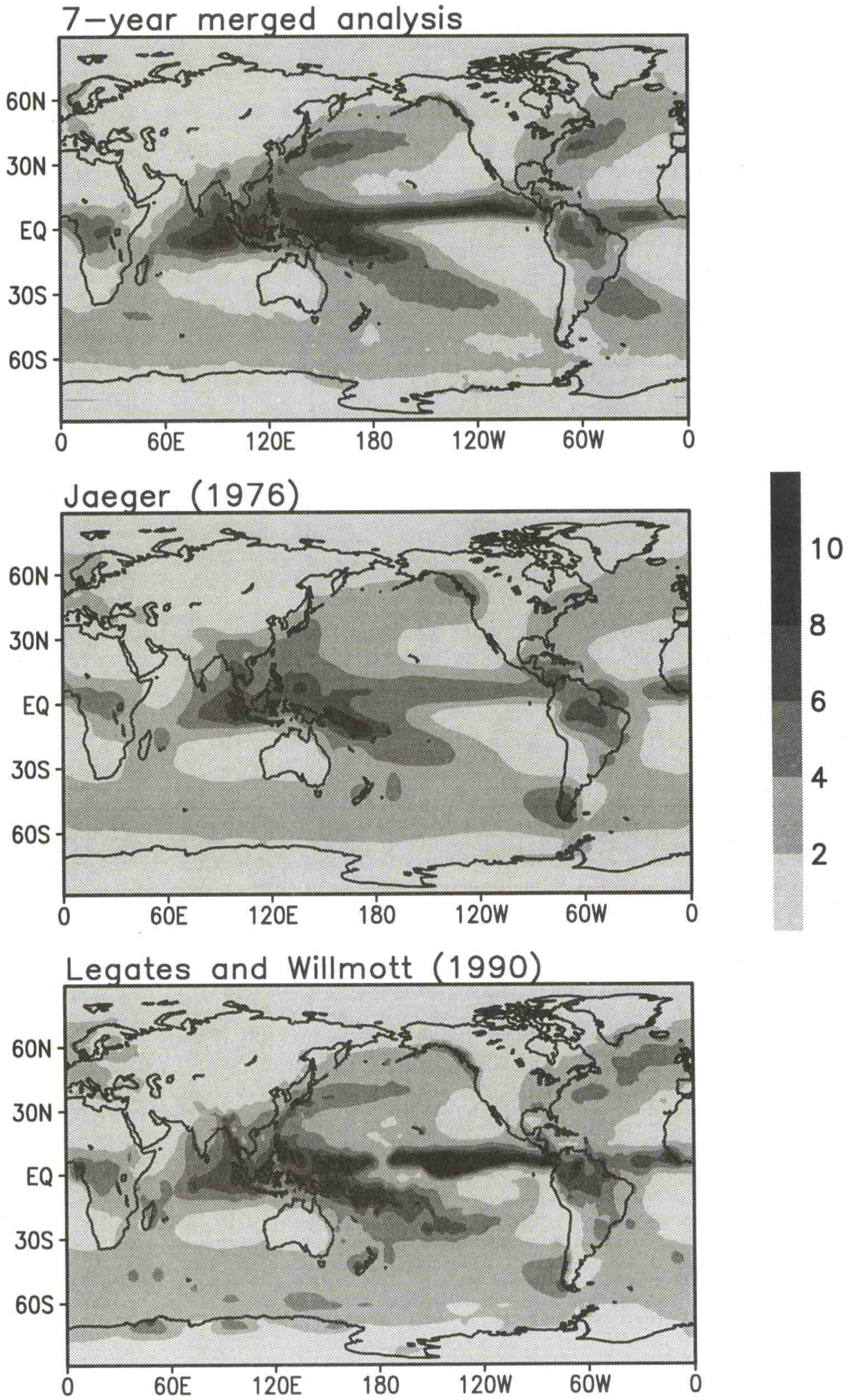

Fig.1 Distributions of annual mean precipitation (mm/day) averaged from the 7–year gauge–based analysis. Long–term means of Jaeger (1976) and Legates and Willmott (1990) are plotted as well for comparison.

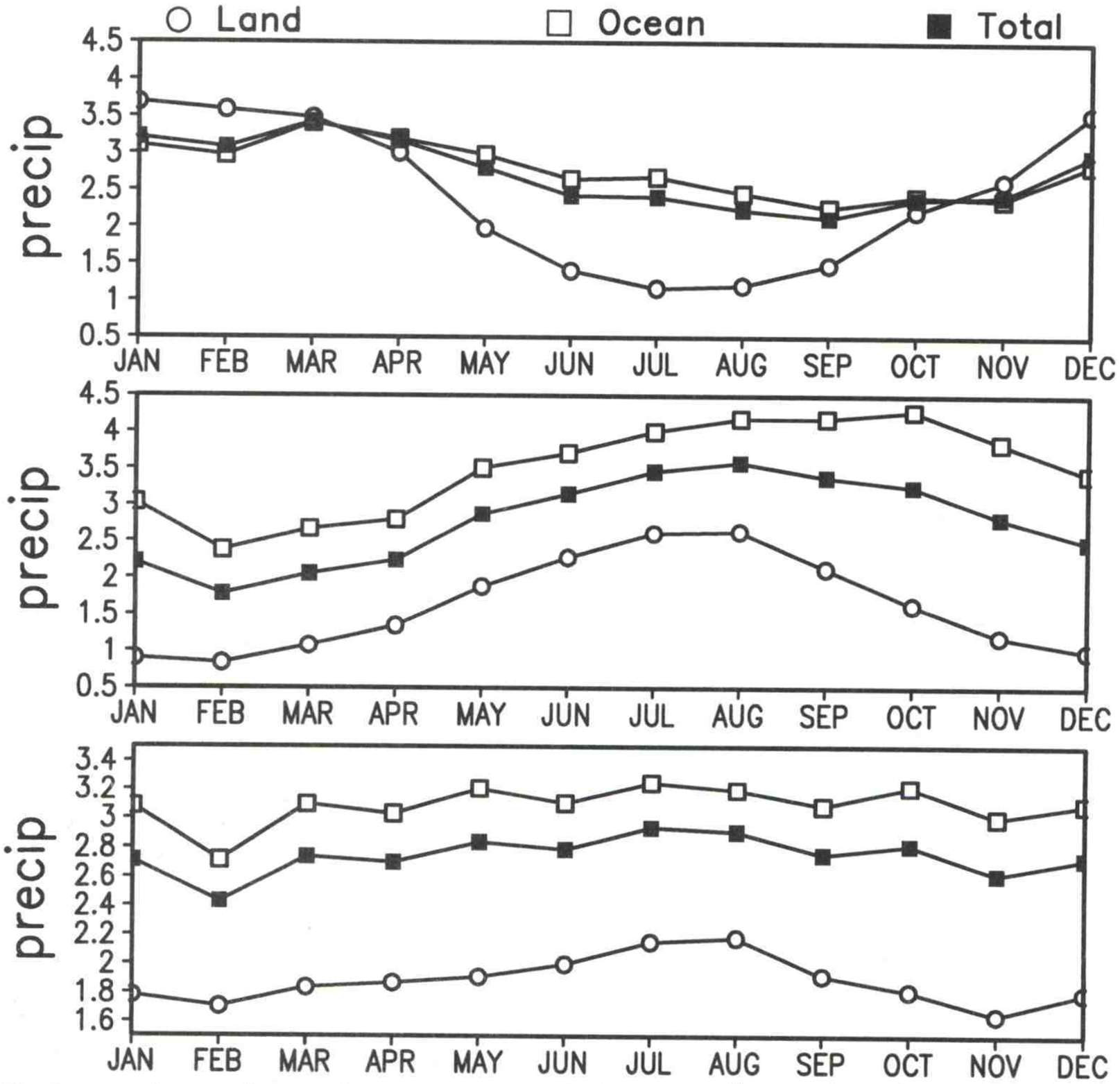

Fig.2 Annual cycles of mean precipitation (mm/day) over Southern Hemisphere (top), Northern Hemisphere (middle) and the entire globe (bottom) as obtained from the 7–year merged analysis.

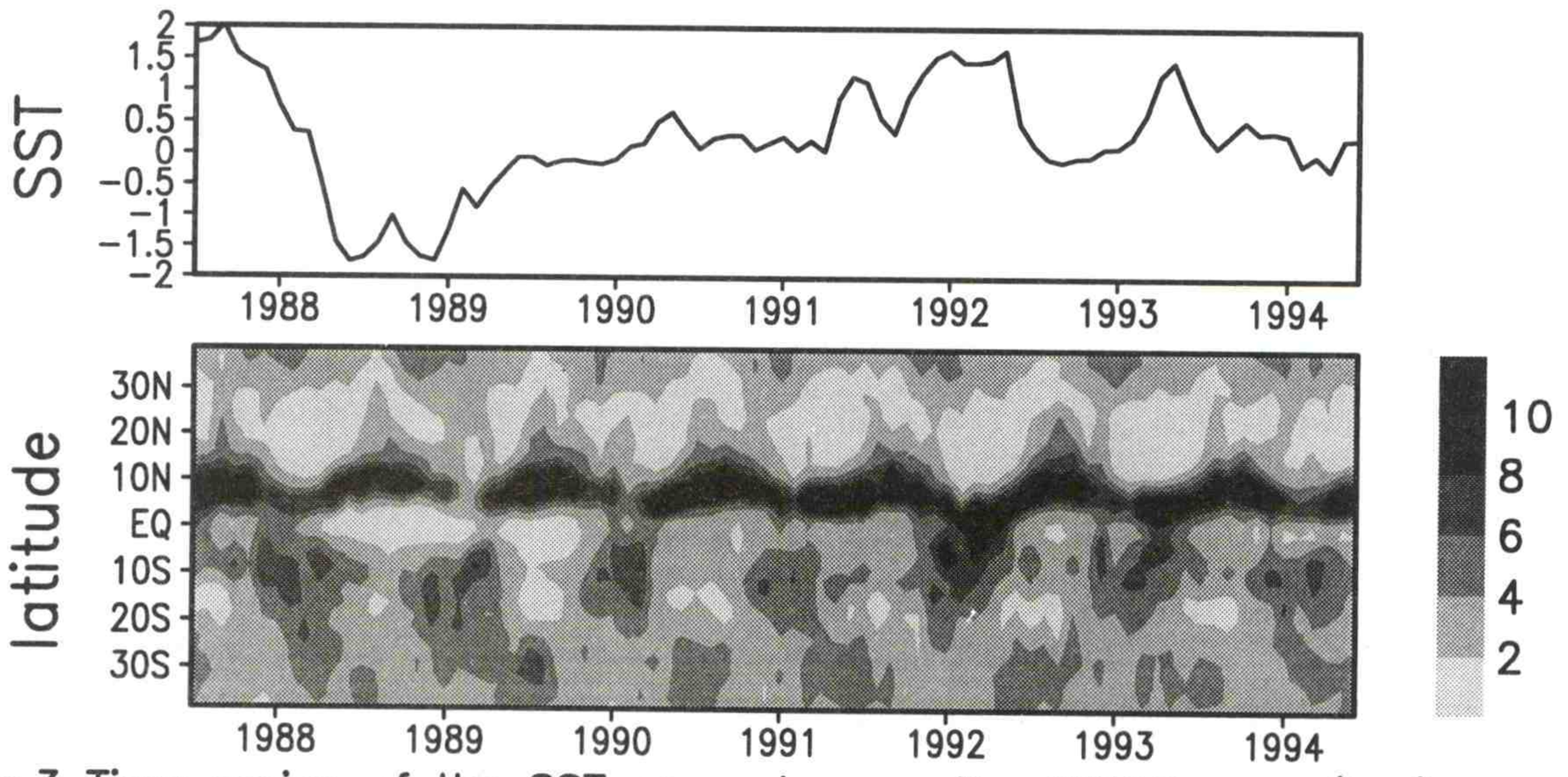

Fig.3 Time series of the SST anomaly over the NINO3 area (top) and Hovermoller diagram for the precipitation (mm/day) averaged over the Pacific (140E – 100W) (bottom).

THE ROLE OF INERTIAL INSTABILITY IN DETERMINING THE STRENGTH AND LOCATION OF NEAR-EQUATORIAL CONVECTION

Robert A. Tomas[1] and Peter J. Webster[2]

1) National Center for Atmospheric Research
Boulder, CO 80307
2) Program in Atmospheric and Oceanic Sciences; Univ. of CO
Boulder, CO 80309

1) INTRODUCTION

Figures 1 a-b show the distribution of mean sea-surface temperature (SST; gray shaded) for February, 1992 in the Indian Ocean and during July, 1992 in the Eastern Pacific, respectively. Superimposed on the diagrams are contours of outgoing longwave radiation (OLR) which are indicators of deep penetrative convection. The heavy bold line represents the zero absolute vorticity contour ($\eta = 0$) at 925 mb for later reference. The distribution and magnitude of the quantities appearing in these diagrams are typical of those that may be found during any month of the same respective season.

Zonally oriented convective features are seen in each of the summer hemispheres, displaced some 4° to 12° from the equator. In these locations convection is very intense, as indicated by OLR values that are among the lowest found anywhere in the tropics. It is frequently assumed that the most intense convection is associated with the warmest SST's, however this is not the case at these locations; the warmest SST's occur elsewhere in both diagram. Also, convection is notably absent at some locations where the SST's are comparable to those found where there is near-equatorial convection . For example, the SST ranges from 27° C to 29° C on both sides of the $\eta = 0$ contour between 55° E and 85°E in Fig. 1a, yet strong convection is present only the southward side. In Fig. 1b, SST's between 27° C and 29° C occur on both sides of the equator but convection is found only in the Northern Hemisphere (NH) with the strongest convection located north of the $\eta = 0$ contour. A clear relationship between high SST's and low OLR does not exist at these locations. These findings also apply during NH summer in the East Atlantic and in the Indian Ocean (Figures not show; see Tomas and Webster, submitted to *Quart. Jour. Roy. Meteor. Soc.*)

Figures 2 a-b show the distribution of mean sea-level pressure (SLP) during February and July, 1992. In both of the regions where there is off-equatorial convection, there is also a strong cross equatorial pressure gradient. Additionally, the local minima in OLR are found equatorward

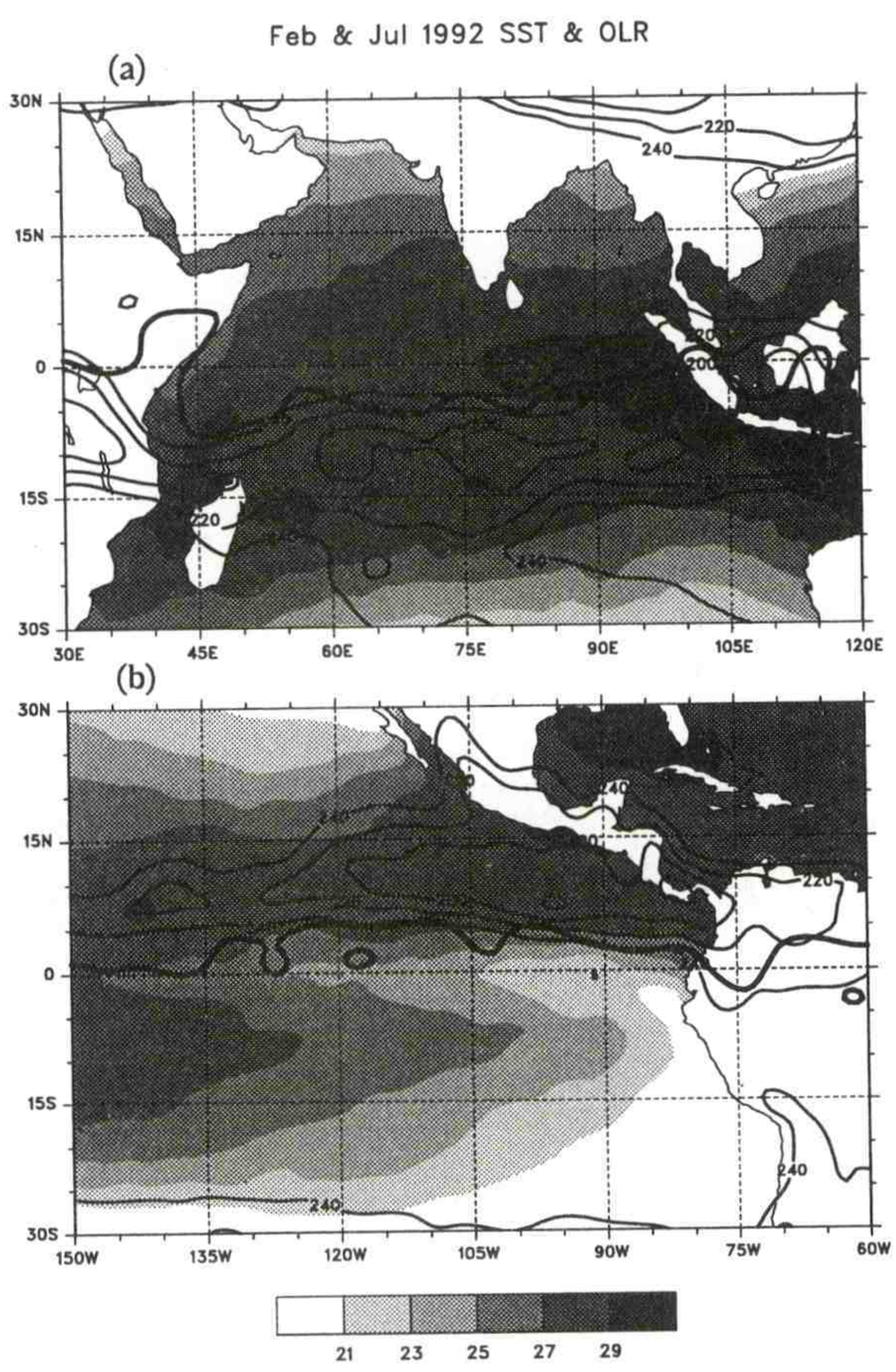

Fig. 1 a-b. The distribution of sea-surface temperature (SST; gray shaded, interval 2 °C) and out-going long-wave radiation measured from satellite (OLR; countur interval 20 W·m^{-2}) during February, 1992 in the Indian Ocean (a) and during July 1992 in the Eastern Pacific (b). The heavy bold line represents the zero absolute vorticity contour ($\eta = \zeta + f = 0$; s^{-1}). Only OLR < 240 W·m^{-2} is shown.

of the local minima in the SLP and not coincident with them. That is, the strongest convection is not observed in the near-equatorial troughs, but rather just equatorward of them.

2) HYPOTHESIS

We propose that there are three necessary conditions that determine the location and strength of near-equatorial convection:

Corresponding author addresses: 1) Robert A. Tomas, National Center for Atmospheric Research, P.O. Box 3000, Boulder, CO 80307–3000; e-mail: tomas@ncar.ucar.edu. 2) Peter J. Webster, Program in Atmospheric and Oceanic Sciences, University of CO, Campus Box 311, Boulder, CO 80309; e-mail: webster@willywilly.colorado.edu.

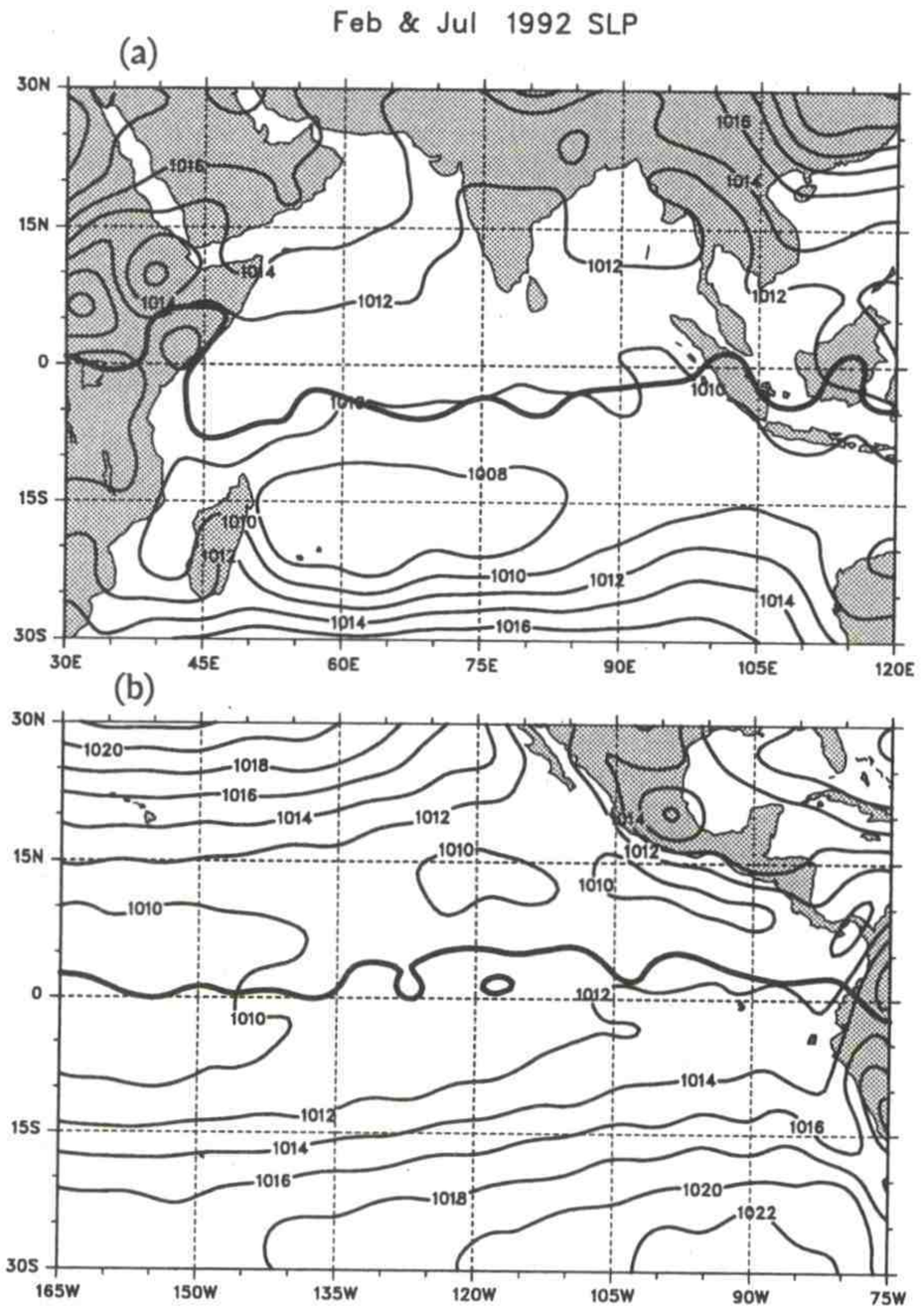

Fig. 2 a-b. The distribution of sea-level pressure (SLP; contour interval 2 mb) during February, 1992 in the Indian Ocean (a) and during July 1992 in the Eastern Pacific (b). The heavy bold line represents the zero absolute vorticity contour ($\eta = \zeta + f = 0; s^{-1}$).

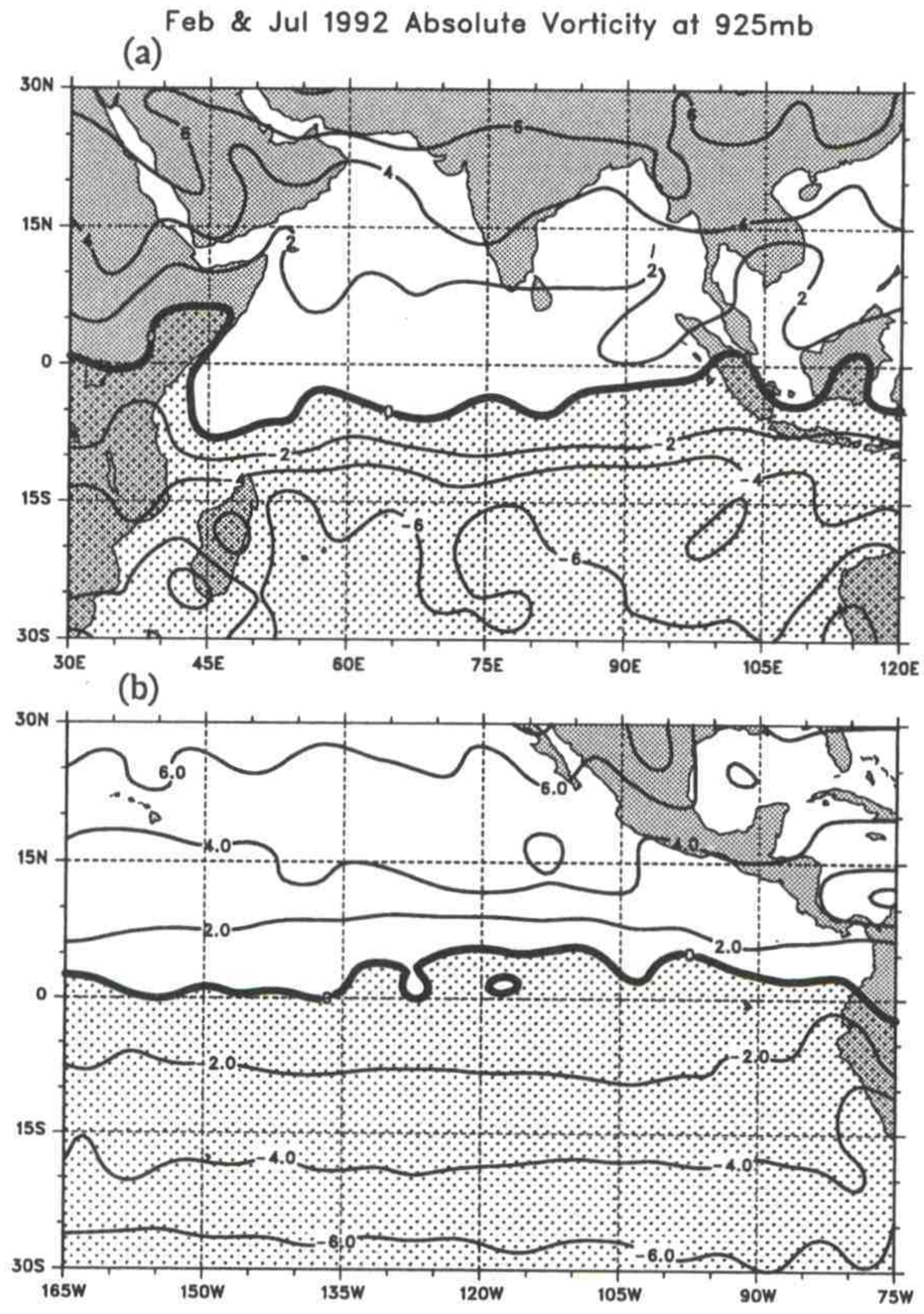

Fig. 3. The mean monthly absolute vorticity distribution ($\eta = \zeta + f = 0; s^{-1}$) at 925 mb in the Indian Ocean during February, 1992 (panel a) and in the Eastern Pacific during July 1992 (panel b). Contours are every $2\times10^{-5}s^{-1}$. Negative absolute vorticity regions are stippled.

i. The flow is inertially (symmetrically) unstable. The instability results from the advection of absolute vorticity across the equator by the strong cross equatorial pressure gradients arising either from the SST distribution about the equator or the unevenly heated distribution of land and ocean such as in the Asian and African regions. The convection itself is produced and enhanced by secondary circulation in the height-latitude plane that render the system stable.

ii. The SST should be close to the maximum tropical SST but not be the maximum overall SST nor even the local SST maximum.

iii. The atmosphere must be locally conditionally unstable where the rising branch of the secondary circulations are located so that the static stability of the atmosphere does not impede or preclude the development of these circulations.

Figures 3a-b show the February and July, 1992 distributions of absolute vorticity on the 925 mb surface, respectively. Where off-equatorial convection was noted in Figs. 1a-b, the zero contour is located some 5° to 8° from the equator and the absolute vorticity is "locally anticyclonic"

A criteria that may be used to determine whether or not a particular flow is symmetrically unstable is:

> If, on an isentropic surface, the absolute vorticity of the flow is of the opposite sign of the local planetary component of vorticity, i.e., that the absolute vorticity is "locally anticyclonic". the flow is symmetrically unstable.

At the lower tropospheric levels in the regions that are the focus of this study, the potential temperature field plotted on constant pressure surface changes little, at most about 5° K over the domain (not shown). In other words, the isentropic surfaces are nearly parallel to isobaric surfaces here. For this case, symmetric instability reduces to inertial instability and the instability criteria for the near-equatorial regions reduces to evaluating the absolute vorticity on a constant pressure surface. Thus, the regions where strong off-equatorial convection was noted are regions that are dynamically (i.e. symmetrically and/or inertially) unstable.

3) INTERPRETATIONS

We employ the parcel method to provide qualitative insight into the processes we expect to occur in the inertially unstable regions. Consider a parcel that is moved horizontally along an isentropic surface so that the local

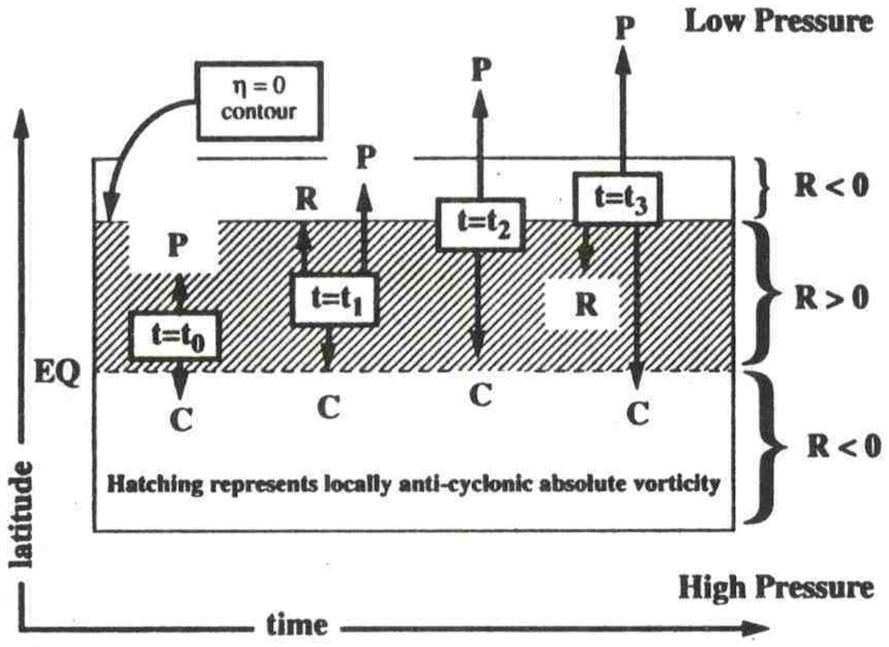

Fig. 4. A schematic diagram illustrating the forces acting on a parcel of air under the influence of a cross-equatorial pressure gradient. The region is assumed to be inertially unstable. The axes on the diagram represent time (abscissa) and latitude (ordinate) and is drawn with orientaion appropriate for northern summer conditions.

buoyancy force can be ignored. Assume a purely zonal basic state flow that is in geostrophic balance:

$$u_g = -\frac{1}{f}\frac{\partial \Phi}{\partial y}. \tag{1}$$

If the parcel's motion does not perturb the pressure field, then it is governed by the following expressions:

$$\frac{du}{dt} = fv = f\frac{dy}{dt}, \tag{2}$$

and

$$\frac{dv}{dt} = f(u_g - u) = -\left(\frac{\partial \Phi}{\partial y} + fu\right). \tag{3}$$

Consider a parcel that is moving with the geostrophic basic state motion at position $y = y_0$. After being displaced a latitudinally by a distance δy, the new zonal velocity of the parcel can be obtained by integrating (2). Thus;

$$u(y_0 + \delta y) = u_g(y_0) + f\delta y \tag{4}$$

The geostrophic wind at the parcel's new location, $y+\delta y$, is approximately:

$$u_g(y_0 + \delta y) = u_g(y_0) + \frac{\partial u_g}{\partial y}\delta y. \tag{5}$$

Substituting (4) and (5) into (3) produces an expression for the meridional acceleration:

$$\frac{dv}{dt} = \frac{d^2(\delta y)}{dt^2} = -f\left(f - \frac{\partial u_g}{\partial y}\right)\delta y. \tag{6}$$

Depending on the sign of the acceleration, the parcel will experience a force that acts either to return it to its original position or to accelerate it in the direction of the displacement. The quantity $(f - \partial u_g/\partial y)$ is the absolute vorticity of the basic flow so that we arrive more formally at the stability condition that if the absolute vorticity is locally anticyclonic, the flow is inertially unstable.

We apply the ideas discussed above to the near equatorial regions where the local absolute vorticity is anticyclonic identified in Figs. 1 and 3, with the aid of a schematic diagram. Figure 4 shows the forces acting on a parcel as it passes through a region that is inertially unstable. That is, the system is under the action of a cross-equatorial pressure gradient. The axes on the diagram represent time (abscissa) and latitude (ordinate) and is drawn with orientation appropriate for northern summer conditions. With respect to the schematic diagram, assume that at time $t = t_0$ a parcel is located in a region where the absolute vorticity is negative north of the equator and is in geostrophic balance. Assume that the parcel is then displaced northward at time $t = t_1$. The zonal velocity changes as a result of this displacement as dictated by (4) but because the environment is inertially unstable, the new zonal velocity of the parcel is sub-geostrophic. The unbalanced pressure gradient force, indicated in the diagram as "R" (residual), acts to accelerate the parcel northward ($R > 0$). At time $t = t_2$, the parcel reaches the zero absolute vorticity contour ($\eta = 0$). At this stage, the acceleration is zero ($R = 0$). Further northward motion (time $t = t_3$) results in the parcel experiencing a southward restoring force ($R < 0$).

Thus, when the zero absolute vorticity contour is found some distance from the equator, the wind will be accelerated on it's equatorward side and decelerated on the poleward side. If this theory is applicable to the real atmospheric system, the signal of these processes should be evident in the divergent wind field. In the following paragraph we use the data described in the appendix to examine the characteristics of the lower-tropospheric divergence fields.

4) LOW-LEVEL DIVERGENT WINDS

In Figs. 5a-b we present the 925 mb divergent winds in vector form with magnitude contoured during February and July 1992. The $\eta = 0$ contour is plotted in bold.

In all the regions identified above where the $\eta = 0$ contour is found some distance away from the equator, there are two consistent relationships between the wind field and the vorticity field:

(i) The divergent wind is always directed such that it advects absolute vorticity across the equator. Presumedly, this process is responsible for the locally anticyclonic absolute vorticity.

(ii) There is a maximum in the divergent wind speed that is nearly bisected by the $\eta = 0$ contour. This is precisely the distribution expected to result from the inertial instability (see Fig. 4). That is, the divergent wind is being accelerated on the equatorward side of the $\eta = 0$ contour and decelerated on the poleward side.

It is important to note how the associated divergence/convergence doublets associated with these local wind maxima contribute to the local vorticity tendency, since it is through this contribution they act to bring the unstable system back into a stable configuration

There are two contributions to the generation of absolute vorticity in the tropics. The vorticity equation scaled for tropical motions is given by:

$$\frac{\partial(\zeta + f)}{\partial t} = -\mathbf{V}\cdot\nabla(\zeta + f) - (\zeta + f)\nabla\cdot\mathbf{V} \tag{7}$$

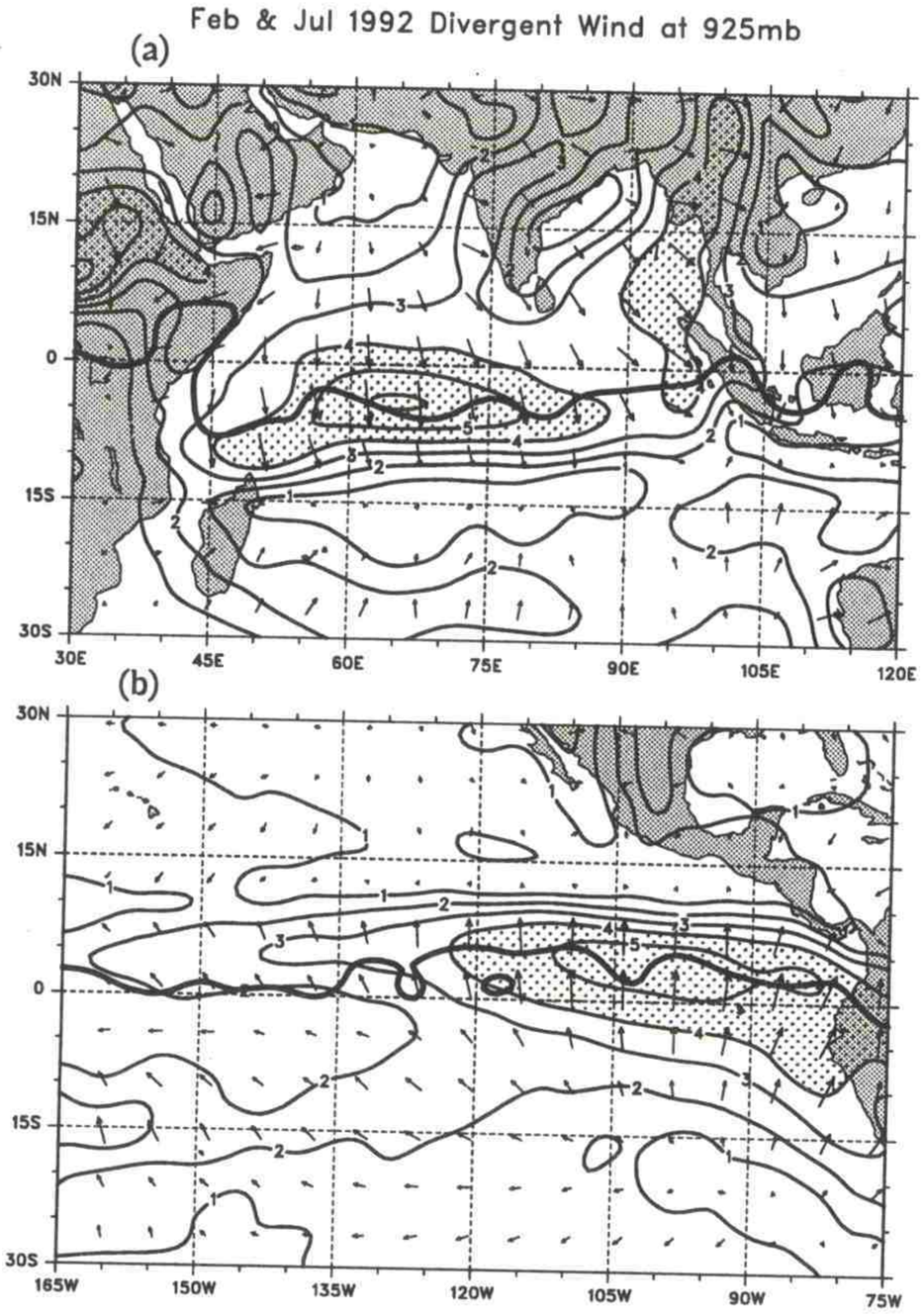

Fig. 5. The mean monthly vector divergent wind distribution at 925 mb during February, 1992 in the Indian Ocean (panel a) and during July, 1992 in the eastern Pacific Ocean (panel b). Contour interval is 1 $m \cdot s^{-1}$ and values $> 4\ m \cdot s^{-1}$ are stippled. The bold line represents the zero absolute vorticity contour.

That is, the local tendency of absolute vorticity is determined by the combination of absolute vorticity advection and stretching. Note that (7) differs from the form found in Holton (1979) in that the advection term involves the total wind field, not just the rotational component. In the regions of interest, the divergent wind field shown in Figs. 5 a-b results in a locally anticyclonic contribution to the tendency through the advection term but the opposite through the divergence term. That is, the location of the wind maximum such that it is centered on the zero absolute vorticity contour (which lies off the equator) results in a contribution to the tendency that acts to return the zero absolute vorticity contour to the equator.

5) THE LATITUDE-HEIGHT CIRCULATIONS

One of the shortcomings of the parcel argument is that environmental air must somehow replace the space vacated by the parcel and it also must disappear from the space where the parcel eventually comes to rest. Thus, the characteristics of the divergent wind fields shown in Figs. 5 a-b along with mass continuity arguments imply the existence of closed circulations in the height latitude plane. Figure 6 shows a schematic diagram generalized from features apparent the plots of the divergent wind fields

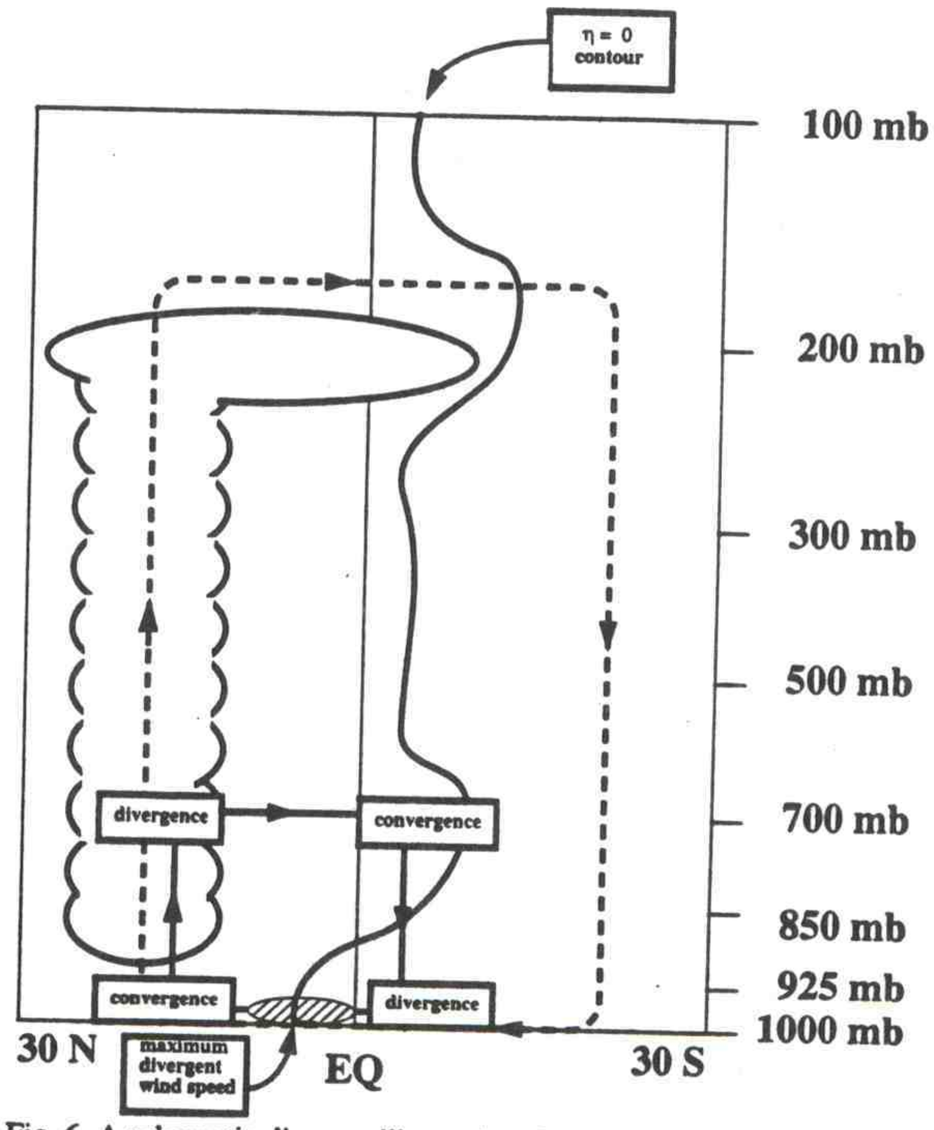

Fig. 6. A schematic diagram illustrating the anticipated circulation in the height-latitude plane in regions where near equatorial inertial instability is occuring.

about the equator. This diagram is oriented to represent advection of negative absolute vorticity into the NH as occurs in the Eastern Pacific during the July 1992 case. The orientation of the circulation would be reversed for the boreal winter case in the Indian Ocean.

In the schematic, two circulations dominate the longitudinal sections. There is a deep, large scale divergent circulation that creates the conditions necessary for the instability by bringing negative absolute vorticity across the equator and into the northern hemisphere. This circulation extends over the entire depth of the troposphere and from 30° S to 20° N. This circulation is driven by the planetary scale cross-equatorial pressure gradient associated with the distribution of land and ocean in the Indian Ocean sector and the SST distribution in the East Pacific. Superimposed on the northern branch of this circulation, there is divergent circulation closer to the equator that is associated with the dynamic instability and the location of the near-equatorial convection.

The atmosphere in the schematic (Fig. 6) is shown to be statically stable with respect to dry adiabatic ascent, indicated by potential temperature values increasing with height. One would expect that this stable state would act to impede or even preclude the development of the near-equatorial circulation resulting from the inertial instability. However, if there is enough moisture at low levels, so that lifted parcels become saturated during forced ascent, it is possible that they may reach their level of free convection and continue to rise on their own. That is, in an atmosphere that is conditionally unstable, the circulations will be enhanced by convection, attaining depths much greater than

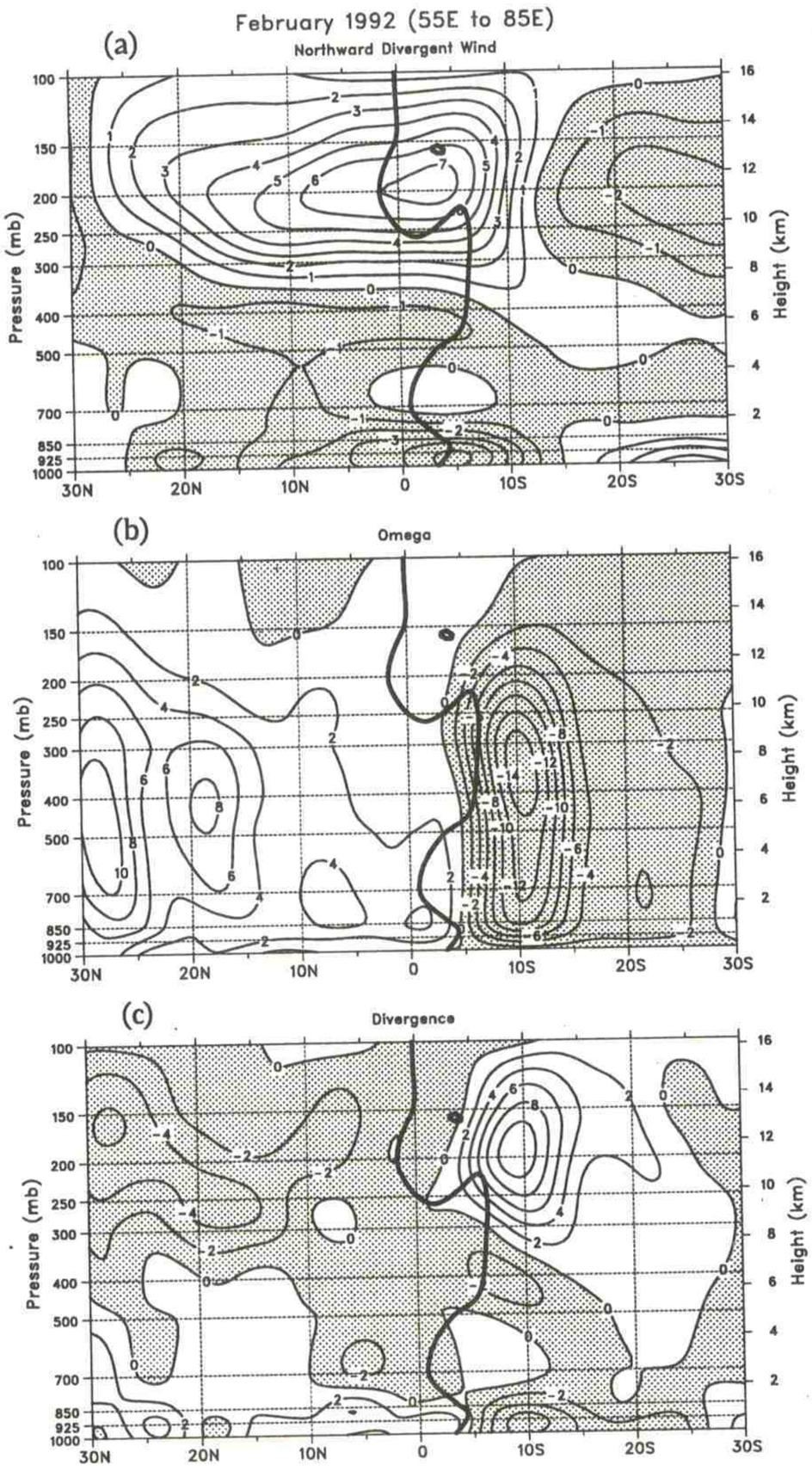

Fig. 7. Latitude-height cross-sections of circulations in the longitude band 55°E to 85°E during February, 1992. The panels depict (a) the northward divergent wind (negative shaded; $m \cdot s^{-1}$), (b) The vertical velocity (dp/dt; negative shaded; $10^{-2} Pa \cdot s^{-1}$) and (c) divergence (negative shaded; 2×10^{-6} s^{-1}). The bold contour represents the zero absolute vorticity contour.

they would in a dry atmosphere. Measurements based on values from the 1000 mb to 850 mb layer show that these regions are conditionally unstable (Figures not show; see Tomas and Webster, submitted to *Quart. Jour. Roy. Meteor. Soc.*).

Figures 7 a-c show a height-latitude cross sections of the zonally averaged divergent flow in the Indian Ocean sector (55°E to 85°E) during February, 1992. The upper panels of the figure show the northward divergent wind with negative (southern) winds stippled. The middle panels show the vertical velocity component (specifically the ω-field: *dp/dt*) with negative (ascending) values stippled. The bottom panels show the divergence. The zero absolute vorticity contour is represented by the bold contour in all panels. Circulation features are reversed during July, 1992 in the Pacific Ocean sector (not shown).

The figure shows the characteristics depicted in the schematic Fig. 6. The poleward branch of the divergent flow is constrained to the lower troposphere generally below 850 mb with a maximum occurring at the position of the zero absolute vorticity contour. A low-level divergence-convergence doublet straddles the $\eta = 0$ contour. The vertical motions concur with the centers of this feature. In the upper troposphere, return flows can be seen near 200 mb and a weaker return flow is seen near 700 mb. Magnitudes of the divergent horizontal flow are between 4 – 6 m s^{-1}. This upper-tropospheric equatorward flow occurs to the southward side of the $\eta = 0$ contour which is positioned just in the winter hemisphere. The reason the $\eta = 0$ has been displaced from one hemisphere to the other in the vertical is because of the reverse sign of absolute vorticity advection occurring in the upper troposphere. In combination, the vertical and horizontal flows define strong latitude-height circulations with the ascending branches tightly bounded just southward of the $\eta = 0$ contour at 925 mb. A comparison of the latitudes of maximum ascent in Fig. 7 with the OLR distributions (Fig. 1) reveals that they match well the regions of convective maxima.

6) SUMMARY

When there is a substantial cross-equatorial pressure gradient such as in the monsoon regions, organized convection occurs off the equator in the summer hemisphere and may not be collocated with the warmest SST or lowest SLP. In this situation, the zero absolute vorticity contour also lies in the summer hemisphere. Thus, between the equator and the zero absolute vorticity contour is a region of locally anticyclonic absolute vorticity and, thus, a dynamically (inertially and/or symmetrically) unstable regime. It is argued that associated with such a region will be a particular low level divergence-convergence doublet centered about the zero absolute vorticity contour. This acts to suppress convection on the equatorward side, amplify convection on the poleward side and encourages convection to be located off the equator.

7) APPENDIX

The SST data and OLR data are from the National Oceanic and Atmospheric Administration, Climate Analysis Center. The wind and pressure data are from European Center for Medium Range Weather Forecasts. All data sets were made available by the National Center for Atmospheric Research.

Tropospheric Equatorial Rossby Waves: Observations and Modeling

Matthew Wheeler and George N. Kiladis[1]

Program in Atmospheric and Oceanic Sciences and Cooperative Institute for Research in Environmental Sciences, University of Colorado, Boulder

1. Introduction

Observations of large-scale (**O**(1000 km)) zonally propagating atmospheric disturbances in the troposphere near the equator have often been interpreted in terms of equatorial wave theory. This theory stems from the seminal work of *Matsuno* [1966] in which the complete set of linear wave solutions of the shallow water equations on an equatorial β-plane were derived. One of these linear wave solutions is the $n = 1$ equatorial Rossby (ER) wave. On the 6- to 30-day time scale, *Kiladis and Wheeler* [1995] (hereafter referred to as KW95) showed that a prominent mode of the observed tropospheric circulation over the equatorial Pacific has a horizontal structure that closely resembles the $n = 1$ ER wave. In that study, however, not all of the observed characteristics of the waves could be explained by the Doppler shifted linear shallow water theory. In particular their phase and group speed relationships versus vertical structure and horizontal extent appeared to be inconsistent.

In this present study, we take a further look at the observational results of KW95 and use a global spectral shallow water model that can maintain a complicated basic flow to gain further insight into the characteristics of the observed waves. It is shown that using a 500-mbar basic flow and a 500 m equivalent depth, initial value problems in the model can reproduce the evolution of the observed composite circulation quite well out to at least a week.

2. Observational Results

The observational data and techniques used in this study are outlined in KW95. Briefly, a cross correlation and regression procedure whereby a 6- to 30-day filtered circulation parameter is regressed against identically filtered wind, outgoing longwave radiation (OLR), and geopotential height data is used to identify predominant large-scale transient circulation modes over the tropics. The data sets are the National Meteorological Center (NMC) daily operational analyses and daily OLR produced by the National Oceanic and Atmospheric Administration (NOAA), with the period of observations used being December-February 1985/1986-1992/1993. In this study, the 850-mbar meridional wind difference between 7.5°N and 7.5°S at the longitude of 160°W is used as the independent variable, or "predictor". The use of this wind difference as the predictor together with the time filtering effectively omits any signatures due to mixed Rossby gravity waves, even-ordered Rossby modes, or Kelvin waves.

Here, in Figure 1a, I show the 850-mbar stream function, wind, and OLR anomalies associated with 1 standard deviation in the predictor from 1 day prior to the peak in the predictor (day -1) to 5 days after the peak (day $+5$). The circulation features in this figure can be seen to be very similar to the structure of the n = 1 ER wave. Also consistent is the enhanced convection (indicated by the negative OLR anomalies) in the convergent poleward flow and suppressed convection in the divergent equatorward flow. The individual circulation dipoles propagate to the west while new circulations develop in their wake to their east. The period of the disturbances in this sequence is about 12 days and there also appears to be slight eastward energy dispersion, an effect that is much more readily discernible in the Hovmueller diagram, Figure 3a. This eastward energy dispersion is significant in the way that it is against the basic zonal flow at this lower-tropospheric level.

Figure 1b shows the 500-mbar circulation associated with the 850-mbar predictor. The circulation pattern is qualitatively quite similar to that at 850 mbar, consistent with the deep equivalent barotropic structure reported by KW95. The observational work of KW95 was also able to link the ER waves with the occurrences of some westerly wind bursts as well as the tendency for the SPCZ cloud band to periodically shift westward with time as seen in Figure 1.

3. Model Results

The observational results have shown the presence of quite deep $n = 1$ ER wave-like circulations over

[1]Now at NOAA Aeronomy Laboratory, Boulder, Colorado.

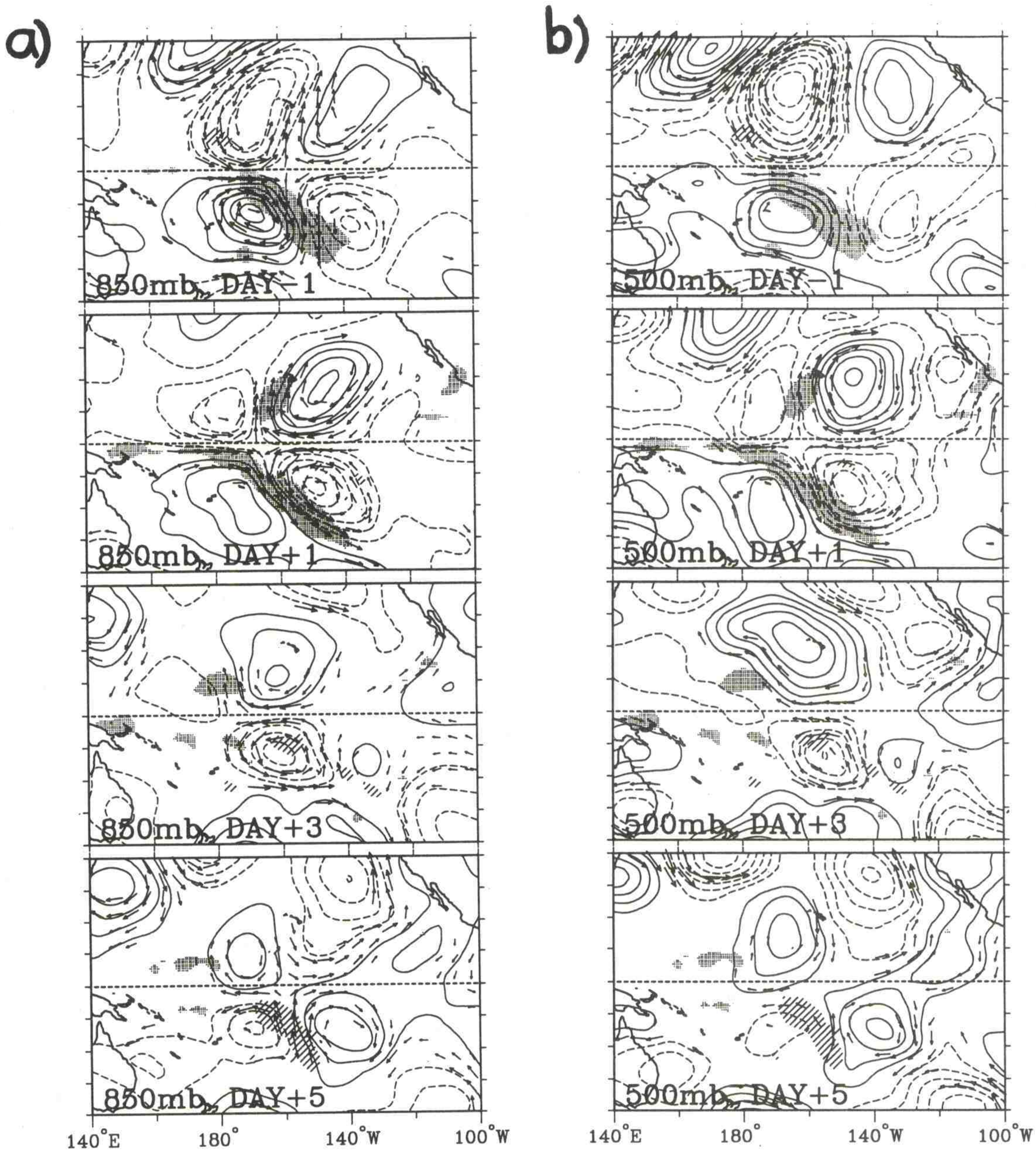

Figure 1. Six- to 30-day (a) 850-mbar, and (b) 500-mbar stream function, wind, and OLR anomalies associated with 1 standard deviation in the 850-mbar meridional wind difference between 7.5°N and 7.5°S at 160°W (2.8 m s^{-1}). The period used was December-February 1985/1986-1992/1993. Contour interval is 0.22 × 10^6 m^2s^{-1} in (a) and 0.3 × 10^6 m^2s^{-1} in (b); shading denotes OLR anomalies less than −4 W m^{-2}, and hatching, OLR anomalies greater than +4 W m^{-2}. Locally statistically significant wind vectors are shown. The largest vectors are about 2.5 m s^{-1}. Day numbers refer to the lag. Latitudinal tick marks are every 10°.

the Pacific. Due to this "deep" nature, and due to the large vertical shear of the basic zonal flow over the tropical Pacific, it becomes an important question as to what basic flow should be used when trying to explain the observations in terms of the single-level shallow water theory. To answer this question, we have used a global spectral shallow water model that maintains a complicated horizontal basic flow through the addition of residual forcing terms. Initial value problems have been performed using zero damping, a horizontal resolution of T42, and very small perturbations ($\sim 10^{-3}$ m s^{-1}) to ensure linearity. The initial perturbation velocity field has been taken from the 850-mbar composite observations (day -1 in Figure 1a, but localized in latitude and longitude by the application of a Gaussian envelope) and model runs have been performed for widely varying values of the equivalent depth and for different basic flows. To prevent the initiation of large amplitude inertiogravity waves, the initial geopotential perturbation is calculated so as to satisfy the nonlinear balance equation.

The best agreement between the model results and the composite observations of Figure 1a was found to be for the equivalent depth of 500 m and using a 500-mbar DJF basic flow. This model run is shown in Figure 2, together with its corresponding Hovmueller diagram in Figure 3b. The similarity of Figures 1a and 2 and also the phase and group speeds indicated in Figures 3a and 3b is amazingly good. Even after 6 days, the initial value problem closely resembles the composite observations, and the tropical portion of the convergence/divergence patterns produced by the modeled waves closely corresponds to the convection anomalies of the composite observations (compare shaded regions in last panels of Figures 1a and 2).

4. Conclusions

In our previous study (KW95) we had some difficulty trying to explain the propagation characteristics of the observed $n = 1$ ER waves in terms of the linear shallow water theory Doppler shifted by the basic zonal flow of the lower troposphere (e.g. the 850-mbar basic zonal flow). Using such a lower tropospheric basic flow necessitated the use of a very small equivalent depth ($\sim$ 30 m) to match the observed westward phase speed ($\sim$ 8 m s^{-1}) of the waves. Such a small equivalent depth, however, was inconsistent with other aspects of the observed waves such as meridional extent or group velocity, and the equiv-

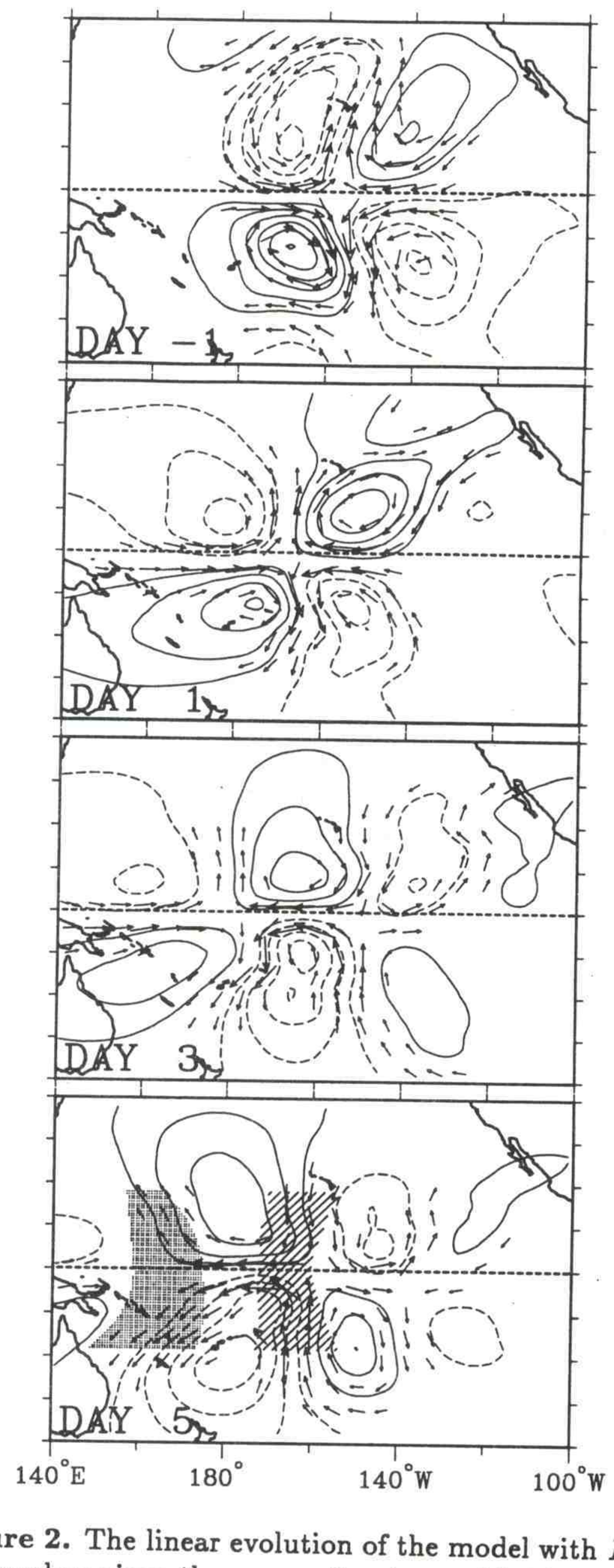

Figure 2. The linear evolution of the model with $H =$ 500 m when given the composite observed initial condition (day -1 in Figure 1a) in the observed 500-mbar DJF basic flow. Contours of perturbation streamfunction (negative contours dashed) and perturbation wind vectors are shown. Convergence (above a certain threshold) equatorward of 20°N and S is shaded and divergence is hatched for the last panel only. Day numbering has been made to correspond with Figure 1.

alent barotropic structure of the ER waves would suggest an equivalent depth that is much greater. Very small equivalent depths were also found to be needed to match the phase speeds of the equatorial wave disturbances observed by *Liebmann and Hendon* [1990] and *Takayabu* [1994] when the 850-mbar zonal flow was used for Doppler shifting. Similar inconsistencies were also found.

In this study it has been shown that the use of the 500-mbar basic flow and an equivalent depth of 500 m can solve these inconsistencies. Indeed, an initial value problem in a shallow water model can reproduce the evolution of the observed composite circulation quite well out to at least a week, confirming the importance of the shallow water dynamics for producing the observed ER waves.

Acknowledgments Thanks to Peter Webster, Klaus Weickmann, Prashant Sardeshmukh, and Gil Compo for guidance. This research was supported by a TOGA COARE grant from the Office of Global Programs at NOAA and the National Science Foundation under grant ATM-9205914.

References

Kiladis, G. N., and M. Wheeler, Horizontal and vertical structure of observed tropospheric equatorial Rossby waves, *J. Geophys. Res., 100,* 22,981-22,997, 1995.

Liebmann, B., and H. H. Hendon, Synoptic-scale disturbances near the equator, *J. Atmos. Sci., 47,* 1463-1479, 1990.

Matsuno, T., Quasi-geostrophic motions in the equatorial area, *J. Meteorol. Soc. Jpn., 44,* 25-43, 1966.

Takayabu, Y. N., Large-scale cloud disturbances associated with equatorial waves, I, Spectral features of the cloud disturbances, *J. Meteorol. Soc. Jpn., 72,* 433-448, 1994.

M. Wheeler, Cooperative Institute for Research in Environmental Sciences, Campus Box 449, University of Colorado, Boulder, Colorado 80309. (e-mail: mwheeler@monsoon.colorado.edu)

(Received December 15, 1995.)

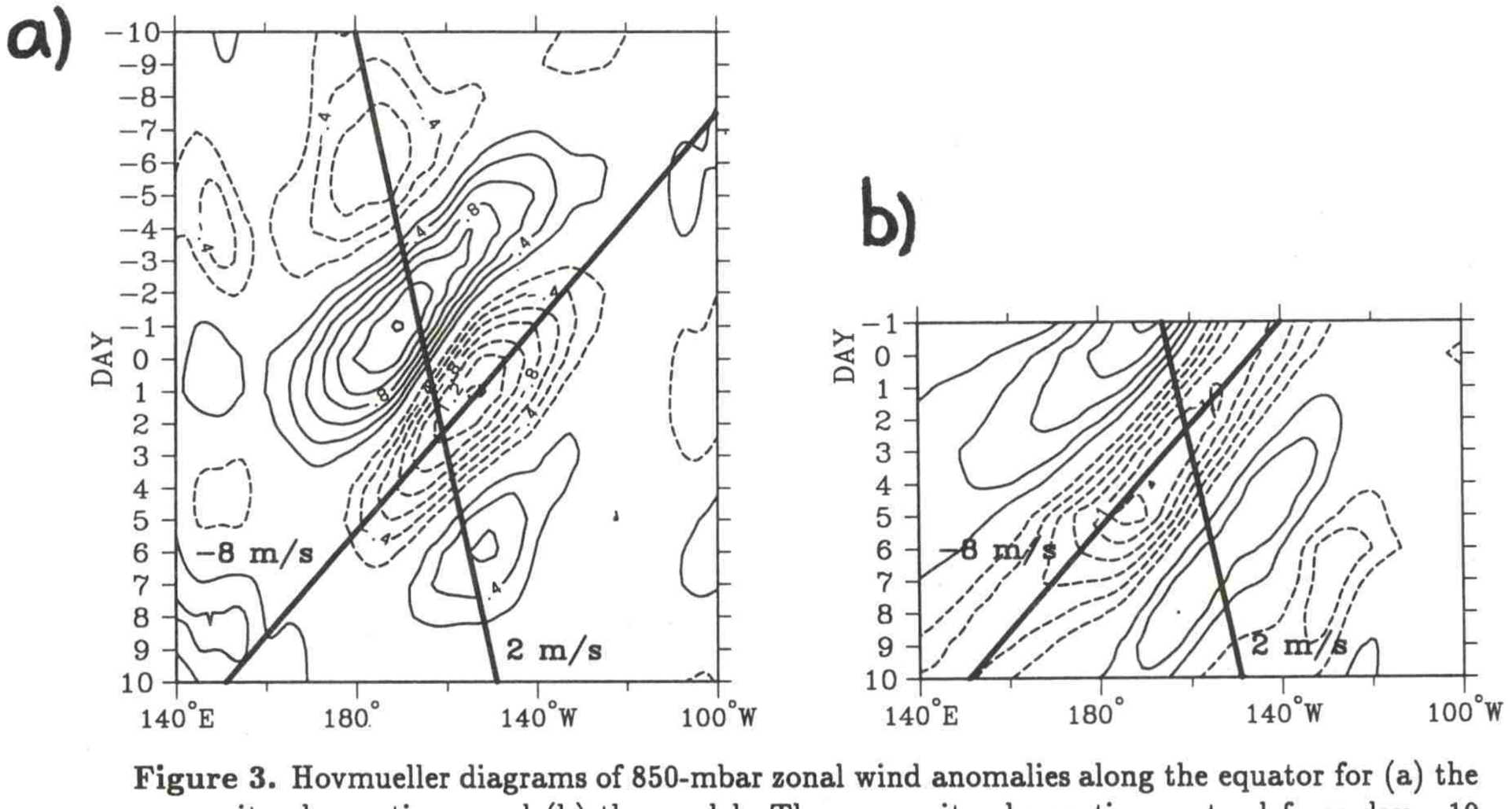

Figure 3. Hovmueller diagrams of 850-mbar zonal wind anomalies along the equator for (a) the composite observations, and (b) the model. The composite observations extend from day −10 through day +10, associated with the pattern shown in Figure 1a. Contour interval is 0.2 m s^{-1}, with negative contours dashed. The model results start at the initial condition of day -1. A phase speed line of −8 m s^{-1} and a group speed line of +2 m s^{-1} are also shown.

ON THE CLIMATOLOGICAL ANNUAL CYCLE IN GLOBAL MEAN ATMOSPHERIC SURFACE PRESSURE AND HYDROLOGY AS REVEALED BY NCEP/NCAR REANALYSIS

H. M. van den Dool, J. Schemm and S. Saha
CPC&EMC/NCEP

1. INTRODUCTION

It has recently been suggested that the continuity equation for total atmospheric mass should contain the sources and sinks of water. If this suggestion is correct, the observed global mean surface pressure ought to have a seasonal cycle of almost 0.5 mb range. This is because the atmosphere is warmest in NH summer, and the water holding capacity of the atmosphere is roughly proportional to temperature. We thus expect the highest global mean pressure in July, and the lowest in January.

We use the ReAnalysis data (Kalnay et al 1996) for the years 1985-89 to show that this minute annual cycle exists, is easily detectable in every single year, and has about the expected magnitude and phase. This finding is consistent with, and expands on, earlier studies of surface pressure using previously available observational or analysed data by Trenberth (1981), Oort(1983) and Christy and Trenberth(1985). **What is new**, however, is that the E-P fields generated by ReAnalysis can be integrated in time to relate the annual variation in total mass (dry air + water vapor) quantitatively to the water sources and sinks.

To explore this issue further we also made the same calculations with an AMIP data set for 1985-89, which is a pure model integration (no interference with observations, other than SST etc). In the AMIP run a continuity equation is used such that the global mean mass is intended to be constant, but we have found that it was not constant in the AMIP output. The ReAnalyisis model (T62L28 MRF), used both for 6hr guess field in the ReAnalysis project and for the long AMIP runs, does not conserve mass exactly and has a small spurious upward trend and a spurious annual cycle. Because total mass is not conserved, water is not conserved (during advection) either.In the AMIP run, the global mean annual mean evaporation is less that the global mean annual mean precip, consistent with a spurious moisture source. In ReAnalysis just the opposite happens: evaporation exceeds precipitation, the 'increments' (i.e. data ingestion) and 'spin-up' being the usual suspects here.

2. EQUATIONS FOR GLOBAL MEAN MASS

Equation	*Nature*	*AMIP*
(1) $\frac{\partial p_*}{\partial t} = g\,[E-P]$	yes	No, $\frac{\partial p_*}{\partial t} = 0$
(2) $\frac{\partial w}{\partial t} = [E-P]$	yes	yes
(3) $\frac{\partial p_*}{\partial t} = g\,\frac{\partial w}{\partial t}$	yes	No

In the above yes(no) means that the equation should (should not) be satisfied in Nature or in AMIP. We trust that ReAnalysis is close to Nature.
In the equations w denotes precipitable water, p* surface pressure, E evaporation, P precipitation, g acceleration of gravity, and t time.
Warnings: ReAnalysis has 'increments', and AMIP and ReAnalysis have spurious mass sources and sinks. Neither are shown in the equations.

3. RESULTS

Fig 1a shows the annual cycle of surface pressure, based on 12 monthly values, each of which is a global mean averaged over 5 years. Relative to the annual mean (984.92 mb) we notice a well-defined annual cycle with a maximum in July, and a minimum in December or January. The range is about 0.40 mb. Fig 1a is the five year average of the time series in Fig 1b (solid line). The annual variation in p* is clear in each single year. The dash-dotted line in Fig 1b represents AMIP. A spurious upward trend (0.75 mb in 5 years) and a spurious annual cycle are produced in this climate run.

Fig.2a shows the climatology of E-P in mm/day, after adjustment. Adjustment means that we made the global annual mean of E-P zero by a season independent correction constant which is different for AMIP and ReAnalysis. This may not be quite right because the spurious mass production has an annual cycle (see Fig.1b). But it does allow an integration in time, the result of which is shown in Fig 2b (ReAnalysis only). The solid line is the same as Fig. 1a, the 'observation' of p*, the dashed line is the theoretical prediction of p* based on E-P, and borrowing the global mean annual mean of p* from Fig 1a. These curves are remarkably similar, particulary from January to July. As long as [E-P] > 0, p* increases and by an amount that is confirmed by surface pressure readings. The decline in p* from July to December shows only modest agreement - [E-P] < 0 suggests a faster and deeper drop in p* than is observed.

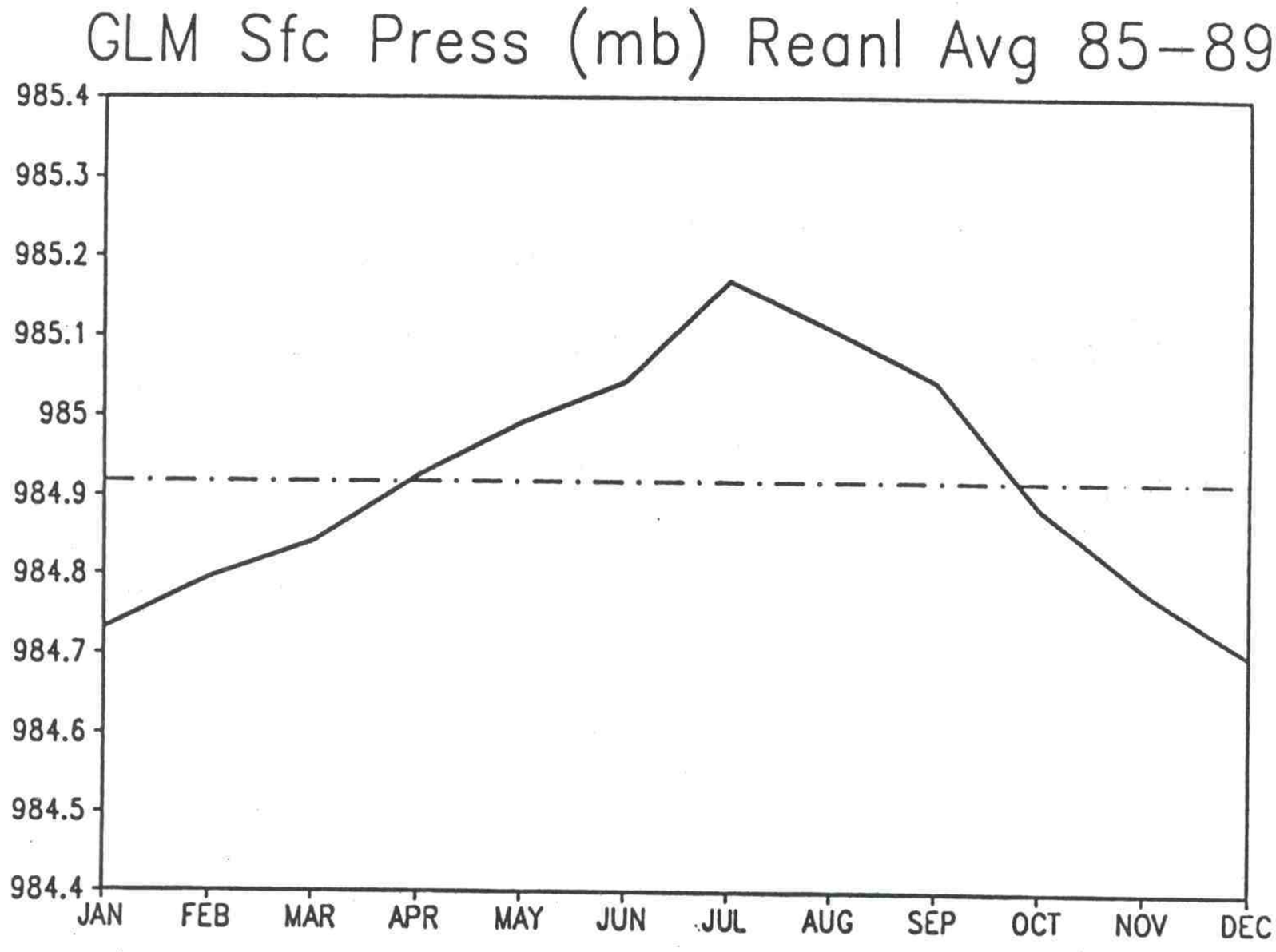

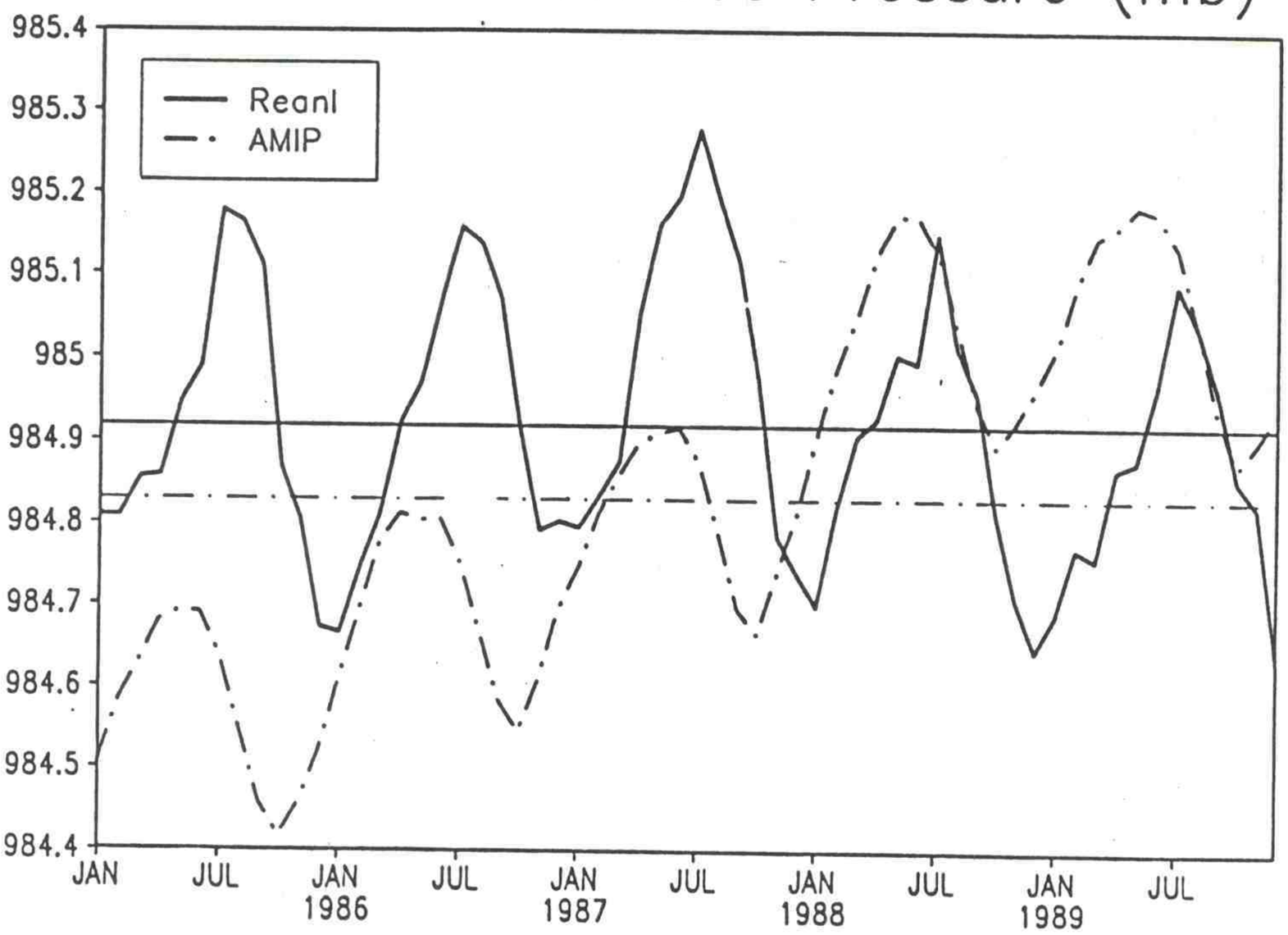

Fig 1. Global, mean monthly surface pressure in mb. **Upper (Fig 1a)**:1985-89 ReAnalysis climatology + annual mean (straight line). **Lower (Fig 1b)**: 1985-89 monthly time series for ReAnalysis (solid) and AMIP (dash dot) and their respective averages (straight lines).

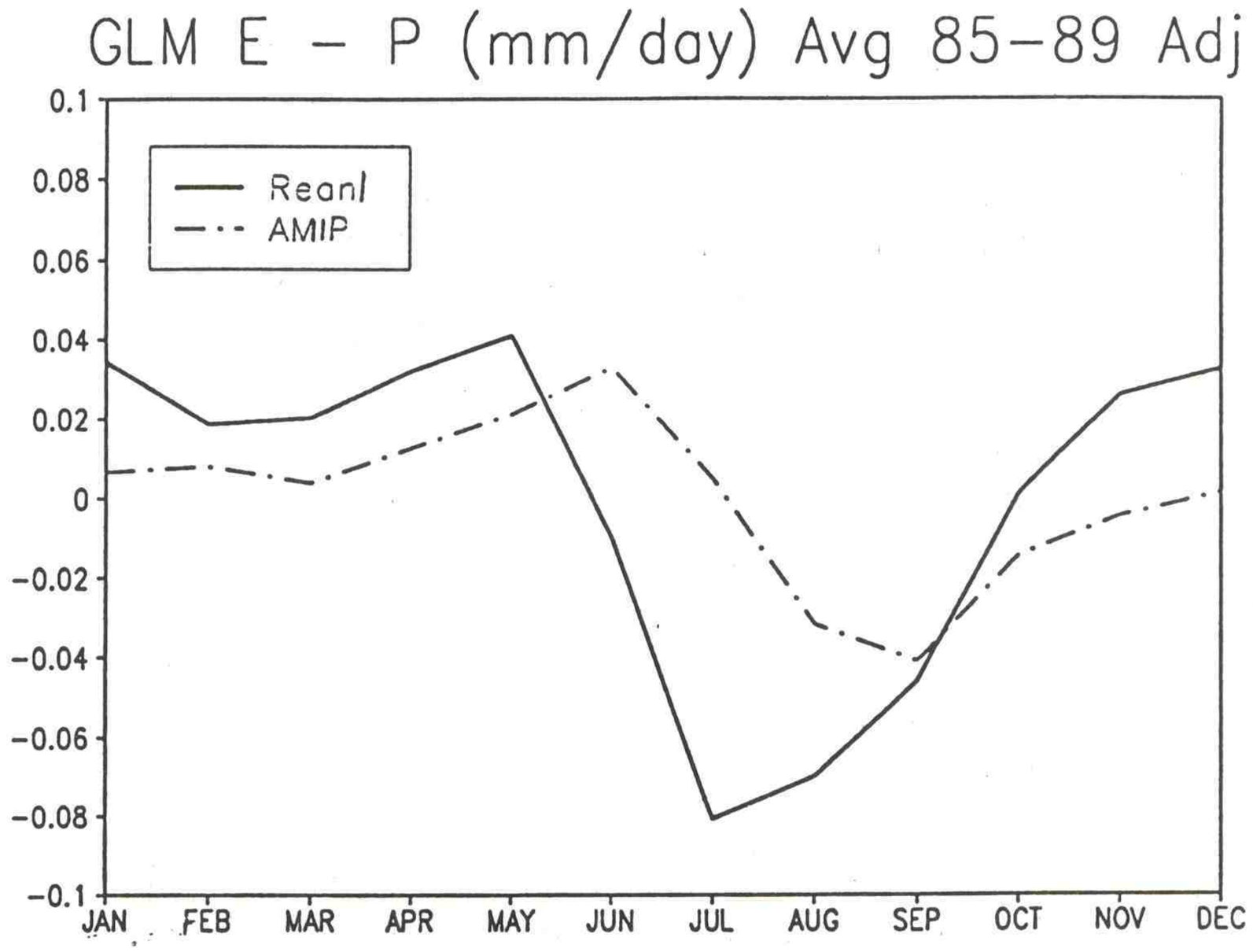

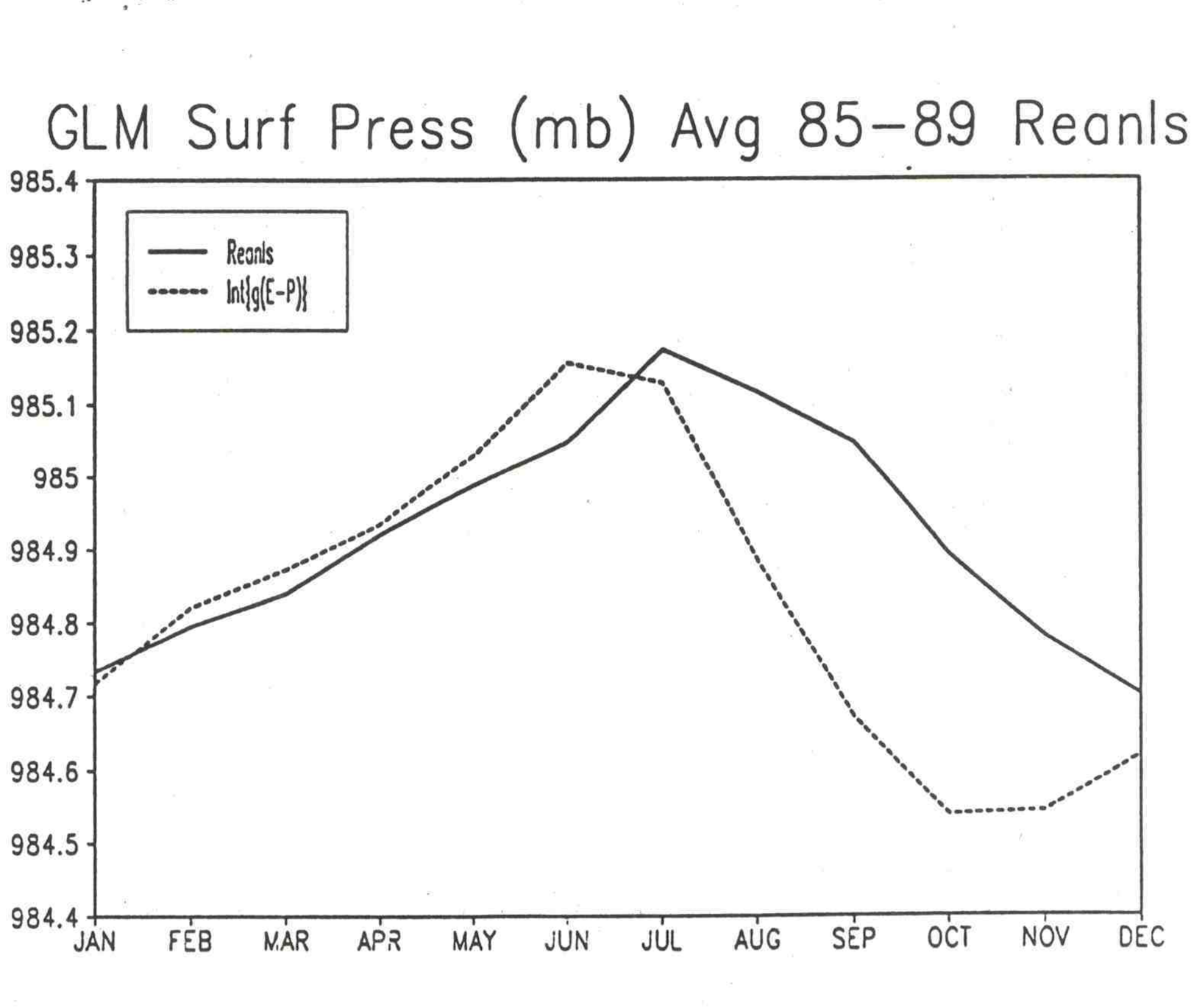

Fig.2 **Upper (Fig 2a)**: 1985-89 climatology of E-P (mm/day) after adjustment. ReAnalysis full line, AMIP dash dot. **Lower (Fig 2b)**: Global mean pressure calculated by integrating [E-P] (dashed) and observed from ReAnalysis (full, same as Fig 1a).

POTENTIAL VORTICITY FLUX DIAGNOSTICS OF THE WINTER MEAN CIRCULATION USING TWO REANALYSIS DATASETS

Jeffrey S. Whitaker and Andrew F. Loughe
CIRES, University of Colorado, Boulder, CO

1. INTRODUCTION.

The conservation and invertibility priniciples for potential vorticity (PV) make it a very useful tool for studying balanced dynamical processes in the atmosphere. However, to date, most studies have utilized PV diagnostics to study synoptic time scale phenomena such as cyclogenesis. Although the PV approach is ideal for studying the general circulation (Hoskins 1991, Haynes and McIntyre 1987) it has rarely been attempted (to our knowldege, Hoerling 1992 is the only such study). Presumably, this is because nonadvective terms in the PV budget associated with diabatic and frictional forces are essential for such studies, and these have been difficult to estimate from the previous generation of global analyses. New assimilated datasets are being produced at various centers which include estimates of unobserved quantities such as diabatic heating rates. In this study we compare some aspects of the winter mean potential vorticity budgets computed with assimilated datasets produced at the National Meteorological Center (NMC) and the NASA's Goddard Space Flight Center (NASA/GSFC). Our goal is to assess the uncertainties in the computation of the budget, especially those terms related to tropical diabatic heating rates.

2. DATA AND ANALYSIS METHODS.

The datasets used were produced by the NASA/GSFC GEOS-I and NMC/NCAR CDAS assimilation systems. For detailed information on these systems, see Schubert et al (1993) and Kalnay et al (1993). The fields used include the models' prognostic variables on sigma levels as well as parameterized quantites, such as convective diabatic heating rates and turbulent dissipation rates. The GEOS-I data are provided on 2 degree latitude by 2.5 degree longitude grid, on 20 sigma levels. The NMC/NCAR prognostic variables are stored as T62 spectral coefficients on 28 sigma levels, while the parameterized fields are output on the corresponding 192 x 94 Gaussian grid. Although both analyses have been completed for the period 1985-1993, our comparative analyses have been completed only for the period December 1985 - February 1986.

There are certain advantages to viewing the PV budget in isentropic coordinates. In particular, the flux of PV has no cross-isentropic component and therefore is purely two-dimensional in isentropic coordinates, even in the presence of diabatic and frictional effect (Haynes and McIntyre 1987). For this reason, we have chosen to interpolate the data from sigma to isentropic coordinates. The interpolation was performed linearly in Exner function for all variables except Montgomery potential (which was treated carefully to avoid created spurious gradients on isentropic surfaces), and consistency with the vertical discretization of the assimilating models was maintained where possible. There are 37 levels in the isentropic dataset, spaced every 5 K between 220 and 400 K. For this study, we will consider only those isentropic surfaces which do not intersect the earth's surface (the "middleworld" and "overworld" in the lexicon of Hoskins 1991).

3. THE PV BUDGET IN ISENTROPIC COORDINATES.

The flux form of the PV equation in isentropic coordinates is

$$\frac{\partial}{\partial t}\sigma Q + \nabla \cdot \mathbf{J} = 0, \tag{1}$$

where $Q = \frac{\zeta_\theta + f}{\sigma}$ is the PV, $\sigma = \frac{-1}{g}\frac{\partial P}{\partial \theta}$ is the isentropic mass density, $\sigma Q = \zeta_\theta + f$ is the isentropic absolute vorticity (or the amount of PV per unit volume) and **J** is the two dimensional PV flux vector given by

$$\mathbf{J} = \mathbf{v}\sigma Q - \mathbf{k} \times (\dot{\theta}\frac{\partial \mathbf{v}}{\partial \theta} - \mathbf{F}). \tag{2}$$

where **F** is the friction force per unit mass. It is implied that $\nabla = \left(\frac{1}{a\cos\phi}\frac{\partial}{\partial\lambda}, \frac{1}{a}\frac{\partial}{\partial\phi}\right)$, $\mathbf{v} = (u,v)$ and all partial derivatives are taken holding θ constant.

The vector **J** can be thought of as being composed of an advective part and a nonadvective part directly related to frictional and diabatic processes. However, for time mean conditions, even the "advective" part of **J** is partially related to diabatic effects. This can be seen by writing the time mean of $\nabla \cdot \mathbf{v}\sigma Q$ as

$$\nabla \cdot \overline{\mathbf{v}\sigma Q} = \nabla \cdot \overline{(\mathbf{v}\sigma)'Q'} + \overline{(\mathbf{v}\sigma)_\psi} \cdot \nabla \bar{Q} + \nabla \cdot \overline{(\mathbf{v}\sigma)_\chi} \bar{Q}, \tag{3}$$

where the overbar denotes a time mean, the prime denotes a transient, and the subscripts ψ and χ denote rotational and divergent parts, respectively. Taking a time mean of the isentropic mass continuity equation yields

$$\nabla \cdot \overline{(\mathbf{v}\sigma)} = -\frac{\partial}{\partial \theta}(\overline{\dot{\theta}\sigma}), \tag{4}$$

so that the divergent part of the time mean isentropic mass flux vector is directly related to diabatic heating, i. e.

$$\overline{(\mathbf{v}\sigma)_\chi} = -\nabla\left[\nabla^{-2}\frac{\partial}{\partial \theta}(\overline{\dot{\theta}\sigma})\right] \tag{5}$$

The last term in (3) represents the flux of PV by the divergent mass circulation in isentropic coordinates. This term is closely related to the "baroclinic Rossby wave source due to diabatic heating" discussed by Hoerling (1992). In that paper, Hoerling showed that analysis of this term concisely illustrates how tropical diabatic heating remotely influences the mid-latitude PV balance.

Inserting (3) into the time mean of (1), taking a zonal mean, integrating over latitude using the boundary conditions at the poles yields

$$\left\langle \overline{(\mathbf{v}\sigma)'Q'} + \overline{(\mathbf{v}\sigma)_\psi}\,\bar{Q} + \overline{(\mathbf{v}\sigma)_\chi}\bar{Q} + \overline{\dot{\theta}\frac{\partial u}{\partial \theta}} - F \right\rangle = 0, \tag{6}$$

where F is the zonal wind tendency due to frictional forces, and the angle brackets denote a zonal mean. An identical result can be obtained directly from the isentropic zonal momentum equation, so (6) may be thought of as the zonal mean isentropic zonal momentum budget.

4. RESULTS FOR DECEMBER - FEBRUARY 1985/86.

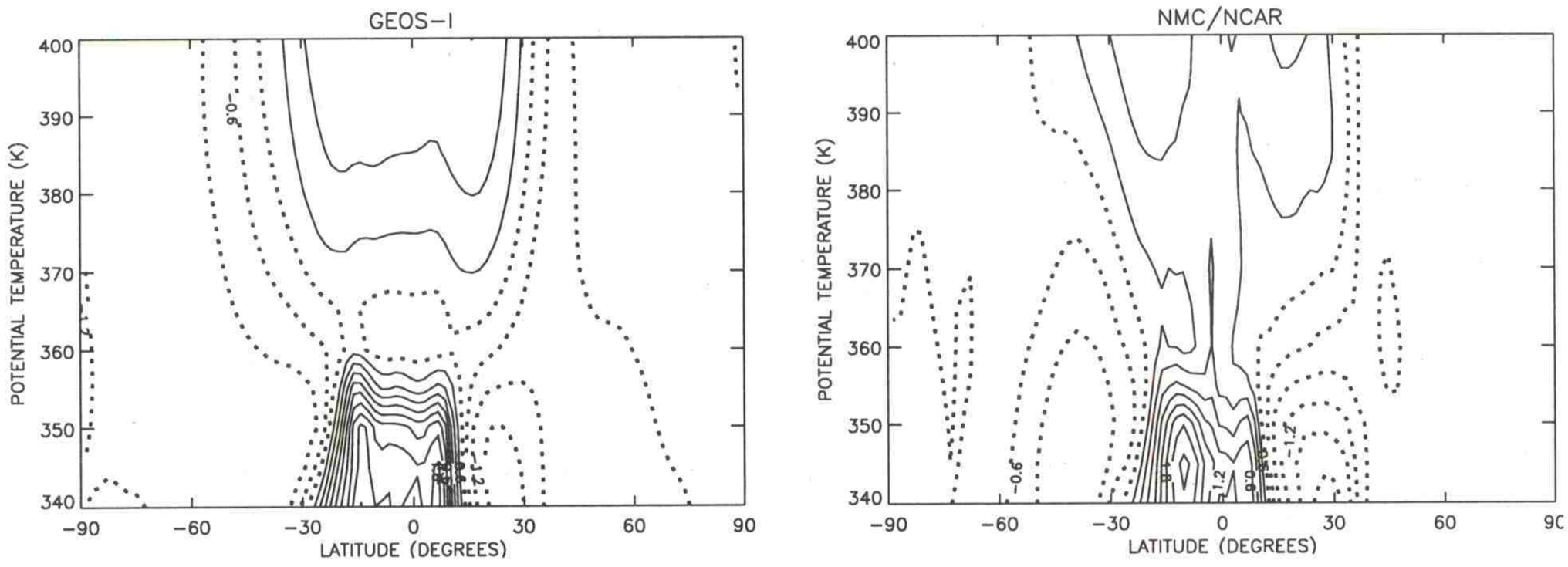

Figure 1: Zonal mean total diabatic heating rate (contour interval 0.3 day^{-1}) produced by the two assimilation systems. Only "middleworld" and "overworld" isentropes are shown (i. e. those isentropes that do not intersect the ground). For reference, the 350 K isentrope is located at about 200 mb on the equator and 175 mb at 60°N.

Fig. 1 shows the zonal mean diabatic heating rates for Dec-Feb 1985/86, produced by the two assimilation systems and interpolated to isentropic coordinates. Only above-ground isentropic levels (> 335 K) are plotted in this and all figures to follow. The two assimilation systems produce qualitatively similar heating fields, with the GEOS-I system producing slightly stronger upper tropospheric convective heating in the tropics, and the NMC/NCAR system producing slightly stronger radiative cooling in the subtropics.

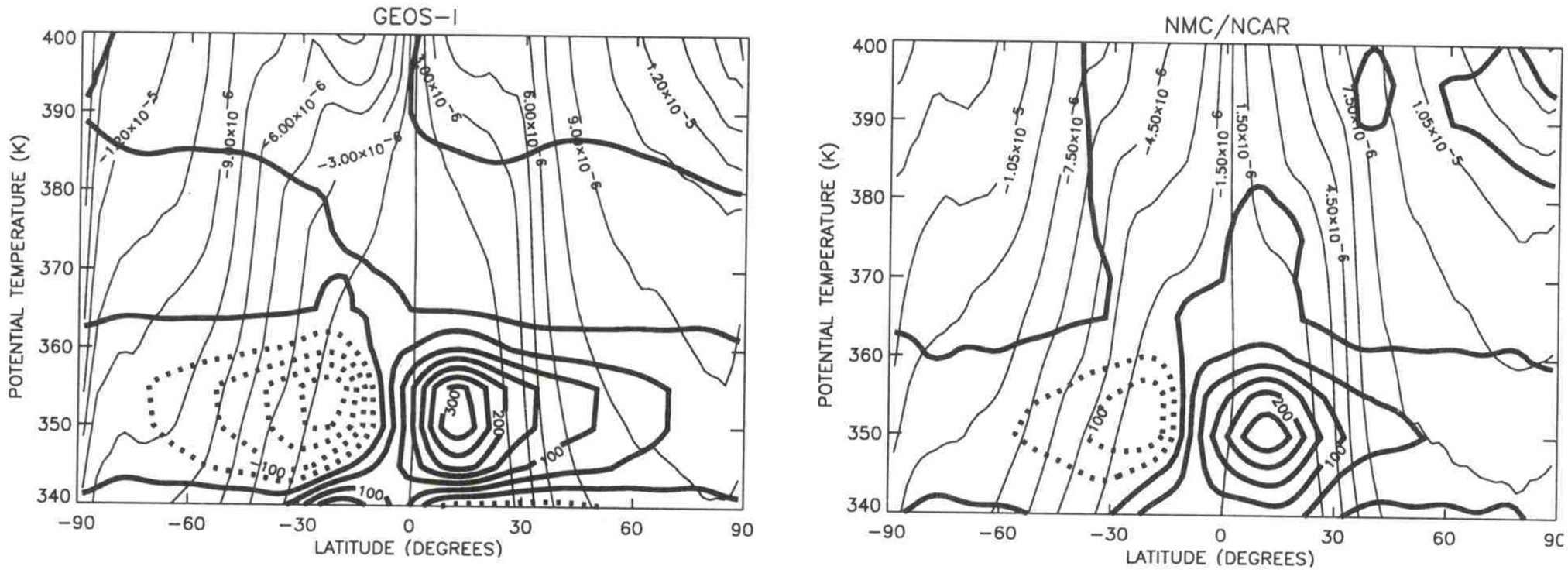

Figure 2: Zonal mean potential vorticity (thin solid, contour interval 1.5 x 10^{-6} $m^2 s^{-1}$ K kg^{-1}) and zonal mean meridional divergent mass flux (thicker contours, interval 50 m^{-1} s^{-1} K^{-1} kg).

Subtle but important differences in the vertical structure of the heating fields become more apparent when the zonal mean isentropic mass flux (computed using (5)) is examined. This quantity is plotted in Fig. 2, along with contours of mean PV. Associated with a stonger vertical gradient of diabatic heating in the tropical upper troposphere, the GEOS-I system clearly has a stronger poleward mass circulation.

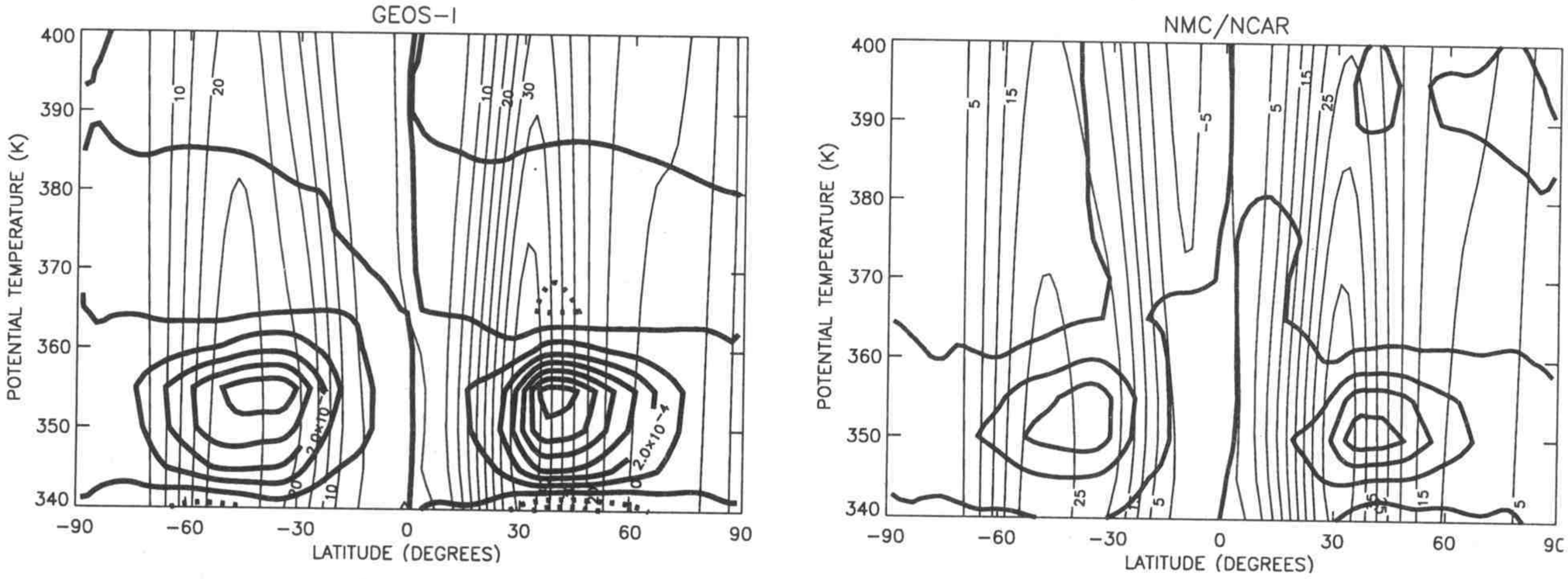

Figure 3: Thin countours are zonal mean zonal wind (contour interval 5 ms^{-1}). Thick contours are zonal mean flux of mean PV by the meridional divergent mass flux (contour interval 1 x 10^{-4} ms^{-2}).

The flux of mean PV by the divergent mass circulation (the third term in equation 6) is shown in Fig. 3, along with the zonal mean zonal wind. The remote effect of tropical diabatic heating on the time mean mid-latitude budgets of PV, and zonal mean zonal wind, is clearly stronger by a factor of two in the GEOS-I analysis. The term associated with cross-isentropic advection of momentum in (1) and (6) is very small outside of the tropics, so that the dominant influence of diabatic heating in the PV budget is through the flux of mean PV by the mean divergent mass flux. In mid-latitudes, this term is balanced principally by eddy fluxes. In other words, the equatorward flux of PV associated with transient eddy activity is approximately balanced by the effect of the poleward mean mass flux

associated directly with diabatic heating. From this perspective, the isentropic mass circulation associated with diabatic heating is trying to rearrange the PV in isentropic layers such that there is dilution at low latitudes and concentration at high latitudes, while the transient eddies are trying to do the opposite. We use the terms "dilution" and "concentration" here since we are discussing only those isentropic layers which do not intersect the ground, so that as a consequence of (1), the total PV per unit volume can neither be created or destroyed within that layer, only rearranged by advective, frictional and diabatic processes (Haynes and McIntyre 1987).

5. SUMMARY.

There are significant differences between the mean PV budgets computed using the GEOS-I and NMC/NCAR reanalysis products, particularly in those terms associated with tropical diabatic heating. In particular, the GEOS-I analysis of diabatic heating implies a much stronger poleward isentropic mass flux, which in turn implies a much stronger tendency for low-PV tropical air to be exported into the extratropics by the isentropic mass circulation. Comparison of the winter mean zonal mean jets and the associated zonal mean isentropic PV gradient at the tropopause produced by the two analysis systems (not shown) indicates that, relative to the NMC/NCAR analysis, both fields are displaced very slightly poleward in the GEOS-I analysis. This is consistent with the expected effect of the enhanced meridional isentropic mass circulation in the GEOS-I assimilation system. If we use the difference between the two analyses as a lower bound on uncertainty, then it appears we can only estimate the effect of diabatic heating in the mean PV budget to within a factor of two. However, if more accurately analyzed quantities which are relatively insensitive to the effects of parameterized diabatic heating in the assimilating model (such as PV and the rotational mass flux) are used to infer the diabatic heating rates in the two analyses, the agreement, and hopefully the accuracy of the estimate, should be improved. This is the spirit of the "χ problem" (Sardeshmukh 1993), and work is underway to apply this technique to the two reanalysis datasets. In addition, we are currently peforming comparisons of interannual variations of the "baroclinic Rossby wave source" associated with ENSO.

ACKNOWLEDGMENTS

This work was made possible through funding from NASA grant 5-2919 and the NOAA Office of Global Programs.

REFERENCES

Haynes, P. H., and M. E. McIntyre, 1987: On the evolution of vorticity and potential vorticity in the presence of diabatic heating and fricitional or other forces. *J. Atmos. Sci.*, **44**, 828-841.

Hoerling, M. P , 1992: Diabatic sources of potential vorticity in the general circulation *J. Atmos. Sci.*, **49**. 2282-2292.

Hoskins, B. J., 1991: Towards a PV-θ view of the general circulation. *Tellus*, **43**, 27-35.

Kalnay, E., M. Kanamitsu, R. Kistler, W. Collins, D. Deavan, L. Gandin, S. Saha, G. White, J. Woollen, Y. Zhu; M. Chelliah, W. Ebisuzaki, J. Janowiak, K.C. Mo, C. Ropelewski, J. Wang; A. Leetmaa, R. Reynolds; and R. Jenne, 1993: The NMC/NCAR CDAS/Reanalysis Project. *NMC Office Note 401*. Available from NMC.

Sardeshmukh, P. D., 1993: The baroclinic χ problem and its application to the diagnosis of atmospheric heating rates. *J. Atmos. Sci.*, **50**, 1099-1112.

Schubert, S. D., R. B. Rood, and J. Pfaendtner, 1993: An assimilated dataset for earth science applications. *Bull. Amer. Meteor. Soc.*, **74**, 2331-2342.

INTERACTION OF TROPICAL HEATING-INDUCED ATMOSPHERIC FLOW WITH MIDLATITUDE OROGRAPHY

Eric DeWeaver and Sumant Nigam
Department of Meteorology, University of Maryland, College Park, MD 20742-2425

1. INTRODUCTION

In observations and simulations, El Niño-related tropical heating anomalies can produce a global atmospheric response. However, the vorticity perturbations forced directly from the equatorial Pacific cannot by themselves explain the associated extratropical climate anomalies: to generate such teleconnected anomalies, the directly forced perturbations must undergo secondary interactions with other components of the climate system. One type of interaction which has received little modeling attention is orographic interaction. As the far-field response to tropical heating has an equivalent barotropic vertical structure, a barotropic model that includes orographic stretching is used to assess the impact of this interaction. For a realistic distribution of El Niño-related tropical divergence, orographic stretching, occurring primarily in the Himalayan/Tibetan region, generates 200 hPa geopotential height anomalies in excess of 40 m in the Pacific/North American sector. The associated zonal wind anomalies in the central Pacific (~5 m/sec) extend the East Asian jet southeastward, as is typical in El Niño winters. The orographic modulation in this model is relatively insensitive to the longitudinal location of the tropical divergence anomaly.

2. METHODOLOGY

To examine the forcing of circulation anomalies accompanying El Niño events, we attempted to simulate the difference in upper-level rotational flow between recent El Niño and La Niña winters using a spectral divergent steady-state barotropic model (Held and Kang, 1987). Specifically, we simulated the 200 hPa streamfunction (Ψ_{200}) differences between the 1987/1988 (El Niño) and 1988/1989 (La Niña) winters. In barotropic diagnoses, the forcing consists of transient vorticity-flux convergence and horizontal divergence fields. The former was calculated from the European Centre for Medium Range Weather Forecasts' (ECMWF) twice-daily operational analyses on a 2.5° latitude-longitude global grid. The horizontal divergence at 200 hPa was obtained both from the ECMWF-analyzed winds and residual diagnoses using

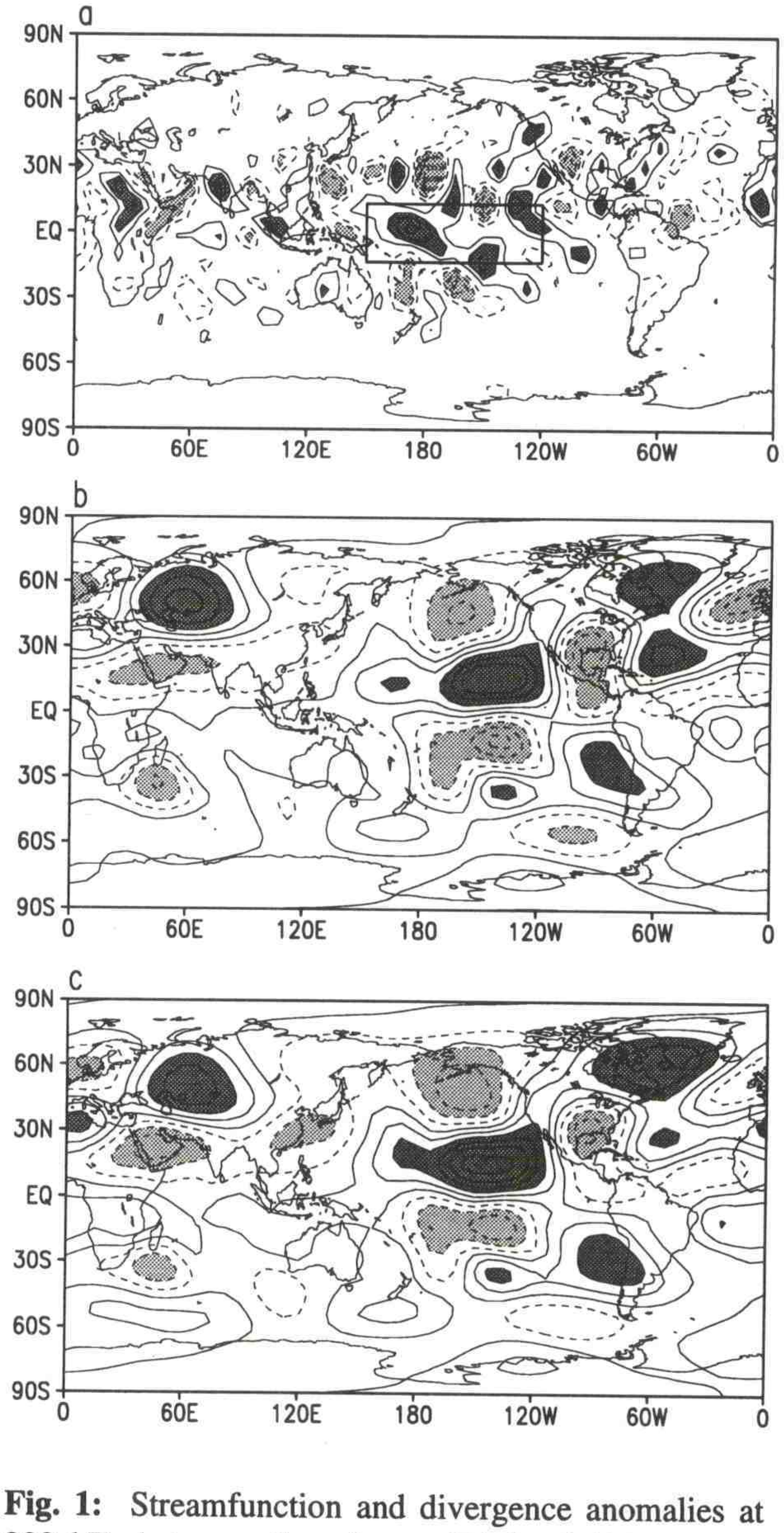

Fig. 1: Streamfunction and divergence anomalies at 200 hPa between the winters (DJF) of 1987/88 and 1988/89. (a) χ-derived divergence anomaly (10^{-6} s^{-1}) with zero contour suppressed, and dark (light) shading for positive (negative) anomalies in excess of $2x10^{-6}s^{-1}$; (b) simulated eddy Ψ_{200} anomaly; (c) eddy Ψ_{200} anomaly from ECMWF analyses. Contour interval is $3x10^6$ m^2 s^{-1}, and values greater (less) than $\pm 6x10^6$ m^2 s^{-1} are heavily (lightly) shaded in (b) and (c).

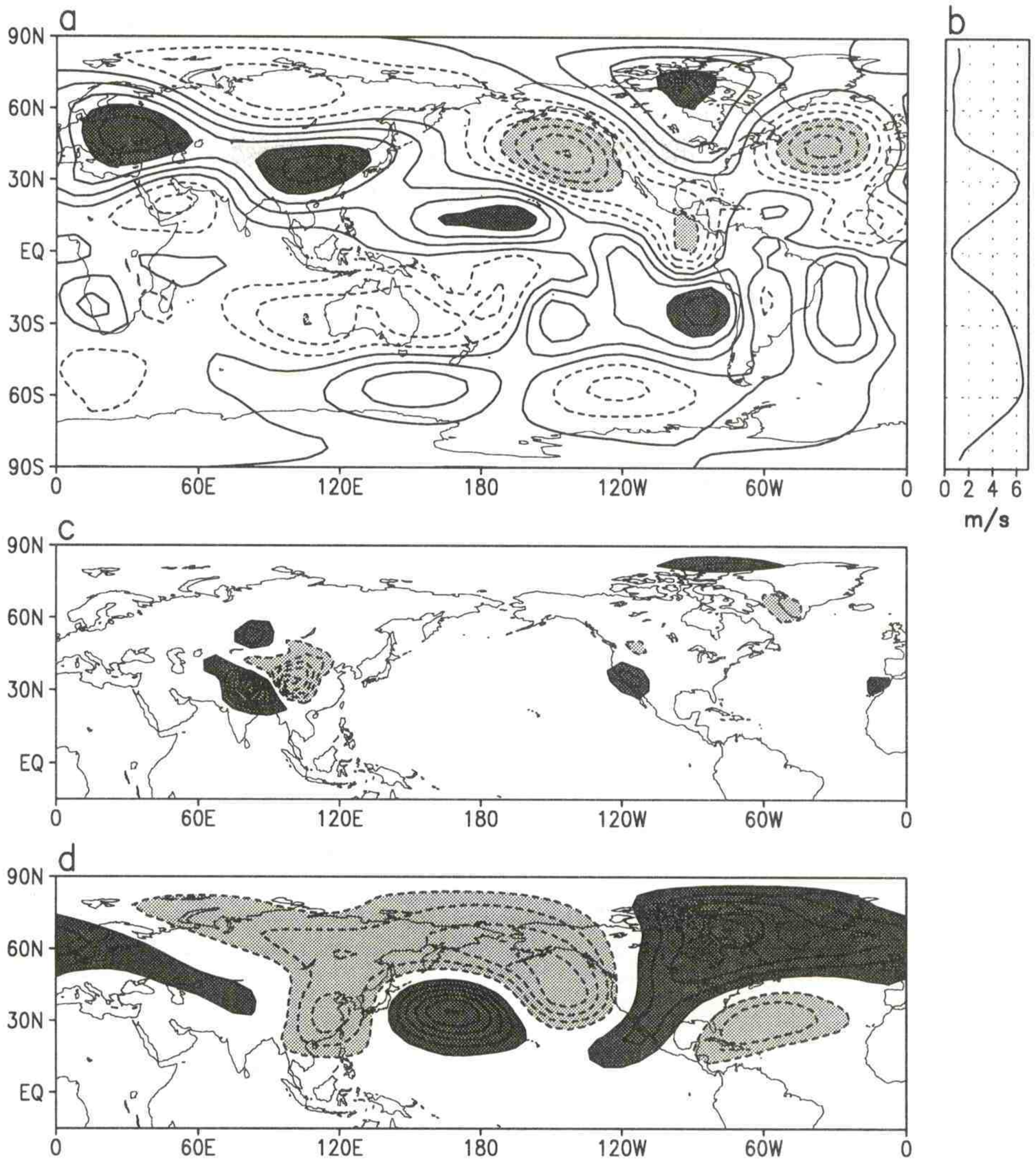

Fig. 2: Model's response to El Niño-related divergence. **(a)** eddy response to divergence in the rectangular region marked in Fig. 1a, with a contour interval of $2x10^6$ m^2 s^{-1} and dark (light) shading for positive (negative) anomalies in excess of $6x10^6$ m^2 s^{-1} ; **(b)** zonal-mean zonal wind corresponding to the solution shown in (a); **(c)** divergence (D in text) generated by the interaction of solutions shown in (a) and (b) with orography, with a contour interval of $2x10^{-7}$ s^{-1} and dark (light) shading for positive (negative) anomalies in excess of $2x10^{-7}$ s^{-1} ; **(d)** eddy response to the divergence in (c), with a contour interval of $1x10^6$ m^2 s^{-1} and dark (light) shading for positive (negative) anomalies in excess of $1x10^6$ m^2 s^{-1} .

the χ-algorithm (Sardeshmukh, 1993). Circulation anomalies were modeled between contrasting winters using a zonally-varying basic state that is the average of the two periods: when the problem is formulated in this manner, the resulting anomaly equation is automatically linear, without neglecting any terms (Schneider, 1988). Thus although the steady model is posed as a linear matrix equation, the anomaly solution is nonlinearly accurate.

Fig. 1 displays the model simulation. The divergence anomaly (panel a), obtained from the χ-algorithm using ECMWF-analyzed divergence as the first guess, has a positive feature over the equator near the dateline, in agreement with the El Niño-related OLR and SST anomalies. The vigorous subsidence over the subtropical north central Pacific is the most significant modification of the first-guess field in the χ-iteration. The model's Ψ_{200} response to forcing by global χ-divergence and anomalous vorticity transients (not shown) is shown in panel (b), while the corresponding observed Ψ_{200} anomaly is shown in panel (c). A pair of anticyclones straddling the equator east of the dateline—a tropical feature characteristic of El Niño

winters—is evident both in observed and simulated anomalies. Extratropical anomalies, including the troughs centered over the Aleutians and the Gulf of Mexico, are also well simulated. χ-divergence and Ψ_{200} simulations are obtained with R15 truncation using (5 day)$^{-1}$ linear dissipation and a fourth-order diffusion coefficient of 1×10^{16} m^{4}s^{-1}.

3. OROGRAPHIC MODULATION OF THE RESPONSE TO TROPICAL HEATING

Having simulated the global streamfunction anomaly, we use the diagnostic model to determine how anomalous forcing from a particular geographic region contributes to the generation of global anomalies. The geographic region of greatest interest is of course the central/eastern tropical Pacific (the rectangular box in Fig. 1a) where the El Niño-related heating is strongest. Fig. 2a shows the model response when forced exclusively by the divergence in the rectangular box in Fig. 1a. To avoid spurious rotational effects, particularly in the zonal-mean response, the global mean of the divergence anomaly is set to zero when obtaining these solutions. The response shown here is quite similar to the model response when forced by the entire tropical strip, or, for that matter, by the idealized source used in Fig. 4.

An interesting feature of Fig. 2a is that both the zonal-mean and eddy winds have large amplitude in mountainous regions. Furthermore, as the mountains are in the far field of the El Niño-related divergence, the tropically forced flow perturbations can be assumed to be equivalent barotropic over the mountains (Held, 1983). In that case, the divergence D due to orographic uplift can be estimated in an off-line calculation by blowing scaled-down winds over the mountains: $D = \alpha \, \vec{V}_\psi \cdot \vec{\nabla} h \, / \, (H_o - h)$. Here H_0 =8 km is the scale height of the atmosphere, h is the height of the mountains, and V_ψ is the tropically forced rotational wind anomaly, scaled down by a factor α=0.3. Fig. 2b shows the orographic divergence D, while Fig. 2c shows the model's response to D. To ensure that the interaction with orography occurs in the far-field, the orographic divergence in panel (c) is obtained with midlatitude mountains only (θ>25°N), although the response to divergence generated by global orography is not substantially different.

The response to D contains large-scale features in the Pacific/North American sector (e.g., the low over the Gulf of Alaska and the ridge extending across North America from Baja California to Greenland) that could substantially modify the directly forced extratropical wave pattern. Furthermore, the zonal wind anomaly associated with this streamfunction perturbation (not shown) is located in the central Pacific, overlapping the eastward end of the East Asian jet. Thus the zonal wind anomaly acts to extend the East Asian jet southeastward, as is typical in El Niño winters. The strength of the orographically induced rotational flow is about one third that of the flow forced directly from the tropics.

4. INCLUDING OROGRAPHIC EFFECTS IN THE LINEAR OPERATOR

The model presented thus far has been a completely literal representation of our physical intuition: tropical heating excites the primary wave pattern, which impinges on the mountains, generating, in a separate calculation, a secondary response which has no further interaction with orography. Although well motivated, this model has an ad hoc character which is both undesirable and unnecessary. A more general model can easily be constructed by including the orographic divergence D in the linear operator rather than treating it as external forcing. When orography is represented explicitly in the time-mean divergent barotropic equation, the resulting stretching term

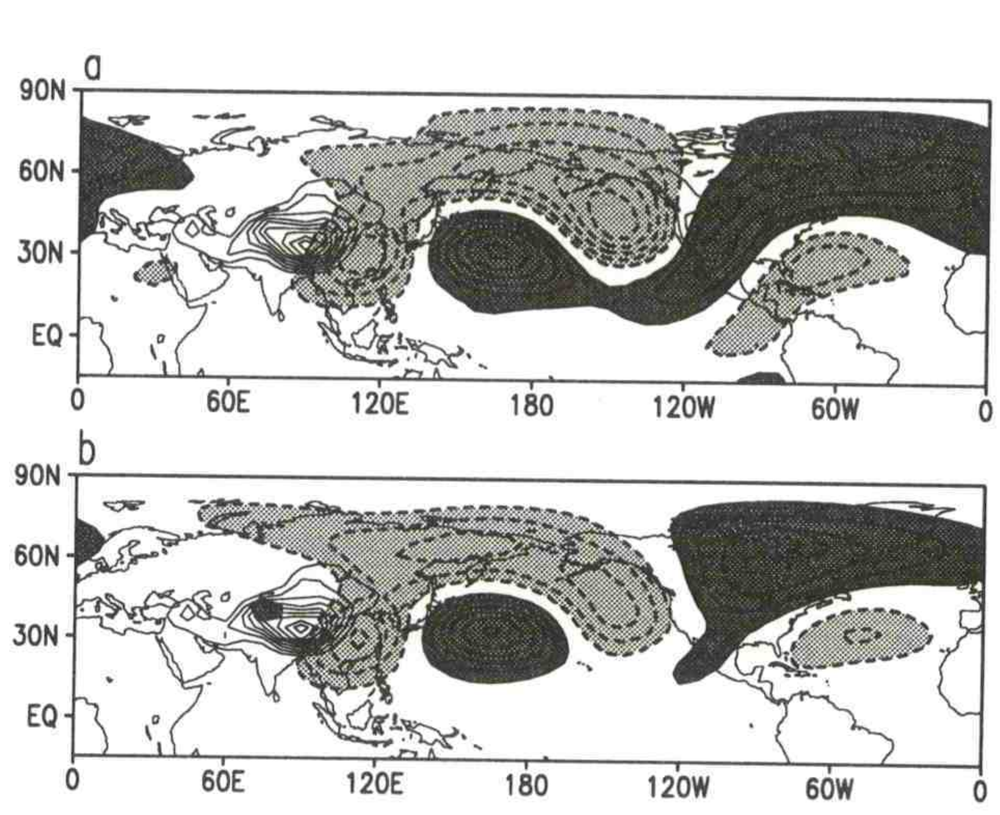

Fig. 3: Modulation of the response to El Niño-related divergence as simulated by a barotropic model with orographic stretching in the operator. **(a)** modulation by extratropical (θ>25°N) mountains; **(b)** modulation by the extratropical eastern hemisphere ($\lambda \leq 180$°E) orography. Contour interval is 1×10^6 m^2 s^{-1} and dark (light) shading is for positive (negative) anomalies in excess of 1×10^6 m^2 s^{-1}. Thin solid lines contour orography in intervals of 500m starting at 500m.

$S = (\nabla^2\psi + f)\,\alpha\,\vec{V}_\psi \cdot \vec{\nabla} h / (H_o - h)$ is quadratic in ψ. However, as the anomaly model is formed by taking the difference between the time-mean equations for the two seasons, the anomalous stretching term is linear in the streamfunction anomaly (Schneider, 1988). With this term in the operator, the model can be written as a single equation which includes both the primary forcing by El Niño-related divergence and the secondary effect of orographic modulation.

Fig. 3a shows the orographic modulation as simulated by the new model. We display the difference between the solution for α=0 (without orographic modulation) and the solution for α=0.3. This difference map is remarkably similar to the secondary wave pattern of Fig. 2d. The similarity suggests that the wave pattern of Fig. 2d has little further interaction with orography, although the new model does allow for such interactions. Further analysis reveals that the anomaly pattern of Fig. 3a is generated primarily by the interaction of the zonally-asymmetric flow with orography. Fig. 3b shows the contributions of the eastern hemisphere orography to the pattern in Fig. 3a. This figure shows the Himalayan/Tibetan complex to be the major locus of orographic interaction. This result is somewhat surprising, given that the primary wavetrain of Fig. 2a appears to impinge more directly on the North American land mass.

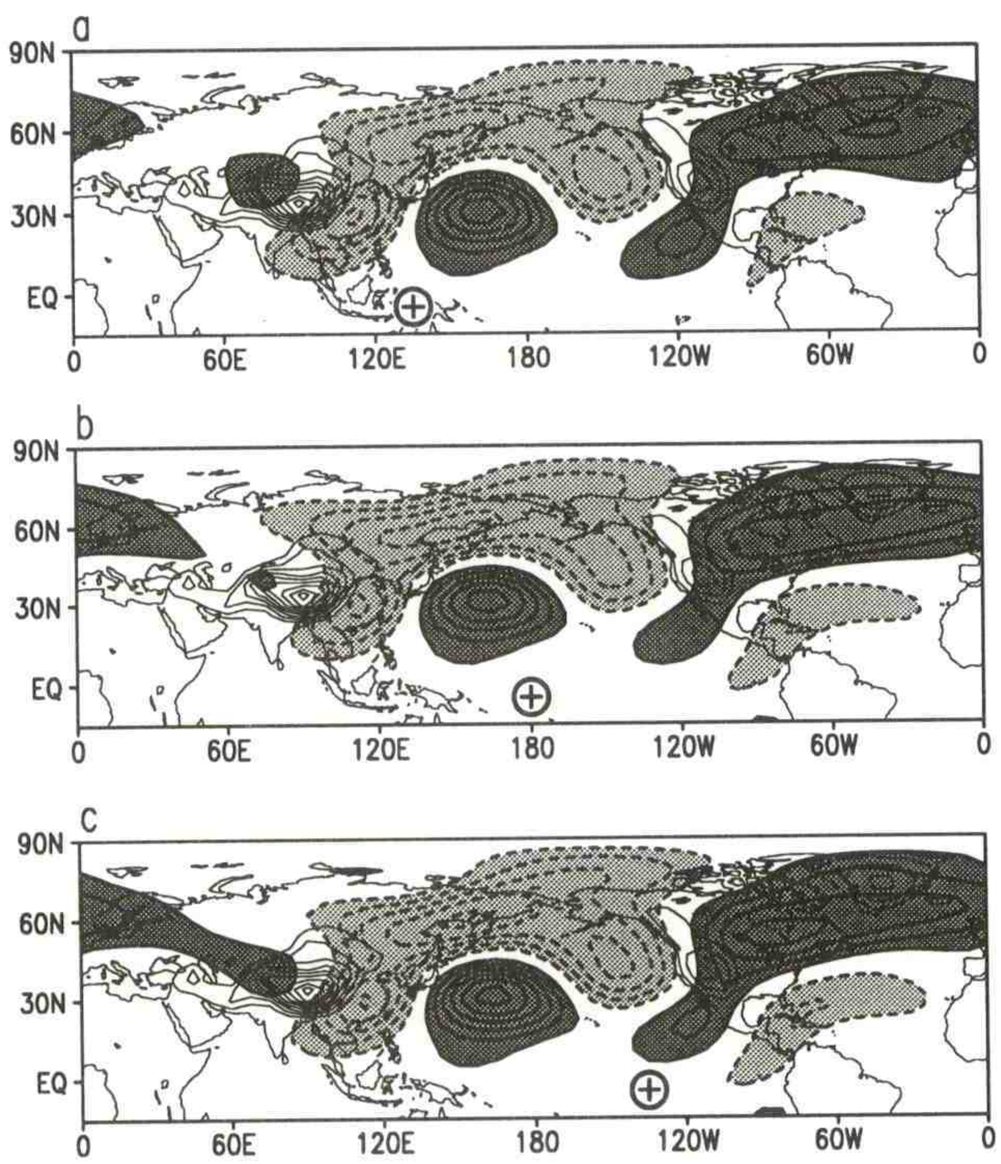

Fig. 4: Modulation of the response to an idealized tropical divergence anomaly placed at 5°S and longitudinally at **(a)** 135°E, **(b)** 180°, and **(c)** 135°W by extratropical (θ>25°N) mountains. Contour interval and orographic contouring as in Fig. 3. Divergence anomalies are ellipses centered on the "+" sign in each panel, with zonal and meridional extent of 60° and 20°, respectively, and maximum amplitude of 6×10^{-6} s^{-1}.

4. SENSITIVITY TEST

In modeling studies, the tropically forced wave pattern over the Pacific/North American sector is relatively insensitive to the longitudinal position of the tropical divergence anomaly (Geisler et al., 1985). However, if the primary wave pattern in the Himalayan-Tibetan region were sensitive to the longitudinal position of the tropical divergence (heating) anomaly, the orographic modulation would be sensitive as well. To ascertain this sensitivity, we performed an experiment in which an idealized tropical divergence anomaly was placed in the equatorial Pacific at three different longitudes. From results shown in Fig. 4, it is clear that even when the divergence anomaly shifts across the Pacific from 135°E to 135°W, the orographic interaction generates anomalies which are qualitatively quite similar. The insensitivity to the heat source location is inherited from the primary wave pattern.

REFERENCES

Geisler, J.E., Blackmon, M.L., Bates, G.T. & Munoz, S., 1985: Sensitivity of January climate response to the magnitude and position of equatorial Pacific sea surface temperature anomalies. *J. Atmos. Sci.*, 42, 865-883.

Held, I.M., & Kang, I.-S., 1987: Barotropic models of the extratropical response to El Niño. *J. Atmos. Sci.*,44, 3576-3586 (1987).

Held, I.M., 1983: in *Large-Scale Dynamical Processes in the Atmosphere* (eds Hoskins, B.J. & Pearce, R.P.) 127-168 (Academic Press, New York, 1983)

Sardeshmukh, P.D., 1993: The baroclinic χ problem and its application to the diagnosis of atmospheric heating rates. *J. Atmos Sci.*, 50, 1099 - 1112.

Schneider, E. K., 1988: A formulation for diagnostic anomaly models. *Pure Appl. Geophys.*, 126, 137-140.

INTRASEASONAL TIME SCALES OF CONVECTION IN GCMs

Kenneth.R. Sperber[1] and Julia M. Slingo[2]

[1]Program for Climate Model Diagnosis and Intercomparison
Lawrence Livermore National Laboratory
P.O. Box 808, L-264, Livermore, CA 94551

[2]Department of Meteorology, Reading University
2 Earley Gate, Whiteknights, P.O. Box 239
Reading, RG6 2AU, United Kingdom

Recently, Slingo et al. (1996) evaluated the ability of 15 atmospheric general circulation models to simulate intraseasonal oscillations as part of a coordinated effort to investigate "Synoptic to Intraseasonal Time Scales" in models participating in the Atmospheric Model Intercomparison Project (AMIP, Gates 1992). From examination of daily upper tropospheric velocity potential and zonal wind (10^oN-10^oS averaged) from the 10-year simulations we have found that no model has successfully captured the dominance of the intraseasonal oscillation (IO). When compared with the velocity potential wave number 1 power spectra from ECMWF analyses, all models fail to capture the observed broad spectral peak of 50-70 days. In most cases the variance at IO time scales is too weak while the models have a tendency to generate too much power (relatively) at higher frequencies. Also, they fail to properly partition the variance between eastward and westward modes. These shortcomings lead to IO propagation that is less coherent than observed. However, there are limited periods when a subset of the models exhibit IO variations that have reasonable periodicity and amplitude, and it is such cases that we concentrate on here to evaluate the ability of the models to simulate the convective evolution of the IO.

November 1987 through May 1988 was observed to be a period of particularly active intraseasonal variability (Matthews et al. 1996), which can be seen in the time-longitude plot of 20-100 day bandpass filtered upper-level velocity potential from ECMWF analyses, shown in Fig. 1. As we are interested in the convective response to passage of the active phase of the IO in the vicinity of the Austral monsoon, we average the filtered velocity potential between 100^o-140^oE to create a time series of IO variability. This IO index is then correlated with seasonally detrended observed OLR. The correlations are computed using pentad averaged IO indices and OLR data at various lags to investigate the evolution of the convective response. To concisely represent this, in Fig. 1 we plot the lag at which the positive correlation (which indicates enhanced convection) between the IO index and the OLR is a maximum. Data is plotted at only those gridpoints at which the coefficient of correlation is significant at $\geq$95% confidence level. Clearly, at negative time lags the enhanced convection occurs to west of region from which we obtained our IO index, and subsequently the convective envelope propagates eastward, extending over Australia and influencing the SPCZ. While the spatial extent of the convective envelope varies somewhat from year to year, it consistently exhibits contiguous eastward propagation from the Indian Ocean through to the Maritime Continent.

The IO displays considerable interannual variability in its activity and, although Slingo et al. (1996) noted a possible link between the strength of the IO and the phase of ENSO, there was little indication from the models that the activity of the IO was systematically modulated by variations in the tropical SSTs. Thus, in order to show the models in their best light, we have examined all winters and selected that during which the IO was strongest and most coherent.

Results from the GLA and UKMO, two models that exhibited the best IO variability of those examined by Slingo et al. (1996), are also shown in Fig. 1. The simulated time-longitude plots of their filtered upper-level velocity potential exhibit similar characteristics relative to the observations, but their convective responses are quite different in that both models fail to represent the coherent eastward convective evolution from the Indian Ocean to the Maritime Continent (this shortcoming also occurs in other years of the simulations, and is also seen in seasonal variance statistics on IO time scales). While they do exhibit eastward propagation of convection from the Maritime Continent into the western Pacific, the extent of the convective envelope is much more latitudinally confined than observed. Models with the weakest IO variability failed to simulate significant and coherent convective evolutions.

We wish to obtain further insight regarding the behavior of the intraseasonal oscillation in the strong versus weak models. If the IO is viewed as a moist Kelvin wave maintained by diabatic heating, as the current paradigm suggests, then models with reduced precipitation in the central Pacific will have conditions in which the wave is more quickly dissipated, and are thus less likely to maintain eastward propagation. To investigate this supposition we have considered the relationship between precipitation and SST in the region 140°E-180°W, 0°-20°S during December-January-February since SSTs in excess of 29°C are found in this region. Figure 2a shows the DJF SST climatology during the AMIP decade (1979/80-1987/88), and Fig. 2b shows the scatter plot of MSU rainfall versus SST in the afore-mentioned region. Linear regression indicates that precipitation increases at the rate of 3.1(mm/day)/°K, with a high degree of coherence between the rainfall and SST as reflected by their pattern correlation of 0.87. The models with the strong IO variability [GLA, UKMO (Figs. 2c-d) and NCAR (not shown)] exhibit a similar rainfall/SST slope and nearly as robust pattern correlations noted in the observations. Those models with the weakest IO activity [ECMWF, MRI (Figs. 2e-f) and LMD (not shown)] tend to produce much less rainfall in this region, have slopes approximately one-half that observed and much weaker pattern correlations which indicates that their convective activity is not as strongly influenced by the SSTs. The following basic conclusion can been reached, that models with the most realistic intraseasonal oscillations appear to have precipitation distributions which are well correlated with warm SSTs, and that these models predominantly employ convective parametrizations which are closed on buoyancy rather than moisture convergence.

Acknowledgments. We would like to thank the AMIP modelling groups for making their output available. This work was performed under the auspices of the U.S. Department of Energy Environmental Sciences Division at the Lawrence Livermore National Laboratory under contract W-7405-ENG-48. Code for the computation of the filter weights was supplied by Dr. Mike Pedder (Reading University).

Gates, W. L., 1992: AMIP: The Atmospheric Model Intercomparison Project. *Bull. Amer. Met. Soc.*, **73**, 1962-1970.

Matthews, A. J., B. J. Hoskins, J. M. Slingo and M. Blackburn, 1996: Development of convection along the SPCZ within a Madden-Julian Oscillation. *Q. J. Roy. Meteorol. Soc.* (accepted).

Slingo, J. M., K. R. Sperber, J. S. Boyle, J.-P. Ceron, M. Dix, B. Dugas, W. Ebisuzaki, J. Fyfe, D. Gregory, J.-F. Gueremy, J. Hack, A. Harzallah, P. Inness, A. Kitoh, W. K.-M. Lau, B. McAvaney, R. Madden, A. Matthews, T. N. Palmer, C.-K. Park, D. Randall, N. Renno, 1996: Intraseasonal oscillations in 15 atmospheric general circulation models: Results from an AMIP diagnostic subproject. *Clim. Dynam.*, (in press).

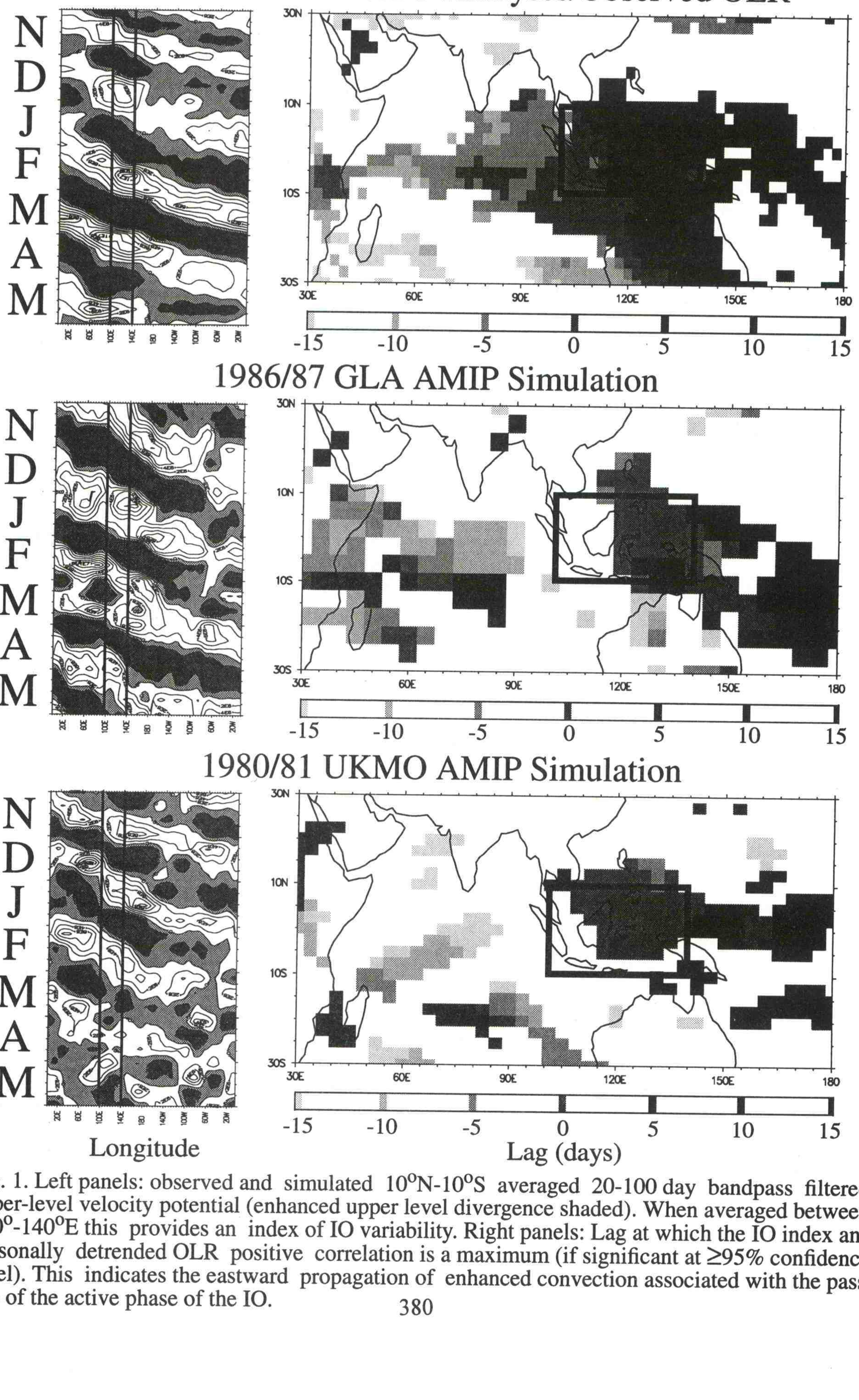

Fig. 1. Left panels: observed and simulated 10°N-10°S averaged 20-100 day bandpass filtered upper-level velocity potential (enhanced upper level divergence shaded). When averaged between 100°-140°E this provides an index of IO variability. Right panels: Lag at which the IO index and seasonally detrended OLR positive correlation is a maximum (if significant at ≥95% confidence level). This indicates the eastward propagation of enhanced convection associated with the passage of the active phase of the IO.

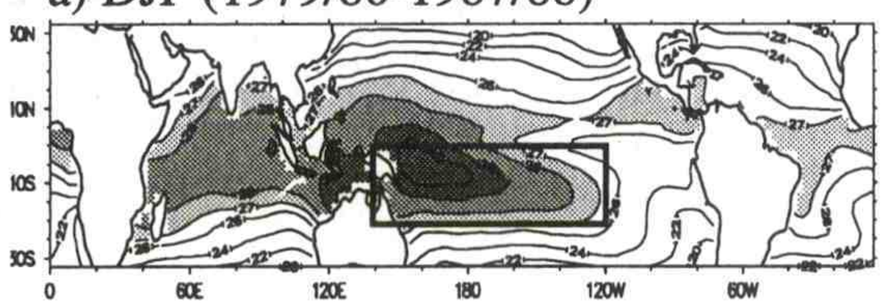

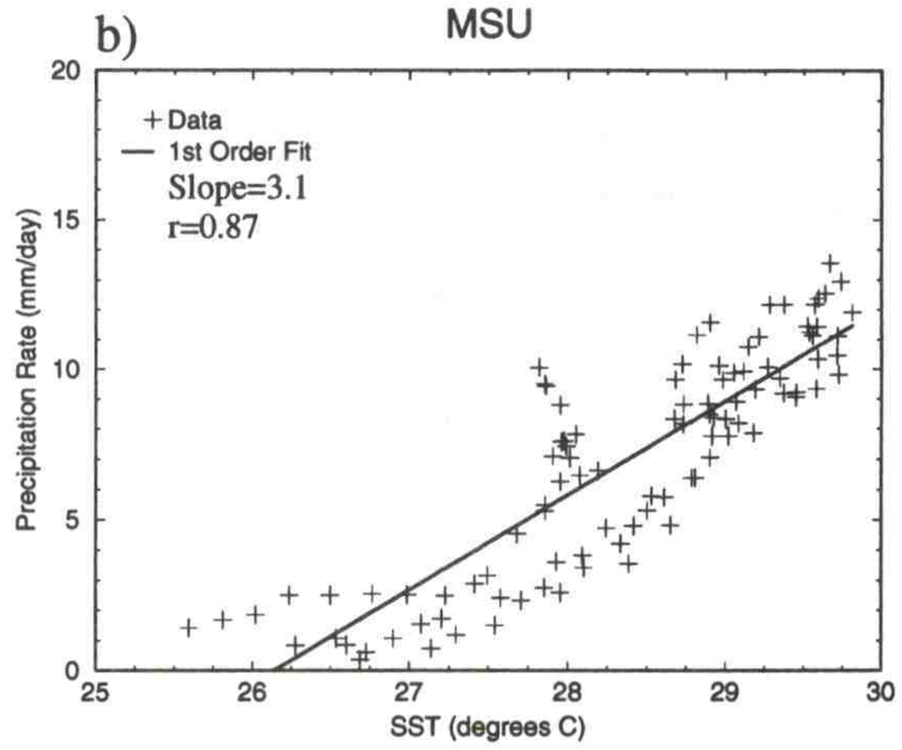

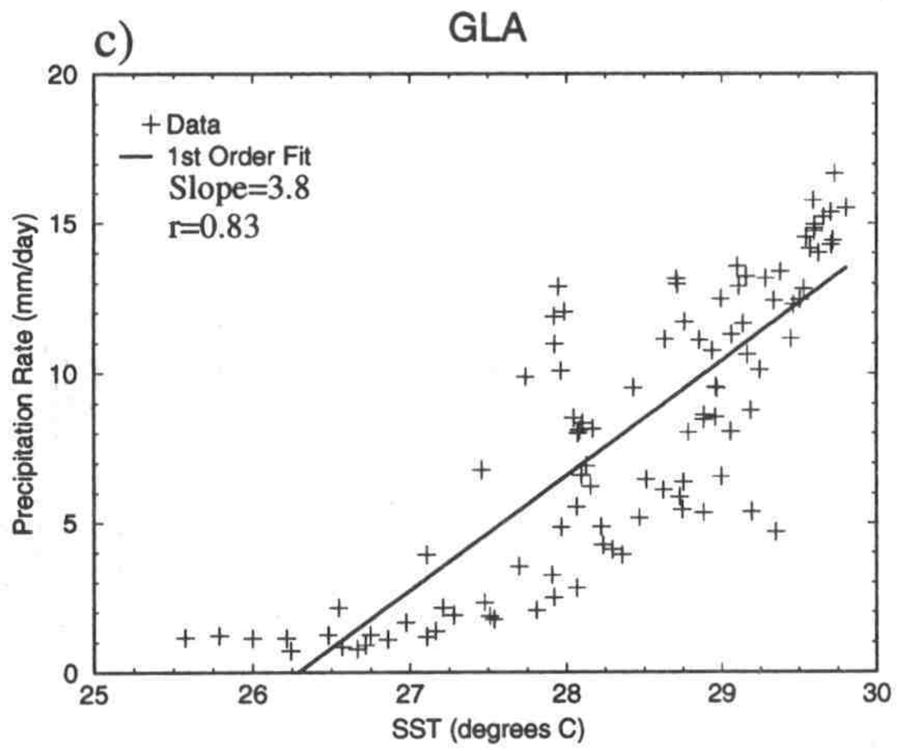

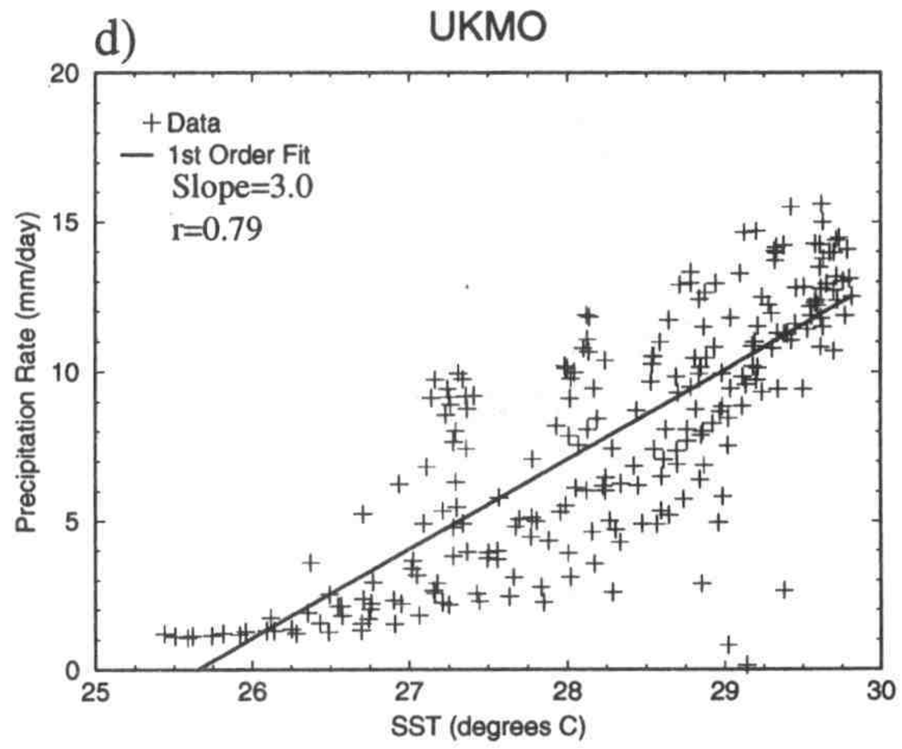

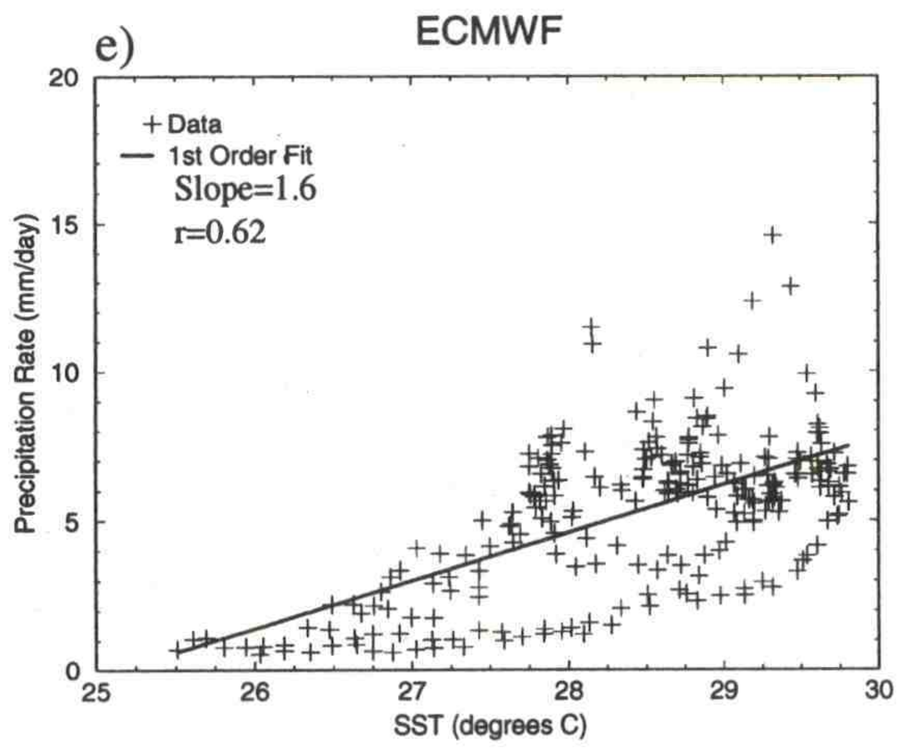

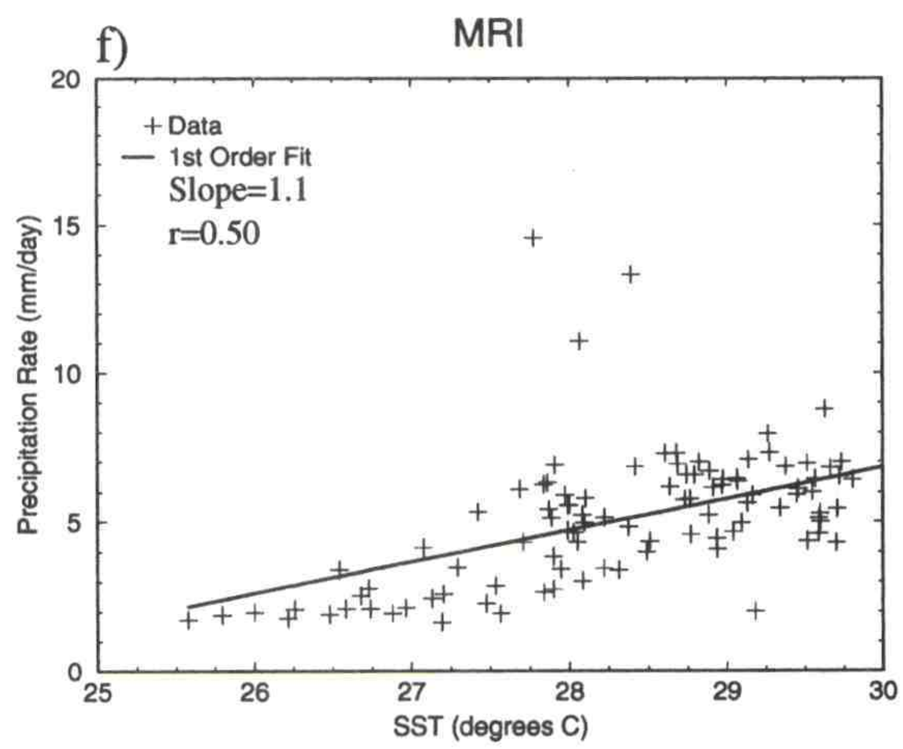

Fig. 2. 1979/80-1987/88 DJF a) SST climatology b) observed rainfall/SST relationship c) GLA rainfall/SST relationship d) UKMO rainfall/SST relationship e) ECMWF rainfall/SST relationship f) MRI rainfall/SST relationship. The GLA and UKMO (ECMWF and MRI) models exhibit strong (weak) intraseasonal variability.

SYSTEMATIC TENDENCY ERROR IN BUDGET CALCULATIONS

Masao Kanamitsu
Climate Prediction Center
National Centers for Environmental Prediction
Washington DC

and

Suranjana Saha
Environmental Modeling Center
National Centers for Environmental Prediction
Washington, D.C.

INTRODUCTION

A budget calculation is one of the most powerful tools for understanding atmospheric and oceanographic phenomena. This technique has been applied at all spatial and temporal scales ranging from the general circulation (e.g., Starr and White, 1951, Lau and Holopainen, 1984) to cumulus convection studies. Despite the popularity of the method, all budget computations suffer from uncertainties, due to computational, observational and many other errors associated with the calculation. The most important problem resulting from the uncertainties in budget calculations is that they seriously contaminate the results, particularly when the residual of a budget calculation is used to estimate desired quantities. For example, estimates of heat transport by the ocean from the residual of the atmospheric heat budget (e.g., Vonder Haar and Oort, 1973; Trenberth, 1979; Masuda, 1988, Trenberth and Solomon, 1994) vary widely. Despite the importance of the estimation of the accuracy, it is normally very difficult to obtain error estimates. Recently there are several activities to produce long series of historic analyses using a uniform analysis and forecast system (Kalnay and Jenne, 1991; Gibson et al., 1994; Schubert et al., 1995; Kalnay et al., 1996). All of these analyses provide some sort of budget calculations as part of the products. Although these analyses are generated by advanced analysis-forecast systems, they still suffer from various errors, and it is important to find some estimate of the errors before the analyses become widely available.

The causes of the errors associated with the budget calculations are diverse. Firstly, observations have inherent limits in the accuracy. The representativeness error of the scale of interest is another source of observation error. When irregularly located observations (both in horizontal and vertical) are interpolated to a regular grid, space and time interpolation errors are introduced. Use of asynoptic observations may further add time interpolation errors to the space interpolation errors. Budget calculations frequently require computation of space and time derivatives, which introduces space and time truncation errors. In addition to these numerical errors, imbalance between mass and motion fields in the analysis generates gravity wave noise, which contaminates budget calculations. Lastly, dynamical and physical models used in the budget equation may introduce errors.

In this paper, we will demonstrate that in data assimilation budget calculations, there is another error, entirely different from the errors mentioned earlier, that significantly reduce the accuracy of the budget calculations. Although it is not explicit, this error also exists in the traditional budget calculations. This particular error is related to the property of the budget equation used in the computation. In the case of a budget based on data assimilation, the error is directly related to the error of the forecast model used in the assimilation and it can also be regarded as a measure of the dependence of the budget calculations upon the forecast model used.

SYSTEMATIC TENDENCY ERROR

The ensemble averaged budget equation can be written as:

$$\frac{1}{N}\sum_{j=1}^{N}\left[(F^{j}_{t=\Delta})_{obs}-F^{j}_{t=0}\right]=\overline{A_{\Delta}}+\overline{B_{\Delta}}+\overline{C_{\Delta}}+\cdots+\overline{\epsilon_{\Delta}}$$

where N is a number of samples in the ensemble, F is the budget variable, A, B, C, are the individual terms in the budget equation, t is time and Δ stands for time step in the budget equation. The subscript *obs* represent observed while no subscript indicates evaluated values, and the over bar indicates ensemble mean. Note that the left hand side is consist of observed value only, while the right hand side is consist of computed quantities. The term ϵ_{Δ} appears on the right hand side, because there is a difference between budget equation produced F at t=Δ and observed F at t=Δ. The term is equivalent to the forecast error of the budget equation used. Since the forecast error is ensemble averaged in the above equation, the error term is the systematic error in the budget equation.
In order to find the relative magnitude of the systematic error terms in the budget equations, budget computations performed for various budget equations and for various budget computation methods were examined.

RESULTS AND CONCLUDING REMARKS

For a time integration budget, we examined two budget calculations; one was a study in which model was integrated for 24 hours using NMC global model, and the other was a budget calculation imbedded into the NMC/NCAR data assimilation. In both studies, the numerical errors, i.e., the vertical interpolation error, spatial truncation error and temporal truncation error are eliminated by using exactly the same numerical scheme as used in the forecast model, and performing the budget calculation on model coordinates. It was found in these studies that the significance of the systematic error term depends upon the spatial scale and also upon the parameter in question, but that the systematic error term is usually at least 10-20 % of the magnitude of the leading terms of the budget equation and is sometimes larger than the leading terms. The error term tends to be large for complex budget calculations such as the energetics in wavenumber domain, and for moisture related budgets. The results from moisture budget is shown in Figure 1.

For the estimation of the systematic error term in the instantaneous tendency budget calculations, the study by Klinker and Sardeshmukh (1992) and a supplemental computation made for the NMC/NCAR reanalysis is studied. These studies showed that the systematic error term in instantaneous tendency calculations tends to be larger than the systematic error term when the model

is integrated for 6-24 hours. This indicates that the systematic tendency term is a significant component of the budget equation regardless of the budget calculation method.

It is noted that the magnitude of the systematic tendency error apparently depends on the forecast model and the analysis system. Although the magnitude of the errors varies from one operational center to the other, the difference is not so large compared to the magnitude of the error itself (a factor of 2-3 difference at the largest among the different data producers). Furthermore, they are decreasing steadily in recent years and are approaching towards similar levels. However, since the systematic tendency error needs to be reduced by a factor of 10 to 100 in order for the error to be negligible compared to other leading terms, the error is still a major source of errors in budget calculations regardless of the producer of the analyses.

The estimation of the accuracy of each term in the RHS of the budget equation requires partitioning the systematic tendency term into various terms. In principle, this is very difficult since the dynamics and the physics of the system of equations are involved in the partitioning. In fact, the partitioning of systematic error is equivalent to the budget study of systematic forecast error. In many such studies, for example in Klinker and Sardeshmukh (1992), and also in KS95 and Kanamitsu and Saha (1994), it is found that it is very difficult to detect the term(s) responsible for the systematic error because there are strong interactions between the dynamical and physical terms, and between the physical processes. Accordingly, it is not possible to estimate the quantitative confidence level of the computed budget by simply comparing the magnitude of the terms in the budget equation with the systematic error term. For example, in the total precipitable water budget, the systematic error term is as large as or even larger than the moisture flux divergence term. This does not necessarily imply that the confidence level of the moisture flux term is low. Rather, moisture flux is obtained from parameters that are directly analyzed, so it should be less dependent on the model than precipitation and evaporation. However, it is very difficult to assign quantitative confidence levels to the budget calculations. There are some attempts to use only the most credible quantities from the analyses and to discard less credible parameters. The use of analyzed moisture convergence together with the observed precipitation is an example of such an attempt. This may suggest that the analysis used for a budget calculation should be verified against independent observations and analyses.

In the future, a number of methods can be considered for reducing the systematic error terms. One method is to integrate the model until the model spin-up/spin-down decreases, and to obtain the budget from the last portion of the integration period. The weakness of this method is that the input analysis fields are modified significantly during the course of the integration. Another possible method is to correct the systematic tendency during data assimilation. This is a rather expensive procedure since data assimilation needs to be performed twice. A more logical approach to the problem is to use a four-dimensional variational data assimilation. Through this approach, if the average of analyzed tendency can be constrained to average of observed time tendency, the systematic error term will be greatly reduced. However, this approach still requires significant research and development. It should be warned that even if the systematic error term is reduced to zero, other errors remain in the budget calculation. The most notable errors may be the errors in the physical processes parameterized in the model. Such errors can only be reduced by improving the parameterizations themselves. The error introduced in the analysis, including errors due to faulty data quality control, can also be significant. In this regard, the systematic tendency error in the budget calculation may give only a lower bound on the accuracy of the budget calculation.

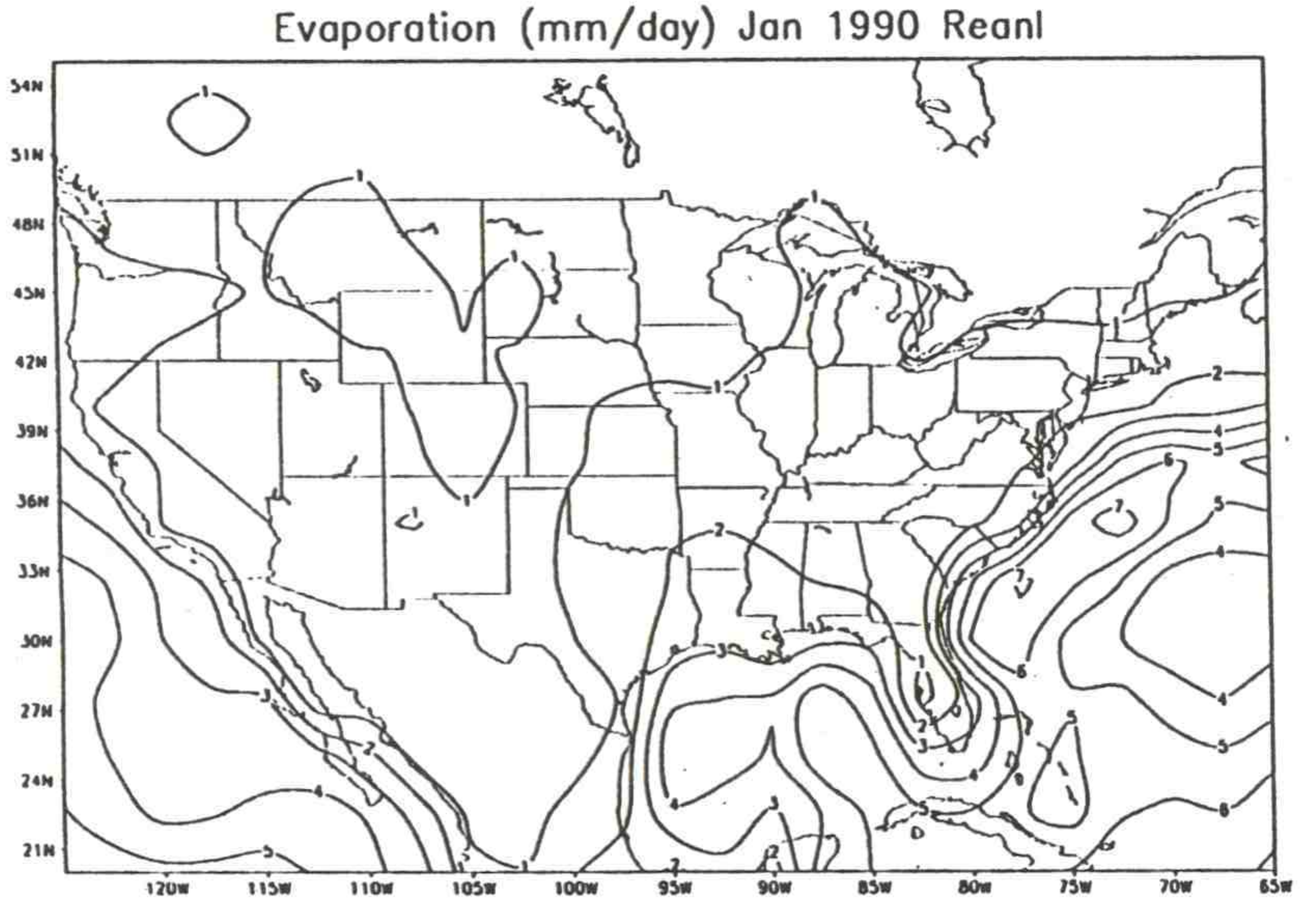

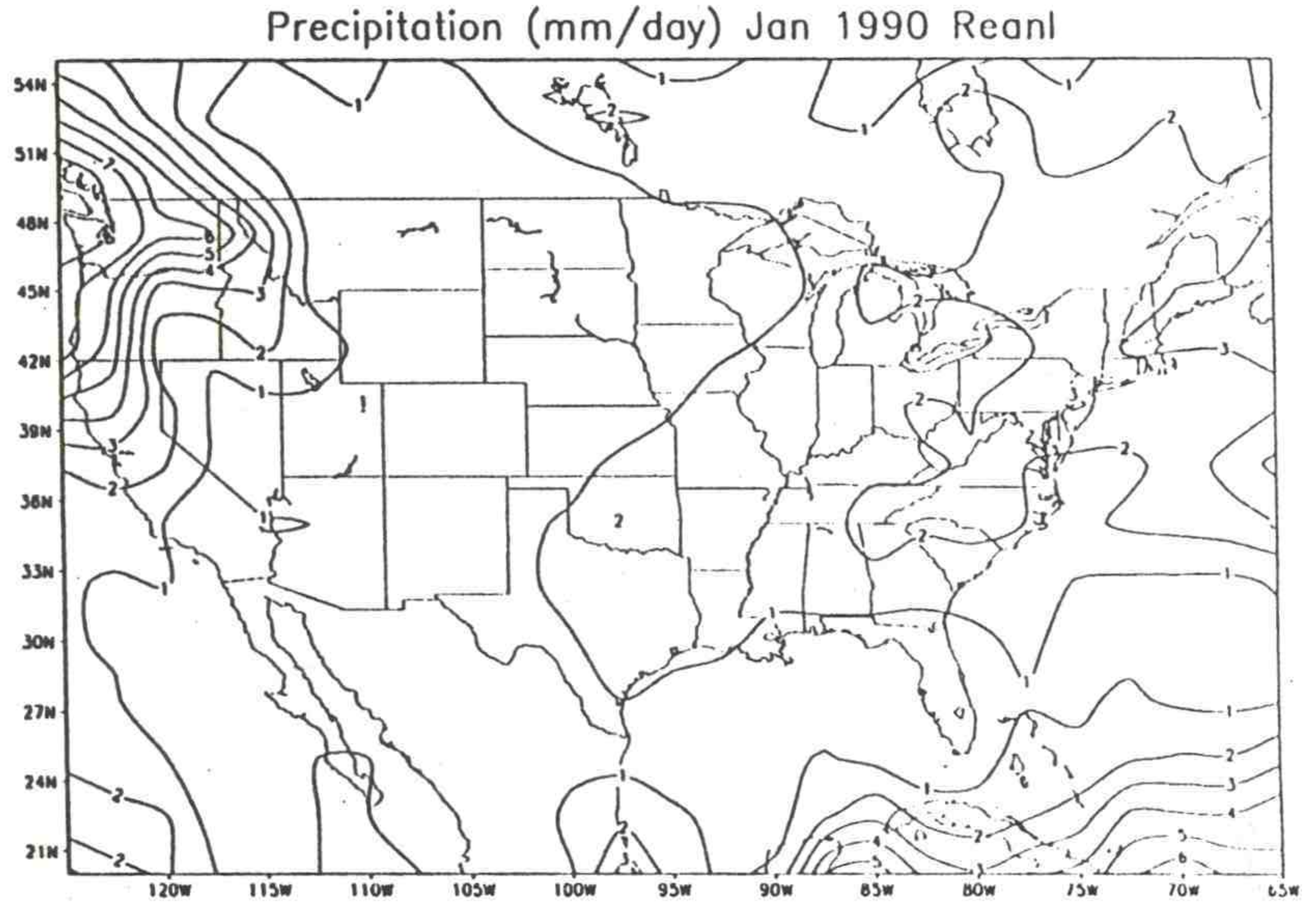

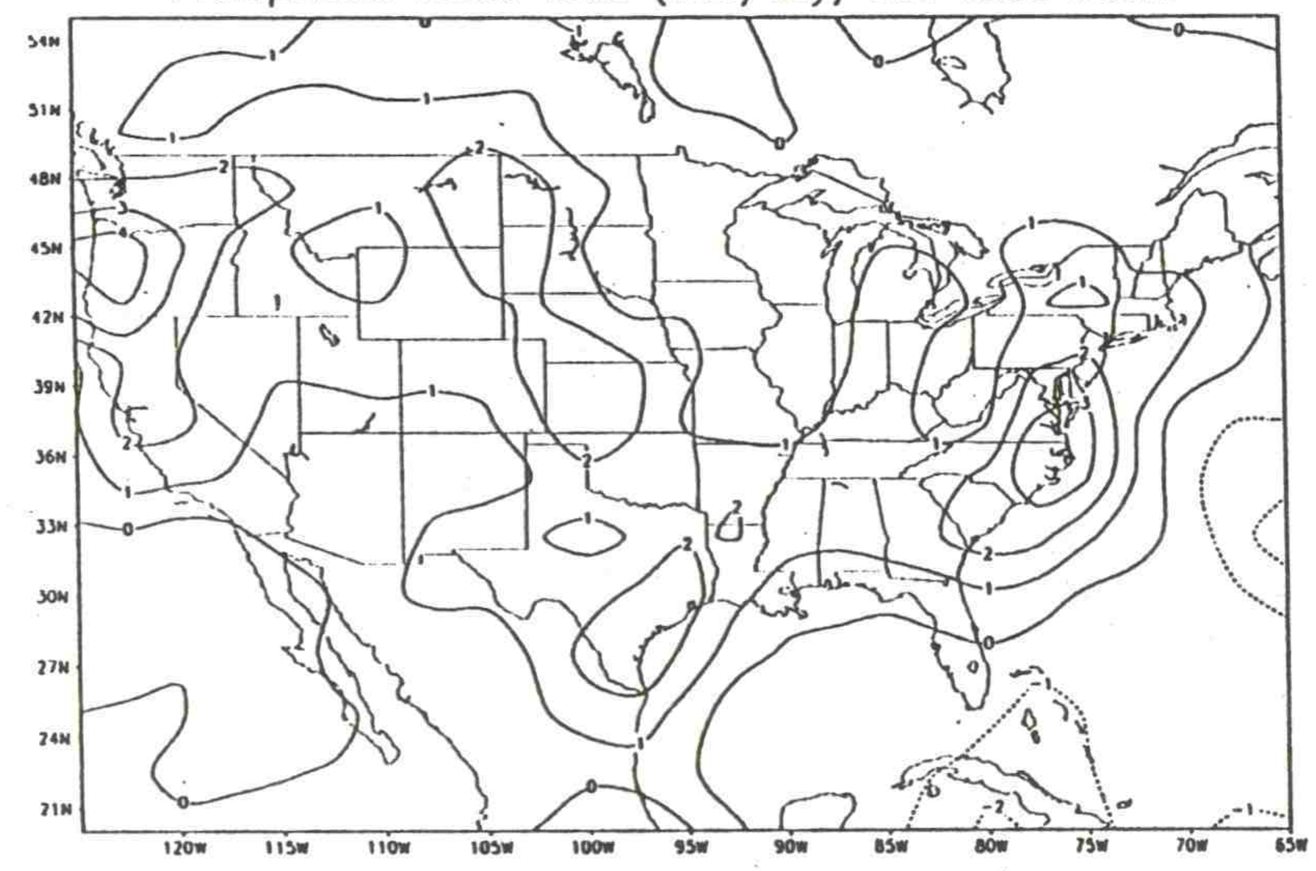

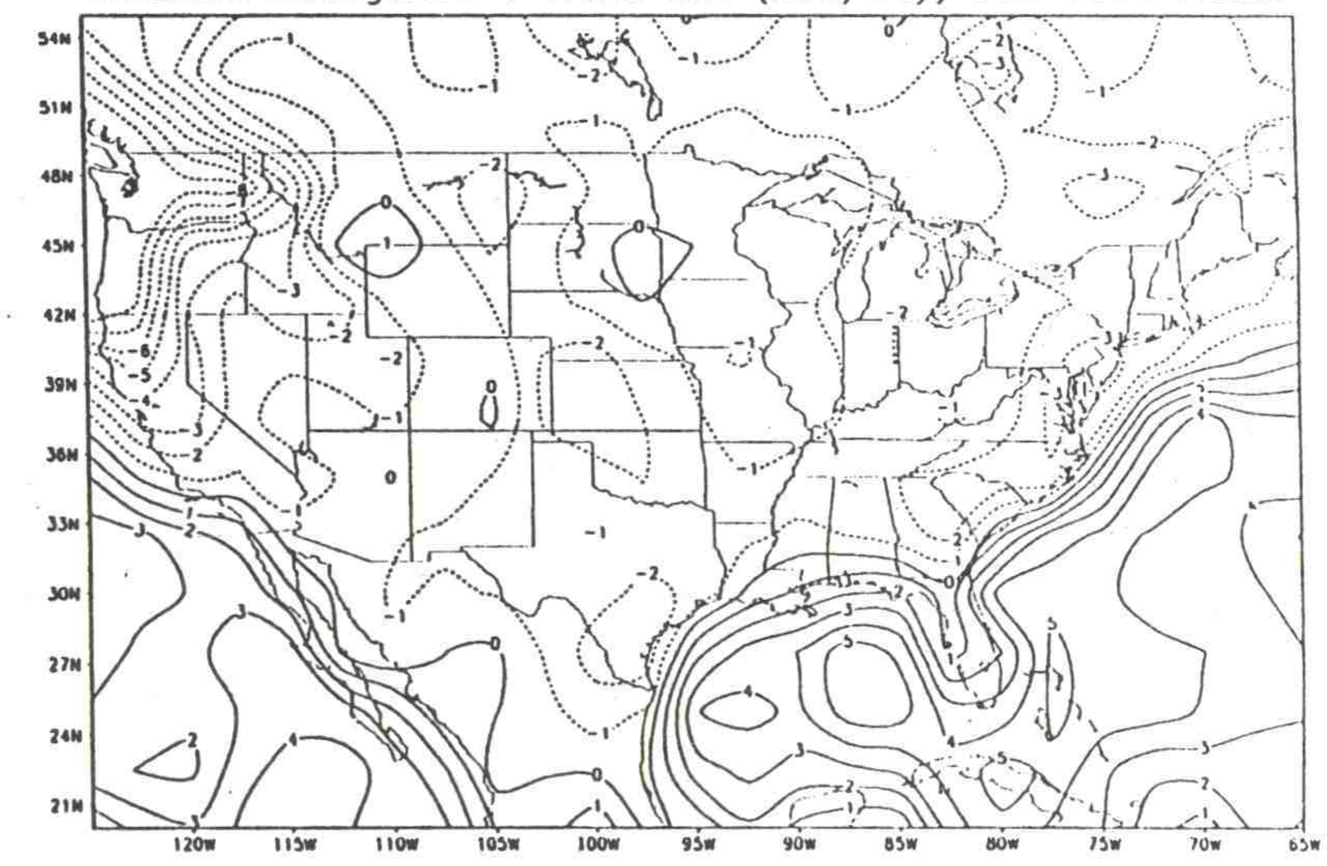

Figure 1. Precipitable water budget for winter of 1990 from NMC/NCAR reanalysis. Evaporation (upper left), precipitation (upper right), systematic tendency (lower left) and column moisture divergence plus horizontal diffusion. Units are mm/day.

Application of Estimated Soil Moisture to Model Climate Simulation

Jin Huang, Huug M. van den Dool and Jae E. Schemm

Climate Prediction Center
National Centers for Environmental Prediction
Washington, DC 20233

Motivation

Nowadays, in most simulations and forecasts with GCMs, soil moisture is interactively driven by the model-calculated precipitation and radiative properties. It is known that the model simulated precipitation is far from satisfactory (the anomaly correlation between simulation and observations is about 0.5 based on NCEP's Reanalysis). Errors in either precipitation or soil moisture could be enlarged through feedback between them and eventually cause unrealistic simulation or forecasts. Ideally, we wish to use the observed soil moisture as a prescribed boundary condition. Unfortunately, the observed soil moisture for an extended period is lacking. We feel that so far the soil moisture estimated with observed precipitation and temperature in a off-line hydrologic model would provide a good retroactive boundary condition.

In order to examine the possible improvements in climate simulation by prescribing soil moisture as a boundary condition, two 10-year (1982-91) integrations are made with NCEP's MRF model (the version used for Reanalysis). The first run (Control run) has interactive soil moisture and the second run (SM run) uses the estimated soil moisture as the prescribed boundary condition. In experimental design, this is analogous to the widespread use of prescribed SST (used also in our 10-year runs) for as long as SST calculated by ocean-atmosphere coupled model remains problematic.

Soil moisture model and data

The off-line model used to estimate the soil moisture is developed by Georgakakos (See details in Huang et al., 1995). In this model, soil moisture is calculated based on the water balance in the soil using observed precipitation and temperature. The components of the water balance in the model are precipitation, evaporation, runoff and ground water loss.

The global monthly precipitation (P) and temperature (T) data are from World monthly station climatology data from NCAR and 344 U.S. climate division data.

Results

Because of the space limitation, the results discussed here will be focused on the simulation of P and T over U.S only. Before using the calculated soil moisture as the prescribed boundary condition for the GCM, we have compared it with the observed soil moisture which is only

available to us in Illinois (1984-91). The anomaly correlation is 0.75, which is higher than that for the reanalysis (Cor= 0.46). The simulation for the climatology with this soil moisture model is also better than that from the reanalysis.

1. Improvement in simulating climatology

Climatologically, the soil moisture prescribed in the SM run is drier in the Northwest U.S. and wetter in the South compared to the soil moisture from the control run. Compared with observations, it is found that the SM run simulates the P and T better than the control run in warm months. As an example, Fig.1 shows the error of simulated June precipitation in the control and the SM runs. The precipitation deficiency/excess in the northwest/south in the SM run are less than those in the control run. The U.S. averaged RMS error of P is decreased from 1.69 to 1.39 (mm/day) and from 2.57°C to 2.21°C for T.

2. Improvement in simulating anomalies

The anomalies for each run and the observation are formed by subtracting its own climatology, ie. the 10 year mean. Here we present an extreme case of 1988 drought. Fig.2 shows the precipitation anomalies of June, 1988 for the observation, the SM and control runs. It is clear that by prescribing soil moisture, the SM run improves simulating the 1988 drought in the mid-west. The SM run can also simulate the above-normal temperature in that area (not shown).

Summary

In this study, we compared two 10-year model runs, one with interactive soil moisture and the other with prescribed soil moisture driven by observed precipitation and temperature. The soil moisture, estimated by the off-line model, is drier in NW U.S. and wetter in South U.S., compared to soil moisture from the control run. Generally, prescribing soil moisture improves the long-term simulation of P and T climatologies in warm months. Prescribing soil moisture also helps simulating the P and T inter-annual variations in extreme cases (e.g., 1988 drought). We have to keep in mind, however, that definitive conclusion about the anomaly simulation can only be based on multiple runs.

Acknowledgement

We thank Dr. Suru Saha in Environmental modeling Center/NCEP for setting up the model run and for her help during the analyses.

References

Huang, J. and H. M. van den Dool and K. Georgakakos, 1995: Analysis of model-calculated soil moisture over the U.S. (1931-93) and applications to long-range temperature forecasts (accepted by *J. of Climate*).

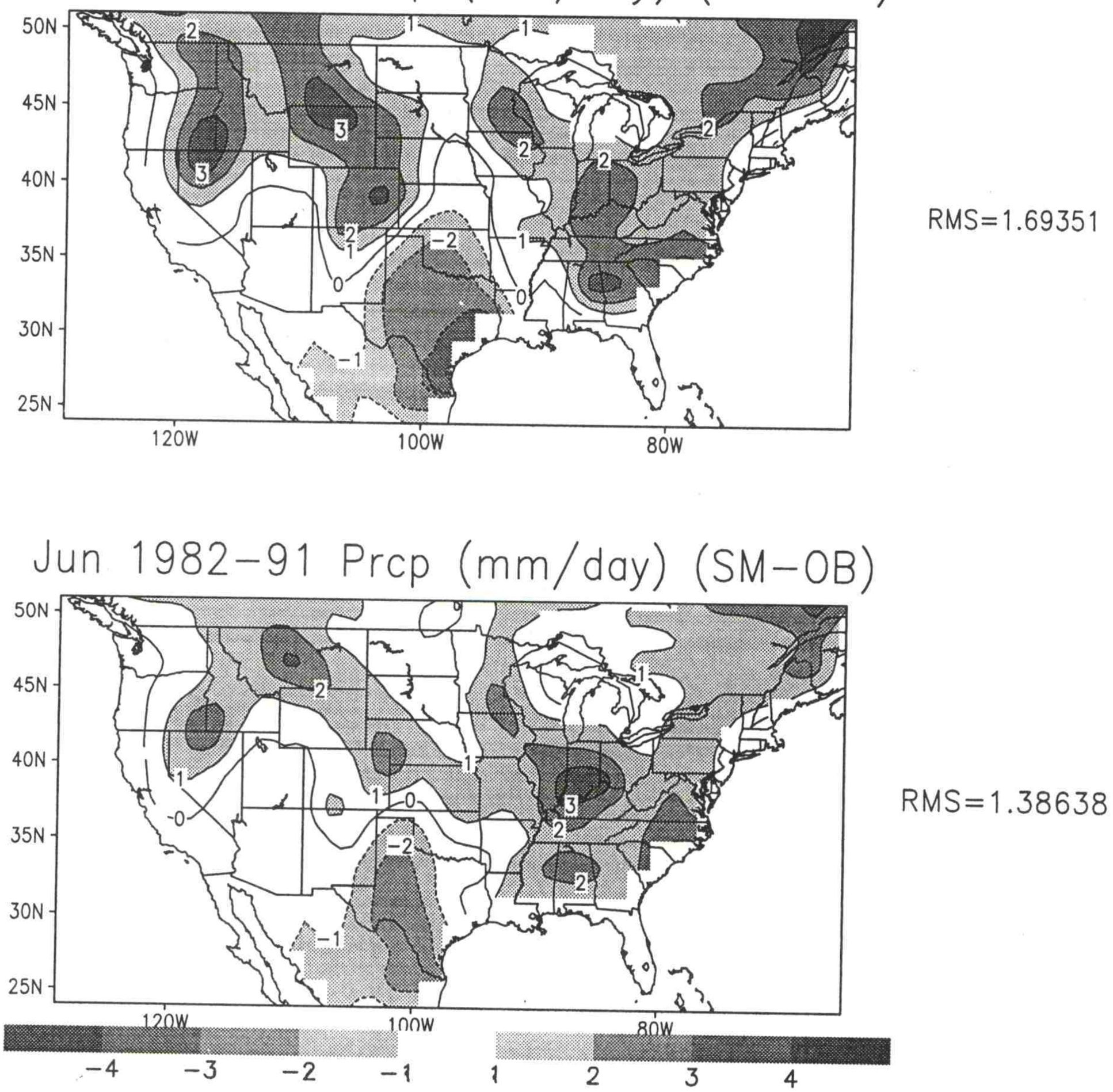

Fig.1 Top panel: The difference of the June precipitation climatology (1982-91) between the control run and the observation. The unit if mm/day. The U.S. averaged RMS is marked by the map. Bottom panel: as the top panel but for the SM run.

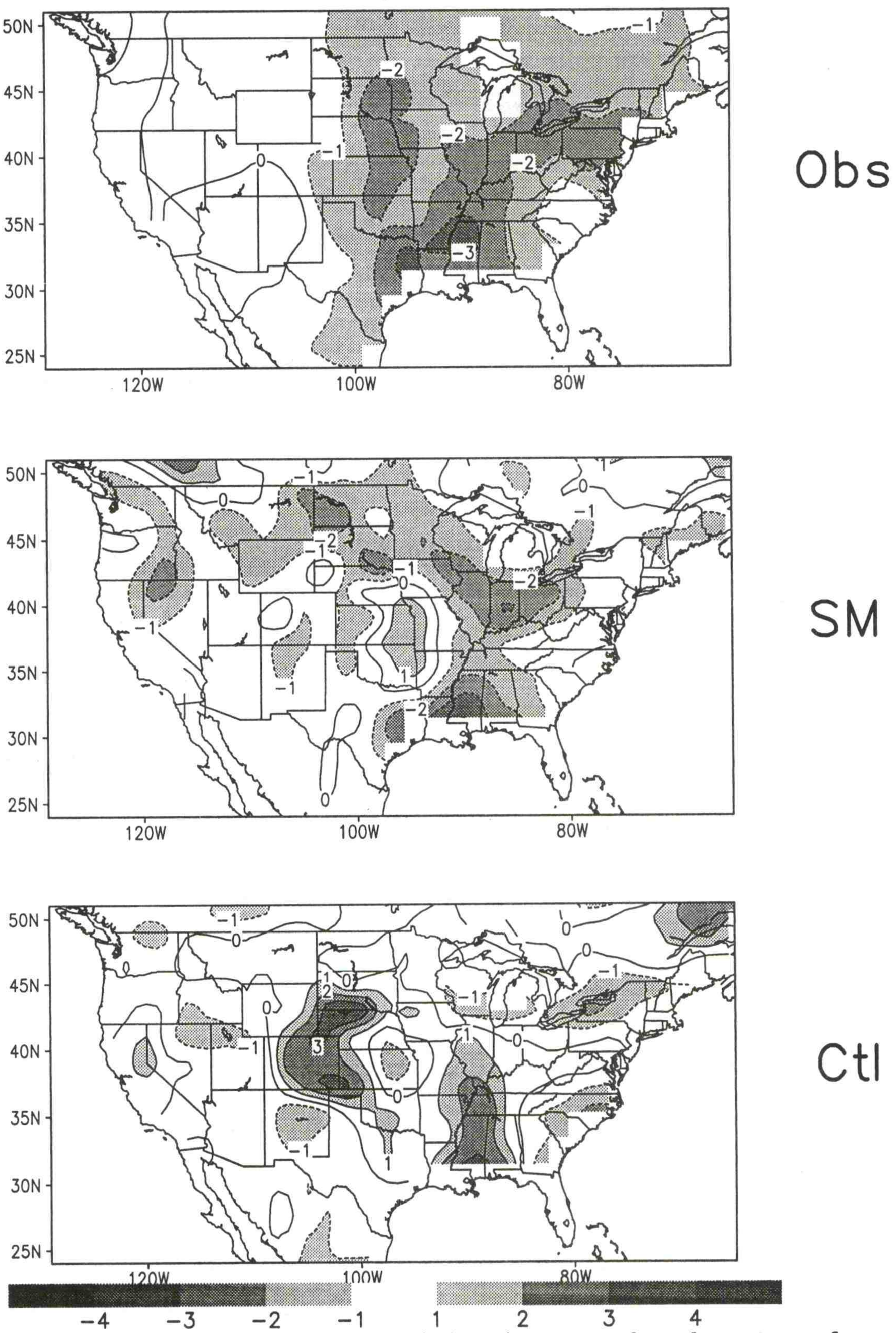

Fig.2 Top panel: The observed precipitation anomaly (departure from 1982-91 average) in June 1988. The middle and bottom panels are for the SM and control runs, respectively.

INHERENT LIMITS TO INTERANNUAL PREDICTABILITY?

Christopher Torrence and Peter J. Webster
Program in Atmospheric and Oceanic Sciences
(http://marigold.colorado.edu/homepage.html)
University of Colorado, Boulder, Colorado 80309–0311

1. Introduction

It is well known that the coupled ocean-atmosphere system appears to possess a spring "predictability barrier." This barrier has been seen in models of interannual variability (e.g. Zebiak and Cane, 1987, Latif and Graham, 1991, Barnston *et al.*, 1994) and in persistence of large-scale statistics (Troup, 1965, Webster, 1995). Thus, predictions of tropical atmosphere and ocean anomalies seem to be limited to a year or less in forecast time. This paper will address the following points:

- Definitions of predictability
- Examples of predictability barrier
- Hypothesis for barrier's existence
- Bridging the barrier
- Interdecadal changes in the barrier

As far as to the inherent limits to interannual predictability, we will see that these limits, if they exist, are highly dependent upon the above points.

2. Definitions of Predictability

Before examining the predictability barrier, it is important to agree on a definition of what is meant by predictability. For models it is relatively straightforward, in some objective sense, to define the predictability as the skill of a forecast compared to reality. This is usually done by computing the root-mean square (rms) difference between the forecast and the true observed values, whether it be a single time series (such as NINO3 sea surface temperature (SST)) or an entire field (such as Pacific basin SST). This can then be normalized to produce a simple observation-prediction correlation.

To get some feel for the degree of predictability before the forecast becomes reality (or doesn't!), it is possible to compute the rms difference between an ensemble of forecasts and compare that to the "expected" standard deviation of the observations, where the expected deviation is just the standard deviation of a long time series. If the spread in forecasts is less than the standard deviation, then some reliability can be attached to the prediction. This assumes that the mean value is also correctly predicted, but since most models consider only anomalies either from their own climatology or that of reality, the mean is assumed to be stationary and zero.

For statistical data analysis, the idea of predictability implies the use of some model. In most cases where statistics such as standard deviations, correlations, and regressions as used, this implies a linear model. This is the idea behind the use of simple persistence as a measure of measuring the forecast ability of a model. The model (which may be a coupled GCM or a simple linear Markov) is being compared against a linear persistence of anomalies.

Therefore, when the term "predictability barrier" is used, it should be noted first of all what type of model is being used, and secondly, what is the definition of predictability. In this study we will be looking at linear correlations and persistence. Thus, we are using a linear regression model and our measure of predictability is the persistence based on this regression.

3. The Predictability Barrier

Many tropical ocean-atmosphere models appear to contain a "predictability barrier" during the boreal (Northern Hemisphere) springtime months of March to May. An example of this can be seen in the Cane-Zebiak model, as shown in Figure 1. The predictability in this case is defined as the correlation between observed and predicted sea surface temperature fields. This barrier causes a substantial decrease in correlations between prediction and observation, with the conclusion that the ocean-atmosphere system seems to be predictable only up to one year in advance (Webster, 1995). Barnston et al. (1994) did an intercomparison of five El Niño-Southern Oscillation (ENSO) models and found that each one exhibited similar decreases in both anomaly correlation and root-mean-square error. Is this then a failure of the models, or a "failure" of the real system?

To answer this question we can examine large-scale statistics of interannual variability. One such measure is the

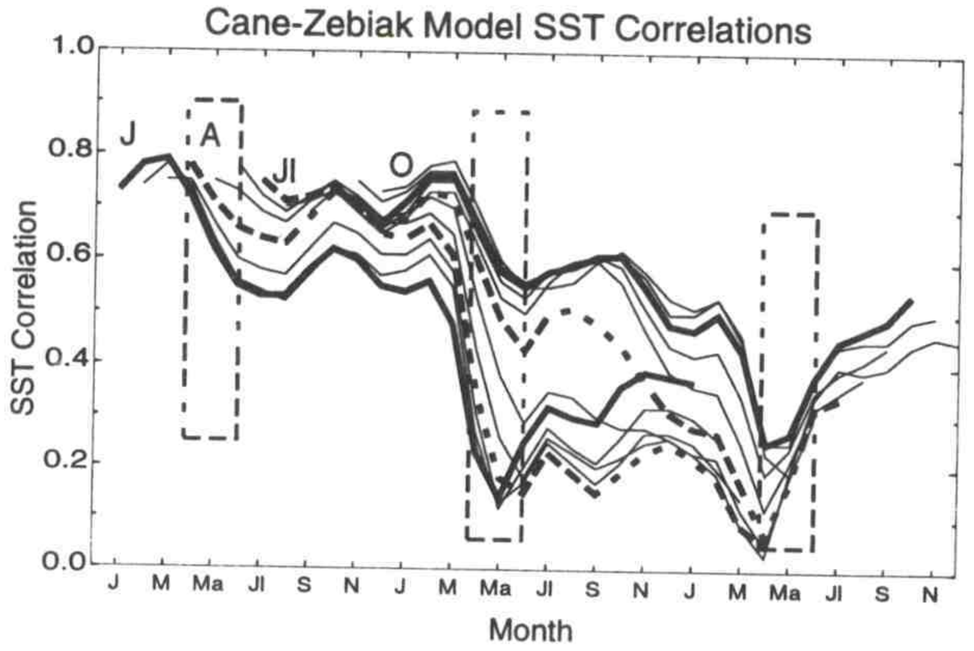

Fig. 1: Correlations between SST predictions and observations in the Cane-Zebiak model. The letters (J,A,Jl,O) mark the starting month of the forecast. From Webster (1995).

Southern Oscillation Index (SOI), defined as the normalized anomalous surface pressure difference between Tahiti in the eastern Pacific and Darwin in the western Pacific. The SOI is thus a measure of variability across the Pacific Ocean basin and can be used to measure the atmospheric component of ENSO. In Figure 2 we construct the lagged correlation between different months from the period 1933–1994. We see that the SOI lagged correlation exhibits the same behavior as the observation-prediction correlation: relatively high correlations for any starting month, followed by a sharp decrease, again between April and May. For predictions starting in April the correlations remain above the 95% significance level until the following May, while for predictions starting in March the drop-off occurs only two months later. We can therefore conclude that, in some sense, the coupled ocean-atmosphere models are capturing the same predictability behavior as the real system.

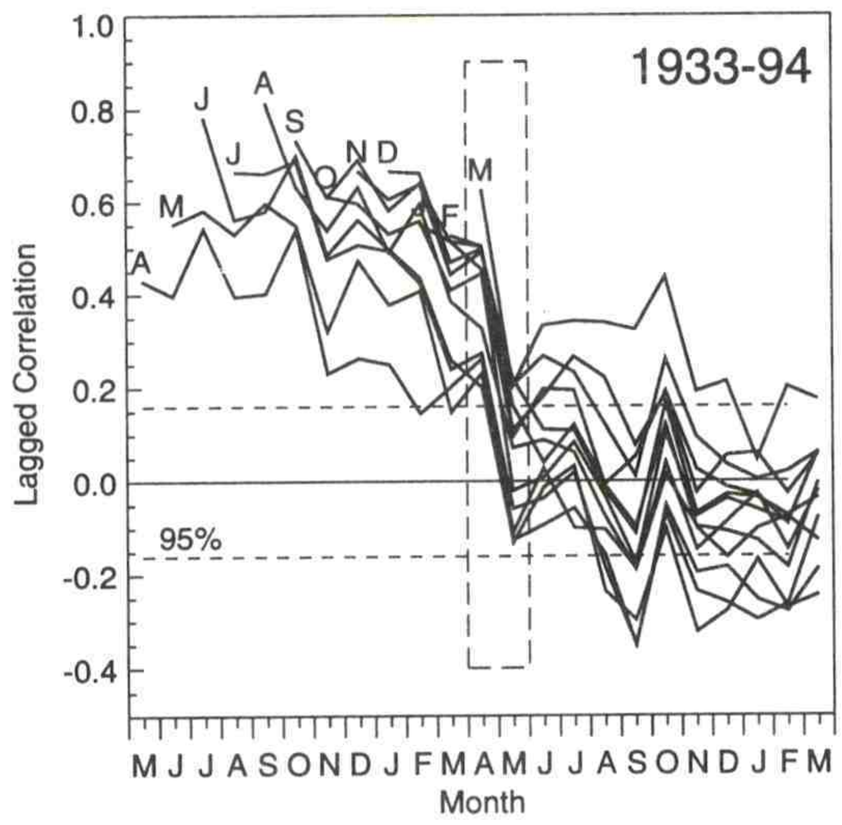

Fig. 2: Lag correlations of the Southern Oscillation Index (SOI) using monthly data from 1933 to 1994. The dotted line marks the 95% significance level, while the dashed box highlights the predictability barrier.

4. Hypothesis

The key to the existence of the predictability barrier is in the development of the warm or cold SST anomalies which lead to an ENSO event. This development is strongly phase locked to the annual cycle, with the transition period occuring during March-May. Webster (1995) and Torrence and Webster (1995) developed the following hypothesis to explain the existence of the spring predictability barrier:

1. *The tropical coupled ocean-atmosphere system becomes decoupled in the boreal spring by the formation of a weak and stable surface thermocline. The formation accompanies the annual cycle of reduced winds and the flat SST gradient across the Pacific Ocean.*
2. *The ocean and the atmosphere system adjust independently: Ocean is unconstrained by wind-stress; atmosphere unconstrained by SST gradient, upwelling, etc.*
3. *Predictability barrier results from the decoupling. Predicting through the barrier depends on the strength of the anomalous thermocline structure and on the anomalous monsoon kick that re-establishes the coupling.*
4. *The anomalous monsoon wind stress in the Pacific Ocean can (a) modify the strong ENSO signal, and (b) restructure interannual variability if ENSO signal is weak.*

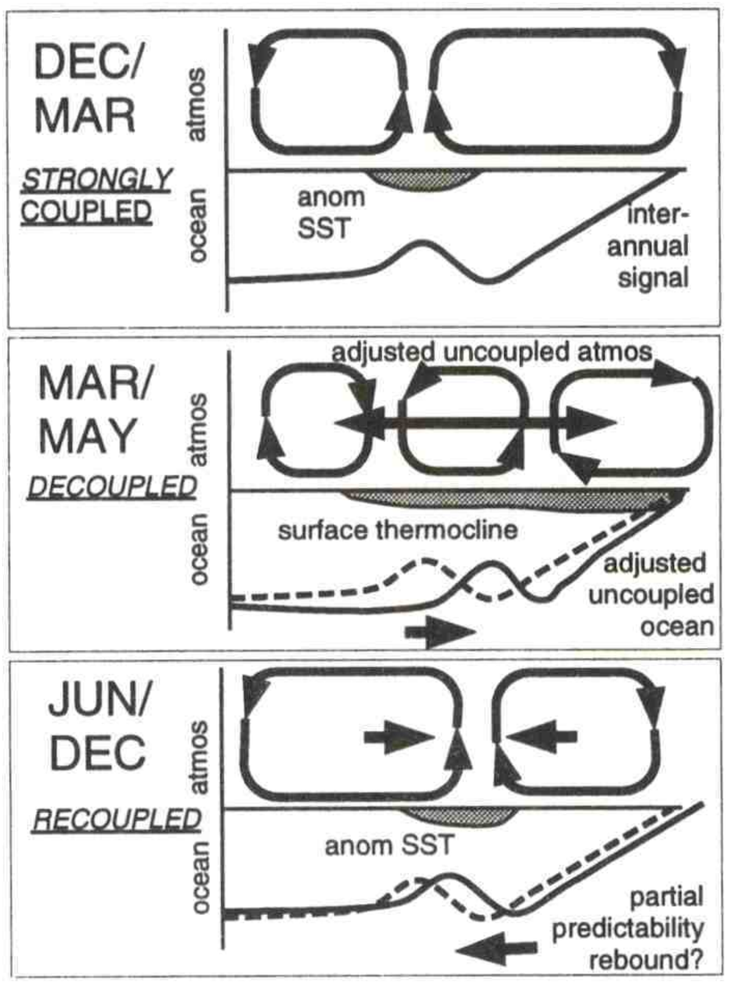

Fig. 3: Annual cycle of ocean-atmosphere coupling in the equatorial Pacific Ocean basin.

This unified hypothesis is illustrated in Figure 3. During most of the year the ocean and atmosphere are strongly coupled, with fluctuations in either system transmitted to the other. However, during March-May, with the weakening trade winds and the development of the thin warm layer over the Pacific basin, the ocean and atmosphere systems become decoupled. Since each system is in its most frail state, both may adjust independently to perturbations such as monsoon strength or subsurface waves. In May-June the trade winds increase, the warm SST layer is eroded, and the two systems become recoupled. However, each system will now be in a different climate state than before, and the new coupling may be very different from pre-spring conditions.

5. Bridging the Barrier

The last two parts of our hypothesis indicate that it may be possible to predict through the barrier. There are at least three possibilities that must be considered:

1. *The statistics used to evaluate the model predictability and statistical persistence are simply inadequate during the spring months when the overall system variance is small,* or
2. *There is missing or incomplete physics in the coupled ocean-atmosphere models, or other nonlinear effects that are not being properly included. It has been suggested that the ocean may possess a "memory" due to the longer time scales and large specific heat, which could explain*

the slight rebound in predictability exhibited by several models and also evident in the SOI lag correlations. or

3. *The spatial scale necessary to successfully model interannual variability is larger than the Pacific basin scale that is used in most models. External influences such as the Indian Ocean or the Southwest Monsoon may cause large perturbations, especially during the springtime.*

Experiments by Webster and Yang (1992) indicate that variations in the intensity of the monsoon may perturb the atmospheric circulation well beyond the monsoon region and can influence the phase, amplitude, and period of the El Niño-Southern Oscillation (ENSO) cycle. During a strong monsoon, convection over the western Pacific warm pool is enhanced, leading to a stronger Walker circulation, and hence stronger trade winds. A stronger Walker circulation inhibits ENSO, causing a longer period between warm events. During a weak monsoon the situation is reversed. Thus it seems that the strength of the annual cycle of the Earth's climate, and more specifically the monsoon, has important consequences for the predictability of interannual variability.

As far as the spatial scale is concerned, it appears that the barrier in the persistence is strongly tied to the pattern of ENSO itself. A map of mean 3–month SST persistence, shown in Figure 4, reveals the important nature of the tropics in prediction of global-scale interannual variability. The largest persistences are found in the central and eastern Pacific, with smaller regions in the Indian and Atlantic. The large region in the central Pacific is also the place of maximum change in persistence during the annual cycle. Hence, Figure 4 is essentially a map of the persistence barrier. It is possible that regions in either the Indian Ocean or the extratropics which do not exhibit a persistence barrier can be then used as predictors during the boreal spring.

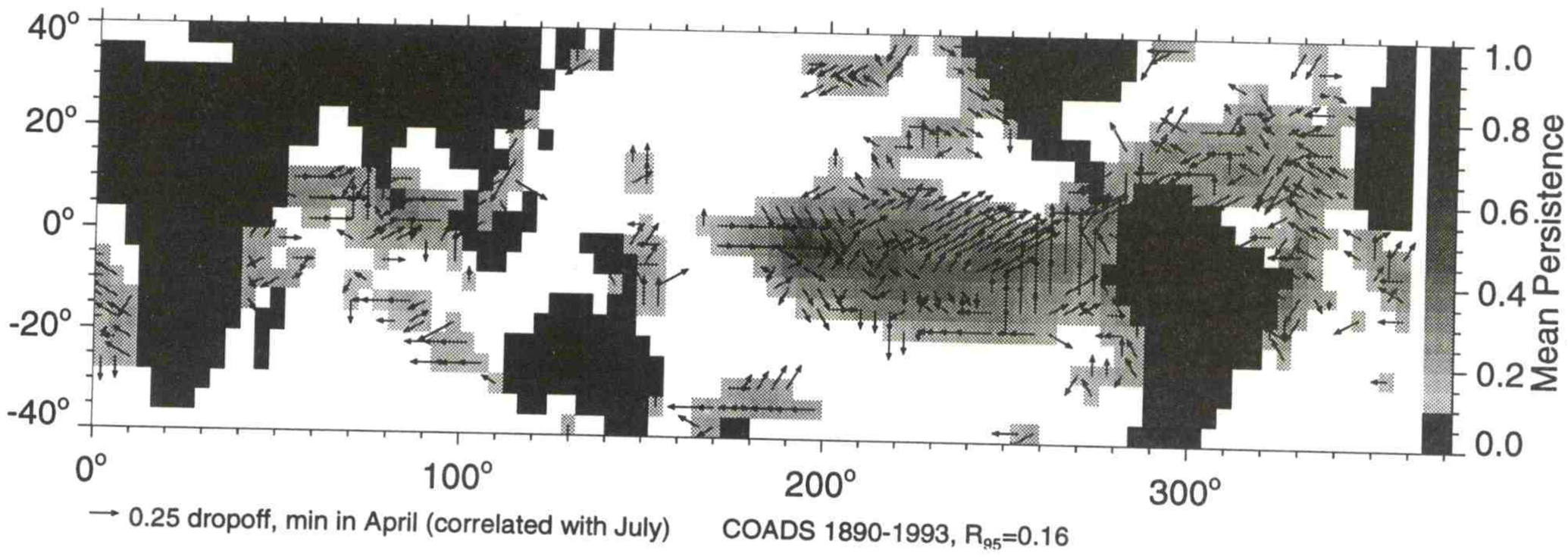

Fig. 4: Mean of the 12 3–month persistences of sea surface temperature from COADS 1890–1993 dataset. The 3–month persistence is defined as the correlation between all 104 January's with all the following April's, etc., for each month of the year, then averaged together. Only regions with mean persistence greater than the 95% significance level (104 D.O.F., 95% sig level = 0.16) are shown. The scale of mean persistence is on the right. The arrows are "harmonic dials" showing the month where the persistence reaches its minimum value. A vertical arrow would represent January, showing that the correlation between all January's with all April's is when the persistence is lowest. The length of the sample vector to the lower left represents a dropoff of 0.25 from the mean value to the minimum, which occured for the (April — July) correlation.

6. Interdecadal Changes

Recent results from the Cane-Zebiak model (Chen *et al.*, 1995) and the Penland linear inverse model (Penland and Sardeshmukh, 1995) indicate the possible disappearance and/or elimination of the predictability barrier. However, before we assume that the barrier has been eliminated due to improved model design, it is worthwhile to determine if the predictability barrier undergoes any long-term variability. Shown in Figure 5(a) is both the running variance of the NINO3 SST and that of the All-India monsoon rainfall index. It is evident that the frequency and amplitude of ENSO events changes dramatically on interdecadal time scales, with low variability during the mid-century and high variance at the beginning and end. This variability seems to be reflected in monsoon rainfall, which suggests a possible connection between these two phenomena. Figure 5(b) shows the effect of these interdecadal changes on our persistence barrier. During times of strong ENSO, or strong phase locking, the persistence barrier is both large and very sharp, while at other times it is much weaker and broader. A close examination of the 1970–1994 period reveals a strong barrier in the 1970's and a much weaker barrier in the 1980's (Balmaseda *et al.*, 1994). This is possibly due to changes in the phase locking of ENSO to the annual cycle, or changes in the basic state itself (Wang, 1995).

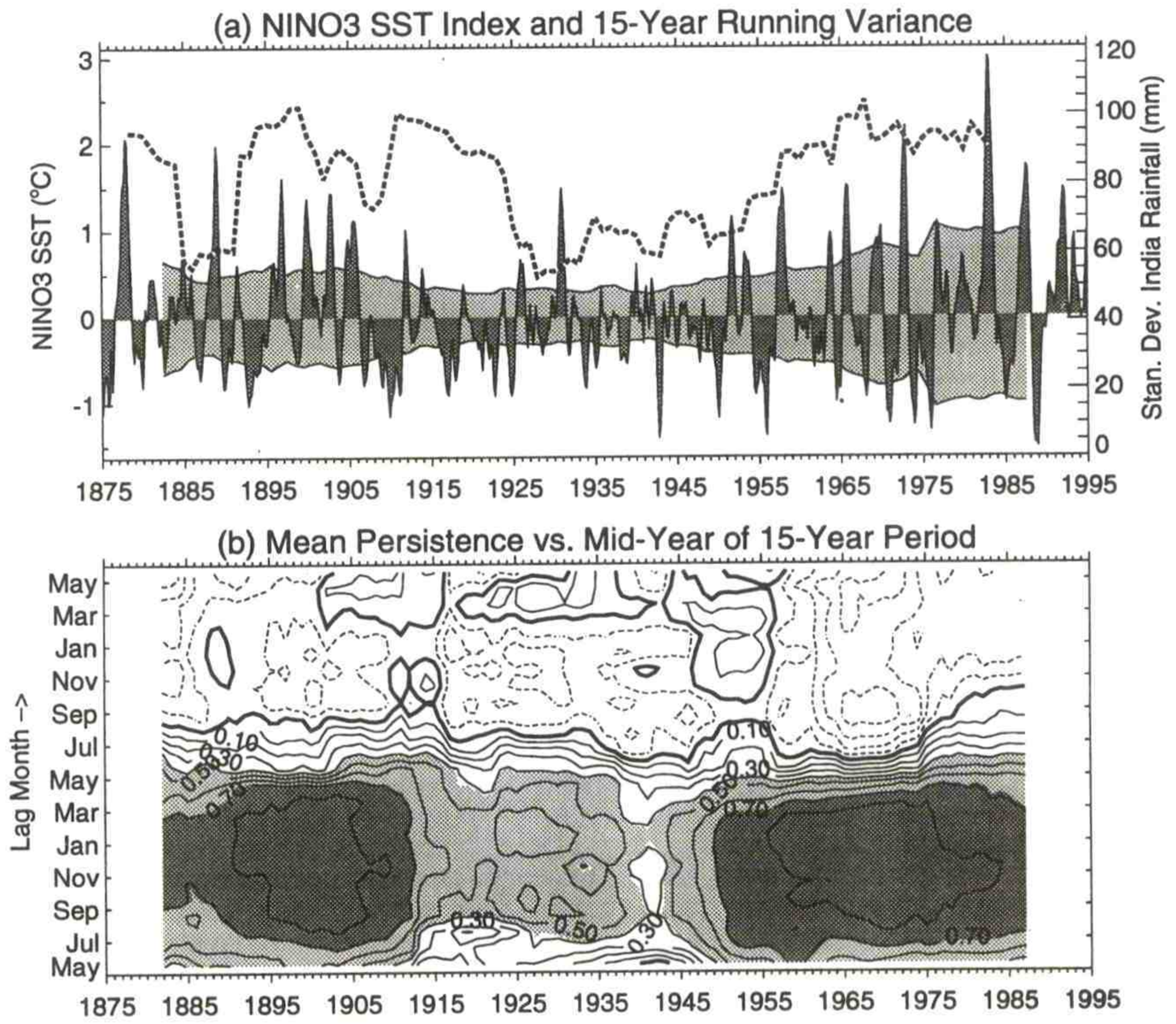

Fig. 5: (a) Running 15–year variance of the NINO3 SST. The original time series is shaded dark, while the running variance is the lighter shading, shown symmetric about the y=0 axis. The thick dashed line is the running 15–year standard deviation of All-India monsoon rainfall. (b) The persistence barrier vs time. This is the mean of all 12 curves (see Figure 2) using a sliding window of width 15 years. The x-axis marks the location of the center of the window, while the y-axis is the lagged month, with time running upwards. The contour interval is every 0.1 correlation.

7. Conclusions

The coupled ocean-atmosphere system has been shown to possess an annual cycle of persistence. This feature has been seen in both coupled ocean-atmosphere models and in basin-wide SST and SLP statistics. This "predictability barrier" appears to be related to the phase locking of the interannual variability of ENSO to the annual cycle of ocean-atmosphere coupling. It is not possible at this time to determine if this represents an inherent limit to interannual predictability, but the promising recent results of the Cane-Zebiak and Penland models show that it may be possible to avoid the barrier. However the presence of interdecadal variability in the strength of the persistence barrier, and especially its weakness during the recent decade, may contribute significantly to the decrease or increase of predictability in models of interannual variability.

References

Balmaseda, M.A., D.L.T. Anderson, and M.K. Davey, 1994: Seasonal dependence of ENSO prediction skill. Technical report, Met. Tech. Note, CTRN 51, Hadley Centre, U.K.

Barnston, A.G., H.M. van den Dool, S.E. Zebiak, T.P. Barnett, M. Ji, D.R. Rodenhuis, M.A. Cane, A. Leetmaa, N.E. Graham, C.R. Ropelewski, V.E. Kousky, E.A. O'Lenic, and R.E. Livezey, 1994: Long-lead seasonal forecasts - where do we stand? *Bull. Am. Meteor. Soc*, **75**, 2097–2114.

Chen, D., S.E. Zebiak, A.J. Busalacchi, and M.A. Cane, 1995: An improved procedure for El Niño forecasting. *Science*, **269**, 1699–1700.

Latif, M. and N.E. Graham, 1991: How much predictive skill is contained in the thermal structure of an OGCM? *TOGA Notes*, **2**, 6–8.

Penland, C. and P.D. Sardeshmukh, 1995: The optimal growth of tropical sea surface temperature anomalies. *J. Climate*, **8**, 1999–2024.

Torrence, C. and P.J. Webster, 1995: The predictability barrier in interannual variability. In *Proceedings of 19th Annual Climate Diagnostics Workshop*, College Park, MD, 14-18 November 1994.

Troup, A.J., 1965: The "southern oscillation". *Quart. J. Roy. Meteor. Soc.*, **91**, 490–506.

Wang, B., 1995: Interdecadal changes in El Niño onset in the last four decades. *J. Climate*, **8**, 267–285.

Webster, P.J., 1995: The annual cycle and the predictability of the tropical coupled ocean-atmosphere system. *Meteor. Atmos. Phys.*, **56**, 33–55.

Zebiak, S.E. and M.A. Cane, 1987: A model El Niño-Southern Oscillation. *Mon. Wea. Rev.*, **115**, 2262–2278.

The Atmospheric Response to Tropical Convection and Implications for Long Range Forecasting

Kingtse C. Mo
Climate Prediction Center
NCEP/NWS/NOAA
Washington D. C. 20233

and

Peitao Peng
Atmospheric and Oceanic Science Program,
Princeton University, Princeton, New Jersey

I. Introduction

Notable advances have been made in seasonal climate prediction over the past few years. Progress in coupled ocean atmosphere system makes it possible to forecast tropical sea surface temperature anomalies in the Pacific up to one year in advance. The important question is whether we are able to utilize this knowledge to improve long range forecasting. Studies by Madden (1976), Shea and Madden (1990) suggested that only boundary forced climate signal has potential for predictability. In this paper, low frequency modes associated with realistic heating anomalies in the tropics are identified by using combined REOF analysis and a linear model.

2. Results

The physically consistent patterns for anomalous rainfall in the tropics and 200 hPa asymmetric stream function anomalies were obtained using the combined rotated EOF analysis. In this note, we concentrate on REOF 1 (Fig.1) which is the ENSO mode and the PNA pattern (Fig.2). The ENSO mode is the only mode having forecast skill in the long term ensemble NCEP climate simulations (Livezey et. al 1996).

The combined REOF modes do not give guidance on cause relationships. A steady state primitive equation model linearized around a wavy basic state is used to determine the tropical forced modes. The linear model was forced by diabetic heating anomalies based on the EOF rainfall composites. For the ENSO pattern, the tropical circulation is forced directly by tropical convection (Fig.3a) but there is no response in midlatitudes. For the PNA pattern, the wavetrain is not directly forced by heating related to tropical rainfall (not shown).

We then forced the atmosphere with different parts of the heating associated with REOF 1 and results are given in Fig.3b-3d. . When the linear model is forced by positive heating anomalies in the central Pacific alone, the response shows a wave train in midlatitudes

(Fig.3b). However, there is no net response to the total heating in midlatitudes. Fig 3c and 3d show cancellations between responses to positive heating anomalies from tropical convection and negative anomalies due to the Hadley and Walker circulations. Results indicate that the response is determined by both positive and negative diabetic heating anomalies. The model needs to capture both the Hadley and Walker circulations related to enhanced convection well in order to have forecast skill in the tropics.

During the ENSO year, the transient vorticity forcing in the North Pacific plays a major role in generating the wavetrains in midlatitudes. While the tropical features are directly related to tropical forcing, the extratropical wavetrain is related to tropical forcing through the transient eddies associated with the shift of the subtropical jet. Since circulations are either linearly forced by the tropics or indirectly linked to tropical convection, this mode has high forecast skill. Different physical mechanisms are involved in generating the PNA wavetrain. The transient vorticity forcing associated with synoptic eddies at the exit region of the jet and diabetic heating in the tropics does not produce the PNA wavetrain. The importance of the stationary non linearity may explain while the model is capable to produce the PNA, it does not appear the same time as observations.

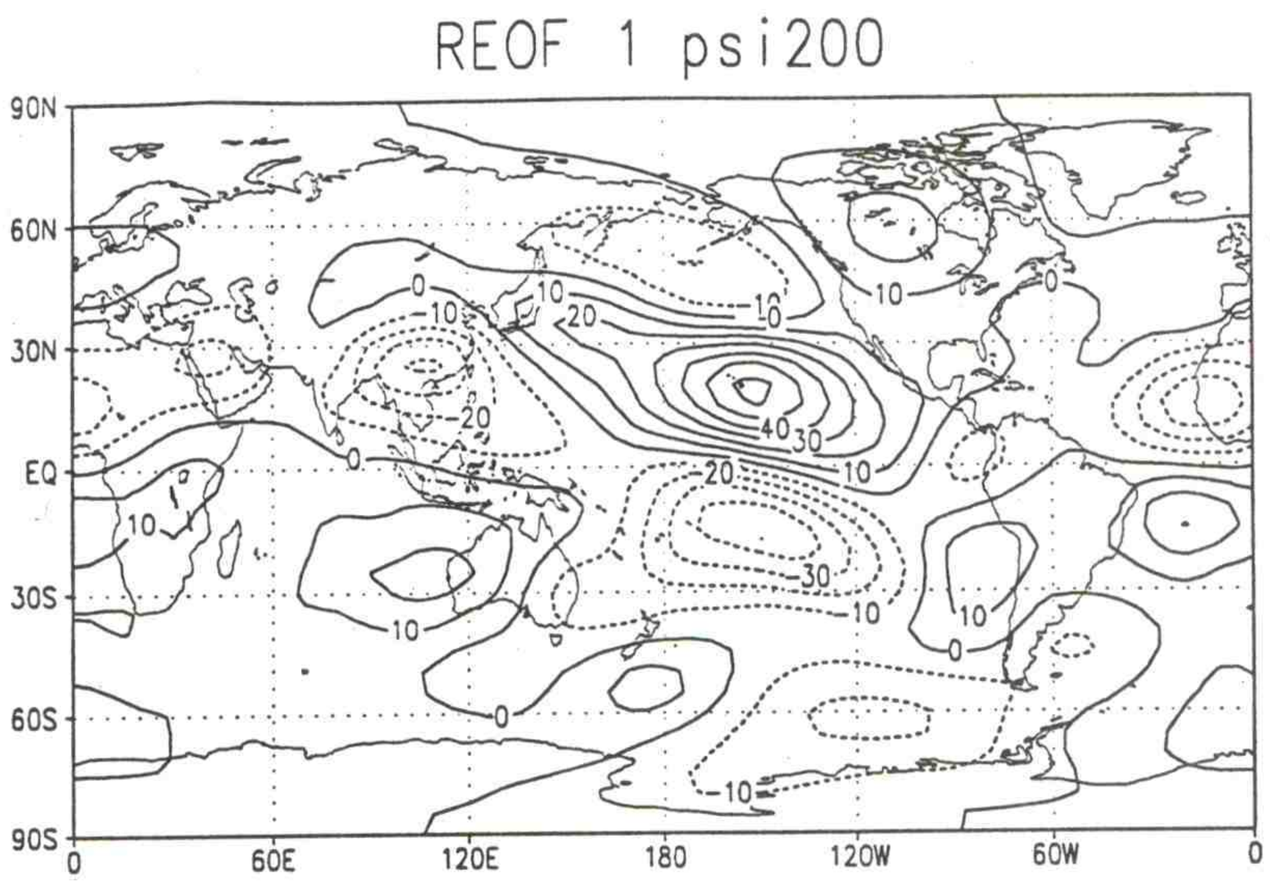

Fig.1 a: REOF 1 composite of 200 hPa asymmetric streamfunction anomalies based on two extremes of PC 1. Contour interval is 2E+06 m^2/s, negative contours are dashed. (b) same as (a), but for rainfall. Contour interval is 1 mm/day .

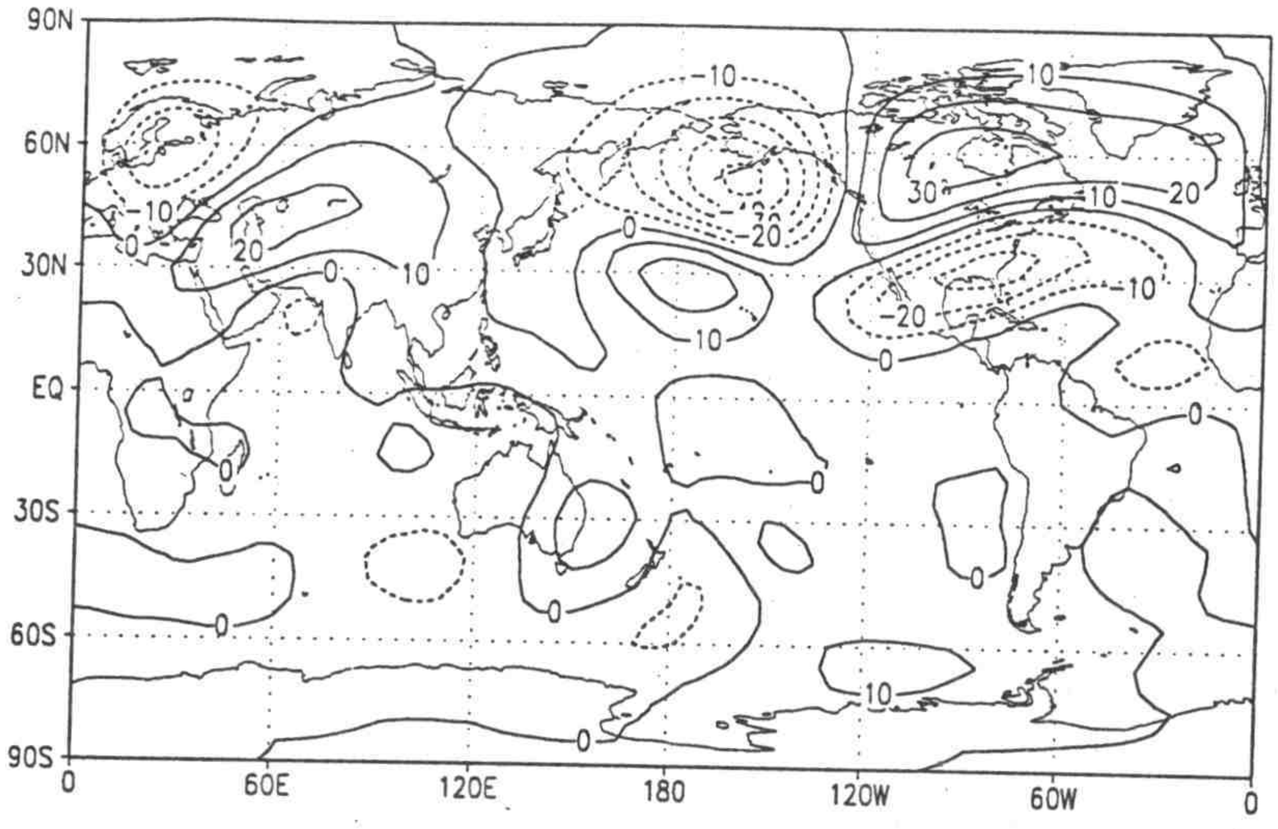

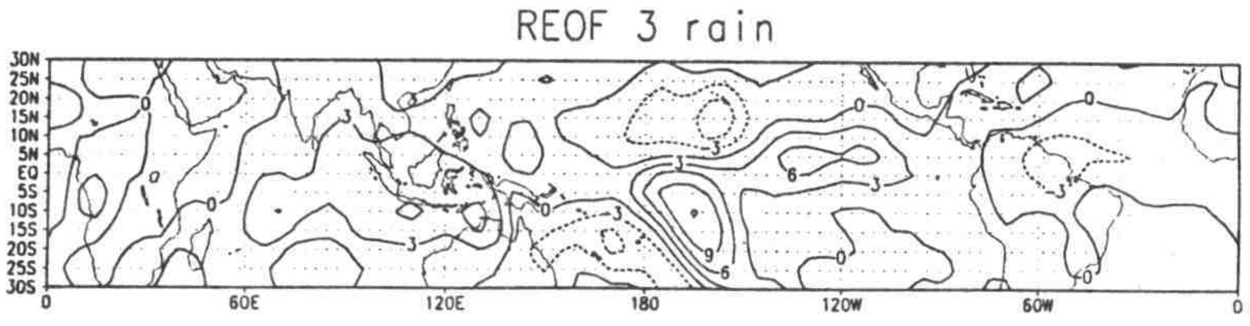

Fig.2: Same as Fig.1, but for the PNA pattern.

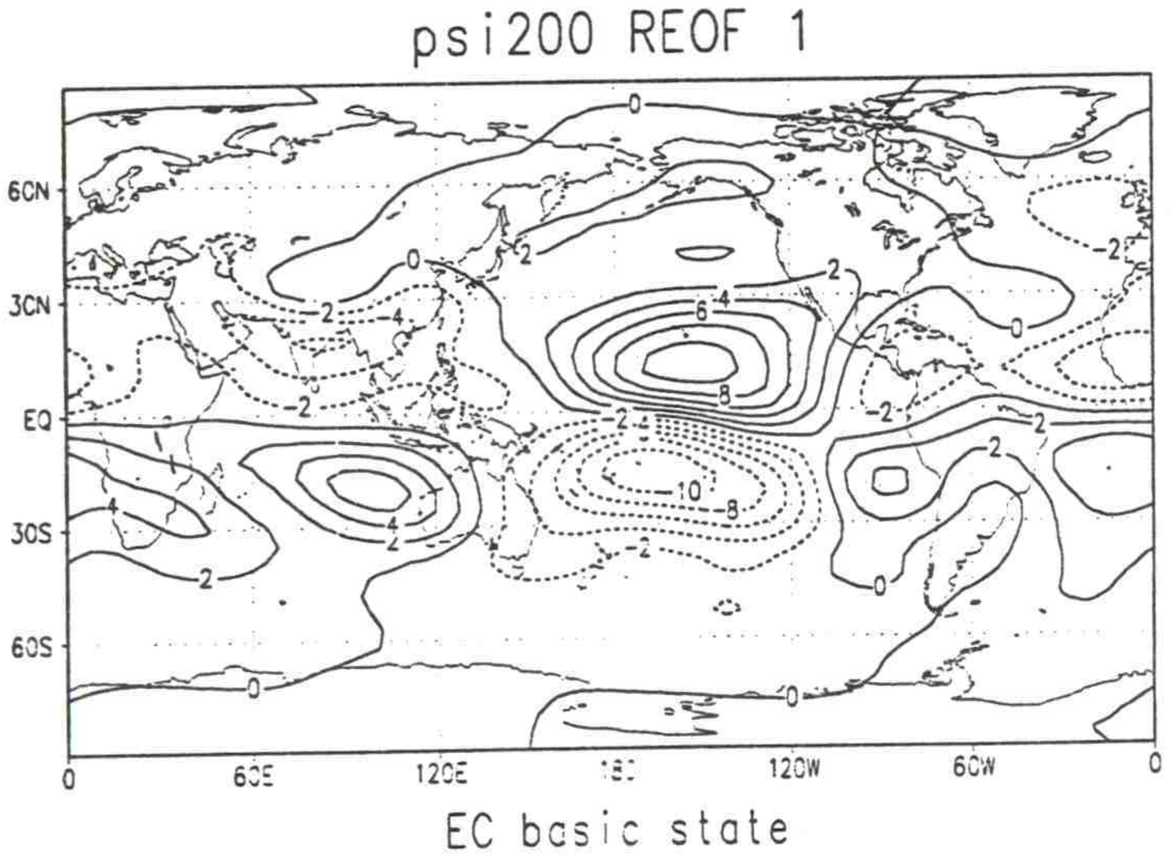

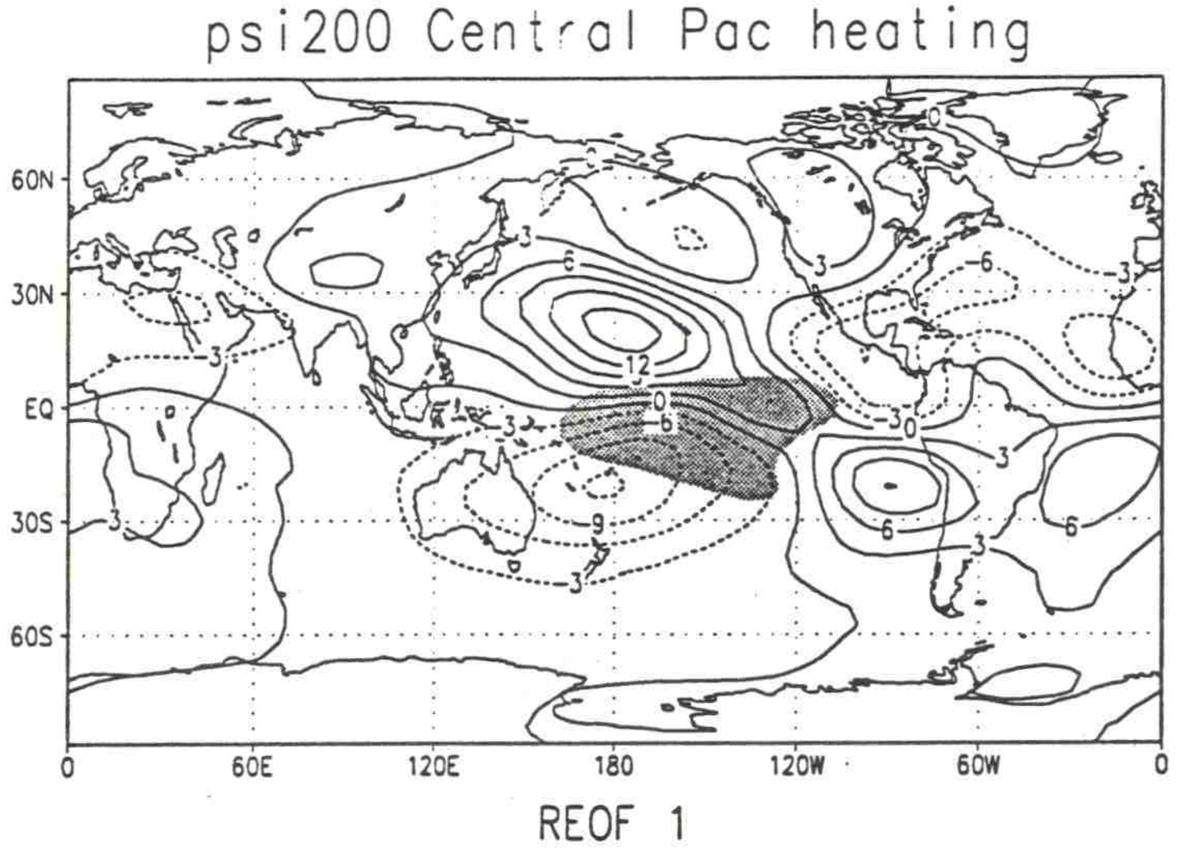

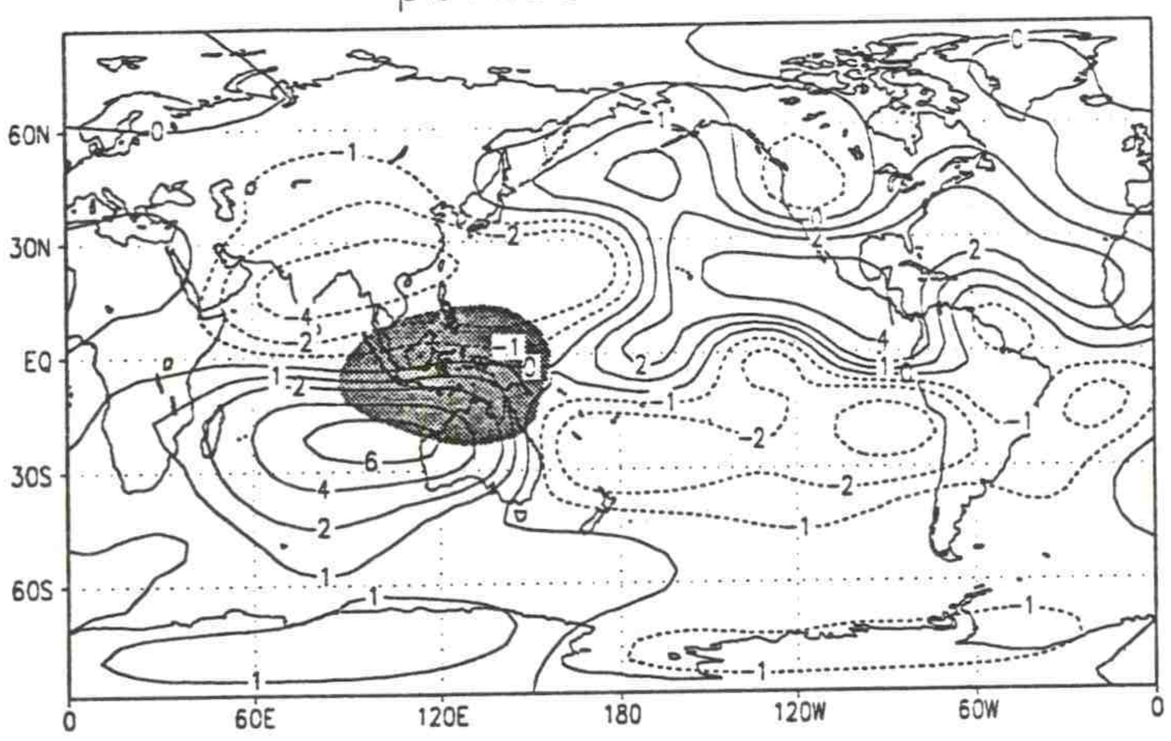

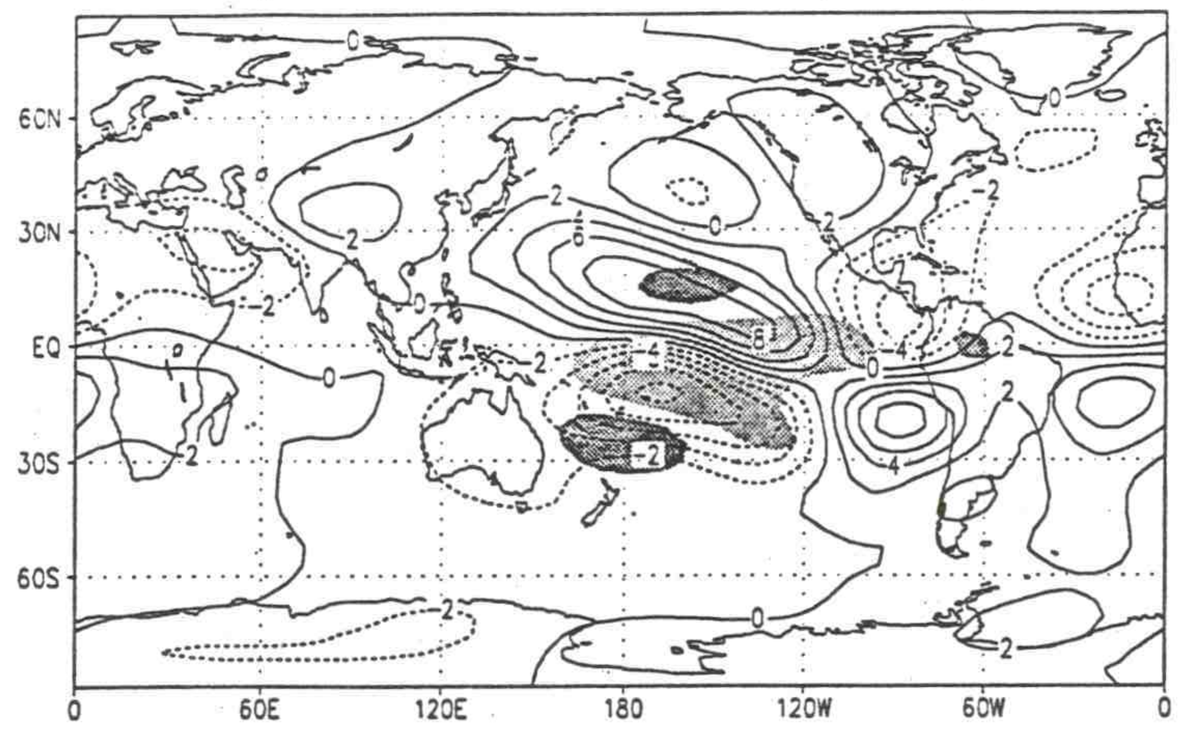

Fig.3: The steady state asymmetric streamfunction response at sigma=0.21 to (a) the total diabatic heating anomalies in Fig.1a, (b) to positive diabatic heating anomalies in the central Pacific alone. (c) to heating anomalies east of 160E and, (d) to heating anomalies west of 160E on the ECMWF basic state. Contour interval is 2E+06 m^2/s. the shading indicates the location of the heating anomalies.

CLIMATE PREDICTION METHODOLOGY

by
William M. Gray
Department of Atmospheric Science, Colorado State University
Fort Collins, Colorado 80523

There is a surprising degree of seasonal to year long climate predictability potential in atmosphere and ocean data sets. The atmosphere has a much longer memory for changes in its future state than one would surmise.

The development of new climate prediction schemes should be based on how the atmosphere-oceans have behaved in the past. This hindcasting methodology appears to offer much more likelihood of higher predictive skill than do climate forecasts made from the initial value numerical model approach.

Variations in Atlantic Seasonal Tropical Cyclone activity and other seasonal climate phenomena variability including ENSO, Asian monsoon rainfall, North African seasonal rainfall, etc. are products of the longer term variability of the global circulation. One cannot explain the variability of these phenomena by looking only at local or regional climate parameters. The global atmosphere functions as a single entity. Our project's climate research in recent years is finding that there are a surprising number of seasonal and yearly predictive signals that reside in the global circulation. These predictive signals include the stratospheric QBO, Singapore 100 mb temperature anomalies, the strength of the northeast Atlantic pressure ridge, multi-month upper tropospheric mean zonal winds and values of multi-monthly surface pressure and rainfall anomalies at various locations around the globe.

There has been a general belief that it is only the ocean, not the atmosphere, has long term predictive signals. This is based on the knowledge that the atmosphere's hydrologic cycle and its kinetic energy dissipation rates operate on a time scale of about ten days. One would not think that the atmosphere would have useful long range predictive signals. Most statistical climate forecast schemes use only sea surface temperature (SST) information. This view of the atmosphere having no long term predictive potential is not correct. There are many long period predictive signals observable within the atmosphere, even if these atmospheric predictive signals are a consequence or proxy response for what is occurring within the oceans. Although the atmosphere may be an ocean forced system, ocean

measurements are typically less accessible and do not extend back in time as long as atmospheric measurements do. One can often learn of the characteristics of the ocean better from atmospheric measurements than from direct but deficient measurements of the ocean itself. We find this to be the case. The atmosphere has much more knowledge as to the future state of the combined atmosphere-ocean system than does the ocean by itself.

The combination of global oceanic and atmospheric measurements allow a substantial degree of statistical skill for seasonal and year duration prediction. Examples of meaningful season to year long statistically predictive are available for seasonal Atlantic hurricane activity, the El-Nino-Southern Oscillation (ENSO), African rainfall, and Asian rainfall. We are presently making such predictions. But these examples are far from complete. We have only scratched the surface. It is to be expected that further observational research will uncover many more atmospheric measurements that can be utilized to allow for skillful season to year-in-advance statistical prediction of other phenomena. We are also exploring the possibility of issuing statistically meaningful outlooks of the what might be expected with regard to changes in the global circulation and various weather phenomena one to three decades into the future. These decadal outlooks are based on Atlantic Ocean conveyor belt alterations.

The methodology for detecting these predictive relationships is based on the assumption that changes in future atmospheric-ocean conditions will mimic those for similar atmospheric-ocean conditions which have occurred in the past. The documentation of past atmospheric and ocean records with sophisticated data storage and retrieval procedures on electric computers is allowing for in-depth analysis of historical weather records not possible in the past. These records throw new light on how the atmosphere and ocean undergo season to year to multi-decadal alterations.

This observationally based research approach is a very promising area for research, but, there has, however, been insufficient resource commitment to it. This is due to:

1. The general belief that few really extended range atmosphere-ocean precursor signals are present in historical data. This is not true, they just haven't been thoroughly investigated.
2. The false notion that the best methodology for climate prediction is that of initial-value numerical modeling.

The likely superiority of the empirical approach to the development of useful climate prediction schemes is due to the complex nature of the atmosphere/ocean system and to

the inability of the numerical models to realistically represent this physical complexity and then forecast this into the future. Imperfect representations of the highly non-linear atmosphere-ocean systems tend to quickly degrade into unrealistic flow states upon long period integration. The specification of the atmosphere's complicated energy and momentum exchange processes, cloud and rainfall processes, cloud versus cloud free and day versus night radiation processes, earth surface to atmospheric exchange processes, etc., etc., cannot now and likely never will be well enough parameterized in coarse grid numerical models such that long-lead climate predictions can be made with much skill — particularly skill which is greater than that of empirical based forecasts.

Although initial value numerical prediction has been a great success story for predictions of 5-10 days (where heavy reliance is placed on extrapolation of the momentum fields) such successes cannot be automatically extrapolated to the very different and much more complicated problem of the prediction on seasonal and yearly time scales. Boundary forced climate models do not utilize knowledge on how the atmosphere-ocean has behaved in the past. They only use current boundary condition. Conceptually one might say that such models lack culture. They employ knowledge of how the detailed physics of the atmosphere works but lack the ability to realistically parameterize this detailed physics with sufficient accuracy millions of time steps into the future in climate simulations. This is not possible.

This does not mean that some effort at climate modeling should not go forward to gain basic knowledge. Improved knowledge can and is coming from climate modeling. Climate models can explore sensitivity to individual parameter alteration on large time scales. Such modeling can help verify or reject various physical hypotheses. But one must realize that climate models are not (and likely never will be) a practical tool for reliable long lead climate prediction. It is important that one make a distinction between general climate understanding and climate forecasting. The two are not the same. It is unfortunate that such a high percentage of climate resources are being expended on climate modeling at the expense of observational and empirical studies which offer a much higher potential for skillful prediction.

The advantage of statistical climate forecasting over boundary condition climate modeling lies in the complex structure of the atmosphere-ocean system. One does not have to understand all of the complicated and involuted physical details of the atmosphere-ocean system to predict it. One only need learn of the time lags of various physically important

climate parameters and how they relate the climate change. In general, physical understanding follows observations rather than the other way around. By contrast, boundary condition numerical modeling requires full knowledge of the complicated physics in advance.

Acknowledgements. The author would like to acknowledge the many beneficial discussions he has had with John Sheaffer, John Knaff and Christopher Landsea. This research has been supported by climate grants from the National Science Foundation and National Oceanic and Atmospheric Administration.

A Multi-Year DERF Experiment at NCEP

J. E. Schemm and H. M. van den Dool, Climate Prediction Center
S. Saha, Environmental Modeling Center
NCEP/NWS/NOAA
Camp Springs, MD 20746

A series of dynamic extended range forecasts (DERF) have been made for a multi-year period from 1985 through 1988 to evaluate their utility for the second week and monthly mean climate predictions issued by the Climate Prediction Center. The GCM used for this purpose is the T62L28 reanalysis version of the NCEP MRF model. Fifty day forecasts are made once a day over the four year period. In these forecasts, sea surface temperature is damped to climatology from the initial condition with a 90-day e-folding time.

Evaluation of forecast skills in terms of 500 mb height anomaly correlation (AC) and root mean squre error (RMSE) is done by verifying the forecasts against the NCEP/NCAR reanlaysis dataset. In addition, attempts have been made to remove part of the model systematic errors by adopting two methods. One is removing bias estimated as an average forecast error over a 30-day training period immediately prior to the forecast initialization date. The other is removing the model climate drift. The climate drift is defined as the departure in the model climatology from the observed. The model climatology is based on a nine year (1985 - 1993) simulation of the AMIP type with the same model.

In Fig. 1, seasonally averaged AC as function of forecast lead is shown for the Northern Hemisphere Extratropics (20N-80N). The removal of systematic error does not have much of impact on the forecast skill in all seasons at all forecast lead times. This is in contrast to the results reported at the last year's workshop (Schemm, et al, 1995), which were based on forecasts during one winter season of 1991/92. This clearly demonstrates that it is neccessary to test a procedure over several seasons before drawing a conclusion on its suitability as an operational process. The winter of 1991/92 happened to be an exceptional period where the bias-based error correction method was very successful.

In Fig. 2, the annual cycle of skill in the second week forecast is examined. In general, the forecast is more skillful during winter months and less skillful during summer months. In addition to the forecasts, a regression procedure was tested to incorporate two dynamic extensions based on the forecasts. The predictors in the regression equation are the first week forecast, second week forecast, extensions of forecast based on an empirical wave propagation method and a simplified vorticity advection method. Details of the two extension methods are referred to Qin and van den Dool (1996). The regression procedure was applied to a limited region encompassing a North American sector (170W-50W, 25N-75N). The procedure was tested in a cross validation mode where coefficients were determined from data over three month segements centered on the month of verification in two years excluding the verifying year. The regression procedure improves forecast skill most of times and provides a significant increase during the fall months.

The skill of 30-day mean forecasts with a 15-day lead is shown in Fig. 3, where forecasts are relatively skillful during the August-September and December-January periods. As expected from Fig. 1, the systematic error corrections do not contribute towards improvement in forecast skill except for a few limited periods. This also indicates the need of a correction procedure dependent on flow regimes. More careful analysis on the DERF experiment data is warranted to elevate the skill of dynamic monthly mean forecasts beyond the level of statistical methods presently utilized for operational predictions.

References

Qin, J. and H. M. van den Dool, 1996: Simple extensions of an NWP model. Mon. Wea. Rev., 124, 277-287.

Schemm, J., H. M. van den Dool and W. Chen, 1994: Un update on dynamic extended range forecast experiments at CAC/NMC. Proceedings of the Nineteenth Annual Climate Diagnostics Workshop, College Park. MD, November 14-18, 1994, 448-451.

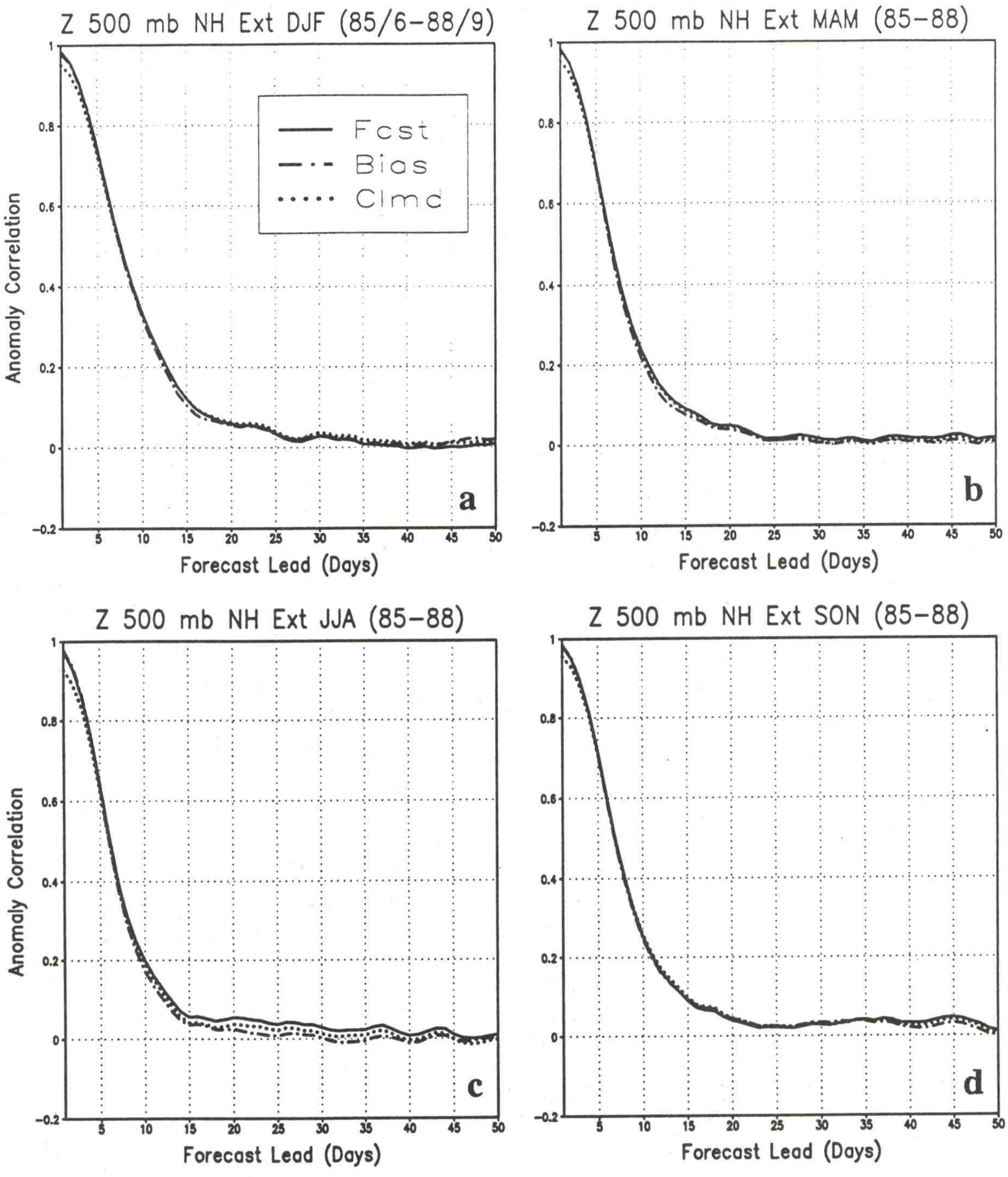

Fig. 1 Anomaly correlation scores of 500 mb height forecast for the Northern Hemisphere Extratropics (20N-80N) averaged over four winter (a), spring (b), summer (c) and fall (d) seasons as function of forecast lead in days. Solid line is for control forecast, dash-dotted line for bias corrected forecast and dotted line for forecast with climate drift removed.

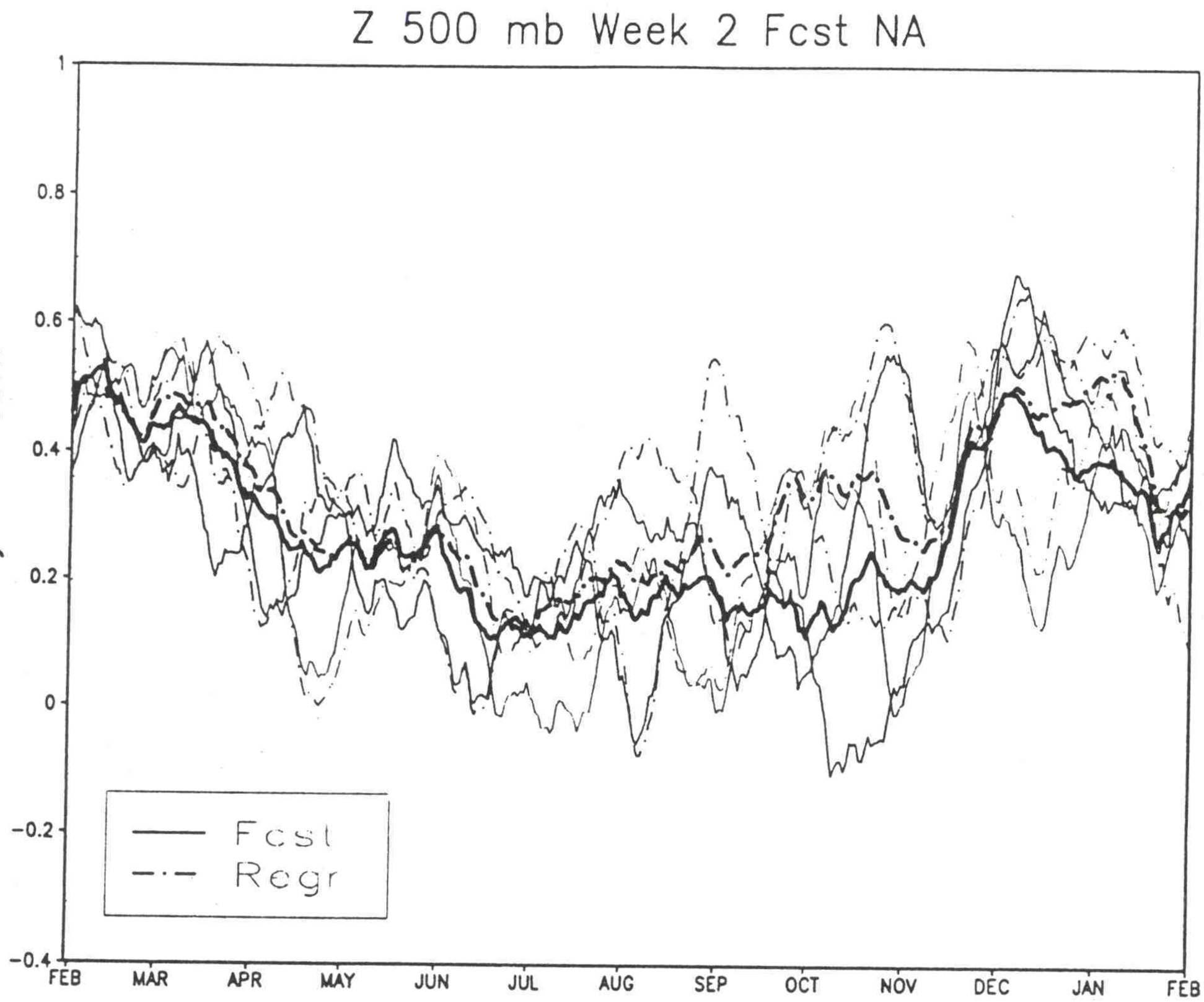

Fig. 2 Anomaly correlation scores of the second week forecast over the North American sector as function of verification date for a year period. Thin lines correspond to scores for individual years and heavy lines for the average over the 1985-1988 period. Solid lines are scores for control forecast and dash-dotted lines scores for the regression procedure.

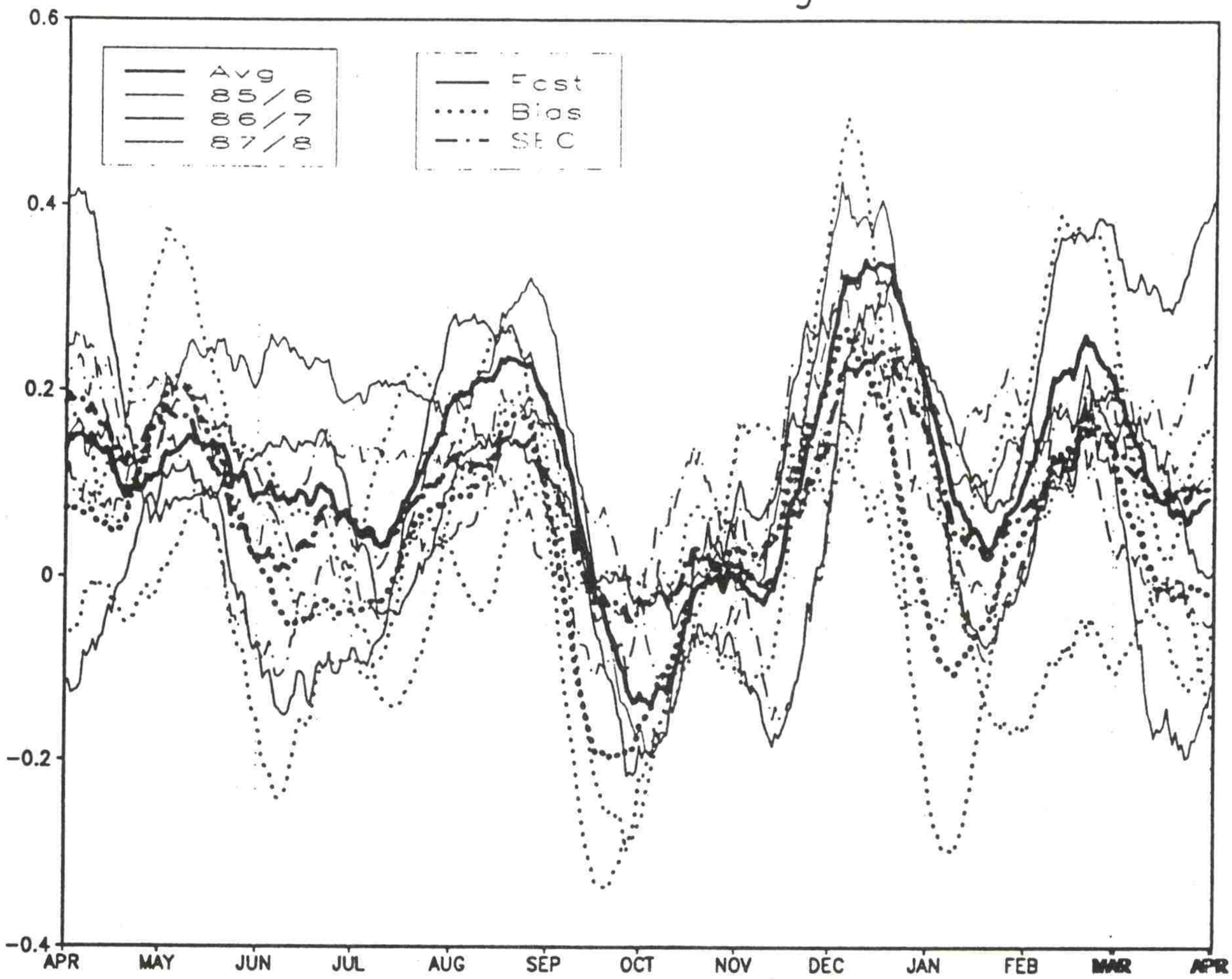

Fig. 3 Anomaly correlation scores of day 16-45 average forecast over the Northern Hemisphere Extratropics as function of verification date over a year. Thin lines correspond to scores for individual years and heavy lines for the average over the 1985-1988 period. Solid lines are for 30-day average scores of control forecast, dotted lines for bias-corrected forecast and dash-dotted lines for forecast with climate drift removed.

Inference of the Potential Predictability of Seasonal Land-Surface Climate from AMIP Ensemble Integrations

Thomas J. Phillips (phillips@tworks.llnl.gov) and Benjamin D. Santer
Program for Climate Model Diagnosis and Intercomparison (PCMDI)
Lawrence Livermore National Laboratory
Livermore, California (USA)

1. Introduction

A number of recent studies of the potential predictability of seasonal climate have utilized AGCM ensemble integrations--i.e., experiments where the atmospheric model is driven by the same ocean boundary conditions and radiative forcings, but is started from different initial states. However, only a few variables of direct relevance to the climate of the land surface (the key locus of human interaction with climate) have been examined. In this study, we infer the potential predictability of 11 climate variables that are indicative of the energetics, dynamics, and hydrology of the land surface (see first column of the Table).

We used a T42L19 ECMWF (cycle 36) AGCM having a land-surface scheme with prognostic temperature and moisture of 2 layers occupying the topmost 0.50 meters of soil, but with monthly climatological values of these fields prescribed below. Six model realizations of decadal climate (for the period 1979-1988) were considered. In each experiment, the SSTs and sea ice extents were those specified for the Atmospheric Model Intercomparison Project (AMIP), and some radiative parameters were prescribed as well (i.e., solar constant = 1365 W m^{-2}; global CO_2 concentration = 345 ppm). However, the initial conditions of the model atmosphere and land surface were different: the first two simulations were initialized from ECMWF analyses, while the initial states of subsequent realizations were assigned values that were the same as those at the last time step of the preceding integration.

2. Methodology

The potential predictability of seasonal climate is often expressed as a ratio of temporal variances:

$$\{ \sigma_T^2 - \sigma_I^2 \}/\sigma_I^2$$

Here σ_I^2 is that part of the total temporal variance σ_T^2 that is attributable to the (unpredictable) internal variability of the climate, which can be estimated from an ensemble of model realizations which vary only in initial conditions. Instead, we inferred the potential predictability of land-surface variables by different measures that more fully utilized the spatio-temporal information available from 6 model realizations. Moreover, because our statistical measures were based on correlations between independent pairs of these realizations, the ensemble size was effectively expanded from n = 6 to N =15 (i.e., n!/[2!(n-2)!]) members.

Because the potential predictability of seasonal climate implies the ability to forecast *interannual variability*, we analyzed the individual seasonal anomaly departures A(x,y,t) of each land-surface variable from the 10-year climatological seasonal cycle--i.e., a time series of ~ 40 anomaly departure maps A(x,y). Our statistical measures included:

- Zero-lag temporal correlations r(x,y) computed at each land grid point (x,y) between pairs of anomaly time series A(x,y,t) of like land-surface variables
- Pattern correlations s(t) computed on land points at each time point t for the same anomaly pairs
- Global measure R, an area-weighted spatial average of r(x,y) over all (~2700) land points (x,y)

- Global measure S, a time average of s(t) over all (~ 40) time points t
- Root-mean-square (RMS) global measure $RS = [(R^2 + S^2)/2]^{1/2}$

For each of these measures, an ensemble mean μ and intraensemble spread δ were computed from N = 15 samples.

Because all these statistics are measures of temporal or spatial *similarity* among the seasonal anomalies of the different realizations of climate, they are *inversely* related to the unpredictable internal variability of the model. It can thus be assumed that the larger the value of the ensemble mean μ of a correlation statistic, and the smaller its intraensemble spread δ, the greater is the associated potential predictability of the seasonal anomalies of the variable. (The inherent weakness of these statistics is that they are measures only of the similarity in temporal or spatial *phase* among the realizations. However, we also examined *amplitude-sensitive* measures of potential predictability such as the variance ratio in the first equation of this section. These results, which present a somewhat brighter picture of the potential predictability of a few land-surface variables in certain seasons, will be reported in a future paper.)

3. Results

Maps of μ and δ of temporal correlations r(x,y) reveal that seasonal continental climate is much more predictable in the tropics--notably over Amazonia, Equatorial Africa, Southern Asia, and Northern Australia (e.g., see maps of Figure 1 for mean sea-level pressure--MSLP). Over extratropical continents, the correlations are mostly < 0.5 for all 11 variables, and some (e.g., surface evaporation, sensible heat flux, and wind stresses) show substantial areas of temporal *anticorrelation* (not shown). These results imply that in the extratropics no one model realization can accurately predict the anomalies of a particular season; however, averaging over an ensemble of realizations can substantially increase the probability of obtaining accurate extratropical seasonal forecasts (Palmer and Anderson 1994, Barnett 1995).

Even in the tropics, there is a considerable range of potential predictability among the model's land-surface variables. For example, tropical MSLP shows broad areas of temporal correlations > 0.5 (Figure 1), while correlations of surface evaporation are this high in only a few scattered equatorial regions (not shown). (Correlations > 0.5 indicate a *practically significant* predictability that would be of potential social value. It should be noted, however, that an ensemble-mean correlation of 0.5 implies that only 25 % of the interannual variance of a seasonal land-surface variable in a given realization is explained, on average, by another realization.)

The time series of μ and δ for the pattern correlation s(t) of the 11 land-surface variables reveals quite different phenomena. In this case, MSLP exhibits numerous instances of negative-valued ensemble-mean s(t) and generally large intraensemble spread δ (not shown), while the surface evaporation shows substantially more coherence (Figure 2). There is also an obvious enhancement of the ensemble-mean pattern correlations of surface evaporation in seasons immediately following the onset of El Niño and La Niña events (e.g. 1982/83, 1984/85, 1986/87). The ENSO signal is present in the pattern correlations of seasonal anomalies of all the other land-surface variables, suggesting that continental seasonal climate is generally more predictable at such times.

The potential predictability of different land-surface variables ranges rather widely in a global sense as well (see Table). The model's soil moisture, MSLP, and surface air temperature are most predictable overall, while the surface fluxes of momentum, sensible heat, and moisture are the least predictable. The hydrological variables and those related to the radiation and temperature at the ground show intermediate levels of global potential predictability.

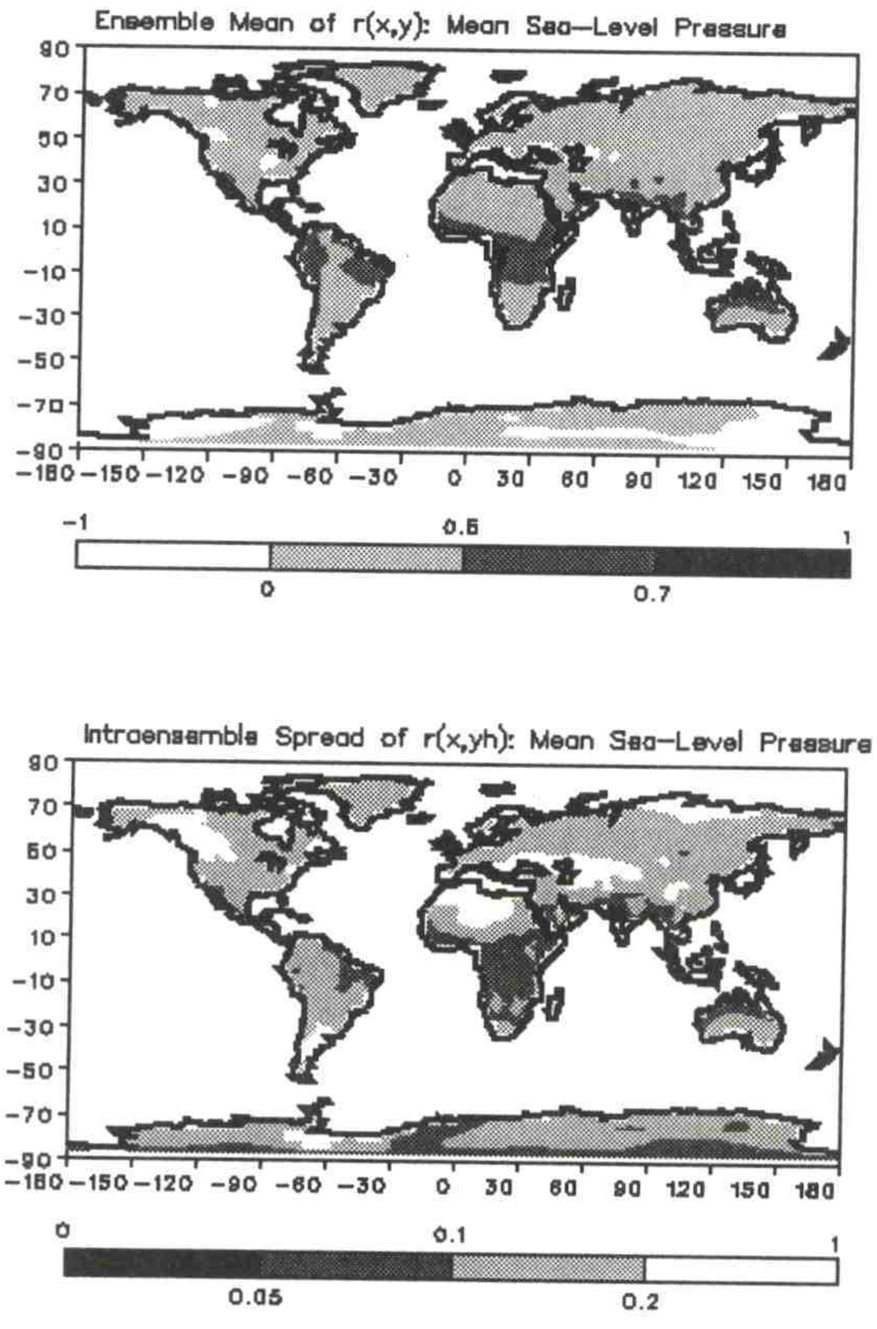

Figure 1: Maps of ensemble mean μ (top) and intraensemble spread δ (bottom) of zero-lag temporal correlations r(x,y) between 15 pairwise-selected realizations of seasonal anomalies of continental mean sea-level pressure (MSLP). Note that darker shading in both panels indicates regions where MSLP is likely to be most predictable in a temporal sense (i.e., areas with relatively high ensemble-mean correlations and low intraensemble spread).

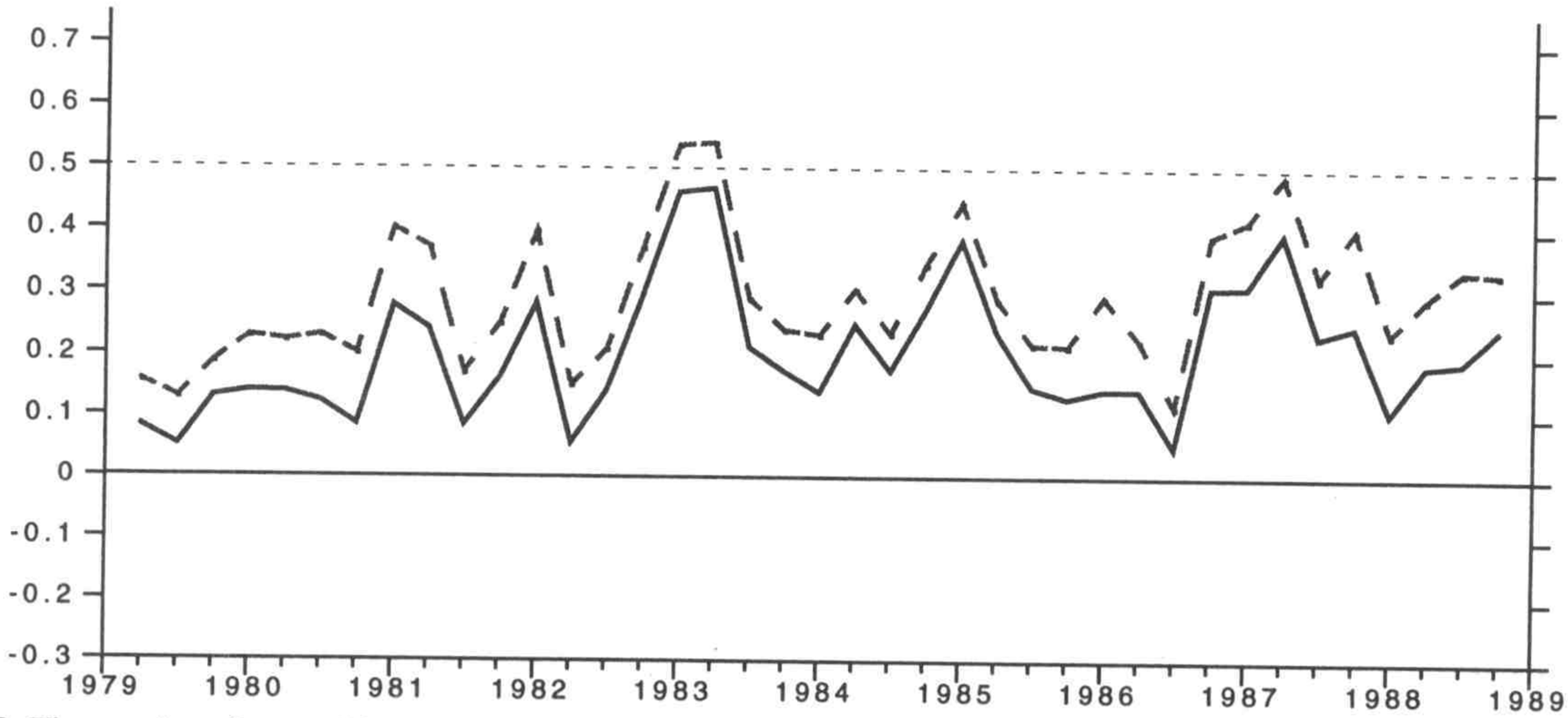

Figure 2: Time series of ensemble mean μ (solid line) and intraensemble spread δ (dashed line) of pattern correlations s(t) between 15 pairwise-selected realizations of seasonal anomalies of continental surface evaporation.

Table: Global measures of the potential predictability of seasonal anomalies of 11 land-surface variables. The variables are ranked in order of the magnitude of the ensemble-mean rms global measure $RS = [(R^2 + S^2)/2]^{1/2}$, where R is an area-weighted average of temporal correlations r(x,y) and S is a time average of pattern correlations s(t).

Variable	**RS**	**R**	**S**
Soil Moisture	0.220	0.203	0.236
Mean Sea-Level Pressure (MSLP)	0.216	0.292	0.090
Surface Air Temperature	0.216	0.266	0.150
Precipitation	0.198	0.145	0.239
Surface Net SW Radiation	0.195	0.205	0.184
Surface Net LW Radiation	0.192	0.203	0.182
Ground Temperature	0.189	0.241	0.116
Surface U-Wind Stress	0.177	0.211	0.133
Surface Evaporation	0.176	0.143	0.203
Surface Sensible Heat Flux	0.172	0.153	0.188
Surface V-Wind Stress	0.155	0.187	0.113

It is likely that the relatively slow spatio-temporal variation of the model's soil moisture contributes to its higher global potential predictability. The apparent absence of a strong connection between the potential predictability of the model's seasonal anomalies of soil moisture and surface evaporation is probably due to the role that the simulated vegetation canopy plays in regulating evaporation. Moisture intercepted by the canopy evaporates directly to the atmosphere, while evapotranspiration of soil moisture is inhibited during times of vegetation stress, such as dry climatic conditions.

From the Table, it can be seen that the S values of seasonal anomalies of soil moisture, precipitation, evaporation, and sensible heat flux are higher than those of MSLP and surface air temperature, while the R values of the latter variables are higher than those of the former. This behavior appears to be related to differences in the characteristic spatial scales of the seasonal anomalies of different variables. For example, in different model realizations it is not unusual for MSLP anomalies in a particular season to be of opposite signs on a continental scale, thereby yielding low values of s(t), and a low S value overall. The seasonal land-surface evaporation anomalies are generally of much smaller scale, so oppositely signed anomalies impact the pattern correlations much less. On the other hand, the temporal variation of the surface evaporation anomalies is more rapid (noisy) than that of the MSLP anomalies, so the R value of the latter is higher.

Some land-surface variables (e.g. MSLP, surface air temperature, precipitation, ground temperature, surface u-wind stress, surface evaporation) exhibit a pronounced asymmetry in their R and S values. We caution that this property may be merely an artifact of different sample sizes. That is, R is obtained by averaging r(x,y) over ~ 2700 land points (x,y), while S represents an average of s(t) over only ~ 40 time points.

References

Barnett, T.P., 1995: Monte Carlo climate forecasting. *J. Climate*, **8**, 1005-1022.

Palmer, T.N., and D.L.T. Anderson, 1994: The prospects for seasonal forcing--A review paper. *Quart. J. Roy. Meteor. Soc.*, **120**, 755-792.

Specification of Continental Temperature and Precipitation Using Global SST

Thomas M. Smith and Anthony G. Barnston

NOAA/National Centers for Environmental Prediction
Climate Prediction Center
Washington, D.C. 20233

A reconstructed global SST data set is used to examine relationships between SST and seasonal mean land-surface temperature and precipitation over most of the globe from 1950-92. The SSTs are from a reconstruction based on COADS observations and spatial covariance scales computed from the 1980s high resolution SST analysis. Land temperature and precipitation data are from global, irregularly distributed networks of stations. Canonical correlation analysis is used to describe the relationships and to give information aiding the physical interpretation of the findings. A sequence of four consecutive three-month periods of global SST anomalies are related to temperature and precipitation anomalies for the fourth period. Skill is assessed using the temporal correlation of the observed values with the model values from cross-validated specifications.

Specification skill is modest except for certain regions and/or times of the year when correlations of 0.6 or greater may occur. Temperature is generally specified with more skill than precipitation. For most of the year temperature specification skill is high in northern South America (Fig. 1). Temperature skill is highest in North America in the JFM season with a secondary maximum in JAS. Across the Sahel region of Africa temperature skill is high in the summer (JAS). There is also temperature skill across southern Europe in JAS. Precipitation skill (Fig. 2) is highest across the Sahel in the wet season (JAS). There is also significant JAS skill in western India and Pakistan, eastern Australia, and eastern tropical South America. In JFM places with high precipitation skill include parts of Australia, South Africa, western Africa, and southeastern and parts of western North America. The central tropical Pacific islands have high skill for both temperature and precipitation specification year round.

Based on an examination of the CCA diagnostics, most skill is found to be related to two modes of oceanic variation. One mode is low-frequency trends in the SST. Trends are responsible for much of the Sahel skill for both temperature and precipitation, for the European JAS temperature skill, and for some of the North American temperature and precipitation skill. The other major mode of oceanic variation is that associated with warm and cool episodes in the tropical Pacific. Skill in all of the tropics, including Sahel Africa, is influenced by these variations, as is skill in North America and Australia.

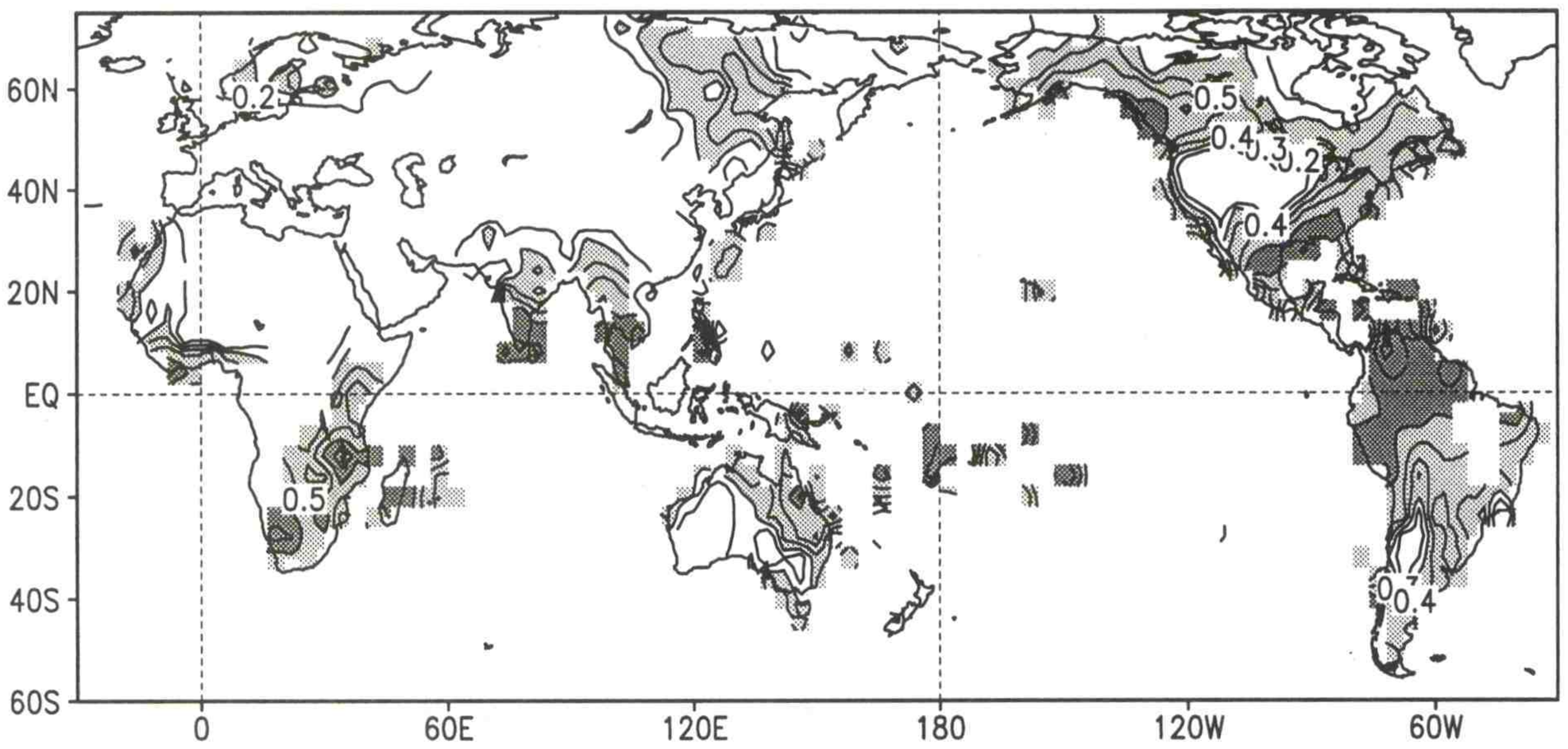

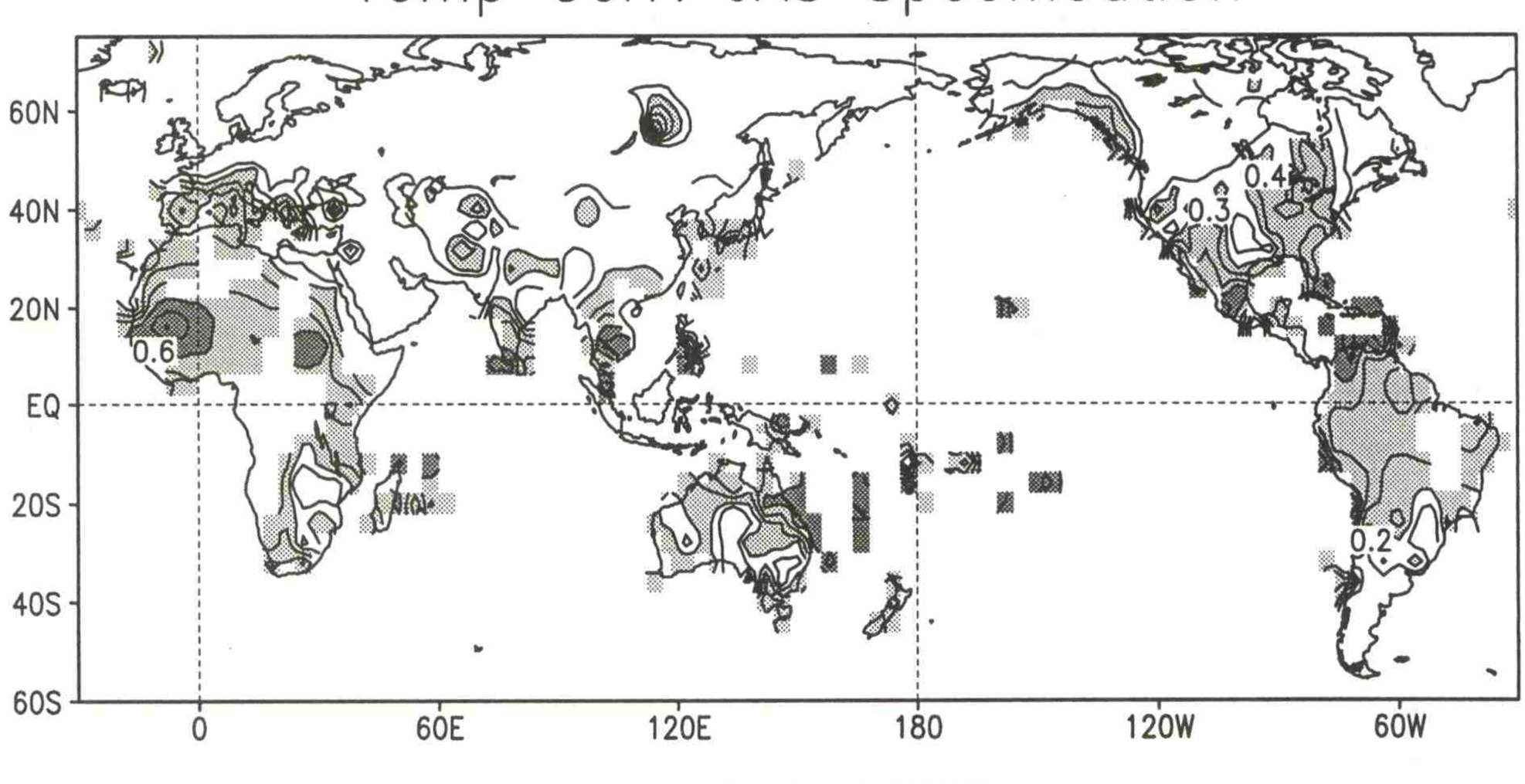

Fig. 1. Land-surface temperature specification skill for the JFM season and the JAS season. Skill is express as temporal correlation of the specification value with the observed value. The contour interval is 0.1, contours less than 0.2 are omitted. Light shading is used for values above 0.3 and dark shading for values above 0.6. Plotting is suppressed in regions with insufficient data.

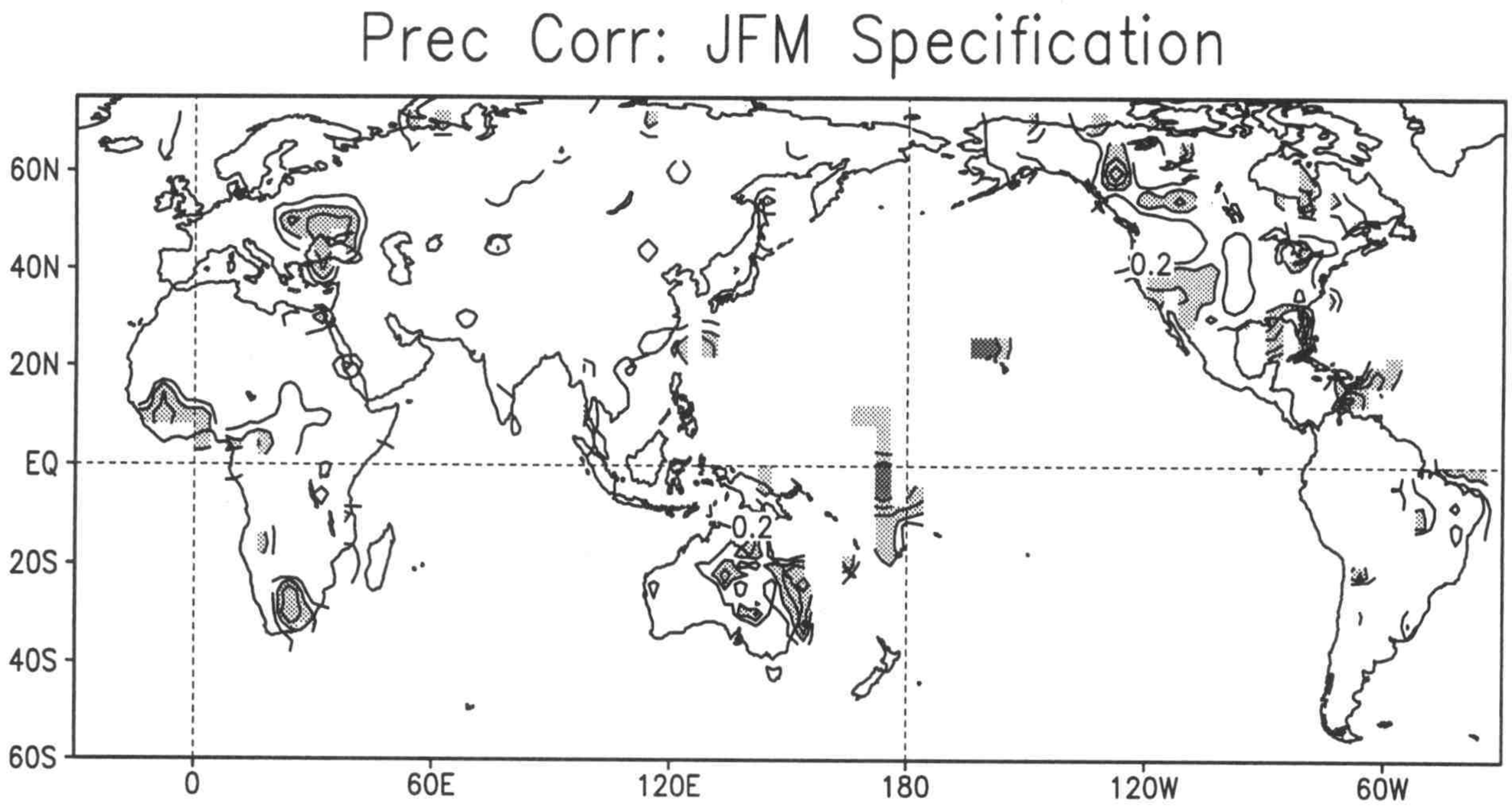

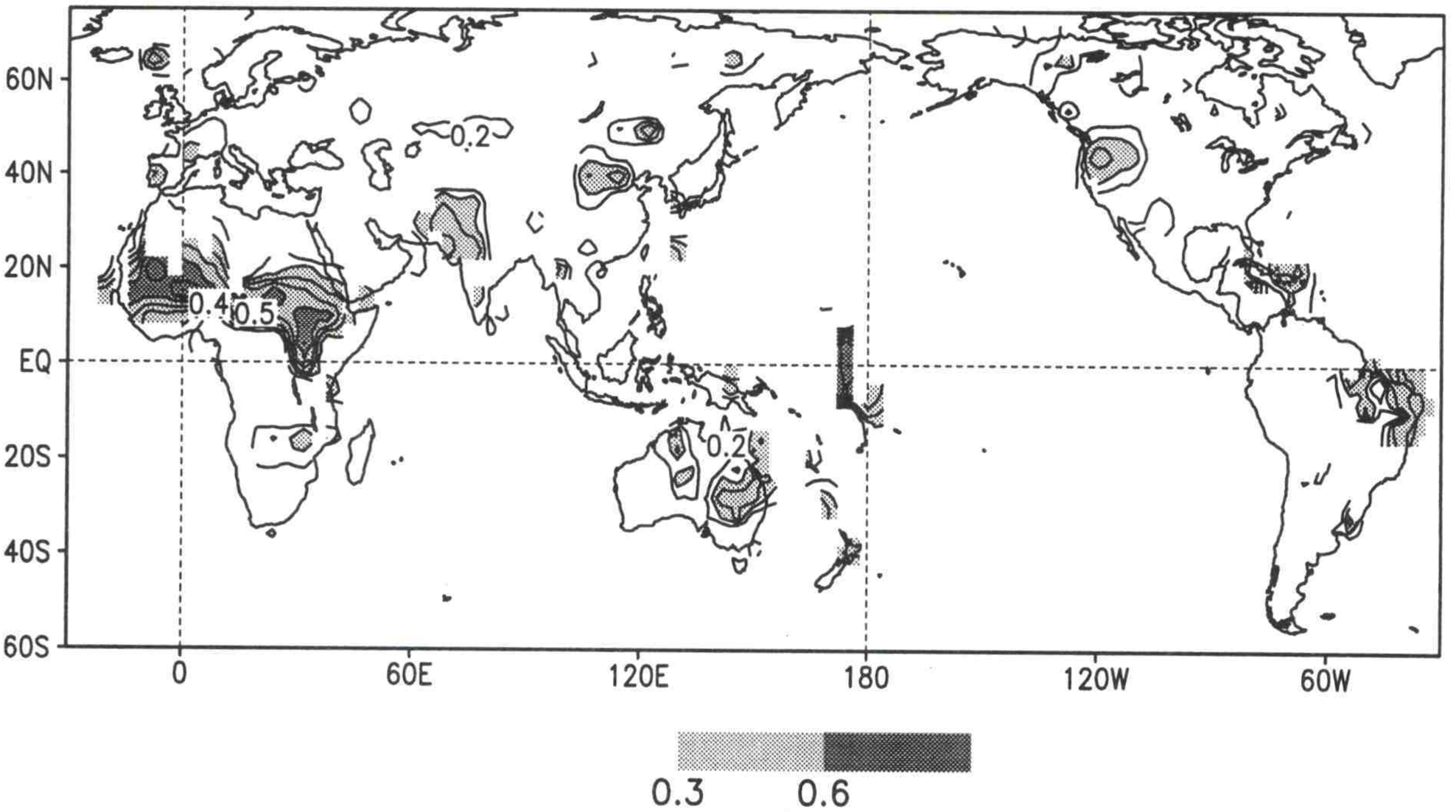

Fig. 2. Land-surface precipitation specification skill for the JFM season and the JAS season. Skill is express as temporal correlation of the specification value with the observed value. The contour interval is 0.1, contours less than 0.2 are omitted. Light shading is used for values above 0.3 and dark shading for values above 0.6. Plotting is suppressed in regions with insufficient data.

TELECONNECTIONS AND SEASONAL RAINFALL PREDICTION IN AFRICA

Wassila Thiao, Anthony G. Barnston, and Vadlamani Kumar

NOAA/NWS/National Centers for Environmental Prediction
Climate Prediction Center

Washington, DC 20233

1. **Introduction**

Recurrent rainfall deficits across Africa during the past several decades have been inimical to the economy of the African nations. In this context, decision-makers and funding agencies often face challenges to make relief plans. Thus, there is a need for climate forecasting, in particular month to season rainfall prediction in Africa. The African Desk, established at the Climate Prediction Center (CPC) of the NWS/NCEP, collected historical data from various sources to experiment with seasonal forecasting in Africa in collaboration with the CPC/Prediction Branch. The technique used is the Canonical Correlation Analysis (CCA) developed at CPC by Anthony Barnston, based on the work of Tim Barnett.

Several forecast experiments are currently being run (U.K. Meteorological Office, Bracknell; Colorado State University, Fort Collins, etc.). Most of these forecasts are experimental and deal with the Sahel, where one can find a fairly good network of raingages. These forecast schemes use statistical approaches based on long-term historical data of sea surface temperature, rainfall and other climatic variables. This paper addresses the possibility of developing an operational seasonal rainfall forecast scheme in Africa using the operational CCA long-range forecast procedure for the Northern Hemisphere mid-latitudes (North America and Europe) (Barnston, 1994, J. Climate, 1513-1564).

After a description in section 2 of the data and technique used in this study, results from the CCA experiments are presented in section 3, and finally, a summary is given in section 4.

2. **Data and Methodology**

a. **Rainfall Data**

Rainfall data from various sources were collected. These include the Food and Agriculture Organization (FAO) of the United Nations, the Global Historical Climatology Network (GHCN), a compilation of global historical data by the U.S. Carbon Dioxide Information Analysis Center (CDIAC) and the National Climatic Data Center (NCDC), The Nile River Project of the NWS/Office of Hydrology, and the Drought Monitoring Center of Zimbabwe. Since all of the sources of data have missing rainfall reports, the data from these various sources were compiled to create a consolidated data base, i.e. the data from the various sources were merged to fill in the gaps. The period 1955-1992 was used as a training period in this study. CCA requires the use of complete long-term historical records to minimize noise induced by gaps in

the use of complete long-term historical records to minimize noise induced by gaps in the data. All the stations with more than 10% of missing reports were removed. Figure 1 shows the distribution of the raingage network used. For these stations, the missing reports were filled with climatology.

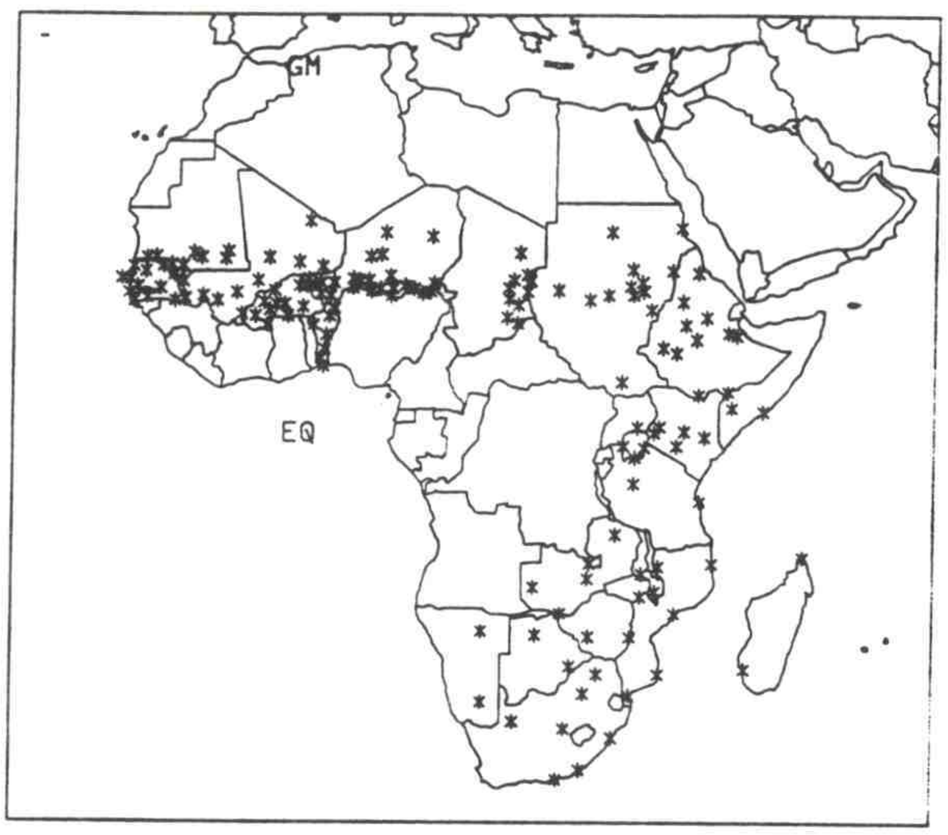

Fig 1: Spatial distribution of raingages over Africa.

b. **CCA Procedure**

CCA is a multivariate linear statistical model that utilizes Northern Hemisphere 700 hpa height, quasi-global SST, precipitation and surface temperature data to forecast monthly and seasonal precipitation and surface temperature with lead times from zero to 13 months. Our definition of lead time is the period between the time the forecast experiment is run and the target period. In these experiments over Africa, only quasi-global gridded SST data at a horizontal resolution of 10°X10° were used as predictors, and precipitation is the predictand. CCA involves several procedures that include: (1) data preprocessing; i.e, standardization of the data, pre-orthogonalization, and (2) the CCA itself, that generates eigenvectors and eigenvalues for predictors and predictands the correlation matrix between the pre-orthogonalized predictors and predictands. Amplitude time series for each CCA mode are also computed. A cross validation is done to test the skill of the forecasts. (For more detail on the CCA technique see Barnston, 1994).

3. **Results**

Several forecast experiments have been performed in this study. Due to the immensity of the continent and for the sake of homogeneity in the rainfall patterns, Africa was divided into three major geographical regions: (1) Sahel extending from 5°N-25°N,45°E-18°W. The rainy season in this region extends from May through October with a peak in JAS. (2) East Africa (8°S-5°N,45°E-30°E). This region is characterized by two rainy seasons in MAM and OND. (3) Southern Africa (35°S-10°S, 50°E-15°E): most of the rainfall in this region occurs during the period November through April with a peak in DJF or JFM.

A first step to the seasonal forecast experiments was to investigate the teleconnection patterns based on seasonal mean precipitation. Seasonal means JAS for Sahel, MAM for eastern Africa, and DJF for southern Africa were computed for the 1955-92 period. These seasonal means serve as a basis for a point correlation analysis. The teleconnection patterns (not shown) exhibited significant spatial correlations within the three regions. The inter-regional correlations were rather low. Thus, we decided to run our forecast experiments for each region. In this paper, only results from the Sahel experiments are shown.

The seasonal rainfall variability and relationship to ENSO was also investigated. The annual cycle of the Sahel rainfall (not

normal rainfall in the 50s extending to the early 70s, and one regime with mostly below normal rainfall starting in the early 70s extending to the 80s and 90s.

The correlation coefficient between rainfall and SST anomalies were -0.44. However, it was noted that during the extremely warm ENSO years for example in 1972, 1982-83, 1992, rainfall amounts were rather low in the Sahel. While in 1988, when SSTs were cold in the equatorial Pacific, rainfall tended to be abundant. Figure 2 displays the seasonal cycle of the CCA average skill over the Sahel at lead times of 1, 4, 7, 10, and 13 months.

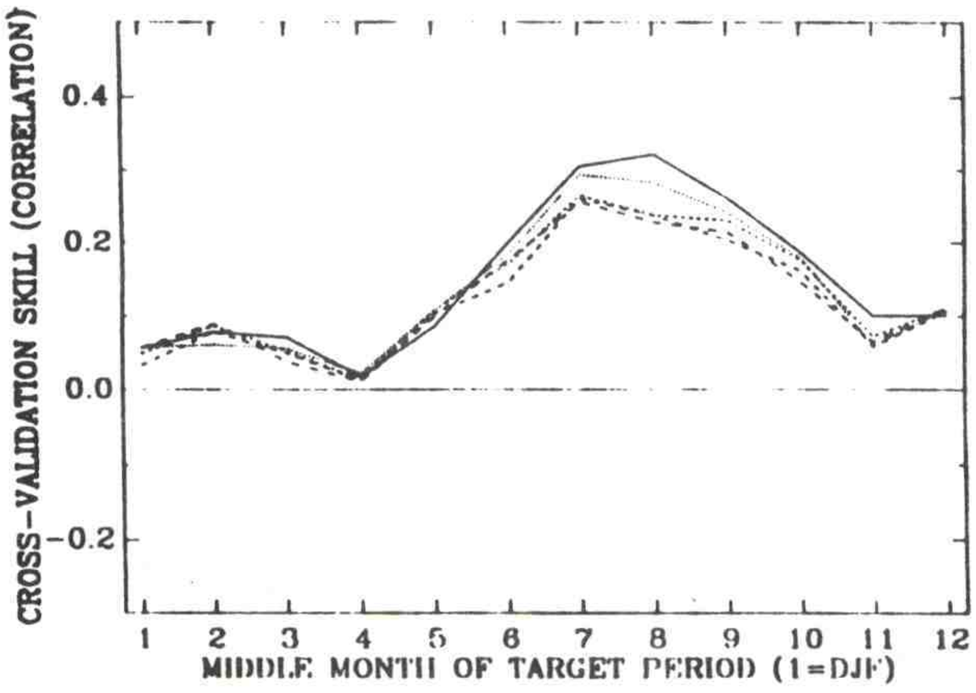

Fig 2. 3-Month precipitation CCA average skill over Sahel.

The numbers indicated in the abscissa represent the middle month of the target periods and in the ordinate are represented the cross validated correlations (CVR). The average skill is highest for JAS, with a CVR of 0.32. Note that the CVR, while low, does not decrease substantially as the lead time increases. In Fig. 3 is represented the geographical distribution of CCA skill at one month lead for the target period of JAS. The picture depicts widespread moderate skills (between 0.4 and 0.5) in parts of central Ethiopia, western Sudan, southern Niger, parts of Burkina Faso, Mali, and Mauritania. Skills are rather low elsewhere. The principal predictor loading patterns (not shown) exhibited negative eigenvalues in the equatorial Pacific. These were associated with positive eigenvalues in the principal predictand loadings, suggesting a contribution of ENSO in determining JAS rainfall in the Sahel. In particular, warm ENSO events tend to suppress rainfall.

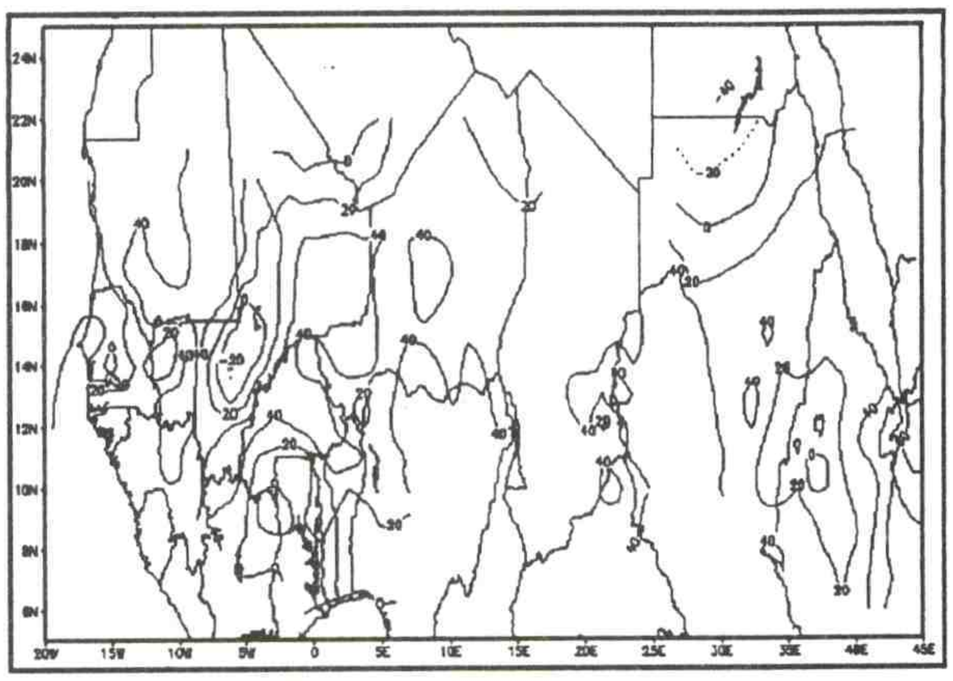

Fig 3. Geographical distribution of CCA skill, one month lead for JAS Sahel rainfall.

The mode 2 CCA predictor loading patterns two seasons prior to the target period is shown in Fig. 4. It reveals a clear dipole, with negative eigenvalues in the northern Atlantic and positive values in the southern Atlantic. The corresponding predictand loadings are mainly negative. This indicates that warm SSTs in the southern Atlantic associated with cooling in the northern Atlantic tend to result in a deficiency in the rainfall in the Sahel during JAS. The CCA predictor time series for the same mode depicted clearly a warming (cooling) trend in the southern (northern) hemisphere. This implies that in addition to ENSO, the Atlantic Ocean plays an important role in modulating rainfall patterns in the Sahel during JAS.

rainfall patterns in the Sahel during JAS.

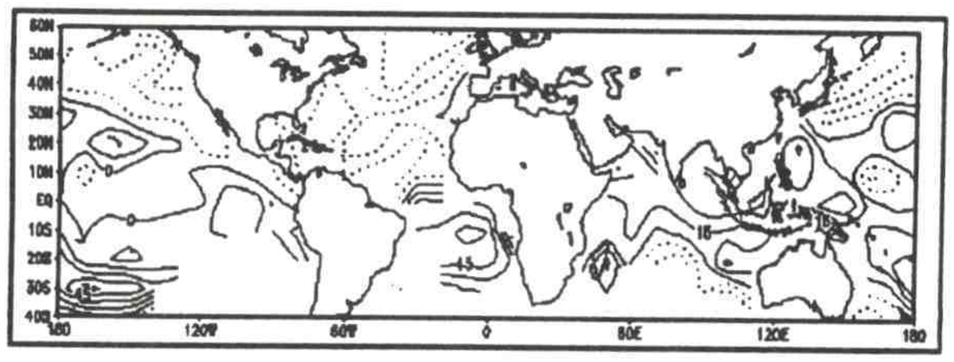

Fig 4a. DJF period SST predictor CCA loading for mode 2.

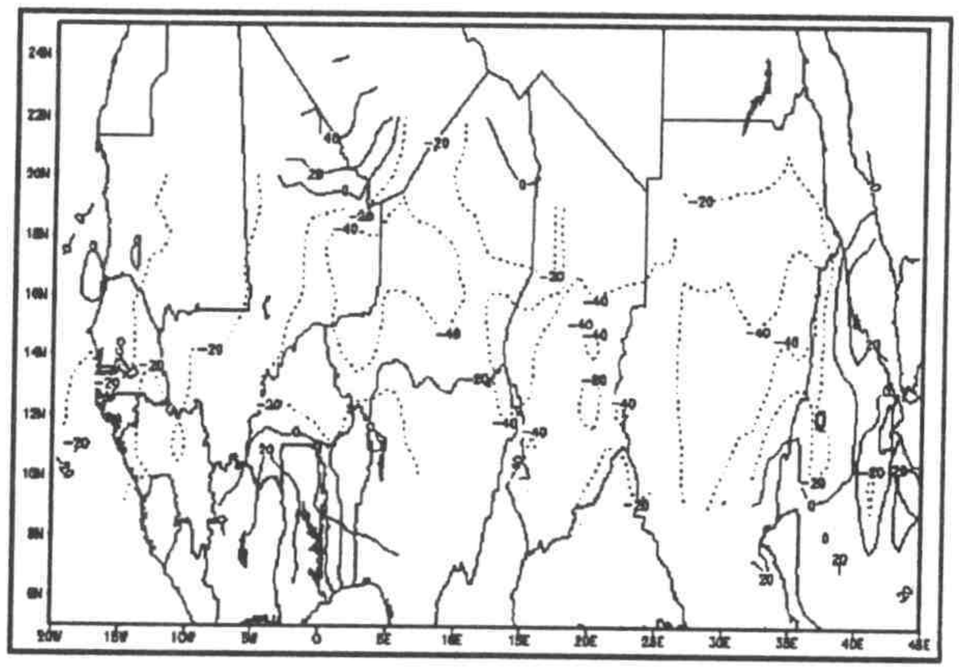

Fig 4b. JAS precipitation predictand loading patterns for mode 2.

4. **Summary**

Historical station data and quasi-global 10°X10° gridded SST data for the period 1955-92 were used to explore long-range precipitation forecasts in Africa. The regions: continent was divided into three geographical Sahel, eastern Africa, and southern Africa. Prior to the forecast experiments, region to region rainfall teleconnections were investigated The presence of spatial coherence in the seasonal rainfall patterns within the three regions were found. Correlations between rainfall and Nino 3 SST anomalies were moderate. However, some correspondence between extreme warm (cold) events and low (abundant) rainfall were found.

The seasonal forecast technique used in this study is the Canonical Correlation Analysis (CCA), a multivariate linear statistical model. Moderate, but localized skills for JAS Sahel rainfall were found. The seasonal cycle of the forecast skill revealed that the skill was higher during the peak of the rainy season. The average skill for JAS at one month lead was 0.32. The skills were lower for JFM southern African rainfall and for OND/MAM eastern African rainfall. The experiments revealed that ENSO has at least an influence in all three regions, but Sahel rainfall has a long-term downward trend related to the interhemispheric SST difference. Thus, CCA has a potential for seasonal rainfall prediction in Africa. Further details in these experiments will be given in Barnston and Thiao (in preparation for submission to *Weather and Forecasting*.)

CLIMATE ENSEMBLE FORECASTING AT CPTEC

P. Nobre, M. L. Abreu, I. F. A. Cavalcanti, M. Quadro and L. Pezzi

Centro de Previsão de Tempo e Estudos Climáticos - CPTEC
Instituto Nacional de Pesquisas Espaciais - INPE
Rodovia Presidente Dutra, Km 40, Cachoeira Paulista, SP, 12630, BRAZIL

ABSTRACT

The first numerical seasonal forecast experiment done at CPTEC for the March-April-May (MAM) 1995 rainy season over northeastern Brazil (Nordeste) is described. Four member ensembles with varying initial conditions are used to obtain the seasonal forecasts. For each initial condition the atmospheric general circulation model is integrated for six months for both climatological and persisted SST anomalies. The MAM rainfall forecast using March 1995 SST conditions closely resembled the observed rainfall distribution. However, the forecasts which used December 1994 and January 1995 SST anomalies were opposite to the observed rainfall anomalies. It is concluded that atmospheric general circulation modeling is capable of predicting seasonal rainfall anomalies over Nordeste, provided accurate tropical SST forecasts are available with sufficient leading time.

Introduction

There is an appreciable amount of observational, theoretical, and general circulation modeling evidence that interannual variability of seasonal rainfall over northeast Brazil (Nordeste) region is strongly modulated by sea surface temperature anomalies over both tropical Atlantic and equatorial Pacific Oceans. Statistical multi linear regression models which explored such dependence on SST have been constructed to forecast seasonal rainfall anomalies over Nordeste. More recently, also atmospheric general circulation models (AGCM) have been used to forecast seasonal rainfall distribution over Nordeste (Graham, 1994, 1995; Shukla, 1994, personal communication). So far, AGCM-ing has shown to be a promising tool towards seasonal forecasts with leading time of months to seasons. The present study describes the numerical seasonal forecast of March-April-May (MAM) 1995 rainfall over Nordeste done at CPTEC. The model used is CPTEC/COLA AGCM with horizontal resolution T62, and 28 levels in the vertical.

Methodology

The numerical experiment consists of four member ensembles, six month long each, starting with slightly different initial conditions (00Z NMC (presently NCEP) analyses for days 27, 28, 29 and 30 November 1994). For each initial condition a control and forecast run are done. Surface boundary conditions for the control runs are climatological SST and soil moisture. For the forecast runs, observed SSTs are used up to the latest month for which observations are available; and persisted SST anomalies during the remaining period. So, for the January forecast, February through June SSTs are calculated as the monthly long term means of each month plus January 1995 SST anomalies at each grid point between 50S and 60N. SST over higher latitudes of both hemispheres are climatological. Boundary conditions over the continents are soil moisture and vegetation types. The AGCM interacts with land surface through SiB model. Soil moisture initial values are modified by SiB during the integration. The first months of

integration use observed SSTs as an attempt to bringing soil moisture values from climatology to more "actual" values. The forecasted rainfall anomalies are the differences between the forecast and control runs, ensemble averaged.

Results

The runs which used December 1994 SST conditions forecasted negative MAM rainfall anomalies over Nordeste (figure not shown). Other runs, using January, February, and March SST respectively, presented progressively higher (positive) rainfall anomalies over Nordeste, as the monthly SST fields approached more and more actual MAM SST. Figure 1 shows the January SST-based and the March SST-based rainfall forecasts for MAM 1995, and the observed rainfall anomalies for the period over Brazil. The January forecast (Fig. 1a) shows negative anomalies over most of central-northern Brazil (north of 15°S). The analyses of OLR and total precipitation over the tropical Atlantic (figures not shown) for the January forecast suggested that the intertropical convergence zone (ITCZ) over the Atlantic would be displaced northward during MAM, resulting negative rainfall anomalies to the south of 5°S. The March forecast (Fig. 1b) shows positive anomalies over northern Nordeste and eastern Amazon, and negative anomalies over eastern and southern Nordeste, and northwestern Amazon. Comparison of these figures with observed rainfall anomalies (Fig. 1c) shows that the March "forecast" (actually it uses March SST to predict MAM rainfall, becoming a mixture of hindcast and forecast) resembles more the observation than the January forecast.

The differences between January and March forecasts of MAM rainfall anomalies are attributed to contrasting SST conditions which dominated over the tropical oceans during those months (Fig. 2). From December to March the warm episode of the 1994/95 ENSO ended (cold anomalies developed over eastern equatorial Pacific), and the tropical Atlantic developed favorable conditions to above-the-average precipitation over Nordeste (the southern tropical Atlantic became warmer than the mean, and the northern tropical Atlantic remained near climatology). Figure 2 shows anomalous SST fields for January 1995, March 1995, and MAM 1995. It is apparent the differences between the SSTA fields for January (Fig2a), while the warm ENSO signal was still evident; March (Fig.2b), when cold anomalies already developed over eastern equatorial Pacific; and the mean MAM SSTA shown in Figure 2c.

The comparison between forecasted and observed values for other variables (figures not shown) revealed that the MAM forecast which used January 1995 SST conditions resembled ENSO-like atmospheric patterns, with anomalous convection displaced eastward over the equatorial Pacific. Whereas the forecast which used March SST anomalies presented large scale anomalous patterns of OLR and winds which resembled the observed patterns for the period.

Conclusions

The experimental seasonal rainfall forecast for the MAM 1995 Nordeste Brazil's rainy season using CPTEC/COLA AGCM suggested that atmospheric general circulation modeling is an useful tool for seasonal forecasting. However, such usefulness depends on long lead accurate tropical SST predictions. For December 1994/March 1995, persisting SST anomalies generated poor forecasts of SST. Consequently, MAM rainfall was poorly forecasted within two months lead time. Nevertheless, using March SST conditions generated encouraging seasonal rainfall hindcast/forecasts.

Present research activities in seasonal climate forecasting done at CPTEC include the use of forecasted SSTs over the equatorial Pacific and tropical Atlantic Oceans as boundary conditions. Also, efforts are being put onto developing statistical and dynamical models to forecast SST anomalies over the tropical Atlantic with three to six months leading time.

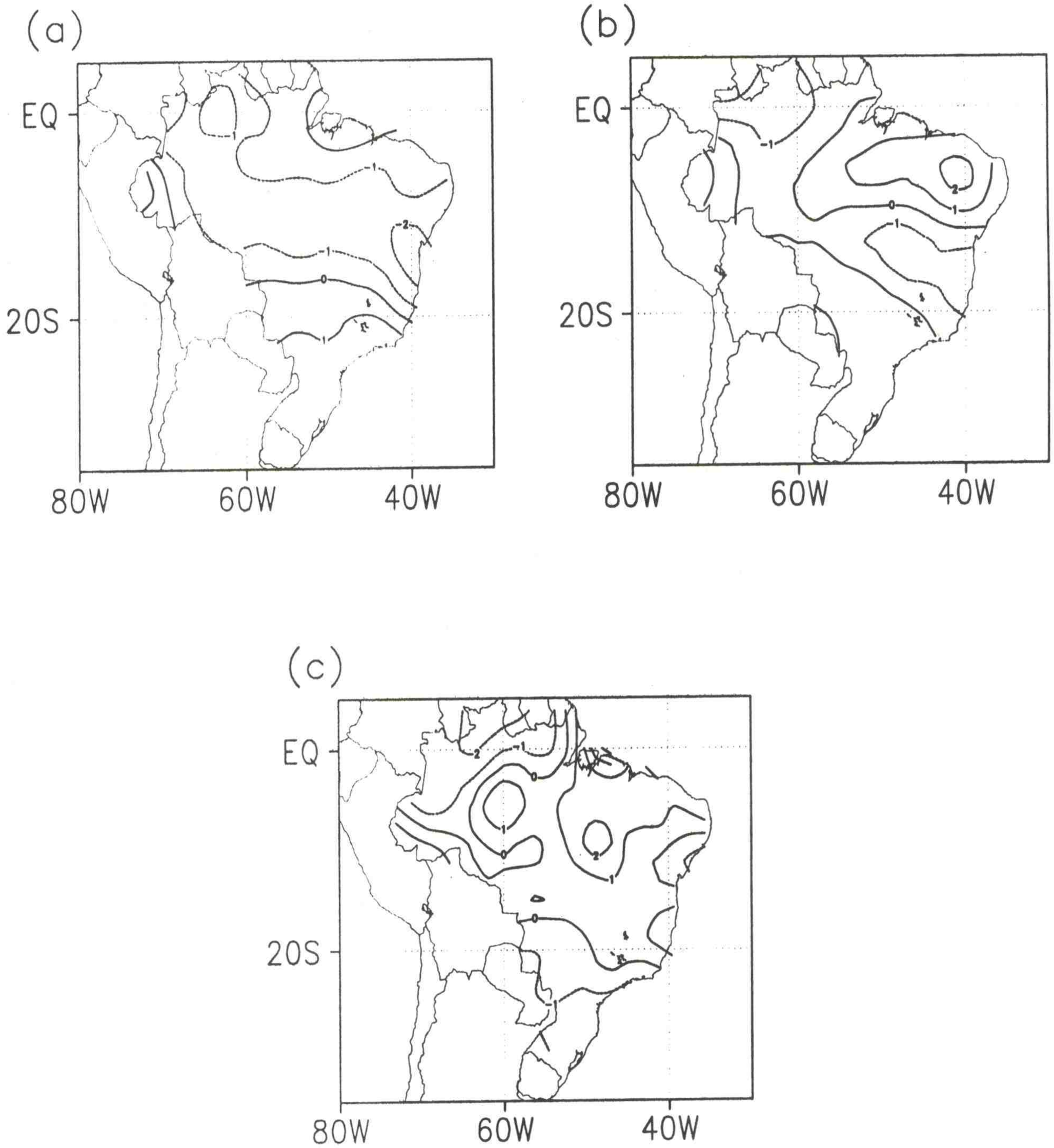

Figure 1 – MAM 1995 rainfall anomalies for (a) January 1995 SSTA forecast, (b) March 1995 SSTA forecast, and (c) observed raingage data. Negative contours are dashed, contour interval is 1 mm/day.

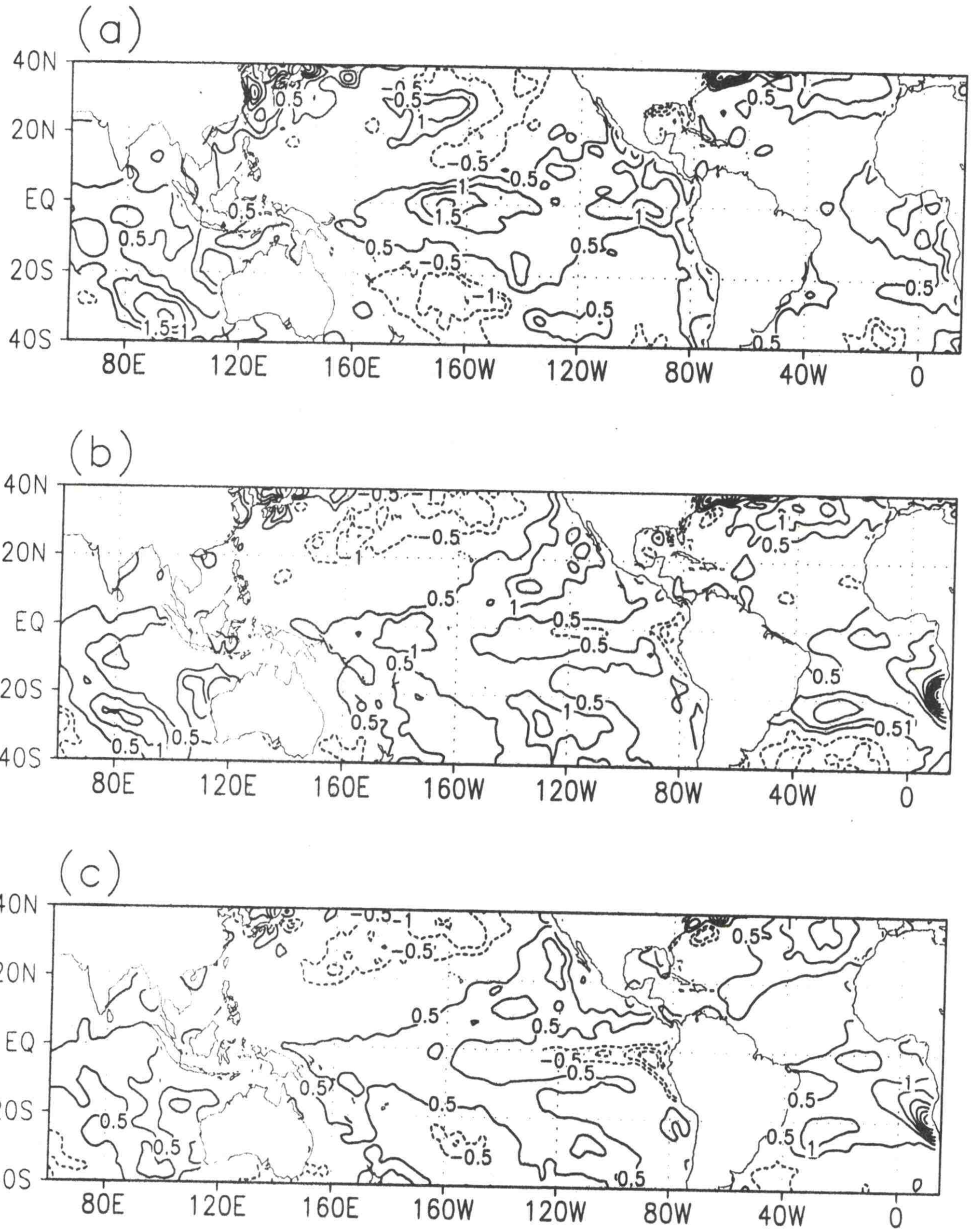

Figure 2 – Sea surface temperature anomalies for (a) January 1995, (b) March 1995, and (c) MAM 1995. Negative contours are dashed, contour interval is 0.5 C.

Seasonal Prediction of Canadian Surface Climate by Canonical Correlation Analysis

by

Amir Shabbar
Atmospheric Environment Service
Environment Canada

I. Introduction

A multivariate linear statistical technique (canonical correlation analysis) is used to explore relationships between low frequency variations in near-global sea surface temperature (SST), Northern Hemisphere 500 mb circulation and Canadian surface temperatures and precipitation. A lead interval of varying length is placed between a series of consecutive predictor periods and a single predictand period. Persistence is used as a control against which the skill of the model is assessed. Using similar technique, Barnston (1994) demonstrated usable skill in the U.S. surface climate. The purpose of this work is to assess the strength of the relationships between large scale circulation patterns and Canadian temperatures and precipitation and to provide skillful guidance for short-term climate forecasts for Canada with a lead time of several months.

II. Data

The data sets cover 35 years from 1955 to 1990 and include 1) quasi-global SST, 2) Northern Hemisphere 500-mb height, 3) Surface temperatures at 51 Canadian stations and 4) Precipitation at 69 Canadian stations. The SST and 500-mb height are used as predictor fields and the Canadian surface temperature and precipitation fields are used as predictands.

The earlier portion of the monthly mean SST data came from COADS, and from 1981 onwards blended ship/satellite data was used. The SST data (obtained from NOAA) covers a 10^{o} by 10^{o} square grid from 40^{o}S to 60^{o}N, some values in the southern oceans are missing however. The 500-mb height data consist of 455 grid point network of 5^{o} latitude by 10^{o} longitude in the Northern Hemisphere (15^{o}N to 80^{o}N). Mean monthly temperature and precipitation data were selected as predictands in this study.

III. Methodology and Data Processing

CCA is well suited to capture pattern-to-pattern relationships between large scale predictors and predictand. In the CCA technique, multi-component predictors are linearly related to multi-component predictands with the specific application of the empirical orthogonal function (EOF) analysis. Eigenanalysis is used to define the structure of the covariance between predictor and predictand with the constraint that the cross data set correlation explained with each successive mode is maximized. Since there are a large number of elements (235 for SST and 455 for 500-mb

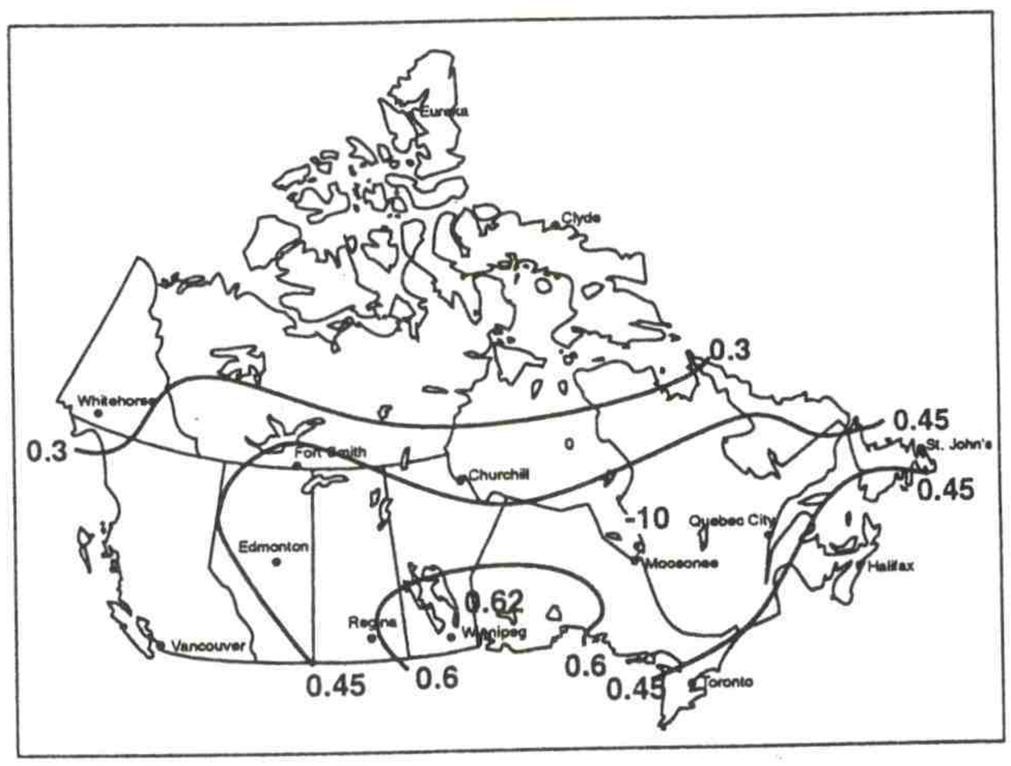

Figure 1. Geographical distribution of CCA skill in forecasting 3-month mean Canadian temperature at 3-month lead. Mean skill is 0.38.

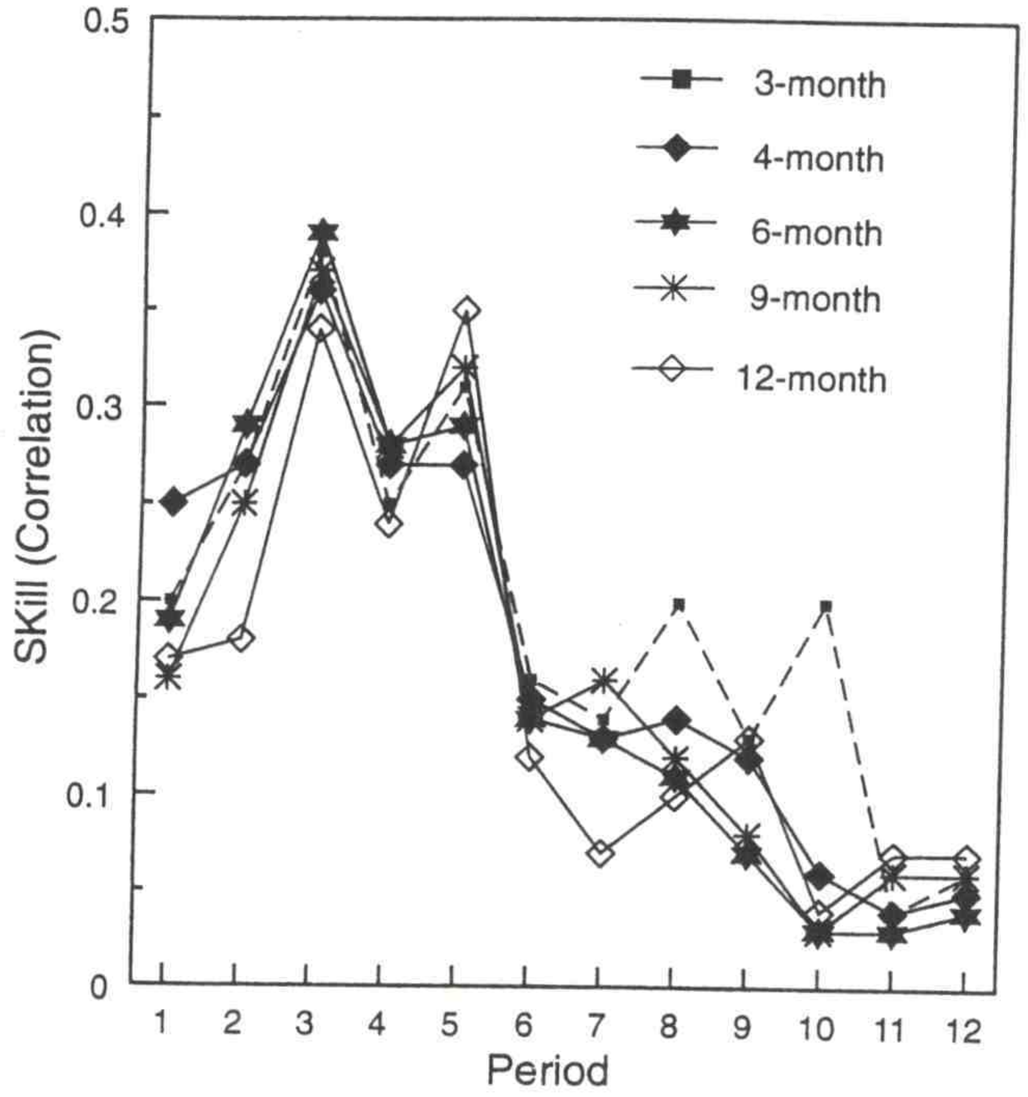

Figure 2. CCA forecast skill averaged over Canada for 3-month mean temperature. SST field is weighted double its natural value. Period 1 represents Jan-Mar period.

height), the data is pre-orthogonalized using the standard EOF analysis. Prior to the CCA analysis, each predictor and predictand data element is standardized so that all elements possess temporal stationarity and are weighted equally. The standardizations ensure that all locations have equal opportunity to participate in the predictive patterns regardless of their latitude and longitude variances. The final preprocessing step before the EOF analysis is interfield weighting. This adjusts the relative weights of two or more predictor fields relative to one another.

The predictor and predictand data sets are then orthogonalized with separate EOF analyses. For the preditor fields, four consecutive prior periods are chosen thus forming an extended EOF analysis. For the predictor data, the first six modes which usually accounts for about 45 percent of the variance, are retained. For the Canadian temperature and precipitation data, the first five modes are used for the CCA analysis. A correlation matrix between each predictor and all predictands is formed. This matrix is then used to obtain CCA eigenvectors and eigenvalues for predictors and predictands. Next, the eigenvectors and the original time series are used to compute an amplitude time series for each mode. This procedure is carried out separately for predictors and predictand. The lead time, or the number of seasons between the final predictor season and the predictand season, is varied from 3 to 12 months. For example, a forecast for Jan-Mar season with a lead time of three months would use all four three-month seasons (Jan-Mar, Apr-Jun, Jul-Sep and Oct-Dec) from the previous year.

IV. Forecast skill evaluation

A more realistic estimate of predictive skill and a minimization of artificial skill can be realized by using a cross-validation scheme. In cross-validation, forecast models are developed using only part of the available data set and then applied to the independent data kept in reserve for testing. Temporal correlation between the series of forecasts and observations is used as a forecast skill measure in this study. As a competitor to CCA forecast, the auto correlation of the Canadian temperature, i.e., persistence is computed.To verify persistence forecasts in a cross-validation framework, the persistence forecasts are formed using a different coefficient as a function of target year, based on the autocorrelation computed from non target years.

V. Results

Cross-validated skill is evaluated for each of the 12 three-month running mean seasons for the 51-station network of Canadian surface temperature. The geographical distribution of skill for Jan-Mar season is shown in Fig. 1. A correlation skill of 0.35 or higher is considered locally statistically significant. Field significance (Livezey and Chen 1983) was evaluated by randomly shuffling the forecast to obervation year correspondence 1000 times and counting the number of times the mean of the 'real' variance statistics over the 51 stations was exceeded by that of the random simulations. The resulting field significance is shown with the map in Fig. 1. A value of 0.05 or lower is considered significant.

Most of Canada south of latitude 60N, from the Rockies to the Newfoundland, exhibits usable skill. The correlation values are the highest over the southeastern prairies. Correlation between the CCA cross-validation forecasts and observations of Canadian temperatures averaged over 51 stations is shown in Fig. 2 for 12 seasons that are one month apart. The lead times between the predictand

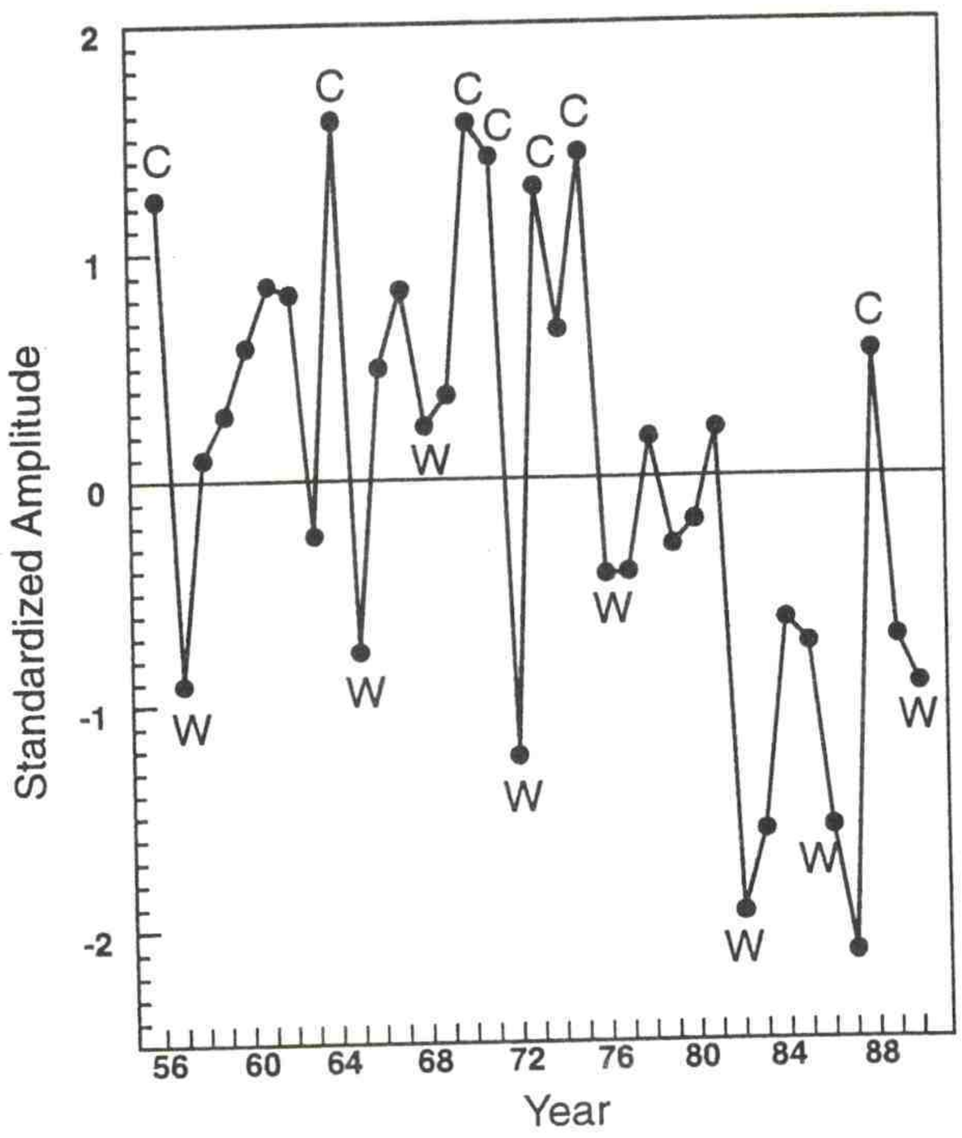

Figure 3. The canonical component predictor time series for mode 1 for the prediction of Jan-Mar Canadian surface temperature.

period and the predictor period range from three months to one year. Clearly, peaks in skill occur in winter and in early spring in Canadian surface temperatures. In this forecast, quasi-global SST is used as predictor. Verification of persistence forecast produces much poorer skill than those obtained by the CCA forecast (not shown). Examination of the canonical loading patterns of SST show that much of the winter predictive skill in Canadian surface temperatures is attributable to the El Nino-Southern Oscillation (ENSO) phenomenon in the tropical Pacific ocean.

The canonical component time series associated with the mode 1 predictor scenario, shown in Fig.3, confirms that ENSO is being described by this mode. The "W" and "C" symbols denote warm and cold ENSO years as identified by Ropelewski and Halpert (1989).

The CCA experiments were performed for 3 month mean precipitation using SST and 500 mb height as predictors. A denser network of surface stations (69 stations approximately equally spaced) was used. The doubly weighted SST was found to produce the best results which will be reported here.

Figure 4 presents the geographical distribution of skill for the Dec-Feb forecast for 3 month lead, with a mean skill score of 0.21 and a field significance of 0.000. Highest skill are found over southwestern Canada, north of Lake Superior, northwestern Arctic and areas surronding Hudson Bay. The Canonical loading patterns of each of the predictor fields (SST and 500-mb height) are examined both by field and time in order to understand the nature of their contribution to the skill.

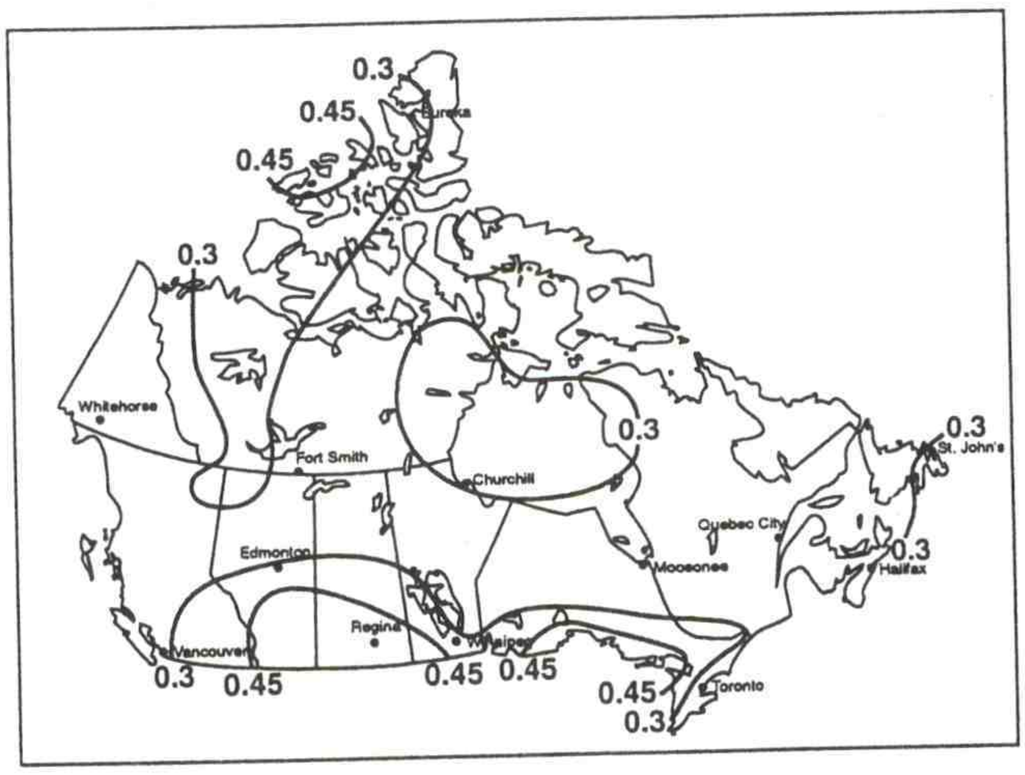

Figure 4. Geographical distribution of CCA skill in forecasting 3-month mean Canadian precipitation at 3-month lead for Dec-Feb. The expected national mean skill is 0.21 and a field significance of 0.000.

The canonical component time series associated with the mode 1 predictor scenario (not

shown) strongly suggests interdecadal trend in the SST field, particularly the cooling trend in the northern oceans where the loadings are high.

In summary, CCA can skillfully predict winter and spring temperature and precipitation with usable skill at a lead time of up to one year in Canada. Fluctuations in ENSO and the interdecadal trend in the SST (particularly cooling in the northern oceans) provide the best source of statistical predictability for the Canadian surface climate.

References

Barnston, A.G., 1994: Linear statistical short-term climate predictive skill in the Northern Hemisphere. *J. Climate*,1, **7**, 513-1564.

Livezey, R. E. and W. Y. Chen, 1983: Statistical field significance and its determination by Monte Carlo techniques. *Mon. Wea. Rev.*, **111**, 46-59.

Ropelewski, C. F. and M. S. Halpert, 1989: Precipitation patterns associated with the highindex phase of the Southern Oscillation. *J. Climate*, **2**, 268-284.

Long Lead Climate Prediction Using Screening Multiple Linear Regression

David A. Unger
National Center for Environmental Prediction
Climate Prediction Center
Washington, DC 20233

INTRODUCTION

Screening multiple linear regression (SMLR) has been tested for use on long lead time predictions of seasonal temperature and precipitation amount. SMLR can be useful to isolate climatic indicators important for seasonal prediction at specific regions and times of year, but is subject to problems associated with artificial predictability, such that real relationships are often obscured by those due to random data variability. Statistical techniques such as canonical correlation analysis (CCA) have been used for climate prediction (Barnston, 1994) and can help reduce the potential for artificial predictability. However, CCA can miss some important information that may not be clearly associated with the large scale predictor-predictand patterns that the technique uses to produce its predictions. This work focuses on the comparative skills of CCA and regression for seasonal forecasts. In order to assess the relative strengths of the two methods, only predictors used in the CCA procedure described in Barnston (1994) are offered to SMLR.

DATA AND PROCEDURES

Predictor data consist of Northern Hemisphere 700-mb heights, near global SSTs and station values of mean temperature and total precipitation amount for the 3-mo period prior to the forecast initial time. Forecasts for the mean temperature and total precipitation in a 3-mo target period were derived with data from 1955 through 1994. Lead times, defined as the time between the end of the predictor period and the start of the target period, of between one and 13 months were tested. Forecasts were produced from single station equations for 59 stations approximately evenly distributed throughout the United States.

All predictors and predictands were expressed as standardized anomalies relative to the developmental data. Precipitation amounts were transformed by taking their square roots prior to standardization to help normalize their distribution. The number of candidate predictors offered for screening was varied from 5 to 600 to test the sensitivity of SMLR to artificial predictability. These tests indicated that independent data skill was highest with about 25 predictors. Most predictors were carefully chosen from gridpoint values in regions of known importance for climate prediction. A few predictors were chosen by examination of data in the first 20 years of the sample, referred to here as the base period. Information from the most recent 20 years was never used for selection of candidate predictors. The SST and 700-mb height predictors were selected from gridpoint values mainly located over the North Pacific, off the west coast of the U. S., and in the western Atlantic. Tropical Pacific SSTs were also used, as well as 700-mb heights over North America.

Initial testing indicated that cross-validation could not be used to estimate predictive skill for SMLR (Unger, 1996) so a variation of a retroactive real time (RRT) validation technique was used instead. A forecast relationship was derived from the base period and applied to the next year's data to obtain independent data results. The case was then added to the developmental sample, and a new relationship was derived and applied to the following year's data. Independent data statistics were accumulated on a year by year basis in exactly the same way as in an operational forecast procedure, except retroactively. Forecasts were obtained for the base period years by application of RRT in reverse: deriving from the future years and applying to the most recent year in the withheld period (now the first half of the sample). Each earlier case

was included in the sample, the relationships rederived and applied to the next earlier case. This bi-directional RRT (BRRT) validation technique enables each available case to contribute to a skill estimate as independent data in a way similar to cross-validation except with a great reduction in the distortion due to redundant sampling (Unger, 1996).

A forward selection screening procedure was used for equation development. The first 5 terms were selected for each equation. Separate statistics were accumulated for each equation length, so that results for all the one, two, three, four and five term equations were calculated. The optimum equation length was then estimated by an objective learning procedure that used the past performance at each RRT trial to "predict" which equation would perform the best on the next. Verification statistics from this "best guess" forecast were also kept separately and were used for the skill estimates presented here.

Verification was based on the correlation coefficient, r, between forecast and observation on the 40 independent cases at each of the 59 stations. A nationwide average correlation coefficient, R, was computed from the root mean squared correlation coefficient at each station, with the signs retained in both the squaring process and the final square root. Field significance was measured by comparison of scores from actual target years against scores determined from 500 randomly shuffled target periods. Field significance expresses the percentage of time that the random forecast series outperformed the actual forecasts.

The skill estimation procedure has been carefully tested with prediction equations derived from random numbers with the same number of candidate predictors and the same sample size as used for the climate predictions presented here. There is a very small positive bias in the skill estimate by BRRT, with R=.06 for a series of random number forecasts rather than the expected R= 0. This small positive bias is balanced to some extent by an underestimate in skill due to over fitting on the samples used for some BRRT trials. The likelihood of a relationship developed from a small sample failing on subsequent independent data decreases with increasing sample size, especially when screening is employed, so that the skill from a relationship developed from the entire sample (available for operational application) is likely to be slightly higher than the estimate from BRRT trials, which have a smaller sample size, on average. The results for individual stations are less reliable than those from nationwide averages, since sampling errors become more prominent. Experiments with random numbers show that typically between three and four stations out of the 59 can be expected by chance to have $r > .3$ given a sample size of 40 cases and 25 candidate predictors.

RESULTS

The annual march of skill for CCA and SMLR-based temperature forecasts for a 1-mo lead time are shown in Figure 1. R is plotted against the final month of the target period so that the Jan-Mar season, for example, is plotted at 3. Fig. 1 shows that the most skillful SMLR forecasts occur more toward the spring than for CCA forecasts. Summertime SMLR skill is approximately the same as CCA's, with small differences due to the fact that the samples are not precisely matched. Most notably, the SMLR predictions do not show the strong skill minima that the CCA forecasts have in transition seasons. Regression forecasts for all months are field significant at better than the 5% level and most at less than .002.

Precipitation forecasts for a 1-mo lead (Fig. 2) show that, SMLR produces a slightly more skillful forecast for most of the year, except for early winter. However, skill levels are quite low and small differences in R when $R < .2$ are probably of little practical significance. Only about half of the monthly SMLR precipitation forecasts are field significant at the 5 percent level or better.

Figures 3 and 4 illustrate the spatial skill characteristics for temperature forecasts at 1 month lead for the Oct.-Dec. target period for SMLR and CCA, respectively. SMLR obtains its advantage over CCA from skillful predictions mostly in the southern half of the country. The predictor selected for this season at most

stations was the SST in the sub-tropical Atlantic Ocean east of Puerto Rico. North Pacific SSTs and the 700-mb height off Southern California were also important at several stations. The fact that the same predictors tended to be chosen at stations in the eastern and western U.S. suggests that they may be associated with a subsequent large scale weather pattern that influences the entire southern portion of the U.S. Note that CCA predictions show areas of some skill where SMLR shows little or none and vice-versa, illustrating that CCA and SMLR frequently complement each other in their regional skill distribution.

Figures 5 and 6 show the annual march of skill for temperature and precipitation forecasts, respectively, from SMLR for the 1, 4, 7, 10 and 13 month leads. Predictions for the 1-mo lead for both elements are clearly more skillful than at longer leads over most of the year for both elements. At longer leads SMLR shows comparatively little dependance on the projection, suggesting, perhaps, that the predictive skill at longer leads may be due to long term trends rather than on specific weather patterns associated with year to year variations in the predictors. For temperature at most longer leads, there is a maximum in winter skill, and a broad, slight maximum from summer through mid fall. The SMLR skill at leads of 7 months and greater is quite similar to CCA skill (not shown, see Barnston, 1994, Fig. 6) over most of the year except for the forecasts for the fall transition season, which are more skillfully predicted by SMLR at all projections.

Precipitation results (Fig. 6) show that there is little or no skill in precipitation forecasts at leads greater than 1-month except for a modest winter maximum for the 4-mo lead and a general tendency for some skill in the fall at most leads. Skill in the late spring and summer is disconcertingly close to the R=.06 found with random numbers, with random data variability producing negative R's for a few seasons and lead times. These results are quite similar to those from CCA (not shown, see Barnston, 1994, Fig. 27), although CCA shows some hint at winter skill beyond the 4 month lead.

One major difference between CCA and the regression procedure is that CCA uses data from a 12-month period prior to the initial forecast time, while only predictors for the three months prior to the initial time were offered to the SMLR. There is some evidence that three months may be too narrow a window on which to base the forecast for some lead times and seasons. The skills of the 4-month lead SMLR forecasts for temperature in the summer and early fall, and for precipitation in the fall, for example, are notably low relative to those at longer projections, indicating that there is information available from earlier periods that is not apparent in the most recent data.

CONCLUSION

SMLR has been investigated and found to be a useful tool for seasonal prediction of temperature and precipitation over the U.S. Temperature forecasts produced by SMLR are most skillful in the late winter and early spring. Precipitation forecasts show some skill in the early fall and late winter but little skill in other seasons. Skill for regression forecasts of seasonal temperature is comparable to that of CCA in the summer, and is higher in the transition seasons, especially in fall. CCA performs better than regression on most projections in early winter. Precipitation forecasts for regression appear to be slightly more skillful than CCA forecasts for most of the year for forecasts of 1-month lead time when averaged over the entire U.S.

REFERENCES

Barnston, A. G., 1994: Linear statistical short-term climate predictive skill in the northern hemisphere. *J. Climate*, 10, 1513-1564.

Unger, D. A., 1996: Skill assessment strategies for screening regression predictions based on a small sample size. *Preprints, Thirteenth Conference on Probability and Statistics in the Atmospheric Sciences*. San Francisco, CA., February 21-23, 1996 (in press).

Figure 1. Annual skill of regression and CCA temperature forecasts. The correlation between forecast and observations at 59 U.S stations for a 1-mo lead time is shown.

Figure 2. Same as Fig. 1 except for precipitation forecasts.

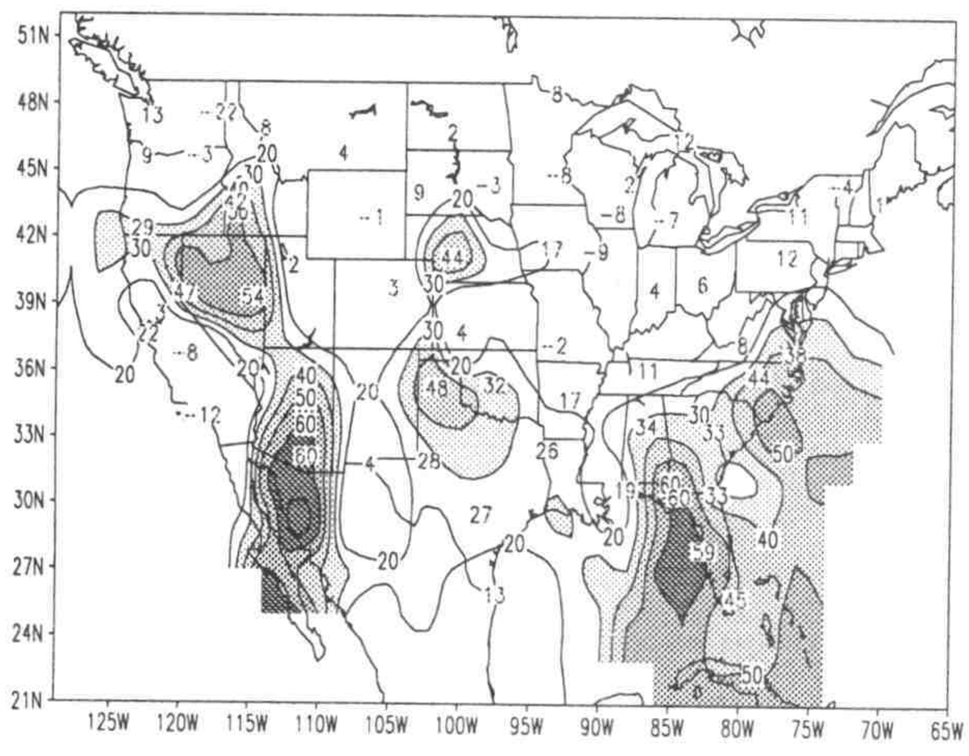

Figure 3. Geographical distribution of regression forecast skill for a 1-mo lead temperature forecast for October-December. The forecast-observation correlation for each station is indicated by the plotted numbers.

Figure 4. Same as Fig. 3 except for CCA forecasts. (Barnston, 1994)

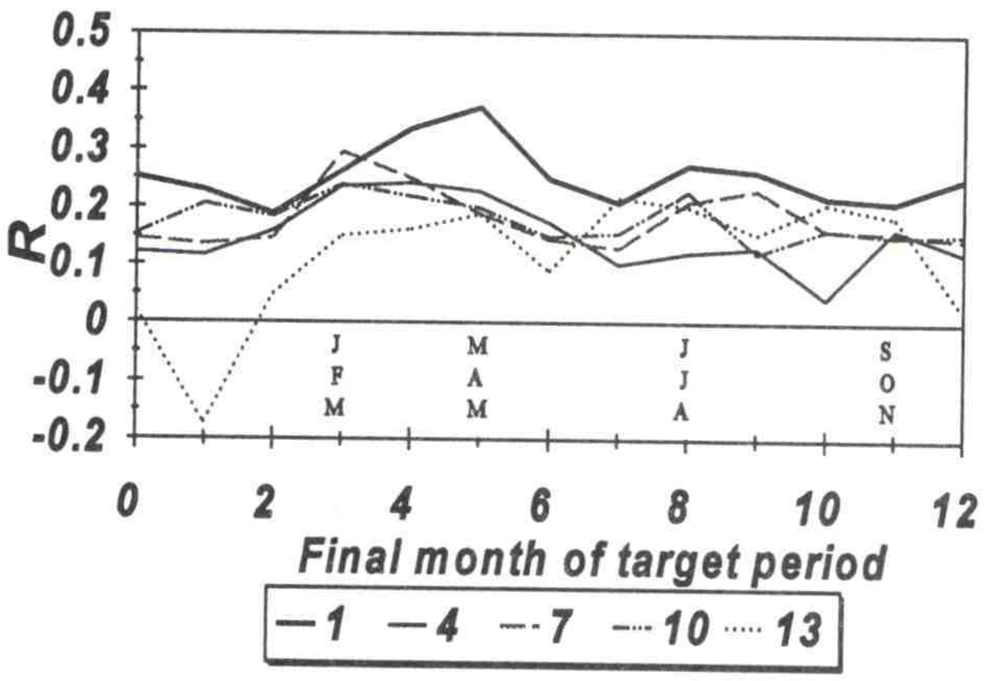

Figure 5. Same as Fig. 1 except for regression forecasts at 1, 4, 7, 10 and 13 month leads.

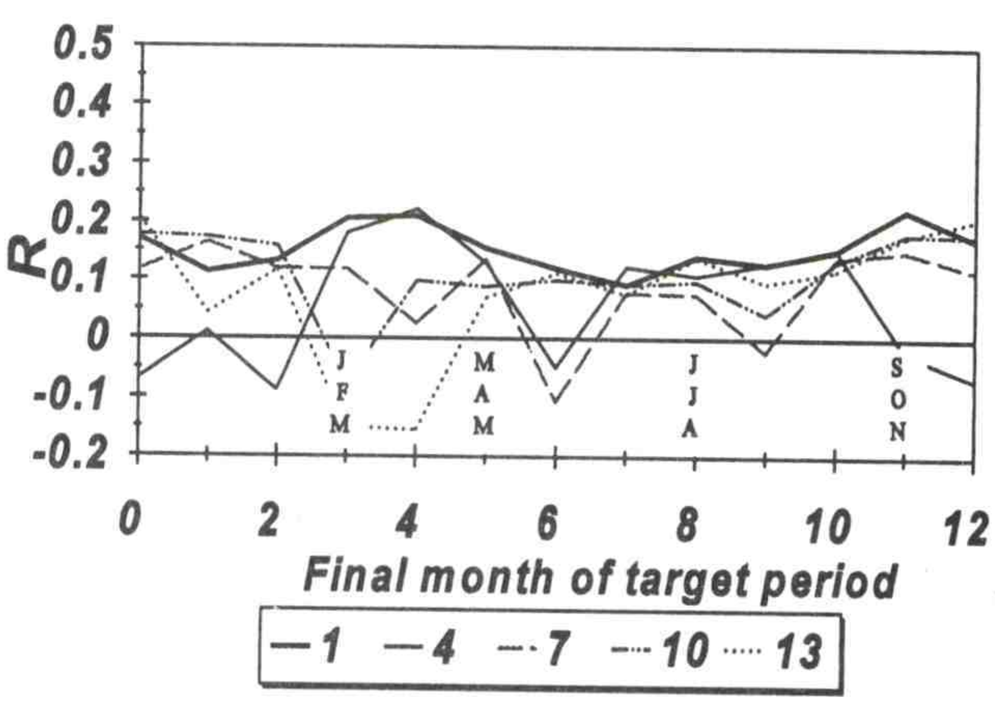

Figure 6. Same as Fig. 1 except for regression forecasts for precipitation at 1, 4, 7, 10, and 13-mo leads.

Potential for Long-Lead Prediction of Seasonal Precipitation over the Pacific Islands Using the NCEP CCA Model

Yuxiang He and Anthony G. Barnston

NOAA/National Centers for Environmental Prediction/Climate Prediction Center
Washington, DC 20233

The statistical short-term climate predictive skills and their sources for seasonal total precipitation in the tropical Pacific islands has been estimated at lead times of up to 13 months using CCA in a cross-validation verification design. The predictor fields, in order of their predictive value, are quasi-global sea surface temperature, Northern Hemisphere 700 mb height, and prior values of the predictand precipitation itself. Four consecutive 3-month predictor periods are used to detect evolving as well as steady-state conditions. Figures 1 and 2 show the correlation skill in the northern and southern tropical Pacific, respectively, as a function of target season and lead time. Figure 3 shows the geographical distribution of the correlation skill for Jan-Feb-Mar forecasts made at 1 month lead, and Fig. 4 does likewise for Jun-Jul-Aug forecasts made at 1, 4 and 7 month lead times. Figure 5 provides a practical illustration of the skill.

Forecasts at 1 month lead time (defined as the time skipped between the end of the final predictor period and the beginning of the target period) have usable skill (Figs. 1, 2) that is generally higher than persistence skill (not shown), with expected correlations of 0.5 or more in late northern winter at some of the stations mainly north of the equator (Fig 3). Expected skill declines moderately quickly as lead time increases (especially in the northern Tropics; Fig. 1), with modest but still usable (>0.3) skill at some stations at 4 months lead. At lead times of 1 year, only a few stations retain usable skill. At such long lead times northern summer is the most skillfully predicted season (Figs. 1, 2, 4).

From the CCA predictor and predictand loading patterns (not shown), the climate variability across the tropical Pacific is seen to be governed largely but not entirely by the ENSO cycle. During the northern winter of mature warm (cold) SO events, there is a strong tendency toward negative (positive) precipitation anomalies across the northern tier of islands from Hawaii to the western Pacific, as well as at near-equatorial stations in the western Pacific and the southern tier of stations. Conversely, positive (negative) anomalies tend to occur near and slightly south of the equator in the central and eastern Pacific, in a band whose north-south width increases eastward. This is completely consistent with the description of ENSO-related precipitation effects given in Ropelewski and Halpert (1987). For forecasts for northern summer a somewhat lower frequency signal appears as the leading CCA mode. This mode describes SO episodes having at least one full year's duration, combined with a worldwide roughly tropical versus extratropical year-long SST anomaly dipole. The northern summer precipitation response is similar to that of the northern winter ENSO response except that the central and eastern basin equatorial response (wet with warm local SST) extends farther to the north and south of the equator and also extends completely across the western basin in the vicinity of the equator. This response is also found for the ENSO mode itself in summer, indicating that it is a seasonal modulation expected for both modes rather than a difference between the two modes.

In forecasting tropical Pacific island precipitation using the predictors described above, CCA implicitly recognizes the ENSO state. Thus, CCA forecasts of ENSO-related tropical Pacific SST likely could also be made using the same predictors. In fact, CCA *is* used to forecast tropical Pacific SST operationally in the Climate Prediction Center (CPC) of the National Centers for Environmental Prediction (NCEP), using the global sea level pressure, tropical Pacific SST and thermocline depth as predictor fields. The capability to forecast ENSO episodes and their tropical Pacific land climate impacts at a usable level of skill encourages commencement of operational forecasting for this region, which could begin during 1996. In addition to maps of the anomaly forecasts and their cross-validated skill estimates, an individual station histogram format for the forecasts and expected skills for the eight U.S.-affiliated stations is proposed.

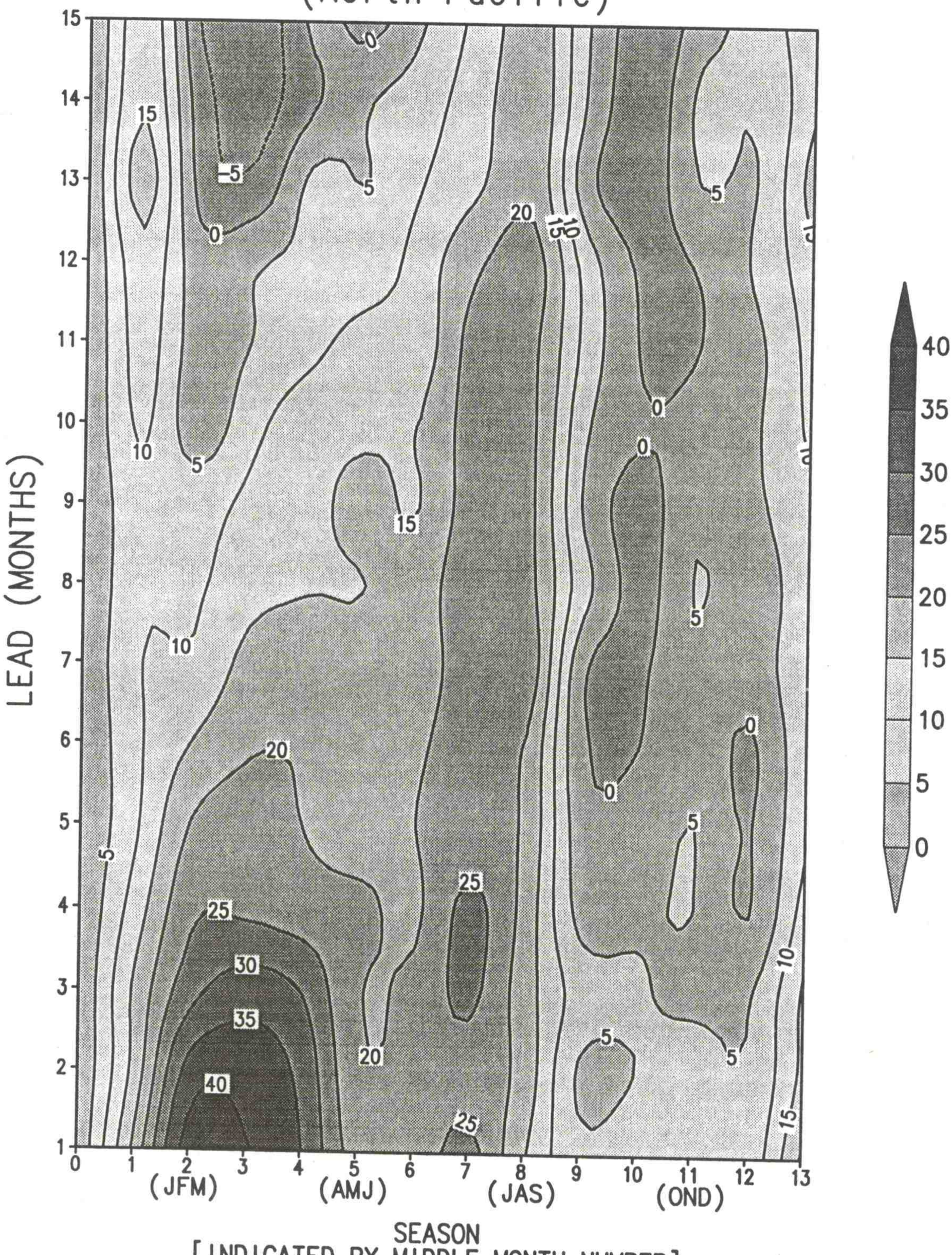

Fig. 1. Lead time-target season cross section of CCA forecast skill for northern tropical Pacific precipitation (correlation X100) using double-weighted SST predictors. The horizontal axis denotes the target season (*not* the forecast start time), and the vertical axis the lead time in months, where 0 is defined as a forecast whose target period begins at the time of the forecast.

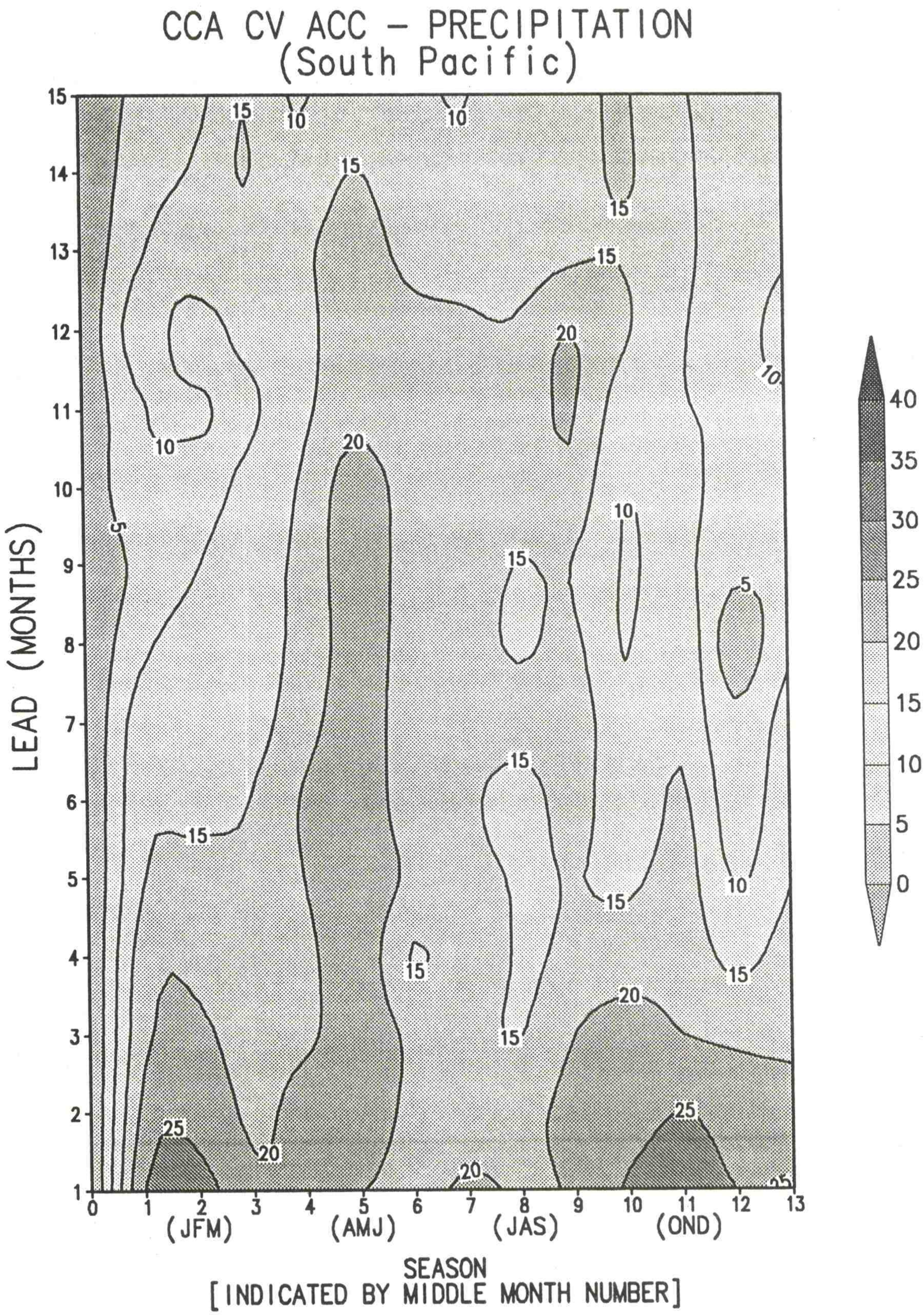

Fig. 2: As in Fig. 1 except for the southern tropical Pacific.

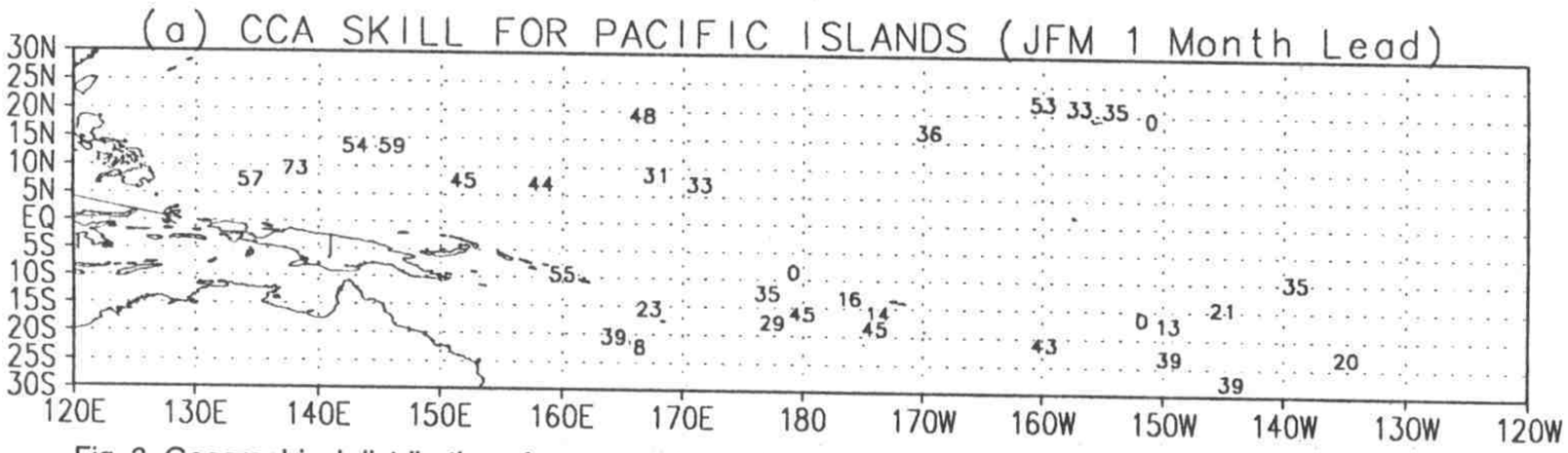

Fig. 3. Geographical distribution of cross-validated CCA skill (correlation X100) in forecasting 3-month precipitation for Jan-Feb-Mar for 33 stations at a lead time of 1 month. Correlations <0 are denoted by 0.

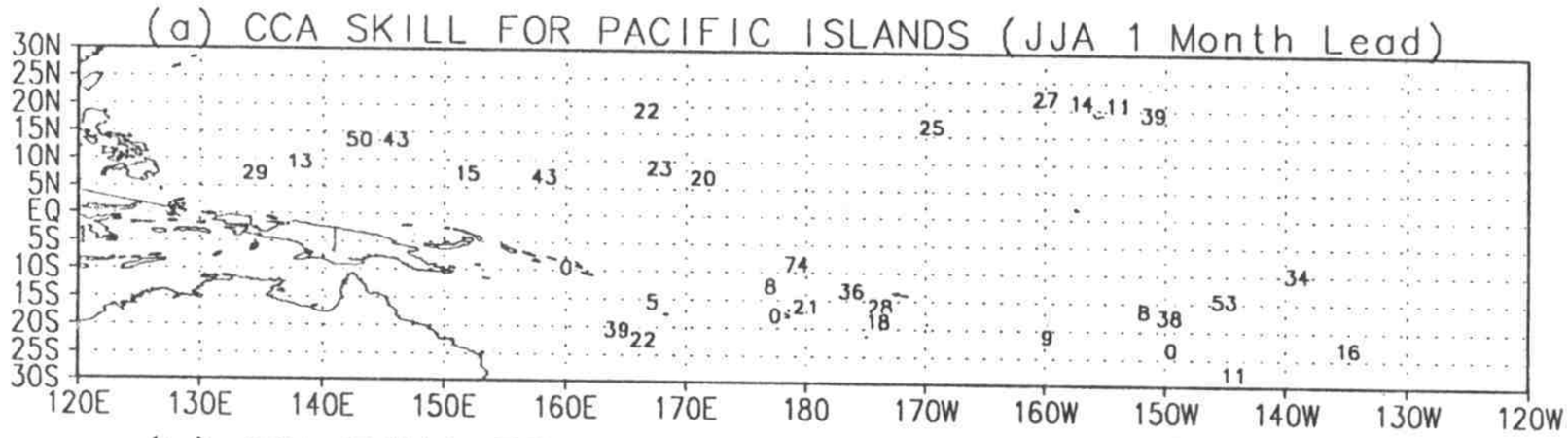

Fig. 4: As in Fig. 3 except for Jun-Jul-Aug at lead times of (a) 1 month, (b) 4 months and (c) 7 months.

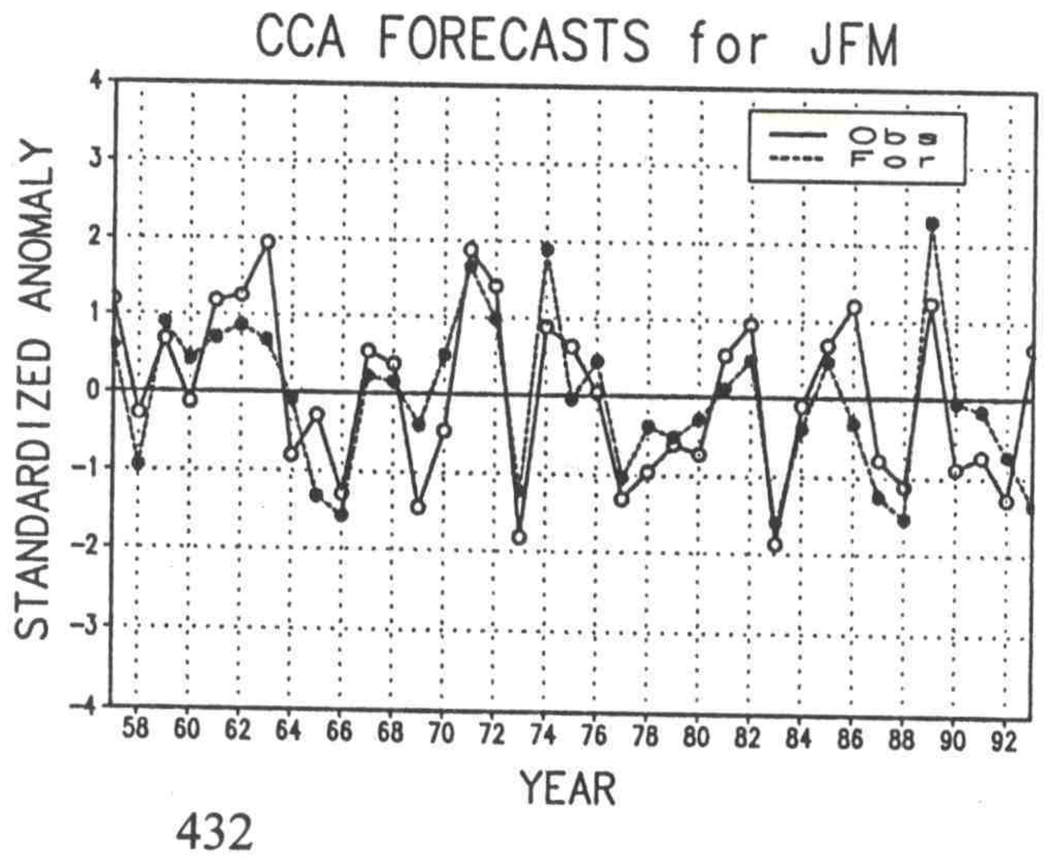

Fig. 5. Yearly time series of forecasts and observations for Yap Island in the northwestern tropical Pacific (9°N, 138° E) Jan-Feb-Mar standardized precipitation anomaly. Forecasts made at 1 month lead (i.e., at end of November; dashed line) and observations (solid line) are shown; correlation is 073. Forecasts are inflated to make their variance equal to that of the observations.

Verification of Seasonal 'Forecasts' from Ensemble GCM Integrations

Jeffrey L. Anderson
Geophysical Fluid Dynamics Laboratory / Princeton University

1. Introduction

The Binned Probability Ensemble (BPE) technique is an extremely simple method for producing a probabilistic forecast from an ensemble of forecast model integrations. The ensemble forecasts are used to partition the real line into a number of bins, each of which can be assumed to have an equal probability of containing the 'true' forecast. The method does not discard any information from the ensemble, and thereby allows users to tailor their own applications in an optimal fashion. The method for producing probabilistic forecasts was successfully tested with perfect model experiments in both a simple initial value problem using the Lorenz convective model, and in a boundary forced problem using an ensemble of AMIP integrations. The method has also been applied at operational centers including the United Kingdom Meteorological Office, the European Centre for Medium-Range Forecasting, and the National Center for Environmental Prediction where it is referred to as Talagrand diagrams.

2. Binned probability ensemble forecasts

Let X be a random variable and let the set x_i, (i = 0, ..., n-1) be samples of this random variable. The x_i can be sorted by value and there is a 1/n chance that sample x_0 is the smallest, a 1/n chance that it is the second smallest, etc. The remaining n-1 samples x_i (i = 1, ..., n-1) partition the real line into n intervals, called bins hereafter. It follows that the probability that the sample x_0 falls into any given bin is 1/n.

As a simple example, suppose a 3 member ensemble forecast is made using an atmospheric forecast model. Three possible initial conditions for the ensemble are selected by randomly sampling from the initial condition distribution and each is then integrated with the numerical model. Suppose that the forecast values of temperature at a given model grid point are 22, 23, and 26. Then, the probability that the true temperature is less than 22 is 1/4, the probability that it is between 22 and 23 is 1/4, the probability that it is between 23 and 26 is 1/4, and the probability that it is greater than 26 is also 1/4.

Model validation can be performed using BPE forecasts. Given an m-sample set of (n-1)-member perfect model ensemble forecasts and the corresponding verifications, the m samples of the bin number containing the true state should be uniformly distributed in the n bins. Since the BPE method is non-parametric, this result does not depend on any of the details of the probability distribution of the forecasts or the initial conditions, so a large set of ensemble forecasts can be grouped for validation without difficulty. The traditional chi-square test can be directly applied to

the BPE results for a set of ensemble forecasts to see how likely it is that the bin distribution is uniform. A small value of chi-square significance means that the distribution of observations in the bins is significantly different from uniform implying that the ensemble forecast is not consistent with the verifications.

In cases where the distribution of the observations in the bins is not uniform, an examination of the frequency with which the observation falls into each of the bins can help to analyze the structure of the model systematic error distribution. This is related to the traditional examination of model bias, however, in this case the chi-square test gives an a priori assessment of the significance of the model systematic error. Bias (in terms of the median, not the mean) in the forecasts can be seen if many of the verifications fall well to one side of the middle bin. Problems with variance of the forecast distributions can be seen if the verifications are clustered in a few neighboring bins, or if many of the verifications are located in bins far away from the center. It is important to recall that the chi-square test is measuring the statistical significance of the difference between the distributions, not the strength of the difference. Given ensembles with many members and a sufficiently large sample of ensemble forecasts, problems with even higher order moments of the forecast distribution can be diagnosed.

3. AMIP Ensemble Integration

The BPE technique is applied to an ensemble of integrations in an atmospheric general circulation model (GCM) that is forced by observed sea surface temperatures (SSTs). The atmospheric model is an 18 level spectral model truncated at T42. The prescribed SSTs are those used for the Atmospheric Model Intercomparison Project (AMIP). An eight member ensemble was integrated for 10 years from 1 January 1979 through 31 December 1988. The initial conditions for the ensembles were taken from analyses for 12 December 1978 through 21 January 1979, sampled every five days. Each of these analyses was then used as an initial condition as if it were the analysis for 1 January 1979. The first 14 months of the ensemble integrations were discarded in an attempt to eliminate direct effects of the initial conditions. The remainder of the integrations were divided into 35 three-month seasonal means extending from MAM (March, April, May) 1980 through SON (September, October, November) of 1988 giving a total of 8 years for the DJF (December, January, February) season and 9 years for all others. An ensemble mean climatology was computed for each of the four seasons, and removed from the individual seasonal fields to produce seasonal mean model anomaly fields. Three model fields, 200 hPa height, 850 hPa temperature, and precipitation are compared to observations here. Validation was done by interpolating data from the model Gaussian grid to the data grid and then performing binning at each data grid point. For all of the observed data fields, seasonal mean climatologies were generated and removed from the individual seasonal means to produce seasonal anomaly fields.

Fig. 1 shows the chi-square significance for the 850 hPa temperatures for MAM. This experiment has 9 bins (since there are 8 ensemble members) and, purely by coincidence, 9 samples (determined by the number of available seasons for which the AMIP integrations are available). Fig. 1 shows that the bias corrected ensemble forecasts are significantly different from the observations over large areas of the globe, particularly over Antarctica, Africa, much of the tropical oceans, and over the Himalayas and southeast Asia. In all other regions, the 8 samples are too

few to resolve differences between the ensemble forecasts and the observations.

An examination of some of the individual grid point binning results for the 850 hPa temperature case can help to analyze the nature of the model's systematic errors as well as revealing why the binning validation and rms results are not always in good agreement (Fig. 2). In almost all areas where Fig. 1 shows a significant difference between the ensemble forecasts and observations, an examination of the bins reveals that the outermost bins are heavily populated while the innermost bins are almost empty. In many cases, for instance for points over Africa and northern South America, almost all of the observations fall in one of the outermost bins, indicating that the observation is colder/warmer than the coldest/warmest forecast. This indicates that the ensemble forecasts do not have enough variability compared to the observations. In other words, the variability of the model ensemble response is not as large as would result if a perfect model were run for the same SST forcings.

The BPE results for the 200 hPa geopotential height field are generally not significantly different from the observations in the extra-tropics, but in the tropics, especially over the oceans, there are a number of areas where the forecasts are significantly different. The individual bins in these significant areas show the same behavior as for the 850 hPa temperatures; the outer bins are heavily populated by the observations.

Unlike the upper air forecasts, the precipitation ensemble forecasts have too little variability in some regions where the forecasts are inconsistent with the observations. In many areas, for instance over North America, the observations are clustered into just a few of the interior bins.

The BPE technique is a powerful tool for evaluating the consistency of ensemble forecasts and verifications. In conjunction with other traditional tools for forecast verification use of the BPE can lead to an increased understanding of the abilities and deficiencies of ensemble forecasts.

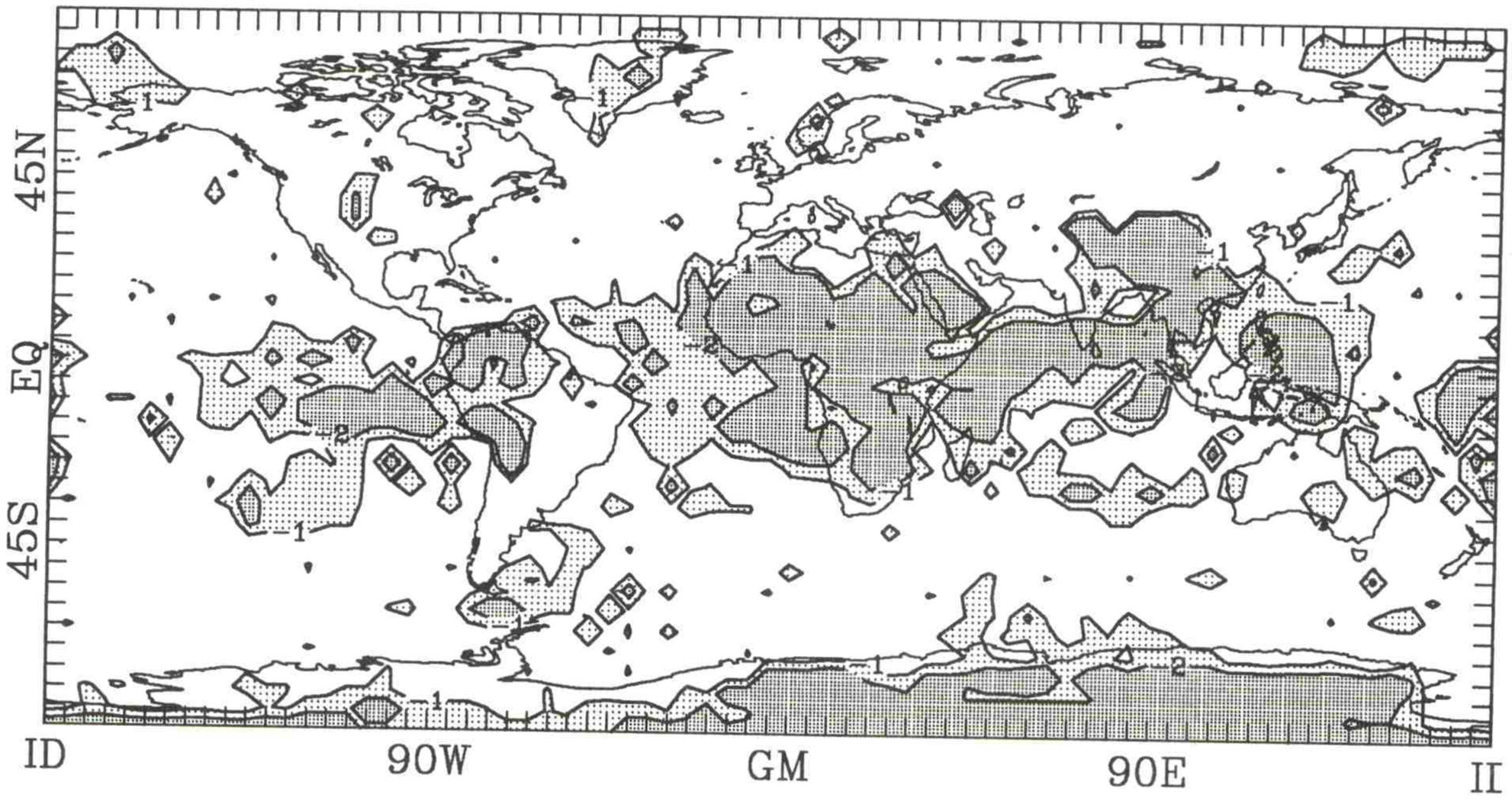

Figure 1: Significance of chi-square tests for BPE validation of 8 member AMIP ensemble 'forecasts' of 850 hPa temperature for MAM. Light (dark) stippled regions have greater than 90% (99%) significance that the ensemble forecasts are inconsistent with the observations.

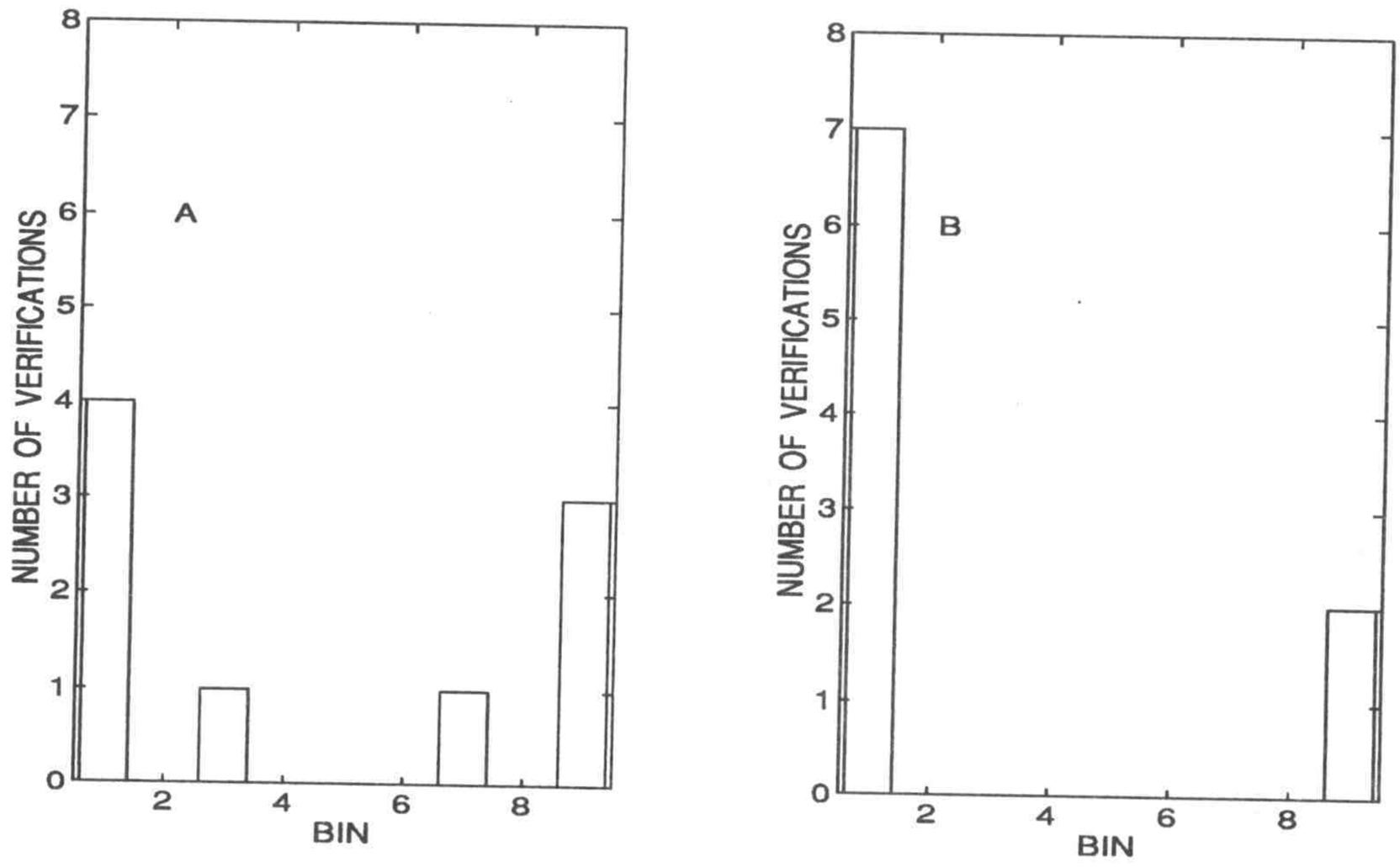

Figure 2: Distribution of observations in bins for MAM 850 hPa temperature for grid point over Africa (A) and over northern South America (B).

PNA-Region Teleconnections to Tropical-Pacific SST Anomalies in Observations and the NCEP Climate Model

R. E. LIVEZEY, M. MASUTANI, M. JI, AND A. LEETMAA

NCEP/NWS/NOAA

We have extensively examined monthly-mean teleconnections over the PNA region to substantial SST anomalies along the equator just east of the dateline in both observational data and an ensemble of 45-year GCM runs (45Y experiment) driven by analyzed SST. This work was motivated by pronounced ensemble responses throughout the calendar year in a 20-year GCM run (J92 experiment), to anomalous SSTs that were fixed to their values in January 1992 (a major ENSO warm event). Tropical convection in our key region (150-180W, 5N-5S) is particularly sensitive to large departures from normal SST. The J92 experiment provides *a priori* predictions of the outcomes of compositing the observations according to the sign and magnitude of SST anomalies there.

Specifically, monthly-mean Northern Hemisphere extratropical 700 hPa heights and U.S. surface temperature and precipitation data have been composited month by month separately for positive and negative key area average SST anomalies that are at least 0.8°C in magnitude. Composite membership is also constrained to not exceed 10 cases. Monthly-mean composites over two- and three-month windows were also constructed with a membership criterion of 1.0°C and no limit on membership to sharpen signals in the single-month window composites that were consistent from month to month. Likewise composites were formed for comparison from arbitrary classification of seven years and five years as major warm and cold ENSO-event years respectively.

Statistical significances of composite signatures were established in a variety of ways: (1) *A priori* predictions of many aspects of composite outcomes from the J92 experiment, (2) signal consistency from month to month (because each month's analysis is sufficiently statistically independent from those for adjacent months), (3) exhaustive local and field significance tests for every composite, and (4) corroboration of features of borderline significance on single-month window composites by similar features of high significance on multiple-month window or ENSO-episode composites. In addition, the per cent of variance of individual members explained by a composite average map was computed for every composite.

Corresponding single-window composites for the 45Y experiment made up of the same cases as the observational composites were also formed and field significance and explained variance calculations performed. Additionally, a Murphy/Epstein skill analysis was performed on every pair of corresponding observed and 45Y experiment composites.

Our intent in this work was to identify and describe to the extent possible tropical equatorial SST signals in our three extratropical data sets. The approach we have taken, use of monthly means and separate composites for positive and negative SST anomalies, was designed to not preclude the discovery of important

nonlinearity or seasonality of these signals. Many previously undocumented examples of both for which a strong case can be made have been identified. The analyses involving multiple-month windows were additionally useful in emphasizing those signals that change little month to month. The 45Y experiment results provided additional support for many aspects of the observed composites, as well as provided evidence of model systematic errors which should be correctable in forecast applications. Because of space limitations only partial sequences of 700 hPa height composites are shown here. Full journal documentation of the entire set of results is currently in preparation.

Fig. 1 is a presentation of the full sequence of monthly mean 700 hPa height anomaly composites for positive SST anomalies, while Fig. 2 contrasts October through March sequences for observed and 45Y experiment composites for negative SST anomalies. Turning now to the composite maps themselves, the warm-SST anomaly sequence in Fig. 1 begins (as expected from previous work) with a clear signature that is notably consistent from January to March. From April through October the composites show a consistent repositioning of the main anticyclonic anomaly over the extratropical PNA region first to the west and then northwest into July and then southeast into October. This scenario was predicted by the J92 experiment but with a delayed start, is reproduced in the 45Y experiment, and receives considerable corroboration form ENSO-episode and multiple-month window composites. The weakest part of the sequence occurs for November and December, but for at least the latter a case can be made through other composites and the model runs for a tendency for reestablishment of the January through March signature. Overall, with both the theoretical support of the model experiments and the empirical evidence presented here there is a substantial case for the existence of a high-latitude, Pacific basin teleconnection to central equatorial Pacific positive-SST anomalies in eleven months of the year.

In contrast to the positive-SST anomaly sequence, the window of the annual cycle with clear negative-SST anomaly teleconnections at 700 hPa is considerably narrower, specifically from October through March (with an echo into April) . These teleconnections (Fig. 2) are particularly interesting from two more standpoints. First, the negative-SST anomaly teleconnections mirror their positive-SST anomaly counterparts in only a very few respects; the SST-anomaly signals are *not linear*! Second, there appear to be three distinct patterns for October to December, January and February, and March respectively with only part of the patterns sharing common characteristics in the December to January and February to March transitions. On the other hand the extent of the common features shared by the October and December composites, which are not field significant in the PNA region, with the November composite which is highly significant, lend considerable support to the signal content in all three maps. The same is true for January (not field significant) and February (highly significant). Note that the 45Y run composites clearly hint at the observed patterns in November and December with a downstream phase error, and a clear shift of patterns for January and February but with much larger phase errors.

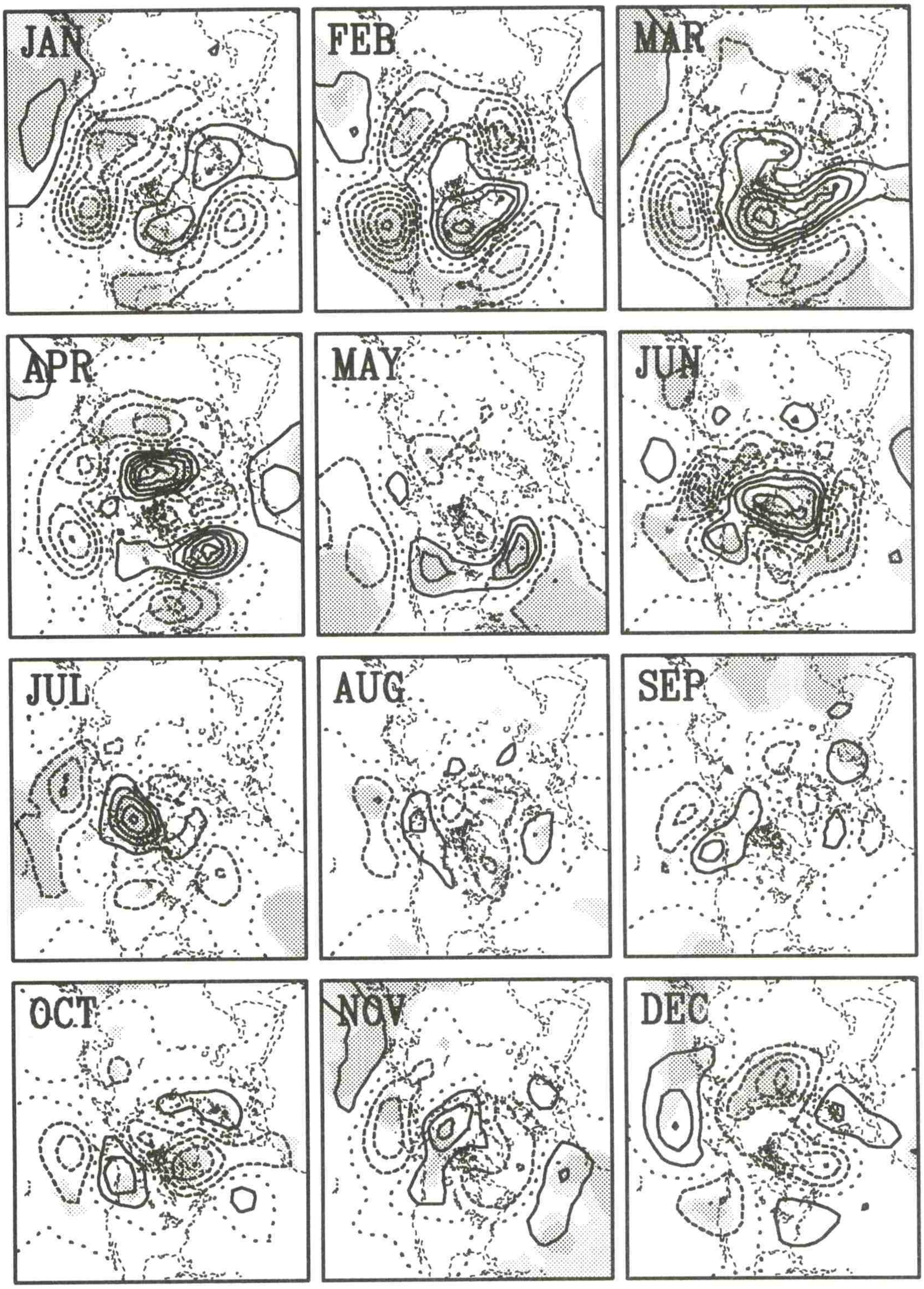

Figure 1. Positive equatorial Pacific SST-anomaly composites of monthly mean 700 hPa height anomalies. Contour interval is 10 meters, solid and dotted lines are positive and zero anomalies respectively. Darkest shading is 5% local significance.

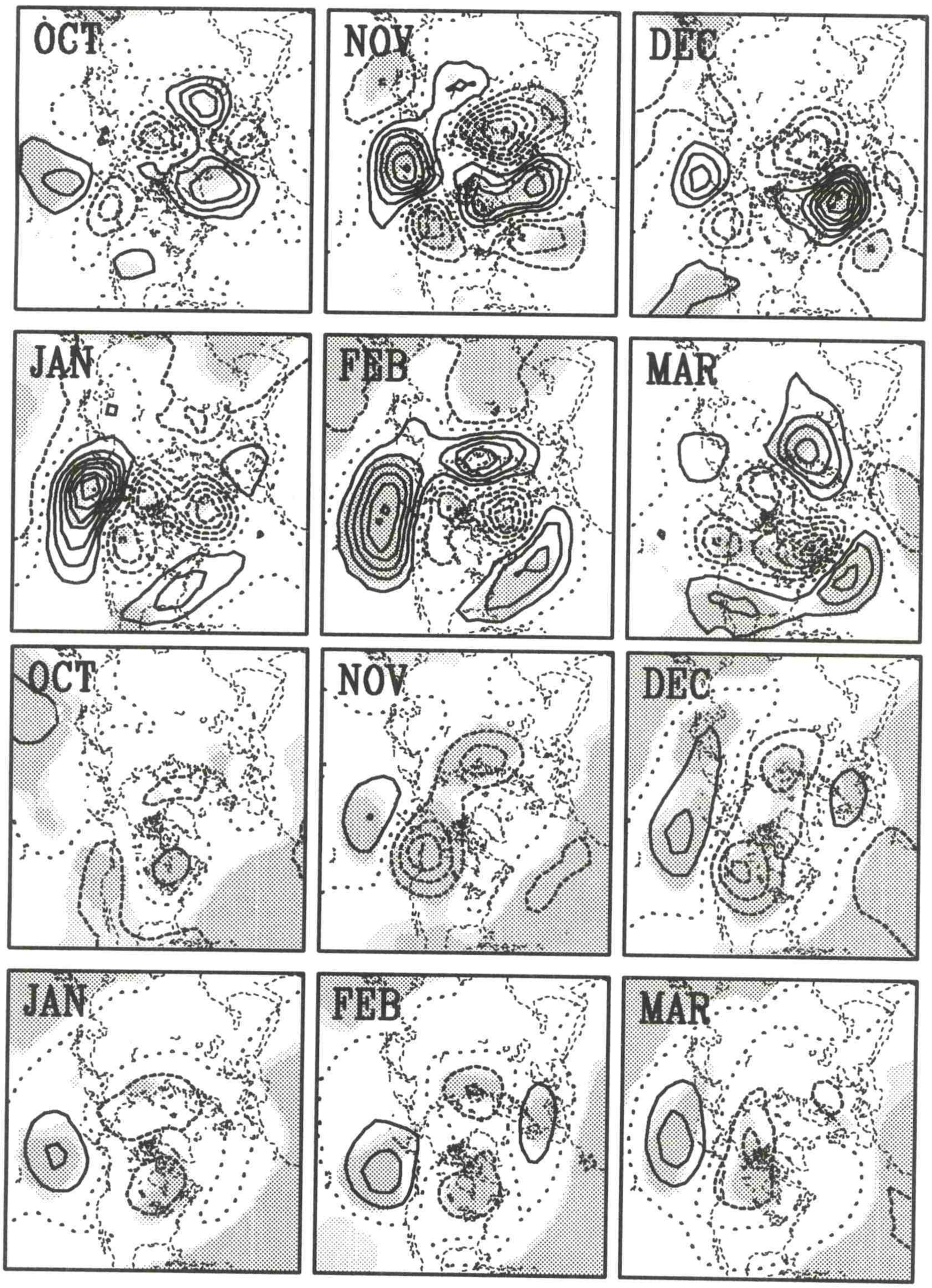

Figure 2. Same as Fig. 1 except for negative SST anomalies. Top are observational composites, bottom model.

*U.S. GOVERNMENT PRINTING OFFICE:1996-404-447/45401